Transactions of the ASME

Journal of Heat Transfer

Published Quarterly by The American Society of Mechanical Engineers

VOLUME 109 • NUMBER 2 • MAY 1987

Transactions of the ASME, Journal of Heat Transfer (ISSN 0022-1481) is published quarterly (Feb., May, Aug., Nov.) for $150 per year by The American Society of Mechanical Engineers, 345 East 47th Street, New York, NY 10017. Second class postage paid at New York, NY and additional mailing offices. POSTMASTER: Send address changes to The Journal of Heat Transfer, c/o THE AMERICAN SOCIETY OF MECHANICAL ENGINEERS, 22 Law Drive, Box 2300, Fairfield, NJ 07007-2300.

CHANGES OF ADDRESS must be received at Society headquarters seven weeks before they are to be effective. Please send old label and new address.

PRICES: To members, $24.00, annually; to nonmembers, $150.00. Add $6.00 for postage to countries outside the United States and Canada.

INDEXED by Engineering Information

ANNOUNCEMENTS

TECHNICAL PAPERS

(Contents continued)

TECHNICAL NOTES

Green's Function Partitioning Procedure Applied to Foil Heat Flux Gages

J. V. Beck
Professor,
Heat Transfer Group,
Department of Mechanical Engineering,
Michigan State University,
East Lansing, MI 48824
Mem. ASME

N. R. Keltner
Supervisor,
Sandia National Laboratories,
Albuquerque, NM 87185
Mem. ASME

This paper presents a new procedure for using Green's functions for transient heat conduction problems. It is developed as part of continuing research on the unsteady surface element (USE) method; the USE method provides a means for combining solutions for two or more different basic geometries. By combining such geometries, problems involving composite media can be solved including problems associated with foil heat flux gages. The new method involves partitioning Green's function solutions over different time domains for each of which only a few terms are needed to describe the Green's functions. The method is illustrated for the two-dimensional problem of a circular foil of finite thickness that is uniformly heated over a circular region and otherwise insulated. It is demonstrated that the method has the potential of providing extremely accurate values since six decimal accuracy is provided. Obtaining such accuracy using classical solution procedures is extremely difficult particularly for the extreme aspect ratios covered in this paper.

1 Introduction

There are several types of foil gages in common use for measuring heat fluxes or energy deposition. The thin circular foil heat flux gage proposed by Gardon [1] has been extensively employed in industry. A number of researchers have reported investigations for many related problems. Keltner and Wildin [2] provide a number of analytical solutions and some experimental results. Analytical results are also given by Riney [3] and Kirchhoff [4]. The transient heat conduction problems treated in these references have analytical solutions in the form of single and double infinite series. Because of the need to evaluate very large numbers of terms, many of these solutions have poor convergence properties. Moreover, such solutions can produce somewhat inaccurate results when large numbers of terms are needed. These are common problems for many analytical solutions in transient heat conduction.

The thin skin calorimeter has been used for aerodynamic heating measurements [5, 6] and for measuring pulsed energy deposition from lasers, ion beams, and other devices. The analysis of these devices has typically involved numerical codes (employing finite differences or elements) or integral equations [6].

This paper presents a new analytical solution method based on the use of Green's functions to solve the problems of poor convergence and inaccuracy inherent in models which involve large geometric aspect ratios and a wide range of dimensionless times. The method can be utilized for a wide variety of linear transient heat conduction problems.

This paper is part of a continuing research effort to develop the unsteady surface element (USE) method [7–12]. The USE method has been particularly useful in the analysis of thermal instrumentation. These analyses typically involve large time ranges, require fine temporal resolution at early times, and have singularities (e.g., corner regions) or near singularities. The method can be either analytical or numerical. One use of the method is for the solution of composite bodies of dissimilar shape that are joined over a relatively small region; an example is the foil heat flux gage which has a small thermocouple wire attached to it as shown in Fig. 1.

In problems of this type the presence of two or more bodies of dissimilar shapes requires evaluation of the solution over a very large range of dimensionless time; eight to ten decades is typical. The USE method is more efficient for these problems than either finite difference or finite element methods which may require a fine grid for small times and a coarser grid covering large regions for large times. The USE method retains the same node spacing for all times and furthermore nodes are needed only at the interface; usually ten or fewer nodes are needed at the interface.

In the USE method, influence functions, which are the solutions to certain basic problems, are used as building blocks. One such basic problem for the foil heat flux gage (thin skin calorimeter) is shown in Fig. 2. The geometry is a circular disk that is insulated everywhere except the central disk area, $0 < r < a$ at $x = 0$. The gage is of finite thickness L. The specific

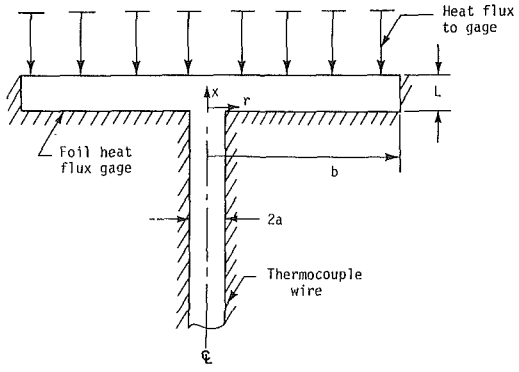

Fig. 1 Foil heat flux geometry. The boundary condition at $r = b$ is insulation for a thin-skin calorimeter and is isothermal for a circular foil heat flux gage.

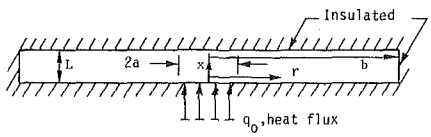

Fig. 2 Basic foil gage problem

Contributed by the Heat Transfer Division for publication in the JOURNAL OF HEAT TRANSFER. Manuscript recieved by the Heat Transfer Division September 26, 1985.

problem treated in this paper is the determination of the average temperature over $0 < r < a$ at $x = 0$ as a function of dimensionless time and for a wide range of aspect ratios of b/a and L/a. This solution can be utilized as an influence function by the USE method to obtain a solution of the errors associated with the conduction heat losses through the thermocouple wire. This type of problem has been considered in [2, 11].

In [13] an analytical "large time" solution for $T(r, x, t)$ is given for a semi-infinite body with a disk source; [14] discusses the same geometry, but is restricted to the average temperature, and accurate small and large time expressions are given. The semi-infinite insulated cylinder is given in [15], an analytical solution of which can take up to thousands of terms for direct evaluation; this slow convergence is mainly due to a time-independent term. The method used in [15] for efficient evaluation of this term, namely by using known early time numerical values, is not as general as the method developed in the present paper which utilizes time partitioning of Green's functions. Different expressions for the Green's functions are used in the various time intervals. Only a few terms are needed to describe the Green's functions in each interval; this is in contrast to the conventional procedure which uses a single expression which may involve single and double infinite series.

A derivation of the general Green's function solution is given in books [16, 17] as well as in a recent paper [18] which includes a compact list of Green's functions for rectangular coordinates. Reference [18] also mentions a numbering system for the solutions and [19] expands on both the numbering system and the table of Green's functions. The numbering notation for Fig. 2 is *R*02*X*22, where *R* is for the radial coordinate, *X* is for the x coordinate, 2 is for the gradient boundary condition, and 0 is for no physical boundary.

The plan of this paper is to give a mathematical statement of the transient heat conduction problem for the foil, a general Green's function solution of the problem, accurate Green's functions, a new procedure of solution which involves time partitioning an integral in the Green's function solution, determination of these time regions, and finally some discussion of results.

2 Mathematical Formulation

The describing partial differential equation for the geometry shown by Fig. 2 is

$$k\left[\frac{1}{r}\frac{\partial}{\partial r}\left(r\frac{\partial T}{\partial r}\right)+\frac{\partial^2 T}{\partial x^2}\right]=\rho c\frac{\partial T}{\partial t} \tag{1a}$$

The symbol T denotes temperature, k denotes thermal conductivity, t denotes time, ρ denotes density, and c denotes specific heat; k, ρ, and c are all assumed constant. The heat flux is constant with time and position at $x = 0$ for $r = 0$ to a

$$-k\left.\frac{\partial T(r, x, t)}{\partial x}\right|_{x=0}=q_0, \qquad 0<r<a \tag{1b}$$

and zero otherwise at $x = 0$. The insulation boundary conditions at $x = L$ and $r = b$ are

$$\left.\frac{\partial T(r, x, t)}{\partial x}\right|_{x=L}=0, \qquad \left.\frac{\partial T(r, x, t)}{\partial r}\right|_{r=b}=0 \tag{1c}$$

The initial temperature distribution is uniform, a constant value of T_0,

$$T(r, x, 0)=T_0 \tag{1d}$$

3 Green's Function Solution

For the gage initially at a temperature T_0 and subjected to a constant heat flux q_0, from $r = 0$ to a and at $x = 0$, the temperature distribution is [18, 19]

$$T(r, x, t)=T_0+(\alpha q_0/k)\int_{\tau=0}^{t}\int_{r'=0}^{a} G(r, x, t; r', 0, \tau)2\pi r' dr' d\tau \tag{2}$$

For the (r, x) coordinates the Green's function can be written as a product of two one-dimensional Green's functions [18]

$$G(r, x, t; r', 0, \tau)=G_R(r, t; r', \tau)G_X(x, t; 0, \tau) \tag{3}$$

and then equation (2) can be written as

$$T(r, x, t)=T_0+(\alpha q_0/k)\int_{\tau=0}^{t} G_X(x, t; 0, \tau)\int_{r'=0}^{a} G_R(r, t; r', \tau)2\pi r' dr' d\tau \tag{4}$$

The emphasis of this paper is upon the average temperature over the heated area

$$\bar{T}(x, t)=T_0+(\alpha q_0/k)\int_{\tau=0}^{t}\pi a^2 G_X(x, t; 0, \tau)\bar{G}_R(t; \tau)d\tau \tag{5}$$

where $\bar{G}_R(t; \tau)$ is given by

$$\bar{G}_R(t; \tau)=(1/\pi^2 a^4)\int_{r=0}^{a} 2\pi r\int_{r'=0}^{a} G_R(r, t; r', \tau)2\pi r' dr' dr \tag{6}$$

The needed Green's functions are functions of t and τ with the functional relation always depending upon the difference, $t-\tau$. To simplify the procedure, the integration of equation (5) is performed over $t-\tau$ from 0 to t rather than over τ from 0 to t (for which $t-\tau$ varies from t to 0). To further simplify the integrations, dimensionless time differences are used

$$t_a^* \equiv \alpha(t-\tau)/a^2 \tag{7a}$$

$$t_L^* \equiv \alpha(t-\tau)/L^2 \tag{7b}$$

Then, equation (5) for $x = 0$ can be written as

$$\bar{T}^+(0, t_a^+)\equiv\frac{\bar{T}(0, t_a^+)-T_0}{q_0 a/k}=\pi a^3\int_0^{t_a^+} G_X(0, t_L^*, 0)\bar{G}_R(t_a^*)dt_a^* \tag{8}$$

Nomenclature

a = radius of heated region
b = radius of disk
c = specific heat
D = integrand in equation (22)
$G(\cdot)$ = Green's function
$I_i(\cdot)$ = modified Bessel function
k = thermal conductivity
L = thickness of disk
q = heat flux
r = radial coordinate
t = time
t_a^* = dimensionless time difference $= \alpha(t-\tau)/a^2$
t_a^+ = dimensionless time $= \alpha t/a^2$
T = temperature
TSAV(n) = integral; see equation (24)
x = axial coordinate
α = thermal diffusivity
ρ = density
τ = dummy time variable

Table 1 Coefficients for the X22 Green's functions

Eq.	I	J	K	II(I,J,K)	KI(I,J,K)	AI(I,J,K)	CI(I,J,K)
(10a)	1	1	1	1	-1	$\pi^{-1/2}$	0
(10a)	1	1	2	3	0	$2\pi^{-1/2}$	1
(10a)	1	1	3	3	0	$2\pi^{-1/2}$	2
(10b)	1	2	1	1	0	1	0
(10b)	1	2	2	2	0	2	π
(10b)	1	2	3	2	0	2	2π

Table 2 Coefficients for radial Green's functions

Eq.	I	J	K	II(I,J,K)	KI(I,J,K)	AI(I,J,K)	CI(I,J,K)
(12)	2	1	1	1	0	1.0	0
(12)	2	1	2	1	1	$-2\pi^{-1/2}$	0
(12)	2	1	3	1	3	$.5\pi^{-1/2}$	0
.	.	.	.	.	.	.	.
.	.	.	.	.	.	.	.
(12)	2	1	7	1	11	$3.22998\pi^{-1/2}$	0
(13)	2	2	1	2	0	.350307417	2.4048256/3
(13)	2	2	2	2	0	.383866200	5.5200781/3
(13)	2	2	3	2	0	.105146524	8.6537279/3
(13)	2	2	4	2	0	.0008193642	11.7915344/3
(13)	2	2	5	2	0	.044399184	14.9309177/3
(13)	2	2	6	2	0	.0257058527	18.0710640/3
(14)	2	3	1	1	-2	.25	0
(14)	2	3	2	1	-4	-.0625	0
.	.	.	.	.	.	.	.
.	.	.	.	.	.	.	.
(16a)	2	4	1	1	0	b^{+-2}	0
(16a)	2	4	2	2	0	$f(b^+)$	$3.8317060/b^+$
(16a)	2	4	3	2	0	$f(b^+)$	$7.0155867/b^+$
.	.	.	.	.	.	.	.
.	.	.	.	.	.	.	.
(16a)	2	4	7	2	0	$f(b^+)$	$16.470630/b^+$

The units of $G_X(\cdot)$ are m^{-1} and those of $\bar{G}_R(\cdot)$ are m^{-2}. The arguments of $G_X(\cdot)$ are now (x, t_L^*, x'). The t_a^* and t_L^* values are related by

$$t_a^* = t_L^* L^{+2} \tag{9a}$$

$$L^+ \equiv L/a \tag{9b}$$

The t_a^+ limit in equation (8), unlike t_a^*, does not imply a time difference; t_a^+ is simply the dimensionless time

$$t_a^+ = \alpha t/a^2 \tag{9c}$$

at which the average temperature is evaluated.

4 Green's Functions

For the boundary conditions shown in Fig. 2, the boundary conditions in the x direction are of the gradient type (ie., second kind) at both $x = 0$ and $x = L$. This is called the $X22$ case. The Green's functions are evaluated only at $x = x' = 0$ and only a few terms are needed if two expressions are used, one for small times and the other for large times. The expression for t_L^* less than 0.25 is

$$LG_{X22}(0, t_L^*, 0) = (\pi t_L^*)^{-1/2}[1 + 2\exp(-1/t_L^*) + 2\exp(-4/t_L^*)] \tag{10a}$$

and for t_L^* greater than 0.25 is

$$LG_{X22}(0, t_L^*, 0) = 1 + 2[\exp(-\pi^2 t_L^*) + \exp(-4\pi^2 t_L^*)] \tag{10b}$$

These two expressions are extremely accurate for the ranges indicated with the greatest inaccuracy being at $t_L^* = 0.25$ where the difference is only in the tenth significant digit. This dimensionless interface time of 0.25 is denoted by t_x^*. For most calculations, only one or two terms of equation (10*a*) or (10*b*) are needed. (The terms in equations (10*a*, *b*) are listed in Table 1 which is described in Appendix A.)

For small dimensionless times, the radial Green's function for the $R02$ case ($0 < r < b$ and insulated at $r = b$) is accurately represented by the one for the infinite radial geometry denoted $R00$ ($0 < r < \infty$). For sufficiently small times the boundary condition at $r = b$ does not affect the average temperature over $0 \le r \le a$. For that reason $\bar{G}_{R00}(\cdot)$ is given first, an exact expression for which is [14]

$$\bar{G}_{R00}(t_a^*) = \left[1 - \exp\left(-\frac{1}{2t_a^*}\right)\left\{I_0\left(\frac{1}{2t^*}\right)_a + I_1\left(\frac{1}{2t_a^*}\right)\right\}\right]\frac{1}{\pi a^2} \tag{11}$$

The presence of the modified Bessel functions, $I_0(\cdot)$ and $I_1(\cdot)$, in (11) makes analytical solutions difficult, and for that reason equation (11) is replaced by three different accurate expressions that are more tractable. Each expression is for a different time region and the first is for $0 < t_a^* < t_{r1}^* = 0.15$, [14]

$$\pi a^2 \bar{G}_{R00}(t;\tau) = 1 - (t_a^*/\pi)^{1/2}[2 - (t_a^*/2) - (3t_a^{*2}/16) - (15t_a^{*3}/64) - (525t_a^{*4}/1024) - (6615t_a^{*5}/2048)] \tag{12}$$

At the time interface, $t_{r1}^* = 0.15$, $a^2\bar{G}_{R00}(t;\tau)$ given by equation (12) is numerically equal to 0.184802 while the exact value given by equation (11) is 0.184804 and thus the error is negligible. The errors in the approximations given herein for G are always greatest at the interface times. The actual quantity of final interest is the temperature which involves time integrations of G. Hence small errors in G near the interfaces result in even smaller errors in the calculated temperatures.

The equation for the second time region, $t_{r1}^* = 0.15 < t_a^* < t_{r2}^* = 0.55$ is

$$\pi a^2 \bar{G}_{R00}(t_a^*) = \Sigma A_n \exp(-\beta_n^2 t_a^*/9) \ldots \tag{13}$$

where $n = 1$ to 6; the A_n values are given as $AI(\cdot)$ and $\beta_n/3$ is given as $CI(\cdot)$ in Table 2. The time index t_{r2}^* denotes the interface between the second and third time regions. This solution is obtained from the analytical solution for the Green's function for a solid cylinder of radius b such that $b = 3a$ and the cylinder is isothermal at $r = b$. The case is denoted $R01$. Only six terms are needed to obtain six significant figure accuracy for $t_a^* = 0.15$. For larger t_a^* values, fewer terms are needed but there is a limit for the maximum t_a^* because the effect of the boundary begins to be important in region $0 < r < a$. The value of $a^2\bar{G}_{R00}$ obtained from equation (13) for $t_a^* = 0.55$ is 0.097634 while the exact value obtained from equation (11) is 0.097643, which results in an error of only -0.009 percent.

For the time range of $t_a^* > t_{r2}^* = 0.55$ the expression for $\bar{G}_{R00}$ is [13]

$$\pi a^2 \bar{G}_{R00}(t_a^*) = v[1 - v + (5v^2/6) - (7v^3/12) + (7v^4/20) - (11v^5/60) + (143v^6/1680) - (143v^7/8064)] \tag{14}$$

$$v \equiv 1/4t_a^* \tag{15}$$

At $t_a^* = 0.55$ the error is only $+0.007$ percent.

For sufficiently large times, the radial boundary condition at $r = b$ becomes important. For this time region the Green's function with an insulation condition at $r = b$ is given by

$$\pi a^2 \bar{G}_{R02}(t_a^*) = \frac{1}{(b^+)^2} + 4\sum_{n=1}^{6} e^{-\gamma_n^2 t_a^*/(b^+)^2}\left[\frac{J_1(\gamma_n/b^+)}{\gamma_n J_0(\gamma_n)}\right]^2 \tag{16}$$

where $b^+ \equiv b/a$. Note that only six terms are needed in equation (16) and further integration is only over time which is relatively simple since t appears linearly in the exponential

function; the Bessel function ratios need be evaluated only once for a given b^+ value. The eigenvalues γ_n are found from

$$J_1(\gamma_n)=0 \tag{17}$$

The first two eigenvalues are $\gamma_1 = 3.831705970$ and $\gamma_2 = 7.015586670$; for others, see [20, p. 409]. Equation (16) is used for dimensionless times larger than

$$t^*_{r3} \equiv (b^+ - 1)^2/12 \tag{18}$$

Equation (18) gives the time region interface between the third and fourth time regions and indicates when the insulation condition at $r = b$ begins to affect the average temperature from $r = 0$ to a. If the summation limit in equation (16) is increased, this equation could be used for small dimensionless times instead of equations (12), (13), and (14). However, thousands of terms may be necessary (as $t^*_a \to 0$, $n \to \infty$).

5 Method for Partitioning the Green's Function Integral

Since different Green's function expressions are needed as time increases, equation (8) must be expressed as several integrals with different integrands and associated integration limits. Assume that there are n time regions indicated by

$$0 < u < t^*_1 \tag{19}$$

$$t^*_1 < u < t^*_2 \tag{20}$$

$$\vdots$$

$$t^*_{n-1} < u < t^*_n \tag{21}$$

Then for t^+_a between t^*_{n-1} and t^*_n, i.e., $t^*_{n-1} < t^+_a < t^*_n$, the integral to be evaluated is

$$\int_0^{t^+_a} D\,du = \int_0^{t^*_1} D_1 du + \int_{t^*_1}^{t^*_2} D_2 du + \ldots + \int_{t^*_{n-1}}^{t^+_a} D_n du \tag{22}$$

where $D_1, \ldots,$ are the Green's function integrands. Notice that $D = D_1$ for $0 < u < t^*_1$, $D = D_2$ for $t^*_1 < u < t^*_2, \ldots$ but in general it is *not* true that $D = D_1 = D_2 = \ldots = D_n$ over the *complete* time domain. By using the D_i expressions over the indicated domains rather than D, the integrations can be performed analytically and then evaluated; furthermore, the computations are much more efficient since the use of a D which is valid for all time domains may require thousands of terms for some time domains. For the integrals in this paper, equation (22) can also be written as

$$\int_0^{t^+_a} D\,du = \int_0^{t^*_1} D_1 du + \left(\int^{t^*_2} D_2 du - \int^{t^*_1} D_2 du\right) + \left(\int^{t^*_3} D_3 du - \int^{t^*_2} D_3 du\right) + \ldots + \left(\int^{t^+_a} D_n du - \int^{t^*_{n-1}} D_n du\right) \tag{23a}$$

$$= \sum_{j=1}^{n-1} \left(\int^{t^*_j} D_j du - \int^{t^*_j} D_{j+1} du\right) + \int^{t^+_a} D_n du = \mathrm{TSAV}(n-1) + \int^{t^+_a} D_n du \tag{23b}$$

The data, i.e., lower integration limit, of the integrals in equation (23) need not be the same for all the integrands, but for a *given* integrand D_j, the *same* datum must be used.

Notice for any dimensionless time t^+_a between t^*_{n-1} and t^*_n that the summation in equation (23b) is the same value. Also notice that the summation in (23b) is denoted TSAV($n-1$). A recursion relation for TSAV(n) is

$$\mathrm{TSAV}(n) = \mathrm{TSAV}(n-1) + \int^{t^*_n} D_n du - \int^{t^*_n} D_{n+1} du \tag{24}$$

where TSAV(0) $\equiv$ 0. If the temperature is calculated at a series of successively larger times, the sums, TSAV(n), need be calculated only once for given values of b^+ and L/a.

An examination of the Green's functions, equations (10a, b), (12), (13) and (14), reveals that there are only three kinds of terms in these functions. The evaluation of these integrals is covered in Appendix A, which also gives a FORTRAN-like notation for the various terms.

6 Time Region Determination

The integrands inside the Green's function integral depend upon the dimensionless time. There are two parts of the integrand in equation (8) to consider: one for the x-direction Green's function $G_{X22}(\bullet)$, and one for the average radial Green's function $\bar{G}_{R02}(\bullet)$. Each part has its own time domains and interface times and the same definition of dimensionless time must be employed for both parts; the dimensionless time based on the radius of the heated region is chosen and is defined by equation (7a).

The x-direction interface dimensionless time based on L is $t^*_x = 0.25$ and based on a is

$$t^*_{ax} = t^*_x L^{*2} = 0.25 L^{+2} \tag{25}$$

The three time interfaces for the radial Green's functions are

$$t^*_{r1} = 0.15 \tag{26a}$$

$$t^*_{r2} = 0.55 \tag{26b}$$

$$t^*_{r3} = (b^+ - 1)^2/12 \tag{26c}$$

An example showing the time regions is instructive; let $b^+ = 25$ and $L^+ = 2$. The t^*_{ax} value is found from equation (25) to be 1.0 and t^*_{r3} is 48. There are then five time regions:

$$0 < t^*_a < 0.15, \quad 0.15 < t^*_a < 0.55, \quad 0.55 < t^*_a < 1 \tag{27}$$

$$1 < t^*_a < 48, \quad 48 < t^*_a \tag{28}$$

For the times less than $t^*_a = 1$, the $X22$ Green's function is equation (10a) and above $t^*_a = 1$, equation (10b) is used. For $0 < t^*_a < 0.15$, equation (12) is used; for $0.15 < t^*_a < 0.55$, equation (13) is used; for $0.55 < t^*_a < 48$, equation (14) is used; and for $t^*_a > 48$, equation (16) is used. For small values of b^+, such as 2, some of the time regions may disappear.

7 Results

Results are presented in two different ways, as very accurate numerical values in tables and as figures. As stated in the beginning of the paper, the temperature of interest is the average value over the heated circular region at the surface of the gage.

Figures 3, 4, and 5 display results for the cases of $L^+ = L/a$ equal to 1, 2, and 10, respectively. The $b^+ = b/a$ values of 2, 5, 10, 25, 50, 100, and 200 are covered. Notice that for a given value of L^+, a curve for a specified value of b^+ follows the $b^+ \to \infty$ curve until some time (about $2t^*_{r3}$) at which the finite b^+ curve increases more rapidly. The shapes of the curves presented in Figs. 3–5 are affected by the radial and axial boundary effects starting at different times. The $b^+ \to \infty$ values for different L^+ values are shown in [14].

Tabulations of the average temperature are given in Table 3 as a function of time for the case of $b^+ \to \infty$; the cases of $L^+ = 1$, 2, and 10 are given. Table 4 contains values for finite values of b^+ and for $L^+ = 1$, 2, and 10. Since the values are

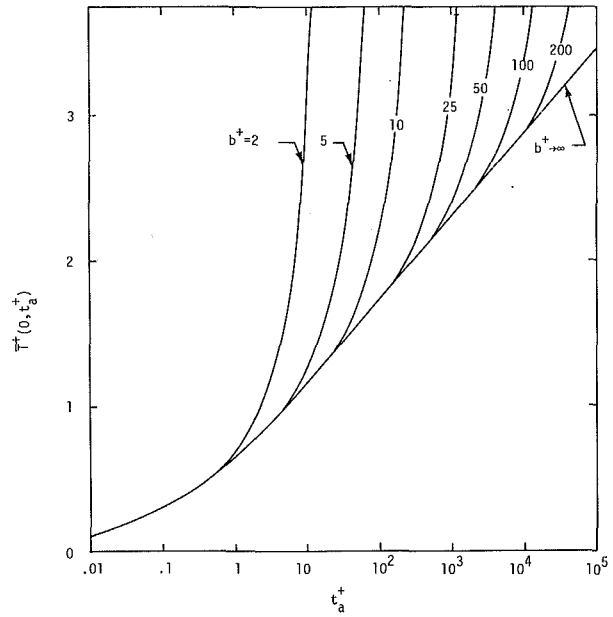

Fig. 3 Average surface temperatures for $L^+ = 1$

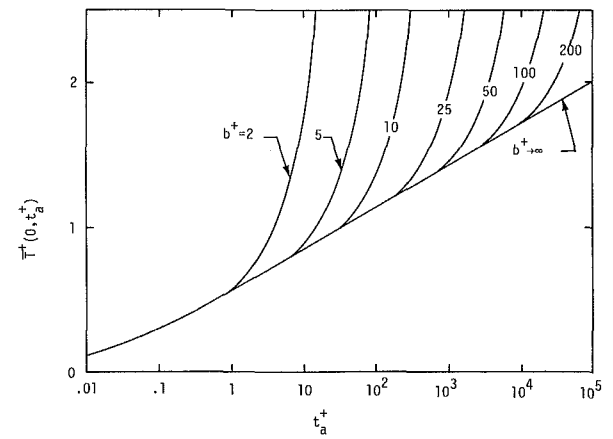

Fig. 4 Average surface temperatures for $L^+ = 2$

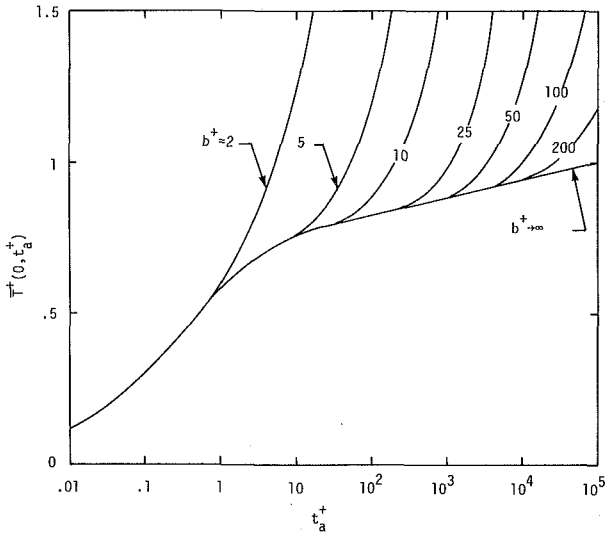

Fig. 5 Average surface temperatures for $L^+ = 10$

Table 3 Average dimensionless temperatures for very large *b/a*

Time	$L^+=1$	$L^+=2$	$L^+=10$
.10	.293982	.293981	.293981
.15	.343440	.343398	.343398
.20	.380992	.380695	.380695
.50	.516123	.503115	.503111
.55	.532119	.515444	.515433
1.00	.642599	.588506	.587630
10.00	1.167761	.856492	.760355
100.00	1.737846	1.141534	.828587
1000.00	2.312931	1.429076	.886095
10000.00	2.888521	1.761871	.943654

Table 4 Average dimensionless temperatures for large times

$\alpha t/a^2$	b^+	$L^+=1$	$L^+=2$	$L^+=10$
.10	2	.292982	.292981	.293981
1.00	2	.663624	.602387	.601495
10.00	2	2.917556	1.738145	1.213459
1.33	5	.701358	.621336	.618486
10.00	5	1.222360	.883792	.771627
100.00	5	4.823379	2.684301	1.162394
6.75	10	1.072434	.808828	.741564
10.00	10	1.167778	.856500	.760358
100.00	10	2.162452	1.353837	.871771
500.00	10	6.162452	3.353837	1.271772
50.00	25	1.565183	1.055203	.811259
100.00	25	1.738569	1.141896	.828659
1000.00	25	3.218497	1.881860	.976652
500.00	50	2.142514	1.343868	.869054
1000.00	50	2.363590	1.454406	.891161
10000.00	50	5.964770	3.254996	1.251279
816.75	100	2.262339	1.403781	.881036
1000.00	100	2.312942	1.429082	.886097
10000.00	100	3.311268	1.928245	.985929
5000.00	200	2.715347	1.630285	.926337
10000.00	200	2.897131	1.721177	.944515
50000.00	200	3.907823	2.226523	1.045585

unchanged for the small dimensionless times only the later times are given in Table 4.

The values are accurate to six decimal places; this accuracy has been verified in part by comparing answers with those obtained using completely different procedures [13]. See also the discussion below equation (12). Extremely accurate values are given for several reasons. The first is to demonstrate that the partitioning method can produce such accuracy and can do it with a very limited number of terms to approximate the Green's functions. Obtaining the same accuracy over the total time range by using a conventional procedure such as separation of variables is extremely difficult. Another reason for providing these accurate values is to give a test case for validating finite difference or element programs.

Summary and Conclusions

A new procedure for solving linear transient conduction problems is given that involves partitioning of Green's functions into time regions. Instead of having a classical solution in terms of a single or double infinite series that covers the complete time domain, finite series for several time domains are used. By using this procedure rather than the classical method, both improved accuracy and decreased computer time can be obtained.

The problem considered herein is that of a circular disk of radius b and finite thickness L, with a heated circular region of radius a. The average temperature over the heated region is

given for wide ranges of b/a and L/a. This multidimensional solution is a fundamental building block, called an influence function, for the unsteady surface element method which can treat composite bodies.

The USE method has been used for thermal modeling of heat transfer instrumentation. The combination of the USE method and Green's function partitioning provides an effective method of solving diverse heat conduction problems such as transient thermal constriction resistance and thermal spreaders for electronic cooling.

Acknowledgments

The research was sponsored by the National Science Foundation under Grant No. MEA 81-21499, and Sandia National Laboratories, which is operated by AT&T Technologies under Contract No. DE-AC04-76DP00789.

References

1 Gardon, R., "An Instrument for the Direct Measurement of Intense Thermal Radiation," *Rev. of Sci. Inst.*, Vol. 24, 1953, p. 366.

2 Keltner, N. R., and Wildin, M. W., "Transient Response of Circular Foil Heat Flux Gages to Radiative Fluxes," *Rev. of Sci. Inst.*, Vol. 46, 1975, pp. 1161–1166.

3 Riney, T. D., "Disk Heated by Internal Source," ASME *Journal of Applied Mechanics*, Vol. 28, 1961, p. 631.

4 Kirchhoff, R. H., "Response of Finite-Thickness Gardon Heat-Flux Sensors," ASME JOURNAL OF HEAT TRANSFER, Vol. 94, 1972, pp. 244–245.

5 Starner, K. E., "Use of Thin Skin Calorimeters for High Flux Arc Jet Measurements," *22nd Annual ISA Conference*, Vol. 22, 1967.

6 Cassagne, B., Kirsch, G., and Bardon, J. P., "Theoretical Analysis of the Errors Due to Stray Heat Transfer During the Measurement of a Surface Temperature by Direct Contact," *International Journal of Heat and Mass Transfer*, Vol. 23, 1980, pp. 1207–1217.

7 Keltner, N. R., and Beck, J. V., "Unsteady Surface Element Method," ASME JOURNAL OF HEAT TRANSFER, Vol. 103, 1981, pp. 759–764.

8 Litkouhi, B., and Beck, J. V., "Intrinsic Thermocouple Analysis Using Multinode Unsteady Surface Element Method," AIAA 18th Thermophysics Conference, Montreal, Canada, June 1–3, 1983, Paper No. AIAA-83-1437; *AIAA Journal*, Vol. 23, 1985, pp. 1609–1614.

9 Litkouhi, B., and Beck, J. V., "Multinode Unsteady Surface Element Method With Application to Contact Conductance Problem," ASME JOURNAL OF HEAT TRANSFER, Vol. 108, 1986, pp. 257–263.

10 Beck, J. V., Keltner, N. R., and Schisler, I. P., "Influence Functions for the Unsteady State Surface Element Method," AIAA 22nd Aerospace Sciences Meeting, Reno, NV, Jan. 9–12, 1984, Paper No. AIAA-84-0492; *AIAA Journal*, Vol. 23, 1985, pp. 1978–1982.

11 Keltner, N. R., and Beck, J. V., "Surface Temperature Measurement Errors," ASME JOURNAL OF HEAT TRANSFER, Vol. 105, 1983, pp. 312–318.

12 Keltner, N. R., Beck, J. V., and Bainbridge, B. L., "Rectangular Heat Source on a Semi-infinite Solid – An Analysis for a Thin Film Heat Flux Gage Calibration," ASME Paper No. 84-HT-46, 1984; submitted to JOURNAL OF HEAT TRANSFER.

13 Beck, J. V., "Large Times Solutions for Temperature in a Semi-infinite Body With a Disk Heat Source," *International Journal of Heat and Mass Transfer*, Vol. 24, 1981, pp. 155–164.

14 Beck, J. V., "Average Transient Temperature Within a Body Heated by a Disk Heat Source," *Heat Transfer, Thermal Control and Heat Pipes*, Vol. 70, Progress in Astronautics and Aeronautics, W. B. Olstad, ed., 1980, pp. 3–20.

15 Beck, J. V., "Transient Temperatures in a Semi-infinite Cylinder Heated by a Disk Heat Source," *International Journal of Heat and Mass Transfer*, Vol. 24, 1981, pp. 1631–1640.

16 Morse, P. M., and Feshbach, H., *Methods of Theoretical Physics*, Vols. I and II, McGraw-Hill, New York, 1953.

17 Ozisik, M. N., *Heat Conduction*, Wiley, New York, 1980.

18 Beck, J. V., "Green's Function Solution for Transient Heat Conduction Problems," *International Journal of Heat and Mass Transfer*, Vol. 27, 1984, pp. 1235–1244.

19 Beck, J. V., "Green's Functions and Numbering System for Transient Heat Conduction," AIAA 19th Thermophysics Conference, Snowmass, CO, June 25–28, 1984, Paper No. AIAA-84-1741; *AIAA Journal*, Vol. 24, 1986, pp. 327–333.

20 Abramowitz, M., and Stegun, I. A., *Handbook of Mathematical Functions*, National Bureau of Standards, Applied Mathematics Series 55, 1964.

APPENDIX A

Basic Terms and Integrals

The Green's functions (10*a*, *b*), (12), (13), and (14) have only three kinds of terms and there are not more than three parameters involved in each

$$A\,u^{k/2},\quad II=1,\quad KI=k,\quad AI=A,\quad CI=0 \tag{A1a}$$

$$A\exp[-C^2u],\quad II=2,\quad KI=0,\quad AI=A,\quad CI=C \tag{A1b}$$

$$A\,u^{-1/2}\exp[-C^2/u],\quad II=3,\quad KI=0,\quad AI=A,\quad CI=C \tag{A1c}$$

The *II*, *KI*, *AI*, and *CI* symbols can be triple-subscripted arrays in FORTRAN, such as $II(I, J, K)$, where $I = 1$ for $G_{X22}(\bullet)$, $I = 2$ for $G_{R02}(\bullet)$; J is an index for the equation number such as $J = 1$ for (10*a*) and $J = 2$ for (10*b*); and K is an index for the location of the term in a summation with $K = 1$ for the first term, $K = 2$ for the second term, etc. The *KI* symbol is another triple-subscripted function, $KI(I, J, K)$ where I, J, and K have the same meanings as for *II*. For the *X*22 Green's functions, see Table 1 and for the *R*02 functions, see Table 2.

The integrals for all the needed combinations of the terms are

II = 1 and 1:

$$\int^{t^*} A_1u^{k_1/2}A_2u^{k_2/2}\,du = A_1A_2\,\frac{2}{k_1+k_2+2}\,t^{*(k_1+k_2+2)/2},\qquad k_1+k_2\neq -2 \tag{A2a}$$

$$\int^{t^*} A_1u^{k_1/2}A_2u^{k_2/2}\,du = A_1A_2\ln t^*,\qquad k_1+k_2=-2 \tag{A2b}$$

II = 1 and 2:

$$\int_\infty^{t^*} A_1u^{k_1/2}A_2e^{-C_2^2u}\,du = -A_1A_2C_2^{-(k_1+2)}\Gamma\left(\frac{k_1+2}{2},\quad C_2^2t^*\right) \tag{A3}$$

II = 2 and 2:

$$\int^{t^*} A_1e^{-C_1^2u}A_2e^{-C_2^2u}\,du = -A_1A_2\,\frac{1}{C_1^2+C_2^2}\,e^{-(C_1^2+C_2^2)t^*} \tag{A4}$$

II = 1 and 3:

$$\int_0^{t^*} A_1u^{k_1/2}A_2u^{-1/2}e^{-C_2^2/u}\,du = A_1A_2C_2^{k_1+1}\Gamma\left(-\frac{k_1+1}{2},\quad \frac{C_2^2}{t^*}\right) \tag{A5}$$

II = 3 and 2:

$$\int_\infty^{t^*} A_1u^{-1/2}e^{-C_1^2/u}A_2e^{-C_2^2u}\,du = -\frac{A_1A_2\sqrt{\pi}}{2C_2}\left[e^{2C_1C_2}\operatorname{erfc}(C_2t^{*1/2}+C_1t^{*-1/2})+e^{-2C_1C_2}\operatorname{erfc}(C_2t^{*1/2}-C_1t^{*-1/2})\right] \tag{A6}$$

In some of the above integrals, data of zero and infinity are used in order to use known functions such as the incomplete gamma function, $\Gamma(i/2, z)$. Relations for evaluating the incomplete gamma function are given in Appendix B.

APPENDIX B

Incomplete Gamma Function of $\Gamma\,[(2k+j)/2, x^2]$

(See Abramowitz and Stegun [20], p. 262).

(*a*) $j=0$; $k=1, 2, 3, \ldots$

$$\Gamma(k, x^2)=e^{-x^2}(k-1)!\sum_{n=0}^{k-1}\frac{x^{2n}}{n!} \tag{B1}$$

(*b*) $j=0$; $k=0, -1, -2, \ldots$. Let $k'=-k$, $k'=0, 1, 2, 3, \ldots$.

$$\Gamma(-k', x^2)=x^{-2k'}E_{k'+1}(x^2) \tag{B2}$$

(*c*) $j=1$; $k=0, 1, 2, 3, \ldots$

$$\Gamma\left(k+\frac{1}{2}, x^2\right)=\Gamma\left(k+\frac{1}{2}\right)\left[\operatorname{erfc}(x)-\frac{1}{x}e^{-x^2}\sum_{i=0}^{k'-1}(-1)^i\Gamma\left(i+\frac{1}{2}\right)x^{2(1-i)}\right] \tag{B4}$$

(*d*) $j=1$; $k=-1, -2, -3, \ldots$. Let $k'=-k$, $k'=1, 2, 3, \ldots$.

$$\Gamma\left(k+\frac{1}{2}, x^2\right)=(-1)^{k'}\frac{1}{\Gamma\left(k'+\frac{1}{2}\right)}\left[\pi\operatorname{erfc}(x)+xe^{-x^2}\sum_{i=1}^{k}\frac{1}{\Gamma(i+1/2)}x^{2(i-1)}\right] \tag{B3}$$

Two-Dimensional Transient Solutions for Crossflow Heat Exchangers With Neither Gas Mixed

G. Spiga
Laboratorio di Ingegneria Nucleare,
Università di Bologna,
40136 Bologna, Italy

M. Spiga
Istituto di Fisica Tecnica,
Università di Bologna,
40136 Bologna, Italy

The two-dimensional transient behavior of gas-to-gas crossflow heat exchangers is investigated, solving by analytical methods the thermal balance equations in order to determine the transient distribution of temperatures in the core wall and in both the unmixed gases. Assuming large wall capacitance, the general solutions are deduced by the Laplace transform method and are presented as integrals of modified Bessel functions on space and time, for a transient response with any arbitrary initial and inlet conditions, in terms of the number of transfer units, capacity rate and conductance ratio. Specializing the entrance temperature and assuming constant initial conditions, the most meaningful transient conditions (such as step, ramp, and exponential responses) have been simulated and the relevant solutions, expressed by means of either integrals or series, have been accurately computed with extremely low computational time. The temperature responses are then presented in graphic form for a wide range of the number of transfer units.

Introduction

Over recent years problems related to crossflow heat exchangers have increased in their importance in a wide range of engineering fields, such as gas turbine regenerators, air–sodium exchangers in nuclear fast breeder reactors, ceramic exchangers for coal-fired and dirty gas applications, phosphoric acid fuel cell power units, and air-conditioning systems. Thermal and hydraulic fundamentals are needed with greater and greater accuracy for a correct and reliable design, for reducing the energy waste, and for preventing dangerous and expensive offlines. Especially in modern high-performance heat transfer units, the systematic use of automatic control devices for the accurate regulation of fluid systems in heat exchangers has stimulated great interest in transient phenomena. Problems such as startup, shutdown, fan failure, and accidents have motivated investigations of thermal response in crossflow heat exchangers. However, an accurate and detailed analysis oriented toward thermal design and modeling is rather lacking. Thus the goal of finding an exact analytical way to predict temperature fields and overall performances during transients is becoming more and more significant, particularly in order to give the designer the possibility of relying on an exact general solution for the time-dependent two-dimensional temperature distributions, very useful for thermal and stress analysis.

While the steady-state solutions for temperature profiles in crossflow heat exchangers have been deeply investigated and are nowadays well known (Baclic and Heggs, 1985), the transient response has received very little attention, probably because of its complexity.

The first paper dealing with the transient behavior of crossflow heat exchangers dates back to Dusinberre (1959), who proposed a finite difference method to describe transients, but resorted to steady-state equations in calculating gas temperatures. Some years later Gartner and Harrison (1965) investigated the transient characteristics of water–air crossflow heat exchangers only for periodic disturbances. Myers et al. (1967) employed an integral technique to obtain an approximate solution for the mean temperatures of the two gases leaving the heat exchanger, for the step response only, assuming the simplifying hypothesis of mixed stepped fluid. Yamashita et al. (1978) investigated the step response by means of finite difference methods, to calculate the exit temperatures. In a recent paper Romie (1983) predicted the exit mean temperatures of the two gases for the step response, resorting to the Laplace transform, and carrying out an accurate investigation about the influence of all governing parameters.

Thus it can be noted that the existing literature deals only with particular features and is generally restricted to: (*i*) calculation of mixed mean exit temperatures; (*ii*) step response.

The aim of this work is the development of a quite general exact analytical solution for the transient two-dimensional temperature distributions, for wall and both gases, in crossflow heat exchangers with neither gas mixed. The paper should thus provide considerable information about the temperature field for any perturbation of the inlet temperatures, and for any value of the governing parameters. The analytical solutions, moreover, constitute reliable benchmarks and can contribute to the development of related computer codes. The general solutions, expressed as integrals of Bessel functions in space and time, or in the alternative equivalent form of rapidly converging series, are then specialized in order to describe step, ramp, exponential responses.

Assumptions and Formulation

The following analysis is concerned with a direct-transfer-type, single-pass, crossflow unit having walls separating the two gas streams. Stream *a* flows through a set of tubes or plates, arranged in a bank, whereas stream *b* threads its way through the spaces at right angles to the bank. The mathematical model is developed resorting to the following usual idealizations:

- no lateral mixing occurs for either gas and no heat is transferred from one flow passage to the next containing the same fluid (neither fluid is mixed);

Contributed by the Heat Transfer Division for publication in the JOURNAL OF HEAT TRANSFER. Manuscript received by the Heat Transfer Division April 14, 1986.

• the physical properties and the fluid capacity rates are uniform and constant;
• the ratios of the thermal capacities of both fluids to the core wall thermal capacity are negligible, as is typical for gas-to-gas exchange units;
• the thermal conductances on both sides are constant and inclusive of wall resistance and fouling;
• the exchanger shell or shroud is adiabatic;
• the mass velocities at the entrance of the heat exchanger on each side are constant and uniform;
• change of flow distribution inside the exchanger and axial heat conduction in fluids are neglected;
• heat transfer area per unit base area as well as heat transfer surface configurations on both sides are constant and distributed uniformly throughout the exchanger.

Inlet temperatures are allowed to be space and time dependent. Introducing the following dimensionless variables

$$t=\frac{(hA)_a}{Mc_w}\tau \qquad x=\frac{(hA)_a}{(mc)_a}\frac{\xi}{L_a} \qquad y=\frac{(hA)_b}{(mc)_b}\frac{\eta}{L_b} \tag{1}$$

the governing differential equations are readily obtained from energy conservation for each gas and for the wall separating the fluids, in the form

$$\frac{\partial T_w}{\partial t}+(1+R)T_w=T_a+RT_b$$
$$\frac{\partial T_a}{\partial x}+T_a=T_w \tag{2}$$
$$\frac{\partial T_b}{\partial y}+T_b=T_w$$

for $t>0$, $0<x<N_a$, $0<y<N_b$, and with initial and inlet conditions

$$T_w(x, y, 0)=f(x, y)$$
$$T_a(0, y, t)=g_a(y, t) \tag{3}$$
$$T_b(x, 0, t)=g_b(x, t).$$

Here and in the sequel the usual dimensionless physical parameters

$$R=\frac{(hA)_b}{(hA)_a} \qquad E=\frac{(mc)_b}{(mc)_a}$$
$$N_a=\frac{(hA)_a}{(mc)_a} \qquad N_b=\frac{(hA)_b}{(mc)_b} \tag{4}$$

$$\mathrm{NTU}=\left\{(mc)_{\min}\left[\frac{1}{(hA)_a}+\frac{1}{(hA)_b}\right]\right\}^{-1}$$

will be used; of course only three of them are independent.

General Solution

In order to solve equations (2), it proves convenient to take a threefold Laplace transform with respect to t, x, y with parameters s, p, q, respectively; the transform of T_w, labeled $\tilde{T}_w$, will be defined as

$$\tilde{T}_w(p, q, s)=\int_0^\infty e^{-qy}dy\int_0^\infty e^{-px}dx\int_0^\infty e^{-st}T_w(x, y, t)dt. \tag{5}$$

Such a technique reduces the problem to a set of algebraic equations, namely

$$\begin{cases}(s+R+1)\tilde{T}_w(p, q, s)-\tilde{T}_a(p, q, s)\\ \qquad -R\tilde{T}_b(p, q, s)=\tilde{f}(p, q)\\ (p+1)\tilde{T}_a(p, q, s)-\tilde{T}_w(p, q, s)=\tilde{g}_a(q, s)\\ (q+1)\tilde{T}_b(p, q, s)-\tilde{T}_w(p, q, s)=\tilde{g}_b(p, s),\end{cases} \tag{6}$$

which can be solved explicitly to yield for the transforms of the sought temperature fields

$$\tilde{T}_w(p, q, s)=\Big[(p+1)(q+1)s+p(q+1)+Rq(p+1)\Big]^{-1}\Big[(p+1)(q+1)\tilde{f}(p, q)+(q+1)\tilde{g}_a(q, s)+R(p+1)\tilde{g}_b(p, s)\Big]$$

$$\tilde{T}_a(p, q, s)=\Big[(p+1)(q+1)s+p(q+1)+Rq(p+1)\Big]^{-1}\Big\{(q+1)\tilde{f}(p, q)+\Big[(q+1)s+(1+R)q+1\Big]\tilde{g}_a(q, s)+R\tilde{g}_b(p, s)\Big\} \tag{7}$$

$$\tilde{T}_b(p, q, s)=\Big[(p+1)(q+1)s+p(q+1)+Rq(p+1)\Big]^{-1}\Big\{(p+1)\tilde{f}(p, q)+\tilde{g}_a(q, s)+\Big[(p+1)s+(1+R)p+R\Big]\tilde{g}_b(p, s)\Big\},$$

Nomenclature

A = heat transfer surface
c = specific heat
E = flow capacitance ratio
f = initial condition
g = inlet condition
h = heat transfer coefficient
I = modified Bessel function of the first kind
L = exchanger length
M = mass of exchanger
m = mass flow rate
N = dimensionless exchanger length
NTU = number of transfer units
R = heat transfer resistance ratio
s, p, q = Laplace transform variables
t = dimensionless time variable
T = dimensionless temperature
x, y = dimensionless space variables
γ = incomplete gamma function
δ = Dirac delta function or Kronecker symbol
ξ, η = space variables
τ = time variable

Subscripts

a = primary fluid
b = secondary fluid
w = solid wall

where each right-hand side is a linear combination of the input data $\tilde{f}$, $\tilde{g}_a$, $\tilde{g}_b$ (arbitrary up to now) with coefficients, given by simple rational functions of p, q, and s, which may be regarded as types of Laplace transforms of Green's functions. The final step in solution procedure is the Laplace inversion of equations (7), which can be accomplished by means of contour integration in the complex plane and residue theory, bearing the convolution theorem in mind. The result reads as

$$T_w(x,y,t)=\int_0^x dx'\int_0^y G_w^w(x-x',\,y-y',\,t)\,f(x',\,y')dy'$$

$$+\int_0^t dt'\int_0^y G_w^a(x,\,y-y',\,t-t')g_a(y',\,t')dy'$$

$$+\int_0^t dt'\int_0^x G_w^b(x-x',\,y,\,t-t')g_b(x',\,t')dx'$$

$$T_a(x,y,t)=\int_0^x dx'\int_0^y G_a^w(x-x',\,y-y',\,t)f(x',\,y')dy'$$

$$+\int_0^t dt'\int_0^y G_a^a(x,\,y-y',\,t-t')g_a(y',\,t')dy'$$

$$+\int_0^t dt'\int_0^x G_a^b(x-x',\,y,\,t-t')g_b(x',\,t')dx' \qquad (8)$$

$$T_b(x,y,t)=\int_0^x dx'\int_0^y G_b^w(x-x',\,y-y',\,t)f(x',\,y')dy'$$

$$+\int_0^t dt'\int_0^y G_b^a(x,\,y-y',\,t-t')g_a(y',\,t')dy'$$

$$+\int_0^t dt'\int_0^x G_b^b(x-x',\,y,\,t-t')g_b(x',\,t')dx',$$

where the weighting functions G follow from the inverse transform of the corresponding coefficients in equations (7). Making use of standard theorems on Laplace transforms, and of the results

$$\int_0^\infty e^{-px}\left(\frac{t}{x}\right)^{j/2} I_j(2t^{1/2}x^{1/2})dx=p^{j-1}e^{t/p}-\delta_{j1} \qquad (9)$$

for $j=0,\ \pm 1$, with $I_{-1}(z)=I_1(z)$, the Green functions are expressed as

$$G_w^w(x,y,t)=e^{-[x+y+(1+R)t]}\left[\delta(x)+\left(\frac{t}{x}\right)^{1/2} I_1(2x^{1/2}t^{1/2})\right]$$

$$\left[\delta(y)+\left(\frac{Rt}{y}\right)^{1/2} I_1(2y^{1/2}R^{1/2}t^{1/2})\right]$$

$$G_w^a(x,y,t)=e^{-[x+y+(1+R)t]}I_0(2x^{1/2}t^{1/2})$$

$$\left[\delta(y)+\left(\frac{Rt}{y}\right)^{1/2} I_1(2y^{1/2}R^{1/2}t^{1/2})\right]$$

$$G_w^b(x,y,t)=Re^{-[x+y+(1+R)t]}$$

$$\left[\delta(x)+\left(\frac{t}{x}\right)^{1/2} I_1(2x^{1/2}t^{1/2})\right]I_0(2y^{1/2}R^{1/2}t^{1/2}) \qquad (10a)$$

$$G_a^w(x,y,t)=e^{-[x+y+(1+R)t]}I_0(2x^{1/2}t^{1/2})$$

$$\left[\delta(y)+\left(\frac{Rt}{y}\right)^{1/2} I_1(2y^{1/2}R^{1/2}t^{1/2})\right]$$

$$G_a^a(x,y,t)=e^{-[x+y+(1+R)t]}\left[\delta(t)+\left(\frac{x}{t}\right)^{1/2} I_1(2x^{1/2}t^{1/2})\right]$$

$$\left[\delta(y)+\left(\frac{Rt}{y}\right)^{1/2} I_1(2y^{1/2}R^{1/2}t^{1/2})\right]$$

$$G_a^b(x,y,t)=Re^{-[x+y+(1+R)t]}I_0(2x^{1/2}t^{1/2})I_0(2y^{1/2}R^{1/2}t^{1/2}) \qquad (10b)$$

$$G_b^w(x,y,t)=e^{-[x+y+(1+R)t]}$$

$$\left[\delta(x)+\left(\frac{t}{x}\right)^{1/2} I_1(2x^{1/2}t^{1/2})\right]I_0(2y^{1/2}R^{1/2}t^{1/2})$$

$$G_b^a(x,y,t)=e^{-[x+y+(1+R)t]}I_0(2x^{1/2}t^{1/2})I_0(2y^{1/2}R^{1/2}t^{1/2})$$

$$G_b^b(x,y,t)=e^{-[x+y+(1+R)t]}$$

$$\left[\delta(t)+\left(\frac{Ry}{t}\right)^{1/2} I_1(2y^{1/2}R^{1/2}t^{1/2})\right]$$

$$\left[\delta(x)+\left(\frac{t}{x}\right)^{1/2} I_1(2x^{1/2}t^{1/2})\right] \qquad (10c)$$

where δ denotes the Dirac delta function, δ_{j1} the Kronecker symbol, and I_n stands for the modified Bessel function of first kind and order n. Equations (8) and (10) provide the complete and exact solution to the heat transfer problem for any initial condition f, and for any inlet condition of the incoming gases, g_a and g_b. The functions G have a physical meaning themselves, since G_j^k represents the temperature distribution in the jth component for a delta pulse of the kth input datum, the other data being zero. So, for instance, $T_a(x,y,t)=G_a^b(x,y,t)$ when $f=g_a=0$ and $g_b(x,t)=\delta(x)\delta(t)$.

The Initial Value Problem

The problem of greatest practical interest is the transient regime induced by a sudden variation of the inlet conditions of one of the two gases at a reference initial time $t=0$. In such a situation, the temperature distribution of both the other gas at its inlet cross section, and solid core at time $t=0$ are assigned and remain unperturbed; the object is to determine the response of the exchanger. It is worth then investigating the initial value problem with, for instance, f (initial core temperature) and g_b (inlet secondary gas temperature) equal to the same constant (that may be set zero by a suitable temperature scaling) and focusing all the attention on the time variations of the other datum g_a, that can be taken as uniform over the inlet section. Specializing thus the results of the previous section to the case $g_a(y,t)=\varphi(t)$, $g_b(x,t)=f(x,y)=0$, and resorting to some properties of the Bessel functions, one is left with the solution

$$T_w(x,y,t)=e^{-x-y}\int_0^t e^{-(1+R)t'}I_0(2x^{1/2}t'^{1/2})I_0(2y^{1/2}R^{1/2}t'^{1/2})$$

$$\varphi(t-t')dt'+e^{-x}\int_0^t e^{-(1+R)t'}I_0(2x^{1/2}t'^{1/2})\varphi(t-t')dt'$$

$$\int_0^y e^{-z}I_0(2z^{1/2}R^{1/2}t'^{1/2})dz \qquad (11)$$

$$T_a(x,y,t)=\varphi(t)e^{-x}+e^{-x-y}\int_0^t e^{-(1+R)t'}\left(\frac{x}{t'}\right)^{1/2}$$

$$I_1(2x^{1/2}t'^{1/2})I_0(2y^{1/2}R^{1/2}t'^{1/2})\varphi(t-t')dt'$$

$$+e^{-x}\int_0^t e^{-(1+R)t'}\left(\frac{x}{t'}\right)^{1/2} I_1(2x^{1/2}t'^{1/2})$$

$$\varphi(t-t')dt' \int_0^y e^{-z} I_0(2z^{1/2}R^{1/2}t'^{1/2})dz$$

$$T_b(x, y, t) = e^{-x} \int_0^t e^{-(1+R)t'} I_0(2x^{1/2}t'^{1/2})$$

$$\varphi(t-t')dt' \int_0^y e^{-z} I_0(2z^{1/2}R^{1/2}t'^{1/2})dz.$$

When $\varphi(t)$ is further specialized, all two-dimensional temperature fields can be computed versus time as integrals of Bessel functions. The mean values on the cross sections can be evaluated by a further integration as

$$\bar{T}_a(x, t) = \frac{1}{N_b} \int_0^{N_b} T_a(x, y, t)dy$$

$$\bar{T}_b(y, t) = \frac{1}{N_a} \int_0^{N_a} T_b(x, y, t)dx \tag{12}$$

and the outlet mean temperatures $\bar{T}_a(N_a, t)$ and $\bar{T}_b(N_b, t)$ are the quantities more interesting from a macroscopic point of view, for control processes. If $\varphi(t)$ is specialized as $\delta(t)$ in equations (11), the Green's functions for the present problem are obtained, namely

$$T_w^G(x, y, t) = e^{-[x+(1+R)t]} I_0(2x^{1/2}t^{1/2})$$

$$\left[e^{-y} I_0(2y^{1/2}R^{1/2}t^{1/2}) + \int_0^y e^{-z} I_0(2z^{1/2}R^{1/2}t^{1/2})dz\right]$$

$$T_a^G(x, y, t) = \delta(t)e^{-x} + e^{-[x+(1+R)t]} \left(\frac{x}{t}\right)^{1/2} I_1(2x^{1/2}t^{1/2})$$

$$\left[e^{-y} I_0(2y^{1/2}R^{1/2}t^{1/2}) + \int_0^y e^{-z} I_0(2z^{1/2}R^{1/2}t^{1/2})dz\right] \tag{13}$$

$$T_b^G(x, y, t) = e^{-[x+(1+R)t]} I_0(2x^{1/2}t^{1/2})$$

$$\int_0^y e^{-z} I_0(2z^{1/2}R^{1/2}t^{1/2})dz,$$

where

$$\int_0^y e^{-z} I_0(2z^{1/2}R^{1/2}t^{1/2})dz = \sum_{k=0}^{\infty} \frac{(Rt)^k}{(k!)^2} \gamma(k+1, y). \tag{14}$$

The response to any inlet datum $\varphi(t)$ is then determined by the Green's functions via the convolution integrals

$$T_w(x, y, t) = \int_0^t T_w^G(x, y, t')\varphi(t-t')dt'$$

$$T_a(x, y, t) = \int_0^t T_a^G(x, y, t')\varphi(t-t')dt' \tag{15}$$

$$T_b(x, y, t) = \int_0^t T_b^G(x, y, t')\varphi(t-t')dt'.$$

Step, Ramp, and Exponential Responses

The explicit analytical expressions for $T_w(x, y, t)$, $T_a(x, y, t)$, $T_b(x, y, t)$, $\bar{T}_a(N_a, t)$, and $\bar{T}_b(N_b, t)$ have been processed for several meaningful choices of $\varphi(t)$, simulating the most common transient operations. In particular the step response ($\varphi = 1$), ramp response ($\varphi = \alpha t$), and exponential response ($\varphi = \exp\alpha t$) have been considered. A much wider range of possible transient responses is covered by these results, since one must bear in mind that, if the input $\varphi(t)$ is a linear combination of the previous cases, the overall output is the same linear superposition of the corresponding outputs. All temperatures have been computed by numerically performing the underlying integrals of Bessel functions; such a procedure does not present any problem, since only integrations of smooth continuous functions on bounded regular domains are involved. Anyway, the results have been checked by comparison with the analytical expressions that can be obtained by permissible power series expansions of the Bessel functions. In this way only elementary integrations of exponentials and powers are left, and all temperatures are expressed as an infinite sum of incomplete gamma functions

$$\gamma(n+1, z) = \int_0^z t^n e^{-t} dt \tag{16}$$

whose computation is very accurate and efficient, since

$$\gamma(n+1, x) = n!\left(1 - e^{-x} \sum_{k=0}^{n} \frac{x^k}{k!}\right) = n! e^{-x} \sum_{k=n+1}^{\infty} \frac{x^k}{k!} \tag{17}$$

and at least one of the two representations converges very fast, according to the different values of n and x. As an example, the series representation of the exponential response is given below

$$T_w(x, y, t) = e^{\alpha t} e^{-x} \sum_{n=0}^{\infty} \frac{\gamma[n+1, (1+R+\alpha)t]}{(1+R+\alpha)^{n+1}}$$

$$\left\{\frac{x^n}{(n!)^2} + \sum_{k=1}^{n} \frac{R^k}{k!(k-1)!} \frac{x^{n-k}}{[(n-k)!]^2} \gamma(k, y)\right\}$$

$$T_a(x, y, t) = e^{\alpha t} e^{-x} + e^{\alpha t} e^{-x}$$

$$\sum_{n=0}^{\infty} \frac{\gamma[n+1, (1+R+\alpha)t]}{(1+R+\alpha)^{n+1}} \left[\frac{x^{n+1}}{n!(n+1)!}\right.$$

$$\left. + \sum_{k=1}^{n} \frac{R^k}{k!(k-1)!} \frac{x^{n-k+1}}{(n-k+1)!(n-k)!} \gamma(k, y)\right]$$

$$T_b(x, y, t) = e^{\alpha t} e^{-x} \sum_{n=0}^{\infty} \frac{\gamma[n+1, (1+R+\alpha)t]}{(1+R+\alpha)^{n+1}}$$

$$\sum_{k=0}^{n} \frac{R^k}{(k!)^2} \cdot \frac{x^{n-k}}{[(n-k)!]^2} \gamma(k+1, y) \tag{18}$$

$$\bar{T}_a(N_a, t) = e^{\alpha t} e^{-N_a} + e^{\alpha t} \frac{e^{-N_a}}{N_b}$$

$$\sum_{n=0}^{\infty} \frac{\gamma[n+1, (1+R+\alpha)t]}{(1+R+\alpha)^{n+1}} \sum_{k=0}^{n} \frac{R^k}{(k!)^2}$$

$$\frac{N_a^{n-k+1}[N_b^{k+1} e^{-N_b} + (N_b - k)\gamma(k+1, N_b)]}{(n-k+1)!(n-k)!}$$

$$\bar{T}_b(N_b, t) = e^{\alpha t} \frac{1}{N_a} \sum_{n=0}^{\infty} \frac{\gamma[n+1, (1+R+\alpha)t]}{(1+R+\alpha)^{n+1}}$$

$$\sum_{k=0}^{n} \frac{R^k}{(k!)^2} \frac{\gamma(k+1, N_b)\gamma(n-k+1, N_a)}{[(n-k)!]^2}.$$

The numerical integration and the series expansion are very inexpensive in terms of computational time. The illustrative examples reported in Figs. 1–12 refer to the option $E = R = 1$ (thus $N_a = N_b = 2$ NTU), and α has been taken to be unity in the ramp and exponential responses. The asymptotic values for $t \to \infty$ in the step response reproduce, of course, the steady conditions with $g_a(y) = 1$ and $g_b(x) = 0$, and are in perfect agreement with previous results available in the literature (Baclic and Heggs, 1985). In addition, it is clear that the propagation speed of disturbances in the present crossflow heat exchanger has been assumed to be well approximated by infinity (as is usual for gas-to-gas exchangers), since the

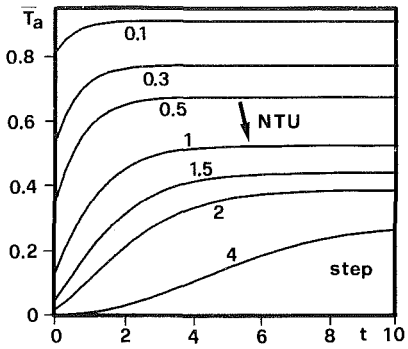

Fig. 1 Mean exit temperature of the stepped gas

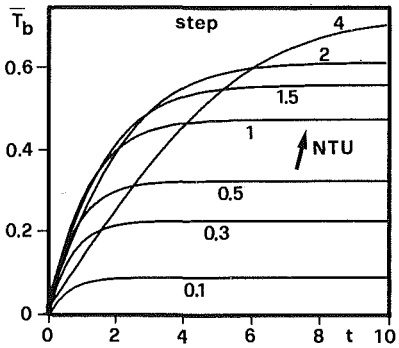

Fig. 2 Mean exit temperature of the unstepped gas

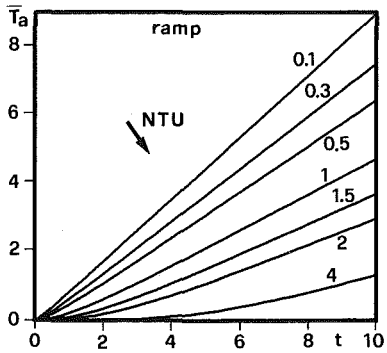

Fig. 3 Ramp response for the mean exit temperature of the hot gas

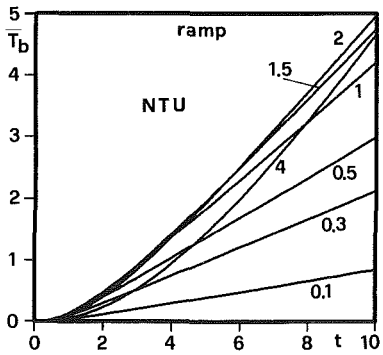

Fig. 4 Ramp response for the mean exit temperature of the cold gas

response times of the heat exchanger are much shorter than the fluid dwell times. Therefore, as it has been pointed out already by Romie (1983), any sudden change taking place at the inlet section $x=0$ is felt immediately, without any time lag, by the whole primary fluid in the unit, only with an exponential

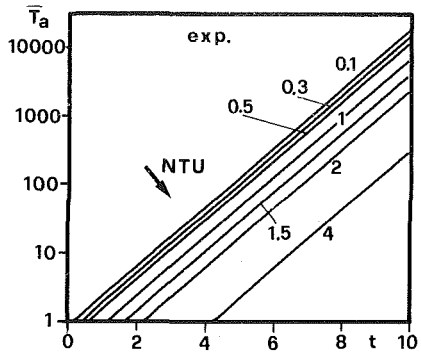

Fig. 5 Exponential response for the mean exit temperature of the hot gas

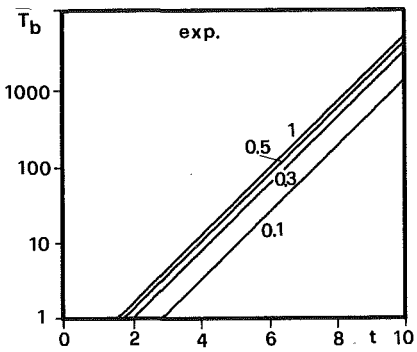

Fig. 6 Exponential response for the mean exit temperature of the cold gas

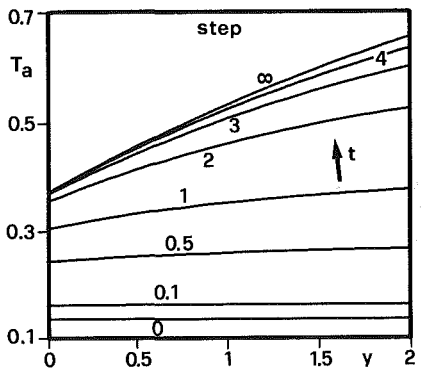

Fig. 7 Spatial distribution of the stepped gas temperature on the exit section

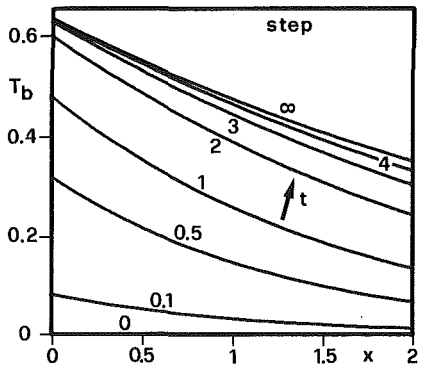

Fig. 8 Spatial distribution of the unstepped gas temperature on the exit section

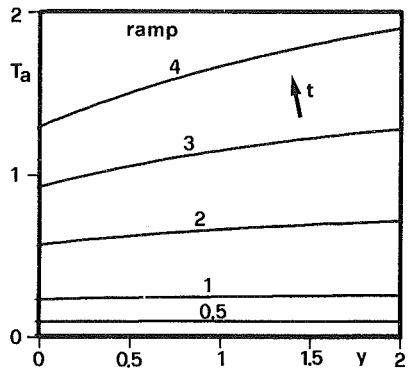

Fig. 9 Ramp response of the spatial distribution for the hot gas temperature in the exit section

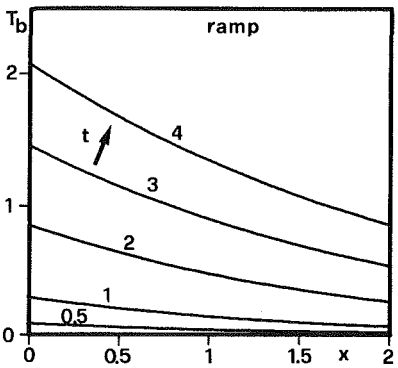

Fig. 10 Ramp response of the spatial distribution for the cold gas temperature in the exit section

damping for increasing x, as described by the first addend of equation (13b). The mean exit temperatures $\bar{T}_a$, and $\bar{T}_b$ have been plotted versus time for a wide range of NTU, for the step (Figs. 1, 2), ramp (Figs. 3, 4) and exponential (Figs. 5, 6) response. The results for the step response (Figs. 1, 2) are quite in agreement with the results contained in Fig. 1(c) of Romie (1983) for NTU $= E = R = 1$; comparisons for other transient cases are not possible because there are no available data in the literature. The spatial distribution of the temperatures for both fluids in their exit sections are then plotted in Figs. 7–10 for various times and NTU $= 1$, for step and ramp responses. At last the transient two-dimensional distributions of the fluid temperatures are shown in Figs. 11, 12 for the step response and NTU $= 1$; they give an immediate and clear insight into the crossflow exchanger behavior. The general solutions can be used easily also to investigate the effects of R and $E \neq 1$

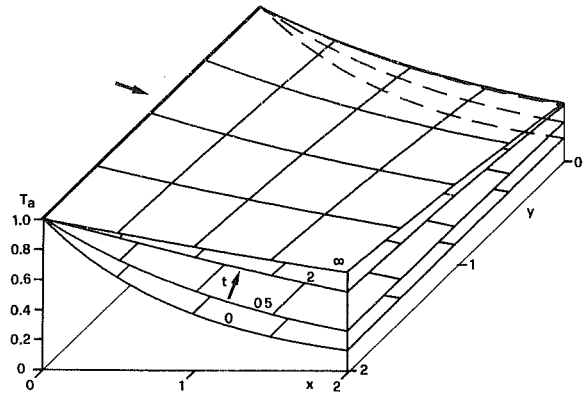

Fig. 11 Two-dimensional transient distribution of the stepped gas temperature

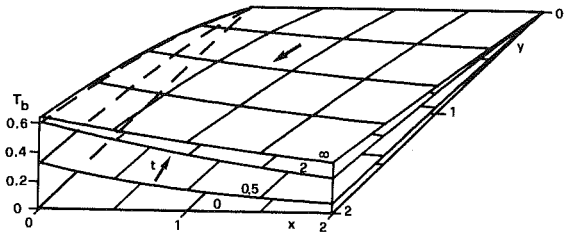

Fig. 12 Two-dimensional transient distribution of the unstepped gas temperature

(interesting for industrial practice); this will be a goal of future work.

Acknowledgments

This work was financially supported by the CNR.

References

Baclic, B. S., and Heggs, P. J., 1985, "On the Search for New Solutions of the Single-Pass Crossflow Heat Exchanger Problem," *Int. J. Heat Mass Transfer*, Vol. 28, pp. 1965–1976.

Dusinberre, G. M., 1959, "Calculation of Transients in a Cross-Flow Heat Exchanger," ASME JOURNAL OF HEAT TRANSFER, Vol. 81, pp. 61–67.

Gartner, J. R., and Harrison, H. L., 1965, "Dynamic Characteristics of Water-to-Air Cross-Flow Heat Exchangers," *Trans. ASHRAE*, Vol. 71, pp. 212–219.

Myers, G. E., Mitchell, J. W., and Norman, R. F., 1967, "The Transient Response of Crossflow Heat Exchangers, Evaporators, and Condensers," ASME JOURNAL OF HEAT TRANSFER, Vol. 89, pp. 75–80.

Romie, F. E., 1983, "Transient Response of Gas-to-Gas Crossflow Heat Exchangers With Neither Gas Mixed," ASME JOURNAL OF HEAT TRANSFER, Vol. 105, pp. 563–570.

Yamashita, H., Izumi, R., and Yamaguchi, S., 1978, "Analysis of the Dynamic Characteristics of Crossflow Heat Exchangers With Both Fluids Unmixed," *JSME Bulletin*, Vol. 21, pp. 479–485.

Second-Law-Based Thermoeconomic Optimization of Two-Phase Heat Exchangers

S. M. Zubair
Assoc. Mem. ASME
Copeland Corporation,
Sidney, OH 45365-0669

P. V. Kadaba
Mem. ASME

R. B. Evans
Mem. ASME

The George W. Woodruff School
of Mechanical Engineering,
Georgia Institute of Technology,
Atlanta, GA 30332-0405

This paper presents a closed-form analytical method for the second-law-based thermoeconomic optimization of two-phase heat exchangers used as condensers or evaporators. The concept of "internal economy" as a means of estimating the economic value of entropy generated (due to finite temperature difference heat transfer and pressure drops) has been proposed, thus permitting the engineer to trade the cost of entropy generation in the heat exchanger against its capital expenditure. Results are presented in terms of the optimum heat exchanger area as a function of the exit/inlet temperature ratio of the coolant, unit cost of energy dissipated, and the optimum overall heat transfer coefficient. The total heat transfer resistance represented by $(1/U = C1 + C2\ Re^{-n})$ *in the present analysis is patterned after Wilson (1915) which accommodates the complexities associated with the determination of the two-phase heat transfer coefficient and the buildup of surface scaling resistances. The analysis of a water-cooled condenser and an air-cooled evaporator is presented with supporting numerical examples which are based on the thermoeconomic optimization procedure of this paper.*

Introduction

In the analysis and design of heat exchangers, it is essential to give due consideration to the rate of entropy generation caused by the irreversible processes that take place inside the heat exchanger. Such considerations are very important from an engineering point of view, since a knowledge of the component irreversibilities that lead to the production of entropy inside an industrial system makes it possible to evaluate the relative contribution of these irreversible processes in terms of the useful work consumed. Such a view along with the aid of the "Second Law of Thermodynamics" makes it possible to express the rate form of the entropy equation as an equality rather than the commonly expressed form of an inequality. This concept of equality has been investigated in some detail by Evans (1966) and the impact of entropy generation on the optimum design of heat exchangers has been studied by McClintock (1951) and Bejan (1977, 1978).

Minimization of the combined cost of entropy generation with the annualized capital cost of the thermal component is generally defined as second-law-based thermoeconomic analysis. This method was first introduced by Tribus and Evans (1962, 1963) using sea water desalination systems as an illustration. A similar approach used to determine the quantities of insulation required for any thermal system having multiple paths for heat exchange between the system and the environment was proposed by Loper (1979). London and Shah (1982, 1983) discussed in detail the thermodynamic irreversibilities that exist in any real engineering system. They also demonstrated a method to attach monetary values to the component irreversibilities generated in the condenser of a powerplant with the purpose of developing various tradeoff factors. The concept of thermoeconomic analysis was recently applied to the design and synthesis of feedwater heaters in steam powerplants by Evans et al. (1983). In this paper, the method is further expanded to develop the design optimization procedures for condensers and evaporators.

Lost Work or Irreversibility

The irreversibilities generated during the operation of heat exchangers are mainly due to the finite temperature difference heat transfer between the hot and cold streams, and those streams experiencing single-phase or two-phase pressure drops within the core, end connections, and piping. The mathematical expressions for the lost work or irreversibility associated with the heat transfer and pressure drops are presented in this section.

Heat Transfer – Lost Work. Consider a general two-fluid heat exchanger operating under steady state as shown schematically in Fig. 1. The two-phase heat exchanger has been shown as a special case in this figure. Using the property values, the rate of entropy generation in such a heat exchanger can be expressed as

$$\dot{S} = \dot{S}_1 + \dot{S}_2 = \dot{m}_1(s_{1,e} - s_{1,i}) + \dot{m}_2(s_{2,e} - s_{2,i}) \tag{1}$$

If the fluid of stream 1 is assumed to be a perfect gas (PG) then

$$\dot{S}_1 = \dot{C}_1[\ln(T_{1,e}/T_{1,i}) + (R/c_p)_1 \ln(P_{1,i}/P_{1,e})] \tag{1a}$$

or if it is an incompressible liquid (ICL)

$$\dot{S}_1 = \dot{C}_1 \ln(T_{1,e}/T_{1,i}) \tag{1b}$$

It may be noted that similar equations can be written if fluid 2 is also a single-phase fluid. Equation (1) can be used directly for the fluids experiencing change of phase.

The two-phase pressure drop experienced by the flowing fluid causes the lowering of saturation temperatures resulting in the reduction of the (pseudo)maximum heat capacity when compared to the traditional value of infinity used for the case

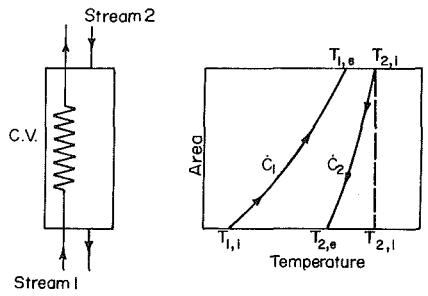

Fig. 1 Heat exchanger and its temperature area diagram: $\dot{C}_1 < \dot{C}_2$

Contributed by the Heat Transfer Division and presented at the National Heat Transfer Conference, Denver, Colorado, August 1985. Manuscript received by the Heat Transfer Division June 6, 1985.

of zero pressure drop. In spite of this reduction, the ratio of the heat capacities ($\dot{C}_{\min}/\dot{C}_{\max}$) will be very nearly equal to the zero value. In this analysis, the temperature effectiveness–N_{tu} relationship for the limiting case of the zero heat capacity ratio has been used. Zubair (1985a) provided quantitative justification for this assumption when applied to several types of heat exchangers. According to Stoecker (1958), for the case of the condenser, if the fraction of superheat when compared to the latent heat of condensation (particularly for the fluorocarbon refrigerants) is small, the assumption of the average maximum heat capacity approaching infinity is still valid. Even in the case of an evaporator having suction gas superheat, the above assumption is equally applicable.

The heat balance for the heat exchanger represented in Fig. 1 is given by

$$\dot{Q} = \dot{C}_1(T_{1,e} - T_{1,i}) = \dot{C}_2(T_{2,i} - T_{2,e}) \tag{2}$$

Coupling this equation with the definition of the temperature effectiveness of the heat exchanger for the case $\dot{C}_1 = \dot{C}_{\min}$

$$\epsilon \triangleq (T_{1,e} - T_{1,i})/(T_{2,i} - T_{1,i}) \tag{3}$$

permits reducing equation (1*b*) for the limiting case of $\dot{C}_{\max} = \infty$, i.e., for a condenser (or evaporator), to

$$\dot{S}_H = \dot{C}_{\min}\left[\ln(\alpha) - \frac{(\alpha-1)\epsilon}{\alpha - 1 + \epsilon}\right] \tag{4}$$

where α is defined by: $\alpha = T_{1,e}/T_{1,i}$; the effectiveness of the heat exchanger is given by

$$\epsilon = 1 - \exp(-N_{tu}) \tag{5}$$

where $N_{tu} = UA/\dot{C}_{\min}$. The lost work corresponding to the heat transfer takes the form

$$T_0\dot{S}_H = \dot{T}_0 C_{\min}\left[\ln(\alpha) - \frac{(\alpha-1)(\exp(N_{tu})-1)}{\alpha\exp(N_{tu}) - 1}\right] \tag{6}$$

Here T_0 is the absolute reference temperature of the natural sink or the thermal reservoir (ambient air or available cooling water source). London (1982) has provided philosophical and pedagogical implications for choices of reference temperatures in thermal designs but recommends that the T_0 described above should be considered as a good choice.

Single-Phase Pressure Drop – Lost Work. It is desirable to keep the pressure drop of the single-phase fluid to a minimum. The lost work associated with this pressure drop needs to be considered. Zubair (1985a) showed that the effect of pressure drop on the temperature is small, and it is included in equation (6). It should be noted that the cost and the power requirements associated with the circulation of this single-phase fluid are expensive; hence, it should be included in any thermoeconomic analysis of heat exchangers. The irreversibility associated with the single-phase pressure drop experienced by the fluid moving through the heat exchanger can be modeled after London and Shah (1983). This relationship is given by

$$T_0\dot{S}_A = (T_0/T_{A,\ln})\dot{m}_{sp}(\Delta P_{sp}/\rho) \tag{7}$$

Additional equations used in the estimation of irreversibilities (lost work) associated with the single-phase pressure drop of the fluid (equation (7)) are presented in Table 1. Here, for the case of a liquid-cooled condenser, turbulent internal flow is considered. The effect of hydrostatic pressure on the lost work will be additive in the expression for the pressure drop. It will not alter the general optimization procedure presented here; but the cost required to overcome this addi-

Nomenclature

A = heat exchanger total heat transfer area on single-phase side, m^2
A_c = heat exchanger minimum flow area, m^2
A_1, A_2 = constants in equation $1/U = A_1 + A_2 V^{-n}$
$C1$, $C2$ = constants in equation $1/U = C1 + C2\ \mathrm{Re}^{-n}$
$\dot{C}$ = capacitance of the heat exchanger, kW/°C
D = diameter of the tubing, m
D_H = hydraulic diameter, m
f = large (Darcy–Weisbach) friction factor (see Table 1)
G = stream mass flux, kg/s-m^2
K_v = cost coefficient associated with single-phase pressure drop (units of $K_v V^m$-\$/m^{2}hr)
L = length of the tubing, m
$\dot{m}$ = mass flow rate, kg/s
N_{tu} = number of heat transfer units
$\dot{Q}$ = heat rate, kW
$\dot{S}$ = entropy generation, kW/K
s = entropy, an extensive property of a system, kJ/kg-K
$T_{A,\ln}$ = log mean temperature of the single-phase fluid, K
$T_{B,\mathrm{avg}}$ = average two-phase temperature, K
T_0 = reference temperature of the system, K (see discussion at the end of equation (6))
U = overall heat transfer coefficient, kW/m^2-C
V = single-phase velocity, m/hr
$\dot{W}$ = pumping power, kW
x = quality of the fluid
$\dot{z}$ = annualized capital cost of owning and maintaining the heat exchanger, \$/m^2-yr
UA = overall heat conductance of the heat exchanger, kW/°C
$T_0\dot{S}$ = lost work or irreversibility, kW
ΔP = pressure drop in the heat exchanger, Pa
ΔT = temperature difference of the fluid, °C
α = exit/inlet temperature ratio of the single-phase fluid = $T_{1,e}/T_{1,i}$
β = ratio of the unit cost of entropy generation associated with irreversible heat transfer to the cost per unit overall heat conductance of the heat exchanger
$\dot{\Gamma}$ = total annual cost of owning and operating the two-phase heat exchanger, \$/yr
γ_{UA} = cost per unit overall heat conductance, \$-°C/kW-hr
ϵ = temperature effectiveness of the heat exchanger
λ = unit cost of lost work, \$/kW-hr

Subscripts

A = single phase
B = two phase
C = Carnot (see β_C in equation (21))
H = heat transfer (see equation (16))
e = exit
f = friction
i = inlet
m = modified (also denotes momentum component in equation (9))
ml = modified
Q = heat transfer (see equation (A1))
sp = single phase
tp = two phase
v = vapor phase
l = liquid phase

Superscript

$*$ = optimum

Table 1 Equations used in estimation of irreversibilities (lost work) associated with pressure drop of single-phase fluid

	$(\Delta p)_{sp}/\rho$	Friction factor	$T_0\dot{S}_A$
Liquid heat exchanger (internal flow)	$\dfrac{fLV^2}{2g_cD}$	$\dfrac{f}{8}=a\,\mathrm{Re}^{-b}$	K'_vAV^{3-b}
Gas/air heat exchanger (external flow)	$\dfrac{G_{\max}^2}{2g_c\rho^2}\dfrac{L}{D_H}\left(\dfrac{D_H}{S_T}\right)^{k1}\left(\dfrac{S_L}{S_T}\right)^{k2}f'$	$f'=c\,\mathrm{Re}^{-d}$	$K''_v\,A\,V_{\max}^{3-d}$

$\mathrm{Re}=\dfrac{\rho VD}{\mu}$; $\mathrm{Re}=\dfrac{G_{\max}D_H}{\mu}$

For turbulent internal flow: $a=0.023$, $m=3-b$, $b=0.2$ after Colburn, $n=1-b$ see Rohsenow (1981)

For inline tube arrangement external flow: $c=1.92$, $d=0.115$, $k1=0.4$, $k2=0.6$, $m=3-d$, $n=1-d$

$D_H=4\dfrac{\text{Free volume in tube bank}}{\text{Exposed surface area of tube}}$ $\qquad K_v=\lambda_AK'_v$ or $\lambda_AK''_v$

$K'_v=2a\dfrac{T_0}{T_{A,\ln}}\dfrac{\rho}{2g_c}\left(\dfrac{\rho D}{\mu}\right)^{-b}$; $\qquad K''_v=c\dfrac{T_0}{T_{A,\ln}}\dfrac{\rho}{2g_c}\dfrac{A_c}{A}\left(\dfrac{L}{D_H}\right)\left(\dfrac{D_H}{S_T}\right)^{k1}\left(\dfrac{S_L}{S_T}\right)^{k2}\left(\dfrac{\rho D_H}{\mu}\right)^{-d}$

tional pressure drop will generate a different numerical result for the optimum velocity. The pressure drop relationships and the associated equations for the estimation of the lost work of an air-cooled evaporator with flow across tube banks having plain and extended surfaces, shown in Table 1, are based on the work of Gunter and Shaw (1945) and that contained in the *Heat Exchanger Design Handbook*, Vol. 2 (1983). The footnote to Table 1 shows the values of typical constants used in the numerical illustrations presented in this paper. The heat exchanger assembly is made out of repeating unit cells, and the hydraulic diameter for such a cell is defined in the footnote to Table 1. The power law correlations suggested in this table have been used for this optimization procedure. In order to preserve this procedure in its entirety, it is recommended that the users consider piecewise power law fits for limited ranges of Reynolds numbers, both for laminar and turbulent flows. Designers usually avoid transitional flows because of the associated hydraulic implications in the design of pumping equipment.

Two-Phase Pressure Drop – Lost Work. The friction factor and the procedure to evaluate the resulting irreversibility due to the pressure drop associated with the two-phase fluid has to be patterned differently from that of the single-phase fluid. In this mode, the vapor phase flow velocity inside the tubes significantly influences the pressure drop. For the purpose of this analysis, the two-phase flow rate at any cross section is treated as a constant. In order to evaluate the irreversibilities in these heat exchangers, the two-phase pressure drop model proposed by London and Shah (1983) is used. According to their model the lost work associated with the two-phase flow can be expressed as

$$T_0\dot{S}_B=(T_0/T_{B,\text{avg}})\dot{m}_{tp}[(\Delta P)_{tp}/(2\rho_v)] \tag{8}$$

It is recognized that the two-phase pressure drops of these heat exchangers are kept at a small value when they are part of a closed thermal system. In such cases the irreversibilities associated with these pressure drops are also small when compared to that associated with the finite temperature difference heat transfer between the two fluids of the heat exchanger. In a refrigeration system, in order to overcome these pressure drops on the two-phase side of the condenser and evaporator, the compressor has to work over a greater pressure difference when compared to the case having zero pressure drop. The incremental cost associated with these inevitable pressure drops can be expensive, and it has a monetary value. Hence, this term needs to be considered in the thermoeconomic analysis. In the case of a multicomponent fluid system, as long as the fraction of the pressure drop with respect to the inlet pressure is negligible, the model discussed by London and Shah (1983) can still be used. These observations clearly demonstrate the need to evaluate the entropy generation term associated with these pressure drops in the condenser and the evaporator in addition to the heat transfer irreversibilities.

Following the method of Traviss et al. (1973), the total pressure drop associated with the two-phase flow for the case when the body forces are neglected can be described as the sum of pressure drops due to frictional effects and momentum changes

$$(\Delta P)_{tp}=(\Delta P_f+\Delta P_m)=\frac{L}{(x_e-x_i)}\int_{x_i}^{x_e}\left[\left(\frac{dP}{dz}\right)_f+\left(\frac{dP}{dz}\right)_m\right]dx \tag{9}$$

where

$$\left(\frac{dP}{dz}\right)_f=\frac{-0.09\mu_v^{0.2}G^{1.8}x^{1.8}}{\rho_vg_cD^{1.2}}(1+2.85\chi_{tt}^{0.523})^2 \tag{10}$$

and

$$\left(\frac{dP}{dz}\right)_m=\frac{-G^2}{\rho_vg_c}\left(\frac{dx}{dz}\right)\left[2x+(1-2x)\left\{\left(\frac{\rho_v}{\rho_l}\right)^{1/3}+\left(\frac{\rho_v}{\rho_l}\right)^{2/3}\right\}-2(1-x)\left(\frac{\rho_v}{\rho_l}\right)\right] \tag{11}$$

The Martinelli parameter (χ_{tt}) in equation (10) is

$$\chi_{tt}=\left(\frac{\mu_l}{\mu_v}\right)^{0.1}\left(\frac{1-x}{x}\right)^{0.9}\left(\frac{\rho_v}{\rho_l}\right)^{0.5} \tag{12}$$

Integrating equation (9) by using equations (10), (11), and (12) results in

$$\Delta P_f=\frac{-LC_1}{(x_e-x_i)}[0.36x^{2.8}+2C_2x^{2.33}(0.43-0.14x-0.29x^2)+C_2^2x^{1.86}(0.54-0.33x)]\Big|_{x_i}^{x_e} \tag{13}$$

where

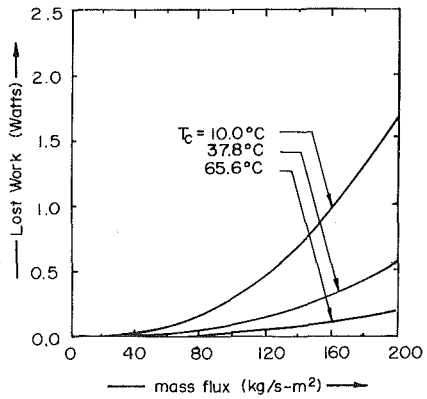

Fig. 2 Effect of condensing temperature on lost work associated with two-phase pressure drop of a heat exchanger

$$C_1 = \frac{0.09\mu_v^{0.2}G^{1.8}}{\rho_v g_c D^{1.2}} \tag{14a}$$

$$C_2 = 2.85\left(\frac{\mu_l}{\mu_v}\right)^{0.053}\left(\frac{\rho_v}{\rho_l}\right)^{0.26} \tag{14b}$$

and

$$\Delta P_m = \frac{-G^2}{\rho_v g_c (x_e - x_i)}\left[x^2 + (x-x^2)\left\{\left(\frac{\rho_v}{\rho_l}\right)^{1/3} + \left(\frac{\rho_v}{\rho_l}\right)^{2/3}\right\} - 2(x - x^2/2)\left(\frac{\rho_\varphi}{\rho_l}\right)\right]\Bigg|_{x_i}^{x_e} \tag{15}$$

The lost work (a measure of irreversibilities) associated with the two-phase pressure drop as a function of mean condensing temperature and the total mass flux for an R-22 condenser is represented in Fig. 2. The increase in lost work due to the pressure drop at a lower condensing temperature for the constant mean flow reflects the effect of decreasing vapor density. The near parabolic nature of increases in the pressure drop as a function of the total mean mass flux at a constant temperature is apparent. Similar trends are expected for the case of an evaporator.

In the design and operation of two-phase heat exchangers, the lost work due to finite temperature difference heat transfer ($T_0\dot{S}_H$) is generally much larger than the values for the two-phase pressure drop shown in Fig. 2. It should be noted that in the following section the cost associated with the lost work due to the two-phase pressure drop is included with the annualized capital cost of owning the heat exchanger itself (see equation (26)).

Thermoeconomic Optimization

The objective of thermoeconomic optimization is to minimize the annualized total cost of owning and operating the system. The total cost is composed of additive terms that measure the cost associated with the lost work (due to the irreversibilities of the heat transfer process, and the pressure drops of the flowing fluids), and the annualized capital costs of the equipment.

In this analysis, the annualized capital cost of owning the heat exchanger is represented as ($\dot{Z} = \dot{z}A + \dot{k}_0$). Here, $\dot{k}_0$ represents the fixed maintenance cost and any other extraneous annual costs that apply to the heat exchanger as a whole. Thus, the total annual cost rate ($\dot{\Gamma}$) for owning and operating the two-phase heat exchanger can be described as

$$\dot{\Gamma} = (\dot{z}A + \dot{k}_0 + \lambda_A T_0 \dot{S}_A + \lambda_B T_0 \dot{S}_B + \lambda_H T_0 \dot{S}_H) \tag{16}$$

The unit costs (λ) shown in equation (16) can be determined by an essergy[1] analysis (a second-law-based thermoeconomic technique) of the interconnecting streams. A typical example of generating such unit costs for essergy transmitting components such as pumps, fans or compressors has been discussed by Zubair et al. (1985b, 1985c). Defining the cost per unit overall heat conductance as

$$\gamma_{UA} = (\dot{z}A + \dot{k}_0 + \lambda_A T_0 \dot{S}_A + \lambda_B T_0 \dot{S}_B)/(UA) \tag{17}$$

and noting the definition of the number of transfer units ($N_{tu} = UA/\dot{C}_{\min}$) results in

$$\dot{\Gamma} = \gamma_{UA}\dot{C}_{\min}N_{tu} + \lambda_H T_0 \dot{S}_H \tag{18}$$

Using equation (6) for the lost work due to heat transfer, the cost equation described above can be written as

$$\dot{\Gamma} = \dot{C}_{\min}\left[\gamma_{UA}N_{tu} + \lambda_H T_0\left\{\ln(\alpha) - \frac{(\alpha-1)(\exp(N_{tu})-1)}{\alpha\exp(N_{tu})-1}\right\}\right] \tag{19}$$

Optimum Number of Transfer Units. Differentiating equation (19) with respect to N_{tu} for a fixed heat rate of the condenser or evaporator, a fixed exit/inlet temperature ratio for the single-phase fluid (α), and fixed cost parameters (λ_H) and (γ_{UA}), leads to the minimization of the overall cost. The resulting dimensionless ratio is

$$\beta \triangleq \frac{\lambda_H T_0}{\gamma_{UA}} = \frac{\{\alpha\exp(N_{tu}^*) - 1\}^2}{(\alpha-1)^2\exp(N_{tu}^*)} \tag{20}$$

Introducing the dimensionless cost parameter β_C, which includes the effect of α, the exit/inlet temperature ratio,

$$\beta_C \triangleq (\beta/\alpha)(\alpha-1)^2 \tag{21}$$

and substituting equation (21) in equation (20) results in a quadratic equation containing the optimum N_{tu} (denoted by *)

$$[\alpha\exp(N_{tu}^*) - 1]^2 - \beta_C[\alpha\exp(N_{tu}^*) - 1] - \beta_C = 0 \tag{22}$$

and the general solution to this quadratic equation is given by

$$[\alpha\exp(N_{tu}^*) - 1] = \left\{\frac{\beta_C \pm \sqrt{\beta_C^2 + 4\beta_C}}{2}\right\} \tag{23}$$

Recognizing that the optimum value of N_{tu}^* in equation (23) is always positive

$$N_{tu}^* = \ln\left[\frac{1}{\alpha}\{1 + (\beta_C/2)\}\{1 + \sqrt{1 + (4/\beta_C)}\}\right] \tag{24}$$

The trends in the variation for the values of the optimum number of transfer units of the heat exchanger (N_{tu}^*) for condensers and evaporators are shown in Fig. 3. The abscissa for this plot is β (ratio of the unit cost of entropy generation associated with irreversible heat transfer to the cost per unit overall heat conductance of the heat exchanger) with α (the ratio of the exit/inlet temperatures of the single-phase fluid) as the parameter. It should be noted that departure of α from unity represents a larger temperature range for the single-phase fluid used in these types of heat exchangers.

Figure 3(*a*) is for the condenser application. For a fixed heat rate, an increase in the value of α, at a constant β, represents an increased temperature range with a corresponding decrease in the heat capacity of the single-phase fluid. This situation will result in a higher value for the optimum number of transfer units. For a given heat capacity of the single-phase fluid, an increase in the value of β can be accomplished either by an increase in the unit cost of lost work due to heat transfer or by lowering the cost per unit overall heat conductance. The

[1] The word essergy means the essential aspect of energy or the useful available energy. This was first introduced by Evans in his doctoral dissertation at Dartmouth (1969). Evans et al. (1983) may be consulted for further discussion on this concept as applied to various types of thermal systems.

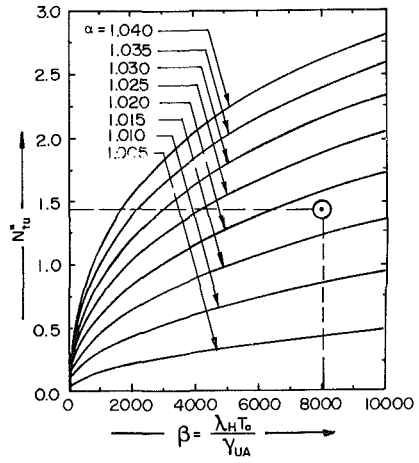

3a. Condenser

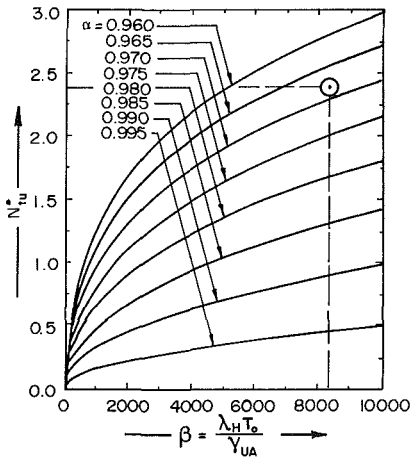

3b. Evaporator.

Fig. 3 Optimum number of transfer units and dimensionless ratio

net result is to increase the value of the optimum number of transfer units of the heat exchanger which implies an increase in the optimum heat transfer area. A similar interpretation applies for the case of the evaporator presented in Fig. 3(*b*). Here, it should be noted that a decrease in the value of α implies that the single-phase fluid used in an evaporator is experiencing a larger temperature difference.

Optimum Single-Phase Fluid Velocity. The optimum single-phase fluid velocity either for finned-tube heat exchangers or for the tube side of shell and tube heat exchangers can be formulated by describing the total heat transfer resistance as $(1/U = C1 + C2\ \mathrm{Re}^{-n})$. This resistance model is patterned after Wilson (1915) and Rich (1973). For the case of a specified geometry and the single-phase fluid flowing in the heat exchanger, the thermal resistance can be reduced to $(1/U = A_1 + A_2 V^{-n})$. By representing the cost of the lost work associated with the single-phase fluid as $\lambda T_0 \dot{S}_A = K_v A V^m$ (the typical values of m are suggested in Table 1), the cost of the heat exchanger per unit heat conductance becomes

$$\gamma_{UA} = \left\{\dot{z} + \frac{\dot{k}_0}{A} + K_v V^m + \frac{\lambda_B T_0 \dot{S}_B}{A}\right\}(A_1 + A_2 V^{-n}) \quad (25)$$

Since equation (25) is being minimized with respect to the single-phase velocity (V), with no change of flow rate and other conditions on the two-phase side, it is possible to define the modified annualized cost of ownership per unit area of the heat exchanger as

$$\dot{z}_m = \dot{z} + \dot{k}_0/A + (\lambda_B T_0 \dot{S}_B/A) \quad (26)$$

so that equation (25) becomes

$$\gamma_{UA} = (\dot{z}_m + K_v V^m)(A_1 + A_2 V^{-n}) \quad (27)$$

Minimizing γ_{UA} with respect to V results in the expression for the optimum condition given by

$$mA_1 K_v V^{m-1} + (m-n)A_2 K_v V^{m-n-1} - nA_2 \dot{z}_m V^{-n-1} = 0 \quad (28)$$

In the typical operation of two-phase heat exchangers, the convective heat transfer coefficient on the two-phase side may be assumed to be large in comparison to the single-phase convective heat transfer coefficient. This assumption implies that the two-phase heat transfer resistance is negligible (case of $A_1 = 0$) and the first term in equation (28) can be eliminated. This situation results in a closed-form solution for the optimum velocity which is given by

$$V^* = \left[\frac{n}{m-n}(\dot{z}_m/K_v)\right]^{1/m} \quad (29)$$

where the values of m, n, and K_v for the tube side of a liquid heat exchanger (internal flow) and the shell side of a gas/air heat exchanger (external flow) are set forth in Table 1. An initial value for the optimum velocity V^* can be estimated by using equation (29), which neglects the two-phase heat transfer resistance. This initial value can be used in a trial and error procedure for determining the final value of the optimum velocity V^* as obtained from equation (28). The difference between these two values of optimum velocities will provide an insight into the extent of the influence of the finite heat transfer resistance of the two-phase fluid on the final optimum velocity. It is noted that in a good heat exchanger design, the use of extended surfaces on the single-phase fluid (gas) side permits balancing of the thermal resistances on both sides of the primary heat transfer surface.

Optimum Area. The designer can use either Fig. 3(*a* or *b*) or the equations that led to the development of these figures for the determination of the optimum N_{tu}. The inlet temperature to the heat exchanger and the temperature ratio of the single-phase fluid α are selected. The cost parameter associated with the definition of β in equation (20) and β_C in equation (21) along with equation (24) permits the determination of the optimum N^*_{tu}. Equation (29) can be used for the selection of the optimum single-phase velocity (V^*) for the case when the thermal resistance on the two-phase fluid side is negligible. For the case when the thermal resistances on both sides of the fluids are comparable, the preliminary estimate of the optimum velocity can be replaced by the final value obtained from the numerical solution of equation (28). Having established these values, the optimum heat transfer area for the heat exchanger with a fixed heat transfer rate is given by

$$A^* = \frac{N^*_{tu}\dot{Q}}{U^* T_{1,i}\,|(\alpha - 1)|} \quad (30)$$

The following illustrative examples depict the use of these equations in obtaining second-law-based optimum heat exchanger parameters as well as providing the basis for generating Fig. 3(*a* and *b*).

Example 1. The condensing area is to be specified for a water-cooled R-22 condenser having a load of 21.1 kW. This value corresponds to a design cooling capacity of 17.6 kW for the refrigeration system having a coefficient of performance of 5.0. Water from a cooling tower at 29.4°C enters the condenser.

A shell and tube condenser will be used. According to the Wilson type representation, the unit overall heat transfer resistance for this type of heat exchanger is assumed to be $(1/U) = A_1 + A_2 V^{-0.8}$ (m²-C/W), where the numerical values for the constants are: $A_1 = 0.000881$, $A_2 = 0.1158$ (turbulent

Table 2 Thermoeconomically optimized parameters of condenser and evaporator

Input	Condenser	Evaporator
Refrigerant	R-22	R-22
Heat load, kW	21.1	17.6
Single-phase fluid medium	Water	Air
Its exit/inlet temperature, °C	35.0/29.4	17.2/26.7
α, exit/inlet absolute temperature ratio	1.0185	0.9683
$\dot{C}_{\min}$, minimum heat capacity, kW/°C	3.768	1.853
Reference temperature, K	294.4	294.4
Operating hours, hr/yr	5000	5000
Tube diameters, o.d./i.d., mm	15.88/14.10	15.88/14.10
No. of tube passes/unit cells	6	5*
λ_H, unit cost of heat transfer, $/kW-hr	0.08	0.10
λ_A, unit cost of moving single-phase fluid, $/kW-hr	0.04	0.04
$\dot{z}_m$, modified annualized cost, $/m^2-yr	13.40	18.84
$\dot{z}_m$, expressed as hourly value based on 5000 hr/yr operation, $/m^2-hr	0.00268	0.00377

Output	Condenser	Evaporator
V^*, optimum velocity, m/hr	3660	4100
U^*, overall heat transfer coefficient, kW/m^2-C	0.9576	1.216
γ_{UA}, cost per unit overall conductance, $-°C/kW-hr	2.93×10^{-3}	3.51×10^{-3}
β, dimensionless ratio		
$\beta \triangleq (\lambda_H T_0/\gamma_{UA})$	8038	8382
$\beta_C \triangleq (\beta/\alpha)(\alpha-1)^2$	2.701	8.699
N^*_{tu}, optimum number of transfer units	1.48	2.39
A^*, optimum surface area, m^2	5.82	3.64
ϵ, temperature effectiveness	0.7724	0.908
T_c or T_e, temperature of refrigerant, °C	36.7	16.2
Appoximate V^*, m/hr	7876†	6221†

*Additional input parameters specified for the unit cell of finned air-cooled evaporator.
Number of fins = 5.9 fins/cm, fin thickness = 0.15 mm, inline arrangement
Number of tube rows in direction of air flow = 3
Number of tube rows in direction of refrigerant flow = 4
Transverse/longitudinal pitch = 44.5/50.8 mm
D_H, hydraulic diameter = 20 mm
†Using equation (29) when refrigerant side heat transfer resistance is neglected.

internal flow) (see Table 1 for other values). Users may want to change these values of A_1 and A_2 based on available experimental results.

The input variables chosen for the design of a thermoeconomically optimum heat exchanger have been presented in Table 2. The important results (output) of this analysis are also shown in this table. They have been arranged in the order in which the numerical evaluations are carried out. In this analysis for the optimum heat exchanger design, only the solution of equation (28) for the optimum single-phase velocity (V^*) is by trial and error.

It may be noted that a proportionate decrease in the value of A_1 and A_2 in equation (27) describing the overall heat transfer resistance will not change the capital cost ($\dot{z}_m$) or the cost of the heat exchanger per unit area ($U\gamma_{UA}$) for the same optimum velocity. However, for a fixed value of thermal resistance on the single-phase fluid side at this optimum velocity, if the remaining thermal resistances of the heat exchanger decrease then the capital cost as well as the cost per unit area of the heat exchanger will also decrease. On the other hand, a decrease in the thermal resistance of the single-phase fluid at this optimum velocity (due to changes in the flow mechanism caused by changes in the arrangement), for a fixed value of the remaining thermal resistances of the heat exchanger, results in increases in the capital cost and the cost per unit area of the heat exchanger. It is recognized that in reality changes in any of the input cost parameters shown in Table 2 will effect the optimum velocity (solution of equation (28)) as well as the optimum N_{tu} and the associated heat exchanger area.

Example 2. The evaporator area is to be specified for an air-cooled, R-22 evaporator having a refrigeration capacity of 17.6 kW. Return air from a building at 26.7°C enters the evaporator of the refrigeration system.

A finned-tube evaporator with an in-line tube arrangement will be used. A Wilson type representation for the unit overall heat transfer resistance of this type of heat exchanger is assumed to be $(1/U)=A_1+A_2V^{-0.885}$ (m^2-C/W) where the numerical values for the constants are: $A_1=0.000508$, $A_2=0.4957$.

Table 1 contains numerical values for the constants used in a heat exchanger of this type. The remaining input variables required for the design of a thermoeconomic heat exchanger are also indicated in Table 2. The development of the solution leading to the optimum N_{tu} and single-phase velocity (V^*) is the same as that for the condenser. Other important output values are presented in this table. The discussions at the end of the previous illustrative example related to the water-cooled condenser also apply to this example.

Discussion

The traditional approach to optimization is to balance the cost of energy consumed in the thermal component against its annualized cost. Bejan (1977, 1978) considered the minimization of irreversibilities in the operation of heat exchangers without considering the capital cost. When the capital cost is ignored, a minimization of irreversibilities is possible if the unit cost of irreversibility (lost work) due to heat transfer (λ_H)

is equal to the unit costs of all other irreversibilities, such as the λ_A and λ_B for the flow friction of the two fluids. Bejan's results do not reflect the possibilities of having different monetary values associated with the different irreversibilities used in his thermoeconomic optimization procedure. His method indicates that if the same monetary values are assigned for the heat transfer and the fluid friction lost work, the optimum solution will differ slightly from the results of this paper because of the dominance of the heat transfer irreversibility.

London and Shah (1982, 1983) in their illustration considered the condenser of a powerplant and discussed the tradeoff between operational irreversibilities and their effects on the other components of the powerplant. In their example, the heat transfer irreversibility amounts to about 50 percent with the remaining accounting for the other irreversibilities of the condenser. They provide a thorough insight into the effects of local changes in the magnitude of lost work on the entire powerplant. In order to achieve this objective, they recognize the need for a better understanding of the physics associated with the heat transfer and the fluid flow characteristics. They recognize that the influence of this additional information leads to iterative solutions for the design of heat exchangers.

Recognizing the need for the systematic design of thermal systems using a second-law-based procedure, this paper presents a closed-form analytical solution for the thermoeconomic optimization of two-phase heat exchangers. In order to achieve better design configurations, the present method paves the way for the more detailed thermoeconomic analysis and design of thermal systems by using the distributed unit cost data for several functional aspects of the components of a thermal system. Additional outputs of the present method are the determination of optimum condensing/evaporating temperatures associated with specific inlet temperatures for the single-phase fluids entering these heat exchangers. These outputs are for any combination of thermoeconomic boundary conditions (reflected in the various selection of constant unit costs such as λ_H and γ_{UA}) used in optimizing the N_{tu} expression in equation (19). These boundary conditions can be further modified to reflect any hidden lost work in the fluid circuits by reflecting changes in the economic conditions governing the thermal system as a whole via feedback approaches as shown by Zubair et al. (1985b).

Conclusions

The thermoeconomic optimization procedure utilizes separate unit costs (λ) *representing monetary values* generated by the second law costing of each of the irreversibilities associated with the heat exchanger. These values are obtained by using annualized capital costs and energy costs as input and using the method outlined by Zubair et al. (1985b). It is a closed-form analytical solution. The present method permits determination of the optimum number of transfer units, the optimum velocity and the optimum area; all derived from the optimum β, the ratio of the unit costs for a given heat rate, and α, the exit/inlet temperature ratio. Incidental to this analysis is the determination of the change of phase temperature of the two-phase fluid.

The parametric study of selected input variables and their effects on the optimum heat exchanger configuration is anticipated. Such results should provide a basis for comparison with those obtained by first law methods, i.e., balancing energy costs with annualized capital costs, or costing all forms of entropy generation alike.

Acknowledgments

The authors of this paper are greatly indebted to the technical and editorial assistance of Mr. Michael R. von Spakovsky, The George W. Woodruff School of Mechanical Engineering, Georgia Institute of Technology.

References

Bejan, A., 1977, "The Concept of Irreversibility in Heat Exchanger Design: Counterflow Heat Exchangers for Gas-to-Gas Applications," ASME JOURNAL OF HEAT TRANSFER, Vol. 97, pp. 374–380.

Bejan, A., 1978, "General Criterion for Rating Heat-Exchanger Performance," *Int. J. Heat Mass Transfer*, Vol. 21, pp. 655–658.

Evans, R. B., Crellin, G. L., and Tribus, M., 1966, "Thermoeconomic Considerations of Sea Water Demineralization," *Principles of Desalination*, K. S. Spiegler, ed., Academic Press, New York, Chap. 2, pp. 21–76.

Evans, R. B., Kadaba, P. V., and Hendrix, W. A., 1983, "Essergentic Function Analysis for Process Design and Synthesis," Vol. 67, pp. 643–660.

Heat Exchanger Design Handbook, 1983, Vol. 2, Hemisphere Publishing Corporation, Washington, pp. 2.2.4-1–2.2.4-17.

London, A. L., 1982, "Economics and the Second Law: An Engineering View and Methodology," *Int. Journal of Heat and Mass Transfer*, Vol. 25, pp. 743–751.

London, A. L., and Shah, R. K., 1983, "Costs of Irreversibilities in Heat Exchanger Design," *Heat Transfer Engineering*, Vol. 4, No. 2, pp. 59–73. (See also comment of Prof. Dr. Ing. Wilfried Roetzel, 1984, followed by author's closure in *Heat Transfer Engineering*, Vol. 5, Nos. 3-4, pp. 15–17.)

Loper, J. L., 1979, "Optimum Insulation Arrangement for Systems Having Multiple Heat Exchange Paths With the Environment," *ASHRAE Transactions*, Vol. 85, Part 2, pp. 296–306.

McClintock, F. A., 1951, "The Design of Heat Exchangers for Minimum Irreversibility," ASME Paper No. 51-A-108.

Rich, D. G., 1973, "The Effect of Fin Spacing on the Heat Transfer and Friction Performance of Multi-row, Smooth Plate Fin-and-Tube Heat Exchangers," *ASHRAE Transactions*, Vol. 79, Part 2, pp. 137–145.

Rohsenow, W. M., 1981, "Heat Exchangers – Basic Methods," *Heat Exchangers: Thermal-Hydraulic Fundamentals and Design*, S. Kakac et al., eds., Hemisphere Publishing Corp., Washington, pp. 429–454.

Stoecker, W. F., 1958, "Water-Cooled and Air-Cooled Condensers," in: *Refrigeration and Air Conditioning*, McGraw-Hill, New York, Chap. 6, p. 104. (See also Stoecker and Jones, 2nd ed., 1982, Chap. 12, pp. 247–248.)

Traviss, D. P., Rohsenow, W. M., and Baron, A. B., 1973, "Forced Convection Condensation Inside Tubes: A Heat Transfer Equation for Condenser Design," *ASHRAE Transactions*, Vol. 73, Part 1, pp. 157–165.

Tribus, M., and Evans, R. B., 1962, "A Contribution to the Theory of Thermoeconomics," UCLA Engr. Dept. Report No. 62-36.

Tribus, M., and Evans, R. B., 1963, "The Thermoeconomics of Sea-Water Conversion," UCLA Engr. Dept. Report No. 62-53.

Wilson, E. E., 1915, "A Basis for Rational Design of Heat Transfer Apparatus," *ASME Transactions*, Vol. 37, pp. 47–82.

Zubair, S. M., 1985a, "Solar Assisted Heat Pump. A Thermoeconomic Design Based on Second Law," Ph.D. Thesis, School of Mechanical Engineering, Georgia Institute of Technology, Atlanta, GA.

Zubair, S. M., Kadaba, P. V., and Evans, R. B., 1985b, "Design Optimization of Two-Phase Heat Exchangers," *ASME Two-Phase Exchanger Symposium* – HTD Vol. 44, pp. 71–81.

Zubair, S. M., Kadaba, P. V., and Evans, R. B., 1985c, "Thermoeconomic Design Optimization of a Refrigeration System: A Second Law Approach," ASME Paper No. 85-WA/HT-20.

APPENDIX A

The heat transfer rate in a heat exchanger can be represented by $\dot{Q} = \dot{C}_{\min}(T_{1,e} - T_{1,i})$. Defining λ_Q as the unit cost of heat transfer, the total cost of the heat exchanger is given by

$$\dot{\Gamma} = \gamma_{UA}\dot{C}_{\min}N_{tu} + \lambda_Q\dot{Q} \tag{A1}$$

Comparing equation (A1) with equation (18), the unit cost of heat transfer of equal value is

$$\lambda_Q \triangleq (\lambda_H T_0 \dot{S}_H/\dot{Q}) \tag{A2}$$

In this paper the optimization procedure is based on a fixed heat transfer rate which, depending on the choices of two-phase temperatures, produces different values of entropy generations associated with the finite temperature difference heat transfer (see equation (4)). Hence, it has been possible to complete the second-law-based optimization procedure. If the value of λ_Q is fixed by an arbitrary selection of its value, the differentiation of equation (A1) will lead to a constant resulting in no first-law-based optimization. Utilizing the procedure of this paper and equation (A2), it is possible to define

a value of λ_Q which may be compared with values available from first-law-based optimization procedures contained in the literature. In a similar manner, it is possible to compute the unit costs λ_{sp} and λ_{tp} associated with $\dot{W}_{sp}$, and $\dot{W}_{tp}$, the pumping powers associated with the flow of the single-phase fluids and the two-phase fluids, i.e.,

$$\lambda_{sp} = (\lambda_A T_0 \dot{S}_A)/\dot{W}_{sp} \text{ and } \lambda_{tp} = (\lambda_B T_0 \dot{S}_B)/\dot{W}_{tp} \quad \text{(A3)}$$

These unit costs can be compared with those obtained by other optimization procedures reported in the literature. However, numerical comparisons are meaningless unless a thorough review of the concepts of the two procedures is made.

Typical development of first-law-based thermoeconomic optimization is possible by starting the analysis utilizing an equation similar to equation (16), i.e.,

$$\dot{\Gamma} = \dot{z}A + \dot{k}_0 + \lambda_{sp}\dot{W}_{sp} + \lambda_{tp}\dot{W}_{tp} + \lambda_Q \dot{Q} \quad \text{(A4)}$$

Utilizing equation (A4), $\dot{z}_{ml}$ is defined such that

$$\dot{\Gamma} = \dot{z}_{ml}A + \lambda_{sp}\dot{W}_{sp} \quad \text{(A5)}$$

A comparable equation utilizing second-law-based concepts would be

$$\dot{\Gamma} = \dot{z}_{ml}A + \lambda_A T_0 \dot{S}_A \quad \text{(A6)}$$

It should be noted that $\dot{z}_m$ used in the main paper has a different value when compared to $\dot{z}_{ml}$, used in this appendix. In the main paper, utilizing the second-law-based optimization procedure, it was possible to obtain at a fixed heat transfer rate not only the optimum velocity of the single-phase fluid V^* by minimizing γ_{UA}, the cost per unit overall heat conductance (equation (27)) but also the optimum N_{tu} (equation (24)) by minimizing $\dot{\Gamma}$, the total cost of owning and operating the two-phase heat exchanger. This second-law-based method also provided the optimum A^*, the heat exchanger surface area. When first-law-based procedures are compared to the procedure of this paper which utilizes distributed cost parameters, the first-law-based procedures exhibit, at best, a limited scope for optimization.

Exact Solution for Unsteady Conjugated Heat Transfer in the Thermal Entrance Region of a Duct

J. Sucec
Professor of Mechanical Engineering,
University of Maine,
Orono, ME 04469
Mem. ASME

By use of the Laplace transformation, an exact analytical solution is developed for the case of transient conjugated heat transfer in the thermal entrance region of a parallel plate duct when the unsteadiness is induced by a sudden change in temperature of the ambient fluid outside the duct walls. The solution is presented for the fastest part of the transient, time domain I, and comparison is made with a finite difference solution and also with the approximate, standard quasi-steady approach which is seen to be appreciably in error for a wide range of conjugation parameter values.

Introduction

Knowledge of transient convective heat transfer is of importance in a number of different physical situations such as the starting, ending, and change in power level transients in gas turbine engines, recuperative and regenerative heat exchangers, and cooling passages in nuclear power reactors.

Practically speaking, most problems of this type are conjugated problems, that is, the temperature distribution in the moving fluid is mutually coupled to the temperature distribution in the solid body over which or through which the fluid flows and therefore one does not have *a priori* knowledge of either the heat flux or the temperature at the interface between the solid and the fluid. Generally, the most severe part of the transient, in terms of time rates and critical material temperatures, occurs in the first time domain, that is, at times less than the time required for the fastest moving fluid particle to travel the distance between the beginning of the body or channel and the downstream point of interest. The two time domains that appear naturally in slug flows are discussed by Siegel [1] while the concept of three time domains for actual nonslug flows is developed in Sucec [2].

The simplest approach to the solution of a transient, conjugated convection problem is the standard, quasi-steady approach which generally employs a constant surface coefficient of heat transfer appropriate to steady-state conditions for a constant temperature surface. Representative contributions of this approximate approach are those of Adams and Gebhart [3] as well as the more recent work of Lu [4]. Solutions can often be found to the problem without resort to the quasi-steady approach if the idealization of a slug flow velocity profile is employed as was done in the exact solutions given by Siegel [5], Sparrow and De Farias [6], and Sucec [7, 8]. Procedures developed to account approximately for thermal energy storage capacity of the fluid, thermal history effects, and nonslug velocity profiles in transient, conjugated problems are provided by Dorfman [9], Karvinen [10, 11], Wang et al. [12], Sucec [2], and Sucec and Sawant [13].

Lin and Shih [14] use an instantaneous local similarity method to solve for the unsteady heat transfer in the thermal entrance region of ducts at small times due to a step change in surface temperature in a nonconjugated situation. Krishnan [15] uses Laplace transforms to get small time solutions, in time domain *I*, in a duct when there is a step change in either heat flux or temperature at the outside of a wall of finite thickness. Drake [16] gets small and large time solutions for the conjugated problem of a finite thickness wall at a two-dimensional stagnation point when the fluid temperature is suddenly changed. Lin et al. [17] use finite differences to solve the problem of fully developed, laminar flow in the thermal entrance region of a circular tube when a transient is induced by a step change in the ambient fluid temperature outside the pipe. In their problem, virtually the entire transient occurs in the first time domain. Their solution procedure is restricted to the case where the thermal capacity of the solid wall is negligible compared to the thermal capacity of the fluid. This is particularly limiting because, in practice, the opposite is often the case.

The work of this article considers a physical situation similar to that of [17], but includes the effect of nonzero thermal energy storage capacity of the wall. An exact solution is developed for the first time domain as well as the approximate quasi-steady solution for comparison purposes. This allows the determination of the importance of the nonzero value of wall energy storage capacity and of the error involved in the use of the simple quasi-steady approach. A finite difference solution by the author yields the extent, in time, of the thermal entrance region as well as permitting further study of the approximate quasi-steady result.

Analysis

Figure 1 depicts the physical situation consisting of a parallel plate duct through which a constant property fluid is flowing in a steady, laminar fashion without appreciable viscous dissipation. Initially, both the flowing fluid and the duct walls

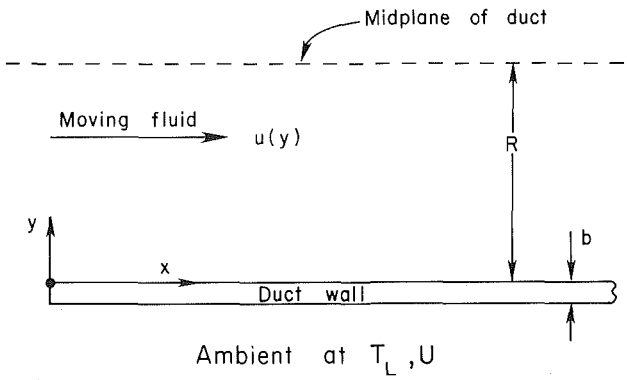

Fig. 1 Symmetric lower half of parallel plate duct

Contributed by the Heat Transfer Division and presented at the ASME Winter Annual Meeting, Miami Beach, Florida, November 17–21, 1985. Manuscript received by the Heat Transfer Division July 29, 1985.

are at a uniform temperature T_i when suddenly the ambient fluid outside the duct undergoes a step change in temperature from T_i to T_L. The overall heat transmission coefficient between the ambient and the duct wall has the value U and the temperature distribution will be lumped in the y direction within the duct wall with axial conduction neglected in both the wall and the fluid. The transient wall temperature distribution in the first time domain, $t < x/u_{\max}$, and the heat flux to the inside flowing fluid are sought. For the conditions just stated and a fully developed velocity profile, the thermal energy equation is given by

$$\frac{\partial T}{\partial t} + u(y)\frac{\partial T}{\partial x} = \alpha \frac{\partial^2 T}{\partial y^2} \tag{1}$$

with initial and boundary conditions

$$t=0, \quad x>0, \quad 0<y<R \quad T=T_i$$

$$x=0, \quad t>0, \quad 0<y<R \quad T=T_i$$

$$y=R, \quad x>0, \quad t>0, \quad \frac{\partial T}{\partial y}=0$$

An energy balance on an element of duct wall along with the conjugation condition that the wall temperature and the fluid temperature must be equal at every x and t yields

$$y=0, \quad x>0, \quad t>0 \qquad U(T_L - T) = -k\left(\frac{\partial T}{\partial y}\right)_{y=0} + \rho_w c_{pw} b \frac{\partial T}{\partial t} \tag{2}$$

These equations are cast into nondimensional form by use of the following variables

$$\phi = (T-T_i)/(T_L-T_i), \ \mathrm{Fo} = \alpha t/R^2,$$

$$\hat{a} = \rho c_p R/\rho_w c_{pw} b, \ X = \alpha x/R^2 u_m, \ Y = y/R, \ S = UR/k,$$

$$\frac{\partial^2 \phi}{\partial Y^2} = \frac{\partial \phi}{\partial \mathrm{Fo}} + \frac{u(Y)}{u_m}\frac{\partial \phi}{\partial X} \tag{3}$$

$$\phi(0, X, Y) = 0, \quad \phi(\mathrm{Fo}, 0, Y) = 0, \quad \frac{\partial \phi}{\partial Y}(\mathrm{Fo}, X, 1) = 0 \tag{4}$$

At

$$Y=0, \quad X>0, \quad \mathrm{Fo}>0 \qquad S(1-\phi) = -\frac{\partial \phi}{\partial y} + \frac{1}{\hat{a}}\frac{\partial \phi}{\partial \mathrm{Fo}} \tag{5}$$

For a fully developed laminar flow in the parallel plate duct, the velocity profile is given by $u(Y) = u_m[3Y - 3Y^2/2]$.

From this, $u_{\max} = 3u_m/2$, and this leads to $\mathrm{Fo} < (2/3)X$ as the range of values of Fo in the first time domain.

Since for $\mathrm{Fo} < (2/3)X$, no fluid which was at the duct entrance at Fo = 0 has yet reached the X of interest, the inlet boundary condition, at $X = 0$, doesn't have to be satisfied in time domain I. Also, since there is no X dependence in the remaining conditions of equations (4) and (5) and no explicit X dependence in the governing equation (3), it follows that $\partial\phi/\partial X = 0$ for $\mathrm{Fo} < (2/3)X$. Thus, setting $\partial\phi/\partial X = 0$ in equation (3) and using the boundary condition of (4), for the thermal entrance region of the duct, gives time domain I, $\mathrm{Fo} < (2/3)X$

$$\frac{\partial^2 \phi}{\partial Y^2} = \frac{\partial \phi}{\partial \mathrm{Fo}} \tag{6}$$

$$\phi(0, X, Y) = 0, \quad \phi(\mathrm{Fo}, X, \infty) \to 0 \tag{7}$$

At

$$Y=0, \ X>0, \ \mathrm{Fo}>0; \quad S(1-\phi) = -\frac{\partial \phi}{\partial Y} + \frac{1}{\hat{a}}\frac{\partial \phi}{\partial \mathrm{Fo}} \tag{8}$$

Define the Laplace transform of ϕ with respect to Fo as

$$\bar{\phi}(Y) = L_{\mathrm{Fo}-p}\phi(\mathrm{Fo}, Y) = \int_0^\infty \phi e^{-p\mathrm{Fo}} d\mathrm{Fo}$$

Using this in equations (6)–(8) and solving yields the transformed wall temperature and flux at $Y = 0$, namely,

$$\bar{\phi}_w = \frac{\hat{a}S}{p[p + \hat{a}\sqrt{p} + \hat{a}S]} \tag{9}$$

$$\bar{q}_w = \frac{k\hat{a}S(T_L - T_i)/R}{\sqrt{p}[p + \hat{a}\sqrt{p} + \hat{a}S]} \tag{10}$$

For the limiting case of zero thermal energy storage capacity of the wall relative to the fluid, $\rho_w c_{pw} b \to 0$, and $\hat{a} \to \infty$, causing equations (9) and (10) to become

Nomenclature

$\hat{a} = \rho c_p R/\rho_w c_{pw} b$ = fluid-to-duct wall thermal energy storage capacity ratio
b = thickness of duct wall
c_p, c_{pw} = specific heats of fluid and duct wall, respectively
erfc = complimentary error function
Fo = $\alpha t/R^2$ = Fourier number
h_x = local surface coefficient of heat transfer
$i = \sqrt{-1}$
I_0 = integral defined by equations (14) and (15)
Im = imaginary part of
k = thermal conductivity of fluid
Nu = $h_x R/k$ = Nusselt number
p = Laplace transform parameter
q_w = heat flux at $y = 0$
R = half height of duct
Re = real part of
$S = UR/k$
t = time
T = local temperature
T_i = initial, and also inlet, temperature
T_B = local bulk mean temperature of fluid
T_L = temperature of ambient outside of duct wall
u, u_m, $u_{\max}$ = local, mass-average, and maximum fluid velocity, respectively
U = overall heat transmission coefficient between ambient and duct wall
$W(z)$ = function related to the error function of complex argument, equation (24)
x = space coordinate along duct
$X = \alpha x/R^2 u_m$
y = space coordinate perpendicular to duct wall
$Y = y/R$
α = thermal diffusivity of the fluid
β_1, β_2 = defined by equation (31)
ρ, ρ_w = mass density of fluid and of duct wall, respectively
σ_1, σ_2 = defined by equations (16) and (17)
$\phi = [T(x, y, t) - T_i]/[T_L - T_i]$ = nondimensional temperature excess ratio

$$\bar{\phi}_w \to \frac{S}{p[\sqrt{p}+S]} \text{ and } \bar{q}_w \to \frac{kS(T_L-T_i)/R}{\sqrt{p}[\sqrt{p}+S]} \tag{11}$$

These two limiting expressions can be inverted with the aid of the tables of transforms in Churchill [18] to yield

$$\hat{a}\to\infty,\ \phi_w = 1 - e^{S^2\mathrm{Fo}}\mathrm{erfc}[S\sqrt{\mathrm{Fo}}] \tag{12}$$

$$q_w = U(T_L-T_i)e^{S^2\mathrm{Fo}}\mathrm{erfc}[S\sqrt{\mathrm{Fo}}] \tag{13}$$

Equations (12) and (13) are the time domain I exact solutions for the parallel plate duct counterpart of the limiting case solved by Lin et al. [17] using finite differences.

For the general case, where $\hat{a}$ can have any value, the following inverse is needed, from equation (9)

$$L^{-1}_{p\to\mathrm{Fo}}\left\{\frac{1}{p[p+\hat{a}\sqrt{p}+\hat{a}S]}\right\} = I_0 \tag{14}$$

This can be put into the following form

$$I_0 = L^{-1}_{p\to\mathrm{Fo}}\left\{\frac{1}{(\sqrt{p})^2[(\sqrt{p})^2+\hat{a}\sqrt{p}+\hat{a}S]}\right\}$$

From Roberts and Kaufman [19] we have

$$L^{-1}_{p\to\mathrm{Fo}}g(\sqrt{p}) = \frac{1}{2\sqrt{\pi}\mathrm{Fo}^{3/2}}\int_0^\infty ze^{-z^2/4\mathrm{Fo}}f(z)dz \tag{15}$$

Comparison with equation (14) leads to the identification

$$g(r) = \frac{1}{r^2[r^2+\hat{a}r+\hat{a}S]} \qquad f(z) = L^{-1}_{r\to z}g(r)$$

Using [19], this can be inverted to give $f(z)$. Then, study of the integral of equation (15) leads to the solution for I_0 and, hence, the wall temperature of equation (9). A similar procedure leads to the inverse of the flux of equation (10). These exact solution functions for ϕ_w and q_w are presented next

$$\sigma_1 = \frac{\hat{a}^2}{4}\left[\sqrt{1-\frac{4S}{\hat{a}}}+1\right]^2 \tag{16}$$

$$\sigma_2 = \frac{\hat{a}^2}{4}\left[1-\sqrt{1-\frac{4S}{\hat{a}}}\right]^2 \tag{17}$$

$$\phi_w = 1-\frac{1}{2}\left\{e^{\sigma_1\mathrm{Fo}}\mathrm{erfc}(\sqrt{\sigma_1\mathrm{Fo}})\left[1-\frac{1}{\sqrt{1-\frac{4S}{\hat{a}}}}\right]\right.$$

$$\left. + e^{\sigma_2\mathrm{Fo}}\mathrm{erfc}(\sqrt{\sigma_2\mathrm{Fo}})\left[1+\frac{1}{\sqrt{1-\frac{4S}{\hat{a}}}}\right]\right\} \tag{18}$$

$4S/\hat{a} < 1$ for the validity of equations (18) and (19)

$$q_w = U(T_L-T_i)\left[\frac{e^{\sigma_2\mathrm{Fo}}\mathrm{erfc}(\sqrt{\sigma_2\mathrm{Fo}})-e^{\sigma_1\mathrm{Fo}}\mathrm{erfc}(\sqrt{\sigma_1\mathrm{Fo}})}{\sqrt{1-\frac{4S}{\hat{a}}}}\right] \tag{19}$$

$$\phi_w = 1-\frac{\hat{a}\sqrt{\mathrm{Fo}}}{\sqrt{\pi}}+\left[\frac{\hat{a}^2\mathrm{Fo}}{2}-1\right]e^{\frac{\hat{a}^2\mathrm{Fo}}{4}}\mathrm{erfc}\left[\frac{\hat{a}}{2}\sqrt{\mathrm{Fo}}\right] \tag{20}$$

$4S/\hat{a} = 1$ for the use of equations (20) and (21)

$$q_w = U(T_L-T_i)\left\{\frac{2\hat{a}\sqrt{\mathrm{Fo}}}{\sqrt{\pi}}-\hat{a}^2\mathrm{Fo}e^{\frac{\hat{a}^2\mathrm{Fo}}{4}}\mathrm{erfc}\left[\frac{\hat{a}}{2}\sqrt{\mathrm{Fo}}\right]\right\} \tag{21}$$

$$\phi_w = 1-\left\{\mathrm{Re}W\left[\frac{\hat{a}}{2}\sqrt{\mathrm{Fo}}\left(\sqrt{\frac{4S}{\hat{a}}-1}+i\right)\right]\right.$$

$$\left. + \frac{\mathrm{Im}W\left[\frac{\hat{a}\sqrt{\mathrm{Fo}}}{2}\left(\sqrt{\frac{4S}{\hat{a}}-1}+i\right)\right]}{\sqrt{\frac{4S}{\hat{a}}-1}}\right\} \tag{22}$$

$4S/\hat{a} > 1$ for use of equations (22) and (23)

$$q_w = \frac{2U(T_L-T_i)}{\sqrt{\frac{4S}{\hat{a}}-1}}\mathrm{Im}W\left[\frac{\hat{a}}{2}\sqrt{\mathrm{Fo}}\left(\sqrt{\frac{4S}{\hat{a}}-1}+i\right)\right] \tag{23}$$

$W(z)$ is a tabulated function (see Abramowitz and Stegun [20]), related to the error function of complex argument as follows

$$W(z) = e^{-z^2}\mathrm{erfc}[-iz] \tag{24}$$

Thus equations (18)–(23), along with equations (12) and (13), constitute the exact analytical solution to the problem over the full range of possible values of $4S/\hat{a}$.

Quasi-Steady Analysis. In this approximate approach, the heat flux at $y = 0$ is cast in terms of Newton's cooling law, where the local bulk mean fluid temperature T_B is used in the driving potential difference, as follows

$$q_{wqs} = h_x(T_w - T_B) \tag{25}$$

Using this in the duct wall energy balance equation (2) leads to

$$\frac{\partial\phi_w}{\partial\mathrm{Fo}} + \hat{a}(\mathrm{Nu}+S)\phi_w = \hat{a}\mathrm{Nu}\phi_B + \hat{a}S \tag{26}$$

where $\mathrm{Nu} = h_xR/k$.

Next, an energy balance on a control volume of fluid R by dx yields

$$h_x(T_w-T_B) = \rho u_m Rc_p\frac{\partial T_B}{\partial x} + \rho Rc_p\frac{\partial T_B}{\partial t} \tag{27}$$

When equation (27) is put into nondimensional form we have

$$\frac{\partial\phi_B}{\partial\mathrm{Fo}} + \frac{\partial\phi_B}{\partial X} = \mathrm{Nu}[\phi_w-\phi_B] \tag{28}$$

The side conditions for equations (26) and (28) are

$$\phi_w(0,X) = \phi_B(0,X) = 0, \quad \phi_B(\mathrm{Fo},0) = 0 \tag{29}$$

Solution of equations (26) and (28), subject to (29), by Laplace transforms for time domain I leads to the quasi-steady solution function

$$\phi_{wqs} = 1+\frac{\hat{a}S}{\sqrt{M^2-4\hat{a}S\mathrm{Nu}}}\left[\left(\frac{\mathrm{Nu}-\beta_1}{\beta_1}\right)e^{-\beta_1\mathrm{Fo}}\right.$$

$$\left. -\left(\frac{\mathrm{Nu}-\beta_2}{\beta_2}\right)e^{-\beta_2\mathrm{Fo}}\right]$$

$$M = \hat{a}(S+\mathrm{Nu})+\mathrm{Nu} \tag{30}$$

$$\beta_1 = [M+\sqrt{M^2-4\hat{a}S\mathrm{Nu}}]/2, \quad \beta_2 = [M-\sqrt{M^2-4\hat{a}S\mathrm{Nu}}]/2 \tag{31}$$

As usual, the constant h_x appropriate to steady, fully developed flow through a duct with a constant wall temperature was used, and this gives the constant value of Nu employed in the solution of equations (28) and (26).

Finite Difference Solution. For the finite difference solu-

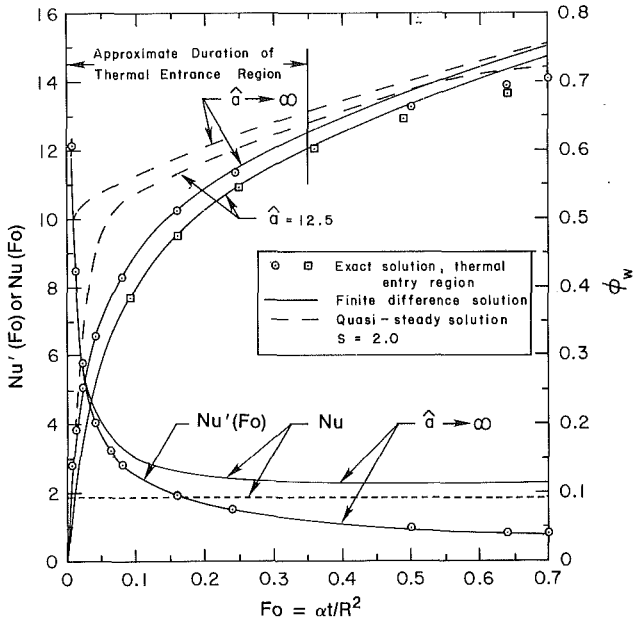

Fig. 2 Wall temperature and Nusselt number response functions

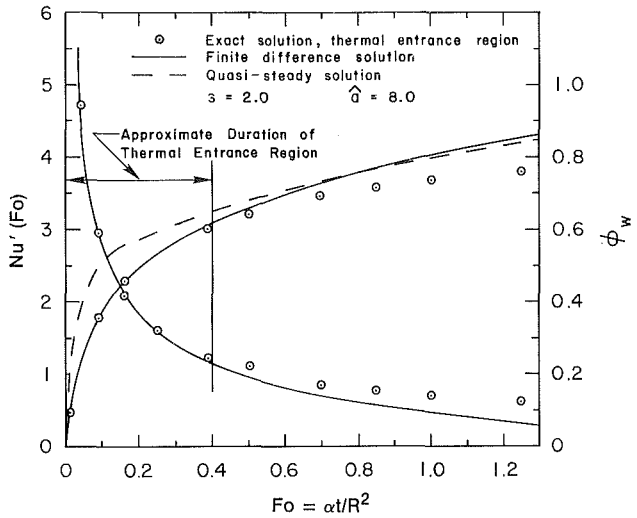

Fig. 3 Wall temperature and Nusselt number response functions

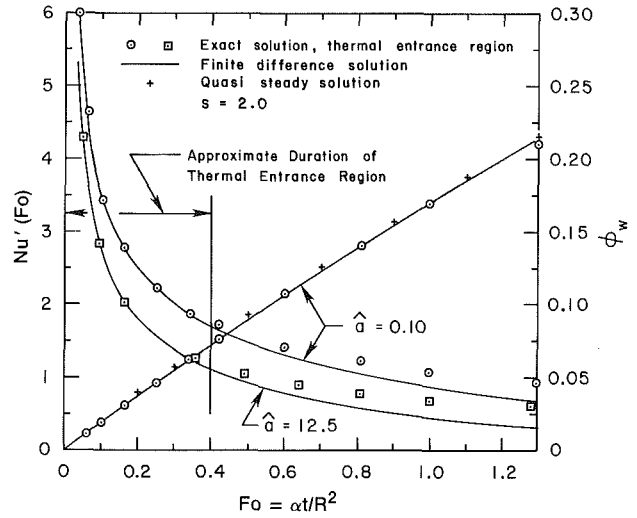

Fig. 4 Wall temperature and Nusselt number response functions

tion of the governing equations (3)–(5), the author made the appropriate modifications to the finite difference equations given by Sucec [2]. Briefly, a set of implicit, unconditionally stable finite difference equations of tridiagonal structure was derived in which upwind differencing was used for the x derivative and standard central differencing for the y second derivatives. Lattice spacing refinement of ΔFo, ΔX, and ΔY was carried to the point where the finite difference solution exhibited no dependence upon their values. A weak check on the integrity of the finite difference solution was made by comparing it to the exact result, available in Kays [22], for steady-state heat transfer in the thermal entry length of an isothermal duct and agreement was found.

Results and Discussion

Since the exact analytical solution in time domain I, given by equations (12), (13), and (18)–(23), is for the thermal entrance region where the temperature at the duct midplane, $y = R$, has not yet changed significantly from T_i, the transient Nusselt number will be based upon the driving potential difference $T_w(\text{Fo}) - T_i$. This will also allow more direct study of the time-varying surface coefficient h, as has been also pointed out by Lin et al. in [17], without the added complication of the time dependency of the bulk mean temperature. Thus,

$$\text{Nu}'(\text{Fo}) = hR/k = \frac{q_w R/k}{\phi_w (T_L - T_i)} \tag{32}$$

Representative response functions for the exact analytical solution, the quasi-steady solution, and for the author's finite difference solution are presented in Figs. 2–4 for the case of $S = UR/k = 2.0$.

Figure 2 gives results for the limiting case of $\hat{a} \to \infty$, negligible thermal energy storage capacity of the duct wall, the case treated by Lin et al. in [17] for the circular tube, and for $\hat{a} = 12.5$. Since the value of $\hat{a} = 12.5$ and $S = 2.0$ corresponds to $4S/\hat{a} < 1$, the exact solution is given by equations (18) and (19) while for $\hat{a} \to \infty$, equations (12) and (13) were used and these results are shown as the circles and squares in the figure. The finite difference results are given by the solid curves while the standard quasi-steady results are given by the dashed curve and the plus symbols. For clarity, the result for Nu'(Fo) when $\hat{a} = 12.5$ is given in Fig. 4.

It is seen that the exact solution and the finite difference solution agree very well until about Fo = 0.35 where the boundary layer character of the solution deteriorates due to the temperature at $y = R$ starting to change significantly from the value T_i. At lower times, such as Fo < 0.25 for $\hat{a} = 12.5$, the agreement is complete as it must be. The exact solution results were continued beyond the thermal entrance region expressly for the purpose of determining the duration of this region by comparison with the finite difference solution which is not limited to this region. On the other hand, the quasi-steady result is in considerable error, especially at times lower than about Fo = 0.50. The quasi-steady solution for these times predicts a much higher wall temperature than actually occurs due to the use of the steady-state Nusselt number for an isothermal duct wall under fully developed conditions of Nu = 1.885 as can be found in Sucec [21]. For comparison purposes the time-varying Nu, using $T_w - T_B$ as the driving potential difference, from the finite difference solution is plotted for $\hat{a} \to \infty$. From these two curves for Nu, it becomes evident why the quasi-steady solution exhibits a large amount of error.

The values of $\hat{a} = 8$ and $S = 2.0$ in Fig. 3 yield $4S/\hat{a} = 1.0$, the singular case for the exact solution where the result is given by equations (20) and (21) for the wall temperature and flux. Again the agreement between the exact solution and the finite difference solution is almost exact until at least Fo = 0.35.

The quasi-steady result, although doing better than at $\hat{a} = 12.5$ or $\hat{a} \to \infty$, still gives very poor predictions for Fo < 0.5.

Finally, in Fig. 4, results are given for $\hat{a} = 0.10$ which, with the value of S, leads to $4S/\hat{a} > 1$ so that the exact solution is given by equations (22) and (23) and is represented by circles in the figure. As mentioned earlier, results for Nu′ (Fo) when $\hat{a} = 12.5$ are also plotted here. As was also the case in the previous two figures, the agreement between the exact solution and the finite difference results for both Nu′ (Fo) and ϕ_w is very good up to Fo $= 0.35$ and the divergence between the two beyond this point is due to the end of the thermal boundary layer character of the flow. Also to be noted is the reasonably good agreement of the standard quasi-steady solution with the exact results and the finite difference results. This comes about as a consequence of $\hat{a} = 0.10$ being low enough to cause a "slow" transient in the wall and fluid so that the fluid is practically proceeding through a succession of instantaneous steady states.

Calculations by the author using representative duct wall thicknesses, materials, and half heights lead to the conclusion that for liquids such as water, values of $\hat{a}$ would be expected to be in the neighborhood of about 10 while for air, $\hat{a}$ values less than 0.10 would often occur. Sample calculations by Sparrow and De Farias [6] also support the value for air as the fluid. Comparing the curves of $\hat{a} = 12.5$ and $\hat{a} \to \infty$ in Fig. 2 indicates that appreciable error could still be introduced in the predicted wall temperature if the limiting value of $\hat{a} \to \infty$ is used as an approximation, as would have to be done with the results of [17].

The exact analytical results given herein are restricted to time domain I, where Fo $< (2/3)X$. Yet, this is not that serious a restriction particularly for the larger values of $\hat{a}$. The results of Lin et al. in [17], as well as in two of their related works [23, 24], indicate that the bulk of the transient is over in the first time domain for $\hat{a} \to \infty$.

Conclusion

An exact analytical solution has been found for the transient conjugated forced convection heat transfer problem in which a step change in the ambient temperature outside a duct instigates the unsteady conditions. Comparison of this solution, which is valid for time domain I in a thermal entrance region, with the finite difference solution indicates that the thermal boundary layer character of the transient persists to Fo ≈ 0.35.

At the high end of the $\hat{a}$ value scale, the standard quasi-steady solution is greatly in error, especially at times Fo $<$ 0.50, because of the use of a steady-state heat transfer coefficient which is far smaller than the actual time-varying heat transfer coefficient. On the opposite end of the $\hat{a}$ scale, $\hat{a}$ very low, the quasi-steady result may be acceptable because of the relative slowness of the transient at low values of $\hat{a}$.

Unacceptable error could be incurred if the results for $\hat{a} \to \infty$ were used as an approximation for lower values of $\hat{a}$ such as $\hat{a} = 8$ and 12.5, which are characteristic of some metal duct wall–liquid combinations. The analytical solution presented applies for all values of $\hat{a}$, from $\hat{a} = 0$ to $\hat{a} \to \infty$.

References

1 Siegel, R., "Transient Heat Transfer for Laminar Slug Flow in Ducts," ASME *Journal of Applied Mechanics*, Vol. 26, 1959, pp. 140–142.

2 Sucec, J., "An Improved Quasi-Steady Approach for Transient Conjugated Forced Convection Problems," *Int. J. Heat Mass Transfer*, Vol. 24, No. 10, 1981, pp. 1711–1722.

3 Adams, D. E., and Gebhart, B., "Transient Forced Convection From a Flat Plate Subjected to a Step Energy Input," ASME JOURNAL OF HEAT TRANSFER, Vol. 86, 1964, pp. 253–258.

4 Lu, P. C., "Perturbation Solutions of Transient Heat Transfer to a Porous Medium From a Fluid Stream," ASME JOURNAL OF HEAT TRANSFER, Vol. 103, 1981, pp. 159–164.

5 Siegel, R., "Forced Convection in a Channel With Wall Heat Capacity and With Wall Heating Variable With Axial Position and Time," *Int. J. Heat Mass Transfer*, Vol. 6, 1963, pp. 607–620.

6 Sparrow, E. M., and DeFarias, F. N., "Unsteady Heat Transfer in Ducts With Time Varying Inlet Temperature and Participating Walls," *Int. Journal Heat Mass Transfer*, Vol. 11, 1968, pp. 837–853.

7 Sucec, J., "Transient Heat Transfer Between a Plate and a Fluid Whose Temperature Varies Periodically With Time," ASME JOURNAL OF HEAT TRANSFER, Vol. 102, 1980, pp. 126–131.

8 Sucec, J., "Unsteady Heat Transfer Between a Fluid With Time Varying Temperature and a Plate: An Exact Solution," *Int. J. Heat Mass Transfer*, Vol. 18, 1975, pp. 25–36.

9 Dorfman, A. Sh., "Solution of the External Problem of Unsteady State Convective Heat Transfer With Coupled Boundary Conditions," *Int. Chem. Engng.*, Vol. 17, 1977, pp. 505–510.

10 Karvinen, R., "Steady State and Unsteady Heat Transfer Between a Fluid and a Flat Plate With Coupled Convection, Conduction and Radiation," *Acta Polytechnica Scandinavika*, ME 73, 1976, pp. 5–36.

11 Karvinen, R., "Some New Results for Conjugated Heat Transfer in a Flat Plate," *Int. J. Heat Mass Transfer*, Vol. 21, 1978, pp. 1261–1264.

12 Wang, R. C. C., Chung, B. T. V., and Thomas, L. C., "Transient Convective Heat Transfer for Laminar Boundary Layer Flow With Effects of Wall Capacitance and Resistance," ASME JOURNAL OF HEAT TRANSFER, Vol. 99, 1977, pp. 514–519.

13 Sucec, J., and Sawant, A. M., "Unsteady Conjugated Forced Convection Heat Transfer in a Parallel Plate Duct," *Int. J. Heat Mass Transfer*, Vol. 27, 1984, pp. 95–101.

14 Lin, H. T., and Shih, Y. P., "Unsteady Thermal Entrance Heat Transfer of Power Law Fluids in Pipes and Plate Slits," *Int. J. Heat Mass Transfer*, Vol. 24, No. 9, 1981, pp. 1531–1539.

15 Krishnan, B., "On Conjugated Heat Transfer in Fully Developed Flow," *Int. J. Heat Mass Transfer*, Vol. 25, No. 2, 1982, pp. 288–289.

16 Drake, D. G., "Unsteady Conjugated Heat Transfer Near a Stagnation Point," *Applied Scientific Research*, Vol. 40, 1983, pp. 199–207.

17 Lin, T. F., Hawks, K. H., and Leidenfrost, W., "Unsteady Thermal Entrance Heat Transfer in Laminar Pipe Flows With Step Change in Ambient Temperature," *Wärme- und Stoffübertragung*, Vol. 17, 1983, pp. 125–132.

18 Churchill, R. V., *Operational Mathematics*, 2nd ed., McGraw-Hill, New York, 1958.

19 Roberts, G. E., and Kaufmann, H., *Tables of Laplace Transforms*, W. B. Saunder, Philadelphia, PA, 1966.

20 Abramowitz, M., and Stegun, I. A., eds., *Handbook of Mathematical Functions With Formulas, Graphs, and Mathematical Tables*, National Bureau of Standards Appl. Math. Ser. 55, 1964.

21 Sucec, J., *Heat Transfer*, Wm. C. Brown, Co., Dubuque, IA, 1985.

22 Kays, W. M., *Convective Heat and Mass Transfer*, McGraw-Hill, New York, 1966.

23 Lin, T. F., Hawks, K. H., and Leidenfrost, W., "Transient Thermal Entrance Heat Transfer in Laminar Pipe Flows With Step Change in Pumping Pressure," *Wärme- und Stoffübertragung*, Vol. 17, 1983, pp. 201–209.

24 Lin, T. F., Hawks, K. H., and Leidenfrost W., "Transient Conjugated Heat Transfer Between a Cooling Coil and Its Surrounding Enclosure," *Int. J. Heat Mass Transfer*, Vol. 26, No. 11, 1983, pp. 1661–1667.

Experimental Investigation of the Augmentation of Forced Convection Heat Transfer in a Circular Tube Using Spiral Spring Inserts

J. P. Chiou
Professor,
Mechanical Engineering Department,
University of Detroit,
Detroit, MI 48221
Mem. ASME

Results of the experimental investigation of a class of spiral spring coil used as a tube side heat transfer augmentative device for a single phase cooling mode operation are presented. SAE 10 engine oil flowing inside the tube is cooled by water flowing outside the tube. This spiral spring insert is inexpensive but it can increase the tube side heat transfer coefficient significantly. Thus its use as an augmentative device is effective. Application of this device in the design of oil coolers is discussed.

Introduction

The use of augmentative techniques, either active or passive, to increase the convective heat transfer coefficient on tube sides has been studied for quite some time [1–5]. One of the passive techniques commonly considered is the use of tube inserts of various types, such as swirl strips, twisted tapes, meshes or brushes, and coil or spiral springs [6–26]. The tube inserts are relatively low in cost, are relatively easy to insert into tubes, and are also relatively easy to take out of the tubes for cleaning operations. Thus they are widely used in industry.

Tube inserts can create one or some combinations of the following conditions, which are favorable for increasing the heat transfer coefficient with a consequent increase in the flow friction:

1 interrupting the development of the boundary layer of the fluid flow and increasing the degree of flow turbulence
2 increasing the effective heat transfer area if the contact between the tube inserts and the tube wall is excellent
3 generating rotating and/or secondary flow

In the heating mode operation, the rotating flow is noted to have favorable centrifugal convection effect [27–31], which can increase the heat transfer coefficient between the flow and the tube wall. In the cooling mode operation, however, the rotating flow may have an adverse centrifugal convection effect which may even reduce the convection heat transfer coefficient. Thus tube inserts which can generate rotating flow (such as swirl strips or twisted tapes) are generally not used in oil coolers; instead coil or spiral springs are used. The spiral spring usually does not generate rotating flow. Thus the flow pressure drop associated with generating the rotating flow can be eliminated.

This paper presents the results of an experimental investigation of the heat transfer and fluid friction characteristics of light engine oil (SAE 10) flowing through a horizontal tube with spiral spring inserts. The oil flow dissipated thermal energy to water flowing outside the tube. The range of the average temperature of the water flow covered in this study was from 104°F to 158°F (40°C to 70°C) approximately. The range of the average temperature of the oil flow covered in this study was from 214°F to 240°F (101°C to 116°C) approximately. Spiral springs of four different wire diameters and four different numbers of turns per unit length were used (see Fig. 1 and Table 1). The coil diameters of the spiral springs were made to be a little smaller than the inside diameter of the tube to permit easy insertion into the tube. The coil was found to touch the tube wall intermittently; and in most cases it touched the bottom part of the tube wall.

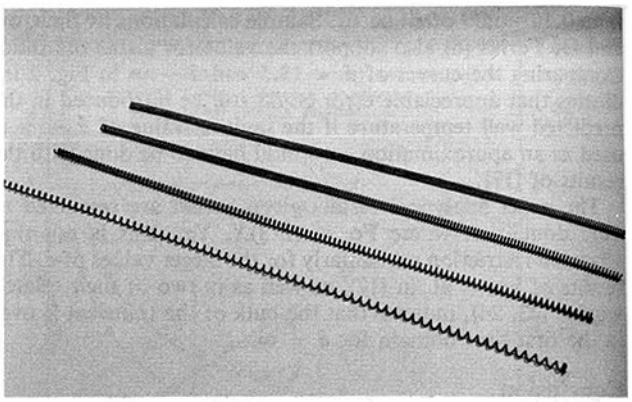

Fig. 1 Spiral spring augmentative devices evaluated

Heat transfer and flow friction data were generated for 16 different tube inserts under various operating conditions. Relations between the heat transfer capability and the fluid pumping power required are presented. Applications of these tube inserts in oil coolers as heat transfer augmentative devices are discussed.

Experimental Apparatus and Procedure

The test apparatus used in this study is shown in Figs. 2–4. A copper tube, sized to an internal diameter of 0.334 in. (0.848 cm) with a test section length of 4.0 ft (1.22 m) was used to evaluate the augmentative devices. This tube was inserted into a 0.750 in. (1.905 cm) i.d. copper tube through which the cooling water flowed. At the ends of this external tube, adaptors were added to seal around the internal tube and to provide an area for attaching pressure taps to measure the fluid pressure drop caused by the different augmentative devices. The internal tube had a fitting added to each end for attachment to the inlet and outlet oil mixing devices. These devices shown in Fig. 3 were required to obtain an accurate measurement of the average oil temperature prior to entering and leaving the test section. Oil temperatures were taken after the mixing mode in each case.

Thermocouples for measuring temperatures of the water and oil flows were installed as shown. Flows were arranged to produce a true counterflow condition for the test section.

Contributed by the Heat Transfer Division for publication in the JOURNAL OF HEAT TRANFER. Manuscript received by the Heat Transfer Division June 23, 1983. Paper No. 83-HT-39.

Table 1 Sixteen different spiral spring inserts used in this investigation

No. of Turns per in. (per m)	Wire Diameter, in. (cm)	Coil Diameter, in. (cm)
3 (118)	0.028 (0.071)	0.278 (0.706)
3 (118)	0.047 (0.119)	0.280 (0.711)
3 (118)	0.062 (0.157)	0.310 (0.787)
3 (118)	0.080 (0.203)	0.297 (0.754)
5 (197)	0.028 (0.071)	0.301 (0.765)
5 (197)	0.047 (0.119)	0.310 (0.787)
5 (197)	0.062 (0.157)	0.313 (0.795)
5 (197)	0.080 (0.203)	0.306 (0.777)
7 (276)	0.028 (0.071)	0.310 (0.787)
7 (276)	0.047 (0.119)	0.306 (0.777)
7 (276)	0.062 (0.157)	0.315 (0.800)
7 (276)	0.080 (0.203)	0.309 (0.785)
9 (354)	0.028 (0.071)	0.315 (0.800)
9 (354)	0.047 (0.119)	0.310 (0.787)
9 (354)	0.062 (0.157)	0.313 (0.795)
9 (354)	0.080 (0.203)	0.316 (0.803)

The fitting, attaching the inner tube to the mixing device, on the outlet and downstream area of test section was used to add the augmentative devices for evaluation. Insertion and removal of these devices was accomplished within a matter of minutes. A straight wire, no greater than the diameter of the device under test, was used to keep the augmentative device in its proper location in the test section. Without this wire, the oil flow would force the device into the mixing section and produce erroneous results.

Water flows were measured by a Cox AN-16 type turbine flow meter with corrections applied for the temperature range covered during the study. Oil flows were measured by a Cox AN-8 type turbine flow meter with corrections applied also. Readout for both flow meters was made on a Cox digital unit which converted cycles per second from the meter to gallons per minute. Temperatures were measured using copper-constantan wires and a Doric 405 digital readout meter. Oil pressure drop was measured by a pressure transducer using a Consolidated Controls Corporation digital readout meter. This method of obtaining oil pressure drop was necessary because the inlet pressures exceed those allowable for a mercury manometer.

Nomenclature

A = heat transfer area of the bare tube (without spring insert), ft^2 (m^2)

c_p = specific heat of the fluid flow at constant pressure, Btu/lbm•°F (kJ/kg °C)

D = inside diameter of the bare tube, ft (m)

E = fluid pumping power required per unit heat transfer area of the bare tube: E (hp/ft^2) = 3600 $M\,\Delta p/(778 \times 2545\,\rho\,A)$ or E (kW/m^2) = $M\Delta p/(\rho A)$

f = Fanning friction factor = $2g_c\,\rho\,r_h\,\Delta p/G^2\,L$

g_c = conversion constant = 32.174 lbm•ft/lbf•s^2 (unity and dimensionless in SI units)

G = flow stream mass velocity, lbm/s•ft^2 (kg/s•m^2)

h = convection heat transfer coefficient, Btu/s•ft^2•°F (kW/m^2•°C)

h^* = ratio of h of tube with spring insert to that of bare tube

j = Colburn j factor = $h\,\mathrm{Pr}^{2/3}/G\,c_p$

K = thermal conductivity of tube wall, Btu/s•ft•°F (kW/m•°C)

L = length of tube, ft (m)

LMTD = Log Mean Temperature Difference between hot and cold flows, °F (°C)

M = fluid mass flow rate, lbm/s (kg/s)

Nu = Nusselt number (based on the inside diameter of the bare tube)

Δp = fluid pressure drop, lbf/ft^2 (kPa)

Pr = Prandtl number

Q = heat transfer rate, Btu/s (kW)

r = radius of the bare tube, ft (m)

r_h = hydraulic radius of the flow passage, ft (m)

Re = Reynolds number (based on the inside diameter of the bare tube)

T = fluid temperature, °F (°C)

ΔT = temperature difference between hot and cold flows, °F (°C)

TURNS/IN, (TURNS/m) = number of turns of the coil per inch or per meter

U = overall convection heat transfer coefficient, Btu/s•ft^2•°F (kW/m^2•°C)

μ = absolute viscosity of fluid, lbm/ft•hr (Pa•s)

ρ = density of fluid, lbm/ft^3 (kg/m^3)

Subscripts

b = based on bulk average temperature

exit = exit of the flow

in = inlet of the flow

o = oil side

w = water side, or based on wall temperature

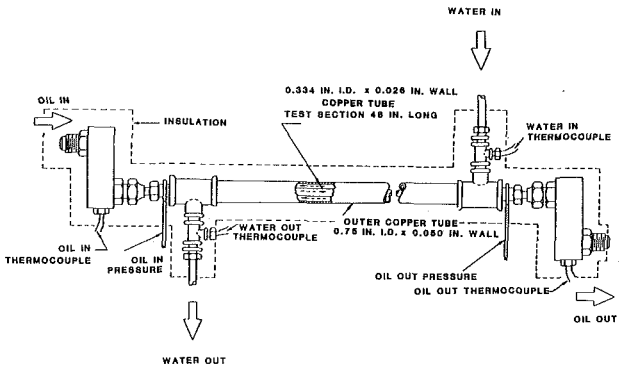

Fig. 2 Arrangement of test section

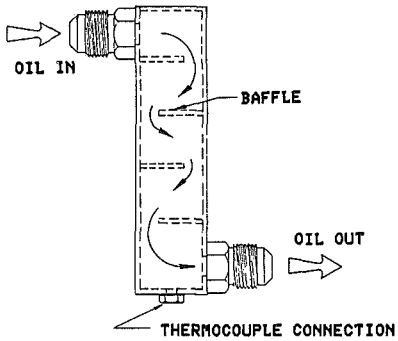

Fig. 3 Inlet and outlet oil mixing device

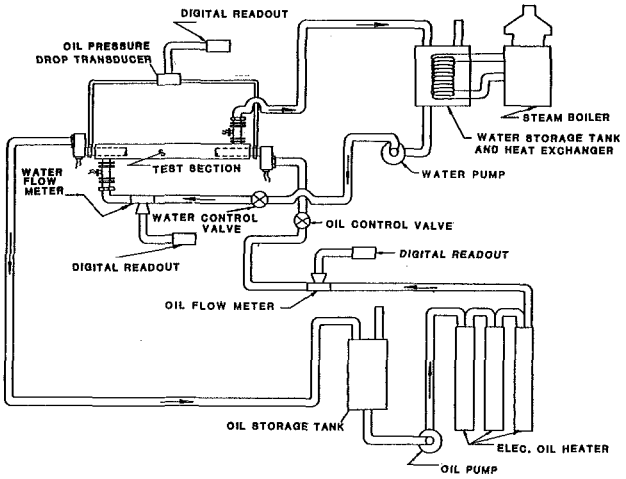

Fig. 4 Schematic of test apparatus

The oil used in this investigation was light engine oil (SAE 10). Oil flow was obtained using a 7.5 hp (5.6 kW) electric motor driven pump on a standard test stand. The oil flow rate was varied from approximately 0.5 gpm to 6.0 gpm (1.9 to 22.7 liters/min). The upper limit of the oil flow rate was determined by the particular augmentative device being studied. The oil was heated by immersion-type electric heaters. The range of the average temperature of the oil flow covered in this study was from 214°F to 240°F (101°C to 116°C) approximately. Thus the average Prandtl number of the oil flow in this study was 90 approximately.

City water was used as cooling water in this study. Water flow was obtained by a 15 hp (11.2 kW) electric motor driven pump on the same test stand. The water was heated by steam. Its temperatures were controlled by the cooling water flowing through a shell and tube type heat exchanger located in the test water circuit. The range of the average temperature of the

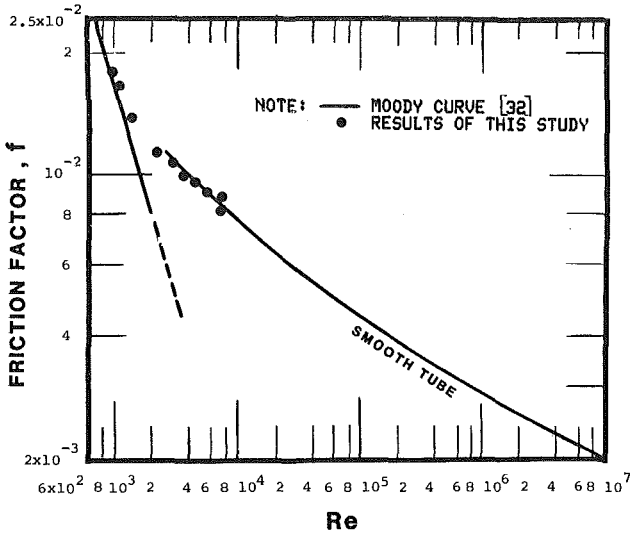

Fig. 5 Comparison of flow friction data—bare tube

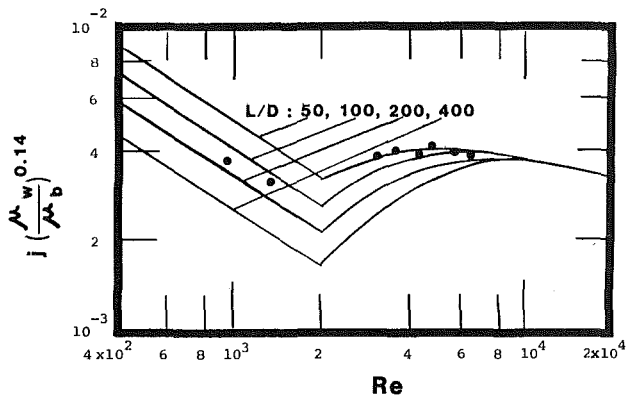

Fig. 6 Comparison of heat transfer data—bare tube; note: ——— published data [37]; ● results of this study, L/D = 143

water flow covered in this study was from 104°F to 158°F (40°C to 70°C) approximately. The water flow rate was controlled at approximately 50 gpm (189.3 liters/min). Under these conditions, the convective heat transfer coefficient on the water side was much higher than that on the oil side.

It is noted that there is much disagreement on heat transfer correlations in an annular flow system. Thus many experimenters interested in determination of the internal convection heat transfer coefficients go to additional effort to assure that the internal tube wall temperatures are measured directly. In this investigation, the water flow rate in the annular space was intentionally kept very high. The range of the ratio hA of the water side to that of the oil side is from about 50 to nearly 100. Therefore the accuracy level of the water side heat transfer coefficient has insignificant effect on that of the oil side in this investigation. It was thus decided that direct measurement of the internal tube wall temperatures was not needed.

In each test run, data for temperatures, flow rates, and fluid pressure drops on both oil and water sides were recorded after steady-state conditions were established. The heat transfer rates calculated based on the operating conditions of both flow sides were found to agree within 3 percent. Test runs of the bare tube (smooth tube without a spring insert) were conducted first. Results of flow friction runs of the bare tube of this study are presented in Fig. 5 together with the f-Re relationships of Moody [32–34] converted in terms of the Fanning friction factor. As shown in this figure, the agreement between results of this study and Moody correlations is excellent.

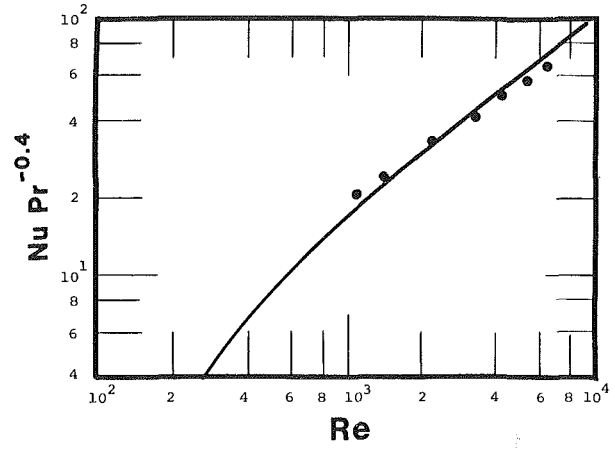

Fig. 7 Comparison of heat transfer data; note: ——— published data [7]; ● results of this study; 0.080 in. wire, 0.333 in. pitch

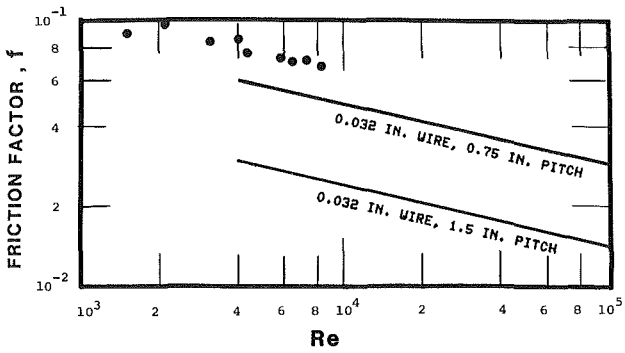

Fig. 8 Comparison of flow friction data; note: ——— published data [36]; ● results of this study; 0.028 in. wire, 0.333 in. pitch

Results of the heat transfer runs of the bare tube of this study are presented in Fig. 6. The heat transfer correlations originally suggested by Sieder and Tate [35] are also presented in this figure. These correlations are generally recommended [33, 35–38] for determining the heat transfer coefficient in circular tubes for all regions of flow, particularly for petroleum oils. The agreement between results of this study and the Sieder–Tate correlations is good in the laminar region and in the regime close to the turbulent flow. It is noted that the flow in the transition region is usually unstable and the fluctuation in heat transfer has been observed [37]. As shown in Fig. 6, the test data in the transition region follow the normal pattern of the Sieder–Tate correlations: Thus the agreement between them is also good.

All the observations mentioned above and in the following sections indicated that the experimental apparatus and the test procedure used in this study can generate reliable data. The estimated magnitudes of the uncertainties of the correlations for both heat transfer and flow friction in this study are approximately 7 percent.

Results and Discussion

The heat transfer rates between oil and water flows across the tube wall in the test section were calculated by

$$Q = (Mc_p)(T_{\text{exit}} - T_{\text{in}}) = U_w A_w(\text{LMTD}) \tag{1}$$

Here

$$\frac{1}{U_w A_w} = \frac{1}{h_o A_o} + \frac{\ln(r_w/r_o)}{2\pi k L} + \frac{1}{h_w A_w} \tag{2}$$

First the convection heat transfer coefficient on the water side h_w was calculated by the following equation [34] based on the equivalent diameter of the annular space

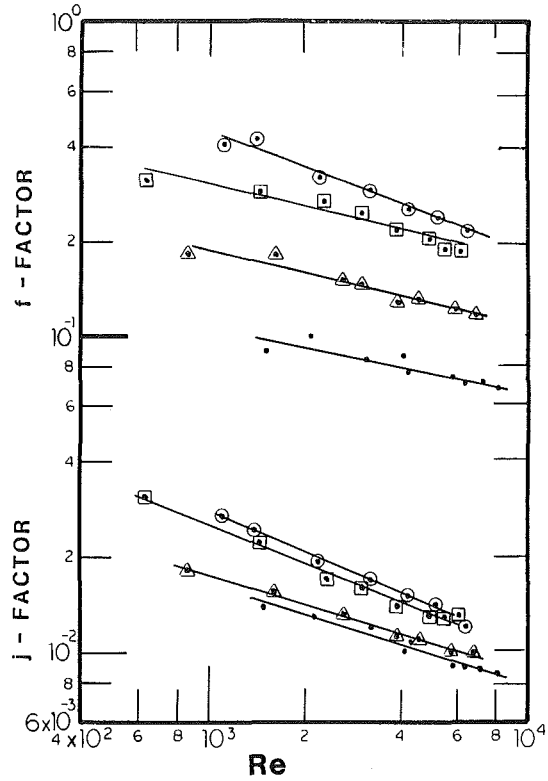

Fig. 9 Flow friction and heat transfer correlations (spring coil of 3 turns/in.); note: wire diameter:

● 0.028 (0.071), Δ 0.047 (0.119), □ 0.062 (0.157), ⊙ 0.080 in. (0.203) (cm)

$$\text{Nu} = 0.023\ \text{Re}^{0.8}\text{Pr}^{0.33} \tag{3}$$

The convection heat transfer coefficient on the oil side h_o was determined by equations (1) and (2). It must be stressed that there is much disagreement on the heat transfer correlations in annular space; thus using equations (1) and (2) may not produce an accurate internal convection heat transfer coefficient h_o. However in this study, the water flow rate in the annular space was intentionally maintained at a very high level. The range of the ratio of $h_w A_w$ to $h_o A_o$ is from about 50 to nearly 100. Under this condition, even if the accuracy of h_w obtained by equation (3) is uncertain, it will not significantly affect the level of accuracy of h_o calculated by equations (1) and (2) as discussed in the previous section.

Heat transfer and flow friction characteristics of oil flowing through a tube with a spiral spring insert in the cooling mode operation do not seem to be available in the literature. Verifications of results of this study were therefore carried out by comparing with available published data obtained in similar systems using water instead of oil. Figure 7 presents such a comparison for the heat transfer characteristics. The curve shown in Fig. 7 is from the case [7, 36] of water flowing through tubes with spiral spring inserts of several configurations. One of these spring inserts is 0.080 in. o.d. wire and 0.375 in. pitch. The data points of this study presented in Fig. 7 are from the case of oil flowing through a tube with similar spiral spring insert (0.080 in. o.d. wire and 3 turns/in., or 0.333 in. pitch). As shown in this figure, the agreement is excellent.

Flow friction data available in literature are scarce even for systems with water flowing through tubes with spring inserts and with the same range of Reynolds number used in this study. Figure 8 presents test results of this study together with two curves of available data [36]. The data points presented are from the case of oil flowing through a tube with spring in-

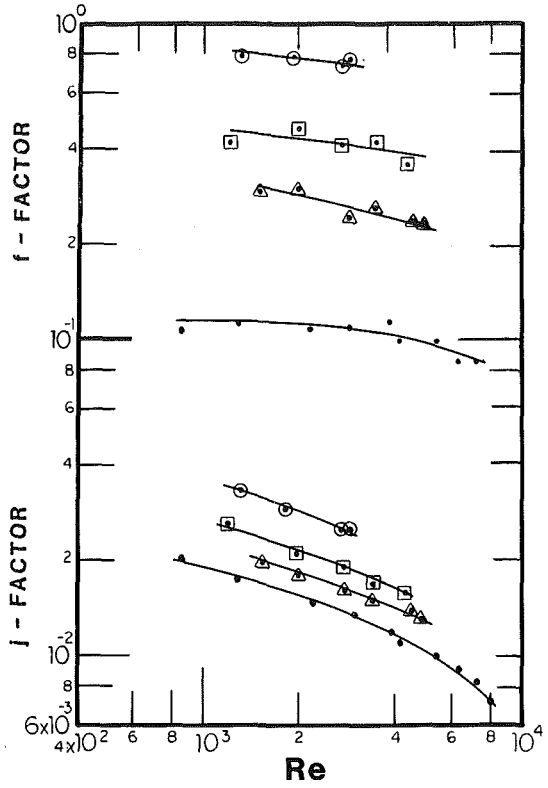

Fig. 10 Flow friction and heat transfer correlations (spring coil of 5 turns/in.); note: wire diameter:

● 0.028 (0.071), Δ 0.047 (0.119), □ 0.062 (0.157), ⊙ 0.080 in. (0.203) (cm)

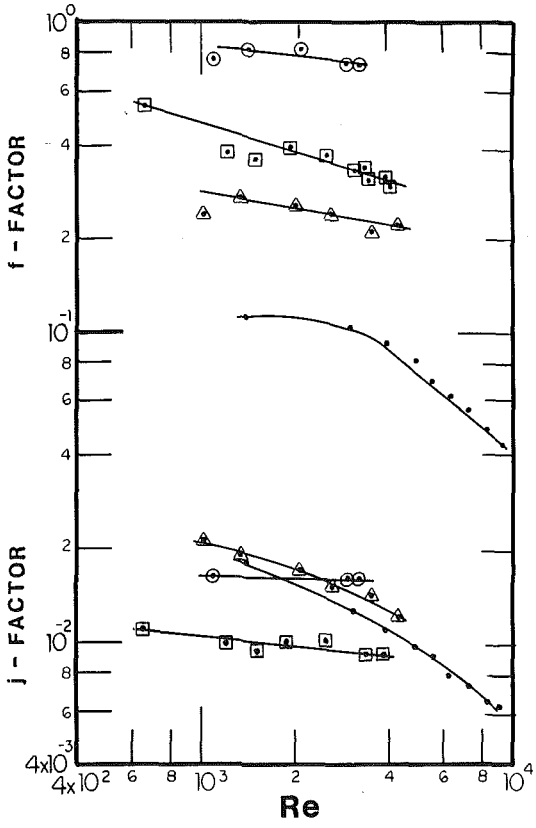

Fig. 11 Flow friction and heat transfer correlations (spring coil of 7 turns/in.); note: wire diameter:

● 0.028 (0.071), Δ 0.047 (0.119), □ 0.062 (0.157), ⊙ 0.080 in. (0.203) (cm)

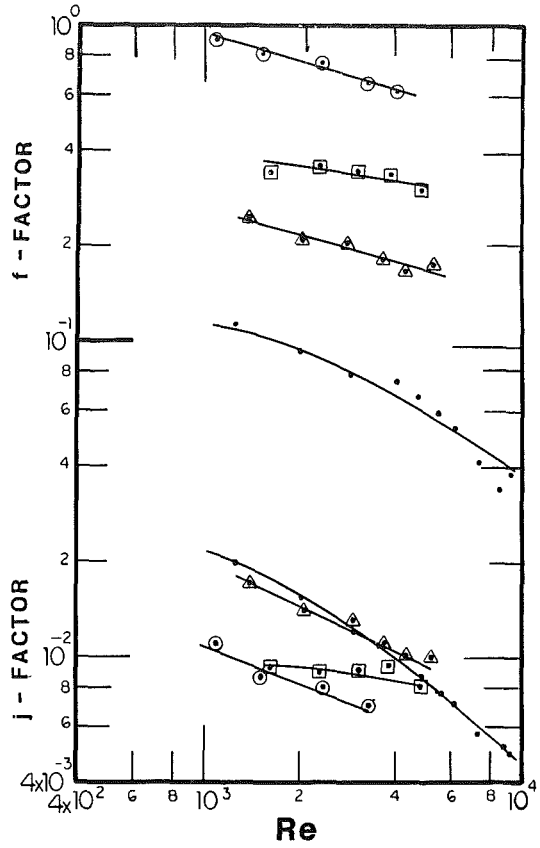

Fig. 12 Flow friction and heat transfer correlations (spring coil of 9 turns/in.); note: wire diameter:

● 0.028 (0.071), Δ 0.047 (0.119), □ 0.062 (0.157), ⊙ 0.080 in. (0.203) (cm)

sert of 0.028 in. o.d. wire and 3 turns/in. (0.333 in. pitch). The curves presented are drawn from data obtained from the case of water flowing through tubes with spring inserts of 0.032 in. o.d. wire and with 0.75 in. and 1.5 in. pitches, respectively. As can be seen the friction factor increases when the spring pitch decreases. Therefore it may be inferred that the test data of this study compare favorably with data obtained by other investigators.

Figures 9 to 12 present the relationships of f-Re and j-Re of all 16 spiral spring inserts studied. For the same Reynolds number, both the f factor and the j factor of the oil flowing in tubes with spring inserts are higher than those of the bare tube. This indicates that the use of the spring insert will increase the tube side heat transfer coefficient. At the same time, the flow friction factor also increases as expected.

The absence of a "dip" zone in the transition region between laminar and turbulent flow can be noted in Figs. 9–12. This is the unique characteristic of fluid flowing through tubes with heat transfer augmentative devices as also observed by others [39].

The increase in the flow friction factor is due to the following effects:

1 the increase of surface area
2 the increase of the disturbance in the main core flow
3 the increase of the disturbance in the laminar sublayer of the boundary layer of the flow

As discussed previously, the principal mechanism for heat transfer enhancement is due to the disruption of the laminar sublayer only. Thus operating conditions influence the flow friction more than the heat transfer. Therefore, when the flow rate increases, or when Reynolds number increases, the flow friction increases relatively faster than the increase in heat

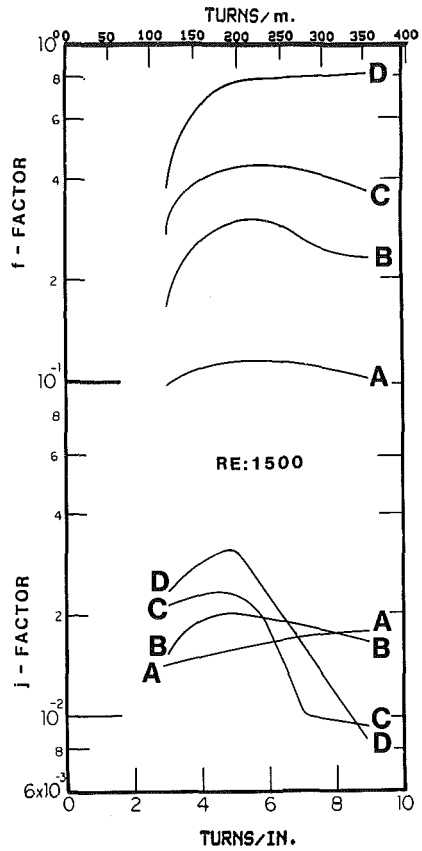

Fig. 13 Flow friction and heat transfer correlations; note: wire diameter:

A 0.028, B 0.047, C 0.062, D 0.080 in.
(0.071) (0.119) (0.157) (0.203) (cm)

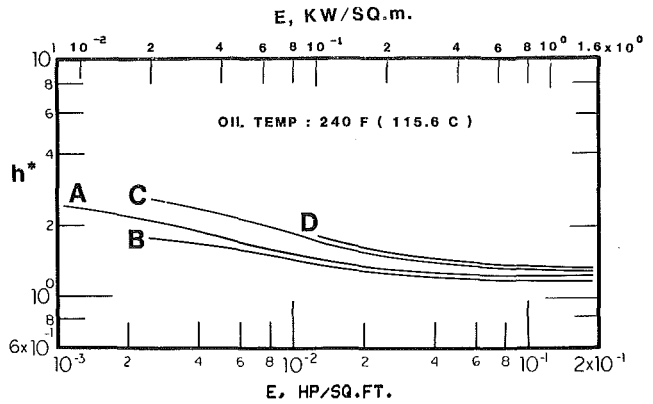

Fig. 14 h^*-E relationships (spring coil of 3 turns/in.); note: wire diameter:

A 0.028, B 0.047, C 0.062, D 0.080 in.
(0.071) (0.119) (0.157) (0.203) (cm)

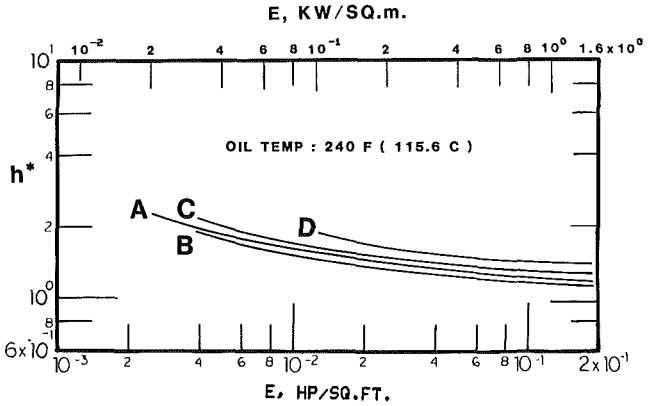

Fig. 15 h^*-E relationships (spring coil of 5 turns/in.); note: wire diameter:

A 0.028, B 0.047, C 0.062, D 0.080 in.
(0.071) (0.119) (0.157) (0.203) (cm)

transfer modulus j. This is the reason why the slope of the f-Re curve is generally lower than that of the j-Re curve for the same wire diameter and for the same spring pitch as shown in Figs. 9–12. However, when the number of turns/in. increases, or when the spring pitch decreases, the situation may change as discussed below.

The maximum thickness of the laminar sublayer of the oil flow of all the cases of this study was found to be around 0.02 in. (0.0508 cm). The smallest wire diameter used was 0.028 in. (0.071 cm). Thus the wire of the spring insert always penetrated out of the laminar sublayer of the flow. The wire element therefore acts as some sort of partition which divides the laminar sublayer into many cells. For the cases of 3 or 5 turns/in., or for the cases of larger distances between the partitions, the development of the disturbance in the laminar sublayer is hardly suppressed by the partitions. As the wire diameter increases, the induced disturbance in the laminar sublayer increases, then both the heat transfer and flow friction increase as shown in Figs. 9 and 10. For the case of 7 or 9 turns/in., or for the cases when the distances between partitions decrease, the partitions will prevent or suppress the effective development of the disturbance in the laminar sublayer, especially when the wire diameter is large. Under this condition, the level of the enhancement of heat transfer decreases significantly, while the level of the flow friction decreases slightly, as shown in Fig. 13. This figure indicates that both the heat transfer and flow friction first increase then decrease as the number of turns/in. of the spring coil increases. At a high number of turns/in., especially if the wire diameter is large, the heat transfer performance decreases so much that it eventually drops below those of the springs with smaller wire diameters. This situation can be observed in Figs. 11–13. In Fig. 12, the heat transfer performance of the spring with wire diameter 0.080 is the lowest among all the cases presented. However, the level of its flow friction is still the highest as also shown in Fig. 12.

The influence of the suppressing effect on the effective development of the disturbance in the laminar sublayer becomes stronger as the flow rate decreases. The heat transfer rate in the low Reynolds number range may drop to such a low level that the direction of the j-Re curve may be nearly horizontal (the case of 0.080 in. wire diameter) as shown in Fig. 11.

Figures 14–17 present the h^*-E relationships for all the cases studied. This relationship is one of the principal evaluation criteria in selecting suitable spiral spring inserts. This criterion is somewhat different from those used by others [41], but is generally used in the compact heat exchanger industry [40]. It must be stressed that h^* is only one of the criteria in selecting the right spring insert as the effective heat transfer augmentative device. Other criteria, such as the cost of the spring, the cost of installation, the cost of maintenance, weight penalty, and others should be carefully evaluated before the final selection can be determined.

As shown in Figs. 14–17, h^* varies from approximately 0.4 to 3.5. When h^* is larger than 1.0, use of the spring insert as a heat transfer augmentative device is more effective than using the bare tube. When h^* is less than 1.0, the reverse is true. There are cases when the size of the heat exchanger cannot be changed, but its heat transfer capability must be increased.

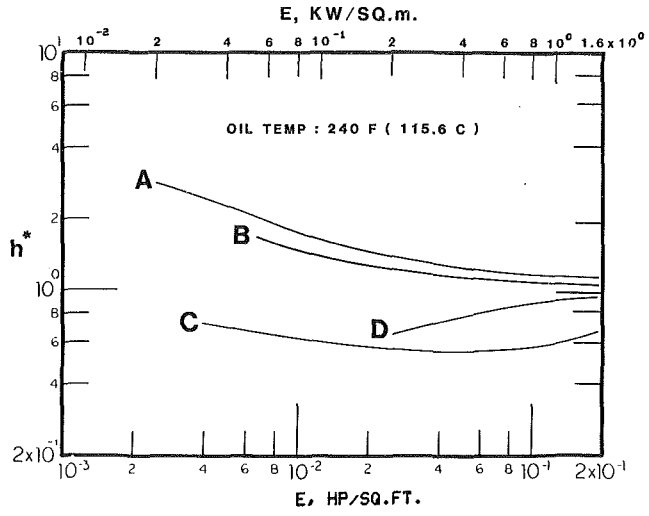

Fig. 16 h^*-E relationships (spring coil of 7 turns/in.); note: wire diameter:

A 0.028, B 0.047, C 0.062, D 0.080 in.
(0.071) (0.119) (0.157) (0.203) (cm)

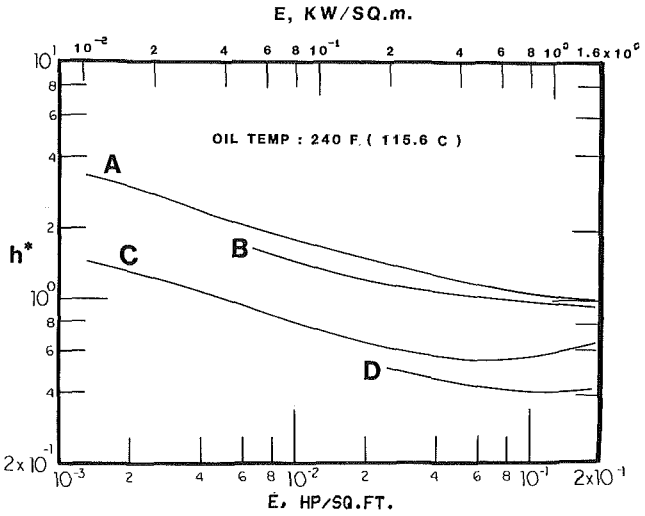

Fig. 17 h^*-E relationships (spring coil of 9 turns/in.); note: wire diameter:

A 0.028, B 0.047, C 0.062, D 0.080 in.
(0.071) (0.119) (0.157) (0.203) (cm)

Then some spring inserts with high heat transfer performance but low h^* may have to be used provided the increase of the fluid pumping power is tolerable.

As also shown in Figs. 14–17, h^* becomes higher when E becomes smaller. Thus use of the spring insert as a heat transfer augmentative device is more effective when the flow rate is low if all other operating parameters are kept unchanged.

Figure 18 shows the relationships of h^* and the wire diameter using turns/in. of the spring coils as parameters. These relationships are presented for $E = 0.0025$ hp/ft^2 (0.02 kW/m^2) and $E = 0.025$ hp/ft^2 (0.2 kW/m^2), respectively. Industrial heat exchangers generally operate in this range.

The spiral spring inserts discussed in this paper had been used successfully in the design of oil coolers for industrial applications. Figure 19 shows the core of a typical oil cooler using this heat transfer augmentative device.

In commercial applications, particularly those on industrial and agricultural tractors, the spring temper of the augmentative device is very important to prevent it from collapsing. In

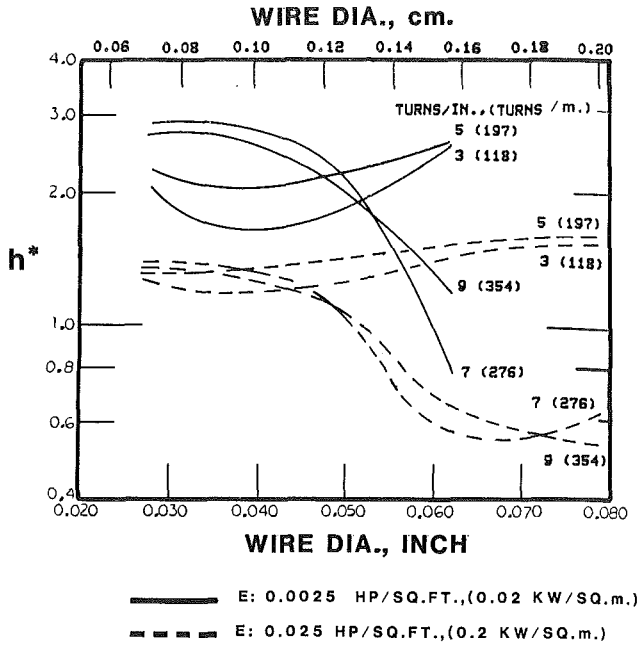

Fig. 18 h^*-wire diameter relationships

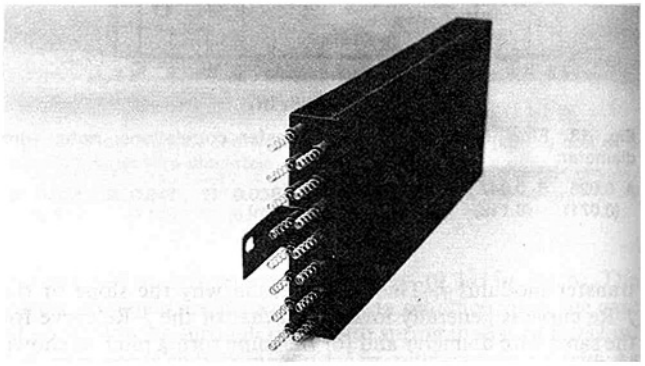

Fig. 19 Core of air-cooled oil cooler using spiral spring augmentative device

some applications, vehicles using heat exchangers with the spiral spring augmentative device remain exposed to very low ambient temperature for extended periods of time. As a vehicle starts and warms up, the oil, which has a high viscosity because of its low temperature, moves as a solid mass through the heat exchanger. If the wire temper is too low, the heavy oil will collapse the spring (so its pitch decreases) and deposit it at one end of the tube. Then there is nothing in the rest of the tube except the bare tube itself. This condition reduces the overall heat transfer performance of the heat exchanger. Thus provision should be made in the heat exchanger for preventing the spring coil from collapsing, especially when the wire diameter is small.

The high temper wire requires close manufacturing control as "spring back" can result in a device whose diameter is outside the acceptable tolerances. Too large a diameter causes assembly problems of the device into the heat exchanger tubes, thus reducing the assembly rate, which becomes costly.

Conclusions

Experimental investigation of a class of spiral spring coil used as heat transfer augmentative device in the cooling of oil flow was carried out. The following conclusions can be drawn from results of this investigation:

1 The spiral spring insert can increase the tube side heat transfer coefficient significantly. For the same fluid pumping power requirement, the heat transfer coefficient of the oil flow in a tube with this type of spring insert can triple that obtained in a tube without augmentative device (bare tube) when the Reynolds number is lower than about 1200. As the Reynolds number increases, the enhancement effect decreases asymptotically. The ratio of the heat transfer coefficient of the oil flow in a tube with spring insert to that in a bare tube reaches a constant value of about 1.5 when the Reynolds number is greater than 6000. Therefore the use of this class of spring insert is generally more effective for the cases when the fluid flow rates are relatively low.

2 In some cases, the use of the spring insert as a heat transfer augmentative device in the cooling mode operation is more effective than use of the bare tube. In other cases, it is less effective. There are cases, however, when the size of the heat exchanger cannot be changed, but its heat transfer rate must be increased. Under this condition, use of the spring insert was found to be desirable provided that the high fluid pressure drop is tolerable.

It is the hope of this writer that this paper may stimulate interest among research workers in the heat transfer field on the use of this class of spiral spring insert as heat transfer augmentative device for the cooling mode operation. It is suggested that the further investigation be carried out both theoretically and experimentally, especially in the low Reynolds number region around 100. This appears to be an area of growing concern as industry is trying to reduce fluid pumping power in order to reduce the operating cost or conserve the energy.

Acknowledgment

The author acknowledges the extensive effort of Mr. W. Melnyk, who set up the test apparatus and obtained the experimental data.

References

1 Bergles, A. E., "Survey and Evaluation of Techniques to Augment Convective Heat and Mass Transfer," *Progress in Heat and Mass Transfer*, Vol. 1, Pergamon Press, New York, 1969, pp. 331–424.

2 Bergles, A. E., and Webb, R. L., eds., *Augmentation of Convective Heat and Mass Transfer*, ASME, New York, 1970.

3 Bergles, A. E., *Research Workshop in Augmentation of Convective Heat Transfer*, Final Report, HTL-8, Engineering Research Institute, Iowa State University, 1975.

4 Bergles, A. E., Webb, R. L., Junkhan, G. H., and Jensen, M. K., *Bibliography on Augmentation of Convective Heat and Mass Transfer*, HTL-31, Engineering Research Institute, Iowa State University, 1983.

5 Webb, R. L., Carnavos, T. C., Park, E. L., Jr., and Hostetler, K. M., eds., *Advances in Enhanced Heat Transfer—1981*, HTD Vol. 18, ASME, New York, 1981.

6 Nakaoka, Z., and Watanabe, A., "Maximum Rate of Heat Transfer With Minimum Loss of Energy," *Proceedings of 7th International Congress of Refrigeration*, Vol. 3, 1936, pp. 221–245.

7 Siegel, L. G., "The Effect of Turbulence Promoters on Heat Transfer Coefficients for Water Flowing in Horizontal Tubes," *Heating, Piping and Air Conditioning*, ASHVE Journal Section, June 1946, pp. 197–204.

8 Sams, E. W., "Heat Transfer and Pressure Drop Characteristics of Wire-Coil Type Turbulence Promoters," Paper presented at Nuclear Reactor Heat Transfer Conference, 1956. Also appears in TID-7529, Part 1, Book 2, Nov. 1957, Technical Information Division, AEC, pp. 390–415.

9 Lopina, R. F., "Heat Transfer and Pressure Drop in Tape-Generated Swirl Flow of Single Phase Water," ASME JOURNAL OF HEAT TRANSFER, Vol. 91, Aug. 1969, pp. 434–442.

10 Kumar, P., and Judd, R. L., "Heat Transfer With Coiled Wire Turbulence Promoters," *Canadian Journal of Chemical Engineering*, Vol. 48, Aug. 1970, pp. 378–383.

11 Kalinin, E. K., Dreitser, G. A., Yarkho, S. A., and Kusminov, V. A., "The Experimental Study of the Heat Transfer Intensification Under Conditions of Forced One and Two-Phase Flow in Channels," in: *Augmentation of Convective Heat and Mass Transfer*, A. E. Bergles and R. L. Webb, eds., ASME, New York, 1970, pp. 80–90.

12 Webb, R. L., Eckert, E. R., and Goldstein, R. J., "Heat Transfer and Friction in Tubes With Repeated-Rib Roughness," *International Journal of Heat and Mass Transfer*, Vol. 14, 1971, pp. 601–617.

13 Kalinin, E. K., and Yarkho, S. A., "Augmentation of Heat Transfer in Gases and Liquids Flowing in Tubes," *Heat Transfer—Soviet Research*, Vol. 4, No. 2, 1972, pp. 79–86.

14 Webb, R. L., Eckert, E. R., and Goldstein, R. J., "Generalized Heat Transfer and Friction Correlations for Tubes With Repeated-Rib Roughness," *International Journal of Heat and Mass Transfer*, Vol. 15, 1972, pp. 180–183.

15 Kalinin, E. K., Dreitser, G. A., and Kozlow, A. K., "An Investigation of Heat Transfer Intensification During Lengthwise Flow Along Tube Bundles With Various Relative Pitches," *International Chemical Engineering*, Vol. 13, No. 1, 1973, pp. 1–4.

16 Klaczak, A., "Heat Transfer in Tubes With Spiral and Helical Turbulators," ASME JOURNAL OF HEAT TRANSFER, Vol. 95, 1973, pp. 557–559.

17 Date, A. W., "Prediction of Fully-Developed Flow in a Tube Containing a Twisted-Tape," *International Journal of Heat and Mass Transfer*, Vol. 17, 1974, pp. 845–859.

18 Hong, S. W., and Bergles, A. E., "Augmentation of Laminar Flow Heat Transfer in Tubes by Means of Twisted-Tape Inserts," ASME JOURNAL OF HEAT TRANSFER, Vol. 98, 1976, pp. 251–256.

19 Royal, J. H., and Bergles, A. E., "Augmentation of Horizontal In-Tube Condensation by Means of Twisted-Tape Inserts and Internally Finned Tubes," ASME JOURNAL OF HEAT TRANSFER, Vol. 100, 1978, pp. 17–24.

20 Marner, W. J., and Bergles, A. E., "Augmentation of Tubeside Laminar Flow Heat Transfer by Means of Twisted-Tape Inserts, Static-Mixer Inserts and Internal Finned Tubes," *Heat Transfer 1978*, Vol. 2, Hemisphere, New York, 1978, pp. 583–588.

21 Bergles, A. E., "Experimental Study of the Augmentation of In-Tube Condensation of R-113," *ASHRAE Trans.*, Vol. 85, Part 2, 1979, pp. 1–14.

22 Webb, R. L., "Toward a Common Understanding of the Performance and Selection of Roughness for Forced Convection," in: *Studies in Heat Transfer*, J. P. Hartnett, T. F. Irvine, E. Pfender, and E. M. Sparrow, eds., Hemisphere and McGraw-Hill, 1979, pp. 257–272.

23 Kalinin, E. K., Dreitser, G. A., and Kostyuk, V. V., "Modern Problems of Heat Transfer Augmentation in Single- and in Two-Phase Flows," in: *Studies in Heat Transfer*, J. P. Hartnett, T. F. Irvine, Jr., E. Pfender, and E. M. Sparrow, eds., Hemisphere and McGraw-Hill, 1979, pp. 457–474.

24 Kalinin, E. K., Dreytser, G. A., Zakirov, S. G., Vakhabov, A. A., Akzamov, Sh. K., and Levin, Ye. S., "Improvement of Heat Transfer in Tubular Heat Exchangers by the Use of Grooved Tubes," *Heat Transfer—Soviet Research*, Vol. 13, No. 4, 1981, pp. 30–40.

25 Nakayama, W., Takahashi, K., and Daikoku, T., "Spiral Ribbing to Enhance Single-Phase Heat Transfer Inside Tubes," *ASME-JSME Thermal Engineering Joint Conference Proceedings*, Y. Mori and W. J. Yang, eds., Vol. 1, ASME, New York, 1983, pp. 365–372.

26 Tanasawa, I., Nishio, S., Takano, K., and Tado, M., "Enhancement of Forced Convection Heat Transfer in Rectangular Channel Using Turbulence Promoters," *ASME-JSME Thermal Engineering Joint Conference Proceedings*, Y. Mori and W. J. Yang, eds., Vol. 1, ASME, New York, 1983, pp. 395–402.

27 Davidson, D. M., "Radiation Fin Augmentation in a Tube With Tape-Generated Swirl Flow," *ASME-JSME Thermal Engineering Joint Conference Proceedings*, Y. Mori and W. J. Yang, eds., Vol. 1, ASME, New York, 1983, pp. 403–410.

28 Kreith, F., and Margolis, D., "Heat Transfer and Friction in Turbulent Vortex Flow," *Applied Scientific Research*, Vol. 9, 1959, pp. 457–473.

29 Gambill, W. R., and Bundy, R. D., "High Flux Heat Transfer Characteristics of Pure Ethylene Glycol in Axial and Swirl Flow," *AIChE Journal*, Vol. 9, 1963, pp. 55–59.

30 Hay, N., and West, P. D., "Heat Transfer in Free Swirling Flow in Pipe," ASME JOURNAL OF HEAT TRANSFER, Vol. 97, 1975, pp. 411–416.

31 Zaherzadeh, N. H., and Jagadish, B. S., "Heat Transfer in Decaying Swirl Flows," *International Journal of Heat and Mass Transfer*, Vol. 18, 1975, pp. 941–944.

32 Moody, L. F., "Friction Factor for Pipe Flow," *Trans. ASME*, Vol. 66, 1944, pp. 671–684.

33 Knudsen, J. G., and Katz, D. L., *Fluid Dynamics and Heat Transfer*, McGraw-Hill, New York, 1958, p. 176 and p. 305.

34 Chapman, A. L., *Heat Transfer*, 4th ed., MacMillan, New York, 1984, p. 255 and p. 290.

35 Sieder, E. N., and Tate, G. E., "Heat Transfer and Pressure Drop of Liquids in Tubes," *Industrial Engineering and Chemistry*, Vol. 28, 1936, pp. 1429–1435.

36 Fraas, A. P., and Ozisik, M. N., *Heat Exchanger Design*, Wiley, 1965, pp. 47–48.

37 Kreith, F., and Black, W. Z., *Basic Heat Transfer*, Harper and Row, New York, 1980, p. 248.

38 McAdams, W. H., *Heat Transmission*, 3rd ed., McGraw-Hill, New York, 1954, p. 241.

39 Marner, W. J., Bergles, A. E., and Chenoweth, J. M., "On the Presentation of Performance Data for Enhanced Tubes Used in Shell-and-Tube Heat Exchangers," ASME JOURNAL OF HEAT TRANSFER, Vol. 105, 1983, pp. 358–365.

40 Kays, W., and London, A. L., *Compact Heat Exchangers*, 3rd ed., McGraw-Hill, New York, 1984.

41 Bergles, A. E., Blumenkrantz, A. R., and Taborek, J., "Performance Evaluation Criteria for Enhanced Heat Transfer Surfaces," *Heat Transfer 1974*, Vol. II, 1974, pp. 239–243.

Second-Law Analysis of Heat Transfer in Swirling Flow Through a Cylindrical Duct

P. Mukherjee

G. Biswas

P. K. Nag

Department of Mechanical Engineering,
Indian Institute of Technology,
Kharagpur 721302 India

A second-law analysis is made on a swirling flow in a cylindrical duct with constant wall temperature. A purely tangential entry of the fluid is considered and a simplified model, consisting of a central air core enclosed by a potential, free vortex region and a boundary layer, is assumed. The approximate hydrodynamic boundary layer equations, and the continuity equation, are set up and solved numerically for the velocity gradients in the boundary layer. Similarly, the temperature gradients within the thermal boundary layer are obtained from the energy equation. The local Nusselt number and rate of entropy generation are calculated and used to evaluate the rate of heat transfer and loss of available energy, respectively. A merit function, defined as the ratio of exergy transferred to the sum of exergy transferred and exergy destroyed, is evaluated for various values of Reynolds number, based on the inlet tangential velocity, and conclusions are drawn about the influence of inlet swirl on irreversibility.

Introduction

This investigation stems from the area of heat transfer augmentation by imparting a swirl to the fluid. Among a number of studies in the relevant field, Kreith and Sonju (1965) have discussed tape-induced turbulent flow through a pipe. Gutstein et al. (1970) have developed a theory based on solid body rotation for a helical vane insert. Bergles et al. (1980) reported a bibliography of different augmentation techniques. Nondecaying swirl flow has been the subject of many investigations (see Kreith and Margolis, 1959; Gambill and Bundy, 1963; Smithberg and Landis, 1964; Hong and Bergles, 1976). Blum and Oliver (1966) and Migay and Golubev (1970) showed that there was significant increase in heat transfer due to free swirling flow. Hay and West (1975) measured the local heat transfer coefficient along the axial direction for air flowing through a slot at the inlet to the pipe. Klepper (1972) used swirl generators at the pipe inlet and studied the performance of swirl flow using nitrogen gas as fluid. Zaherzadeh and Jagdish (1975) carried out experimental investigation of decaying swirl flow created by tangential vane swirls at the inlet of the test section. An analytical study of the heat transfer characteristics in decaying turbulent swirl flow generated by short twisted tapes placed at the entrance of the test section was carried out by Algifri and Bhardwaj (1985). They showed that the augmentation in the local heat transfer can be as high as 80 percent and an initial length of about 60 tube diameters is important to augmentation. Sparrow and Chaboki (1984) performed an experimental study on swirl-affected turbulent air flow and heat transfer in a tube. The swirling motion enhanced heat transfer substantially in the initial portion of the tube. Compared with the enhancements encountered in the conventional thermal entrance region in a nonswirling pipe flow, those associated with swirl were found to be remarkably greater. Junkhan et al. (1985) conducted experimental studies of three different turbulator inserts for fire tube boilers. Two commercial turbulators, consisting of narrow, thin metal strips bent and twisted in zig-zag fashion to allow a periodic contact with tube wall, displayed 135 and 175 percent increase in heat transfer coefficient at a high Reynolds number. A third turbulator consisting of a twisted strip, with width slightly less than the tube diameter, provided a 65 percent increase in the heat transfer coefficient while the increase in the friction factor was small as compared to the other two turbulator inserts.

Simultaneous release of hot air at one end and cold air at the other end due to a high-velocity swirling flow of compressible fluids is observed in Ranque–Hilsch vortex tubes. Refrigeration potential is obtained by creating a colder stream at the center through a low-pressure zone. Detailed analyses of vortex tube refrigerators have been discussed in many investigations. Among these the investigations of Hartnett and Eckert (1957), Merkulov (1960), Metenin (1960), and Parulekar (1961) are notable.

However, one aspect of swirling flow which is yet to be analyzed is the irreversibility associated with imparting a swirl. Bejan (1982) has shown that irreversibility, quantified by the rate of entropy generation, plays a very significant part in convective heat transfer processes. Irreversibility of a process is estimated from total production of entropy in the process. The method of second-law analysis seeks to evaluate the rate of entropy generation in various processes and then seeks to minimize the same by a suitable adjustment of flow parameters. Thus the analyses of heat transfer in ducts with constant heat flux (Bejan, 1978), flat plates, cylinders in cross flow and rectangular ducts (Bejan, 1979), heat exchangers (Bejan, 1977), and cryogenic apparatus (Bejan and Smith, 1975) are of importance. Sarangi and Chowdhury (1982) have analyzed counterflow heat exchangers to account for the entropy generated due to axial conduction and have derived an expression for optimum wall conductivity.

This study presents a method of evaluating the rate of entropy generation for swirling flow in a cylindrical duct. Based on an evaluation of the irreversibility, this study draws some conclusions about the effect of swirl on the availability.

Flow Model

The simplified flow model assumes a swirling flow produced by tangential entry of the fluid into the cylindrical duct. The flow field has been considered to consist of the following three zones (Fig. 1):

(*a*) the central air core,
(*b*) the potential core of free vortex outside the central air core, and
(*c*) the zone of boundary layer near the wall of the duct.

The temperature distribution in the fluid flowing along the duct is as follows:

Contributed by the Heat Transfer Division for publication in the JOURNAL OF HEAT TRANSFER. Manuscript received by the Heat Transfer Division July 19, 1985.

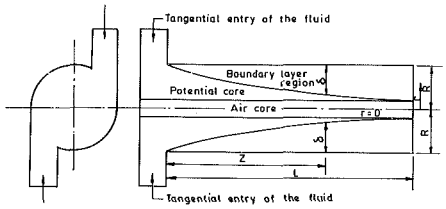

Fig. 1 Hydrodynamic picture inside the duct according to the theoretical model

(*a*) At the inlet, the fluid has the same initial temperature T_0 across the whole cross section.

(*b*) Downstream from the inlet, the fluid temperature at the wall is the same as the wall temperature T_w and decreases radially toward the core.

(*c*) Farther downstream, the thermal boundary layer grows in size.

(*d*) For a very long duct, the temperature across the cross section becomes almost equal and approaches the wall temperature T_w.

The approximate hydrodynamic boundary layer equations for laminar, steady-state flow of an incompressible, purely viscous Newtonian fluid, flowing symmetrically with respect to the axis $r = 0$ in cylindrical polar coordinates are given by Som and Biswas (1985) as

$$\frac{1}{\rho}\frac{\partial p}{\partial r}=\frac{V_\phi^2}{r} \tag{1}$$

$$V_r\frac{\partial V_\phi}{\partial r}+V_z\frac{\partial V_\phi}{\partial z}=\frac{\mu}{\rho}\frac{\partial}{\partial r}\left[\frac{\partial V_\phi}{\partial r}\right] \tag{2}$$

$$V_r\frac{\partial V_z}{\partial r}+V_z\frac{\partial V_z}{\partial z}=-\frac{1}{\rho}\frac{\partial p}{\partial z}+\frac{\mu}{\rho}\frac{\partial}{\partial r}\left[\frac{\partial V_z}{\partial r}\right] \tag{3}$$

The equation of continuity is

$$\frac{\partial V_r}{\partial r}+\frac{\partial V_z}{\partial z}=0 \tag{4}$$

The thermal boundary layer equation is given by

$$V_r\frac{\partial \theta}{\partial r}+V_z\frac{\partial \theta}{\partial z}=\alpha\frac{\partial^2\theta}{\partial r^2} \tag{5}$$

where the viscous dissipation terms are neglected and θ (the excess temperature over the inlet temperature) is $T - T_0$.

The boundary layer momentum integrals are obtained by the usual Pohlhausen method of integrating equations (2) and (3) through a hydrodynamic boundary layer having thickness δ and equation (5) through a thermal boundary layer of thickness δ_t. The radial component of velocity is eliminated with the help of equation (4). Finally, the tangential and axial momentum integrals are obtained as

$$-\frac{\Omega}{(R-\delta)}\int_{R-\delta}^{R}\frac{\partial V_z}{\partial z}\,dr+\int_{R-\delta}^{R}\frac{\partial}{\partial z}\,(V_zV_\phi)\,dr=\frac{\mu}{\rho}\left[\frac{\partial V_\phi}{\partial r}\right]_{R-\delta}^{R} \tag{6}$$

$$2\int_{R-\delta}^{R}V_z\frac{\partial V_z}{\partial z}\,dr-\int_{R-\delta}^{R}\frac{\Omega^2}{(R-\delta)^3}\frac{d\delta}{dz}=\frac{\mu}{\rho}\left[\frac{\partial V_z}{\partial r}\right]_{R-\delta}^{R} \tag{7}$$

and the energy integral as

$$\int_{R-\delta_t}^{R}\frac{\partial}{\partial z}\,(V_z\theta)=\alpha\left[\frac{\partial\theta}{\partial r}\right]_{r=R} \tag{8}$$

Equations (6) and (7) are solved by taking the polynomial distribution of velocity components as

$$V_z=\frac{\Omega E}{R}\,(\eta-2\eta^2+\eta^3)=\frac{\Omega E}{R}f(\eta) \tag{9}$$

$$V_\phi=\frac{\Omega}{R}\,(2\eta-\eta^2)=\frac{\Omega}{R}\,\phi(\eta) \tag{10}$$

where

$$\eta=\frac{(R-r)}{\delta} \tag{11}$$

so that η varies from 0 to 1.0 through the boundary layer. With these simple assumptions for the functions $f(\eta)$ and $\phi(\eta)$ two variable quantities E and δ determine the boundary

Nomenclature

c_p = specific heat at constant pressure, J/kg•K
dV^* = nondimensional volume element, defined in equation (33)
D = duct diameter, m
E = velocity parameter, defined in equation (9)
Ec = Eckert number, defined in equation (32)
G = parameter defined in equation (16)
h = heat transfer coefficient, W/m²•K
I = irreversibility, W
K = thermal conductivity of fluid, W/m•K
L = duct length, m
M = merit function, defined in equation (40)
Ns = total rate of entropy generation defined in equation (35)
Ns_1 = local rate of entropy generation
Ns_3 = rate of entropy generation per unit volume defined in equation (30)
Nu_z = local Nusselt number = h_zD/K
$\overline{\mathrm{Nu}}$ = average Nusselt number = h_cD/K
P = fluid pressure, Pa
Pr = Prandtl number = $\mu C_P/K$
Q = heat transfer rate, W
Q_a = exergy transfer accompanying energy transfer Q, W
q = heat flux, W/m²
r = radial dimension, m
R = duct radius, m
Re = Reynolds number based on the inlet tangential velocity
$\dot{S}$ = total rate of entropy generation, W/K
$\dot{S}_3$ = rate of entropy generation per unit volume, W/m³•K
T = fluid temperature, K
T_a = ambient temperature, K
T_b = bulk temperature of fluid, K
T_0 = inlet fluid temperature, K
T_w = wall temperature, K
V_r = radial velocity, m/s
V_z = axial velocity, m/s
V_ϕ = circumferential velocity, m/s
z = axial dimension, m
z_1 = z/D
α = thermal diffusivity of fluid, m²/s
δ = hydrodynamic boundary layer thickness, m
δ_t = thermal boundary layer thickness, m
θ_b = $T_b - T_0$, K
θ_w = $T_w - T_0$, K
μ = fluid viscosity, N•s/m²
ρ = fluid density, kg/m³
σ = θ_w/T_w
σ_a = T_a/T_w
τ = shear stress of the fluid, N/m²
Ω = circulation constant, m²/s

layer at any point, so that E and δ are functions of z only and can therefore be determined by using momentum integrals (6) and (7). The kinematic boundary conditions are: $V_z=0$, $V_\phi=0$ at $r=R$; $V_z=0$, $\partial V_z/\partial r=0$, $V_\phi=\Omega/(R-\delta)$, $\partial V_\phi/\partial r=0$ at $r=R-\delta$. As the analysis points out, the tangential velocity of equation (10) does not satisfy the kinematic condition at the boundary layer interface. But to get along harmoniously with the laminar boundary layer theory ($\delta/R << 1$), $(\Omega/R)/(1-(\delta/R))$ can be approximated as Ω/R. A similar treatment was discussed in the swirl problem of Taylor (1950). Equation (8) is solved by taking the polynomial distribution of temperature as

$$\theta=\theta_w(1-2\eta_t+\eta_t^2) \tag{12}$$

where

$$\eta_t=\frac{(R-r)}{\delta_t} \tag{13}$$

and the thermal boundary conditions are: $\theta=\theta_w$ at $r=R$, i.e., at the wall; and $\theta=0$, $\partial\theta/\partial r=0$ at $r=R-\delta_t$, i.e., at the thermal boundary layer interface. The equations are nondimensionalized by writing $\delta_1=\delta/R$, $\delta_{t_1}=\delta_t/R$, $z_1=z/D$. $\partial\theta_w/\partial z$ is equated to zero to account for the constant wall temperature boundary condition. Finally the equations reduce to

$$\frac{d\delta_1}{\partial z_1}=\frac{225GE}{(E^2+105\delta_1)\delta_1} \tag{14}$$

$$\frac{dE}{dz_1}=\frac{60G}{\delta_1^2}-\frac{225GE^2}{(E^2+105\delta_1)\delta_1^2} \tag{15}$$

$$G=\frac{4}{\mathrm{Re}} \tag{16}$$

The Reynolds number Re is defined on the basis of the inlet tangential velocity and the diameter of the duct as

$$\mathrm{Re}=\frac{\rho V_{\phi_i}D}{\mu}$$

where $V_{\phi_i}=\Omega/R$

$$\frac{d\delta_{t_1}}{dz_1}=\frac{A_{11}}{E\left[\frac{\delta_R}{6}-\frac{\delta_R^2}{5}+\frac{\delta_R^3}{15}\right]} \tag{17a}$$

where

$$A_{11}=E\frac{d\delta_1}{dz_1}\left(\frac{1}{12\delta_R^2}-\frac{2}{15\delta_R^3}+\frac{1}{20\delta_R^4}\right)-\frac{dE}{dz_1}\delta_{t_1}\left(\frac{1}{12\delta_R}-\frac{1}{15\delta_R^2}+\frac{1}{60\delta_R^3}\right)+\frac{8}{\delta_{t_1}\mathrm{Re\ Pr}}$$

for $\mathrm{Pr}>1$, and

$$\frac{d\delta_{t_1}}{dz_1}=\frac{A_{22}}{E\left[\frac{\delta_R^2}{15}-\frac{\delta_R^3}{30}\right]} \tag{17b}$$

where

$$A_{22}=E\frac{d\delta_1}{dz_1}\left(-\frac{1}{12}+\frac{2\delta_R}{15}-\frac{\delta_R^2}{20}\right)-\frac{dE}{dz_1}\delta_1\left(\frac{1}{12}-\frac{\delta_R}{15}+\frac{\delta_R^2}{60}\right)+\frac{8}{\delta_{t_1}\mathrm{Re\ Pr}}$$

for $\mathrm{Pr}<1$, where

$$\mathrm{Pr}\sim\delta_R \quad \text{and} \quad \delta_R=\frac{\delta}{\delta_t} \tag{18}$$

In the case of $\mathrm{Pr}=1$, equations (17*a*) and (17*b*) yield the same expression for the growth of the thermal boundary layer

$$\frac{d\delta_{t_1}}{dz_1}=-\frac{dE}{dz_1}\frac{\delta_1}{E}+\frac{240}{\delta_{t_1}E\ \mathrm{Re\ Pr}}$$

Equations (14) and (15) are first solved simultaneously using the fourth-order Runge-Kutta method to get the values of δ_1, E, $d\delta_1/dz_1$, and dE/dz_1 at different sections down the duct. Using these values, equation (17*a*) or (17*b*) is similarly solved to get the values of δ_{t_1} along the duct.

Nusselt Number

The local Nusselt number is given by

$$\mathrm{Nu}_z=h_zD/K \tag{19}$$

where

$$h_z=\frac{-K\left[\frac{\partial\theta}{\partial r}\right]_{\mathrm{wall}}}{(\theta_w-\theta_b)} \tag{20}$$

$$\theta_b=T_b-T_0$$

$$\theta_w=T_w-T_0$$

and T_b, T_w are the bulk temperature of the fluid and the wall temperature, respectively. Combining equations (12), (19), and (20), the expression for the local Nusselt number becomes

$$\mathrm{Nu}_z=\frac{4}{\delta_{t_1}(1-\theta_b/\theta_w)} \tag{21}$$

The bulk temperature in excess of the free-stream temperature is given by

$$\theta_b=\frac{\int_{R-\delta_t}^{R}V_z\cdot\theta\cdot r\,dr}{\int_{R-\delta_t}^{R}V_z\cdot r\cdot dr} \tag{22}$$

which leads to

$$\frac{\theta_b}{\theta_w}=\frac{1}{\delta_R^2}\left[1-\frac{4}{5\delta_R}+\frac{1}{5\delta_R^2}\right]\text{for Pr}>1 \tag{23a}$$

$$\frac{\theta_b}{\theta_w}=\left[1-\frac{4}{5}\delta_R+\frac{1}{5}\delta_R^2\right]\text{for Pr}<1 \tag{23b}$$

From a knowledge of δ_1, δ_{t_1} at various sections, local values of δ_R and hence θ_b/θ_w and Nu_z have been calculated. These values have been averaged to obtain the average Nusselt number $\overline{\mathrm{Nu}}$.

Entropy Generation

The rate of entropy generation per unit volume is given by Kirkwood and Crawford (1952) and Bird et al. (1960) as

$$\dot{S}_3=-\frac{1}{T^2}(q\cdot\nabla T)-\frac{1}{T}(\tau:\nabla V) \tag{24}$$

The first term on the right-hand side of equation (24) may be written as

$$-\frac{1}{T^2}(q\cdot\nabla T)=\frac{K}{T^2}\left[\left(\frac{\partial T}{\partial r}\right)^2+\frac{1}{r^2}\left(\frac{\partial T}{\partial\phi}\right)^2+\left(\frac{\partial T}{\partial z}\right)^2\right] \tag{25}$$

The second term of the right-hand side of equation (25) is zero for an axisymmetric case. As it was suggested by Bejan (1979), the axial conduction effect can be neglected for $\mathrm{Pe}>>4$. Invoking the simplification $(\partial T/\partial z)^2<<(\partial T/\partial r)^2$, we get

$$-\frac{1}{T^2}\,(q\cdot\nabla T)=\frac{K}{T^2}\left(\frac{\partial T}{\partial r}\right)^2=\frac{K}{T^2}\left(\frac{\partial \theta}{\partial r}\right)^2 \tag{26}$$

The second term on the right-hand side of equation (24) is expanded as

$$(\tau:\nabla V)=\tau_{rr}\left(\frac{\partial V_r}{\partial r}\right)+\tau_{\phi\phi}\left(\frac{1}{r}\frac{\partial V_\phi}{\partial \phi}+\frac{V_r}{r}\right)$$
$$+\tau_{zz}\left(\frac{\partial V_z}{\partial z}\right)+\tau_{r\phi}\left[r\frac{\partial}{\partial r}\left(\frac{V_\phi}{r}\right)+\frac{1}{r}\frac{\partial V_r}{\partial \phi}\right]$$
$$+\tau_{\phi z}\left[\frac{1}{r}\frac{\partial V_z}{\partial \phi}+\frac{\partial V_\phi}{\partial z}\right]+\tau_{rz}\left[\frac{\partial V_z}{\partial r}+\frac{\partial V_r}{\partial z}\right] \tag{27}$$

Expressing the shear stresses in terms of the viscosity and the corresponding velocity gradient, equating gradients in the ϕ directions to zero, as the flow is axisymmetric, and neglecting gradients in the axial direction as they are small compared to the other terms, equation (27) can be written as

$$-\frac{1}{T}\,(\tau:\nabla V)=\frac{\mu}{T}\left[\left(\frac{\partial V_\phi}{\partial r}\right)^2+\left(\frac{\partial V_z}{\partial r}\right)^2\right] \tag{28}$$

Using equations (26) and (28), equation (24) becomes

$$\dot{S}_3=\frac{K}{T^2}\left[\left(\frac{\partial \theta}{\partial r}\right)^2\right]+\frac{\mu}{T}\left[\left(\frac{\partial V_\phi}{\partial r}\right)^2+\left(\frac{\partial V_z}{\partial r}\right)^2\right] \tag{29}$$

As expected, the irreversibility indicator $\dot{S}_3$ contains two additive parts, one due to conduction in the presence of a nonzero temperature gradient, and the other accounting for the viscous dissipation of mechanical power throughout the flow.

Equation (29) is evaluated by substituting expressions for θ, V_ϕ, and V_z from equations (12), (10), and (9). The temperature variation over the thermal boundary layer is negligible as compared with the absolute temperature at any radius. Hence T can be substituted by any characteristic reference temperature. Here the wall temperature has been considered as the reference temperature, hence $T \approx T_w$. A similar approach was suggested by Bejan (1979).

This finally leads to

$$Ns_3=\frac{\dot{S}_3R^2}{K}=\sigma^2\left[-\frac{1}{\delta_{t_1}}\,(-2+2\eta_t)\right]^2$$
$$+\mathrm{Ec}\,\mathrm{Pr}\left[\left[\frac{1}{\delta_1}\,(2-2\eta)\right]^2+\left[\frac{E}{\delta_1}\,(1-4n+3\eta^2)\right]^2\right] \tag{30}$$

where

$$\sigma=\theta_w/T_w \tag{31}$$

and

$$\mathrm{Ec}=(\Omega/R)^2/(c_pT_w) \tag{32}$$

and Ns_3 is a nondimensional rate of entropy generation per unit volume.

To evaluate the total rate of entropy generation, $\dot{S}_3$ is integrated to obtain

$$\dot{S}=\int\dot{S}_3\,dV$$

This integration is carried out by first defining a nondimensional volume element

$$dV^*=\frac{dV}{2R^3}=2\pi\left(\frac{r}{R}\right)d\left(\frac{r}{R}\right)d\left(\frac{z}{D}\right) \tag{33}$$

which may also be expressed as

$$dV^*=2\pi(1-\eta\delta_1)(\delta_1\,d\eta)\,dz_1 \text{ for } \mathrm{Pr}>1 \tag{34a}$$

or

$$dV^*=2\pi(1-\eta_t\delta_{t_1})(\delta_{t_1}\,d\eta_t)\,dz_1 \text{ for } \mathrm{Pr}<1 \tag{34b}$$

Hence the integration is modified as follows

$$\dot{S}=\int\dot{S}_3\,dV=\int\frac{Ns_3K}{R^2}\,dV^*2R^3$$

or

$$Ns=\frac{\dot{S}}{2KR}=\int Ns_3\,dV^* \tag{35}$$

Substituting equations (30) and (34) into equation (35), the nondimensional rate of entropy generation Ns becomes

$$Ns=\int_0^{L/D}\int_0^1 Ns_3\,2\pi(1-\eta\delta_1)\delta_1\,d\eta\;dz_1 \tag{36a}$$

for $\mathrm{Pr}>1$

$$Ns=\int_0^{L/D}\int_0^1 Ns_3\,2\pi(1-\eta_t\delta_{t_1})\delta_{t_1}\,d\eta_t\;dz_1 \tag{36b}$$

for $\mathrm{Pr}<1$

Local values of entropy generation Ns_1 can be obtained by carrying out the inner integral. This gives the entropy generated in a cross section.

Since the numerical values of all terms in the integrand are known over the prescribed range from previous analyses, the integration is carried out by a summation process to obtain a numerical value of Ns.

Merit Function

From this analysis, it is possible to evaluate both the rate of energy transferred usefully as well as the destruction of exergy due to irreversibilities.

If Q is the total rate of heat transfer, then

$$Q=h_c(T_w-T_b)2\pi RL$$
$$=\overline{\mathrm{Nu}}KR\theta_w\left(1-\frac{\theta_b}{\theta_w}\right)2\pi\,\frac{L}{D} \tag{37}$$

The rate of exergy transfer accompanying energy transfer at the rate of Q is given by Moran (1982) as

$$Q_a=Q\left[1-\frac{T_a}{T_w}\right]$$
$$=Q[1-\sigma_a] \tag{38}$$

where T_a, the ambient temperature, has been considered as the exergy reference environment temperature and T_w, the wall temperature, has been considered as a suitable temperature at the surface where the heat transfer takes place. If $\dot{S}$ is the total rate of entropy generation, the destruction of exergy is

$$I=T_a\dot{S}$$
$$=(T_a/T_w)\,T_w\dot{S}$$
$$=\sigma_aT_wNs2KR \tag{39}$$

A merit function is defined as the ratio of exergy transferred to the sum of exergy transferred and exergy destroyed

$$M=\frac{Q_a}{Q_a+I} \tag{40}$$

Introducing equations (37)–(39), equation (40) becomes

$$M=\frac{\overline{\mathrm{Nu}}\left(1-\frac{\theta_b}{\theta_w}\right)(1-\sigma_a)}{\overline{\mathrm{Nu}}\left(1-\frac{\theta_b}{\theta_w}\right)(1-\sigma_a)+\frac{1}{\pi}\left(\frac{D}{L}\right)\frac{\sigma_a}{\sigma}\,Ns} \tag{41}$$

This merit function is now evaluated for various flow parameters. The merit of the merit function lies in its simultaneous accountability of exergy and its destruction which is caused by irreversibilities associated with energy transport and momentum transport. Irreversibilities due to external interaction and internal dissipative effects are together taken care of by this parameter. Another widely used

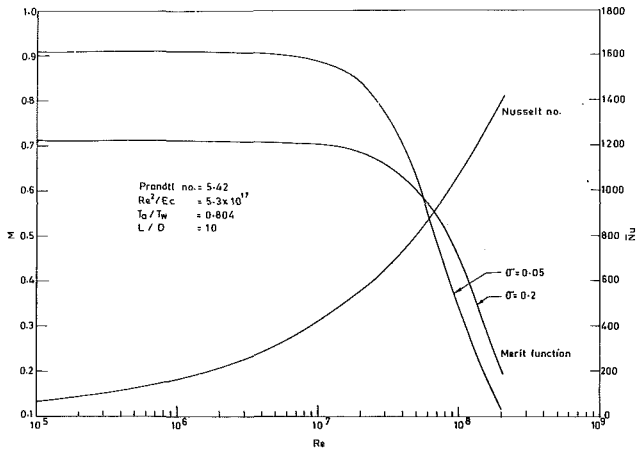

Fig. 2 Variation of $\overline{Nu}$ and M with Reynolds number (based on inlet tangential velocity)

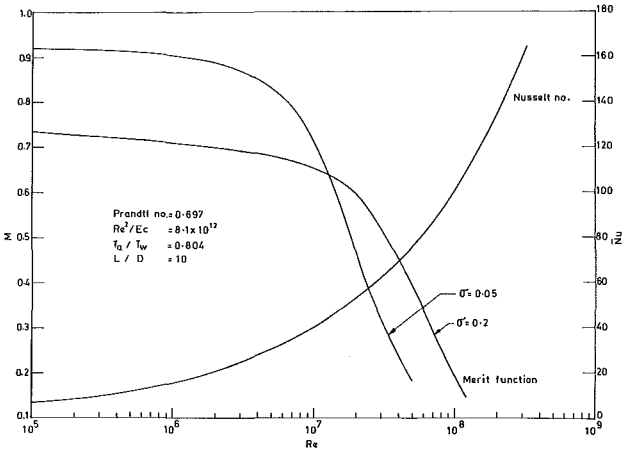

Fig. 3 Variation of $\overline{Nu}$ and M with Reynolds number (based on inlet tangential velocity)

parameter in the study of the second law is the dimensionless irreversibility (I/Q). The dimensionless irreversibility also can summarize the second-law analysis in a nice way. However, as we are interested in finding out energy transferred usefully, i.e., available energy as a function of total energy interaction in a particular energy transfer process, it would be quite meaningful to express the results in terms of M. Further it may be pointed out that I/Q is obtainable by reorganizing the expression for M. Therefore depiction of the study in terms of the merit function is not an entirely new idea but a different way to express the same physical laws of nature. However, it might be noted that equation (40) is a type of second-law efficiency (Moran, 1982).

Results and Discussion

Numerical evaluation of the Nusselt number, as well as the merit function M, is carried out for two different cases: (*i*) $\delta < \delta_t$, i.e., $Pr < 1$; and (*ii*) $\delta > \delta_t$, i.e., $Pr > 1$. The results are shown in Figs. 2 and 3. In each case, the effects of inlet swirl velocity, i.e., the Reynolds number, on these two variables are shown. To ensure that the variation in Reynolds number is due to change of the swirl velocity only and not due to changes in fluid properties or duct diameter, the ratio Re^2/Ec is kept constant.

From these graphs, it is evident that the Nusselt number definitely increases with swirl, i.e., Reynolds number. However, it is also evident that beyond a certain value of swirl, the merit function M takes a sharp plunge. Close observation depicts that up to a certain value of Reynolds number

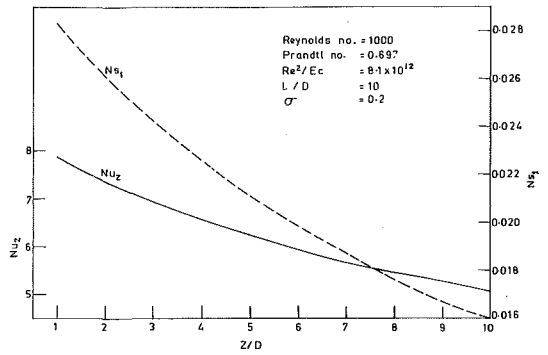

Fig. 4 Variation of Nu_z and Ns_1 along axial direction

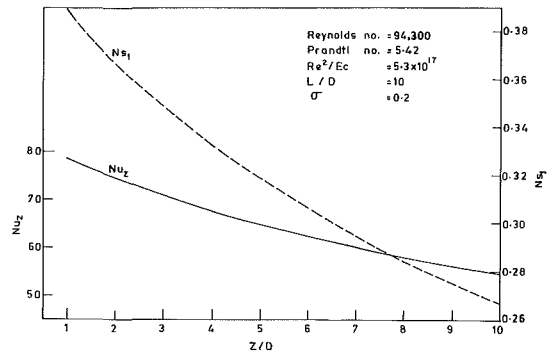

Fig. 5 Variation of Nu_z and Ns_1 along axial direction

there is a steady and slow rise in the Nusselt number. Here, the increase in irreversibility associated with the increase in exergy transfer occurs at a relatively lower rate; hence, merit function becomes independent of Reynolds number. Beyond a certain range of Reynolds number ($Re \approx 10^7$ in Fig. 2 and $Re \approx 10^6$ in Fig. 3), there is a sharp increase in Nusselt number at the price of high irreversibility with a drastic decrease in available energy. Below this critical range of Reynolds number, M is also a strong function of σ. The greater the temperature difference, the greater will be the unavailable energy. This is quite obvious and follows the law of degradation of energy. Figures 4 and 5 show the variation of local Nusselt number as well as the local entropy generation number at various cross sections along the duct for two different cases with Prandtl number lower and greater than one. It appears from the figures and computed data that the flow regime ($z/D = 10$), shown here, is not fully developed. It is well known that augmentation in heat transfer is generally dominant in the developing region. The local Nusselt number follows a decaying trend of variation from a very high to an asymptotic constant value along the length of the duct. Decrease in local Nusselt number along the axial direction in any developing flow is attributed to the growth of thermal boundary layer. When thermal boundary layer grows progressively, the temperature gradient at the wall decreases. Development of hydrodynamic boundary layer also gives rise to a decrease in the velocity gradient at the wall. These two phenomena exert influence on the local entropy generation number, which decreases rapidly to a smaller value along the tube length in a developing flow.

Concluding Remarks

This method of second-law analysis provides an insight into the irreversibilities associated with swirling flow. Besides providing an upper limit on the Reynolds number, it can also be used to evaluate the total losses incurred in heat transfer of

swirl duct flow. The study forms a basis for calculating and minimizing the irreversibility in thermal design involving a variety of heat transfer processes pertaining to efficient energy conversion. The analysis can be extended to other convective heat transfer configurations associated with different types of internal turbulence promoters for selection of best fitted insert for a particular process. A similar type of investigation can also be conducted to optimize the performance of vortex tube refrigeration devices.

References

Algifri, A. H., and Bhardwaj, R. K., 1985, "Prediction of Heat Transfer for Decaying Turbulent Swirl Flow in a Tube," *International Journal of Heat and Mass Transfer*, Vol. 28, pp. 1637–1643.

Bejan, A., 1977, "The Concept of Irreversibility in Heat Exchanger Design," ASME JOURNAL OF HEAT TRANSFER, Vol. 99, pp. 374–380.

Bejan, A., 1978, "General Criterion for Rating Heat Exchanger Performance," *International Journal of Heat and Mass Transfer*, Vol. 21, pp. 655–658.

Bejan, A., 1979, "A Study of Entropy Generation in Fundamental Convective Heat Transfer," ASME JOURNAL OF HEAT TRANSFER, Vol. 101, pp. 718–725.

Bejan, A., 1982, "Second Law Analysis in Heat Transfer and Thermal Design," *Advances in Heat Transfer*, J. P. Hartnett and T. F. Irvine, Jr., eds., Vol. 15, pp. 1–58.

Bejan, A., and Smith, J. L., Jr., 1975, "Heat Exchangers for Vapour Cooled Conducting Supports of Cryostats," *Adv. Cryog., Engg.*, Vol. 21, pp. 247–256.

Bergles, A. E., Webb, R. L., Junkhan, G. H., and Jensen, M. K., 1980, "Bibliography on Augmentation of Convective Heat and Mass Transfer," Heat Transfer Laboratory, Department of Mechanical Engineering, Iowa State University, Ames, IA.

Bird, R. B., Stewart, W. E., and Lightfoot, E. N., 1960, *Transport Phenomena*, Wiley, New York, pp. 350–351.

Blum, H. A., and Oliver, L. R., 1966, "Heat Transfer in Decaying Vortex System," ASME Paper No. 66-WA/HT-62.

Gambill, W. R., and Bundy, R. D., 1963, "High Heat Flux Heat Transfer Characteristics of Pure Ethylene Glycol in Axial and Swirl Flow," *AIChE Journal*, Vol. 9, pp. 55–59.

Gutstein, M. U., Converse, G. L., and Peterson, J. R., 1970, "Theoretical Analysis and Measurement of Single Phase Pressure Losses and Heat Transfer for Helical Flow in a Tube," NASA TN D-6097.

Hartnett, J. P., and Eckert, E. R. G., 1957, "Experimental Study of the Velocity and Temperature Distribution in a High Velocity Vortex Type Flow," *Trans. ASME*, Vol. 79, pp. 751–755.

Hay, N., and West, P. D., 1975, "Heat Transfer in Free Swirling Flow in a Pipe," ASME JOURNAL OF HEAT TRANSFER, Vol. 97, pp. 411–416.

Hong, S. W., and Bergles, A. E., 1976, "Augmentation of Laminar Flow Heat Transfer by Means of Twisted Tape Inserts," ASME JOURNAL OF HEAT TRANSFER, Vol. 98, pp. 252–256.

Junkhan, G. H., Bergles, A. E., Nirmalan, V., and Ravigururajan, T., 1985, "Investigation of Turbulators for Fire Tube Boilers," ASME JOURNAL OF HEAT TRANSFER, Vol. 107, pp. 354–360.

Kirkwood, J. G., and Crawford, B., Jr., 1952, "The Macroscopic Equations of Transport," *Journal of Physical Chemistry*, Vol. 56, pp. 1048–1051.

Klepper, O. H., 1972, "Heat Transfer Performance of Short Twisted Tapes," *AIChE Symposium Series*, Vol. 69, pp. 87–93.

Kreith, F., and Margolis, D., 1959, "Heat Transfer and Friction Factor in Turbulent Vortex Flow," *Applied Scientific Research*, Vol. 8, pp. 457–473.

Kreith, F., and Sonju, O. K., 1965, "The Decay of a Turbulent Swirl in a Pipe," *Journal of Fluid Mechanics*, Vol. 22, pp. 257–271.

Merkulov, A., 1960, "The Vortex Refrigerator," *Journal of Refrigeration*, Vol. 3, pp. 16–17.

Metenin, V., 1960, "Experimental Investigation of the Operation of a Vortex Refrigerator," *Journal of Refrigeration*, Vol. 3, pp. 45–47.

Migay, V. K., and Golubev, L. K., 1970, "Friction and Heat Transfer in Turbulent Swirl Flow With a Variable Swirl Generator in a Pipe," *Heat Transfer—Soviet Research*, Vol. 2, pp. 68–73.

Moran, M. J., 1982, *Availability Analysis: A Guide to Efficient Energy Use*, Prentice Hall, Englewood Cliffs, NJ, pp. 58, 85.

Parulekar, B. B., 1961, "The Short Vortex Tube," *Journal of Refrigeration*, Vol. 4, pp. 74–80.

Sarangi, S., and Chowdhury, K., 1982, "On the Generation of Entropy in Counter Flow Heat Exchangers," *Cryogenics*, Vol. 22, pp. 63–65.

Smithberg, E., and Landis, F., 1964, "Friction and Forced Convection Heat Transfer Characteristics in Tube With Twisted Tape Swirl Generator," ASME JOURNAL OF HEAT TRANSFER, Vol. 86, pp. 39–49.

Som, S. K., and Biswas, G., 1985, "Convective Heat Transfer in a Superimposed Streaming and Swirling Flow Through a Cylindrical Duct," *Wärme- und Stoffübertragung*, Vol. 19, pp. 31–39.

Sparrow, E. M., and Chaboki, A., 1984, "Swirl Affected Turbulent Fluid Flow and Heat Transfer in a Circular Tube," ASME JOURNAL OF HEAT TRANSFER, Vol. 106, pp. 766–773.

Taylor, G. I., 1950, "The Boundary Layer in the Converging Nozzle of a Swirl Atomizer," *Quarterly Journal of Mechanics and Applied Mathematics*, Vol. 3, pp. 129–139.

Zaherzadeh, N. H., and Jagdish, B. S., 1975, "Heat Transfer in Decaying Swirl Flow," *International Journal of Heat and Mass Transfer*, Vol. 18, pp. 941–944.

Heat Transfer From an Open- or Closed-Bore Cylinder Situated Longitudinal to a Freestream

S. S. Kang

E. M. Sparrow

Department of Mechanical Engineering,
University of Minnesota,
Minneapolis, MN 55455

Wind tunnel experiments were performed to determine the local response of the heat transfer at the outer surface of a longitudinal cylinder to geometry-related differences in the pattern of fluid flow. Among the three investigated configurations, one was a cylinder with an open bore through which fluid could pass, while in the second the bore was closed at its downstream end, creating an upstream-open-ended cavity. In the third configuration, the upstream face of the cylinder was impenetrable and blunt. The Reynolds number ranged from 7700 to 47,000. For all cases, the axial distribution of the Nusselt number was characterized by an initial increase, followed by the attainment of a maximum and a monotonic decrease, reflecting the occurrence of flow separation and of post-reattachment boundary layer development. The magnitude and location of the maximum were configuration dependent, with that for the open configuration being highest and occurring first, and that for the blunt face configuration being lowest and occurring last; the cavity configuration gave intermediate results. Upstream of the maxima, the Nusselt numbers were arranged in the same order as at the maximum, with a configuration-related spread of 50 percent. Well downstream of the maxima, the ordering was reversed and the spread was in the 5 percent range. Tight, configuration-independent correlations were achieved both for the maximum Nusselt number and for the Nusselt numbers in the downstream region.

Introduction

This paper is concerned with the response of the heat transfer characteristics of a circular cylinder situated longitudinal to a uniform freestream to geometry-induced changes of the pattern of fluid flow. The physical situations to be investigated are pictured schematically in Fig. 1. Figure 1(*a*) depicts a cylinder with an unconstricted hollow bore, so that a portion of the freestream flow approaching the upstream face may pass through the bore while the remainder passes around the face. This configuration will hereafter be referred to as the open configuration. In Fig. 1(*b*), the bore is closed at its downstream end, thereby forming a cavity. Although a portion of the flow may enter the cavity at its open end, an equal amount of fluid must exit the same end. In the situation depicted in Fig. 1(*c*), the bore is closed at its upstream end so that, from the standpoint of the fluid flow, the upstream face of the cylinder is an impenetrable surface. This case will be designated as the blunt face configuration.

The geometric differences among the configurations described in Fig. 1 will affect the nature of the radial outflow along the upstream face caused by the blocking action of the cylinder. The turning of the flow at the intersection of the upstream face and the outer surface of the cylinder should also be affected, as should the size and shape of the separation bubble associated with the turning. The main focus of the present experiments is to measure the distribution of the local heat transfer coefficient along the outer surface of the cylinder in the presence of these differing patterns of fluid flow.

During the course of the experiments, the Reynolds number Re_D was varied from about 7500 to 47,000 in nine steps. At each Reynolds number and for each of the configurations of Fig. 1, the local heat transfer coefficient was measured at 22 axial stations deployed along the outer surface of the cylinder. The design heating condition was uniform wall heat flux, with corrections made for extraneous conduction and radiation. Circumferential uniformity was achieved at all of the investigated operating conditions. The experiments were performed in a wind tunnel, so that the heat transfer medium was air.

Several aspects of the results will be highlighted. These include the effect of the cylinder configuration on the local Nusselt number distribution for each fixed Reynolds number and the effect of the Reynolds number on the local Nusselt number distribution for each configuration. The Nusselt numbers in the region downstream of the separation bubble were amenable to correlation, as were the maximum Nusselt numbers in the separated region. Comparison will be made with the literature whenever possible.

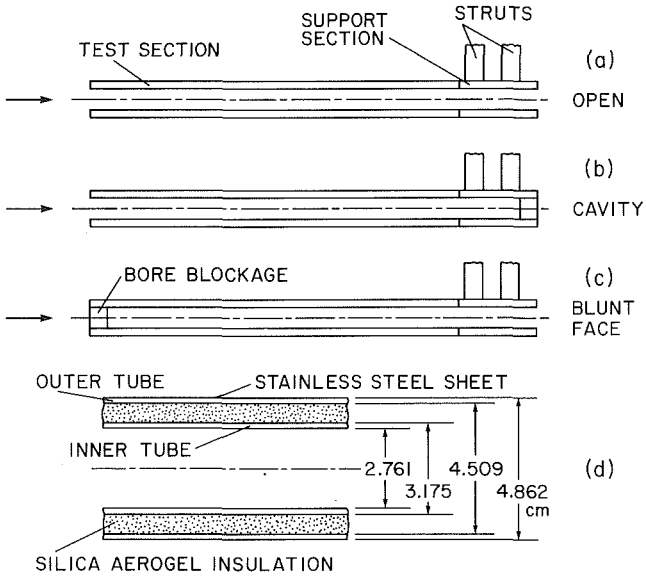

Fig. 1 Schematic diagrams of the investigated geometric configurations of the longitudinally oriented cylinder

Contributed by the Heat Transfer Division for publication in the JOURNAL OF HEAT TRANSFER. Manuscript received by the Heat Transfer Division February 25, 1986.

With regard to the literature, there appears to be no prior work for the open and cavity configurations. For the blunt face cylinder, a limited set of local Nusselt number distributions were measured in [1], while in [2], a photometric mass transfer technique was used which yielded maximum separated-region Sherwood numbers as well as local Sherwood number distributions downstream of the separation bubble. In the available heat transfer analyses for the longitudinal cylinder [3–5], the issue of leading edge separation was ignored, so that work cannot be associated with any of the configurations investigated here. A more extensive literature survey covering other aspects of the longitudinal cylinder problem (e.g., cylinders with nosepieces, fluid flow without heat transfer) is available in the thesis [6] on which this paper is based.

Experiments

The main features of the experimental apparatus will now be described, with details available in [6]. As indicated in Fig. 1(*a*), the forward portion of the longitudinal cylinder served as the test section, while the rear portion served to support the test section in cantilever fashion. Heating occurred only at the outer surface of the test section.

The cylinder was suspended from the upper wall of the wind tunnel by struts attached to the support section. Overall, the cylinder had a streamwise length of 59.7 cm, with respective lengths of 49.3 cm and 10.4 cm for the test section and the support section. The outer and bore diameters of the cylinder were 4.862 and 2.761 cm, respectively.

The test section was an assembly of several components, as depicted in Fig. 1(*d*). The bore was formed by an aluminum tube (i.d. = 2.761 cm, o.d. = 3.175 cm) whose streamwise length (59.7 cm) spanned both the test section and the support section. To form the outer surface of the test section, a laminated phenolic tube (i.d. = 4.509 cm) was first machined to an outer diameter of 4.852 cm and then covered with a tight-fitting sheet of 0.00508-cm-thick stainless steel shim stock. The exposed surface of the stainless steel sheet served as the heated outer surface of the longitudinal cylinder. No nonuniformities of the sheet thickness could be detected with a micrometer having a 0.0001-in. vernier.

The upstream face of the cylinder was an annular aluminum disk whose bore was shrunk-fit over the inner (aluminum) tube and whose outer edge was machined with a back-facing step to provide a seat for the upstream end of the outer (phenolic) tube. The shrink-fit ensured excellent electrical contact at the bore of the disk, while excellent contact between the outer edge of the disk and the stainless steel sheet was achieved through the application of silver paint. At the downstream end of the test section, an annular disk made of Delrin plastic bridged between the inner and outer tubes. The machining and assembly were performed so that the intersections of the front face of the cylinder with the inner and outer cylindrical surfaces were square and perpendicular and that the face itself was continuous at the intersection of the inner tube and the annular disk.

Before the assembly procedure, the exposed surface of the stainless steel sheet was hand-lapped to a high luster. Measurements of the emissivity of an identically prepared surface by a Gier–Dunkle heated cavity reflectometer yielded a value of 0.10. Also, prior to the assembly, the rear face of the sheet had been instrumented with thermocouples and voltage taps, respectively affixed with minute drops of structural and silver-loaded epoxy.

The thermocouples were made from 0.00762-cm-dia, Teflon-coated chromel and constantan wire that had been calibrated specifically for these experiments. Chromel-constantan was chosen because of its relatively low thermal conductivity and high sensitivity. The thermocouples were deployed along a line parallel to the axis of the cylinder at 22 axial stations whose coordinates will be evident from the data to be presented later. At two stations, the third and the twentieth, four thermocouples were installed at 90 deg intervals around the circumference in order to verify the circumferential uniformity of the temperature distribution. The voltage taps, of which there were four, were made from 0.00762-cm-dia, Teflon-coated constantan wire, also chosen for its low thermal conductivity. The positions of the thermocouples and voltage taps were read with an optical cathetometer to within 0.001 cm.

To accommodate the thermocouple and voltage tap wires, grooves had been machined into the outer surface of the phenolic tube. The grooves were circumferential so that the wires would lie along isothermal lines. At the terminus of each groove, a radial hole was provided to enable the wires to pass into the annular space between the inner and outer tubes. The wires were drawn axially through the annular space, from which they exited through an aperture in the Delrin disk at the downstream end. Once the wires were in place, the annular space was filled with silica aerogel insulation whose thermal conductivity was 85 percent that of air. A total of eight thermocouples were installed on the front and rear disks and on the inner tube of the test section.

The support section consisted of a pair of aluminum sleeves situated one behind the other and followed by a specially machined aluminum lock nut. All three components had identical outer diameters equal to that of the test section and an inner diameter which enabled them to be assembled over the inner tube. The forward sleeve was electrically connected to the stainless steel sheet (the connections were internal to the cylinder) but was electrically isolated from the other portion of the support system and from the inner tube. On the other hand, the rear sleeve and the lock nut were in electrical contact with the inner tube. These electrical contacts were designed to establish a series circuit for heating the stainless steel sheet, as will be discussed shortly.

Nomenclature

D = diameter of outer surface of cylinder
h = local heat transfer coefficient = $q/(T_w - T_\infty)$
h_{max} = maximum value of h
k = thermal conductivity
Nu_D = local Nusselt number = hD/k
$Nu_{D,max}$ = maximum value of $Nu_D = h_{max}D/k$
Nu_x = local Nusselt number = hx/k
$(Nu_x)_{max}$ = value of Nu_x at h_{max} and x_{max}
Pr = Prandtl number
q = local convective heat flux
Re_D = Reynolds number = $U_\infty D/\nu$
Re_x = local Reynolds number = $U_\infty x/\nu$
$(Re_x)_{max}$ = local Reynolds number at $x_{max} = U_\infty x_{max}/\nu$
T_w = local wall temperature
T_∞ = freestream temperature
U_∞ = freestream velocity
x = axial coordinate measured from upstream face
x_{max} = position of Nusselt number maximum
ϵ = emissivity
ν = kinematic viscosity
σ = Stefan–Boltzmann constant

The support struts were thin stainless steel plates (0.19 cm thick) with rounded leading and trailing edges. Each strut was fabricated with an aluminum-filled groove to increase its electrical conductivity. In addition, in the forward strut, there was a second groove through which the thermocouple and voltage tap wires were channeled. The groove was subsequently covered to present a smooth surface to the air flow.

The upper ends of the struts terminated in a plexiglass mounting plate which formed a portion of the upper wall of the wind tunnel. The mounting plate was designed to allow two degrees of freedom in the positioning of the cylinder (to achieve a circumferentially uniform temperature distribution). It was also equipped with connectors for the attachment of the thermocouple and voltage tap wires and with binding posts for electrical interconnection of the struts and the power supply.

The electrical circuit through the apparatus may now be traced. It was a series circuit which, along the path of current flow, included the rear binding post, rear strut, and rear sleeve; the inner tube; the front face of the cylinder; the stainless steel sheet (outer surface of the cylinder); and internal bus system; and the forward sleeve, forward strut, and forward binding post. Electric power was supplied by a d-c source stable to 0.01 percent. Voltage and current measurements, the latter performed with the aid of a calibrated shunt, were made to 1 μV.

The foregoing description of the longitudinal cylinder has dealt with the open configuration (Fig. 1(*a*)), i.e., where the bore of the inner tube was unconstricted. The cavity and blunt face configurations were modifications of the open configuration, achieved by inserting a precisely machined, O-ring-equipped plexiglass disk into the bore. Special care was taken in the positioning of the inserted disk for the blunt-face case to ensure that the resulting surface of the face was perfectly flat.

The experiments were performed in a low-turbulence wind tunnel (0.4–0.5 percent turbulence intensity) having a 2.4-m-long test section with a 30.48 × 60.96 cm rectangular cross section (width × height). The freestream velocity was measured upstream of the cylinder by an impact tube in conjunction with a wall static tap. Measurements of the velocity and static pressures were made with a Baratron solid-state, capacitance-type pressure meter having a resolution of 10^{-3} Torr.

The freestream temperature was measured by two thermocouples situated to the side of the cylinder. All thermocouple voltages were read and recorded to 1 μV by a programmable datalogger.

The data runs were performed in groups of three at a fixed airspeed, respectively for the open, cavity, and blunt-faced configurations in that order. An equilibration period of 1½ hours was allowed between each data run.

Data Reduction

The local heat transfer coefficient was evaluated at each of the instrumented axial stations on the outer surface of the cylinder. If q and T_w, respectively, represent the heat flux and surface temperature at any such station, then

$$h = q/(T_w - T_\infty) \tag{1}$$

where T_∞ is the freestream temperature. Circumferential uniformity of T_w was achieved to within ±1 percent of $(T_w - T_\infty)$ or better, and the two thermocouple readings for T_∞ were always identical. The local heat flux q was determined by first prorating the overall power dissipation and then correcting for radiation and conduction losses, with the validity of the prorating being supported by the linearity of the voltage variation along the cylinder.

The local radiation loss was computed from

$$\epsilon\sigma(T_w^4 - T_\infty^4) \tag{2}$$

with $\epsilon = 0.10$. Typically, the radiation correction was about 2-3 percent of the electrical dissipation at the lower Reynolds numbers and about 1-2 percent at the higher Reynolds numbers. The corrections were greatest at the downstream end of the test section because of the higher temperatures prevailing there.

The conduction corrections were determined from numerical solutions described in detail in [6]. The solution domain was a composite annular cylinder made up of the phenolic tube and the silica aerogel insulation. Since the temperatures on all the boundaries of the solution domain were available from the experimental data, the temperature field within the domain was readily obtained numerically, from which the local conduction heat fluxes at the outer surface of the cylinder followed directly. A finite-difference grid consisting of 24 × 15 points (axial × radial) was used for the solutions.

Representative conduction corrections are listed in Table 3-2 of [6]. As expected, the largest corrections occurred for the open configuration, since in that case the air passing through the bore of the inner tube served as a heat sink. Typical corrections for the open configuration were in the 5 percent range, while the typical corrections for the other two configurations were in the 2–3 percent range. Somewhat larger corrections were encountered at the extreme upstream and downstream ends of the test section at lower Reynolds numbers (see Table 3-2 of [6]).

The local heat transfer coefficients were represented in dimensionless terms by either of two Nusselt numbers, Nu_D and Nu_x, respectively defined as

$$\mathrm{Nu}_D = hD/k, \qquad \mathrm{Nu}_x = hx/k \tag{3}$$

where D denotes the outer diameter of the cylinder, and x is the axial coordinate measured from the upstream face of the cylinder. Similarly, two Reynolds numbers, Re_D and Re_x, were used in the presentation of results, where

$$\mathrm{Re}_D = U_\infty D/\nu, \qquad \mathrm{Re}_x = U_\infty x/\nu \tag{4}$$

In the determination of U_∞, there was no need to apply a blockage correction since the cross-sectional blockage of the wind tunnel by the cylinder was less than 1 percent.

The thermophysical properties appearing in the Nusselt and Reynolds numbers were evaluated at the freestream temperature. Variable properties were not a significant issue since the wall-to-freestream temperature differences were on the order of 5°C. The Nusselt and Reynolds numbers are believed to be accurate to 2 percent.

Effect of Cylinder Configuration

The first focus of the presentation of results is the effect of the geometric configuration of the cylinder on the local Nusselt number distribution along its outer surface. This information is conveyed in Figs. 2–4. In each figure, results are displayed for three values of the Reynolds number Re_D: 7700, 10,000, and 13,000 in Fig. 2; 19,000, 25,700, and 31,200 in Fig. 3; and 36,300, 40,000, and 47,000 in Fig. 4. For each Reynolds number, the local Nusselt number Nu_D is plotted as a function of the dimensionless streamwise coordinate x/D for the three investigated geometric configurations, as identified by the respective data symbols appearing at the upper right in each figure. Since the cylinder diameter is constant, the distribution of Nu_D is a true reflection of the distribution of the local heat transfer coefficient. To separate the results for the various Reynolds numbers in each figure, different abscissa origins are used for each Reynolds number.

The Nusselt number distributions have a common shape for all of the investigated operating conditions. Starting near the leading edge, the Nusselt number increases at first, attains a maximum, and then decreases monotonically. These

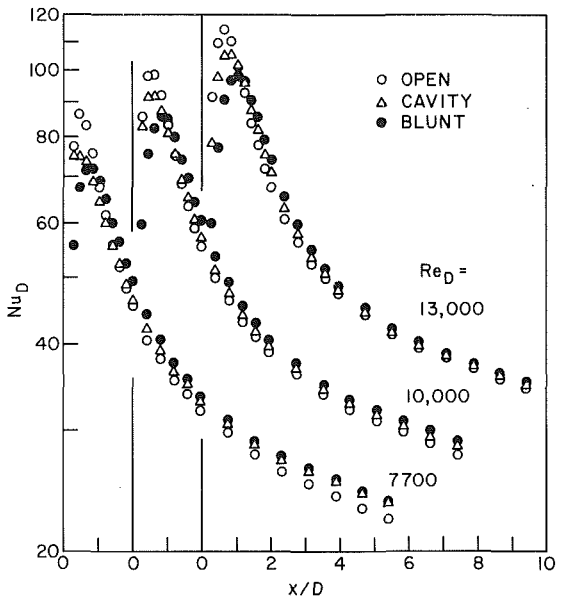

Fig. 2 Effect of the geometric configuration of the cylinder on the local Nusselt number distribution, $Re_D = 7700$, 10,000, and 13,000

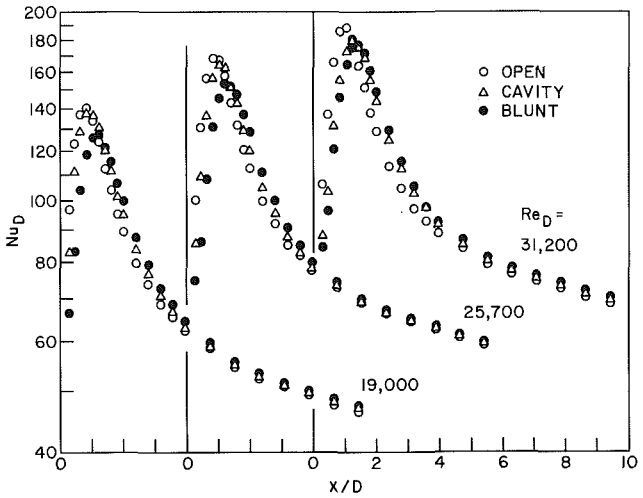

Fig. 3 Effect of the geometric configuration of the cylinder on the local Nusselt number distribution, $Re_D = 19{,}000$, 25,700, and 31,200

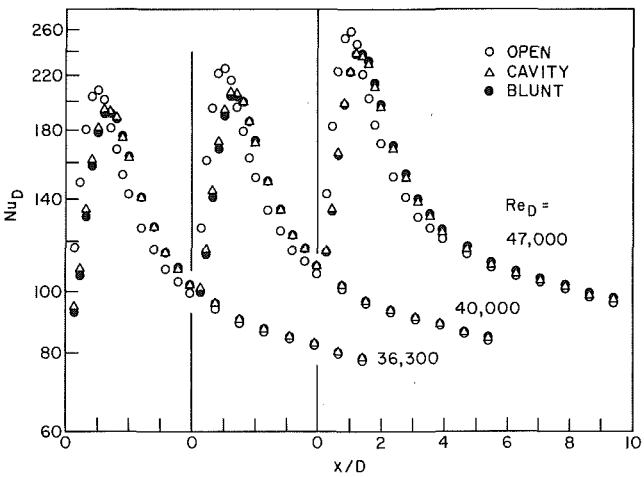

Fig. 4 Effect of the geometric configuration of the cylinder on the local Nusselt number distribution, $Re_D = 36{,}300$, 40,000, and 47,000

characteristics reflect a pattern of fluid flow which includes separation of the flow at the outer edge of the upstream face of the cylinder, the subsequent reattachment of the flow on the cylindrical surface, and the post-reattachment boundary layer development.

As expected, the specifics of the geometric configuration of the cylinder are felt most strongly on the upstream portion of the cylindrical surface and to a lesser extent on the downstream portion. Of particular note is that for a given Reynolds number, both the maximum Nusselt number $Nu_{D,max}$ and the location x_{max}/D of the maximum are configuration dependent. In general, the largest $Nu_{D,max}$ for a given Re_D corresponds to the open configuration and the least to the blunt face configuration, with the cavity configuration falling between. The spread in $Nu_{D,max}$ is about 20 percent at $Re_D = 7700$ and about 10 percent at $Re_D = 47{,}000$.

Furthermore, x_{max} is generally smallest for the open configuration and largest for the blunt face configuration, as illustrated by the respective x_{max}/D values of 0.50 and 0.80 at $Re_D = 7700$ and of 1.00 and 1.33 at $Re_D = 47{,}000$. This illustration also bears witness to the trend that x_{max} increases with Re_D. Except at $Re_D = 7700$, x_{max} for the cavity configuration falls between the others. The relation between x_{max} and the point at which the flow reattaches to the cylinder is dealt with in [8].

In the region of x/D upstream of the smallest x_{max}/D for a given Reynolds number, Nu_D depends on the configuration with the same ordering as for $Nu_{D,max}$. At a given x/D in this region, the configuration dependence may bring about a variation in Nu_D as large as 50 percent. For x/D values between the smallest x_{max}/D and a downsteram location in the range from $x/D = 1.2$ to 1.8 depending on the Reynolds number, the Nu_D distributions for the different configurations cross as they descend from their respective maxima. Because of the crossings, there is not a consistent configuration-dependent ordering of the Nu_D values.

Beyond the crossings, a new ordering of the Nu_D distributions, opposite to that encountered upstream, emerges. In particular, the highest Nu_D are now those of the blunt face configuration, followed by those for the cavity and the open configurations, in that order. Up to $x/D = 4$, the overall differences between the distributions remains appreciable (up to 16 percent), and their relative positions with respect to each other continue to evolve. However, for $x/D > 4$, a virtually unchanging relationship among the distributions appears to have been established (except, perhaps, at the lower Reynolds numbers). In this region, the overall configuration-related spread of the Nusselt number data is in the 5 percent range – 7 percent for $Re_D = 7700$ and 3 percent for $Re_D \geq 36{,}300$. Within this spread, the data are consistently ordered according to configuration as noted in the foregoing.

The configuration-related Nusselt number characteristics described in the foregoing paragraphs can be readily rationalized. Among the three configurations, the extent of the flow blockage and the corresponding vigor of the radial outflow along the upstream face of the cylinder are greatest for the blunt face case, intermediate for the cavity case, and least for the open case. As a consequence, the length and thickness of the separation bubble are similarly ordered. Longer, thicker separation bubbles correspond to larger x_{max} and smaller $Nu_{D,max}$, as encountered in the experiments. Furthermore, the longer the bubble, the less is the boundary layer development at a given downstream station and the higher is Nu_D there. Therefore, all of the observed characteristics are plausible.

Effect of Reynolds Number

Attention is next turned to the effect of the Reynolds number on the Nusselt number distribution for a given

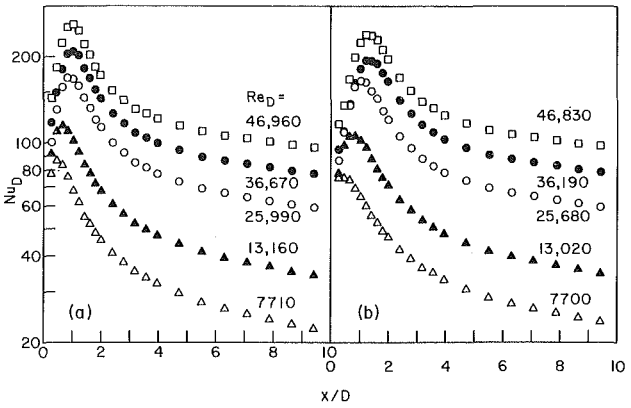

Fig. 5 Effect of the Reynolds number on the local Nusselt number distribution: (*a*) open configuration, (*b*) cavity configuration

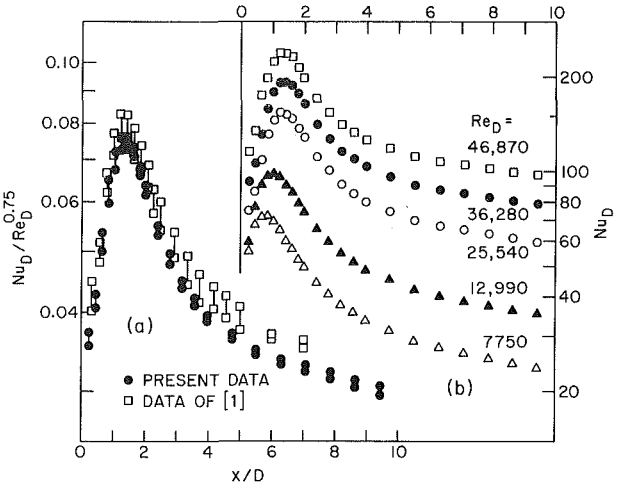

Fig. 6 (*a*) Comparison of Nusselt numbers for the blunt face configuration with those of [1]; (*b*) effect of the Reynolds number on the local Nusselt number distribution for the blunt face configuration

geometric configuration of the cylinder, and Figs. 5 and 6 have been prepared for this purpose. In Fig. 5(*a*), the Nu_D versus x/D data for the open configuration are plotted for five of the nine Reynolds numbers for which experiments were performed. Similar presentations are made in Figs. 5(*b*) and 6(*b*) for the cavity and the blunt face configurations (Fig. 6(*a*) will be discussed shortly).

Turning first to Fig. 5(*a*), the expected increase in the general level of the Nusselt number with increasing Reynolds number is readily apparent. However, the extent of the increase is by no means uniform along the length of the cylinder. This observation can be quantified by ratioing the maximum Nusselt number with that at the most downstream station. At $Re_D = 7710$, the value of the ratio is nearly 4, while at $Re_D = 36{,}670$ and 46,960, the ratio is about 2.75. The nonuniform response of different portions of the Nusselt number distribution to changes in the Reynolds number is consistent with the presence of zones of markedly different types of fluid flow, i.e., a separated region and a boundary layer region. Furthermore, the laminar or turbulent nature of the flows in the respective zones may also affect the results; for example, the flow may be laminar in one zone and turbulent in the other.

Further inspection of Fig. 5(*a*) confirms the downstream movement of the location x_{max} of the maximum Nusselt number as the Reynolds number increases. The greatest sensitivity of x_{max} to the Reynolds number appears to occur at the lower Reynolds numbers, whereas x_{max} is virtually invariant at higher Reynolds numbers. This invariance suggests that the separated region may have become fully turbulent. For the investigated range of Reynolds numbers, x_{max}/D varied from 0.50 to 1.00 for the open configuration.

Figures 5(*b*) and 6(*b*), which respectively correspond to the cavity and the blunt configurations, display the same qualitative characteristics as those just discussed in connection with Fig. 5(*a*) for the open configuration. There are, however, certain differences in detail. In particular, the response of the different portions of the Nusselt number distribution to the Reynolds number is more uniform than before. This is witnessed by the ratio of the maximum Nusselt number to that at the most downstream station. For the cavity and the blunt configurations, this ratio is equal to 3.0 – 3.2 for $Re \cong 7700$ and to about 2.5 for $Re > 36{,}000$. The corresponding ratios are ~4 and 2.75 for the open configuration.

Another difference discernible from the figures is in the magnitude of x_{max}. For the cavity configuration, x_{max}/D ranges from 0.45 to 1.30 over the investigated range of Reynolds numbers, while for the blunt configuration, the corresponding increase is from 0.80 to 1.33. As was true for the open configuration, x_{max} is more sensitive to the Reynolds number at the lower end of the range.

With regard to the literature, it has already been noted in the Introduction that local Nusselt number results of the type presented here are available only for the blunt face configuration, as published in [1]. There, data were collected in the Reynolds number range from 25,200 to 53,600 and presented in terms of the $Nu_D/Re_D^{0.75}$ ratio. The present data for the blunt face configuration for Re_D between 25,700 and 47,000 will be compared with those of [1] in Fig. 6(*a*), where $Nu_D/Re_D^{0.75}$ is plotted versus x/D. In the figure, pairs of data points connected by a vertical line are used to indicate the Reynolds-number-related spread of the data. This spread is substantially smaller for the present data than it is for the data of [1], despite the fact that the $Re_D^{0.75}$ scaling is from [1].

An overall inspection of Fig. 6(*a*) indicates that the Nusselt numbers of [1] are higher than the present values. In the separated region, the differences are fairly small, but farther downstream, deviations in excess of 10 percent are encountered. It is believed that the departures are due to the inadequate treatment of the heat loss corrections in [1]. No mention was made there of the surface of the cylinder having been polished, so that radiation losses might well have been 3–6 percent but were not taken into account. Also, the conduction corrections were made on the basis of temperature measurements at only three locations.

A more quantitative perspective on the dependence of the local Nusselt number on the Reynolds number is conveyed by plotting Nu_D versus Re_D at several representative axial stations. Such a presentation is made in Fig. 7 for the open and the cavity configurations and in Fig. 8 for the blunt face configuration. The discussion of the results will begin with Fig. 8.

In Fig. 8(*a*), Nu_D–Re_D distributions are plotted at five axial stations. One of them, $x/D = 0.269$, is in the separated region (at the first measurement station). The other four stations are downstream of the Nu_D maximum. At all of the latter stations, the data obey a power law of the form

$$Nu_D = CRe_D^n \tag{5}$$

and the solid lines passed through the data represent least-squares fits of equation (5). However, at $x/D = 0.269$, the data do not follow a regular pattern. To explore this latter behavior more fully, data at a succession of small x/D stations, with x/D greater than 0.269, have been plotted in Fig. 8(*b*), and the irregularity already noted at $x/D = 0.269$ is seen to persist to $x/D = 0.642$, after which a more regular pattern emerges. Similar behavior occurred for the open and cavity configurations, but to achieve a compact presentation format, the small x/D data have been omitted from Fig. 7.

If the slopes of the least-squares lines in Figs. 7 and 8 are ex-

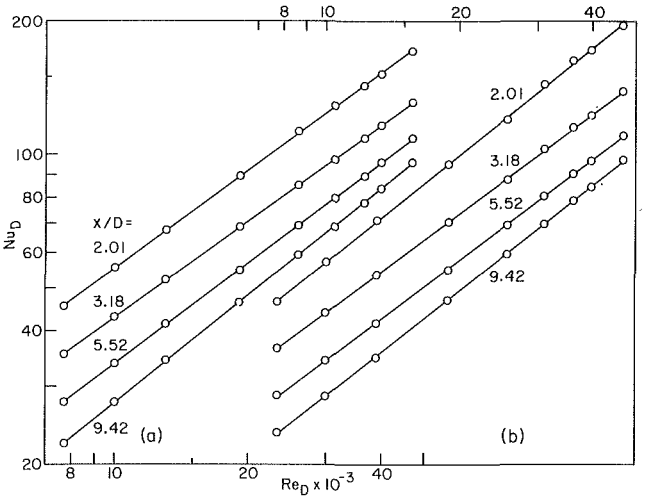

Fig. 7 Nusselt-Reynolds relationship at various fixed axial stations: (*a*) open configuration, (*b*) cavity configuration

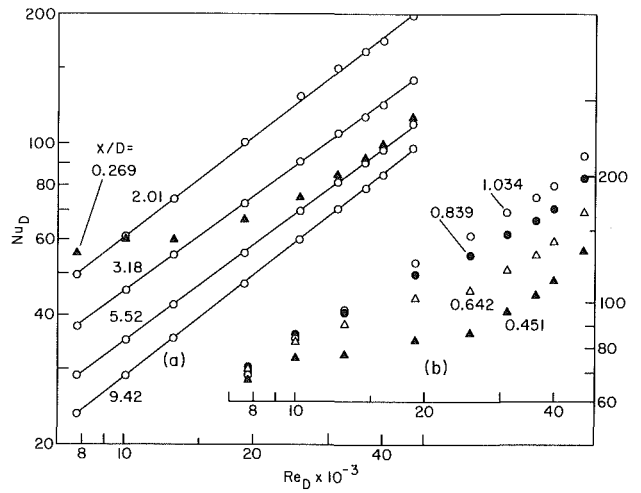

Fig. 8 Nusselt-Reynolds relationship at various fixed axial stations for the blunt face configuration

amined, a definite pattern can be discerned. There is a decrease in the slope between the stations at $x/D=2.01$ and 3.18, followed by an increase in slope as x/D increases. The relatively high slope at $x/D=2.01$ reflects the downstream movement of x_{max} with increasing Reynolds number. The increase of the slope at stations beyond $x/D=3.18$ is a reflection of the progressive increase of the turbulence in the developing boundary layer. At the last station, $x/D=9.42$, the exponent in equation (5) is in the range from 0.785 to 0.802, depending on the configuration. These values are in the neighborhood of $n=0.8$, which is widely used as the Reynolds number exponent for fully turbulent flows.

The foregoing observation suggests that the Nusselt numbers in the downstream region may not be significantly affected by the presence of the separation bubble situated on the upstream portion of the cylinder. This, in turn, prompted the rephrasing of the data in terms of the conventional boundary layer variables Nu_x and Re_x. For $x/D \geq 4.5$ and $Re_x \geq 10^5$, the data were very tightly correlated by the least-squares representation

$$Nu_x = 0.0426 Re_x^{0.767} \quad (6)$$

Of the 88 data points which were used to obtain the least-squares fit, 81 percent fell within ±2 percent of the correlating line, 93 percent fell within ±3 percent, and all the data were included in a ±5 percent band. Note that the correlation was based on the data for the blunt and the cavity configurations but not on those for the open configuration. This choice was

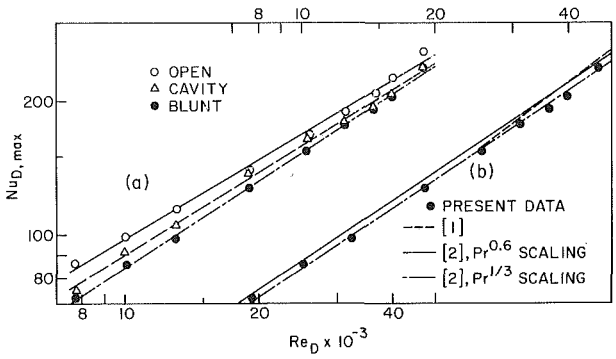

Fig. 9 Maximum Nusselt numbers in the $Nu_{D,max}$ versus Re_D format: (*a*) present results, (*b*) comparison with the literature

made because the latter are not as universal as the former. The Nu_x values from equation (6) exceed the corresponding flat plate values by about 15 percent.

The data of [1] were found to fall 8–16 percent above equation (6), for reasons already discussed. In order to use the data of [2] for comparison, it was necessary to transform them from a Schmidt (or Prandtl) number of 0.616 to the present Prandtl number of 0.713. If a $Pr^{0.6}$ scaling is used (as recommended by [2]), the transformed data lie about 1–2 percent below equation (6). For a $Pr^{1/3}$ scaling (as indicated in most textbooks), the transformed data are about 5 percent below the equation. Since the present experiments correspond to uniform wall heat flux while those of [2] are for uniform wall temperature, the present data are expected to lie above the data of [2].

Maximum Nusselt Numbers

The maximum Nusselt numbers are of particular interest, and the $Nu_{D,max}$ data for each of the three geometric configurations have been brought together in Fig. 9(*a*), where they are plotted against Re_D. The data have been fit with least-squares, power-law representations having the form of equation (5), and the corresponding straight lines are drawn in the figure. Note that the $Nu_{D,max}$ data display somewhat greater deviations from the correlating lines than did the downstream Nusselt number data presented in Figs. 7 and 8. These deviations reflect the likelihood that the maximum Nu_D values obtained using fixed, discrete measurement stations differ somewhat from the true maximum values.

The figure confirms that $Nu_{D,max}$ is configuration dependent – arranged in increasing order for the blunt, cavity, and open configurations. On the other hand, the slopes of the $Nu_{D,max}$ versus Re_D curves are arranged in decreasing order for the same sequence of configurations. As a consequence, the configuration-related spread of $Nu_{D,max}$ decreases as the Reynolds number increases.

The present $Nu_{D,max}$ results for the blunt configuration are compared with those of [1, 2] in Fig. 9(*b*). At the lowest Re_D value of [1] (~25,000), the comparison yields agreement within 2 percent; however, at higher values of Re_D, there are deviations in the 5–7 percent range. The comparison with [2] again depends on the scaling rule that is employed. If the scaling is performed with $Pr^{0.6}$, there is a 4–5 percent deviation between the present results and those of [2], while if a $Pr^{1/3}$ scaling is used, excellent agreement prevails. The latter scaling is represented by the equation

$$Nu_{D,max} = 0.202 Re_D^{2/3} Pr^{1/3} \quad (7)$$

which contains the familiar 2/3 power of the Reynolds number.

Although the maximum Nusselt numbers for the three configurations were distinct when plotted in the $Nu_{D,max}$–Re_D format of Fig. 9, they can be tightly correlated when the

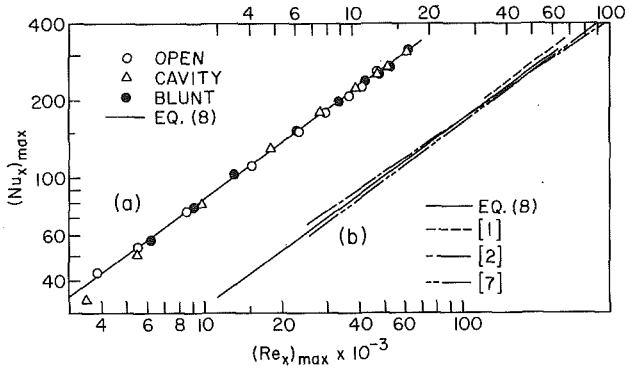

Fig. 10 Maximum Nusselt numbers in the $(Nu_x)_{max}$ versus $(Re_x)_{max}$ format: (a) present results, (b) comparison with the literature

$(Nu_x)_{max}$-$(Re_x)_{max}$ format is used. This finding is exhibited in Fig. 10(*a*). The equation of the least-squares correlating line is

$$(Nu_x)_{max} = 0.103(Re_x)_{max}^{0.726} \tag{8}$$

where

$$(Nu_x)_{max} = h_{max}x_{max}/k, \qquad (Re_x)_{max} = U_\infty x_{max}/\nu \tag{9}$$

Significant departures from the correlating line occur only at one or two isolated points. The relation between x_{max} and Re_D is presented in [8].

A comparison of the $(Nu_x)_{max}$ correlation of equation (8) with the literature is made in Fig. 10(*b*). It should be noted that the line attributed to [1] in the figure is actually a modification of the correlation given in the reference. In particular, the correlation was altered by using $x_{max}/D = 1.3$ instead of 1.4 as specified in [1], because it is a better representation of the data. With regard to [2], equation (7) was transformed to the new format by using $x_{max}/D = 1.10$ for $Re_D = 6000$ and $x_{max}/D = 1.15$ for $Re_D \geq 10{,}000$, with a straight line between 6000 and 10,000. In addition, Fig. 10(*b*) also contains a line representing the results of [7] for a thick flat plate with various nose shapes.

Inspection of the figure shows that the results of [1, 2, 7] lie within a ±7 percent band of the correlation (8). This excellent agreement, especially considering the various nose shapes of [7], suggests that equation (8) has a high degree of generality.

Concluding Remarks

The experiments performed here have provided definitive information about the response of the heat transfer at the outer surface of a longitudinally oriented cylinder to flow field differences brought about by differences in geometric configuration. In one configuration, the bore of the cylinder was open so that fluid could pass through it. In another, the downstream end of the bore was closed, thereby forming a cavity open at its upstream end. In the third configuration, the upstream face of the cylinder was impenetrable. Heating was confined to the outer surface of the cylinder. The Reynolds number range extended from 7700 to 47,000.

In all cases, the local Nusselt number at the cylindrical surface increased at first, attained a maximum, and then decreased monotonically. These characteristics reflected the presence of a separation bubble on the forward portion of the cylindrical surface and the post-reattachment boundary layer development.

The location of the Nusselt number maximum was configuration dependent, as was the value of the maximum. The maximum for the open configuration was attained first and was highest, while that for the blunt face configuration was attained last and was lowest. Upstream of the locations of the maxima, the Nusselt numbers for the open configuration were again the highest, by as much as 50 percent in some cases. In the region where the maxima were attained, the order of the Nusselt numbers underwent a reversal, so that in the downstream region the Nusselt numbers for the blunt face configuration were highest and those for the open configuration were lowest. For $x/D > 4$, the configuration-related spread of the data was on the order of 5 percent.

The maximum Nusselt numbers were very tightly correlated by equation (8), which also agreed with literature information for a thick flat plate with various nose pieces. The downstream-region Nusselt numbers were very well represented by equation (6).

References

1 Ota, T., and Kon, N., "Heat Transfer in an Axisymmetric Separated and Reattached Flow Over a Longitudinally Blunt Cylinder," ASME JOURNAL OF HEAT TRANSFER, Vol. 99, 1977, pp. 155–157.

2 Kottke, V., Blenke, H., and Schmidt, K. G., "Determination of the Local and Average Mass Transfer on Thick Plates in Parallel Flow With Flow Separation and Reattachment," *Wärme- und Stoffübertragung*, Vol. 10, 1977, pp. 217–232.

3 Seban, R. A., and Bond, R., "Skin Friction and Heat Transfer Characteristics of a Laminar Boundary Layer on a Cylinder in Axial Incompressible Flow," *Journal of the Aeronautical Sciences*, Vol. 18, 1951, pp. 671–675.

4 Kelly, H. R., "A Note on the Laminar Boundary Layer on a Cylinder in Axial Incompressible Flow," *Journal of the Aeronautical Sciences*, Vol. 19, 1952, p. 634.

5 Sparrow, E. M., Eckert, E. R. G., and Minkowycz, W. J., "Heat Transfer and Skin Friction for Turbulent Boundary Layer Flow Longitudinal to a Cylinder," ASME JOURNAL OF HEAT TRANSFER, Vol. 85, 1963, pp. 37–43.

6 Kang, S. S., "Heat Transfer From a Hollow-Bore Circular Cylinder Situated Longitudinal to a Freestream Flow," Ph.D. Thesis, Department of Mechanical Engineering, University of Minnesota, Minneapolis, MN, 1985.

7 Ota, T., and Kon, N., "Heat Transfer in the Separated and Reattached Flow Over Blunt Flat Plates – Effect of Nose Shape," *International Journal of Heat and Mass Transfer*, Vol. 22, 1976, pp. 197–206.

8 Sparrow, E. M., Kang, S. S., and Chuck, W., "Relation Between the Points of Flow Reattachment and Maximum Heat Transfer for Regions of Flow Separation," *International Journal of Heat and Mass Transfer*, in press.

J. Davalath
Graduate Student.
Student Mem. ASME

Y. Bayazitoglu
Associate Professor.
Assoc. Mem. ASME

Mechanical Engineering and
Materials Science,
Rice University,
Houston, TX 77001

Forced Convection Cooling Across Rectangular Blocks

Conjugate heat transfer for two-dimensional, developing flow over an array of rectangular blocks, representing finite heat sources on parallel plates, is considered. Incompressible flow over multiple blocks is modeled using the fully elliptic form of the Navier–Stokes equations. A control-volume-based finite difference procedure with appropriate averaging for the diffusion coefficients is used to solve the coupling between the solid and fluid regions. The heat transfer characteristics resulting from recirculating zones around the blocks are presented. The analysis is extended to study the optimum spacing between heat sources for a fixed heat input and a desired maximum temperature at the heat source.

Introduction

A two-dimensional problem of conjugate heat transfer for laminar incompressible flow over multiple rectangular blocks with uniformly distributed heat sources, as illustrated in Fig. 1, is studied. Three blocks are considered in a horizontal channel in order to take into account thermal entrance effects. The problem represents a mathematical model for integrated circuit (IC) components placed on horizontal circuit boards. As solid-state circuits are miniaturized, large amounts of heat are generated due to flow of current through gates and connections of smaller areas within a silicon chip. As computing and gate switching speed increases in a chip, heat generation increases. Circuit miniaturization has advanced to such an extent that heat dissipation capability of a system design has become one of the primary limiting factors. The primary consideration in thermal design is to minimize the maximum temperature at the chip for a given set of design criteria. Temperature distributions must be calculated within the package to assess reliability of solder joints and devices accurately under thermal stress. Recent advances in computing speed, and improved packaging density in modern digital computers, can be attributed to convection heat transfer research resulting in novel thermal designs for handling high heat dissipation densities.

In most computers, IC components are mounted in a densely packed array such that the heights of the components are of the same *order of magnitude* as the height of the channel. The heat sources are finite, and unevenly distributed on the PC (printed circuit) board. In general, integrated circuit chips are packaged in either plastic or ceramic, with metal leads protruding from the packages. The materials selected have thermal properties such that most of the resistance to heat flow is due to convective resistance of the fluid.

The problem of analyzing convection in the fluid and conduction in the solid is complicated by complex geometry and different thermal properties of the materials. An equivalent roughness factor cannot be assumed for the discrete components in modeling the flow field since the devices disturb the core flow significantly. Most heat transfer analyses (Mahalingam and Reed, 1984; Waller et al., 1983) consist of a resistor-network model in the solid, assuming a constant convection heat transfer coefficient at the surface of the package. The convection boundary condition is also applied assuming a constant environment temperature. For a finite-sized block in a rectangular channel, the heat transfer from the block surface is a function of both position and thermal properties. In addition, the bulk fluid temperature rises as it absorbs the heat generated by the blocks.

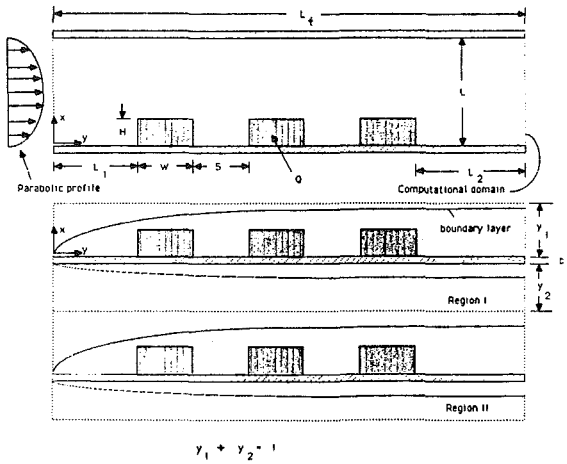

Fig. 1 Flow perpendicular to the rectangular blocks between horizontal printed circuit boards. Thermal periodicity is observed in Regions I and II, each having similar thermal boundary layers on both sides of the plate.

In this study, IC devices are idealized as rectangular blocks with uniform conductivity. The heat source is uniformly distributed in the volume of the blocks. The components obstruct the flow, resulting in recirculation zones between blocks and downstream from the last block. In the entrance region, the heat transfer varies from block to block. All of the above effects are accurately modeled, generating sufficient heat transfer data (Nusselt number) to assist in the proper design of electronic cooling systems.

The numerical model presented here is limited to two dimensions. The geometry is defined such that the blocks and the horizontal plates are continuous in the third dimension. In general, IC components are arranged in rows in such a way that the spacing between components in each row is small compared to the spacing between the rows. For a PC board, the length of each row (length or width of the PC board) is at least one order of magnitude higher than the width of each component. Therefore, the two-dimensional model for the flow and temperature fields provides a good approximation.

Several books (Krause, 1983; Steinberg, 1976; Sloan, 1985) have been published describing thermal design considerations in cooling electronic equipment. These books do not give elaborate analytical treatment for any application. Bergles (1972) and Simons (1983) have completed surveys of cooling techniques applied to electronic devices, but do not consider detailed mathematical models of any relevant problems. Two general purpose packages called TNETFA and TAMS have been developed by Ellison (1984) for general purpose modeling of conduction of PC boards and components in different geometries (horizontal or vertical). These models assume cor-

Contributed by the Heat Transfer Division for publication in the JOURNAL OF HEAT TRANSFER. Manuscript received by the Heat Transfer Division October 1, 1985.

relation equations for calculating the convection heat transfer coefficient.

Although a number of papers have been published in the general area of convective cooling of electronic components, little work has been carried out for simulating finite sources on horizontal plates. Jaluria (1985) has completed an extensive survey of papers in natural convection cooling for finite heat sources placed in various geometries. A numerical simulation of combined forced and free connection in horizontal parallel plates has been studied by Kennedy and Zebib (1982, 1983) using the vorticity–stream function formulation. This study involves a zero-thickness heat source placed on either the bottom or top wall. A recent paper by Zebib and Wo (1985) considers forced convection of a single electronic component in a horizonal geometry, neglecting free convection. Braaten and Patankar (1984) assessed the heat transfer enhancement by free convection for flow along the length of the blocks. In their analysis, the primary flow along the length of the components is assumed fully developed and buoyancy forces induce secondary flow, resulting in improvement in heat transfer. In this study, attention is focused on the heat transfer characteristics of developing flow perpendicular to the rectangular blocks considering forced convection.

Mathematical Model and Numerical Approach

The problem consists of flow between parallel plates with multiple blocks containing distributed heat sources, as depicted in Fig. 1, where the fluid enters with a parabolic profile from one end and leaves at the other end of the plates carrying the heat dissipated by the blocks. The two-dimensional Navier–Stokes equations for incompressible elliptic flow, using the nondimensionalization described in the nomenclature, are as follows:

Governing Equations:

Continuity:

$$\frac{\partial u}{\partial x}+\frac{\partial v}{\partial y}=0 \tag{1a}$$

Momentum equations:

$$u\frac{\partial u}{\partial x}+v\frac{\partial u}{\partial y}=\frac{\nu^*}{\mathrm{Re}}\left(\frac{\partial^2 u}{\partial x^2}+\frac{\partial^2 u}{\partial y^2}\right)-\frac{\partial p}{\partial x} \tag{1b}$$

$$u\frac{\partial v}{\partial x}+v\frac{\partial v}{\partial y}=\frac{\nu^*}{\mathrm{Re}}\left(\frac{\partial^2 v}{\partial x^2}+\frac{\partial^2 v}{\partial y^2}\right)-\frac{\partial p}{\partial y} \tag{1c}$$

Energy equation:

$$u\frac{\partial \theta}{\partial x}+v\frac{\partial \theta}{\partial y}=\frac{k^*}{\mathrm{Pe}\,c^*}\left(\frac{\partial^2\theta}{\partial x^2}+\frac{\partial^2\theta}{\partial y^2}\right)+\frac{1}{\mathrm{Pe}\,c^*}\frac{1}{wh}f(\Omega) \tag{1d}$$

where ν^* is the ratio of the viscosity of the material in the domain to the viscosity of the fluid. For the fluid, this parameter is one. In the numerical treatment of the Navier–Stokes equations, the ratio ν^*/Re for the block can be set to an infinitely large value such as 10^3 or 10^4 to simulate a solid. As a result of this procedure, the simultaneous conjugate solution of Navier–Stokes equations for fluid and solid will yield close to zero (10^{-5} or below) velocities for the block, satisfying the no-slip boundary condition along the block faces. In the energy equation, $f(\Omega)$ is a step function which is set to zero everywhere except the block

$$f(\Omega)=\begin{cases}1, & \Omega=\text{block}\\ 0, & \Omega=\text{fluid}\end{cases} \tag{1e}$$

The volume of the heat source, characterized by the product (wh), appears in the source term of the energy equation. It should be noted that the smaller this quantity, the larger the maximum temperature in the center of heat source. k^* and c^* are the thermal conductivity and unit thermal capacity ratios, respectively, of solid to fluid. In the fluid domain, k^* and c^* are both set equal to one. For the solid region, the effect of c^* can be eliminated since the solid velocity is identically zero. Therefore, c^* is set equal to one for both regions. Depending upon the thermal properties of the block and plate, k^* is different from one in the solid region.

Boundary Conditions: No-slip boundary conditions are applied at the two parallel plates as follows:

at $0<x<l_t;\ y=0$: $u, v=0$ (2a)

at $0<x<l_t;\ y=1$: $u, v=0$ (2b)

at $x=0;\ 0<y<1$: $u=6y(1-y),\ v=0$ (2c)

at $x=l_t;\ 0<y<1$: $\dfrac{\partial u}{\partial x}=0,\ \displaystyle\int_0^1 u\,dy=1,\ v=0$ (2d)

The fluid enters the domain with a fully developed parabolic profile. Axial diffusion is set to zero at the exit, to satisfy closure for the elliptic problem. Also, at the plate exit, the x-component velocity (u) is calculated to satisfy conservation of

Nomenclature

b = dimensionless plate thickness
c^* = ratio of solid to fluid unit thermal capacities $=(\rho C_p)_s/(\rho C_p)_f$
$f_i(x, y)$ = curve defining the solid–fluid interface
H, h = dimensional and dimensionless height of blocks; $h=H/L$
k_f = thermal conductivity of the fluid
k_s = thermal conductivity of the solid
k^* = ratio of solid to fluid thermal conductivities $= k_s/k_f$
k^*_{plate} = ratio of plate to fluid thermal conductivities $= k_{\mathrm{plate}}/k_f$
L = plate spacing
L_1, l_1 = dimensional and dimensionless length of plate upstream from the blocks; $l_1=L_1/L$
L_2, l_2 = dimensional and dimensionless length of plate downstream from the blocks; $l_2=L_2/L$
L_t, l_t = dimensional and dimensionless plate length; $l_t=L_t/L$
n = coordinate normal to the solid–fluid interface
Nu = local Nusselt number
Nu_m = mean Nusselt number for a block
P, p = dimensional and dimensionless pressure; $p=P/\rho U_0^2$
$(\rho C_p)_s$ = solid unit thermal capacity
$(\rho C_p)_f$ = fluid unit thermal capacity
Pe = Peclet number $=(U_0/L)/\alpha_f=1/(\mathrm{Re\ Pr})$
q = heat dissipation density (heat per unit volume) $= Q/(WH)$

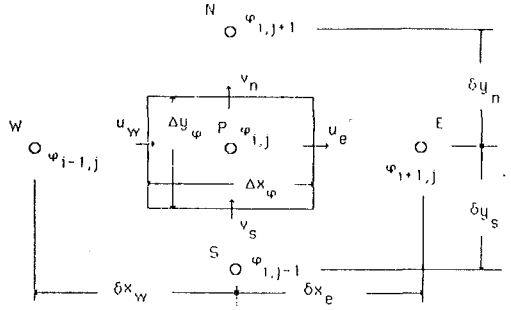

Fig. 2 Local cell geometry for convection and diffusion of property ϕ

mass (boundary condition 2*c*) with the pressure set to zero. For flow over three blocks, the downstream length L_2 was suitably chosen by trial and error to ensure that the recirculation zone was inside the computational domain. This is important for satisfying the elliptic equations in the numerical procedure. The boundary condition on the energy equation depends on the problem considered. In this study two different problems are considered.

Problem 1: Insulated Plates. The boundary conditions for fluid and the bottom of the block are:

$$\text{at} \quad x=0;\ 0<y<1:\ \theta=0 \tag{3a}$$

$$\text{at} \quad x=l_t;\ 0<y<1:\ \partial\theta/\partial x=0 \tag{3b}$$

$$\text{at} \quad 0<x<l_t;\ y=0:\ \partial\theta/\partial y=0 \tag{3c}$$

$$\text{at} \quad 0<x<l_t;\ y=1:\ \partial\theta/\partial y=0 \tag{3d}$$

This implies that the nondimensionalized fluid inlet temperature is zero. The upper and lower plates are insulated. This condition will yield the maximum expected temperature in both the solid and the fluid regions. The plate length is chosen long enough so that there is no axial conduction at the exit. The above boundary conditions are sufficient for the elliptic solution of the energy equation in the rectangular domain.

Problem 2: Conducting Plates. The domain of calculation for conducting plates is shown in Fig. 1. The domain is bounded by the lines, $x=0$, l_t and $y=-(b+y_2)$, y_1, where b is the dimensionless thickness of the plates and y_1 and y_2 are suitably chosen so that the boundary layers are within the domain of calculation. The boundary conditions for temperature are:

$$\text{at} \quad x=0;\ -(b+y_2)<y<-b:\ \theta=0 \tag{4a}$$

$$\text{at} \quad x=0;\ -b<y<0:\ \partial\theta/\partial x=0 \tag{4b}$$

$$\text{at} \quad x=0;\ 0<y<y_1:\ \theta=0 \tag{4c}$$

$$\text{at} \quad x=l_t:\ -(b+y_2)<y<y_1:\ \partial\theta/\partial x=0 \tag{4d}$$

$$\text{at} \quad 0<x<l_t;\ y=y_1:\ \partial\theta/\partial y=0 \tag{4e}$$

$$\text{at} \quad 0<x<l_t;\ y=y_1:\ \partial\theta/\partial y=0 \tag{4f}$$

The heat flux is set to zero at the upper and lower boundaries in the fluid. This is a necessary condition to simulate periodic temperature solution in the y direction. The upstream and downstream temperature conditions for the fluid are the same as in the problem with insulated plates. The boundary condition (4*b*) is employed to neglect heat loss through the edge of the plate.

Interface Condition: For all cases, the boundary conditions (matching conditions) at the fluid–solid interface for the energy equation are

$$T_f(f_i(x,y)=0)=T_s(f_i(x,y)=0) \tag{5a}$$

where $f_i(x, y)=0$ is the curve defining the solid–fluid interface.

$$k_s \frac{\partial T}{\partial n} s\Big|_{f_i(x,y)=0} = k_f \frac{\partial T}{\partial n} f\Big|_{f_i(x,y)} \tag{5b}$$

The derivative with respect to n represents the gradient normal to the curve $f_i(x, y)=0$ at any point on the interface.

Numerical Method: A numerical procedure called SIMPLE is used to solve the basic conservation equations (momentum, heat, mass, etc.). The finite difference mesh consists of many rectangular control volumes using a staggered grid system. Different control volumes are used for x-, y-direction momentum equations, and continuity. All scalar quantities (such as pressure and temperature) are defined at the intersection of any two grid lines. The U and V velocities are defined on the scalar control volume faces. The following is a general formulation for the diffusion–convection equation, which can be applied to both the momentum and energy equations. Figure 2 shows the local cell geometry. Let ϕ be any property for which the conservation equation is as follows

$$\frac{\partial}{\partial x}(u\phi)+\frac{\partial}{\partial y}(v\phi)=\frac{\partial}{\partial x}\left(\Gamma\frac{\partial\phi}{\partial x}\right)+\frac{\partial}{\partial y}\left(\Gamma\frac{\partial\phi}{\partial y}\right)+S_\phi \tag{6}$$

Application of central differencing for the diffusion terms and upwind differencing for the convective terms gives

Nomenclature (cont.)

Q = heat input per unit length in each block
Re = Reynolds number = U_0L/ν
S, s = dimensional and dimensionless spacing between blocks; $s=S/L$
T = temperature
T_f = temperature of fluid along the solid–fluid interface
T_0 = inlet temperature of the fluid (ambient temperature)
T_s = temperature of solid along the solid–fluid interface = T_f
U_0 = average velocity
U, u = dimensional and dimensionless axial velocity; $u=U/U_0$
V, v = dimensional and dimensionless transverse velocity; $v=V/U_0$
W, w = dimensional and dimensionless width of blocks; $w=W/L$
X, x = dimensional and dimensionless x coordinate; $x=X/L$
Y, y = dimensional and dimensionless y coordinate; $y=Y/L$
θ = dimensionless temperature = $(T-T_0)/(Q/k_f)$
θ_b = dimensionless bulk temperature
θ_w = dimensionless temperature of lower plate and the surface of the blocks
ν = kinematic viscosity
ν^* = ratio of viscosity of the solid block to the viscosity of the fluid (an arbitrary large number $\sim 10^{10}$)
ρ = density
Ω = domain of calculation

$$a_p\phi_{i,j} = a_E\phi_{i+1,j} + a_W\phi_{i-1,j} + a_N\phi_{i,j+1} + a_S\phi_{i,j-1} \quad (7)$$

where

$$a_E = \Gamma \frac{\Delta y_\phi}{\delta x_{\phi e}} + [-u_e, 0]\Delta y_\phi \quad (8a)$$

$$a_W = \Gamma \frac{\Delta y_\phi}{\delta x_{\phi w}} + [u_w, 0]\Delta y_\phi \quad (8b)$$

$$a_N = \Gamma \frac{\Delta x_\phi}{\delta y_{\phi n}} + [-v_n, 0]\Delta x_\phi \quad (8c)$$

$$a_S = \Gamma \frac{\Delta x_\phi}{\delta y_{\phi s}} + [v_s, 0]\Delta x_\phi \quad (8d)$$

a_E, a_W, a_N, and a_S are coefficients of ϕ_E, ϕ_W, ϕ_N, and ϕ_S, respectively.

Discretized Equations: Applying the above discretization procedure for x- and y-momentum and energy equations gives

$$a_p U_{i,j} = a_E U_{i+1,j} + a_W U_{i-1,j} + a_S U_{i,j-1} + \Delta y_u (P_{i-1,j} - P_{i,j}) \quad (9)$$

$$a_p V_{i,j} = a_E V_{i+1,j} + a_W V_{i-1,j} + a_N V_{i,j+1} + a_S V_{i,j-1} + \Delta x_v (P_{i,j-1} - P_{i,j}) \quad (10)$$

$$a_P \theta_{i,j} = a_E \theta_{i+1,j} + a_W \theta_{i-1,j} + a_N \theta_{i,j+1} + a_S \theta_{i,j-1} + \frac{\Delta x \Delta y f(i,j)}{\mathrm{Pe}\, c^*\, wh} \quad (11)$$

Equations (9), (10), and (11) give a system of linear equations for the solution of U, V, and θ at the interior nodes as i varies from 1 to N and j varies from 1 to M. There are several ways of solving this system. One can construct a coefficient matrix of order $(M \times N)$ and band width $(2K+1)$, where $K = \min$ of $[M, N]$. The solution to the system can be obtained by a standard banded matrix solver. As K becomes large, the computation time increases drastically. A line-by-line tridiagonal matrix algorithm is applied to solve this system of equations. This solution is fast, but the overall solution for the domain is obtained by several sweeps. Although this technique is iterative, it takes less computer time for large number of nodes in the domain. Solution of the momentum equation using the above discretization is based on a guessed pressure field. The pressure is corrected to satisfy continuity at the end of each iteration. To derive the pressure correction equation, we define the following:

$$P = P^* + P' \quad (12a)$$

$$U = U^* + U' \quad (12b)$$

$$V = V^* + V' \quad (12c)$$

The starred values (U^* and V^*) represent the flow solution given by the pressure P^*. By applying the above in the discretized momentum and continuity equations and simplifying, a linear system can be obtained for P' (pressure correction) as follows:

$$a_p P'_{i,j} = a_W P'_{i-1,j} + a_E P'_{i+1,j} + a_S P'_{i,j-1} + a_N P'_{i,j+1} + b \quad (13)$$

where

$$a_E = \frac{\Delta y_u^2}{a_{u(i+1,j)}} \quad (14a)$$

$$a_W = \frac{\Delta y_u^2}{a_{u(i,j)}} \quad (14b)$$

$$a_N = \frac{\Delta x_v^2}{a_{v(i,j+1)}} \quad (14c)$$

$$a_S = \frac{\Delta x_v^2}{a_{v(i,j)}} \quad (14d)$$

a_u and a_r are central coefficients in the discretized momentum equations for U and V at the specified nodes. The solution to P' at each iteration is obtained by solving the linear system (13) with the coefficients defined in (14).

Note that for a two-dimensional domain involving an $M \times N$ set of interior pressure nodes, there are $M \times (N-1)$ unknowns for U and $(M-1) \times N$ unknowns for V. Appropriate finite-difference equations are used to apply the boundary conditions for U and V at the wall, inflow and outflow boundaries. In solving the steady momentum equations in this step, underrelaxation of 0.5 is applied to the velocities to prevent instability and divergence due to nonlinearity in the Navier–Stokes equations. For the pressure correction equation, a Neumann boundary condition ($\partial P'/\partial n = 0$) must be employed to satisfy continuity. If the iterative line-by-line TDMA is used to obtain the solution, the solution either tends to diverge or is too slow in convergence. Therefore, the system of equations for P' is solved block iteratively using a band matrix solver. The computer code is structured similar to the TEACH-T computer package (Gosman, 1976), which also incorporates the SIMPLE algorithm.

After a steady-state solution is obtained for the flow field, the temperature distribution is solved by discretizing the energy equation (1d), which is similar to the pressure correction equation. Because the energy equation is linear for laminar forced convection, only one iteration is needed, with the discretization equation solved by many sweeps of the line-by-line TDMA. The diffusion coefficient is discontinuous in the energy equation at the solid–fluid interface. Based on property conservation, an equivalent diffusion coefficient is defined for the interface.

A nonuniform mesh with a large concentration of nodes in regions of steep gradients, such as close to the walls and blocks, is employed. The computational region consists of 86 grid lines in the x direction, and 42 grid lines in the y direction. Starting with a parabolic velocity profile in the entire region and a zero velocity in the modules, the flow solution program took about 150 iterations to converge. These computations, performed on an NAS/9000 computer, took about 300–500 CPU seconds depending upon the Reynolds number, for the flow field. After solving for the flow field, the temperature field for forced convection took another 80–100 seconds to converge (multiple sweeps of line-by-line TDMA) depending upon the Peclet number.

Results and Discussion

The dimensionless parameters that must be specified for the system are Re, Pr, k^*_{block}, k^*_{plate}, w, h, and s. Thus the nondimensionalized problem is much more general than the original dimensional formulation. Notice that for pure forced convection problems, the solution is independent of the strength of the heat source. Temperature is a linear function of the heat source magnitude. Since seven basic dimensionless parameters are required to characterize the system, a comprehensive analysis of all combinations of problems is not practical. The results will represent only a small fraction of the possible situations, and will illustrate the effect of several critical parameters. The fixed input parameters that were used in all the cases were: $w = 0.5$, $h = 0.25$, $l_1 = 3.0$, $l_2 = 9.5$. This is representative of the most common size of an IC component relative to the spacing between consecutive boards. This corresponds approximately to the dimensional parameters: $L = 1$ in., $W = 0.5$ in., $H = 0.25$ in., $L_1 = 3$ in., $L_2 = 9.5$ in. The upstream and downstream lengths of the plates were chosen to eliminate the entrance effect in the fluid flow and to satisfy continuity at the exit. This ensures that the outflow boundary condition of a fully developed profile for the velocity has no effect on the flow solution around the blocks. The other values, viscosity of fluid, thermal properties of fluid and solid,

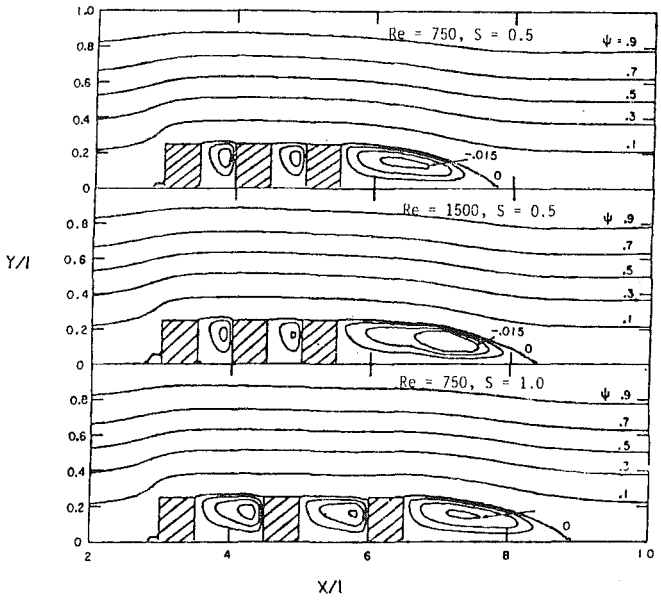

Fig. 3 Streamlines for steady flow over three blocks

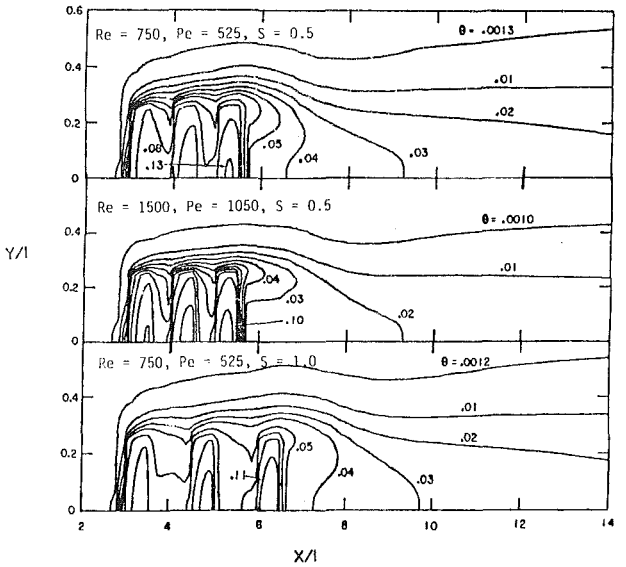

Fig. 4 Dimensionless temperature contours for forced convection from three blocks, with insulated plates

bulk velocity of the cooling fluid, etc., are varied. All of these effects are summarized in the parameters Re, Pr, and k^* for both the block and the plate. Based on the above parameters, the analysis is divided into the following two problems: (*a*) forced convection from three blocks with insulated plates; (*b*) forced convection from three blocks with conducting plates.

To verify the computer program for steady-state solution of the Navier–Stokes equation, isothermal flow between two parallel plates was selected as a test problem. A numerical solution for U, V, and P was obtained up to an additive constant for the pressure. Due to the relative nature of pressure, the pressure can be prescribed arbitrarily at any internal node. Convergence was declared when the maximum change in dimensionless U and V after each successive iteration was less than 10^{-4}. The computer program, when tested for various Reynolds numbers, yielded consistent results for the centerline velocity profile. This solution converged as the mesh size was decreased. The test solution compared well with an independent study by Morihara et al. (1973). This example illustrates that the SIMPLE algorithm is a reliable algorithm for solving problems in transport phenomena.

Fluid flow over one block is solved using the same problem parameters studied by Zebib and Wo (1985). These values are: $w = 0.96$ and $h = 0.10$. The streamline plot agrees with Zebib's solution (1985) within 2 percent for the region neighboring the block. The current model assumes a uniform conductivity throughout the solid region, whereas Zebib's study (1985) considers a complex internal geometry of the component, made up of composite materials to simulate the various conduction paths from the center of the chip to the board and the environment. However, his study is limited to one particular application of IC components. Therefore the temperature solution could not be compared with his results.

Forced Convection With Insulated Plates. The model used in the current study to analyze conjugate heat transfer from three blocks is shown in Fig. 1. The conductivities of IC components are generally an order of magnitude higher than the fluid conductivity. Most applications employ a plastic mold compound for the packaging material. The thermal conductivity for a typical mold compound is 0.142 to 0.262 W/m°C. This approximately corresponds to a conductivity ratio $k^* = 10$ for the heat-generating block with air as the cooling fluid. Spacings of 0.25, 0.5, 0.75, and 1.0 were chosen for this analysis. To consider a range of values in the laminar regime, Re = 100, 750, 1000, and 1500 were used to study the flow field and corresponding forced convection. Prandtl numbers of 0.1 and 2 were used to simulate different fluids, along with 0.7 for air.

Figure 3 displays distribution of stream function for Reynolds numbers of 750 and 1500 at block spacings of 0.5, and for Re = 750 and spacing = 1.0. The streamlines were generated by computing the stream function, $\psi = \int u dy$, and plotting contours. Several interesting features are observed from these plots. First, the streamlines are considerably distorted in the channel due to presence of the blocks. The velocity distribution is parabolic at both the entrance and exit of the two plates. However, this distribution changes rapidly as the fluid turns the corner of the first block. Downstream from the third block, it takes much longer to return to parabolic distribution. Second, there is no recirculation zone ahead of the first block for the range of Reynolds numbers investigated (100 to 1500). Third, the fluid forms recirculating zones between every block. The size of the recirculation increases between the blocks as the spacing increases from 0.5 to 1.0. Even at the largest spacing ($s = 1.0$), the recirculating cell completely occupies the region between blocks. For the range of spacings considered for flow over IC's, the recirculating cell is attached to all three walls between components. The fluid flow solution in this problem is similar to flow over a cavity.

The core flow introduces a shear layer in the fluid driving the recirculating flow, just as a moving plate over an enclosed cavity. There is a very steep velocity gradient in the fluid as it turns the corner around the blocks. This is similar to a secondary boundary layer starting from the top left corner of the block. This effect increases the heat transfer by convection. As the Reynolds number increases, the extent of distortion in core flow profiles due to presence of blocks increases. The streamline distribution shows that the center of recirculation between blocks shifts to the right for increasing Reynolds numbers. For all Reynolds numbers studied, a long recirculation zone is observed downstream from the last block.

The length of recirculation zone downstream from the last block increases as the Reynolds number increases. By increasing the Reynolds number, momentum in the fluid is increased, resulting in a longer travel length in the fluid before reattachment. The flow patterns, including the shape of recirculating zones, play an important role in transporting heat from the blocks and in determining temperature distributions in both the fluid and the blocks.

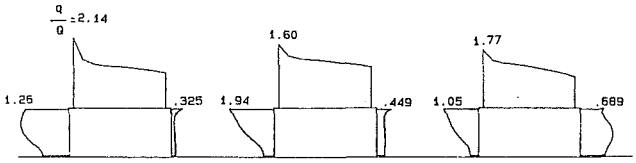

Fig. 5 Local heat flux profile for insulated plates: s = 0.50, Re = 750, and Pr = 0.7

Temperature contours for spacings of 0.5 and two different values of Reynolds numbers are given in Fig. 4 for Pr = 0.7. The temperature contours for the above Reynolds numbers at Pr = 0.7 and spacing 1.0 are also shown in Fig. 17. Notice that the hot spots are in the center of the blocks along the lower wall, since the lower wall is kept insulated. The thermal boundary layer thickness at the end of the channel is less than 0.60 for large Peclet numbers (Pe > 500). An interesting feature is that the boundary layer thickness increases over the blocks and decreases downstream from the blocks. This is different from a thermal boundary that develops from a flat finite heat source placed along the bottom wall. For flow over a heated bottom plate, the thermal boundary layer thickness increases along the length of the plate. In this problem the distortion in the boundary layer shape arises partly due to the reduced cross-sectional area of the core flow and transverse conduction in the fluid from the top surface of each block. In each case, the maximum temperature occurs in the center of last block downstream.

The temperature distribution between the blocks is similar to temperature distribution in flow over a cavity. This distribution is similar to the computations by Chen and Yoon (1983) for flow over an expansion in a pipe, with a step change in temperature at the cavity walls. At large Reynolds numbers the distribution of temperature contours penetrates deep into the space between blocks creating a large potential difference between the blocks and the fluid temperature. This reduces the convective resistance of the fluid in the boundary layer over the blocks.

Conservation of energy was checked by balancing energy input to the three blocks with the energy convected out by the fluid at the exit of the plates. The error in global energy balance is within 2 percent for all Peclet numbers. This is probably due to truncation error in the finite-difference equations.

The local Nusselt number along the surface of the blocks may be expressed from the local heat transfer coefficient as

$$\mathrm{Nu} = \frac{hl}{k_f} = -\frac{1}{\theta_w}\frac{\partial\theta}{\partial y}\bigg|_w \qquad \text{(top face of block)} \qquad (15a)$$

$$\mathrm{Nu} = -\frac{1}{\theta_w}\frac{\partial\theta}{\partial x}\bigg|_w \qquad \text{(left and right faces of the block)} \qquad (15b)$$

The mean Nusselt number for each block is calculated as follows

$$\mathrm{Nu}_m = \frac{1}{A}\int_A \mathrm{Nu}\, dA \qquad (16)$$

where A is the surface area of the block exposed to the fluid. The local heat flux profile with insulated plates for spacing $s = 0.5$, Re = 750, Pr = 0.7 is presented in Fig. 5. The local Nusselt number and the dimensionless wall temperature for each of the three blocks is presented at Re = 100, 750, 1000, and 1500 and Pr = 0.7 (Fig. 6). The x-coordinate system used for local Nusselt number includes the vertical surfaces of the blocks. The heat flux distribution varies several orders of magnitude between the side surfaces and top surfaces of the block. Maximum heat flux occurs at the top surface of each

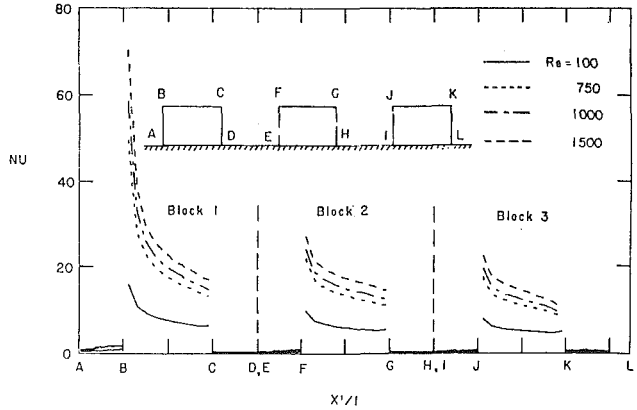

Fig. 6(a) Local Nusselt number for forced convection with insulated plates: s = 0.50 and Pr = 0.7

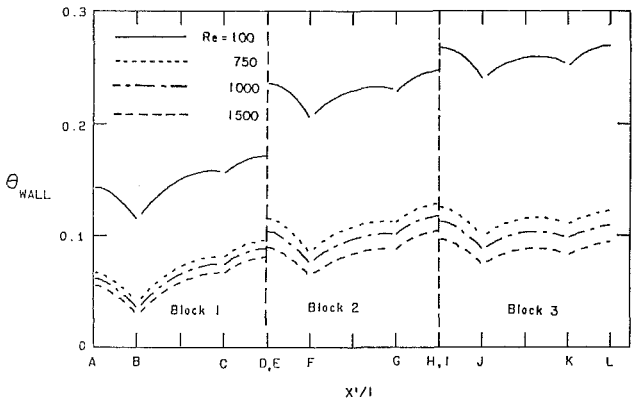

Fig. 6(b) Dimensionless wall temperature with insulated plates: s = 0.50 and Pr = 0.7

Table 1 Correlation constants for mean Nusselt numbers in forced convection with insulated plates; $100 \le \mathrm{Re} \le 1500$ and $0.1 \le \mathrm{Pr} \le 2.0$

	Constants		
Block number	A	B	C
1	0.69085	0.43655	0.410806
2	0.57419	0.40087	0.377710
3	0.48004	0.39578	0.364050

block, since this surface is parallel to the flow direction. As the fluid turns around the corner at points B, F, and J, the Nusselt number reaches a peak because of the presence of a secondary boundary layer beginning at the leading edge of top surface. In general, the Nusselt number increases as both Re and Pr increase.

The mean Nusselt number varies approximately linearly on a logarithmic scale with respect to Reynolds number over the range 100 to 1500. Using least-squares method to get a linear fit on a log–log–log plot of Nu versus (Re, Pr), the following empirical expressions may be derived

$$\mathrm{Nu} = A\mathrm{Re}^B\mathrm{Pr}^C \qquad (18)$$

The constants A, B, and C are tabulated in Table 1 for each of the three blocks.

In general, electronic component designers are interested in the maximum temperature at the chip. The reliability and the function of the electronic devices depend on this maximum temperature. The effect of different cooling fluid velocities (Reynolds number) and Prandtl number on the maximum temperature ($\theta_{\max}$) is presented in Fig. 7. This result shows that

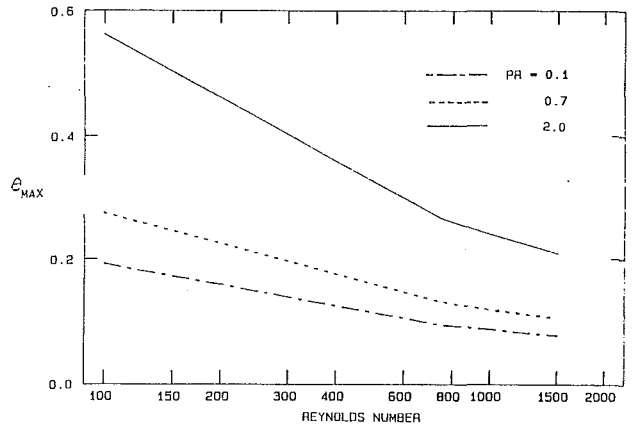

Fig. 7 Dimensionless maximum temperature (in block 3) as a function of Reynolds and Prandtl numbers with insulated plates: $s = 0.50$

Table 2 Correlation constants for mean Nusselt numbers in forced convection with conducting plates; $750 \le Re \le 1500$ and $Pr = 0.7, 2.0$

	Constants		
Block number	A	B	C
1	1.09064	0.37406	0.38605
2	0.89287	0.34568	0.33571
3	0.67149	0.36757	0.31054

Table 3 Heat transfer through the bottom surface of plate; $Re = 750$, $Pr = 0.7$, and spacing $= 0.50$

k^*_{plate}	Percent of total heat generated in blocks
10	46.0
5	44.3
1	32.8

the maximum temperature decreases as a function of Reynolds number. Variation with the Prandtl number is also shown.

Forced Convection With Conducting Plates. In most applications (especially main-frame computers), layers of PC boards with IC components are arranged as shown in Fig. 1. The heat generated by the blocks has two distinct paths. It reaches the surface by conduction and convects away by the fluid stream, or it travels below to the PC board and eventually to the fluid flowing over the board. The thermal conductivity of the plate determines the ratio of heat divided between these two primary paths. For a finite conductivity of the plate (same order of magnitude as the block conductivity), an accurate heat transfer model must include conjugate conduction through the PC board coupled to the fluid flow and the block. Therefore, the heat loss to the PC board cannot be neglected.

The analysis for this problem can be complex if multiple layers of PC boards are included in the domain of calculation. Zebib and Wo (1985) assume a constant heat transfer coefficient on the lower surface of the plate to estimate heat loss through the board. This will introduce large errors because the heat input from the blocks on the top surface of the plate is discrete and nonuniform. To reduce the complexity in this analysis, a rectangular domain that cuts through the fluid stream above the blocks and below the plate can be considered for solution of the energy equation. The flow field is the same through each channel as calculated by the flow solver. For large Peclet numbers ($Pe > 500$), the boundary layers from each surface of the plate can be assumed independent (as shown in Fig. 1). Hence, a zero-heat flux boundary condition is applied at $y = y_1$ and $y = -(b + y_2)$, for all values of x. With

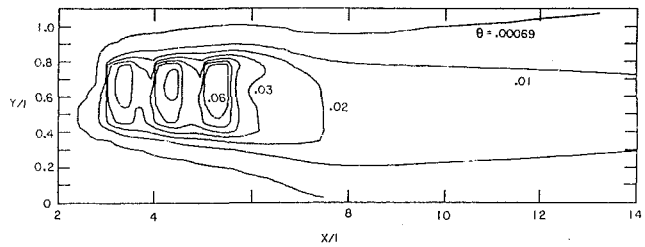

Fig. 8 Dimensionless temperature contours for forced convection from three blocks with conducting plates: $s = 0.50$, $Re = 750$, $Pr = 0.7$, $Pr = 525$, $k^*_{plate} = 10$

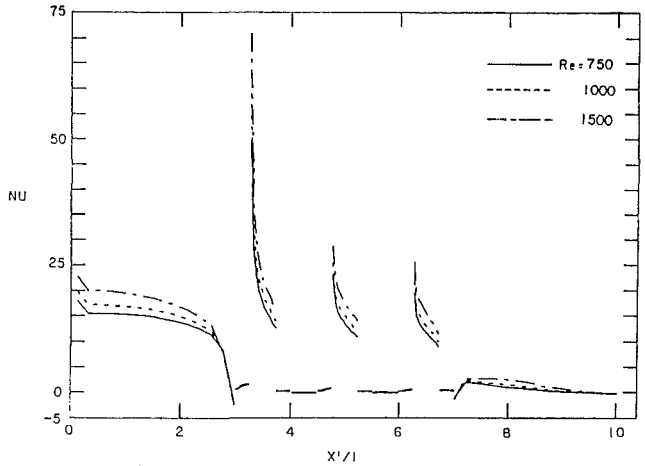

Fig. 9(a) Local Nusselt number (top surface) for forced convection with conducting plates: $s = 0.50$, $Pr = 0.7$, and $k^*_{plate} = 10$

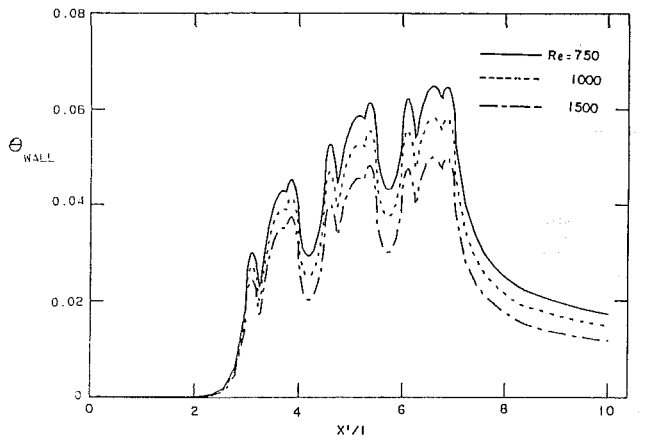

Fig. 9(b) Dimensionless wall temperature (top surface) with conducting plates: $s = 0.50$, $Pr = 0.7$, and $k^*_{plate} = 10$

a given velocity field, and thermal properties for the block and plates, the energy equation can be solved for forced convection with a conducting plate. The following parameters were selected in this study: $k^*_{block} = 10$, $b = 0.10$, and $k^*_{plate} = 10$.

Temperature contours for spacing $= 0.5$, $Re = 750$, and $Pr = 0.7$ are shown in Fig. 8. This shows that the temperature contours extend in both directions (fluid above the blocks and below the plate) equally, indicating the importance of heat loss through the PC board. The local Nusselt number and dimensionless wall temperature along the top and bottom surfaces of the plate are shown in Figs. 8 and 9, respectively, for $Re = 750$, 1000, and 1500. In this study, only $Pr = 0.7$ is considered to satisfy the assumption of zero heat flux along the top and bottom boundaries of the domain. For small Peclet numbers ($Pe < 500$), this assumption is not valid, as the thermal

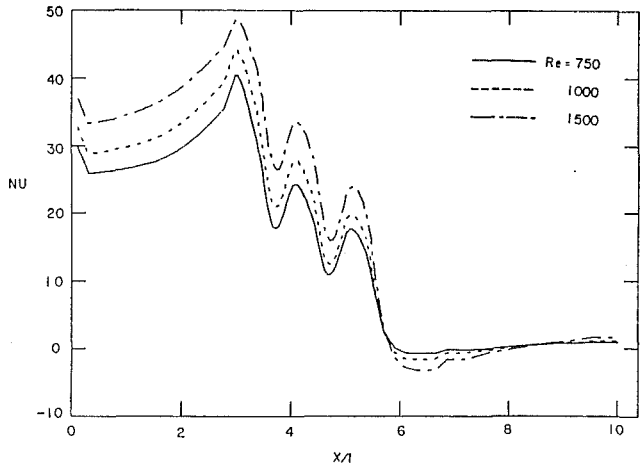

Fig. 10(*a*) Local Nusselt number (bottom surface) for forced convection with conducting plates: s = 0.50, Pr = 0.7, and $k^*_{plate} = 10$

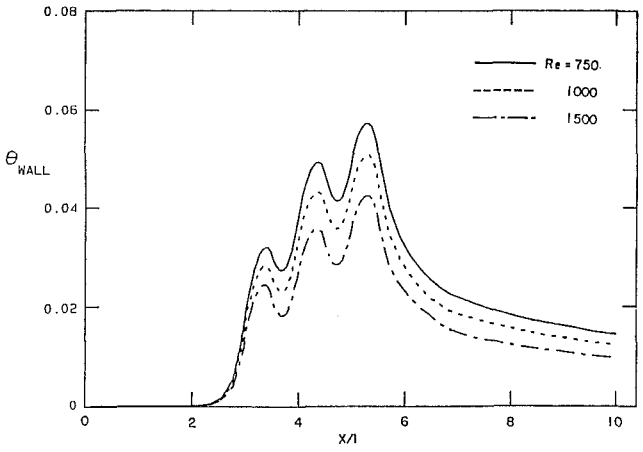

Fig. 10(*b*) Dimensionless wall temperature (bottom surface) with conducting plates: s = 0.50, Pr = 0.7, and $k^*_{plate} = 10$

boundary layers from the two walls in the channel mix and transition to fully developed heat transfer begins.

Qualitatively, the distribution of local Nusselt number on the top surface is similar to the case with insulated plates. A periodic variation of Nusselt number on the bottom surface is observed, with a decreasing mean. The peak in each cycle occurs at an x value corresponding to the left face of each block. This clearly suggests that the heat loss distribution is in fact not a constant but a continuous function of x. The heat input to the board is discrete. Although the thermal conductivity of the plate is uniform, the heat flux below varies along the plate length. Correlation constants for the mean Nusselt numbers in each block can be obtained similar to the procedure used in obtaining equation (18). The constants A, B, and C for forced convection with conducting plates are presented in Table 2.

The conductivity of the plate is significant in determining the maximum temperature in the block. To study the effect of different conductivities, k^* of 1 and 5 are used for the plate (PC board) at Re = 750 and Pr = 0.7. The Nusselt number did not vary significantly for different conductivities of the plate. However, the total heat transferred to the fluid below the plate varies (Table 3). As k^* for the plate is decreased from 10 to 1, total heat transfer decreases from 44 to 33 percent.

Conclusions

A model for numerical prediction of viscous flow and forced convection between parallel plates with finite block heat sources has been developed. The analysis for the blocks (representing IC components) is treated by assuming different material properties in the appropriate differential equations. The rectangular blocks change the incoming parabolic velocity field considerably resulting in recirculating zones between the blocks. Although each block generates a constant rate of heat, the heat flux varies as a function of position on all three surfaces (left, right, and top) exposed to the fluid stream. Velocity and temperature fields are obtained for different spacings, Reynolds numbers, Prandtl numbers, conducting plate, and an insulated plate. Mean Nusselt number correlations are presented for different Re and Pr numbers with and without insulated plates.

References

Bergles, A. E., Chu, R. C., and Seely, J. H., 1972, "Survey of Heat Transfer Techniques Applied to Electronic Equipment," *Proceedings, ASME Winter Annual Meeting*, ASME, New York.

Braaten, M. E., and Patankar, S. V., 1984, "Analysis of Laminar Mixed Convection in Shrouded Arrays of Heated Rectangular Blocks," *Proceedings, The 22nd National Heat Transfer Conference and Exhibition*, L. C. Witte, ed., Niagara Falls, NY.

Chen, C. J., and Yoon, Y. W., 1983, "Finite Analytic Numerical Solution Axisymmetric Navier-Stokes and Energy Equations," ASME JOURNAL OF HEAT TRANSFER, Vol. 105, pp. 639-645.

Ellison, G. N., 1984, *Thermal Computations for Electronic Equipment*, Van Nostrand Reinhold Company, New York.

Gosman, A. D., and Ideriah, F. J. K., 1976, "TEACH-T: A General Purpose Computer Program for Two-Dimensional, Turbulent, Recirculating Flows," in: *Calculation of Recirculating Flows*, Department of Mechanical Engineering, Imperial College, London.

Jaluria, Y., 1985, "Natural Convection Cooling of Electronic Equipment," Technical Report, Dept. of Mechanical and Aerospace Engineering, Rutgers University, New Brunswick, NJ.

Kennedy, K. J., and Zebib, A., 1982, "Combined Forced and Free Convection Between Parallel Plates," *Proceedings, Seventh International Heat Transfer Conference*, Hemisphere Publishing, New York, Paper No. 82-IHTC-152.

Kennedy, K. J., and Zebib, A., 1983, "Combined Free and Forced Convection Between Horizontal Parallel Planes: Some Case Studies," *International Journal of Heat and Mass Transfer*, Vol. 26, pp. 471-474.

Kraus, A. D., and Bar-Cohen, A., 1983, *Thermal Analysis and Control of Electronic Equipment*, Hemisphere Publishing Corp., Washington, DC.

Mahalingam, L. M., and Reed, D. J., 1984, "Bipolar Device Packaging – Electrical, Thermal and Mechanical Stress Considerations," *Solid State Technology*, Vol. 17, No. 5, pp. 167-172.

Morihara, H., and Cheng, R. T., 1973, "Numerical Solution of the Viscous Flow in the Entrance Region of Parallel Plates," *Journal of Computational Physics*, Vol. 11, pp. 550-572.

Patankar, S. V., 1980, *Numerical Heat Transfer and Fluid Flow*, Hemisphere Publishing Company, New York.

Patankar, S. V., 1978, "A Numerical Method for Conduction in Composite Materials, Flow in Irregular Geometries and Conjugate Heat Transfer," *Proceedings, Sixth International Heat Transfer Conference*, Toronto, Vol. 3, p. 297.

Simons, R. E., 1983, "Thermal Management of Electronic Packages," *Solid State Technology*, Oct., pp. 131-137.

Sloan, J. L., 1985, *Design and Packaging of Electronic Equipment*, Van Nostrand Reinhold Company, New York.

Waller, D. L., Fox, L. R., and Hannemann, R. J., 1983, "Analysis of Surface Mount Thermal and Thermal Stress Performance," *IEEE Transactions on Components, Hybrids, and Manufacturing Technology*, Vol. CHMT-6, pp. 257-266.

Walter, K. T., and Larsen, P. S., 1981, "The FON Method for the Steady Two-Dimensional Navier-Stokes Equations," *Computers and Fluids*, pp. 365-371.

Zebib, A., and Wo, Y. K., 1985, "A Two-Dimensional Conjugate Heat Transfer Model for Forced Air Cooling of an Electronic Device," presented at the International Electronic Packaging Conference, Orlando, FL, Oct. 22-24, 1985.

Heat (Mass) Transfer for Circular Jet Impingement on a Confined Disk With Annular Collection of the Spent Air

E. M. Sparrow

Z. X. Xu

L. F. A. Azevedo

Department of Mechanical Engineering,
University of Minnesota,
Minneapolis, MN 55455

Heat (mass) transfer experiments have been performed for a single circular jet impinging perpendicular to a confined disk, with the spent air being collected in an annulus which surrounds the jet delivery tube. This configuration provides precise control of the surface area affected by the impinging jet and also assures complete collection of the spent air. During the course of the experiments, parametric variations were made of the dimensionless separation distance between the jet origin and the impingement disk, of the ratio of disk diameter to the jet diameter, and of the Reynolds number. It was found that the heat (mass) transfer coefficient at the impingement surface increased substantially with a decrease in the jet diameter. Furthermore, for the smaller diameter jet, there was an optimum separation distance at which a maximum value of the heat (mass) transfer coefficient was achieved. For a jet of larger diameter, the transfer coefficient decreased monotonically as the separation distance increased.

Introduction

Jet impingement has been widely investigated because of the relatively high heat transfer coefficients which are provided by this mode of fluid flow. Investigations of jet impingement are often classified according to whether a single jet or multiple jets participate in the heat transfer process [1]. In the case of multiple jets, a major issue is the outflow path of the spent fluid, since this path affects the extent to which the individual jets interact with each other. On the other hand, for a single jet, no particular note has been taken of the collection of the spent fluid. In the heretofore-investigated, single round-jet configurations, the collection generally occurred after the impinged fluid had completed its radial spread over the impingement surface and had passed beyond the outer rim of the surface [1].

In the present paper, consideration is given to a novel single jet configuration in which the impingement heat transfer coefficients are affected by the nature of the spent fluid collection. A schematic diagram of the investigated jet impingement configuration is presented in Fig. 1. As seen there, the impingement fluid, air, is delivered through a circular tube and is collected in an annular flow passage which surrounds the delivery tube. The outer bounding surface of the annulus extends downward in skirt-like fashion and seats at the outer rim of the impingement surface, thereby confining the jet.

The aforementioned configuration enables precise control of the surface area affected by the impinging jet. Also, total collection of the spent air is assured, which may be a relevant consideration if the spent fluid contains heat energy or chemical components which can be reclaimed or if it contains toxic components which require special handling. Furthermore, compared with other possible arrangements for total collection of the spent fluid, the concentric annulus is relatively compact. The total collection feature coupled with the high heat transfer coefficients which characterize jet impingement are attractive for heat storage systems such as regenerators.

The fluid delivery-collection arrangement pictured in Fig. 1 gives rise to a flow pattern adjacent to the impingement surface that differs markedly from the radial wall jet that is characteristic of previously investigated, single impinging round jets. In particular, the requirement that the flow execute a 180 deg turn in order to exit the impingement zone and the presence of blockage at the rim of the impingement surface create a strong axial velocity component directed away from the surface. This significantly altered flow pattern should affect the impingement-surface heat transfer coefficients.

As indicated in Fig. 1, the problem is described by three geometric parameters: (1) the separation distance S between the jet origin and the impingement surface, (2) the jet diameter D_j at the tube exit, and (3) the diameter D of the impingement

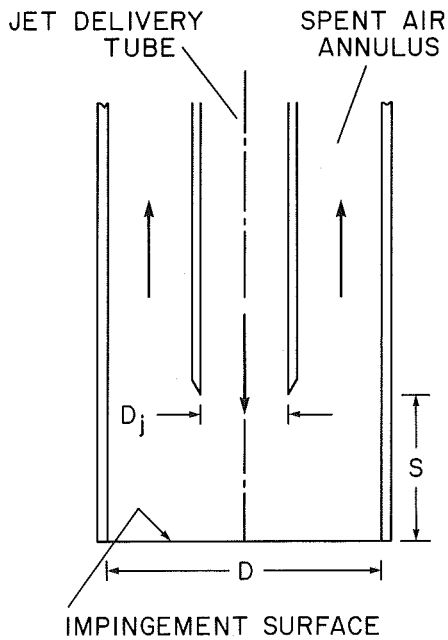

Fig. 1 Schematic diagram of the investigated jet impingement configuration

Contributed by the Heat Transfer Division for publication in the JOURNAL OF HEAT TRANSFER. Manuscript received by the Heat Transfer Division May 14, 1986.

surface. In dimensionless terms, these reduce to the ratios S/D_j and D/D_j. The experiments were performed for S/D_j varying from 1 to 5 in as many as seven steps and for D/D_j values of 1.51 and 2.20. For each geometry characterized by S/D_j and D/D_j, the jet Reynolds number, based on conditions at the exit of the jet delivery tube, spanned an overall range which extended from 7000 to 80,000.

The main focus of the work was to determine average impingement-surface mass transfer coefficients as a function of the aforementioned parameters. The thus-determined Sherwood numbers (dimensionless mass transfer coefficients) can be transformed to Nusselt numbers for heat transfer by using the analogy between the two processes. If $Sh \sim Sc^m$ and $Nu \sim Pr^m$, the analogy yields $Nu/Sh = (Pr/Sc)^m$.

Experiments

As implied in the foregoing, the experimental work was carried out for mass transfer rather than for heat transfer. The specific mass transfer process used in the experiments was the sublimation of naphthalene in air. The naphthalene technique affords higher accuracy than is commonly obtainable in heat transfer experiments and is free of heat-transfer-type extraneous losses (e.g., conduction and radiation losses). Furthermore, the use of the naphthalene technique makes for apparatus simplicity and flexibility. The boundary condition at the subliming surface, uniform concentration of the sublimed vapor, is analogous to uniform wall temperature in the corresponding heat transfer problem.

Apparatus. The description of the experimental apparatus is facilitated by reference to the longitudinal sectional view presented in Fig. 2. The apparatus was operated in the open-circuit mode and in suction. Air was drawn from the temperature-controlled, naphthalene-free laboratory room into the inlet of the jet delivery tube. The air traversed the length of the tube, which had been chosen to ensure hydrodynamically developed flow, and emerged as a free jet. After impinging on the naphthalene surface, the spent air was collected in the annulus surrounding the delivery tube. Three radially oriented exit ports, spaced 120 deg apart around the circumference, were provided at the downstream end of the annulus. The air which exited through the three ports was merged into a header, from which it was ducted to a flowmeter (a calibrated rotameter), a control valve, and finally to a blower situated in a service corridor adjacent to the laboratory. The naphthalene-enriched, compression-heated discharge of the blower was vented outside the building.

As seen in Fig. 2, the two-tube system (the jet delivery tube and the outer tube of the annulus) was fitted with a pair of collars, one at the inlet/exit end of the apparatus and the other at the test section end. Both collars, made of brass, were precisely machined to fit over the outer tube with minimal clearance. The former served both to close the downstream end of the annulus and to support the inner tube concentrically with the other tube. The latter provided a recessed housing

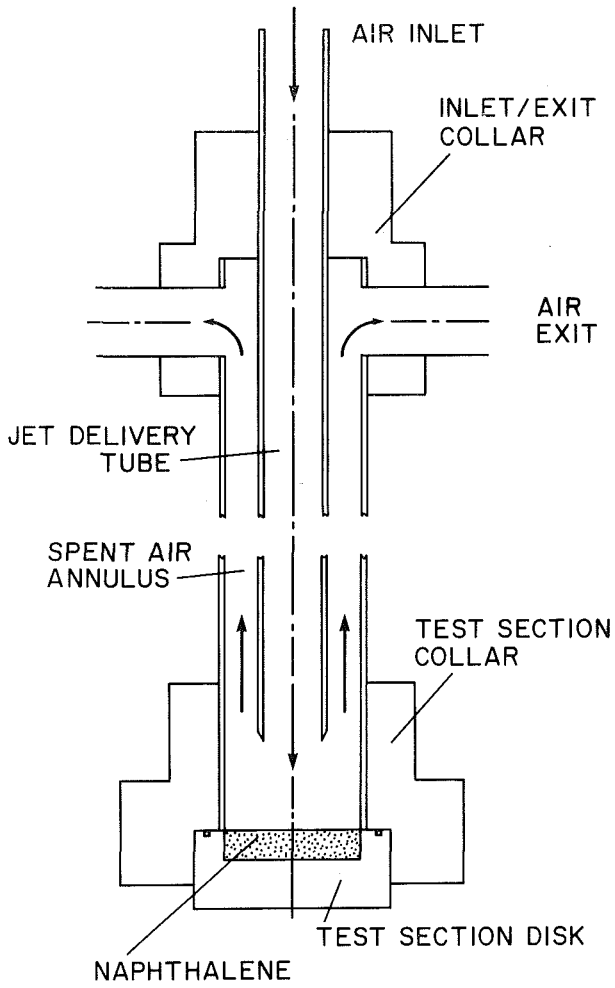

Fig. 2 Longitudinal sectional view of the experimental apparatus

to seat the mass transfer test section. Silicone rubber was used to seal the interfaces between the collars and the other components of the apparatus, unless otherwise noted.

The test section consisted of an aluminum disk (aluminum was used to minimize weight) and the naphthalene impingement surface which was cast into a 0.75-cm-deep cavity machined in the disk. The diameter of the impingement surface, already designated as D in Fig. 1, was made identical to the outer diameter of the annulus. An O-ring was used to prevent leaks at the interface between the disk and the collar. To ensure a positive seal and to lock the test section in place in the collar, quick-acting clamps (not shown), which could be engaged or disengaged in seconds, were mounted so as to press firmly against the rear face of the disk.

Nomenclature

A = area of impingement surface
C = coefficient in equation (5)
D = diameter of impingement surface
D_j = diameter of jet delivery tube
$\mathfrak{D}$ = mass diffusion coefficient
K = impingement-surface mass transfer coefficient
ΔM = change of mass during data run
n = exponent in equation (5)
Re = Reynolds number at jet origin $= 4\dot{w}/\mu\pi D_j$
S = separation distance between jet origin and impingement surface
Sc = Schmidt number
Sh = impingement-surface Sherwood number
$\dot{w}$ = mass flow rate in jet delivery tube
μ = viscosity
ν = kinematic viscosity
ρ = density
ρ_{nj} = density of naphthalene vapor in jet
ρ_{nw} = density of naphthalene vapor at impingement surface
τ = duration of data run

To facilitate the casting of the naphthalene, a hole (not shown) was drilled along the axis of the disk from its rear face through to the bottom of the cavity. This hole was used to introduce molten naphthalene into the cavity during the casting process. In addition to the pour hole, two smaller, off-axis holes were drilled through the disk to enable the escape of air displaced by the poured naphthalene. One of the smaller holes also served as a channel through which a thermocouple was passed. The thermocouple junction was cast into the exposed surface of the naphthalene.

In addition to the concentricity of the tubes enforced by the inlet/outlet collar, positive centering was also provided at two other axial stations. At each station, three specially machined, fine-diameter pins, deployed 120 deg apart around the circumference, passed radially through the annulus and contacted the other surface of the jet delivery tube. To facilitate the centering, the mass transfer test section was removed and a fixture inserted which held the tubes in precise concentricity. The pins were then tightened to preserve the concentricity. Care was taken in selecting the axial locations of the centering stations to ensure that the pins did not inhibit the free entry of the air flow into the annulus.

Two different jet delivery tubes were used during the course of the experiments, with respective inner diameters of 1.580 and 2.300 cm. Both tubes were 114.3 cm long, with a wall thickness of 0.159 cm. The tubes were selected for straightness and surface finish. As indicated in Fig. 2, the downstream end of each tube was beveled at 45 deg to eliminate the effect of the wall thickness. After the tubes had been cut to length and beveled, they were carefully deburred and subsequently polished.

A single outer tube was used throughout the experiments. It had an inner diameter of 3.480 cm, a wall thickness of 0.159 cm, a length of 101.6 cm, and was also selected on the basis of straightness and surface finish. The outer tube was of brass, and the inner tubes were of aluminum.

In view of the foregoing, it may be noted that the jet diameter D_j at the tube exit took on values of 1.580 cm and 2.300 cm, while the diameter D of the impingement surface was 3.480 cm. This yielded D/D_j ratios of 1.51 and 2.20. For each D/D_j (i.e., for each of the inner tubes), the separation distance S between the jet origin and the impingement surface was varied parametrically. These variations were accomplished with the aid of precisely machined gages (accurate to 0.001 cm) which were inserted into the test section end of the apparatus (with the test section removed).

Mention may also be made of a second test section, alternate to the mass transfer test section, used for measurement of the pressure at the impingement surface. The pressure test section was an aluminum disk having overall dimensions identical to those of the mass transfer disk. It was equipped with three 0.10-cm-dia pressure taps, one at the center of the disk and the other two symmetrically placed 1.65 cm to either side of the center. The measured pressures were used in the data reduction for the mass transfer experiments and also to verify the symmetry of the flow (via the two off-center pressure taps).

With regard to instrumentation, mention has already been made of the flowmeter and of the thermocouple embedded in the naphthalene. A second thermocouple was used to measure the temperature of the air entering the apparatus. Both thermocouples were made from precalibrated, 0.0254-cm-dia chromel and constantan wire and were read to 1 μV by a programmable datalogger. The pressures were read from either water or mercury manometers, as appropriate, in conjunction with a barometer. The sublimation-related change of mass of the mass transfer test section during a data run was determined with an electronic analytical balance having a resolution of 0.00001 g and a capacity of 166 g. A stopwatch with a resolution of 0.01 s was used to clock the duration of the data runs.

Experimental Procedure. In preparation for each data run, a fresh naphthalene impingement surface was cast. As a prelude to the casting, the naphthalene remaining in the test section disk from the preceding run was removed by melting and evaporation. Then, the disk was placed on a highly polished stainless steel plate with the cavity facing downward, and the thermocouple was inserted into the cavity and fixed so that it contacted the plate. Molten naphthalene was then introduced into the cavity through the aforementioned pour hole. After solidification was completed, the test section disk was separated from the plate. The finish of the thus-exposed naphthalene surface was comparable to that of the plate against which it has been cast. The newly cast naphthalene surface was capped with a Delrin (plastic) cover which totally suppressed sublimation, and the mass transfer test section was placed in the laboratory to achieve thermal equilibrium.

Each data run was characterized by D/D_j, S/D_j, and Re. The geometric parameters D/D_j and S/D_j were set using the components described in the preceding section of the paper and no further elaboration is needed here. For the selected Reynolds number Re, the impingement-surface pressures were first determined by making use of the pressure test section. The mass transfer run was initiated with a thermal equilibration period in which the mass transfer test section was put in place in the apparatus but shielded from the air flow by a 0.005-cm-thick stainless steel disk. During the equilibration period, the impingement surface thermocouple was read periodically. Once steady state had been achieved, the test section was removed from the apparatus, covered, and weighed.

After the weighing, the test section was returned to the apparatus, and the data run proper was initiated. During the run, the impingement surface temperature and the air temperature were read periodically by the datalogger (10 to 15 readings), while the rotameter float position and the air pressure at the rotameter were read and recorded manually. The duration of the run was selected to limit the mean sublimation-related recession of the impingement surface to 0.0025 cm (a mass loss of about 0.027 g). Durations ranging from four minutes to one and a half hours were used to accommodate the investigated range of Reynolds numbers and geometric parameters.

At the termination of the run, the mass transfer test section was removed from the apparatus and covered. It was then weighed. Then, all steps between the before-run and after-run weighings were repeated, except for the air flow period, following which a third weighing was performed. The difference between the second and third weighings reflected the extraneous mass losses associated with the handling of the test section. These losses were found to be on the order of 0.1 percent of the mass transfer to the impinging jet and were, therefore, neglected.

Data Reduction. The mass transfer results will be presented in dimensionless form in terms of the Sherwood number Sh, which is the mass transfer counterpart of the Nusselt number. The Sherwood number is defined as

$$\mathrm{Sh} = KD/\mathfrak{D} \tag{1}$$

where K is the average mass transfer coefficient for the impingement surface, and $\mathfrak{D}$ is the mass diffusion coefficient. Note that the diameter D of the impingement surface has been used as the characteristic length in the Sherwood number.

The mass diffusion coefficient can be eliminated from equation (1) by introducing the definiton of the Schmidt number Sc $= \nu/\mathfrak{D}$, so that

$$\mathrm{Sh} = (KD/\nu)\mathrm{Sc} \tag{2}$$

For naphthalene diffusion in air, Sc = 2.5 [2], with a possible uncertainty of two percent. Furthermore, in view of the minute amounts of naphthalene vapor present, ν was

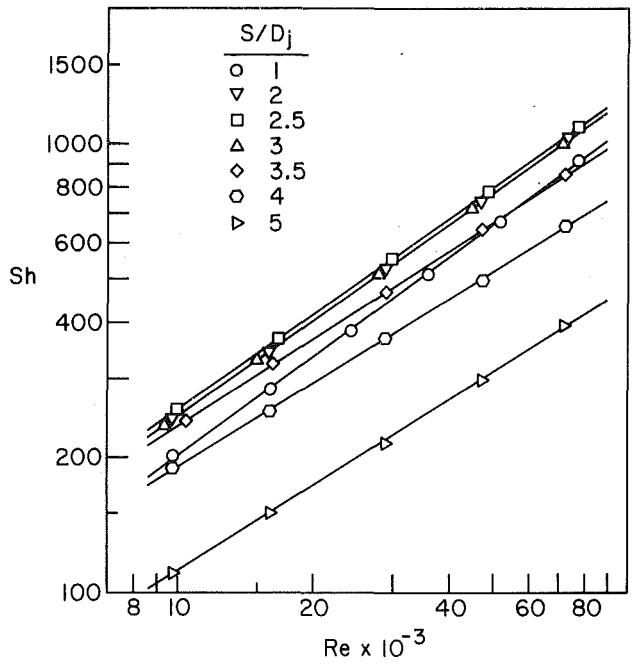

Fig. 3 Response of the impingement-surface Sherwood number to the Reynolds number, D/D_j = 2.20 (smaller diameter jet)

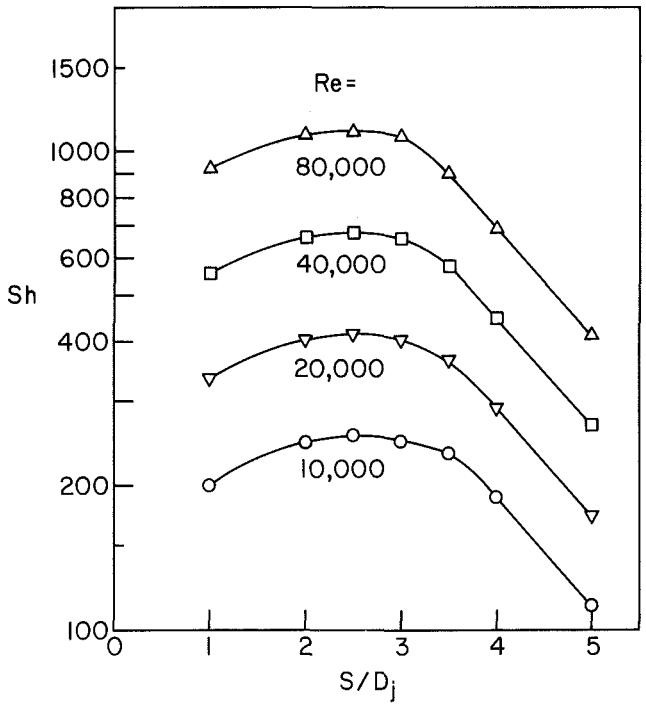

Fig. 4 Response of the impingement-surface Sherwood number to the separation distance, D/D_j = 2.20 (smaller diameter jet)

evaluated as the kinematic viscosity of air, with the density ρ corresponding to the pressure at the impingement surface. The air temperature, which was used in the evaluation of ρ and μ, was virtually identical to the impingement surface temperature.

The mass transfer coefficient K appearing in equation (2) was evaluated from its definition

$$K = (\Delta M/\tau A)/(\rho_{nw} - \rho_{nj}) \tag{3}$$

In this equation, ΔM is the change of mass during the data run, τ is the duration of the run, and A is the area of the impingement surface. In the denominator, ρ_{nw} and ρ_{nj} respectively denote the densities of naphthalene vapor at the impingement surface and in the jet at the exit of the delivery tube. For the conditions of the present experiments, $\rho_{nj} = 0$. For the determination of ρ_{nw}, solid-vapor equilibrium was assumed to exist at the subliming surface. The vapor pressure of the naphthalene at the surface was computed from the vapor pressure–temperature relation given in [2] using the measured surface temperature as input. Then, with the vapor pressure and the surface temperature as inputs, ρ_{nw} was obtained from the perfect gas law.

The jet Reynolds number was evaluated as that of the air flow exiting the jet delivery tube, i.e.,

$$\mathrm{Re} = 4\dot{w}/\mu\pi D_j \tag{4}$$

in which $\dot{w}$ is the mass flow rate of the air which passed through the delivery tube, as found from the air density and volumetric flow rate at the rotameter.

Results and Discussion

The impingement-surface Sherwood numbers will be presented in two formats. In one, the dependence of the Sherwood number on the Reynolds number will be highlighted, while the second focuses attention on the variation of the Sherwood number with the separation distance between the jet origin (i.e., the tube exit) and the impingement surface. These results will be presented separately for the two investigated ratios of the impingement surface diameter to the jet origin diameter. Subsequently, a comparison will be made between the two diameter ratios.

Smaller Diameter Jet. The presentation will begin with the results for the smaller of the two jet diameters, which corresponds to D/D_j = 2.20. Figure 3 shows the response of the Sherwood number to variations of the Reynolds number over the range from about 9500 to 80,000. The data appearing in the figure are parameterized by values of the dimensionless separation distance S/D_j equal to 1, 2, 2.5, 3, 3.5, 4, and 5. Note that the original research plan did not include the noninteger S/D_j values (2.5 and 3.5), but these were subsequently added in order to clarify the variation of Sh with S/D_j.

From the figure, it is seen that at each fixed separation distance, there is a logarithmically linear increase of Sh with Re, resulting in the power-law form

$$\mathrm{Sh} = C\mathrm{Re}^n \tag{5}$$

The straight lines which pass through the data points are least-squares fits of equation (5). It is seen that the data are virtually free of scatter and are very well described by the fitted lines. Note that a single line has been used to represent the data for S/D_j = 2 and 3.

Initial appearances to the contrary, there is a readily identifiable ordering of the various S/D_j curves. The results for S/D_j = 2, 2.5, and 3 cluster in a tight band which forms the upper bound of the data presented in the figure. Since the results for S/D_j = 1, 3.5, 4, and 5 fall below the aforementioned cluster, it is clear that there is a maximum in the variation of Sh with S/D_j. This variation and the maximum will be explored shortly in greater detail.

Further inspection of Fig. 3 shows that there is an overall decrease in the slope of the Sh versus Re distributions as S/D_j increases. These slopes can be characterized by the exponent n of equation (5), with $n \sim 0.73$ for S/D_j = 1, ~ 0.7 for S/D_j = 2–3, ~ 0.65 for S/D_j = 3.5, and ~ 0.625 for S/D_j = 4–5. Note that the slope is virtually independent of S/D_j in the range where Sh attains a maximum and similarly for larger values of S/D_j.

The variation of Sh with the separation distance S/D_j is highlighted in Fig. 4, which was constructed as a crossplot of Fig. 3. Correspondingly, the symbols appearing in Fig. 4 are crossplot points rather than actual data points. Smooth curves have been passed through the data for continuity. Results are given for Re = 10,000 to 80,000, which spans the investigated range.

From the figure, it is seen that the form of the Sh versus S/D_j distribution is common to all of the Reynolds numbers. Starting at $S/D_j = 1$, the Sherwood number increases but levels off and attains a maximum at $S/D_j = 2.5$. The increase in Sh between $S/D_j = 1$ and 2.5 is 20-25 percent. The maximum itself is rather flat, and the variation of Sh is only about three percent in the range between $S/D_j = 2$ and 3. Beyond $S/D_j = 3$, the decrease of Sh with S/D_j grows steeper, culminating in what appears to be a semilogarithmic linear variation. The value of Sh at $S/D_j = 5$ is about 40 percent of that at the maximum. It is also seen that the separation between adjacent curves tends to narrow with increasing S/D_j, reflecting the aforementioned decrease in the exponent n (equation (5)) with S/D_j.

The occurrence of a maximum in the Sh versus S/D_j distributions is reminiscent of literature information (e.g., [3-6]) on the local impingement-point Nusselt number for the conventional single-jet configuration (i.e., collection of the spent fluid beyond the extremities of the impingement surface). In that literature, the Nu versus S/D_j distributions also displayed a maximum. Although the present results pertain to the average transfer coefficient while the aforementioned literature was concerned with a local transfer coefficient, the same rationalization of the maximum is applicable.

At small separation distances, for which an undisturbed core exists within the jet, the velocity of the impinging core will be virtually unchanging as the separation distance increases. However, measurements have shown that the turbulence level within the core increases. As a result, the transfer coefficient increases with increasing separation distance. With further increases in separation distance, the core is engulfed by the jet mixing process, so that the impingement velocity decreases and, subsequently, the turbulence also decreases. This brings about a postmaximum decrease in the transfer coefficient.

Information on the variation of the average Sherwood or Nusselt number with S/D_j for the conventional single-jet configuration is presented in Fig. 10 of [1]. Unfortunately, the figure is virtually incomprehensible because the curve designations given in the legend appear to be unrelated to the curves presented in the figure. Nevertheless, it is noteworthy that that figure does contain curves which display well-defined maxima such as those of the present Fig. 4. However, the maxima of Fig. 10 of [1] occur at about $S/D_j = 6$, in contrast to the present maxima which occur at $S/D_j = 2.5$. In this regard, it may be noted that the maxima for the aforementioned impingement-point transfer coefficients for the conventional single-jet configuration were also attained at about $S/D_j = 6$ [3-6].

From the foregoing, it may be concluded that for the present confined impingement surface and annular collection of the spent air, the maximum transfer coefficient occurs at a smaller separation distance than that for the conventional single-jet configuration. This finding is plausible, since the annular collection tends to deplete the jet, reducing both the velocity and the turbulence level.

Larger Diameter Jet. Attention will now be turned to the results for the larger of the two jet diameters, which corresponds to $D/D_j = 1.51$. In Fig. 5, the Sherwood number is plotted as a function of the Reynolds number over the range from 7000 to about 65,000. The data are parameterized by the separation distance $S/D_j = 1, 2, 3, 4$, and 5.

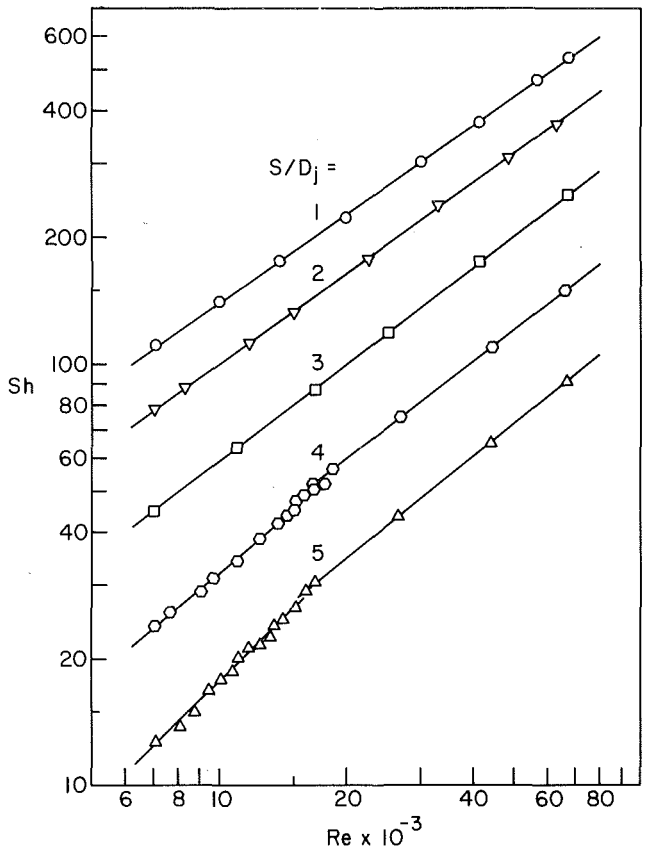

Fig. 5 Response of the impingement-surface Sherwood number to the Reynolds number, $D/D_j = 1.51$ (larger diameter jet)

For each of the smaller separation distances $S/D_j = 1$, 2, and 3, the data fall squarely on a straight line, and the lines drawn in the figure are least-squares fits having the form of equation (5). However, for each of the two larger separation distances, the data do not fall on a single straight line. Rather, there appear to be two distinct Reynolds number ranges, with a breakpoint at about 16,000, in which the data follow different power laws of the form (5). Since the presence of the lower range did not follow the expected pattern (i.e., a single power law for the entire Re range), a substantial amount of data were collected in that range. The lines passed through the data for $S/D_j = 4$ and 5 are least-squares fits.

The aforementioned low-Reynolds-number tails for $S/D_j = 4$ and 5 are believed due to enfeebled impingement. The enfeeblement may be attributed to the relatively low initial velocity of the jet, the relatively large separation distance, and the tendency of the annular collection to deplete the jet.

Further inspection of Fig. 5 reveals that the Sherwood numbers are ordered in a regular pattern with S/D_j, with those for $S/D_j = 1$ falling highest, those for $S/D_j = 2$ next highest, etc. Therefore, Sh decreases monotonically with S/D_j for $S/D_j \geq 1$. This is to be contrasted with the maximum encountered for the $D/D_j = 2.20$ case (i.e., the smaller jet diameter). Another contrast relates to the slope of the Sh versus Re curves (i.e., the exponent n of equation (5)). In Fig. 5, the slope increases with increasing S/D_j (n increases from about 0.7 to 0.8 as S/D_j increases from 1 to 5 (upper range of Re)). On the other hand, as noted earlier, the slope of the curves in Fig. 4 decreases with increasing S/D_j.

A crossplot of Fig. 5, yielding Sh as a function of S/D_j, is presented in Fig. 6. Results are shown for the same Reynolds numbers between 10,000 and 80,000 as were used in parameterizing Fig. 4. Inpection of Fig. 6 confirms the just-stated conclusion that the Sherwood number decreases

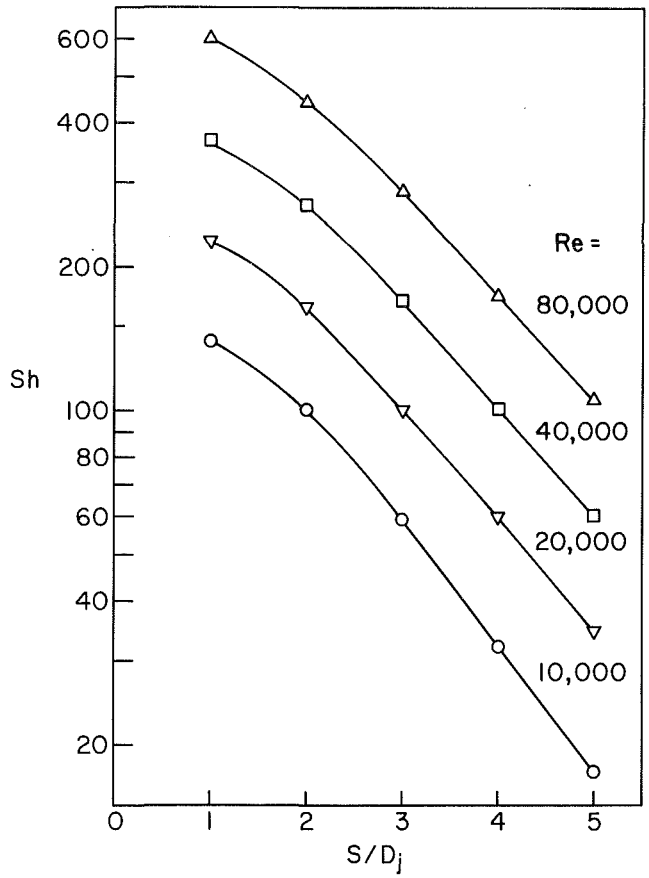

Fig. 6 Response of the impingement-surface Sherwood number to the separation distance, D/D_j = 1.51 (larger diameter jet)

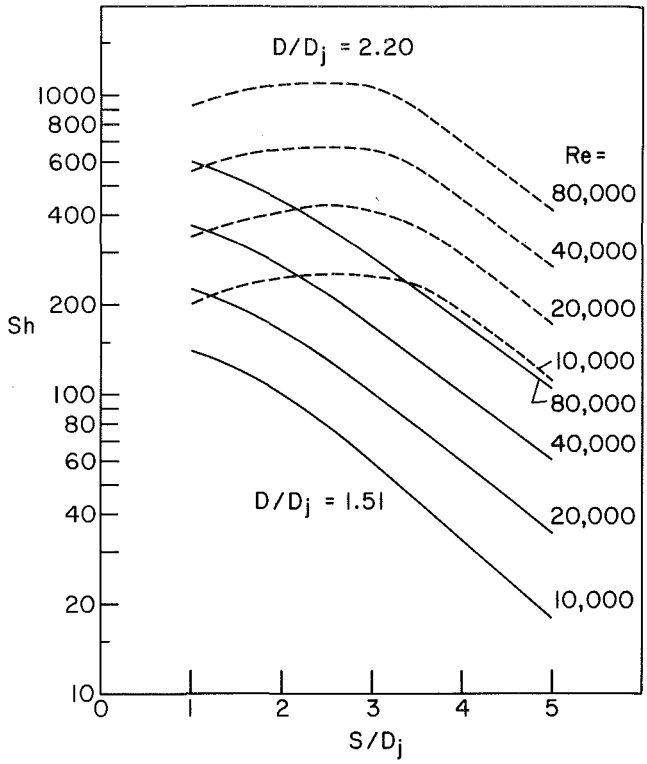

Fig. 7 Comparison of the Sherwood numbers for the smaller and larger diameter jets

monotonically with the separation distance. Starting at S/D_j = 1, the decrease initially grows steeper but then becomes semilogarithmically linear. The separation between adjacent curves increases with S/D_j, reflecting the increases of the exponent n of equation (5).

Comparison of the Jets. It is relevant to compare the results for the two D/D_j ratios, and Fig. 7 has been prepared for this purpose. In the figure, Sh is plotted as a function of S/D_j for parametric values of Re. The results for D/D_j = 2.20, taken from Fig. 4, are plotted as dashed lines, while those for D/D_j = 1.51 are taken from Fig. 7 and plotted as solid lines. Inspection of the figure reveals significant qualitative and quantitative differences between the two sets of results.

In particular, the Sherwood numbers for the smaller jet delivery tube (D/D_j = 2.20) are appreciably greater than those for the larger jet delivery tube (D/D_j = 1.51). The deviations are smallest at S/D_j = 1, where the Sh values for D/D_j = 2.20 exceed those for D/D_j = 1.51 by about 50 percent. The largest deviations occur at S/D_j = 5. At that separation distance, the Sh for D/D_j = 2.20 are 4–6 times greater than those for D/D_j = 1.51. The other major difference between the two sets of results is the respective monotonic and nonmonotonic variations of Sh with S/D_j, as already discussed.

It is relevant to rationalize the difference between the two sets of results. In this regard, it may be noted that for the conventional single-jet configuration, it is shown in Fig. 10 of [1] that the shape of the variation of the average Sherwood number with S/D_j is sensitive to D/D_j. That figure contains some Sh distributions that are monotonic with S/D_j and others that are not; however, owing to the aforementioned mismatch between the legend and the curves, it is not possible to identify the D/D_j values which correspond to the various distributions.

In the present experiments, there are noteworthy velocity field differences between the two cases: (*a*) at a fixed Reynolds number, the mean velocity at the jet origin for the larger delivery tube is 69 percent of that of the smaller delivery tube and (*b*) at a fixed value of S/D_j, the separation distance S is 45 percent greater for the larger tube than for the smaller tube. These two characteristics suggest that a jet emerging from the larger delivery tube was more affected by the depletion of air from the jet due to the annular collection, diminishing the vigor of the impingement. Both the impingement velocity and turbulence level were probably decreasing functions of S/D_j, giving rise to the measured monotonic decrease of Sh with S/D_j for the larger-jet case.

Concluding Remarks

The impingement mass/heat transfer characteristics have been experimentally investigated for a novel single jet configuration characterized by a confined impingement surface and by annular collection of the spent air. This configuration provides precise control of the surface area affected by the impinging jet and also assures complete collection of the spent air. Three parameters were varied during the course of the experiments: the dimensionless separation distance S/D_j between the jet delivery tube and the impingement surface, the ratio D/D_j of the impingement surface diameter to the delivery tube diameter, and the Reynolds number.

The Sherwood numbers (dimensionless mass transfer coefficients) at the impingement surface were found to be quite sensitive to the D/D_j ratio. The larger the value of D/D_j (i.e., a smaller delivery tube for a given impingement surface), the larger are the impingement surface Sherwood numbers. Furthermore, the nature of the variation of the Sherwood number with the S/D_j separation distance depends on D/D_j. At larger D/D_j (smaller delivery tube), the Sherwood number initially

increases with S/D_j, attains a maximum at $S/D_j = 2.5$, and then decreases with further increases in S/D_j. On the other hand, for smaller D/D_j (larger delivery tube), the Sherwood number decreases monotonically with S/D_j. For all cases, the Sherwood number increases monotonically with the Reynolds number, with the data being well represented by power laws of the form $\mathrm{Sh} = C\mathrm{Re}^n$.

References

1 Martin, H., "Heat and Mass Transfer Between Impinging Gas Jets and Solid Surfaces," in: *Advances in Heat Transfer*, Vol. 13, Academic Press, New York, 1977, pp. 1-60.

2 Sogin, H. H., "Sublimation From Disks to Air Streams Flowing Normal to Their Surfaces," *Trans. ASME*, Vol. 80, 1958, pp. 61-71.

3 Gardon, R., and Cobonpue, J., "Heat Transfer Between a Flat Plate and Jets of Air Impinging on It," *Proc. 2nd Int. Heat Transfer Conf.*, 1962, pp. 454-460.

4 Gardon, R., and Akfirat, J. C., "The Role of Turbulence in Determining the Heat Transfer Characteristics of Impinging Jets," *Int. J. Heat Mass Transfer*, Vol. 8, 1965, pp. 1261-1272.

5 Gauntner, J. W., Livingood, J. N. B., and Hrycak, P., "Survey of Literature on Flow Characteristics of a Single Turbulent Jet Impinging on a Flat Plate," NASA Technical Note D-5652, 1970.

6 Sparrow, E. M., Goldstein, R. J., and Rouf, M. A., "Effect of Nozzle-Surface Separation Distance on Impingement Heat Transfer for a Jet in a Crossflow," ASME JOURNAL OF HEAT TRANSFER, Vol. 97, 1975, pp. 528-533.

Exponential Wake Structure of Heated Turbulent Boundary Layers at Elevated Levels of Free-Stream Turbulence

P. Sepri
Associate Professor,
Dept. of Aerospace and
Mechanical Engineering,
University of Oklahoma,
Norman, OK 73019

The wake region of a turbulent boundary layer is demonstrated to exhibit simple exponential behavior at elevated levels of free-stream turbulence. As a predictive tool, the computer code STANCOOL has been modified to include FST effects in heated turbulent boundary layers. Preliminary comparisons with experimental data indicate improvements in computational capability, although further development of the code is required. From these comparisons, three new results are offered: (1) At elevated levels of FST, several statistical profiles in the boundary layer wake region decay exponentially into the free stream; (2) $\overline{v'T'}$ decays at half the rate of the mean velocity and temperature; (3) analytical expressions are provided for $\overline{u'v'}$ and $\overline{v'T'}$ in this case.

Introduction

The primary objective of the present article is the reporting of a novel characterization of the outer region of a turbulent boundary layer in the presence of a high degree of free-stream turbulence (FST). From experimental data it is concluded that the mean defects of velocity and temperature decay exponentially with a linear argument into the free stream under such conditions. Analytical forms are derived for the Reynolds stress and $\overline{v'T'}$ in this "wake region" from the momentum and energy equations. It is shown that current mixing length models do not reproduce the exponential decay, although the computational performance may be improved through a modification including an FST term.

The transports of heat and momentum across a turbulent boundary layer are often influenced in practical cases by a nontrivial degree of FST. However, most of the fundamental studies concerned with turbulent boundary layers have dealt with low levels of FST, and thus, an adequate data base has not been available to investigators seeking to model its influences. Recent descriptions of FST effects on the structure of heated turbulent boundary layers have been reported by Simonich and Bradshaw [1], Bayley and Priddy [2], and Pedisius et al. [3]. Additional background material may be obtained from [4–12]. In the present article, considerable reference is made to the excellent experimental data published recently by Blair [13–19]. His measurements include extensive turbulence statistics and profiles in the boundary layer adjacent to a heated flat plate, for which the FST is varied parametrically. Although Blair has reported his findings in two journal articles [13, 14], he has also documented comprehensive tables of data in UTRC reports [15–19]. These constitute a detailed source for purposes of code verifications and turbulence study in general.

In order to provide further support for the present observations, a search has been conducted for other relevant data. It is shown that the recent data taken by Hancock [20, 21] and the earlier data reported by Kline et al. [22] strengthen the case for the wake model proposed herein. Other investigations, which might have a bearing on the present work, have proven to yield only peripheral or inconclusive information. The earlier well-established works by Favre et al. [23, 24] do not report cases of FST intensity levels higher than approximately 1.8 percent, and for such cases the exponential wake structure does not occur. The recent articles by Kottke [25, 26] treat the issue of heat transfer in separated regions downstream of steps, but profile data are not presented, and the attendant FST levels appear to be low. The highly relevant work by Evans [27] introduces an alternative wake model in extension to the landmark investigation of Coles [28]. However, the exponential nature of the wake appears to have eluded observation by Evans.

One motivation for the continuing investigation of FST effects has come from the area of gas turbine technology. A key to improved turbine design lies in the effective prediction of the turbine blade heating environment. With such information blades may be designed to yield longer lifespans in hotter ambients. It is clear that turbine blades are subjected to high levels of FST, although actual levels vary with operating conditions [2]. It is particularly useful to develop accurate yet economical codes for heating computations because it is exceedingly difficult and costly to obtain detailed experimental information from tests involving simulated conditions, much less from actual engine performance tests. Several codes [29] have been developed in the industry for this purpose, among which is STAN5 [30, 31] developed by Crawford and Kays. One objective of the present work has been to modify STANCOOL (a more recent version of STAN5) so as to predict better the effects of FST. As a first step, only the basic geometry of the flat plate is considered herein. Turbulence modeling of the actual turbine blade environment introduces many additional complexities.

A widely used approach in calculations of turbulent heat transfer involves the introduction of the turbulent Prandtl number (Pr_t), through which heat transport is likened to the relatively more studied momentum transport in the manner of the Reynolds analogy. The deviation in the Reynolds analogy is often described at a solid surface by the local ratio of the Stanton number to half of the skin friction coefficient, $2St/C_f$, which is termed the Reynolds analogy factor, with unity denoting a perfect analogy. Earlier investigations [8–12] have conflicted in their reports of the dependence of turbulent heating on the level of FST, some even claiming no effect. More recent data [1–3, 15] indicate that the Reynolds analogy factor increases with increasing FST intensity. In codes such as STANCOOL it is desirable that heating calculations incorporate an accurate model of Pr_t throughout the extent of the boundary layer, so that total profiles are accurately predicted.

Contributed by the Heat Transfer Division for publication in the JOURNAL OF HEAT TRANSFER. Manuscript received by the Heat Transfer Division April 21, 1986.

An early empirical expression for the Pr_t profile is attributed to Rotta [32], and other more recent formulations appear in [33, 34]. Experimental data of Pr_t profiles in heated boundary layers appear in [35–38]. In Fig. 1 are summarized the results of several investigations, both analytical and experimental, concerning the variation of Pr_t in a heated turbulent boundary layer. The general trends are: (1) large variations in the near-wall region, (2) a fairly constant intermediate region, and (3) a pronounced decline in the outer region (for all except [38]). It should be noted that experimental inaccuracies become large in both the wall and outer regions, in which the largest variations of Pr_t are observed.

At present there appears to be little information concerning the influence of FST on the Pr_t profile. Blair [15] reports a general rise in the Pr_t profile as FST increases, but also that the near wall region exhibits the reversed trend. In addition to the intensity level of FST, it has also become clear that turbulence integral length scales in the FST have an influence on the structure of the boundary layer. Hancock and Bradshaw [21] report for unheated boundary layers that the most influential length scales are those of the order of the boundary layer thickness, which has also been noted in [3, 6]. Presumably, the integral length scales have a corresponding effect on Pr_t.

Upon the availability of Blair's data, MacArthur [39] undertook a preliminary evaluation of the predictive capability of two options in STANCOOL. These options are comprised of a standard mixing length model and a model incorporating the turbulence kinetic energy equation [30]. Although the comparisons yielded favorable results in some cases, significant departures were noted in other cases in two respects; namely, the onset and duration of transition, and the level of heat transfer with increasing FST. Unexpectedly, MacArthur's comparisons revealed that occasionally the two computational options agreed with each other better than either did with the data. While the mixing length model does not provide a mechanism for FST effects, it was anticipated that the kinetic energy option would introduce these effects via the external boundary condition.

Sepri and Ebert [40] continued MacArthur's study with the objective of seeking a turbulence model that reflects an improved prediction of FST effects. The highlights and continuation of that investigation are reported herein. Since the code has been developed by Crawford and Kays, and since

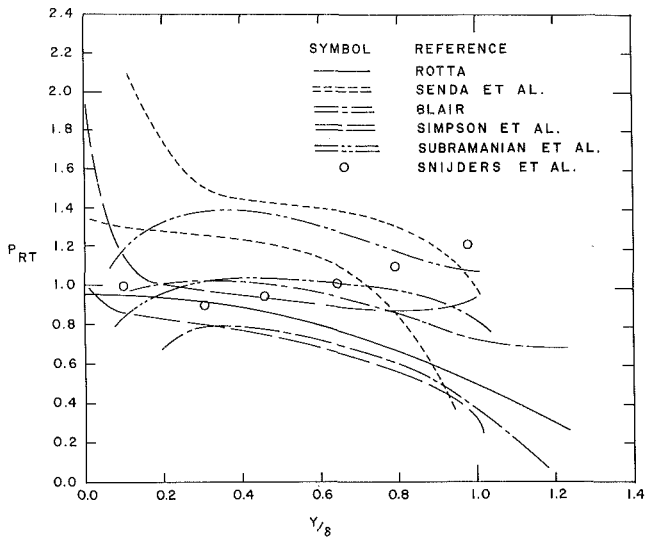

Fig. 1 Comparison of Pr_t data for boundary layer flows

commentary and descriptions of its operation and assumptions appear elsewhere [30, 31] such details will be excluded here. Of the transition models introduced by several users, the present work has utilized the options derived from van Driest and Blumer [41], Abu-Ghannam and Shaw [42], Dhawan and Narasimha [43], and Chen and Thyson [44]. However, in order to distinguish between FST effects on transition models and FST effects on the downstream boundary layer, in some cases the code option has been utilized to fix the transition location to agree with Blair's experimental transition. A preliminary turbulence model based on the work by Miyazaki and Sparrow [45] has been utilized with the result of improved comparison with Blair's data.

Turbulence Model

In his preliminary evaluations, MacArthur [39] concentrated on Stanton number comparisons, which reflect net heat transfer effects at the wall. In an effort to observe underlying causes for the aforementioned discrepancies, Sepri and Ebert [40] compared selected computations of profiles in the boundary layer with Blair's data. As is evident from several

Nomenclature

A = correlation factor related to FST [equation (1)]
A_T = integration factor in equation (15)
B = factor defined below equation (13)
B_T = integration factor in equation (15)
$B_{1,2}$ = thermal correlation factors related to FST [equation (5)]
C_f = skin friction coefficient
C_p = specific heat at constant pressure
$\bar{H}$ = total mean enthalpy
I = turbulence intensity $\equiv \bar{q}/\bar{u}$
l = Prandtl mixing length
$\mathcal{O}$ = order of magnitude
Pr = molecular Prandtl number
Pr_t = turbulent Prandtl number $\equiv \nu_t/\kappa_t$
$\bar{q}$ = turbulence kinetic energy per unit mass $= \overline{[(u')^2 + (v')^2 + (w')^2]^{1/2}}$
Re_δ = Reynolds number based on boundary layer thickness
St = Stanton number
$\bar{T}$ = mean temperature
$\bar{u}$ = mean streamwise velocity component
$\hat{u}$ = $\bar{u}/\bar{u}_e$
$\overline{u'v'}$ = Reynolds number
u_τ = friction velocity $\equiv (\tau_w/\rho_w)^{1/2}$
$\bar{v}$ = mean normal velocity component
$\overline{v'H'}$ = turbulent enthalpy flux
$\overline{v'T'}$ = turbulent thermal flux
x = streamwise coordinate
y = coordinate normal to surface
α = exponential decay factor [equation (6)]
β = wall value of exponential velocity form [equation (6)]
δ = boundary layer thickness
η = y/δ
κ_t = turbulent thermal conductivity
μ = first coefficient of viscosity
ν_t = turbulent (eddy) viscosity
$\bar{\rho}$ = mean fluid density
τ_w = mean wall shear stress

Subscripts

e = boundary layer edge condition
w = boundary layer wall condition

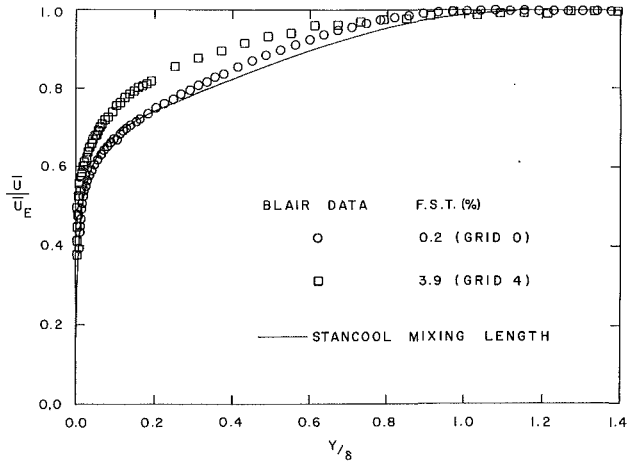

Fig. 2 Mean velocity profiles compared at high and low FST; Blair data [15] taken at $x = 2.13$ m

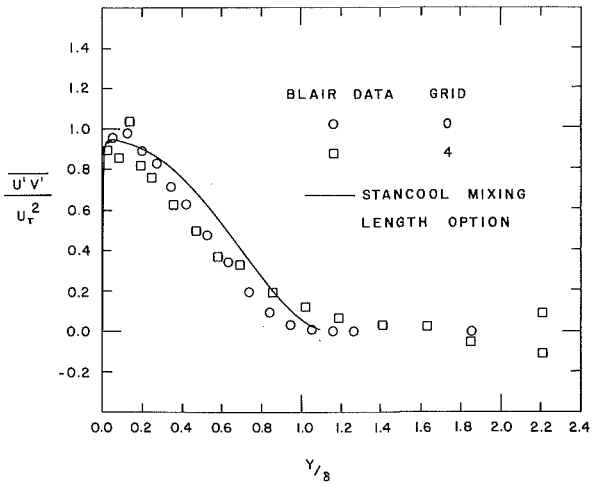

Fig. 3 Comparison of Reynolds stress at high and low FST; Blair data [15] taken at $x = 2.13$ m

works [1, 13, 21, 22, 27] the mean velocity and temperature profiles become fuller with increasing FST, and there is a corresponding diminishing of Coles' wake function [46]. Sample comparisons between STANCOOL computations in the mixing length mode and the data for mean velocity are displayed in Fig. 2. Although there is reasonable agreement at a low level of FST (0.2 percent), there is a clear mismatch in both mean velocity and Reynolds stress profiles (Fig. 3) at the higher FST level (3.9 percent). These comparisons are made at the experimental station $x = 2.13$ m for the case of zero pressure gradient [15]. Since MacArthur's evaluation indicated that no major differences resulted between the two STANCOOL options, the present approach has been to alter the existing mixing length model to account for FST effects. It is evident from Figs. 2 and 3 that the presence of FST alters the mean boundary layer structure significantly. Presumbly, the profile mismatches can be corrected if the $\overline{u'v'}$ model incorporates correct FST effects.

The effect of FST on heating near the stagnation point of a cylinder placed transverse to the flow has been investigated by Miyazaki and Sparrow [45]. In that work a mixing length model was proposed with some success which alters the usual one with terms proportional to the level of FST. A heuristic basis for this model (explained in [45]) relies on the previous experimental observations by Belov et al. [47], who noted that the turbulence intensity in the boundary layer is augmented during the presence of FST by a growth which is linear with

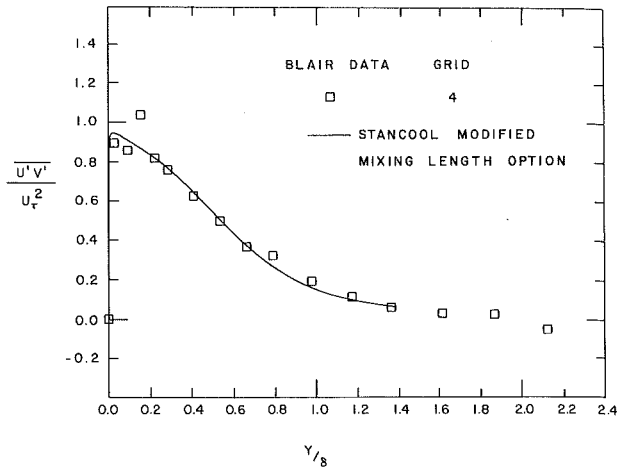

Fig. 4 Improved computational model at high FST ($x = 2.13$ m, $A = 1.4$)

distance from the wall and which is also linear with FST intensity. Utilizing this observation, Miyazaki and Sparrow proposed the Reynolds stress model

$$\overline{-u'v'} = l^2 \left|\frac{\partial \bar{u}}{\partial y}\right| \frac{\partial \bar{u}}{\partial y} + Al\bar{u}_e I_e \left(\frac{y}{\delta}\right) \frac{\partial \bar{u}}{\partial y} - \overline{u_e' v_e'} \left(\frac{y}{\delta}\right)^2 \tag{1}$$

Here, I_e is the local FST intensity and A is a dimensionless correlation coefficient adjustable in the model. It should be noted that the last term in equation (1) contributes to a Reynolds stress that continues to grow beyond the boundary layer edge whenever the free-stream correlation does not vanish. In many cases $u_e'v_e'$ does vanish, and no numerical discrepancy arises. However, external to the boundary layer this term cannot be correct in principle, and presumably the model is not meant to extend beyond the boundary layer edge. For the present work, $u_e'v_e'$ does indeed vanish, and therefore the mixing length model is assumed to have the form

$$\overline{-u'v'} = \nu_t \frac{\partial \bar{u}}{\partial y} \tag{2}$$

where

$$\nu_t = l^2 \left|\frac{\partial \bar{u}}{\partial y}\right| + Al\bar{u}_e I_e (y/\delta) \tag{3}$$

Furthermore, the mixing length l remains unaltered as given by the options available in STANCOOL. Values for A have been selected parametrically to exhibit the range of variations possible with this computational model.

To complete the model, it is also necessary to assume a form for $\overline{v'T'}$ (or Pr_t) which contains the influence of FST. In parallel with the Reynolds stress, the initial model is taken to be

$$\overline{-v'T'} = \kappa_t \frac{\partial \bar{T}}{\partial y} \tag{4}$$

where

$$\kappa_t = B_1 l^2 \left|\frac{\partial \bar{u}}{\partial y}\right| + B_2 l\bar{u}_e I_e (y/\delta) \tag{5}$$

Here, the coefficients B_1 and B_2 may be adjusted to reflect experimental trends observed for Pr_t. Clearly, unity Pr_t may be obtained by selecting $B_1 = B_2 = A$.

Computational Results

The simple alteration of the mixing length model mentioned

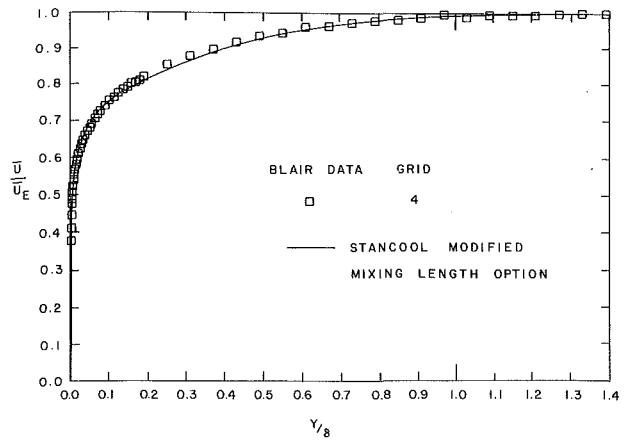

Fig. 5 Mean velocity profile at high FST compared with improved computational model (x = 2.13 m, A = 2.0)

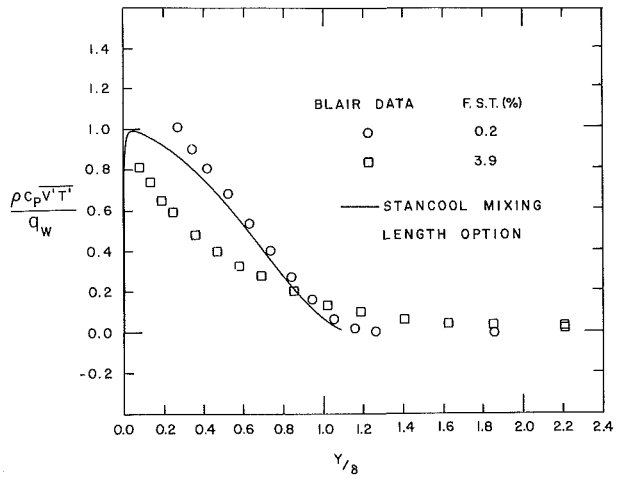

Fig. 6 Effect of FST on turbulent heat flux; Blair data [15] taken at x = 2.13 m; original computational model

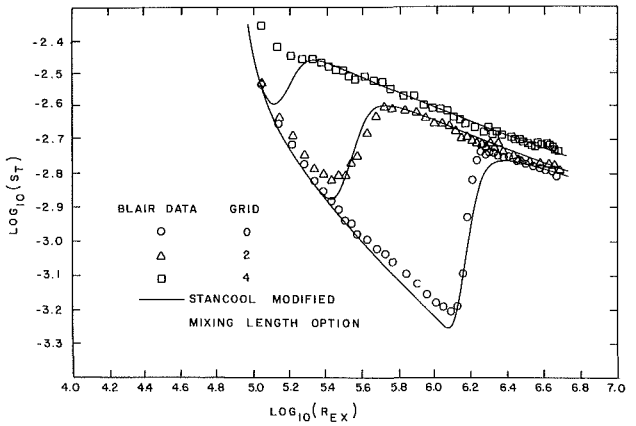

Fig. 7 Effect of FST on wall heat transfer distribution; improved computational model with transition location matched to experiment

above yields improved results at higher levels of FST, although certain discrepancies also arise.

A comparison between Blair's data and the calculated Reynolds stress profiles (3.9 percent FST) is shown in Fig. 4 for the value 1.4 for A. An improvement is shown over the earlier comparison in Fig. 3, so that now, the inner level of $\overline{u'v'}$ is diminished while the outer decay is prolonged. Accordingly, the mean velocity profile exhibits an improvement as shown in Fig. 5, although a mild mismatch is still apparent. In fact, a curious incompatibility is inherent in this model; namely, the parameter A could be chosen to result in an excellent fit of either $\bar{u}$ or $\overline{u'v'}$ with the data, but both profiles could not be simultaneously matched with the same value of A. Although this model exhibits a good trend, it is clearly an oversimplification. However, this computational result represents a secondary conclusion of the present article.

Previous investigators [1, 3, 4] have suggested that FST should alter the structure of the outer part of the boundary layer while the wall region should remain unaltered in character except for an increased value for the friction velocity u_τ. The model expressed by equations (2) and (3) is in accord with this notion since the FST term diminishes rapidly in comparison to the gradient term as the wall is approached. However, scrutiny of Blair's data and numerical experimentation with the model have indicated that the FST influence may extend into the wall region as well. In Fig. 6 are shown turbulent heat flux profiles at two levels of FST. The usual wall region is characterized as being a constant flux layer in which the total heat flux remains at its wall value. In Fig. 6 the dimensionless heat flux should exhibit the value of unity in such a wall layer. For the lowest level of FST (0.2 percent), the wall layer appears to comprise approximately the inner 20 percent of the boundary layer thickness (as inferred from the data). However, as the FST increases, the data indicate that the wall layer diminishes in extent greatly, and may even disappear at the highest level of FST (3.9 percent). In the computational model, it is possible to choose a value of A for which the outer part of the boundary layer is well matched to the mean velocity and temperature data. However, the corresponding values for C_f and St overpredict the measured wall values. Conversely, if the value for A is reduced so that the C_f and St comparison is good, then the outer profiles have a significant mismatch, although the comparison is improved over that of the original mixing length model. A possibility for further improvement of the mixing length model lies in the alteration of the wall region as well as the wake region with varying FST. An example of the present prediction of wall heat transfer (equations (2)–(5)) is displayed in Fig. 7, in which St is shown for three levels of FST (grids 0, 2, 4). In these cases, the location of the transition in STANCOOL was forced to agree with Blair's experiment, so as to remove this separate uncertainty from the calculations.

Exponential Wake Structure

The main novelty reported herein concerns the observation of an exponential character to the wake defects of mean velocity, temperature, and $\overline{v'T'}$ at higher levels of FST. This observation leads to an altered form of Coles' wake function in the presence of FST. In the process of comparing Blair's data with STANCOOL computations, it was convenient to represent the profiles in a variety of graphical formats. In order to highlight the decay of mean velocity into the free stream, the logarithm of the wake defect, $\log[(\bar{u}_e - \bar{u})/\bar{u}_e]$, is plotted versus y/δ as shown in Fig. 8. In such a format, the differences between the computational model and the data are magnified in the outer part of the boundary layer, whereas in the usual linear plot the data and the calculations appear to be almost superimposed. The mean velocity data in Fig. 8 have been measured [16] with a pitot tube traverse. It is striking that Blair's data fall on a straight line for the outer 80 percent or more of the boundary layer at high FST (3.9 percent). Blair has also reported profiles [15] measured with hot wires, and these are shown in Fig. 9. Here, the boundary layer defect at lower FST (0.2 percent) does not exhibit the linear exponential decay which is seen for the higher FST case (3.9 percent). These graphs also illustrate that the boundary layer thickness

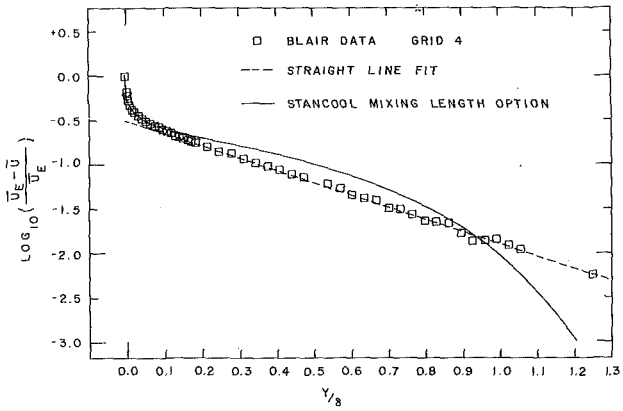

Fig. 8 Exponential wake deficit at high FST; Blair data [16] taken with pitot tube at $x \approx 2.13$ m

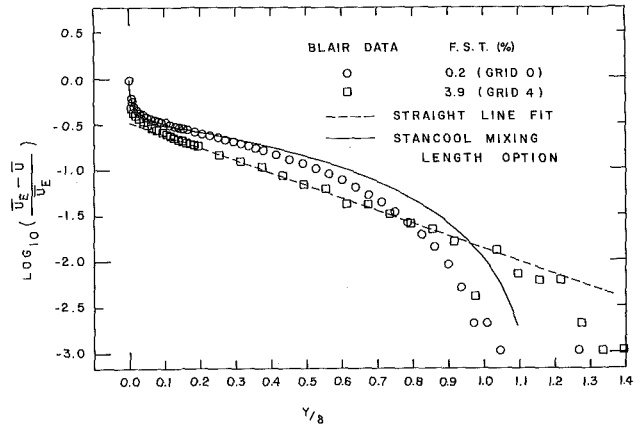

Fig. 9 Effect of FST on exponential wake structure; Blair data [15] taken with hot wires at $x = 2.13$ m

δ is sensitive to the degree of FST. Blair's reported values have been used in constructing these graphs.

A search of the literature has not revealed previous mention of this exponential decay, and the author believes it to be a noteworthy new observation. In order to add credence to the existence of the exponential form, data have been extracted from two other investigations and are replotted in Figs. 10–12 in the semilogarithmic format. In Fig. 10 are shown Hancock's [20] data for the case of low FST (<1 percent) at three downstream stations on his flat plate. It is clear that the wake defects approach the free stream more rapidly than can be characterized by a linear exponential, and this is attributed to the effect of intermittency. In contrast, some of Hancock's data for the case of high FST (6–2.5 percent) are exhibited in Fig. 11. The solid straight lines appearing in Fig. 11 have been added to demonstrate the linear exponential decay. The square symbols denote data taken farther downstream, at which stations the local FST has decayed to 2.55 percent. It is evident that the linear exponential decay manifests itself as a limiting case at higher FST. Although further plots of Hancock's data are not presented here, there is also an indication that the turbulence length scale influences the wake defect as a parameter additional to the FST intensity. A large scale FST appears to decrease the linearity of decay somewhat as compared to that of a small scale FST.

The earlier data of Kline et al. [22] are shown replotted in Fig. 12. These data correspond to a fixed streamwise location ($x = 49$ cm) and a fixed external velocity ($u_e = 30.5$ m/s). The level of FST is varied parametrically by the insertion of various grids. It is clear that the wake defect approaches the linear characterization progressively as the FST is increased.

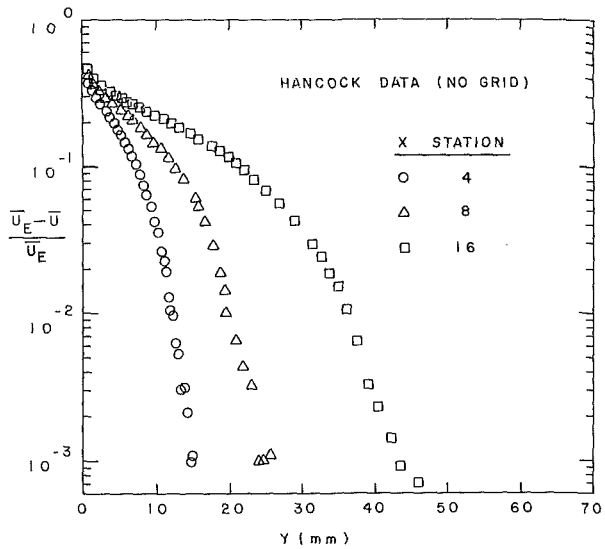

Fig. 10 Nonlinear exponential wake structure at low FST

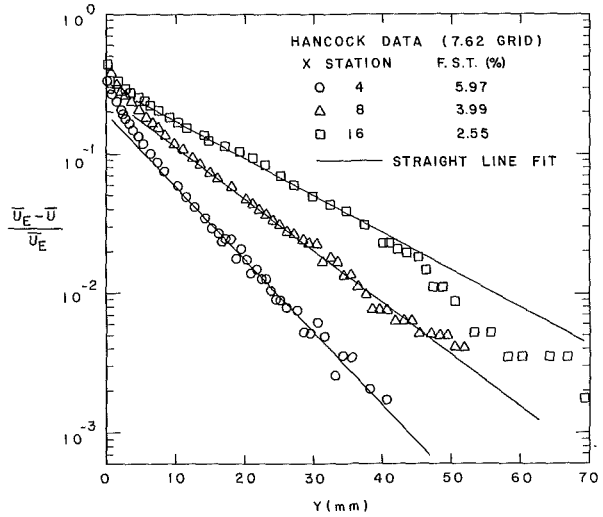

Fig. 11 Linear exponential wake structure at high FST

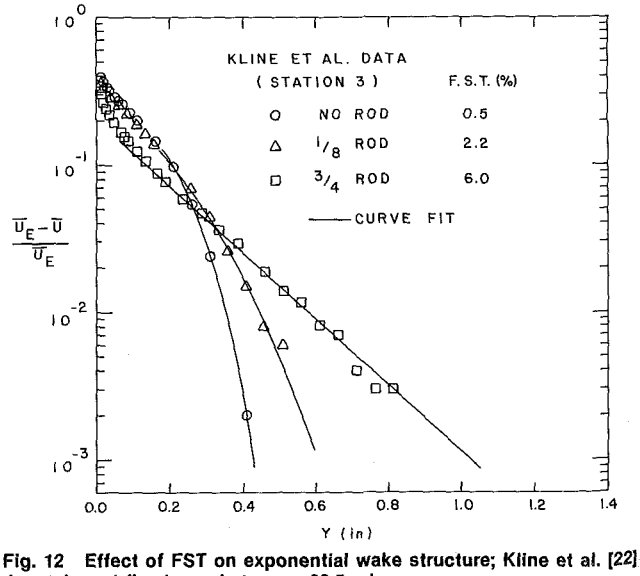

Fig. 12 Effect of FST on exponential wake structure; Kline et al. [22] data taken at fixed x and at $u_e = 30.5$ m/s

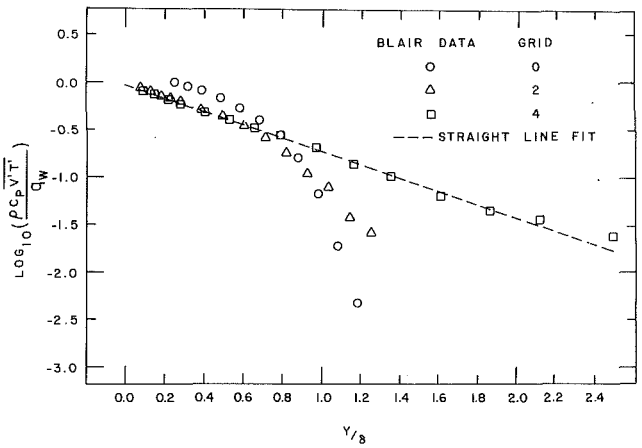

Fig. 13 Effect of FST on turbulent heat transfer profile; Blair data [15] taken at $x = 2.13$ m

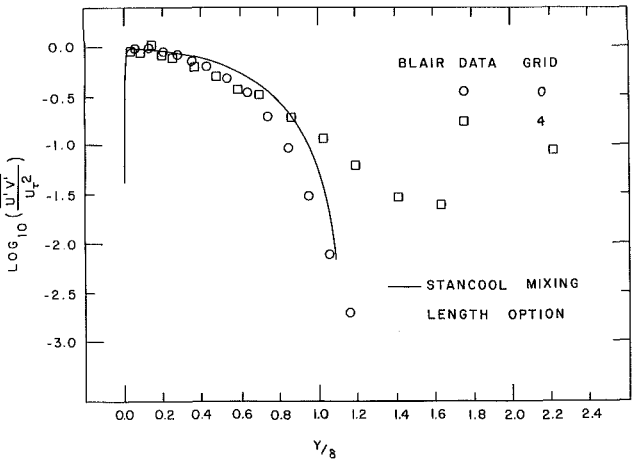

Fig. 14 Effect of FST on Reynolds stress profile; linear decay not achieved at high FST; Blair data [15] taken at $x = 2.13$ m

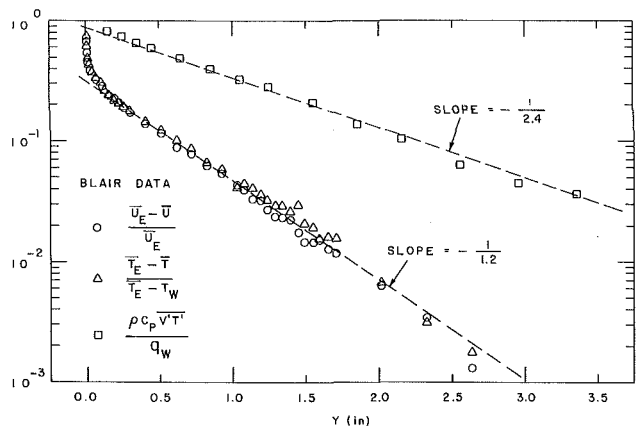

Fig. 15 Turbulent heat transfer decay compared with mean defect decay; Blair data [15] at $x = 2.13$ m (grid 4)

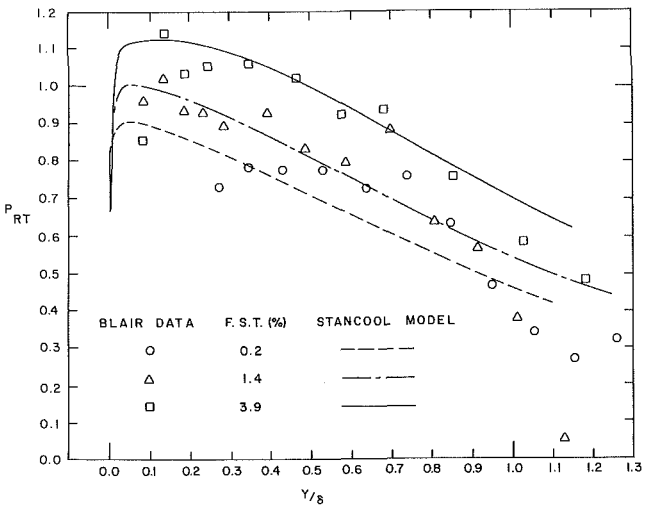

Fig. 16 FST effect on Pr_t profile; Blair data [15] taken at $x = 2.13$ m

The solid lines in Fig. 12 have been added for the sake of emphasizing the trends of the sparse data and of the straight limit.

Although other data relevant to the boundary layer wake at high FST may have been published, these have not as yet come to the attention of the author. No data have emerged which contradict the present observations.

A search through Blair's published data has led to the following preliminary characterizations of the exponential decay.

1 Both the mean velocity and mean temperature profiles exhibit the form

$$\frac{\bar{u}_e - \bar{u}}{\bar{u}_e} = \frac{1}{\beta} \exp[-\alpha y/\delta] \tag{6}$$

$$\frac{\bar{T}_e - \bar{T}}{\bar{T}_e - T_w} = \frac{1}{\beta} \exp[-\alpha y/\delta] \tag{7}$$

Blair's data indicate the approximate values: $\alpha, \beta \cong \sqrt{10}$.

2 The exponential behavior does not occur for FST levels lower than approximately 3 percent. In these cases the free-stream velocity and temperatures are approached more rapidly than the linear exponential rate. This is attributed to the effects of turbulence intermittency.

3 Since all of the observed data at high levels of FST [15–19, 20, 22] exhibit the exponential, it is conjectured here that this may represent a limiting form for the turbulent mixing process which may hold for all higher levels of FST.

4 After a short distance downstream of the leading edge of the flat plate (approximately 0.6 m) equations (6) and (7) represent good approximations for all subsequent wake profiles with varying x, indicating a self-similar scaling to exist with the local boundary layer thickness $\delta(x)$.

5 The $\overline{v'T'}$ profiles also exhibit a limiting exponential character as seen in Fig. 13. However, the corresponding $\overline{u'v'}$ profiles appear not to have such a form (Fig. 14), owing to a fundamental difference in their nature. However, the tendency toward the exponential behavior is exhibited by $\overline{u'v'}$ as well. By symmetry arguments for Blair's channel flow it is clear that $\overline{u'v'}$ must have a zero crossing outside of the boundary layer, whereas $\overline{v'T'}$ does not. In the logarithmic format this zero crossing precludes the existence of a straight line for $\overline{u'v'}$ in the far wake region. This discussion is pursued further in regard to Pr_t below.

6 It is extremely noteworthy that the exponential decay rate of $\overline{v'T'}$ at high FST appears to be exactly *one half* of that corresponding to the rates for $\bar{T}$ and $\bar{u}$, as shown in Fig. 15. The straight lines in this figure do not represent "best fits," but rather, they have been drawn with slopes differing by a factor of two. This difference in slopes leads to a dilemma discussed in the next section which remains to be resolved.

A separate observation is made here concerning the variation of the turbulent Prandtl number Pr_t across the boundary layer. As mentioned earlier, the Pr_t profile plays an important role in calculations of turbulent heat transport in codes such as STANCOOL. However, Pr_t is not a quantity that is directly measured, and past accounts of its behavior have led to a variety of models and considerable discussion concerning its

true behavior. Blair's data exhibit a remarkable feature which deserves comment and which may also have a bearing on previously published Pr_t profiles. Shown in Fig. 16 are Blair's Pr_t data for varying levels of FST along with the modified model (resulting from equations (3) and (5)) used in STANCOOL. Two trends are evident. First, there is a general increase in Pr_t as the level of FST is increased, with the exception of the near wall region in which Blair [15] suggests a reversed trend. Second, Pr_t values are seen to decline greatly toward the boundary layer edge and beyond. In fact, in some instances Blair reports negative values for Pr_t beyond the boundary layer edge! Although experimental error becomes increasingly dominant as y increases, the trends in the measurements are too consistent to dismiss, and these are also observed in other data shown in Fig. 1. An explanation might be offered in terms of channel flow contamination of the data, owing to the shallow height of the tunnel used by Blair (approximately 20 cm). It was noted earlier that at high FST the turbulence structure clearly extends beyond the usual definition of the boundary layer edge. In fact, toward the most downstream stations of measurement (2.13 m), Blair's data indicate that the structure is nonuniform even at the channel centerline, whereas the boundary layer thickness is roughly of half that height. Therefore, it is very likely that channel flow effects have increasingly influenced Blair's Pr_t measurements in the outer wake regions. Since only the upper wall is heated, the $\overline{v'T'}$ profile maintains an unchanged sign throughout the channnel height, whereas $\overline{u'v'}$ must change sign near the tunnel centerline by reason of symmetry. However, since the upper and lower boundary layers are not matched in thickness, it is probable that $\overline{u'v'}$ and $\partial\bar{u}/\partial y$ have zero crossings at different y locations, thereby invalidating the usual mixing length approach. Such a circumstance can lead to negative values for Pr_t. It is therefore conjectured here that true boundary layer measurements, uncontaminated by channel effects, would not exhibit such large decreases in Pr_t in the wake region as were measured by Blair. It is further noted that an actual turbine configuration may give rise to Blair's observed effect concerning Pr_t, owing to the close spacing of the blades.

Deductions From Observations

In view of the observed exponential behavior in the wake region, it is possible to deduce the corresponding mathematical forms for the turbulent fluxes, $\overline{u'v'}$ and $\overline{v'T'}$, by integration of the mean equations. As a result, the original mixing length form in equations (2) and (3) receives further support and also some modification. The argument is summarized as follows.

Assuming that equations (6) and (7) represent the mean velocity and temperature profiles in the wake region of the turbulent boundary layer, the ideal gas equation requires that the mean density profile take the form

$$\frac{\bar{\rho}_e}{\bar{\rho}} = 1 + \left[\frac{T_w}{\bar{T}_e} - 1\right]\frac{1}{\beta}\exp[-\alpha y/\delta] \tag{8}$$

provided the mean pressure remains invariant with y according to the boundary layer approximation. Thus, a hot fluid element adjusts rapidly by expansion to a lower density in order to maintain a uniform pressure.

Given equations (6) and (8) for $\bar{u}$ and $\bar{\rho}$, the mean equation for conservation of mass is analytically integrated to yield the following profile for $\bar{v}$. Here, density–velocity correlations are neglected, and α and β are assumed to be constants.

$$\frac{\bar{\rho}\bar{v}}{\bar{\rho}_e\bar{u}_e} = \frac{\bar{v}_e}{\bar{u}_e} - \left[\frac{\delta}{\bar{T}_e}\frac{dT_w}{dx} + \frac{T_w}{\bar{T}_e}\frac{d\delta}{dx}\left(1+\alpha\frac{y}{\delta}\right)\right] \frac{\exp[-\alpha y/\delta]}{\alpha\beta} + \mathcal{O}(\exp[-2\alpha y/\delta]) \tag{9}$$

The higher order terms vanish identically if $T_w = \bar{T}_e = \text{const.}$ The usual mean momentum equation is assumed to be applicable

$$\frac{\partial}{\partial x}(\bar{\rho}\bar{u}^2) + \frac{\partial}{\partial y}(\bar{\rho}\bar{u}\bar{v}) = \frac{\partial}{\partial y}\left[\mu\frac{\partial\bar{u}}{\partial y} - \bar{\rho}\overline{u'v'}\right] \tag{10}$$

Upon integration, equation (10) takes the form

$$\bar{\rho}\overline{u'v'} = \mu\frac{\partial\bar{u}}{\partial y} + \bar{\rho}_e\bar{u}_e\bar{v}_e - \bar{\rho}\bar{u}\bar{v} + \frac{\partial}{\partial x}\int_y^\infty \bar{\rho}\bar{u}^2 dy \tag{11}$$

Here, the Reynolds stress is assumed to vanish outside of the boundary layer. Although equation (11) is not a closure relation which is independent of the momentum equation, it may be viewed as an exact description (within the boundary layer assumptions) of the Reynolds stress, provided the mean velocity profile is known. Equation (11) may be re-arranged as follows

$$-\bar{\rho}\overline{u'v'} = \bar{u}_e[\bar{\rho}_e\bar{v}_e - \bar{\rho}\bar{v}] - \bar{\rho}\bar{v}[\bar{u}_e - \bar{u}] - \mu\frac{\partial\bar{u}}{\partial y} - \frac{\partial}{\partial x}\int_y^\infty \bar{\rho}(\bar{u}-\bar{u}_e)^2 dy + \bar{u}_e^2\frac{\partial}{\partial x}\int_y^\infty(\bar{\rho}-\bar{\rho}_e)dy \tag{12}$$

In the wake region of many boundary layers, the last three terms are of secondary importance. First, turbulent transport dominates over molecular transport in the wake region. Second, the quadratic integrand diminishes rapidly as the boundary layer edge is approached. Third, the density effect is negligible in incompressible boundary layers. The advantage achieved in equation (12) is that an explicit limiting form is demonstrated for the Reynolds stress in terms of the mean velocity field in the outer region of the boundary layer. It is apparent that the Reynolds stress counterbalances the entrainment of external momentum into the boundary layer.

For the case of high FST, equations (8), (9), and (11) lead to the analytical result

$$\frac{-\overline{u'v'}}{\bar{u}_e^2} = \frac{\partial\hat{u}}{\partial\eta}\left\{B + \frac{\partial\hat{u}}{\partial\eta}\left[\frac{B}{\alpha}\left(\frac{T_w}{\bar{T}_e}-1\right) + \frac{1}{2\alpha^3}\frac{d}{dx}\left(\frac{T_w\delta}{\bar{T}_e}\right)\right]\right\} \tag{13}$$

where

$$\hat{u} \equiv \bar{u}/\bar{u}_e$$

$$\eta \equiv y/\delta$$

$$B \equiv \frac{1}{\alpha^2}(1+\alpha\eta)\frac{d\delta}{dx} - \frac{1}{\mathrm{Re}_\delta} - \frac{\bar{v}_e}{\alpha\bar{u}_e}$$

Here, the exponential character of $\bar{u}$ has been used again to express the Reynolds stress in terms of mean velocity gradients. Furthermore, exponentials of third power and greater have been neglected in the above. These higher order terms vanish identically for an isothermal boundary layer. The terms which are linear in the velocity gradient correspond to the dominant terms discussed in equation (12).

The form obtained for $\overline{u'v'}$ in equation (13) is strikingly similar to the Miyazaki and Sparrow model given in equation (3), and therefore this model appears to have further support. It is emphasized that equation (13) is not meant to be applicable in the near-wall region in which the exponential behavior is not observed. There are three additional terms appearing in equation (13) which do not appear in the earlier model. In comparison to the other terms, Re_δ^{-1} is negligible for the fully turbulent boundary layer, and may therefore be discarded in approximation. The two other constant terms appearing in B are comparable to the y/δ term and should be retained in general. Here, the factor multiplying y/δ depends on x explicitly, whereas in the initial model based on equation (3) the factor A was considered to be constant.

A parallel deduction from the energy equation leads to a noteworthy dilemma. The applicable mean equation for total energy is assumed to be

$$\frac{\partial}{\partial x}(\bar{\rho}\bar{u}\bar{H})+\frac{\partial}{\partial y}(\bar{\rho}\bar{v}\bar{H})=\frac{\partial}{\partial y}\left\{\frac{\mu C_p}{\mathrm{Pr}}\frac{\partial \bar{T}}{\partial y}-\bar{\rho}\overline{v'H'}+\frac{\mu}{2}\frac{\partial}{\partial y}[\bar{u}^2+\bar{q}^2]\right\} \quad (14)$$

where $\bar{H}\simeq C_p\bar{T}+1/2[\bar{u}^2+\bar{q}^2]$ and $\overline{v'H'}\cong C_p\overline{v'T'}+\overline{v'u'}\,\bar{u}$. Various correlations involving density fluctuations have been discarded as being negligible in the above, in the usual manner [21]. By use of the exponentials given in equations (6) and (7), the above is integrated to give a result of the form

$$C_p\frac{\overline{v'T'}}{\bar{u}_e^3}=\left\{A_T(x)+\frac{y}{\delta}B_T(x)\right\}\exp\left[-\alpha\frac{y}{\delta}\right]+\text{higher order exponentials} \quad (15)$$

For the high FST cases the experimental results for $\overline{v'T'}$ consistently follow the form shown in Fig. 15, in which the decay rate is one half that of the mean velocity and mean temperature. However, integration of the energy equation leading to equation (15) gives the result that the slowest rate of decay of $\overline{v'T'}$ is identical to that of $\bar{u}$ and $\bar{T}$, not the half power. Furthermore, the appearance of the y/δ factor in equation (15) suggests that the semilogarithmic plot should not yield a straight line, in contrast to experimental observation. Such a mismatch in form is not reconciled by adjusting the magnitude of the coefficients; and therefore, there appears to be an inconsistency, which remains to be resolved.

Conclusions

The main results of this article may be summarized in four parts:

1 It is demonstrated that the mixing length hypothesis may be extended to turbulent boundary layer flows involving elevated levels of FST by utilizing the model proposed by Miyazaki and Sparrow as a first approximation. This model, expressed by equations (2)–(5), has been incorporated into the computer code STANCOOL. Computational results have been compared with the recent experimental data compiled by Blair and the comparison demonstrates an improved description, both for mean profiles of temperature and velocity and for the turbulent fluxes of momentum and heat. The model requires further development in the wall region, however.

2 A striking new observation has emerged in the wake portion of a turbulent boundary layer. As the FST is increased parametrically, the deficits of mean velocity and mean temperature approach a form that decays exponentially into the free stream with a linear argument. This behavior appears to extend from $y/\delta \simeq 0.2$ to well beyond the boundary layer edge. The exponential behavior is not observed for FST intensities less than approximately 2–3 percent. The graphs of $\overline{u'v'}$ and $\overline{v'T'}$ also exhibit approaching linear exponential behavior, although the $\overline{u'v'}$ profile cannot achieve this limit in channel flow owing to its zero crossing external to the boundary layer. In contrast, the $\overline{v'T'}$ graph shows the remarkable fact that its exponential decay is exactly half the rate of the mean velocity and temperature deficits. An explanation is not as yet offered.

3 By utilization of the observed exponential forms for $(\bar{u}_e-\bar{u})/\bar{u}_e$ and $(\bar{T}-\bar{T}_e)/(T_w-\bar{T}_e)$, the equations of motion and energy are integrated to provide explicit functional forms for $\overline{u'v'}$ and $\overline{v'T'}$ in the wake region. These results are similar to the form of the Miyazaki and Sparrow model which has proposed earlier as a result of separate arguments. However, it also appears that FST may influence the wall region of a turbulent boundary layer as well as the wake region, which is contrary to several earlier assertions. In contrast, the integration leading to $\overline{v'T'}$ yields a result which is incompatible with the slow half power decay into the free stream that is observed in Blair's data. Although it is likely that this dilemma may not be numerically significant, it is an important conceptual issue for continued investigation.

4 Since the heat transfer computation in STANCOOL, and also in other similar codes, relies on Pr_t modeling, Blair's data have been scrutinized for this purpose. It is observed that Pr_t declines rapidly outside of the boundary layer and that some values even become negative. An explanation is offered for this anomaly in terms of channel flow effects which influence $\overline{u'v'}$ and $\overline{v'T'}$ in different ways. Although this influence is probably numerically small over the major part of the turbulent boundary layer, it may be more correct to model a slower decay of Pr_t into the free stream than the data indicate.

Acknowledgments

The author is grateful for the excellent computer assistance provided by Mr. John L. Ebert during the summer 1984 phase of this research. Mr. Charles MacArthur and Dr. Richard Rivir are thanked for their initial motivation and many helpful discussions. Financial assistance from AFOSR is gratefully acknowledged under Contract F49620-82-C-0035 which was administered under the auspices of the Southeastern Center for Electrical Engineering Education.

References

1 Simonich, J. C., and Bradshaw, P., "Effect of Free-Stream Turbulence on Heat Transfer Through a Turbulent Boundary Layer," ASME JOURNAL OF HEAT TRANSFER, Vol. 100, 1978, pp. 671–677.

2 Bayley, F. J., and Priddy, W. J., "Effects of Free-Stream Turbulence Intensity and Frequency on Heat Transfer to Turbine Blading," ASME *Journal of Engineering for Power*, Vol. 103, 1981, pp. 60–64.

3 Pedisius, A. A., Kazimekas, P.-V. A., and Slanciauskas, A. A., "Heat Transfer From a Plate to a High-Turbulence Air Flow," *Heat Transfer—Soviet Research*, Vol. 11, No. 5, 1979, pp. 125–134.

4 McDonald, H., and Kreskovsky, J. P., "Effect of Free Stream Turbulence on the Boundary Layer," *Int. J. Heat Mass Transfer*, Vol. 17, 1974, pp. 705–716.

5 Hall, J. D., and Gibbings, J. C., "Influence of Stream Turbulence and Pressure Gradient Upon Boundary Layer Transition," *Journal of Mechanical Engineering Science*, Vol. 14, No. 2, 1972, pp. 134–146.

6 Meier, H. U., and Kreplin, H.-P., "Influence of Freestream Turbulence on Boundary-Layer Development," *AIAA Journal*, Vol. 18, No. 1, 1980, pp. 11–15.

7 Krishnamoorthy, V., "Effect of Turbulence on the Heat Transfer in a Laminar and Turbulent Boundary Layer Over a Gas Turbine Blade," ASME Paper No. 82-GT-146, 1982.

8 Junkhan, G. H., and Serovy, G. K., "Effects of Free-Stream Turbulence and Pressure Gradient on Flat-Plate Boundary-Layer Velocity Profiles and on Heat Transfer," ASME JOURNAL OF HEAT TRANSFER, Vol. 89, 1967, pp. 169–176.

9 Kestin, J., "The Effect of Free-Stream Turbulence on Heat Transfer Rates," *Advances in Heat Transfer*, Vol. 3, T. F. Irvine, Jr., and J. P. Hartnett, eds., Academic Press, London, 1966.

10 Sugawara, S., Sato, T., Hirosyasa, K., and Osaka, H., "The Effect of Free-Stream Turbulence on Heat Transfer From a Flat Plate," NACA TM 1441, 1958.

11 Feiler, C. E., and Yaeger, E. B., "Effect of Large-Amplitude Oscillations on Heat Transfer," NASA TR R-142, 1962.

12 Edwards, A., and Furber, B. N., "The Influence of Free-Stream Turbulence on Heat Transfer by Convection From an Isolated Region on a Plane Surface in Parallel Air Flow," *Proc. Inst. Mech. Engrs.*, London, Vol. 1970, 1956, p. 941.

13 Blair, M. F., "Influence of Free-Stream Turbulence on Turbulent Boundary Layer Heat Transfer and Mean Profile Development, Parts I & II," ASME JOURNAL OF HEAT TRANSFER, Vol. 105, 1983, pp. 33–47.

14 Blair, M. F., "Influence on Free-Stream Turbulence on Boundary Layer Transition in Favorable Pressure Gradients," ASME *Journal of Engineering for Power*, Vol. 104, 1982, pp. 743–750.

15 Blair, M. F., "The Effects of Free-Stream Turbulence on the Turbulence Structure and Heat Transfer in Zero Pressure Gradient Boundary Layers," United Technologies Research Center Report No. R82-915634-2, East Hartford, CT, Nov. 1982.

16 Bair, M. F., "Final Data Report—Vol. I—Velocity and Temperature Profile Data for Zero Pressure Gradient, Fully Turbulent Boundary Layers," UTRC Report No. R81-914388-15, E. Hartford, CT, Jan. 1981.

17 Blair, M. F., "Final Data Report—Vol. II—Velocity and Temperature Profile Data for Accelerating, Transitional Boundary Layers," UTRC Report No. R81-914388-16, E. Hartford, CT, Jan. 1981.

18 Blair, M. F., "Combined Influence of Free-Stream Turbulence and Favorable Pressure Gradients on Boundary Layer Transition and Heat Transfer," UTRC Report No. R81-914388-17, E. Hartford, CT, Mar. 1981.

19 Blair, M. F., "The Influence of Free-Stream Turbulence on the Zero Pressure Gradient Fully Turbulent Boundary Layer,"' UTRC Report No. R80-914388-12, E. Hartford, CT, Sept. 1980.

20 Hancock, P. E., "The Effect of Free-Stream Turbulence on Turbulent Boundary Layers," Ph.D. Dissertation, Imperial College, London, 1980.

21 Hancock, P. E., and Bradshaw, P., "The Effect of Free-Stream Turbulence on Turbulent Boundary Layers," ASME *Journal of Fluids Engineering*, Vol. 105, 1983, pp. 284–289.

22 Kline, S. J., Lisin, A. V., and Waitman, B. A., "Preliminary Experimental Investigation of Effect of Free-Stream Turbulence on Turbulent Boundary Layer Growth,"' NASA TND-368, Mar. 1960, pp. 1–60.

23 Favre, A., Gaviglio, J., and Dumas, R., "Space-Time Double Correlations and Spectra in a Turbulent Boundary Layer," *Journal of Fluid Mechanics*, Vol. 2, Part 4, 1957, pp. 313–342.

24 Favre, A., Gaviglio, J., and Dumas, R., "Further Space-Time Correlations of Velocity in a Turbulent Boundary Layer," *Journal of Fluid Mechanics*, Vol. 3, Part 4, 1958, pp. 344–356.

25 Kottke, V., "Heat, Mass, and Momentum Transfer in Separated Flows," *Int. Chemical Eng.*, Vol. 24, No. 1, 1984, pp. 1–12.

26 Kottke, V., "Techniques for the Visualization of Gas Flows," *Int. Chemical Engineering*, Vol. 22, No. 2, 1982, pp. 206–216.

27 Evans, R. L., "Freestream Turbulence Effects on Turbulent Boundary Layers in an Adverse Pressure Gradient," *AIAA Journal*, Vol. 23, No. 11, 1985, pp. 1814–1816.

28 Coles, D., "The Law of the Wake in a Turbulent Boundary Layer," *Journal of Fluid Mechanics*, Vol. 1, 1956, pp. 191–226.

29 Daniels, L. D., and Browne, W. B., "Calculation of Heat Transfer Rates to Gas Turbine Blades," *Int. J. Heat Mass Transfer*, Vol. 24, No. 5, 1981, pp. 871–879.

30 Crawford, M. E., and Kays, W. M., "STAN5—A Program for Numerical Computation of Two-Dimensional Internal and External Boundary Layer Flows," NASA CR-2742, Nov. 1976.

31 Gaugler, R. E., "Some Modifications to, and Operational Experiences With, the Two-Dimensional, Finite Difference, Boundary-Layer Code, STAN5," ASME Paper No. 81-GT-89, 1981.

32 Rotta, J. C., "Temperaturverteilungen in der Turbulenten Grenzchsicht an der Ebenen Platte," *Int. J. Heat Mass Transfer*, Vol. 7, 1964, pp. 215–228.

33 Reynolds, A. J., "The Prediction of Turbulent Prandtl and Schmidt Numbers," *Int. Journal of Heat and Mass Transfer*, Vol. 18, 1975, pp. 1055–1069.

34 Wassel, A. T., and Catton, I., "Calculation of Turbulent Boundary Layers Over Flat Plates With Different Phenomenological Theories of Turbulence and Variable Turbulent Prandtl Number," *Int. J. of Heat and Mass Transfer*, Vol. 16, 1973, pp. 1547–1563.

35 Senda, M., Suzuki, K., and Sato, T., "Turbulence Structure Related to the Heat Transfer in a Turbulent Boundary Layer With Injection," *Turbulent Shear Flows*, Vol. 2, Springer-Verlag, 1980, pp. 143–157.

36 Subramanian, C. S., and Antonia, R. A., "Effect of Reynolds Number on a Slightly Heated Turbulent Boundary Layer," *Int. J. Heat Mass Transfer*, Vol. 24, No. 11, 1981, pp. 1833–1846.

37 Simpson, R. L., Whitten, D. G., and Moffat, R. J., "An Experimental Study of the Turbulent Prandtl Number of Air With Injection and Suction," *Int. J. Heat Mass Transfer*, Vol. 13, 1970, pp. 125–143.

38 Snijders, A. L., Koppius, A. M., and Neiuwvelt, C., "An Experimental Determination of the Turbulent Prandtl Number in the Inner Boundary Layer for Air Flow Over a Flat Plate," *Int. J. Heat Mass Transfer*, Vol. 26, No. 3, 1983, pp. 425–431.

39 MacArthur, C. D., 'Prediction of Free-Stream Turbulence Effects on Boundary Layer Heat Transfer—An Evaluation of the Heat Transfer Code STAN5," 1983 USAF-SCEEE Graduate Student Summer Support Program, Contract No. F49620-82-0035, Sept. 16, 1983.

40 Sepri, P., and Ebert, J. L., "Calculation of Enhanced Heating in Turbulent Boundary Layers Influenced by Free Stream Turbulence," 1984 USAF-SCEEE Summer Faculty Research Program, Final Report for Contract No. F49620-82-C-0035, 1984.

41 van Driest, E. R., and Blumer, C. B., "Boundary Layer Transition: Free Stream Turbulence and Pressure Gradient Effects," *AIAA Journal*, Vol. 1, 1963, pp. 1303–1306.

42 Abu-Ghannam, B. J., and Shaw, R., "Natural Transition of Boundary Layers—The Effects of Turbulence, Pressure Gradient, and Flow History," *Journal of Mechanical Engineering Science*, Vol. 22, No. 5, 1980, pp. 213–228.

43 Dhawan, S., and Narasimha, R., "Some Properties of Boundary Layer Flow During Transition From Laminar to Turbulent Motion," *Journal of Fluid Mechanics*, Vol. 3, 1958, pp. 418–436.

44 Chen, K. K., and Thyson, N. A., "Extension of Emmons' Spot Theory to Flows on Blunt Bodies," *AIAA Journal*, Vol. 9, No. 5, 1971, pp. 821–825.

45 Miyazaki, H., and Sparrow, E. M., "Analysis of Effects of Free-Stream Turbulence on Heat Transfer and Skin Friction," ASME JOURNAL OF HEAT TRANSFER, Vol. 99, 1977, pp. 614–619.

46 Coles, D. E., "Turbulent Boundary Layers in Pressure Gradients: A Survey Lecture Prepared for the 1968 AFOSR-IFP-Stanford Conference on Computation of Turbulent Boundary Layers," Rand Corp. Memorandum RM-6142-PK, Oct. 1969.

47 Belov, I. A., Gorshkov, G. F., Komarov, V. S., and Terpigor'ev, V. S., "Influence of Jet Turbulence on Flow in the Boundary Layer Near the Wall," translated from *Zhurnal Prikladnoi Mekhaniki i Tekhnicheskoi Fiziki*, No. 6, 1982, pp. 77–82.

Boundary-Layer Treatment of Forced Convection Heat Transfer From a Semi-infinite Flat Plate Embedded in Porous Media

M. Kaviany
Department of Mechanical Engineering and Applied Mechanics,
The University of Michigan,
Ann Arbor, MI 48109

The effect of the presence of an isotropic solid matrix on the forced convection heat transfer rate from a flat plate is studied using the integral method. The closed-form solutions found are in good agreement with the available numerical results and also with the results obtained using a finite difference approximation and the expansion method. For large values of the flow resistance (due to the presence of the solid matrix), the asymptotic value for the heat transfer rate shows a Prandtl number dependency of 1/2 power, while the results for the intermediate values of the resistances show a 1/3 power dependency. The effect of the presence of the solid matrix on the heat transfer rate is shown through a regime diagram marking the boundaries of the regime of no significant alteration, the non-Darcian regime, and the Darcian regime.

1 Introduction

It has been found (Vafai and Tien, 1981; Vafai, 1984) that in laminar boundary-layer flows over a flat plate, the presence of a solid matrix creates flow resistances which are proportional to the velocity (first and second-order terms being the most dominant (Beaver and Sparrow, 1969)) and this tends to make the velocity distribution more uniform. The heat transfer rate at the interface of the plate and the porous media increases as a result of this homogeneity. This increase has an upper bound which is reached when the thickness of the thermal boundary layer becomes much larger than the momentum boundary-layer thickness (i.e., Darcian regime). This problem has been extensively studied by Vafai and Tien (1981) for developed velocity fields using mostly a numerical technique. However, convenient closed-form solutions for determining the extent of the influence of the presence of the solid matrix on the heat transfer rate are not available. The usefulness of the closed-form solutions can be appreciated when it is noted that in the graphic presentation of the effect of the presence of a solid matrix on the heat transfer rate, as the resistance to the flow varies, the Prandtl number also changes.

In this study as an extension to the results of Vafai and Tien (1981), the integral method, as applied to the natural and mixed convection problems in the Darcy regime (Cheng, 1978), has been applied in order to obtain closed-form and relatively accurate solutions for the heat transfer rate. The expansion method and a finite difference approximation are also used for validation of the solutions of the integral method.

2 Analysis

Assuming that: (*a*) the magnitude of the free-stream velocity is maintained and the flow is steady state and two-dimensional; (*b*) the boundary-layer approximations hold; and (*c*) the properties are constant, the conservation equations for fluid flow through isotropic and saturated porous media can be written[1] as (Vafai and Tien, 1981)

$$\frac{\partial u}{\partial x}+\frac{\partial v}{\partial y}=0 \tag{1}$$

$$u\frac{\partial u}{\partial x}+v\frac{\partial u}{\partial y}=-\frac{1}{\rho}\frac{dp}{dx}-\frac{\nu\epsilon}{K}u-\frac{F\epsilon^2}{K^{1/2}}u^2+\nu\frac{\partial^2 u}{\partial y^2} \tag{2}$$

$$u\frac{\partial T}{\partial x}+v\frac{\partial T}{\partial y}=\alpha_e\frac{\partial^2 T}{\partial y^2} \tag{3}$$

where the contribution of the viscous dissipation to the energy equation is neglected. It should be noted that in the problem considered the free-stream velocity, rather than the axial pressure gradient, is prescribed.

The boundary conditions are

$$y,\ x<0: u=u_\infty,\quad T=T_\infty \tag{4a}$$

$$y=0,\quad x>0: u=v=0,\ T=T_w \tag{4b}$$

$$y\to\infty,\quad x>0: u=u_\infty,\quad T=T_\infty \tag{4c}$$

Since at a sufficiently large distance from the wall the flow field is uniform, the free-stream axial pressure gradient required for maintaining the velocity u_∞ must follow

$$\frac{1}{\rho}\frac{dp}{dx}=-\frac{\nu\epsilon}{K}u_\infty-\frac{F\epsilon^2}{K^{1/2}}u_\infty^2 \tag{2a}$$

Then, equation (2) becomes

$$u\frac{\partial u}{\partial x}+v\frac{\partial u}{\partial y}=\frac{\nu\epsilon}{K}(u_\infty-u)+\frac{F\epsilon^2}{K^{1/2}}(u_\infty^2-u^2)+\nu\frac{\partial^2 u}{\partial y^2} \tag{2b}$$

In equation (2*b*), for small permeabilities the pressure gradient is just balanced by the first and second-order solid matrix resistances, i.e., the boundary and the development terms are not significant (equation (2*a*)). For higher permeability media, near the leading edge the development term is significant, while the shear stress term remains significant for a larger distance (Vafai and Tien, 1981). The thickness of the momentum and thermal boundary layers and the regions over which the development and shear stress terms are significant will be discussed later.

3 Solutions

In the following, the solutions to equations (1)-(3) are

[1] These equations are semi-empirical and are based on treatment of the combination of the solid and fluid phases as a continuum. For high velocities and large porosities the interpore mixing and the resulting gradient destructions may have to be included (Kaviany, 1986).

Contributed by the Heat Transfer Division for publication in the JOURNAL OF HEAT TRANSFER. Manuscript received by the Heat Transfer Division March 25, 1986.

found through the application of: (*a*) a finite difference approximation, (*b*) the expansion method for the case of $F=0$, and (*c*) the integral method.

3.1 Finite Difference Approximation. The Falkner-Skan transformations (Cebeci and Bradshaw, 1984) of equations (1)–(3) are made using

$$\psi = (u_\infty \nu x)^{1/2} f, \quad u = \frac{\partial \psi}{\partial y}, \quad v = -\frac{\partial \psi}{\partial x} \tag{5}$$

$$\eta = \left(\frac{u_\infty}{\nu x}\right)^{1/2} y \tag{6}$$

$$\theta = \frac{T - T_w}{T_\infty - T_w} \tag{7}$$

The emerging momentum and energy equations are

$$f''' + \frac{1}{2} f f'' = x\left(f' \frac{\partial f'}{\partial x} - f'' \frac{\partial f}{\partial x}\right) - \xi_x (1 - f') - \Psi_x (1 - f'^2) \tag{8}$$

$$\theta'' + \frac{1}{2} \mathrm{Pr}_e f \theta' = \mathrm{Pr}_e x\left(f' \frac{\partial \theta}{\partial x} - \theta' \frac{\partial f}{\partial x}\right) \tag{9}$$

where

$$\xi_x = \frac{\nu \epsilon x}{K u_\infty} = \frac{\gamma_x^2}{\mathrm{Re}_x} \text{ and } \Psi_x = \frac{F \epsilon^2}{K^{1/2}} x$$

are the dimensionless first and second-order flow resistances due to the presence of the solid matrix. Note that ξ_x contains both the dimensionless porous media shape parameter γ_x and the fluid inertia parameter (Reynolds number) Re_x.

The boundary conditions are

$$\eta,\ x \le 0: \quad f' = 1, \quad \theta = 1 \tag{10a}$$

$$\eta = 0,\ x \ge 0: \quad f = f' = \theta = 0 \tag{10b}$$

$$\eta \to \infty,\ x \ge 0: \quad f' = \theta = 1 \tag{10c}$$

Solutions to equations (8) and (9) subject to these boundary conditions are found using the Box finite difference approximation method as described by Keller (1978) and applied successfully by Cebeci and Bradshaw (1984). The Newton iteration method was applied to the emerging difference equations.

For the constant free-stream velocity situation considered, the presence of the solid matrix tends to make the velocity distribution more uniform. Initially the edge of the momentum boundary layer was taken to be that for $\xi_x = \Psi_x = 0$ (i.e., when similarity of the velocity field exists). Although it is known that the momentum boundary layer thickness decreases as ξ_x and Ψ_x increase, the results were always examined in order to insure that η_∞ was sufficiently large.

3.2 Expansion Method. In order to validate the numerical solutions obtained using the finite difference approximation, some solutions were obtained using the expansion method. For the case of $\Psi_x = 0$ and for small values of ξ_x an expansion was made in ξ_x around the solution for $\xi_x = 0$. The results for the first and second-order approximations are already available,[2] but for completeness the results for up to the third order are given below.

By taking a solution of the form

$$f = \sum_{i=0}^{\infty} f_i \xi_x^i$$

where $f_i = f_i(\eta)$ only, we have

$$f_0''' = -\frac{1}{2} f_0 f_0'' \tag{11a}$$

$$f_1''' = f_0' f_1'' - \frac{3}{2} f_0'' f_1 - \frac{1}{2} f_0 f_1'' - (1 - f_0') \tag{11b}$$

$$f_2''' = 2 f_0' f_2' + f_1'^2 - \frac{3}{2} f_1 f_1'' - \frac{1}{2} f_0 f_2'' - \frac{5}{2} f_2 f_0'' + f_1' \tag{11c}$$

$$f_3''' = 3 f_0' f_3' + 3 f_1' f_2' - \frac{7}{2} f_0'' f_3 - \frac{5}{2} f_1'' f_2 - \frac{3}{2} f_2'' f_1 - \frac{1}{2} f_0 f_3'' + f_2' \tag{11d}$$

subject to the following boundary conditions

[2] Note that for $F=0$, equation (2*b*) is identical to the equation describing the flow of a conducting fluid in the presence of a transverse magnetic field (fixed relative to the fluid) (Rossow, 1957). In this case the resistance due to the presence of the magnetic field (insteady of the rigid matrix) is also proportional to the velocity. This commonness of some particular MHD flows and flows through porous media can make available the solutions and insights earned in one field for application in the other field.

Nomenclature

c_f = friction coefficient
f = a similarity function, given in equation (5)
F = empirical constant in the second-order resistance
k_e = effective thermal conductivity, W/m-K
K = permeability, m^2
$\mathrm{Nu}_x = q_0'' x/(T_w - T_\infty) k_e$ = Nusselt number
p = pressure, N/m^2
$\mathrm{Pe}_x' = \mathrm{Pr}_e \mathrm{Re}_x$ = Peclet number
$\mathrm{Pr}_e = \nu/\alpha_e$ = effective Prandtl number
q_0'' = wall heat flux, W/m^2
$r = \Delta/\delta$ = ratio of thermal to momentum boundary layer thickness
$\mathrm{Re}_x = u_\infty x/\nu$ = Reynolds number
T = temperature, K
u, v = velocity components parallel and perpendicular to the plate, m/s
x, y = coordinate axes parallel and perpendicular to the plate, m
α_e = effective thermal diffusivity, m^2/s
$\gamma_x = (x^2 \epsilon/K)^{1/2}$ = dimensionless porous media shape parameter
$\Gamma_x = (3/8)\xi_x + (54/105)\Psi_x$ = total resistance to the flow due to presence of the solid matrix
δ = momentum boundary layer thickness, m
Δ = thermal boundary layer thickness, m
ϵ = porosity
$\eta = (u_\infty/\nu x)^{1/2} y$
$\theta = (T - T_w)/(T_\infty - T_w)$ = dimensionless temperature
ν = kinematic viscosity, m^2/s
$\xi_x = \gamma_x^2/\mathrm{Re}_x$ = first-order resistance
ρ = fluid density, kg/m^3
ψ = stream function, m^2/s
$\Psi_x = F\epsilon^2 x/K^{1/2}$ = second-order resistance

Subscripts and Superscripts

e = effective
w = wall condition
x = based on x
∞ = free-stream condition
$\bar{}$ = dimensionless
$'$ = differentiation with respect to η

Table 1 Computed values of $f_i''(0)$

i	0	1	2	3
$f_i''(0)$	0.3324	1.145	−1.380	3.604

$$f_i(0) = f_i'(0) = 0 \qquad i = 0, 1, 2, 3 \tag{12a}$$

$$f_0'(\eta_\infty) = 1, \quad f_i'(\eta_\infty) = 0 \qquad i = 1, 2, 3 \tag{12b}$$

The solution to equation (11*a*) is the available Blasius solution and the solution to equation (11*b*) is also available from the MHD studies (Rossow, 1957). The solutions for these as well as for $i=2$, 3 are given in Table 1. The fourth-order Runge-Kutta-Gill method for solving the initial value problems, as described in (Romanelli, 1960) was applied.

Since the expansion method is only used to validate the numerical and integral results for small values of ξ_x, and as will be shown complete agreement has been found between the numerical and expansion method, this exercise was not extended to the energy equation. Also, further numerical results on the effects of the second-order resistance on the wall heat transfer rate and the wall shear stress are already available (Vafai and Tien, 1981).

3.3 Integral Method. The standard integral method as described by Kays and Crawford (1980) is applied to equations (1) and (2) for two different flow regimes. In the non-Darcian regime the velocity distribution is nonuniform, i.e., the shear stress at the interface of the plane surface and the porous media is finite. In the Darcian regime the velocity distribution is nearly uniform.

3.3.1 Non-Darcian Regime. Following the conventional boundary-layer analyses (e.g., Kays and Crawford, 1980), the temperature and velocity distributions are prescribed as

$$\frac{u}{u_\infty} = \frac{3}{2}\frac{y}{\delta} - \frac{1}{2}\frac{y^3}{\delta^3} \tag{13a}$$

$$\theta = \frac{3}{2}\frac{y}{\Delta} - \frac{1}{2}\frac{y^3}{\Delta^3} \tag{13b}$$

While the presence of the solid matrix does not significantly alter the temperature profile, as will be discussed later, this velocity profile becomes less acceptable as the Darcian regime is approached. This will be remedied by adapting a uniform velocity distribution for the Darcian regime.

Based on these, the approximate integral momentum and energy equations become

$$\frac{39}{280}\frac{d\delta}{d\bar{x}} = \frac{3}{2}\frac{1}{\bar{\delta}}\frac{1}{\mathrm{Re}_x} - \frac{3}{8}\xi_x\bar{\delta} - \frac{54}{105}\Psi_x\bar{\delta} = \frac{3}{2}\frac{1}{\bar{\delta}}\frac{1}{\mathrm{Re}_x} - \Gamma_x\bar{\delta} \tag{14}$$

$$\frac{dr}{d\bar{x}} = \frac{10}{\mathrm{Pe}_x'}\frac{1}{2r^2\bar{\delta}^2\left(1-\frac{r^2}{7}\right)} - \frac{\frac{r}{2}-\frac{r^3}{28}}{\bar{\delta}\left(1-\frac{r^2}{7}\right)}\frac{d\bar{\delta}}{d\bar{x}} \tag{15}$$

where $r=\Delta/\delta$, and $\Gamma_x=(3/8)\ \xi_x+\ (54/105)\ \Psi_x$ is total resistance to the flow due to the solid matrix. Note that $\bar{\delta}=\delta/x$. Equations (14) and (15) are subject to the initial conditions

$$\delta(0) = 0 \tag{16a}$$

$$\Delta(0) = 0 \tag{16b}$$

The normalized interface shear stress and heat transfer rates are given as

$$f''(0) = \frac{c_f}{2}\mathrm{Re}_x^{1/2} = \frac{3}{2}\frac{1}{\bar{\delta}\mathrm{Re}_x^{1/2}} \tag{17}$$

$$\theta'(0) = \frac{\mathrm{Nu}_x}{\mathrm{Re}_x^{1/2}} = \frac{3}{2}\frac{1}{\bar{\Delta}\mathrm{Re}_x^{1/2}} \tag{18}$$

where $f''(0)$ and $\theta'(0)$ are used only for comparison with the numerical and expansion solutions. Equations (14) and (15) are solved numerically and the singularities are avoided by using the results of $\Gamma_x=0$ for very small values of x.

Hydrodynamically Developed Flow. As will be discussed, the presence of the solid matrix accelerates the hydrodynamic development and after a short distance from the leading edge the momentum boundary-layer thickness attains a constant value, i.e., for $d\delta/dx=0$. Examination of equations (14) and (15) shows that

$$\bar{\delta} = \left(\frac{3}{2}\frac{1}{\mathrm{Re}_x\Gamma_x}\right)^{1/2}, \quad f''(0) = \left(\frac{3}{2}\right)^{1/2}\Gamma_x^{1/2} \tag{19a}$$

$$\frac{r^3}{3} - \frac{r^5}{35} = \frac{10\Gamma_x}{3\mathrm{Pr}_e} \tag{19b}$$

$$\theta'(0) = \left(\frac{3}{2}\right)^{1/2}\frac{\Gamma_x^{1/2}}{r} \tag{19c}$$

r Near Unity. From equation (19*b*) and by applying the expression for fully developed values of δ (given above) and also for r of near unity (thermal and momentum boundary-layer thicknesses are of the same order of magnitude), the following closed-form solutions emerge. For $r^3/3 > r^5/35$ we have

$$r = \left(\frac{10\Gamma_x}{\mathrm{Pr}_e}\right)^{1/3}, \text{ or } \bar{\Delta} = \left(\frac{3}{2}\right)^{1/2} 10^{1/3}\frac{1}{\mathrm{Re}_x^{1/2}\mathrm{Pr}_e^{1/3}\Gamma_x^{1/6}} \tag{20a}$$

then

$$f''(0) = \left(\frac{3}{2}\Gamma_x\right)^{1/2} \tag{20b}$$

$$\theta'(0) = \left(\frac{3}{2}\right)^{1/2}\frac{1}{10^{1/3}}\Gamma_x^{1/6}\mathrm{Pr}_e^{1/3} \tag{20c}$$

In the next section, by comparing these approximate solutions with the numerical solutions: (*a*) the length x required before $d\delta/dx=0$, i.e., the momentum development length x_{md}, and (*b*) the range of validity of equations (20*b*), (20*c*), will be determined.

3.3.2 Darcian Regime. For this regime equation (13*b*) will be used for the temperature distribution, but the velocity distribution will be taken to be uniform, i.e., $u=u_\infty$. Then the energy equation becomes

$$\frac{dr}{d\bar{x}} = \frac{4}{\mathrm{Pe}_x'}\frac{1}{\bar{\delta}^2 r} \tag{21a}$$

Using this, substituting for δ from equation (19*a*), and integrating (note that δ does not vary with x), we have

$$r = \left(\frac{8}{\mathrm{Pe}_x'\bar{\delta}^2}\right)^{1/2} = \frac{16}{3}\left(\frac{\Gamma_x}{\mathrm{Pr}_e}\right)^{1/2} \tag{21b}$$

then

$$\bar{\Delta} = 8^{1/2}\frac{1}{\mathrm{Pr}_e^{1/2}\mathrm{Re}_x^{1/2}} = 8^{1/2}\mathrm{Pe}_x'^{1/2} \tag{21c}$$

$$\theta'(0) = \frac{3}{2}\frac{1}{8^{1/2}}\mathrm{Pr}_e^{1/2} \tag{21d}$$

Note that the thermal boundary layer thickness and the dimensionless heat transfer rate are independent of the value of Γ_x. This is in agreement with the results obtained by Vafai and Tien (1981) for uniform flow, where by using an exact analysis it was found that

$$\theta'(0) = \left(\frac{\mathrm{Pr}_e}{\pi}\right)^{1/2} = 0.56\ \mathrm{Pr}_e^{1/2}$$

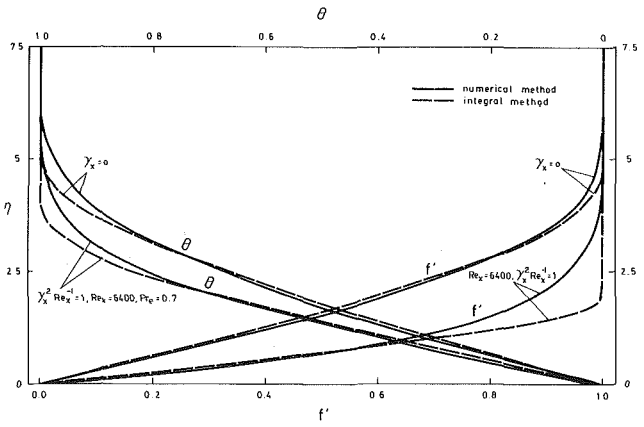

Fig. 1 Comparison of the temperature and velocity distributions obtained from the application of the numerical and integral methods. The results are for $\Psi_x = 0$.

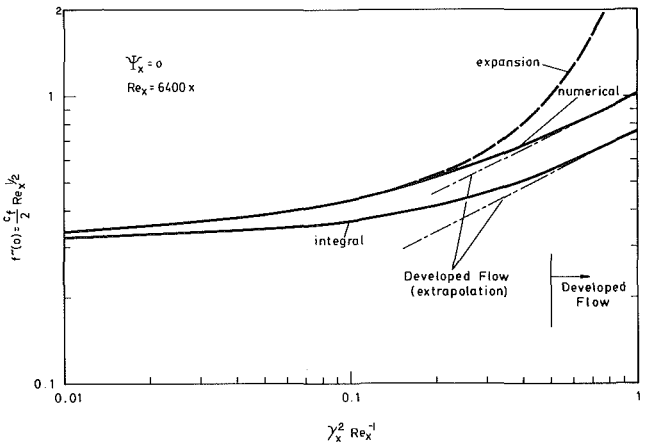

Fig. 2 Comparison of the magnitudes of the dimensionless wall shear stress obtained from the application of the numerical, expansion, and integral methods. Also shown are extrapolations based on the assumption of developed flow field.

4 Results and Discussion

As was shown in the last section, the integral method can lead to rather simple closed-form solutions which can be used to develop a regime diagram. In the following, the validity of these solutions is examined by comparing the results for the velocity and temperature distributions, the normalized shear stress at the wall, and the normalized heat flux at the wall, to the numerical solutions. Then, a regime diagram for normalized heat transfer rate is developed.

Figure 1 shows how the boundary layer thickness and the velocity and temperature profiles are affected when a solid matrix is present. The results are for $\xi_x = 1$ and $Pr_e = 0.7$.[3] As expected the velocity distribution changes toward the conventional uniform profile which is used when the viscous shear stress term is neglected, i.e., the velocity slip at the wall is allowed (large Γ_x limit). Note that the effect of the presence of the solid matrix is more significant on the velocity distribution than on the temperature distribution.

Figure 2 shows the normalized wall shear stress as determined by the three methods. As expected for large values of ξ_x the expansion method leads to erroneous results. For $\xi_x < 0.2$ the agreement between the Box method and the expansion method is complete. Compared to the numerical results the integral method underpredicts the magnitude of $f''(0)$. This difference reaches an asymptotic value of approximately 24 percent.

[3] Note that $Pr_e = \nu/\alpha_e$ and α_e changes as the solid matrix changes. Therefore the constant values used for Pr_e are not physically very meaningful. However, the closed-form solutions which are presented are valid for any set of (Pr_e, Γ_x).

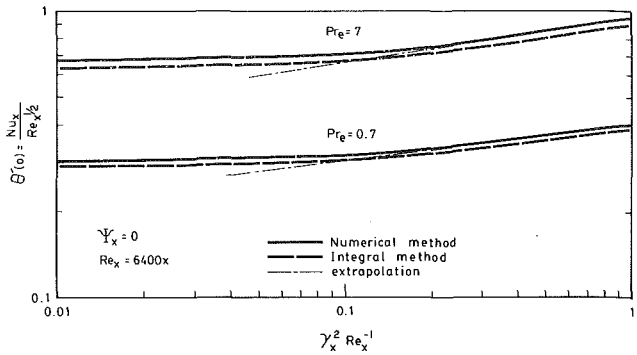

Fig. 3 Comparison of the magnitudes of the normalized wall heat transfer rate obtained using the numerical and integral methods for $Pr_e = 0.7$ and 7. Also shown are extrapolations based on developed flow field.

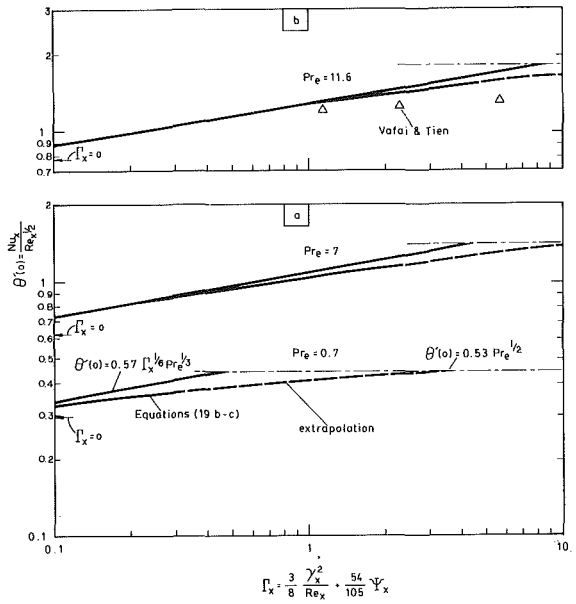

Fig. 4(*a*) Comparison of the various approximate solutions found using the integral method. The results are for $Pr_e = 0.7$ and 7. (*b*) Comparison of the results obtained using the integral method with the numerical results of Vafai and Tien (1981).

Figure 3 compares the results of the Box method and integral methods for normalized wall heat transfer rate for $Pr_e = 0.7$ and 7. The results show a rather good agreement (within less than 5 percent) between the two solutions. The range of ξ_x presented is rather small for a thorough comparison, but similar agreements have been found for larger values of ξ_x. Note that for $\xi_x > 0.2$ the variation in $\theta'(0)$ approaches an asymptotic behavior. Equations (19*b*) and (19*c*) describe these asymptotes. Note that equation (19*b*) is limited to $r < (35/3)^{1/2}$ and beyond this a different velocity profile has to be specified (e.g., for large r the velocity distribution in the thermal boundary layer is nearly uniform, i.e., Darcian regime).

In the Darcian regime the effect of the wall no-slip condition penetrates only a small distance into the fluid-saturated porous medium and therefore inside the thermal boundary layer the velocity is nearly uniform and the results given by equations (21*a–d*) hold. Figure 4(*a*) shows the results of the integral method for magnitudes for Γ_x large enough that the flow fields are already hydrodynamically developed. Also shown are the approximate results for values of r near unity (i.e., equation (20*c*)), the Darcian result (i.e., equation (21*d*)), as well as the results for $r < (35/3)^{1/2}$ (i.e., equations (19*b*, *c*)).

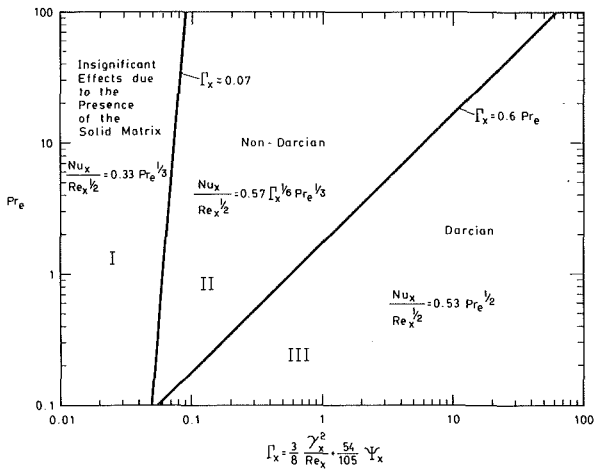

Fig. 5 A regime diagram showing the regimes of (a) no significant alteration in the normalized heat transfer rate, and (b) significant alteration in heat transfer rate (non-Darcian and Darcian).

Note that due to limitations on equation (19*b*) the result for both small and large values of r cannot be obtained. Examinations of the results show how the Darcian regime is approached and that in the Darcian regime the value of the normalized heat transfer rate is independent of the value of the resistance. This has already been observed (Vafai and Tien, 1981) and equation (21*d*) describes this asymptotic value and its Prandtl number dependency.

Figure 4(*b*) compares the results obtained using the integral method with those obtained numerically by Vafai and Tien (1981) for $Pr_e = 11.6$. The agreement can be considered good, except that their results show a more gradual approach to the Darcian regime compared to the extrapolated solution based on the integral solution.

The foregoing comparisons show that the integral method can lead to meaningful and relatively accurate predictions of the heat transfer rate at the interface of the wall and the saturated porous media.

Based on the results presented, a regime diagram for heat transfer rate is given in Fig. 5. The independent variables are Pr_e and Γ_x. For small values of Γ_x, there is no change in the normalized heat transfer rate (regime I). As ξ_x increases the momentum boundary-layer thickness decreases and the heat transfer rate increases. For r near unity (and to a good approximation even for larger values of r) the normalized heat transfer rate is given by equation (20*c*). This is designated as non-Darcian regime (regime II), since the thickness of the thermal boundary layer is of the order of the thickness of the momentum boundary layer. Also, since as Pr_e increases the ratio of the thermal to momentum boundary layer remains of the order unity for even larger values of Γ_x, therefore, the non-Darcian regime extends to higher value of Γ_x as the Prandtl number increases. For even larger values of Γ_x, the asymptotic regime or the Darcian regime (regime III) is reached, when the thermal boundary layer is much larger than the momentum boundary layer thickness. Equation (21*d*) describes the normalized heat transfer rate.

5 Conclusion

The effect of the presence of a solid matrix, exerting first and second-order resistances to a constant free-stream velocity flow over a semi-infinite plate, is examined by applying the integral method. The results confirm the findings of others and provide closed-form solutions for normalized heat transfer rate. Three regimes have been identified.

Regime I. The effect of the presence of the solid matrix is not significant and the boundary for this regime is given by

$$\Gamma_x \leq 0.07$$

Regime II. The non-Darcian regime; the ratio of thermal to momentum boundary layer is of the order of unity ($r \sim 1$) and

$$\bar{\delta} = \left(\frac{3}{2}\frac{1}{\mathrm{Re}_x}\frac{1}{\Gamma_x}\right)^{1/2}, \quad r = \left(\frac{10}{\mathrm{Pr}_e}\Gamma_x\right)^{1/3},$$

$$\theta'(0) = 0.57\Gamma_x^{1/6}\mathrm{Pr}_e^{1/3}$$

or

$$\mathrm{Nu}_x = 0.57\Gamma_x^{1/6}\mathrm{Re}_x^{1/2}\mathrm{Pr}_e^{1/3}$$

For $F=0$, $\delta = (4K/\epsilon)^{1/2}$ and the momentum development length required for reaching this constant thickness is about $0.9\ Ku_\infty/\nu$. These confirm the findings of Vafai and Tien (1981) and Kaviany (1984).

The non-Darcian regime is confined between

$$\Gamma_x > 0.07 \text{ and } \Gamma_x < 0.6\ \mathrm{Pr}_e$$

Regime III. The Darcian regime; $r >> 1$ and

$$\theta'(0) = 0.53\ \mathrm{Pr}_e^{1/2} \text{ or } \mathrm{Nu}_x = 0.53\ \mathrm{Pe}_x'^{1/2}$$

where the Prandtl number dependency has changed from the power of 1/3 for the non-Darcian regime to 1/2 for the Darcian regime.

References

Beaver, C. S., and Sparrow, E. M., 1969, "Non-Darcy Flow Through Porous Media," ASME *J. Appl. Mech.*, Vol. 36, pp. 711–714.

Cebeci, T., and Bradshaw, P., 1984, *Physical and Computational Aspects of Convective Heat Transfer*, Springer-Verlag, New York, pp. 406–428.

Cheng, P., 1978, "Convective Heat Transfer in Porous Layers by Integral Methods," *Letters in Heat and Mass Transfer*, Vol. 5, pp. 243–252.

Kaviany, M., "Laminar Flow Through a Porous Channel Bounded by Isothermal Parallel Plates," *Int. J. Heat Mass Transfer*, Vol. 28, pp. 851–858.

Kaviany, M., 1986, "Gradient Destruction in Flow Through a Rigid Matrix," *J. Fluid Mech.*, pp. 221–230.

Kays, W. M., and Crawford, M. E., 1980, *Convective Heat and Mass Transfer*, McGraw-Hill, New York, pp. 144–147.

Keller, H. B., 1978, "Numerical Methods in Boundary-Layer Theory," *Ann. Rev. Fluid Mech.*, Vol. 10, pp. 417–433.

Romanelli, H. J., 1960, "Runge-Kutta Methods for the Solution of Ordinary Differential Equations," in: *Mathematical Methods for Digital Computers*, Ralston and Wilf, eds., Wiley, Vol. 1, pp. 110–120.

Rossow, V. J., 1957, "On Flow of Electrically Conducting Fluids Over a Flat Plate in the Presence of a Transverse Magnetic Field," NACA Technical Note 3971.

Vafai, K., 1984, "Convective Flow and Heat Transfer in Variable-Porosity Media," *J. Fluid Mech.*, Vol. 147, pp. 233–259.

Vafai, K., and Tien, C.-L., 1981, "Boundary and Inertia Effects on Flow and Heat Transfer in Porous Media," *Int. J. Heat Mass Transfer*, Vol. 24, pp. 195–203.

Instabilities of Steady, Periodic, and Quasi-Periodic Modes of Convection in Porous Media

S. Kimura[1]

G. Schubert

Department of Earth and Space Sciences,
University of California,
Los Angeles, CA 90024

J. M. Straus

Space Sciences Laboratory,
The Aerospace Corporation,
Los Angeles, CA 90009

Instabilities of steady and time-dependent thermal convection in a fluid-saturated porous medium heated from below have been studied using linear perturbation theory. The stability of steady-state solutions of the governing equations (obtained numerically) has been analyzed by evaluating the eigenvalues of the linearized system of equations describing the temporal behavior of infinitesimal perturbations. Using this procedure, we have found that time-dependent convection in a square cell sets in at Rayleigh number Ra = 390. The temporal frequency of the simply periodic ($P^{(1)}$) convection at Rayleigh numbers exceeding this value is given by the imaginary part of the complex eigenvalue. The stability of this ($P^{(1)}$) state has also been studied; transition to quasi-periodic convection (QP_2) occurs at Ra ≈ 510. A reverse transition to a simply periodic state ($P^{(2)}$) occurs at Ra ≈ 560; a slight jump in the frequency of the $P^{(2)}$ state occurs at Ra between 625 and 640. The jump coincides with a second narrow (in terms of Ra) region of quasi-periodicity.

1 Introduction

It is well known that with increasing Rayleigh number Ra thermal convection in a porous layer heated from below undergoes a transition from steady to time-dependent flow. The existence of time-dependent convection was first described in [1, 2]; numerical simulations in [3, 4] also indicated the existence of time-dependent convection. These investigations showed that the transition from steady (S) flow to time-dependent motion takes place at a value of Ra in the range 300-400. The behavior of convection in a square cross section of fluid-saturated porous material at values of Ra as large as ≈1000 has been defined more accurately in [5-7]. In particular, it has been found that the first transition to time-dependent flow occurs at Ra ≈ 390 and leads to a simply periodic state $P^{(1)}$. Further transitions occur at higher Ra: to a quasi-periodic state $QP_2^{(1)}$ with two basic frequencies at Ra between 500 and 520; to a second simply periodic state $P^{(2)}$ at Ra ≈ 565; and to a nonperiodic (chaotic) state NP at values of Ra in excess of ≈900. In the $P^{(1)}$ regime the fundamental frequency f_1 was found to vary as $Ra^{7/8}$ and the average Nusselt number $\overline{Nu} \propto Ra^{2/3}$; in $P^{(2)}$, $f_1 \propto Ra^{3/2}$ and $\overline{Nu} \propto Ra^{11/10}$. The chaotic NP state is characterized by spectral peaks at at least three fundamental frequencies superimposed on broad-band background noise.

Accurate evaluation of the values of Ra at which these transitions take place has been difficult. This is because the numerical calculations, which typically make use of spectral or pseudo-spectral techniques, require long computational times before the character of the solution's temporal dependence can be determined with confidence. (Calculations involving 30,000-50,000 time steps have been used in previous work.) This has necessarily limited the number of computations that have been carried out. The transitions from one type of time-dependent convection to another (e.g., $QP_2^{(1)} \rightarrow P^{(2)}$) are rather subtle, and an accurate determination of the value of Ra at the transition cannot be made from computations at widely spaced values of Ra.

The present paper describes an alternate technique which facilitates accurate identification of the values of Ra at which these transitions occur and the dominant frequencies of the resultant time-dependent flows. As described below, the present linear perturbation theory predicts the transition $S \rightarrow P^{(1)}$ in a square cross section to occur at Ra = 390 and the frequency of oscillation at the transition to be $f_{cr} = 83/\Delta\tau$, where $\Delta\tau$ is the thermal diffusion time across the square. These values are in excellent agreement with the numerical simulations previously carried out. The stability of the $P^{(1)}$ state has also been studied here, allowing a clear evaluation of the Rayleigh number at the $P^{(1)} \rightarrow QP_2^{(1)}$ transition and the fundamental frequencies of oscillation in the $QP_2^{(1)}$ state; this has been difficult and time-consuming in previous analyses because of the existence of spurious frequencies, associated with decaying modes of oscillation, which are seen in power spectra of the time series. Finally, the perturbation theory used here has allowed us to identify a previously unknown discontinuity in the frequency of the $P^{(2)}$ state which occurs in the range Ra = 625-640. The discontinuity coincides with a second quasi-periodic $QP_2^{(2)}$ solution regime.

The paper is organized as follows: Section 2 gives a brief discussion of the mathematical formulation of the problem. Section 3 deals with the transition $S \rightarrow P^{(1)}$, while Section 4 describes the subsequent transitions. Finally, Section 5 is dedicated to a summary and concluding remarks.

2 Mathematical Formulation and Numerical Scheme

The mathematical formulation of the present work is identical to that of [8] and will be described only briefly here. Assuming Darcy's law and the Boussinesq approximation to hold, a single differential equation may be derived

$$\frac{\partial}{\partial \tau} \nabla^2 \phi = -\phi_{\xi\xi} \nabla^2 \phi_\xi + \phi_{\xi\xi} \nabla^2 \phi_\xi + \nabla^4 \phi + \mathrm{Ra} \phi_{\xi\xi} \qquad (1)$$

where the nondimensional horizontal velocity $u = -\phi_{\xi\zeta}$, the nondimensional vertical velocity $w = \phi_{\xi\xi}$, and the Rayleigh number $\mathrm{Ra} = \alpha g \rho^2 K c d \Delta T / \mu k$. Here, τ is the time, nondimensionalized in units of $\Delta\tau = d^2 \rho c / k$, and ζ and ξ are measured in units of d (see nomenclature for definitions of symbols). The boundary conditions imposed are that the top ($\zeta = 1$) and bottom ($\zeta = 0$) boundaries are isothermal and that the vertical ($\xi = 0, 1$) boundaries are insulating.

[1] Present address: The Government Industrial Research Institute, Tohoku Agency of Industrial Science and Technology, MITI 4-2-1, Nigatake, Sendai, 983, Japan.

Contributed by the Heat Transfer Division and presented at the 4th AIAA/ASME Heat Transfer Conference, Boston, Massachusetts, June 2-4, 1986. Manuscript received by the Heat Transfer Division February 14, 1986.

A solution for equation (1) satisfying the boundary conditions can be constructed by forming a series using as basis functions the eigenfunctions of the linear part of equation (1)

$$\phi(\tau, \zeta, \xi) = \sum_{n=1}^{\infty} \sum_{j=0}^{\infty} \Phi_{nj}(\tau) \sin n\pi\zeta \cos j\pi\xi \tag{2}$$

Substitution of the series in equation (2), truncated with $n+j \leq N$ where N is a positive integer referred to as the truncation number, into equation (1) leads to a set of nonlinear differential equations describing the temporal behavior of the Φ_{nj}. In the interest of computational efficiency, a further restriction on the ϕ_{nj} has been applied. The sum $(n+j)$ has been taken as an even integer, so that N is also even. As discussed in detail in [5], this restriction is equivalent to imposing certain physically plausible assumptions of symmetry of the flow. Numerical calculations made without applying this condition indicate that these symmetries, in fact, do characterize the flow for $\mathrm{Ra} \leq 800$. All of the calculations reported here were carried out with $N=26$. In general, these equations have been integrated forward in time using the pseudospectral method first suggested in [9, 10]. The advantage of this procedure, as compared with the direct approach taken in [8], is that the evaluation of spatial derivatives is more accurate in spectral space than in physical space whereas the evaluation of the nonlinear terms in equation (1) is more efficient in physical space than in spectral space.

The Nusselt number Nu is the ratio of the horizontally averaged upward heat flux to that which would occur by conduction alone in the absence of convection. Because we take $w=0$ at the horizontal boundaries, all of the heat flux must be carried by conduction there, and we can calculate Nu from

$$\mathrm{Nu}(\tau) = 1 - \sum_{n=1}^{N} \frac{n^3\pi^3}{\mathrm{Ra}} \Phi_{n0}(\tau) \tag{3}$$

The nature of the time-dependent convection will be characterized by the spectral content of the Nusselt number time series.

3 The Transition S→P(1)

In order to study the transition S→P(1), we consider the stability of solutions of equation (1) with the left side of the equation set identically to zero. With expression (2) substituted into equation (1), the steady state is represented by a set of nonlinear algebraic equations $E_{nj}=0$. Once the Φ_{nj} which satisfy these equations have been found using a Newton-Raphson scheme, the transition S→P(1) can be investigated by applying small perturbations to the values of the Φ_{nj}

$$\Phi_{nj} = \Phi_{nj}^{(0)} + \delta_{nj} e^{(\sigma_r + i\sigma_i)t} \tag{4}$$

where $\Phi_{nj}^{(0)}$ = base (steady) state values and δ_{nj} is a perturbation. Substitution of this expression into equation (2) and then into equation (1) and linearization (with the δ_{nj} considered to be small) leads to a matrix whose eigenvalues are the σ's. By writing $\epsilon_{ij} = \delta_{ij} \exp(\sigma_{ij} t)$, we obtain the following explicit representation for the variational equation

$$\dot{\epsilon}_{ij} = J_{ijkl} \epsilon_{kl} \tag{5}$$

where J_{ijkl} is the Jacobian matrix evaluated from $\Phi_{nj}^{(0)}$ in equation (4). These eigenvalues give the growth (damping) rates (σ_r) and frequencies ($f = |\sigma_i|/2\pi$) of possible time-dependent flows to which the steady-state solution is unstable. Thus, the transition S→P(1) is indicated by σ_r changing from negative to positive as a function of Ra with $\sigma_i \neq 0$ (a Hopf bifurcation). Our computer codes were tested by evaluating the critical Rayleigh number for the onset of convection from a motionless basic state. In this case, the actual value $\mathrm{Ra}_c = 4\pi^2$ for a square cross section was found to an accuracy of 0.05 percent. (In this case, of course, $\sigma_i = 0$.)

Figure 1 shows the situation, in the σ_r–σ_i plane, for the S→P(1) transition. The calculations were carried out at Ra = 370, 380, and 390 with the truncation parameter $N=26$. This value of N is larger than that used in previous work at these values of Ra and therefore should lead to very accurate results. The eigenvalues occur as complex-conjugate pairs, and, in this case, there are two sets of pairs with values of σ_r near zero (and none at larger positive values). A single pair of eigenvalues approaches the vertical axis from the left as Ra ap-

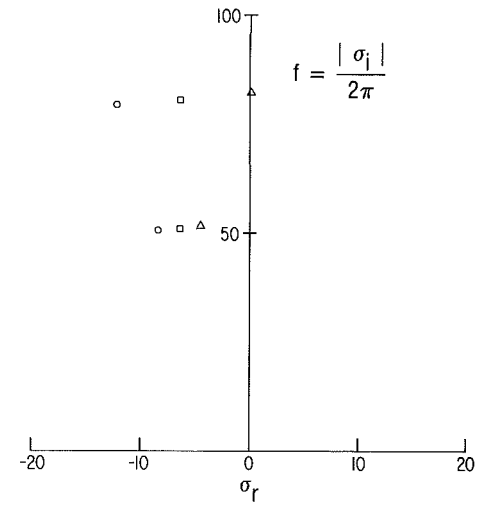

Fig. 1 Results of the eigenanalysis for the S→P(1) transition: ○ Ra = 370, □ Ra = 380, Δ Ra = 390

Nomenclature

c = specific heat of fluid
d = thickness of square cross section of porous medium
f = frequency
g = gravitational acceleration
k = average thermal conductivity of fluid and solid matrix
J = Jacobian
K = permeability of solid matrix
N = truncation number
Nu = Nusselt number
Ra = Rayleigh number
ΔT = excess temperature of bottom boundary relative to top boundary
u = horizontal velocity
w = vertical velocity
α = thermal expansion coefficient of the fluid
δ_{nj} = perturbations to Φ_{nj}
ϵ_{ij} = perturbations to Φ_{nj}
ζ = nondimensional vertical coordinate
μ = fluid viscosity
ξ = nondimensional horizontal coordinate
ρ = fluid density
σ = complex eigenvalue for the time dependence of perturbations to Φ_{nj}; σ_r (real part) is the growth rate, σ_i (imaginary part) is the circular frequency
τ = nondimensional time
ϕ = velocity potential
Φ_{nj} = coefficients of expansion for ϕ

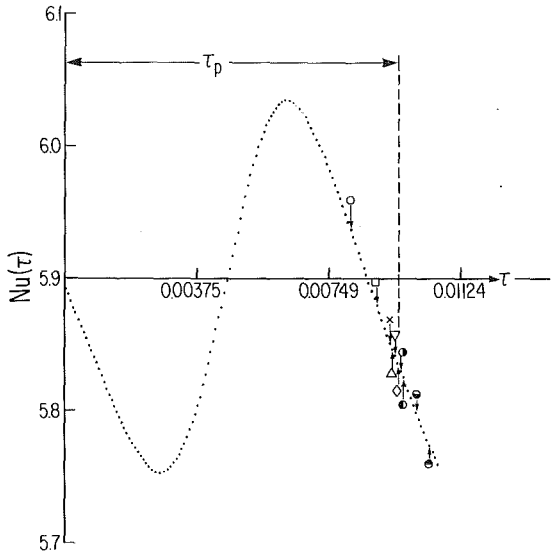

Fig. 2 Nu versus τ for one cycle of oscillation at Ra = 510. The symbols identify the locations in τ at which averaging of the Φ_{nj} was terminated for the eigenanalysis illustrated in Fig. 3. τ_p is the period of oscillation.

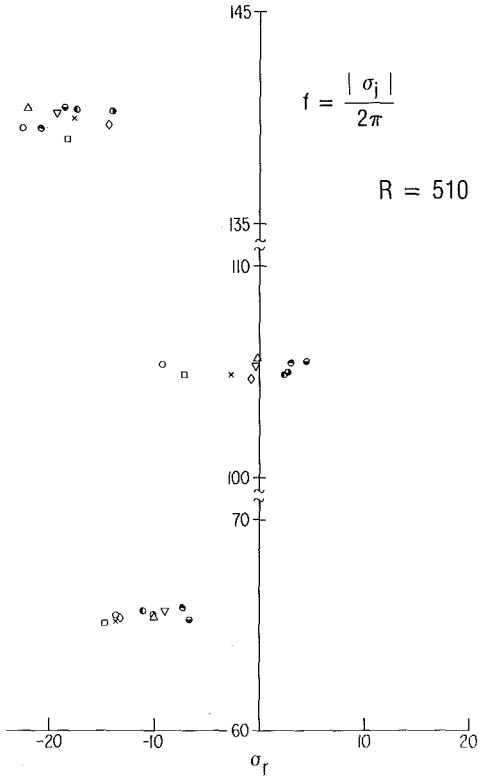

Fig. 3 Results of the eigenanalysis at Ra = 510; the symbols correspond to those in Fig. 2

proaches 390. The value Ra = 389.7 is thereby derived for the $S \rightarrow P^{(1)}$ transition, in excellent agreement with that derived in previous work [4, 6]. The corresponding oscillation frequency f is $|\sigma_i|/2\pi = 82.5$. This is approximately 1–2 percent of the diffusion time defined by pcd^2/k. This value confirms the earlier results described in [6, 7].

4 The Transitions $P^{(1)} \rightarrow QP_2^{(1)}$ and $QP_2^{(1)} \rightarrow P^{(2)}$ and the Frequency Discontinuity $P^{(2)} \rightarrow P^{(3)}$

The $P^{(1)}$ state exists for Ra exceeding ≈ 390. As Ra is increased further, the transition $P^{(1)} \rightarrow QP_2^{(1)}$ is indicated by the appearance of a second complex conjugate pair of eigenvalues with $\sigma_r > 0$. However, since the basic state in this case is time-dependent, rather than steady, the eigenvalues are time-dependent and the analysis is more complicated. Although there exists a general mathematical statement (the Floquet theorem) regarding the stability of a periodic solution, the application of this theorem to determine the stability of general systems such as equation (5) is extremely difficult. Instead, we extend our previous analysis for the stability of the steady-state case by hypothesizing that the $P^{(1)}$ state is stable if for all σ_k (except the pair of complex-conjugate eigenvalues of equation (5) corresponding to the basic oscillation)

$$\psi_k(T) = \exp(\bar{\sigma}_k T) < 1 \tag{6}$$

where

$$\bar{\sigma}_k = \frac{1}{T}\int_0^T \sigma_k(\tau)d\tau \tag{7}$$

and T is the period of oscillation of the $P^{(1)}$ state. The implementation of expressions (6) and (7) appears to be relatively straightforward. However, accurate evaluation of $\psi_k(T)$ requires the calculation of the σ_k at a large number of values of τ; this, in turn, still requires a substantial amount of computing. A more economical approach would be to make use of a set of time-averaged spectral coefficients as a base state

$$\bar{\Phi}_{nj} = \frac{1}{T}\int_0^T \Phi_{nj}(\tau)d\tau \tag{8}$$

and then apply the stability analysis described above. We tested this approach with the $P^{(1)}$ state at Ra = 510. Figure 2 shows a single oscillation of Nu and the positions in τ at which the time-averaging process (initiated at $\tau = 0$) was terminated for the calculation of the eigenvalues shown in Fig. 3. As τ approaches the period T, a single pair of complex-conjugate eigenvalues crosses the imaginary axis, so that $\sigma_r > 0$. The predicted frequency, $f \approx 105$, agrees exactly with the numerical simulations reported previously in [7].

More detail regarding this transition is given in Figs. 4–6, which show the results of the eigenvalue analysis at Ra = 500, 510, and 520, respectively. (The direct numerical simulations reported in [7] indicate that the $P^{(1)} \rightarrow QP_2^{(1)}$ transition takes place with Ra somewhere between 510 and 520.) In each figure, the eigenvalues calculated using the time-averaged set of Φ_{nj} are shown as solid dots, while the other symbols indicate instantaneous eigenvalues calculated during a single oscillation. Intercomparison of these three figures shows clearly the trend of σ_r to become positive with increasing Ra. The majority of the instantaneous eigenvalues at Ra = 520, which is already in the $QP_2^{(1)}$ state, have positive real parts. The frequencies ($|\sigma_i|/2\pi$) of $\approx$ 110 and $\approx$ 140 at Ra = 520 agree with those found by direct numerical integration (Fig. 7), which also shows power at a frequency of $\approx$ 30. The eigenanalysis, then, indicates that the frequencies $f = 110$ and 140 are fundamental, while $f \approx 30 \approx 140 - 110$ is due to frequency locking. The third frequency in Figs. 4–6, $f \approx 65$, is seen to be of little importance in Fig. 7; this can be understood by noting that the eigenvalues with $f \approx 65$ generally have $\sigma_r < 0$.

It is known from our earlier numerical experiments that a transition from the $QP_2^{(1)}$ state to another simply periodic state $P^{(2)}$ takes place somewhere between Ra = 560 and Ra = 570. Figures 8 and 9 show this clearly. The eigenvalues with the largest real parts ($f \approx 155$) at Ra = 560 (Fig. 8) continue to have $\sigma_r > 0$ at Ra = 570 (Fig. 9), while those with $f \approx 120$ retreat to the negative σ_r half-plane as Ra increases from 560 to 570. This is a clear indication of the reverse transition $QP_2^{(1)} \rightarrow P^{(2)}$ and shows that the frequency of the $P^{(2)}$ regime begins at $f \approx 155$.

The $P^{(2)}$ state exists for values of Ra up to $\approx$ 625, where

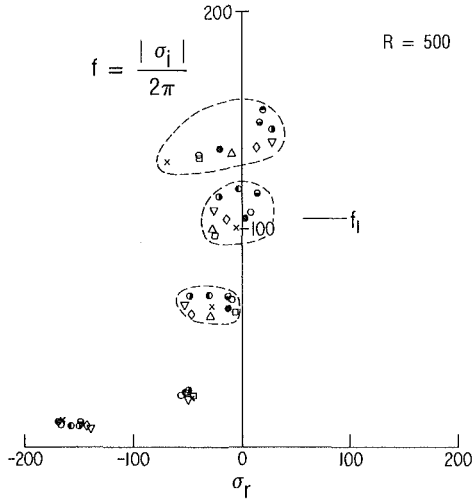

Fig. 4 Results of the eigenanalysis at Ra = 500. The open symbols give instantaneous eigenvalues at various places within a single oscillation, while the solid circles are the eigenvalues obtained using Φ_{nj}. f_1 is the frequency obtained in a direct numerical integration.

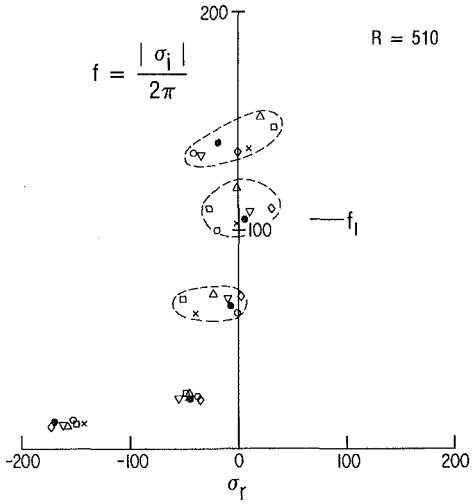

Fig. 5 Same as Fig. 4, but for Ra = 510

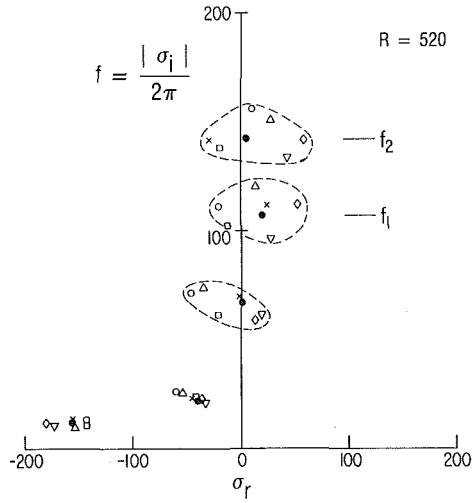

Fig. 6 Same as Fig. 5, but for Ra = 520; f_1 and f_2 indicate the frequencies obtained from numerical experiments

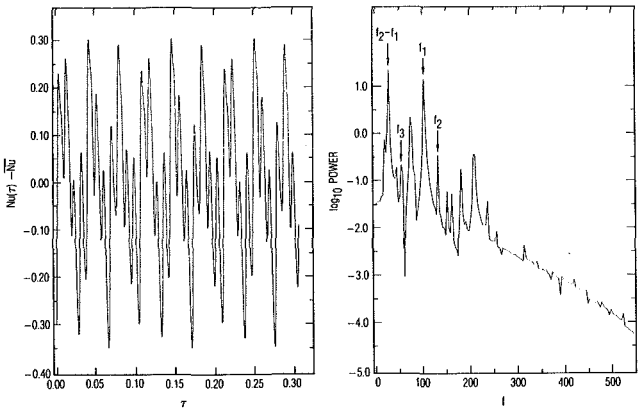

Fig. 7 The time series $Nu(\tau)-\overline{Nu(\tau)}$ and its power spectrum at Ra = 520

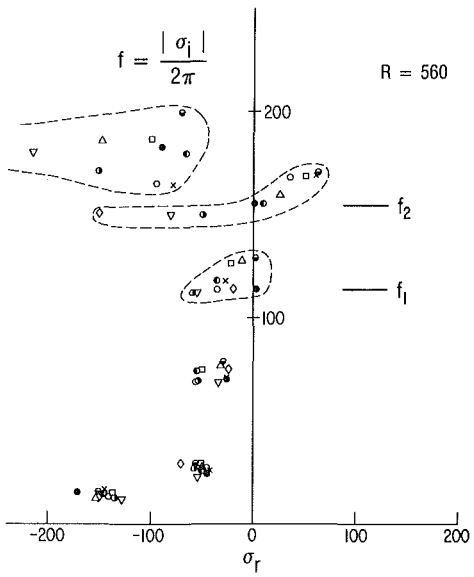

Fig. 8 Same as Fig. 4, but for Ra = 560, which is in the $QP_2^{(1)}$ state

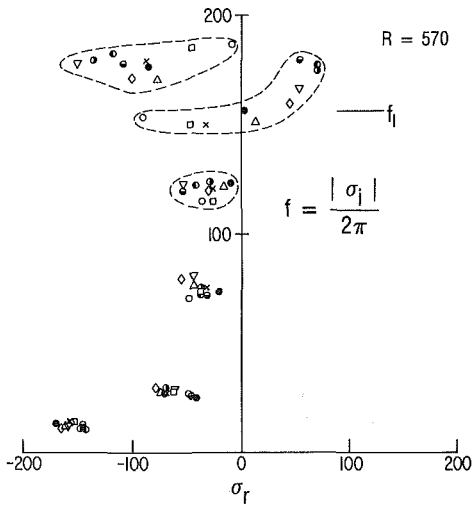

Fig. 9 Same as Fig. 4, but for Ra = 570, which is in the $P^{(2)}$ state

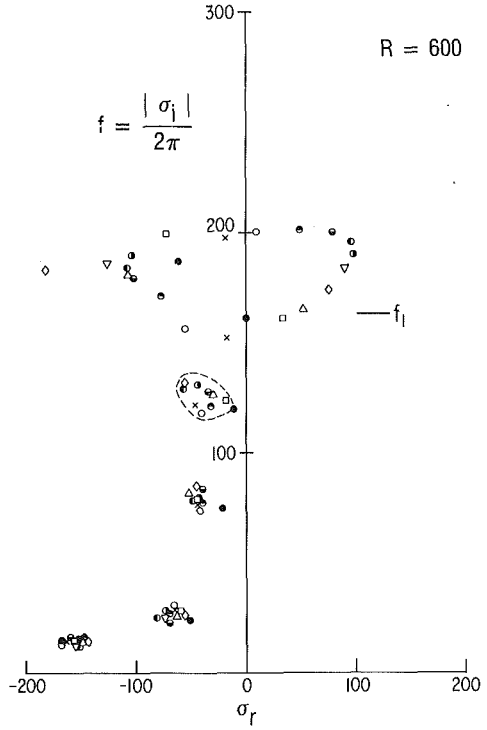

Fig. 10 Same as Fig. 4, but for a $P^{(2)}$ state with Ra = 600

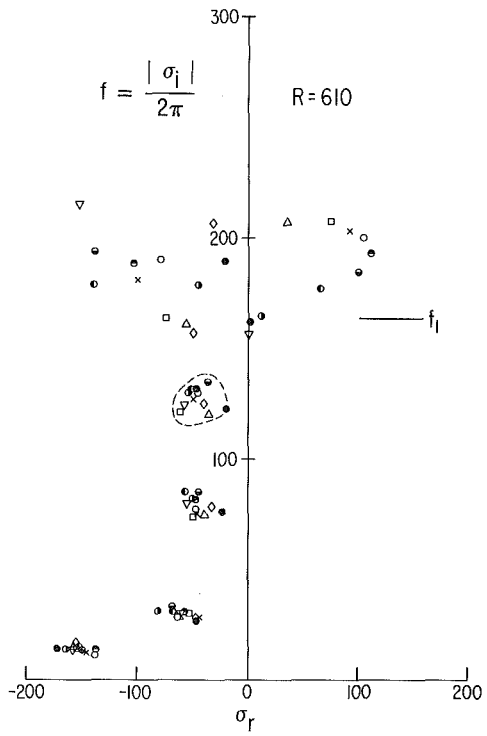

Fig. 11 Same as Fig. 4, but for a $P^{(2)}$ state with Ra = 610

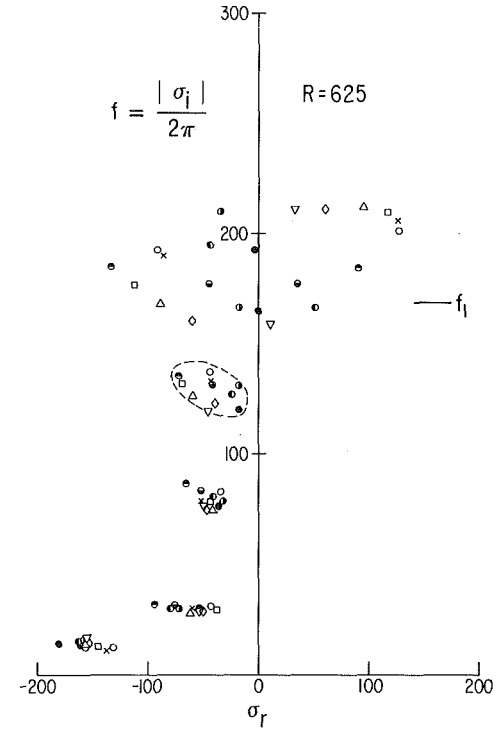

Fig. 12 Same as Fig. 4, but for a $P^{(2)}$ state with Ra = 625

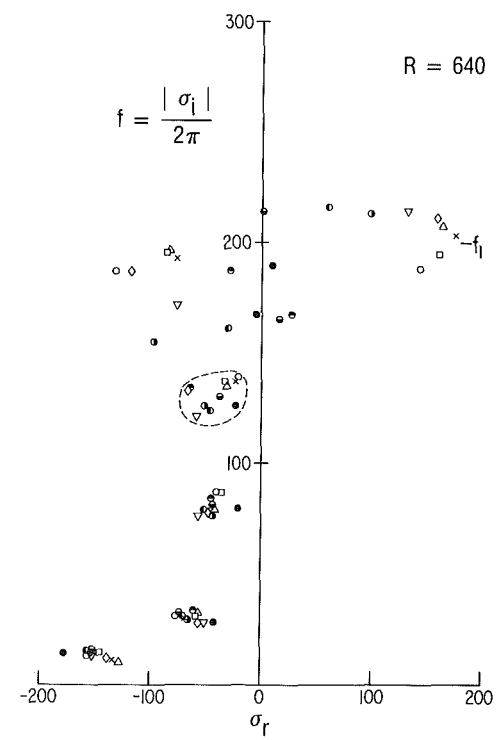

Fig. 13 Same as Fig. 4, but for a $P^{(3)}$ state with Ra = 640

another event occurs. To see this clearly, we show, in Figs. 10–13, the behavior of the eigenvalues in the range Ra = 600 to 640. Immediately obvious is that the two sets of eigenvalues identified in the Ra = 560–570 range, with frequencies of ≈ 120 and ≈ 150, have increased in frequency and have overlapped in the frequency range 160–220. The eigenvalues based on the time-averaged Φ_{nj} appear with frequencies ≈ 190 and ≈ 165; the former has σ_r increasing as Ra increases, while the latter has σ_r decreasing with increasing Ra. Comparison of the solid dots in Figs. 12 and 13 shows that a transition from the $P^{(2)}$ state, with $f \approx 165$, takes place at a value of Ra ≈ 630. Thus, the eigenanalysis points to a discontinuity in the frequency trend. Additional direct numerical integrations indicate that this discontinuity takes place via a second quasi-periodic $QP_2^{(2)}$ state which exists in a narrow range of values of Ra near Ra = 630.

5 Summary and Conclusions

We have described a practical method for studying transitions from steady to periodic states and from periodic to quasi-periodic flows. We have applied the procedure to thermal convection in a square cross section of fluid-saturated porous material heated from below. Both the Rayleigh numbers at which these transitions occur and the characteristics of the temporal behavior at the transitions have been investigated. We have established the following transition sequence

$$S \rightarrow P^{(1)} \rightarrow QP_2^{(1)} \rightarrow P^{(2)} \rightarrow QP_2^{(2)} \rightarrow P^{(3)}$$

A further transition, to a nonperiodic (chaotic) NP state, has been observed in the numerical experiments at $Ra \approx 900$ reported in [7]. This transition is characterized by the growth of Φ_{nj} with $(n+j)$ equal to an odd integer; the restriction, used in the present analysis, that $(n+j)$ be even precludes the study of this transition using the procedures which we have developed. This transition will be studied using an extended eigenanalysis procedure in the future.

The method described herein should be applicable in many other situations in which the stability of a time-dependent state is of interest. Although not based on a rigorous mathematical foundation, the concept of evaluating the stability of the time-mean state of a time-dependent flow appears to be useful, as indicated by the excellent agreement between the results of the present analysis for the $P^{(1)} \rightarrow QP_2^{(2)}$ transition and the direct numerical integration of the full equation (1).

Acknowledgments

This work was supported by NSF Grant MEA82-18600 at UCLA and by the Aerospace-Sponsored Research Program.

References

1 Combarnous, M., and Le Flur, B., "Transfert de Chaleur par Convection Naturelle dans une Couche Poreuse Horizontale," *C. R. Acad. Sci. Paris*, Vol. 269B, Oct. 1969, pp. 1009–1012.

2 Caltagirone, J. P., Cloupeau, M., and Combarnous, M., "Convection Naturelle Fluctuate dans une Couche Poreuse Horizontale," *C. R. Acad. Sci.*, Vol. 273B, Feb. 1971, pp. 258–262.

3 Horne, R. N., and O'Sullivan, M. J., "Oscillatory Convection in a Porous Medium Heated From Below," *J. Fluid Mech.*, Vol. 66, Nov. 1974, pp. 339–352.

4 Caltagirone, J. P., "Thermoconvective Instabilities in a Horizontal Porous Layer," *J. Fluid Mech.*, Vol. 72, Nov. 1975, pp. 269–287.

5 Schubert, G., and Straus, J. M., "Three-Dimensional and Multicellular Steady and Unsteady Convection in Fluid-Saturated Porous Media at High Rayleigh Number," *J. Fluid Mech.*, Vol. 94, Sept. 1979, pp. 25–38.

6 Schubert, G., and Straus, J. M., "Transitions in Time-Dependent Thermal Convection in Fluid-Saturated Porous Media," *J. Fluid Mech.*, Vol. 121, Aug. 1982, pp. 301–313.

7 Kimura, S., Schubert, G., and Straus, J. M., "Route to Chaos in Porous Medium Thermal Convection," *J. Fluid Mech.*, Vol. 166, June 1986, pp. 305–324.

8 Straus, J. M., "Large Amplitude Convection in Porous Media," *J. Fluid Mech.*, Vol. 64, June 1974, pp. 51–63.

9 Orszag, S. A., "Numerical Simulation of Incompressible Flows Within Simple Boundaries," *Stud. in Appl. Math.*, Vol. 50, Dec. 1971, pp. 293–327.

10 Gottlieb, D., and Orszag, S. A., *Numerical Analysis of Spectral Methods: Theory and Applications*, SIAM, 1977.

J. T. Hong[1]
Graduate Research Assistant.

Y. Yamada
Visiting Scholar.

C. L. Tien
Professor.
Fellow ASME

Department of Mechanical Engineering
University of California,
Berkeley, CA 94720

Effects of Non-Darcian and Nonuniform Porosity on Vertical-Plate Natural Convection in Porous Media

This work examines analytically the effects of non-Darcian and nonuniform permeability conditions on the natural convection from a vertical plate in porous media. The non-Darcian effects, which include the no-slip and inertia effects, decrease the flow and heat transfer rate, while the nonhomogeneity effect enhances the heat transfer. For packed spheres, in particular, the nonhomogeneity in permeability due to the packing of spheres near the solid wall results in a strong flow-channeling effect that significantly increases the heat transfer. The effect of transverse thermal dispersion is also examined. This dispersion effect causes an increase in the heat transfer.

Introduction

Natural convection in a porous medium has attracted considerable attention in several areas. These include geophysics, oil recovery techniques, thermal insulation engineering, packed-bed catalytic reactors, and heat storage beds. Excellent review articles are provided by Cheng [1, 2] and Combarnous [3]. Most of existing analytical studies for natural convection in porous media are based on Darcy's law which cannot account for the no-slip boundary condition at the interface between the porous media and the solid wall. The neglect of the no-slip condition has little effect on the pressure drop calculations, since the major part of the pressure drop is due to the porous medium. This may not be the case for heat transfer which consists primarily of boundary phenomena. When heat transfer is considered, the modification of the velocity profile in the near-wall region due to the no-slip boundary condition may have noticeable effects on the heat transfer. To account for the no-slip wall effect, Brinkman's extension of Darcy's law [4] should be used. Darcy's law also becomes inadequate when the flow Reynolds number based on the mean pore diameter is of the order of one or greater, because the inertia force is no longer negligible in comparison to the viscous force [5]. The non-Darcian effects, i.e., the no-slip wall and inertia effects, on forced convection heat transfer were analyzed by Vafai and Tien [6] for constant-porosity media. Both the wall and inertia effects decrease the velocity in the thermal boundary layer, broaden the temperature distribution, and reduce the heat transfer rate. These non-Darcian effects should exhibit the same influence on the natural convection heat transfer.

In some applications, the permeability of the porous medium is not uniform. The nonhomogeneity in permeability due to the porosity variation can be found particularly in packed beds of spheres. The measurements of Benenati and Brosilow [7] show a distinct porosity variation with a high-porosity region close to the solid wall in packed beds. The variable porosity near an impermeable boundary leads to the occurrence of a maximum velocity close to the boundary. This wall-channeling phenomenon has been reported by a number of investigators such as Schertz and Bishoff [8], Schwartz and Smith [9], and was numerically predicted by Chandrasekhara and Vortmeyer [10] for isothermal packed beds. Very few works [11] have been conducted to investigate this effect on heat transfer, which depends strongly on flow behavior near the boundary. The present analytical study will consider this nonuniform porosity effect together with the non-Darcian effects for flat-plate natural convection heat transfer in porous media. A similar but simpler problem was analyzed for the first time by Cheng and Minkowycz [12] who employed Darcy's law and the boundary layer approximation to get a similarity solution for a power law variation of surface temperature. Later, the inertia effect on heat transfer was considered by Plumb and Huenefeld [13]. The effect due to the no-slip boundary condition was studied by several investigators [14, 15] where Brinkman's extension of Darcy's law was employed. In the case when inertia effects are prevalent, the transverse thermal dispersion effect is expected to become important. Plumb [16] studied this dispersion effect on both forced and buoyancy-induced boundary layers with slip boundary condition at the wall. The present analytical study discusses all the abovementioned non-Darcian and nonhomogeneity effects on flow and heat transfer in packed-sphere beds, showing that the nonhomogeneity effect is dominating among them. The dispersion effect is also studied with the no-slip boundary condition included. The results show that the heat transfer is increased due to the transverse thermal dispersion. This is similar to what has been found by Plumb [16]. However, due to the inclusion of the no-slip wall effect, present results show smaller values in heat transfer compared to Plumb's results when the nonhomogeneity effect is not included.

Mathematical Formulations

Consider the basic problem of the buoyant boundary layer flow along a heated vertical plate with temperature T_w embedded in a fluid-saturated porous medium with temperature T_∞. The coordinate along the plate is denoted by x and that perpendicular to it is denoted by y. The following common assumptions are made for the formulation: The fluid and the porous medium are in local thermal equilibrium; and the Boussinesq approximation is valid. The porosity ϵ is also assumed to vary exponentially with the distance y from the wall as an approximation to account for the effect of the nonhomogeneity such as in packed beds of spheres [7]

$$\epsilon = \epsilon_\infty [1 + \xi \exp(-\zeta y/d)] \tag{1}$$

where ξ and ζ are empirical constants which depend on the packing of the spheres near the solid boundary and d is the sphere diameter. Both ξ and ζ must be determined experimen-

[1]Present address: Department of Mechanical Engineering, Tatung Institute of Technology, Taipei, Taiwan, Republic of China.

Contributed by the Heat Transfer Division for publication in the JOURNAL OF HEAT TRANSFER. Manuscript received by the Heat Transfer Division July 16, 1984.

tally. In the present study, the value for ξ is chosen so that the porosity at wall is equal to ϵ_w, which is the average porosity for the region of one half diameter from the wall. The value for ζ is determined so that the porosity variation is similar to that obtained by the experiments [7]. The present study neglects the oscillations of the porosity, which are considered to be secondary. The emphasis here is on the decay of the porosity from the solid boundary, which has the primary effect.

Based on the above assumptions, the governing equations, which are derived by using volume-averaged principles and empirical results [6, 17], are given by

$$\frac{\partial u}{\partial x}+\frac{\partial v}{\partial y}=0 \tag{2}$$

$$\frac{\mu u}{K(y)}+\rho C(y)u^2=-\frac{\partial p}{\partial x}+\rho g\beta(T-T_\infty)+\frac{\mu}{\epsilon}\nabla^2 u \tag{3}$$

$$\frac{\mu v}{K(y)}+\rho C(y)v^2=-\frac{\partial p}{\partial y}+\frac{\mu}{\epsilon}\nabla^2 v \tag{4}$$

$$u\frac{\partial T}{\partial x}+v\frac{\partial T}{\partial y}=\nabla\cdot(\alpha_e\nabla T) \tag{5}$$

where u and v are the velocity components in the x and y directions; T, P, and g are the temperature, pressure, and the gravitational constant; ρ, μ, and β are the density, viscosity, and thermal expansion coefficient of the fluid; $\alpha_e=k_e/(\rho_f c_f)$ is the effective thermal diffusivity of the porous medium with $\rho_f c_f$ denoting the product of density and specific heat of the fluid, and k_e is the effective thermal conductivity of the saturated porous medium; $K(y)$ and $C(y)$ are the permeability and the inertia coefficient of the porous medium and are represented respectively by the well-known correlations [18]

$$K=\frac{d^2\epsilon^3}{150(1-\epsilon)^2} \tag{6}$$

$$C=\frac{1.75(1-\epsilon)}{\epsilon^3 d} \tag{7}$$

The second and last terms in equations (3) and (4) account for the inertia and no-slip effects in the porous medium respectively. It should also be noted that a convective term $\rho\mathbf{u}\cdot\nabla\mathbf{u}$ has already been neglected in the present analysis. This follows the suggestions by Vafai and Tien [6] as well as by Catton [17].

The effective thermal diffusivity α_e in equation (5) is assumed to have two components, i.e., $\alpha_e=\alpha_0+\alpha'$, where α_0 is the effective molecular thermal diffusivity and α' is the effective thermal diffusivity due to the transverse thermal dispersion. The dispersion thermal diffusivity is known to be a complicated function of velocity [5]. Following the assumption employed by Plumb [16], the dispersion diffusivity is assumed to be proportional to the streamwise velocity components, i.e., $\alpha'=\gamma u d$, where γ may be expected to vary from approximately 1/7 to 1/3.

The boundary conditions for equations (2)–(5) are

$$u=v=0,\ T_w=T_\infty+E\ x^n \text{ at } y=0 \tag{8}$$

$$u=0,\ T\to T_\infty \text{ at } y\to\infty \tag{9}$$

where the wall temperature of the plate is assumed to be a power law function of distance x from the origin with constant coefficient E.

The continuity equation is automatically satisfied by introducing the stream function ψ as

$$u=\frac{\partial\psi}{\partial y},\qquad v=-\frac{\partial\psi}{\partial x} \tag{10}$$

Boundary Layer Solution

Let δ_m and δ_t be the scales for the momentum and thermal boundary layer thicknesses, and consider $\delta_m<<\delta_t<<x$. Then the order-of-magnitude scaling analysis shows

$$u\sim O(\rho g\beta\Delta T K_\infty/\mu)\sim O(\alpha_0\hat{\mathrm{Ra}}_x/x) \tag{11}$$

$$\delta_m\sim O(K_\infty^{0.5}) \tag{12}$$

$$\delta_t\sim O\left(\frac{x}{\hat{\mathrm{Ra}}_x^{0.5}}\right) \tag{13}$$

$$\psi\sim O(\alpha_0\hat{\mathrm{Ra}}_x^{0.5}) \tag{14}$$

where $\Delta T=T_w-T_\infty$ and $\hat{\mathrm{Ra}}_x=\rho g\beta\Delta T K_\infty x/\mu\alpha_0$ is the local

Nomenclature

C = inertia coefficient, equation (7)
Da_x = local Darcy number = K_∞/x^2
d = particle diameter
E = constant, equation (8)
f = dimensionless stream function
$\hat{\mathrm{Gr}}$ = modified Grashof number = $\rho^2 g\beta(T_w-T_\infty)K_\infty^2 C_\infty/\mu^2$
g = gravitational constant
h = heat transfer coefficient
K = permeability
k_e = effective conductivity
L_h = characteristic length for the porosity variation near the wall
Nu_x = Nusselt number
n = constant, equation (8)
p = pressure
q = local heat flux
$\hat{\mathrm{Ra}}_x$ = local Darcy-Rayleigh number = $\rho g\beta(T_w-T_\infty)K_\infty x/\mu\alpha_0$
$\hat{\mathrm{Ra}}_d$ = Darcy-Rayleigh number based on particle diameter = $\rho g\beta(T_w-T_\infty)K_\infty d/\mu\alpha_0$
T = temperature
u = velocity parallel to surface
v = velocity normal to surface
x = streamwise coordinate
y = cross-stream coordinate
α_e = effective thermal diffusivity
α_0 = effective molecular thermal diffusivity
α' = effective thermal diffusivity due to dispersion
β = coefficient of thermal expansion
γ = thermal dispersion coefficient
δ_m = hydrodynamic boundary layer thickness
δ_t = thermal boundary layer thickness
ϵ = porosity
ζ = porosity-variation parameter, equation (1)
η = dimensionless cross-stream coordinate
η_d = dimensionless particle diameter
η_T = dimensionless thermal boundary layer thickness
θ = dimensionless temperature
μ = fluid viscosity
ξ = porosity-variation parameter, equation (1)
ρ = fluid density
ψ = stream function

Subscripts

∞ = at a distance from the wall
w = evaluated at wall

Superscripts

$'$ = differentiation with respect to η

Darcy-Rayleigh number based on the permeability K_∞ in the bulk region. Boundary layer approximations reduce equations (3)-(5) to

$$\frac{\mu u}{K(y)} + \rho C(y) u^2 = -\frac{\partial p}{\partial x} + \rho g\beta(T - T_\infty) + \frac{\mu}{\epsilon}\frac{\partial^2 u}{\partial y^2} \quad (15)$$

$$u\frac{\partial T}{\partial x} + v\frac{\partial T}{\partial y} = \frac{\partial}{\partial y}\left(\alpha_e \frac{\partial T}{\partial y}\right) \quad (16)$$

Equations (13) and (14) suggest the following nondimensional variables

$$\eta = \frac{y}{\delta_t} = \frac{y}{x}\hat{\mathrm{Ra}}_x^{0.5} \quad (17)$$

$$f = \frac{\psi}{\alpha_0 \hat{\mathrm{Ra}}_x^{0.5}} \quad (18)$$

and the nondimensional temperature can be defined as

$$\theta = \frac{T - T_\infty}{T_w - T_\infty} \quad (19)$$

In terms of these new variables, the velocity components are given by

$$u = \frac{\alpha_0 \hat{\mathrm{Ra}}_x}{x} f' \quad (20)$$

$$v = -\alpha_0 \hat{\mathrm{Ra}}_x^{0.5}\left[\frac{\partial f}{\partial x} + (n+1)\frac{f}{2x} - (n-1)\frac{\eta}{2x}\frac{\partial f}{\partial \eta}\right] \quad (21)$$

and the boundary layer equations can be transformed into local similarity equations

$$-\frac{\mathrm{Da}_x \hat{\mathrm{Ra}}_x}{\epsilon} f''' + \left(\frac{K_\infty}{K}\right) f' + \left(\frac{C}{C_\infty}\right)\hat{\mathrm{Gr}}(f')^2 = \theta \quad (22)$$

$$(1 + \gamma \hat{\mathrm{Ra}}_d f')\theta'' + \left(\frac{1+n}{2} f + \gamma \hat{\mathrm{Ra}}_d f''\right)\theta' - n f'\theta = 0 \quad (23)$$

where $\hat{\mathrm{Ra}}_d = g\beta\Delta T K_\infty d/\nu\alpha_0$.

The above equations are subjected to the following dimensionless boundary conditions

$$f(\mathrm{O}) = f'(\mathrm{O}) = \theta(\mathrm{O}) - 1 = \mathrm{O} \quad (24)$$

$$f'(\infty) = \theta(\infty) = \mathrm{O} \quad (25)$$

where the primes indicate differentiation with respect to η.

The modified Grashof number $\hat{\mathrm{Gr}}$ and the local Darcy number Da_x in equation (22) are defined as

$$\hat{\mathrm{Gr}} = \rho^2 g\beta\Delta T K_\infty^2 C_\infty/\mu^2 \quad (26)$$

$$\mathrm{Da}_x = K_\infty/x^2 \quad (27)$$

The local heat transfer rate along the surface of the flat plate can be computed from

$$q = -k_e \frac{\partial T}{\partial y}\Big|_{\mathrm{o}} \quad (28)$$

where k_e is the effective conductivity of the porous media. With the aid of equations (17), (19), and (8), equation (28) can be rewritten as

$$q = k_e E^{1.5}\left(\frac{\rho g\beta K_\infty}{\mu\alpha_0}\right)^{0.5} x^{(3n-1)/2}[-\theta'(x, \mathrm{O})] \quad (29)$$

It is noted that with the no-slip wall effect neglected, $n = 1/3$ corresponds to the case of constant wall heat flux [12]. When the wall effect is considered, $n = 1/3$ no longer represents the constant wall heat flux case. However, since the wall effect is usually very small, the heat flux for $n = 1/3$ is only a weak function of x. For the present study, only the results for the constant wall temperature ($n = 0$) will be presented.

The heated transfer results can be represented by the Nusselt number Nu_x, which is defined as $\mathrm{Nu}_x = hx/k_0 = qx/k_0(T_w - T_\infty)$, where h is the local heat transfer coefficient. The definition of the Nusselt number and equation (29) combine to give

$$\mathrm{Nu}_x/\hat{\mathrm{Ra}}_x^{0.5} = -\frac{\alpha_e}{\alpha_0}\theta'(x, \mathrm{O}) \quad (30)$$

Note that the no-slip wall effect introduces nonsimilarity. The heat transfer parameter, $\mathrm{Nu}_x/\hat{\mathrm{Ra}}_x^{0.5}$, varies with the distance x. In the limiting case without the wall effect, the heat transfer parameter becomes a constant along the plate.

Numerical solutions for equations (22) and (23) with the boundary conditions (24) and (25) have been obtained by using a modified version of the adaptive finite difference solver (PASVAR) [19]. The method employs deferred corrections and adaptive meshes are automatically produced in order to detect and resolve mild boundary layers and other sharp gradient situations. The next section presents numerical results with a focus on the wall, inertia and nonhomogeneity effects by neglecting the dispersion effect. Results on dispersion effects will then follow.

Table 1 Range of variables used in numerical computations

d, mm	ϵ_∞	ξ	ζ	$T_w - T_\infty$	α_e	T_m	Results
3	0.371	0.35	3	15.4, 29.4 43.8, 80.0	1.338 α_f	30.0, 37.0 44.2, 52.0	Table 2
5	0.390	0.43	3	10.0, 60.0	3.750 α_f	23.0, 50.0	Table 3

Table 2 Numerical results for $\mathrm{Nu}_x/\hat{\mathrm{Ra}}_x^{0.5} = -\theta'(x, \mathrm{O})$, $d = 3$ mm

$\hat{\mathrm{Gr}}$	x, mm	$\mathrm{Da}_x\hat{\mathrm{Ra}}_x \times 10^4$	WnIH	WIH	WnInH	WInH	nWnIH	nWIH	nWnInH	nWInH
0.087	15	28.43	0.420	0.410	0.552	0.526	0.444	0.432	0.671	0.611
	51	8.36	0.431	0.420	0.529	0.504				
	189	2.26	0.437	0.425	0.499	0.478				
	441	1.05	0.439	0.427	0.485	0.465				
0.197	15	55.26	0.412	0.393	0.555	0.510	0.444	0.419	0.710	0.596
	51	16.25	0.426	0.404	0.543	0.495				
	189	4.39	0.434	0.411	0.514	0.470				
	441	1.88	0.437	0.414	0.495	0.455				
0.542	15	130.1	0.398	0.362	0.544	0.467	0.444	0.391	0.755	0.548
	51	38.28	0.417	0.374	0.554	0.462				
	189	10.3	0.429	0.382	0.534	0.442				
	441	4.43	0.434	0.385	0.514	0.429				

Table 3 Numerical results for $Nu_x/\hat{Ra}_x^{0.5} = -\theta'(x, O)$, $d = 5$ mm

$\hat{Gr}$	x, mm	$Da_x\hat{Ra}_x \times 10^4$	WnIH	WIH	WnInH	WInH	nWnIH	nWIH	nWnInH	nWInH
0.064	30	10.35	0.429	0.421	0.558	0.535	0.444	0.435	0.761	0.687
	100	3.11	0.436	0.427	0.522	0.501				
	250	1.24	0.439	0.430	0.498	0.481				
	500	0.62	0.440	0.431	0.484	0.468				
2.18	25	231.2	0.390	0.310	0.562	0.404	0.444	0.331	0.953	0.483
	125	46.23	0.415	0.320	0.589	0.390				
	250	23.12	0.423	0.323	0.579	0.379				
	500	11.56	0.429	0.325	0.561	0.369				

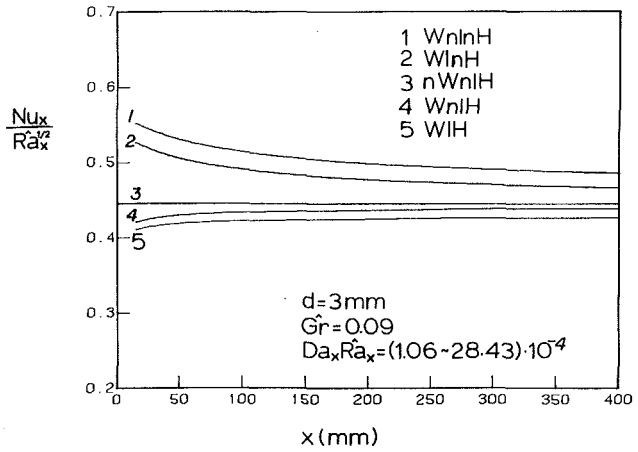

Fig. 1 Comparison of local heat transfer parameter

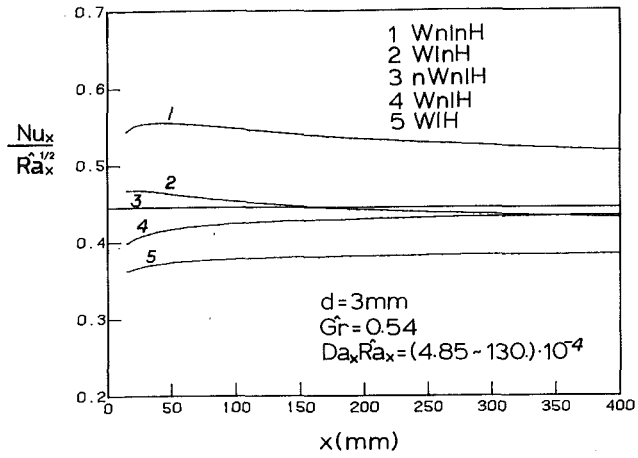

Fig. 2 Comparison of local heat transfer parameter

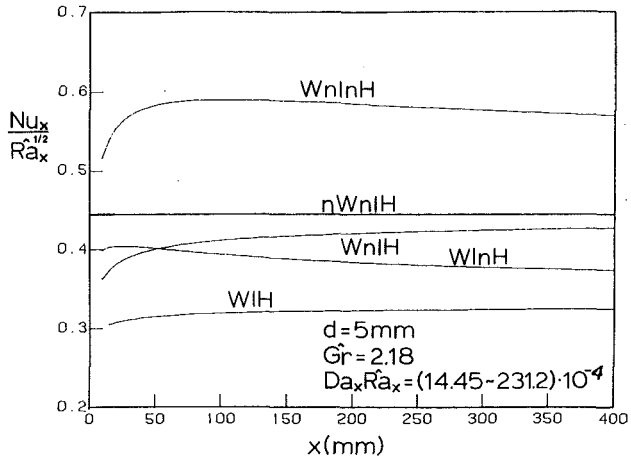

Fig. 3 Comparison of local heat transfer parameter

Results With Dispersion Effects Neglected

The dispersion effect can be neglected by setting $\hat{Ra}_d = 0$ in equation (23). Table 1 shows the range of the variables used in the numerical calculations. Two particle sizes have been considered and the properties of the fluid have been evaluated at the mean film temperature T_m. Results for the heat transfer parameter $Nu_x/\hat{Ra}_x^{0.5}$ are shown in Tables 2 and 3 as well as in Figs. 1–3. Since various effects are considered, the following symbols are used: WIH, which refers to Wall (due to no-slip boundary condition), Inertia, and Homogeneity effects; nWnInH, which refers to no Wall, no Inertia, and non-Homogeneity effects, etc. Notice that nWnIH is the case considered by Cheng and Minkowycz [12], and nWIH is the case studied by Plumb and Huenefeld [13]. It is seen that the no-slip wall and inertia effects decrease the velocity and the heat transfer rate, while the wall-channeling effect, due to the nonhomogeneity in porosity, enhances the heat transfer. Typical velocity and temperature profiles with various effects are presented in Figs. 4 and 5. Figure 4 shows the predicted dimensionless velocity and temperature profiles near the leading edge, while Fig. 5 shows the results for positions downstream. The following subsections describe the main feature of the wall, inertia, and nonhomogeneity effects, respectively, and also compare the calculated results with the existing experimental ones.

Wall Effect. The wall effect due to the no-slip boundary condition at the solid wall is effective in a length scale of $K^{0.5}$ where the viscous resistance term and the Darcy resistance term have the same order of magnitude. For natural convection heat transfer, the importance of the wall effect is governed by the parameter $Da_x\hat{Ra}_x$. By equations (12) and (13), it can be shown that $(\delta_m/\delta_T)^2 \sim O(Da_x\hat{Ra}_x)$; therefore, the parameter $Da_x\hat{Ra}_x$ characterizes the ratio of the momentum to the thermal boundary layer thickness. If the value for this number is small enough, as in the usual case for most porous media, the wall effect is negligible, and the first term in equation (22) can be dropped. In addition, if the porous medium is uniform, equations (22)–(25) reduce to equations reported previously [13] and the result is the same as the nWIH case in the present study. Furthermore, since $Da_x\hat{Ra}_x$ is inversely proportional to the square root of x, the wall effect will be more pronounced near the leading edge. This is seen clearly from Figs. 1–3 (and also from Tables 2 and 3). These figures show that when only the wall effect is considered (WnIH), the decrease in the heat transfer parameter is more pronounced near the leading edge when compared with the case where the

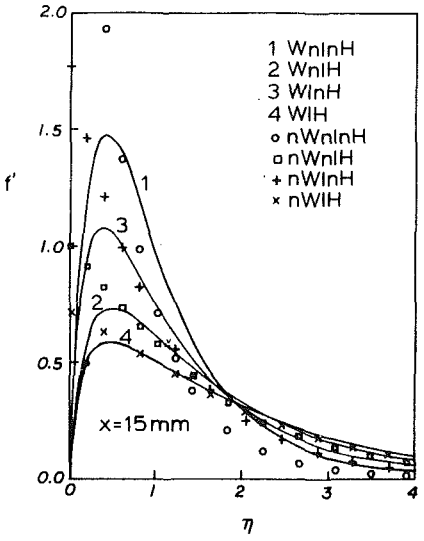

Fig. 4(a)

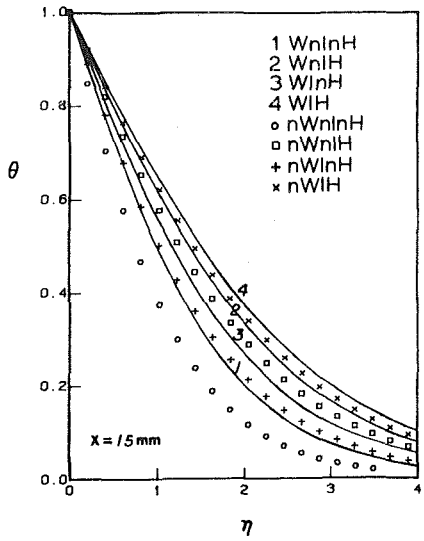

Fig. 4(b)

Fig. 4 Velocity and temperature profiles at $x = 15$ mm for $d = 3$ mm, Gr = 0.542

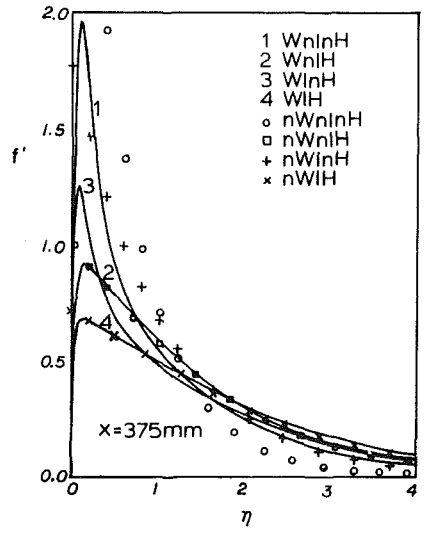

Fig. 5(a)

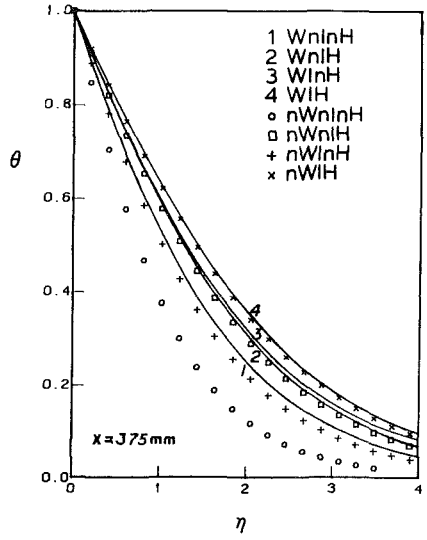

Fig. 5(b)

Fig. 5 Velocity and temperature profiles at $x = 375$ mm for $d = 3$ mm, Gr = 0.542

slip boundary condition is assumed (nWnIH). The variation of the wall effect along the heated plate can also be seen from the velocity profiles shown in Figs. 4(*a*) and 5(*a*). Near the leading edge, Fig. 4(*a*), the wall effect is more significant and the profiles are quite different from what would be obtained from a slip boundary assumption. At downstream locations, Fig. 5(*a*), the wall effect seems to be restricted in a very small viscous sublayer and the total profile looks similar to that obtained from a slip boundary assumption.

As mentioned above, the no-slip wall effect is usually small for packed spheres since the permeability is small. However, for high-porosity porous media, such as foam metals, the permeability can be very high, $10^{-5} \sim 10^{-6}$ m^2. In this case, the wall effect cannot be neglected under certain circumstances. For example, for a foam metal with a permeability of 10^{-6} m^2 and a characteristic length x of 0.5 m, the wall parameter $\mathrm{Da}_x\hat{\mathrm{Ra}}_x$ under a temperature difference of 80°C, such as that considered in Table 1, is equal to 4.3; therefore the wall effect is significant. Furthermore, for high-porosity media, the flow velocity is usually so high that the inertia effect is more important than that in the packed spheres.

Inertia Effect. The inertia effect, which is dependent on the modified Grashof number, tends to thicken the thermal and hydrodynamic boundary layers and to reduce the magnitude of the vertical velocity (Figs. 4 and 5). For Grashof numbers less than 0.1, this effect is negligible [13]. Tables 2 and 3 clearly show the dependence of the heat transfer parameter $\mathrm{Nu}_x/\hat{\mathrm{Ra}}_x^{0.5}$ on the Grashof number. The Grashof number is seen to be proportional to the particle diameter d to the third power from equations (6), (7), and (26); therefore, the inertia effect depends strongly on the particle size. For porous media with small particles and low porosities (Table 2), the permeability is small, thus showing negligible inertia effect unless the temperature difference is very large. On the other hand, for porous media with large particles and high porosities (Table 3), $\hat{\mathrm{Gr}}$ can be quite large even for normal temperature difference. For the same heated plate, Figs. 1–3

show that the inertia effect increases along the plate because the fluid particles pick up more and more energy along the plate and are accelerated to have higher velocities when they approach the downstream locations. This is seen more clearly for higher values of $\hat{Gr}$ (Figs. 2 and 3).

The present results also show that the inertia effect is more important when the nonhomogeneity effect is considered. Since in nonuniform porous media, such as packed-sphere beds, the permeability near the wall is much higher than that in the bulk region, the real Grashof number near the wall is thus higher than that defined in equation (26). For the case with $\hat{Gr} = 2.18$ in Table 2, when the nonhomogeneity effect is considered and the inertia effect is neglected (nWnInH), a big increase in heat transfer due to the flow channeling near the wall can be obtained, a more than 100 percent increase from the nWnIH case. However, with both the inertia and nonhomogeneity effects considered together (nWInH), the predicted enhancement in heat transfer would be substantially reduced to about only 9 percent. Therefore, for packed spheres, when the wall-channeling effect is considered, the inertia effect should also be considered so that the heat transfer will not be overestimated.

Nonhomogeneity Effect. The effect of wall-channeling due to the porosity variation near the wall is to increase heat transfer. With the wall and inertia effects neglected, the enhancement in heat transfer due to the variation of porosity (nWnInH) for the 3 mm particles is 51 ~ 70 percent (Table 2) and is 71 ~ 115 percent for the 5 mm particles (Table 3) when compared with the nWnIH case under the conditions given in Table 1. While the inclusion of the no-slip condition hardly reduces the heat transfer for homogeneous porous media, the wall effect can be very significant for nonhomogeneous media. When inertia effect is also considered, the heat transfer is further reduced. This inertia effect is negligible when the Grashof number is small and is quite significant at large Grashof numbers as discussed earlier. When all three effects are considered, the heat transfer can be either increased or decreased depending on the competition between these three mechanisms. Figures 1–3 clearly show the interactions among these effects under various conditions.

For packed spheres, the porosity variation is confined in a region near the wall which is characterized by a length L_h. At a distance L_h away from the wall, the porosity value will approach that of the bulk region. It is expected that the length L_h is only a function of the sphere diameter and the characteristic length of the packed bed and is independent of the downstream location. The variation of the ratio of this length to the thermal boundary layer thickness will describe the local heat transfer variation due to the nonhomogeneity near the wall. Near the leading edge, the thermal boundary layer thickness δ_t is very small, thus showing very large L_h/δ_t. Since the thermal boundary layer thickness δ_t grows with x, L_h/δ_t will decrease with increasing x. This means that near the leading edge, most of the fluid within the thermal boundary layer will have a high velocity, while downstream, a smaller portion of fluid within the thermal boundary layer has a high velocity. Therefore, when the effect of porosity variation is considered, $\mathrm{Nu}_x/\hat{\mathrm{Ra}}_x^{0.5}$ will decrease as x increases. The trend is clearly shown in Figs. 1–3 (WInH and WnInH). The opposite trend near the leading edge is due to the wall effect, which decreases the heat transfer and is significant near the leading edge. However, since the wall-channeling effect is dominant, the values of the heat transfer parameter are still higher than those downstream. The velocity profiles in Figs. 4 and 5 show that near the leading edge (Fig. 4) the region of velocity overshooting due to the wall-channeling effect occupies larger portions of the thermal boundary layer than that downstream (Fig. 5). This can be seen more clearly by the variation of the ratio η_d/η_T shown in Table 4, where η_T is the nondimensional thermal boundary layer thickness, which is defined as the point where θ has a value of 0.01, and η_d is the nondimensional length for L_h if $L_h = d$ is assumed. Table 4 shows the decrease of η_d/η_T with increasing x. This observation confirms the argument given above.

Table 4 Nondimensional particle diameters and thermal boundary layer thicknesses for $d = 3$ mm, $\hat{Gr} = 0.54$

x, mm	η_d	η_T	$\frac{\eta_d}{\eta_T}$
15	3.89	5.64	0.67
87	1.62	6.29	0.26
159	1.20	6.51	0.18
231	0.99	6.51	0.15
303	0.86	6.51	0.15
375	0.78	6.51	0.12

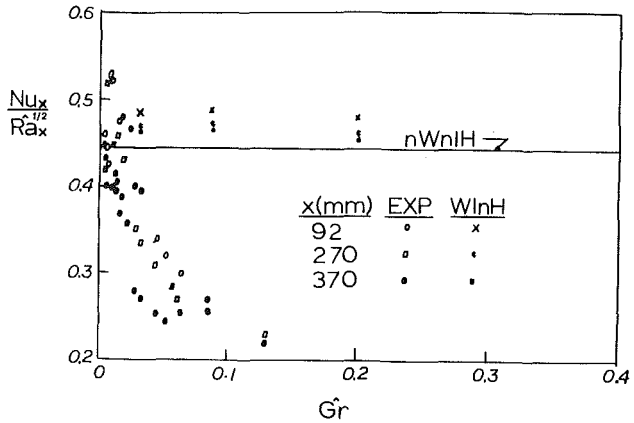

Fig. 6 Comparison of theoretical and experimental results [20]

Comparison With Experimental Data. Figure 6 shows the comparison between the theoretical predictions and the experimental data [20]. The theoretical results consider both the non-Darcian and the nonhomogeneity effects. Of the various effects, the nonhomogeneity effect is dominating (see Tables 2 and 3); therefore, the calculated results for the WInH case show enhancement over the nWnIH case which is the same case as that considered by Cheng and Minkowycz [12], while the experimental data are much lower than the nWnIH case except those at small Grashof numbers. The discrepancy between the theoretical predictions and the experimental data is quite large especially at large Grashof numbers. The reduction in heat transfer due to the inertia effect cannot describe such a large decrease in $\mathrm{Nu}_x/\hat{\mathrm{Ra}}_x^{0.5}$ for large Grashof numbers. Although the experimental data do not show the enhancement due to the wall-channeling effect, the decrease in the heat transfer parameter along the plate follows the same trend when the nonhomogeneity effect is dominant.

Results With Dispersion Effects Considered

When the inertia effect is prevalent, the thermal dispersion in porous media is expected to become important. Plumb [16] studied this problem by neglecting the wall effect and assuming a linear relationship between the dispersion thermal diffusivity and the streamwise velocity components, i.e.,

$$\alpha' = \gamma\, u\, d$$

The present study extends Plumb's work by including the wall (due to no-slip condition) and nonhomogeneity effects (due to the porosity near the wall). The value for γ should be determined from experiment. For the present study, a fixed value of 0.2 is employed since the main interest is to study

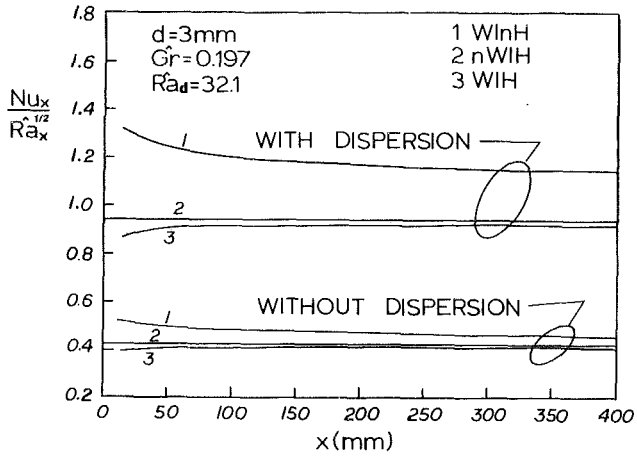

Fig. 7 Effect of dispersion on local heat transfer parameter

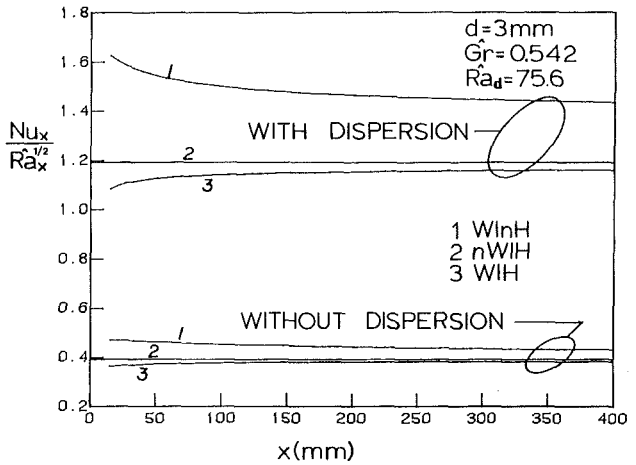

Fig. 8 Effect of dispersion on local heat transfer parameter

qualitatively the dispersion effect in the presence of wall and nonhomogeneity effects. Figures 7 and 8 show the results of the present study where the heat transfer parameter is calculated by

$$\frac{\mathrm{Nu}_x}{\hat{\mathrm{Ra}}_x^{0.5}} = -\frac{\alpha_e}{\alpha_0}\,\theta'(x, \mathrm{O}) = -[1+\gamma\hat{\mathrm{Ra}}_d\, f'(\mathrm{O})]\theta'(x, \mathrm{O}) \quad (31)$$

It is noted that $f'(\mathrm{O})$ is a maximum for the case when the wall effect is neglected; whereas, when the wall effect is considered, $f'(\mathrm{O})$ vanishes. Because the different assumptions about the wall velocity, the results of the temperature gradient at wall, $-\theta'(\mathrm{O})$, are quite different. For cases with the wall effect considered, $-\theta'(x, \mathrm{O})$ is always increased due to the dispersion effect. On the contrary, dispersion will decrease $-\theta'(x, \mathrm{O})$ when the slip boundary condition is assumed. Despite the disagreement in the prediction of the wall temperature gradient, all the results show that dispersion effect will increase heat transfer. Actually, when the wall effect is considered, the temperature gradient for most of the thermal boundary layer decreases, similar to the case when the wall effect is neglected, only for a very small region near the wall where the temperature gradient is increased. Therefore, Plumb's results (with wall effect neglected) can be regarded as the outer solution for the cases which include the no-slip wall effect. The differences between these two cases are due to the convective heat loss within the small region near the wall. For most porous media, this region is very small. Therefore, the differences are small as can be seen from Figs. 7 and 8. Figures 7 and 8 also show that when the nonhomogeneity and dispersion effects are both considered, the heat transfer is enhanced tremendously.

Conclusions

Various effects for natural convection from a vertical flat plate embedded in a porous medium are investigated analytically. The wall-channeling and the dispersion effects tend to enhance the heat transfer, while the wall and inertia effects decrease the heat transfer. Whether the heat transfer will be increased or decreased as compared to the Darcy flow depends on the competition among these mechanisms. Other conclusions of this study are:

1 Both the no-slip wall and nonhomogeneity effects are more pronounced near the leading edge and decrease with increasing distance downstream. The nonhomogeneity effect tends to increase heat transfer while the no-slip effect decreases it.

2 At high Grashof numbers, both inertia and dispersion effects become important. The inertia effect decreases the heat transfer while the dispersion effect increases it.

3 The no-slip wall effect is negligible for low-porosity media. However, for small apparatus with high permeability, this effect may not be neglected.

4 Both wall and inertia effects are more pronounced for nonhomogeneous media, because the flow overshoot near the wall is decreased dramatically due to these two effects; therefore, the enhancement due to the wall-channeling effect is largely reduced.

References

1 Cheng, P., "Heat Transfer in Geothermal Systems," *Advances in Heat Transfer*, Vol. 14, 1978, pp. 1–105.

2 Cheng, P., "Natural Convection in a Porous Medium: External Flows," NATO Advanced Study Institute on Natural Convection: Fundamentals and Applications, Izmir, Turkey, July 16–27, 1984.

3 Combarnous, M. A., "Natural Convection in Porous Media and Geothermal Systems," *Proceedings of the 6th International Heat Transfer Conference*, Vol. 6, 1978, pp. 45–59.

4 Brinkman, H. C., "A Calculation of the Viscous Force Extended by a Flowing Fluid on a Dense Swarm of Particles," *Appl. Sci. Res.*, Vol. A1, 1947, pp. 26–34.

5 Scheidegger, A. E., *The Physics of Flow Through Porous Media*, University of Toronto Press, Toronto, 1974.

6 Vafai, K., and Tien, C. L., "Boundary and Inertia Effects on Flow and Heat Transfer in Porous Media," *Int. J. Heat Mass Transfer*, Vol. 24, 1981, pp. 195–203.

7 Benenati, R. F., and Brosilow, C. B., "Void Fraction Distribution in a Beds of Spheres," *AIChE J.*, Vol. 8, 1962, pp. 395–361.

8 Schertz, W. M., and Bishoff, K. B., "Thermal and Material Transport in Non-isothermal Packed Beds," *AIChE J.*, Vol. 15, 1969, pp. 597–604.

9 Schwartz, C. E., and Smith, J. M., "Flow Distribution in Packed Beds," *Ind. Eng. Chem.*, Vol. 45, 1958, pp. 1209–1218.

10 Chandrasekhara, B. C., and Vortmeyer, D., "Flow Model for Velocity Distribution in Fixed Porous Beds Under Isothermal Conditions," *Wärme- und Stoffübertragung*, Vol. 12, 1979, pp. 105–111.

11 Denloye, A. O. O., and Botterill, J. S. M., "Heat Transfer in Flowing Packed Beds," *Chem. Eng. Sci.*, Vol. 32, 1977, pp. 461–465.

12 Cheng, P., and Minkowycz, W. J., "Free Convection About a Vertical Flat Plate Embedded in a Porous Medium With Application to Heat Transfer From a Dike," *J. of Geophysical Research*, Vol. 82, 1977, pp. 2040–2044.

13 Plumb, O. A., and Huenefeld, J. C., "Non-Darcy Natural Convection From Heated Surfaces in Saturated Porous Media," *Int. J. Heat Mass Transfer*, Vol. 24, 1981, pp. 765–768.

14 Evans, G. H., and Plumb, O. A., "Natural Convection From a Vertical Isothermal Surface Embedded in a Saturated Porous Medium," ASME Paper No. 78-HT-55, 1978.

15 Hsu, C. T., and Cheng, P., "Brinkman's Model for Free Convection About a Flat Plate in a Porous Medium," *Int. J. Heat Mass Transfer*, Vol. 28, 1985, pp. 683–697.

16 Plumb, O. A., "The Effect of Thermal Dispersion on Heat Transfer in Packed Bed Boundary Layers," *ASME–JSME Joint Thermal Conference Proceedings*, Vol. 2, 1983, pp. 17–21.

17 Catton, I., "Natural Convection Heat Transfer in Porous Media," NATO Advanced Study Institute on Natural Convection: Fundamentals and Applications, Izmir, Turkey, July 16–27, 1984.

18 Ergun, S., "Fluid Flow Through Packed Columns," *Chem. Eng. Progress*, 1952, pp. 89–94.

19 Lentini, M., and Pereyra, V., "An Adaptive Finite Difference Solver for Nonlinear Two-Point Boundary Problems With Mild Boundary Layers," *SIAM J. Num. Anal.*, Vol. 14, 1977, pp. 91–111.

20 Verma, A. K., M.S. Thesis, University of Hawaii, 1980.

Natural Convection Flow and Heat Transfer Between a Fluid Layer and a Porous Layer Inside a Rectangular Enclosure

C. Beckermann

S. Ramadhyani

R. Viskanta

Heat Transfer Laboratory,
School of Mechanical Engineering,
Purdue University,
West Lafayette, IN 47907

A numerical and experimental study is performed to analyze the steady-state natural convection fluid flow and heat transfer in a vertical rectangular enclosure that is partially filled with a vertical layer of a fluid-saturated porous medium. The flow in the porous layer is modeled utilizing the Brinkman–Forchheimer–extended Darcy equations. The numerical model is verified by conducting a number of experiments, with spherical glass beads as the porous medium and water and glycerin as the fluids, in rectangular test cells. The agreement between the flow visualization results and temperature measurements and the numerical model is, in general, good. It is found that the amount of fluid penetrating from the fluid region into the porous layer depends strongly on the Darcy (Da) and Rayleigh (Ra) numbers. For a relatively low product of $Ra \times Da$, the flow takes place primarily in the fluid layer, and heat transfer in the porous layer is by conduction only. On other hand, fluid penetrating into a relatively highly permeable porous layer has a significant impact on the natural convection flow patterns in the entire enclosure.

1 Introduction

Interest in natural convection fluid flow and heat transfer in porous media has been motivated by a broad range of applications, including geothermal systems, crude oil production, storage of nuclear waste materials, ground water pollution, fiber and granular insulations, solidification of castings, etc. A comprehensive review of the literature is available (Cheng, 1978). In a wide variety of such problems, the physical system can be modeled as a two-dimensional, rectangular enclosure filled with a homogeneous porous medium, with the vertical walls held at different temperatures and the connecting horizontal walls considered adiabatic. In the past two decades, numerous experimental and theoretical investigations have been devoted to the steady-state natural convection flow and heat transfer in such enclosures. In many real situations, however, the porous medium consists of several layers of different permeability. In addition, the enclosure might contain simultaneously a (free) fluid and a porous layer. A typical example of this is a situation where porous insulation material occupies only a small fraction of the space between two walls. The fluid flow and heat transfer can be significantly reduced because of the large frictional resistance offered by the porous insulation.

The present study is motivated by natural convection in a solidifying casting. Because of the extended freezing temperature range of an alloy, a mushy zone might exist, consisting of a fine meshwork of dendrites growing into the melt region. In the past, fluid flow in this mushy zone has been modeled as natural convection in a porous medium (Fisher, 1981). There has been some controversy on the importance of fluid flow between the pure melt region and the porous mushy zone. Most investigators have neglected this phenomenon in their analyses. However, penetration of fluid into the mushy zone can significantly alter the local temperatures and concentrations in the mushy zone and, eventually, the chemical homogeneity and grain structure of the solidified casting. Hence, the objective of the present study is to investigate the natural convection flow and heat transfer in such a system, idealized as a vertical rectangular enclosure partially filled with a vertical porous layer.

Research devoted to natural convection in layered porous media is relatively new. A recent review of the subject has been provided by Tien and Hong (1985). Sun (1973), Nield (1977), and Somerton and Catton (1982) have studied convective instabilities in the case where a horizontal fluid is superposed above a porous layer, but no study has been found in the open literature concerning the vertical case considered here. Of related interest is the numerical investigation of Poulikakos and Bejan (1983) who have considered a vertical rectangular enclosure with vertical layers of various permeability porous media. Tong and Subramanian (1983) and Lauriat and Mesguich (1984) have investigated natural convection in vertical rectangular enclosures that are vertically divided into a fluid and a porous layer, the two being separated by an impermeable wall.

In the present study, fluid flow is permitted to take place between the fluid and porous layers (i.e., the partition is permeable). The flow is modeled by utilizing the Brinkman–Forchheimer–extended Darcy equations for the porous layer. The predictions of the model are verified by conducting experiments in rectangular test cells using flow visualization and temperature measurements. The heat transfer and fluid flow phenomena in the present physical system are further investigated through a number of numerical experiments. However, in view of the large number of governing parameters, no attempt has been made to present a complete parametric study.

2 Analysis

2.1 Model Equations. The physical situation and coordinate system are shown in Fig. 1. The horizontal extent of the fluid layer is s, while the overall dimensions of the rectangular enclosure are H and L. It is assumed that the flow is steady, laminar, incompressible, and two-dimensional. The thermophysical properties of the fluid are assumed constant, except for the density in the buoyancy term in the momentum

Contributed by the Heat Transfer Division and presented at the 4th AIAA/ASME Thermophysics and Heat Transfer Conference, Boston, Massachusetts, June 1–4, 1986. Manuscript received by the Heat Transfer Division March 14, 1986.

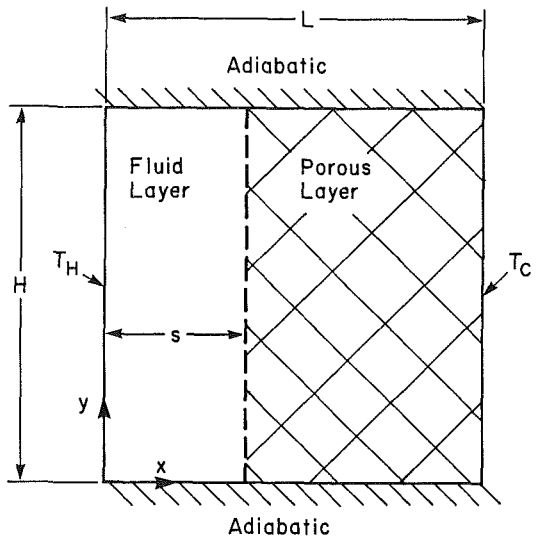

Fig. 1 Schematic of the physical model and coordinate system

equations. The porous medium is considered homogeneous and isotropic and is saturated with a fluid which is in local thermodynamic equilibrium with the solid matrix. The governing conservation equations for the fluid and the porous layer will be written separately. For the fluid layer, we have:

Continuity:

$$\frac{\partial U}{\partial x}+\frac{\partial V}{\partial y}=0 \tag{1}$$

Momentum:

$$\rho\left(U\frac{\partial U}{\partial x}+V\frac{\partial U}{\partial y}\right)=-\frac{\partial P}{\partial x}+\frac{\partial}{\partial x}\left(\mu_f\frac{\partial U}{\partial x}\right)+\frac{\partial}{\partial y}\left(\mu_f\frac{\partial U}{\partial y}\right) \tag{2}$$

$$\rho\left(U\frac{\partial U}{\partial x}+V\frac{\partial U}{\partial y}\right)=-\frac{\partial P}{\partial y}+\frac{\partial}{\partial x}\left(\mu_f\frac{\partial V}{\partial x}\right)+\frac{\partial}{\partial y}\left(\mu_f\frac{\partial V}{\partial y}\right)+\rho g\beta(T-T_c) \tag{3}$$

Energy:

$$\rho c_{pf}\left(U\frac{\partial T}{\partial x}+V\frac{\partial T}{\partial y}\right)=\frac{\partial}{\partial x}\left(k_f\frac{\partial T}{\partial x}\right)+\frac{\partial}{\partial y}\left(k_f\frac{\partial T}{\partial y}\right) \tag{4}$$

The conservation equations for the porous layer are based on a non-Darcian model, incorporating the Brinkman and Forchheimer extensions to account for viscous and inertia effects, respectively. The importance of these extensions is discussed in Beckermann et al. (1986a and 1987), who have found that both extensions must be included simultaneously for a high permeability porous medium (i.e., a high Darcy number), while the importance of Forchheimer's extension increases with decreasing Pr/R_k. In terms of the superficial (Darcian) velocity, the governing equations for the porous layer are (Tien and Hong, 1985; Georgiadis and Catton, 1984):

Continuity:

$$\frac{\partial U_D}{\partial x}+\frac{\partial V_D}{\partial y}=0 \tag{5}$$

Momentum:

$$0=-\frac{\partial P}{\partial x}+\frac{\partial}{\partial x}\left(\mu_{\text{eff}}\frac{\partial U_D}{\partial x}\right)+\frac{\partial}{\partial y}\left(\mu_{\text{eff}}\frac{\partial U_D}{\partial y}\right)-\left(\frac{\mu_f}{K}+\frac{\rho C}{\sqrt{K}}\,|\mathbf{U}_D|\right)U_D \tag{6}$$

$$0=-\frac{\partial P}{\partial y}+\frac{\partial}{\partial x}\left(\mu_{\text{eff}}\frac{\partial V_D}{\partial x}\right)+\frac{\partial}{\partial y}\left(\mu_{\text{eff}}\frac{\partial V_D}{\partial y}\right)+\rho g\beta(T-T_c)-\left(\frac{\mu_f}{K}+\frac{\rho C}{\sqrt{K}}\,|\mathbf{U}_D|\right)V_D \tag{7}$$

Energy:

$$\rho c_{pf}\left(U_D\frac{\partial T}{\partial x}+V_D\frac{\partial T}{\partial y}\right)=\frac{\partial}{\partial x}\left(k_{\text{eff}}\frac{\partial T}{\partial x}\right)+\frac{\partial}{\partial y}\left(k_{\text{eff}}\frac{\partial T}{\partial y}\right) \tag{8}$$

The boundary conditions for the governing equations for both the fluid and the porous layer are the no-slip condition at the impermeable walls of the enclosure as well as the constant temperature and zero heat flux conditions at the vertical and horizontal walls, respectively. The two sets of equations are coupled by the following matching conditions at the porous/fluid layer interface

$$T|_{x=s^-}=T|_{x=s^+} \tag{9a}$$

$$k_f\frac{\partial T}{\partial x}\Big|_{x=s^-}=k_{\text{eff}}\frac{\partial T}{\partial x}\Big|_{x=s^+} \tag{9b}$$

$$U|_{x=s^-}=U_D|_{x=s^+},\quad V|_{x=s^-}=V_D|_{x=s^+} \tag{9c}$$

Nomenclature

A = aspect ratio = H/L
c_p = specific heat, J/kg K
C = inertial coefficient, see equation (11)
Da = Darcy number = K/L^2
g = gravitational acceleration, m/s^2
$\bar{h}$ = average convective heat transfer coefficient, W/m^{2}K
H = height of enclosure, m
k = thermal conductivity, W/mK
K = permeability of the porous medium, m^2
L = length of enclosure, m
$\overline{\mathrm{Nu}}$ = average Nusselt number = $\bar{h}L/k_f$
P = pressure, Pa
p = dimensionless pressure = $PL^2/(\rho\alpha_f^2)$
Pr = Prandtl number = ν_f/α_f
Ra = Rayleigh number = $g\beta(T_H-T_C)L^3/(\nu_f\alpha_f)$
R_k = ratio of thermal conductivities = k_{eff}/k_f
s = fluid layer thickness, m
S = dimensionless fluid layer thickness = s/L
T = temperature, K
u = dimensionless x-component velocity = UL/α_f
U = x-component velocity, m/s
v = dimensionless y-component velocities = VL/α_f
V = y-component velocity, m/s
x = horizontal coordinate, m
X_p = binary parameter, see equation (13)
y = vertical coordinate, m
α = thermal diffusivity = $k_f/\rho c_{pf}$, m^2/s
β = coefficient of thermal expansion, K^{-1}
ϵ = porosity of the porous medium
η = dimensionless vertical coordinate = y/L
θ = dimensionless temperature = $(T-T_C)/(T_H-T_C)$
μ = dynamic viscosity, Ns/m^2
ν = kinematic viscosity, m^2/s
ξ = dimensionless horizontal coordinate = x/L
ρ = fluid density, kg/m^3

Subscripts

b = beads
C = cold
D = Darcy
eff = effective
f = fluid
H = hot

$$P|_{x=s^-} = P|_{x=s^+} \tag{9d}$$

$$\mu \frac{\partial U}{\partial x}\Big|_{x=s^-} = \mu_{\text{eff}} \frac{\partial U_D}{\partial x}\Big|_{x=s^+} \tag{9e}$$

$$\mu\left(\frac{\partial V}{\partial x}+\frac{\partial U}{\partial y}\right)\Big|_{x=s^-} = \mu_{\text{eff}}\left(\frac{\partial V_D}{\partial x}+\frac{\partial U_D}{\partial y}\right)\Big|_{x=s^+} \tag{9f}$$

Equations (9*a*), (9*b*), (9*c*), and (9*d*) express the continuity of temperature, heat flux, normal and tangential velocities, and pressure, respectively, across the fluid/porous layer interface. Equations (9*e*) and (9*f*) are the matching conditions for the deviative normal and shear stresses. Note that equations (9*d*) and (9*e*) taken together imply matching of the total normal stress at the interface. Equation (9*f*) represents an extension of the shear stress matching condition of Neale and Nader (1974) for flow which is not parallel to the fluid/porous layer interface. Obviously, matching of the stresses at the interface can only be accomplished if Brinkman's extension is used in the momentum equations for the porous layer.

The values for the permeability K and the inertia coefficient C in the momentum equations for the porous layer are given by Ergun (1952) for packed beds of beads of diameter d_b and porosity ϵ

$$K = \frac{d_b^2 \epsilon^3}{175(1-\epsilon)^2} \tag{10}$$

$$C = \frac{1.75}{\sqrt{175}}\,\epsilon^{-3/2} \tag{11}$$

In addition, models for the effective properties (μ_{eff} and k_{eff}) of the porous medium are needed. It has been found that taking $\mu_{\text{eff}} = \mu_f$ in Brinkman's extension provides good agreement with experimental data (Neale and Nader, 1974; Lundgren, 1972) and is adopted in the present work. Various models for the effective thermal conductivity k_{eff} have been proposed (Combarnous and Bories, 1975). In the present study, a nonlinear equation derived by Veinberg (1967) is used, which is claimed to be universally applicable for a medium with randomly distributed spherical inclusions

$$k_{\text{eff}} + \epsilon\left(\frac{k_b - k_f}{k_f^{1/3}}\right)k_{\text{eff}}^{1/3} - k_b = 0 \tag{12}$$

2.2 Dimensionless Equations. Instead of solving the governing equations separately for each layer, the equations are combined into one set by introducing the following binary parameter

$$X_p(\xi,\eta) = \begin{cases} 1 & \text{if in porous layer } 0<\epsilon<1 \\ 0 & \text{if in fluid layer } \epsilon = 1 \end{cases} \tag{13}$$

Introducing dimensionless variables (see the Nomenclature), the combined conservation equations for the fluid and porous layer can be written as:

Continuity:

$$\frac{\partial u}{\partial \xi}+\frac{\partial v}{\partial \eta} = 0 \tag{14}$$

Momentum:

$$(1-X_p)\left(u\frac{\partial u}{\partial \xi}+v\frac{\partial u}{\partial \eta}\right) = -\frac{\partial p}{\partial \xi}+\text{Pr}\left(\frac{\partial^2 u}{\partial \xi^2}+\frac{\partial^2 u}{\partial \eta^2}\right)-X_p\left(\frac{\text{Pr}}{\text{Da}}+\frac{C}{\sqrt{\text{Da}}}|\mathbf{u}|\right)u$$

$$(1-X_p)\left(u\frac{\partial v}{\partial \xi}+v\frac{\partial v}{\partial \eta}\right) = -\frac{\partial p}{\partial \eta}+\text{Pr}\left(\frac{\partial^2 v}{\partial \xi^2}+\frac{\partial^2 v}{\partial \eta^2}\right)-X_p\left(\frac{\text{Pr}}{\text{Da}}+\frac{C}{\sqrt{\text{Da}}}|\mathbf{u}|\right)v+\text{RaPr}\theta \tag{15, 16}$$

Energy:

$$u\frac{\partial \theta}{\partial \xi}+v\frac{\partial \theta}{\partial \eta} = (X_p(R_k-1)+1)\left(\frac{\partial^2 \theta}{\partial \xi^2}+\frac{\partial^2 \theta}{\partial \eta^2}\right) \tag{17}$$

By combining the governing equations for the two regions, the fluid and the porous media are treated as a single medium with its properties depending on the location within the enclosure. The advantage of this formulation is that it ensures the satisfaction of the matching conditions at the fluid/porous layer interface and, thus, simplifies the numerical solution procedure (refer to the following section). It is interesting to consider the limiting case when the porous medium has a high porosity, because this situation should closely approximate natural convection in a purely fluid enclosure. In this limit, as $\text{Da} \to \infty$ and $R_k \to 1$, the governing equations on the porous side begin to resemble the fluid side equations. Indeed, the principal difference between the porous and fluid side equations is the absence of inertia terms in the momentum equations for the porous side. At moderate Rayleigh numbers, since inertia effects are small, the present formulation is able to reproduce the velocity and temperature distributions corresponding to a purely fluid enclosure when Da is assigned a very large value (Beckermann et al., 1986a). The boundary conditions for the combined equations are given in dimensionless form as

$$\begin{aligned} &\theta = 1, \quad u = v = 0 \text{ at } \xi = 0, \quad 0 \le \eta \le A \\ &\theta = 0, \quad u = v = 0 \text{ at } \xi = 1, \quad 0 \le \eta \le A \\ &\frac{\partial \theta}{\partial \eta} = 0, \quad u = v = 0 \text{ at } \eta = 0, \quad 0 \le \xi \le 1 \\ &\frac{\partial \theta}{\partial y} = 0, \quad u = v = 0 \text{ at } \eta = A, \quad 0 \le \xi \le 1 \end{aligned} \tag{18}$$

The results for the total heat transfer rate across the enclosure will be presented in terms of the Nusselt number defined as

$$\overline{\text{Nu}} = \frac{\bar{h}L}{k_f} = -\frac{1}{A}\int_0^A (X_p(R_k-1)+1)\frac{\partial \theta}{\partial \xi}\Big|_{\substack{\xi=1 \\ \text{or} \\ \xi=0}} d\eta \tag{19}$$

According to this definition, the actual heat transfer rate is referenced to the heat transfer by conduction if the entire enclosure is filled with the fluid alone.

2.3 Numerical Procedure. The combined continuity, momentum, and energy equations (14)–(17) were solved numerically using the SIMPLER algorithm (Patankar, 1980). The control-volume formulation utilized in this algorithm ensures continuity of the convective and diffusive fluxes as well as overall momentum and energy conservation. The harmonic mean formulation adopted for the interface diffusion coefficients between two control volumes can handle abrupt changes in these coefficients (for example, if $R_k \neq 1$) without requiring an excessively fine grid, for example, at the porous/fluid layer interface.

The mesh size required for sufficient numerical accuracy depended mainly on the Rayleigh and Darcy numbers. For most of the numerical experiments, a grid of 25×25 nodal points ensured independence of the solution on the grid. The nodal points were uniformly distributed in the y direction, while the distribution along the x direction was slightly skewed to have a greater concentration of points near the vertical

Table 1 Summary of experimental conditions ($A = 1.0, S = 0.5$)

Test No.	Test cell/ fluid	d_b [mm]	Ra	Pr	Da	C	R_k	Ra•Da
1	small t.c./water	1.6	3.028×10^{7}	6.97	7.354×10^{-7}	0.6124	1.397	22.3
2	small t.c./water	6.0	3.028×10^{7}	6.97	1.296×10^{-5}	0.5647	1.383	392.4
3	large t.c./glycerin	1.6	3.471×10^{6}	12630	3.985×10^{-8}	0.6124	2.315	0.14
4	large t.c./glycerin	6.0	3.471×10^{6}	12630	7.112×10^{-7}	0.5647	2.259	2.47

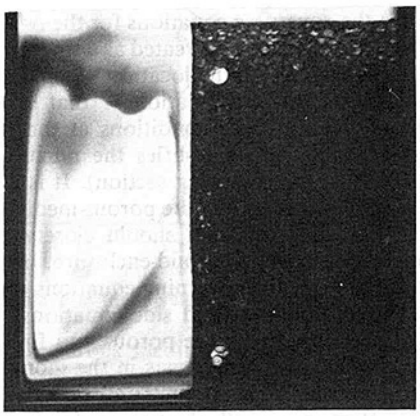

Fig. 2(a) Flow visualization

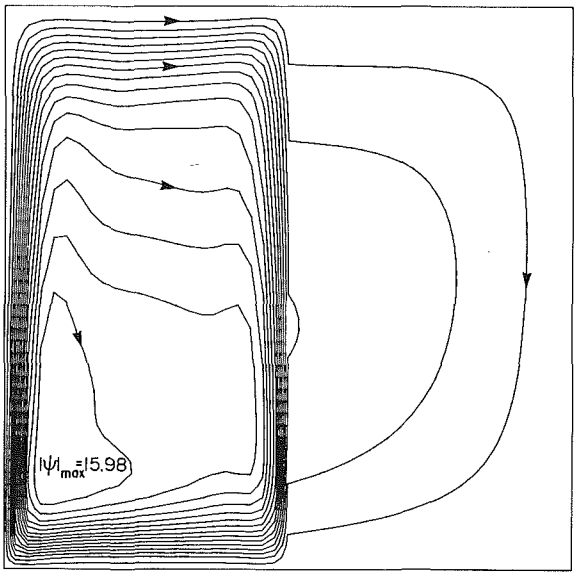

Fig. 2(b) Streamlines (equal increments)

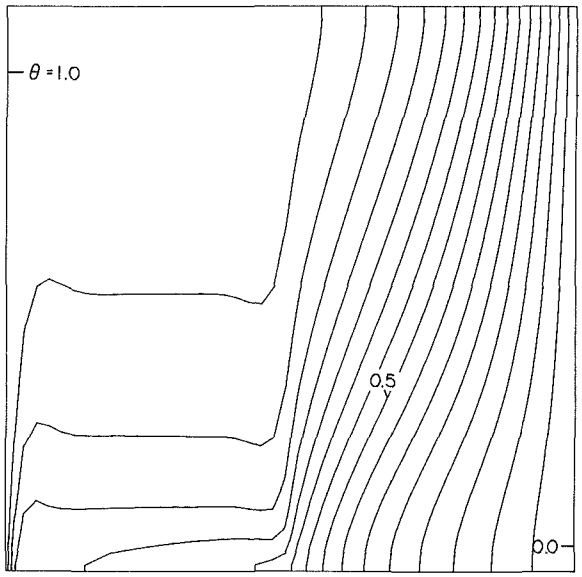

Fig. 2(c) Isotherms (equal increments)

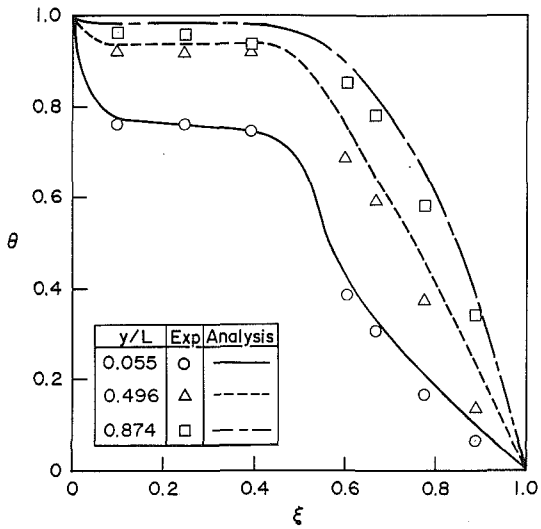

Fig. 2(d) Temperature profiles

Fig. 2 Experimental and predicted results for experiment 1 (water/small glass beads)

boundaries. For the comparisons with the experimental results (refer to Section 4), a grid of 50×50 nodal points was used. The iteration procedure was terminated when the dependent variables agreed to four significant digits. Convergence of the numerical solution was also checked by comparing the Nusselt numbers obtained along the two vertical side walls, equation (19). The agreement between the two values was always better than 0.1 percent. The calculations were performed on a CYBER 205 computer and required between 50 and 500 CPU seconds (depending on the mesh size and the Rayleigh and Darcy numbers). A test of the accuracy of the numerical algorithm was obtained by comparing the results to those reported in the literature for the limiting cases of a fully porous and a fully fluid enclosure. The results of these comparisons are given by Beckermann et al. (1986a).

3 Experiments

3.1 Test Cell and Instrumentation. Natural convection experiments were performed in two different test cells of square cross section partially filled with a porous medium. The smaller test cell had inside dimensions of 4.76 cm in height and width and 3.81 cm in depth, while the larger test cell measured 20.32 cm in height and width and 3.0 cm in depth. In both test cells, the two vertical sidewalls, which served as the heat source/sink, were multipass counterflow heat exchangers machined out of a copper plate. For flow visualization purposes, the vertical front and back walls were made of plexiglass. The horizontal top and bottom walls were made of acrylic and phenolic plates, respectively. The test cells were insulated with 5.09-cm-thick Styrofoam.

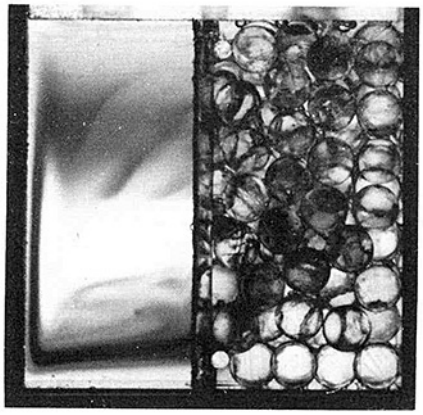

Fig. 3(*a*) Flow visualization

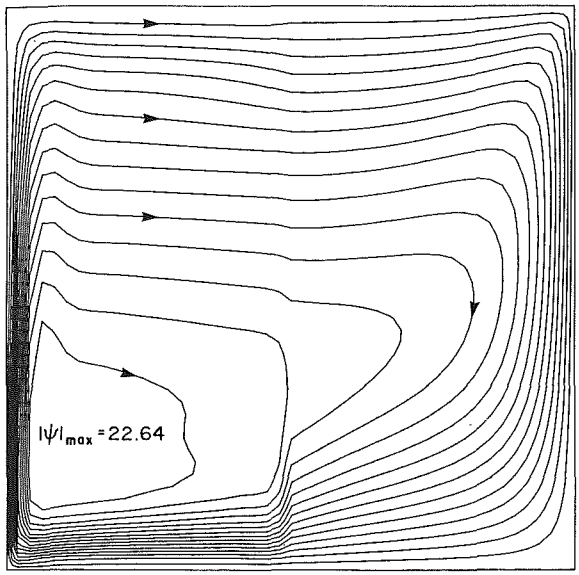

Fig. 3(*b*) Streamlines (equal increments)

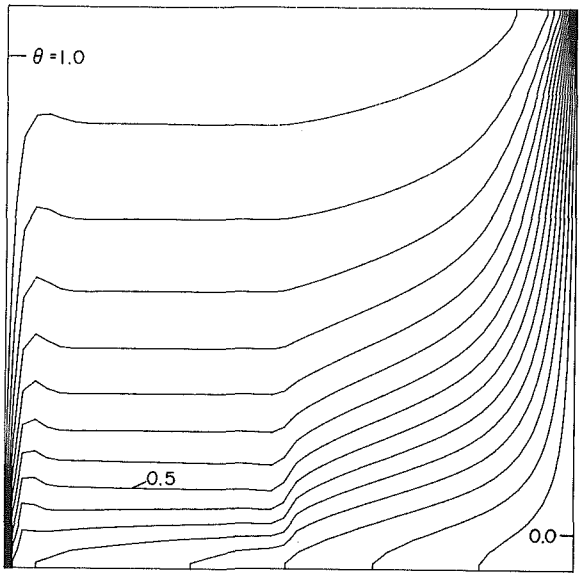

Fig. 3(*c*) Isotherms (equal increments)

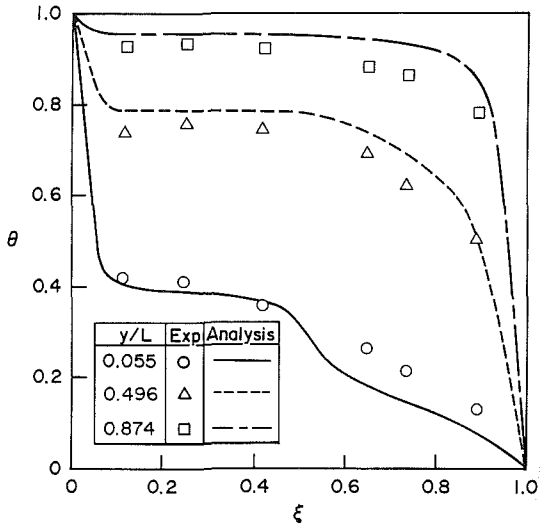

Fig. 3(*d*) Temperature profiles

Fig. 3 Experimental and predicted results for experiment 2 (water/large glass beads)

The temperatures of the copper heat exchangers were measured with five thermocouples epoxied separately into five small-diameter holes which were drilled close to the surface of the copper plates. The temperature distribution in the smaller test cell was measured using a movable thermocouple probe sheathed in a 1.27 mm o.d. stainless steel tube. The position of the thermocouple bead in the test cell was determined with a slide caliper. It was estimated that the position of the bead could be determined to within ± 0.5 mm. It should also be noted that the structure of the porous medium was slightly disturbed due to the movement of the thermocouple probe especially in the case of the large glass beads. This disturbance, however, is believed to have had a relatively small influence on the temperature measurements. After each movement of the thermocouple probe, the system was allowed to reach steady state again.

Measurement of the temperature distribution in the larger test cell was made with 28 thermocouples with a wire diameter of 0.127 mm which were placed in three different plexiglass rakes. The three rakes were located along the center line at heights of 2.86, 10.16, and 17.78 cm measured from the bottom of the test cell. All thermocouples were calibrated with an accuracy of ± 0.1°C.

3.2 Test Materials. Spherical glass beads were used as the porous medium. The beads were of soda-lime glass with diameters of 1.59 and 6.0 mm. The properties used were for a soda-lime glass with a chemical composition closely matching that of the glass beads used in this study (Weaver, 1985). The glass beads were held in place by a fine fiberglass screen supported by small diameter glass rods. The porosity of the screen was much higher than the porosity of the glass beads, while the mesh size was only slightly smaller than the diameter of the glass beads. It is believed that the screen had a negligible influence on the flow and heat transfer between the porous and fluid layers. In all experiments, the porous medium was a vertical layer occupying half of the test cell. The porosity was measured separately for each size glass bead (Weaver, 1985). For the large diameter glass beads, the increase in porosity near the walls of the test cells is more significant (considering the relatively small depth of the test cells) resulting in a higher value of the average porosity.

The fluids used were once-distilled, degasified water for the smaller test cell and chemical grade glycerin for the larger test cell. With the various combinations of fluids, glass beads, and test cells, it was possible to cover a broad range of the relevant dimensionless parameters. The values of the dimensionless parameters for the four experiments selected for comparison

with the numerical results are summarized in Table 1. All properties were evaluated at a temperature of $(T_H + T_C)/2$.

3.3 Experimental Procedures. In preparing for the experiment, one half of the test cell was first filled with the glass beads. Then, the water/glycerin was carefully siphoned into the test cell to ensure that no air was trapped in the matrix or to prevent air from mixing with the fluid. A mixture of alcohol and water was circulated through the two heat exchangers from two constant temperature baths. After the system reached steady state (after at least 12 hr), the thermocouple output was read using a data logger.

Flow visualization experiments were performed in the small test cell by injecting a Calcoid Blue ink/water solution at the top of the cold heat exchanger. The test cell was illuminated from the back through the plexiglass windows by using a white light source and a diffusing white glass plate. The dye was allowed to convect with the flow for some time and the entire test cell was then photographed from the front. No flow visualization was performed in the larger test cell with glycerin as the fluid.

4 Results and Discussion

4.1 Comparison of Predictions With Experiments. With the two different glass bead sizes used in the experiments in the smaller test cell, it was possible to cover a relatively broad range of Darcy numbers (from about 7.4×10^{-7} to 1.3×10^{-5}), while the other dimensionless parameters were approximately constant. The results of these experiments, together with the pertinent numerical predictions, are shown in Figs. 2 and 3. The values of the governing parameters corresponding to the figures are listed for the respective experiments in Table 1. It can be seen from both the flow visualization and the predicted streamlines, that with increasing permeability (i.e., Darcy number) the flow penetrates progressively more into the porous layer. In the case of the small glass beads (Fig. 2), the flow is almost completely confined to the fluid layer and is not able to penetrate into the porous layer. A boundary layer develops at the porous/fluid layer interface. On the other hand, in the case of the large glass beads (Fig. 3), the porous layer offers much less resistance to the flow and natural convection takes place in the entire cavity. For both sizes of glass bead, the streamlines show sharp changes in the slope at the fluid/porous layer interface. When the flow enters the porous matrix at the upper region of the test cell, the streamlines bend upward. Due to the strong downflow along the fluid/porous layer interface, the streamlines bend downward when the flow leaves the porous region. The above observations indicate that the porous matrix exerts a strong influence on the velocity component parallel to the interface (resulting in a high velocity gradient on the fluid side), while the normal velocity component is relatively unaffected. Both velocity components are actually continuous across the fluid/porous layer interface. Also, the center about which the flow circulates is moved toward the lower left corner of the test cell when compared to natural convection in a vertical cavity filled with a homogeneous medium.

In general, the agreement between the flow patterns revealed by the flow visualization experiments and the numerically predicted streamlines is good. With the dye injection method employed in the present study, it was not possible, however, to visualize the flow patterns in the porous layer. This is mainly due to scattering of the light by the glass beads. The sharp bending of the streamlines at the fluid/porous layer interface cannot be seen on the photographs (Figs. 2*a* and 3*a*), but it was observed during the experiments. It should also be kept in mind that, especially in

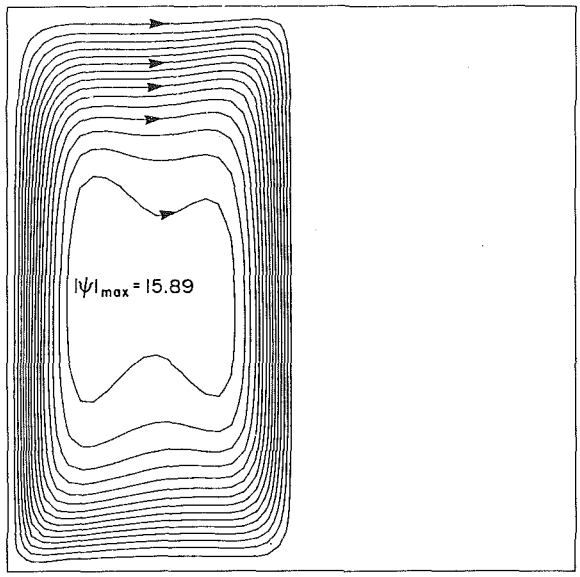

Fig. 4(*a*) Streamlines (equal increments)

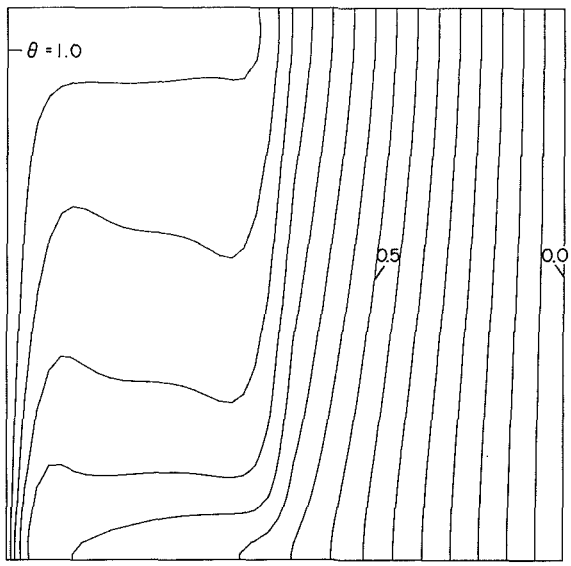

Fig. 4(*b*) Isotherms (equal increments)

Fig. 4 Numerical predictions for experiment 4 (glycerin/large glass beads)

the case of the large glass beads, there are relatively large nonuniformities in the porosity of the porous layer because of the presence of the walls. In reality, the porosity at the wall is always equal to one. This effect is, however, not taken into account in the model. It is also recognized that in experiment 2, the small size of the porous layer relative to the diameter of the glass beads might invalidate the assumptions of homogeneity and isotropy used in the derivation of the governing equations for the porous medium. The good agreement between the flow visualization and the predicted streamlines (Figs. 3*a* and 3*b*) indicates, however, that this problem is not too severe for the conditions of experiment 2.

The above observations are further supported by the predicted isotherm patterns shown in Figs. 2(*c*) and 3(*c*). In the case of the small glass beads (Fig. 2*c*) the isotherms in the porous layer are almost vertical and equally spaced, indicating that heat transfer is mainly by conduction. On the other hand, in the fluid layer, there exists a thermally stratified core in the center region with thermal boundary layers along the hot wall

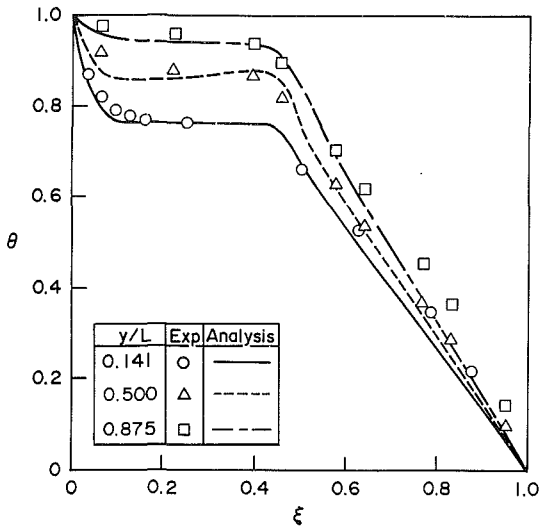

Fig. 5(*a*) Experiment 3

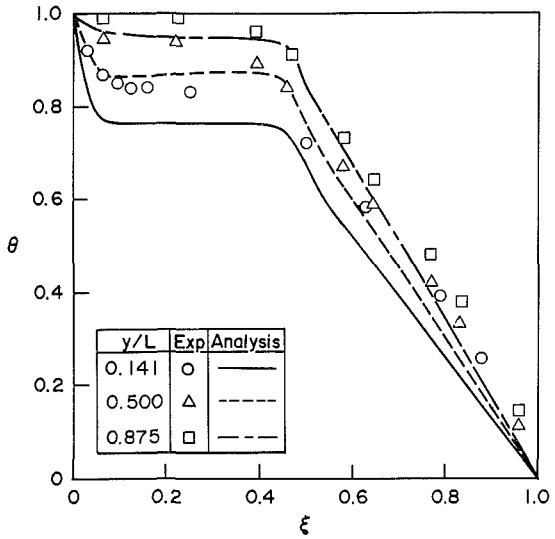

Fig. 5(*b*) Experiment 4

Fig. 5 Experimental and predicted temperature profiles (glycerin/large glass beads)

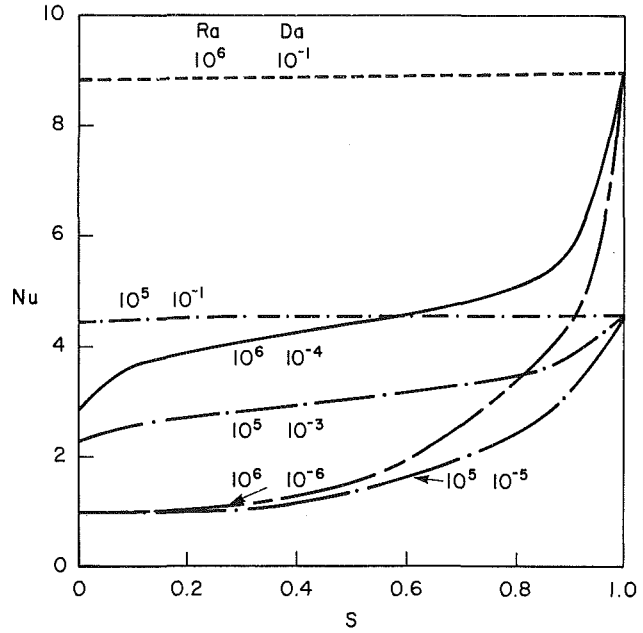

Fig. 6 Effect of fluid layer thickness on the Nusselt number (Pr = 1.0, R_k = 1.0, A = 1.0, C = 0.55)

and the porous/fluid layer interface, indicating strong natural convection flow. In the case of the large glass beads (Fig. 3*c*), the isotherms show that the fluid is thermally stratified throughout the test cell, while there are thermal boundary layers of different thickness at the hot and cold walls. In other words, the penetrating fluid causes the heat in the porous layer to be transferred convectively. In both cases, the isotherms show "cusps" at the porous/fluid layer interface which can be attributed to the natural convection flow and the difference in the thermal conductivity between the porous and fluid layers.

A quantitative comparison between measured and predicted temperatures is shown in Figs. 2(*d*) and 3(*d*). As mentioned earlier, temperature measurements were taken at three different heights in the small test cell. The general agreement between measured and predicted temperatures is good, and the differences in the temperature distributions between the experiments with the small and large glass beads are well predicted by the numerical model. It should be noted that the data trends become somewhat exaggerated due to the dimensionless representation. In reality, the discrepancies between the measured and predicted temperatures are less than about ± 1°C. A large part of these discrepancies is possibly due to the inaccuracies in determining the exact position of the movable thermocouple probe (refer to Section 3). Again, nonuniformities in the porosity at the walls are expected to produce a considerable difference between the numerical model and the experiments in the relatively small test cell of the present study.

In order to validate the model for various Rayleigh and Prandtl numbers as well as for different thermal conductivity ratios, experiments were also performed in a larger test cell with glycerin as the fluid (refer to Table 1). Although the same diameter glass beads were used in the experiments in the larger test cell, the Darcy numbers are two orders of magnitude lower than in the smaller test cell because of the larger length scale (i.e., L). Due to the high viscosity of glycerin, the Rayleigh number is one order of magnitude lower and the Prandtl number is much higher than in the experiments with water. Also, the thermal conductivity ratio is higher in the case of glycerin.

The predicted streamlines and isotherms for the case of the large glass beads (experiment 4) are illustrated in Fig. 4. (The numerical results for experiment 3 are presented in Beckermann et al. (1986a).) It can be seen that even for the large glass beads, the flow is almost completely confined to the fluid layer and very little penetration of glycerin into the porous layer takes place. Accordingly, the heat transfer in the porous layer is mainly by conduction (Fig. 4*b*). The streamlines in the fluid layer (Fig. 4*a*) show a behavior similar to what would be expected for natural convection in a vertical enclosure of the same aspect ratio as the fluid layer. In other words, even for the large glass beads the porous layer acts almost like a solid wall.

The measured and predicted temperature profiles for both sizes of glass beads (Figs. 5*a* and 5*b*) show that approximately 70 percent of the total temperature drop across the test cell takes place in the porous layer. The agreement between the slopes of the measured and predicted temperature profiles in the porous layer is very good, indicating the correctness of the model adopted for the effective thermal conductivity [equation (12)]. Also, the agreement is good for the general trend of the temperature profiles in the fluid layer. Both the measured and predicted temperature profiles show strong discontinuities in the slope at the porous/fluid layer interface which is due to the large differences in the thermal conductivities of the two

layers. The relatively large discrepancies in the absolute values of the temperatures in the case of the large glass beads (Fig. 5*b*) can be attributed to the larger nonuniformities in the porosity at the walls of the relatively thin test cell. In addition, the viscosity of glycerin varies by almost an order of magnitude over the temperature range in the present experiments (10°C). Both of the above effects are not taken into account in the model.

In summary, the comparison between measured and predicted data shown above established some confidence in the numerical model of the present study. Several "real" effects, namely, porosity and property variations, need more attention to obtain better agreement between experimental and numerical results.

4.2 Effect of Fluid Layer Thickness on the Nusselt Number. The effects of various fluid layer thicknesses S on the Nusselt number were determined numerically and are illustrated in Fig. 6. As expected, for (unrealistically) high Darcy numbers (i.e., $\mathrm{Da}=0.1$), the porous layer has nearly no effect on the heat transfer across the enclosure. The flow penetrates completely into the porous layer and natural convection is only slightly reduced. On the other hand, in the case of relatively low Darcy numbers (i.e., $\mathrm{Da}=1\times10^{-6}$ and $\mathrm{Da}=1\times10^{-5}$) the Nusselt number decreases sharply with decreasing fluid layer thickness. For these Darcy (and Rayleigh) numbers, only a small amount of fluid enters the porous layer, and the porous layer acts almost like a solid wall (see also Fig. 5). A further decrease in the Darcy number (for the same Rayleigh number) has practically no influence on the functional relationship between the Nusselt number and the fluid layer thickness. This observation is also supported by the fact that for an impermeable partition between the porous and fluid layers (Tong and Subramanian, 1983), the predicted decrease in the Nusselt number with decreasing fluid layer thickness is very similar to the decrease predicted for low Darcy numbers in the present study.

Quite different behavior can be seen for $\mathrm{Da}=1\times10^{-4}$ and $\mathrm{Da}=1\times10^{-3}$. Here, a small addition of a porous layer causes a sharp decrease in the Nusselt number. The decrease in the Nusselt number is, however, less sharp and approximately linear for further increases in the porous layer thickness and is again more pronounced when the enclosure is almost completely occupied by the porous layer (i.e., $S < 0.1$). This phenomenon can be explained by the fact that for Darcy numbers of the order of 1×10^{-4} (and a Rayleigh number of 1×10^{6}), the flow does penetrate into the porous layer. In this case, the penetrating fluid significantly alters the fluid flow in the fluid layer, i.e., the flow in the fluid layer is not similar to the natural convection patterns seen in a vertical enclosure of that aspect ratio (see also Figs. 2*a* and 3*a*). Hence, decreasing the thickness of the fluid layer has a completely different effect on the Nusselt number than in the case of low Darcy numbers where the flow is simply blocked by the porous layer.

In order to provide a quantitative criterion for the importance of penetration of fluid into the porous layer for the present physical system, many more numerical and experimental studies are needed. In particular, the effects of variations in the other dimensionless parameters, namely Pr, A, and R_k, need to be investigated. The experimental and numerical results (refer to Table 1 and Fig. 6, respectively) as well as additional numerical studies (Beckermann et al., 1986b) indicate, however, that the product $\mathrm{Ra}\times\mathrm{Da}$ should be greater than about 50 in order for penetration of fluid into the porous layer to be significant.

The coupling of the fluid flow in the porous and fluid layers is of particular importance in the solidification of castings. Here, the dendrites growing into the melt can form a highly permeable porous layer. The flow penetrating into the dendritic meshwork will not only alter the local conditions in this region but may also influence the natural convection patterns in the entire casting.

5 Conclusions

A model has been developed for natural convection in vertical enclosures containing simultaneously a fluid layer and a porous layer. The numerical results show good agreement with experiments conducted utilizing various glass beads, fluids, and test-cell sizes.

The effect of fluid layer thicknesses on the Nusselt number has been numerically investigated for various Rayleigh and Darcy numbers. It has been found that, if fluid penetrates into the porous layer, the natural convection patterns in the entire enclosure are significantly altered when compared to fully porous or fluid enclosures. The degree of penetration of fluid into the porous layer depends roughly on the product of the Rayleigh and Darcy numbers, which should be greater than about 50 in order for penetration to be significant.

Acknowledgments

The work reported in this paper was supported, in part, by the National Science Foundation under Grant No. CBT-8313573. Computer facilities were made available by Purdue University Computer Center.

References

Beckermann, C., Ramadhyani, S., and Viskanta, R., 1986a, "Natural Convection Flow and Heat Transfer Between a Fluid Layer and a Porous Layer Inside a Rectangular Enclosure," in: *Natural Convection in Porous Media*, V. Prasad and N. A. Hussein, eds., ASME, New York, pp. 1–12.

Beckermann, C., Viskanta, R., and Ramadhyani, S., 1986b, "Natural Convection in Vertical Enclosures Containing Simultaneously Fluid and Porous Layers," submitted to *Journal of Fluid Mechanics*.

Beckermann, C., Viskanta, R., and Ramadhyani, S., 1987, "A Numerical Study of Non-Darcian Natural Convection in a Vertical Enclosure Filled With a Porous Medium," *Numerical Heat Transfer* (in press).

Cheng, P., 1978, "Heat Transfer in Geothermal Systems," *Advances in Heat Transfer*, Academic Press, New York, Vol. 14, pp. 1–105.

Combarnous, M. A., and Bories, S. A., 1975, "Hydrothermal Convection in Saturated Porous Media," *Advances in Hydroscience*, Academic Press, New York, Vol. 10, pp. 231–307.

Ergun, S., 1952, "Fluid Flow Through Packed Columns," *Chemical Engineering Progress*, Vol. 48, pp. 89–94.

Fisher, K. M., 1981, "The Effects of Fluid Flow on Solidification of Industrial Castings and Ingots," *Physico Chemical Hydrodynamics*, Vol. 2, pp. 311–326.

Georgiadis, J., and Catton, I., 1984, "Prandtl Number Effect on Benard Convection in Porous Media," ASME JOURNAL OF HEAT TRANSFER, Vol. 108, pp. 284–290.

Lauriat, F., and Mesguich, F., 1984, "Natural Convection and Radiation in an Enclosure Partially Filled With a Porous Insulation," ASME Paper No. 84-WA/HT-101.

Lundgren, T. S., 1972, "Slow Flow Through Stationary Random Beds and Suspensions of Spheres," *Journal of Fluid Mechanics*, Vol. 51, pp. 1865–1874.

Neale, G., and Nader, W., 1974, "Practical Significance of Brinkman's Extension of Darcy's Law," *Canadian Journal of Chemical Engineering*, Vol. 52, pp. 475–478.

Nield, D. A., 1968, "Onset of Thermohaline Convection in a Porous Medium," *Water Resources Research*, Vol. 4, pp. 553–560.

Patankar, S., 1980, *Numerical Heat Transfer and Fluid Flow*, Hemisphere, New York.

Poulikakos, D., and Bejan, A., 1983, "Natural Convection in Vertically and Horizontally Layered Porous Media Heated From the Side," *International Journal of Heat and Mass Transfer*, Vol. 26, pp. 1805–1813.

Somerton, C. W., and Catton, I., 1982, "On the Natural Convection of Superposed Porous and Fluid Layers," ASME JOURNAL OF HEAT TRANSFER, Vol. 104, pp. 160–165.

Sun, W. J., 1973, "Convective Instability in Superposed Porous and Free Layers," Ph.D. Dissertation, University of Minnesota, Minneapolis, MN.

Tien, C. L., and Hong, J. T., 1985, "Natural Convection in Porous Media Under Non-Darcian and Non-uniform Permeability Conditions," in: *Natural Convection*, S. Kakac et al., eds., Hemisphere, Washington, DC.

Tong, T. W., and Subramanian, E., 1983, "Natural Convection in Rectangular Enclosures Partially Filled With a Porous Medium," *ASME-JSME Thermal Engineering Joint Conference*, ASME, New York, Vol. 1, pp. 331–338.

Veinberg, A. K., 1967, "Permeability, Electrical Conductivity, Dielectric Constant and Thermal Conductivity of a Medium With Spherical and Ellipsoidal Inclusions," *Soviet Physics—Doklady*, Vol. 11, pp. 593–595.

Weaver, J. A., 1985, "Solid-Liquid Phase Change Heat Transfer in Porous Media," MSME Thesis, Purdue University, West Lafayette, IN.

Prandtl Number Dependence of Natural Convection in Porous Media

T. Jonsson

I. Catton

Mechanical, Aerospace, and Nuclear Engineering Department, School of Engineering and Applied Science, University of California, Los Angeles, Los Angeles, CA 90024

The effect of Prandtl number of a medium on heat transfer across a horizontal layer was measured. Stainless steel particles of diameters 1.6, 3.2, and 4.8 mm, glass particles of diameters 2.5 and 6.00 mm, and lead particles of diameter 0.95 mm were used with silicon oil, water, and mercury as working fluids. The bed height was varied from 2.5 to 12 cm. Experimental results are presented showing Nusselt number as a function of medium Rayleigh number with the effective Prandtl number, defined as the product of medium Prandtl number and Kozeny-Carmen constant, serving as a parameter. Correlations for Nusselt number are given for effective Prandtl number less than 0.1 and for effective Prandtl number greater than 0.1, which corresponds to an infinite effective Prandtl number. For the steel-water case the wavenumber is shown as a function of medium Rayleigh number.

Introduction

Many processes and systems of current interest involve heat and mass transfer in porous media. As research proceeded on this topic, it became apparent that there are a number of fundamental problems dealing with transport in porous media which have not been sufficiently addressed. One such problem is buoyancy-driven flow in a horizontal layer. This work has been motivated by practical applications in areas such as thermal insulation, geothermal engineering, pollutant dispersal in aquifers, dynamics of snow layers, coolability in a LMFBR, and the storage of nuclear waste in deep geologic repositories. In all these areas, both experimental and theoretical work has been done to determine the nature of the flow field and heat transfer rate in a variety of saturated porous materials and flow domains.

To describe heat transfer in porous media, one uses an equivalence between the heterogeneous porous medium, made up of a solid matrix and a saturating fluid, and a fictitious continuum for which an energy equation is defined that is similar to that used in homogeneous fluids. This is the most common practice and the one being used here. In Fig. 1 the physical model for the problem of interest is shown. We consider a horizontal porous layer saturated with fluid, bounded from above and below by parallel, rigid, and perfectly conducting plates. When the temperature difference $T_H - T_C$ characterized by the dimensionless parameter Rayleigh number Ra is not too great, heat is transported by conduction. However, when the Rayleigh number exceeds a certain critical value Ra_c, the colder and denser fluid at the top tends to "topple over." The fluid becomes unstable and two-dimensional cellular patterns appear. It is postulated by some that increasing the Rayleigh number further results in three-dimensional cellular patterns and finally in chaotic motion, which is difficult to model physically.

The Prandtl number has not been accounted for in any previously reported work, because the inertia terms in the momentum equation have been omitted. In recent work by Georgiadis and Catton (1984) the mixed finite difference-Galerkin scheme of McDonough (1980) was used to solve the governing equations. A wave-number selection based on the theory of Glansdorff and Prigogine (1971) was introduced and the Prandtl number effect was taken into account using a nonlinear fluid motion equation. Their results are in good agreement with experimental work by Combarnous (1970) and the present work.

The number of experimental investigations dealing with the porous layer problem is surprisingly small. In addition to the work by Elder (1967a) and Wooding (1958) are the experiments by Combarnous (1970) and Kaneko et al. (1974). Combarnous presented data for a large number of systems, such as glass-water, lead-water, polypropylene-water, and glass-oil up to Rayleigh numbers of 50 times critical. He observed a difference in heat transfer for different systems that is not accounted for by previous work.

For additional and more detailed overviews of natural convection in porous media and especially its application to geothermal systems, the articles by Combarnous and Bories (1975), Combarnous (1978), and Cheng (1978) should be consulted.

To our knowledge no experimental measurements aimed directly at studying the effect of Prandtl number in natural convection in a horizontal porous layer have been presented. The porous layers studied in this work are glass-water, steel-water, glass-oil, and lead-mercury. The glass beds were made of particles of sizes 2.5 and 6.0 mm. The steel particles were 1.6, 3.2, and 4.8 mm, and the lead particles 0.95 mm in diameter. The bed height was varied from 2.5 to 12.0 cm. Before describing the experimental study that is the primary result of this work, we briefly present the theoretical background that will lead us to the proper parameters for correlation of the data.

Theoretical Background

The physical model being studied is shown in Fig. 2. The

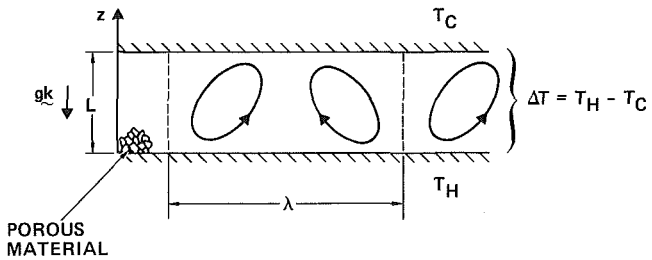

Fig. 1 Physical model

Contributed by the Heat Transfer Division for publication in the JOURNAL OF HEAT TRANSFER. Manuscript received by the Heat Transfer Division July 29, 1985.

solid matrix, consisting of spherical beads, is treated as a spatial discontinuity in the flow field. Thus the balance equations, as far as hydrodynamics is concerned, are written for the interstitial fluid while the porous walls form the boundaries of the flow field. By averaging the microscope equations over a small volume and introducing certain interstitial relationships, one recovers a momentum equation describing the seepage, or superficial, velocity (see Georgiadis, 1985, or Jonsson, 1984). The resulting equation is the Forcheimer-Brinkman motion equation

$$\frac{1}{\epsilon}\frac{\partial \mathbf{q}}{\partial t} = -\frac{1}{\rho_f}\nabla P + \frac{\nu_f}{\epsilon}\nabla^2\mathbf{q} - q\mathbf{e}_z - \left[\frac{\nu_f}{\mathcal{P}} + \frac{b}{\mathcal{P}}|\mathbf{q}|\right]\mathbf{q} \quad (1)$$

In order to nondimesionalize these equations the following scalings are used: time, $[L^2/\alpha_m]$, $\alpha_m = k_m/(\rho c)f$; length, $[L]$; temperature $[\Delta T]$, $\Delta T = T_H - T_C$; pressure, $[\rho_f \nu_f \alpha_m / L^2]$. The steady-state, dimensionless form of the equations of motion and continuity now become

$$\nabla \cdot \mathbf{q} = 0 \quad (2)$$

$$\frac{1}{\epsilon}\nabla^2\mathbf{q} - \frac{1}{\mathrm{Da}}\mathbf{q} + \mathrm{Ra}T^*\mathbf{e}_z - \nabla P^* = \frac{1}{\mathrm{Pr}_m \mathrm{KC}}|\mathbf{q}|\mathbf{q} \quad (3)$$

where the following dimensionless parameters have been introduced: Prandtl number of the medium, $\mathrm{Pr}_m = \nu_f/\alpha_m$; Darcy number, $\mathrm{Da} = \mathcal{P}/L^2$; Rayleigh number, $\mathrm{Ra} = g\beta\Delta T L^3/\nu_f\alpha_m$; Kozeny-Carmen constant, $\mathrm{KC} = \mathcal{P}/(bL)$. A parameter frequently used to correlate experimental data is a combination of the above, medium Rayleigh number, $\mathrm{Ra}_m = \mathrm{RaDa}$. For convenience the medium Rayleigh and Prandtl numbers will be referred to as just Rayleigh and Prandtl numbers.

In equation (3) we see that the Prandtl number appears directly due to the inclusion of the inertia term. Thus, omitting the inertia term is equivalent to assuming an infinite Prandtl number. Experimental as well as numerical studies show that this is a reasonable assumption for Prandtl numbers greater than 11. In equation (3) we also see the Prandtl number and the Kozeny-Carmen constant appear as a product, which implies that they should be replaced by a single number, the effective Prandtl number

$$\mathrm{Pr}_e = \mathrm{Pr}_m \mathrm{KC} \quad (4)$$

and that the length scale enters here as well as through specification of the Rayleigh number.

We assume that local thermal equilibrium exists between the solid and liquid phase, an assumption verified experimentally by Wong and Dybbs (1976). Thus, we adopt a one-equation model for the spatial average temperature that characterizes the energy transport in the porous medium. Neglecting viscous dissipation, assuming constant thermophysical properties and scaling, the steady-state energy equation is

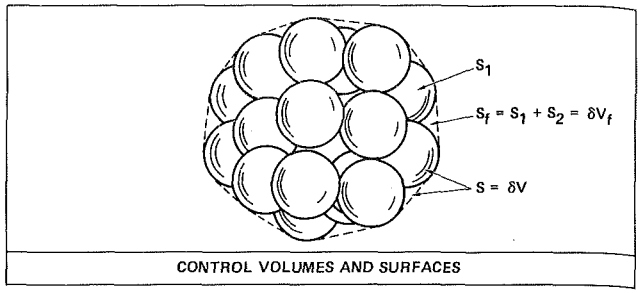

Fig. 2 Control volumes and surfaces

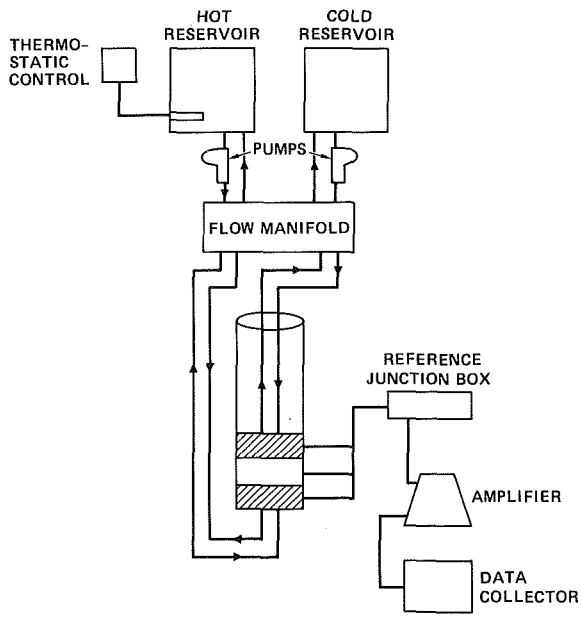

Fig. 3 Schematic of experimental apparatus

$$\mathbf{q} \cdot \nabla T = \nabla^2 T \quad (5)$$

No new parameters are introduced. The heat transfer augmentation resulting from convection is scaled with the conduction heat transfer yielding

$$\mathrm{Nu} = \frac{k_{\mathrm{eff}}}{k_m} \quad (6)$$

Natural Convection Experiment

A schematic of the experimental apparatus is shown in Fig. 3. The convection cell (Fig. 4) consists of a 17.5-cm i.d. plexiglass tube, bounded from above and below by heat meters.

Nomenclature

a = $2\pi L/\gamma$ = wavenumber (dimensionless)
b = inertial resistance coefficient
c = thermal capacity
Da = particle diameter
$\mathbf{e}_z$ = vector
f = body force vector
g = acceleration of gravity
k = thermal conductivity
KC = Kozeny-Carman coefficient
L = porous layer thickness
Nu = Nusselt number
$\mathcal{P}$ = permeability
P = pressure
Pr = Prandtl number
Pr_e = Pr_mKC effective Prandtl number
q = filtration velocity
Ra = Rayleigh number
u = velocity
U = conductance of epoxy layers
t = time
T = temperature
α = thermal diffusivity
β = coefficient of thermal expansion
ΔT = temperature difference
ϵ = porosity
λ = wavelength
μ = dynamic viscosity
ν = kinematic viscosity
ρ = density

Subscripts

C = cold wall
eff = effective
f = fluid
H = hot wall
m = porous medium
0 = reference value

Superscripts

* = perturbation

Table 1 Measured bed thermal conductivity and porosity

System	$k_{m,meas.}$, W/mK	$k_{m,calc.}$, W/mK	$\epsilon_{meas.}$
4.8-mm steel in water	3.3	10.1	0.393
2.5-mm glass in water	0.9	0.67	0.393
6.0-mm glass in water	1.1	1.03	0.394
2.5-mm glass in oil	0.6	0.32	0.395
6.0-mm glass in oil	0.6	0.39	0.394
0.95-mm lead in mercury	11.3	24.3	0.395

Each heat meter is made of two 1/4 in. copper plates separated by a thin layer of epoxy. Thermocouples are attached to each copper plate, and the thermal resistance of the epoxy layer is determined. Once the heat meters are calibrated by heating from above with several different fluids and plate spacings, heat transfer measurements across the convection cell can be made. The data acquisition system was calibrated by imposing a known EMF in place of the thermocouple EMF. The thermocouple signal is led through a zero reference junction box, then amplified before it is read by a digital computer. The computer converts the signal to temperature readout and calculates the Nusselt number. The experimental procedure will be discussed in detail below, but first some properties of the porous medium will be looked at.

Bed Properties. An important property of the porous medium is the medium thermal conductivity k_m. In prior investigations a typical mixing rule has usually been applied

$$k_m = \epsilon k_f + (1-\epsilon)k_s \tag{7}$$

In the present work k_m is measured by applying a stabilizing heat flux. In Table 1 comparison is made between measured and calculated values for k_m. The measurements are in significant disagreement with calculations. The reason equation (9) fails to give the desired result is that thermal conductivity is a complicated function of the bed materials and geometry. Simple addition should not be expected to be very accurate.

Another important property of the porous medium is the permeability, which can be calculated directly using Kozeny–Carmen equation

$$\mathcal{P} = \frac{d^2}{36k_0}\frac{\epsilon^3}{(1-\epsilon)^2} \tag{8}$$

When the porous medium is made of identical spherical beads, d is the bead diameter and $k_0 = 4.8$ (Wyllie and Gregory, 1955). The permeability can also be measured using Forchheimer's modification to Darcy's law

$$\frac{dP}{dz} = \frac{\mu}{\mathcal{P}}u + \frac{b}{\mathcal{P}}u^2 \tag{9}$$

where b is the turbulent or inertial coefficient. The second term is not too important if one is interested in low-velocity forced flow. It will be seen, however, that it does play a role in natural convection flows. Given two measurements of pressure drop versus flow rate one can obtain the permeability and turbulent coefficient. Experiments have been run to determine the permeabilities of most of the porous media systems used in the present work. The fluid used in making permeability measurements was water. Results are shown in Table 2 along with permeability values calculated from equation (10). The values are seen to be in reasonable agreement with one another.

Ergun (1952) showed that the internal resistance coefficient in the Kozeny–Carmen constant could be calculated within tolerable accuracy. The expression is

$$b = 0.0117d/(1-\epsilon) \tag{10}$$

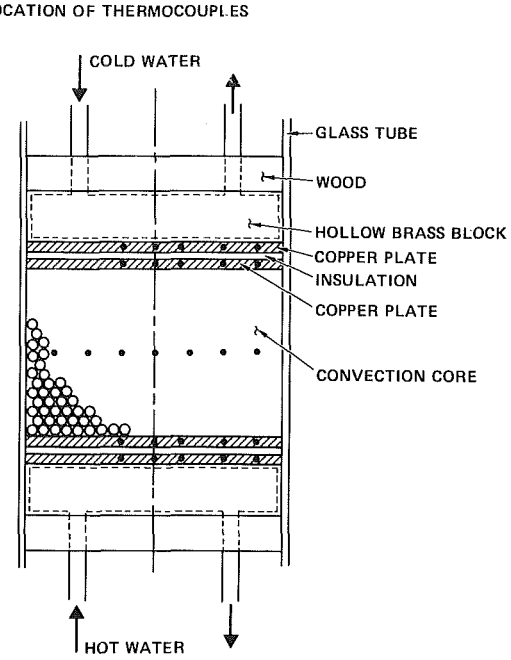

Fig. 4 Convection cell

Experimental Procedure. The experimental procedure is straightforward. First, the core of the convection cell is packed. Clean particles are saturated with the working liquid and then poured into the convection cell. The top heat meter is then lowered down to the top of the porous layer and fastened in place. The convection cell is shaken gently to level the bed and release any trapped air. Before the convection measurements begin the thermal conductivity of the porous medium is determined by applying a stabilizing temperature gradient to the porous layer. Then a destabilizing temperature gradient is applied to the porous layer by passing hot water through the bottom heat meter and cold water through the top heat meter. The average temperature of the cell is kept within a few degrees of room temperature to minimize heat losses. Once the heat fluxes are approximately equal and constant with time, it is assumed that steady state has been reached. This takes between 2 and 4 hrs depending on the porous medium being used. At this point temperature measurements begin, and at the same time the heater in the hot reservoir is turned off and no more ice is added to the cold reservoir. This results in a very slowly decreasing temperature gradient across the porous layer, so readings of Nusselt number at several Rayleigh numbers are obtained, while the Prandtl number is assumed to be constant for each run.

To determine the wavenumber, two strings of thermocouples are placed in the midplane of the porous medium, perpendicular to each other. Seven thermocouples are in each string. The deviation from average temperature is plotted as a function of radial distance, which typically results in the form of a sine wave, as shown in Fig. 5. The peaks correspond to upflow of hotter fluid, while the valleys correspond to downflow of colder fluid.

At this point a question might arise whether true steady-state results are obtained, because the temperature is changing with time. Sun (1970) used a lumped-capacitance model to derive an expression for Nusselt number. An important parameter in his analysis is the time constant of the system, defined as

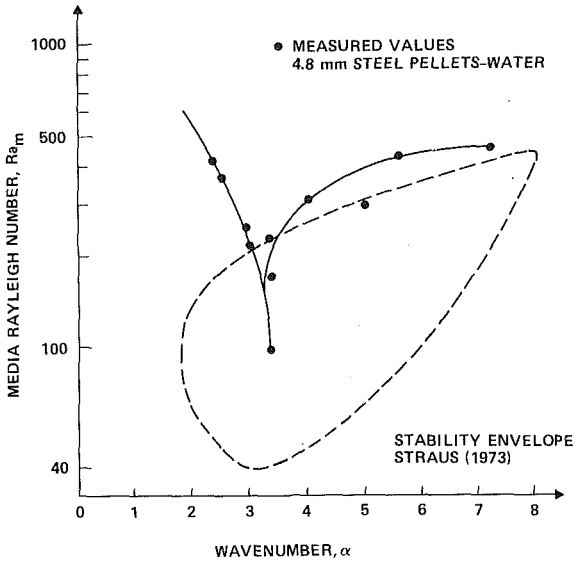

WAVENUMBER RESULTS FOR STEEL-WATER

Fig. 5 Wavenumber measurements

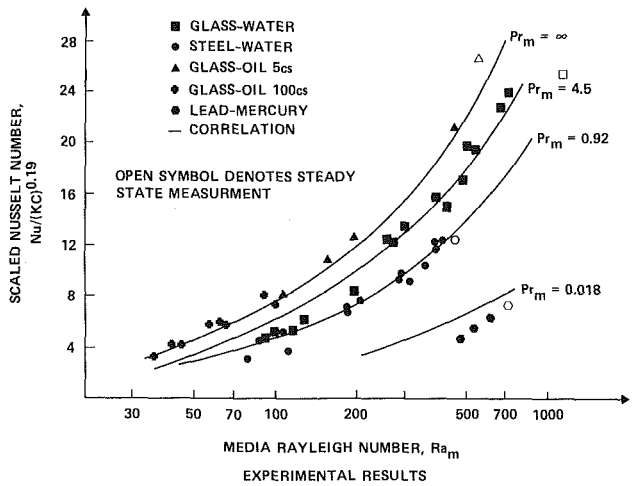

EXPERIMENTAL RESULTS

Fig. 6 Experimental results

$$\tau = \frac{c_m}{u_m} \tag{11}$$

where c_m is the thermal capacitance (mass times specific heat) of each heat meter assembly, and u_m is the thermal conductance. τ can be measured by conducting two runs with different decay rates. τ was not measured in this work, but Arnold (1978) measured it for a similar, but less massive system and found that τ was always on the order of 0.009 hr. Assuming that τ is of the same order here, we estimate the transient effects on the results to be very small. To insure that this was the case, moderate initial temperature differences were used so that each run would take several hours to complete. To be sure that the slow transient decay did not cause error in the assumption of steady state, several steady-state data points were obtained for comparison and the Nusselt number was found to be very close (see Fig. 7).

Error Analysis. The uncertainty in the experimental data can be considerable due to the following sources: The temperature measurements are accurate to 0.2°C; the porosity of the bed may vary from 0.38 to 0.42 which implies an uncertainty of about 4.0 percent; the height of the porous layer is measured to within 0.1 cm. Thermophysical properties are assumed to be constant with temperature, and known with no uncertainty. Using the assumptions that the errors are random, one can express the fractional overall error as the square root of the sum of the squares of the fractional error of each contributor. Doing so yields the following expected errors in the three parameters arising in this work:

$$\frac{\partial \mathrm{Nu}}{\mathrm{Nu}} = 0.13 \tag{12}$$

$$\frac{\partial \mathrm{Ra}}{\mathrm{Ra}} = 0.223 \tag{13}$$

$$\frac{\partial \mathrm{Pr}_e}{\mathrm{Pr}_e} = 0.17 \tag{14}$$

Table 2 Permeability values

System	Measured, m^2	Calculated, m^2
2.5-mm glass	$5.5*10^{-9}$	$6.09*10^{-9}$
6.0-mm glass	$3.7*10^{-8}$	$3.51*10^{-8}$
1.6-mm steel	$2.1*10^{-9}$	$2.49*10^{-9}$
4.8-mm steel	$1.9*10^{-8}$	$2.24*10^{-8}$
0.95-mm lead		$9.28*10^{-10}$

Results and Discussion

The experimental results for the six systems in Table 1 are presented in this section, along with a comparison with earlier experimental and numerical results. Correlations are given for heat transfer as a function of media Rayleigh number and the effective Prandtl number. Discussion of the results is also included.

Experimental Results. Experimental results were obtained for each of the six systems listed in Table 1. The results are presented in terms of the Nusselt number Nu using the measured thermal conductivity given in Table 1. The ordinate is the medium Rayleigh number Ra_m. The Rayleigh number is based on the measured value of permeability listed in Table 2.

The results are brought together in Fig. 6, where results for all the systems are shown. To demonstrate the Prandtl number effect itself, the Nusselt number is divided by KC to the power of 0.19, where the exponent comes from the data correlation. Figure 6 shows clearly how the heat transfer varies between the systems due to difference in Prandtl number. The data for Prandtl numbers greater than 11 fall on a single curve, which corresponds to infinite Prandtl number. For lower Prandtl numbers, the Nusselt number is obviously strongly dependent on the Prandtl number.

A correlation was sought that would relate Nusselt number to Rayleigh number and effective Prandtl number. The correlation is

$$\mathrm{Nu} = 0.118\ \mathrm{Ra}_m^{0.65}\mathrm{Pr}_e^{0.19} \qquad \mathrm{Pr}_e < 0.1$$

$$\mathrm{Nu} = 0.147\ \mathrm{Ra}_m^{0.65} \qquad \mathrm{Pr}_e > 0.1 \tag{15}$$

The correlation is shown in Fig. 6 by the solid curves. We can see considerable scatter of experimental results around those curves, which comes partly from the experimental errors discussed below, and partly because of the effect of Darcy number. Equation (5) implies that the Darcy number should directly affect the heat transfer results, by means other than just being included in the Rayleigh number. The above correlations should therefore be looked at as an intermediate measure until enough data are available to give statistically significant meaning to a correlation involving Da. The Darcy number for each case was measured by Jonsson (1984) and can be found in Table 3.

Table 3 Experimental data

System	L, cm	Da	Pr_m	KC	Pr_e	Ra_m	Nu
	3.2	3.58×10^{-5}	4.5	0.0114	0.0513	199.0	3.7
	3.2	3.58×10^{-5}	4.5	0.0114	0.0513	308.0	5.8
	3.2	3.58×10^{-5}	4.5	0.0114	0.0513	499.0	7.3
	4.2	2.08×10^{-5}	4.5	0.0087	0.0392	95.0	1.9
Glass–water	4.2	2.08×10^{-5}	4.5	0.0087	0.0392	100.0	2.2
$d=6$ mm	4.2	2.08×10^{-5}	4.5	0.0087	0.0392	111.0	2.2
	4.2	2.08×10^{-5}	4.5	0.0087	0.0392	135.0	2.3
	7.0	7.48×10^{-6}	4.5	0.00523	0.0235	551.0	7.2
	7.0	7.48×10^{-6}	4.5	0.00523	0.0235	684.0	8.3
	7.0	7.48×10^{-6}	4.5	0.00523	0.0235	953.0	8.6
	10.2	5.28×10^{-7}	3.9	0.00149	0.00581	287.0	3.6
	10.2	5.28×10^{-7}	3.9	0.00149	0.00581	396.0	4.6
Glass–water	10.2	5.28×10^{-7}	3.9	0.00149	0.00581	528.0	5.7
$d=2.5$ mm	14.3	2.68×10^{-7}	3.9	0.00107	0.00416	266.0	3.4
	14.3	2.68×10^{-7}	3.9	0.00107	0.00416	411.0	4.1
	14.3	2.68×10^{-7}	3.9	0.00107	0.00416	724.0	6.3
	3.9	1.56×10^{-5}	0.92	0.00750	0.00690	180.0	2.7
	3.9	1.56×10^{-5}	0.92	0.00750	0.00690	113.0	1.5
	3.9	1.56×10^{-5}	0.92	0.00750	0.00690	205.0	3.0
Steel–water	3.9	1.56×10^{-5}	0.92	0.00750	0.00690	295.0	3.6
$d=4.8$ mm	7.8	3.90×10^{-6}	0.92	0.00375	0.00345	356.0	3.6
	7.8	3.90×10^{-6}	0.92	0.00375	0.00345	399.0	4.2
	7.8	3.90×10^{-6}	0.92	0.00375	0.00375	468.0	4.3
Steel–water	7.0	4.80×10^{-6}	0.92	0.00418	0.00385	291.0	3.3
	7.0	4.80×10^{-6}	0.92	0.00418	0.00385	400.0	4.1
$d=4.8$ mm	7.0	4.80×10^{-6}	0.92	0.00418	0.00385	413.0	4.3
Steel–water	2.7	3.50×10^{-6}	0.92	0.00564	0.00519	79.4	1.2
	2.7	3.50×10^{-6}	0.92	0.00564	0.0519	89.1	1.7
$d=1.6$ mm	2.7	3.50×10^{-6}	0.92	0.00564	0.00519	108.0	1.9
Steel–water	4.3	3.41×10^{-6}	0.92	0.00453	0.00417	169.0	2.4
$d=3.2$ mm	4.3	3.41×10^{-6}	0.92	0.00453	0.00417	317.0	3.4
	2.5	1.49×10^{-6}	0.018	0.00232	4.17×10^{-5}	712.0	2.3
Lead–mercury	2.5	1.49×10^{-6}	0.018	0.00232	4.17×10^{-5}	618.0	2.0
$d=0.95$ mm	2.5	1.49×10^{-6}	0.018	0.00232	4.17×10^{-5}	532.0	1.8
	2.5	1.49×10^{-6}	0.018	0.00232	4.17×10^{-5}	494.0	1.5
	5.2	2.03×10^{-6}	15.7	0.00293	0.0460	111.0	2.7
Glass–oil 5cs	5.2	2.03×10^{-6}	15.7	0.00293	0.0460	164.0	3.6
	5.2	2.03×10^{-6}	15.7	0.00293	0.0460	198.0	4.2
$d=2.5$ mm	7.3	1.21×10^{-6}	15.7	0.00209	0.0328	462.0	6.5
	7.3	1.21×10^{-6}	15.7	0.00209	0.0328	560.0	7.5
	4.7	1.66×10^{-5}	236.0	0.00778	1.836	42.5	1.7
	4.0	2.29×10^{-5}	236.0	0.00915	2.159	42.7	1.8
Glass in	4.0	2.29×10^{-5}	236.0	0.00915	2.159	57.6	2.4
100 cs oil	3.7	2.68×10^{-5}	236.0	0.00989	2.334	35.3	1.4
$d=6$ mm	6.2	9.55×10^{-6}	236.0	0.00590	1.392	65.4	2.1
	6.2	9.55×10^{-6}	236.0	0.00590	1.392	94.3	2.9
	5.7	1.13×10^{-5}	236.0	0.00642	1.515	63.2	2.3
	5.7	1.13×10^{-5}	236.0	0.00642	1.151	107.4	3.0

Figure 7 compares the Nusselt number correlations with measured values. We see that most of the empirical values fall within 10 percent of the measured values, which gives us some confidence in the above correlations. Figures 8–11 give a more detailed picture of each system being tested.

The wavenumber results for the steel–water case are shown in Fig. 12. For a particular Rayleigh number there are two possible wavenumbers. Which one is chosen in each case does not seem to be easily predictable. It is a function of initial conditions which we were not able to fix in our experiment. The stability envelope calculated by Straus (1974) for infinite horizontal layer and Prandtl number is also shown. The measured wavenumbers for the right-hand branch fall near enough to the upper part of the stability envelope to give it some credibility. The steel pellets saturated with water yield a medium Prandtl number of 0.9. A larger Prandtl number will probably shift the curve more to the left, if Bénard convection similarities exist, casting some doubt on the balloon boundaries.

The temperature measurements used to measure the wavenumber were made in each and every run, but only for the steel–water porous layer did they yield a clear result. For

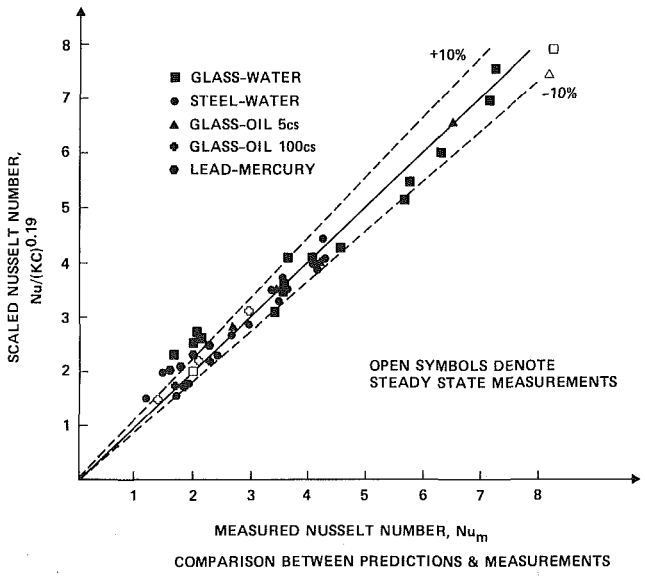

Fig. 7 Comparison between predictions and measurements

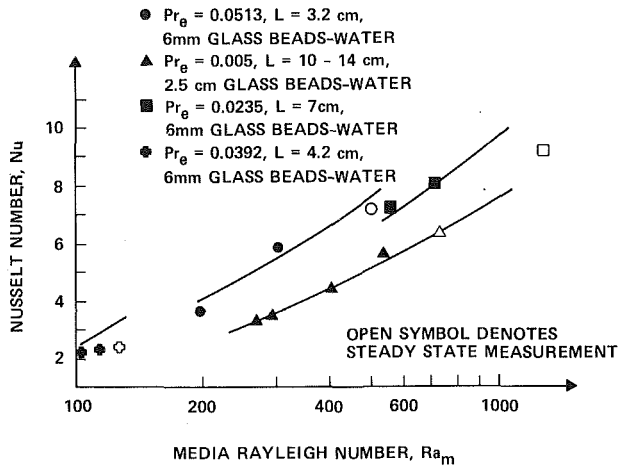

HEAT TRANSFER RESULTS FOR GLASS-WATER

Fig. 8 Experimental results, glass-water

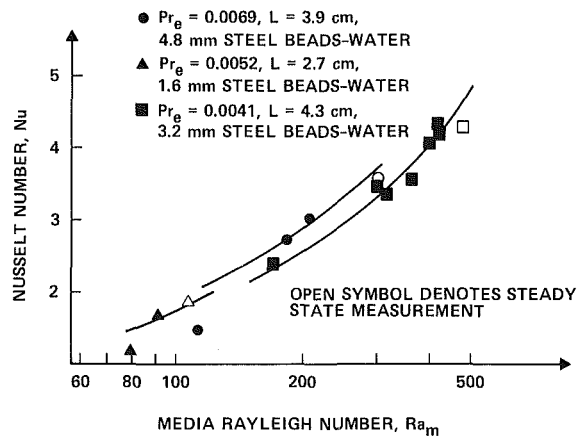

HEAT TRANSFER RESULTS FOR STEEL-WATER

Fig. 9 Experimental results, steel-water

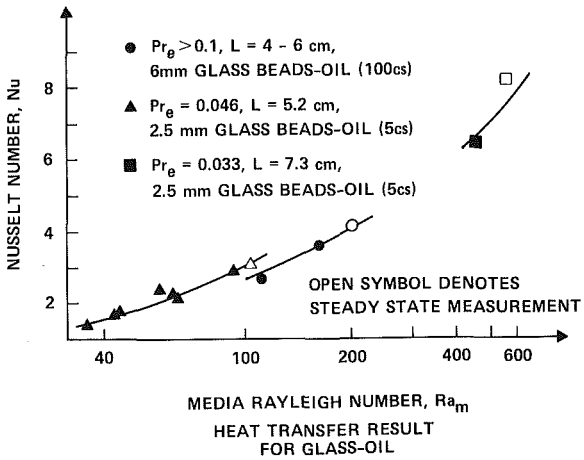

Fig. 10 Experimental results, glass-oil

other systems we were not able to calculate the wavenumber from experimental data because no wavelike temperature distribution was observed. Possible reasons for this are that for higher Prandt number layers, the amplitude of the temperature distribution is so small that it was absorbed into the error in the temperature measurements. For lower Prandtl number layers, runs were made at high Rayleigh numbers, where three-dimensional rolls exist. With the current apparatus those rolls cannot be detected.

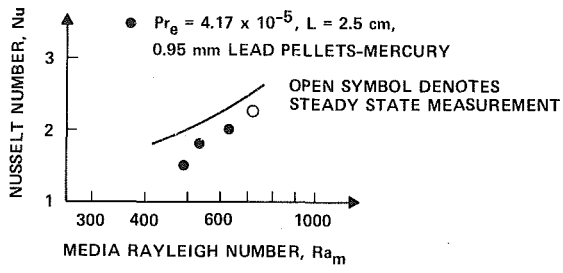

HEAT TRANSFER RESULT LEAD-MERCURY

Fig. 11 Experimental results, lead-mercury

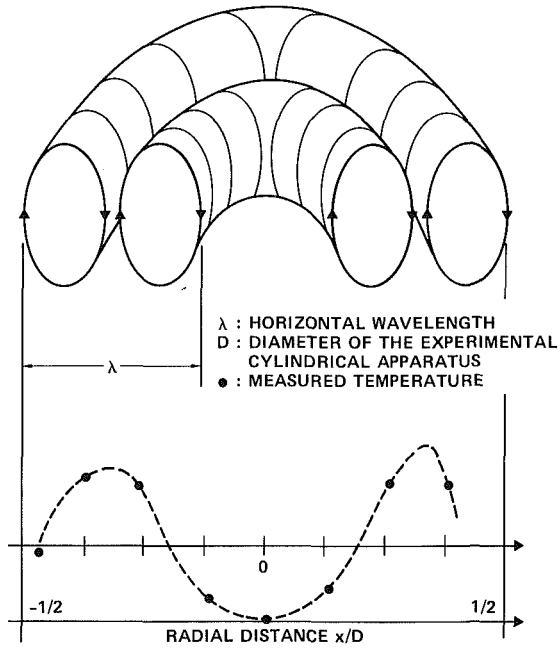

POSTULATED SHAPE OF THE CORRECTION CELLS
AND TEMPERATURE HORIZONTAL PROFILE

Fig. 12 Wavenumber results, steel-water

Comparison With Earlier Work. Here comparison of present work is made to experimental results presented by Combarnous and Bories (1975) and to numerical work by Georgiadis and Catton (1984). Combarnous and Bories presented experimental results for several different systems, such as glass-oil, glass-water, and quartz-water. They did not show what their exact geometric configuration was (plate spacing) so the effective Prandtl number could not be calculated from their data. For glass-water $1/Pr_e$ is typically of the order 20-40 and for glass-oil, 0.6-20, depending on the viscosity of the oil. In Fig. 13 their results are plotted along with the present results and the numerical results by Georgiadis and Catton.

For the glass-oil system our results compare well with the numerical results while results by Combarnous and Bories show considerably higher heat transfer.

For the water-glass system all the results compare well for $Ra_m < 250$ but above that the curves diverge, the numerical results showing less heat transfer than experimental. The reason for this most likely lies in the fact that when Ra_m is between 250 and 300 the steady-state two-dimensional convection pattern breaks down, and unsteady three-dimensional convection begins. Experiments show an increase in slope of the heat transfer curve at that point, which has not been accounted for in the numerical analysis.

For the lead-mercury case, no prior experimental data are available, but present experimental results are in good agree-

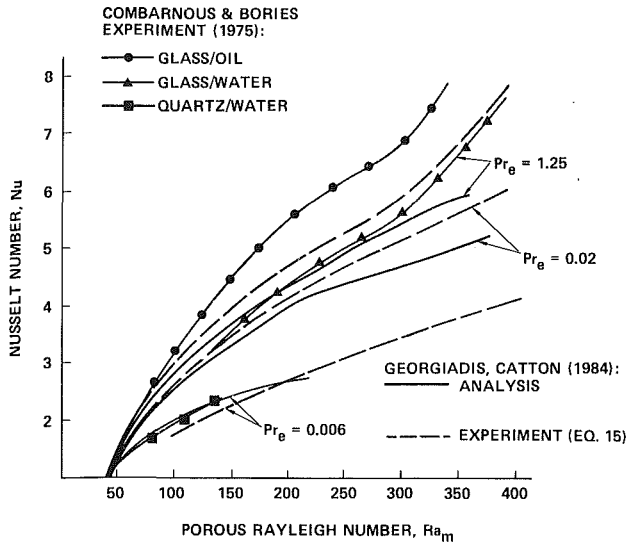

Fig. 13 Comparison with the work of others

ment with the numerical predictions of Georgiadis and Catton (1984).

Conclusions

The following conclusions may be drawn from this experimental study:

1 The Prandtl number and the Kozeny–Carmen constant appear as a product allowing an effective Prandtl number Pr_e to be defined that is a function of layer and medium geometry as well as fluid properties.

2 The experimental data presented in this paper clearly indicate that the Prandtl number has a significant effect on the magnitude of the heat transfer across a differentially heated fluid saturated porous layer, especially for low values of the Prandtl number.

3 For effective Prandtl numbers greater than 0.1, the Nusselt number no longer increases with increasing Prandtl number and it can be assumed to be infinite.

4 The effective Prandtl number varies inversely with layer thickness. This means that no matter how large the medium Prandtl number is, there will be a layer thickness that is large enough that inertial effects will become important. This should be contrasted with Bénard convection where the Prandtl number appears without a geometric parameter.

5 The wide variation between predictions of thermophysical properties and their measured values requires that they be measured for each system, and moreover the thermal conductivity should be measured for each run. The inability to accurately predict medium thermophysical properties may be another source of scatter in reported results.

6 A measured nonuniqueness in wavenumber was found for water-saturated beds of steel particles. The nonuniqueness cannot be explained by the results of this study. Similar nonuniqueness can be found in the analysis of Georgiadis and Catton [1984]. Both the experiment and the analysis yield the same Nusselt number at different values of the wavenumber.

7 The large amount of disparity found in previously reported results can be, at least in part, explained by the dependence of the effective Prandtl number on the plate spacing. The other major contributor is not knowing the medium thermophysical properties.

Acknowledgments

This work was supported by the Basic Sciences Division of the Department of Energy under Grant DOE 34-76FR12021. The assistance of Ben Alexander in accomplishing the experimental effort and Phyllis Gilbert for enabling us to report it is gratefully acknowledged.

References

1 Arnold, N. N., "Heat Transfer by Natural Convection in Enclosed Rectangular Cavities," Ph.D. Thesis, University of California, Los Angeles, CA, 1978.

2 Aziz, K., and Combarnous, M., "Prediction Theoretique du Transfert de Chaleur par Convection Dans une Couche Poreuse Horizontale," *Comptes Rendus Academie Science*, Ser. B, Vol. 271, 1970, pp. 813–815.

3 Beck, J. H., "Convection in a Box of Porous Material Saturated With Fluid," *International Journal of Heat and Mass Transfer*, Vol. 15, 1972, pp. 1377–1383.

4 Bories, S., "Comparison des Previsions d'une Non-lineare et des Resultats Experimentaux en Convection Naturelle Dans une Couche Poreuse Saturee Horizontale," *Comptes Rendus Academie de Science*, Ser. B, Vol. 271, 1970, pp. 169–172.

5 Busse, F., and Joseph, D., "Bounds for Heat Transport in a Porous Layer," *Journal of Fluid Mechanics*, Vol. 54, 1972, pp. 521–543.

6 Cheng, P., "Heat Transfer in Geothermal Systems," *Advances in Heat Transfer*, Vol. 14, 1978, pp. 1–105.

7 Combarnous, M. A., "Convection Naturelle et Convection Mixte en Milieu Poreux," Ph.D. Thesis, University of Paris, France, 1970.

8 Combarnous, M. A., "Natural Convection in Porous Media and Geothermal Systems," *VI International Heat Transfer Conference*, Toronto, 1978.

9 Combarnous, M. A., and Bories, S. A., "Hydrothermal Convection in Saturated Porous Media," *Advances in Hydroscience*, Vol. 10, 1975, pp. 231–307.

10 Elder, J. W., "Steady Free Convection in a Porous Medium Heated From Below," *Journal of Fluid Mechanics*, Vol. 27, 1967, pp. 29–48.

11 Elder, J. W., "Transient Convection in Porous Medium," *Journal of Fluid Mechanics*, Vol. 27, 1967, pp. 609–623.

12 Ergun, S., "Fluid Flow Through Packed Columns," *Chemical Engineering Progress*, Vol. 48, 1952, pp. 89–94.

13 Georgiadis, J., "Numerical Study of the Inertial Effect on Natural Convection in an Infinite Horizontal Fluid-Saturated Porous Layer," M.Sc. Thesis, University of California, Los Angeles, CA, 1985.

14 Georgiadis, J., and Catton, I., "Prandtl Number Effect on Bénard Convection in Porous Media," presented at the ASME National Heat Transfer Conference, Niagara Falls, NY, 1984.

15 Glansdorff, P., and Prigogine, I., *Thermodynamic Theory of Structure, Stability and Fluctuations*, Wiley-Interscience, New York, 1971.

16 Gupta, V. P., and Joseph, D. D., "Bounds for Heat Transport in a Porous Layer," *Journal of Fluid Mechanics*, Vol. 57, 1973, pp. 491–514.

17 Horton, C. W., and Rogers, F. T., "Convection Currents in a Porous Medium," *Journal of Applied Physics*, Vol. 16, 1945, pp. 367–370.

18 Jonsson, T., "Prandtl Number Dependence of Natural Convection in Porous Medium," M.Sc. Thesis, University of California, Los Angeles, CA, 1984.

19 Kaneko, T., Mohtadi, M. F., and Aziz, K., "An Experimental Study of Natural Convection in Inclined Porous Media," *International Journal of Heat and Mass Transfer*, Vol. 17, 1974, pp. 485–496.

20 Katto, Y., and Masouka, T., "Criterion for the Onset of Convection in a Fluid in Porous Media," *International Journal of Heat and Mass Transfer*, Vol. 10, 1967, pp. 297–309.

21 Lapwood, E. R., "Convection of a Fluid in a Porous Medium," *Proceedings of the Cambridge Philosophical Society*, Vol. 44, 1948, pp. 508–521.

22 Malkus, W. V. R., and Veronis, G., "Finite Amplitude Cellular Convection," *Journal of Fluid Mechanics*, Vol. 4, 1958, pp. 225–260.

23 McDonough, J. M., "The Rayleigh-Bénard Problem on a Horizontal Unbounded Domain: Determination of the Wavenumber of Convection," Ph.D. Thesis, University of California, Los Angeles, CA, 1980.

24 Palm, E., Weber, J., and Kvernvold, O., "On Steady Convection in a Porous Medium," *Journal of Fluid Mechanics*, Vol. 2, 1972, pp. 273–285.

25 Ruth, D. W., "A Model for Convection in Horizontal Porous Media Layers," 1980, Paper No. AIAA-80-0090. AIAA 18th Aerospace Sciences Meeting, Pasadena, CA.

26 Somerton, C. W., "Natural Convection and Boiling in Porous Media," Ph.D. Thesis, University of California, Los Angeles, CA, 1982.

27 Straus, J. M., "Large Amplitude Convection in Porous Media," *Journal of Fluid Mechanics*, Vol. 64, 1974, pp. 51–63.

28 Sun, W. M., "Effects of Arbitrary Wall Conduction on Radiation on Free Convection in a Cylinder," Ph.D. Thesis, University of California, Los Angeles, CA, 1970.

29 Wooding, R. A., "Steady State Free Thermal Convection of Liquid in a Saturated Permeable Medium," *Journal of Fluid Mechanics*, Vol. 2, 1957, pp. 273–285.

30 Wooding, R. A., "An Experiment on Free Thermal Convection of Water in Saturated Permeable Material," *Journal of Fluid Mechanics*, Vol. 3, 1958, pp. 582–600.

31 Wong, K., and Dybbs, A., "An Experimental Study of Thermal Equilibrium in Liquid Saturated Porous Media," *International Journal of Heat and Mass Transfer*, Vol. 18, 1976, pp. 234–235.

32 Wyllie, M. J. R., and Gregory, A. R., "Fluid Flow Through Unconsolidated Porous Aggregates," *Ind. Eng. Chem.*, Vol. 47, 1955, pp. 1379–1388.

An Improved Approach to Conductive Boundary Conditions for the Rayleigh-Bénard Instability

J. H. Lienhard V
Department of Applied Mechanics
and Engineering Sciences
and
Project in Nonlinear Science,
University of California at San Diego,
La Jolla, CA 92093
Student Mem. ASME

A technique is developed for predicting the stability limit of conductively coupled horizontal fluid layers heated from below and cooled above. The approach presented gives exact solutions of the stability problem and is numerically much simpler than previous multilayer solutions. Critical Rayleigh numbers are obtained for the case of three and four fluid layers separated by equally spaced identical midlayers of various thicknesses and conductivities with isothermal outer walls and for the symmetric two-layer problem with outer walls of finite thermal conductivity. Other configurations are considered briefly.

Introduction

Natural convection in parallel arrays of fluid layers is a problem of current technical interest. The most outstanding example of a coupled fluid layer array is the set of cover layers on a flat plate solar collector. In this example, as in many others, the basic design objective is convection suppression, to reduce heat loss. A necessary first step toward suppressing convection is prediction of the stability limit of the quiescent state of the fluid.

To date only the two-layer problem has been studied. Gershuni and Zhukhovitskii [1] considered the stability of a pair of identical fluid layers separated by a conducting midlayer, allowing the outer boundaries to be either isothermal or of the same conductivity as the midlayer. They found approximate solutions using the Galerkin method. Catton and Lienhard [2] generalized the problem to allow for fluid layers of differing heights, considering isothermal outer boundaries; their solutions were obtained using a higher order Galerkin approximation.

Here, I consider the stability of the one-dimensional conductive state of an array of horizontal fluid layers heated from below and cooled above. A general technique is formulated for obtaining exact solutions of the stability problem in an arbitrary number of layers when the thermal coupling is by conduction through intermediate solid layers (the important problem of radiative coupling is not treated here). The method follows standard techniques of stability analysis and relies on manipulation of the boundary conditions to simplify the equations to be solved. The resulting computational procedure is much simpler and yields higher accuracy than the previous multilayer solutions.

The heart of the procedure is the formulation of a third kind thermal boundary condition dependent upon the wavenumber and, more generally, a coupling parameter which must be iterated. While third kind conditions were first discussed for the single layer more than fifty years ago by Low [8], only in 1968 was a wavenumber-dependent condition considered by Nield [11], in the context of a conductive boundary slab. Apparently, no subsequent work has dealt with conductive boundaries.

The Effect of Midlayer Conduction on Multilayer Stability

The physical behavior of multilayer instability is discussed in detail by Catton and Lienhard [2] in the context of a two-layer system. The general features of the instability are, at the simplest level, just like those of the ordinary Bénard instability. Once the temperature gradient in a fluid layer becomes large enough, the release of buoyant energy by fluid motion exceeds the associated viscous dissipation and convection ensues. However, heat conduction through adjacent solid layers modifies the stability limit of a layered system and allows thermal interactions between adjacent fluid layers.

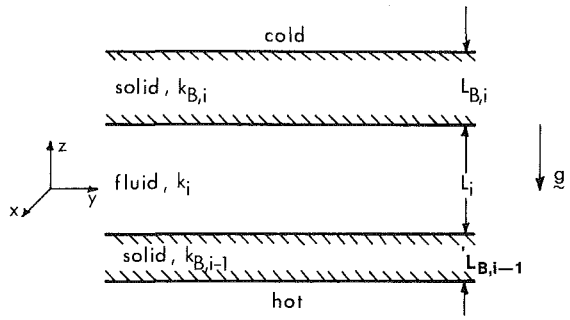

Fig. 1 Archetypical configuration for coupled layers

When fluid layers are coupled by a conducting midlayer, a thermal disturbance in one layer of wavelength λ is present in the adjacent layers at the same wavelength. Thus, if one layer has a higher Rayleigh number than an adjacent layer, we may think of it as becoming unstable at some critical Ra and driving convection in the adjacent layer, even if the latter might otherwise be stable. In no case can one layer in a thermally interacting group be quiescent while convection occurs in the others. If the thermal coupling is weak, however, the amplitude of convection in one layer may be much less than in others.

The thermal conductivity and thickness of the midlayers are the dominant parameters affecting the stability of a layered system. Thicker, more conductive layers tend to damp out thermal disturbances, resulting in weaker coupling between the layers. Thin midlayers allow less damping of thermal disturbances, resulting in greater thermal coupling. In general, when the thermal interaction of the layers is stronger, the stability of an individual layer is lower. Poorly conducting midlayers allow less dissipation of thermal disturbances and result in hot and cold spots along the midlayer, lowering the stability of individual fluid layers.

When considering the stability limit of a layered system, one must distinguish between the overall Rayleigh number of the layered system and the Rayleigh number of an individual fluid layer. The overall critical Rayleigh number may be increased indefinitely by adding more layers (for a fixed overall temperature difference) and by making the midlayers less con-

Contributed by the Heat Transfer Division and presented at the 23rd National Heat Transfer Conference, Denver, Colorado, August 4-7, 1985. Manuscript received by the Heat Transfer Division November 5, 1985.

ductive. The individual layer critical Rayleigh number always varies between 1708 (isothermal boundaries) and 720 (fixed heat flux boundaries), with associated critical wavenumbers of 3.12 and 0, respectively. One other important critical Rayleigh number is 1296 (with wavenumber 2.56) which occurs for a single layer with one isothermal and one fixed heat flux wall.

The results presented here focus on the individual layer critical Rayleigh number. The critical wavenumber is largely ignored, both for brevity and because it varies between the above limits, more or less in tandem with the critical Rayleigh number and in a fairly regular fashion.

Governing Equations

Our analysis begins with the usual disturbance equations for horizontally unbounded, plane solid and fluid layers. The archetypical geometry is illustrated in Fig. 1. A fluid layer is bounded by rigid, conducting solids above and below. The thermal conditions imposed at the outer boundaries of the solid layer are arbitrary. These conditions will be prescribed later in the context of particular problems. The basic temperature gradient is in the negative z direction.

Perturbation and normal mode analysis of the Oberbeck-Boussinesq equations leads to the following sixth-order O.D.E. for the normal mode amplitude of the temperature disturbance, Θ_i, in a fluid layer i [1, 3]

$$\left\{-\frac{s_i}{\mathrm{Pr}}+(D_i^2-a_i^2)\right\}\{-s_i+(D_i^2-a_i^2)\}(D_i^2-a_i^2)\Theta_i = -a_i^2\mathrm{Ra}_i\Theta_i \tag{1}$$

where the dimensional temperature disturbance in layer i is

$$T_i' = \Delta T_i \cdot \Theta_i(z_i)\exp[s_i t_i + i(a_{x_i}x_i + a_{y_i}y_i)]$$

Here all quantities (except T_i') are cast in the scales of layer i. In particular, Pr is the Prandtl number, $\mathrm{Ra}_i = (g\beta/\nu\alpha)L_i^3\Delta T_i$ is the Rayleigh number of layer i, $a_i^2 = a_{x_i}^2 + a_{y_i}^2 = 2\pi L_i/\lambda$ is the wavenumber for layer i, and ΔT_i—the temperature scale for this layer—is the temperature difference across layer i.

We state without proof that instability will occur by passage through a marginal state in which disturbances neither decay nor grow characterized by $s_i = 0$. This assertion, known as exchange of stabilities, has been proven for various boundary conditions on a single layer (see, e.g. [1, 3]) and for a pair of coupled fluid layers [4]. The proof for an arbitrary number of solid and fluid layers involves only more algebra than the proof in [4]. To find the critical Rayleigh number, we therefore need only consider the case $s_i = 0$ in (1)

$$(D_i^2 - a_i^2)^3\Theta_i = -a_i^2\mathrm{Ra}_i\Theta_i \tag{2}$$

The general solution of the above equation was found long ago by Pellew and Southwell [5] and is

$$\Theta_i = A\cosh(qz_i) + A^*\cosh(q^*z_i) + A_0\cos(q_0z_i) + B\sinh(qz_i) + B^*\sinh(q^*z_i) + B_0\sin(q_0z_i) \tag{3}$$

where $(\ )^*$ denotes a complex conjugate and

$$q_0 = a_i(\tau-1)^{1/2}$$

$$q^2 = a_i^2\left(1+\frac{1}{2}\tau(1\pm i\sqrt{3})\right)$$

with

$$\mathrm{Ra}_i = a_i^4\tau^3$$

Here we may take $z_i \in (-1/2, 1/2)$. The coefficients in (3) will be chosen to satisfy the six boundary conditions on Θ which we shall develop presently.

We are interested in situations in which the thermal disturbance will be carried into the solid layers above and below the fluid layer. In these layers

$$\frac{\partial T_B}{\partial t_B} = \nabla_B^2 T_B \tag{4}$$

where $(\ )_B$ denotes a value in the solid. This equation has been nondimensionalized with the scales: length—L_B, the thickness of the solid layer; time—L_B^2/α_B; temperature—ΔT_B, the temperature difference across the solid layer. Perturbing

Nomenclature

A = midlayer to fluid layer aspect ratio = $L_B/2L_i$; A_{ij} = $L_{B_j}/2L_i$

a_i = dimensionless wavenumber in layer i = $2\pi L_i/\lambda$

D_i = dimensionless z derivative in layer i

h = heat transfer coefficient, assumed spatially uniform

k = thermal conductivity (of fluid unless subscripted with B or 0)

L_i, L_{B_j} = thickness of fluid layer i and thickness of midlayer j, respectively

M, N = coefficients of even, odd portions of midlayer thermal disturbance

Ra_i = Rayleigh number of fluid layer i = $(g\beta/\nu\alpha)L_i^3\Delta T_i$

Ra_c = critical Rayleigh number of layer i

Ra_T = overall Rayleigh number

Re = real part of a complex number

s_i = dimensionless disturbance growth rate in layer i

T_i' = temperature disturbance in layer i

X_B = fluid to solid layer conductivity ratio = k/k_B; $X_{B_{ij}} = k_i/k_{B_j}$

X_0 = fluid layer to outer wall conductivity ratio = k/k_0

Greek Letters

α = even/odd disturbance amplitude ratio = M/N; α_B is the thermal diffusivity of a solid layer

γ = fluid layer Biot number = (hL_i/k_i)

γ_e = cover plate Biot number = (hL_B/k_B)

$\Delta T_i, \Delta T_{OA}$ = temperature difference across layer i and across entire multilayer array, respectively

Θ = dimensionless normal mode thermal disturbance amplitude

Λ = coefficient of third kind boundary condition: $\Theta' = \Lambda\Theta$; definition varies by context

$\Lambda_{Ui}, \Lambda_{Li}$ = coefficient at upper and lower boundaries of fluid layer i, respectively

λ = dimensional disturbance wavelength

Subscripts and Superscripts

$(\ )_i$ = a variable in layer i

$(\ )_B, (\ )_{B_j}$ = a variable in a solid layer or boundary, in barrier j

$(\ )'$ = differentiation with respect to z_i

equation (4) and analyzing the disturbance into normal modes yields

$$\left\{-s_B+(D_B^2-a_B^2)\right\}\Theta_B=0 \tag{5}$$

The physical wavelength and growth rate (λ and σ) are common to the fluid and solid layers so that

$$\lambda=\frac{2\pi}{a_i}L_i=\frac{2\pi}{a_B}L_B \Rightarrow a_B=\frac{L_B}{L_i}a_i$$

and, with exchange of stabilities,

$$s_i=s_B=0$$

in the marginal state. The solution of equation (5) with $s_B = 0$ is

$$\Theta_B=M\cosh(a_Bz_B)+N\sinh(a_Bz_B),\quad z_B\in\left(-\frac{1}{2},\frac{1}{2}\right) \tag{6}$$

with the constants M and N to be found from the thermal boundary conditions on the solid layer. Commonly, this requires simultaneous solution for all the constants arising in the entire set of fluid and solid layers.

Boundary Conditions

Boundary conditions are required for the vertical velocity disturbance w_i and the fluid and solid temperature disturbances T_i and T_B.

At a rigid, horizontal boundary we have

$$\mathbf{v}=(u,\ v,\ w)=0$$

and, with the continuity equation

$$\frac{\partial u}{\partial x}+\frac{\partial v}{\partial y}+\frac{\partial w}{\partial z}=\frac{\partial w}{\partial z}=0$$

at the boundaries. By (2) these are equivalent to

$$(D_i^2-a_i^2)\Theta_i=(D_i^2-a_i^2)D_i\Theta_i=0 \tag{7}$$

The thermal boundary conditions on a fluid layer match temperature and heat flux to those of the bounding solids. In physical variables

$$T_i=T_B,\quad -k_i\frac{dT_i}{dz}=-k_B\frac{dT_B}{dz}$$

or, in terms of the nondimensional disturbances

$$\Theta_i=\left(\frac{k_i}{k_B}\right)\left(\frac{L_B}{L_i}\right)\Theta_B$$

and

$$D_i\Theta_i=D_B\Theta_B \tag{8}$$

Note that the thermal boundary conditions are generally not symmetric about the fluid layer and the even and odd functions in Θ_i cannot be separated as in the symmetric case.

We may use equations (7) to reduce the number of free constants in equation (3). Conditions (7) apply at each boundary of the fluid layer ($z_i = \pm 1/2$), and, by taking advantage of the even/odd behavior of the cos/cosh and sin/sinh functions in the expression for Θ_i, we find

$$\begin{bmatrix}\cosh(q/2) & \cosh(q^*/2)\\ q\sinh(q/2) & q^*\sinh(q^*/2)\end{bmatrix}\begin{bmatrix}(q^2-a^2)A\\ (q^{*2}-a^2)A^*\end{bmatrix}=A_0(q_0^2+a^2)\begin{bmatrix}\cos(q_0/2)\\ -q_0\sin(q_0/2)\end{bmatrix} \tag{9}$$

and

$$\begin{bmatrix}\sinh(q/2) & \sinh(q^*/2)\\ q\cosh(q/2) & q^*\cosh(q^*/2)\end{bmatrix}\begin{bmatrix}(q^2-a^2)B\\ (q^{*2}-a^2)B^*\end{bmatrix}=B_0(q_0^2+a^2)\begin{bmatrix}\sin(q_0/2)\\ +q_0\cos(q_0/2)\end{bmatrix} \tag{10}$$

These equations may be solved directly (e.g., by Cramer's rule) to find A/A_0, B/B_0, and their conjugates, cutting the number of unknown coefficients from six to two.

Finally, we observed that if no forcing of the system's thermal disturbance is imposed the boundary conditions will be homogeneous, and we must choose particular values of Ra to obtain nontrivial solutions for Θ which satisfy equations (7) and (8). The smallest of the eigenvalues Ra must be minimized as a function of wavenumber to obtain the critical Rayleigh number.

The Appearance and Use of Third Kind Thermal Boundary Conditions

We are interested in developing a technique for collapsing the coupling conditions (8) into a single condition applied directly to the fluid layer, thereby avoiding the need to solve simultaneously for the constants and Rayleigh numbers in all fluid and solid layers. The simplest example of such an approach was given by Sparrow et al. [6] in 1964. They considered the case in which the medium adjacent to the fluid layer could be characterized by a spatially uniform heat transfer coefficients as

$$-k_i\frac{dT}{dz}=\pm h(T-T_\infty) \tag{11}$$

where the minus sign applies when $T_\infty > T$. Perturbing this condition and scaling with ΔT_i, L_i produces

$$\Theta_i'=\mp\left(\frac{hL_i}{k_i}\right)\Theta_i=\mp\Lambda\Theta_i \tag{12}$$

a third kind condition depending on a constant Λ (which is a Biot number here). For Bénard-type problems the plus sign applies at the (hot) lower surface if the direction of increasing z is taken to be vertically upward. Equation (12) is applied directly to the fluid layer and allows us to ignore the details of the disturbance to the external medium.

Of particular interest are the two limiting cases:

$\Lambda\to\infty\Rightarrow\Theta_i=0$ isothermal wall

$\Lambda\to 0\Rightarrow\Theta_i'=0$ fixed heat flux wall

One may show analytically that the critical Rayleigh number will increase monotonically as Λ is increased, in agreement with the results of Sparrow et al.

A somewhat more advanced example is obtained when the bounding surface is a semi-infinite wall of thermal conductivity k_B. Here the appropriate solution of equation (5) is

$$\Theta_B=M\exp(-a_Bz_B),\quad z_B\in(0,\ \infty) \tag{13}$$

if $z_B = 0$ at the boundary of the fluid and z_B is scaled with L_i. Substitution into condition (8) gives

$$\Theta_i=\left(\frac{k_i}{k_B}\right)M\,e^{-a_Bz_B}$$

$$\Theta_i'=-M\,a_Be^{-a_Bz_B}=-M\,a_ie^{-a_iz_B}$$

in light of the scaling. We may form a single third kind condition by eliminating M between these equations

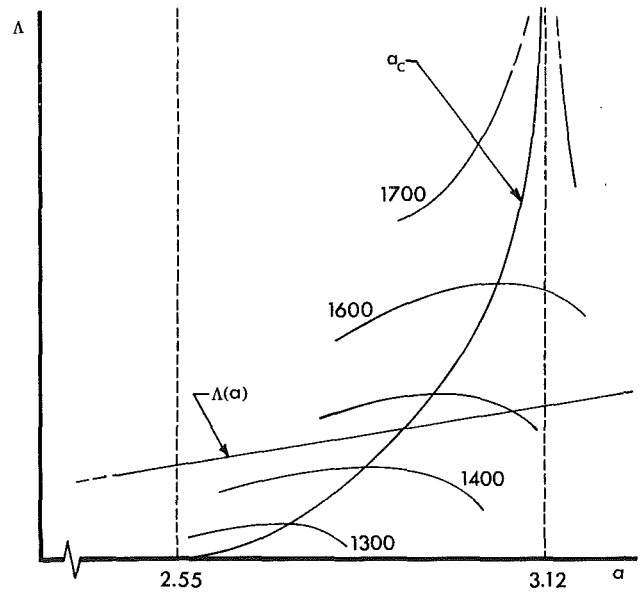

Fig. 2 Level curves of the Rayleigh number as a function of Λ and a

$$\Theta_i' = -\left(\frac{a_i}{k_i/k_B}\right)\Theta_i = -\left(\frac{a_i}{X}\right)\Theta_i \tag{14}$$

with X defined as indicated. At a lower surface, z_B will have opposite orientation and the minus sign in equation (1) becomes a plus sign.

For this problem $\Lambda = (a_i/X)$ is wavenumber dependent, and the calculation of the critical Rayleigh number will include a constrained variation of the parameter Λ with a_i. Note, however, that simultaneous solution for M, the coefficients of Θ, and Ra is no longer required. We need consider only the fluid layer and the disturbance in the wall requires no better specification that equation (13).

The wavenumber dependence of Λ has a marked effect on the stability limit of the fluid layer. The cases of equations (12) and (14) are contrasted in Fig. 2, assuming for example that Λ applies on top with the lower surface isothermal. The figure shows schematically the level curves of $\mathrm{Ra}(a, \Lambda)$. The curve a_c is the locus of critical wavenumbers for given $\Lambda \neq \Lambda(a)$, viz., the result of using equation (12). The critical Rayleigh numbers for fixed Λ lie on this curve. On the other hand, when $\Lambda = a/X$ the critical Rayleigh number for a given X corresponds to the lowest Ra level curve intersecting the line $\Lambda = (1/X)a$. Of particular importance is the observation that these points do not generally lie on the curve a_c for constant Λ. Hence, there is not a unique curve for $\mathrm{Ra}_c = \mathrm{Ra}_c(a, \Lambda(a))$ if $\Lambda(a)$ is arbitrary.

To this point our remarks have been organizational. We are now in a position to tackle some previously unsolved problems.

The Two-Layer Problem With Finite Outer Wall Conductivity

We consider here the problem of two identical fluid layers separated by a finite thickness and conductivity midlayer and bounded by identical outer walls of finite conductivity (Fig. 3). This configuration is symmetric about the centerline of the midlayer. Lienhard and Catton [7] found that disturbances of the two layer system with isothermal outer walls are either even or odd about the midlayer centerline when the fluid layers are of equal height. This will also be true when the outer walls are not isothermal.

For even disturbances, the midlayer thermal perturbation must be

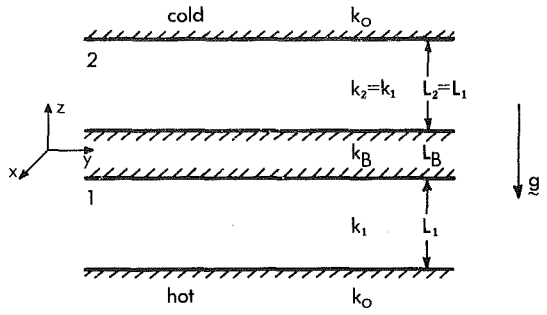

Fig. 3 The symmetric two-layer configuration

$$\Theta_B(z_B) = M \cosh(a_B z_B) \tag{15}$$

and for odd modes

$$\Theta_B(z_B) = N \sinh(a_B z_B) \tag{16}$$

We may substitute these general forms into equations (8) and eliminate M and N. The result for even disturbances is

$$\left.\begin{aligned}\Theta_1'(1/2) &= -\Lambda_e \Theta_1(1/2)\\ \Theta_2'(-1/2) &= \Lambda_e \Theta_2(-1/2)\end{aligned}\right\} \tag{17}$$

with

$$\Lambda_e = \left(\frac{a_1}{X_{B_1}}\right)\tanh(a_1 A) \tag{18}$$

and $X_{B_1} = k_1/k_B$, $A = L_B/2L_1$. For the odd modes we find

$$\Lambda_0 = \left(\frac{a_1}{X_{B_1}}\right)\coth(a_1 A) \tag{19}$$

Observe that $\Lambda_e \leq \Lambda_0$ for a given two-layer system; as noted above Ra_c increases monotonically with Λ, so even modes will always occur before odd modes. This agrees with the results of [7].

The thermal conditions at the outer walls were developed in the preceding section and are

$$\left.\begin{aligned}\Theta_1'(-1/2) &= \Lambda_w \Theta_1(-1/2)\\ \Theta_2'(1/2) &= -\Lambda_w \Theta_2(1/2)\end{aligned}\right\} \tag{20}$$

with $\Lambda_w = a_1/X_{0_1}$, $X_{0_1} = k_1/k_0$. The eigenvalue problems for the two layers are the same. In agreement with physical intuition, the layers must become unstable simultaneously (at the same Rayleigh number). Accordingly, we need solve the problem only for one layer, say the first.

The equations to be solved are algebraic. Equation (6) is substituted into equations (17) and (20); equations (9) and (10) are used to eliminate A, A^*, B, and B^* in favor of A_0 and B_0. The result is

$$\begin{bmatrix}\mathcal{C}_1 & \mathcal{C}_2\\ \mathcal{C}_3 & \mathcal{C}_4\end{bmatrix}\begin{bmatrix}A_0\\ B_0\end{bmatrix} = 0$$

where the $\mathcal{C}_i$ are uninteresting functions of Ra, a, Λ_e, and Λ_w which we have relegated to the Appendix. For nontrivial solutions we must have

$$\mathcal{C}_1\mathcal{C}_4 - \mathcal{C}_2\mathcal{C}_3 = 0 \tag{21}$$

For a given a, Λ_e, and Λ_w this equation has roots for varius Ra. To solve for the stability limit Ra_c, the smallest of these roots was located using bisection and then minimized as a function of wavenumber using parabolic fit of $\mathrm{Ra}(a)$ and the requirement $d\mathrm{Ra}/da = 0$. Calculations made in double precision FORTRAN on a Vax-11 yielded the results in Table 1. These results are believed accurate to the number of figures shown.

Table 1 Critical Rayleigh numbers for the two-layer system

A = 0.001

X_{B_1} \ X_0	0.0	0.1	0.3	1.0	3.0	10.0	∞
0.0	1707.76	1667.96	1607.18	1492.66	1391.00	1329.56	1295.78
0.0003	1668.56	1627.90	1565.65	1447.85	1342.74	1279.06	1244.04
0.001	1596.97	1554.73	1489.67	1364.98	1251.56	1181.69	1142.89
0.003	1483.85	1439.71	1371.02	1235.88	1105.60	1016.89	956.69
0.01	1374.40	1330.31	1261.32	1123.52	985.59	884.11	792.00
0.1	1304.95	1262.17	1195.12	1060.58	924.45	822.50	727.20
1.0	1296.71	1254.16	1187.44	1053.51	917.83	816.06	720.72
∞	1295.78	1253.25	1186.58	1052.71	917.09	815.35	720.00

A = 0.01

X_{B_1} \ X_0	0.0	0.1	0.3	1.0	3.0	10.0	∞
0.0	1707.76	1667.96	1607.18	1492.66	1391.00	1329.56	1295.78
0.001	1694.03	1653.93	1592.64	1477.02	1374.23	1312.07	1277.90
0.01	1596.95	1554.71	1489.65	1364.96	1251.54	1181.67	1142.87
0.03	1483.83	1439.69	1371.00	1235.86	1105.58	1016.88	956.69
0.1	1374.38	1330.29	1261.30	1123.51	985.58	884.10	792.00
1.0	1304.95	1262.17	1195.12	1060.58	924.45	822.49	727.20
10.0	1296.71	1254.16	1187.44	1053.51	917.83	816.06	720.72
∞	1295.78	1253.25	1186.58	1052.71	917.09	815.35	720.00

A = 0.1

X_{B_1} \ X_0	0.0	0.1	0.3	1.0	3.0	10.0	∞
0.0	1707.76	1667.96	1607.18	1492.66	1391.00	1329.56	1295.78
0.03	1667.45	1626.82	1564.59	1446.84	1341.78	1278.12	1243.12
0.1	1594.60	1552.43	1487.47	1362.96	1249.71	1179.93	1141.18
0.3	1481.23	1437.22	1368.74	1234.03	1104.19	1015.86	956.22
1.0	1372.95	1328.98	1260.16	1122.69	985.08	883.84	792.00
3.0	1324.51	1281.30	1213.60	1077.91	940.97	838.85	744.00
10.0	1304.76	1262.00	1194.98	1060.48	924.39	822.47	727.20
∞	1295.78	1253.25	1186.58	1052.71	917.09	815.35	720.00

A = 0.3

X_{B_1} \ X_0	0.0	0.1	0.3	1.0	3.0	10.0	∞
0.0	1707.76	1667.96	1607.18	1492.66	1391.00	1329.56	1295.78
0.03	1690.44	1650.39	1589.17	1473.68	1371.00	1308.90	1274.76
0.1	1654.49	1613.91	1551.74	1434.01	1328.87	1265.13	1230.07
0.3	1577.79	1536.02	1471.67	1348.32	1236.08	1166.91	1128.48
1.0	1452.47	1409.19	1341.80	1209.03	1080.64	992.82	932.78
3.0	1363.40	1320.07	1252.25	1116.81	981.28	881.74	792.00
10.0	1318.28	1275.40	1208.20	1073.47	937.42	835.90	741.60
∞	1295.78	1253.25	1186.58	1052.71	917.09	815.35	720.00

A → ∞

X_{B_1} \ X_0	0.0	0.1	0.3	1.0	3.0	10.0	100.0	∞
0.0	1707.76							
0.1	1667.96	1628.02						
0.3	1607.18	1566.93	1505.29					
1.0	1492.66	1451.68	1388.53	1267.47				
3.0	1391.00	1349.22	1284.33	1157.50	1037.89			
10.0	1329.56	1287.29	1221.24	1090.02	961.13	872.10		
100.0	1299.41	1256.91	1190.30	1056.72	921.90	821.91	753.34	
∞	1295.78	1253.25	1186.58	1052.71	917.09	815.35	740.99	720.00

Table 2 Rayleigh numbers for $A/X_B = 1$ at various A

A	Ra_c	a_c	% Error, Ra	% Error, b.c.	Column 5 / Column 4
0.001	1330.31	2.50	0	-	-
0.01	1330.29	2.50	0.0013	0.021	20.7
0.1	1328.98	2.50	0.10	2.04	20.4
0.3	1320.07	2.51	0.77	15.4	20.0

The basic trends in the critical Rayleigh number Ra_c as a function of A and X_{B_1} were discussed in [2] for $X_{0_1} = 0$. The results for finite X_{0_1} are entirely as expected, viz., decreased stability as the outer walls become less conductive and thus less able to dissipate thermal disturbances. Observe that as X_{B_1} and $X_{0_1} \to \infty$ we recover the limiting case $Ra_c = 720$, $a = 0$ first found in [6].

The limit $A \to 0$ is most profitably discussed with reference to equations (18) and (19). Edwards and Ulrich (see [9]) found that they could correlate Catton and Lienhard's Ra_c values as a function of the single parameter A/X_{B_1} for smaller values of A. To understand how this parameter (not to be confused with the conductance ratio AX_{B_1}) becomes important, we let $A \to 0$ in equation (18) and find

$$\Lambda_e \sim a_1^2 \left(\frac{A}{X_{B_1}}\right), \quad A \to 0 \tag{22}$$

The group A/X_{B_1} is indeed the appropriate single parameter for small A. A calculation shows that this approximation introduces less than 1.0 percent error in the boundary conditions if $a_1 A \leq 0.175$ (or ≤ 10 percent error if $a_1 A \leq 0.585$). However, the resultant error in Ra_c is much smaller, as illustrated in Table 2. For the case considered by Edwards and Ulrich $X_{0_1} = 0 \Rightarrow a_1 \geq 2.5 \Rightarrow A \leq 0.23$ for 10 percent boundary conditions error; thus, they were able to collapse data for $A \lesssim 0.3$ onto a single curve with high accuracy.

Conversely, from equation (19)

$$\Lambda_0 \sim \frac{1}{AX_{B_1}}, \quad A \to 0$$

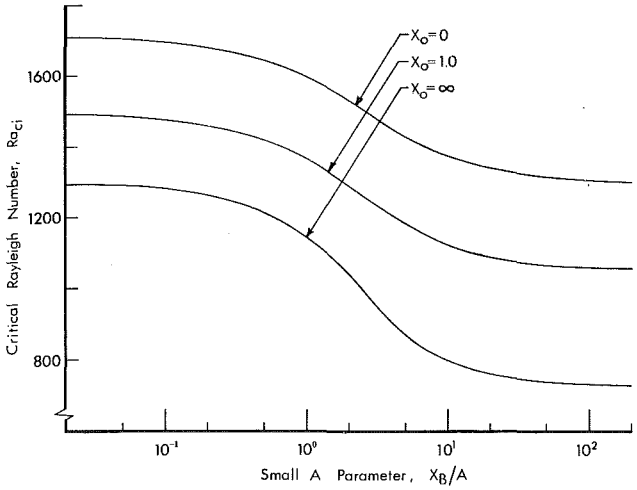

Fig. 4 Critical Rayleigh number of the two-layer problem

Table 3 Single layer with nonisothermal walls; present (PW); Hurle, Jakeman, and Pike (HJP); Gershuni and Zhukhovitskii (GZ)

X_0 \ X_{B_1}		0.0	0.5	1.0	2.0	∞
X_{B_1}	PW	1707.762	1415.093	1267.471	1116.412	720.000
	HJP	1707.762	1415.093	1267.471	1116.412	720
	GZ	1708	1415	1269	1117	720.0

X_{B_1} \ X_0		0.1	1.0	10.0	∞
0.0	PW	1667.96	1492.66	1329.56	1295.78
	GZ	1668	1496	1337	1304
∞	PW	1253.25	1052.71	815.35	720.00
	GZ	1260	1054	815	720.0

which is a midlayer to fluid layer conductance ratio. While $A \rightarrow 0$ gives rise to a fixed heat flux boundary conditions for even modes (horizontal dissipation of heat negligible), the limit produces as isothermal wall condition for odd modes (horizontal dissipation dominant). Of particular importance is the observation that A/X_{B_1} is only a meaningful parameter for the special case of even two-layer modes with $A \rightarrow 0$. Nonetheless, A/X_{B_1} provides a useful characterization of the stability limit for this case.

The critical Rayleigh number is plotted as a function of A/X_{B_1} for various X_{0_1} in Fig. 4, using values for $A = 0.001$. These universal curves also represent Ra_c for $A = 0.01$, 0.1, and 0.3 to within about 1 percent. We also note that, to within a tenth of a percent, $A = 1.0$ coincides with $A = \infty$.

The case $A \rightarrow \infty$ is essentially a single layer with outer walls of different conductivity ratios X_{B_1} and X_{0_1}. The case $X_{B_1} = X_{0_1}$ was solved exactly by Hurle et al. [10] and the general case was solved approximately by Gershuni and Zhukhovitskii [1]. A comparison to those works is made in Table 3.

The case $X_{0_1} = 0$ was approximated in [2]. A comparison of the present exact solutions to the former approximate solutions (Table 4) shows Catton and Lienhard's Ra_c values to be accurate to about 0.6 percent for thin midlayers and 0.02 percent for $A = 1.0$, the worst errors occurring for $X_{B_1} = 0(1)$.

Finally, a few calculations were made for the odd modes of

Table 4 Comparison to Catton and Lienhard (CL), $X_0 = 0$

X_{B_1}	A	0.01	0.1	0.3	1.0
0	PW	1707.76	-	-	-
	CL	1708	-	-	-
0.2	PW	1338.49	1525.71	1612.08	1634.67
	CL	1345.3	1527.9	1612.7	1634.9
1.0	PW	1304.95	1372.95	1452.47	1491.90
	CL	1312.6	1378.5	1454.7	1492.2
100	PW	1295.87	1296.69	1298.12	1299.36
	CL	1299.8	1297.5	1298.5	1299.6

Table 5 Odd modes of the two-layer system, $A = 0.1$

X_0 \ X_B	0.1	1.0	10.0	100.0
0	1694.965	1609.318	1400.371	1309.836
0.1	1655.331	1570.484	1360.753	1267.868
1.0	1408.697	1399.015	1182.588	1072.172
10.0	1318.172	1239.070	1011.321	859.441
∞	1284.511	1205.946	975.458	807.893

the two-layer system. The coefficient Λ_0, however, is exactly the boundary condition employed by Nield [11] in his study of a single layer with one isothermal wall and a finite conductivity, finite thickness slab covering the other isothermal wall. Therefore, since the results for $X_{0_1} = 0$ have already been found by Nield, we give only a brief table (Table 5) illustrating the effect of taking $X_{0_1} > 0$.

General Midlayer Disturbances; Multilayer Arrays

The preceding results were easily obtained because the midlayer disturbances could be found *a priori* by symmetry considerations. More general configurations lack such symmetry, however, and we must develop a more systematic approach for these cases.

Recall the general solution for Θ_B (equation (6)). Defining $\alpha = M/N$ $(-\infty < \alpha < \infty)$, we obtain

$$\Theta_{B_j} = N_j(\alpha_j \cosh(a_{B_j} z_{B_j}) + \sinh(a_{B_j} z_{B_j}))$$

where the subscript j denotes the jth solid layer. Elimination of N between conditions (8) as before produces

$$\Theta_i' = \Lambda_{ij}\Theta_i$$

with

$$\Lambda_{ij} = \left(\frac{a_i}{X_{B_{ij}}}\right)\left\{\frac{\cosh(a_i A_{ij}) \pm \alpha \sinh(a_i A_{ij})}{\alpha \cosh(a_i A_{ij}) \pm \sinh(a_i A_{ij})}\right\} \tag{23}$$

wherein the minus sign applies at the upper surface of a fluid layer ($z_{B_j} = -1/2$; $z_i = 1/2$) and

$$A_{ij} = \left(\frac{L_{B_j}}{2L_i}\right), \quad a_{B_j} = 2A_{ij}a_i, \quad \text{and} \quad X_{B_{ij}} = \frac{k_i}{k_{B_j}}$$

We have successfully removed one of the two unknowns. To solve for the remaining unknown, α, we require an additional constraint. At this point, we observe that, for given α, we may solve directly for Ra in a particular fluid layer by substituting the appropriate Λ's into equation (21) and proceeding as before. This suggests an iterative solution for α subject to a

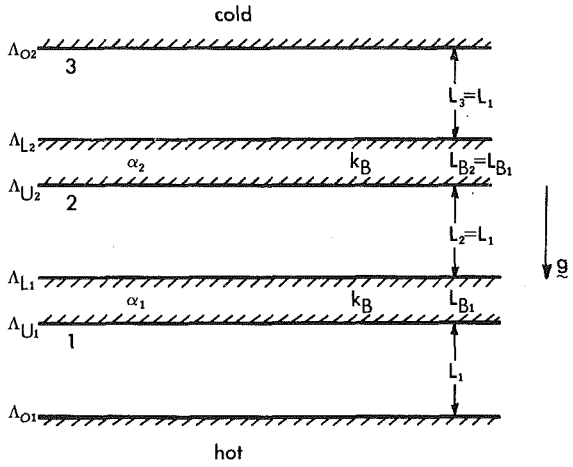

Fig. 5 The symmetric three-layer configuration

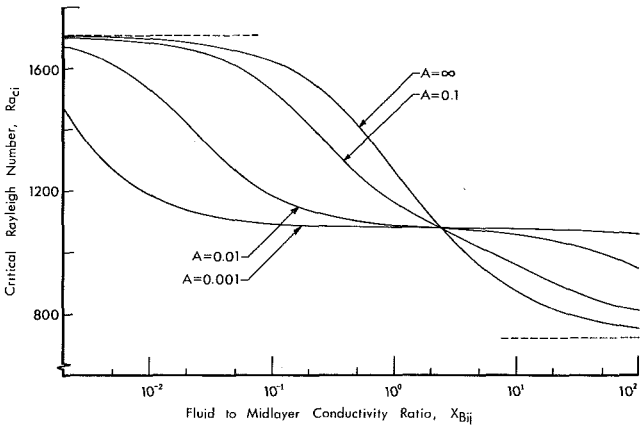

Fig. 6 Critical Rayleigh number of the three-layer problem

matching condition which we now develop for a multilayer array.

We seek a relationship between the Rayleigh numbers of the various fluid layers at onset. In the marginal state, one-dimensional conduction prevails. Accordingly, we may use the "voltage divider" to find ΔT_i

$$\Delta T_i = \frac{(\Delta T_{OA})(L/k)_i}{\sum_j (L/k)_j + \sum_j (L/k)_{B_j}} \tag{24}$$

where ΔT_{OA} is the temperature difference between the outermost boundaries of the fluid layers. From this

$$(\mathrm{Ra}_i/\mathrm{Ra}_j) = (L_i/L_j)^4 \tag{25}$$

if each layer has the same fluid. Thus, we may solve for α_j and Ra_i by iterating guesses for the α's until equation (25) is satisfied throughout. Notice that we need only find the roots of equation (21) corresponding to each layer's Λ's—no more complicated eigenvalue problem need be solved. We have reduced the multilayer problem to a set of one layer problems. Presently, we shall illustrate this approach for the three-layer problem. Before doing so, we note that equation (25) allows us to relate the individual layer critical Rayleigh number to the overall critical Rayleigh number Ra_T which is of interest to the designer. The result is

$$\mathrm{Ra}_T \equiv \left(\frac{g\beta}{\nu\alpha}\right)\left(\sum_j L_j + \sum_j L_{B_j}\right)^3 \Delta T_{OA}$$

$$= \mathrm{Ra}_i \left(\frac{k}{L}\right)_i \left(\sum_j L_j + \sum_j L_{B_j}\right)^3 \left(\sum_j \left(\frac{L}{k}\right)_j + \sum_j \left(\frac{L}{k}\right)_{B_j}\right)$$

We note in passing that convective heat transfer behavior for multilayer problems is best described in terms of Ra_T (see, e.g., [7]). The basic trend in the heat transfer rate is that, when the critical value of Ra_T decreases, the heat transfer at a given supercritical Ra increases. However, from the preceding equation we see that Ra_T and Ra_i need not vary in the same direction as a function of conductivity or aspect ratios (see the discussion in [2]). Thus, some care is required in inferring the effects of midlayer conductivity and thickness on heat transfer from stability results for Ra_i.

Three-Fluid Layer Stability

When a fluid layer is partitioned with two identical midlayers, evenly spaced, the resulting configuration is symmetric about the centerline of the innermost fluid layer (Fig. 5). Symmetry considerations show that $\alpha_1 = -\alpha_2$ and $\Lambda_{U2} = \Lambda_{L1}$; therefore, we need solve only for α_2, say. (In asymmetric situations both α's must be found; this is possible, but more complication than needed for illustration.) The eigenvalue problems in layers one and three are equivalent.

For convenience, we take the outermost boundaries to be isothermal ($\Lambda_{0_i} \to \infty$). Layer three has the boundary conditions

$$\Theta_3(1/2) = 0$$

$$\Theta_3'(-1/2) = \Lambda_{L2}\Theta_3(-1/2)$$

with

$$\Lambda_{L2} = \left(\frac{a_3}{X_{B_{32}}}\right)\left\{\frac{\cosh(a_3A_{32}) + \alpha_2 \sinh(a_3A_{32})}{\alpha_2 \cosh(a_3A_{32}) + \sinh(a_3A_{32})}\right\} \tag{26}$$

while layer two has

$$\Theta_2'(1/2) = \Lambda_{U2}\Theta_2(1/2)$$

$$\Theta_2'(-1/2) = -\Lambda_{L1}\Theta_2(-1/2) = -\Lambda_{U2}\Theta_2(-1/2)$$

with

$$\Lambda_{U2} = \left(\frac{a_2}{X_{B_{32}}}\right)\left\{\frac{\cosh(a_2A_{22}) - \alpha_2 \sinh(a_2A_{22})}{\alpha_2 \cosh(a_2A_{22}) - \sinh(a_2A_{22})}\right\} \tag{27}$$

Observe that

$$a_3 = a_2 \quad \text{and} \quad A_{32} = A_{22}$$

The matching condition (25) becomes

$$\mathrm{Ra}_2 = \mathrm{Ra}_3$$

Solutions for this geometry were obtained iteratively. With a guess for α_2, Ra_3 was found by solving equation (21) with

$$\Lambda_U = \infty, \quad \Lambda_L = \Lambda_{L2}$$

and Ra_2 from equation (21) with

$$\Lambda_U = \Lambda_L = \Lambda_{U2}$$

The α_2 root of $(\mathrm{Ra}_3 - \mathrm{Ra}_2)(\alpha) = 0$ was then obtained via bisection. (Note that sharp changes in the function $(\mathrm{Ra}_3 - \mathrm{Ra}_2)(\alpha)$ made more sophisticated root-finding procedures, such as the secant method, unsuitable.) After obtaining the root α_2, the function $\mathrm{Ra}_i(a)$ was minimized as before.

The three-layer stability limit is presented in Table 6 and Fig. 6 for various A and X_B. Basic trends in Ra_{c_i} are as expected. When $X_B \to 0$, $\mathrm{Ra}_{c_i} \to 1708$ (isothermal midlayers) and when $X_B \to \infty$, $\mathrm{Ra}_{c_i} \to 720$ (fixed heat flux midlayers). These limits, together with $A \to \infty$ (single layer with identical, finite outer wall conductivities), respresent decoupling of the fluid layers.

Table 6 Critical Rayleigh numbers for the three-layer system

$A_{ii} = 0.001$

$X_{B_{ii}}$	$-\alpha_2$	a_i	Ra_i
0.005	365.007	2.27	1270.78
0.01	209.323	2.19	1187.49
0.02	112.572	2.16	1137.41
0.05	47.1581	2.15	1104.24
0.1	23.9591	2.15	1092.61
0.2	12.0781	2.15	1086.67
0.5	4.85546	2.15	1083.03
1.0	2.43182	2.14	1081.72
2.0	1.21718	2.14	1080.92
5.0	0.487393	2.14	1079.95
10.0	0.244104	2.14	1078.82
20.0	0.122277	2.14	1076.74
50.0	0.0492742	2.13	1070.73
100.0	0.0249956	2.11	1061.05

$A_{ii} = 0.1$

$X_{B_{ii}}$	$-\alpha_2$	a_i	Ra_i
0.005	9.04824	3.10	1696.87
0.01	8.96797	3.07	1686.22
0.02	8.79883	3.03	1665.61
0.05	8.29346	2.92	1609.08
0.1	7.47959	2.75	1530.34
0.2	6.05125	2.52	1417.30
0.5	3.56912	2.26	1257.23
1.0	2.08358	2.16	1164.85
2.0	1.16421	2.10	1096.96
5.0	0.555987	1.99	1020.04
10.0	0.347477	1.86	960.88
20.0	0.239858	1.68	904.05
50.0	0.165709	1.42	842.18
100.0	0.132730	1.22	807.62

$A_{ii} = 0.01$

$X_{B_{ii}}$	$-\alpha_2$	a_i	Ra_i
0.005	86.9031	2.92	1612.61
0.01	78.0692	2.76	1536.03
0.02	62.7325	2.53	1425.47
0.05	36.4911	2.27	1270.64
0.1	20.9289	2.19	1187.27
0.2	11.2578	2.16	1136.98
0.5	4.71905	2.15	1103.22
1.0	2.40015	2.14	1090.59
2.0	1.21259	2.14	1082.65
5.0	0.491045	2.13	1073.09
10.0	0.249515	2.11	1062.23
20.0	0.129106	2.08	1043.51
50.0	0.0585810	1.98	999.03
100.0	0.0357651	1.85	950.82

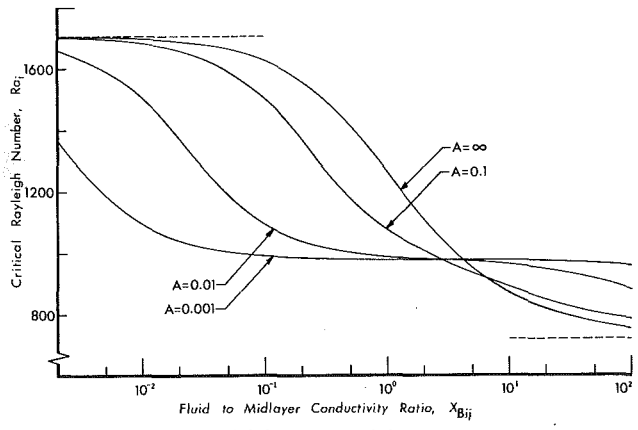

Fig. 7 Critical Rayleigh number of the four-layer problem

Observe that the curves for varius A cross at $X_B \simeq 2.4$. Here $\alpha = -1$ and we see from equations (26) and (27) that the Λ's are independent of A at this point and equal to (a_i/X_B). To the left, $\alpha_2 < -1$ and midlayer disturbances are dominantly even; to the right, midlayer disturbances are dominantly odd. As $A \to 0$ there is a large region over which $Ra_{c_i} \simeq 1080$ irrespective of X_B (viz., within a certain range *midlayer conductivity is unimportant for thin midlayers*). In this region $-\alpha X_B \simeq 2.4$, as one might deduce by formally setting $A = 0$ in equations (26) and (27); expansion of equations (26) and (27) shows that this region is characterized by $1 \gg |\alpha| aA \gg (aA)^2$. Accordingly, we find the [empirical] result that

$$Ra \simeq 1080, \quad a \simeq 2.14$$

when

$$(a_i A)^2 \ll 2.4\left(\frac{a_i A}{X_B}\right) \ll 1$$

However, an attractive conclusion such as (22) is not found for the three-layer problem.

Symmetric Four-Layer Array

If a fluid layer is partitioned with three evenly spaced, identical midlayers we have symmetry about the center of the innermost midlayer. Reductions similar to those used in the two and three-layer cases show that we need use only a single α and a pair of layers having

$$\Theta_4(1/2) = 0 \qquad \text{(say)}$$

$$\Theta_4'(-1/2) = \Lambda_{L4}\Theta_4(-1/2)$$

$$\Theta_3'(1/2) = \Lambda_{U3}\Theta_3(1/2)$$

$$\Theta_3'(-1/2) = \Lambda_{L3}\Theta_3(-1/2)$$

with

$$\Lambda_{L4} = \left(\frac{a_4}{X_{B_{43}}}\right)\left\{\frac{\cosh(a_4A_{43}) + \alpha_3 \sinh(a_4A_{43})}{\alpha_3 \cosh(a_4A_{43}) + \sinh(a_4A_{43})}\right\}$$

$$\Lambda_{U3} = \left(\frac{a_3}{X_{B_{33}}}\right)\left\{\frac{\cosh(a_3A_{33}) - \alpha_3 \sinh(a_3A_{33})}{\alpha_3 \cosh(a_3A_{33}) - \sinh(a_3A_{33})}\right\}$$

Table 7 Critical Rayleigh numbers for the four-layer system

A_{ii} = 0.001

$X_{B_{ii}}$	$-\alpha_3$	a_i	Ra_i
0.005	288.969	2.04	1192.28
0.01	161.266	1.94	1096.33
0.02	85.3790	1.91	1040.44
0.05	35.4119	1.89	1004.19
0.1	17.9379	1.89	991.62
0.2	9.02782	1.89	985.22
0.5	3.62590	1.89	981.31
1.0	1.81586	1.89	979.93
2.0	0.909067	1.89	979.08
5.0	0.364419	1.89	978.11
10.0	0.182772	1.88	977.02
20.0	0.0919105	1.88	975.05
50.0	0.0374406	1.87	969.49
100.0	0.0192864	1.84	960.92

A_{ii} = 0.01

$X_{B_{ii}}$	$-\alpha_3$	a_i	Ra_i
0.005	70.5713	2.89	1598.56
0.01	63.8184	2.69	1509.11
0.02	51.3663	2.38	1377.34
0.05	28.9029	2.04	1192.16
0.1	16.1297	1.94	1096.12
0.2	8.54649	1.91	1040.04
0.5	3.55188	1.89	1003.20
1.0	1.80402	1.89	989.68
2.0	0.913255	1.88	981.40
5.0	0.373372	1.87	972.04
10.0	0.192665	1.85	962.18
20.0	0.102307	1.81	946.49
50.0	0.0482971	1.71	912.89
100.0	0.0302173	1.58	879.24

A_{ii} = 0.1

$X_{B_{ii}}$	$-\alpha_3$	a_i	Ra_i
0.005	7.42090	3.09	1695.39
0.01	7.36231	3.07	1683.27
0.02	7.23779	3.02	1659.77
0.05	6.86719	2.89	1594.87
0.1	6.23853	2.68	1503.35
0.2	5.07408	2.38	1369.52
0.5	2.92593	2.02	1180.07
1.0	1.68672	1.90	1076.27
2.0	0.949694	1.83	1005.79
5.0	0.466513	1.71	936.81
10.0	0.296231	1.59	891.11
20.0	0.205361	1.43	850.03
50.0	0.141446	1.20	806.30
100.0	0.112737	1.04	781.94

Table 8 Comparison of exact solution to Sparrow et al. approximate model

A = 0.01

X_B \ Y	1	3	10
(Ra_{sp}) Exact	(1398.508)	(1497.594)	(1607.104)
0.01	1648.346	1653.344	1665.496
	3.00	3.02	3.05
0.1	1483.324	1541.551	1617.780
	2.78	2.91	3.02
1.0	1407.859	1497.192	1594.400
	2.75	2.89	3.01

A = 0.1

X_B \ Y	1	3	10
(Ra_{sp})	(1398.508)	(1497.594)	(1607.104)
0.1	1641.724	1645.910	1655.666
	3.00	3.01	3.04
1.0	1460.544	1494.599	1529.101
	2.76	2.85	2.92
10.0	1344.928	1353.619	1357.887
	2.64	2.66	2.67

$$\Lambda_{L3} = \left(\frac{a_3}{X_{B_{32}}}\right) \tanh\,(a_3 A_{32})$$

and

$$\mathrm{Ra}_{c3} = \mathrm{Ra}_{c4}$$

$$a_3 = a_4; \quad X_{B_{32}} = X_{B_{33}} = X_{B_{34}}; \quad A_{32} = A_{33} = A_{43}$$

Results of this calculation are given in Table 7 and Fig. 7. The behavior of the critical Rayleigh number is qualitatively very similar to the three layer case, but for each value of A the stability limit is lower. The curves for each A do not have a common intersection point because the third kind condition on the center layer is quite different from those on the outer midlayers. We again find a flattening of the stability curve for thin midlayers in a region characterized by the same inequality as the three-layer flat spot but having instead

$$\mathrm{Ra} \approx 980, \quad a \approx 1.89$$

Comparison to Experiments

At present a very limited amount of experimental data is available for multilayer arrays. Ulrich [9] obtained critical Rayleigh numbers of 1319 for a symmetric two-layer system and of 1154 for a symmetric three-layer system, both having isothermal outer walls and thin Teflon midlayers (A = 0.001, X = 0.01). Hollands and Wright [12] obtained a critical Rayleigh number of ~1220 for the same type of two-layer configuration. All three points are within 6 percent or better of the predictions made herein and thus agree to well within the experimental uncertainty of the data.

Limitations of the Sparrow et al. Model

To come full circle, we may apply our generalized approach to the prototype convective condition with which we began

(equation (11)). This model, from Sparrow et al. [6], applies a convective thermal boundary condition directly to the upper surface of a rigidly bounded fluid layer, neglecting the possible effects of horizontal conduction in the cover plate. We wish to assess the validity of this assumption.

If a single fluid layer 1 is covered by a conductive slab B having above it a uniform heat transfer coefficient h, we easily find that

$$\alpha_B = -\frac{(\gamma_e S + a_B C)}{(a_B S + \gamma_e C)}$$

where $\gamma_e = (hL_B/k_B)$, $S = \sinh(a_B/2)$, and likewise for C. Substitution into equation (23) and some algebra yield the thermal coefficient at the top of the fluid layer

$$\Lambda_U = \left(\frac{a_1}{X_B}\right)\left\{\frac{1+(a_B/\gamma_e)\left(\frac{2SC}{S^2+C^2}\right)}{(a_B/\gamma_e)+\left(\frac{2SC}{S^2+C^2}\right)}\right\} \tag{28}$$

Following [6], we define $\gamma = (hL_i/k_i) = 2AX_B/\gamma_e$. Some analysis then shows that

$$\Lambda \simeq \gamma$$

only if

$$a_1^2\left(\frac{L_B}{L_1}\right)^2 \ll \gamma_e \ll 1 \tag{29}$$

As a typical example for solar collectors, consider a 1/8 in. glass cover plate (mean length: 0.75 m) over an air layer with an 11 mph wind (300 K) above. Then

$$\gamma_e \approx 0.025 \ll 1$$

and, if $a_1 \approx 3$, the first inequality of (29) might be satisfied if $L_1 \approx 7\ 1/2$ in. A more reasonable value would be $L_1 = 1$ in., however, an exact solution for this value using equation (28) yields

$$\mathrm{Ra}_1 = 1687.9, \quad a_1 = 3.08$$

Here $\gamma \cong 10$ and the Sparrow et al. approximation yields

$$\mathrm{Ra}_1 = 1607.1, \quad a_1 = 3.03$$

While the error is only 5 percent of the absolute Ra_i, it represents 20 percent (80/(1708 − 1296)) of the possible variation in Ra_i. Clearly, the Sparrow et al. approximation should not be used indiscriminantly. Some additional values are given in Table 8 to help put this example in perspective.

Finally, we remark that the result of [2] that maximum stability occurs for evenly spaced midlayers will only be true when the outer bounding surfaces are of the same conductivity. In general, maximum stability is achieved by placing the midlayer closer to the less conductive boundary. Exactly how much closer must be determined by further study.

Summary and Conclusions

- The procedure developed herein facilitates simple, exact calculation of the stability limit of arbitrary combinations of fluid layers, conductive midlayers, and conductive boundaries.
- The wavenumber dependence of the fluid layer thermal boundary condition drastically affects the stability limit of that layer.
- The stability limit of the symmetric two-layer system with conductive boundaries is as given in Table 1.
- Previous approximate solutions of the single layer, conductive wall problem and the two-layer problem have been reasonably accurate.
- The stability limit of the three and four-layer systems with identical, evenly spaced midlayers and isothermal boundaries is as given in Tables 6 and 7.
- Cover plate conduction can strongly affect stability with the convective boundary condition of Sparrow et al. [6].
- The present solutions are in good agreement with available experimental data.

References

1 Gershuni, G. Z., and Zhukhovitskii, E. M., *Convective Stability of Incompressible Fluids*, Israel Program for Scientific Translations, Jerusalem, 1976.

2 Catton, I., and Lienhard, J. H. V., "Thermal Stability of Two Fluid Layers Separated by a Solid Interlayer of Finite Thickness and Thermal Conductivity," ASME JOURNAL OF HEAT TRANSFER, Vol. 106, 1984, pp. 605–612.

3 Chandrasekhar, S., *Hydrodynamic and Hydromagnetic Stability*, Clarendon Press, Oxford, 1961.

4 Lienhard, J. H. V., "Thermal Instability and Heat Transfer in a Singly Partitioned Horizontal Fluid Layer," Master's Thesis in Engineering, UCLA, 1984.

5 Pellew, A., and Southwell, R. V., "On Maintained Convective Motion in a Fluid Heated from Below," *Proc. Roy. Soc. (London) A*, Vol. 176, 1940, pp. 312–343.

6 Sparrow, E. M., Goldstein, R. J., and Jonsson, V. K., "Thermal Instability in a Horizontal Fluid Layer: Effect of Boundary Conditions and Nonlinear Temperature Profile," *J. Fluid Mech.*, Vol. 18, 1964, pp. 513–528.

7 Lienhard, J. H. V., and Catton, I., "Heat Transfer Across a Two-Fluid-Layer Region," ASME JOURNAL OF HEAT TRANSFER, Vol. 108, 1986, pp. 198–205.

8 Low, A. R., "On the Criterion for Stability of a Layer of Viscous Fluid Heated From Below," *Proc. Roy. Soc. (London) A*, Vol. 125, 1929, pp. 180–195.

9 Ulrich, T. R., "Heat Transfer Across a Multi-Layered Air Enclosure," Master's Thesis in Engineering, UCI, 1984.

10 Hurle, D. T. J., Jakeman, E., and Pike, E. R., "On the Solution of the Bénard Problem With Boundaries of Finite Conductivity," *Proc. Roy. Soc. (London) A*, Vol. 296, 1967, pp. 469–475.

11 Nield, D., "The Rayleigh–Jeffreys Problem With Boundary Slab of Finite Conductivity," *J. Fluid Mech.*, Vol. 32, 1968, pp. 393–398.

12 Hollands, K. G. T., and Wright, J. L., "Heat Loss Coefficients and Effective Products for Flat-Plate Solar Collectors With Diathermanous Covers," *Solar Energy*, Vol. 30, 1983, pp. 211–216.

APPENDIX

This appendix gives the functions $\mathcal{C}_i$ used in equation (21). Boundary conditions of the form

$$D\Theta + \Lambda_U\Theta = 0, \quad z = 1/2$$

$$D\Theta - \Lambda_L\Theta = 0, \quad z = -1/2$$

applied to equation (3) produce the $\mathcal{C}_i$ indicated in the text as

$$\mathcal{C}_1 = -q_0 \sin(q_0/2) + \Lambda_U \cos(q_0/2) + 2\,\mathrm{Re}\left\{\frac{A}{A_0}(q\sinh(q/2) + \Lambda_U \cosh(q/2))\right\}$$

$$\mathcal{C}_2 = q_0 \cos(q_0/2) + \Lambda_U \sin(q_0/2) + 2\,\mathrm{Re}\left\{\frac{B}{B_0}(q\cosh(q/2) + \Lambda_U \sinh(q/2))\right\}$$

$$\mathcal{C}_3 = q_0 \sin(q_0/2) - \Lambda_L \cos(q_0/2) - 2\,\mathrm{Re}\left\{\frac{A}{A_0}(q\sinh(q/2) + \Lambda_L \cosh(q/2))\right\}$$

$$\mathcal{C}_4 = q_0 \cos(q_0/2) + \Lambda_L \sin(q_0/2) + 2\,\mathrm{Re}\left\{\frac{B}{B_0}(q\cosh(q/2) + \Lambda_L \sinh(q/2))\right\}$$

in which B/B_0 and A/A_0 may be evaluated from equations (9) and (10).

Effect of Insulated/Uninsulated Channel Walls on Heat Transfer From a Horizontal Finned Tube in a Vertical Channel

E. M. Sparrow

M. A. Ansari

Department of Mechanical Engineering,
University of Minnesota,
Minneapolis, MN 55455

Measurements were made of the combined natural convection and radiation heat transfer from a horizontal finned tube situated in a vertical channel open at the top and bottom. In one set of experiments, both walls of the channel were heavily insulated, while in a second set of experiments, one of the insulated walls was replaced by an uninsulated metallic sheet. In general, the heat transfer coefficients were found to be lower with the metal wall in place, but only moderately. With the finned tube situated at the bottom of the channel, the differences in the heat transfer coefficients corresponding to the two types of walls were only a few percent. When the tube was positioned at the mid-height of the channel, larger differences were encountered, but in the practical range of Rayleigh numbers, the differences did not exceed 5 percent.

Introduction

In common practice (e.g., space-heating applications), horizontal finned-tube heaters are installed between parallel vertical walls open at the top and bottom. The channel formed by the walls is a passageway through which air is drawn by buoyancy – entering at the bottom, passing in crossflow over the heater, and exiting at the top. The buoyancy which drives the flow results from the density decrease sustained by the air as it contacts the heated surfaces during its passage through the channel. These surfaces include not only the tube and the fins but also the channel walls, which are heated by radiation from the tube and fins.

The higher the temperature level of the channel walls, the greater is their contribution to the buoyancy. The temperature level of the walls depends not only on their radiation properties (emissivity, absorptivity) but also on the heat losses through the walls to the outside. The greater these losses, the lower is the wall temperature and the smaller is the contribution of the walls to the buoyancy.

From the foregoing, it appears that by insulating the channel walls, the buoyancy can be maximized, thereby enhancing the rate of heat transfer from the finned-tube heater. On the other hand, the absence of insulation, while making for diminished buoyancy, opens up an additional path of heat transfer from the finned tube to the outside, via radiation from the finned tube to the channel walls. Therefore, from the standpoint of the rate of heat transfer at the finned tube, it is uncertain whether higher values will be achieved with insulated or uninsulated channel walls.

In practical installations of finned-tube heaters (e.g., for space heating), one of the two walls of the channel can be regarded as insulated – typically, gypsum board backed by various types of insulation. The other wall is typically made of sheet metal. The exposed face of the sheet metal is, in effect, a vertical plate which exchanges heat by natural convection and radiation with the surroundings.

The objective of the present investigation is to establish the effect of the presence or absence of channel wall insulation on the rate of heat transfer from a horizontal finned-tube heater. To this end, experiments were performed utilizing a channel with one wall insulated and the other wall of sheet metal. The thus-obtained finned-tube heat transfer rates (Nusselt numbers) were compared with those measured in [1] using a channel in which both of the walls were insulated. Aside from the aforementioned difference in one of the channel walls, the apparatus used here and in [1] was identical, thereby making for a definitive comparison of results. The experiments (and the comparisons) encompassed two different vertical positions of the finned tube in the channel, four values of the clearance between the fin tips and the channel walls, and a 12-fold variation of the Rayleigh number.

Experiments

The essential features of the experimental setup are illustrated in Fig. 1, which shows the two types of channels being considered. Figure 1(*a*) depicts a channel where both the walls are insulated, while for the channel of Fig. 1(*b*), one of

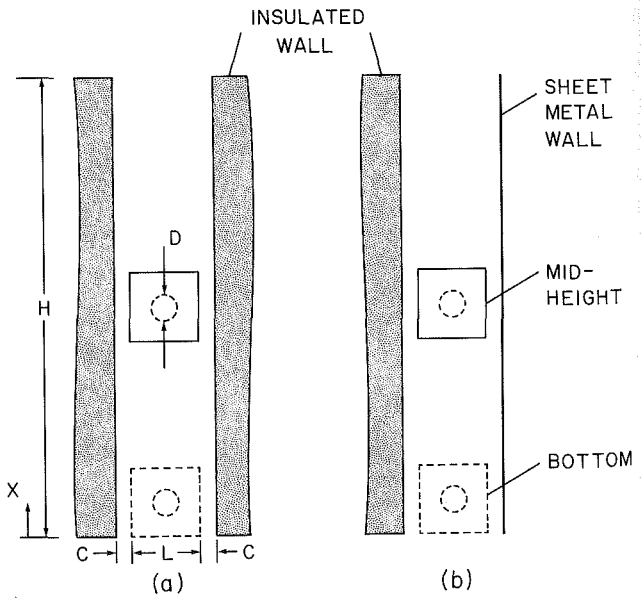

Fig. 1 Illustration of the two types of channels under investigation

Contributed by the Heat Transfer Division for publication in the JOURNAL OF HEAT TRANSFER. Manuscript received by the Heat Transfer Division April 16, 1986.

the insulated walls is replaced by a sheet metal wall. As already noted, experimental results for the configuration of Fig. 1(*b*) are obtained here and compared with those of [1] for the configuration of Fig. 1(*a*).

The fins and the tube were both of copper, with all surfaces exposed to the airflow being spray-painted with a high-temperature black paint having a measured emissivity of 0.87. The finned tube was synthesized by alternately stacking annular rings (outer diameter D) and square fins (side length L), with the assembly being performed in a furnace, with solder introduced at all contacting faces to yield a unit in which the fins were, in effect, integral with the tube. A specially designed electric heater, wound to provide both circumferentially and axially uniform heating, was positioned in the bore of the tube. The temperature of the tube wall was measured by 11 fine-gage, precalibrated thermocouples deployed along the length of the tube and around its circumference. The thermocouple junctions were situated 0.025 cm from the exposed surface of the tube.

The external dimensions and radiation surface properties of the finned tube correspond to those used in practice. The dimensions (in cm) are: $D = 3.188$, $L = 8.128$, S (interfin spacing) $= 0.584$, and t (fin thickness) $= 0.0508$. The axial pitch ($S + t$) corresponds to four fins per inch, and a total of 49 fins were utilized. The outboard fin at each end of the finned tube was very well insulated (11½ cm thickness of insulation). The flow channel was made up of the two principal walls shown in Fig. 1 plus two end walls. Each of the insulated principal walls was a composite structure consisting of a 1.27-cm-thick plywood sheet backed by an insulation pack made up of 5 cm of polystyrene and 9 cm of fiberglass. To ensure the flatness of the plywood, angle-iron braces were affixed to its rear face. The front face was sanded smooth and covered with plasticized contact paper (measured emissivity = 0.855) which presented a hydrodynamically smooth surface to the airflow. The sheet-metal principal wall was 0.16 cm thick, braced from behind to ensure flatness, and spray-painted black (measured emissivity = 0.89). Each of the end walls was fabricated from a contact-paper-faced sheet of polystyrene backed by fiberglass, yielding a total insulation thickness of 11½ cm.

To avoid extraneous conduction losses, the finned tube was suspended from above by nylon line. The experiments were performed in a windowless, unventilated room, with the instrumentation and power supply situated in an adjacent service corridor.

During the course of the experiments, the finned tube was positioned at either of the two elevations illustrated in Fig. 1, respectively designated as *bottom* and *mid-height*. The clearance C between the fin tips and the adjacent channel wall was varied parametrically, encompassing the values $C/L =$ 0.078, 0.156, 0.234, and 0.469. For each geometric configuration, the temperature difference between the tube wall and the ambient was varied in 7–8 steps to yield a 10- to 12-fold variation of the Rayleigh number. The channel height was held fixed at the value $H/L = 10$ for all the experiments.

Results and Discussion

Results will now be presented for the combined natural convection and radiation heat transfer from the finned tube. From the standpoint of practice, it is the combined heat transfer that is relevant rather than the separate natural convection and radiation components.

The combined-mode heat transfer coefficient h was evaluated from

$$h = Q/A(T_w - T_\infty) \tag{1}$$

in which A is the total heat transfer surface area (i.e., the exposed surfaces of the fins and the tube), T_w is the tube wall temperature, T_∞ is the ambient temperature, and Q is the combined rate of heat transfer. For a dimensionless representation, the heat transfer coefficient may be rephrased as a Nusselt number, and the temperature difference ($T_w - T_\infty$) which drives the natural convection flow may be expressed as a Rayleigh number, that is,

$$\mathrm{Nu} = hS/k,\ \mathrm{Ra} = [g\beta(T_w - T_\infty)S^3/\nu^2]\mathrm{Pr} \tag{2}$$

where the interfin spacing S has been used as the characteristic dimension. The thermophysical properties were evaluated at a reference temperature ½($T_w + T_\infty$), except that $\beta = 1/T_\infty$.

The main issue to be addressed here is the *difference* in the heat transfer rates (or in the Nusselt numbers) for the two channel wall configurations illustrated in Fig. 1. To this end, the results of [1], which correspond to Fig. 1(*a*), will be brought together with the present experimental data, which are for the configuration of Fig. 1(*b*).

The heat transfer results of [1] were presented in terms of the ratio Q/Q^* (=Nu/Nu*). In this ratio, Q (and Nu) pertain to the finned tube situated in the channel, while Q^* (and Nu*) correspond to the finned tube in free space (no channel). The use of the Q/Q^* ratio was motivated by the fact that its magnitude relative to unity is a direct index to whether in-channel positioning of the finned tube is enhancing.

To conform with [1], the present results will also be cast in the Q/Q^* (=Nu/Nu*) ratio. This is in no way a complication, since a comparison of the Q/Q^* values for the configurations of Figs. 1(*a*) and 1(*b*) yields exactly the same percentage differences as does a comparison of the actual Q values. Note that Nu* and Q^* can be obtained from Fig. 3 of [1].

The heat transfer results are presented in Figs. 2–4, each of which conveys information for a specific clearance between the fin tips and the channel wall ($C/L = 0.078$ in Fig. 2 and 0.469 in Fig. 4) or for a pair of clearances ($C/L = 0.156$ and 0.234 in Fig. 3). In each figure, Q/Q^* (=Nu/Nu*) is plotted as a function of the Rayleigh number. The results for the channel with two insulated walls are represented by lines (the actual data are plotted in [1]), while the data points correspond to the channel having one wall of uninsulated sheet metal. Each figure conveys results for both the mid-height and bottom positions of the finned tube.

An overview of Figs. 2–4 indicates that, in general, the finned-tube heat transfer rates are lower when one of the channel walls is uninsulated sheet metal than when both walls

Nomenclature

C = clearance between fin tip and channel wall
D = tube diameter
H = height of channel
k = thermal conductivity
L = side length of square fin
Nu = in-channel, finned-tube Nusselt number
Nu* = free-space, finned-tube Nusselt number
Q = in-channel, finned-tube heat transfer rate
Q^* = free-space, finned-tube heat transfer rate
Ra = Rayleigh number
S = interfin spacing
T_{cw} = channel wall temperature
T_w = tube wall temperature
T_∞ = ambient temperature
t = fin thickness
X = vertical coordinate
β = coefficient of thermal expansion
ν = kinematic viscosity

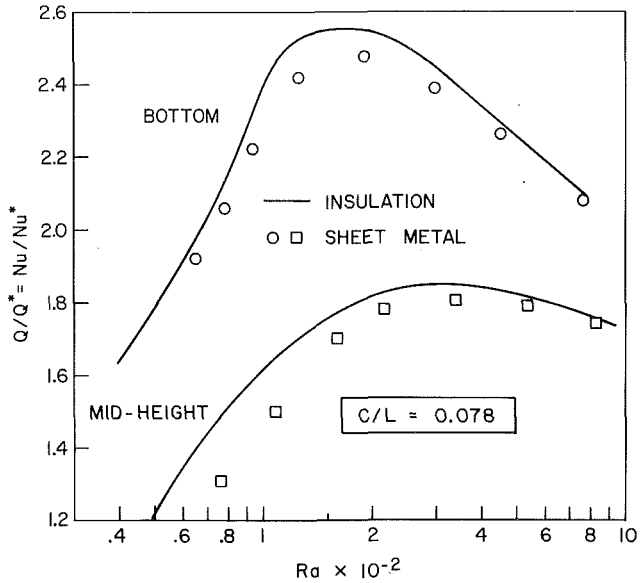

Fig. 2 Finned-tube heat transfer results for the two types of channels; clearance *C/L* = 0.078

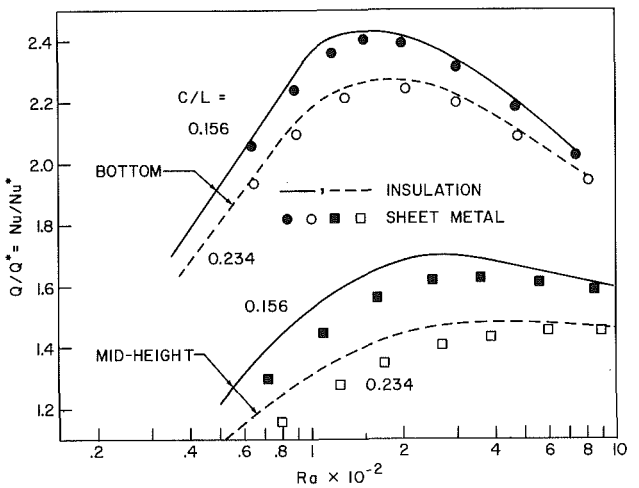

Fig. 3 Finned-tube heat transfer results for the two types of channels; clearances *C/L* = 0.156 and 0.234

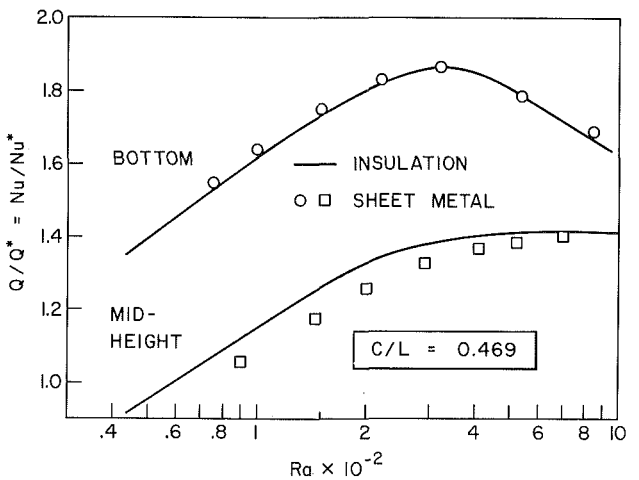

Fig. 4 Finned-tube heat transfer results for the two types of channels; clearance *C/L* = 0.469

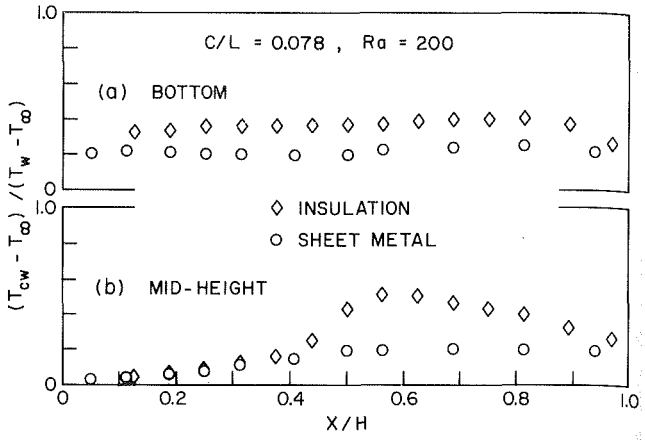

Fig. 5 Representative temperature distributions along the channel walls for the two types of channels

are insulated. Therefore, the reduction in the wall-induced buoyancy which is brought about by the absence of the insulation outweighs the additional heat loss path from the uninsulated wall to the ambient. As will now be elaborated, the changes in the heat transfer rates due to the replacement of an insulated wall by an uninsulated sheet metal wall are moderate.

The response of the heat transfer to the insulation/sheet metal alternatives is somewhat affected by the position of the finned tube in the channel. When the finned tube is at the bottom of the channel, the heat transfer is relatively insensitive to the alternatives. In particular, for the smallest clearance gap $C/L = 0.078$ (Fig. 2), the heat transfer data for the case of the uninsulated metal wall are 1–4 percent lower than those for the insulated wall case. Even these slight deviations tend to wane as C/L increases, so that at $C/L = 0.469$ (the largest clearance), the results for the two cases are within 1½ percent of each other (with the results for the uninsulated metal-wall case actually falling higher).

With the finned tube at the mid-height of the channel, the heat transfer results are somewhat more sensitive to the insulation/sheet metal alternatives. At the $C/L = 0.078$ clearance, deviations in excess of 10 percent occur at the lower Rayleigh numbers, but these deviations decrease and virtually disappear as Ra increases. This same pattern is encountered at the other clearances, but the deviations at the lower Rayleigh numbers are smaller (about 7 percent).

As discussed in the Introduction, the replacement of an insulated channel wall with an uninsulated sheet metal wall should result in a reduction of the wall temperature. This expectation is verified by the representative wall temperature distributions shown in Fig. 5. On the ordinate, the channel wall temperature T_{cw} is plotted in the dimensionless group $(T_{cw} - T_\infty)/(T_w - T_\infty)$. The abscissa is the dimensionless vertical position along the wall, with X measured upward and $X = 0$ at the bottom of the wall (see Fig. 1). The data in part (*a*) of the figure correspond to the bottom positioning of the finned tube, and those in part (*b*) are for the mid-height positioning. The data designated *insulation* were measured along one of the insulated walls of the channel depicted in Fig. 1(*a*), while those designated *sheet metal* were measured along the sheet metal wall of the channel of Fig. 1(*b*).

Inspection of the figure shows that the presence or absence of insulation has a substantial effect on the magnitude of the wall temperature. For the case of the bottom-positioned finned tube, the reduction in the temperature at the uninsulated sheet metal wall occurs all along the height of the channel. On the other hand, for the mid-height positioning, deviations in the temperatures of the insulated wall and the uninsulated sheet metal wall start at the channel mid-height

and continue throughout the upper portion of the channel. The reductions in temperature at the uninsulated sheet metal wall bring about a decrease in the wall-induced buoyancy which, in turn, reduces the heat transfer at the finned tube.

Concluding Remarks

The results obtained here have demonstrated that the heat transfer from a finned tube positioned at the bottom of a vertical channel is virtually independent of whether both walls of the channel are insulated or one wall is an uninsulated metal sheet. In this regard, it should be noted that the bottom positioning of the finned tube is the most advantageous one from the standpoint of practice, since it yields the highest heat transfer coefficients. With the tube positioned at the midheight of the channel, the heat transfer was found to be slightly more sensitive to the insulation/sheet metal alternatives. However, for the range of Rayleigh numbers appropriate to practice, the differences in the heat transfer due to the different types of walls do not exceed 5 percent.

References

1 Sparrow, E. M., Ansari, M. A., Stryker, P. C., and Ruiz, R., "Enhanced Heat Transfer From a Horizontal Finned Tube Situated in a Vertical Channel," ASME JOURNAL OF HEAT TRANSFER, Vol. 108, 1986, pp. 62–69.

Experimental and Numerical Studies of Cold Inflow at the Exit of Buoyant Channel Flows

Vijay Modi[1]

K. E. Torrance
Fellow ASME

Sibley School of Mechanical and Aerospace Engineering,
Cornell University,
Ithaca, NY 14853

Experimental and numerical studies of the separation of a smooth attached buoyant flow from the inner wall of a duct, as the duct discharges into a quiescent environment, are reported. The associated penetration of neutrally buoyant ambient fluid into the duct is called cold inflow. The experimental study was carried out for air flows over ranges of Reynolds and Froude numbers, based on duct radius, of Re = 2400 to 3300 and Fr = 0.68 to 2.69. The experiments provide information on the onset and extent of cold inflow in a turbulent flow regime. Spatial profiles of fluctuating temperature reveal a wedge-shaped cold inflow region at the wall near the exit when Fr is decreased below a critical value. The numerical study examines the influence of Re and Fr on the structure of the cold inflow phenomenon at moderate Reynolds numbers (Re = 200 to 500 and Fr = 1 to 5). Steady-state, two-dimensional, laminar flow solutions reveal a region of downward-flowing cold air near the wall of the duct which leads to premature separation of the wall boundary layer. The separated boundary layer merges into the buoyant jet above the duct exit.

1 Introduction

Most buoyant jets appear to "separate" from the wall at the lip of the exit duct. Examples are smoke stacks, cooling towers, faucets, and orifice discharges. However, under certain conditions (usually a low inertia/buoyancy force ratio) the jets may separate before reaching the lip of the duct. Such separation is usually accompanied by the penetration of neutrally buoyant ambient fluid into the duct (cold inflow). This phenomenon can impair the performance of a device such as a cooling tower by reducing the available draft height.

Two situations susceptible to separation and cold inflow are shown in Fig. 1. Cold inflow is observed in natural-draft cooling towers under conditions of low draft velocities and large exit diameters (Baer et al., 1977; Moore, 1978), but is not as evident in tall smoke stacks which have large draft velocities. To introduce the relevant parameters we define the following model problem. A fluid of density ρ_1 and kinematic viscosity ν flows through a duct of characteristic half-width (or radius) b, with a bulk velocity U, to emerge into an otherwise quiescent environment. The environment is at a higher density ρ_0. The length of the duct is h; however, the duct flow may separate at some distance x_s. Gravity g acts to provide a body force to the duct flow in the direction of bulk motion. Even though in an actual situation wall roughness and crosswinds in the exit region may have significant effects, we shall not take them into consideration. Moreover, the duct walls are assumed to be insulated. The dimensionless parameters that emerge are the Reynolds number Re based on duct width, the Froude number Fr, and the aspect ratio A defined as

$$\mathrm{Re} = Ub/\nu, \qquad \mathrm{Fr} = \rho_0 U^2/g(\rho_0 - \rho_1)b, \qquad A = h/b \quad (1)$$

Typical values of these parameters for cooling towers and smoke stacks are shown in Fig. 1.

The idea of a critical Froude number will now be introduced. For a given duct (h/b) and a given Reynolds number, the separation location will presumably vary with the Froude number. The flow is less likely to separate at large Froude numbers, since the flow has sufficient inertia to overcome any such tendency. Under these circumstances the flow leaves the duct at the very lip. However, as the Froude number is decreased, at some critical value, the flow may begin to separate prior to the lip. That Froude number, Fr_c, is referred to as the critical Froude number and it will in general depend on the Reynolds number

The experiments of Jörg and Scorer (1967) addressed the critical conditions for cold inflow. They studied negatively buoyant, downward-directed jets of salt water emerging into a fresh water tank through a glass tube. In the laminar flow regime, they found the existence of a critical Froude number for "small values of the buoyancy and tube diameter, when the Reynolds number was below about 600 and the laminar profile was established at the tube mouth." Neither the value of the Froude number, nor the range of Reynolds numbers over which the relationship was verified, were specified. The limitation to small values of buoyancy and tube diameters was not explained nor were bounds given. For the turbulent flow regime they found that, "for a fair range of Reynolds number," ReFr = constant ($\simeq 2000$) at critical conditions.

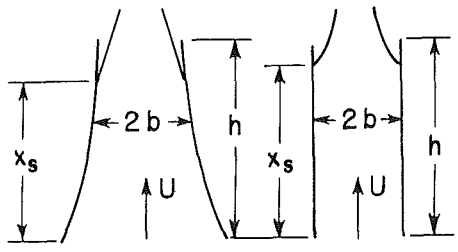

	Cooling Tower	Smoke Stack
U	3 m/s	10 m/s
b	50 m	3 m
h	100 m	30 m
$\Delta\rho/\rho$	0.1	0.1
Re	$0(10^7)$	$0(10^6)$
Fr	0(1)	0(10)
Pr	0(1)	0(1)
h/b	0(1)	0(10)

Fig. 1 Two situations susceptible to separation and cold inflow. Characteristic dimensions and parameters are listed. The flow separation point is at x_s.

[1]Present address: Department of Aeronautics and Astronautics, Gas Turbine Laboratory, Massachusetts Institute of Technology, Cambridge, MA 02139.

Contributed by the Heat Transfer Division for publication in the JOURNAL OF HEAT TRANSFER. Manuscript received by the Heat Transfer Division April 7, 1986.

However, they also found a strong dependence of the constant on the shape of the velocity profile near the wall. Since the shape of the velocity profile at the wall may be influenced by the Reynolds number, it is not possible to generalize their results to wider ranges of Reynolds and Froude numbers.

In a related problem, Sparrow et al. (1984) observed flow reversals (cold inflow) during natural convection in an open-ended vertical channel with asymmetric heating of the walls. One of the walls was heated, and cold inflow was observed along the opposing, unheated wall near the top of the channel; water was the working fluid. The heating rate was expressed in terms of a Rayleigh number Ra, based on spacing between walls and the difference in temperature between the heated wall and the ambient fluid at discharge from the duct. At low Rayleigh numbers, a very small, but constant, distance of penetration of the cold inflow was observed. At Rayleigh numbers above a critical value (Ra $\approx$ 35,000), the penetration distance of the inflow increased linearly with Ra. The flows were laminar, steady, and essentially two dimensional; the cold inflow process did not influence the rate of heat transfer on the heated wall.

More recently, Modi and Moore (1987) examined the cold inflow process in the range of very large Reynolds numbers. Attention was focused on a laminar boundary layer and its separation from the wall, in a vertical, buoyant channel flow. An idealized problem was considered, in which a thin, wall boundary layer was matched to an external potential flow. The potential flow consisted of the flow in the duct, and the buoyant plume following discharge from the duct. The separation streamline was analyzed using free streamline theory and a triple-deck, boundary-layer matching procedure. The critical conditions for separation were determined, in terms of Reynolds and Froude numbers, in the limit of large Fr and the duct Reynolds number approaching infinity. In this limit, the distance to the separation point x_s was found to vary as $\mathrm{Fr}^{16/9}/\mathrm{Re}^{1/9}$. This represents a very weak dependence on Reynolds number, suggesting the use of high Reynolds number experiments to study the basic structure of the cold inflow process in chimneys and cooling towers. The paper by Modi and Moore (1987) was based on the thesis of Modi (1984). That thesis included experiments at large Re, and numerical computations at moderate Re, that form the subject of the present paper.

In this paper separate, but complementary, experimental and numerical investigations of the cold inflow phenomenon are reported. Idealized geometries are considered. The laboratory experiments focus on the turbulence structure and global behavior of the cold inflow phenomenon at a duct Reynolds number, equation (1), of about 3000. A short, axisymmetric, vertical duct was employed; heated air was the working fluid. The Froude number was varied, but significant variations of the Reynolds number were not possible for reasons cited later. The flow in the separated region was observed to be time dependent and three dimensional. However, time-averaged measurements of mean and root-mean-square (rms) temperatures clearly demonstrate the Froude number dependence and shape of the separation zone. In the numerical investigation, finite difference approximations of the time-dependent, two-dimensional Navier–Stokes equations were integrated to obtain steady-state laminar flow solutions at moderate Reynolds numbers (Re = 200 to 500). The calculations reveal the flow structure and shape of the separation zone, and the influences of the Reynolds and Froude numbers on the separation process.

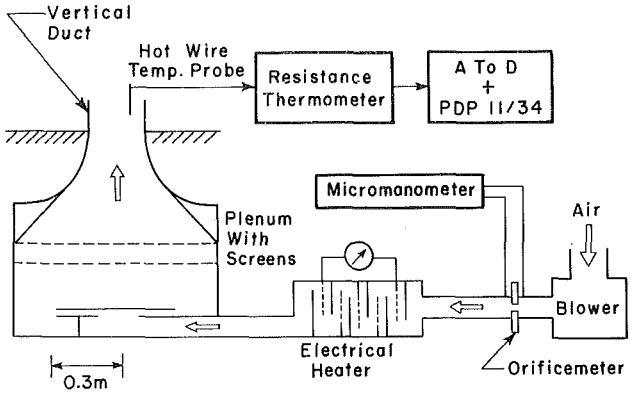

Fig. 2 Schematic of the experimental apparatus

The experimental and numerical studies are reported in Sections 2 and 3 of this paper. Section 4 provides a summary and concluding remarks.

2 Experimental Study

An experiment was set up to study cold inflow. The experiment was limited in scope, but was intended to provide information on the onset, size, and structure of the inflow phenomenon in a turbulent flow regime. In the experiment, heated and conditioned air is discharged from a short, vertical duct into an otherwise quiescent environment (see Fig. 2). The mean flow in the duct is upward. During inflow events, cool ambient air enters around the inner periphery of the duct, and flows downward along the wall in a direction opposite to the mean flow in the duct. The structure of the cold inflow phenomenon is deduced from temperature measurements inside the duct. Some flow visualization with smoke was also employed.

Apparatus. A schematic of the experiment is shown in Fig. 2. The apparatus was designed to supply heated air through a duct at a known temperature and velocity. The choice of operating parameters is dictated by a desire to have

Nomenclature

A = aspect ratio = h/b
b = duct half-width (or radius)
Fr = Froude number = $\rho_0 U^2/g(\rho_0-\rho_1)b$
g = acceleration of gravity
h = duct length
Pr = Prandtl number = ν/α
Ra = Rayleigh number = $g\beta(T_1 - T_0)b^3/\nu\alpha$
Re = Reynolds number = Ub/ν
T = dimensionless temperature = $(T'-T_0')/(T_1'-T_0')$
T_0' = ambient fluid temperature
T_1' = warm fluid temperature
x = dimensionless axial coordinate
x_s = location of separation point
y = dimensionless radial or normal coordinate
u = dimensionless axial velocity
U = bulk velocity
v = dimensionless radial or normal velocity
α = thermal diffusivity
β = volume thermal expansion coefficient
ν = kinematic viscosity
ρ = density
ψ = dimensionless streamfunction
ω = dimensionless vorticity

Subscripts

0 = ambient condition
1 = warm fluid condition

Superscript

′ = dimensional temperature

Froude numbers low enough to produce cold inflow, mean velocities high enough for accurate measurement, and reasonable power requirements for heating. It was possible to satisfy these requirements for air only over a very limited range of duct Reynolds numbers, due to the variation of the density and viscosity of air with temperature (see Modi, 1984), thus limiting the Re range that could be studied in the experiments. The instrumentation allowed measurements of the mean duct velocity, and the mean and rms local temperatures.

The flow path in Fig. 2 is as follows: Filtered air (from outside the laboratory room) is pumped by a 2 hp blower through an orifice flowmeter and a 9 kW electrical heater. The air flow rate is controlled by a bypass valve on the blower, and the electrical heating rate is controlled by a variable voltage transformer. The heated air then flows through an adiabatic flow-mixing duct into a plenum chamber of 87.5 cm square cross section. After passing through a series of screens, the flow enters an axisymmetric, conical, converging section consisting of a cone connected to an ASME nozzle. The converging section goes from 87.5 cm diameter to 25 cm diameter over a height of 40 cm. The converging section connects to a straight, vertical duct of circular cross section. The straight duct has an inside diameter of 25 cm and a height of 12.5 cm. The duct projects 12.5 cm above a 1.5 m by 3 m horizontal groundplane.

The heated flow exits the duct into a laboratory room which is free of drafts. The room is 3 m by 4.6 m by 2.4 m high. The buoyant jet leaves the room through a hole in the ceiling, which is located 1.5 m above the exit of the duct. The plenum chamber and the nozzle were wrapped with 10 cm of fiberglass insulation to reduce heat losses. The last straight section of the duct, which projects out of a wooden groundplane, was wrapped with asbestos tape insulation.

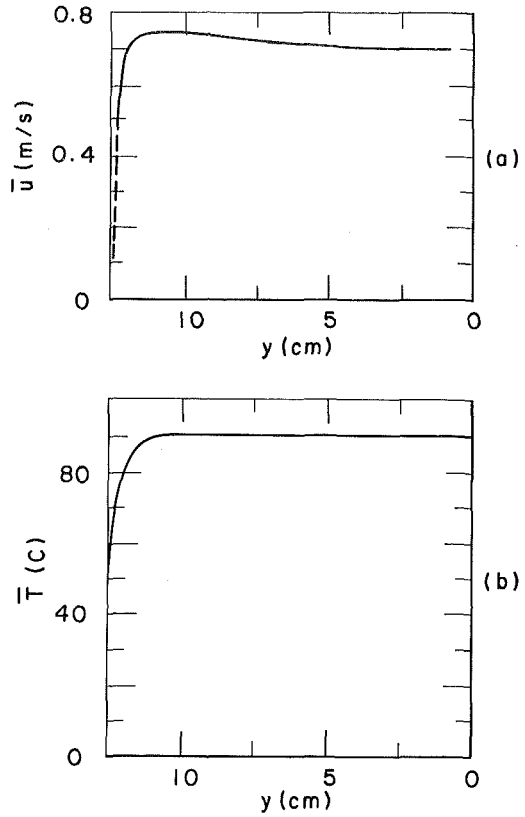

Fig. 3 Radial profiles in the duct in the absence of cold inflow for Re = 3300, Fr = 2.69: (*a*) mean velocity $\bar{u}$; (*b*) mean temperature $\bar{T}$

Measurements. In the experiment, mean exit velocities from 0.2 m/s to 1 m/s could be achieved, with exit temperatures of up to 120 K above ambient. Initial attempts were made to measure temperature and velocity simultaneously in the cold inflow region (the region of flow separation). However, due to extremely low velocities, large temperature fluctuations, and flow reversals in the region, this was not possible. Local velocities could be measured only in regions far removed from the separated flow region. Indeed, the only local measurements that could be made in the separated region were the mean and rms fluctuating temperatures. These were made with a TSI (Thermo Systems, Inc.) Model 1244 hot-wire probe, Model 1050 hot-wire anemometer circuit, and Model 1040 temperature circuit. The system consists of a bridge circuit and amplifier in an open loop configuration, with the hot wire used as a resistance thermometer. The high-frequency response of the resistance thermometer at the velocities of interest was limited to 100 Hz. Since all fluctuations of interest were at 5 Hz or lower, this limitation was of no concern. A two-point linear calibration guaranteed an accuracy of ± 1.25 K. Mean and rms fluctuating temperatures were measured by sampling 1024 points at a rate of 10 Hz over a time period of 102.4 s. The rms fluctuating temperatures are reported as a percent fraction of the difference between duct centerline and ambient temperatures.

The mean flow rate in the duct (needed to determine the Froude number and duct Reynolds number) was measured with the orificemeter (located upstream of the air heater) and micromanometer (capable of reading to ± 0.05 cm of water). Local velocities were measured with a hot wire using a nonlinear form of King's law where the coefficients A and B in $\mathrm{Nu} = A + B\mathrm{Re}^n$ are polynomial functions $A_1 + A_2T + A_3T^2$ and $B_1 + B_2T + B_3T^2$, respectively, in the temperature T. The six unknown coefficients and the exponent n are determined by calibrating the hot wire at seven known temperatures ranging from 30°C to 130°C. This allowed calibration of the hot wire to ± 3 percent of the centerline mean velocity at exit. Additional details on the experiment are provided in the thesis by Modi (1984).

Experimental Results. The experimental results consist of velocity and temperature measurements in the duct in the absence of cold inflow, time traces of fluctuating temperatures in the boundary region of the duct during cold inflow, and spatial profiles of the fluctuations to establish the size and geometry of the inflow region. The Froude number ranged from 0.68 to 2.69, and the duct Reynolds number from 2400 to 3300. In what follows, we implicitly assume that we are in a high Re regime, such that the cold inflow process is only a weak function of Re (Modi and Moore, 1987). We interpret our results as essentially indicating the Fr number dependence of the cold inflow process in this limit.

Profiles of mean velocity and mean temperature in the duct, in the absence of separation and cold inflow, are shown in Figs. 3(*a*) and 3(*b*), respectively. These profiles are representative of conditions without flow separation. The profiles, at Fr = 2.69 and Re = 3300, were obtained 8 cm below the exit plane of the duct. The profiles are symmetric and show a uniform core temperature and a slight dip in velocity near the duct centerline (a result of the flow acceleration in the converging section). The velocity and temperature boundary layers are 1 cm and 1.5 cm thick, respectively. The rms velocity fluctuations are about 1 percent of the mean velocity, and the rms temperature fluctuations are less than 1.5 percent in the wall boundary layer, and less than 0.1 percent outside the boundary layer. The profiles in Fig. 3 provide a baseline against which to assess the impact of cold inflow.

We next examine the effect of lowering the Froude number to encourage separation and cold inflow. Time traces of the fluctuating temperature at a location close to the exit corner provide graphic evidence of cold inflow. Three such traces are shown in Fig. 4 for Fr = 1.40, 1.18, and 1.00 at Re = 3000,

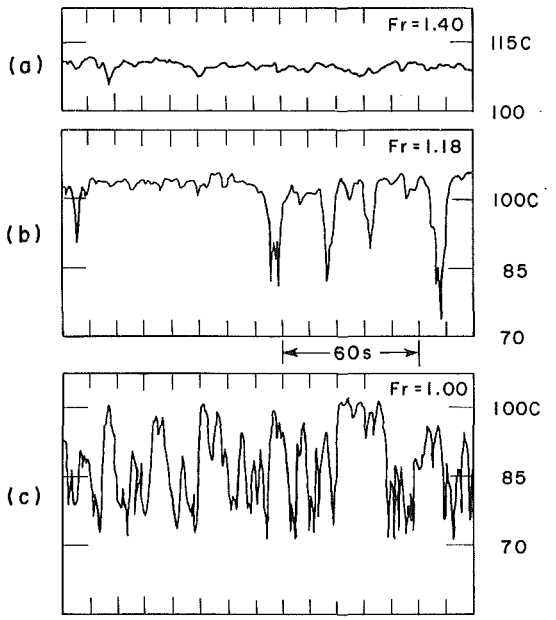

Fig. 4 Time traces of the fluctuating temperature in the duct at a position close to the exit lip: (a) Fr = 1.40, Re = 3000; (b) Fr = 1.18, Re = 2800; (c) Fr = 1.00, Re = 2600. The duct centerline temperature and the ambient temperature are 120°C and 30°C, respectively.

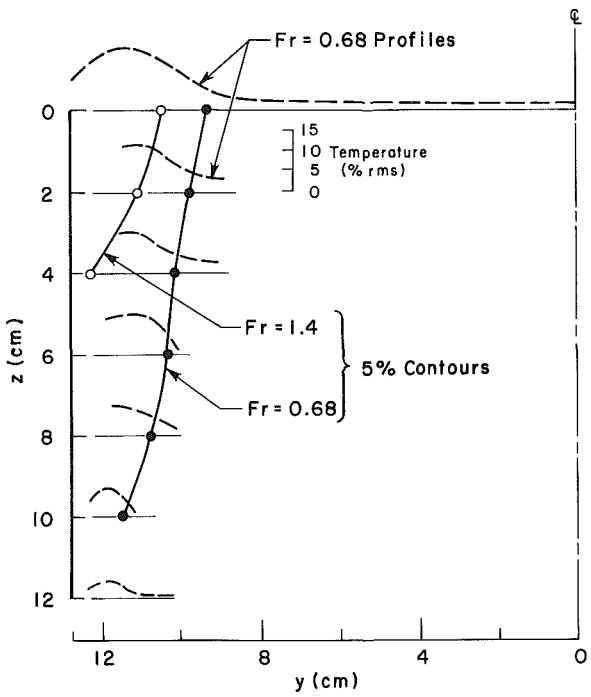

Fig. 5 Radial profiles of rms fluctuating temperature in the duct (dashed lines), Fr = 0.68, Re = 2400. Contours of the 5 percent rms fluctuating temperature are shown for Fr = 0.68 and 1.4. z is measured downward from the exit lip.

2800, and 2600, respectively. The duct centerline temperature for these traces is 120°C and the ambient temperature is 30°C. The measurement location was 0.5 cm below the exit plane and 1.6 cm away from the wall. As the Froude number is decreased from 1.4 to 1.18, intermittent bursts of cold air, each lasting a few seconds, appear. A further reduction to Fr = 1.0 leads to vigorous mixing between cold ambient fluid and warm duct fluid, as illustrated by the large fluctuations in temperature. The maximum fluctuating temperature is less than the duct centerline temperature, the minimum is above the ambient temperature, and the mean temperature has been reduced relative to the case without cold inflow. The traces provide clear evidence of cool ambient air plunging into the duct and mixing with warm air in the separated region.

Flow visualization with smoke was carried out as the Fr number was lowered. The visual observations confirm the cold inflow events associated with the large temperature minima in Fig. 4, and reveal that the cold inflow bursts occur randomly around the periphery of the duct. This was confirmed by making long-time-average measurements of the rms fluctuating temperature around the duct periphery. These measurements indicate that the time-averaged temperature profiles are axisymmetric, although at each instant the flow is not axisymmetric. As the Froude number is lowered, the bursts penetrate deeper and occur more frequently.

Spatial profiles of the rms fluctuating temperature provide an indication of the size and geometry of the separated or cold inflow region. Profiles at seven horizontal planes for Fr = 0.68 and Re = 2400 are shown by dashed lines in Fig. 5. The upper profile corresponds to the duct exit plane, at which the temperature fluctuations range from 15 percent near the duct wall (where inflow initiates) to 1.5 percent in the duct core. The fluctuations near the wall are an order of magnitude larger than those observed in the absence of separation. The profiles at lower planes show both a reduction in the maximum fluctuations and a narrowing of the radial span of the fluctuations. The profiles allow the size of the cold inflow zone to be estimated.

One way to estimate the size is to sketch contours of constant fluctuating intensity. Arbitrarily selecting the 5 percent contour, contours for Fr = 0.68 and 1.4 are shown in Fig. 5. The Reynolds numbers were 2400 and 3000, respectively. Clearly, the 5 percent contour indicates a greater size for the inflow region at Fr = 0.68 than at Fr = 1.4. The separated region is seen to be a wedge-shaped zone near the wall, growing in size with diminishing Froude number and associated with turbulent mixing of ambient and duct fluids. Measurements at Fr = 2.0 and Re = 3200 show no increase in rms temperature fluctuations near the wall similar to those shown in Fig. 5. This suggests that the critical Froude number for the present duct geometry, for Re $\approx$ 3000, is between 1.4 and 2.0.

The experiments reveal that cold inflow arises from the separation of the wall boundary layer inside the duct, and that inflow is confined to the near-wall region. In that region, the axisymmetric shape of the duct may not be a factor. To understand the separation process in detail, it would appear desirable to carry out high Reynolds number turbulent flow calculations in some time-averaged form. However, during cold inflow, turbulence is generated by both shear and buoyancy forces, which interact in a complicated way. Under such conditions the turbulence generation process is incompletely understood, and a turbulent flow numerical calculation would be fraught with uncertainties. Therefore, it was decided to consider a much simpler problem to see if the basic features of the boundary layer separation and the resulting cold inflow could be reproduced. Accordingly, a laminar flow numerical study was carried out in a planar geometry, at moderate Reynolds numbers, with care taken to describe accurately the boundary layer and flow reversal processes. This study is described in the next section.

3 Numerical Study

A numerical study of cold inflow was carried out for the geometry sketched in Fig. 6. A stream of warm fluid at temperature T_1' is shown emerging from a duct of half-width b into an ambient region of denser, and cooler, fluid at temperature T_0'. Numerical solutions of the governing elliptic

equations were obtained for Reynolds numbers from 200 to 500, and for Froude numbers from 1 to 5.

Geometry. In Fig. 6, fluid of uniform velocity U is shown entering the duct at $x = 0$. The fluid discharges from the duct at a height $x = h$. The ambient fluid is assumed to be at rest except for possible motions induced by the buoyant flow. For simplicity, we assume symmetry about the duct midplane. The computational domain is bounded by the six numbered surfaces shown in Fig. 6.

Special consideration is required at the exit corner of the duct (that is, at $x = h$, $y = b$). In the absence of buoyancy, flow separation would occur at this corner. In the presence of buoyancy, the separation location can move into the duct. Clearly, the separation process will depend upon the geometry of the corner, on the thickness of the wall boundary layers on either side of the corner, and, at the moderate Reynolds numbers considered in this section, on the flow structure of the separated zone itself. Normally, in chimneys and cooling towers, the exit edge of the duct would be a sharp lip (with a 180 deg corner), located well above the surrounding ground level. To simplify, we have moved the groundplane up to $x = h$ and treat it as a free (slip) surface. This creates a 90 deg corner (which is easier to model computationally) and eliminates the boundary layer on the outside wall. We treat the inner wall of the duct as a no-slip surface, and allow for the growth of boundary layers (one starting at $x = 0$ and associated with the duct velocity profile development, and the other starting at $x = h$ and associated with possible cold inflow).

Governing Equations. The flow is assumed to be governed by the time-dependent, constant-property, two-dimensional Boussinesq equations which are, in nondimensional, vorticity-stream function form

$$u = \frac{\partial \psi}{\partial y}, \qquad v = -\frac{\partial \psi}{\partial x} \tag{2}$$

$$\omega = -\nabla^2 \psi \tag{3}$$

$$\frac{\partial \omega}{\partial t} + \bar{\nabla} \cdot (\bar{v}\omega) = \frac{1}{\mathrm{Re}} \nabla^2 \omega - \frac{1}{\mathrm{Fr}} \frac{\partial T}{\partial y} \tag{4}$$

$$\frac{\partial T}{\partial t} + \bar{\nabla} \cdot (\bar{v} T) = \frac{1}{\mathrm{RePr}} \nabla^2 T \tag{5}$$

The equations have been scaled with a reference time b/U, reference length b, and reference temperature difference $(T_1' - T_0')$. The parameters which appear in the governing equations are the Reynolds, Froude, and Prandtl numbers. An additional parameter, the aspect ratio A, appears from the geometry of the problem. Thus, the governing parameters are

$$\mathrm{Re} = \frac{Ub}{\nu}, \qquad \mathrm{Fr} = \frac{U^2}{g\beta(T_1' - T_0')b},$$

$$\mathrm{Pr} = \frac{\nu}{\alpha}, \qquad A = h/b \tag{6}$$

where β and α are the volumetric thermal expansion coefficient and thermal diffusivity of the fluid, respectively.

Boundary Conditions. Equations (2)–(5) are to be solved by prescribing appropriate boundary and initial conditions for the computational domain sketched in Fig. 6.

The initial conditions are taken to be those of an inviscid, nonbuoyant, uniform jet of diameter $2b$ and temperature $T = 1$, moving vertically through, and without interaction with, a stationary ambient medium at temperature $T = 0$. Thus, at $t = 0$

$$\psi = y, \quad \omega = 0, \quad T = 1 \text{ in the jet} \tag{7}$$

$$\psi = 1, \quad \omega = 0, \quad T = 0 \text{ elsewhere} \tag{8}$$

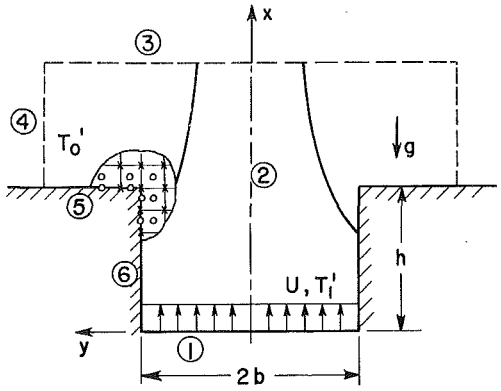

Fig. 6 Schematic of the geometry considered for the numerical solutions

In principle, the steady-state solution of equations (2)–(5) for the present geometry should be independent of the initial conditions. Indeed, this was found to be true for several test cases.

We next turn to the boundary conditions to be applied on the numbered, bounding surfaces in Fig. 6. We take the inlet flow (through surface 1) to be of uniform velocity, $u = 1$, and uniform temperature, $T = 1$. Further, we assume the boundary is sufficiently far upstream of any separated zone on the wall so as to be unaffected by the upstream influence of separation. The imposed boundary conditions are

$$\psi = y, \qquad \omega = 0, \qquad T = 1 \tag{9}$$

Along the symmetry boundary (surface 2) we have

$$\psi = \omega = 0, \qquad \frac{\partial T}{\partial y} = 0 \tag{10}$$

At the open boundaries (surfaces 3 and 4), some approximation is required. Ideally, these boundary conditions should be weak, so that a solution in the computational domain approximates the solution for an infinite, ambient medium above $x = h$. Therefore we apply weak derivative conditions and a directional convective flux condition. On surface 3

$$\frac{\partial^2 \psi}{\partial x^2} = \frac{\partial^2 \omega}{\partial x^2} = 0$$

$$\frac{\partial^2 T}{\partial x^2} = 0 \quad \text{if} \quad u > 0; \quad T = 0 \quad \text{if} \quad u < 0 \tag{11}$$

The same conditions apply on surface 4 by replacing x with y and u with v. We take the solid bounding surfaces 5 and 6 to be adiabatic. Thus, at the slip-wall boundary (surface 5), we have

$$\psi = 1, \qquad \omega = \frac{\partial T}{\partial x} = 0 \tag{12}$$

and at the no-slip boundary (surface 6)

$$\psi = 1, \qquad \frac{\partial \psi}{\partial y} = \frac{\partial T}{\partial y} = 0 \tag{13}$$

We note that the conditions applied on the open boundaries (equation (11)) are consistent with the recommendations of Thoman and Szewczyk (1966), Roache and Mueller (1970), Briley (1971), and Roache (1982), and allow for both outflow and inflow at the boundary. The thermal conditions allow for a second derivative constraint on outflow and convection of ambient air on inflow.

Numerical Method. The computational domain was divided into discrete volumes, as sketched in the insert in Fig. 6. Vorticity and temperature are defined at the geometric centers of control volumes, and the stream function at the corners. This is an ω–ψ staggered mesh, which gives full control volume

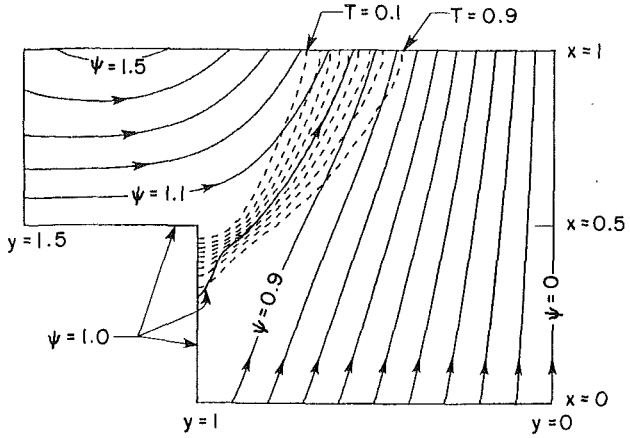

Fig. 7 Streamlines (solid lines) and isotherms (dashed lines) for a calculated flow with cold inflow, Re = 500 and Fr = 2

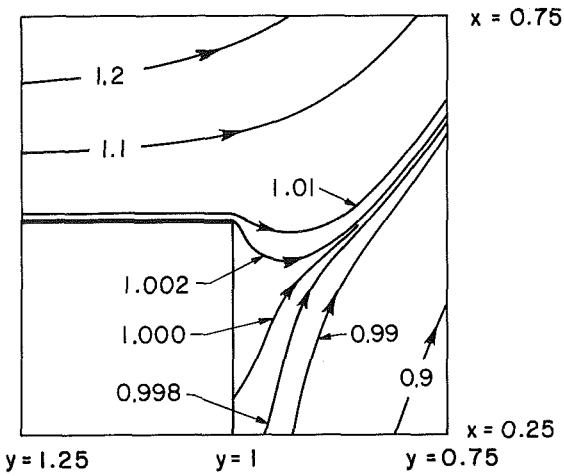

Fig. 8 Streamline detail in the region of flow reversal and separation, Re = 500 and Fr = 2

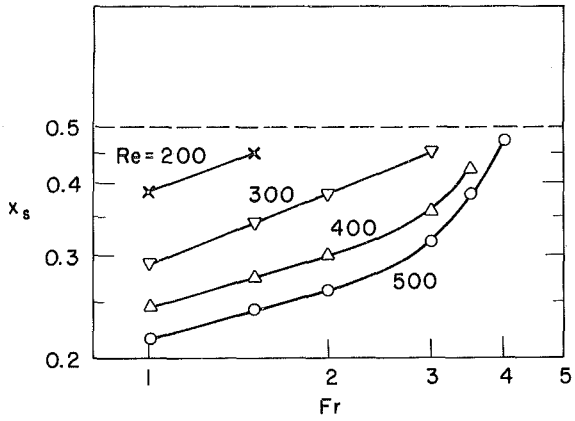

Fig. 9 Calculated distance x_s to flow separation on the duct wall as a function of Fr and Re; dashed line denotes the duct exit plane

coverage of the domain and assists with diagnostic checks of energy and vorticity conservation (Wong and Raithby, 1979).

The discrete equations are formed by using finite volume or control volume principles (Torrance, 1985). Convective and diffusive fluxes between control volumes are evaluated using a power-law approximation (Patankar, 1980) to the exact exponential solution. The time discretization and integration is carried out with the alternating-direction-implicit (ADI) method. The transient equations are free of formal stability restrictions on the temporal and spatial meshes. However, the time steps were typically limited to a small multiple of the diffusive relaxation time for a control volume in order to preserve accuracy. The ω–ψ Poisson equation (3) was discretized with three-point central differences in each spatial coordinate and by averaging adjacent values of ω to get ω values on the ψ grid. The ω–ψ equation was solved at each time step by iteration (one Gauss–Seidel sweep followed by optimized successive overrelaxation). The calculation sequence advanced T, ω, and ψ in sequence over a time step. Iteration over a time step was not done to update the boundary values of ω, and to update the transport velocities to midpoint time levels to achieve full second-order time accuracy.

The boundary conditions (9)–(13) were incorporated into the discrete equations. Special points to be noted include: On the open boundaries, ψ was found by integrating discrete approximations of $\partial^2\psi/\partial y^2 = -\omega$ on the horizontal open boundary, and $\partial^2\psi/\partial x^2 = -\omega$ on the vertical open boundary, with ω known from the solution of equation (4) and the ω boundary condition (11). The boundary values for ψ were then used during the iteration of the ω–ψ equation in the interior. The second derivative conditions in equation (11) at the open boundaries essentially set the longitudinal diffusion terms to zero. Their adaptation into a power-law scheme has been discussed by Patankar (1980). Remaining points include: The zero heat flux condition is readily incorporated since full control volumes are used throughout, and adjacent to all boundaries (Torrance, 1985). The vorticity boundary condition at the no-slip wall is evaluated using the EDS scheme of Wong and Raithby (1979).

A nonuniform Cartesian mesh was used, such that the highest resolution was available in the boundary layer region. The ratio of adjacent cell sizes was always less than or equal to 1.10. The cell aspect ratio was limited to 4. A different mesh was used at each Reynolds number, such that the cell Reynolds number based on the smallest cell was held constant at about 11. This allows meaningful cross comparisons of flows at different Reynolds numbers. The number of cells varied from 15 $\times$ 15 at Re = 200 to 30 $\times$ 30 at Re = 500. A uniform mesh calculation was carried out by using the same cell size as the smallest cell in a nonuniform mesh calculation, and resulted in virtually the same solution. This check was necessary since the spatial accuracy of the scheme can be guaranteed only for a uniform mesh. Further details of the computational procedure are available in Modi (1984).

Numerical Results. Using the numerical method outlined in the previous section, solutions have been obtained for the geometry shown in Fig. 6 by carrying a transient solution forward in time until steady state was achieved. Four parameters appear in the problem formulation, as listed in equation (6). Of these parameters, the Prandtl number and duct aspect ratio were held fixed at Pr = 1 and $h/b = 0.5$, respectively. The domain of computation was also held fixed. Several trial runs were carried out to ensure that the domain was large enough so that the location of the open boundaries did not influence any flow separation regions inside the duct. This was achieved by locating the upper boundary at $x = 1$ and the left boundary at $y = 1.5$. Efforts were focused on the remaining two parameters, the Reynolds and Froude numbers, and their influence on cold inflow.

Results are presented in terms of streamlines and isotherms for one representative case (Figs. 7 and 8). The quantity of prime interest, however, is the location x_s of flow separation on the vertical wall of the duct. This quantity is of interest for design purposes, since the duct length beyond x_s does not help produce draft. x_s is defined by the position where the wall vorticity goes to zero (as determined by linear interpolation of the computed wall vorticities). Since the duct exit is located at $x = 0.5$, a lower value of x_s implies the presence of premature

separation, or cold inflow. The effect of Re and Fr on x_s is shown in Fig. 9.

Two-dimensional contour diagrams of streamlines (solid lines) and isotherms (dashed lines) are shown in Fig. 7 for Re = 500 and Fr = 2. The duct midplane (to the right) corresponds to $\psi = 0$. The ψ contours increase in steps of 0.1 away from the midplane up to a value of $\psi = 1.5$ in the upper left of the diagram. The separation streamline and the solid walls correspond to $\psi = 1.0$. The streamline touching the solid wall of the duct is the separation streamline, and clearly indicates the presence of cold inflow. ψ values greater than 1.0 denote ambient fluid which has been drawn in from the left boundary. Near the exit corner of the duct, ambient fluid flows around the duct edge and into the duct. This is shown in more detail in Fig. 8, which is an enlargement (with more streamlines) of the flow field near the corner of the duct.

Also shown in Fig. 7 are the isotherms, which increase in steps of 0.1 from the ambient region toward the interior of the duct. The isotherms illustrate the diffusive exchange of heat between the cold ambient air and the warm duct fluid. Away from the separation zone on the wall of the duct, the isotherms are distributed almost symmetrically with respect to the $\psi = 1$ separation streamline. The temperature field thus shows that the $\psi = 1$ streamline is the boundary between duct fluid and ambient fluid.

Near the wall there is an apparent kink in the dividing streamline. This is located near the edge of the wall boundary layer. Thus, the process of flow separation appears to take place within a zone dominated by the wall boundary layer. The slowly moving fluid in the separated region (the region between the dividing streamline and the wall) also shows evidence of having been heated to higher temperatures. Due to the lower velocities in this zone, heat diffusion becomes important, and the isotherms are no longer symmetric about the separation streamline ($\psi = 1$).

The overall appearance of the streamlines and the separation zone suggests strong convection in the streamwise direction right up to the point of separation. Therefore, it seems likely that any instabilities in the separated region would not have an upstream-propagating influence on the location of the separation point.

The calculation shown in Fig. 7 was obtained with a 30 × 30 mesh. The cells in the channel region were uniform in the x direction but increased in size away from the duct wall. The separated flow region inside the duct spans nine cells in the x direction and six cells in the y direction. The contours have not been smoothed, and the overall smoothness suggests that the flow is well resolved by the mesh. There is some arbitrariness in locating the separation point of the dividing streamline at the wall (due to extrapolation). In subsequent discussions the separation location is found by interpolating the wall vorticity.

We next examine the influence of Re and Fr on the location of the separation point x_s. This is illustrated in Fig. 9. We observe that with increasing buoyancy (lower Fr) the separation location moves upstream into the channel. This behavior is expected since buoyancy accelerates the duct flow relative to the ambient. This leads to a narrowing of the plume, and streamlines within the duct are observed to move away from the wall. An increase in buoyancy leads to a larger deceleration at the wall, and the separation point moves further upstream. In the absence of buoyancy, separation would occur at the very top of the duct, $x_s = 0.5$, since there would be no mechanism to create an adverse pressure gradient at the wall. Thus, we would expect a critical Froude number to exist, at which the duct flow would just begin to separate prematurely. We found it difficult to find an exact value for this parameter numerically because as the separation zone shrinks in size with increasing Fr, the zone becomes increasingly difficult to resolve on a finite grid.

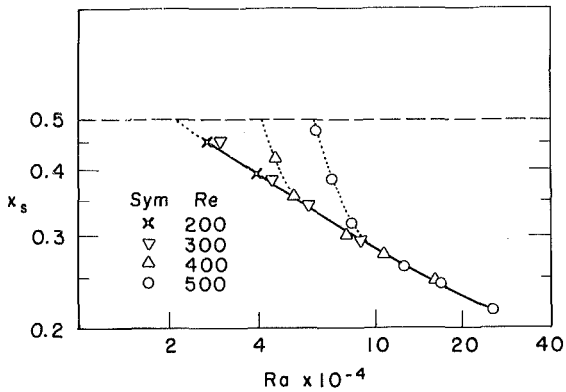

Fig. 10 Calculated distance x_s to flow separation on the duct wall as a function of Ra and Re; dashed line at $x_s = 0.5$ denotes the duct exit plane

The Reynolds number dependence of x_s can also be examined with the aid of Fig. 9. The separation point x_s is seen to move into the duct with increasing Re. This occurs while the wall boundary layer and the thickness of the cold inflow region are thinning. At the higher values of Re, the rate of change of x_s with Re diminishes. This trend is consistent with the prediction of Modi and Moore (1987), who use a high Reynolds number, laminar boundary layer analysis to predict that $x_s \sim \mathrm{Re}^{-1/9}$ as Re approaches infinity. This is a very weak dependence on Re, but not inconsistent with the extrapolation of the results in Fig. 9 to higher values of Re.

At low Reynolds numbers, the strong dependence on Re in Fig. 9 suggests that other reference quantities might be more appropriate for nondimensionalizing the governing equations. This is also apparent by inspection of the vorticity transport equation (4). At low values of Re, we expect the convection terms on the left to be zero, and the two terms on the right side to balance one another. Since time has been scaled with b/U, this limit causes some difficulty as Re → 0. The difficulty can be eliminated by using a reference time based on thermal diffusion, b^2/α. With this reference time, no parameters appear in the energy equation (5), and, in the viscous limit, the vorticity equation reduces to

$$0 = \nabla^2 \omega'' - \mathrm{Ra} \frac{\partial T}{\partial y} \tag{14}$$

where ω'' is scaled with the diffusion time scale. Thus, the only dimensionless group appearing in the governing equations is the Rayleigh number, defined as

$$\mathrm{Ra} = \mathrm{Re}^2 \mathrm{Pr}/\mathrm{Fr} = g\beta(T_1 - T_0)b^3/\nu\alpha \tag{15}$$

The remaining parameters appear through the boundary data and are Re and the channel aspect ratio, $A = h/b$.

Thus, in the limit of low Re, we expect Ra to be one of three important nondimensional parameters. The results in Fig. 9 are regraphed in Fig. 10 with Ra on the abscissa. Clearly all of the linear portions of the curves in Fig. 9 group onto a common curve, which represents the viscous-dominated limit. Inertial effects becomes important, relative to viscosity and buoyancy respectively, as either Re or Fr increase. This explains why data for Re = 400 and 500 in Fig. 10 depart from the viscous limit. Clearly, Ra is the appropriate parameter to represent the viscous-dominated regime.

The viscous behavior in Fig. 10 is fully consistent with the experimental observations of cold inflow reported by Sparrow et al. (1984) for a very different configuration. They observed cold inflow on an unheated wall of an open-ended natural convection channel. They always observed a small amount of cold inflow on the unheated wall (i.e., x_s never actually achieved the full channel height, but was very close). This may explain our inability to fill in the dotted extension of the

viscous curve in Fig. 10, which we attributed to an inability to refine the mesh sufficiently. For Ra above a critical value ($\approx$4400 based on channel half-width), Sparrow et al. (1984) observed that the amount of penetration increased linearly with Ra. This is essentially the behavior shown for the viscous regime in Fig. 10, in which the penetration (or the distance between the horizontal dashed line and x_s) increases with Ra for Ra $\gtrsim$ 22,000. The present numerical calculations and the experiments of Sparrow et al. (1984) lead to different critical Ra values. This is undoubtedly due to differences in the heating conditions in the two studies and to large differences in the channel aspect ratios (present calculations, $h/b = 0.5$; experiments of Sparrow et al. (1984), $h/b \approx 40$).

4 Summary and Conclusions

The experimental study provides qualitative evidence (Fig. 4) of the onset of cold inflow as the Froude number is reduced below a critical value (between Fr = 1.4 and 2.0) in a turbulent flow regime (Re $\approx$ 3000). The inflow process was time dependent. Spatial profiles of rms fluctuating temperatures (Fig. 5) show that the time-averaged cold inflow region is a wedge-shaped zone near the wall, and is associated with the turbulent mixing of ambient and duct fluids. The measurements provide quantitative information on the growth of the cold inflow region with diminishing Froude number. It is found that cold inflow arises from the separation of the wall boundary layer and that inflow is confined to the near-wall region.

Numerical solutions of the governing elliptic equations were obtained for Reynolds numbers from 200 to 500, and for Froude numbers from 1 to 5. These solutions yield steady-state flows which provide quantitative information on the cold inflow region (Figs. 7 and 8), and on the effect of Reynolds and Froude numbers on the size of the cold inflow region. The latter is displayed in terms of the separation location on the wall (Fig. 9). The separation location is found to move upstream into the channel with increasing buoyancy (lower Fr), an effect that would be important at all Reynolds numbers, since it is buoyancy that is responsible for the deceleration at the wall. Increasing the Reynolds number also moves the separation point further into the duct. This is particularly significant at lower Reynolds numbers, suggesting a viscous-dominated regime with the Rayleigh number as one of the important parameters. This parametric dependence is shown in Fig. 10. A viscous regime is apparent in which the penetration of cold inflow increases with Rayleigh number for Ra > 22,000.

The present studies show that cold inflow is associated with the premature separation of the wall boundary layer in a buoyant channel flow. Such separation can lead to a loss of draft height in a cooling tower or a chimney. The present paper provides information on the onset and structure of the cold inflow process.

Acknowledgments

We are grateful to Professor Franklin K. Moore for insightful and constructive comments throughout the course of this work. We acknowledge the partial support of the National Science Foundation under grants ENG-7926404, ENG-7602516, and MEA-8401489.

References

Baer, E., Ernst, G., and Wurz, D., 1977, "Untersuchung zur Schwadenströmung in den Kronen von Naturzugkühltürmen," VDI Kühlturmseminar, Düsseldorf, May 25, 1977, Inst. f. Technische Thermo., U. Karlsruhe.

Briley, W. R., 1971, "A Numerical Study of Laminar Separation Bubbles Using the Navier-Stokes Equations," *Journal of Fluid Mechanics*, Vol. 47, pp. 713–736.

Jörg, O., and Scorer, R. S., 1967, "An Experimental Study of Cold Inflow Into Chimneys," *Atmospheric Environment*, Vol. 1, pp. 645–654.

Modi, V., 1984, "A Study of Laminar Separation in Buoyant Channel Flows," Ph.D. Thesis, Cornell University, Ithaca, NY, 175 pp.

Modi, V., and Moore, F. K., 1987, "Laminar Separation in Buoyant Channel Flows," *Journal of Fluid Mechanics* (in press).

Moore, F. K., 1978, "Cold Inflow and Its Implications for Dry Tower Design," *Proceedings of the 2nd Conference on Waste Heat Management and Utilization*, University of Miami, Miami Beach, FL, Dec. 4–6, 1978.

Patankar, S. V., 1980, *Numerical Heat Transfer and Fluid Flow*, Hemisphere/McGraw-Hill, New York.

Roache, P. J., 1982, *Computational Fluid Dynamics*, rev., Hermosa Publishers, Albuquerque, NM.

Roache, P. J., and Mueller, T. J., 1970, "Numerical Solutions for Laminar Separated Flows," *AIAA Journal*, Vol. 8, pp. 530–538.

Sparrow, E. M., Chrysler, G. M., and Azevedo, L. F., 1984, "Observed Flow Reversals and Measured-Predicted Nusselt Numbers for Natural Convection in a One-Sided Heated Vertical Channel," ASME JOURNAL OF HEAT TRANSFER, Vol. 106, pp. 325–332.

Thoman, D. C., and Szewczyk, A. A., 1966, "Numerical Solutions of Time Dependent Two-Dimensional Flow of a Viscous, Incompressible Fluid Over Stationary and Rotating Cylinders," Technical Report 66-14, Heat Transfer and Fluid Mechanics Laboratory, Department of Mechanical Engineering, University of Notre Dame, Notre Dame, IN.

Torrance, K. E., 1985, "Numerical Methods in Heat Transfer," *Handbook of Heat Transfer Fundamentals*, 2nd ed., W. M. Rohsenow et al., eds., McGraw-Hill, New York, Ch. 5, pp. 5.1–5.85.

Wong, H. H., and Raithby, G. D., 1979, "Improved Finite-Difference Methods Based on a Critical Evaluation of the Approximation Errors," *Numerical Heat Transfer*, Vol. 2, pp. 139–163.

Steady, Two-Dimensional, Natural Convection in Rectangular Enclosures With Differently Heated Walls

K. S. Chen

J. R. Ho

Department of Mechanical Engineering,
National Sun Yat-Sen University,
Kaohsiung, Taiwan 800,
Republic of China

J. A. C. Humphrey

Department of Mechanical Engineering,
University of California,
Berkeley, CA 94720
Mem. ASME

Numerical results are presented for steady natural convection in two-dimensional rectangular enclosures in which the side walls, top wall, and bottom wall are at uniform temperatures θ_s, θ_t, and θ_b, respectively, and $\theta_s > \theta_t > \theta_b$. Rayleigh numbers ranging from 10^4 to 10^7 and aspect ratios of 1 and 1.5 were investigated. The top wall was modeled as an impermeable rigid surface or an impermeable free-moving boundary. The calculations reveal two flow regions. In the upper part of the enclosure two large counterrotating cells appear, separated by a descending plume of fluid. Near the bottom wall the flow is almost motionless and stably stratified. The temperature in the central portion of the enclosure is almost uniform due to mixing by the recirculating cells. A temperature inversion occurs near the top wall and is particularly noticeable at high Rayleigh numbers. At high Rayleigh numbers the flow breaks up into smaller cells. The result is that each main recirculation region develops a secondary counterrotating eddy within it. The condition of a free surface as the top wall boundary condition significantly affects the circulation and heat transfer throughout the flow domain. Numerical experiments reveal the extent to which the flow field in the enclosure is affected by an asymmetric specification of side-wall temperature boundary conditions.

1 Introduction

It has been recognized that the growth of single crystals by the Czochralski technique (Hurle, 1977) is influenced by the fluid dynamics and heat transport characteristics of the process. The flow in the melt, due to natural convection, surface tension gradient, and crucible or crystal rotation has a profound influence on the interface shape, surface striations, defect density, and crystal integrity. There are a number of numerical, analytical and experimental works that simulate various aspects of these effects; see, for example, Laudise (1979), Carruthers (1977), Schwabe and Scharmann (1981), Simpkins and Dudderar (1981), Ostrach (1983), Simpkins and Chen (1985, 1986), Miller and Pernell (1981), and Simpkins (1981). However, the causes of misshapen and nonuniform crystal growth are still not well understood due to the complexity of the process.

The experimental studies of Miller and Pernell (1981) and Simpkins (1981) are of particular interest to this work. The first study involved heating the side walls of an open cylinder containing water. The authors characterized the flow into three regions when the temperature of the bottom wall is below that of the side walls. From the top to the bottom surfaces the regions are: (*i*) a thin surface layer; (*ii*) a convection region with essentially uniform temperature; and (*iii*) a motionless region, the so-called "stagnant" region. In a rectangular container with hot side walls and cooled top and bottom surfaces, Simpkins (1981) observed the appearance of two large recirculation cells, separated by a descending plume, in the upper portion of the container. The plume was fed by thin boundary layers adjacent to the vertical walls, and it would only sink to a critical depth in the container. Below this depth the flow was not strictly stagnant but moved very slowly relative to the motion in the upper layer. The top surfaces in these two works were free of motion and held at approximately constant temperatures. The experimental condition in Simpkins (1981) was for a Rayleigh number o(10^7) and aspect ratio o(1).

To complement the above experimental works, it is the purpose of this study to investigate numerically the buoyancy-driven flow in an enclosure in which the side-wall temperatures are higher than that of the bottom wall. The top wall is either rigid or represents a free surface, and is kept at an intermediate uniform temperature. Flow and heat transport in the recirculation cells, descending plume and stagnant layer, and the influence of free surface effects and asymmetric boundary conditions, are presented and discussed for $Pr = 7$, a Rayleigh number range 10^4 to 10^7, and aspect ratios (width/height) of 1 and 1.5. The calculated results compare fairly well with the available experimental data.

It should be noticed that the flow due to a heat source (such as a fire) located on the bottom wall of a symmetric enclosure strongly resembles (when inverted) the flow of interest here. For example, a detailed analysis has been performed by Rehm et al. (1982), but neglecting the molecular diffusion of momentum and heat which are crucial to this study. In contrast to the heat-source/plume configuration, the descending plume problem of interest here has received considerably less attention; see, for example, Simpkins and Chen (1985) and Simpkins (1985).

It is recognized that the practical realization of the present problem is bound to exhibit some degree of three dimensionality and unsteadiness. In this regard, the investigations of Humphrey and Bleinc (1985) and Simpkins (1985) are especially relevant. The top half of a vertical plate was cooled and the bottom half was heated by Humphrey and Bleinc (1985). This configuration induced boundary layer flows of opposing sign to collide halfway along the plate. The resulting flow was essentially two dimensional until Rayleigh numbers larger than 10^8 were imposed, at which point the motion in the collision region became three dimensional and unsteady, with time and length scales commensurate with the boundary layer

Contributed by the Heat Transfer Division and presented at the ASME Winter Annual Meeting, Anaheim, California, December 1986. Manuscript received by the Heat Transfer Division April 7, 1986.

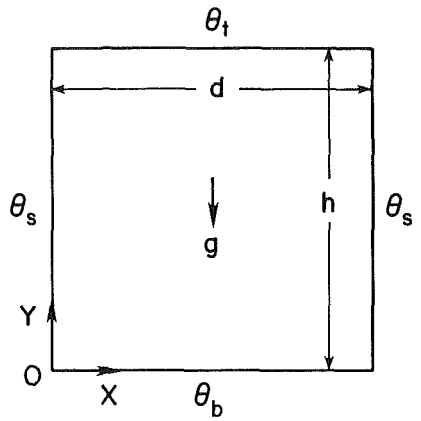

Fig. 1 Schematic of two-dimensional enclosure and coordinates. For the case of interest $\theta_s > \theta_t > \theta_b$.

length and time scales. In the present, more stable flow configuration, the maximum Rayleigh investigated was 10^7 and, therefore, the assumption of two-dimensional flow is not unrealistic.

Unsteadiness of the plume leaving the top surface of the enclosure where the turning boundary layers collide is discussed by Simpkins (1985). Measurements obtained by Simpkins (1985) in an enclosure of aspect ratio unity and $\mathrm{Ra} = 7 \times 10^6$ revealed a meandering plume of changing length. The periodicity determined was about 30 s for a value $(T_b - T_t)/(T_s - T_t) = -4.5$. Experimental attempts failed to stabilize the meandering of the collision region, and hence of the plume. In the present study $(T_b - T_t)/(T_s - T_t) = -2.39$ and, while we cannot rule out the possible meandering of a plume corresponding to our calculation conditions, its periodicity should be greater than 30 s. The results presented here were obtained with a time-dependent calculation scheme that evolved to steady state *without* displaying oscillatory motions of the type just described.

2 Governing Equations and Solution Procedure

Consider a two-dimensional rectangular enclosure filled with fluid, such as is shown in Fig. 1. The two side walls are maintained at the same temperature θ_s, while the top and bottom surfaces are kept at the lower temperatures θ_t and θ_b, respectively. Employing the Boussinesq approximation, the nondimensional equations describing laminar flow in stream function and vorticity form are

$$\frac{\partial \omega}{\partial \tau} + U\frac{\partial \omega}{\partial X} + V\frac{\partial \omega}{\partial Y} = \mathrm{Ra}\,\mathrm{Pr}\frac{\partial \theta}{\partial X} + \mathrm{Pr}\nabla^2\omega \tag{1}$$

$$\frac{\partial \theta}{\partial \tau} + U\frac{\partial \theta}{\partial X} + V\frac{\partial \theta}{\partial Y} = \frac{\partial^2 \theta}{\partial X^2} + \frac{\partial^2 \theta}{\partial Y^2} \tag{2}$$

$$\nabla^2\psi = -\omega \tag{3}$$

$$\frac{\partial \psi}{\partial Y} = U, \qquad \frac{\partial \psi}{\partial X} = -V \tag{4}$$

The initial and boundary conditions are

$\tau = 0$: $\quad U = V = 0, \quad \theta = 0$ (5*a*)

$\tau > 0$:

$X = 0$ or 1: $\quad \psi = \dfrac{\partial \psi}{\partial X} = 0, \quad \theta = 1$ (5*b*)

$Y = 0$: $\quad \psi = \dfrac{\partial \psi}{\partial Y} = 0, \quad \theta = 0$ (5*c*)

$Y = AR$: $\quad \psi = \dfrac{\partial \psi}{\partial Y} = 0, \quad \theta = 0.7053$

(rigid top surface) (5*d*)

$$\psi = \frac{\partial \psi}{\partial X} = 0, \quad \theta = 0.7053$$

(free top surface) (5*e*)

$$\omega = -\mathrm{Ma}\frac{\partial \theta}{\partial X} = 0$$

(free top surface) (5*f*)

Note that in this study $AR = 1$ or 1.5, and the top surface is kept at a temperature between that of the bottom and side walls. Equation (5*d*) is used if the top wall represents a rigid surface. In this case, the vorticity is calculated by linear extrapolation from two interior points adjacent to the boundary.

Nomenclature

AR = aspect ratio = h/d
d = width of cavity shown in Fig. 1
g = gravitational acceleration
h = height of cavity shown in Fig. 1
Ma = Marangoni number defined in equation (6)
Nu_s = mean value of Nusselt number on side wall, defined in equation (8)
Pr = Prandtl number = ν/α
q = average heat flux from side wall
Ra = Rayleigh number = $g\beta(T_s - T_b)d^3/\nu\alpha$
T = absolute temperature
u = velocity in x direction
U = dimensionless velocity in x direction = ud/α
v = velocity in y direction
V = dimensionless velocity in y direction = vd/α
x = horizontal coordinate shown in Fig. 1
X = dimensionless horizontal coordinate = x/d
y = vertical coordinate shown in Fig. 1
Y = dimensionless vertical coordinate = y/d
α = thermal diffusivity of fluid
β = thermal expansion coefficient of fluid
γ = surface tension gradient defined in equation (7)
δ = thermal layer thickness on the bottom wall
Δ = difference
θ = dimensionless temperature = $(T - T_b)/(T_s - T_b)$
μ = dynamic viscosity of fluid
ν = kinematic viscosity of fluid
σ = surface tension coefficient
τ = dimensionless time = $t\alpha/d^2$
ψ = dimensionless stream-function defined in equation (4)
ω = dimensionless vorticity defined in equation (3)
Ω = relaxation parameter

Superscripts

p = iteration number

Subscripts

b = bottom wall
i, j = subscripts denoting X and Y grid node
s = side wall
t = top wall

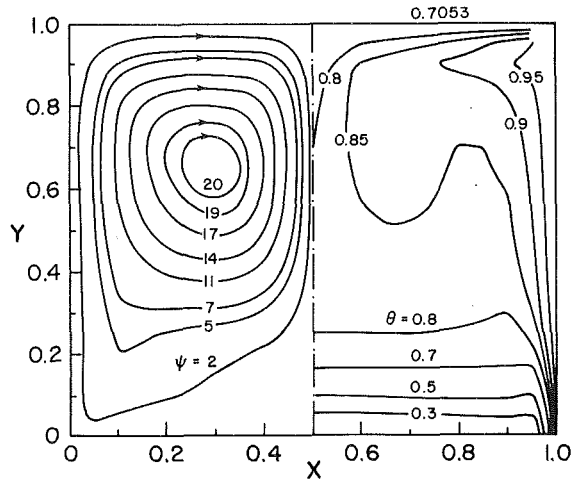

Fig. 2 Streamline and isotherm contours in an enclosure with $Ra = 10^6$, $AR = 1.0$, and rigid upper surface

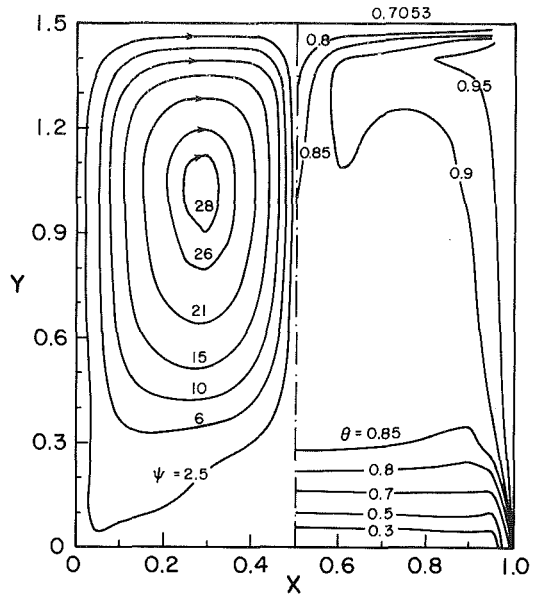

Fig. 3 Streamline and isotherm contours in an enclosure with $Ra = 10^6$, $AR = 1.5$, and rigid upper surface

Equations (5*e*, 5*f*) are used instead if the top wall represents a free surface. Ma in equation (5*f*) is the Marangoni number defined by

$$\mathrm{Ma} = -\frac{\gamma d \Delta T}{\alpha \mu} \tag{6}$$

where $\Delta T = T_s - T_b$. In the above equation γ is defined by

$$\gamma = -\frac{d\sigma}{dT} \tag{7}$$

where σ is surface tension of the fluid. The derivation of equation (5*f*) is given in the appendix. Since the free surface is held at constant temperature, surface tension gradients do not drive the flow and so the value of vorticity at the free surface vanishes.

Equations (1)–(5) are solved in the following manner. Given the field values at time $n\Delta\tau$, the vorticity and temperature at time $(n+1)\Delta\tau$ are calculated by the ADI method from equations (1) and (2), respectively, as described in Wilkes and Churchill (1966). The stream function is then computed from equation (3) using the successive overrelaxation (S.O.R.) method. Finally, the new values of U and V are computed by a central difference approximation to equation (4). 41 × 41 grid points are used for the case of aspect ratio 1, and 41 × 61 for the aspect ratio 1.5. This level of grid refinement guaranteed not fewer than 2 grid points within the side-wall boundary layers at the highest Rayleigh number investigated. In solving the stream function by the S.O.R. method, the convergence criterion within each time step is

$$\left| \frac{\psi_{i,j}^{p+1} - \psi_{i,j}^{p}}{\psi_{i,j}^{p+1}} \right| \leq 5.0 \times 10^{-5}$$

All the results presented here correspond to steady-state conditions. As in Wilkes and Churchill (1966), steady state is presumed to have been reached when

$$\left| \frac{\mathrm{Nu}_s^{p+1} - \mathrm{Nu}_s^{p}}{\mathrm{Nu}_s^{p+1}} \right| \leq 5.0 \times 10^{-6}$$

where Nu_s is the average Nusselt number on the vertical side wall given by

$$\mathrm{Nu}_s = \left[\int_0^{AR} \frac{\partial \theta}{\partial X} \bigg|_{X=0} dY \right] / AR \tag{8}$$

3 Results and Discussion

Prior to the calculations, numerical tests were conducted to check the accuracy of the ADI procedure by reference to the flow generated by differentially heating the side walls of a rectangular enclosure while keeping the top and bottom walls adiabatic. The results were compared with the benchmark solution of de Vahl Davis (1981). They are reported in Chen (1985) and substantiate the correctness of the numerical calculation procedure.

The computation time depends on the numerical time step $\Delta\tau$, the Rayleigh number, the number of grid points, and the S.O.R. parameter Ω. For a 41 × 41 grid, with $\Delta\tau = 2.0 \times 10^{-4}$ and $\Omega = 1.73$, the CPU time is approximately 4000 s on a CDC CYBER 170/815 when $\mathrm{Ra} = 10^4$–10^6; and about 9000 s when $\Delta\tau = 1.0 \times 10^{-5}$ and $\mathrm{Ra} = 10^7$.

Figure 2 shows the streamlines and isotherms for $\mathrm{Ra} = 10^6$ and $AR = 1$ in an enclosure with a rigid upper surface. Along each side wall an upward flow is induced by natural convection. The two side-wall streams turn inward respectively at the top wall corners, flow along the top wall (to which they lose heat), and collide at $X = 0.5$. At this point the streams merge and "jet" or "plume" downward, along the symmetry plane of the enclosure. As the plume penetrates the bulk of the cooler fluid, it entrains fluid of increasing temperature. Heat is lost to the cold bottom surface as the plume descends further and splits into two streams each of which flows along the bottom wall, eventually to reach the side walls thus forming two recirculating cells.

The descending plume sinks to a critical depth of about $Y = 0.26$, below which the fluid is almost motionless. This layer of essentially motionless fluid is termed the stagnant layer by Miller and Pernell (1981). Figure 2 shows that the isotherms are almost parallel to the bottom surface in the stagnant layer and, therefore, that the heat transfer is conduction dominated.

Figure 3 shows corresponding results for $\mathrm{Ra} = 1.0 \times 10^6$ and $AR = 1.5$. The resulting flow pattern is basically the same as for the previous case. However, the thermal boundary layer on the vertical wall is thinner and well developed. In addition, the temperature distribution is more uniform in the central portion of the enclosure, and the circulation strength in each cell is stronger, due to the increased heat transfer from the larger side walls.

Figure 4 shows the streamlines and isotherms for $\mathrm{Ra} = 10^7$ and $AR = 1.0$, again for the case of a rigid upper surface. When compared with the case with $\mathrm{Ra} = 10^6$ in Fig. 2, the results show that the circulation strength at $\mathrm{Ra} = 10^7$ has

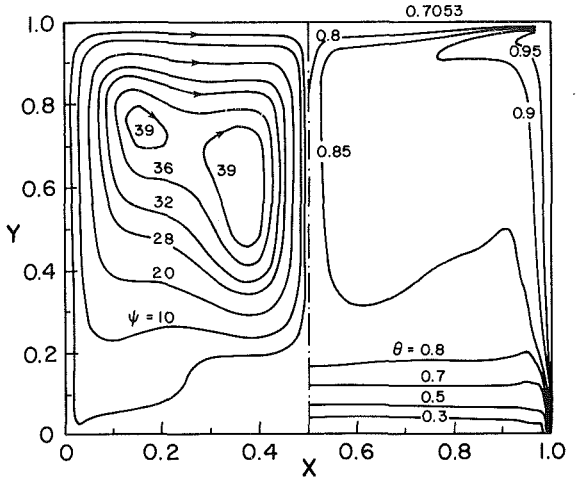

Fig. 4 Streamline and isotherm contours in an enclosure with $Ra = 10^7$, $AR = 1.0$, and rigid upper surface

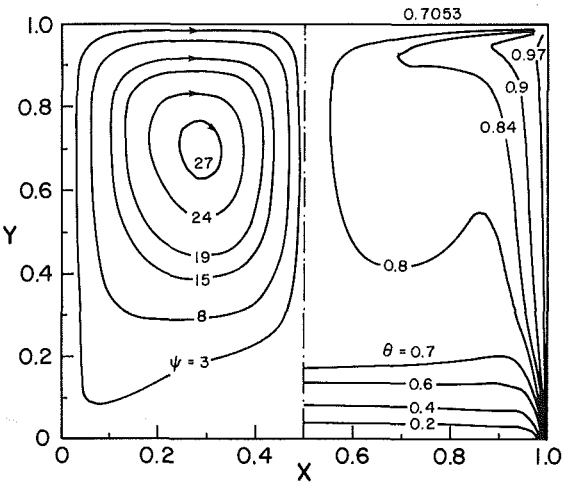

Fig. 5 Streamline and isotherm contours in an enclosure with $Ra = 10^6$, $AR = 1.0$, and free upper surface

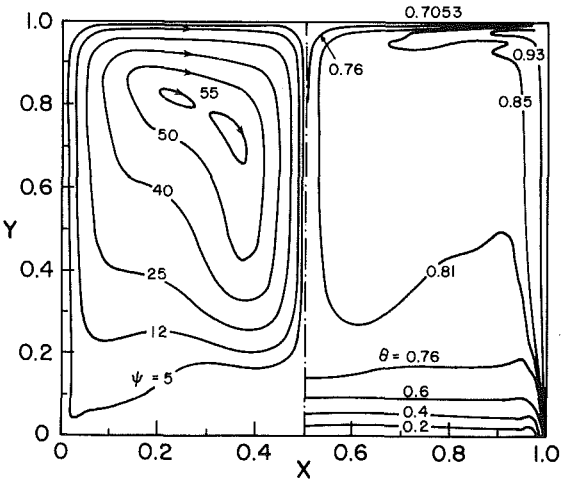

Fig. 6 Streamline and isotherm contours in an enclosure with $Ra = 10^7$, $AR = 1.0$, and free upper surface

almost doubled, due to the increased driving force. The strong circulation is accompanied by the appearance of a secondary eddy within each main cell.

To illustrate free surface effects, calculations were performed using the boundary conditions given by equations (5*e*)

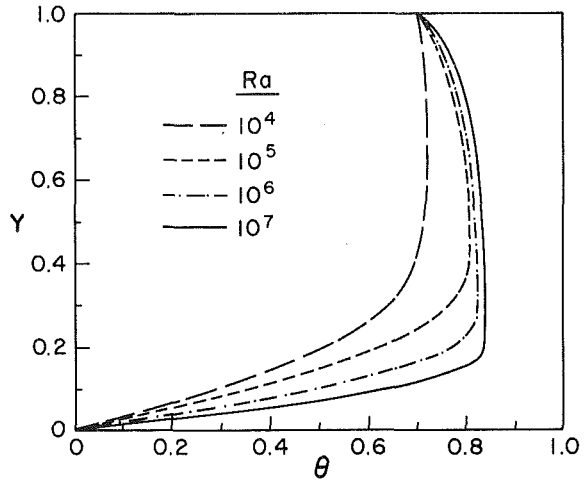

Fig. 7 Temperature profiles along the enclosure height at the center plane, $X = 0.5$, for various Rayleigh numbers (rigid upper surface)

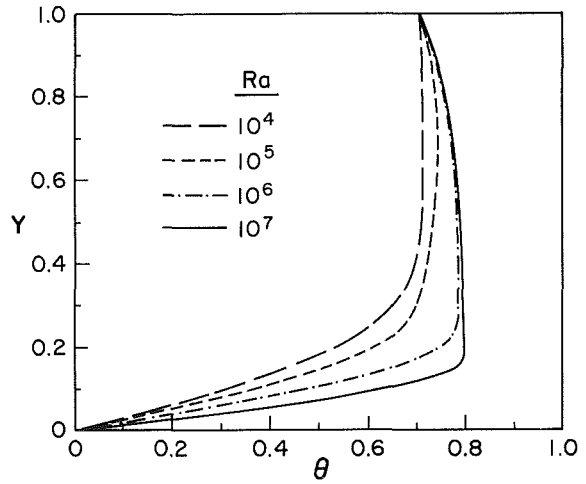

Fig. 8 Temperature profiles along the enclosure height at the center plane, $X = 0.5$, for various Rayleigh numbers (free upper surface)

and (5*f*). Figures 5 and 6 show the resulting streamlines and isotherms for $Ra = 10^6$ and 10^7, respectively, with $AR = 1.0$. A comparison between the streamlines corresponding to Figs. 2 and 5 and Figs. 4 and 6 reveals that, for the same Ra and AR, the circulation strength is larger in the free surface case. This is especially noticeable at the higher Ra. In addition, the center of the circulation cell is displaced upward when the top surface is free to move. A comparison between the corresponding isotherms shows that the thermal boundary layers along the side and bottom walls for the free surface flow condition are thinner than those for a rigid surface condition.

None of the above cases displayed evidence of recirculation zones in the lower layer near each corner of the cavity as found by Simpkins (1985). While this may reflect a lack of sufficient grid refinement to calculate the flow in its full details, we note that the effect is very small (Simpkins, 1986) and is unlikely to alter substantially any of the conclusions of this work.

Figures 7 and 8 show vertical temperature profiles in a square enclosure at the center plane, $X = 0.5$, for $Ra = 10^4 - 10^7$, for rigid and free upper boundary conditions, respectively. These results confirm that the flow field is stably stratified in the bottom stagnant region and that as Ra increases the stagnant layer becomes thinner. The temperature in the enclosure center is essentially uniform, but an inversion arises near the top surface at higher Ra. These results are in good qualitative agreement with those observed experimental-

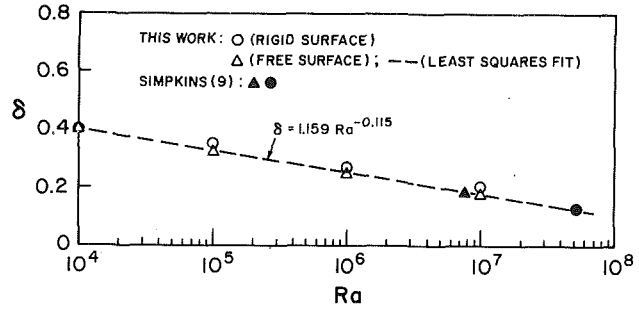

Fig. 9 Thermal layer thickness on the bottom wall of an enclosure with AR = 1 as function of Rayleigh number

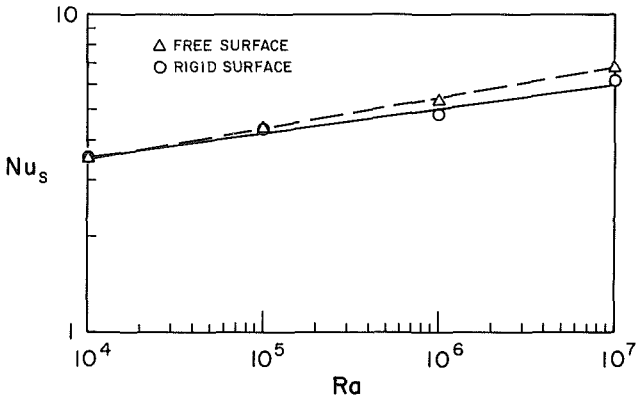

Fig. 10 Average Nusselt number on the side wall as function of Rayleigh number

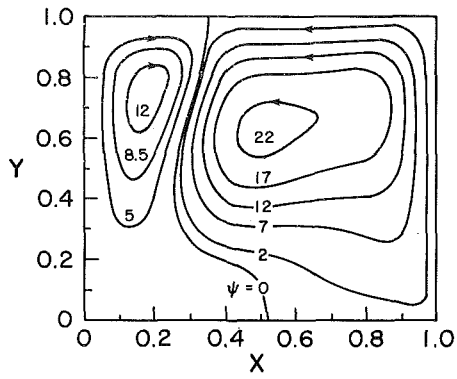

Fig. 11(*a*) Streamline contours in an enclosure with Ra = 10^6, *AR* = 1.0, and rigid upper surface

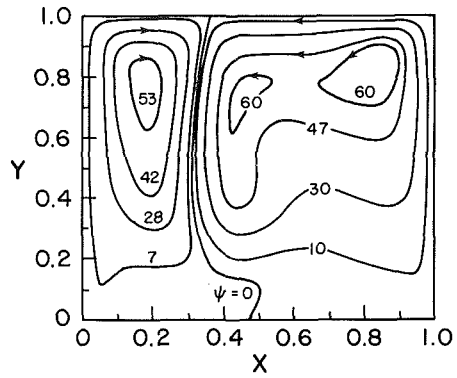

Fig. 11(*b*) Streamline contours in an enclosure with Ra = 10^7, *AR* = 1.0, and free upper surface

ly by Simpkins (1981), who performed experimental observations in enclosures with a free upper surface.

The influence of the free surface is also exhibited in Fig. 8, when compared with Fig. 7. The comparison shows that: (*i*) The temperature inversion near the upper surface becomes smaller; (*ii*) the temperature is more uniformly distributed; and (*iii*) the bottom thermal layer becomes thinner, in the free surface case. These results are consistent with the stronger circulation strength observed for the free upper surface condition.

The bottom layer thickness δ versus Ra is presented in Fig. 9 for both rigid and free upper boundaries, together with the experimental data from Simpkins (1981). It can be seen that δ decreases with Rayleigh number according to $Ra^{-0.115}$. The predictions for the free surface condition compare very well with the experimental findings by Simpkins (1981) even though the upper surface boundary conditions do not correspond exactly. Unfortunately, it has not been possible to conduct similar detailed comparisons of velocity and temperature profiles with the results of others. In the case of velocity, the data are simply unavailable; although we note that in Simpkins (1985) there is a reference to forthcoming measurements. Data for temperature have been reported by Miller and Pernell (1981) and Simpkins (1981) but, because the configurations and/or aspect ratios investigated differ from those of this study, exact comparisons cannot be made.

The mean Nusselt number of a vertical side wall Nu_s is shown as a function of Ra in Fig. 10. The results show that Nu_s for the free surface case is larger than that for the rigid. The following correlations were derived from the calculations:

$$Nu_s = 1.43\ Ra^{0.097} \text{ (free upper surface)} \quad (9)$$

$$Nu_s = 1.75\ Ra^{0.077} \text{ (rigid upper surface)} \quad (10)$$

Numerical experiments were performed to investigate the sensitivity of the flow in the enclosure to an asymmetric

Table 1 Calculated values of side-wall Nusselt number for symmetric and asymmetric side-wall temperature boundary conditions

		Rigid Upper Surface		Free Upper Surface	
Ra	Boundary Condition	left (colder) wall	right (hotter) wall	left (colder) wall	right (hotter) wall
10^4	Sym.	3.5409	3.5408	3.5408	3.5406
	Asym.	3.5264	4.2631	3.5247	4.2645
	(%)	(-0.41)	(20.4)	(-0.45)	(20.4)
10^5	Sym.	4.3244	4.3245	4.3578	4.3579
	Asym.	3.7830	4.9424	3.9458	5.1520
	(%)	(-12.5)	(14.3)	(-9.5)	(18.2)
10^6	Sym.	4.8472	4.8472	5.3099	5.3099
	Asym.	4.4345	6.2594	4.9722	6.8987
	(%)	(-8.5)	(29)	(-6.4)	(30)
10^7	Sym.	6.1432	6.1432	6.9755	6.9757
	Asym.	5.4262	8.3123	6.5339	9.5109
	(%)	(-12)	(35)	(-6.3)	(36)

specification of the side-wall boundary conditions. This was readily accomplished by fixing $\theta_s = 1.1$ on the right-hand side of the enclosure shown in Fig. 1 while specifying the remaining boundary conditions as explained above. Figure 11(*a*) illustrates the extent and magnitude of the artificially induced asymmetry for the case Ra = 10^6 in a square enclosure with a rigid upper surface. Qualitatively similar flow patterns were observed at the other values of Ra, irrespective of whether the top boundary was a rigid or free-moving surface. However, at Ra = 10^7 the free-moving surface case displayed the interesting eddy structure shown in Fig. 11(*b*). Comparing with the streamlines shown in Fig. 6, it is seen that the effect of the asymmetry is to intensify the motion of the secondary eddy in the main right-hand cell, while eliminating the secondary eddy in the main left-hand cell. The corresponding effect of the asymmetry on the temperature fields, in square enclosures

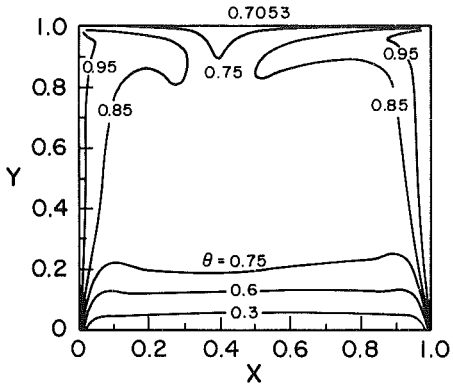

Fig. 12(a) Isotherm contours in an enclosure with Ra = 10^6, $AR = 1.0$, and rigid upper surface

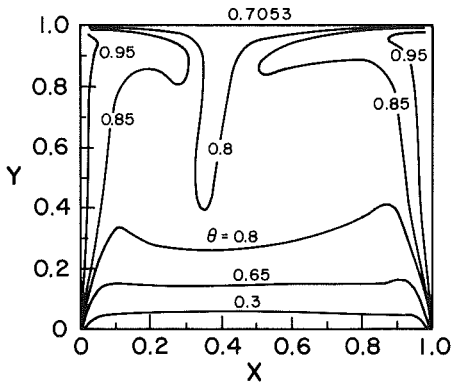

Fig. 12(b) Isotherm contours in an enclosure with Ra = 10^6, $AR = 1.0$, and free upper surface

with rigid and free-moving top surfaces, respectively, is shown in Figs. 12(*a*, *b*) for Ra = 10^6.

Table 1 presents calculated values of side-wall Nusselt numbers for conditions corresponding to symmetric and asymmetric specifications of the side-wall temperatures. In all cases, irrespective of whether the top surface is rigid or free, the hotter side wall experiences a proportionately larger increase in Nu_s than the corresponding decrease experienced by the cooler side wall. (That this is the case is readily seen from the percentage changes shown in parentheses in the table.) The table also shows that between Ra = 10^4 and 10^5 the *rate of increase* in Nu_s on the hotter side wall, induced by the asymmetry, is substantially reduced (20.4 percent to 14.3 percent for an enclosure with rigid upper surface) but that it is restored to high values at Ra = 10^6 and 10^7 (29 percent, 35 percent). A corresponding but less substantial variation is shown by the cooler wall between Ra = 10^5 and 10^6, where the *rate of decrease* in Nu_s is temporarily reduced. The interpretation of this finding is complicated, due to the interactions that arise between the flow in each main cell and the portions of the horizontal boundaries with which each cell is in contact. This question is the subject of continuing research by one of us (JACH) in a related experiment at the University of California, Berkeley.

4 Conclusions

A numerical study was conducted for conditions of natural convection in a rectangular enclosure in which the side walls are hotter than the top wall, and the top wall is hotter than the bottom wall. Symmetric and asymmetric side-wall boundary conditions for temperature were considered. Calculations were performed for Ra = 10^4 to 10^7, and $AR = 1.0$ and 1.5. Two enclosure configurations, one with a rigid top wall, the other with a free-moving fluid surface, were investigated. Comparisons between the calculations and limited experimental data show good agreement. The following major conclusions can be drawn from this study:

1 Steady-state, two-dimensional, numerical simulations indicate that there are two regions in the flow field of the enclosure configuration studied. In the upper part, two large cells separated by a descending plume circulate in mutually counterrotating directions. The plume sinks to a limited depth, below which lies a fluid layer that is essentially motionless.

2 Temperature profiles along the cavity height at the midplane, $X = 0.5$, indicate that the bottom layer of fluid in the enclosure is stably stratified. In the enclosure center, the fluid temperature is essentially uniform, due to strong mixing by the recirculating cells. A temperature inversion, especially strong at high Ra, occurs near the top layer.

3 When the aspect ratio increases at a fixed Ra, the circulation strength increases, with thinner boundary layers arising along the vertical side walls of the enclosure.

4 At high Rayleigh number, e.g., Ra = 10^7, the circulation strength increases and a secondary eddy develops within each of the two larger main cells filling the enclosure.

5 The thickness of the stratified fluid layer in the bottom of the enclosure varies with Rayleigh number according to $\delta = 1.159\ \mathrm{Ra}^{-0.115}$.

6 For equal Ra and AR, the free surface enclosure flow reveals: (1) larger circulation strength; (2) higher heat transfer rates; and (3) smaller bottom layer thickness, relative to the rigid surface case.

7 The flow and heat transfer in the enclosure are strongly affected by an asymmetric specification of the side-wall temperatures. The asymmetry induces a disproportionately higher increase in the Nusselt number of the hotter side wall relative to the decrease in Nusselt that arises at the colder side wall.

Acknowledgments

One of us (JACH) gratefully acknowledges the financial support provided by the Department of Energy under grant No. DE-FG03-85ER13397. We are grateful to Ms. Loris C-H. Donahue for the typing of this manuscript. The authors' names are listed in alphabetical order.

References

Carruthers, J. R., 1977, *Preparation and Properties of Solid State Materials*, Wilcox and Lefever, eds., Marcel Dekker, New York, Vol. 3.

Chen, K. S., 1985, "The Heat Transfer Study in Czochralski Crystal Growth," Mid-term report to National Science Council, NSC-74-0401-E110-06, Taiwan, ROC.

de Vahl Davis, G., 1981, "Natural Convection of Air in a Square Cavity: An Accurate Numerical Solution," Report 1981/FMT/1, University of N.S.W., Kensington, Australia.

Humphrey, J. A. C., and Bleinc, C., 1985, "On the Structure of the Flow Due to the Collision of Opposed, Vertical, Free Convection, Boundary Layers," *Int. Comm. Heat and Mass Transfer*, Vol. 12, pp. 233–240.

Hurle, D. T. J., 1977, "Hydrodynamics in Crystal Growth," in: *Crystal Growth and Materials*, E. Kaldis and H. J. Scheel, eds., North Holland, Vol. 2, pp. 549–569.

Laudise, R. A., 1970, *The Growth of Single Crystals*, Prentice-Hall Inc., New York.

Miller, D. L., and Pernell, T. L., 1981, "The Temperature Distribution in a Simulated Garnet Czochralski Melt," *J. Crystal Growth*, Vol. 53, pp. 523–529.

Ostrach, S., 1982, "Low Gravity Fluid Flows," *Ann. Rev. Fluid Mech.*, M. Van Dyke, J. V. Wehausen, and J. L. Lumley, eds., Annual Reviews Inc., Vol. 14, pp. 313–345.

Ostrach, S., 1983, "Fluid Mechanics in Crystal Growth – The 1982 Freeman Scholar Lecture," *J. Fluid Engrg.*, Vol. 105, pp. 5–20.

Rehm, R. G., Baum, H. R., and Barnett, P. D., 1982, "Buoyant Convection Computed in a Vorticity, Stream-Function Formulation," *J. of Res.*, Nat. Bur. Stand., Vol. 87, No. 2, pp. 165–185.

Schwabe, D., and Scharmann, A., 1981, "Marangoni Convection in Open Boat and Crucible," *J. Crystal Growth*, Vol. 52, pp. 435–449.

Simpkins, P. G., 1981, "On Descending Plumes in Containers," *Bulletin Am. Phys. Soc.*, Vol. 26, No. 8, p. 1277.

Simpkins, P. G., and Dudderar, T. D., 1981, "Convection in Rectangular

Cavities With Differentially Heated End Walls," *J. Fluid Mech.*, Vol. 110, pp. 433–456.

Simpkins, P. G., and Chen, K. S., 1985, "Natural Convection in Horizontal Containers With Applications to Crystal Growth," in: *Natural Convection: Fundamentals and Applications*, S. Kakac, W. Aung, and R. Viskanta, eds., Hemisphere Publishing Corporation, Washington, DC.

Simpkins, P. G., 1985, "Convection in Enclosures at Large Rayleigh Numbers," in: *Stability in Convective Flows*, W. S. Saric and A. A. Szewczyk, eds., ASME, HTD-Vol. 54, pp. 39–47.

Simpkins, P. G., and Chen, K. S., 1986, "Convection in Horizontal Cavities," *J. Fluid Mech.*, Vol. 166, pp. 21–39.

Simpkins, P. G., 1986, Personal Communication.

Villers, D., and Platten, J. K., 1985, "Marangoni Convection in Systems Presenting a Minimum in Surface Tension," *Physico-Chemical Hydrodynamics*, Vol. 6, No. 4, pp. 435–451.

Wilkes, J. O., and Churchill, S. W., 1966, "The Finite-Difference Computation of Natural Convection in a Rectangular Enclosure," *AIChE J.*, Vol. 12, pp. 161–166.

APPENDIX

For a free fluid surface subjected to a temperature gradient, the shear stress along the surface is balanced by the surface tension gradient according to Ostrach (1982) and Villers and Platten (1985)

$$\mu \frac{\partial u}{\partial y} = \frac{\partial \sigma}{\partial x} = \frac{\partial \sigma}{\partial T} \frac{\partial T}{\partial x} \tag{A1}$$

The nondimensional form of the above equation is

$$\frac{\partial U}{\partial Y} = \mathrm{Ma} \frac{\partial \theta}{\partial X} \tag{A2}$$

or

$$\frac{\partial^2 \psi}{\partial Y^2} = \mathrm{Ma} \frac{\partial \theta}{\partial X} \tag{A3}$$

where Ma is the Marangoni number defined by equation (6) in the text. Since $V = 0$ and $\partial \psi / \partial X = 0$ at the free surface, so also

$$\frac{\partial^2 \psi}{\partial X^2} = 0 \tag{A4}$$

Substitution of equations (*A*3) and (*A*4) into equation (3) yields equation (5*f*) in the text.

Natural Convection From Isothermal Cubical Cavities With a Variety of Side-Facing Apertures

A. M. Clausing
Professor of Mechanical Engineering.
Mem. ASME

J. M. Waldvogel
Graduate Research Assistant.

L. D. Lister
Graduate Research Assistant.

Department of Mechanical
and Industrial Engineering,
University of Illinois at Urbana-Champaign,
Urbana, IL 61820

An experimental investigation of heat transfer by natural convection from a smooth, isothermal cubic cavity with a variety of side-facing apertures is described in this paper. The study was motivated by the desire to predict the convective loss from large solar thermal-electric receivers and to understand the mechanisms which control this loss. Hence, emphasis is placed on the large Rayleigh number, Ra, regime with large ratios of the cavity wall temperature T_w *to the ambient temperature* T_∞. *A cryogenic wind tunnel with test section temperatures which are varied between 80 K and 310 K is used to facilitate deduction of the influences of the relevant parameters and to obtain large temperature ratios without masking the results by radiative heat transfer. A 0.4-m cubic cavity, which is mounted in the side wall of this tunnel, is used. The area of the aperture* A_a *and its location are key variables in this study. The data which are presented cover the ranges:* $1 < T_w/T_\infty < 3$, $L^2/18 \le A_a \le L^2$, *and* $3 \times 10^7 < Ra < 3 \times 10^{10}$.

Introduction

The problem which precipitated the title investigation is the determination of convective energy loss from large solar receivers. This loss is one of the biggest uncertainties in the determination of the efficiency of solar thermal-electric receivers and the economic viability of the solar alternative. The determination of the convective energy loss is difficult because of (*i*) the complex geometries and the complexity of the convective flow from and within open cavities; (*ii*) the large Rayleigh numbers Ra of interest, that is, the difficulty of experimentally modeling large buoyant forces; and (*iii*) the large ratios of the wall temperature to the ambient temperature T_w/T_∞, that is, the difficulty of experimentally simulating these hot cavities without the convective energy flow being masked by radiative heat transfer. The assumption of constant properties is clearly not applicable, and the role of the additional dimensionless group T_w/T_∞ must be established.

Some convective loss data are available from tests conducted on full-scale solar receivers (see, e.g., Clausing, 1983a). Unfortunately, these isolated data points contain large uncertainties because of the large radiative energy fluxes which are present in such tests. In addition, these data points provide little information on the important mechanisms or on the functional dependency of the convective loss on the controlling parameters. Hence, these data are of limited value in trying to predict convective losses from other cavity configurations.

On the other hand, in controlled laboratory tests with small-scale models, it is difficult to satisfy the relevant modeling laws because of the large size and the high temperature of solar receivers. For example, the excellent experimental study of convective losses from a five-sided, cubic cavity by LeQuere et al. (1981) is in a Rayleigh number regime which is completely outside the fully turbulent, high Ra regime of interest in solar receivers. Also, the ratio of the wall temperature T_w to the ambient temperature T_∞ is near unity, whereas typically ratios between 2 and 4 are of interest in solar thermal-electric receivers. No studies to date have considered the importance of the size and location of the aperture or the influence of the temperature ratio over any significant range.

The objectives of this investigation are to understand the mechanisms which control the convective energy flow out of or into cavities for a variety of aperture configurations and to derive expressions to enable the prediction of this convective energy transport. An understanding of the mechanisms will enable the estimation of this energy transport for other geometries and provide ways of reducing the importance of this loss mechanism in solar receivers. The results will also be applicable to other problems such as the convective energy transport between building zones which are connected by an open passageway. In this application, the large Rayleigh number regime is again of interest, and separating the energy transported by convection from that transported by radiation is still a problem.

Large solar receivers are modeled in the correct regimes in the title investigation by using the cryogenic wind tunnel at the University of Illinois at Urbana-Champaign (UIUC). The UIUC cryogenic facility is a variable ambient temperature tunnel which can operate with test section temperatures between 310 K and 80 K. The main advantages of this liquid-nitrogen-cooled facility in the title investigation are (*i*) the ability to generate large Rayleigh numbers, (*ii*) the ability to cover large ranges in the parameters of interest by changing only the ambient temperature (this feature greatly facilitates deducing the influences of the relevant dimensionless groups), (*iii*) the ability to generate large ratios of the cavity wall temperature to the

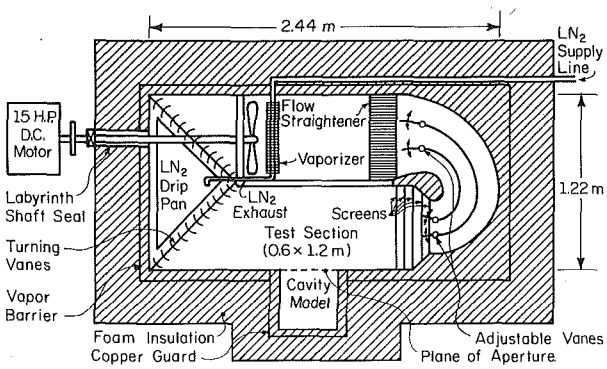

Fig. 1 Top view of the UIUC cryogenic facility

Contributed by the Heat Transfer Division and presented at the ASME Winter Annual Meeting, Anaheim, California, December 1986. Manuscript received by the Heat Transfer Division May 12, 1986.

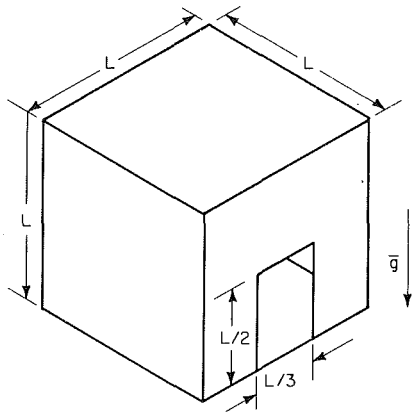

Fig. 2 Isometric view of cubic cavity model

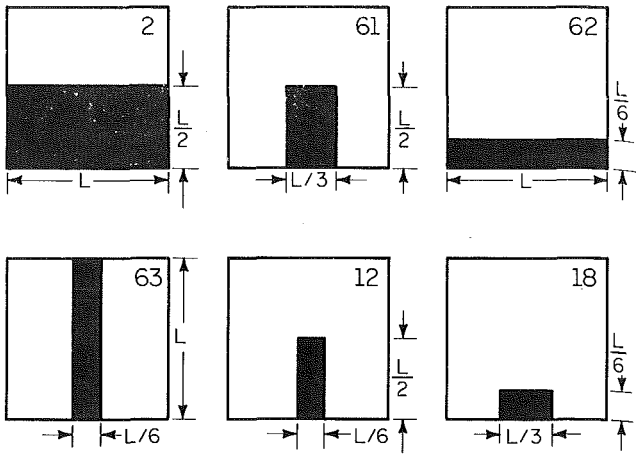

Fig. 3 Aperture configurations investigated

ambient temperature T_w/T_∞, without the results being masked by thermal radiation (in general, the radiative mode has been virtually eliminated), and (*iv*) the elimination of extraneous convective currents. Previous natural convection data which were obtained from the UIUC facility (Clausing, 1983b) agree well with data obtained from full-scale models at operating temperatures greater than 300 K as well as with data taken at high pressures (pressures between 1 and 70 atm).

Experimental Apparatus and Procedure

The newly remodeled UIUC cyrogenic facility is illustrated in Fig. 1. It is a variable-speed recirculating wind tunnel with a 1.2 m high by 0.6 m wide, rectangular test section. The test section temperature T_∞ is reduced for the cryogenic tests by the vaporization of liquid nitrogen in a serpentine finned-tube heat exchanger. The heat exchanger is located just downstream of two 0.5-m-dia cast aluminum fans. Gaseous nitrogen is used as the working fluid in cryogenic tests, and air is used in experiments which are conducted with $T_\infty > 290$ K. The 11.5 kW fan motor is operated at low rpm to increase the efficiency of the heat exchanger and to ensure an isothermal test section prior to a test. The motor is shut off 30 s before a test to ensure quiescent surroundings.

A cubic cavity, $L \times L \times L$ where $L = 0.4$ m, with a variety of side-facing apertures was chosen for the investigation. An isometric view of the model is given in Fig. 2. Six of the aperture configurations are shown in Fig. 3. The apertures are referenced by the respective aperture number AN, which is also indicated in Fig 3. The seven configurations being investigated are AN equal to 1, 2, 61, 62, 63, 12, and 18 where the aperture area is L^2/AN if the units digit is dropped from the 60 series. The five full sides of the cube are smooth, isothermal, active surfaces. If the aperture area is less than L^2, the remaining portion of the sixth side, the aperture mask, is an adiabatic surface.

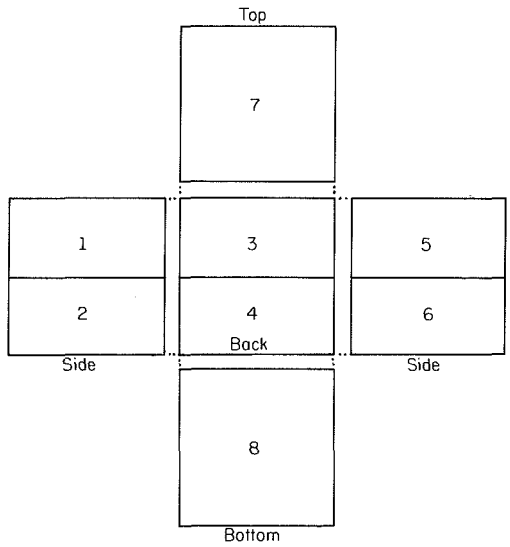

Fig. 4 Unfolded view of cavity and eight calorimeters

A transient technique is used to deduce the convective loss from the cavity and the individual heat transfer rates from the interior surfaces of the cavity. Specifically, the five active sides consist of eight polished 6061-T6 aluminum alloy plates or calorimeters. The 6.35-mm-thick calorimeters are configured as shown in Fig. 4. The top and bottom plates are full sides,

Nomenclature

A = area, m^2
b = defined by equation (5)
C = defined by equation (14)
c_p = specific heat, J/kg-K
f = defined by equation (5)
g = acceleration of gravity, m/s^2 or defined by equation (5)
h = heat transfer coefficient, W/m^2-K
k = thermal conductivity, W/m-K
L = length, m
m = mass, kg
$\dot{m}$ = mass flow rate, kg/s
q = heat flow rate, W
T = temperature, K
T^* = $(T - T_\infty)/(T_z - T_\infty)$
α = thermal diffusivity, m^2/s
β = volume coefficient of expansion, K^{-1}
ϵ = emissivity
ρ = density, kg/m^3
ν = kinematic viscosity, m^2/s
Nu = Nusselt number = hL/k
Pr = Prandtl number = ν/α
Ra = Rayleigh number = $g\beta\Delta TL^3/(\nu\alpha)$

Subscripts

a = aperture
b = bulk value or buoyancy
c = cavity
cz = convective zone
f = based on film temperature
l = laminar/transitional boundary
t = transitional/turbulent boundary
tot = total
tr = transitional regime
w = wall condition or width
z = initial condition
∞ = ambient condition

Superscripts

$'$ = quantity based on total area
$*$ = dimensionless quantity

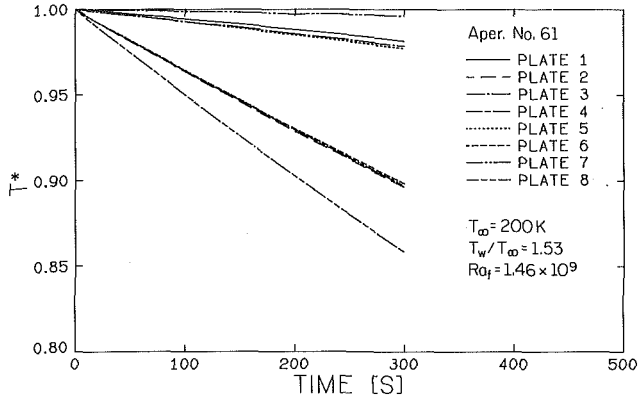

Fig. 5 Dimensionless plate temperatures for a typical test

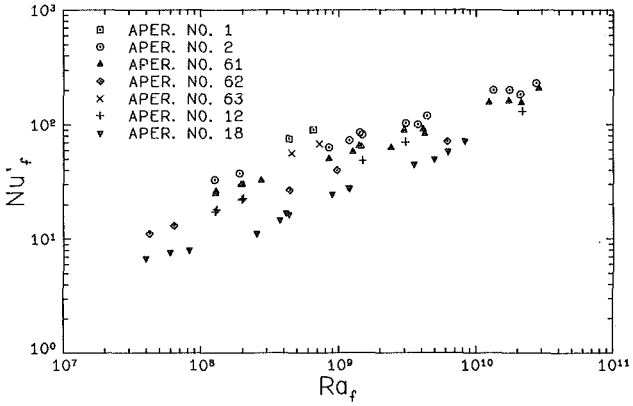

Fig 7 The influence of Ra on Nu′ for various apertures

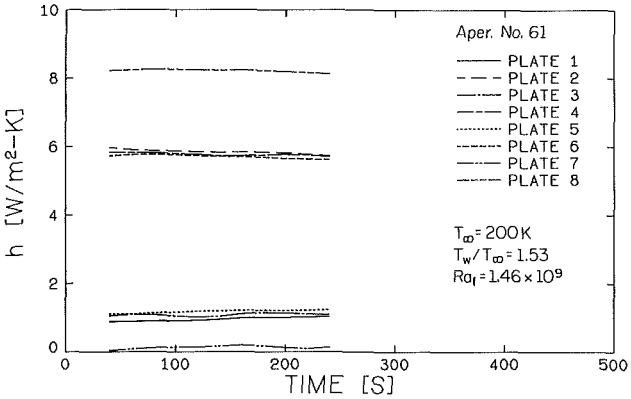

Fig. 6 Individual heat transfer coefficients for a typical test

0.4 m by 0.4 m, and the three active walls each consist of two 0.2 m by 0.4 m plates. The calorimeters are heated on the back side with thin foil heaters whose thermal mass is negligible relative to the aluminum plates. The calorimeters are thermally isolated from each other to enable the determination of the individual rates of heat transfer over each of the eight surfaces. The average heat transfer coefficient over each calorimeter is deduced from the rate of cooling of the respective calorimeter after all heaters are shut off.

The model is mounted outside of the test section with the plane of the aperture in the outside wall as illustrated in Fig. 1. The five active sides of the model, going from inside to outside, consist of: the eight calorimeters, a 25-mm envelope of urethane insulation, five independently heated copper guards which correspond to the five active sides, a second 25-mm envelope of urethane insulation, and a second heated, copper guard. The second guard is a one-piece copper envelope which is thermally attached to the tunnel walls. It enables the guarding of the calorimeters when the desired cavity temperature lies below the room ambient temperature ($\simeq$ 300 K). The exterior copper shell of the model is covered by approximately 0.2 m of insulation.

The aperture mask, if required, is constructed of a 6.35-mm-thick removable sheet of polystyrene insulation with foil facing to provide a low thermal mass, high thermal resistance wall. The aperture mask is slid down a dual track, aluminum channel to form the desired configuration. The second track holds a solid sheet of the same insulation which is slid over the aperture during heating. At the initiation of a test run, the solid sheet is raised to the top lip of the aperture.

The convective heat flow from the ith calorimeter during a test run is determined from

$$q_i = -m_i c_p (dT_{w,i}/dt) - q_{r,i} \tag{1}$$

where $q_{r,i}$ is the radiative loss from the surface. It is determined by solving the ten-surface enclosure problem with the assumptions of gray, diffuse, uniformly irradiated surfaces. The published emissivity data for polished 6061-T6 aluminum was approximated by $\epsilon = 0.04 + (6 \times 10^{-5}\ \mathrm{K}^{-1})T_w$. It should be noted that the radiative heat transfer from the cavity to the surroundings, even at the largest T_w/T_∞ ratios, was less than 2, 4, and 11 percent of the total heat transfer at ambient temperatures less than 160, 210, and 310 K, respectively.

The respective average heat transfer coefficient over surface i is calculated by: $h_i = q_i \times \{A_i(T_{w,i} - T_\infty)\}$. Note that T_∞ is used as the reference temperature in the definition of all heat transfer coefficients. The energy convected out of the aperture q is

$$q = \sum_{i=1}^{8} q_i \tag{2}$$

where the q_i are determined using equation (1). The Nusselt number Nu′ is defined as

$$\mathrm{Nu}' \equiv h' L_c/k \tag{3}$$

where $h' \equiv q/\{A_{\mathrm{tot}}(T_w - T_\infty)\}$, and A_{tot} is the total active area in the cavity, $5L^2$. A prime is used to denote a quantity that is based on the total active cavity area.

Twenty-six thermocouples are used to determine the temperatures of the calorimeters, while grids of 16 and 6 thermocouples are used to determine the temperature distributions of the gas inside the cavity and in the test section, respectively. During a test run, the data acquisition system scans the 48 channels continuously at the rate of 12 channels per second, records the converted temperatures in the RAM of a microcomputer, averages the readings on each of the eight plates as well as other ensembles of interest, and graphically displays the specified key temperatures and/or average temperatures. At the completion of the test run, the data are written on a diskette and subsequently uploaded to the mainframe computer for further processing and plotting.

In a typical test run, the eight calorimeters and the two sets of guards are all heated to within ±0.1 K of the desired initial temperature T_z. If the test is the first at that temperature, the model and guards are held at this temperature for a minimum of 30 min. This requirement assures that the insulation between the guards and the calorimeters is at the same temperature as the calorimeters.

Results

Figures 5 and 6 show typical results for a 300 s test run with aperture configuration 61. The dimensionless temperature T^*

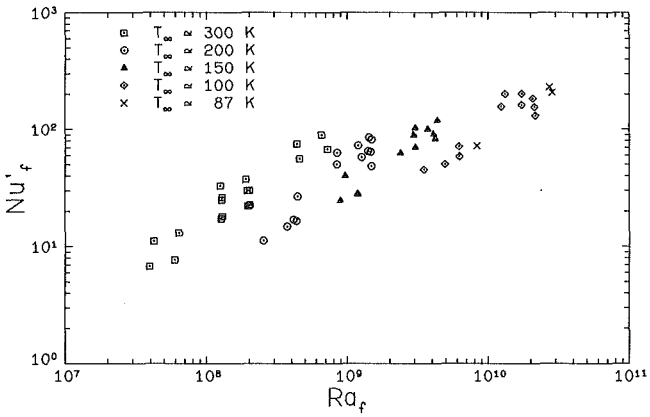

Fig. 8 The influence of Ra on Nu′ at various T_∞

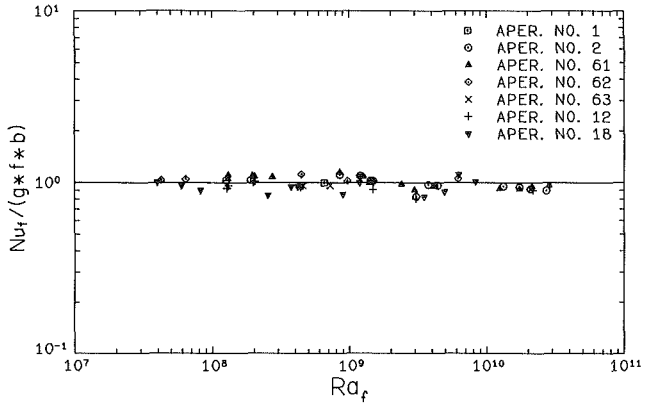

Fig. 9 Comparison of correlation, equation (5), and all data

for surface i which is shown in Fig. 5 is defined as $(T_i - T_\infty)/(T_z - T_\infty)$. The drastic differences in the heat transfer rates from the various surfaces in the cavity are clearly evident. The temperature of Plate 7, the top of the cavity, decreased by only 0.41 K during the 300 s test run, whereas the bottom, Plate 8, decreased by 15.0 K. The rate of convective energy loss from the bottom surface is over two orders of magnitude larger than that from the top surface of the cavity. For aperture numbers 61, 12, and 18, the rate of energy loss from the upper *half* of the cavity is approximately an order of magnitude smaller than that from the lower half for all values of Ra, T_w/T_∞, and T_w which are investigated. The symmetry, the smoothness of the temperature versus time and h versus time curves, and the small values of h and ΔT, which are consistently resolved, clearly attest to the accuracy of the experiment.

Figure 7 shows the extent of the natural convection data. All properties are based on the film temperature, $T_f = (T_w + T_\infty)/2$, unless indicated otherwise by the appropriate subscript. The height of the aperture L_a plus $L/2$ is the characteristic length L_c, which is used in the definitions of Nu and Ra. This definition was chosen based on the ability to correlate the experimental data, as will be shown in the following section. Since Nu is typically proportional to $Ra^{1/3}$ for turbulent natural convection, h is independent of L_c; therefore, the definition of L_c is irrelevant in this regime. The data given in Fig. 7 cover the ranges: $1 < T_w/T_\infty < 3$, $3 \times 10^7 < Ra < 3 \times 10^{10}$, and 80 K $< T_\infty <$ 310 K. A comparison of the results for aperture numbers 1 and 63 shows only a small difference in Nu in spite of the factor of six difference in the aperture area. On the other hand, corresponding Nu for 62 are much smaller than those for 61, yet the aperture areas are equal. Clearly, the location and the configuration of the aperture are of extreme importance. The scatter in the data for any given aperture at approximately equal values of Ra is mainly a consequence of the strong influence of T_w/T_∞ (see Fig. 7). Figure 8 is a graph which is identical to Fig. 7 except that the plotting symbol in Fig. 8 indicates the ambient temperature at which the respective data points were obtained. The data encompass all aperture configurations; hence the aperture number corresponding to a given data point must be obtained from Fig. 7. An examination of these two figures shows the large range in the Rayleigh number which is obtained with this signel model by changing the ambient temperature T_∞.

Correlations

The dimensionless groups which govern the heat transfer by natural convection from an isothermal cubic cavity are deduced from a dimensional analysis of the general, compressible form of the governing equations. The simplifying assumptions are: a laminar flow of a Newtonian fluid, a perfect gas, a nonparticipating gas, negligible viscous dissipation, and negligible work done by compression. The dependent variables, c_p/c_{pf}, μ/μ_f, and k/k_f, are general functions of only the absolute temperature ratio T/T_f. With these assumptions, one obtains

$$\mathrm{Nu}' = h'L_c/k = f_1(\mathrm{Ra}, \mathrm{Pr}, T_w/T_\infty, L_a^*, L_w^*, x^*, y^*) \qquad (4)$$

where an asterisk denotes a dimensionless group. The last four groups are: the height of the aperture, the width of the aperture, and the x and y coordinates of the centroid of the aperture, respectively, all referenced to the characteristic length L_c. Thus, even a simple, isothermal cubic cavity with a single, rectangular aperture gives rise to four geometric parameters. Including the group T_w/T_∞ enables one to arrive at equation (4) without making the Boussinesq approximation. The influences of variable properties are taken into account with the absolute temperature ratio T_w/T_∞; hence, equation (4) is not restricted to values of this parameter near unity. This is contrasted with commonly used procedures: the reference temperature method and the property ratio method.

Instead of trying to delineate the influences of four geometric parameters, a nearly impossible task, consider the physics of the problem. Clausing (1983a) hypothesized that: (*i*) the horizontal plane passing through the upper lip of the aperture is nearly adiabatic, (*ii*) the gas in the region above this plane is relatively stagnant, and (*iii*) the ability to heat the air inside the portion of the cavity below this plane, the "convective zone," often controls the convective loss from large, hot cavities. This suggests the following: (*i*) The dependence on geometry can be reduced and the cubic cavity results can be generalized by basing the definition of h on the area in the convective zone, that is, $h \equiv q/\{A_{cz} \cdot (T_w - T_\infty)\}$. In contrast, h' was based on the total cavity area. (*ii*) Factoring the quantity $b \equiv (T_w - T_b)/(T_w - T_\infty)$ out of the correlation for Nu would simplify deducing the balance of the correlation. Since T_b is an unknown, a means of determining b needs to be derived. Note that $0 < b < 1$ and b approaches one as Ra approaches infinity. The proposed correlation is

$$\mathrm{Nu} = hL_c/k = qL_c/\{A_{cz}(T_w - T_\infty)k = g \cdot f \cdot b \qquad (5)$$

where:

(*i*) g, a function of Ra, is the constant property correlation for the natural convection from the interior surfaces to the fluid in the convective zone which is at the bulk temperature T_b. A gas with Pr $\simeq$ 0.7 is assumed.

(*ii*) f, a function of Ra and T_w/T_∞, is the quantity which accounts for variable property influences. The limit of f, as T_w/T_∞ approaches one, is one.

(*iii*) b, a function of Ra, T_w/T_∞ and geometry, accounts

for values of T_b which are significantly different than T_∞. b is a transformation between the case of natural convection between surfaces at T_w and a fluid at T_∞, which is described by $g \cdot f$, and the actual heat transfer from the surfaces at T_w to a fluid at T_b.

Consider first the definition of A_{cz}. The experimental results showed that the horizontal plane passing through the upper lip of the aperture was nearly adiabatic. The small heat flux across this plane is approximated by defining A_{cz} as: (the wall area below the horizontal plane passing through the upper lip of the aperture) + (the aperture area A_a). Note that the limits of A_{cz}, as A_a approaches zero and L^2, are zero and $5L^2$, respectively.

The correlations g and f were derived using procedures similar to those described by Clausing (1983b), the results given by Clausing (1983b), the results of an investigation of a horizontal plate study in progress, and the data given in Fig. 7. They are:

Regime I, $Ra < 3.8 \times 10^8 \equiv Ra_l$

$$g = 0.63\ \mathrm{Ra}^{1/4} \tag{6}$$

$$f_l = 1 \tag{7}$$

Regime II, $Ra_l < Ra < 1.6 \times 10^9 \equiv Ra_t$

$$g = 0.63\ \mathrm{Ra}^{1/4} \tag{8}$$

$$f_{tr} = (f_t - 1)\{(\mathrm{Ra}^{1/3} - \mathrm{Ra}_l^{1/3})/(\mathrm{Ra}_t^{1/3} - \mathrm{Ra}_l^{1/3})\} + 1 \tag{9}$$

Regime III, $Ra > Ra_t$

$$g = 0.108\ \mathrm{Ra}^{1/3} \tag{10}$$

$$f_t = 0.2524 + 0.9163(T_w/T_\infty) - 0.1663(T_w/T_\infty)^2 \tag{11}$$

The subscript on f is used to denote the three regimes: laminar, transitional, and turbulent. The physical basis for equation (9) is given by Clausing (1983b). $g \cdot f$ is a continuous function throughout the three regimes regardless of the values of Ra and T_w/T_∞.

Consider next the remaining part of the correlation, the function b. The rate of convective heat exchange within the cavity, which is also the rate of energy transport out of the aperture q, follows from the definition of h and equation (5) as

$$q = (g \cdot f \cdot b) k A_{cz} (T_w - T_\infty)/L_c \tag{12}$$

Clausing (1983a) proposed an approximate expression for the convective energy transport out of the aperture. It is derived as follows. If one assumes that the average temperature of the exiting gas is T_c and $(T_c - T_\infty) = 2(T_b - T_\infty)$, then

$$q = 2\dot{m} c_{p\infty} (T_b - T_\infty) \tag{13}$$

The mass flow rate $\dot{m}$ is determined from

$$\dot{m} = C \rho_\infty V_b A_a \tag{14}$$

where C is an empirical constant, and V_b is defined as

$$V_b = \{2g\beta_\infty (T_b - T_\infty) L_a\}^{1/2} \tag{15}$$

If viscous forces are neglected and a linear variation in temperature from T_∞ at $z = 0$ to T_c at $z = L_a$ is assumed, a fluid element would accelerate, due to the buoyant force acting on it, to the velocity V_b. If hot air were flowing out of the aperture with the velocity V_b over the upper half of the aperture area at an average temperature elevation of $2(T_b - T_\infty)$, C would be equal to 0.5. Having no experimental data on which to base this constant, Clausing (1983a) conjectured a value of 0.25 for C. In this investigation, C equal to 0.18 was found to correlate the data well.

If q is eliminated by equating equations (12) and (13), $\dot{m}$ and V_b are eliminated by substituting equations (14) and (15), respectively, and 0.18 is substituted for the empirical constant C, one obtains

$$b = 1 - 1.57\left[\frac{g \cdot f \cdot b (k_f/k_\infty)}{(\mathrm{Ra}_\infty \mathrm{Pr}_\infty L_a^*)^{1/2} \cdot (A_a/A_{cz})}\right]^{2/3} \tag{16}$$

This equation is of the form

$$b = z(b, \mathrm{Ra}, T_w/T_\infty, L_a^*, A_a/A_{cz}) \tag{17}$$

Equation (16) is a nonlinear function of b and must be solved iteratively. Thus, equation (5) is quite different from the classical empirical correlation. In the 102 cases which were considered, equation (16) was solved by successive substitutions, and no convergence problems were experienced.

Figure 9 illustrates the complete correlation, specifically , a plot of $\mathrm{Nu}/(g \cdot f \cdot b)$ versus Ra. One should note the following:

(*i*) The data span three regimes, and f varies from a constant, one, in Regime I to values as large as 1.50 in Regime III. (*ii*) The uncertainties in the regime boundaries and the errors in the prediction of small values of the function b give rise to more scatter at small Ra numbers. The correlation is not applicable to small cavities (for example, small electronic components) but is expected to give excellent predictions for large cavities such as buildings and solar central receivers. (*iii*) The maximum deviation of any data point from Correlation (5) is 20 percent. Ninety percent of the data lie within ±12 percent of this correlation. In comparison, the largest dimensional rate of heat exchange was 61 times larger than the smallest.

Conclusions

The following conclusions are drawn from this study of natural convective heat transfer from isothermal cavities in gases:

(*i*) The horizontal plane which passes through the upper lip of the aperture is a nearly adiabatic plane. Hence, the geometry of the portion of the cavity which lies above this plane has little influence on the convective loss, and the data can be effectively correlated only if the definition of the heat transfer coefficient is based on the surface area which lies below this plane. This conclusion remains valid even for values of T_w/T_∞ near unity.

(*ii*) Although the data ranged from the laminar regime where f is unity to the fully turbulent regime where f is as large as 1.50, good agreement exists in all three regimes between the data and the correlations. The film temperature is the most convenient reference temperature, if all three regimes are being considered, because f is unity in the laminar regime for this reference temperature. Large differences occurred in the turbulent regime between data for a given aperture configuration at the same Rayleigh number because of the influence of variable properties.

(*iii*) The slope of a line drawn through the uncorrelated data given in Fig. 7 for any given aperture is dependent on the aperture size and configuration. Hence, a correlation of the form $\mathrm{Nu} = C \cdot \mathrm{Ra}^m$ would require a different value of m for each aperture even with identical values of T_w/T_∞. Introduction of the function b enables the correlation of the data for all apertures with a single equation.

(*iv*) In spite of the simple model which is used to predict the temperature in the convective zone of the cavity T_b, and the strong influence of correlation b, good agreement was obtained. The value of b ranged from 0.93 to 0.43 which corresponds to $0.07 < (T_b - T_\infty)/(T_w - T_\infty) < 0.57$. Correlation (5) is unusual in that the factor b must be determined iteratively, and the expression for this quantity stems from an analytical model.

(*v*) By introducing the area in the convective zone and the

factor b, the number of geometric parameters which need to be considered was reduced from 4 to 2, L_a^* and A_a/A_{cz}. In addition, Correlation (5) should prove to be applicable to a wide variety of cavity geometries and not simply to a cubic configuration.

Acknowledgments

The authors gratefully acknowledge the financial support of the National Science Foundation in sponsoring this research.

References

Clausing, A. M., 1983a, "Convective Losses From Cavity Receivers—Comparisons Between Analytical Predictions and Experimental Results," ASME *Journal of Solar Energy Engineering*, Vol. 105, No. 1, pp. 29–33.

Clausing, A. M., 1983b, "Natural Convection Correlations for Vertical Surfaces, Including Influences of Variable Properties," ASME JOURNAL OF HEAT TRANSFER, Vol. 105, No. 1, pp. 138–143.

LeQuere, P., Penot, F., and Mirenayat, M., 1981, "Experimental Study of Heat Loss Through Natural Convection From an Isothermal Cubic Open Cavity," *Proceedings DOE/SERI/SNLL Workshop on Convective Losses From Solar Receivers*, SNLL Report SAND81-8014, Livermore, CA, pp. 165–174.

Natural Convection Along a Finite Vertical Plate

R. Yang

L. S. Yao

Department of Mechanical and Aerospace Engineering, Arizona State University, Tempe, AZ 85287

The discrepancy between the measured mean heat flux for natural convection on a finite vertical plate and the solution of Pohlhausen, Schmidt, and Beckmann has been known for a long time; no theoretical explanation has ever been provided. In this paper, a double-deck structure is introduced to account for the trailing-edge effect. This solution shows that the flow accelerates near the training edge due to the geometric discontinuity which leads to a decreased flow constraint. An inward normal flow is induced by the local flow acceleration and generates a change in the displacement of the thin viscous layer near the plate. Consequently a pressure disturbance is developed and transmits information upstream. The heat flux and wall shear stress both increase due to this flow acceleration. Even though the effect on the total heat flux is small, the local heat flux is modified substantially. Thus the smaller effects due to the leading edge, the displacement, and the wake cannot be the reason for the discrepancy.

1 Introduction

Natural convection in a cavity has been a popular research topic for the past several years. Since many parameters, such as aspect ratio and orientation relative to the gravitational acceleration, appear in this problem, a large number of numerical simulations and experimental investigations have been reported. So far no general analytical solution is available. The key difficulty is that the boundary-layer approximation is not valid near the corners of the cavity where the flow turns, and near the reverse stagnation point where two boundary layers collide. In this paper, we study the merging of two parallel boundary layers. This problem is simpler than, but is relevant to, the problem of the collision of two boundary layers driven by body forces.

The boundary layer along a vertical, heated plate (see Fig. 1) is probably the first natural-convection problem which was studied. Since Schmidt and Beckmann [1], and Pohlhausen [2], both the analytical solution [3–6] and the measured heat transfer data [7–10] have been continuously improved. A very long list would be required to exhaust the published literature for this problem.

Since the boundary-layer equations are parabolic and are not affected by downstream activities, the flow near the trailing edge of a finite plate cannot be adequately described by the boundary-layer equations alone. Although the solution for the near plume, analogous to Goldstein's [11] near-wake solution, was obtained by Yang [12], it is singular at the trailing edge. Thus, a flow structure which can smoothly join the boundary layer and the thermal plume at the trailing edge is needed.

Messiter and Liñán [13] demonstrated that the discontinuous change in boundary conditions at the trailing edge implies large derivatives in the wall region. This results in a large local flow acceleration over a short distance, although the modification of the velocity is small. Thus, away from the thin region near the plate, the velocity profile deviates only slightly from the boundary-layer solution. The flow perturbations are inviscid in nature, and cannot satisfy the nonslip condition on the plate. A viscous sublayer is developed near the plate; the solution in this region determines the local heat flux and the wall shear stress. This structure is known as a "double deck" (Fig. 2). The existence of a similar structure has been demonstrated near the edge of a rotating disk [14]. It is worth noting that the double deck shares many similarities with the triple deck near the trailing edge of a flat plate in a uniform stream [15–17].

The double-deck theory shows that a disturbance inside a boundary layer driven by body forces (equivalently, a flow in which the motion outside of the boundary layer is much slower than that inside) can have an upstream influence to a distance of $0(\epsilon^{6/7})$, where $\epsilon \equiv \mathrm{Gr}^{-1/4}$. Messiter and Liñán adopted the natural-convection boundary layer along a finite vertical flat plate as a model problem to explain this double-deck structure and showed that the boundary-layer solution on the plate can smoothly join the solution of the thermal plume above the plate. However, they did not actually solve the perturbation equations.

In the following, we will show that the dimensions of the main deck are $0(\epsilon^{6/7} \times \epsilon)$ while those for the lower deck are $0(\epsilon^{6/7} \times \epsilon^{9/7})$. The trailing edge correction to the mean Nusselt number Nu is then $0(\epsilon^{1/7})$ which is larger than the other corrections due to the leading edge, the displacement effect, and the

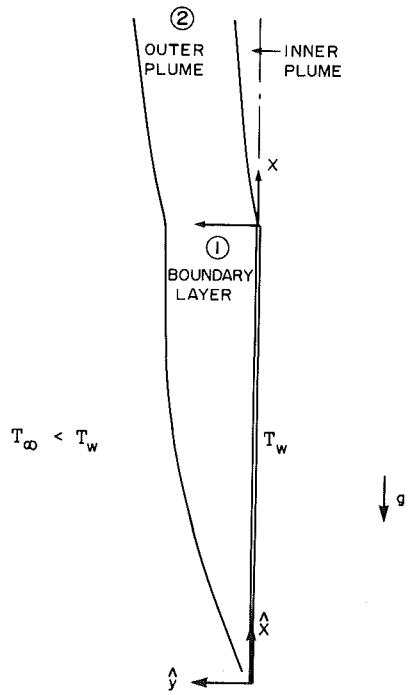

Fig. 1 Physical model and coordinates

Contributed by the Heat Transfer Division for publication in the JOURNAL OF HEAT TRANSFER. Manuscript received by the Heat Transfer Division June 12, 1985.

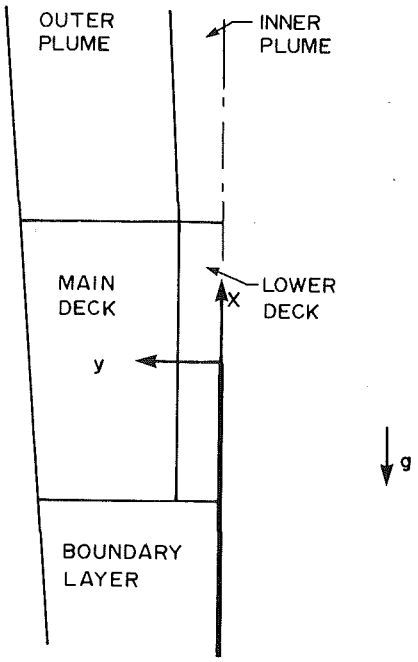

Fig. 2 Trailing edge of the plate

wake effect over the remainder of the plate. The trailing-edge structure suggested by Martynenko [5] has the dimensions $0(\epsilon^2 \times \epsilon^2)$, which implies a much shorter upstream effect and is physically incorrect. Consequently his model leads to a smaller trailing-edge correction (of $0(\epsilon)$) to Nu. In the present work, we numerically integrate the double-deck equations and compare the results with the available data.

In section 2, we briefly present the boundary-layer and plume solutions in order to provide consistent matching conditions for the double deck. In order to simplify the computation, Yang's plume solution is transformed to eliminate the explicit dependence of the boundary-layer solution. The predictions of the velocity and temperature profiles agree well with measurement and elucidate the physics of the problem. Comparison of the numerical results with experimental data shows that the trailing-edge effect on the total heat flux is small. A plausible explanation of the discrepancy between the measured mean heat flux of a finite vertical plate and the natural-convection boundary-layer solution for small Grashof numbers is the existence of a flow circulation which can have a forced-convection effect on the plate.

2 Analysis and Numerical Results

The solutions for the natural-convection boundary layer and the thermal plume are well known, and are briefly described below in order to establish a set of consistent notation to carry out the double-deck analysis. The dimensionless form of the equations of continuity, momentum, and energy with the Boussinesq approximation (Fig. 1) are

$$\frac{\partial \hat{u}}{\partial \hat{x}}+\frac{\partial \hat{v}}{\partial \hat{y}}=0$$

$$\hat{u}\frac{\partial \hat{u}}{\partial \hat{x}}+\hat{v}\frac{\partial \hat{u}}{\partial \hat{y}}=-\frac{\partial \hat{p}}{\partial \hat{x}}+\hat{\theta}+\epsilon^2\left[\frac{\partial^2 \hat{u}}{\partial \hat{x}^2}+\frac{\partial^2 \hat{u}}{\partial \hat{y}^2}\right] \tag{1}$$

$$\hat{u}\frac{\partial \hat{v}}{\partial \hat{x}}+\hat{v}\frac{\partial \hat{v}}{\partial \hat{y}}=-\frac{\partial \hat{p}}{\partial \hat{y}}+\epsilon^2\left[\frac{\partial^2 \hat{v}}{\partial \hat{x}^2}+\frac{\partial^2 \hat{v}}{\partial \hat{y}^2}\right]$$

$$\hat{u}\frac{\partial \hat{\theta}}{\partial \hat{x}}+\hat{v}\frac{\partial \hat{\theta}}{\partial \hat{y}}=\frac{\epsilon^2}{\mathrm{Pr}}\left[\frac{\partial^2 \hat{\theta}}{\partial \hat{x}^2}+\frac{\partial^2 \hat{\theta}}{\partial \hat{y}^2}\right]$$

The appropriate forms of these equations for the boundary layer, the plume, and the double deck are derived by rescaling equations (1).

Natural-Convection Boundary Layer. The scales for the natural-convection boundary layer are well known: The thickness of the boundary layer and the normal velocity are $0(\epsilon)$. The expansions for the velocity components, the pressure, and the temperature are

$$\begin{aligned}\hat{u} &= (4\hat{x})^{1/2} f_b'(\eta_b)+\ldots\\ \hat{v} &= -\epsilon(4\hat{x})^{-1/4}[3f_b-\eta_b f_b']+\ldots\\ \hat{p} &= 0+\ldots\\ \hat{\theta} &= h_b(\eta_b)+\ldots\end{aligned} \tag{2}$$

where $\eta_b = y_b/(4x_b)^{1/4}$ is the similarity variable, and $x_b=\hat{x}$, $y_b=\hat{y}/\epsilon$. The substitution of equations (2) into equations (1) and neglecting terms of higher orders yields

$$\begin{aligned}&f_b'''+3f_b f_b''-2f_b'^2=-h_b\\ &\frac{1}{\mathrm{Pr}}h_b''+3f_b h_b'=0\end{aligned} \tag{3}$$

where the prime denotes the derivative with respect to the independent variable. The associated boundary conditions are

$$\begin{aligned}f_b(0) &= f_b'(0)=0, \quad h_b(0)=1\\ f_b'(\infty) &= h_b(\infty)\to 0\end{aligned} \tag{4}$$

Many different forms of solution of equations (3) satisfying condition (4) are available [3]. The numerical solutions calculated for this study can be found in [18].

Thermal Plume Above the Heated Vertical Plate. The

Nomenclature

A = displacement function
a = constant introduced in equation (7)
f = stream function
g = gravitational acceleration
Gr = Grashof number $=\beta g L^3(T_w-T_\infty)/\nu^2$
h, H = temperature function
H_b = $h_b(x_b=1)$
L = length of the plate
Nu = mean Nusselt number
$\hat{p}$ = $\bar{p}/\rho U_0^2$ = pressure
Pr = Prandtl number $=\nu/\alpha$
Ra = Gr•Pr
T = temperature
$\hat{u}$ = $\bar{u}/U_0$ = axial velocity
U_b = $\sqrt{2}f_b'(x_b=1)$
U_0 = $[g\beta L(T_w-T_\infty)]^{1/2}$ = characteristic velocity
$\hat{v}$ = $\bar{v}/U_0$ = normal velocity
$\hat{x}$ = $\bar{x}/L$ = axial coordinate
$\hat{y}$ = $\bar{y}/L$ = normal coordinate
α = thermal diffusivity
β = coefficient of volumetric expansion
γ = $\int_0^\infty U_b^2 dy_1$
ϵ = $(\mathrm{Gr})^{-1/4}$
η = similarity variable
$\hat{\theta}$ = $(T-T_\infty)/(T_w-T_\infty)$
λ = $\sqrt{2}h_b''(0)$
μ = $(1/\sqrt{2})\ h_b'(0)$
ν = kinematic viscosty
ρ = density of fluid
ψ = stream function

Subscripts

b = quantities associated with the boundary layer
p = quantities associated with the plume
1 = quantities associated with the main deck
w = plate surface conditions
∞ = ambient conditions

near-plume solutions is needed in order to provide the matching condition for the double deck. The near-plume solution consists of two parts, an inner plume and an outer plume (see Fig. 2). For the inner plume, the expansions of the dependent variables are

$$\begin{aligned}\hat{u} &= (3x_p)^{1/3}\lambda^{2/3}f_p' + \ldots \\ \hat{v} &= -\epsilon[(3x_p)^{-1/3}\lambda^{1/3}(2f_p - \eta f_p') + \ldots] \\ \hat{p} &= 0 \\ \hat{\theta} &= 1 + (3x_p)^{1/3}\lambda^{-1/3}\mu h_p(\eta) + \ldots\end{aligned} \tag{5}$$

where $x_p = \hat{x} - 1$, $y_p = \hat{y}/\epsilon$, and $\eta = \lambda^{1/3}y_p/(3x_p)^{1/3}$. The governing equations for f_p and h_p can be obtained by substituting equations (5) into equations (1) and collecting terms of equal powers of x_p. The result is

$$\begin{aligned}f_p''' + 2f_p f_p'' - (f_p')^2 = 0 \\ \frac{1}{\mathrm{Pr}}h_p'' + 2f_p h_p' - f_p' h_p = 0\end{aligned} \tag{6}$$

The required conditions for the inner plume become

1. $\eta = 0, f_p(0) = f_p''(0) = h_p'(0) = 0$ (7a)

(symmetry condition)

2. $\eta \to \infty, f_p' = h_p \to \eta + a$ (7b)

The expansions for $y_p \sim 0(1)$ (outer plume) are then

$$\begin{aligned}\hat{u} &= U_b(y_p) + (3x_p)^{1/3}\psi_p'(y_p) + \ldots \\ \hat{v} &= -\epsilon[(3x_p)^{-2/3}\psi_p(y_p) + \ldots] \\ \hat{p} &= 0 \\ \hat{\theta} &= H_b(y_p) + (3x_p)^{1/3}H_p(y_p) + \ldots\end{aligned} \tag{8}$$

The governing equations for ψ_p and h_p can be obtained from equations (8) and (1). They are

$$\begin{aligned}U_b\psi_p' - \psi_p U_b' = 0 \\ U_b H_p - \psi_p H_b' = 0\end{aligned} \tag{9}$$

The solutions are

$$\begin{aligned}\psi_p &= a\lambda^{-1/3}U_b \\ H_p &= a\lambda^{-1/3}H_b'\end{aligned} \tag{10}$$

The constant a can be determined from the numerical solution of equation (6) and

$$a = \lim_{\eta\to\infty}[(2f_p)^{1/2} - \eta] = 0.6185 \tag{11}$$

Double Deck. Since the y component of the velocity in the plume is singular at $x_p = 0$, a double deck [13] is suggested to join the solutions of the natural-convection boundary layer and the thermal plume (see Fig. 2). Intuitively, one expects that the parabolic differential equations which describe the fluid motion in the boundary layer and in the plume may not be valid near the trailing edge of the plate. Locally, the equations of motion should be of elliptic-type differential equations. On the other hand, the leading term of the outer-plume solution is identical to that of the natural convection boundary layer. This suggests that the boundary-layer solution is still the leading term of the local solution in the neighborhood of the trailing edge. The elliptic type of equations govern the next-order terms. This naturally leads to the double-deck structure described below.

Following [13], the sizes of the main deck are ($\epsilon^{6/7} \times \epsilon$). The stretched coordinates become

$$\begin{aligned}x_1 &= \frac{\hat{x} - 1}{\epsilon^{6/7}} \\ y_1 &= \frac{\hat{y}}{\epsilon} = y_p\end{aligned} \tag{12}$$

The expansions of the dependent variables are

$$\begin{aligned}\hat{u} &= U_b(y_1) + \epsilon^{2/7}u_1(x_1, y_1) + \ldots \\ \hat{v} &= \epsilon^{3/7}v_1(x_1, y_1) + \ldots \\ \hat{p} &= \epsilon^{4/7}p_1(x_1, y_1) + \ldots \\ \hat{\theta} &= H_b(y_1) + \epsilon^{2/7}\theta_1(x_1, y_1) + \ldots\end{aligned} \tag{13}$$

The governing equation can be derived from substituting equations (13) into equations (1). They are

$$\begin{aligned}\frac{\partial u_1}{\partial x_1} + \frac{\partial v_1}{\partial y_1} = 0 \\ U_b\frac{\partial u_1}{\partial x_1} + v_1\frac{\partial U_b}{\partial y_1} = 0 \\ U_b\frac{\partial v_1}{\partial x_1} = -\frac{\partial p_1}{\partial y_1} \\ U_b\frac{\partial \theta_1}{\partial x_1} + v_1\frac{\partial H_b}{\partial y_1} = 0\end{aligned} \tag{14}$$

The solutions of the above equations can be expressed as

$$\begin{aligned}u_1 &= U_b'(y_1)A_1(x_1) \\ v_1 &= -U_b(y_1)A_1'(x_1) \\ p_1 &= A_1''(x_1)\int_{y_1}^{\infty}[U_b(y_1)]^2 dy_1 \\ \theta_1 &= H_b'(y_1)A_1(x_1)\end{aligned} \tag{15}$$

where $A_1(x_1)$ represents the displacement of the thin viscous layer (lower deck), and can be determined from the solution of the lower deck. Since $\hat{u}(-\infty, y_1) \to U_b(y_1)$ and $u_1(-\infty, y_1) \to 0$, $A_1(-\infty) \to 0$.

Since the restraining force on the plate is removed at $x_1 = 0$, the flow accelerates near $y_1 = 0$. The corresponding displacement effect requires a small inward mass flow toward $y_1 = 0$. The flow acceleration responding to the strong streamline curvature induces a pressure gradient in y direction. This pressure gradient introduces the net force acting on the fluid in the lower deck.

A lower deck is introduced mainly due to the fact that the solution (15) does not satisfy the wall condition on the plate. The thickness of the lower deck is $0(\epsilon^{9/7})$. Therefore, the expansions of the dependent variables, which match with the variables of the surrounding regions, are

$$\begin{aligned}\hat{u} &= \epsilon^{2/7}\gamma^{1/7}\lambda^{3/7}u(x, y) + \ldots \\ \hat{v} &= \epsilon^{5/7}\gamma^{-1/7}\lambda^{4/7}v(x, y) + \ldots \\ \hat{p} &= \epsilon^{4/7}\gamma^{2/7}\lambda^{6/7}p(x, y) + \ldots \\ \hat{\theta} &= H_b(0) + \epsilon^{2/7}\gamma^{1/7}\lambda^{-4/7}\mu\theta(x, y) + \ldots \\ A_1 &= \gamma^{1/7}\lambda^{-4/7}A(x)\end{aligned} \tag{16}$$

where $x = \gamma^{-3/7}\lambda^{5/7}x_1$ and $y = \epsilon^{-9/7}\gamma^{-1/7}\lambda^{4/7}\hat{y}$.

By substituting equations (16) into equation (1), we obtain the governing equations

$$\begin{aligned}\frac{\partial u}{\partial x} + \frac{\partial v}{\partial y} = 0 \\ u\frac{\partial u}{\partial x} + v\frac{\partial u}{\partial y} = -\frac{\partial p}{\partial x} + \frac{\partial^2 u}{\partial y^2} \\ \frac{\partial p}{\partial y} = 0 \\ u\frac{\partial \theta}{\partial x} + v\frac{\partial \theta}{\partial y} = \frac{1}{\mathrm{Pr}}\frac{\partial^2 \theta}{\partial y^2}\end{aligned} \tag{17}$$

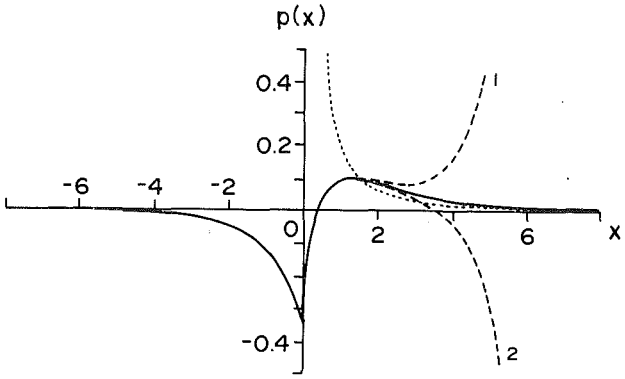

Fig. 3 Pressure distribution. Dashed curves are trial solutions; the dotted curve is the asymptotic form.

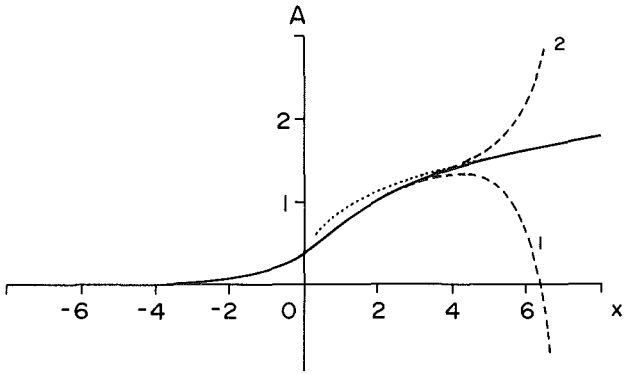

Fig. 4 Displacement function

which are parabolic-type partial differential equations. Since p has to be determined from the main deck, and the solution of equations (17) provides the required matching condition for the main deck, the coupling of equations (15) and (17) results in a mechanism to transfer the disturbance upstream from the trailing edge.

Expansion (16) must match with boundary-layer solution as $x \to -\infty$, so that

$$u \to y \qquad \theta \to y \tag{18a}$$

As $y \to \infty$, they must also match with the main deck

$$u \to y + A(x) \qquad \theta \to y + A(x) \tag{18b}$$

Thus, the physical meaning of $A(x)$ is clearly revealed by equation (18b) and represents the lower-deck displacement. The wall conditions for $x<0$ and $y=0$ are

$$u = v = \theta = 0 \tag{18c}$$

The centerline conditions ($x>0$, $y=0$) are

$$\frac{\partial u}{\partial y} = v = \frac{\partial \theta}{\partial y} = 0 \tag{18d}$$

As $x \to \infty$, the main deck matches with the outer plume and the lower deck matches with the inner plume. This results in

$$A(x) \to a(3x)^{1/3} \tag{18e}$$

Finally, since the normal pressure gradient vanishes across the lower deck, we have

$$P = -A''(x) \tag{19}$$

which provides a relation of pressure and displacement functions.

The numerical method used to solve (14) is essentially identical to the one used in [6]. The equations (14) are integrated

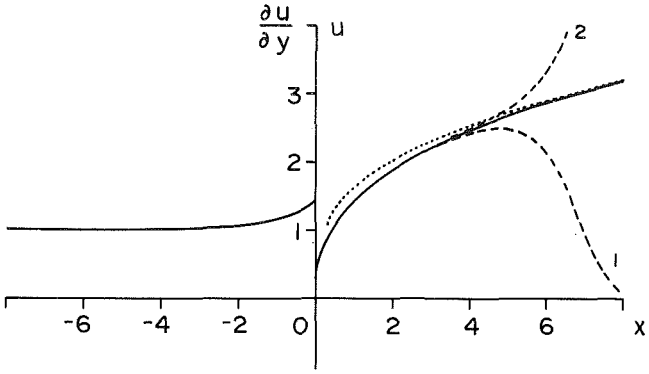

Fig. 5 Wall shear stress for $x \le 0$ and centerline velocity for $X \ge 0$

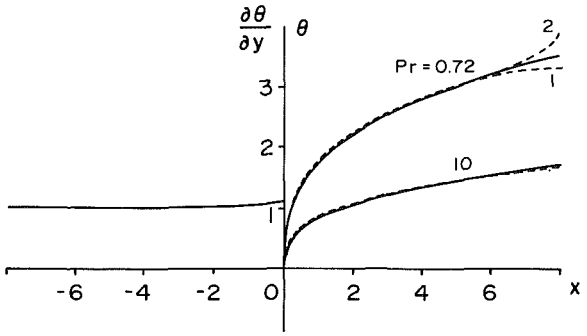

Fig. 6 Heat flux and centerline temperature

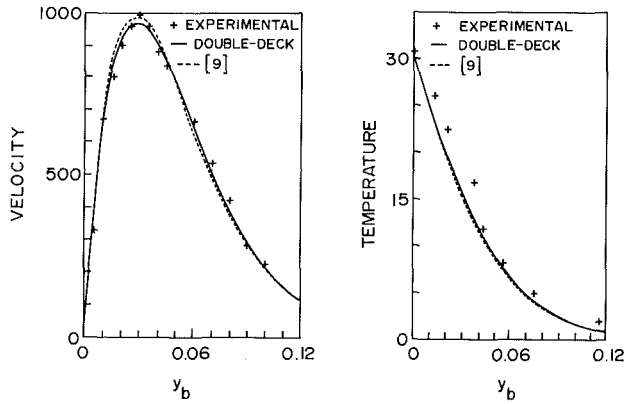

Fig. 7 The comparison of the double-deck solution (Pr = 0.72, Gr = 3 × 10^6) with the experimental data and the numerical results of [9] at the trailing edge

from $x_{-\infty} = -10$ to a point well downstream ($x_\infty = 10$). A detailed numerical procedure and the results are given in [18].

The induced pressure p is plotted in Fig. 3. The favorable pressure gradient develops along the plate near the trailing edge. The pressure increases in the plume region and eventually recovers and matches with the ambient pressure. The dotted line represents the asymptotic solution of the double deck for large x. The agreement of the numerical solution and the asymptotic solution ensures the convergence. The displacement A is plotted in Fig. 4. The continuous distribution of A indicates that the double deck indeed provides a smooth junction between the boundary-layer solution and that of the plume. The discontinuity of the axial pressure gradient at the trailing edge is acceptable as a solution of the Navier–Stokes equations. In Fig. 5, the increase of the wall shear near the trailing edge due to the flow acceleration agrees with our expectation. Also, the centerline velocity accelerates from zero at the trailing edge and smoothly merges with that of the near plume solution. The enhanced heat flux is presented in Fig. 6.

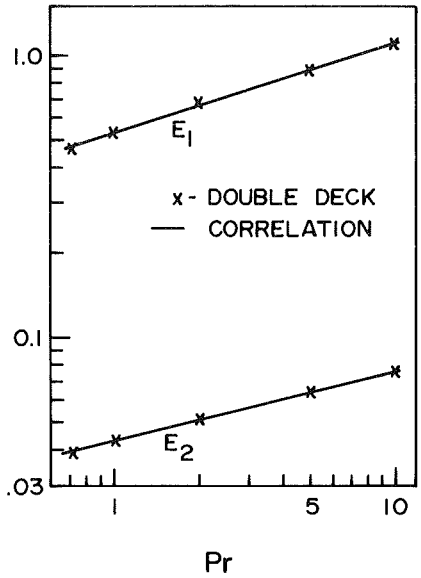

Fig. 8 Coefficients for $\overline{Nu}$

The value for $Pr = 10$ is slightly larger than that for $Pr = 0.72$, but two curves cannot be distinguished on the scale of the figure. The monotonical increase of θ along $y = 0$ indicates that the centerline temperature decreases from the wall temperature at the trailing edge toward the ambient temperature as the fluid rising from the plate.

In Fig. 7, the composite expansions of the velocity and the temperature at the trailing edge are compared with the experimental data and with the numerical solution of the Naiver-Stokes equations in [9]. The accuracy of the double-deck solution is shown better than the full numerical solution. This is likely due to the fact that the lower deck is extremely thin. A direct numerical solution of the Navier-Stokes equations requires a large number of computational nodes in order to obtain enough resolution of the flow field.

3 Correlations and Discussion

Ede [8] compared the Ostrach solution with the data of Schmidt and Bechmann. The agreement is satisfactory for $10^6 < Ra < 10^7$. The similarity solution underpredicts the total heat flux for Ra either lower or higher than the above mentioned range. The discrepancy for $Ra > 10^7$ can be attributed to flow transition and turbulence. The discrepancy for $Ra < 10^6$ is usually explained as being due to the boundary-layer displacement effect, the leading-edge, and the wake. All three effects are of $0(\epsilon)$ which is smaller than the trailing-edge effect, which is shown below to be $0(\epsilon^{-1/7})$.

The mean Nusselt number in terms of the length of the plate and the difference of the plate and the ambient temperatures can be estimated as

$$\overline{Nu} = -\epsilon^{-1}\int_0^1 \frac{\partial h_b}{\partial y_b}(x_b, 0)dx_b$$

$$-\epsilon^{-1/7}\mu\gamma^{3/7}\lambda^{-5/7}\int_{-\infty}^{0}\left(\frac{\partial\theta}{\partial y}\bigg|_{y=0} - 1\right)dx \qquad (20)$$

The first term on the right-hand side is the heat flux due to the natural-convection boundary layer. The second term represents the correction due to the trailing edge. A simple correlation is derived from equation (20) with the numerical data for $Pr = 0.72$, 1, 2, 5, and 10. It is

$$\overline{Nu} = 0.534Pr^{0.314}Gr^{1/4} + 0.043Pr^{0.25}Gr^{1/28} \qquad (21)$$

The exponents of Pr in the above equation are obtained by plotting the numerical results in a log-log scale as shown in Fig. 8. It is disappointing to find out that the numerical value of the constant in the second term in equation (21) is very small. This means that the local modification of the heat flux near the trailing edge is significant, but its contribution to the total heat flux is rather limited. This behavior is partially due to the short axial extent of the double deck. Thus, the even smaller effects due to the leading edge, the boundary-layer displacement, and the wake cannot be the reason for the discrepancy between the experimental data and the theory. A possible explanation can be put forward on the flow circulation induced by a heat source inside a room, or by other reasons. The induced drift can have a forced-convection effect on a heated vertical plate. The measured data are actually for mixed convection, and not for pure natural convection. Of course, this forced-convection effect is relatively significant for a slightly heated plate, and its effect is eventually overwhelmed by the natural-convection effect for a highly heated plate [19]. It is not easy to quantify this effect because the magnitude of the drift depends on the thermal condition and the setup of the room, and the outside temperature.

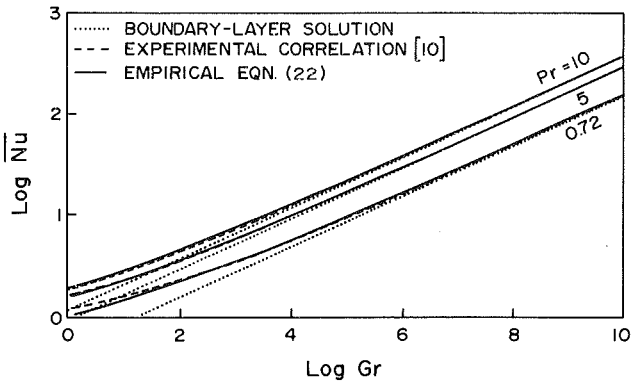

Fig. 9 Comparison of $\overline{Nu}$

Before a definite conclusion can be made about the above argument, it was decided to develop a correlation by adjusting the constant which reflects the contribution of the trailing edge. The constant was adjusted according to the available experimental data. The resulting correlation is

$$\overline{Nu} = 0.534Pr^{0.314}Gr^{1/4} + 0.528Pr^{0.129}Gr^{1/28} \qquad (22)$$

The correlation is compared with the one by Churchill and Chu [10], which appears to fit the widest range of the available data. Since the form of their correlation is rather complex and is quite different from (22), the correlations are compared for $Pr = 0.72$, 5, and 10 in Fig. 9. It is clear that the agreement is excellent.

In conclusion, the double-deck solution clearly shows that the flow accelerates near the trailing edge due to the sudden change of the geometry which results in decrease of the flow constraint. The heat flux increases due to this local flow acceleration. Even though its effects on the total heat flux is small, it modifies the local heat flux substantially.

Acknowledgments

The authors wish to express appreciation to M. K. Ellingsworth of the Office of Naval Research for generous research support under award number N00014-81-K-0428.

References

1 Schmidt, E., and Beckmann, W., "Das Temperatur und Geschwindigkeitsfeld von einer Warme abgebenden, senkrenchten Platte bei naturlicher Konvektion," *Forschg. Ing.-Wes.*, Vol. 1, 1930, pp. 391-404.

2 Pohlhausen, E., "Der Warmeaustausch zwischen festen Korpern und Flussigkeiten mit kleiner Reibung und kleiner Warmeleitung," *ZAMM*, Vol. 1, 1921, pp. 115-121.

3 Ostrach, S., "An Analysis of Laminar Free-Convection Flow and Heat

Transfer About a Flat Plate Parallel to the Direction of the Generating Body Forces," NACA TR 1111, 1953.

4 Sparrow, E., and Gregg, J., "Laminar Free Convection From a Vertical Plate With Uniform Surface Heat Flux," *Trans. ASME*, Vol. 78, 1956, pp. 435–440.

5 Martynenko, O. G., "Laminar Free Convection from a Vertical Plate," *Int. J. Heat Mass Transfer*, Vol. 27, 1984, pp. 869–881.

6 Merkin, J. H., and Smith, F. T., "Free Convection Boundary Layers Near Corners and Sharp Trailing Edges," *J. of Appl. Math. and Phys. (ZAMP)*, Vol. 33, 1982, pp. 36–52.

7 Eichhorn, R., "Measurement of Low Speed Gas Flows by Particle Trajectories," *Int. J. Heat & Mass Transfer*, Vol. 5, 1962, pp. 915–928.

8 Ede, A. J., "Advances in Free Convection," *Advances in Heat Transfer*, Vol. 4, 1967, pp. 1–64.

9 Hardwick, N., and Levy, E., "Study of the Laminar Free Convection Wake Above an Isothermal Vertical Plate," ASME JOURNAL OF HEAT TRANSFER, Vol. 95, 1973, pp. 289–294.

10 Churchill, S. W., and Chu, H. H. S., "Correlating Equations for Laminar and Turbulent Free Convection From a Vertical Plate," *Int. J. Heat Mass Transfer*, Vol. 18, 1975, pp. 1323–1329.

11 Goldstein, S., "Concerning Some Solutions of the Boundary Layer Equations in Hydrodynamics," *Proc. Cambridge Philosophical Soc.*, Vol. 26, 1930, pp. 1–26.

12 Yang, K. T., "Laminar Free-Convection Wake Above a Heated Vertical Plate," ASME *J. Appl. Mech.*, Vol. 31, 1964, pp. 131–138.

13 Messiter, A., and Liñán, A., "The Vertical plate in Laminar Free Convection," *J. of Appl. Math. and Phys.*, Vol. 27, 1976, pp. 633–651.

14 Smith, F., "A Note on a Wall Jet Negotiating a Trailing Edge," *Q. J. Mech. Appl. Math.*, Vol. 31, 1978, pp. 473–479.

15 Stewartson, K., "On the Flow Near the Trailing Edge of a Flat Plate," *Proc. R. Soc. London A*, Vol. 306, 1968, pp. 275–290.

16 Stewartson, K., "On the Flow Near the Trailing Edge of a Flat Plate II," *Mathematika*, Vol. 16, 1969, pp. 106–121.

17 Messiter, A., "Boundary Layer Flow Near the Trailing Edge of a Flate Plate," *SIAM J. Appl. Math.*, Vol. 18, 1970, pp. 241–257.

18 Yang, R., "Natural Convection Heat Transfer on a Finite Vertical Flat Plate," M.S. Thesis, Department of Mechanical and Aerospace Engineering, Arizona State University, Tempe, AZ 1985.

19 Yao, L. S., "Two-Dimensional Mixed Convection Along a Flat Plate," ASME JOURNAL OF HEAT TRANSFER, Vol. 109, 1987, this issue.

The Effects of Side-Wall Conduction on Natural Convection in a Slot

G. D. Mallinson
Associate Professor,
Department of Mechanical Engineering,
The University of Auckland,
Auckland, New Zealand

A numerical model for the interaction between natural convection in a slot and conduction in the side walls that are parallel to the plane of the slot is described. Two-dimensional equations containing source terms which account for the viscous and thermal coupling between the fluid and the walls are solved by a finite difference method. The model neglects radiation effects. Solutions for a slot of square cross section filled with a high Prandtl number fluid and heated from below are compared with the results of a Galerkin analysis made by Frick [8] and with solutions obtained by a fully three-dimensional model. Solutions for a slot filled with air and heated from the side are also validated by comparison with three-dimensional solutions. The data produced by the model predict that the more conventional Hele Shaw analysis overestimates heat transfer when the slot aspect ratio is greater than 0.05. Perfectly conducting walls are shown to reduce the rate of heat transfer by the fluid but to increase the strength of the flow. Some effects of walls that are neither adiabatic nor perfectly conducting are assessed.

1 Introduction

Natural convection in the air space between a solar collector and its cover plate can be suppressed by filling the space with a series of partitions which divide the space into a series of slots with their planes aligned normal to the collector surface. It is usual to arrange the partitions so that the slots are aligned with their planes across the direction of slope of the collector. However, recent research [1] has shown that more effective suppression can be achieved for some angles of slope if the slots are aligned up the slope.

In many cases of practical interest, the convection within the slots takes the form of a series of rolls with their axes normal to the partitions. In slots aligned up the slope of the collector a single roll can occur in each slot if the angle of inclination of the collector exceeds 24 deg [1]. When multiple rolls occur, the essential mechanisms of the convection can be understood by studying the convection in vertical slots between two horizontal isothermal surfaces, a situation which corresponds to a solar collector which is not inclined. If the partition spacing is very small, the convective flow closely resembles that in a porous medium heated from below and is amenable to analysis using the Hele Shaw approximation as reported, for example, by Elder [2], Hartline and Lister [3], and Frick and Clever [4].

Experiments with models of solar collectors, of which those by Smart et al. [5] are recent examples, indicate that the thermal properties of the partition material can have a significant effect on the convection. The correct modeling of the interaction between the wall and the convecting fluid may be important for the case of air-filled cavities when partitions are most likely to behave somewhere between the limiting conditions of adiabatic and perfectly conducting. Meyer et al. [5] present a numerical analysis which accounts for wall/fluid interaction for situations where the roll axes are aligned parallel to the walls as may occur when cross slope partitions divide the space into a series of approximately square cross section cavities which span the full width of the collector. The walls, in this case, influence the coupling between rolls. Kim and Viskanta [7] have considered the coupling between convection in an infinitely long cavity of square cross section and conduction in the four bounding surfaces.

The work reported here concentrates on convection in slots between upslope partitions, the spacing between which is between 0.05 and 0.25 times the distance between the collector and its cover plate. The objective was to produce a model which could be extended to the single role convection observed by Symons et al. [1].

The slot convection has been modeled by a finite difference analysis in which the conventional Hele Shaw approximation is modified to account approximately for the effects of diffusion and advection of vorticity in the plane of the slot. A fully two-dimensional set of equations is retained so that the model may be eventually applied to a single roll in a slot having a large upslope length-to-height ratio. This contrasts with the approach used by Frick [8] to model convection in slots heated from below whereby plane flow solutions were sought while still retaining three-dimensional temperature and stream function fields.

Wall/fluid interaction has been modeled by deriving a separate equation for the temperature at the partition/fluid interface. This extends the conventional approach, summarized by Koster and Muller [9], whereby the properties of the wall are incorporated into average parameters used to represent the combined wall/fluid system.

The model has been applied, in the first instance, to a slot of square cross section heated from below. These results can be compared directly with the analysis of Frick [8]. A full three-dimensional analysis has been applied to this problem and to a cavity heated from the side to provide further validation of the model. Exploratory solutions for the side heating case have been obtained to determine the conditions under which side walls may be classified as adiabatic or perfectly conducting. These results have also been used to determine the limits of validity of the conventional Hele Shaw model.

2 Mathematical Models

2.1 Three-Dimensional Model. The slot, as shown in Fig. 1, has dimensions L_x, L_y, and L_z and can be tilted so that the z axis is directed up the slope and makes an angle ϕ with the horizontal plane. L_y is much smaller than either L_x or L_z. The

Contributed by the Heat Transfer Division and presented at the National Heat Transfer Conference, Niagara Falls, NY, August 1984. Manuscript received by the Heat Transfer Division December 20, 1984.

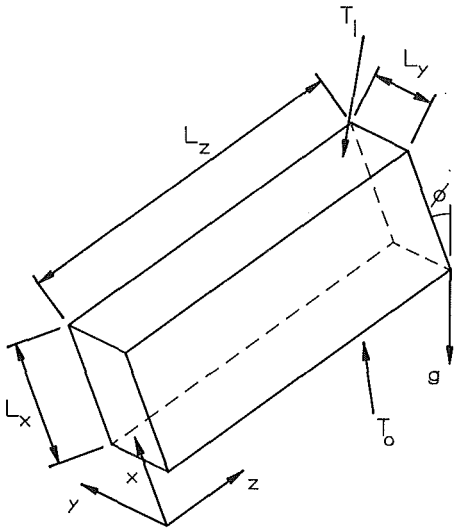

Fig. 1 Slot dimensions and orientation

x boundaries of the slot are isothermal with the temperature of the boundary at $x=0$ being the greater (i.e., $T_0 > T_1$). Using L_x, κ_f/L_x, and $\rho_0\kappa_f^2/L_x^2$ as the scale factors for distance, velocity, and pressure, and defining $\theta = (T-T_1)/(T_0-T_1)$, the equations governing steady Boussinesq convection are

$$\mathbf{v}\cdot\nabla\mathbf{v} = -\nabla P - \mathrm{RaPr}\theta\hat{\mathbf{g}} + \mathrm{Pr}\nabla^2\mathbf{v} \tag{1}$$

$$\nabla\cdot\mathbf{v} = 0 \tag{2}$$

$$\mathbf{v}\cdot\nabla\theta = \nabla^2\theta \tag{3}$$

Ra and Pr are the Rayleigh and Prandtl numbers, respectively.

These equations can be expressed in terms of the vorticity ζ, and a vector potential Ψ, defined by

$$\mathbf{v} = \nabla\times\Psi; \qquad \nabla\cdot\Psi = 0 \tag{4}$$

The curl of equation (1) yields

$$\nabla\times(\zeta\times\mathbf{v}) = -\mathrm{RaPr}(\nabla\times\theta\hat{\mathbf{g}}) + \mathrm{Pr}\nabla^2\zeta \tag{5}$$

and the equation relating vorticity and the vector potential is

$$\nabla^2\Psi = -\zeta \tag{6}$$

Boundary conditions for Ψ and ζ can be derived from the relevant boundary conditions for velocity. For a plane boundary perpendicular to an axis of the Cartesian coordinate system, the condition of zero volume flux through the boundary leads to the condition that Ψ is normal to the boundary and that its gradient at the boundary is zero. At the $z=0$ boundary, for example,

$$\psi_1 = \psi_2 = \partial\psi_3/\partial z = 0 \tag{7}$$

The boundary conditions for ζ depend on whether the boundary is rigid (or nonslip) or free (perfect slip). The conditions at $z = 0$ when that boundary is rigid are

$$\zeta_1 = -\partial^2\psi_1/\partial z^2, \qquad \zeta_2 = -\partial^2\psi_2/\partial z^2, \qquad \zeta_3 = 0 \tag{8}$$

When the same boundary is free, the boundary conditions are

$$\zeta_1 = \zeta_2 = 0, \qquad \partial\zeta_3/\partial z = 0 \tag{9}$$

The boundary conditions for θ at $x=0$ and $x=1$ are

$$\theta = 1 \text{ and } \theta = 0, \text{ respectively.} \tag{10}$$

For this study, the z boundaries are assumed to be adiabatic so that

$$\partial\theta/\partial z = 0 \qquad \text{at } z=0 \text{ and } z=A_z \tag{11}$$

A full three-dimensional analysis can be applied to the above equations using the finite difference method described by Mallinson and de Vahl Davis [10]. Second-order finite difference approximations are used throughout and steady-state

Nomenclature

A_w = L_w/L_x = nondimensional wall thickness
A_y = L_y/L_x = cavity aspect ratio in y versus x
A_z = L_z/L_x = cavity aspect ratio in z versus x
$f(y)$ = y variation for velocity, vorticity, and stream function
$g(y)$ = y variation for wall temperature
$\mathbf{g}$ = gravitational vector
$g_\phi(\theta)$ = $(\partial\theta/\partial z)\cos\phi - (\partial\theta/\partial x)\cdot\sin\phi$ = directional term for vorticity generation
$h(y)$ = y variation for fluid temperature
k_f = thermal conductivity of the fluid
k_w = thermal conductivity of the wall
L_w = width of side wall
L_x, L_y, L_z = dimensions of cavity in x, y, and z directions
Nu = overall Nusselt number
Nu_f = Nusselt number for fluid
Nu_w = Nusselt number for side wall
P = pressure
Pr = ν/κ_f = Prandtl number
Ra = $g\beta_f L_x^3(T_0-T_1)/(\nu\kappa_f)$ = Rayleigh number
Ra_{HS} = $\mathrm{Ra}A_y^2/12$ = Hele Shaw Rayleigh number
T = temperature
T_0 = temperature of hot boundary at $x = 0$
T_1 = temperature of cold boundary at $x = 1$
u, v, w = velocity components in x, y, and z directions
$\bar{u}$ = y-averaged velocity in x direction
$\mathbf{v}$ = velocity vector
$\bar{w}$ = y-averaged velocity in z direction
x, y, z = nondimensional Cartesian coordinates
α = k_f/k_w = fluid/wall conductivity ratio
β = L_y/L_w = slot/wall width ratio
β_f = fluid coefficient of thermal expansion
ζ = vorticity vector
$\zeta_1, \zeta_2, \zeta_3$ = x, y, and z components of vorticity
$\bar{\zeta}_2$ = y-averaged value of y vorticity
θ = $(T-T_1)/(T_0-T_1)$ = nondimensional temperature
θ_b = value of θ at fluid/wall interface
θ_f = nondimensional fluid temperature
$\tilde{\theta}_f$ = y-averaged deviation of θ_f from θ_b
θ_f^* = y-averaged value of θ_f
θ_w = nondimensional wall temperature
$\tilde{\theta}_w$ = y-averaged deviation of θ_w from θ_b
θ_w^* = y-averaged value of θ_w
κ_f = thermal diffusivity for the fluid
ν = kinematic viscosity
ρ_0 = reference density
ϕ = angle of inclination of the cavity
Ψ = vector potential for velocity
ψ_1, ψ_2, ψ_3 = x, y, and z components of Ψ
$\bar{\psi}$ = y-averaged stream function
∇_2^2 = $\partial^2/\partial x^2 + \partial^2/\partial z^2$

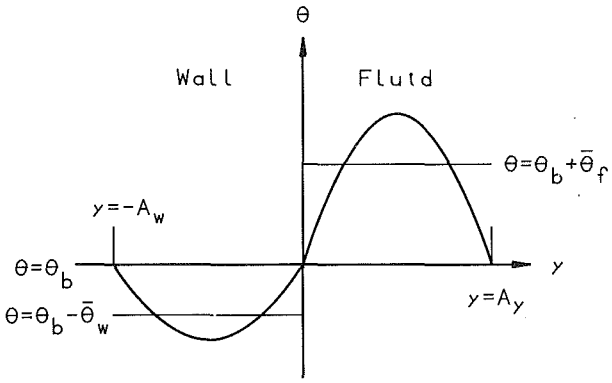

Fig. 2 Schematic representation of the variation of nondimensional temperature with y

solutions are generated by an alternating direction implicit iterative procedure.

This analysis can be applied to slots where the y boundaries are either adiabatic or perfectly conducting. The adiabatic conditions for θ are

$$\partial\theta/\partial y = 0 \qquad \text{at } y = 0 \text{ and } y = A_y \tag{12}$$

The conditions for perfectly conducting boundaries are

$$\theta = 1 - x \qquad \text{at } y = 0 \text{ and } y = A_y \tag{13}$$

The full three-dimensional analysis can, in principle, be applied to any rectangular cavity. However, when large differences in cavity dimensions occur the demands on the computer resource can become excessive.

The iterative procedure used to obtain the steady-state solutions is analogous to a stepwise progression through time: Instabilities arising from nonlinear coupling between the finite difference equations impose an effective time step limit which is proportional to the square of the smallest mesh interval. In the case of a slot with $A_y = 0.1$ and $A_z = 1$, the smallest mesh intervals occur in the y direction and restrict the time step to be approximately 0.01 times that which could be used to produce a solution for a slot with $A_y = 1$. Since the time scale for the convection is dictated by the dimensions of the slot in the x and z directions, the time step restriction means that the $A_y = 0.1$ solution requires approximately 100 times the computer time used to produce an $A_y = 1$ solution. Certainly the effort required to obtain the three-dimensional solutions described later in this paper increased as A_y decreased and became prohibitively excessive for $A_y < 0.1$.

2.2 Two-Dimensional Model

2.2.1 Vorticity Equation. The large solution times for the three-dimensional model provided motivation to develop a model for which the solution method is independent of the y aspect ratio. Sample calculations for a slot with $A_y = 0.16$ and $A_z = 7.5$ with an $11 \times 11 \times 31$ mesh indicated that the x and z components of velocity were within 2 percent of a parabolic variation in the y direction. Moreover, the y velocity component was typically two orders of magnitude smaller than the other two components. This evidence suggested that the flow in the slot could be regarded as being closely approximated by fully developed viscous flow between parallel plates.

Accordingly the velocity field was assumed to be represented by

$$u = f(y)\bar{u}(x, z), \qquad v = 0, \qquad w = f(y)\bar{w}(x, z) \tag{14}$$

where

$$f(y) = 6y(A_y - y)/A_y^2 \tag{15}$$

Making these substitutions, it follows that $\bar{u}$ and $\bar{w}$ can be generated from a stream function $\bar{\psi}$ such that

$$\bar{u} = -\partial\bar{\psi}/\partial z \text{ and } \bar{w} = \partial\bar{\psi}/\partial x \tag{16}$$

The three components of vorticity are

$$\zeta_1 = f'(y)\bar{u}, \qquad \zeta_2 = \bar{\zeta}_2 f(y), \qquad \zeta_3 = -f'(y)\bar{w} \tag{17}$$

where

$$\bar{\zeta}_2 = \partial\bar{u}/\partial z - \partial\bar{w}/\partial x \tag{18}$$

The y component of vorticity is related to the stream function by

$$\nabla_2^2\bar{\psi} = -\bar{\zeta}_2 \tag{19}$$

where

$$\nabla_2^2 = \partial^2/\partial x^2 + \partial^2/\partial z^2 \tag{20}$$

After substitution and integration over y, the vorticity transport equation becomes

$$\frac{1.2}{\text{Pr}}\left[\frac{\partial}{\partial x}(\bar{\zeta}_2\bar{u}) + \frac{\partial}{\partial z}(\bar{\zeta}_2\bar{w})\right] = \text{Ra}g_\phi(\theta_f^*) + \nabla_2^2\bar{\zeta}_2 - 12\bar{\zeta}_2/A_y^2 \tag{21}$$

where

$$g_\phi(\theta) = \cos\phi\ \partial\theta/\partial z - \sin\phi\ \partial\theta/\partial x \tag{22}$$

The y-averaged temperature field is denoted by θ_f^*.

Note that the x and z components of vorticity, although nonzero, do not influence the y-averaged velocity field. This decoupling arises from the assumption that the flow is plane and means that the solution is independent of the nonlinear interactions between these components. The flow predicted by equation (21) is insensitive to vorticity generated by temperature gradients in the y direction.

2.2.2 Temperature Equations. The temperature variation in the y direction is assumed to take the form shown in Fig. 2. $\bar{\theta}_f$ and $\bar{\theta}_w$ are the mean deviations from the interface temperature of the fluid and wall temperatures, respectively. The side wall at a y boundary is assumed to have thickness L_w measured to the interface with the fluid in an adjacent slot. This renders the analysis directly applicable to a system of slots. Alternatively, the wall can be regarded as being of thickness $L_w/2$, with the outer boundary satisfying the adiabatic condition $\partial\theta/\partial y = 0$. The dimension L_w is converted to an aspect ratio, $A_w = L_w/L_x$, for use in the nondimensional equations. The thermal and geometric factors influencing the coupling between the wall and the fluid are denoted by α and β where

$$\alpha = k_f/k_w \text{ and } \beta = A_y/A_w = L_y/L_w \tag{23}$$

The temperature in fluid is assumed to be approximated by

$$\theta_f = \bar{\theta}_f(x, z)h(y) + \theta_b(x, z) \tag{24}$$

If the (x, z) variation of heat flux through the wall/fluid interface is assumed to be negligible compared with the variations in the y direction, it follows that $h''(y)$ is proportional to $f(y)$ and that an appropriate form for $h(y)$ is

$$h(y) = 5(y^4 + A_y^3 y - 2A_y y^3)/A_y^4 \tag{25}$$

Substitution into equation (3) and integration over the cavity width yields

$$\frac{51}{42}\left[\frac{\partial}{\partial x}(\bar{\theta}_f\bar{u}) + \frac{\partial}{\partial z}(\bar{\theta}_f\bar{w})\right] = \nabla_2^2\bar{\theta}_f - 10\bar{\theta}_f/A_y^2 + \left\{\nabla_2^2\theta_b - \frac{\partial}{\partial x}(\theta_b\bar{u}) - \frac{\partial}{\partial z}(\theta_b\bar{w})\right\} \tag{26}$$

The temperature in the wall can be approximated by

$$\theta_w = \theta_b(x, z) - \bar{\theta}_w(x, z)g(y) \tag{27}$$

where

$$g(y) = -6(yA_w + y^2)/A_w^2 \tag{28}$$

The equation for wall temperature is

$$\nabla_2^2(\theta_b - \bar{\theta}_w) = -12\bar{\theta}_w/A_w^2 \tag{29}$$

Equations (29) and (26) are coupled by the continuity of wall heat flux through the interface, leading to

$$\bar{\theta}_w = 1.2(\alpha/\beta)\bar{\theta}_f \tag{30}$$

so that equation (29) can be replaced by

$$\nabla_2^2(\theta_b - \bar{\theta}_w) = -10(\alpha/\beta)\bar{\theta}_f/A_w^2 \tag{31}$$

Equation (31) can be used with equation (26) to generate an equation for θ_b

$$\frac{\partial}{\partial x}(\theta_b\bar{u}) + \frac{\partial}{\partial z}(\theta_b\bar{w}) = [1 + 1/(\alpha\beta)]\nabla_2^2\theta_b$$

$$+ \left\{\left[1 - 1.2/\beta^2\right]\nabla_2^2\bar{\theta}_f - 1.214\left[\frac{\partial}{\partial x}(\bar{\theta}_f\bar{u}) + \frac{\partial}{\partial z}(\bar{\theta}_f\bar{w})\right]\right\} \tag{32}$$

Equations (26) and (32) are convection-diffusion equations for $\bar{\theta}_f(x, z)$ and $\theta_b(x, z)$, respectively, with the coupling terms in curly brackets acting as source/sink terms. The y-averaged fluid and wall temperatures, θ_f^* and θ_w^*, can be evaluated using

$$\theta_f^* = \theta_b + \bar{\theta}_f \text{ and } \theta_w^* = \theta_b - \bar{\theta}_w = \theta_b - 1.2(\alpha/\beta)\bar{\theta}_f \tag{33}$$

2.2.3 Limiting Thermal Conditions. The thermal interaction between the partitions and the fluid in the slot depends on the nondimensional groups α and β. The following special cases can be identified.

Thin walls—adiabatic. Thin adiabatic walls correspond to $\beta \to \infty$ and $\alpha > o(1)$. The limiting forms of equations (26) and (32) imply that

$$\bar{\theta}_f = 0 \text{ and } \frac{\partial}{\partial x}(\theta_b\bar{u}) + \frac{\partial}{\partial z}(\theta_b\bar{w}) = \nabla_2^2\theta_b \tag{34}$$

Thick walls—adiabatic. If $\beta \to 0$, the walls are thick. Provided $\alpha >> \beta$, equation (26) will approach $\nabla_2^2\bar{\theta}_f = 0$ to the first order so that $\bar{\theta}_f = 0$ and the fluid behaves as if the walls were adiabatic. The appropriate form for equation (32) is

$$\frac{\partial}{\partial x}(\theta_b\bar{u}) + \frac{\partial}{\partial z}(\theta_b\bar{w}) = (1 + 1/(\alpha\beta))\nabla_2^2\theta_b \tag{35}$$

Perfectly conducting walls. Walls with a high thermal conductivity imply that $\alpha \to 0$. Equations (30) and (31) imply that

$$\bar{\theta}_w = 0 \text{ and } \nabla_2^2\theta_b = 0 \tag{36}$$

The mean deviation of the fluid temperature from the interface temperature is governed by equation (26).

2.3 Heat Transfer. The heat flux through the wall/fluid system can be calculated by evaluating individual Nusselt numbers for the wall and fluid and then evaluating an overall Nusselt number. The individual Nusselt numbers are given by

$$\mathrm{Nu}_f = \frac{1}{A_z}\int_0^{A_z} -\frac{\partial\theta_f^*}{\partial x}\bigg|_{x=0} dz \tag{37}$$

$$\mathrm{Nu}_w = \frac{1}{A_z}\int_0^{A_z} -\frac{\partial\theta_w^*}{\partial x}\bigg|_{x=0} dz \tag{38}$$

In each case the derivative is approximated by a three-point forward difference expression and the integration uses Simpson's rule. The overall Nusselt number is given by

$$\mathrm{Nu} = (k_w A_w \mathrm{Nu}_w + k_f A_f \mathrm{Nu}_f)(A_w k_w + A_f k_f)$$

$$= (\mathrm{Nu}_f + \alpha\beta\mathrm{Nu}_w)/(1 + \alpha\beta) \tag{39}$$

The Nusselt numbers for the three-dimensional solutions are calculated similarly with the exception that the integrations in equations (37) and (38) are replaced by double integrations over y and z.

If the walls are thin and adiabatic, $\mathrm{Nu}_w = \mathrm{Nu}_f$. If the walls are perfectly conducting, $\mathrm{Nu}_w = 1$.

2.4 Hele Shaw Model. Convection between closely spaced parallel planes has been previously modeled using the Hele Shaw approximations that the flow is fully developed and that the transport of vorticity is dominated by diffusion in the y direction. If these assumptions are made, equation (21) can be replaced by

$$0 = \mathrm{Ra}g_\phi(\theta_f^*) - 12\bar{\zeta}_2/A_y^2 \tag{40}$$

If the walls are thin and adiabatic, the convection is determined by the single nondimensional number

$$\mathrm{Ra}_{\mathrm{HS}} = \mathrm{Ra}A_y^2/12 \tag{41}$$

which is called the Hele Shaw Rayleigh number.

If the walls are thick and k_f/k_w is such that the adiabatic condition still holds, the velocity can be rescaled by the factor $(1 + 1/(\alpha\beta))$ and the appropriate single nondimensional number characterizing the flow and convection is

$$\mathrm{Ra}_{\mathrm{HS}} = \mathrm{Ra}A_y^2 k_f/12(k_f + k_w A_w/A_y) \tag{42}$$

which is the Hele Shaw Rayleigh number defined by Hartline and Lister [3].

Hele Shaw experiments usually have walls which fit into this category. For example, the apparatus used by Hartline and Lister [3] had $\beta = 0.08$ and $\alpha = 3.36$. This value of α is too small to ensure that the walls behave as perfectly as adiabatic boundaries if they were thinner, with $\beta \simeq 1$ say.

3 Results

3.1 Convection in a Slot Heated From Below. Frick [8] predicted heat transfer in a slot having the x boundaries horizontal ($\phi = 0$) and filled with a high Prandtl number fluid by using a Galerkin technique in which the temperature and two scalar potentials for velocity were expanded as series of orthogonal functions. Two types of solutions were obtained. The first type used both scalar potentials and can be regarded as being equivalent to the full three-dimensional model described here. The second type used a single scalar potential and corresponded to the assumption of plane flow but retained the three dimensionality of the scalar potential and the temperature.

Frick's analysis produced estimates of the critical Rayleigh number and preferred wavenumber which for adiabatic side walls and small A_y was shown to correspond to a roll of square cross section.

The estimation of the wavenumber of the convection in a layer heated from below is difficult to obtain with a finite difference method. There are two techniques that can be used. The first is to solve the equations for the case of very large A_z and let the solution, following an applied disturbance, settle to the appropriate multiroll form. Unless the number of mesh points is very large, the solution method will act as a digital filter and have a significant effect on the ensuing wavenumber. The second technique is to solve the equations for a single roll for a range of wavelengths and use an appropriate indicator, such as a maximum in the rate of heat transfer, to determine the preferred wavelength. Either technique involves a prohibitive amount of computation, especially when a three-dimensional model is used.

Accordingly, the solutions obtained here for comparison with Frick's results relied on his predicted wavenumber. For a single roll that is one of a series between two horizontal isothermal boundaries, the appropriate conditions for the z boundaries are that they are adiabatic and perfect slip.

Predictions using a 41 × 41 mesh for A_y equal to ∞, 1/3, 0.2, 0.1, and 0.05 are shown in Fig. 3. Also shown are Hele Shaw solutions using the same mesh for A_y equal to 0.1 and 0.05. The broken lines represent Frick's predictions transferred from Fig. 2 in [8]. Generally, the two-dimensional model predicts Nusselt numbers that are slightly higher (ap-

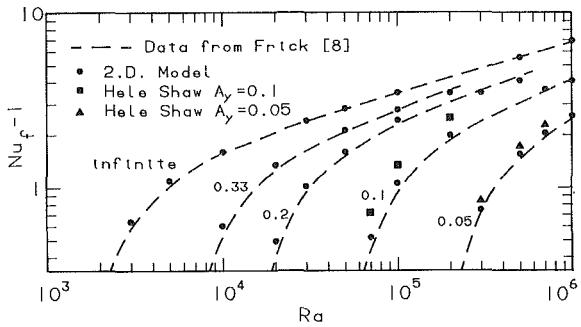

Fig. 3 Cavity heated from below, $A_z = 1$, $Pr = 10^4$ and adiabatic side walls: dependence of Nu_f on Ra. A_y values as marked. (41 × 41 mesh used for two-dimensional model).

proximately 2 percent) than those reported by Frick, especially when Ra is near the critical value. As Ra increases, the finite difference solutions approach the Galerkin solutions. It should be remembered, however, that the assumed wavenumber may not be appropriate for the highest values of Ra shown in Fig. 2 and for the $A_y = \infty$ and $A_y = 1/3$ solutions.

The Hele Shaw Nusselt numbers are higher than those predicted when the x–z diffusion of vorticity is taken into account. The disparity increases as A_y increases. The reasons for this will be considered later in this paper.

Sample Nusselt numbers calculated by the three-dimensional model are given in Table 1. The three-dimensional solutions all used a 21 × 21 mesh in the x–z cross section. Results for meshes with 11 and 21 y planes are listed in the table and can be compared with two-dimensional solutions for a 21 × 21 x–z mesh. Two-dimensional solutions for a 41 × 41 x–z mesh are also tabulated to establish the link, via Fig. 3, with Frick's [8] data. Generally, the coarser two-dimensional mesh produces 2–3 percent increases in Nusselt numbers referenced to the 41 × 41 mesh values. The two-dimensional results for a 21 × 21 mesh are within 1.5 percent of the three-dimensional results which use the same cross-sectional mesh and 21 y planes. This means that the two-dimensional model represents the three-dimensional effects with an accuracy which is comparable to, if not better than, that with which the cross-sectional flow is modeled.

The three-dimensional solutions which use only 11 y planes underpredict the heat transfer by about 10 percent, which suggests that at least 21 y planes are required to achieve an accuracy which is comparable to the cross-sectional accuracy. This requirement appears to be independent of the value of A_y so that the number of y planes cannot be reduced in an effort to decrease computational effort as $A_y \to 0$. A three-dimensional solution for $A_y = 0.1$ required up to 5 hr computer time on an IBM4341 computer whereas the corresponding two-dimensional solution could be obtained in less than 3 min. Three-dimensional solutions for $A_y < 0.1$ proved to be impracticable on the same computer.

3.2 Convection in a Slot Heated From the Side. Solutions presented here for the side-heated cavity ($\phi = 90$) concentrate on the case of a square cross section in the x–z plane ($A_z = 1.0$) with air as the convecting fluid. The majority of solutions are for $Pr = 0.71$, with a few for $Pr = 10$ to investigate the influence of Prandtl number for $Pr > 0.7$. (Numerical experiments indicated that increasing Pr beyond 10 resulted in less than 0.5 percent change in Nu_f.) All solutions have used a 21 × 21 mesh in the x–z cross section.

3.2.1 Adiabatic Side Walls. Stream function and temperature contour maps for $Ra = 1.5 \times 10^5$, $Pr = 0.71$, and $A_y = 0.2$ and 0.1 are compared in Fig. 4 with the infinite A_y solution and the Hele Shaw solution for $A_y = 0.1$. The infinite A_y solution exhibits the secondary rolls that are

Table 1 Cavity heated from below, $A_z = 1$, $Pr = 10^4$: sample values of Nu_f as predicted by the two-dimensional and three-dimensional models

Ra	A_y	Two-dimensional model		Three-dimensional model	
		41×41	21×21	21×11×21	21×21×21
10^5	0.1	2.06	2.09	1.89	2.02
2×10^5	0.1	2.99	3.07	2.85	3.06
3×10^4	0.2	2.02	2.04	1.82	2.01
5×10^4	0.2	2.60	2.64	2.40	2.58

characteristic of moderate Ra convection in this cavity. The stream function contour map closely resembles the flow visualization for $Ra = 2 \times 10^5$ published by Linthorst et al. [12]. As explained by Mallinson and de Vahl Davis [11], the positions of the secondary rolls are determined by the balance between advection and diffusion of vorticity away from the top-right and bottom-left corners where the horizontal temperature gradients and consequent vorticity generation are greatest. For $Pr = 0.71$, both advection and diffusion affect the flow field. If advection is diminished, the rolls align closer to the corners where vorticity is generated. The flow in a cavity with $A_y = 0.2$ exhibits such alignment, suggesting that advection has been diminished, having been dominated by the vorticity sink which represents viscous interaction between the fluid and the stationary partitions. For $A_y = 0.1$, this sink is stronger and swamps both advection and diffusion. The flow is then very similar to that predicted by the Hele Shaw model which neglects the advection and x–z diffusion terms in the vorticity transport equation.

The Hele Shaw solution for $A_y = 0.2$ resembles that in Fig. 4(*d*) rather than exhibiting the double secondary roll flow shown in Fig. 4(*b*), suggesting that the Hele Shaw model may not represent the convection accurately for $A_y > 0.2$.

Heat transfer results for adiabatic side walls are summarized by the solid lines in Fig. 5. The rate of heat transfer for a given value of Ra decreases as A_y decreases and the impedance created by the viscous drag of the walls increases. The effect of the side walls is greater for lower values of Ra, an observation which is in agreement with a similar observation for $\phi = 0$ made by Frick and Clever [4].

Comparison with the Hele Shaw analysis can be made by plotting the Nusselt number against the Hele Shaw Rayleigh number defined by equation (41). For adiabatic side walls, this Rayleigh number embodies the dependence on A_y, and results for all values of A_y collapse onto a single line. As shown in Fig. 6, the Hele Shaw model increasingly overestimates the heat transfer as A_y increases. For Ra = 10 say, the Hele Shaw model predicts that $Nu_f = 8.73$ for a slot with $A_y = 0.1$. This compares with $Nu_f = 7.5$ or 9.6 as predicted by the present model for $A_y = 0.1$ and infinite A_y, respectively. If $A_y = 0.2$, the Hele Shaw analysis predicts that $Nu_f = 13$ which is unrealistically higher than the infinite A_y value.

The present model and the Hele Shaw analysis are in close agreement for $A_y = 0.05$. These results and those presented in Fig. 3 for the cavity heated from below suggest an upper limit of $A_y = 0.05$ for the validity of the Hele Shaw analysis.

The variation of Nu_f with A_y is shown in Fig. 7 for $Ra = 1.5 \times 10^5$ and $Ra = 3 \times 10^5$. In each case, Nu varies from the Hele Shaw prediction for $A_y < 0.05$ to approach asymptotically the two-dimensional prediction as $A_y \to \infty$. The rapid departure from the Hele Shaw model once A_y is greater than 0.05 should be noted. For $Ra = 3 \times 10^5$, the variation of Nu_f with A_y for $Pr = 10$ has been shown. The infinite A_y analysis predicts an increase in Nu_f as Pr changes from 0.71 to 10. This effect diminishes with decreasing A_y.

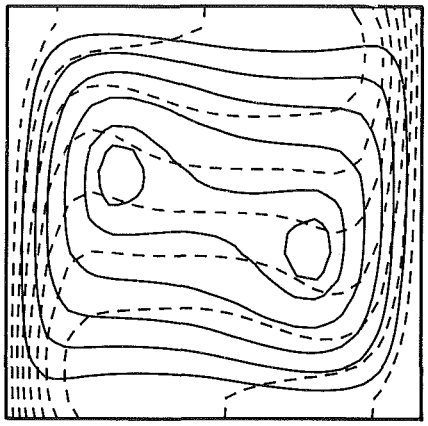

Fig. 4(a)

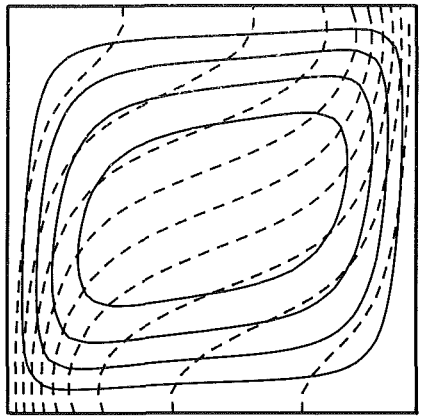

Fig. 4(c)

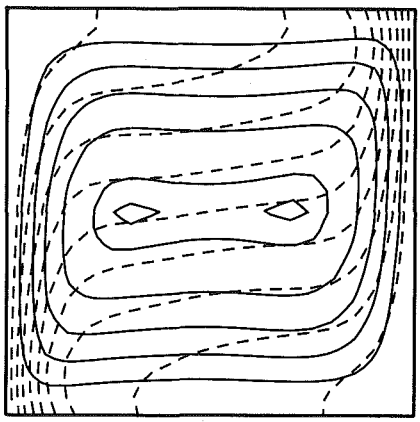

Fig. 4(b)

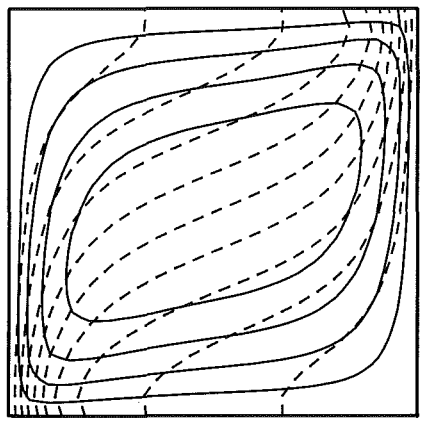

Fig. 4(d)

Fig. 4 Cavity heated from the side, $A_z = 1$, Pr = 0.71, Ra = 1.5×10^5 and adiabatic side walls: contour maps of stream function (solid lines) and temperature (broken lines); (a) infinite A; (b) $A_y = 0.2$; (c) $A_y = 0.1$; (d) $A_y = 0.1$ with Hele Shaw approximation

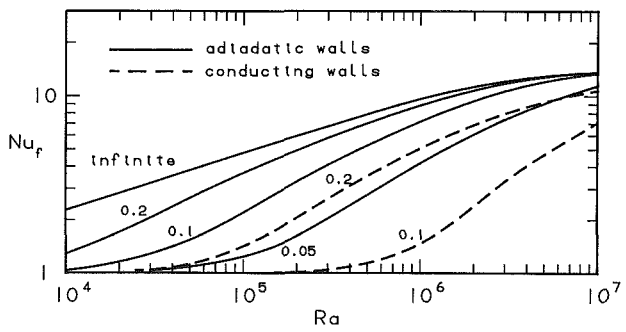

Fig. 5 Cavity heated from the side, $A_z = 1$ and Pr = 0.71; dependence of Nu_f on Ra for adiabatic and perfectly conducting side walls. A_y values as marked. (21 x 21 mesh used for two-dimensional model.)

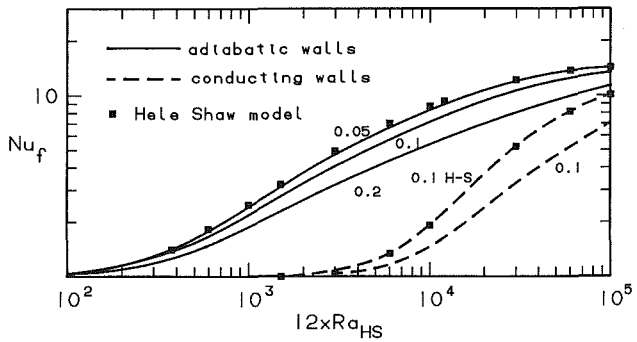

Fig. 6 Cavity heated from the side: $A_z = 1$ and Pr = 0.71: dependence of Nu_f on Ra_{HS} for adiabatic and perfectly conducting side walls. A_y values as marked. (Hele Shaw data for adiabatic side walls are independent of A_y).

Data obtained using the three-dimensional model are shown in Fig. 7 for comparison. The two-dimensional model is certainly adequate for $A_y < 0.1$ and is still within 4 percent of the three-dimensional model for $A_y < 1.0$. The data in Fig. 7 suggest that three-dimensional effects are greatest for $A_y \simeq 0.5$.

3.2.2 Conducting Side Walls. The relationship between Nu_f and Ra for cavities with perfectly conducting walls is shown by the broken lines in Figs. 5 and 6 for $A_y = 0.2$ and $A_y = 0.1$. In both cases, the replacement of adiabatic walls by conducting walls causes a significant reduction in Nu_f.

If the Hele Shaw approximation is made, Nu_f is overestimated, as shown in Fig. 6, where the results for a cavity with $A_y = 0.1$ have been plotted against Ra_{HS}. For nonadiabatic walls, the Hele Shaw model is not characterized by a single nondimensional group: The scaling which produces Ra_{HS} is relevant for only one value of A_y. Irrespective of the way that vorticity transport is modeled, the prediction is that conducting walls retard convection but once convection commences the rate of increase of Nu_f with Ra can be greater than for the corresponding adiabatic side wall case. This observation was made, from experiments with a cavity heated from below, by Koster [13]. Data presented in Fig. 8 indicate that

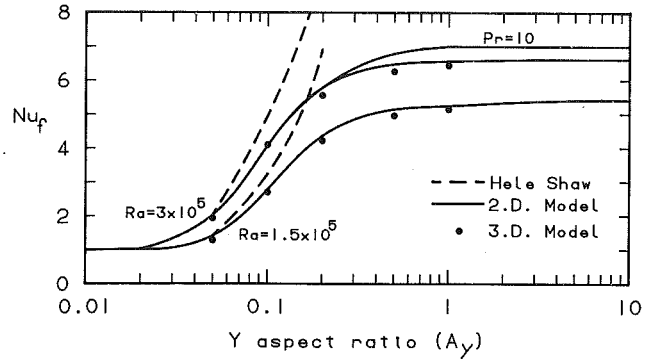

Fig. 7 Cavity heated from the side, $A_z = 1$ and adiabatic side walls: dependence of Nu_f on A_y. All data for $Pr = 0.71$ unless marked otherwise. Ra values as marked. (21 x 21 mesh for two-dimensional model, 21 x 11 x 21 mesh for three-dimensional model).

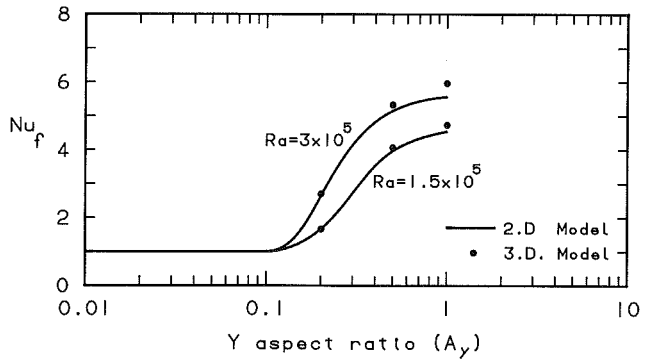

Fig. 8 Cavity heated from the side, $A_z = 1$, $Pr = 0.71$ and perfectly conducting side walls: dependence of Nu_f on A_y. Ra values as marked.

the two-dimensional model predicts Nu_f within 1 percent of the values predicted by the three-dimensional analysis for $A_y \leq 0.1$, and within 6 percent for $A_y \leq 1.0$.

The stream function map for $Ra = 3 \times 10^5$, $Pr = 0.71$, and $A_y = 0.2$ for a cavity with perfectly conducting side walls is shown in Fig. 9(*a*). The corresponding Hele Shaw flow is shown in Fig. 9(*b*). Without the diffusion of vorticity in the plane of the slot, higher temperature gradients in the corners of the cavity are maintained by the Hele Shaw model resulting in higher overall heat transfer.

The flow field in Fig. 9(*a*) resembles a low Ra uniroll flow in a cavity of infinite A_y. However, the resemblance is misleading. The stream function maximum for Fig. 9(*a*) is 33.2 compared with 10.9 for a flow in a cavity with adiabatic walls and $A_y = 0.2$ or 14.37 for a flow with no side wall interaction. Although heat transfer by the fluid is reduced by the presence of the conducting walls, the strength of the fluid motion is increased. The conducting walls, by offering an impedance to convective distortion of the temperature field, maintain horizontal temperature gradients over a large section of the cavity and the total production of vorticity is greater than if the walls were not present.

Calculations made for walls that are not perfectly conducting indicate consistent behavior between the two limiting conditions. Figure 10 shows the results of sample calculations for a cavity with $Ra = 3 \times 10^5$, $Pr = 0.71$, $A_y = 0.2$, and $A_w = 0.02$ for varying α. For this cavity, $\beta = 10$ so that the walls can be classed as being thin. In Fig. 10, Nu is plotted against $\alpha\beta$. The data suggest that the adiabatic condition exists for $\alpha\beta < 100$ and the perfectly conducting case for $\alpha\beta < 0.1$. The behavior of the overall Nusselt number Nu is shown by the broken line in Fig. 10. As the wall conduction increases, the contribution made by Nu_f to the total heat transport diminishes. For this example, by the time the perfect conduction condition is

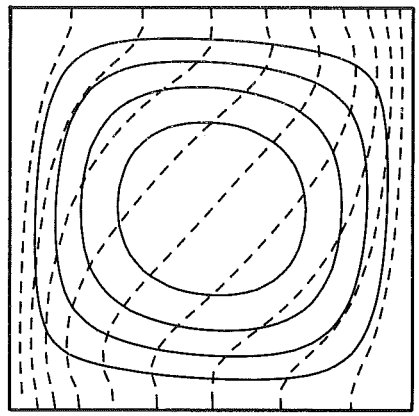

Fig. 9(*a*)

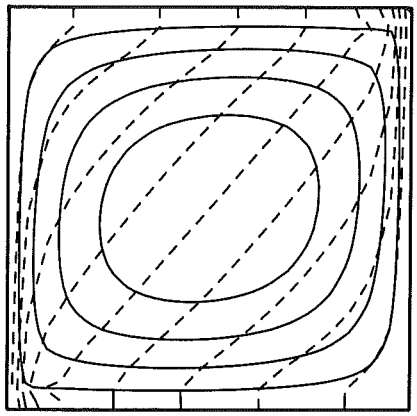

Fig. 9(*b*)

Fig. 9 Cavity heated from the side, $A_z = 1$, $Pr = 0.71$ and perfectly conducting walls: contour maps of stream function (solid lines) and temperature (broken lines) for $Ra = 3 = 10^5$; (*a*) $A_y = 0.2$; (*b*) $A_y = 0.2$, Hele Shaw approximation

reached, the contribution made by convection by the fluid is small.

If the sample calculation used for Fig. 10 was for an air-filled cavity with perspex side walls, the relevant parameter values would be $\alpha = 0.15$ and $\alpha\beta = 1.5$. The width of the side walls would have to be decreased by at least an order of magnitude to achieve the adiabatic condition. Whereas the perspex walls may perform adequately as adiabatic boundaries for a water-filled cavity ($\alpha\beta = 35$), they cannot perform adequately for an air-filled cavity.

4 Conclusions

The two-dimensional model, generated by making the assumption that the y variation of the x and z velocity components can be separated as a parabolic function, can be used to obtain numerical solutions which predict, in a consistent manner, the interaction of side walls (y boundaries) with a convecting fluid.

For the case of a slot heated from below, the model has been validated for adiabatic side walls via comparison with a Galerkin analysis made by Frick [8] and with a full three-dimensional analysis.

For the case of a slot of square cross section filled with air and heated from the side, the two-dimensional model is in good agreement with the three-dimensional analysis for adiabatic and perfectly conducting side walls.

Perfectly conducting walls have been shown to decrease the heat transfer by the fluid but to increase the strength of the fluid motion.

The results for the cases of side heating and heating from below indicate that the Hele Shaw model, which neglects

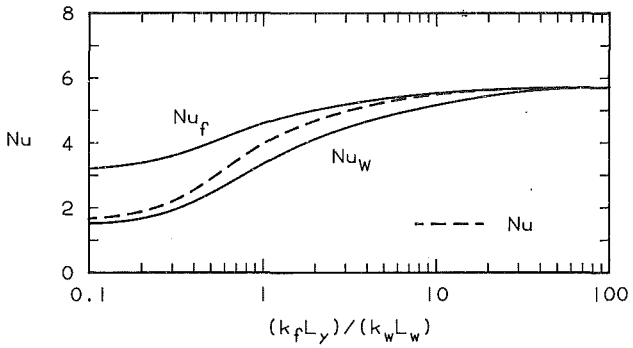

Fig. 10 Cavity heated from the side, $A_z = 1$, $Pr = 0.71$, $A_y = 0.2$, $\beta = 10$, and $Ra = 3 \times 10^5$: dependence of Nu, Nu_f, and Nu_w on $(k_fL_y)/(k_wL_w)$ (or $\alpha\beta$)

advection and cross-sectional diffusion of vorticity, overpredicts heat transfer for $A_y > 0.05$.

A sample calculation for imperfect walls indicates that $0.1 \leq \alpha\beta \leq 100$ corresponds to conditions between the limiting cases of perfectly conducting or adiabatic side walls.

References

1 Symons, J. G., and Peck, M. K., "Natural Convection Heat Transfer Through Inclined Longitudinal Slots," ASME JOURNAL OF HEAT TRANSFER, Vol. 106, 1984, pp. 824–829.

2 Elder, J. W., "Transient Convection in a Porous Medium," *Journal of Fluid Mechanics*, Vol. 27, 1967, pp. 609–623.

3 Hartline, B. K., and Lister, C. R., "Thermal Convection in a Hele-Shaw Cell," *Journal of Fluid Mechanics*, Vol. 79, 1977, pp. 379–389.

4 Frick, H., and Clever, R. M., "The Influence of Side Walls on Finite-Amplitude Convection in a Layer Heated From Below," *Journal of Fluid Mechanics*, Vol. 114, 1982, pp. 467–480.

5 Smart, D. R., Hollands, K. G. T., and Raithby, G. D., "Free Convection Heat Transfer Across Rectangular Celled Diathermanous Honeycombs," ASME JOURNAL OF HEAT TRANSFER, Vol. 102, 1980, pp. 75–80.

6 Meyer, B. A., Mitchel, J. W., and El-Wakil, M. M., "The Effect of Thermal Properties on Natural Convection in Inclined Rectangular Cells," ASME JOURNAL OF HEAT TRANSFER, Vol. 104, 1982, pp. 111–117.

7 Kim, D. M., and Viskanta, R., "Study of the Effects of Wall Conductance on Natural Convection in Differentially Oriented Square Cavities," *Journal of Fluid Mechanics*, Vol. 44, 1984, pp. 153–176.

8 Frick, H., "The Effect of Thermal Boundary Conditions on the Heat Transport in Vertical Channels Heated From Below," *International Journal of Heat and Mass Transfer*, Vol. 36, 1983, pp. 681–688.

9 Koster, J. N., and Muller, U., "Free Convection in Vertical Gaps," *Journal of Fluid Mechanics*, Vol. 125, 1982, pp. 429–451.

10 Mallinson, G. D., and de Vahl Davis, G., "The Method of the False Transient for the Solution of Coupled Elliptic Equations," *Journal of Computational Physics*, Vol. 12, 1973, pp. 435–461.

11 Mallinson, G. D., and de Vahl Davis, G., "Three Dimensional Natural Convection in a Box: a Numerical Study," *Journal of Fluid Mechanics*, Vol. 83, 1977, pp. 1–31.

12 Linthorst, S. J. M., Schinkel, W. M. M., and Hoogendoorn, C. J., "Flow Structure With Natural Convection in Inclined Air-Filled Enclosures," ASME JOURNAL OF HEAT TRANSFER, Vol. 103, 1981, pp. 535–539.

13 Koster, J. N., "Heat Transfer in Vertical Gaps," *International Journal of Heat and Mass Transfer*, Vol. 25, 1982, pp. 426–428.

Radiation-Induced Buoyancy-Driven Flow in Rectangular Enclosures: Experiment and Analysis

B. W. Webb
Assoc. Mem. ASME

R. Viskanta
Fellow ASME

Heat Transfer Laboratory,
School of Mechanical Engineering,
Purdue University,
West Lafayette, IN 47907

Experiments have been performed to study the rate of internal radiative heating on the natural convective motion in a vertical rectangular enclosure irradiated from the side. A Mach–Zehnder interferometer has been used to determine the temperature field, and a fluorescing dye injection technique was employed to illustrate the flow structure with water as the working fluid. A theoretical model is developed for predicting the absorption of thermal radiation and the subsequent buoyancy-driven flow. Predictions based on spectral calculations for the radiation flux divergence agree well with the experimental data.

Introduction

Radiation-induced buoyancy-driven flow is encountered in such technologies as laser fusion, crystal growth, processing of glass and other semitransparent materials, photochemical reactions, and collection and utilization of solar energy. The primary driving force for the natural convective motion in such systems is the volumetric absorption of thermal radiation in semitransparent materials. Most often the absorption of radiant energy in these materials is strongly wavelength dependent. The heat transfer and fluid flow may also be strongly affected by other variables such as the magnitude of the incident flux and its spectrum, the system geometry, reflectivity of the solid surfaces forming the enclosure, etc. This paper presents experimental and analytical results of an investigation of radiation-induced natural convective motion in a vertical rectangular enclosure.

There has been considerable work treating the interaction between radiation and natural convection in vertical slots and enclosures. Two previous investigations have presented the stability characteristics of radiation-absorbing vertical fluid layers (Arpaci and Bayazitoglu, 1973; Hassab and Ozisik, 1979). The effect of radiation exchange between surfaces of an enclosure bounding a nonparticipating fluid has also been studied both experimentally (Kim and Viskanta, 1984a) and analytically (Larson and Viskanta, 1976; Kim and Viskanta, 1984b). Some recent papers have treated analytically the effects of radiation on the natural convective motion of a radiatively participating gas in rectangular enclosures (Lauriat, 1982a; Lauriat, 1982b; Shih and Ren, 1983; Chang et al., 1983; Desreyaud and Lauriat, 1985).

All of the aforementioned investigations have treated the effects of radiation exchange on heat transfer in fluid layers bounded by differentially heated walls, a situation in which buoyant enclosure flow would exist anyway. Problem physics are expected to be quite different if the primary driving force for the buoyancy-driven flow is the volumetric absorption (deposition) of radiant energy by the fluid. This paper presents experimental results describing heat transfer and natural convective fluid motion in a vertical fluid layer resulting primarily from absorption of incident thermal radiation from an external source. A theoretical model is developed to predict the local rate of radiant energy deposition in the fluid and the resulting natural convective motion. Predictions from the theoretical model are compared to experimental results for the purpose of validating the model.

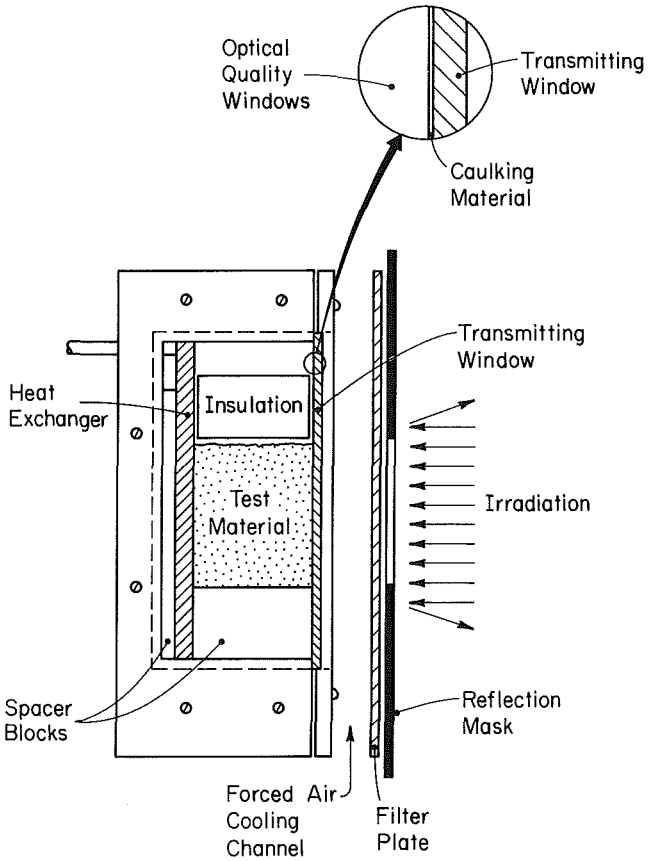

Fig. 1 Schematic of test apparatus

Experiments

Test Apparatus. Experiments have been performed to determine the temperature distribution and natural convective flow field in a rectangular enclosure arising from absorption of an externally incident radiation flux. To this end, a test cell was designed and constructed capable of use with a Mach–Zehnder interferometer and established flow visualization techniques. As shown in Fig. 1, the test cell consists of an acrylic C-shaped

Contributed by the Heat Transfer Division for publication in the JOURNAL OF HEAT TRANSFER. Manuscript received by the Heat Transfer Division June 2, 1986.

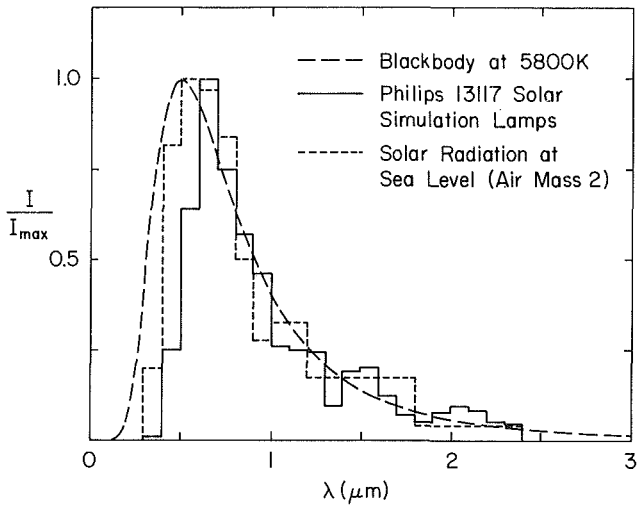

Fig. 2 Power spectrum of high-temperature lamps

frame which houses acrylic spacer blocks (for control of the cavity aspect ratio) and a heat exchanger. The heat exchanger was fabricated by milling serpentine countercurrent channels in a solid block of 1.27-cm-thick copper. Six copper-constantan thermocouples were situated flush with the heat exchanger surface through small drilled holes at various locations and were used to monitor the temperature uniformity over the fluid-exposed surface. The heat exchanger was then painted with a special solar absorber coating whose spectral absorption characteristics were known (3M Brand ECP-2200 Solar Absorber Coating). Thermally regulated fluid from a constant-temperature bath was circulated through the heat exchanger. In all tests the temperature variation across the coated surface was less than 0.3°C.

Optical quality windows were employed as front and back walls for the enclosure, providing optical access both for visualizing the flow and as a requirement for use in the Mach–Zehnder interferometer system. The windows were pressed against C-shaped O-rings located in milled grooves on each side of the primary test cell frame by acrylic faces. Six screws on either face of the optical quality windows were used to give the somewhat independent adjustment necessary for the initial infinite fringe setting of the interferometer. The front transmitting plate made of 0.63-cm-thick float glass was pressed against the optical quality windows with a flexible caulking sealing material in the joint. Despite reducing the thickness of the caulking material to less than 0.3 mm, a very thin vertical layer of the fluid field was not resolvable at the transmitting window by the Mach–Zehnder interferometer. The top of the acrylic test cell frame was left open for filling the enclosure. The upper free surface of the test fluid was insulated by inserting a 5-cm block of styrofoam insulation covered with duct tape snugly into the cell. Room temperature cooling air was forced through the channel formed by the filter plate and transmitting window with a four-speed centrifugal fan. Air proved to be an adequate cooling fluid since the majority of the lamp radiant energy is in spectral regions where the glass is effectively transparent (see Fig. 2). The purpose of the reflection mask placed over the filter plate was to allow only the test fluid to be exposed to the incident radiation flux. The average air velocity in the cooling channel was measured with an air velocity meter (TSI Model 1650), and the convective heat transfer coefficient at the glass-air interface was estimated to be 60 W/m^2K using accepted internal flow correlations (Incropera and DeWitt, 1985).

Once assembled the entire test cell was insulated with 5 cm of styrofoam insulation. Final interior dimensions were $4.8 \times 14.5 \times 4.1$ cm wide. The cell was mounted rigidly in the test leg of a Mach–Zehnder interferometer with 25-cm optics. An energy balance on the insulated test cell showed that heat loss to the ambient always amounted to less than 1 percent of the radiant energy incident on the fluid layer.

Radiation Source. Quartz halogen lamps with parabolic dichroic mirrors (Philips 13117) were used as the radiation source. The lamps offer the advantage that they simulate quite well the solar spectrum at sea level. As seen in the power spectrum of Fig. 2, radiation from the lamps is only slightly less concentrated in the visible than the solar spectrum, with virtually all energy lying in the spectral range 0.3–2.4 μm. Four of the circular lamps were arranged in a flexible frame for two-dimensional adjustment. The frame was adjusted to op-

Nomenclature

A = aspect ratio of cavity = H/D
D = depth of cavity, Fig. 4
F = local radiation flux
F° = radiation flux incident on test fluid (after being transmitted through the window)
$\bar{h}$ = average heat transfer coefficient at glass–air interface, Fig. 4
H = height of cavity, Fig. 4
k^* = thermal conductivity ratio = k_g/k
Pr = fluid Prandtl number = ν/α
q^* = local convective heat flux, equation (16)
Q^*_{rad} = local fraction of total absorbed radiant energy, equation (15)
Ra* = modified Rayleigh number = $g\beta F^\circ D^4/k\nu\alpha$
t = transmitting glass wall thickness
T = local temperature
U, V = dimensionless velocities = $(u, v)D/\alpha$
x, y = coordinates, Fig. 4
α = thermal diffusivity
β = thermal expansion coefficient
γ = interreflection function = $1-\rho_w\rho(\mu)e^{-2\tau_D/|\mu|}$
θ = dimensionless temperature = $(T - T_w)/(F^\circ D/k)$; or angle from normal of beam incident flux, Fig. 4
κ = absorption coefficient
λ = wavelength
μ = direction cosine, cos θ, Fig. 4
ν = kinematic viscosity
ξ, η = dimensionless coordinates = $(x, y)/D$
ρ = density or reflectivity
τ = transmissivity or optical depth, $\tau_\lambda = \int_0^x \kappa_\lambda dx$
τ_D = fluid layer opacity, $\tau_{D\lambda} = \int_0^D \kappa_\lambda dx$
Φ = dimensionless radiation flux = F/F°

Subscripts

b = beam component
d = diffuse component
g = glass
w = wall
λ = spectral quantity
∞ = ambient conditions

Superscripts

$^\circ$ = radiation quantity at $x = D$

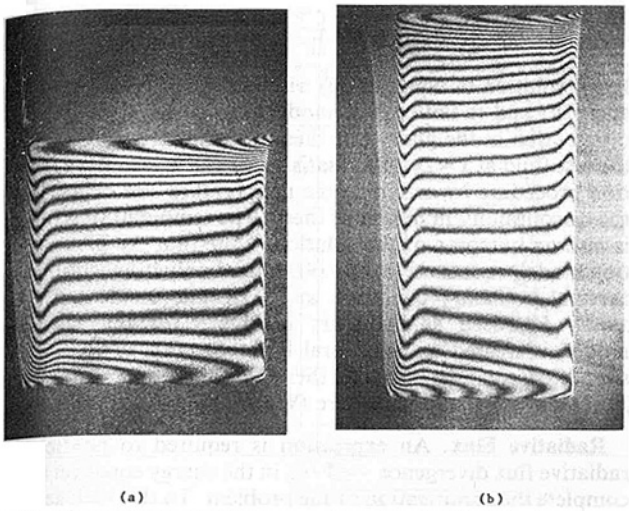

Fig. 3 Mach-Zehnder interferograms for water, incident flux level 1300 W/m^2, enclosure aspect ratios of (*a*) $A = 1.0$ and (*b*) $A = 2.0$

timize uniformity of the radiation flux over the transmitting window. A spatial uniformity of the irradiation of ±9 percent on the average was achieved over a typical 9 cm exposed test fluid height. Uniformity over the 4 cm exposed test cell width proved to be ±2 percent. The lamp optimization also revealed that radiation from the lamps closely approximates a totally beam (collimated) flux. This approximation will be used in the analytical part of the paper. Details of the lamp configuration may be found elsewhere (Webb, 1986).

Test Procedure. Deionized water was used as the test fluid. This was selected because the radiative and thermophysical properties are well-established. The water was degasified by boiling for approximately one hour. The fluid was allowed to cool and the test cell was then filled to the desired level. The test cell and fluid were allowed to equilibrate overnight, after which the optical quality windows and Mach-Zehnder interferometer were adjusted to achieve the "infinite fringe" condition. This insures that any subsequent variation in intensity is a result only of thermal disturbances in the system. The constant-temperature bath was set (near ambient temperature to reduce heat loss) and the regulated fluid was circulated through the heat exchanger. Both the centrifugal fan and the radiation lamps were turned on. The magnitude of the radiation flux was then measured at approximately eight locations over the exposed fluid. The average of these measurements was used in characterizing the flux level. Eight to ten hours were allowed for the system to reach steady state. Mach-Zehnder interference images were then recorded and flow visualization was performed if desired by injection of the fluorescing dye. It was found that the tracer fluorescence was brilliant enough for adequate photography when exposed to a 100-mW argon ion laser without extinguishing the high-temperature lamps. Interferograms were always recorded prior to performing the flow visualization so that the presence of the fluorescein tracer would not affect the index of refraction of the water. Additionally, new experiments were always begun by filling the test cell with fresh water.

Experimental Results. Figures 3(*a*) and 3(*b*) show typical interferograms for a radiation flux incident on the water layer of $F^\circ = 1300$ W/m^2 for enclosure aspect ratios of 1.0 and 2.0, respectively. The cooled wall and cooling air temperatures were 23.1°C and 22.3°C, respectively. It should be underlined that throughout the paper the magnitude of the total radiation flux incident on the water layer F° is determined from that measured experimentally. The transmittance of the two 0.64-cm-thick float glass plates was determined by a ray-tracing technique (Siegel and Howell, 1981) and was found to

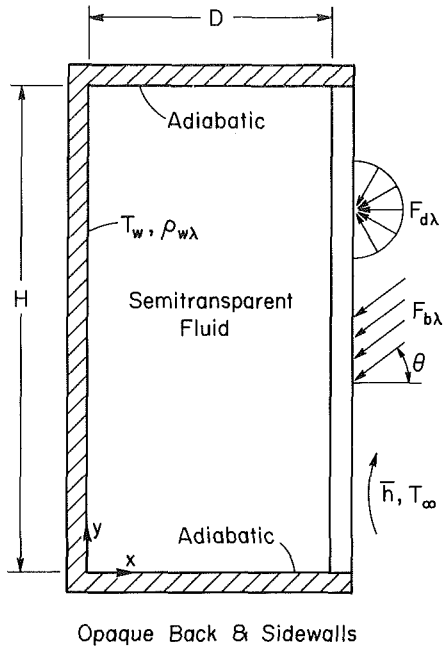

Fig. 4 Model coordinate system and pertinent parameters

be 61 percent based on the spectral transmittance of float glass (PPG, 1972). This agrees well with the 64 percent transmittance measured experimentally for two similarly spaced float glass plates irradiated at the same distance from the lamps. The difference in the fringe densities at the two vertical walls seen in Figs. 3(*a*) and 3(*b*) is indicative of absorption of radiation; higher fringe density at the cooled (heat exchanger) wall indicates higher convective heat transfer there. Interferograms were interpreted and lines of constant intensity converted to isotherms using the methods outlined in the literature (Hauf and Grigull, 1970; Eckert and Goldstein, 1976). Each fringe in this system corresponds to an approximate temperature difference of 0.14°C. Boundary layers are present on both vertical walls, the boundary layer at the cooled wall being the thinnest. The interior core of the enclosure is stagnant and stably stratified. Deviations from the desired adiabatic condition at the top and bottom boundaries are evident, although slight. Calculation of the local convective heat flux at the opaque wall from the interferograms was not possible due to the extremely high fringe densities there. Results for lower Rayleigh numbers were qualitatively similar.

The fluid flow structure may be inferred from the interferograms in Fig. 3. Fluid is heated by absorption of thermal radiation near the transmitting wall and rises to the top of the cavity. The fluid flows along the top free surface and is drawn into the thin boundary layer at the opaque wall, falling as it cools. The interior core appears to be stagnant. The flow pattern inferred here from the interferograms has been corroborated by the flow visualization experiments and will be presented in a later section.

Analysis

Physical Model. Consider a vertical layer of semitransparent fluid as shown in Fig. 4. One vertical wall is opaque with known spectral reflectivity and is maintained at constant temperature. The opposite vertical wall is semitransparent and serves to confine the fluid and transmit the external radiant energy incident upon it. The two horizontal boundaries are assumed adiabatic, the upper one being a free surface.

The radiation flux incident at $x = D$ penetrates the fluid layer and is absorbed, resulting in local volumetric heating and

subsequent buoyancy-driven flow. The radiation flux is assumed to be one-dimensional. The flow is assumed to be steady, two-dimensional, and laminar. The thermophysical properties are taken to be constant and the Boussinesq approximation is invoked, allowing for density variations in the flow field only insofar as they contribute to natural convective motion.

Governing Equations. Introducing the dimensionless variables defined in the Nomenclature, and under the assumptions outlined in the foregoing, the partial differential equations governing the transport of mass, momentum, and energy may be written as:

Mass:

$$\frac{\partial U}{\partial \xi}+\frac{\partial V}{\partial \eta}=0 \tag{1}$$

Momentum:

$$U\frac{\partial U}{\partial \xi}+V\frac{\partial U}{\partial \eta}=-\frac{\partial P}{\partial \xi}+\mathrm{Pr}\left[\frac{\partial^2 U}{\partial \xi^2}+\frac{\partial^2 U}{\partial \eta^2}\right] \tag{2}$$

$$U\frac{\partial V}{\partial \xi}+V\frac{\partial V}{\partial \eta}=-\frac{\partial P}{\partial \eta}+\mathrm{Pr}\left[\frac{\partial^2 V}{\partial \xi^2}+\frac{\partial^2 V}{\partial \eta^2}\right]+\mathrm{Ra}^*\mathrm{Pr}\theta \tag{3}$$

Energy:

$$U\frac{\partial \theta}{\partial \xi}+V\frac{\partial \theta}{\partial \eta}=\frac{\partial^2 \theta}{\partial \xi^2}+\frac{\partial^2 \theta}{\partial \eta^2}-\frac{d\Phi}{d\xi} \tag{4}$$

Note that the momentum and energy equations are strongly coupled through the buoyancy and convective terms. The boundary conditions completing the specification of the problem are stated as follows:

$$\eta=0, \qquad U=V=\frac{\partial \theta}{\partial \eta}=0 \tag{5a}$$

$$\eta=A, \qquad \frac{\partial U}{\partial \eta}=V=\frac{\partial \theta}{\partial \eta}=0 \tag{5b}$$

$$\xi=0, \qquad U=V=\theta=0 \tag{5c}$$

$$\xi=1, \qquad U=V=0 \tag{5d}$$

$$\theta=\theta_g, \quad k^*\frac{\partial \theta_g}{\partial \xi}=\frac{\partial \theta}{\partial \xi} \tag{5e}$$

The thermal boundary condition at $\xi=1$, equation (5*e*), requires continuity of both temperature and local heat flux at the glass–fluid interface. Since the transmitting wall is long and slender and the convective cooling at the glass–air interface is quite high, heat transfer through the transmitting wall can be assumed one-dimensional. The equation governing energy transport in the glass window may then be stated in dimensional form as

$$k_g\frac{d^2T_g}{dx'^2}-\frac{dF}{dx'}=0 \tag{6}$$

with boundary conditions

$$x'=0, \qquad T_g=T(D,y) \tag{7a}$$

$$x'=t, \qquad -k_g\frac{dT_g}{dx'}=\bar{h}(T-T_\infty) \tag{7b}$$

The local radiation flux in the glass is approximated by a simple gray exponential model of the form

$$F(x')=-\tau^\circ G^\circ e^{-\bar{\kappa}_g(t-x')} \tag{8}$$

where $\tau^\circ G^\circ$ is the flux transmitted into the glass across the air–glass interface. In writing this expression interreflections of radiation between the two interfaces were ignored (Viskanta and Anderson, 1975). The mean absorption coefficient $\bar{\kappa}_g$ was determined by a weighted average over the spectrum of the irradiation as follows:

$$\bar{\kappa}_g=\int_0^\infty \tau_\lambda^\circ G_\lambda^\circ \kappa_\lambda d\lambda \Big/ \int_0^\infty \tau_\lambda^\circ G_\lambda^\circ d\lambda \tag{9}$$

Exact solution of equation (6) with boundary conditions (7*a*) and (7*b*) and radiation flux model (8) yields the temperature distribution in the glass. The thermal boundary condition for the test fluid at $x=D$ is then satisfied iteratively in the calculation procedure by matching the temperature and heat flux at the discontinuity in materials there. The temperature $T(D, y)$ is also an outcome of the solution. Note that the gray radiation model, equations (8) and (9), is used only in specifying the thermal boundary condition at $x=D$. The incident flux at $x=D$, F_λ°, used as boundary condition for the radiation model, is treated on a spectral basis. Specific details of the simplified treatment of the thermal boundary condition at $x=D$ may be found elsewhere (Webb, 1986).

Radiative Flux. An expression is required to predict the radiative flux divergence $-d\Phi/d\xi$ in the energy equation (4) to complete the specification of the problem. To this end, several additional assumptions relative to the radiation transfer in the system are invoked. As stated earlier, radiant energy transfer is assumed to be one-dimensional. The fluid layer is assumed to be nonemitting, an assumption justified by the fact that relatively low temperatures are found in the system and emission will be in spectral regions where the fluid is effectively opaque. The flux incident on the fluid layer is approximated as the sum of diffuse and beam components, $F^\circ=F_d^\circ+\mu^\circ F_b^\circ$. Scattering is assumed to be negligible. However, the model is also valid for radiant transfer in materials for which scattering is predominantly in the forward direction. The opaque wall of reflectivity $\rho_{w\lambda}$ is assumed to be a diffuse reflector. This model for the deposition of radiation flux was first formulated for the study of radiant transfer in stagnant horizontal layers of water (Viskanta and Toor, 1972), and was validated experimentally (Snider and Viskanta, 1975). The expressions for the spectral radiative flux and the flux divergence, nondimensionalized here are, respectively,

$$-\Phi_\lambda(\xi)=2\left[\frac{1}{2}\mu^\circ\tau(\mu^\circ)\Phi_{b\lambda}^\circ e^{-(\tau_{D\lambda}-\tau_\lambda)/\mu}/\gamma(\tau_{D\lambda},|\mu_i'|)+\Phi_{d\lambda}^\circ T_3(\tau_{D\lambda}-\tau_\lambda)-\Phi_{b\lambda}^* E_3(\tau_\lambda)\right] \tag{10}$$

and

$$-\frac{d\Phi_\lambda}{d\xi}=2\tau_{D\lambda}\left[\frac{1}{2}(\mu^\circ/\mu)\tau(\mu^\circ)\Phi_{b\lambda}^\circ e^{-(\tau_{D\lambda}-\tau_\lambda)/\mu}/\gamma(\tau_{D\lambda},|\mu_i'|)+\Phi_{d\lambda}^\circ T_2(\tau_{D\lambda}-\tau_\lambda)+\Phi_{b\lambda}^* E_2(\tau_\lambda)\right] \tag{11}$$

where the flux at the opaque wall is given by

$$\Phi_{b\lambda}^*=2\rho_{w\lambda}\left[\frac{1}{2}\mu^\circ\tau(\mu^\circ)\Phi_{b\lambda}^\circ e^{-\tau_{D\lambda}/\mu}/\gamma(\tau_{D\lambda},|\mu_i'|)+\Phi_{d\lambda}^\circ T_3(\tau_{D\lambda})\right] \tag{12}$$

The exponential and transmission integrals are given by

$$E_n(x)=\int_0^1 e^{-x/\mu}\mu^{n-2}d\mu \tag{13a}$$

$$T_2(x)=\int_0^1 \tau(\mu')e^{-x/\mu}(\mu'/\mu)d\mu'/\gamma(\tau_D,|\mu_i'|) \tag{13b}$$

$$T_3(x)=\int_0^1 \tau(\mu')e^{-x/\mu}\mu' d\mu'/\gamma(\tau_D,|\mu_i'|) \tag{13c}$$

Under the framework of the model proposed here the spectral radiation flux incident on the fluid layer F_λ° is calculated by a ray-tracing method (Siegel and Howell, 1981) based on the spectral transmittance of the float glass filter plate and transmitting window. The modification of the radiation spectrum emitted by the lamps in the presence of the filter plate and transmitting window is therefore properly handled. This

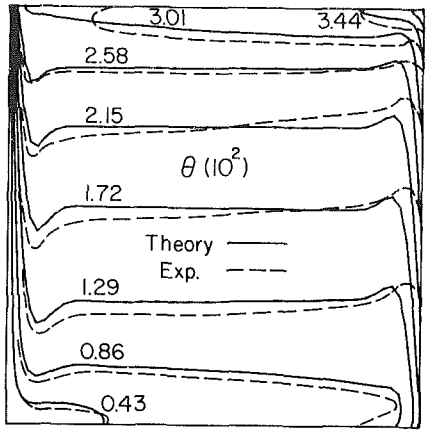

Fig. 5(a)

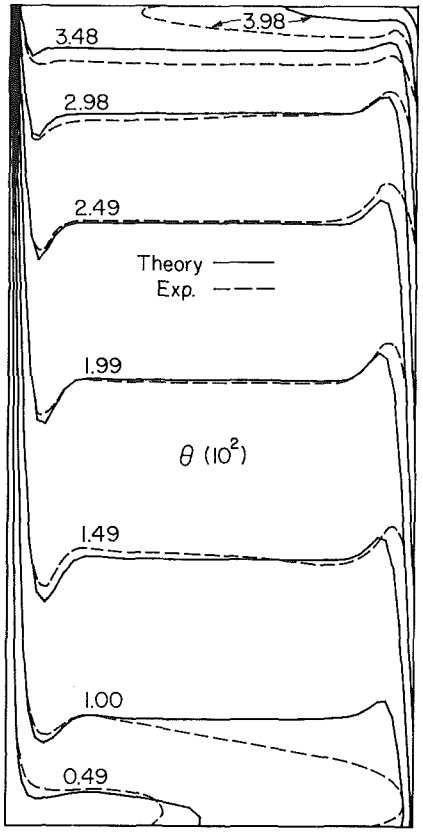

Fig. 5(b)

Fig. 5 Predicted and experimentally measured isotherms for nominal Rayleigh numer $Ra^* = 2.3(10^8)$, (a) $A = 1.0$ and (b) $A = 2.0$

flux F_λ° serves as the boundary condition for the radiative transfer equation and is assumed known just inside the fluid layer. Consequently, the surface reflectivity $\rho(\mu^\circ) = 0$, which yields $\tau(\mu^\circ) = 1$. Then the transmission integral functions $T_2(x)$ and $T_3(x)$ reduce to exponential integral functions of the same order. This simplification results in a slight error since the reflectivity at the transmitting wall–test fluid interface is not rigorously accounted for. However, this error is negligible since that reflectivity is of order 0.005. The external radiation flux is modeled as entirely collimated based on experiments, and is assumed to be normally incident.

Method of Solution. The conservation equations of mass, momentum, and energy, and their boundary conditions, equations (1)–(5), along with the expression for the radiation flux divergence, equation (11), complete the mathematical formulation of the problem. A closed-form analytical solution is not possible. The equations were therefore solved numerically. The control volume scheme of Patankar (1980) was used to reduce the governing partial differential equations to a set of nominally linear-algebraic equations. The SIMPLER algorithm was employed to treat the coupling between pressure and momentum. Nodes were clustered near the vertical walls in order to accurately model thin boundary layers and large gradients in the radiative flux. A power-law clustering scheme was used with vertical control surfaces being generated, for example, according to the formula

$$\xi_i = \frac{1}{2}\left(\frac{i-1}{M}\right)^m, \qquad i = 1,2, \ldots, M+1 \tag{14}$$

where $2M$ is the number of control volumes across the depth of the domain $0 \le \xi \le 1$. It was found that an exponent $m = 1.75$ provided good resolution of the spatial flux gradient at $\xi = 1$ and velocity and thermal boundary layers at $\xi = 0$ and 1. A grid size study on computational meshes from 14×14 to 40×40 control volumes was conducted to demonstrate grid independence of the results after which the 40×40 grid was selected. The difference in the magnitude of the maximum stream function was less than 1 percent between the 30×30 and 40×40 control volume grids. Nodes were clustered near the solid walls in order to resolve the fine thermal and hydrodynamic boundary layer expected there. Iterations were terminated when radiant energy absorption integrated over the layer depth matched the sum of heat transfer by convection to the isothermal wall and heat transfer to the ambient from the transmitting wall to within 0.1 percent.

The expression for the radiation flux divergence, equation (11), was used to calculate the source term in the energy equation at each node. The spectral absorption coefficient of water (Goldstein and Penner, 1964; Hale and Querry, 1973) varies nearly seven orders of magnitude in the spectral range of interest. It ranges from about 10^{-2} m^{-1} at 0.5 μm to about 10^4 m^{-1} at 2.0 μm. This makes the definition of an appropriate gray model absorption coefficient impossible. As a result, calculations were carried out on a spectral basis. The spectrum of the radiation source was divided into 20 wavelength intervals over which the absorption coefficient was assumed constant. The spectral transmittance of the filter plate and transmitting wall was also determined on this basis to give the spectral flux at the transmitting wall–water interface F_λ°. Contributions from each spectral band were summed to give the total radiation flux divergence. Twenty spectral bands were deemed adequate to accurately resolve the strong wavelength dependence of water absorption.

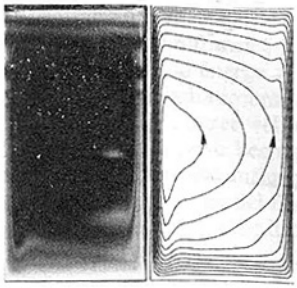

Fig. 6 Comparison of flow visualization results with predicted streamlines ($\Delta\psi = \psi_{max}/12$) for $Ra = 2.26(10^8)$, $A = 2.0$

Results and Discussion

Comparison With Experiment. Predicted isotherms are compared to those measured experimentally for a nominal $Ra^* = 2.3$ (10^8), $Pr = 6.05$, and enclosure aspect ratios of 1 and 2 in Figs. 5(a) and 5(b), respectively. Very good agreement is seen in the prediction of the thermal boundary layer at the

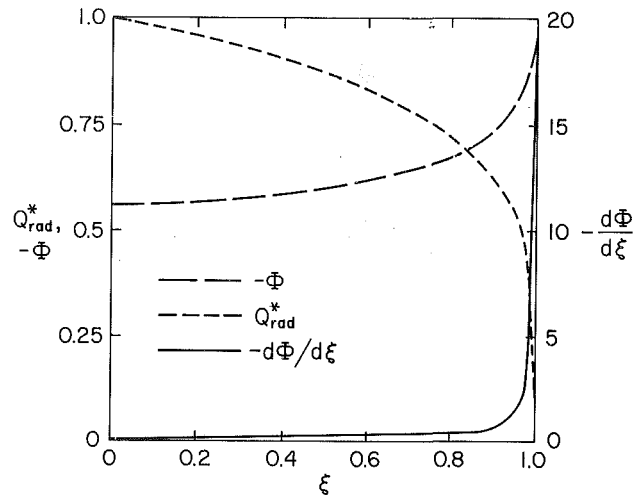

Fig. 7 Profile of the predicted total radiative flux and flux divergence, and local fraction of total radiant energy absorbed based on spectral absorption coefficient for water

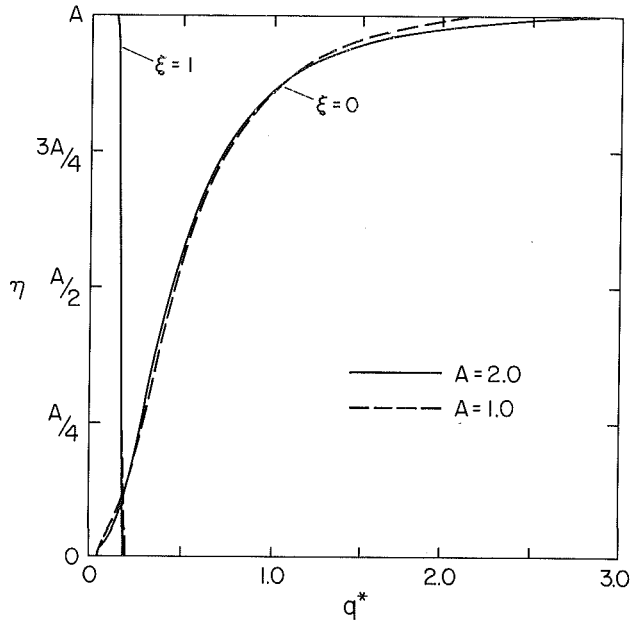

Fig. 8 Profiles of the convective heat flux to the test fluid at the cooled wall and transmitting wall for Ra = 2.26(10^8), A = 1.0 and A = 2.0

cooled wall and in the central stagnant core. Discrepancies at the top and bottom horizontal boundaries are due to the experimental inability to achieve an adiabatic condition. The discrepancy at the top free surface may also be attributed somewhat to free surface effects; the surface tension forces and subsequent flow were not accounted for. Only fair agreement is seen between model predictions and experimental data at the transmitting wall. Local temperatures here are predicted only moderately well by the special treatment of the thermal boundary condition at the glass-water interface. The discrepancies may be attributed to the difficulty in accurately predicting the high gradients in the flux divergence at $\xi = 1$. As will be shown later, the predicted radiative flux divergence drops dramatically in a very thin layer of fluid near $\xi = 1$. There is then an obvious difficulty in resolving accurately the internal radiative heating with a finite number of computational nodes. Additionally, the radiation band model used to treat the spectral dependence of the absorption coefficient effectively averages κ_λ over each wavelength interval. The predicted radiative flux will certainly be more sensitive to the band model employed in wavelength regions where the absorption coefficient κ_λ is large and/or its variation with wavelength is great.

Another source of error is the difficulty in specifying the local cooling at the glass-air interface. This was handled on an average basis over the height of the transmitting glass wall. However, the good agreement at the cooled wall and in the central core of the enclosure suggests that the simplified boundary condition at $\xi = 1$ accounts for global absorption and subsequent convective heat transfer from the transmitting window to the test fluid. As will be shown later, the formation of a boundary layer near $\xi = 1$ is largely a result of radiant energy absorption by the water in the infrared part of the spectrum where the absorption coefficient and the radiation flux divergence $-d\Phi/d\xi$ are very high.

A photograph of the fluorescein dye flow visualization for $A = 2$, $Ra^* = 2.26(10^8)$ is compared to model predictions in Fig. 6. The fluorescing dye was injected at the top against the cooled wall. The dye fell quickly along the wall to the cavity floor where it turned and formed a curious hump. The hydrodynamic boundary layer was so thin at the cooled wall that traces of the dyed fluid were torn off by the shear layer at different heights and penetrated the stagnant core. These ribbons of tracer migrated slowly across the stagnant central zone and were entrained in the boundary layer at the transmitting wall. This is evident in the photograph. The fluid is heated both volumetrically and convectively near the glass wall and rises to the top. Here again it turns, forming another hump although not as apparent nor intense as the one in the opposite corner at the bottom. The general flow pattern is predicted quite well by the model. Thin hydrodynamic boundary layers are evident at both walls, being thinner, however, at the cooled wall. The large slowly rotating mass of fluid at the interior of the cavity is evident in both predicted and visualized flow structure. The velocity humps at the base of the cooled wall and the top of the transmitting wall are also predicted by the model. These humps appear to be the natural hydrodynamic mechanism for expansion from thin to thicker velocity boundary layers. The flow pattern loses the centrosymmetry characteristic of natural convection in cavities with differentially heated side walls. The eddy center has been displaced to a position very near the cooled wall. This is due to the fact that the force driving the fluid motion, internal radiative heating, is able to penetrate the fluid layer and heat more directly the fluid in the interior of the cavity.

Radiative Transfer. Figure 7 shows the profile of the predicted radiative flux and flux divergence, based on the spectral calculations for equation (10). Also illustrated is the local fraction of total radiant energy absorbed calculated from

$$Q^*_{rad} = 1 - \int_0^\xi \left(-\frac{d\Phi}{d\xi}\right) d\xi \Big/ \int_0^1 \left(-\frac{d\Phi}{d\xi}\right) d\xi \qquad (15)$$

The high absorption of radiation at $\xi = 1$ near the transmitting wall is due to the extremely high absorption coefficient of water in the near-infrared part of the spectrum. Nearly 25 percent of the radiant energy from the high-temperature lamps lies in the spectral region $\lambda > 1.2$ μm, where the absorption coefficient is 100 m^{-1} or higher. Consequently, virtually all of the energy in this spectral range is deposited in a very thin fluid layer near $\xi = 1$. One can see from Fig. 7 that about 60 percent of the total radiant energy deposited is absorbed in the first 20 percent of the fluid layer. This explains in part the thermal and hydrodynamic boundary layer development at the transmitting wall. The remaining 40 percent of the total energy absorbed is able to penetrate the fluid and heat the internal layers.

Heat Transfer. The predicted local convective heat flux to the test fluid at the cooled and transmitting walls was

calculated from the converged temperature field by evaluating the derivative

$$q^*(\eta) = \frac{\partial \theta}{\partial \xi}\Big|_{\xi=0 \text{ or } 1} \tag{16}$$

The profiles of the convective heat flux are shown in Fig. 8 for $A = 1$ and 2. A dimensionless heat flux is presented rather than a Nusselt number because there is no appropriate temperature difference on which to base a Nusselt number. The special treatment of the thermal boundary condition at $\xi = 1$ predicts very little variation in heat flux over the height of the transmitting wall. This is not surprising in light of the weak variation of the temperature gradient $\partial\theta/\partial\xi$ along the height of the transmitting wall seen experimentally (see Fig. 3) for both aspect ratio cavities. As expected for the high Rayleigh number studied the convective heat flux at the cooled wall varies dramatically over the height of the cooled wall. Most of the heat transfer takes place near the top where warm fluid first contacts the isothermal wall. Convective heat transfer near the base of the cooled wall is very low. The high variation of q^* along the cooled wall is a consequence of convection-dominated heat transfer at high Rayleigh number.

It is interesting that based on a normalized coordinate ($0 \le \eta \le A$) the local convective heat transfer varies little for $A = 1$ and 2. The major difference is near $\eta = A$ where results for $A = 2$ show somewhat higher heat flux. The local heat flux at the transmitting wall for the two different aspect ratios studied is virtually the same. These trends suggest that for the cases studied here the local heat transfer is nearly independent of aspect ratio in a cavity where the natural convective flow is primarily the result of absorption of thermal radiation.

Based on predictions for the radiation flux field, approximately 45 percent of the total flux incident at the glass–water interface F° is absorbed in the fluid layer. The remainder penetrates the fluid layer unattenuated and is absorbed by the near-black heat exchanger surface. This is a consequence of the fact that the absorption coefficient is low in spectral regions where much of the irradiation is concentrated.

A portion of the total energy input to the fluid layer is due to surface heating from the transmitting wall. Model predictions reveal that 70 percent of the total energy input to the system (internal radiative heating + convective surface heating at the transmitting wall) is from the direct absorption of radiation. While some of the flow and heat transfer is due to convective surface heating at the transmitting wall (about 30 percent), the primary driving force is the volumetric absorption of thermal radiation by the fluid.

Conclusions

Experiments have been performed to determine the temperature field and flow structure for radiation-induced natural convection in a vertical rectangular enclosure irradiated from the side. A Mach–Zehnder interferometer was used to map the temperature field, and fluorescing dye injection was used as a technique for visualizing the flow patterns. The experimental results showed thin hydrodynamic boundary layers at the vertical walls, being thinner, however, at the cooled wall. Interferograms illustrate that for $Ra^* = 2.3(10^8)$, a convection regime prevails with thin thermal boundary layers at the vertical walls and a stagnant, stably stratified central core. The absorption of radiation in the fluid is manifested by a difference in interference fringe densities at the vertical boundaries. The flow structure loses completely the centrosymmetry characteristic of natural convection in cavities with differentially heated walls.

A theoretical model has been developed for predicting the internal radiative heating of the fluid and subsequent buoyancy-induced motion. The two-dimensional conservation equations of mass, momentum, and energy are solved in conjunction with a one-dimensional radiation model. Predictions based on spectral band calculations agree well with experimental data. Parametric calculations have been performed with the model presented to determine the influence of Rayleigh number, fluid Prandtl number, gray model fluid layer opacity on the temperature and flow fields, and the detailed results are described elsewhere (Webb, 1986).

Acknowledgments

One of the authors (B.W.W.) wishes to acknowledge support of his graduate studies by an Eastman Kodak Co. Graduate Fellowship. Computer facilities were made available by the Purdue University Computing Center.

References

Arpaci, V. S., and Bayazitoglu, Y., 1973, "Thermal Stability of Radiating Fluids: Asymmetric Slot Problem," *Physics of Fluids*, Vol. 16, pp. 589–593.

Chang, L. C., Yang, K. T., and Lloyd, J. R., 1983, "Radiation-Natural Convection Interactions in Two-Dimensional Complex Enclosures," ASME JOURNAL OF HEAT TRANSFER, Vol. 105, pp. 89–95.

Desreyaud, G., and Lauriat, G., 1985, "Natural Convection of a Radiating Fluid in a Vertical Layer," ASME JOURNAL OF HEAT TRANSFER, Vol. 107, pp. 710–712.

Eckert, E. R. G., and Goldstein, R. J., 1976, "Optical Measurement of Temperature," in: *Measurements in Heat Transfer*, 2nd ed., R. J. Goldstein, ed., Hemisphere, Washington, DC.

Goldstein, R., and Penner, S. S., 1964, "The Near-Infrared Absorption of Liquid Water at Temperatures Between 27 and 209°C," *Journal of Quantitative Spectroscopy and Radiative Transfer*, Vol. 4, pp. 441–451.

Hale, G. M., and Querry, M. R., 1973, "Optical Constants of Water in the 200-nm to 200-μm Wavelength Region," *Applied Optics*, Vol. 12, pp. 555–563.

Hassab, M. A., and Ozisik, M. N., 1979, "Effects of Radiation and Convective Boundary Conditions on the Stability of Fluid in an Inclined Slender Slot," *International Journal of Heat and Mass Transfer*, Vol. 22, pp. 1095–1105.

Hauf, W., and Grigull, U., 1970, "Optical Methods in Heat Transfer," in: *Advances in Heat Transfer*, Vol. 6, J. P. Hartnett and T. F. Irvine, eds., Academic Press, New York, pp. 133–366.

Incropera, F. P., and DeWitt, D. P., 1985, *Introduction to Heat Transfer*, Wiley, New York.

Kim, D. M., and Viskanta, R., 1984a, "Heat Transfer by Conduction, Natural Convection, and Radiation Across a Rectangular Cellular Structure," *International Journal of Heat and Fluid Flow*, Vol. 5, pp. 205–213.

Kim, D. M., and Viskanta, R., 1984b, "Effect of Wall Conduction and Radiation on Natural Convection in a Rectangular Cavity," *Numerical Heat Transfer*, Vol. 7, pp. 449–470.

Larson, D. W., and Viskanta, R., 1976, "Transient Combined Laminar Free Convection and Radiation in a Rectangular Enclosure," *Journal of Fluid Mechanics*, Vol. 78, pp. 65–85.

Lauriat, G., 1982a, "Combined Radiation-Convection in Gray Fluids Enclosed in Vertical Cavities," ASME JOURNAL OF HEAT TRANSFER, Vol. 104, pp. 609–615.

Lauriat, G., 1982b, "Numerical Study of the Interaction of Natural Convection With Radiation in Nongray Gases in a Narrow Vertical Cavity," in: *Heat Transfer—1982*, Hemisphere, Washington, Vol. 2, pp. 153–158.

PPG Industries Technical Bulletin, 1972, "Float Glass."

Patankar, S. V., 1980, *Numerical Heat Transfer and Fluid Flow*, McGraw-Hill, New York.

Shih, T. M., and Ren, A. L., 1983, "Combined Convective and Radiative Recirculating Flows in Enclosures," in: *Natural Convection in Enclosures—1983*, I. Catton and K. E. Torrance, eds., ASME, New York, pp. 49–57.

Siegel, R., and Howell, J. R., 1981, *Thermal Radiation Heat Transfer*, 2nd ed., Hemisphere, Washington.

Snider, D. M., and Viskanta, R., 1975, "Radiation-Induced Thermal Stratification in Surface Layers of Stagnant Water," ASME JOURNAL OF HEAT TRANSFER, Vol. 97, pp. 35–39.

Viskanta, R., and Toor, J. S., 1972, "Radiant Energy Transfer in Waters," *Water Resources Research*, Vol. 8, pp. 595–608.

Viskanta, R., and Anderson, E. E., 1975, "Heat Transfer in Semitransparent Solids," in: *Advances in Heat Transfer*, Vol. 11, T. F. Irvine, Jr. and J. P. Hartnett, eds., Academic Press, New York, pp. 317–441.

Webb, B. W., 1986, "Radiation-Induced Melting of Semitransparent Materials," Ph.D. Thesis, Purdue University, West Lafayette, IN.

Mixed-Convection Flow and Heat Transfer in the Entry Region of a Horizontal Rectangular Duct

F. P. Incropera
A. L. Knox
J. R. Maughan

Heat Transfer Laboratory,
School of Mechanical Engineering,
Purdue University,
West Lafayette, IN 47907

Entry-region hydrodynamic and thermal conditions have been experimentally determined for laminar mixed-convection water flow through a horizontal rectangular duct with uniform bottom heating. Direct heating of 0.05 mm stainless steel foil was used to minimize wall conduction, and the foil was instrumented to yield spanwise and longitudinal distributions of the Nusselt number. Flow visualization revealed the existence of four regimes corresponding to laminar forced convection, laminar mixed convection, transitional mixed convection, and turbulent free convection. The laminar mixed-convection regime was dominated by ascending thermals which developed into mushroom-shaped longitudinal vortices. Hydrodynamic instability resulted in breakdown of the vortices and subsequent transition to turbulent flow. The longitudinal distribution of the Nusselt number was characterized by a minimum, which followed the onset of mixed convection, and subsequent oscillations due to development of the buoyancy-driven secondary flow.

Introduction

For laminar flow in horizontal channels heated from below, buoyancy forces are known to induce secondary flows which enhance heat transfer and induce transition to turbulence. In an early study performed for airflow between isothermal parallel plates (Mori and Uchida, 1966), the secondary flow was observed to be in the form of longitudinal vortex rolls and, for Rayleigh numbers less than approximately 18,000, linear stability analysis yielded a roll pitch λ which was twice the plate spacing H. This existence of *first-type vortex rolls*, for which the roll height corresponds to the plate spacing, was confirmed by flow visualization for values of H up to approximately 15 mm, beyond which λ was independent of H. For larger Rayleigh numbers, stability analysis suggested *second-type vortex rolls* for which $\lambda \approx H$ and the roll height is $H/2$.

Longitudinal rolls were predicted in subsequent three-dimensional, thermal entry-region solutions for which streamwise diffusion was neglected. For uniform wall heat flux, Cheng et al. (1972) found that, with increasing Rayleigh number, the length of the thermal entry region decreased, while heat transfer enhancement in the fully developed region increased. Moreover, irrespective of aspect ratio in the range $0.2 \leq A \leq 5$, the secondary flow was predicted to consist of two large rolls which encompassed the cross-stream plane, implying that the roll pitch varied with aspect ratio from $0.2H$ to $5H$. Although similar trends were predicted for uniform wall temperature (Ou et al., 1974), the secondary flow decayed and heat transfer enhancement diminished as the mean fluid temperature approached the wall temperature.

In experiments performed for fully developed air flow between isothermal plates, Ostrach and Kamotani (1975) confirmed the existence of the first-type vortex rolls ($\lambda \approx 2H$) for Rayleigh numbers in the range $1708 < \mathrm{Ra} < 8000$, but questioned the independence of λ on H for $H > 15$ mm. In subsequent experiments (Kamotani and Ostrach, 1976; Kamotani et al., 1979), which were performed for larger Rayleigh numbers up to 2×10^5 and included the thermal entry region, flow visualization suggested the existence of second-type rolls ($\lambda \approx H$). Formation of a roll was attributed to a column of fluid (a thermal) which ascended from the bottom plate. It was suggested that, with increasing longitudinal coordinate z, shear forces induced by the main flow cause the thermal to bifurcate and curl back to the heated surface such that, when viewed in the spanwise plane, the boundaries of the secondary flow are mushroom shaped. Heat transfer measurements revealed a departure from forced convection behavior in the entry region and significant heat transfer enhancement in a fully developed region. Secondary flow in the form of longitudinal rolls or mushroom-shaped vortices, as well as attendant heat transfer enhancement, has also been reported for stratified, gas–liquid flow over a horizonal plate (Hung and Davis, 1974; Davis and Choi, 1977), for water in parallel flow over a heated horizontal plane (Gilpin et al., 1978; Imura et al., 1978), and for air flow along an embedded line source (Smith et al., 1986).

The thermal entry region solutions of Cheng et al. (1972) and Ou et al. (1974) were extended to a larger aspect ratio ($A = 10$) by Cheng and Ou (1982). In contrast to the previous solutions, the secondary flow was predicted to begin with sidewall rolls which grew with increasing z, inducing the formation of neighboring vortices and eventually producing 12 rolls for the entire cross-stream plane ($\lambda = 1.67H$). Onset of the secondary flow corresponded to a departure of the Nusselt number from the forced convection limit, and, with increasing z, Nu increased continuously from a characteristic minimum to a value associated with fully developed conditions. Although predicting similar behavior for the variation of Nu with z, the three-dimensional combined entry region solution of Abou-Ellail and Morcos (1983) yielded secondary flows in the form of two large rolls for $1 \leq A \leq 4$.

More recently, experiments were performed for laminar water flow in the thermal entry region of a horizontal duct (Osborne and Incropera, 1985). The experiments were characterized by uniform bottom heating, although conditions were strongly influenced by conjugate effects. Buoyancy-induced heat transfer enhancement was significant, and the Nusselt number data were correlated in terms of the inverse Graetz and Rayleigh numbers. Although the variation of Nu with z approached a fully developed condition, it was not characterized by a minimum in Nu. Flow visualization revealed plumes rising from the bottom surface and, in combination with fluid temperature measurements, suggested the existence of spatially and temporally random conditions. Failure to detect longitudinal rolls and a minimum in the Nu–z distribution may have been due to conjugate effects and/or to limitations in the flow visualization and measurement techniques.

Contributed by the Heat Transfer Division for publication in the JOURNAL OF HEAT TRANSFER. Manuscript received by the Heat Transfer Division April 7, 1986.

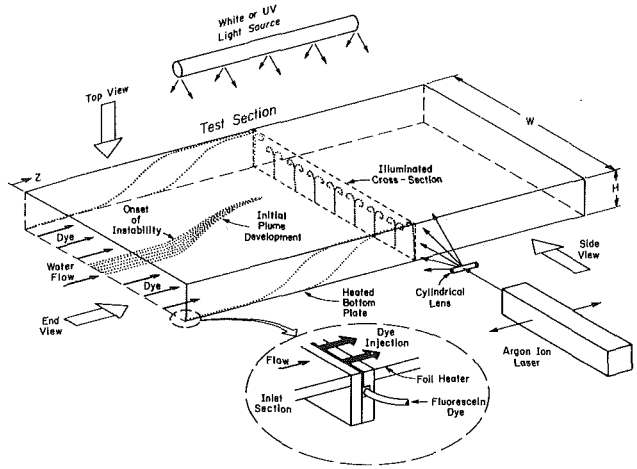

Fig. 1 Schematic of water flow channel

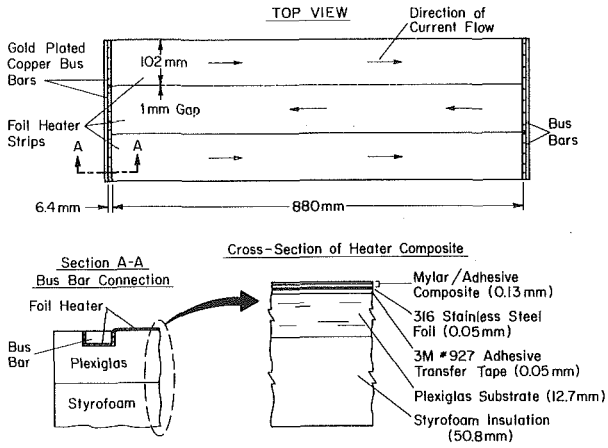

Fig. 2 Schematic of heater design

In a recent three-dimensional simulation of the combined entry region with uniform bottom heating (Incropera and Schutt, 1985), Nusselt number predictions revealed a characteristic minimum in the Nu–z distribution and significant enhancement over the forced convection limit. However, instead of a continuous approach to a fully developed value, there was an oscillatory variation of Nu with z following the minimum.

The experiments of this study were performed in an attempt to resolve some of the conflicting trends concerning laminar mixed convection in horizontal rectangular ducts. Matters of particular interest include the nature of the secondary flow, the longitudinal distribution of the Nusselt number, and the possible role of conjugate effects. In executing the experiments, attempts were made to minimize wall conduction and to achieve good spatial resolution in both the flow visualization and heat transfer measurements.

Experimental Procedures

The experiments were performed in the horizontal water channel shown schematically in Fig 1. The channel was constructed with acrylic side and top walls to facilitate flow visualization, which was performed using two different types of dye and lighting. A single stream of blue-black dye was injected along the midline of the heated bottom plate and illuminated with white light. When observed from the side, the dye clearly revealed the longitudinal station corresponding to onset of the secondary flow. To determine the structure of the secondary flow, sheets of fluorescein dye were injected along the bottom and illuminated with ultraviolet light, when viewed from the top of the channel, and with slit lighting from an argon ion laser, when viewed from the upstream end of the channel. The laser and cylindrical lens could be traversed longitudinally to provide an end view of different flow cross sections.

A requirement of the research was to develop a heater which could maintain a uniform heat flux over a large (308 mm × 880 mm) surface area, while minimizing wall conduction effects. The final design, shown in Fig. 2, consisted of a 2 mil (0.05 mm) stainless steel foil which was adhered to an acrylic substrate with a 2 mil (0.05 mm) transfer tape and shielded from the water by a 5 mil (0.13 mm) mylar/adhesive composite sheet. The foil was cut into three 102 mm wide × 880 mm long strips, and copper bus bars were used to connect the strips in series. The foil was mechanically joined to the copper bus bars, which were gold plated to prevent oxidation. Thermal conditions in proximity to the bus bar were investigated by applying liquid crystal sheets to the surface. The sheets revealed a sharp color change at the bus bar interface which, together with electrical resistance measurements, indicated negligible preheating by the bus bar.

Although concern has been expressed for the extent to which a uniform surface heat flux may be achieved by direct electrical heating (Tarasuk and Castle, 1983), good uniformity has been reported for 0.025 mm (Goldstein and Behbahani, 1982) and 0.076 mm (Eibeck and Eaton, 1984) stainless steel foils, as well as for gold-plated dielectric materials (Hippensteele et al., 1983; Baughn et al., 1984). Similarly, for the conditions of this study, electrical measurements made at various locations on the foil, as well as use of the liquid crystal sheets, indicated the existence of uniform surface heating. Flow visualization and use of the liquid crystal sheets also indicated a negligible influence on hydrodynamic and thermal conditions of the 1 mm gap between foil strips.

The heater composite was mounted on an acrylic/styrofoam base and used as the bottom surface of the rectangular channel. Experiments were performed for sidewall heights of 30.5 and 61.0 mm, thereby providing aspect ratios of approximately 10 and 5, respectively. The heater was installed immediately downstream of the flow straightener, providing a combined

Nomenclature

A = aspect ratio = W/H
g = gravitational acceleration
Gr_D^* = modified Grashof number = $g\beta_T q_b (2H)^4/k\nu^2$
Gz = Graetz number = $2H \cdot \mathrm{Re}_D \mathrm{Pr}/z$
h = convection coefficient
H = plate spacing
k = thermal conductivity
Nu = Nusselt number = $h(2H)/k$
Pr = Prandtl number
q = heat rate per unit area
Re_D = Reynolds number = $w_m(2H)/\nu$
T = temperature
w_m = mean longitudinal velocity
W = channel width
x, y, z = spanwise, vertical, and longitudinal coordinates
β_T = thermal expansion coefficient
λ = pitch (wavelength) of longitudinal rolls
ν = kinematic viscosity

Subscripts

b = bottom surface of channel
D = characteristic length ($D \equiv 2H$)
m = mixed mean fluid condition
o = entrance condition

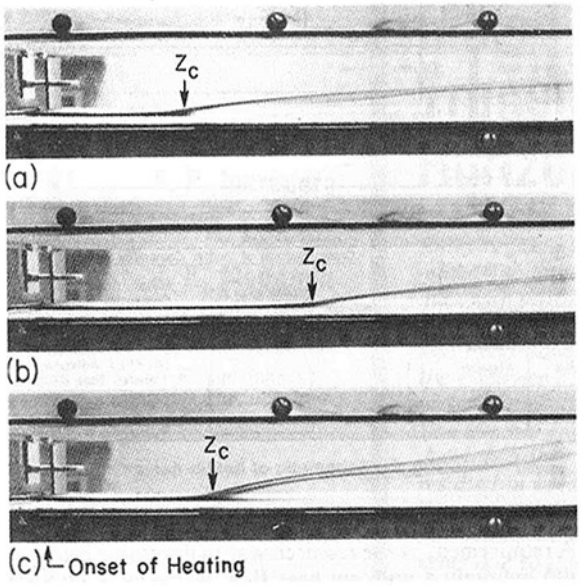

Fig. 3 Side view of secondary flow induced by bottom heating: (*a*) $Re_D = 1500$, $Gr_D^* = 3 \times 10^8$, (*b*) $Re_D = 1500$, $Gr_D^* = 1.5 \times 10^8$, (*c*) $Re_D = 1000$, $Gr_D^* = 1.5 \times 10^8$

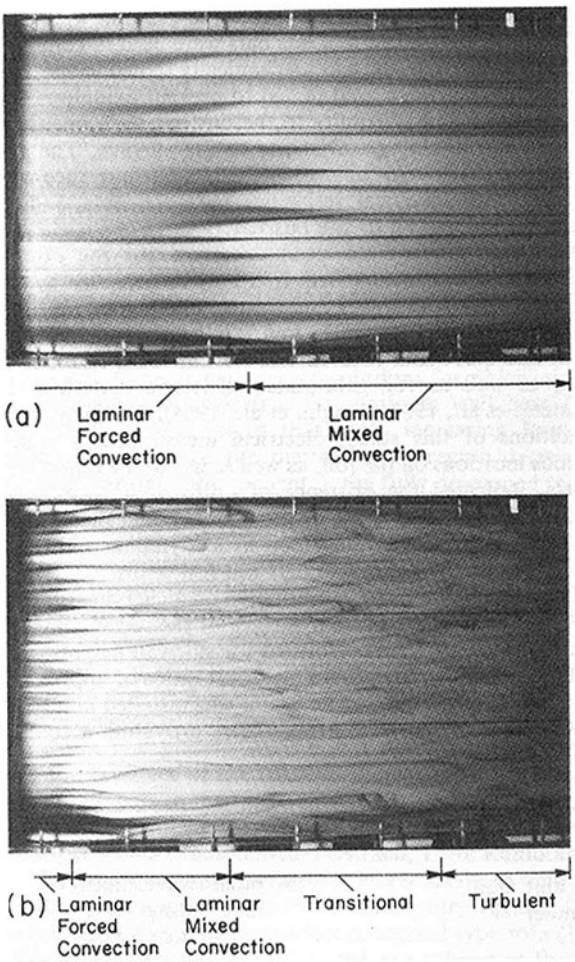

Fig. 4 Top view of fluorescein dye revealing onset of buoyancy-driven secondary flow and transition to turbulence ($Re_D = 500$): (*a*) $Gr_D^* = 5 \times 10^6$, (*b*) $Gr_D^* = 3 \times 10^7$

entry region, and power was provided by a 40V-60A d-c supply, which permitted operation up to a maximum heat flux of 4500 W/m^2. Instrumentation and operation of the water loop which supplies the channel are described by Osborne and Incropera (1985).

Fifty-eight thermocouples, calibrated to within 0.05°C, were inserted through 1.59 mm holes in the plexiglass substrate and bonded to the foil heater by a thermally conducting epoxy. The thermocouples were installed at selected longitudinal stations along the midplane and along two columns at spanwise locations 114.3 mm (Column A) and 57.2 mm (Column B) off the midplane. To enhance resolution near the entrance, the longitudinal spacing between thermocouples decreased with decreasing z. The surface temperature was obtained by correcting the thermocouple reading for the temperature drop across the mylar/adhesive layer which separates the foil from the water. The temperature drop is proportional to the heat flux and was estimated to vary from 0 to 2°C for $0 \leq q_b \leq 4500$ W/m^2. Allowing for a possible error of 100 percent in this estimate, the corresponding error in the surface-to-fluid temperature difference could range from 13 to 22 percent for the conditions of this study. Uncertainties in the heat flux, which was obtained from voltage measurements for the heater and a calibrated shunt, and the water flow rate were estimated to be 2 and 1 percent, respectively.

To estimate heat losses to the surroundings, as well as the longitudinal redistribution of the surface heat flux due to wall conduction effects, a two-dimensional conjugate analysis was performed. The analysis, which considered the actual heater composite of Fig. 2 and assumed pure forced convection for a combined entry region, revealed heat losses of less than 1 percent and a surface heat flux redistribution of less than 1.5 percent.

With the mixed mean temperature $T_m(z)$ obtained from a fluid energy balance, the local convection coefficient was evaluated from the measurements, $h_b(x, z) = q_b/[T_b(x, z) - T_m(z)]$, and used to calculate a local Nusselt number $Nu_b(x, z)$. An average Nusselt number $Nu_b(z)$ was computed from the spanwise average of the surface-to-fluid temperature difference. The Nusselt numbers, as well as other dimensionless parameters, were based on $2H$, the hydraulic diameter for infinite parallel plates. The experiments were performed for combined entry-region conditions, with aspect ratios of 5 and 10, $480 \leq Re_D \leq 2020$, and $4.5 \times 10^6 \leq Gr_D^* \leq 5 \times 10^9$.

Results

Flow Visualization. Side views of a single streak of dye injected at the channel inlet along the midline of the bottom plate are shown in Fig. 3. The dye moves along the bottom surface until it reaches a position z_c, at which it ascends from the surface due to onset of a buoyancy-driven secondary flow. Contrasting results for the three conditions, it is evident that the onset point is advanced by increasing Gr_D^* and/or decreasing Re_D. For prescribed conditions the onset point, as well as the path of the secondary flow, exhibited a quasi-steady behavior for which low-frequency, small-amplitude oscillations were observed. The oscillations are attributed to the sensitivity of the buoyancy-driven flow to small, uncontrollable disturbances in surface and/or inlet conditions.

The structure of the secondary flow was determined by injecting a thin sheet of fluorescein dye over the entire width of the bottom surface and observing the channel from the top and end. The top view of Fig. 4 suggests the existence of four flow regimes corresponding to laminar forced convection, laminar mixed convection, transitional flow, and turbulent flow. In Fig. 4(*a*) the uniform distribution of dye near the leading edge corresponds to the laminar, forced-convecton region, where the dye moves along the channel bottom. The laminar, mixed-convection region begins with onset of the buoyancy-driven flow, which corresponds to plumes rising from the bottom surface at discrete spanwise locations. The

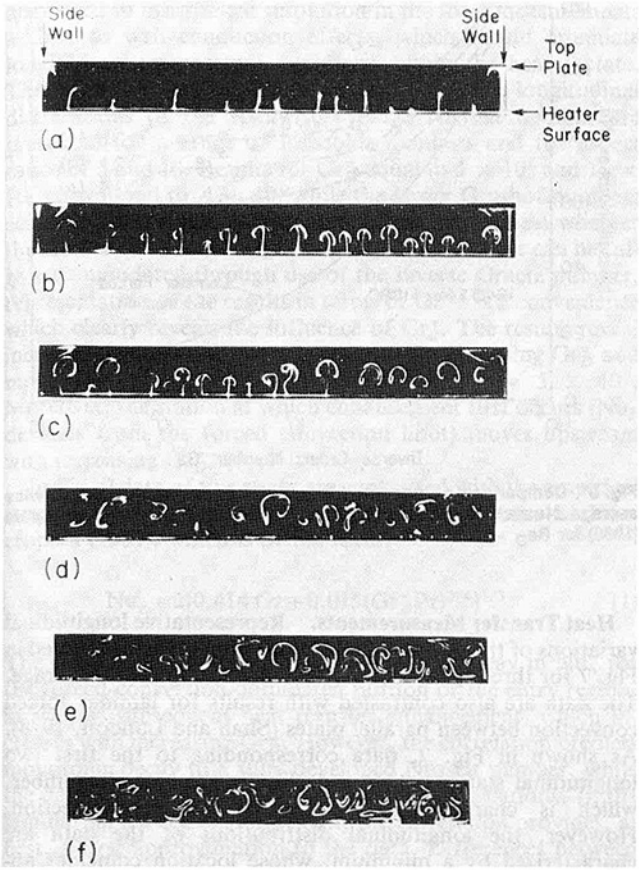

Fig. 5 End view of channel cross section at six longitudinal stations in the laminar, mixed-convection and transitional regions ($Re_D = 500$, $Gr_D^* = 3.7 \times 10^7$): (a) $Gz^{-1} = 7.7 \times 10^{-4}$, (b) $Gz^{-1} = 1.7 \times 10^{-3}$, (c) $Gz^{-1} = 2.5 \times 10^{-3}$, (d) $Gz^{-1} = 3.9 \times 10^{-3}$, (e) $Gz^{-1} = 5.8 \times 10^{-3}$, (f) $Gz^{-1} = 6.4 \times 10^{-3}$

plumes are visible as longitudinal streaks of concentrated dye. They are supplied by dyed fluid from adjoining locations, which is, in turn, replenished by cool, undyed fluid descending from the channel core. The ascending and descending warmer and cooler fluid, respectively, forms longitudinal vortices which remain approximately parallel in the laminar, mixed-convection region, until spanwise oscillations due to hydrodynamic instabilities mark the onset of a transitional regime (Fig. 4(*b*)). The streaks remain wavy until oscillations become strong enough to induce complete spanwise mixing and individual streaks are no longer identifiable. The strong mixing and irregular flow conditions are indicative of turbulence. Contrasting Figs. 4(*a*) and 4(*b*), it is evident that onset of the different regimes is advanced with increasing Grashof number.

Clarification of flow conditions in the second and third regions was obtained from end views of sheets of laser light in the cross-stream plane, where development of the secondary flow was tracked by illuminating cross sections at various longitudinal positions. Figure 5 indicates that secondary flow in the laminar mixed convection region is associated with plumes, which first appear as small buds (Fig. 5(*a*)). With increasing z, the buds form small plumes which grow and subsequently adopt a mushroom shape, with small vortices forming above a narrow stem (Fig. 5(*b*)). The plumes persist at downstream locations, maintaining approximately the same shape, but growing slightly (Fig. 5(*c*)). Farther downstream, at a location corresponding to onset of waviness in the longitudinal streaks of Fig. 4, the plumes and vortices begin to oscillate and interact in the cross-stream plane (Fig. 5(*d*)). The interactions become stronger, and the plumes subsequently break up, as the flow becomes well mixed in the cross-stream plane (Figs. 5(*e*, *f*)).

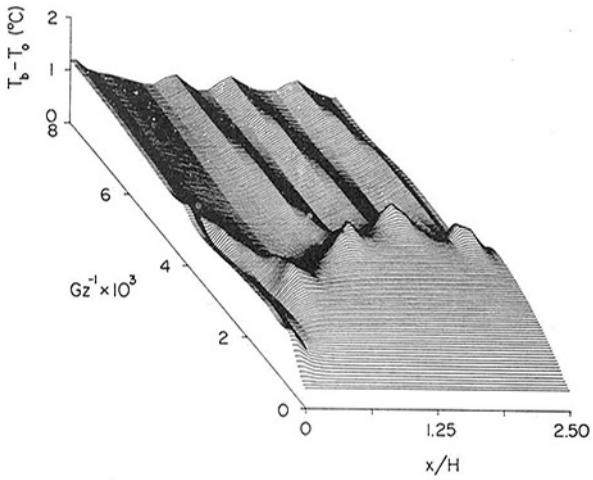

Fig. 6 Predicted longitudinal and spanwise distribution of bottom plate temperature for $A = 5$, $Re_D = 500$, $Gr_D^* = 2.5 \times 10^6$, $Pr = 6.5$

The laminar, mixed-convection region exhibited quasi-steady behavior, which was characterized by a low-frequency, small-amplitude drift of the plumes and vortices. As mentioned previously, the drift is attributed to unavoidable disturbances in the inlet and/or surface conditions. In contrast, unsteady flow in the transitional region was characterized by random, high-frequency, large-amplitude oscillations which significantly altered the structure of the vortices. The onset of such oscillations is attributed to a second instability which increases mixing and results in transition to turbulence.

The foregoing trends for the laminar forced and mixed convection regions are consistent with those predicted by the three-dimensional model of Incropera and Schutt (1985). In Fig. 6 results of representative predictions are depicted in terms of the spanwise and longitudinal variation of the bottom plate temperature. From symmetry, spanwise representation of the results may be restricted to the region bounded by one sidewall ($x/H = 0$) and the midline ($x/H = 2.5$ for $A = 5$). The initial continuous rise in T_b with increasing Gz^{-1} is characteristic of laminar forced convection. However, the precipitous decline in T_b, which occurs at $Gz^{-1} \approx 2 \times 10^{-3}$, is due to onset of a buoyancy-driven secondary flow, and the downstream ridges in the spanwise variation of T_b are indicative of thermals originating from the bottom plate. This behavior is consistent with the observations of Figs. 4 and 5. Predictions of thermal and velocity fields within the fluid reveal a secondary flow which is dominated by thermally driven vortices.

The results of this study may also be contrasted with those obtained from experiments performed for water flow over an isothermally heated flat plate (Gilpin et al., 1978; Imura et al., 1978) and for airflow between parallel plates (Akiyama et al., 1971; Hwang and Liu, 1976; Kamotani et al., 1976, 1979). The water flow experiments also suggested a transition from laminar forced convection to turbulent free convection, through the development and breakdown of longitudinal vortices. Significant spanwise oscillations, or swaying, of the vortices were reported to exist in the transitional regime. However, the quasi-steady conditions associated with plume behavior in the laminar mixed-convection region of this study were not reported for the previous studies. This difference may be due to the absence of sidewalls in the previous flat-plate experiments. Although steady secondary flow conditions were observed in the airflow experiments, the results of Akiyama et al. and Hwang and Liu suggested the existence of large longitudinal convection cells, rather than the mushroom-shaped thermals of the present study. The results of this study

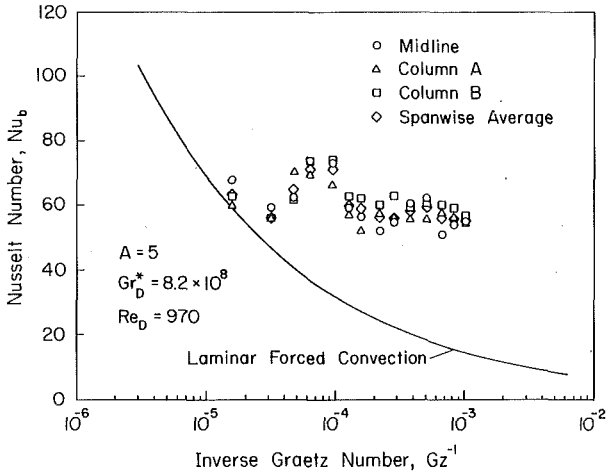

Fig. 7 Longitudinal distribution of bottom plate Nusselt number for selected spanwise locations and the spanwise average (Re_D = 970, Gr_D^* = 8.2 × 10^8)

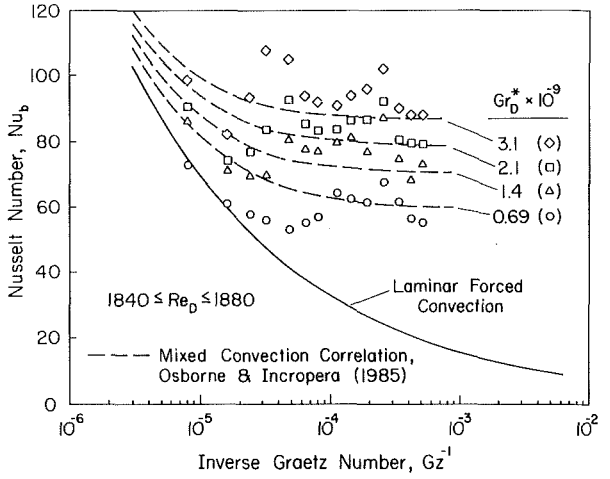

Fig. 9 Comparison of measured longitudinal distribution of spanwise average Nusselt number with correlation of Osborne and Incropera (1985) for $Re_D \approx 1860$ and $A = 5$

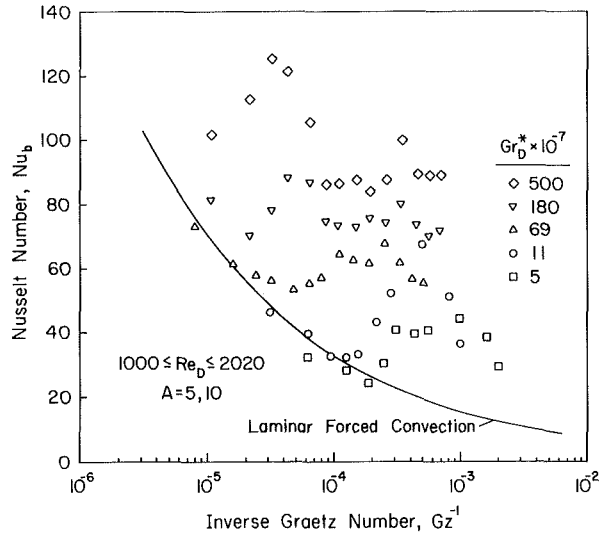

Fig. 8 Longitudinal distribution of spanwise average Nusselt number for selected Grashof numbers (1000 ≤ Re_D ≤ 2020, A = 5, 10)

are, however, consistent with the observations of Kamotani et al., as well as those of Smith et al. (1986) for secondary flow driven by a line source. The existence of steady secondary flow in a laminar mixed convection region is also consistent with observations of cellular convection in horizontal flow of a liquid film (Davis and Choi, 1977).

While the width of the mushroom-shaped vortex pairs in the laminar mixed convection region was not perfectly uniform across the heated surface, the number of pairs was found to be independent of z and to increase with increasing Gr_D^*. For $Gr_D^* < 1.5 \times 10^7$ the number of pairs was approximately equal to $A/2$, but with increasing Gr_D^* to 8.0×10^8, the number increased to approximately $4A$, while vortex shape, size, and spacing became more irregular. Since a vortex pair, which corresponds to one wavelength, is associated with each plume, the foregoing results suggest that the wavelength is $\lambda \approx 2H$ for $Gr_D^* < 1.5 \times 10^7$ and that it decreases continuously to $\lambda \approx H/4$ with increasing Gr_D^*. This behavior is consistent with the results of Gilpin et al. (1978) and Davis and Choi (1977), who observed a continuous reduction in λ with increasing Grashof number. However, the results differ from those of Mori and Uchida (1966) and Kamotani and Ostrach (1976), who suggested the existence of second-type vortex rolls ($\lambda = H$) for Rayleigh numbers exceeding 8000.

Heat Transfer Measurements. Representative longitudinal variations of the bottom plate Nusselt number are presented in Fig. 7 for three spanwise locations and the spanwise average. The data are also contrasted with results for laminar forced convection between parallel plates (Shah and London, 1978). As shown in Fig. 7, data corresponding to the first two longitudinal stations show a decline in the Nusselt number, which is characteristic of laminar forced convection. However, the longitudinal distributions of the data are characterized by a minimum, whose location coincides approximately with the observed onset of laminar mixed-convection conditions. At this point the effect of heat transfer enhancement by the secondary flow exceeds that of heat transfer reduction due to thermal boundary layer development in the entry region. The subsequent increase in Nu_b is due to the effect which the secondary flow has on disrupting the thermal boundary layer and advecting cooler fluid from the core of the channel to the bottom surface. As the secondary flow intensifies, the Nusselt number continues to increase until a maximum value is reached. It is surmised that, beyond this point, the secondary flow has completed a full cycle, returning fluid which originated with an ascending plume to the plate. Because the temperature of this fluid exceeds the inlet temperature, its ability to cool the plate is diminished. This interpretation is confirmed by a three-dimensional numerical simulation of laminar mixed convection (Incropera and Schutt, 1985). The appearance of a second minimum in Nu_b and the subsequent oscillations may be attributed to secondary flow development in the laminar mixed-convection region and to onset of the transitional and turbulent regions. In these regions Nusselt numbers substantially exceed those associated with laminar forced convection and are better approximated (within 20 percent) by results corresponding to turbulent free convection (Fujii and Imura, 1972). The oscillations appear to decay with the transition to turbulent flow.

Spanwise variations in the Nusselt number increased with increasing Gr_D^* and were typically characterized by slightly smaller values for column A (nearest the wall), as well as small differences between longitudinal stations corresponding to the maxima and minima. Such variations are an expected consequence of the three dimensionality of the flow and are consistent with model predictions (Incropera and Schutt, 1985). Nevertheless, major trends associated with longitudinal variations are satisfactorily depicted by the spanwise average.

The existence of longitudinal Nusselt number oscillations was confirmed in all of the experiments of this study, and the inability of previous experiments to reveal such oscillations is

attributed to insufficient resolution in the local measurements and/or to wall conduction effects, which would attenuate longitudinal temperature variations within the heater plate. The effect of Gr_D^* is shown in Fig. 8, where longitudinal distributions of the spanwise average Nusselt number are presented for a range of Reynolds numbers and for aspect ratios of 5 and 10. Results for Gr_D^* equal to 5×10^7 and 11×10^7 correspond to $A = 10$, while the larger Grashof numbers correspond to $A = 5$. Although it is presently unclear whether the effects of channel height and Reynolds number can be fully accommodated through use of the inverse Graetz number, representation of the results in terms of Gz^{-1} is a convenience which clearly reveals the influence of Gr_d^*. The results reveal increased heat transfer enhancement with increasing Gr_D^* and more than a fourfold enhancement for $Gr_D^* = 5 \times 10^9$. Moreover, the station at which enhancement first occurs (Nu_b deviates from the forced convection limit) moves upstream with increasing Gr_D^*.

In Fig. 9 data of this study are contrasted with the empirical laminar mixed convection correlation of Osborne and Incropera (1985), which is of the form

$$Nu_b = 2[0.414\ Gz + 0.015(Gr_D^* Pr)^{3/4}]^{1/3} \quad (1)$$

The correlation and the data both reveal a decay in Nu_b for the forced-convection-dominated portion of the entry region, as well as subsequent heat transfer enhancement, which increases with increasing Gr_D^*. However, the correlation predicts monotonic decay to a fully developed Nusselt number, while the data are characterized by longitudinal oscillations. In the laminar mixed convection region, the correlation provides, at best, a first approximation to the data. Differences between the results are attributed to conjugate effects, which strongly influenced the previous experiments but were minimized in the present experiments. In the turbulent region, however, there is good agreement between the correlation and the data.

Summary

The experiments of this study indicate that, when efforts are made to minimize conjugate effects, laminar mixed convection in a horizontal channel is characterized by a developing secondary flow which induces oscillations in the longitudinal Nusselt number distribution. The secondary flow is driven by thermals which originate at regular spanwise intervals and culminate in the formation of counterrotating vortex pairs. Nearly steady behavior in the laminar mixed-convection region is followed by spanwise plume oscillations and interactions in a transition region and complete mixing in a turbuent region. For the experimental conditions of this study, a fully developed, laminar, mixed convection flow could not be achieved. As longitudinal oscillations in the laminar mixed-convection region were decaying, transition to turbulence occurred before they decayed to zero.

Acknowledgments

We are grateful for support of this work by the National Science Foundation under Grant No. CBT-8316580. One of us (J.R.M.) is grateful for fellowships provided by the Chevron Corporation and the NL Industries Foundation.

References

Abou-Ellail, M. M. M., and Morcos, S. M., 1983, "Buoyancy Effects in the Entrance Region of Horizontal Rectangular Channels," ASME JOURNAL OF HEAT TRANSFER, Vol. 105, pp. 924–928.

Akiyama, M., Hwang, G. J., and Cheng, K. C., 1971, "Experiments in the Onset of Longitudinal Vortices in Laminar Forced Convection Between Horizontal Plates," ASME JOURNAL OF HEAT TRANSFER, Vol. 93, pp. 335–341.

Baughn, J. W., Takahashi, R. K., Hoffman, M. A., and McKillop, A. A., 1984, "Local Heat Transfer Measurements Using an Electrically Heated Thin Gold-Coated Plastic Sheet," *New Experimental Techniques in Heat Transfer—1984*, ASME HTD-31, pp. 9–17.

Cheng, K. C., Hong, S. W., and Hwang, G. J., 1972, "Buoyancy Effects on Laminar Heat Transfer in the Thermal Entrance Region of Horizontal Rectangular Channels With Uniform Wall Heat Flux for Large Prandtl Number Fluid," *International Journal Heat Mass Transfer*, Vol. 15, pp. 1819–1836.

Cheng, K. C., and Ou, J. W., 1982, "Convective Instability and Finite Amplitude Convection in the Thermal Entrance Region of Horizontal Rectangular Channels Heated From Below," *Proceedings Seventh International Heat Transfer Conference*, U. Grigull et al., eds., Hemisphere, Washington, D.C., Vol. 2, pp. 189–194.

Davis, E. J., and Choi, C. K., 1977, "Cellular Convection With Liquid-Film Flow," *Journal of Fluid Mechanics*, Vol. 81, Part 3, pp. 565–592.

Eibeck, P. A., and Eaton, J. K., 1984, "Heat Transfer Effects of Longitudinal Vortices Embedded in a Turbulent Boundary Layer," ASME Paper No. 84-HT-21.

Fujii, T., and Imura, H., 1972, "Natural Convection Heat Transfer From a Plate With Arbitrary Inclination," *International Journal Heat Mass Transfer*, Vol. 15, pp. 755–767.

Gilpin, R. R., Imura, H., and Cheng, K. C., 1978, "Experiments on the Onset of Longitudinal Vortices in Horizontal Blasius Flow Heated From Below," ASME JOURNAL OF HEAT TRANSFER, Vol. 100, pp. 71–77.

Goldstein, R. J., and Behbahani, A. I., 1982, "Impingement of a Circular Jet With and Without Cross Flow," *International Journal Heat Mass Transfer*, Vol. 25, pp. 1377–1382.

Hippensteele, S. A., Russel, L. M., and Stepka, F. S., 1983, "Evaluation of a Method for Heat Transfer Measurements and Thermal Visualization Using a Composite of a Heater Element and Liquid Crystals," ASME JOURNAL OF HEAT TRANSFER, Vol. 105, pp. 184–189.

Hung, S. C., and Davis, E. J., 1974, "The Onset of Natural Convection and Its Enhancement of Heat Transfer in Stratified Gas-Liquid Flow," *International Journal Heat Mass Transfer*, Vol. 17, pp. 1357–1364.

Hwang, G. J., and Liu, C. L., 1976, "An Experimental Study of Convective Instability in the Thermal Entrance Region of a Horizontal Parallel-Plate Channel Heated From Below," *Canadien Journal Chemical Engineering*, Vol. 54, pp. 521–525.

Imura, H., Gilpin, R. R., and Cheng, K. C., 1978, "An Experimental Investigation of Heat Transfer and Buoyancy Induced Transition From Laminar Forced Convection to Turbulent Free Convection Over a Horizontal Isothermal Heated Plate," ASME JOURNAL OF HEAT TRANSFER, Vol. 100, pp. 429–434.

Incropera, F. P., and Schutt, J. A., 1985, "Numerical Simulation of Laminar Mixed Convection in the Entrance Region of Horizontal Rectangular Ducts," *Numerical Heat Transfer*, Vol. 8, pp. 707–729.

Kamotani, Y., and Ostrach, S., 1976, "Effect of Thermal Instability on Thermally Developing Laminar Channel Flow," ASME JOURNAL OF HEAT TRANSFER, Vol. 98, pp. 62–66.

Kamotani, Y., Ostrach, S., and Miao, H., 1979, "Convective Heat Transfer Augmentation by Means of Thermal Instability," ASME JOURNAL OF HEAT TRANSFER, Vol. 101, pp. 222–226.

Mori, Y., and Uchida, Y., 1966, "Forced Convective Heat Transfer Between Horizontal Flat Plates," *International Journal Heat Mass Transfer*, Vol. 9, pp. 803–817.

Osborne, D. G., and Incropera, F. P., 1985, "Laminar Mixed Convection Heat Transfer for Flow Between Horizontal Parallel Plates With Asymmetric Heating," *International Journal Heat Mass Transfer*, Vol. 28, pp. 207–217.

Ostrach, S., and Kamotani, Y., 1975, "Heat Transfer Augmentation in Laminar Fully Developed Channel Flow by Means of Heating From Below," ASME JOURNAL OF HEAT TRANSFER. Vol. 97, pp. 220–225.

Ou, J. W., Cheng, K. C., and Lin, R. C., 1974, "Natural Convection Effects of Graetz Problem in Horizontal Rectangular Channels With Uniform Wall Temperature for Large Pr," *International Journal Heat Mass Transfer*, Vol. 17, pp. 835–843.

Shah, R. K., and London, A. L., 1978, *Laminar Flow Forced Convection in Ducts*, Advances in Heat Transfer—Supplement 1, Academic Press, pp. 179–182, 192–193.

Smith, M. C., Haines, D. A., and Main, W. A., 1986, "Some Characteristics of Longitudinal Vortices Produced by Line-Source Heating in a Low-Speed Wind Tunnel," *International Journal Heat Mass Transfer*, Vol. 29, pp. 59–68.

Tarasuk, J. D., and Castle, G. S. P., 1983, "Temperature Distribution in an Electrically Heated Wide Metallic Foil," ASME JOURNAL OF HEAT TRANSFER, Vol. 105, pp. 210–212.

L. S. Yao
Department of Mechanical and Aerospace Engineering,
Arizona State University,
Tempe, AZ 85287
Mem. ASME

Two-Dimensional Mixed Convection Along a Flat Plate

1 Introduction

Free convection can have a significant effect on forced flows over solid bodies. It can alter the flow field and hence the heat transfer rate and wall-shear distribution. The simplest physical model is two-dimensional, mixed forced and and free convection along a flat plate. Understanding of the fundamental mechanism of this interaction can help those who need to estimate the heat transfer rate and pumping power for more complex geometries of practical interest. Recent examples can be found in the areas of reactor safety, combustion flames, and solar collectors, as well as building energy conservation.

Extensive studies [1–20] have been conducted on mixed convection along vertical, horizontal, or inclined surfaces. It has been generally recognized that $\xi = (\mathrm{Gr}/\mathrm{Re}^2)_x$ is the governing parameter for a vertical plate. Forced convection exists as a limit when ξ goes to zero which occurs at the leading edge, and the free-convection limit can be reached when the value of the parameter becomes large. Perturbation solutions have been developed for both limits since both forced convection and free convection have similarity solutions. Empirical patching of two perturbation solutions has also been carried out to provide a solution which covers the whole range of ξ. A finite-difference solution [20] has been obtained by applying an algebraic transformation $z = 1/(1+\xi^2)$. This transformation transforms the semi-infinite domain of $\xi(0 - \infty)$ to a finite z domain $(1 - 0)$. The solution clearly demonstrates that a local nonsimilar solution, which ignores the history effect of a boundary-layer flow, is inadequate.

For a horizontal plate, the axial pressure gradient induced by the buoyancy force is $0(\mathrm{Gr}/\mathrm{Re}^{5/2})$. Numerous solutions have been developed by considering the free-convection effect as a perturbation quantity. Again, forced convection exists as a limit for small $\mathrm{Gr}/\mathrm{Re}^{5/2}$ and the free-convection limit can be reached as the parameter approaches infinity. The critical difference between the flow over a horizontal plate and a vertical plate has been pointed out by Cheng and his co-workers [22, 23]. The buoyancy force normal to the plate can induce a vortex instability. The governing parameter for the development of this instability is $\mathrm{Gr}/\mathrm{Re}^{3/2}$.

In this paper, we re-examine this problem. For a vertical plate, we show that two limits can exist for $\xi \to \infty$, depending on whether $\mathrm{Re} \to 0$, or $\mathrm{Gr} \to \infty$. The mixed-convection, boundary-layer solution is valid for the limit $\mathrm{Re} \to \infty$. The solution for the limit, $\mathrm{Re} \to 0$, is the free-convection solution, but the forced-convection effect cannot be obtained by solving mixed-convection, boundary-layer equations alone. Also, we demonstrate by order-of-magnitude arguments that $\mathrm{Gr}/\mathrm{Re}^{5/2}$ is not the governing parameter for mixed convection along a horizontal plate. For an inclined plate, as long as no vortex instability develops, $\mathrm{Gr}/\mathrm{Re}^2$ is the sole parameter for mixed-convection flows. This conclusion is confirmed by recent measurements [24]. The physical model of the analysis is kept simple in order to point out the important physics; thus, the forced flow is assumed along the same direction as the free convection (assisting flow), Fig. 1, and the value of the Prandtl number is set to one (Pr = 1).

2 Vertical Plates

2.1 $\mathrm{Re} \to \infty$ and $\mathrm{Gr}/\mathrm{Re}^2$ Finite. The Navier–Stokes and energy equations with the Boussinesq approximation for an inclined plate are

$$\frac{\partial \bar{u}}{\partial \bar{x}} + \frac{\partial \bar{v}}{\partial \bar{y}} = 0 \tag{1a}$$

$$\bar{u}\frac{\partial \bar{u}}{\partial \bar{x}} + \bar{v}\frac{\partial \bar{u}}{\partial \bar{y}} = \frac{-1}{\rho}\frac{\partial \bar{p}}{\partial \bar{x}} + \beta g(T - T_\infty)\cdot\cos\gamma + \nu\nabla^2\bar{u} \tag{1b}$$

$$\bar{u}\frac{\partial v}{\partial \bar{x}} + \bar{v}\frac{\partial v}{\partial \bar{y}} = \frac{-1}{\rho}\frac{\partial p}{\partial \bar{y}} + \beta g(T - T_\infty)\cdot\sin\gamma + \nu\nabla^2\bar{v} \tag{1c}$$

$$\bar{u}\frac{\partial T}{\partial \bar{x}} + \bar{v}\frac{\partial T}{\partial \bar{y}} = \alpha\nabla^2 T \tag{1d}$$

where γ is the angle of inclination of the plate with respect to the direction of gravitational acceleration.

2.1.1 Upstream Series Solution. Consider a uniform upward flow U parallel to a vertical plate. The dimensionless variables are defined as

$$u = \frac{\bar{u}}{U_\infty}, \quad v = \frac{\bar{v}}{U_\infty}\cdot\mathrm{Re}^{1/2} \quad \text{(velocities)} \tag{2a}$$

$$p = \frac{\bar{p}}{\rho U_\infty^2}, \quad \theta = \frac{T - T_\infty}{T_w - T_\infty} \quad \text{(pressure and temperature)} \tag{2b}$$

$$x = \frac{\bar{x}}{l}, \quad y = \frac{\bar{y}}{l}\cdot\mathrm{Re}^{1/2} \quad \text{(coordinates)} \tag{2c}$$

$$\mathrm{Re} = \frac{U_\infty l}{\nu} \quad \text{(Reynolds number)} \tag{2d}$$

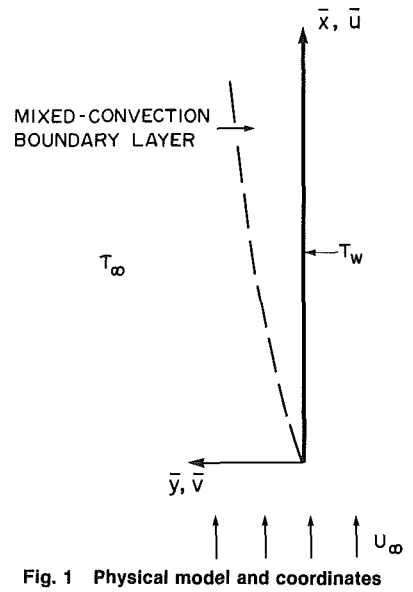

Fig. 1 Physical model and coordinates

Contributed by the Heat Transfer Division and presented at the ASME Winter Annual Meeting, Miami Beach, Florida, November 1985. Manuscript received by the Heat Transfer Division June 28, 1985.

$$\mathrm{Gr}=\frac{\beta g(T_w-T_\infty)l^3}{\nu^2} \qquad \text{(Grashof number)} \tag{2e}$$

The length scale l is introduced for convenience in order to show the magnitude of different transport mechanisms and the proper limiting procedures needed to obtain the governing equations. Since the flat-plate problem does not have a characteristic length, l can not appear in the final form of the solution.

Substitution of equations (2) into equations (1), and then taking the limit $\mathrm{Re} \to \infty$ with $\mathrm{Gr}/\mathrm{Re}^2$ finite, yields

$$\frac{\partial u}{\partial x}+\frac{\partial v}{\partial y}=0 \tag{3a}$$

$$u\frac{\partial u}{\partial x}+v\frac{\partial u}{\partial y}=-\frac{\partial p}{\partial x}+\frac{\mathrm{Gr}}{\mathrm{Re}^2}\cdot\theta+\frac{\partial^2 u}{\partial y^2} \tag{3b}$$

$$\frac{\partial p}{\partial y}=0 \tag{3c}$$

$$u\frac{\partial \theta}{\partial x}+v\frac{\partial \theta}{\partial y}=\frac{1}{\mathrm{Pr}}\frac{\partial^2\theta}{\partial y^2} \tag{3d}$$

The boundary conditions associated with the above equations are simply the no-slip condition at the wall and the asymptotic free-stream conditions far away from the plate. Equation (3c) indicates that the pressure inside the boundary layer equals the ambient pressure, and the pressure gradient along the x direction is therefore zero. The buoyancy force in equation (3b) is proportional to $\mathrm{Gr}/\mathrm{Re}^2$. This suggests that the solution can be expanded as an asymptotic series in $\mathrm{Gr}/\mathrm{Re}^2$. This series solution is valid for small $\mathrm{Gr}/\mathrm{Re}^2$, that is, for a forced-convection, dominated flow only. We will demonstrate below that the actual parameter which determines the magnitude of the buoyancy force is $(\mathrm{Gr}/\mathrm{Re}^2)_x$, which is linearly proportional to x. Therefore, the free-convection effect is always small near the leading edge of a plate, and the forced-convection limit is the solution of the problem at the leading edge, $x = 0$. The solution of equations (3) can be expressed as

$$u=\frac{\tilde{u}}{U_\infty}=f_0'(\eta)+2\cdot\left(\frac{\mathrm{Gr}}{\mathrm{Re}^2}\right)_x\cdot f_1'(\eta)+\ldots \tag{4a}$$

$$v=\frac{\tilde{v}}{U_\infty}[2\mathrm{Re}_x]^{1/2}=(\eta f_0'-f_0)+2\cdot\left(\frac{\mathrm{Gr}}{\mathrm{Re}^2}\right)_x\cdot(\eta f_1'-3f_1)+\ldots \tag{4b}$$

$$\theta=\frac{T-T_\infty}{T_w-T_\infty}=\theta_0(\eta)+2\cdot\left(\frac{\mathrm{Gr}}{\mathrm{Re}^2}\right)_x\cdot\theta_1(\eta)+\ldots \tag{4c}$$

where $\eta = y/\sqrt{2}x = y \cdot (U/2\nu x)^{1/2}$ is the Blasius variable and is independent of l. The equations which describe the functions f_0, f_1, θ_0, and θ_1 can be obtained by substituting equations (4) into equations (3) and collecting terms of equal order in $(\mathrm{Gr}/\mathrm{Re}^2)_x$. They are

$$f_0'''+f_0f_0''=0 \tag{5a}$$

$$\frac{1}{\mathrm{Pr}}\theta_0''+f_0\theta_0'=0 \tag{5b}$$

and

$$f_1'''+f_0f_1''-2f_0'f_1'+3f_0''f_1'=-\theta_0 \tag{6a}$$

$$\frac{1}{\mathrm{Pr}}\theta_1''+f_0\theta_1'-2f_0'\theta_1=-3f_1\theta_0 \tag{6b}$$

Equations (5) are the usual equations for forced convection along a flat plate and equations (6) represent the first-order, free-convection effect. Their solutions with the proper boundary conditions are available in [25], and therefore will not be repeated here. The important physics, revealed by equations (4), is that the forced-convection flow exists only at the leading edge of the plate, and the free-convection effect grows downstream along the plate. The asymptotic solution, equation (4), is valid only when $(\mathrm{Gr}/\mathrm{Re}^2)_x$ is small, i.e., near the leading edge. However, the proper scales for a mixed-convection boundary layer which covers the entire plate can be derived from equations (4), and will be described in the next section. We will also demonstrate that the series solution (4) is included in the downstream numerical solution. The only advantage in seeking the upstream series solution is that the series solution reveals the analytical structure of a mixed-convection boundary layer; the downstream solution can only be obtained by a numerical integration of the boundary-layer equations.

2.2 Downstream Mixed-Convection Boundary Layer. The dimensionless variables derived from equations (4) are

$$u=\frac{\tilde{u}}{U_\infty},\quad v=\frac{\tilde{v}}{U_\infty}\cdot[2\mathrm{Re}_x]^{1/2} \tag{7a}$$

$$\theta=\frac{T-T_\infty}{T_w-T_\infty},\quad p=\frac{\tilde{p}}{\rho U_\infty^2} \tag{7b}$$

$$\xi=\left(\frac{\mathrm{Gr}}{\mathrm{Re}^2}\right)_x=\frac{\mathrm{Gr}}{\mathrm{Re}^2}\cdot\frac{\tilde{x}}{l},\quad \eta=\tilde{y}\left[\frac{U_\infty}{2\nu\tilde{x}}\right]^{1/2}=\frac{y}{\sqrt{2x}} \tag{7c}$$

The axial-length scale is derived from equations (4) when $(\mathrm{Gr}/\mathrm{Re}^2)_x$ becomes 0(1). This marks the distance where the free-convection effect has grown to a magnitude which cannot be treated as a perturbed quantity. Explicitly, $x/l \sim \mathrm{Re}^2/\mathrm{Gr}$ is the axial distance where the free-convection effect becomes as important as the forced-convection effect. This distance becomes shorter for a larger overheating (or a larger Gr), and is longer for a higher speed flow (or a larger Re). It is worth noting that expressing equations (4) in terms of the

Nomenclature

f = stream functions, equations (4) and (6)
g = gravitational acceleration
Gr = Grashof number = $\beta g l^3 \Delta T/\nu^2$; $\mathrm{Gr}_x = \beta g x^3 \Delta T/\nu^2$
k = thermal conductivity
Nu = Nusselt number
p = pressure
Pr = Prandtl number = ν/α
Re = Reynolds number = $U l/\nu$; $\mathrm{Re}_x = U x/\nu$
T = temperature
u, v = velocities
x, y = coordinates
α = thermal diffusivity
β = thermal expansion coefficient
γ = inclined angle
ϵ = expansion parameter = $\mathrm{Gr}/\mathrm{Re}^2$
η = Blasius variable
θ = dimensionless temperature, equation (1)
ν = kinematic viscosity
τ = wall shear stress

Superscripts

$\tilde{}$ = dimensional quantities
$'$ = upstream region

Subscripts

∞ = free-stream condition
w = wall condition

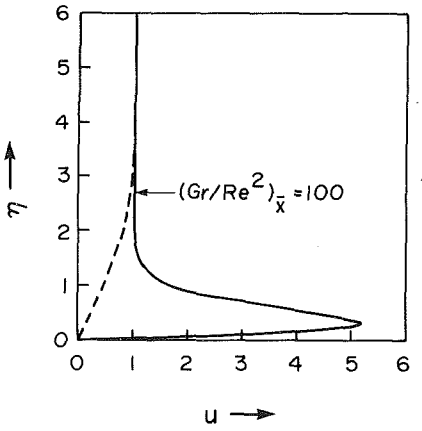

Fig. 2 Axial-velocity profile for $\xi = 0$ and 100

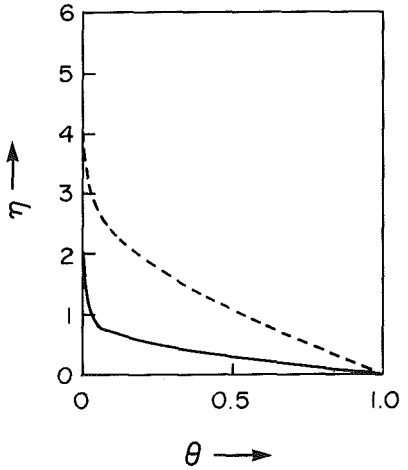

Fig. 3 Temperature distribution for $\xi = 0$ and 100

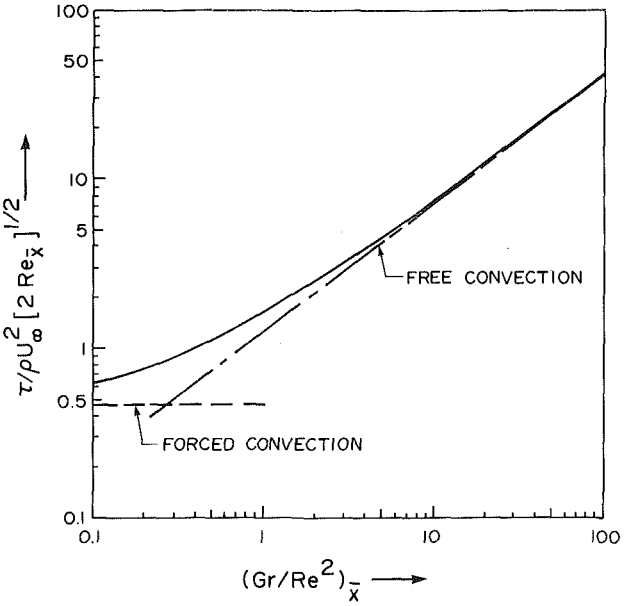

Fig. 4 Wall shear

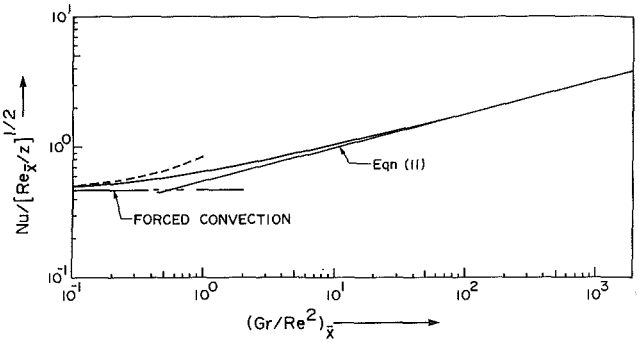

Fig. 5 Nu distribution

downstream dimensionless variables, equations (7), shows that the upstream solutions are a series in ξ. This is another way of saying that the upstream solution is valid only within a small distance from the leading edge of the plate.

The mixed-convection, boundary-layer equations can be obtained by substituting equations (7) into equations (1). After taking the limit Re $\to \infty$, they become

$$(2\xi)\cdot\frac{\partial u}{\partial \xi} - \eta\frac{\partial u}{\partial \eta} + \frac{\partial v}{\partial \eta} = 0 \tag{8a}$$

$$(2\xi)u\frac{\partial u}{\partial \xi} + (v-\eta u)\frac{\partial u}{\partial \eta} = 2\xi\theta + \frac{\partial^2 u}{\partial \eta^2} \tag{8b}$$

$$(2\xi)u\frac{\partial \theta}{\partial \xi} + (v-\eta u)\frac{\partial \theta}{\partial \eta} = \frac{1}{\mathrm{Pr}}\frac{\partial^2 \theta}{\partial \eta^2} \tag{8c}$$

The associated boundary conditions are

$$(i)\ u = v = 0 \text{ and } \theta = 1 \text{ at } \eta = 0 \tag{9a}$$

$$(ii)\ u \to 1 \quad \text{and } \theta \to 0 \text{ as } \eta \to \infty \tag{9b}$$

Taking the limit $\xi \to 0$, equations (8) reduce to the equations for forced convection. Their similarity solutions can be readily obtained, which provide the required leading-edge condition for the computation of the mixed-convection boundary layer. It is worth noting that equation (8*b*) shows that the magnitude of the buoyancy force increases downstream. A finite-difference solution of equations (8) was obtained by marching from $\xi = 0$ to 2000. The grid size along the η direction was set at 0.01 and the variable $\Delta\xi$ was used. A value of $\Delta\xi \approx 0.05$ was required near the leading edge and $\Delta\xi$ as large as 20 was used for $\xi \geq 200$. A total of 240 ξ stations was used in the computation and the CPU time was less than one and a half minutes for the IBM 380. The grid sizes have been reduced to 0.1 for $\xi \geq 20$ and 1 for $\xi \geq 200$ to check the accuracy. The numerical results presented below are believed to be accurate to the third decimal point, and are much better than one tenth of one percent.

A typical axial-velocity profile is plotted in Fig. 2 for ξ = 100. The forced-convection profile, dotted line, is also included for comparison. It shows that the buoyancy force accelerates the flow near the plate and thins the boundary layer. This results in a high heat transfer rate and wall shear stress for a mixed-convection boundary layer. The corresponding temperature distributions are presented in Fig. 3. The large temperature gradient for mixed convection relative to forced convection is clear.

The axial distribution of the wall shear stress is plotted in Fig. 4. The forced-convection and free-convection limits are also plotted for comparison. The mixed-convection wall shear approaches asymptotically that of the free convection for $\xi >$ 40. The Nusselt number, plotted in Fig. 5, is defined in terms of $T_w - T$ and x. The solid line is the numerical result for mixed convection. The short dotted line is the upstream series solution which deviates from the numerical solution at ξ = 0.1. This indicates that the series solution coincides with the downstream numerical solution for $\xi \leq 0.1$. Both curves merge with the forced-convection limit

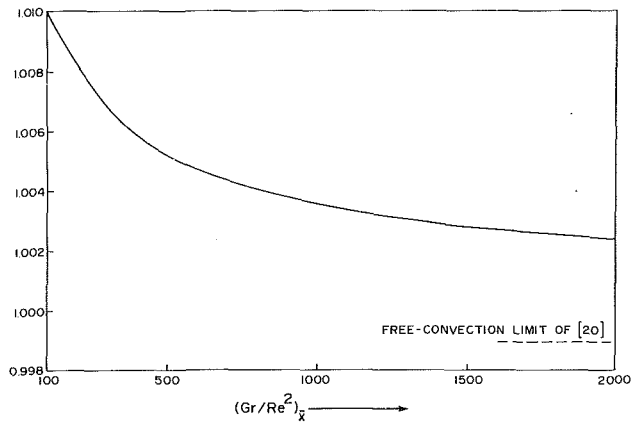

Fig. 6 Ratio of $(Nu)_{mixed}/(Nu)_{free}$

$$Nu \cdot \left[\frac{Re_x}{2}\right]^{-1/2} = -0.4696 \tag{10}$$

at the leading edge, $\xi = 0$. The mixed-convection heat transfer rate seems to merge with the free-convection limit

$$Nu \cdot \left[\frac{Re_x}{2}\right]^{-1/2} = 0.5671 \left[\frac{Gr}{Re^2}\right]_x^{1/4} \tag{11}$$

for a vertical flat plate in Fig. 5. A careful examination of the numerical results indicates, however, that the mixed-convection Nu asymptotically approaches the free-convection limit very slowly. If one uses 1 percent as a criterion, then the mixed-convection Nu merges with the free-convection limit at $\xi = 500$. The ratio of the mixed-convection Nu and the free-convection Nu is plotted in Fig. 6. It shows that this ratio keeps on slowly declining even at $\xi = 2000$. The dotted line in Fig. 5 is the ratio calculated from [20]. Due to the different definitions of Nusselt number used in this paper and in [20], it is only possible to compare the values of Nu in the sense $\xi \to \infty$. The value from [20] is 0.9989 which is within the accuracy of the numerical method.

It is clear that the free-convection effect is cumulative, and the formulation described above is only valid for large Re. Near the leading edge of the plate, forced convection is the dominant mode. The value of Gr determines the required distance before free convection becomes important. Free convection becomes the dominant mode when $Gr/Re^2 \to \infty$. The previous perturbation solution for a free-convection, dominated flow obtained by solving the parabolic boundary-layer equations alone is incorrect since the equations are solved by marching against the flow direction. In the next section, a correct way to find the solution for a free-convection, dominated flow will be outlined.

2.2 $Gr \to \infty$ and Re ~ 0(1). This limit corresponds to the case of a heated vertical plate set in a very slow, upward stream. Free convection is the dominant mode over the entire plate. Since the length scale for this problem is the distance measured from the leading edge of the plate, the Reynolds number can be large for large x even though the free-stream velocity is very small. In the following, we will show that the forced convection will alter the heat transfer slightly for $\bar{x} < \nu/U_\infty$. Downstream from this location, the flow is free convection. This is because the analysis described in the above section becomes valid and the value Gr/Re^2 which is linearly proportional to x approaches infinity. Thus, the value of Re is considered to be 0(1) in the following analysis.

2.2.1 Outer Flow. The dimensionless variables are defined as

$$U = \frac{\bar{u}}{\bar{W}}, \quad V = \frac{\bar{v}}{\bar{W}} \tag{12a}$$

$$\Theta = \frac{T - T_\infty}{T_w - T_\infty}, \quad \mathbf{P} = \frac{\bar{P}}{\rho \bar{W}^2} \tag{12b}$$

$$x = \frac{\bar{x}}{l}, \quad y = \frac{\bar{y}}{l} \tag{12c}$$

and

$$\bar{W} = [\beta g \cdot (T_w - T_\infty) \cdot l]^{1/2} \tag{12d}$$

Substitution of equations (12) into equations (1) results in

$$\frac{\partial U}{\partial x} + \frac{\partial V}{\partial y} = 0 \tag{13a}$$

$$U\frac{\partial U}{\partial x} + V\frac{\partial U}{\partial y} = -\frac{\partial \mathbf{P}}{\partial x} + \Theta + \epsilon^2\left(\frac{\partial^2 U}{\partial x^2} + \frac{\partial^2 U}{\partial y^2}\right) \tag{13b}$$

$$V\frac{\partial V}{\partial x} + V\frac{\partial U}{\partial y} = -\frac{\partial \mathbf{P}}{\partial y} + \Theta + \epsilon^2\left(\frac{\partial^2 V}{\partial x^2} + \frac{\partial^2 V}{\partial y^2}\right) \tag{13c}$$

$$U\frac{\partial \Theta}{\partial x} + V\frac{\partial \Theta}{\partial y} = -\frac{\epsilon^2}{Pr}\left(\frac{\partial^2 \Theta}{\partial x^2} + \frac{\partial^2 \Theta}{\partial y^2}\right) \tag{13d}$$

where $\epsilon = Gr^{-1/4}$ and the free-stream velocity becomes $\epsilon^2 Re$. Since the displacement effect of the free-convection boundary layer is $0(\epsilon)$, the perturbation series are expanded in terms of ϵ. They are

$$\left.\begin{aligned} \Phi &= \Phi_0 + \epsilon\,\Phi_1 + \epsilon^2\,\Phi_2 + \ldots \\ P &= P_0 + \epsilon\,P_1 + \epsilon^2\,P_2 + \ldots \\ \Theta &= \Theta_0 + \epsilon\,\Theta_1 + \epsilon^2\,\Theta_2 + \ldots \end{aligned}\right\} \tag{14}$$

where Φ is the velocity potential and

$$U = \frac{\partial \Phi}{\partial x}, \quad V = \frac{\partial \Phi}{\partial y} \tag{15}$$

Since there is no conduction outside of the boundary layer, $\Theta_0 = \Theta_1 = \Theta_2 = 0$. Substitution of equations (14) into equations (13), and collecting terms of equal powers of ϵ, results in

$$\nabla^2 \Phi_i = 0 \quad (i = 0, 1, 2) \tag{16}$$

The boundary conditions for Φ_0 are homogeneous; therefore, Φ_0 = constant. This represents that there is no zeroth-order fluid motion. The boundary conditions for Φ_1, which represent the consequence of the displacement effect of the zeroth-order boundary layer (free-convection boundary layer) described in Section 2.2.2, are quiescent fluid far away from the plate, and on the plate

$$\frac{\partial}{\partial y}\Phi_1(x, 0) = v_0(x, \infty) \tag{17}$$

where $v_0(x, \infty)$ is the normal velocity of the zeroth-order boundary layer. The solution of Φ_1 for a finite plate has been given by Yang and Jerger [21], which is a good approximation to a semi-infinite plate since $v_0(x, \infty)$ quickly drops to zero as x increases.

Φ_2 represents the perturbation induced by the slow forced flow. Its boundary conditions are

$$\frac{\partial \Phi_2}{\partial x} = Re \tag{18a}$$

far away from the plate and

$$\frac{\partial \Phi_2}{\partial y} = v_1(x, \infty) \tag{18b}$$

on the plate, where $v_1(x, \infty)$ is the normal velocity of the first-order boundary layer. Its solution can be obtained by the same method used by Yang and Jerger to find Φ_1. Since the effect of the forced convection is extremely small for the case $Gr \to \infty$, its solution has only academic interest, and therefore is not

given here. In the next section, the boundary-layer equations will be derived to complete this formulation.

2.2.2 Boundary Layers. Since the outer flow does not satisfy the no-slip condition on the plate, a thin viscous layer with heat conduction exists near the plate. The dimensionless variables are

$$v=\frac{V}{\epsilon},\quad r=\frac{y}{\epsilon},\quad \text{and } u=U, \text{ etc.} \tag{19}$$

The expansions which match with the outer expansions (14) are

$$\left.\begin{aligned} u&=u_0+\epsilon\, u_1+\epsilon^2\, u_2+\ldots\\ v&=v_0+\epsilon\, v_1+\epsilon^2\, v_2+\ldots\\ p&=p_0+\epsilon\, P_1+\epsilon^2\, p_2+\ldots\\ \theta&=\theta_0+\epsilon\,\theta_1+\epsilon^2\,\theta_2+\ldots \end{aligned}\right\} \tag{20}$$

The equations of the zero-order boundary layer can be obtained by substituting equations (19) and (20) into equations (13) and collecting terms independent of ϵ; the result is

$$\left.\begin{aligned} &\frac{\partial u_0}{\partial x}+\frac{\partial v_0}{\partial r}=0\\ &u_0\,\frac{\partial u_0}{\partial x}+v_0\,\frac{\partial u_0}{\partial r}=-\frac{\partial p_0}{\partial x}\,\theta_0+\frac{\partial^2 u_0}{\partial r^2}\\ &\frac{\partial p_0}{\partial r}=0\\ &u_0\,\frac{\partial \theta_0}{\partial x}+v_0\,\frac{\partial \theta_0}{\partial r}=\frac{1}{\mathrm{Pr}}\,\frac{\partial^2\theta_0}{\partial r^2} \end{aligned}\right\} \tag{21}$$

and the boundary conditions are

$$\left.\begin{aligned} &(i)\ x=0,\ u_0=\theta_0=0\\ &(ii)\ x>0;\ r=0,\ u_0=v_0=0,\ \theta_0=1,\\ &\qquad r\to\infty,\ u_0,\ \theta_0\to 0 \end{aligned}\right\} \tag{22}$$

The solution of equations (21), which satisfies conditions (22), is the free-convection boundary layer along a vertical flat plate, a well-known result. v_0 evaluated at $r\to\infty$ represents the displacement effect and is needed to find the first-order outer flow Φ_1; see equation (17).

Similarly the equations of the first-order boundary layer are

$$\left.\begin{aligned} &\frac{\partial u_1}{\partial x}+\frac{\partial v_1}{\partial r}=0\\ &u_0\,\frac{\partial u_1}{\partial x}+v_0\,\frac{\partial u_1}{\partial r}+u_1\,\frac{\partial u_0}{\partial r}+v_1\,\frac{\partial u_0}{\partial r}\\ &\qquad=-\frac{\partial p_1}{\partial x}+\theta_1+\frac{\partial^2 u_1}{\partial r^2}\\ &\frac{\partial p_1}{\partial r}=0\\ &u_0\,\frac{\partial \theta_1}{\partial x}+v_0\,\frac{\partial \theta_1}{\partial r}+u_1\,\frac{\partial \theta_0}{\partial r}+v_1\,\frac{\partial \Theta_0}{\partial r}\\ &\qquad=\frac{1}{\mathrm{Pr}}\,\frac{\partial_2\theta_1}{\partial r^2} \end{aligned}\right\} \tag{23}$$

The associated boundary conditions are

$$\left.\begin{aligned} &(i)\ x=0,\ u_1=\theta_1=0\\ &(ii)\ x>0;\ r=0,\ u_1=v_1,\ \theta_1=0,\\ &\qquad r\to\infty,\ u_1\to U_1(x,0),\ \theta_1\to 0 \end{aligned}\right\} \tag{24}$$

where $U_1(x, 0) = (\partial/\partial x)\,\Phi_1(x, 0)$ is the axial velocity of the first-order outer flow evaluated on the plate. The solution of equations (23) satisfying the boundary conditions (24) can be found in [21]. The results, $v_1(x, \infty)$, provide the required wall condition to find Φ_2; see equation (18*b*).

The effect of the forced flow is $0(\epsilon^2)$, the second-order boundary layer. The equations are

$$\left.\begin{aligned} &\frac{\partial u_2}{\partial x}+\frac{\partial v_2}{\partial r}=0\\ &u_0\frac{\partial u_2}{\partial x}+v_0\,\frac{\partial u_2}{\partial r}+u_1\,\frac{\partial u_1}{\partial r}+v_1\,\frac{\partial u_1}{\partial r}+u_2\,\frac{\partial u_0}{\partial x}\\ &\qquad+v_2\,\frac{\partial u_0}{\partial r}=-\frac{\partial p_2}{\partial x}+\theta_2+\frac{\partial^2 u_2}{\partial r^2}+\frac{\partial^2 u_0}{\partial x^2}\\ &u_0\frac{\partial v_0}{\partial x}+v_0\,\frac{\partial v_0}{\partial r}=-\frac{\partial p_2}{\partial r}+\frac{\partial^2 v_0}{\partial r^2}\\ &u_0\frac{\partial \theta_2}{\partial x}+v_0\,\frac{\partial \theta_2}{\partial r}+u_1\,\frac{\partial \theta_1}{\partial x}+v_1\,\frac{\partial \theta_1}{\partial r}+u_2\,\frac{\partial \theta_0}{\partial x}\\ &\qquad+v_2\,\frac{\partial \theta_2}{\partial r}=\frac{1}{\mathrm{Pr}}\left(\frac{\partial^2\theta_2}{\partial r^2}+\frac{\partial^2\theta_2}{\partial x^2}\right) \end{aligned}\right\} \tag{25}$$

The associated boundary conditions are

$$\left.\begin{aligned} &(i)\ x=0,\ u_2=\frac{\partial}{\partial x}\,\Phi_2(0,0),\ \theta_2=0\\ &(ii)\ x>0;\ r=0,\ u_2=v_2,\ \theta_0=0,\\ &\qquad r\to\infty,\ u_1=\frac{\partial}{\partial x}\,\Phi_2(x,0),\ \theta_2\to 0 \end{aligned}\right\} \tag{26}$$

The structure of equations (25) differs from that of equations (21) and (22). The normal pressure gradient is not zero across the boundary layer, but the pressure distribution within the thin boundary layer can be obtained by solving the third equation in (25). Once the pressure distribution is determined, u_2, v_2, and θ_2, which are governed by a set of parabolic differential equations, can be solved straightforwardly.

From the above analysis, it is clear that the forced-convection effect is $0(\epsilon^2)$, and is smaller than that due to the displacement of the free-convection boundary layer. Even though the effect is small, the formulation clarifies the physics which has been misunderstood for many years.

In conclusion, it is clear that the free-convection limits for $\mathrm{Re} > 1$ and $\mathrm{Re} < 1$ are different. For $\mathrm{Re} > 1$, the free convection becomes large when $\mathrm{Gr}/\mathrm{Re}^2 \to \infty$. Here the value of Gr determines the required distance for the forced-convection effect to fade away. On the other hand, when $\mathrm{Re} < 1$, free convection is the dominant mode all over the plate, and the forced-convection effect is $0(\epsilon^2)$. All previous work which tried to find the limiting solution as $\mathrm{Gr}/\mathrm{Re}^2 \to \infty$ and $\mathrm{Re} \to 0$ by solving the boundary-layer equations alone are incorrect.

3 Horizontal Plates

For a horizontal plate ($\gamma = 90$ deg), the set of dimensionless variables, equations (2), can also be used to find the magnitude of the terms in the governing equations. The y-momentum equation (1c) becomes

$$\mathrm{Re}^{-1/2}\left[u\frac{\partial v}{\partial x}+v\frac{\partial v}{\partial y}\right]=-\mathrm{Re}^{1/2}\cdot\frac{\partial p}{\partial y}+\frac{\mathrm{Gr}}{\mathrm{Re}^2}\theta$$
$$+\mathrm{Re}^{-1/2}\cdot\frac{\partial v}{\partial y^2}+\mathrm{Re}^{-1/3}\cdot\frac{\partial v}{\partial x^2} \quad (27)$$

Since the onset of the vortex instability due to buoyancy occurs at $0(\mathrm{Gr}/\mathrm{Re}^2)$, a proper asymptotic limit can be taken only after the order of magnitude of $\mathrm{Gr}/\mathrm{Re}^2$ is determined. From equation (27), there are three choices: $0(\mathrm{Re}^{-1/2})$, $0(1)$, or $0(\mathrm{Re}^{1/2})$. We will discuss these cases in detail.

If the buoyancy force is of the same order as the inertia forces, i.e., $\mathrm{Gr}/\mathrm{Re}^2 \sim 0(\mathrm{Re}^{-1/2})$, the limiting form of equation (13) simply states that the buoyancy force is of the same order as the displacement effect, which is $0(\mathrm{Re}^{-1})$ for a flat plate. This implies that the onset of vortex instability due to the normal buoyancy force can be analyzed by adopting the Blasius profile as the base flow. Including the nonparallel effect, which is $0(\mathrm{Re}^{-1/2})$ in linear stability analysis [22], is consistent since the buoyancy effect on the base flow is small and is of $0(\mathrm{Re}^{-1})$. Physically, this scaling suggests that the vortex instability develops within a distance $x/l \sim 0(\mathrm{Re}/\mathrm{Gr}^{2/3})$ from the leading edge of the plate. This scaling agrees with measurement [23].

In the case where $\mathrm{Gr}/\mathrm{Re}^2 \sim 0(1)$, the axial pressure gradient induced by the buoyancy force is of the same order as the nonparallel effect in the stability analysis. A consistent base flow should then include the free-convection effect. On the other hand, the scaling indicates that the effect of the induced axial-pressure gradient becomes important at a distance, $x \sim \mathrm{Re}^2/\mathrm{Gr}$ ($\gg \mathrm{Re}/\mathrm{Gr}^{2/3}$ for $\mathrm{Gr} \sim \mathrm{Re}^2$) from the leading edge of the plate which is far downstream from the location where the vortex instability starts to develop. A similar argument can be used to rule out the possibility that $\mathrm{Gr}/\mathrm{Re}^2$ is $0(\mathrm{Re}^{1/2})$. The conclusion is that neither $\mathrm{Gr}/\mathrm{Re}^2$ nor $\mathrm{Gr}/\mathrm{Re}^{5/2}$ is a parameter for mixed-convection problems along a horizontal flat plate.

4 Inclined Plates

Equations (1) clearly show that the direct free-convection effect is proportional to $\cos\gamma$ while the vortex instability depends on $\sin\gamma$. Two effects cannot be added together by assuming that they are linearly independent, since the buoyancy force parallel to the plate can alter the velocity profile of the base flow substantially. The onset condition for the vortex instability estimated for a horizontal plate cannot be applied to an inclined plate without redoing the linear stability analysis. On the other hand, the parameter which can be used to correlate vortex instabilities should be $(\mathrm{Gr}\cdot\sin\gamma/\mathrm{Re}^{3/2})_x$. For an inclined plate, if the vortex instability is not developed, $\mathrm{Gr}/\mathrm{Re}^2\cdot\cos\gamma$ will be the governing parameter.

5 Conclusion

It is clear that the governing parameter for a mixed-convection boundary-layer solution along a vertical plate is $\mathrm{Gr}/\mathrm{Re}^2$, if $\mathrm{Re} \to \infty$. Rigorously speaking, forced convection exists only at the leading edge, and the natural-convection effect gradually increases downstream. For small Re, the governing parameters are $\mathrm{Gr}^{-1/4}$ and Re. In this case natural convection is the dominant mode over the entire plate and the forced-convection effect is even smaller than the displacement effect of the natural-convection boundary layer.

For a horizontal plate, a vortex instability can be expected. Thus, the governing parameter is $\mathrm{Gr}/\mathrm{Re}^{3/2}$, and not $\mathrm{Gr}/\mathrm{Re}^{5/2}$, as suggested by some previous works. For an inclined plate, $\mathrm{Gr}/\mathrm{Re}^2\sin\gamma$ is again the governing parameter as long as the angle of inclination is less than about 85 deg; experimental evidence shows that instability does not occur in that range.

References

1 Sparrow, E. M., and Gregg, J. L., "Buoyancy Effects in Forced-Convection Flow and Heat-Transfer," ASME *J. Appl. Mech.*, Vol. 81, 1959, pp. 133–134.

2 Mori, Y., "Buoyancy Effects in Forced Laminar Convection Flow Over a Horizontal Flat Plate," ASME JOURNAL OF HEAT TRANSFER, Vol. 83, 1961, pp. 479–482.

3 Acrivos, A., "On the Combined Effect of Forced and Free Convection Heat Transfer in Laminar Boundary Layer Flows," *Chem. Eng. Sci.*, Vol. 21, 1966, p. 343.

4 Sparrow, E. M., and Minkowycz, W. J., "Buoyancy Effects on Horizontal Boundary-Layer Flow and Heat Transfer," *Int. J. Heat Mass Transfer*, Vol. 5, 1962, pp. 505–511.

5 Merkin, J. H., "The Effect of Buoyancy Forces on the Boundary-Layer Flow Over a Semi-infinite Vertical Flat Plate in a Uniform Free Stream," *J. Fluid Mech.*, Vol. 35, 1969, pp. 439–450.

6 Lloyd, J. R., and Sparrow, E. M., "Combined Forced and Free Convection Flow on Vertical Surfaces," *Int. J. Heat Mass Transfer*, Vol. 13, 1970, pp. 434–438.

7 Redekopp, L. C., and Chartwat, A. F., "Role of Buoyancy and the Boussinesq Approximation in Horizontal Boundary Layers," *J. Hydronautics*, Vol. 6, 1972, pp. 34–39.

8 Robertson, G. E., Seinfeld, J. H., and Leal, G. E., "Combined Forced and Free Convection Flow Past a Horizontal Flat Plate," *AIChE Journal*, Vol. 19, 1973, pp. 998–1008.

9 Hieber, C. A., "Mixed Convection Above a Heated Horizontal Surface," *Int. J. Heat Mass Transfer*, Vol. 16, 1973, pp. 769–785.

10 Wilks, G., "Combined Forced and Free Convection Flow on Vertical Surfaces," *Int. J. Heat Mass Transfer*, Vol. 16, 1973, pp. 1958–1964.

11 Hieber, C. A., "Mixed Convection Above a Heated Horizontal Surface," *Int. J. Heat Mass Transfer*, Vol. 16, 1973, pp. 769–785.

12 Leal, L. G., "Combined Forced and Free Convection Heat Transfer From a Horizontal Flat Plate," *Z. Angew. Math. Phys.*, Vol. 24, 1973, pp. 20–42.

13 Chen, T. S., Sparrow, E. M., and Mucoglu, A., "Mixed Convection in Boundary Layer Flow on a Horizontal Plate," ASME JOURNAL OF HEAT TRANSFER, Vol. 99, 1977, pp. 66–71.

14 Mucoglu, A., and Chen, T. S., "Mixed Convection on Inclined Surfaces," ASME JOURNAL OF HEAT TRANSFER, Vol. 101, 1979, pp. 422–426.

15 Moutsoglou, A., Tzuoo, S. K. L., and Chen, T. S., "Mixed Convection in Boundary Layer Flows Over Inclined Surfaces," *AIAA 15th Thermo-physics Conference*, Snowmass, CO, July 14–16, 1980, Paper No. AIAA-80-1525.

16 Ramachandran, N., Armaly, B. F., and Chen, T. S., "Mixed Convection Over Horizontal Plate," ASME JOURNAL OF HEAT TRANSFER, Vol. 105, 1983, pp. 420–423.

17 Chen, T. S., and Armaly, B. F., "Mixed Convection in Laminar Boundary-Layer Flow," in: *Natural Convection: Fundamentals and Applications*, Proc. of the NATO ASI, July 16–27, 1984, S. Kakac, W. Aung, and R. Viskanta, eds., Hemisphere, New York, 1985.

18 Fernandez-Pello, A. C., and Law, C. K., "On the Mixed-Convective Flame Structure in the Stagnation Point of a Fuel Particle," *19th Symp. (Int.) on Combustion*, 1983, pp. 1037–1044.

19 Fernandez-Pello, A. C., and Pagni, P. J., "Mixed Convective Burning of a Vertical Fuel Surface," *Proc. ASME-JSME Thermal Engineering Joint Conf.*, Vol. 4, 1983, pp. 295–301.

20 Raju, M. S., Liu, X. R., and Law, C. K., "A Formulation of Combined Forced and Free Convection Past Horizontal and Vertical Surfaces," *Int. J. Heat Mass Transfer*, Vol. 27, 1984, pp. 2215–2224.

21 Yang, K. T., and Jerger, E. W., "First-Order Perturbations of Laminar Free-Convection Boundary Layers on a Vertical Plate," ASME JOURNAL OF HEAT TRANSFER, Vol. 86, 1964, pp. 107–115.

22 Wu, R. S., and Cheng, K. C., "Thermal Instability of Blasius Flow Along Horizontal Plates," *Int. J. Heat Mass Transfer*, Vol. 19, 1976, pp. 907–913.

23 Gilpin, R. R., Imura, H., and Cheng, K. C., "Experiments on the Onset of Longitudinal Vortices in Horizontal Blasius Flow Heated From Below," ASME JOURNAL OF HEAT TRANSFER, Vol. 100, 1978, pp. 71–77.

24 Ramachandran, N., Armaly, B. F., and Chen, T. S., "Measurements of Laminar Mixed Convection From an Inclined Surface," ASME Winter Annual Meeting, Miami Beach, FL, Nov. 17–21, 1985.

25 Yao, L. S., "Free and Forced Convection in the Entry Region of a Heated Vertical Channel," *Int. J. Heat Mass Transfer*, Vol. 26, 1983, pp. 65–72.

An Experimental Study of High Rayleigh Number Mixed Convection in a Rectangular Enclosure With Restricted Inlet and Outlet Openings

L. Neiswanger
Research Assistant.

G. A. Johnson
Research Assistant.

V. P. Carey
Associate Professor.

Department of Mechanical Engineering,
University of California,
Berkeley, CA 94720

Measured local heat transfer data and the results of flow visualization studies are reported for cross-flow mixed convection in a rectangular enclosure with restricted inlet and outlet openings at high Rayleigh number. In this study, experiments using water as the test fluid were conducted in a small-scale test section with uniformly heated vertical side walls and an adiabatic top and bottom. As the flow rate through the enclosure increased, the enhancement of heat transfer, above that for natural convection alone, also increased. The variation of the local heat transfer coefficient over the heated surface was found to be strongly affected by the recirculation of portions of the forced flow within the enclosure. Mean heat transfer coefficients are also presented which were calculated by averaging the measured local values over the heated surface. A correlation for the mean heat transfer coefficient is also proposed which agrees very well with the experimentally determined values. A method of predicting the flow regime in this geometry for specified heating and flow conditions is also discussed.

Introduction

Convective transport under the combined influence of a vertical buoyancy force and an imposed horizontal flow occurs in a number of important technological applications. Cross-flow mixed convection circumstances of this type may arise, for example, during heat transfer from vertical walls in buildings, in the cooling of electronic circuit boards, heat loss from central solar receivers, and mixed convection in horizontal heat exchanger tubes at low flow rates.

Virtually all previous studies of this type of flow circumstance fall into one of two categories: (1) mixed convection internal flows in horizontal tubes and ducts, or (2) external boundary layer mixed convection resulting from a horizontal forced flow over a vertical surface. Previous studies of mixed convection in horizontal tubes with an isothermal wall condition have recently been summarized by Yousef and Tarasuk (1982). Experimental studies of mixed convection in uniformly heated horizontal tubes have been conducted by McComas and Eckert (1966), Mori et al. (1966), Shannon and Depew (1968), Petukhov et al. (1967), Bergles and Simons (1971), and Hong et al. (1974).

A number of theoretical and numerical analyses of mixed convection in uniformly heated horizontal tubes have also been conducted (see, for example, Faris and Viskanta, 1969; Newell and Bergles, 1970; Cheng et al., 1972; and Cheng and Ou, 1974). In addition, external cross-flow mixed convection has been investigated in previous studies by Young and Yang (1963), Eichhorn and Hasan (1980, Evans and Plumb (1982a, 1982b), Siebers et al. (1983), and Rahman and Carey (1986a, 1986b).

The studies described above have provided considerable insight into the characteristics of mixed convection flows of this type. However, none of these studies have specifically considered high Rayleigh number mixed convection flows near vertical walls in enclosures. Flows of this type may commonly arise in building heat transfer circumstances due to the interaction of a horizontal flow, due to ventilation, with a buoyancy-driven flow along the wall resulting from the difference between the wall temperature and bulk air temperature. For such circumstances, the characteristic Rayleigh number is usually large ($> 10^{10}$) and buoyancy effects are confined to a thin boundary layer near the walls. Characteristic values of Reynolds number associated with air motion due to ventilation or infiltration are usually less than 5000 in most builidngs.

This type of high Rayleigh number mixed convection flow is also similar to flows which arise in electronics cooling when a fan drives a horizontal flow of air through a cabinet containing heat-dissipating electronic components on vertical circuit boards.

Because buoyancy is confined to a relatively thin boundary layer region, there are some similarities between the flows for these conditions and the external boundary layer flows studied by Evans and Plumb (1982a) and Siebers et al. (1983). However, because the walls are part of an enclosure, the flow near the walls in a room is expected to interact with the core flow in a stronger manner than the idealized boundary-layer flows in these studies.

In this regard, the mixed convection flows in a building are similar to mixed convection flows in horizontal tubes. However, the previous studies of mixed convection in horizontal tubes described above all consider flows at Rayleigh numbers of 10^7 or lower, which is much lower than typical Rayleigh numbers for building heat transfer circumstances. Hence, the results of these previous studies do not appear to be directly applicable to flows of this type.

The experimental investigation described here was conducted to obtain a better understanding of cross-flow mixed convection at high Rayleigh number in enclosures with inlet and outlet "doorways." This circumstance relates closely to mixed convection flows found in buildings and electronics cooling applications. A special test section was used in the experiments which had uniformly heated side walls, adiabatic top and bottom walls, and restricted inlet and outlet openings

Contributed by the Heat Transfer Division for publication in the JOURNAL OF HEAT TRANSFER. Manuscript received by the Heat Transfer Division April 21, 1986.

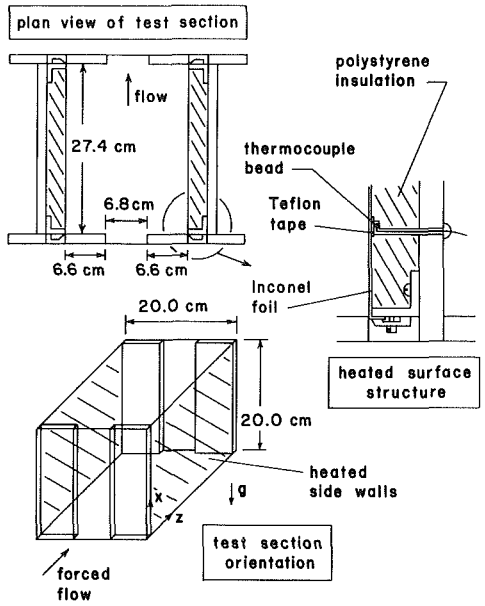

Fig. 1 Test section for mixed convection experiments

in the end walls. The heated side walls were instrumented to provide direct measurements of the local heat transfer coefficients at 32 locations over the surface.

Using water as the test fluid, experiments were conducted at high values of Rayleigh number and moderate values of Reynolds number. The distribution of the local heat transfer coefficient over the heated surfaces was determined experimentally for wide ranges of these parameters. The variation of the local heat transfer coefficient was found to be related to the flow behavior observed in flow visualization experiments.

Mean heat transfer coefficients over the entire wall surface were also determined from the measured local data. A heat transfer correlation for mixed convection flow has been developed which agrees well with our data. In addition, flow regime criteria were also developed which indicate the conditions corresponding to natural convection dominated flow, forced convection dominated flow, and a mixed convection regime where both effects are important.

Experimental Apparatus

Experimental studies of mixed convection in a rectangular enclosure with finite inlet and exit openings were conducted using the test section shown in Fig. 1. Within the enclosure, the cross section normal to the forced-flow direction is a square 20.0 cm high and 20.0 cm wide, and the inside length of the enclosure is 27.4 cm. The top and bottom walls of the test section are made of 12.7-mm-thick transparent acrylic plastic. This permitted us to observe the flow when employing flow visualization techniques.

For the tests with water reported here, the heat transfer through the plastic was negligible, so the top and bottom walls were essentially adiabatic. The end walls were also made of acrylic plastic, and were essentially adiabatic during these experiments. A rectangular opening running from the bottom to the top in the center of each of the end walls permitted a horizontal flow to pass through the test section. These openings were 6.7 cm wide, or about one third of the enclosure width.

As seen in Fig. 1, along each of the vertical side walls, two jaw assemblies are used to stretch a 0.0264-mm-thick sheet of Inconel foil over a 25.4 mm thick layer of polystyrene foam insulation. This foil was also bonded to the surface of the insulation, except at the thermocouple locations. This foil is very uniform in thickness ($\pm$ 0.00013 mm) so that when electric current passes through it, a uniform heat flux condition is imposed along the vertical walls of the enclosure. The polystyrene insulation virtually elminates heat loss to the surroundings, so all the applied heat flux is delivered entirely to the water. In addition, due to the thinness of the Inconel foil, conduction of heat in the wall structure is negligible.

Local wall temperatures were determined using copper-constantan thermocouples installed behind the foil as shown in Fig. 1. The thin layer of Teflon tape between each thermocouple bead and the foil prevents electrical interactions which might affect thermocouple readings, while maintaining good thermal communication between the bead and the foil. Thermocouple wires leaving the test section were sealed using RTV silicone to prevent water leakage. One side wall of the test section was instrumented with 32 thermocouples distributed over the surface of the wall. The opposite side wall had six thermocouples installed to verify symmetry in the thermal transport from the two walls. Two thermocouples mounted on a support rod at different elevations in the entrance of the test section were used to determine the ambient (and core-flow) water temperature.

Nomenclature

a = exponent in equation (4)
A_c = test section cross-sectional area = $x_m L$
d = hydraulic diameter of test section = $4A_c/2(L + x_m)$
F = function of Prantdl number defined by equation (5*b*)
g = gravitational acceleration
Gr_x = Grashof number = $g\beta x^3 \Delta t/\nu^2$
h = local heat transfer coefficient = $q''/(t_w - t_\infty)$
h_{nc} = h value for pure natural convection
$\bar{h}$ = mean surface heat transfer coefficient
$\bar{h}_{nc}$ = $\bar{h}$ value for natural convection alone
$\bar{h}_{fc}$ = $\bar{h}$ value for forced convection alone
k = fluid thermal conductivity
L = horizontal dimension of enclosure
$\dot{m}$ = mass flow rate through test section
Pr = Prandtl number
q'' = surface heat flux
Ra_x^* = local Rayleigh number = $g\beta x^4 q''/k\nu\alpha$
Ra_{xm}^* = Rayleigh number based on x_m = $g\beta x_m^4 q''/k\nu\alpha$
Re_d = channel Reynolds number = Wd/ν
Re_z = local Reynolds number = Wz/ν
Re_{zm} = Reynolds number based on z_m = Wz_m/ν
t_w = local wall temperature
t_∞ = ambient (core) temperature
W = mean horizontal velocity in test section
x = vertical coordinate
x_m = overall height of heated wall
y = horizontal coordinate normal to heated wall
z = horizontal coordinate parallel to heated wall
z_m = overall length of heated wall
α = fluid thermal diffusivity
β = fluid coefficient of thermal expansion
Γ = parameter defined by equations (7*c*) and (7*d*)
δ = horizontal dimension of inlet and exit openings
ν = fluid kinematic viscosity

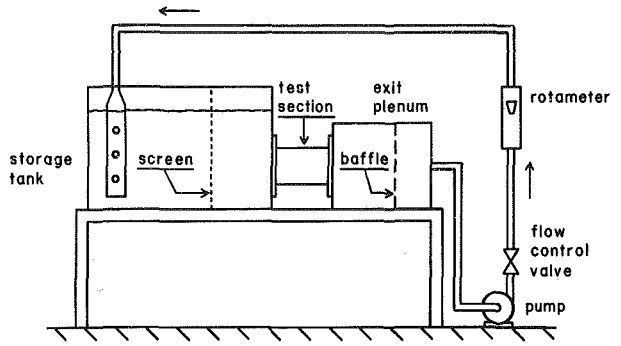

Fig 2 Schematic of test system used for mixed convection experiments

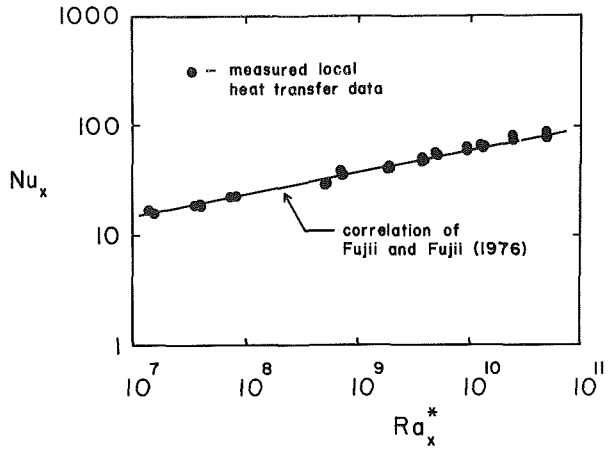

Fig. 3 Comparison of measured local heat transfer data for natural convection with the correlation of Fujii and Fujii (1976)

The flow of water through the test section was supplied by the flow system shown schematically in Fig. 2. Water from the storage reservoir flowed into the test section and was discharged into the exit plenum. The water then passed through the pump and flow meter and was returned to the inlet reservoir through an overhead pipe.

The storage reservoir has a capacity of 246 liters. The water return line splits in two just before entering the reservoir to reduce the kinetic energy of the flow. Below the water level in the tank, each return line has a staggered hole pattern around its circumference and a capped end. This distributes water as evenly as possible, for greater flow uniformity in the tank.

One layer of nylon window-screen material was located about halfway between the water return and the test section inlet to help damp out flow irregularities. Flow visualization studies indicated that the inlet flow was, in fact, laminar and very symmetric with respect to the rectangular inlet cross section. The exit plenum is slightly larger than the test section, having a capacity of 76 liters. An acrylic plastic distribution plate with a staggered array of small holes was installed inside the exit plenum to prevent premature flow constriction in the test section.

Plumbing lines in the water circulation loop were 31.8-mm (inside) diameter PVC pipe. To help isolate the test section from pump vibration, flexible rubber pipe couplers were used to connect the pump inlet and outlet to the hard piping in the system. Calibrated rotameters, manufactured by King Instruments, with ranges of 4 to 38 liter/min were used to determine the water flow rate. A low-range or a high-range centrifugal pump was used in the system, depending on the flow rate desired in the experiment.

The electric power required to heat the walls of the test section was provided by a Sorensen DCR40-40B 1800 watt regulated d-c power supply. A specified current up to 45 A was passed through the Inconel foil, establishing a uniform heat flux at the walls of up to 1900 W/m^2. The current through the foil was determined by measuring the voltage drop across a large shunt resistor of known resistance in the circuit. This measurement and the voltage drop across the foil were determined using a Hewlett Packard 3466A digital multimeter. Copper-constantan thermocouples in the test section were read using an Omega two-pole selector switch and a precision Fluke digital readout.

As described above, this experimental system permitted testing over Rayleigh number (Ra^*_{xm}) and inside channel Reynolds number (Re_d) ranges of $5 \times 10^9 < Ra^*_{xm} < 10^{11}$ and $670 < Re_d < 10{,}500$. The lower limits of these ranges were determined by the minimum flow and heat flux conditions where accurate measurements are possible. The upper limits are dictated by the ouptut capacity of the equipment. For almost all of our data, the wall to core-flow temperature difference was between 3 and 6°C, although a few points were below 3°C. For all our experiments, the core flow was within 2°C of the surrounding room temperature. As noted above, for these conditions, heat transfer through the top and bottom acrylic walls of the test section was negligible. For our instrumentation, the resulting uncertainty in the measured values of the heat transfer coefficient is estimated to be ± 9 percent. The uncertainties in the measured heat flux and flow rate are estimated to be ± 3 percent and ± 5 percent, respectively.

In addition to the heat transfer measurements, flow visualization studies were also done for selected experiments using a gravity-driven dye injection system. Dye was stored above the test section in a bottle with a drip valve. A thin plastic tube connected the exit of the bottle to a brass injector tube with an inside diameter of approximately 1 mm. With the drip valve open, a steady stream of slowly moving dye was released into the flow at the location of the injector, which could be placed anywhere in the test section. The subsequent motion of the dye was then observed visually. A water-soluble blue food coloring was ued as the dye.

Experimental Procedure and Results

Before conducting the mixed convection experiments, two sets of preliminary tests were run. The first preliminary tests were a series of natural convection experiments with no forced flow through the test section. The end walls were removed for these tests to permit the test section to exchange fluid more freely with the adjacent tanks. This eliminated the tendency for warm fluid to accumulate in the test section during these experiments. In these tests, measurements of the local surface heat transfer coefficient were obtained over the entire heated surface for several values of applied heat flux. The local Nusselt number was thereby obtained for values of the local Rayleigh number, Ra^*_x, ranging from 10^7 to 5×10^{10}.

Flow visualization studies for these conditions indicated that the flow was entirely laminar, even for the highest heat flux levels. The measured local Nusselt number data at several wall locations are compared to the laminar natural convection correlation of Fujii and Fujii (1976) for a uniform flux surface in Fig. 3. It can be seen that the data are in excellent agreement over the entire surface, and at all heat flux levels tested.

At thermocouple locations very near the entrance and exit of the test section, the measured h values were slightly higher due to lateral entrainment of colder fluid into the boundary layer from the reservoir or exit plenum. However, even at these locations, agreement of the data with the correlation is quite good. The excellent agreement between the correlation and our data for these conditions verified that our thermocouples were reading properly and the heat flux measurements and data reduction procedure were correct.

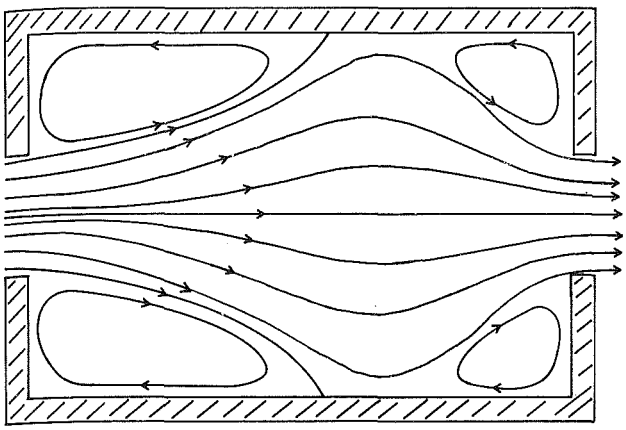

Fig. 4(a)

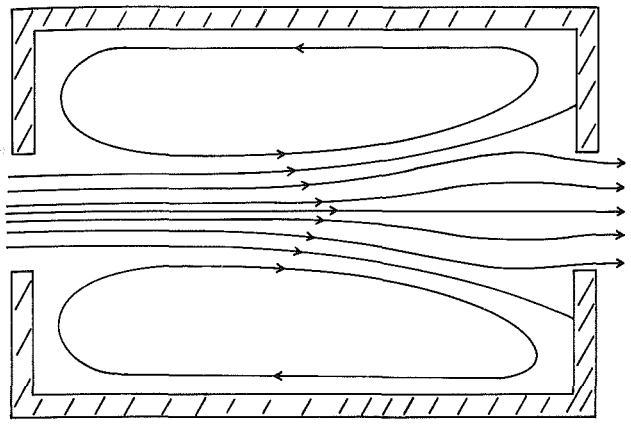

Fig. 4(b)

Fig. 4 Observed pattern of the horizontal velocity field: (a) $Re_{zm} < 5000$, (b) $Re_{zm} > 5000$

The second set of preliminary tests was a series of flow visualization studies to examine the characteristics of the horizontal forced flow through the test section with no heat input at the walls. Using the dye-injection technique, it was found that, for the entire range of flow rates tested here, the entrance flow into the test section was smooth, laminar, and symmetric. Inside the test section, the horizontal flow near the middle of the vertical walls was observed to be in one of the two patterns shown in Fig. 4. The flow rate through the enclosure will be quantified in terms of a wall-length Reynolds number Re_{zm}. Note that this parameter is related to the channel Reynolds number Re_d as

$$Re_d = 0.730\, Re_{zm} \tag{1}$$

The flow within the enclosure was observed to be turbulent for $Re_{zm} > 2000$, which includes most of the flow rates tested here. At flow rates corresponding to $Re_{zm} < 5000$, the entering flow expanded, resulting in a stagnation point generally about half way along the side wall. The resulting flow pattern is shown in Fig. 4(*a*). The position of this stagnation point was often observed to fluctuate by as much as 4 cm. For these circumstances, the horizontal velocity along the side wall appeared to be strongest near the exit end.

For $Re_{zm} > 5000$, the flow pattern usually looked like that shown in Fig. 4(*b*). The flow rate through the test section was generally too rapid to allow significant expansion and there was no stagnation point along the side wall. The coldest fluid impinges on the side wall at the exit end of the enclosure. All fluid near the wall was moving in the direction opposite to that of the core flow. However, this flow pattern was sometimes observed to be unstable, occasionally alternating between the patterns shown in Figs. 4(*a*) and 4(*b*).

The flow patterns described above were characteristic of the horizontal flow over most of the central portion of the enclosure. As expected, this pattern broke down near the top and bottom due to the presence of these surfaces. Later flow visualization studies conducted with heated walls indicated that the buoyancy effect near the walls did not strongly affect the horizontal flow pattern in the center of the enclosure. The observed horizontal flow behavior was consistent with that shown in Fig. 4. Upward flow along the walls was simply superimposed on the horizontal flow pattern.

Upon completing the preliminary studies described above, experiments were then conducted with both heating and cross flow through the test section. After setting the power input to the foil wall heaters and the pump flow, the system was allowed to stabilize for approximately 15 min. Then the thermocouple readings were recorded and, in some cases, flow visualization results were noted.

For each combination of flow and heat flux conditions, three sets of data were recorded to assess the repeatability of the results. In most cases, all three sets were virtually identical. However, in a few instances, small but significant differences were found. Such differences were encounterd only at high flow rates. The differences appeared to be the result of the unsteadiness of the flow near the reattachment point, or the alternating of the flow between the two patterns shown in Fig. 4 at high flow rates. For the few instances where such variations were found, the data which best represent the average of the three recorded data sets are presented here.

For each combination of flow rate and surface heat flux, the surface thermocouple measurements and the measured heat flux were used to determine the local heat transfer coefficient h at each of the 32 thermocouple locations. For each location, the ratio h/h_{nc} was also calculated, where h_{nc} is the local heat transfer coefficient for laminar natural convection flow at the same heat flux. The value of h_{nc} was calculated using the correlation of Fujii and Fujii (1976)

$$h_{nc} = \frac{k}{x}\left[\frac{\mathrm{Pr}}{4+9\ \mathrm{Pr}^{1/2}+10\ \mathrm{Pr}}\right]^{1/5} (\mathrm{Ra}_x^*)^{1/5} \tag{2}$$

Hence, the amount by which h/h_{nc} exceeds one directly indicates the enhancement of the local heat transfer coefficient due to forced convection effects.

The measured variation of h/h_{nc} over the instrumented vertical wall of the test section is plotted in Figs. 5–8 for four different combinations of flow rate and heat flux. These figures also indicate the relative locations of the embedded thermocouples on the heated surface.

As in the unheated experiments, the nature of the flow in the test section below $Re_{zm} = 5000$ was distinctly different from that above 5000. The principle difference was that the horizontal flow reattached to the vertical side walls about halfway through the test section for $Re_{zm} < 5000$, whereas no reattachment occurred for $Re_{zm} > 5000$. Near the walls, fluid from the horizontal core flow was entrained in a buoyancy-driven flow which moved upward along the wall until it reached the top of the test section. At the top, the flow turned and moved horizontally toward the center of the test section along the top wall. As expected, the strength of the buoyancy-driven flow near the walls increased as the Rayleigh number Ra_{xm}^* increased.

In general, for $Re_{zm} < 1500$, the flow near the heated walls resembled pure natural convection laminar flow with a superimposed weak horizontal drift. As seen in Fig. 5, the enhancement of heat transfer beyond that for natural convection alone is small at $Re_{zm} = 930$. Although the horizontal flow impinges on the sidewalls (see Fig. 4(*a*)) near the center of the wall ($z/z_m \sim 0.5$), there is little, if any, effect on the heat transfer there. For this value of Re_{zm}, the only significant enhancement occurred near the exit end of the heated wall where cold fluid from the center of the test section impinges

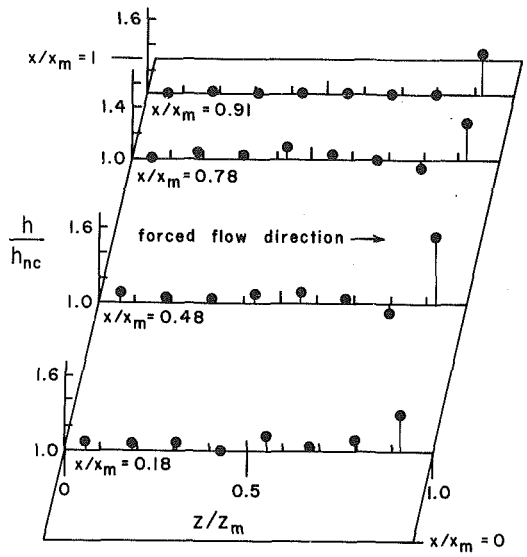

Fig. 5 Measured variation of the enhancement ratio, h/h_{nc}, over the heated surface for $Ra^*_{xm} = 8.65 \times 10^{10}$ and $Re_{zm} = 930$

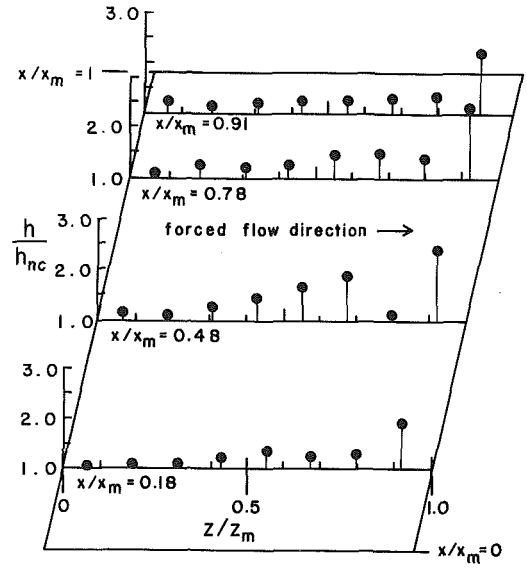

Fig. 6 Measured variation of the enhancement ratio, h/h_{nc}, over the heated surface for $Ra^*_{xm} = 7.02 \times 10^{10}$ and $Re_{zm} = 2340$

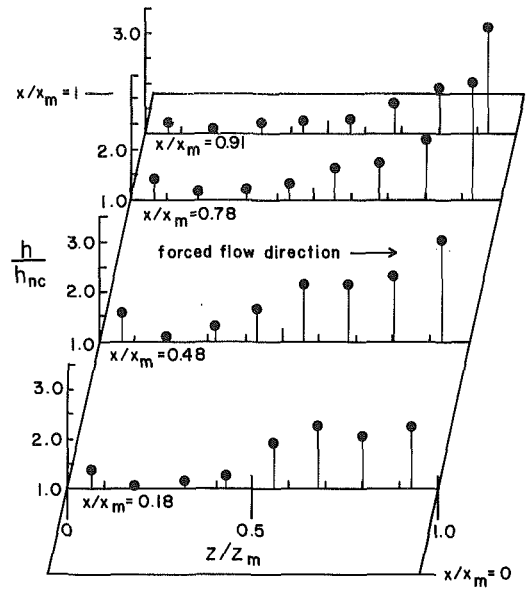

Fig. 7 Measured variation of the enhancement ratio, h/h_{nc}, over the heated surface for $Ra^*_{xm} = 1.58 \times 10^{10}$ and $Re_{zm} = 2250$

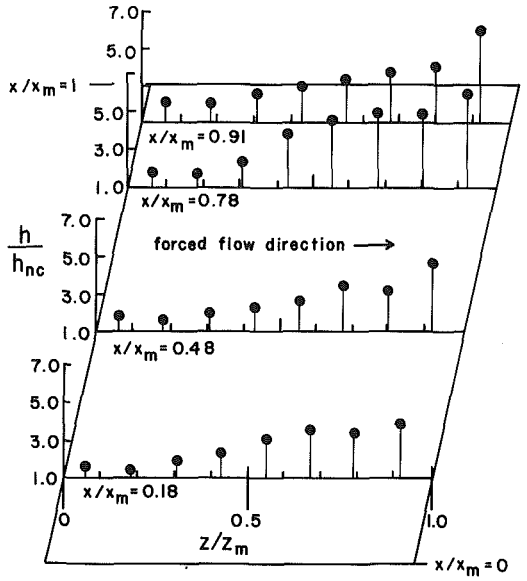

Fig. 8 Measured variation of the enhancement ratio, h/h_{nc}, over the heated surface for $Ra^*_{xm} = 8.70 \times 10^{10}$ and $Re_{zm} = 11{,}600$

on the wall. However, even at this location, only 20 to 60 percent enhancement is found. Low levels of enhancement were observed for all our experiments at $Re_{zm} < 1500$.

Figure 6 shows the distribution of h/h_{nc} for $Re_{zm} = 2340$ at a value of Ra^*_{xm} near that for Fig. 5. Similar results are plotted for about the same Reynolds number with a slightly lower value of Ra^*_{xm} in Fig. 7. At this level of Reynolds number, the core flow appeared to be turbulent. Very near the vertical sidewalls, the flow appeared to be laminar or weakly turbulent. The horizontal flow pattern appeared to be like that shown in Fig. 4(*a*).

It can be seen in Fig. 6 that the peak enhancement occurs near the exit end of the heated wall. About halfway up the sidewall there is a region where the enhancement peaks at about $z/z_m = 0.65$. This corresponds approximately to the location where flow from the core was observed to impinge on the sidewall, as seen in Fig. 4(*a*). However, this second peak is almost nonexistent near the top and bottom of the heated wall. This may be due to the effects of the top and bottom walls on the horizontal flow. It can also be seen that overall, the level of enhancement is higher than that observed at $Re_{zm} = 930$ for about the same Ra^*_{xm}.

The results shown in Fig. 7 also indicate a maximum enhancement near the exit end of the wall. The enhancement is also high near $z/z_m = 0.6$, although a strongly distinctive peak is not found there, even at $x/x_m = 0.48$. The flow visualization studies indicated that the location of the stagnation point in the horizontal flow near $z/z_m = 0.6$ varies with time for these conditions. This may be part of the reason for the lack of a distinctive peak in the heat transfer at this location. It can also be seen from Figs. 6 and 7 that for about the same Re_{zm} values, the relative enhancement is sightly greater for lower Ra^*_{xm}. This is somewhat expected since the heat transfer coefficient for natural convection alone is lower for lower Ra^*_{xm}, and a given cross-flow effect can therefore have a greater relative effect on transport. The enhancement of about 50 percent near the inlet end of the heated wall suggests that

there may have been an undetected additional recirculation zone there that brought colder fluid from the core flow into the region near the wall. As seen in Fig. 6, there was no such enhancement near the inlet edge at higher heating rates (larger Ra^*_{xm}).

Figure 8 shows the distribution of h/h_{nc} for $Re_{zm} = 11{,}600$ at a value of Ra^*_{xm} near those for Figs. 5 and 6. The horizontal flow pattern for this condition was similar to that shown in Fig. 4(*b*). It can be seen that again, the enhancement is greatest near the exit end of the heated wall. Since fluid from the core flow first impinges on the side walls near the exit end, and the flow circulates toward the inlet end, it is not surprising that the enhancement increases monotonically from the inlet to the exit end. It is also noteworthy that the enhancement is very large at the exit end. The heat transfer coefficient is five to seven times that for natural convection alone. This suggests that over most of the surface, the transport is dominated by this reversed portion of the horizontal flow.

For each combination of flow rate and heat flux tested, the local heat transfer measurements were used to calculate the mean heat transfer coefficient over the entire heated surface. The heated surface was divided into 32 area elements with a surface thermocouple at the center of each element. The mean heat transfer coefficient $\bar{h}$ was then calculated as

$$\bar{h} = \frac{1}{x_m z_m} \sum_{i=1}^{32} A_i h_i \tag{3}$$

where A_i is the area of the ith element, and h_i is the measured local heat transfer coefficient at the thermocouple location at the center of this element. This summation approximates the integral average of h over the entire surface.

To develop a correlating equation to match $\bar{h}$ data calculated as described above, it is postulated here that the mixed convection heat transfer coefficient is given by

$$\bar{h} = (\bar{h}^a_{nc} + \bar{h}^a_{fc})^{1/a} \tag{4}$$

where $\bar{h}_{nc}$ aand $\bar{h}_{fc}$ are the mean heat transfer coefficients for natural convection alone at the specified heating condition, and forced convection alone at the same flow conditions, respectively.

At low heat flux and high flow rate, the flow is expected to be forced-convection dominated so that $\bar{h} \approx \bar{h}_{fc}$. Conversely, at high heat flux and low flow rate, the flow is expected to be natural-convection dominated and $\bar{h} \approx \bar{h}_{nc}$. Between these extremes, it is assumed that the overall $\bar{h}$ can be determined from a superposition of the two effects in the manner described by equation (4).

The preliminary experiments indicated that, for the conditions studied here, a laminar natural convection boundary-layer flow exists over the entire heated surface when there is no forced flow present. The value of $\bar{h}_{nc}$ in equation (4) was therefore calculated using the laminar correlation of Fujii and Fujii (1976). The following relation for $\bar{h}_{nc}$ was obtained by determining the integrated average of h, as given by equation (2), over the entire surface

$$\bar{h}_{nc} = \left(\frac{5k}{4x_m}\right)[F(\mathrm{Pr})\mathrm{Ra}^*_{xm}]^{1/5} \tag{5a}$$

where

$$F(\mathrm{Pr}) = \mathrm{Pr}/(4 + 9\,\mathrm{Pr}^{1/2} + 10\,\mathrm{Pr}) \tag{5b}$$

In the limit of high Reynolds number, it was observed that the $\bar{h}$ data obtained from our experiments could be correlated in terms of Reynolds number alone, suggesting that the flow had reached the forced-convection dominated limit. The high Reynolds number data are well correlated by the relation

$$\bar{h}_{fc} = 0.50(k/z_m)\mathrm{Pr}^{0.6}\mathrm{Re}^{0.6}_{zm} \tag{6}$$

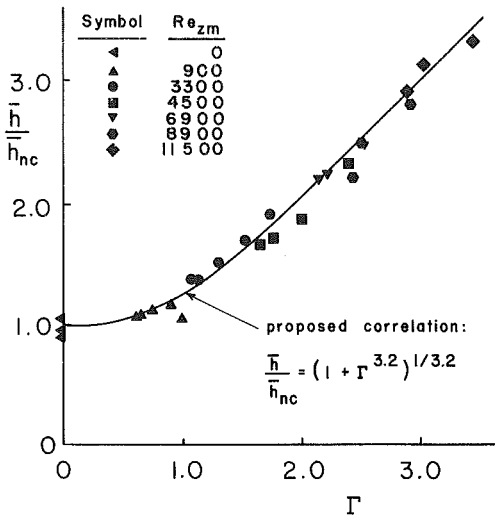

Fig. 9 Comparison of the experimentally determined values of the mean heat transfer coefficient with the proposed correlation for cross-flow mixed convection in the enclosure

For turbulent forced convection boundary layer flow at moderate Prandtl number, the correlation of Kays and Crawford (1980) indicates that h should vary about proportional to $\mathrm{Pr}^{0.6}$. Since the high Reynolds number flows near the surface appear to be turbulent and boundary layer in nature, the postulated relation for $\bar{h}$ above includes a factor of $\mathrm{Pr}^{0.6}$. However, this dependence on Pr has not been verified over a wide range of Prandtl number. All data reported here correspond to values of Pr between 6.11 and 6.94. The constant factor in equation (6) was obtained by optimizing the fit to the high Reynolds number data.

Using equations (5) and (6) to evaluate $\bar{h}_{nc}$ and $\bar{h}_{fc}$ in equation (4), an optimization scheme was used to minimize the rms deviation between the correlation (4) and the values of $\bar{h}$ calculated from the experimental data. The optimal value of a was thereby found to be 3.2. The proposed correlation can then be written as

$$\bar{h}/\bar{h}_{nc} = [1 + \Gamma^{3.2}]^{1/3.2} \tag{7a}$$

where

$$\bar{h}_{nc} = \left(\frac{5k}{4x_m}\right)[F(\mathrm{Pr})\mathrm{Ra}^*_{xm}]^{0.2} \tag{7b}$$

$$F(\mathrm{Pr}) = \mathrm{Pr}/(4 + 9\,\mathrm{Pr}^{1/2} + 10\,\mathrm{Pr}) \tag{7c}$$

and

$$\Gamma = \bar{h}_{fc}/\bar{h}_{nc} = \frac{0.40(x_m/z_m)\mathrm{Pr}^{0.6}\mathrm{Re}^{0.6}_{zm}}{[F(\mathrm{Pr})\mathrm{Ra}^*_{xm}]^{0.2}} \tag{7d}$$

A relation of the form given by equation (4) was also used by Siebers et al. (1983) to correlate heat transfer data for mixed convection near a heated vertical flat plate in a horizontal forced flow. It is interesting to note that they also found that an exponent of $a = 3.2$ best fit their data in both the laminar and turbulent regimes.

The experimentally determined $\bar{h}$ values for the heated sidewalls of the enclosure are compared with the correlation given by equations (7*a*)-(7*d*) in Fig. 9. It can be seen that the agreement between the measured data and the correlation is quite good. For all the data points, the difference between the measured values and the correlation is less than the uncertainty of the measurements. Even the data for $Re_{zm} < 2000$, where the forced flow is laminar, agree well with the correlation.

It can be seen in Fig. 9 that, as expected, the data approach the natural convection limit ($\bar{h}/\bar{h}_{nc} = 1$) at small values of Γ,

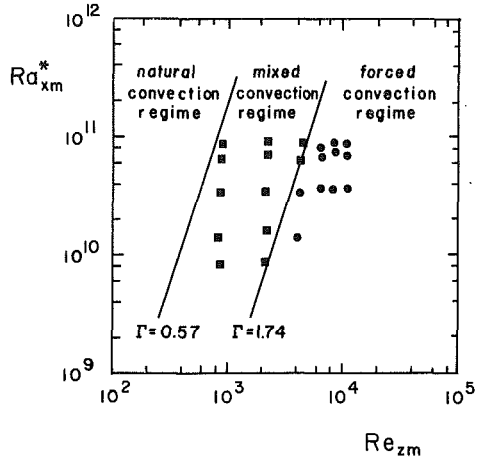

Fig. 10 Flow regime map for convection heat transfer from the vertical sidewalls of an enclosure with restricted inlet and exit openings

and the forced convection limit ($\bar{h}/\bar{h}_{nc} = \Gamma$) at large values of Γ. It is possible, therefore, to distinguish between the natural, mixed and forced convection regimes by comparing the correlation predictions of $\bar{h}/\bar{h}_{nc}$ with these limits. The natural convection regime was arbitrarily taken to correspond to conditions for which $\bar{h}$ is within 5 percent of the value for natural convection alone at the specified heat flux. Since this implies that $1.0 \leq \bar{h}/\bar{h}_{nc} < 1.05$, the correlation given by (7) requires that $\Gamma < 0.57$ in the natural convection regime.

Similarly, the forced convection regime was taken to correspond to conditions where $\bar{h}$ is within 5 percent of the value for purely forced convection flow at the same flow rate. Using equations (7) with $\bar{h}/\bar{h}_{nc} = 1.05\ \Gamma$, it can be shown that the forced-convection regime must correspond to $\Gamma > 1.74$. The range $0.57 \leq \Gamma \leq 1.74$ thus corresponds to the mixed convection regime where both forced convection and natural convection effects are important.

These conclusions are shown graphically in Fig. 10. The data points shown indicate all the combinations of Re_{zm} and Ra^*_{xm} for which experiments were done in this study. The boundaries of the flow regimes, corresponding to $\Gamma = 0.57$ and $\Gamma = 1.74$, are also shown.

It should be noted that the flow regime boundaries shown in Fig. 10 apply only to the specific Prandtl number and height-to-length ratio (x_m/z_m) for our experimental circumstances. Only by specifying these parameters can a constant Γ condition be transformed into a line on the flow regime map in terms of Ra^*_{xm} and Re_{zm}. In addition, the limiting values of Γ which define the boundaries of the flow regimes are specific to the aperture-width ratio (δ/L) for our test section. These values may vary if this ratio is changed. Figure 10 is therefore not a general flow regime map, but a specific one for our experimental condition. However, for δ/L near 0.34 and x_m/z_m near 0.73, the boundaries defined by $\Gamma = 0.57$ and $\Gamma = 1.74$ are expected to be generally applicable to internal flows of the type considered here.

Conclusions

Measurements of local heat transfer coefficients have been obtained for cross-flow mixed convection at high Rayleigh number in a rectangular enclosure with restricted inlet and exit openings. These experiments were conducted in a small-scale test section with uniformly heated vertical side walls and an adiabatic top and bottom, using water as the test fluid.

For the mixed convection circumstances studied here, the heat transfer from the vertical sidewalls is dictated by the interaction of upward buoyancy with recirculating portions of the horizontal flow near the walls. At $Re_{zm} < 2000$, our flow visualization studies indicated that the flow throughout the test section was laminar, whereas for $Re_{zm} \geq 2000$, the flow appeared to be turbulent. For $Re_{zm} < 5000$, two distinct recirculation regions were observed near each heated vertical wall. Above $Re_{zm} = 5000$, a single large recirculation near each sidewall was most often observed.

As the flow rate, and Re_{zm}, increased, the enhancement of the heat transfer coefficient, above that for natural convection alone, generally increased over the entire surface. For all conditions tested, the local enhancement is largest near the exit end of the heated vertical wall. This peak in the enhancement is associated with the impingement of recirculating colder fluid from the horizontal core flow against the sidewall at this location. At flow rates corresponding to $Re_{zm} < 2000$, little enhancement of the heat transfer coefficient is found beyond that for natural convection alone. At the highest flow rates (Re_{zm} near 11,000) the local enhancement was as much as a factor of six higher.

The measured local heat transfer coefficients were also used to calculate the mean heat transfer coefficient averaged over the entire heated sidewall. The calculated $\bar{h}$ values determined in this way for the high Reynolds number values were found to be well correlated by equation (6). Using this correlation for the forced-convection limit and the relation of Fujii and Fujii (1976) for laminar natural convection, a correlation has been developed which agrees very well with our data in the mixed convection regime where both natural and forced-convection effects are important.

Based on the heat transfer correlation developed here, regimes of natural, mixed, and forced convection were also specified in terms of the Γ parameter defined by equation (7*d*). The range $\Gamma < 0.57$ corresponds to the natural convection dominated regime, whereas the forced-convection regime corresponds to $\Gamma > 1.74$. The range $0.57 \geq \Gamma \leq 1.74$ corresponds to the mixed convection regime where both mechanisms have an important effect on heat transfer.

The results of this experimental study provide new insight into the flow behavior and heat transfer mechanisms for flows of this type. However, strictly speaking, the heat transfer correlation and conclusions regarding the flow regime transitions are applicable only for the Prandtl number ($Pr \sim 6.7$) and geometry ($x_m/z_m = 0.73$, $\delta/L = 0.34$) considered here. Clearly there is a need for more data for other geometries and Prandtl numbers before the effects of geometry variations and fluid property changes on the flow and heat transfer can be fully assessed for flows of this type.

Acknowledgments

Support for this research was provided by the Solar Energy Research Institute under subcontract number XX-4-04038-1 and the National Science Foundation under grant number CBT-8451781. The efforts of Loris C.-H. Donahue in preparation of this manuscript are also appreciated.

References

Bergles, A. E., ans Simons, R. R., 1971, "Combined Forced and Free Convection for Laminar Flow in Horizontal Tubes With Uniform Heat Flux," *International Journal of Heat and Mass Transfer*, Vol. 14, pp. 1989–2000.

Cheng, K. C., Hong, S. W., and Hwang, G. J., 1972, "Buoyancy Effects on Laminar Heat Transfer in the Thermal Entrance Region of Horizontal Rectangular Channels With Uniform Wall Heat Flux For Large Prandtl Number Fluids," *International Journal of Heat and Mass Transfer*, Vol. 15, pp. 1819–1836.

Cheng, K. C., and Ou, J.-W., 1974, "Free Convection Effects on Graetz Problem for Large Prandtl Number Fluids in Horizontal Tubes With Uniform Wall Heat Flux," *Proc. 5th Int. Heat Transfer Conf.*, Paris, Vol. 3, pp. 159–163.

Eichhorn, R., and Hasan, M. M., 1980. "Mixed Convection About a Vertical Surface in Cross-Flow: a Similarity Solution," ASME JOURNAL OF HEAT TRANSFER, Vol. 102, pp. 775–777.

Evans, G. H., and Plumb, O. A., 1982a, "Laminar Mixed Convection From

a Vertical Heated Surface in a Cross-Flow," ASME JOURNAL OF HEAT TRANSFER, Vol. 104, pp. 554–558.

Evans, G. H., and Plumb, O. A., 1982b, "Numerical and Approximate Numerical Solution to a Three-Dimensional Mixed Convection Boundary Layer Flow," *Numerical Heat Transfer*, Vol. 5, pp. 287–298.

Faris, G. N., and Viskanta, R., 1969, "An Analysis of Laminar Combined Forced and Free Convection Heat Transfer in a Horizontal Tube," *International Journal of Heat and Mass Transfer*, Vol. 12, pp. 1295–1309.

Fujii, T., and Fujii, M., 1976, "The Dependence of Local Nusselt Number on Prandtl Number in the Case of Free Convection Along a Vertical Surface With Uniform Heat Flux," *International Journal of Heat and Mass Transfer*, Vol. 19, pp. 121–122.

Hong, S. W., Marcos, S. M., and Bergles, A. E., 1974, "Analytical and Experimental Results for Combined Forced and Free Laminar Convection in Horizontal Tubes," *Proc. 5th Int. Heat Transfer Conf.*, Tokyo, Vol. 3, pp. 159–163.

Kays, W. M., and Crawford, M. E., 1980, *Convective Heat and Mass Transfer*, McGraw-Hill, New York, NY.

McComas, S. T., and Eckert, E. R. G., 1966, "Combined Free and Forced Convection in a Horizontal Circular Tube," ASME JOURNAL OF HEAT TRANSFER, Vol. 88, pp. 147–153.

Mori, Y., Fugatami, K., Tokunda, S., and Nakamura, M., 1966, "Forced Convective Heat Transfer in Uniformly Heated Horizontal Tubes," *International Journal of Heat and Mass Transfer*, Vol. 9, pp. 453–463.

Newell, P. H., and Bergles, A. E., 1970, "Analysis of Combined Free and Forced Convection for Fully Developed Laminar Flow in Horizontal Tubes," ASME JOURNAL OF HEAT TRANSFER, Vol. 92, pp. 83–93.

Petukhov, B. S., and Polyakov, A. F., 1967, "Experimental Investigation of Viscogravitational Fluid Flow in a Horizontal Tube," *High Temp.*, Vol. 5, pp. 75–81.

Plumb, O. A., 1980, 'The Effect of Crossflow on Natural Convection From Vertical Heated Surfaces," ASME Paper No. 80-HT-71.

Rahman, M. M., and Carey, V. P., 1986a, "Transient Cross-Flow Mixed Convection Adjacent to an Isothermal Vertical Plate in Air," *Proc. 8th Int. Heat Transfer Conf.*, San Francisco, Vol. 3, pp. 1439–1444.

Rahman, M. M., and Carey, V. P., 1986b, "Steady and Transient Mixed Convection Near a Vertical Uniformly Heated Surface Exposed to a Horizontal Fluid Flow," *Numerical Heat Transfer*, Vol. 10, pp. 327–347.

Shannon, R. L., and Depew, C. A., 1968, "Combined Free and Forced Laminar Convection in a Horizontal Tube With Uniform Heat Flux," ASME JOURNAL OF HEAT TRANSFER, Vol. 90, pp. 353–357.

Siebers, D. L., Schwind, R. G., and Moffat, R. J., 1983, "Experimental Mixed Convection Heat Transfer From a Large Vertical Surface in a Horizontal Flow," SAND 83-8225, Sandia National Laboratories, Livermore, CA.

Young, R. J., and Yang, K. T., 1963, "Effect of Small Cross-Flow and Surface Temperature Variation on Laminar Free Convection Along a Vertical Plant," ASME *J. Applied Mechanics*, pp. 252–256.

Yousef, W. M., and Tarasuk, J. D., 1982, "Free Convection Effects on Laminar Forced Convective Heat Transfer in a Horizontal Isothermal Tube," ASME JOURNAL OF HEAT TRANSFER, Vol. 104, pp. 145–158.

Experiments on Melting of Unfixed Ice in a Horizontal Cylindrical Capsule

B. W. Webb
Assoc. Mem. ASME

M. K. Moallemi
Assoc. Mem. ASME

R. Viskanta
Fellow ASME

School of Mechanical Engineering,
Purdue University,
West Lafayette, IN 47907

Melting of unrestrained ice in a horizontal cylindrical capsule has been investigated experimentally to determine the interaction of fluid flow induced by motion of the solid and natural convection with density inversion of the water–ice system. During the melting process the ice is drawn by buoyancy to the top of the heated cylinder where close-contact melting occurs. Natural convection-dominated melting whose intensity depends on wall temperature prevails in the liquid region below. Three distinct flow regimes were identified for the cylinder wall temperatures of 3.5, 7, and 12°C studied. The flow structure for temperatures below the inversion point is similar to that for melting of unfixed n-heptadecane reported previously. Photographs of flow regimes are presented, and dependence of the solid–liquid interface morphology on the flow structure is discussed.

Introduction

Melting and solidification phenomena are encountered extensively in nature and many technologically important processes. Casting of metals, freeze-drying of foodstuffs, growth of pure crystals from melts and solutions, freezing and thawing of moist soil, and latent heat-of-fusion thermal energy storage are a few of the important applications which have motivated research in this area. Previous investigations have sought to characterize the heat transfer and fluid flow in solid–liquid phase change systems from both theoretical and experimental perspectives in a variety of geometric configurations and boundary conditions. These studies have employed "ordinary" phase change materials, i.e., the density of the liquid phase decreases with increasing temperature. Recent reviews summarize prior work in this area (Viskanta, 1983; Viskanta, 1985).

One very important geometric arrangement for technical applications is the phase change process inside horizontal cylindrical enclosures. This configuration has been studied extensively for ordinary materials (primarily paraffins) both experimentally (Rieger et al., 1983; Ho and Viskanta, 1984) and theoretically (Pannu et al., 1980; Saitoh and Hirose, 1982; Rieger et al., 1983; Ho and Viskanta, 1984). In these studies the solid phase change material was maintained at a fixed position inside the heated horizontal cylinder throughout the melting process. An analytical and experimental study of melting of restrained ice inside a horizontal cylinder has also been reported by Rieger and Beer (1986). The findings of this investigation showed that the flow structure in the melt is strongly dependent on the cylinder temperature due to the density inversion of water at 4°C. Other studies have characterized transient natural convection of water in horizontal cylinders in the absence of phase change (Cheng and Takeuchi, 1976; Cheng et al., 1978; Gilpin, 1975). Results of these investigations have also shown radically different flow structure as the wall temperature is lowered through the maximum density point.

It is obvious that the melting behavior of a solid in a horizontal cylinder will be quite different if the solid is not restrained. In this case the solid is free to respond to the net force acting upon it. If the solid phase has higher density than the liquid phase the solid will sink to the bottom of the cylinder. Conversely, if the solid phase is lighter than the liquid phase the unmelted solid will be drawn by buoyancy to the top of the cylinder. In either case, a region of close-contact melting will arise between the solid and the heated wall. As a result of the motion of the solid, new melt will be squeezed out of the small gap separating the solid from the cylinder. This effective forced flow will penetrate the melt pool in the remainder of the cylindrical cavity and interact with the natural convective motion that may exist there. Then there exist two zones where the heat transfer mechanisms controlling the local melting rate are quite different. In the close-contact zone conduction is the dominant mode of heat transfer, whereas the presence of warm fluid controls heat transfer to the solid–liquid interface in the melt pool. The close-contact region will produce more rapid melting since the heat source and phase change material are separated by only a very thin fluid layer. The effectiveness of heat transfer in close-contact melting has been demonstrated by Moallemi et al. (in press). Melting in the melt pool region, although less rapid than that in the close-contact region, may also account for a portion of the total melting rate of the solid.

Heat transfer during melting of an unfixed solid phase change in an enclosure has received only limited research attention. Nicholas and Bayazitoglu (1980) and Moore and Bayazitoglu (1982) studied melting of an unrestrained solid in horizontal cylindrical and spherical geometries, respectively, primarily from a theoretical viewpoint. Melting of unfixed PCM (phase change material) in an inclined cylinder was investigated by Sparrow and Myrum (1985). An extensive study considering melting of an unfixed solid in a horizontal cylinder was conducted by Bareiss and Beer (1984). Two different paraffins were used as phase change material, and excellent agreement was found between experimental data and predictions of an integral solution to the model equations.

All of the aforementioned investigations treating melting of unfixed solids in enclosures have employed materials of nearly linear density–temperature relationship in the liquid phase. This paper reports results of a study on melting heat transfer of unfixed ice in a horizontal cylindrical capsule. The effect of water density inversion at 4°C on the flow structure is illustrated. The effect of flow regimes obtained at different wall temperatures on the solid–liquid interface is also presented.

Experiments

Test Apparatus. The experimental test cell is shown in Fig.

Contributed by the Heat Transfer Division and presented at the 4th AIAA/ASME Thermophysics and Heat Transfer Conference, Boston, Massachusetts, June 1–4, 1986. Manuscript received by the Heat Transfer Division February 28, 1986.

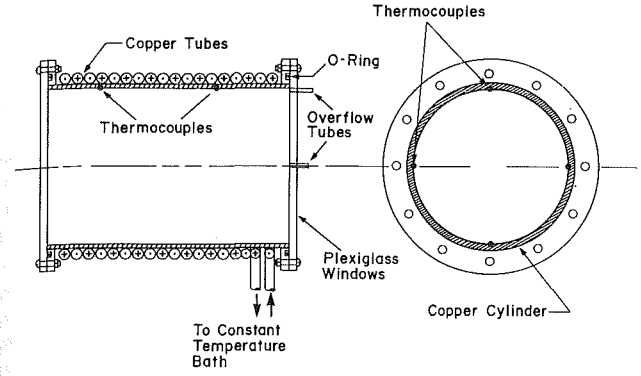

Fig. 1 Schematic of experimental setup

1. The test apparatus consists of a copper cylindrical tube 15.2 cm in length with 9.8 cm i.d. and 0.32 cm wall thickness. Small copper tubing was wrapped tightly around the large cylinder in a countercurrent fashion and good thermal contact was ensured between the two by joining the surfaces with high thermal conductivity grease. Temperature-regulated fluid from a constant temperature bath was circulated through the small countercurrent tubing to give a heated boundary at the test cylinder interior. Thermocouples were located on the test cell interior at angle increments of 90 deg, as well as in the supply and return tubes leading to the constant temperature bath. The cylinder was enclosed at the ends by 0.64-cm-thick plexiglass disks which were tightened against rubber O-rings in a plexiglass ring affixed to the copper cylinder. Small holes drilled at two locations in one of the plexiglass end disks were used as overflow tubes for expansion or contraction of the ice upon change of phase. Once assembled the cylindrical surface of the cylinder (and heat exchanger tubes) was covered by 2.5 cm of foam rubber insulation. The plexiglass ends were intentionally left exposed to the ambient so that slight end melting would provide a lubricating fluid layer, reducing friction against the plexiglass ends upon solid motion.

Test Procedure. The water was carefully degassed prior to each experiment to prevent liberation of bubbles at the solid-liquid interface during melting. This was accomplished by boiling the deionized water for approximately one hour. The cylindrical solid for each test was prepared by solidifying the degassed PCM in a mold of the same size as the test apparatus. Once solidified, the mold was heated slightly and the solid PCM was ejected. The ice cylindrical test samples were stored in a freezer for approximately 16 hr. This equilibration period provided an initial solid subcooling of about 15°C. At test time the sample to be studied was removed, and three small holes were drilled radially into the cylinder at a given axial location. The holes were then filled with dilute dye. The dyed liquid solidified in the holes, later to be released on melting to reveal the flow structure. This method insures that the dyed tracer fluid is introduced at a temperature in equilibrium with the new melt, and the resulting motions accurately represent the flow field. Standard optical techniques for visualizing the flow structure (shadowgraph, Mach-Zehnder interferometry, etc.) were not attempted because of the difficulty associated with the complex relationship between refractive index and temperature for water in the temperature range between 0 and 8°C.

Table 1 Comparison of close-contact and melt pool wall temperatures

$T_{w,\text{close-contact}}$	$T_{w,\text{melt pool}}$
1.8°C	3.5°C
5.3	7.0
7.6	12.0

Two small markers were also attached flush with the end of the cylindrical solid. These markers were to be used as reference points in separating the contribution of melting in the close-contact region from that occurring in the melt pool. However, this proved impossible due to slight rotation of the solid bulk. The PCM was then placed in the test apparatus, and the remaining volume was filled with degasified water and closed while fluid below the fusion temperature was circulated through the heat exchanger tubes. This procedure eliminated the problem of major ice expansion damaging the test apparatus upon freezing. The experiments were begun by impulsively circulating heated fluid through the heat exchanger tubes. Thermocouple temperatures were recorded at preselected time intervals and the melt fraction and flow structure (as revealed by the dilute dye liberated on melting) were photographed.

Results and Discussion

General Observations. Despite efforts to insure that the heated cylinder wall was maintained at a uniform temperature, variations in the local heat transfer resulted in circumferential nonuniformities in the cylinder temperature. High heat transfer at the close-contact melting zone resulted in lower temperatures there, whereas low heat transfer to the melt pool yielded higher temperatures. Although there was considerable circumferential temperature nonuniformity around the entire cylinder, the wall temperature variation within each of the two zones of different melting mechanisms was much lower. Lowest wall temperatures were localized in the region of close-contact melting, while quite uniform higher temperatures were found in the melt pool zone. Maximum measured circumferential wall temperature variations within the two different zones was of the order of 0.5°C. The average temperature in the close-contact melting zone is compared to that measured in the melt pool region in Table 1. The difference in wall temperature between the two zones of different melting mechanisms is experimentally unavoidable. A simple energy balance at the heated cylinder wall reveals that the heat transfer coefficient in the close-contact melting zone is easily two orders of magnitude higher than that in the melt pool. This calculation is based on the qualitative experimental observation that the majority of the melting occurs in the close-contact region, even for the highest wall temperature

Nomenclature

c = specific heat of liquid
Fo = Fourier number = $\alpha t/R^2$
Δh_f = latent heat of fusion
L = length of capsule
R = radius of cylinder or density inversion buoyancy parameter = $(T_{\max} - T_w)/(T_m - T_w)$
Ste = Stefan number = $c(T_w - T_m)/\Delta h_f$
t = time
T = temperature
V = melted volume
V_0 = initial volume = $\pi R^2 L$
α = thermal diffusivity of liquid
ρ = density

Subscripts

l = liquid-phase quantity
m = melting-point quantity
s = solid-phase quantity
w = wall quantity

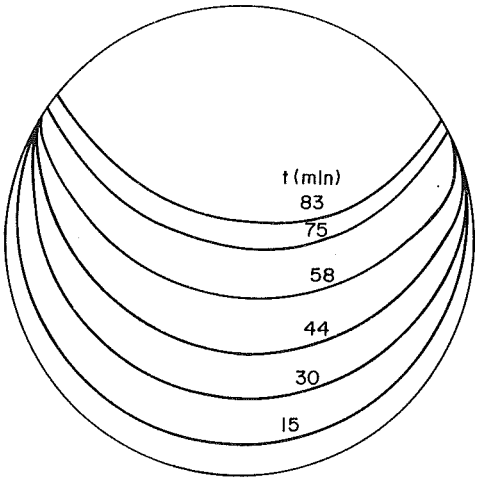

Fig. 2 Melting sequence and solid bulk position versus time for $T_w = 3.5°C$

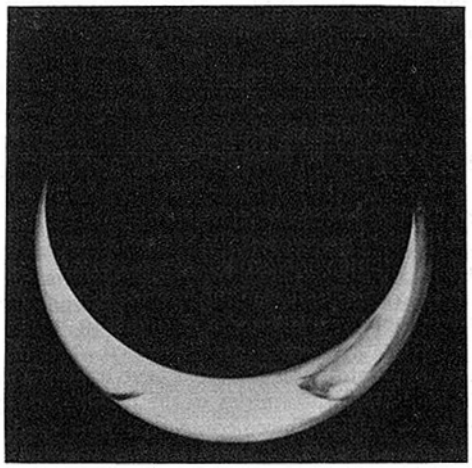

Fig. 3 Visualized flow structure for ice, $T_w = 3.5°C$, $t = 28$ min

case where the natural convective motion will be shown to be most intense. Since the emphasis of this investigation is the characterization of flow in the melt pool and its interaction with the new melt squeezed out of the close-contact gap, the cases studied have been described according to the nominal wall temperature in the melt pool. The close-contact zone wall temperature is used (in the Stefan number) only when global melting rates are compared.

Axial variations of the wall temperature were minimal. The maximum axial wall temperature difference occurred for the higher cylinder wall temperature experiments, never exceeding 0.4°C. The lowest wall temperature case ($T_w = 3.5°C$) showed virtually no measurable axial variation in the wall temperature. A temporal rise of all temperatures was also observed over the duration of each experiment. The cylinder wall temperatures rose from 1 to 3°C depending on wall temperature over a typical test period as the resistance to heat transfer increased with higher melt fraction. The unmelted solid was observed to rotate in some tests, particularly those with lower wall temperature. The rotation always occurred early in the melting process and always proceeded in the same direction. In each test, solid bulk rotation terminated before 40 percent of the initial volume had melted. The rotation speed was much lower than the velocity of the melt squeezed from the close-contact gap and thus, its effect on the flow regime is deemed negligible. The rotation is attributed to the slight circumferential nonuniformities in the wall temperature described previously. It is believed that the temperature variations and slight solid rotation do not affect significantly the trends reported here.

A typical melting process is depicted in Fig. 2, where the solid position at several times has been reproduced from the photographs for a nominal wall temperature of 3.5°C. Because of its lower density the unfixed solid ice rises to the top of the cylindrical cavity where good thermal contact with the heated wall results in intensive melting there. The upward motion of the solid causes the new melt to be squeezed out of the gap at the close-contact region into the melt pool below. It was not possible to photograph the liquid film separating the solid from the top of the heated cylinder as the gap was too thin to be detected. Slight melting was observed to take place on the underside of the solid bulk, although the melting rate here was much lower than that in the close-contact region. The same general behavior was observed for the tests at higher wall temperatures.

Flow Structure in Absence of Density Inversion. The flow field in the 3.5°C nominal wall temperature experiment is presented in the photograph in Fig. 3. New melt is squeezed out of the gap in the close-contact melting zone and flows down along the cylinder wall. Part of the fluid separates from the wall and flows upward along the solid toward the close-contact zone, forming weak recirculation cells in the corners. As time advances the separation point on the cylinder wall moves upward such that the recirculation cells remain approximately the same size. A large pool of stagnant melt, fed by the remainder of the fluid flowing down along the wall, forms in the bottom of the cavity and grows with time. This pool is stably stratified, since fluid is heated as it flows down along the wall and increases in density to a maximum in the cavity bottom at T_w. The effective forced flow induced by the upward motion of the solid is buoyancy-assisted by the increased density due to heating. Consequently, new melt replaces the upward-moving solid in the stably stratified pool at the cavity bottom.

Melting behavior analogous to the $T_w = 3.5°C$ ice-water experiment has also been observed for melting of *n*-heptadecane ($T_m = 21.4°C$) at a heated wall temperature of 31.0°C, and is reported elsewhere (Webb et al., 1986). For the paraffin, the solid phase is more dense than the liquid, so the unmelted solid bulk sinks to the bottom. New melt is forced out of the gap at the bottom of the cavity and flows up along the cylinder wall. Part of the flow separates, and flows downward along the cold solid, forming weak recirculation zones. As with the $T_w = 3.5°C$ ice case, a stably stratified stagnant melt pool is formed which grows with time. However, in the paraffin experiment, the formation of the stagnant pool is the result of decreasing density due to heating, and the stagnant pool forms at the top of the cavity. Again, the effective forced flow due to solid motion is assisted by the density change due to heating. This phenomenon is illustrated schematically for both the ice and paraffin systems in Fig. 4, where the flow structure and stagnant melt pool for the ice and paraffin systems are seen to be inverted images of each other. Again, this is observed in ice only for $T_w < 4°C$. Higher wall temperatures invoke the influence of the density inversion, as will be illustrated in the sections to follow.

Density Inversion Effects. The visualized flow field for $T_w = 12°C$, relatively far from the 4°C density inversion, is illustrated by the photograph in Fig. 5. Unlike the flow structure seen in the $T_w = 3.5°C$ experiment, new melt is squeezed out of the gap at the top of the cylinder and flows down along the solid. The fluid rising along the wall causes the new melt to travel along the interface until its increased density causes it to fall. At the bottom of the cavity the falling dye divides into two streams. One stream feeds the two-dimensional cell which rises along the wall toward the close-contact gap, and the

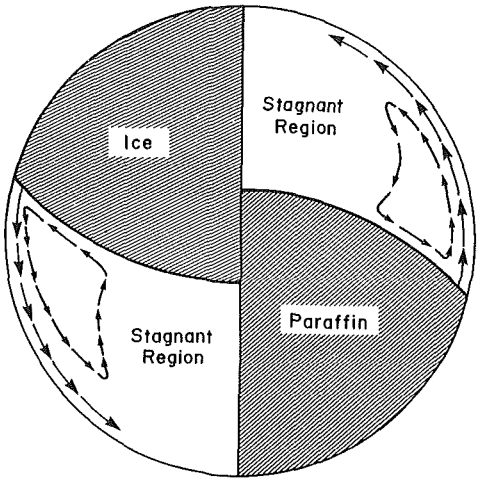

Fig. 4 Schematic of flow regime for ice ($T_w < 4°C$) and *n*-heptadecane

Fig. 5 Visualized flow structure for ice, T_w 12°C, $t = 16$ min 15 s

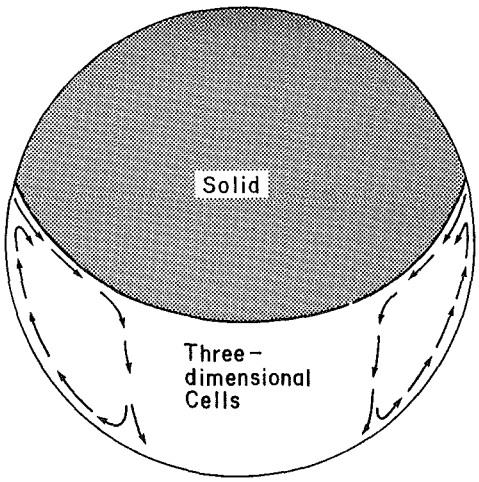

Fig. 6 Schematic of flow regime for ice, $T_w = 12°C$

other joins complex three-dimensional flow and roll cells rising from the cylinder bottom. The three-dimensional flow beneath the solid is evidenced by the mixing of the dye seen in the photographs. Plumes rising from the cylinder bottom may also be observed. As seen in the flow schematic of Fig. 6, the recirculation cells at the sides of the cylinder are observed to be largely two dimensional, whereas the flow beneath the solid

Fig. 7 Visualized flow structure for ice, $T_w = 7°C$, $t = 12$ min

caused by heating from below is strongly three-dimensional. The complex flow structure in the cavity bottom is responsible for nonuniform melting at the lower surface of the solid to be shown later. No attempt was made to characterize the flow in terms of a relevant Rayleigh number. The complex and transient melt cavity geometry makes the selection of an appropriate characteristic length difficult. Density inversion effects also preclude a clear-cut definition of the thermal expansion coefficient. One parameter has been proposed for characterizing the flow structure in water systems near its density inversion (Gebhart et al., 1979)

$$R = \frac{T_{\max} - T_w}{T_m - T_w} \tag{1}$$

where $T_{\max}$ is the temperature corresponding to maximum density (3.98°C). Positive or negative values of R indicate the difference in the buoyancy force relative to the density extremum. The values of the density inversion buoyancy parameter corresponding to the $T_w = 3.5$, 7, and 12°C cases considered here are $R = -0.14$, 0.43, and 0.67, respectively. These radically different flow regimes which depend on wall temperature have been predicted theoretically and observed experimentally for natural convection of water in the absence of phase change in a horizontal cylinder with wall cooling through the density inversion point (Cheng and Takeuchi, 1976; Cheng et al., 1978; Gilpin, 1975).

The effect of the density inversion is more pronounced for the $T_w = 7°C$ results presented in Fig. 7. Much like the weak recirculation cells found for the $T_w = 3.5°C$ test, the melt from the close-contact region flows down along the wall. A portion then lifts away from the wall and flows up along the bottom of the solid. The remainder of the stream forms a second cell. Only one of these second cells is seen in the photograph on the right side of the cavity rotating counterclockwise. A second cell from the dye tracer is inferred and shown by the solid line in the flow schematic, Fig. 8. The asymmetry in the flow field was observed in all tests at $T_w = 7°C$. However, the positions of the secondary recirculation cells were not reproducible. It is suggested that the flow regime in the cavity bottom for this intermediate wall temperature lies in a transition regime, the structure changing from the stably stratified zone seen for $T_w = 3.5°C$ to the complex three-dimensional rolls seen for $T_w = 12°C$. Experimental determination of a "critical" wall temperature demarcating transition between the flow regimes found at wall temperatures well above and below the density inversion point is infeasible due to the unavoidable wall temperature variations discussed previously. Observation of the dye for $T_w = 7°C$ reveals that the flow is two-dimensional both in the recirculation zones near the close-contact zone and below the solid bulk. This is supported by photographs of the

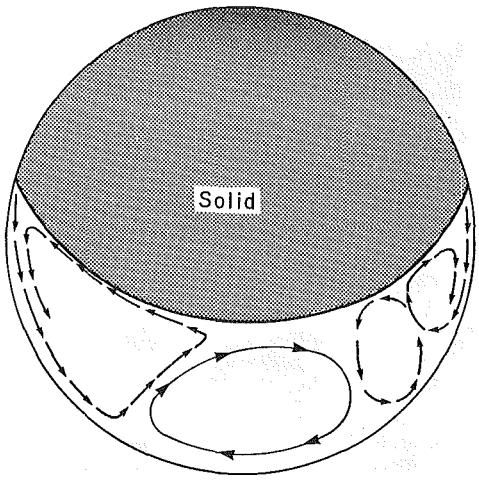

Fig. 8 Schematic of flow regime for ice, $T_w = 7°C$

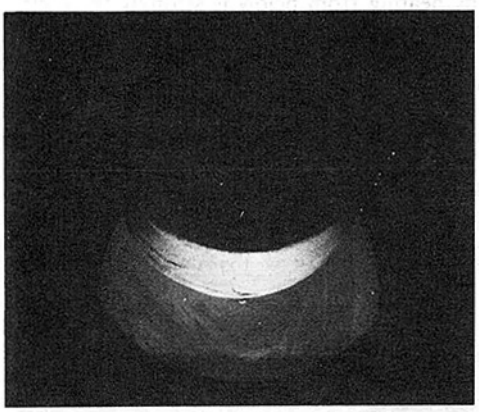

Fig. 9(a)

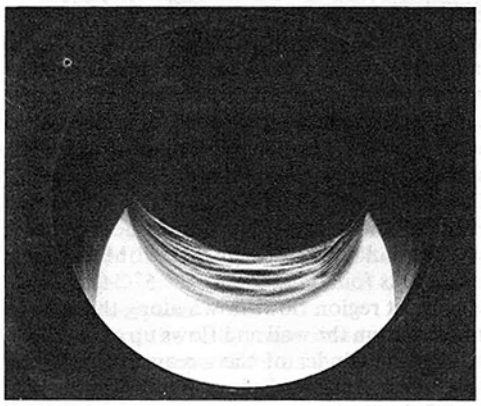

Fig. 9(b)

Fig. 9 Solid-liquid interface morphology for ice: (a) $T_w = 7°C$; (b) $T_w = 12°C$

solid–liquid interface morphology presented in the next section.

Solid–Liquid Interface Morphology. The solid–liquid interface was photographed at an angle to the solid axis in order to understand the influence of the flow regime on local melting. The results for wall temperatures of 7 and 12°C are shown in Figs. 9(*a*) and 9(*b*), respectively. The interface for $T_w = 7°C$ is very smooth with the only axial variations in local melting being confined to a very small region near the windows – a result of heat gain from the ambient. The existence of the smooth interface corroborates the observation of two-

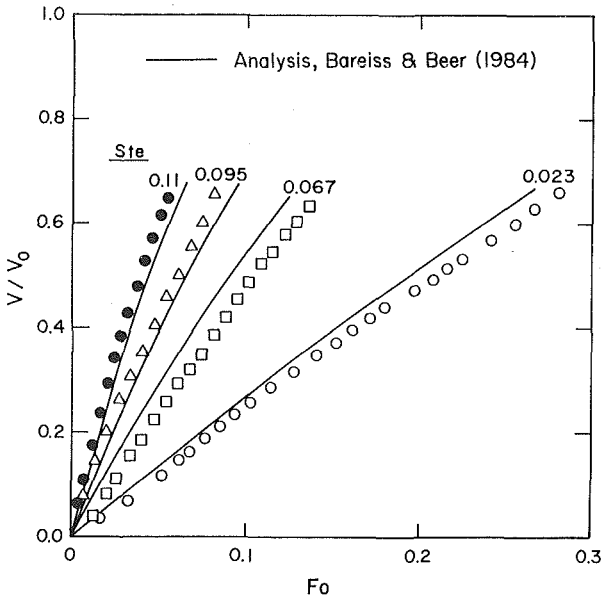

Fig. 10 Melt fraction versus dimensionless time with predictions: open symbols, ice; solid symbols, *n*-heptadecane (from Webb et al., 1986).

dimensional flow beneath the solid discussed in the preceding section. The solid–liquid interface for $T_w = 3.5°C$ was similar to the interface for $T_w = 7°C$, as one would expect for the stagnant zone shown in Fig. 3.

By contrast, note the ridges and grooves in the interface of Fig. 9 for $T_w = 12°C$. Clearly the three-dimensional flow manifested by the dye tracer in Fig. 5 results in axially nonuniform melting of the solid bottom. Similar three-dimensional cells were reported by Herrmann et al. (1984) who investigated the melting characteristics of ice around a horizontal cylinder. They suggested that the grooves formed might be the result of Görtler vortices (Schlichting, 1979) arising from instabilities in the laminar boundary layer along the concave melt front. Rieger and Beer (1986) also observed axially nonuniform melting along the top surface of restrained ice melting in a horizontal cylinder. They concluded that the ridges were the result of the onset of thermal instabilities, perturbing the initially two-dimensional rolls to the three-dimensional vortices observed. Such is the case qualitatively in the present investigation. The two-dimensional cells observed in Figs. 7 and 8 for $T_w = 7°C$ intensify as the cylinder wall temperature is increased. The more intense heating from below at higher wall temperatures produces a thermal instability; fluid is heated at the cylinder floor and rises to the bulk solid where melting causes it to cool. The cooled fluid then returns to the cylinder floor. The most natural flow regime favoring this behavior is the three-dimensional rolls observed, with the associated axial variations in the local melting rate. It is the combination of unstable fluid heating from below and the density inversion that results in the complex vortex motion and ridges evidenced.

Melting Rates. The timewise behavior of the melt fraction for the ice tests is shown in Fig. 10. Also shown is the result for melting of unfixed paraffin reported elsewhere (Webb et al., 1986). The Stefan number characterizing the melting rate for each case is based on the timewise average wall temperature in the close-contact region since the majority of the melting occurs there. The trends are as expected – higher Stefan numbers result in higher melting rates. Attempts made to correlate the data in terms of the product FoSte, the conventional time scale used in melting heat transfer, proved unsuccessful. The product FoSte is a relevant dimensionless time only when melting is dominated by conduction and melt accumulates between heat

source and interface. Consequently, it is not surprising that it fails to correlate the data for the system studied here where motion of the bulk solid squeezes new melt out of the gap, preventing accumulation of liquid.

Bareiss and Beer (1984) developed a model to predict the global melting rate of unfixed PCM in a horizontal cylindrical capsule. The model accounted for melting of the solid exposed to the melt pool by a correlation based on quasi-steady natural convection. Predictions based on their model, with melting from the melt pool neglected, are also shown in Fig. 10. In general, the agreement is quite good since most of the melting takes place in the close-contact zone. However, if local melting rates are of interest the consideration of the detailed flow regimes observed here would be necessary.

Conclusions

Melting of unrestrained ice in a horizontal cylindrical capsule has been investigated experimentally. Three distinct flow regimes depending on wall temperature were identified. For wall temperatures below the density inversion point the flow structure is the inverted image of the case for melting of paraffin – forced fluid flow out of the close-contact gap due to motion of the bulk solid is buoyancy-assisted by fluid density change upon heating. At wall temperatures relatively far above the density inversion point the flow exhibits two-dimensional recirculation cells near the solid bulk sides, and strong three-dimensional rolls and plumes in the cavity bottom. Wall temperatures closer to the density inversion point display transition behavior, the flow being characterized by multiple two-dimensional cells in the melt. The existence of the flow regimes is corroborated by the solid–liquid interface morphology.

No effort has been made to predict analytically the flow structure and melting rate, as has been done by others referenced earlier for two-dimensional systems. Complex and sometimes three-dimensional flow prevails in the system studied here. Currently available algorithms for predicting the temperature distribution and solid–liquid interface position in two-dimensional melting systems for ordinary fluids are still very costly (Webb and Viskanta, 1986). The three-dimensional nature of the flow and strongly temperature-dependent fluid properties make any attempt to model mathematically the system discussed infeasible.

Acknowledgments

One of the authors (B.W.W.) wishes to acknowledge the financial assistance of his graduate studies by an Eastman Kodak Company Graduate Fellowship. This work was partially supported by the National Science Foundation under Grant No. MEA-8313573.

References

Bareiss, M., and Beer, H., 1984, "An Analytical Solution of the Heat Transfer Process During Melting of an Unfixed Solid Phase Change Material Inside a Horizontal Tube," *International Journal of Heat and Mass Transfer*, Vol. 27, pp. 739–746.

Cheng, K. C., Takeuchi, M., and Gilpin, R. R., 1978, "Transient Natural Convection in Horizontal Water Pipes With Maximum Density Effect and Supercooling," *Numerical Heat Transfer*, Vol. 1, pp. 101–115.

Cheng, K. C., and Takeuchi, M., 1976, "Transient Natural Convection of Water in a Horizontal Pipe With Constant Cooling Rate Through 4°C," ASME JOURNAL OF HEAT TRANSFER, Vol. 98, pp. 581–587.

Gebhart, B., Bendell, M. S., Shauleatullah, H., 1979, "Buoyancy-Induced Flows Adjacent to Horizontal Surfaces in Water Near its Density Extremum," *International Journal of Heat and Mass Transfer*, Vol. 22, pp. 132–149.

Gilpin, R. R., 1975, "Cooling of a Horizontal Cylinder of Water Through Its Maximum Density Point at 4°C," *International Journal of Heat and Mass Transfer*, Vol. 18, pp. 1307–1315.

Herrmann, J., Leidenfrost, W., and Viskanta, R., 1984, "Melting of Ice Around a Horizontal Isothermal Cylindrical Heat Source," *Chemical Engineering Communications*, Vol. 25, pp. 63–78.

Ho, C.-J., and Viskanta, R., 1984, "Heat Transfer During Inward Melting in a Horizontal Tube," *International Journal of Heat and Mass Transfer*, Vol. 27, pp. 705–716.

Katayama, K., Saito, A., Utoka, Y., Saito, A., Matsu, H., Mae Kawa, H., and Saifullah, A., 1981, "Heat Transfer Characteristics of the Latent Heat Thermal Energy Storage Capsule," *Solar Energy*, Vol. 27, pp. 91–97.

Moallemi, M. K., Webb, B. W., and Viskanta, R., in press, "An Experimental and Analytical Study of Close-Contact Melting," ASME JOURNAL OF HEAT TRANSFER.

Moore, F. E., and Bayazitoglu, Y., 1982, "Melting Within Spherical Enclosures," ASME JOURNAL OF HEAT TRANSFER, Vol. 104, pp. 19–23.

Nicholas, D., and Bayazitoglu, Y., 1980, "Heat Transfer and Melting Front Within A Horizontal Cylinder," ASME *Journal of Solar Energy Engineering*, Vol. 102, pp. 229–232.

Pannu, J., Joglekar, G., and Rice, P. A., 1980, "Natural Convection to Cylinders of Phase Change Material Used for Thermal Storage," *AIChE Symposium Series*, Vol. 76, pp. 47–55.

Rieger, H., Projahn, U., Bareiss, M., and Beer, H., 1983, "Heat Transfer During Melting Inside a Horizontal Tube," ASME JOURNAL OF HEAT TRANSFER, Vol. 105, pp. 226–234.

Rieger, H., and Beer, H., 1986, "The Influence of Density Anomaly of Water on the Melting Process of Ice Inside a Horizontal Cylinder," ASME JOURNAL OF HEAT TRANSFER, Vol. 108, pp. 166–173.

Saitoh, T., and Hirose, K., 1982, "High Rayleigh Number Solutions to Problems of Latent Heat Thermal Energy Storage in a Horizontal Cylindrical Capsule," ASME JOURNAL OF HEAT TRANSFER, Vol. 104, pp. 545–553.

Schlichting, H., 1979, *Boundary Layer Theory*, McGraw-Hill, New York.

Sparrow, E. M., and Myrum, T., 1985, "Inclination-Induced Direct-Contact Melting in a Circular Tube," ASME JOURNAL OF HEAT TRANSFER, Vol. 107, pp. 553–540.

Viskanta, R., 1983, "Phase-Change Heat Transfer," in: *Solar Heat and Storage: Latent Heat Materials*, G. A. Lane, ed., CRC Press, Boca Raton, FL, pp. 153–222.

Viskanta, R., 1985, "Natural Convection in Melting and Solidification," in: *Natural Convection: Fundamentals and Applications*, S. Kakac et al., eds., Hemisphere, Washington, DC, pp. 845–877.

Webb, B. W., and Viskanta, R., 1986, "Analysis of Heat Transfer During Melting of a Pure Metal From an Isothermal Vertical Wall," *Numerical Heat Transfer*, Vol. 9, pp. 539–558.

Webb, B. W., Moallemi, M. K., and Viskanta, R., 1986, "Phenomenology of Melting of Unfixed Phase Change Material in a Horizontal Cylindrical Capsule," ASME Paper No. 86-HT-10.

S. K. Roy

S. Sengupta

University of Miami,
Coral Gables, FL 33124

The Melting Process Within Spherical Enclosures

Introduction

Cylindrical and spherical enclosures are most commonly used for the storage of phase change materials. A relatively large amount of literature on the melting/freezing process is available for the cylindrical geometry as compared to the spherical case. The effects of unequal solid and liquid densities on the melting process for the spherical geometry have been considered only in one study in which Moore and Bayazitoglu [1, 2] obtained numerical solutions for the isothermal enclosure for about half the melting process, a limitation imposed by the coordinate system used. Results of their study showed good agreement with their experimental data for Ste = 0.05 and 0.1 with a maximum deviation of about 10 percent in the predicted interface position.

In this note, an analysis of the problem assuming a constant wall temperature and a higher solid density, covering the entire melting process, is presented. The method used is an extension of Bareiss and Beer's [3] analysis of the melting process in cylindrical enclosures, but unlike their study no simpifying assumption for the film thickness has been made. In fact, an earlier analysis by this investigator using such a relation gave results which failed to agree with experimental data from [1, 2].

Governing Equations

Figure 1 shows the geometry used to describe the problem. The sphere is originally filled with the phase change material (PCM) in its solid phase at its melting point. At time $t>0$, a step change in wall temperature is imposed. The melting process is modeled using the following assumptions:

1 The process is quasi-steady. Therefore, the weight of the solid core and the liquid above it, which is assumed to be stagnant, is exactly balanced at every instant by the force due to the pressure in the film of molten material below which is being continuously forced upward. Since the final results show that the velocity at the end of the film is very small, the assumption that the fluid above is stagnant is not violated. The velocity profile in the liquid film is also quasi-steady and changes only with the film thickness which varies with time.

2 Heat transfer is assumed to take place by one-dimensional conduction through the liquid film. No melting occurs at the upper surface of the solid core. Experimental observations by Moore and Bayazitoglu [1, 2] indicate that this assumption is valid for low values of Ste except for a short time at the initial stages of melting, with the upper surface remaining almost spherical throughout the melting process. Numerical investigations of melting within a cylindrical enclosure by Said and Sengupta [4] and Prasad and Sengupta [5] also showed that convection plays a small role in the overall process.

3 The process is considered to be axisymmetric, and the normal velocity in the film and its derivative are assumed to be very small. A no-slip condition exists both at the solid wall and the lower melt interface.

4 The pressure at the junction between the thin film below the solid and the upper liquid region is assumed to be equal to the static pressure at that point.

5 For mathematical simplicity, the area of the melt surface at the bottom of the solid is calculated as the area of the sphere subtending the same solid angle. The volume of the solid core and the body force in the liquid film are evaluated in a similar manner. Since the results show that the film thickness is very small relative to the dimensions of the sphere, any error due to this assumption is marginal.

6 A preliminary analysis showed that the force due to shear stress is relatively small and it is therefore neglected.

The governing equations therefore are:

(*a*) *Geometric Conditions*

$$\cos\theta_A = s/2R \tag{1}$$

$$V_s = \pi(16R^3 - 12sR^2 + s^3)/12 \tag{2}$$

$$\frac{ds}{dt} = \frac{m(0)}{\rho_s} - \frac{1}{\rho_s}\frac{d\delta(0)}{dt} \tag{3}$$

where $s(0) = 0$.

(*b*) *Energy Balance*

$$k\Delta T/\delta = mh_f \tag{4}$$

(*c*) *Mass Balance*

$$m(2\pi R \sin\theta \cdot Rd\theta) = d\left[\int_{R-\delta}^{R} v 2\pi r \sin\theta dr\right] \tag{5}$$

where $-\rho_s \frac{dV_s}{dt} = \int_0^{\theta_A} m(2\pi R \sin\theta \cdot Rd\theta)$.

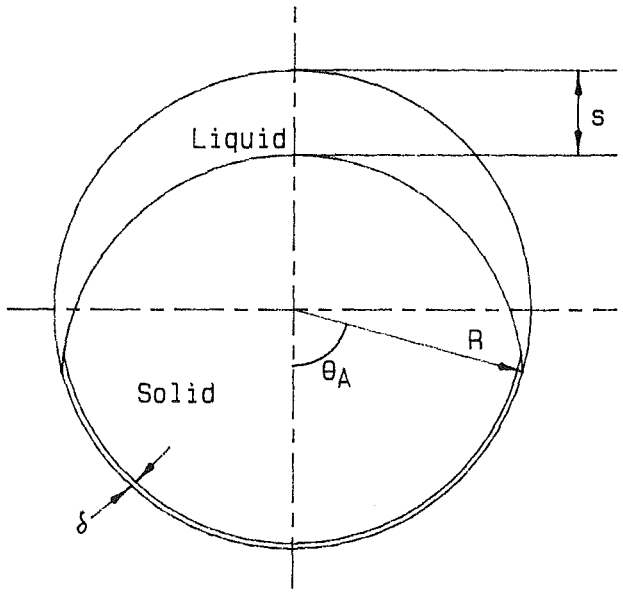

Fig. 1 Problem geometry

Contributed by the Heat Transfer Division and presented at the ASME Winter Annual Meeting, Miami Beach, Florida, November 17-21, 1985. Manuscript received by the Heat Transfer Division October 2, 1985.

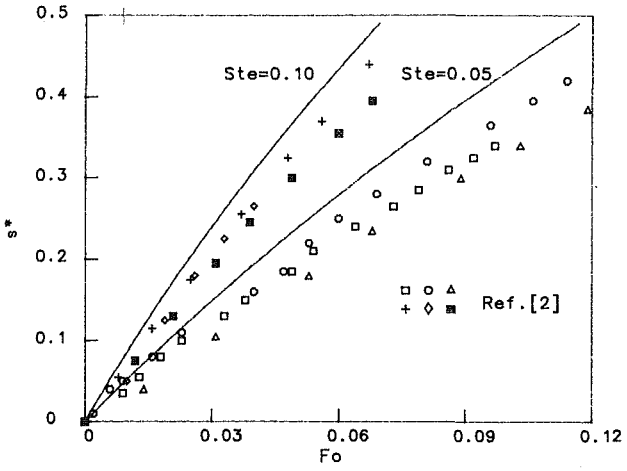

Fig. 2 Comparison of s^* with experimental data from [2]

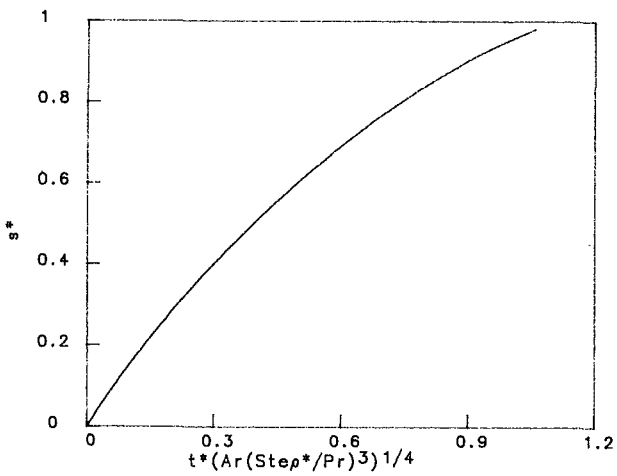

Fig. 3 Variation of s^* with time

(d) Fluid Flow Equations in Film and Force Balance

$$\frac{\partial}{\partial\theta}(v\sin\theta)=0 \tag{6}$$

$$\frac{\mu\partial}{r\partial r}\left(r^2\frac{\partial v}{\partial r}\right)=\frac{dp}{d\theta}+\rho gR\sin\theta \tag{7}$$

$$\int_0^{\theta_a} p\cos\theta(2\pi R\sin\theta\cdot Rd\theta)=\rho_s V_s g$$

$$+\left[\int_0^{\theta_a}\rho gR(1+\cos\theta)\cdot 2\pi R\sin\theta\cdot Rd\theta-\rho gV_s\right] \tag{8}$$

where $p(\theta_A)=\rho gR(1+\cos\theta_A)$, $v(R-\delta)=v(R)=0$.

Solution and Results

The governing equations are suitably normalized and solutions for the drop rate, melt flux distribution, film thickness, and Nusselt numbers are obtained. The drop rate is given by

$$\frac{ds^*}{dt^*}=\left[\frac{m^*(0)}{\left(1+\delta^*(0)\dfrac{(1+2s^*)}{4(2+s^*)(1-s^*)}\right)}\right] \tag{9}$$

The melt flux distribution can be obtained from

$$m^*(\theta)=\left[\frac{1}{12}\mathrm{Ar}\left(\frac{\mathrm{Ste}\rho^*}{\mathrm{Pr}}\right)^3\frac{(1-s^*)(2+s^*)}{(c-\cos\theta)}\right]^{1/4} \tag{10}$$

where c is the real root of the cubic equation

$$(c-(5+3s^*)/8)=(c-s^*)^{3/4}(c-1)^{1/4}$$

Details of the method of solution and expressions for the other parameters are given in [6]. It can be seen from equation (9) that, if $\delta^*(0)<<1$, then the expressons for the drop rate and the melt flux at $\theta=0$ become identical. For the range of parameters normally encountered, this is indeed true.

It should be noted at this stage that these results will be valid only for the range of parameters where the model assumptions hold. The assumption that heat transfer takes place only by one-dimensional conduction in the film is satisfied only when

$$\frac{\mathrm{Ar}^{1/4}}{\rho^*}\left(\frac{\mathrm{Ste}\rho^*}{\mathrm{Pr}}\right)^{9/4}<\frac{2.8\sin\theta}{[(1-s^*)(2+s^*)]^{1/4}(c-\cos\theta)^{3/4}} \tag{11}$$

Equation (9) was solved numerically using a fourth-order Runge-Kutta method for Ste = 0.05 and 0.10 and $R=32.72$ mm for octadecane and results have been compared with experimental data from [2] in Fig. 2. All property values (except for ρ_s which was at 25°C and C_p) were evaluated at the melting point of octadecane of 28°C. Good agreement with the experimental data can be seen. The maximum deviation from the experimental results is about 16 percent.

Two main parameters are found to affect the melt rates. The temperature differences has a large effect with the drop rate being proportional to $(\mathrm{Ste}\rho^*/\mathrm{Pr})^{3/4}$. The ratio of the net gravitational force acting on the liquid film to the viscous force in the film, given by Ar, directly affects the pressure in the film and thus the melt rate. The melt rate also increases as the difference between the solid and liquid density increases. Higher melt rates also result when Ar is high due to a higher radius since the volume to lower surface area ratio increases as the radius of the enclosure increases. Figure (3) shows the variation of s^* with $t^*\times(\mathrm{Ste}\rho^*/\mathrm{Pr})^{3/4}\times(\mathrm{Ar})^{1/4}$ when $\delta^*<<1$. The melting rate can be seen to reduce with time. This is caused by an increase in the film thickness as the melting progresses.

Nomenclature

Ar = Archimedes number = $(\rho_s-\rho)D^3/\rho_s\nu^2$
Fo = Fourier number = $\alpha t/R^2$
h_f = latent heat of melting
m = melt flux at lower surface = $Dm/\rho_s\nu$
Nu = Nusselt number = hD/k
p = pressure = $(p-\rho gR(1+\cos(\theta)))/(\rho_s-\rho)gR$
r = radial coordinate = r/D
s = drop of interface at $\theta=\pi[s/D]$
Ste = Stefan number = $C_p\Delta T/h_f$
t = time = $\nu t/D^2$
ΔT = difference between wall and melting temperature
v = fluid velocity in film in θ direction = $v/\sqrt{(\rho_s-\rho)gD/\rho}$
V_s = volume of solid core
δ = thickness of film
ρ_s = density of solid
ρ^* = nondimensional density = ρ/ρ_s

Superscript

* = normalized variable

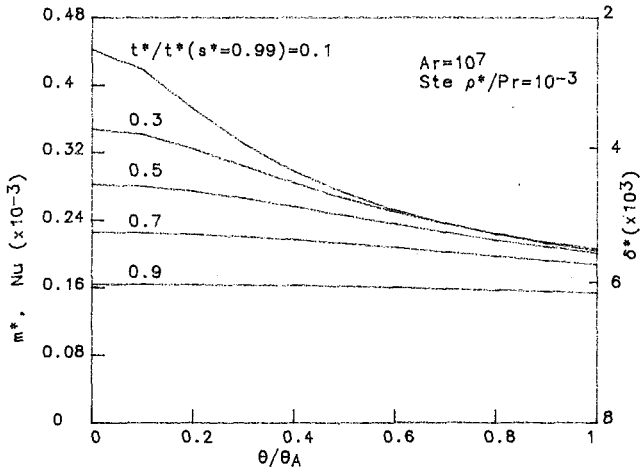

Fig. 4 Variation of m^*, δ^*, and Nu with angle

The nondimensionalized melt flux, film thickness, and Nusselt number distributions are plotted in Fig. 4. Since equation (9) cannot be integrated exactly until $s^* = 1.0$, the time has been normalized with respect to time required to reach $s^* = 0.99$. Highest melt rates occur for small values of θ. Also, as time increases, the melt rate decreases and tends to become more uniform over the surface. The variation of the film thickness is the inverse of the melt rate. Thus the film thickness increases with time since the solid volume decreases at a faster relative rate than the supporting surface area, resulting in a lower melting rate as seen earlier. The heat transfer rate controls the melting rate. The melting rate is therefore directly proportional to the Nusselt number.

Conclusions

A simple axisymmetric model has been developed and an analytical solution for the melting rate at the lower surface of the solid core has been obtained. The predicted melting rate shows good agreement with previously published experimental data. The melting rate increases with an increase in the temperature difference between the wall and the solid, the size of the enclosure and the difference between the solid and liquid densities. It decreases with an increase in the latent heat of melting and the viscosity of the fluid. Results of this investigation also show that the film thickness is minimum, and the melting flux and Nusselt numbers are maximum, at $\theta = 0$. The melting rate is also found to decrease with time, beause the film thickness increases as the gravitational force decreases more rapidly compared to the surface area supporting the core as it melts.

References

1 Moore, F., and Bayazitoglu, Y., "Melting Within a Spherical Enclosure," ASME JOURNAL OF HEAT TRANSFER, Vol. 104, 1982, pp. 19–23.

2 Moore, F., "Melting Within a Spherical Enclosure," M.S. Thesis, Rice University, TX, 1981.

3 Bareiss, M., and Beer, H., "An Analytical Solution of the Heat Transfer Process During Melting of an Unfixed Solid Phase Change Material Inside a Horizontal Enclosure," *Int. J. Heat Mass Transfer*, Vol. 27, 1984, pp. 739–746.

4 Said, E., and Sengupta, S., "Phase Change Heat Transfer Inside a Horizontal Tube: Effects of Rayleigh Number," ASME/NHTC Paper No. 84-HT-4, Buffalo, NY, Aug. 1984.

5 Prasad, A., and Sengupta, S., "Numerical Investigation of Melting Inside a Horizontal Cylinder Including Effects of Natural Convection," *Heat Transfer and Fluid Flow in Solar Thermal Systems*, ASME SED Vol. 1, 1985, pp. 19–26.

6 Roy, S. K., and Sengupta, S., "An Analysis of the Melting Process Within a Spherical Enclosure," *Heat Transfer and Fluid Flow in Solar Thermal Systems*, ASME SED Vol. 1, 1985, pp. 27–32.

Transient Melting of a Metal Plate by a Penetrating Plasma Arc

Y. F. Hsu

B. Rubinsky

University of California,
Department of Mechanical Engineering,
Berkeley, CA 94720

A study was performed on the heat transfer and the fluid flow during transient melting of a metal plate subjected to stationary, penetrating plasma-arc heating. An integral method of solution was used for this simplified, first-order simulation of plasma-arc metal processing. The results of the study reveal the importance of the workpiece thickness, plasma-penetrating hole size, and gravity on the melting process and the molten fluid flow. The study also shows that plasma-arc metal processing seems to be a low-efficiency manufacturing process with only 7 percent of the plasma energy contributing to the melting.

Introduction

The plasma arc is a concentrated energy source commonly used in welding and cutting processes. It is composed of a partially ionized gas stream produced by forcing an inert gas to flow through an electric field and emerge from a constricting orifice. With its high energy density and velocity, the plasma arc, when impinging on the workpiece, can create a hole in the molten liquid pool and penetrate through it. Depending on the operating parameters employed, this hole may either become self-healing or remain open as the arc transverses along the workpiece. A "keyhole" welding process occurs in the self-healing case, in which the molten metal in front of the arc flows around the arc column and resolidifies behind the arc. On the other hand, a cutting operation is achieved if the hole remains open (O'Brien, 1968). Studies have been made on plasma-arc metalwork processes. For example, Metcalfe and Quigley (1975a, b) investigated the relative importance of the convection and radiation heat transfer mechanisms during welding. Tomsic and Barhorst (1984) investigated the keyhole plasma-arc welding of aluminum with application to welding of the space shuttle external tank. Welding experiments were performed to develop proper welding procedures and parameter settings (Lancaster, 1984). Most of the studies on plasma-arc welding that have appeared in the open literature are experimental with little emphasis on the supportive analysis.

In this paper the transient melting of a metal plate subjected to stationary plasma-arc heating is analyzed. This study may enhance our understanding of the heat transfer related phenomena during plasma-arc metalwork processes. The melting process studied in this paper is induced by a thermal plasma arc flowing through a predrilled hole in a metal plate. As the plasma heat is transferred via radiation and convection to the solid surface, the solid surrounding the plasma arc melts, and a moving solid–liquid interface appears. The molten liquid flows due to both the gravity and the shear force induced by the high-velocity plasma arc. As a result, a moving liquid–plasma interface and a flowing liquid film are expected to occur.

Analytical studies on similar phase change problems involving flowing liquid films and moving interfaces can be found in the open literature. Studies on the condensation of saturated vapor on vertical melting surfaces, of materials characterized by large Prandtl numbers and small Stefan numbers were performed by Contreras and Thorsen (1975), Epstein and Cho (1976), and Taghavi-Tafreshi and Dhir (1982a, 1982b).

The problem studied in this paper is different since the metallic system is characterized by a low Prandtl number (less than 0.05) and a large Stefan number. This paper employs the integral method approach to analyze the plasma-induced melting process. As a first-order approximation, a simplified one-dimensional heat conduction model is assumed in the solid region and a two-dimensional heat convection model is assumed in the molten liquid region. Correlations developed for the plasma flow in a tube by Schmidt and Leppert (1970), and Hunn and Moffat (1974) are applied to simulate the heat flux and the shear at the plasma–liquid interface. The study focuses on the heat transfer, fluid flow, and melting phenomena which occur during the heating of a stainless steel plate by a penetrating plasma arc.

Analysis

A study was performed on the transient melting process in a metal plate subjected to plasma-arc heating. The plate, with a predrilled hole of radius R_0, is assumed to extend to infinity in the radial (r) direction but has a finite thickness of L in the axial (z) direction. A schematic description of the system is shown in Fig. 1. At time zero, a high-temperature plasma arc starts to flow, in the direction of gravity, through the predrilled hole. Since the diameter of the predrilled hole is larger than that of the arc torch, it is assumed that all the plasma arc will flow through the keyhole. The initial temperature of the whole plate is assumed to be uniform at T_0. As the heat is continuously transferred from the plasma arc into the metal plate, the heat-affected zone in the solid is expanding with time. In this analysis, a heat penetration depth δ_s is used to indicate the varying size of this heat-affected zone.

The initial conduction process continues until the

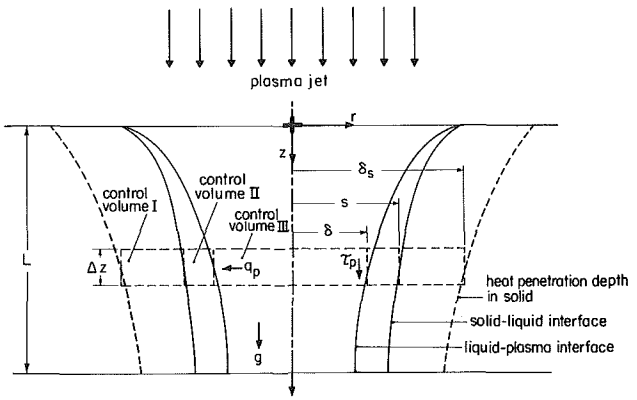

Fig. 1 Physical model used to study the transient melting of a solid undergoing plasma heating

Contributed by the Heat Transfer Division for publication in the JOURNAL OF HEAT TRANSFER. Manuscript received by the Heat Transfer Division February 4, 1986.

temperature of the solid surrounding the plasma reaches its melting point, then the melting process begins. Flow is induced in the molten region by gravity and shear from the plasma arc. Consequently the location of the solid–liquid interface s and the position of the liquid–plasma interface δ will vary in time along the axial direction. Simplifying assumptions were made to facilitate the study of this plasma-induced transient melting process. The liquid-metal flow in the molten region is assumed laminar. The axial conduction in both the solid and liquid region is assumed negligible relative to the axial convection in the liquid region. This assumption, which is commonly used in the heat transfer analyses of boundary layer flows, also implies that the top and bottom surfaces of the metal plate can be considered adiabatic. In this first-order study, the interfacial curvature effects are neglected in a way similar to that proposed by Epstein and Cho (1976), Taghavi-Tafreshi and Dhir (1982), and Contreras and Thorsen (1975). The assumption that negligible metal vaporization occurs at the liquid–plasma interface and that surface tension effects are negligible is confirmed by the final results of this study. It is assumed that radiation from plasma is absorbed at the plasma–liquid interface and is not transmitted through the liquid. Homogeneous, isotropic, and temperature-independent properties are assumed in both solid and liquid regions. The effect of the density change on the phase transformation is neglected.

During the initial pure conduction process, the heat from the plasma is transferred into the solid. The nondimensionalized energy equation in the solid region in which the axial conduction is neglected is

$$\mathrm{Ste}\,\frac{k_L}{k_s}\,\frac{\partial\theta_s}{\partial t}=\frac{1}{r}\,\frac{\partial}{\partial r}\left(r\,\frac{\partial\theta_s}{\partial r}\right);\quad 1\le r\le\delta_s,\quad 0\le z\le 1 \tag{1}$$

Note that in metallic systems the Stefan number Ste is large and therefore transient effects cannot be neglected. The boundary conditions associated with equation (1) are

$$\frac{\partial\theta_s}{\partial r}=-\frac{R_0 q_p}{k_s(T_b-T_m)};\qquad \text{at } r=1,\ 0\le z\le 1 \tag{2}$$

$$\theta_s=\theta_0;\qquad \text{at } r=\delta_s,\ 0\le z\le 1 \tag{3}$$

where q_p is the heat flux transferred from the plasma to the workpiece. The initial condition is

$$\theta_s=\theta_0;\quad \text{at } t=0,\ 1\le r<\infty,\ 0\le z\le 1 \tag{4}$$

In the solution of equation (1) by the integral method an additional boundary condition is used, typical to that method

$$\frac{\partial\theta_s}{\partial r}=0;\ \text{at } r=\delta_s,\ 0\le z\le 1 \tag{5}$$

The transient melting process begins when the solid surface temperature reaches its melting point. The starting time of this process is denoted by t_s. It is assumed that at the onset of the melting process the heat penetration depth δ_s and the temperature in the solid region θ_s are known from the solution of equations (1)–(5). During melting the nondimensional continuity equation of the incompressible molten metal liquid flow is

Nomenclature

C = thermal capacity of the metal, J/kg-K
f = friction factor = $(2\,\tau_p)/(\rho_m u_m^2)$
g = 9.8 m/s^2
h = plasma enthalpy
h_{sL} = latent heat of fusion, J/kg
k = conductivity, W/m-K
L = thickness of the workpiece, m
Nu = Nusselt number of the plasma flow = $q_p(2r^*)/[(k_m/C_m)(h_m-h_w)]$
P_1, P_2 = dimensionless parameters in equation (9)
Pr = Prandtl number for liquid metal = $\mu/(\rho\alpha)$
q_p = heat flux released from plasma, W/m^2
q_w = heat flux from the liquid region to the solid–liquid interface, W/m^2
R_0 = radius of the predrilled hole, m
Re = Reynolds number of the plasma flow = $(\rho_m u_m(2r^*))/\mu_m$
r^*, r = radial coordinate, m; dimensionless radial coordinate, $r=r^*/R_0$
s^*, s = radial distance, m; dimensionless radial distance of the solid–liquid interface $s=s^*/R_0$
Ste = Stefan number = $C_s(T_b-T_m)/h_{sL}$
T = liquid metal temperature, K
T_s = solid metal tempeature, K
T_0 = initial solid temperature, K
T_b, T_m = boiling, melting temperature of the metal, K
t^*, t = time, s; dimensionless time $t=(k_L(T_b-T_m)t^*)/(\rho h_{SL}R_0^2)$
t_s = dimensionless time when the pure conduction mode ends
U_0 = reference velocity, m/s, in equation (9)
u^*, u = axial velocity, m/s; dimensionless axial velocity of the liquid metal $u=u^*/U_0$
u_δ = dimensionless liquid velocity on the plasma–liquid interface
u_m = plasma mean velocity, m/s
v^*, v = radial velocity, m/s; dimensionless radial velocity of the liquid metal $v=v^*/U_0$
z^*, z = axial coordinate, m; dimensionless axial coordinates $z=z^*/L$
z^+ = nondimensional axial distance = $z^*/(r^*\mathrm{Re}_m\mathrm{Pr}_m)$
α = thermal diffusivity, m^2/s
δ^*, δ = radial distance, m; dimensionless radial distance of the plasma–liquid interface $\delta=\delta^*/R_0$
δ^*_s, δ_s = radial distance, m; dimensionless radial distance of heat effected zone $\delta_s=\delta_s^*/R_0$
ζ = dimensionless coordinate = $(r-s)/(\delta_s-s)$
η = dimensionless coordinate = $(s-r)(s-\delta)$
θ, θ_s = dimensionless liquid, solid temperature; $\theta=T/(T_b-T_m)$, $\theta_s=T_s/(T_b-T_m)$
θ_0, θ_m = dimensionless initial, melting temperature; $\theta_0=T_0/(T_b-T_m)$, $\theta_m=T_m/(T_b-T_m)$
μ = viscosity, kg/m-s
ξ = dimensionless coordinate = $(\delta_s-r)/(\delta_s-1)$
ρ = metal density, kg/m^3
ρ_m = plasma density at local mixed-mean temperature, kg/m^3
τ_p = shear stress at the plasma–liquid interface, N/m^2

Superscript

* = dimensional quantities

Subscripts

0 = initial condition
L = liquid
m = at mixed-mean temperature
s = solid
w = at wall temperature

$$\frac{\partial}{\partial r}(rv)+\frac{\partial}{\partial z}(ru)=0; \quad s\le r\le\delta, \quad 0\le z\le 1 \tag{6}$$

Based on assumptions listed at the beginning of this section, the nondimensional axial direction momentum equation, which includes the effects of the body forces in that direction, and the nondimensional axial-direction energy equation in the liquid region can be simplified as

$$P_1\frac{\partial u}{\partial t}+v\frac{\partial u}{\partial r}+u\frac{\partial u}{\partial z}=(P_2\mathrm{Pr})\frac{1}{r}\frac{\partial}{\partial r}\left(r\frac{\partial u}{\partial r}\right)+1; \quad \delta\le r\le s; \quad 0\le z\le 1 \tag{7}$$

$$P_1\frac{\partial \theta}{\partial t}+v\frac{\partial \theta}{\partial r}+u\frac{\partial \theta}{\partial z}=P_2\frac{1}{r}\frac{\partial}{\partial r}\left(r\frac{\partial \theta}{\partial r}\right); \quad \delta\le r\le s; \quad 0\le z\le 1 \tag{8}$$

where θ is the dimensionless liquid temperature and

$$P_1=\frac{k_L}{\rho_s}\frac{T_b-T_m}{h_{sL}R_0^2}\frac{L}{U_0}; \quad P_2=\frac{\alpha_L L}{R_0^2U_0}; \quad U_0=(gL)^{1/2} \tag{9}$$

The energy equation which governs the heat conduction in the solid is

$$\mathrm{Ste}\frac{k_L}{k_s}\frac{\partial\theta_s}{\partial t}=\frac{1}{r}\frac{\partial}{\partial r}\left(r\frac{\partial\theta_s}{\partial r}\right); \quad s\le r\le\delta_s, \quad 0\le z\le 1 \tag{10}$$

The temperature at the solid–liquid interface is the melting temperature for metal

$$\theta=\theta_s=\theta_m; \quad \text{at } r=s,\ 0\le z\le 1 \tag{11}$$

The energy balance at the solid–liquid interface is

$$\frac{\partial s}{\partial t}=\frac{k_s}{k_L}\frac{\partial\theta_s}{\partial r}-\frac{\partial\theta}{\partial r}; \quad \text{at } r=s,\ 0\le z\le 1 \tag{12}$$

Based on the assumption that all the plasma heat is absorbed by the liquid at the plasma–liquid interface, the dimensionless interfacial energy balance on the plasma–liquid interface becomes

$$\frac{\partial\theta}{\partial r}=-\frac{R_0q_p}{k_L(T_b-T_m)}; \quad \text{at } r=\delta,\ 0\le z\le 1 \tag{13}$$

Nonslip conditions are imposed at the solid–liquid boundary

$$u=0,\ v=0; \quad \text{at } r=s,\ 0\le z\le 1 \tag{14}$$

Since this analysis assumes no metal vaporization at the liquid–plasma interface, mass cannot flow across this interface. Therefore, the liquid velocities at this interface must satisfy the following conservation equation

$$v-u\frac{\partial\delta}{\partial z}=P_1\frac{\partial\delta}{\partial t}; \quad \text{at } r=\delta,\ 0\le z\le 1 \tag{15}$$

The plasma-induced shear is related to the liquid velocity gradient by

$$\frac{\partial u}{\partial r}=-\frac{R_0\tau_p}{\mu_L U_0}; \text{ at } r=\delta,\ 0\le z\le 1 \tag{16}$$

The liquid velocity at the plasma-entrance elevation is

$$u=0 \text{ at } \delta\le r\le s,\ z=0 \tag{17}$$

The integral method was used to solve the problem described here. This method is commonly used in the investigations of boundary layer flows over a fixed solid boundary. In the present study, however, the situation is much more complicated than in typical studies of boundary layer flows since here the solid–liquid boundary is moving and its moving rate depends on the heat flux transferred to the solid–liquid interface. To cope with this problem, a new parameter, the heat flux transferred from the liquid region to the liquid–solid interface (q_w), is introduced into the formulation.

The three unknowns associated with the liquid flow, namely, liquid film thickness ($s-\delta$), liquid surface velocity u_δ, and the heat flux into the liquid–solid interface q_w, are then determined based on integral forms of the liquid's continuity, momentum, and energy equations. The heat conduction into the solid region can be calculated by using the integral energy equation of the solid region. The moving rate of the solid–liquid interface is then calculated from the energy balance at the solid–liquid interface.

The following steps are taken in the solution procedure. First, describing differential equations are converted into integral forms. By substituting both the velocity and temperature profiles, which represent the expected radial distributions of velocity and temperature in the liquid, into these equations, a set of first-order partial differential equations is obtained. Finally a finite difference approximation is introduced to convert these differential equations into algebraic equations, from which the numerical solution is found. Details are explained below.

By integrating equations (6)–(8) over the radial direction (control volume II in Fig. 1) and applying the interfacial conditions, i.e., equations (11), (14), (15), and (16), the integral forms of the liquid's continuity, momentum, and energy equations are, respectively,

$$\frac{\partial}{\partial z}\int_\delta^s urdr=P_1\delta\frac{\partial\delta}{\partial t}; \quad t>t_s, \quad 0\le z\le 1 \tag{18}$$

$$P_1\frac{\partial}{\partial t}\int_\delta^s urdr+\frac{\partial}{\partial z}\int_\delta^s u^2rdr=(P_2\mathrm{Pr})\left(s\frac{\partial u}{\partial s}\Big|_{r=s}+\frac{R_0\delta}{\mu_L\sqrt{gL}}\tau_p\right)+\frac{1}{2}(s^2-\delta^2); \quad t>t_s, \quad 0\le z\le 1 \tag{19}$$

$$P_1\frac{\partial}{\partial t}\int_\delta^s\theta rdr+\frac{\partial}{\partial z}\int_\delta^s u\theta\, rdr-P_1\theta_m s\frac{\partial s}{\partial t}=P_2\left(s\frac{\partial\theta}{\partial s}\Big|_{r=s}+\frac{R_0\delta}{k_L(T_b-T_m)}q_p\right); \quad t>t_s,\ 0\le z\le 1 \tag{20}$$

Likewise, integrations of both equation (1) and equation (10) over the heat-affected zone in the solid (control volume I in Fig. 1) yield the following integral equations

$$\frac{\partial}{\partial t}\int_1^{\delta_s}\theta_s rdr-\theta_0\delta_s\frac{\partial\delta_s}{\partial t}=\frac{1}{\mathrm{Ste}}\frac{R_0q_p}{k_L(T_b-T_m)}; \quad 0\le t\le t_s, \quad 0\le z\le 1 \tag{21}$$

$$\frac{\partial}{\partial t}\int_s^{\delta_s}\theta_s rdr+\theta_m s\frac{\partial s}{\partial t}-\theta_0\delta_s\frac{\partial\delta_s}{\partial t}=-\frac{1}{\mathrm{Ste}}\frac{k_s}{k_L}s\frac{\partial\theta_s}{\partial r}\Big|_{r=s}; \quad t>t_s,\ 0\le z\le 1 \tag{22}$$

In deriving the above equations, conditions (2), (3), (5), and (11) are used.

As in standard integral method procedures, it is necessary to assume radial distributions of the liquid downflow velocity u, liquid temperature θ, and solid temperature θ_s to evaluate terms in equations (18)–(22). In this study, the following profiles are used

$$u=u_\delta\eta; \quad 0\le\eta=\frac{s-r}{s-\delta}\le 1 \tag{23}$$

$$\theta=\theta_m+(s-\delta)\frac{R_0}{k_L(T_b-T_m)}\left[q_w\eta+\frac{1}{2}(q_p-q_w)\eta^2\right]; \quad 0\le\eta\le 1 \tag{24}$$

$$\theta_s=\theta_0+\frac{1}{2}\frac{R_0q_p}{k_s(T_b-T_m)}(\delta_s-1)\xi^2; \quad 0\le t\le t_s; \quad 0\le\xi=\frac{\delta_s-r}{\delta_s-1}\le 1 \tag{25}$$

$$\theta_s=\theta_0+(\theta_m-\theta_0)(1-2\zeta+\zeta^2);\quad t>t_s,\quad 0\le\zeta=\frac{r-s}{\delta_s-s}\le 1 \tag{26}$$

where u_δ is the liquid velocity at the plasma–liquid interface and q_w is the heat flux transferred from the liquid to the solid–liquid interface. As can be seen, profiles assumed here satisfy boundary equations (2), (3), (5), (11), (13), and (14).

Substitutions of the assumed profiles into equations (18)–(22) lead to the following first-order partial differential equations

$$\frac{\partial}{\partial z}\left[u_\delta(s-\delta)\left(\frac{1}{6}s+\frac{1}{3}\delta\right)\right]=P_1\delta\frac{\partial\delta}{\partial t};\quad t>t_s,\quad 0\le z\le 1 \tag{27}$$

$$P_1\frac{\partial}{\partial t}\left[u_\delta(s-\delta)\left(\frac{1}{6}s+\frac{1}{3}\delta\right)\right]+\frac{\partial}{\partial z}\left[u_\delta^2(s-\delta)\left(\frac{1}{12}s+\frac{1}{4}\delta\right)\right]=(P_2\mathrm{Pr})\left(\frac{R_0\delta}{\mu_L\sqrt{gL}}\tau_p-\frac{s}{(s-\delta)}u_\delta\right)+\frac{1}{2}(s^2-\delta^2);$$

$$t>t_s,\quad 0\le z\le 1 \tag{28}$$

$$sq_w+\frac{P_1}{P_2}\frac{\partial}{\partial t}\left[(s-\delta)^2\left(\frac{1}{8}s+\frac{5}{24}\delta\right)q_w\right]+\frac{1}{P_2}\frac{\partial}{\partial z}\left[u_\delta(s-\delta)^2\left(\frac{7}{120}s+\frac{3}{20}\delta\right)q_w\right]=\delta q_p+\frac{P_1}{P_2}\frac{k_L(T_b-T_m)}{R_0}\theta_m s\frac{\partial s}{\partial t}-\frac{P_1}{P_2}\frac{\partial}{\partial t}\left[\frac{1}{2}\frac{k_L(T_b-T_m)}{R_0}\cdot\theta_m(s^2-\delta^2)+(s^2-\delta^2)\left(\frac{1}{24}s+\frac{1}{8}\delta\right)q_p\right]-\frac{1}{P_2}\frac{\partial}{\partial z}\left[u_\delta\frac{k_L(T_b-T_m)}{R_0}\theta_m(s-\delta)\left(\frac{1}{6}s+\frac{1}{3}\delta\right)+(s-\delta)^2u_\delta\left(\frac{1}{40}s+\frac{1}{10}\delta\right)q_p\right];\quad t>t_s,\quad 0\le z\le 1 \tag{29}$$

$$\frac{\partial}{\partial t}\left[\left(\delta_s-1\right)^2\left(\frac{1}{12}\delta_s+\frac{2}{4}\right)\right]=\frac{2}{\mathrm{Ste}}\frac{k_s}{k_L};\quad 0\le t_s\le t,\quad 0\le z\le 1 \tag{30}$$

$$\frac{\partial}{\partial t}\left[(\delta_s-s)\left(\frac{1}{12}\delta_s+\frac{1}{4}s\right)\right]+s\frac{\partial s}{\partial t}=\frac{2}{\mathrm{Ste}}\frac{k_s}{k_L}\frac{s}{(\delta_s-s)};\quad t>t_s,\quad 0\le z\le 1 \tag{31}$$

Using the assumed temperature profiles, equations (12) can be written as

$$\frac{\partial s}{\partial t}=\left[\frac{R_0q_w}{k_L(T_b-T_m)}-\frac{k_s}{k_L}\frac{(\theta_m-\theta_0)}{(\delta_s-s)}\right];\ t>t_s,\quad 0\le z\le 1 \tag{32}$$

For known distributions of the plasma heat flux q_p and shear stress τ_p, five unknowns, namely u_δ, δ, q_w, δ_s, and s, appear in the formulations. They can be calculated by simultaneously solving equations (27)–(32).

Following is a description of the solution procedure. In the initial pure conduction period, equation (30) is solved to obtain the heat penetration depth in the solid. This calculation continues until the solid surface temperature reaches the melting temperature. Because of the nonuniform axial heating, pure conduction and partial melting may occur in different regions simultaneously.

During the partial melting period, only the solid metal that is near the plasma-jet entrance undergoes a phase change, and the rest of the material remains in solid state. The molten liquid generated in the top section of the plate can flow downward and pass over the downstream solid wall, which might still be relatively cool. Resolidification of this downflowing liquid may occur. For simplicity, this possible resolidification mechanism is neglected in this work. Since in the initial partial melting period the thickness of the resolidified layer is thin relative to the radius of the hole, the change in radius of the solid domain upon resolidification is also neglected in the analysis.

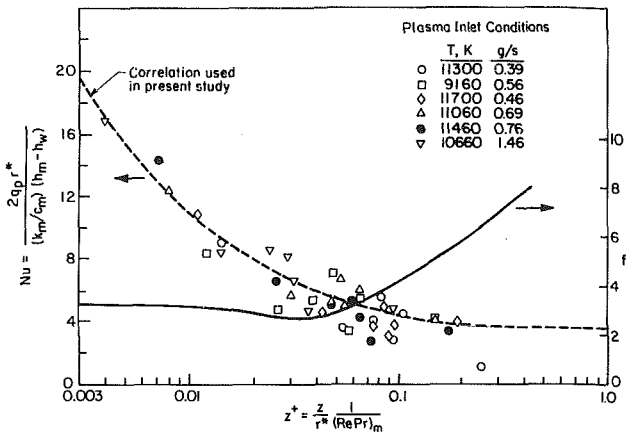

Fig. 2 Heat transfer and friction factor correlation for plasma flow in a tube

In this study the partially melting mode is simulated by simultaneously solving equations (27), (28), (29), (31), and (32) only down to the axial location where there is no net energy left for phase change. Beyond this location, the radius of the solid region is assumed unchanged, and only equations (27) and (28) are solved for the liquid film motion.

As the process continues, the full melting mode will be reached and the solid at the bottom section of the plate will start to melt. During this period, the transient characteristics of the process are investigated by solving equations (27), (28), (29), (31), and (32).

The first-order partial differential equations describing the heat transfer process were solved using an Euler backward finite difference approximation for the time derivative terms, and during each time step, an Euler forward finite difference approximation for the derivatives in the axial direction. The solution proceeds element by element along the axial direction, while at each element the unknowns are determined by an iterative procedure. Typical finite difference elements are shown as control volumes in Fig. 1. Details on the finite difference equations can be found in Hsu (1986).

The correlations used to evaluate the Nusselt number Nu and the friction factor f for plasma flow through the keyhole are shown in Fig. 2 as a function of the nondimensional distance z^+. The correlations were developed by Schmidt and Leppert (1970), Hunn (1972), and Hunn and Moffat (1974) for argon-plasma flow in the entrance region of a circular tube (12.7 mm in diameter) at a constant wall temperature of 417 K. The plasma conditions at the inlet are given in Fig. 2 and happen to be typical conditions during plasma-arc metalwork processes (O'Brien, 1986; Lancaster, 1984). Since it was shown during the development of these correlations that in the entrance region the plasma radiation plays a more significant role than the convection, the correlations in Fig. 2 should be applicable in this problem as a first-order approximation, despite the different flow geometry. (The need for more accurate plasma heat transfer and fluid flow correlations in the study of plasma-arc metalwork processes is recognized by the authors and research is currently being performed on this topic.)

The axial variation in the local mean temperature of the plasma jet, the local heat flux q_p, and friction factor f were determined by performing local energy balances on the plasma

Table 1 Properties of 304 stainless steel

Density, ρ (kg/m^3)	7200.
Solid conductivity, k_s (W/m-K)	24.29
Liquid conductivity, k_L (W/m-K)	17.81
Thermal capacity, C (kJ/kg-K)	0.693
Liquid viscosity, μ_L (kg/m-s)	6.416×10^{-4}
Latent heat, h_{sL} (kJ/kg)	265.2
Melting temperature, T_m (°C)	1427.
Boiling temperature, T_b (°C)	2807.

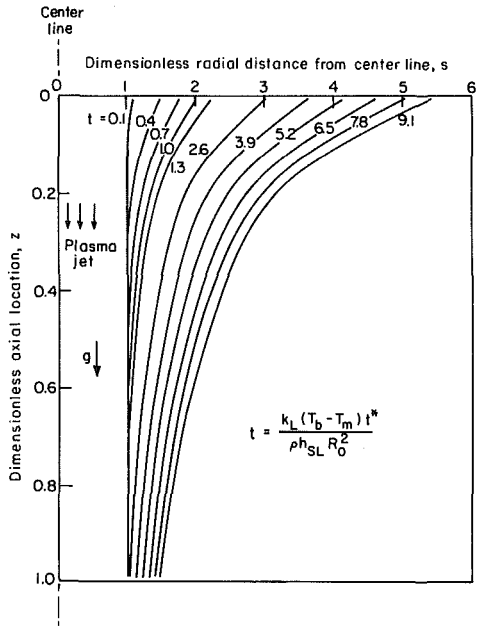

Fig. 3 Solid-liquid interface position versus time

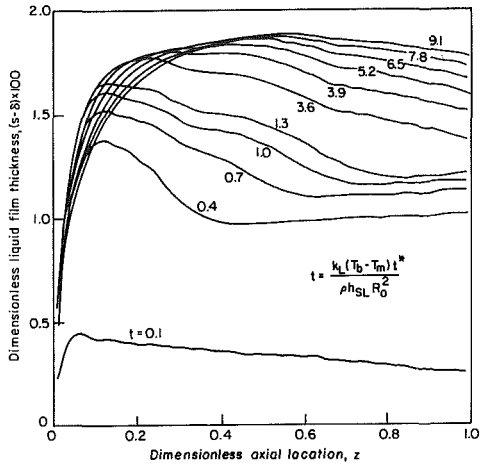

Fig. 4 Liquid film thickness versus time

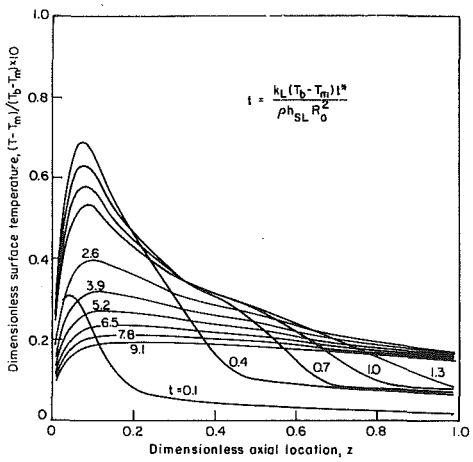

Fig. 5 Liquid surface temperature versus time

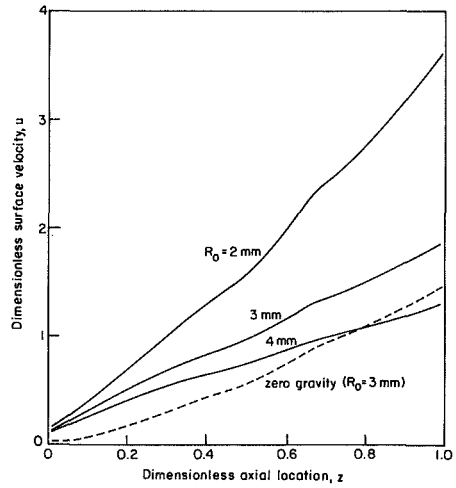

Fig. 6 Liquid surface velocity

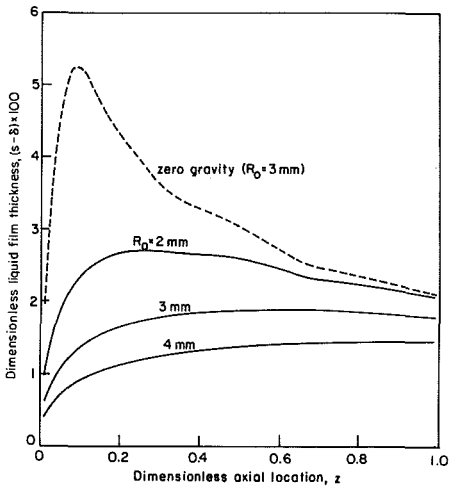

Fig. 7 Liquid film thickness

flow for each finite difference element (control volume III of Fig. 1). The heat released from the plasma in this control volume and the local friction factor are calculated from Fig. 2 for the thermal conditions of the plasma entering the control volume. By subtracting the heat released from the energy content of the incoming plasma, the thermal conditions of the plasma as it leaves the control volume are determined and used for the next control volume. The temperature-dependent properties of argon plasma listed in Kays (1955) were used in this study.

Results and Discussions

For a better understanding of the heat and fluid flow phenomena that occur during plasma-arc metal processing, a study was performed on the transient melting of a 20-mm-thick AISI 304 stainless steel plate (Table 1) at an initial temperature of 50°C subjected to plasma-arc heating. A plasma arc of argon, with a flow rate of 0.5 g/s and an inlet mean temperature of 15,000 K, was considered to flow in the direction of gravity through a 3-mm hole, predrilled in the

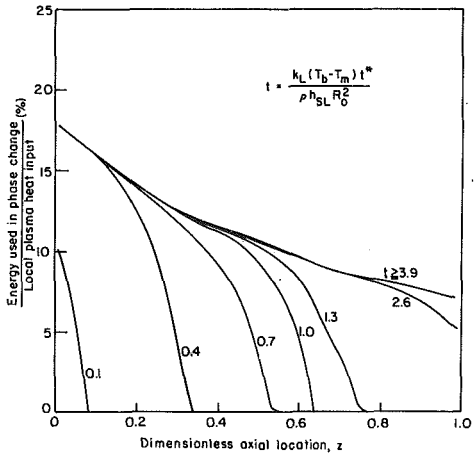

Fig. 8 Percentage of local plasma heat input used to melt solid

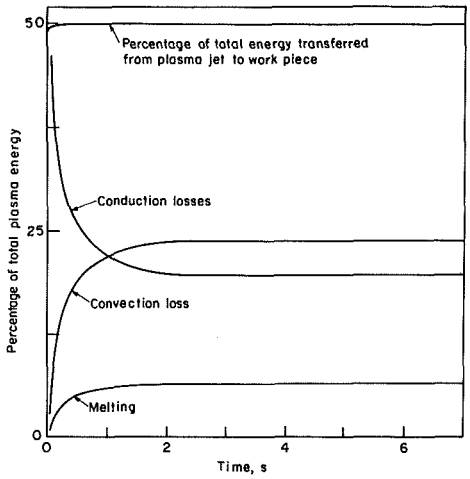

Fig. 9 Integrated heat input

plate. These plasma inlet conditions are typical in plasma metalwork processes. The numerical results discussed in this section were obtained using a convergence criterion on the order of 0.4 percent of the solution. This is also the accuracy of the solution. The lack of smoothness in some of the curves in Figs. (4)–(7) is related to the use of this convergence criterion.

Figure 3 shows the position of the solid–liquid interface as a function of time. The results indicate that the melting is much faster near the entrance of the plasma jet. This is caused by the nonuniform axial heating resulted from the cooling of the plasma-arc jet as it flows through the "keyhole." Although the model presented here does not rigorously simulate a welding process, the results indicate a potential problem in the welding of thick plates caused by the cooling of the plasma jet as it flows through the keyhole. Because of this nonuniform axial heating it is obvious that in thicker plates the weld pool will vary in the axial direction resulting in a variable weld quality.

The liquid film thickness at different times is shown in Fig. 4. Both gravity and plasma shear drive the flow. The liquid film thickness increases quickly at the onset of the melting process but it does not vary significantly at later times. First, the thickness of the liquid boundary layer increases in the axial direction; however, downstream the thickness starts to decrease. This is caused by the gradual decrease in the radius of the keyhole (shown in Fig. 3) and the consequent increase in plasma–liquid shear stress.

The surface temperature of the liquid at the liquid–plasma interface is shown for different times in Fig. 5. It can be seen that the liquid temperature is always below 1600°C. Based on an empirical formula for the evaporation rate for iron under vacuum as a function of temperature, developed by Dushman and Lafferty (1962), the maximal rate of evaporation for steel at 1600°C was calculated. The results show that this evaporation rate is about 0.03 percent of the steel melting rate and that the energy related to the evaporation is only 0.15 percent of the plasma heat input. Therefore the assumption of negligible metal vaporization made at the beginning of this work is justified. Figure 5 shows that the temperature gradient along the axial direction on the liquid plasma interface is less than 11°C/m. The shear stress induced by surface tension can be evaluated from the temperature gradient in the axial direction and the dependence of surface tension on temperature as given by Chan et al. (1984). The results show that this value does not exceed 4 percent of the shear stress τ_p induced by the plasma jet and is therefore negligible in this first-order study. The surface temperature is initially high near the entrance of the plasma-arc jet and decreases downstream as the plasma temperature decreases. With time the temperature of the surface decreases since the keyhole becomes larger and consequently, according to Fig. 2, the heat transfer coefficient decreases. This result seems to indicate the importance of the keyhole diameter on the melting process.

The effect of the initial size of the keyhole on the liquid film conditions involved in the melting of stainless steel is depicted in Figs. 6 and 7. Figure 6 shows the liquid surface velocity at a certain instant in time, while Fig. 7 shows the liquid film thickness at the same time. Three cases with initial keyhole radii of 2, 3, and 4 mm were considered in this study. The same plasma inlet conditions were used in these cases: mean temperature of 15,000 K and mass flow of 0.5 g/s. A decrease in hole size for the same plasma inlet conditions has two opposite effects. On one hand it causes an increase in molten fluid flow velocity because of the higher plasma shear stress. On the other hand it increases the liquid film thickness because of the higher heat transfer. The results indicate the importance of the keyhole size on the fluid flow processes during plasma-arc melting processes.

Also included in these two figures is a hypothetical case in which the effect of gravity is neglected. Since the driving force on the liquid motion is reduced, a slower liquid flow and a thicker film are expected. Note that the effect of neglecting gravity is more prominent at the top section of the plate where the plasma flow channel is wider. These results illustrate the importance of gravity on fluid flow during metal processing. In practical applications plasma-arc metal processing will be performed at different orientations relative to gravity. The results shown here indicate that the quality of the process might be affected by the workpiece orientation.

To evaluate a metalwork process it is important to be able to determine the fraction of the total energy distributed among the different modes of heat transfer, i.e., conduction, phase transformation, and convection. Figure 8 shows the energy fraction contributing to phase transformation as a function of both the axial location and time. In the melting of stainless steel, this fraction varies from 17.7 percent at the top to 7.1 percent at the bottom of the plate. This is a small fraction of the total heat input in the workpiece. Note that during the initial stage of the process only the top section of the solid surrounding the plasma jet undergoes phase change. The melting front, however, moves downward as plasma heating continues. These results imply that only a small fraction of the total energy goes toward the melting process. A significant portion of the energy is lost by both conduction and convection.

In Fig. 9 an integration of the energy transferred by the different modes of heat transfer along the keyhole axis shows

that, following the initial transients, about 50 percent of the plasma energy is transferred to the workpiece while 50 percent of the plasma energy is lost as the plasma jet exits the keyhole. It was interesting to observe that this percentage varied with time less than 1 percent. These results also show that plasma-arc melting might be a rather low-efficiency process in which only 7 percent of the total plasma energy contributes to the melting of the workpiece, 20 percent is lost by conduction in the solid, and 23 percent is removed by molten liquid convection.

Conclusions

A first-order approximation study using an integral method of solution was performed to investigate the heat transfer, the fluid flow, and the transient melting process in metals undergoing keyhole-plasma heating. An analysis of the melting process in a plate of stainless steel has shown that the melting process will vary significantly along the axis of the keyhole which might affect the quality of the process result in thick plates of metal. Results indicate that the size of the keyhole and gravity will affect the fluid flow of the molten liquid and the melting process. Plasma-arc metal processing seems to have low efficiency with significant heat transfer losses by conduction in the workpiece by convection in the molten liquid, and by energy transport away from the plasma efflux.

Acknowledgments

This research was supported by a gift from the FMC Corporation, Welding Engineering Group, headed by Mr. K. L. Keck. The authors would like to express their appreciation to Messrs. K. L. Keck and D. Witkowski for suggesting this topic of research and for the continuous consultations.

References

Chan, C., Mazumder, J., and Chen, M. M., 1984, "A Two-Dimensional Transient Model for Convection in Laser Melted Pool," *Metallurgical Trans.*, Vol. 15A, pp. 2175–2184.

Contreras, W., and Thorsen, R. S., 1975, "Transient Melting of a Solid Heated by a Condensing Saturated Vapor – Case 1: Negligible Interface Curvature," ASME JOURNAL OF HEAT TRANSFER, Vol. 97, pp. 570–575.

Dushman, S., and Lafferty, J. M., 1962, *Scientific Foundations of Vacuum Technique*, 2nd ed., Wiley, NY, pp. 691–701.

Epstein, M., and Cho, D. H., 1976, "Laminar Film Condensation on a Vertical Melting Surface," ASME JOURNAL OF HEAT TRANSFER, Vol. 98, pp. 108–113.

Hunn, B. D., 1972, "Radiative Heat Transfer From an Argon Plasma in Tube Flow," Ph.D. Dissertation, Stanford University, Stanford, CA.

Hunn, B. D., and Moffat, R. J., 1974, "Radiative Heat Transfer From a Plasma in Tube Flow," *Int. J. Heat Mass Transfer*, Vol. 17, pp. 1319–1328.

Hsu, Y., 1986, "Numerical Studies on Heat Transfer and Fluid Flow During Plasma-Arc Metalwork Processes," Ph.D. Thesis, University of California, Berkeley, CA.

Kays, W. M., 1955, "Numerical Solutions for Laminar Flow Heat Transfer in Circular Tubes," ASME JOURNAL OF HEAT TRANSFER, Vol. 77, pp. 1265–1274.

Lancaster, J. F., 1984, *The Physics of Welding*, Pergamon Press, p. 268.

Metcalfe, J. C., and Quigley, M. B. C., 1975, "Heat Transfer in Plasma-Arc Welding," *Welding J.*, Vol. 54, pp. 99–103.

Metcalfe, J. C., and Quigley, M. B. C., 1975, "Keyhole Stability in Plasma Arc Welding," *Welding J.*, Vol. 64, pp. 401–404.

O'Brien, R. L., 1968, "Arc Plasma for Joining, Cutting and Surfacing," Welding Research Council, No. 131.

Schmidt, P. S., and Leppert, G., 1970, "Heat Transfer From Plasma in Tube Flow," ASME JOURNAL OF HEAT TRANSFER, Vol. 92, pp. 483–489.

Taghavi-Tafreshi, K., and Dhir, V. K., 1982a, "Analytical and Experimental Investigation of Simultaneous Melting-Condensation on a Vertical Wall," ASME JOURNAL OF HEAT TRANSFER, Vol. 104, pp. 24–33.

Taghavi-Tafreshi, K., and Dhir, V. K., 1982b, "Shape Change of an Initially Vertical Wall Undergoing Condensation-Driven Melting," ASME JOURNAL OF HEAT TRANSFER, Vol. 105, pp. 235–240.

Tomsic, M., and Barhorst, S., 1984, "Keyhole Plasma Arc Welding of Aluminum With Variable Polarity Power," *Welding J.*, Vol. 13, pp. 25–32.

Hsing-Pang Liu
Center for Electromechanics.

J. R. Howell
E.C.H. Bantel Professor,
Dept. of Mechanical Engineering and
Center for Energy Studies.
Fellow ASME

The University of Texas
at Austin,
Austin, TX 78758

Scale Modeling of Radiation in Enclosures With Absorbing/Emitting and Isotropically Scattering Media

Exchange factor analysis has been shown to be an alternative to zonal analysis in enclosures with participating media. An experimental measurement of exchange factors for a cubic enclosure has been done, and practical problems associated with the measurements are discussed. The effects of isotropic scattering and absorption-isotropic re-emission processes are known to be the same for their contribution to energy exchange paths in systems with equal optical thickness. The measurement of these exchange factors is achieved by using an enclosure containing a near-isotropically scattering medium. The heat transfer results for the pure radiation case are demonstrated by using these experimentally determined exchange factors in the analysis, and are compared with the analytical results.

Introduction

The Hottel zonal method remains the most widely used method for radiative transfer analysis in industrial furnaces [1, 2]. Despite certain serious drawbacks, this method continues to be studied and improved because of its mathematical simplicity. The drawbacks of the zonal method include the difficulty of adequately representing complex geometries and the tedious calculations required to determine the "exchange areas" that describe the geometry and attenuation characteristics of a gas–surface system. Although exchange areas are available in the literature for elemental volumes in rectangular parallelepipeds, right circular cylinders, and cones, exchange areas for the more complex geometries, such as industrial process furnaces and utility furnaces, are not generally available. Exchange areas are quite difficult to compute for complex geometries and cannot be determined experimentally.

An alternative formulation, the exchange factor method, is available that overcomes some of the geometric restrictions of the zonal method [3]. In the exchange factor method, the exchange factors, which replace the direct-exchange areas of the zonal method, are used to write energy balances for each area and volume element in the system. The energy balance equations result in a set of coefficients that relate the independent variables, the surface element radiosities (W_i) and the volume element emissive powers (E_γ), of the system, and these coefficients are in some cases more easily obtained this way than through the zonal method.

Exchange factors have the advantage over direct-exchange areas that they can in principle be determined experimentally. The formulation of the equations of radiative energy exchange is no more difficult using exchange factors than in the zonal method. The goal of the present work is to design, construct, and use an experimental apparatus to measure the values of exchange factors. The experimental system is used to determine factors for a simple cubic geometry where known factors are available in order to check for accuracy. At successful completion of this work, a method will have been established for determining exchange factors in a complex geometry typical of an industrial furnace.

The Exchange Factor Method

As in the zonal method, the enclosure is divided into discrete area and volume elements. The exchange factors replace the direct-exchange areas of the zonal method and can be defined as follows:

- $\overline{FS_iS_j}$ = fraction of energy leaving surface A_i and incident on surface A_j by all possible paths within the enclosure, excluding wall reflections
- $\overline{FS_iG_\gamma}$ = average number of mean paths (based on the total extinction coefficient) traveled by energy leaving surface A_i before absorption or scattering in V_γ
- $\overline{FG_\gamma S_i}$ = fraction of energy emitted by volume V_γ and incident on surface A_i by all possible paths within the enclosure, excluding wall reflections
- $\overline{FG_\gamma G_\mu}$ = average number of mean paths (based on the total extinction coefficient) traveled by energy originating as an energy source in V_γ before absorption or scattering in V_μ

Other interpretations for $\overline{FS_iG_\gamma}$ and $\overline{FG_\gamma G_\mu}$ are described in [3]. Since exchange factors account for energy absorbed, re-emitted, and scattered anywhere in the enclosure, they can be experimentally measured.

Energy balances may be written in terms of exchange factors for each area and volume element in the system, resulting in a set of linear algebraic equations. For an enclosure that is not in radiative equilibrium, i.e., including sources in the medium, the energy balance on a surface element A_i of a total of N surface elements is

$$W_iA_i = \epsilon_iA_iE_i + \rho_i\left\{\sum_{j=1}^{N}\overline{FS_jS_i}W_jA_j + \sum_{\gamma=1}^{\Gamma}\overline{FG_\gamma S_i}Q_\gamma\right\} \quad (1)$$

The energy balance on a volume element V_γ of a total of Γ volume elements is

$$(4aV)_\gamma E_\gamma = (1-\omega_0)\left\{\sum_{i=1}^{N}\overline{FS_iG_\gamma}W_iA_i + \sum_{\mu=1}^{\Gamma}\overline{FG_\mu G_\gamma}Q_\mu\right\} + Q_\gamma \quad (2)$$

The unknowns W_i and E_γ can be calculated from the $N + \Gamma$ energy balance equations.

Consider, for the purposes of exploring the properties of exchange factors, an isothermal, black-walled enclosure which is in radiative equilibrium. Since there is no net energy exchange between any pair of volume and/or area elements, the following relationships must hold [3, 4]

Contributed by the Heat Transfer Division and presented at the ASME National Heat Transfer Conference, Denver, Colorado, August 1985. Manuscript received by the Heat Transfer Division December 23, 1985.

$$A_i\overline{FS_iS_j} = A_j\overline{FS_jS_i} \tag{3}$$

$$A_i\overline{FS_iG_\gamma} = (4aV)_\gamma\overline{FG_\gamma S_i} \tag{4}$$

$$(4aV)_\gamma\overline{FG_\gamma G_\mu} = (4aV)_\mu\overline{FG_\mu G_\gamma} \tag{5}$$

For such an enclosure with N surface and Γ volume elements, all of the energy leaving any given surface must be incident on the bounding surfaces. That implies

$$\sum_{j=1}^{N}\overline{FS_iS_j} = 1 \tag{6}$$

Note $\overline{FS_iS_i} \neq 0$ in the above equation.

In the same case, the energy emitted by a volume element must eventually strike an enclosure surface. Therefore

$$\sum_{i=1}^{N}\overline{FG_\gamma S_i} = 1 \tag{7}$$

By definition, the values of the $\overline{FGG}$ factors increase as the optical thickness of the medium increases, because repeated absorption, re-emission and scattering of energy will occur when the medium is optically thick. They may be greater than unity if the optical thickness becomes large enough. Energy that originates in a volume element ultimately must reach the enclosure surfaces; hence, no conservation law for $\overline{FGG}$ can be established.

Note that although exchange factors are defined for and measured in a black-walled enclosure, they are used in analysis of any gray-diffuse surfaced enclosure, with or without radiative equilibrium. The factors themselves depend only on enclosure geometry and the extinction coefficient of the medium.

Basically, exchange factors may be obtained by two ways. For a simple enclosure (e.g., a cube) with known direct-exchange areas, the relationships between exchange factors and direct-exchange areas of [3] can be used to calculate the exchange factors. But the exchange factors must be determined experimentally for enclosures with complex geometries where the direct-exchange areas are totally unknown. In such an experimental determination of exchange factors, the assumptions present in the exchange factor (and zonal) analysis should be met as closely as possible. These include diffusely emitting sources; diffusely absorbing surface sinks; and an isotropic participating medium. The purpose of this paper is to describe the results of a program for measuring exchange factors, and the methods used to meet the necessary conditions as closely as possible.

It must be realized that any analytical results obtained from exchange factor or zonal analysis have a degree of uncertainty in comparison with actual results, because few real systems approach the assumed conditions in the analysis. In the work presented here, we are forced to construct a system that meets the assumptions, or, where that is not possible, to apply corrections to the measured results that account for the nonideal behavior of the measurements. In this way, the measured factors should be correct for use in the analysis; the analytical results will still include the idealized assumptions.

Energy conservation may not be exactly met by a set of individually calculated or measured exchange factors due to the errors associated with either numerical integration or experiment. Therefore, exchange factors usually must be scaled or smoothed to satisfy the conservation laws of equations (6) and (7).

A least-squares smoothing method for exchange factors as well as for Hottel's exchange areas has been developed by Larsen [4, 5]. In his smoothing technique, the method of Lagrange multipliers has been used to determine the necessary adjustments for a set of factors. By applying this method, the [*FSS*] may be smoothed to meet energy conservation constraints while minimizing the disturbance of the original estimates.

The scaling of [*FGS*] as described in [4] causes each row of the matrix of factors to be multiplied by the same scalar. In other words, the original "shape" of [*FGS*] is not altered.

Exchange Factor Measurement Analysis

For an absorbing/emitting, and isotropically scattering medium in radiative equilibrium, energy emitted by an enclosure surface is absorbed and scattered in the medium, and the energy is then re-emitted and scattered isotropically, and eventually will be absorbed by one of the enclosure surfaces. If the medium is replaced by a pure isotropically scattering medium, the energy transport will be identical as long as both systems have the same optical thickness. This was shown analytically for the exchange factor formulation in [3, 4]. Of course, the scattering medium must not absorb the radiative energy at the wavelength being measured; this is especially important when optically thick media are simulated.

To determine exchange factors experimentally, a black-walled enclosure of the necessary geometry was constructed

Nomenclature

a = absorption coefficient, cm^{-1}
A = area, cm^2
C = scattering cross section of sphere, cm^2; modifier on incident energy
d = particle diameter, cm
D = distance between centers of light source and detector, cm
E = emissive power, W/cm^2
$\overline{FSS}$, $\overline{FSG}$, $\overline{FGS}$, $\overline{FGG}$ = exchange factors defined in text
[*FSS*], [*FGS*] = bracketed factors refer to that group (matrix) of factors
L = enclosure dimension, cm
m = relative index of refraction
N = number density of spheres, cm^{-3}; number of surface elements
q = heat flux, W/cm^2
Q = heating rate of volume element, W; energy per unit time, W
S = relative angular sensitivity
V = volume of gas element, cm^3
W = radiosity, W/cm^2
x = size parameter
Γ = number of volume elements
ϵ = emissivity
λ = wavelength, cm
ρ = reflectivity
σ = scattering coefficient, cm^{-1}
τ = optical thickness
ω_0 = scattering albedo = $\sigma/(\sigma + a)$

Subscripts

a = actual quantity
d = detector
m = measured quantity
i, j = indices associated with surface elements
γ, μ = indices associated with volume elements

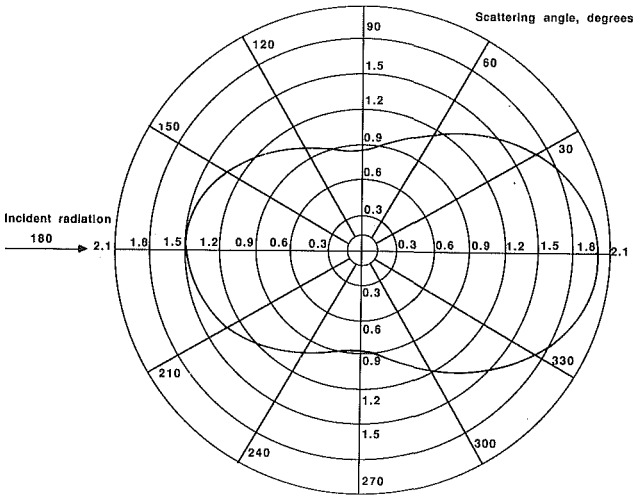

Fig. 1 Scattering phase function of 0.091-μm diameter latex spheres (incident wavelength 0.6328 μm)

and filled with a nonabsorbing, near-isotropically scattering medium. Energy from a source to a detector was then measured. "Energy transfer by all possible paths" is automatically included in this measurement. A stirred transparent liquid with neutral density scattering spheres was used, and the enclosure optical thickness could be varied by changing the sphere number density. In such an experiment, the nonideal properties of the diffuse light source, nonunity wall absorptivity, nonisotropic scattering, and nonisotropically sensitive detector must all be considered.

Choice of Scattering Medium. Aqueous suspensions of polystyrene latex spheres, manufactured by Dow Chemical Company, were used in the experiment. Mie scattering theory predicts that the anisotropic nature of the phase function becomes pronounced for large particles. Small particles with mean diameter 0.091 μm and a standard deviation of 6.4 percent, measured by electron microscope, were chosen. Generally, the particles can be treated as being monodispersed if the standard deviation of diameter is less than 10 percent [6]. These particles were shown to be nonabsorbing to visible light [7].

In order to take advantage of the particle's low absorptivity and allow convenient optical alignment of the experimental devices, monochromatic visible light from a helium–neon laser (wavelength 0.6328 μm) with random polarization was used in the experiment. This laser has 4 mW output power and long-term stability (less than 5 percent power variation in 8 hr).

The particle's refractive index at a wavelength of 0.6328 μm is 1.5882 [8]. The particle concentration was diluted by adding pure water and thoroughly dispersing the spheres. Double-distilled water with 17 MΩ-cm resistivity was used to dilute the latex in the experiment, and its refractive index is 1.3321 for 0.6328 μm wavelength and room temperature [9].

Water is a selective absorber for radiative transmission. For 0.6328 μm wavelength radiation, the absorption coefficient of water is 0.0029 cm^{-1} [10]. For optical thicknesses 1, 2, and 4, the scattering albedos are 0.965, 0.982, and 0.991, respectively. The effect of water absorption becomes less important for media with high sphere number density.

Determination of Scattering Phase Function and Scattering Coefficient. We determined the scattering phase function and the relationship between scattering coefficient and particle concentration from Mie scattering theory. The size parameter x is defined as:

$$x = \pi d/\lambda \tag{8}$$

Substituting the known values into the above expression, we obtain the size parameter $x = 0.602$. With the known x and the relative refractive index of the particles $m = 1.192$, it was found that the scattering pattern fell into the Rayleigh–Gans scattering domain with the scattering cross section of the sphere having a value of $C = 3.25 \times 10^{-13}$ cm^2 [11]. The relative scattering phase function is plotted as a function of scattering angle, and is shown in Fig. 1.

The scattering coefficient σ is defined as:

$$\sigma = C \cdot N \tag{9}$$

where the number density of scattering spheres N can be related to the particle concentration.

Because the polystyrene particle is nonabsorbing to visible laser light, the optical thickness τ of an enclosure (neglecting water absorption) can be expressed as

$$\tau = \sigma \cdot L = C \cdot N \cdot L \tag{10}$$

A given optical thickness may be obtained by adjusting the particle concentration.

The measurements of exchange factors should be performed by using ideal isotopically scattering media, but this idealized scattering behavior cannot be obtained in a real experiment. In practice, Rayleigh scattering is the closest approach to isotropic scattering. Due to the constraints of the wavelength of the visible light source, the absorbing properties of the particles, and the smallest particle diameter available from the manufacturer, Rayleigh–Gans scattering [11] was the closest to Rayleigh scattering we could achieve. However, the scattering phase function becomes less important for multiple scattering in optically thick media.

Other Experimental Considerations. A colloidal dispersion in which the dispersed phase remains essentially as discrete, single particles on a long time scale is said to be stable. In the polymerization of polystyrene latex, a sulfonate type surfactant and a persulfate initiator are adsorbed onto the particles. Both the sulfonate and sulfate groups impart a negative surface charge to the particles to insure stability. Woods and Krieger [12] showed that polymer latex, with diameters less than 0.5 μm, would remain stable indefinitely and could be considered to behave in aqueous suspension as independent rigid spheres. For latex of diameters greater than 0.5 μm, appreciable settling on storage was noted.

The present work compares the measured exchange factors with those of the zonal analysis [3, 4]. The zonal method assumes the intensity of all the energy leaving the enclosure surface does not vary with angular direction; hence, a diffuse light source is required in the exchange factor measurement. In this work a spatial filter, which was composed of a microscope objective and a magnetically captured pinhole, was used to convert the collimated laser beam into an expanding spherical wavefront, free from unwanted intensity variations. The expanded laser light was then directed onto a white flashed opal glass.

The opal glass (optical diffuser), with diameter 50 mm and thickness 3 mm, was obtained from the Ealing Corporation. When illuminated by a defocused beam of light, the glass transmits as a true Lambertian source (i.e., directional radiated energy proportional to the cosine of the angle measured away from the normal of the surface). This glass was tested in order to check its diffusing property. During the test, a helium–neon laser was modulated by a mechanical chopper, then went through the spatial filter, and finally was directed onto the opal glass. The signal detection unit, located on a tripod-mounted radiometer, consisted of a 20.32-cm-dia focusable collecting optics system and a PbS detector providing an 8-milliradian field of view for this measurement. A light spot projector mounted inside the radiometer optics served as an aid in aiming and focusing the unit at the desired

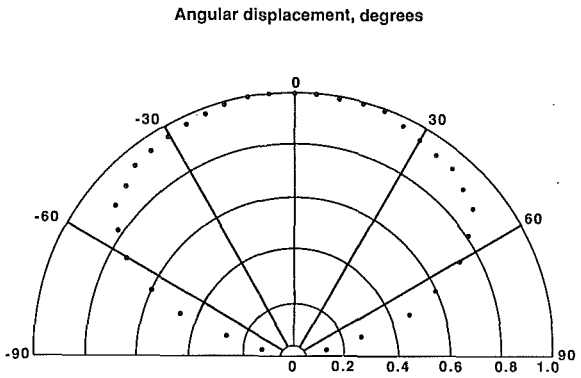

Fig. 2 Angular sensitivity diagram of uncovered eye-response photodiode

target. The detected signal then went to a radiometer control console which included a lock-in amplifier and associated control electronics for signal processing. The measured signals at various angles of incidence (relative to normal incidence) were divided by the cosine of the corresponding incident angles, and the quantities after division were directly proportional to the radiative intensities of the opal glass at different directions. The results indicated that the opal glass indeed was an excellent optical diffuser. The above test was performed in air, but the diffusing characteristics will remain the same if the surrounding medium is changed to water.

To measure the surface-to-surface exchange factors, a 3.175-cm square surface element detector was made with nine uncovered (the front filter glass was removed) eye-response photodiodes, which were evenly distributed on the detecting element. The sensitive area of each photodiode was 0.97 mm^2, and the typical dark current was 4 pA. The light detected by these nine photodiodes was assumed to represent that detected by the whole detecting element on a relative basis. Because of the large variation of incident angles onto the detector for possible light source and detector pair locations in the model, a sensitivity diagram (relative sensitivity versus angular displacement) of the uncovered photodiode, shown in Fig. 2, was measured in double-distilled water for the purpose of correcting the experimental results for the sensitivity of the photodiodes to incident angle.

For the measurement of surface-to-gas exchange factors, a 3.175-cm cubic detector was constructed with four photodiodes on top and five photodiodes on each of the other walls. There were several holes on the walls of this cubic detector to allow the scattering medium to fill the inside so that the radiation field was disturbed as little as possible by the presence of the detector. The hole area was 20 percent of the surface area of the cubic detector. The central hole on the top of the cubic detector was connected to the position-control device which was located outside the model and controlled by a microcomputer.

Consistent with the definitions of exchange factors, the enclosure walls should be perfectly black. The interior surfaces of the enclosure were coated with black paint with absorptivity 0.96 to closely approach ideal black boundaries. A schematic diagram of the experimental system is shown in Fig. 3.

Measurement of $\overline{FSS}$ Factors

A cube made of clear acrylic plates, with sides of 12.7 cm interior dimension and evenly divided into 64 ($4\times4\times4$) volume elements, was filled with aqueous suspensions of polystyrene latex spheres. There are 16 square surface elements (3.175 cm $\times$ 3.175 cm) on each of the six enclosure walls. The interior walls were constructed of removable panels for the purpose of varying the detector location.

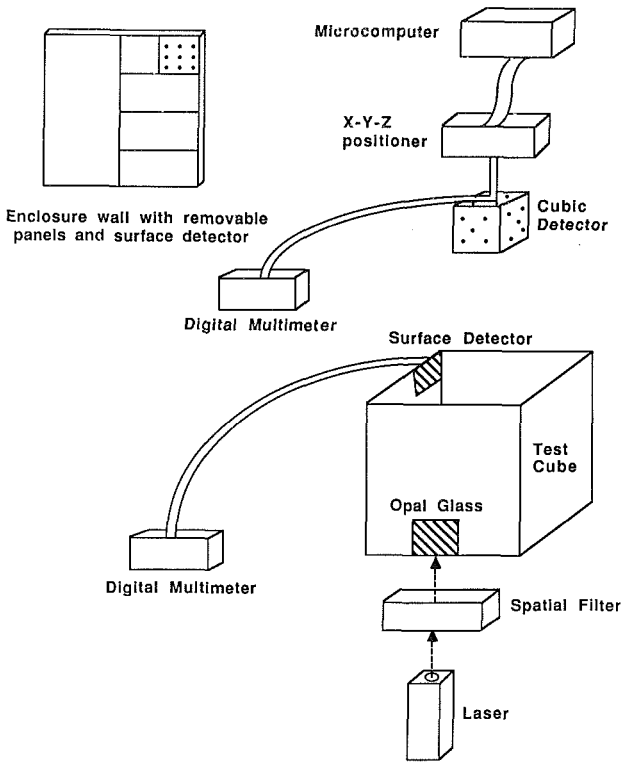

Fig. 3 Schematic diagram of the experimental system

For the measurement of $\overline{FSS}$ factors, two of the removable panels were built of several small pieces in order to locate the opal glass and detector. These small pieces could be combined by inserting various sets of locating pins between them to produce the desired positions of light source and detector. Both the opal glass source window and the surface detector were 3.175 cm square, and could thus be assembled with the other small pieces. When all the panels were assembled within the container, the interior dimensions formed a 12.7-cm cube exactly, and the opal glass and the detector were integral parts of the enclosure walls. Slots on the back of the detector panel allowed the leads, which were connected to the photodiodes, to go to the measuring device outside the cube. Except for the opal glass and photodiodes, all the other interior surfaces were coated with black paint.

The front filter glass of each photodiode on the surface detector was removed to avoid total internal reflection at the medium/glass interface. Without removing the filter glass, total reflection will occur at those detector positions with angles of incidence (relative to the light source position) larger than 49 deg ($\simeq \sin^{-1}(1/1.332)$).

Before and after the measurements on a given enclosure wall (16 measurements for all surface elements on a wall), we measured the total incident energy (into the cube) by placing the detector flush against the opal glass. The variation with time of total energy incidence was considered by linearly interpolating between these two values according to the measuring sequence of each surface element. It took about 3 min to measure an individual data point. Dividing the measured incident energy of a surface element by the total energy incident on the enclosure, we obtained the $\overline{FSS}$ factors.

It was difficult to combine a light source and detector to measure the $\overline{FS_iS_i}$ factor; therefore, the energy scattered back to the light source itself was obtained by extrapolating from the measurements of adjacent surface elements.

Because the photodiodes were not isotropically sensitive, the detected signal did not represent the incident energy to a given surface element. In the measurement of $\overline{FSS}$ factors, there were 96 possible detector positions for a fixed position of

light source if we disregarded the symmetry. With a given medium optical thickness inside the cubic enclosure, it was difficult to estimate the distribution of angles of incidence of the scattered light for every possible pair of light source and detector positions. The modifier which was used to correct the measured factors was a combination of two parts: (1) the product of direct transmittance and the angular sensitivity to the directly transmitted energy and (2) the product of the indirectly scattered light and an optical thickness dependent function which governs the incident distribution of the indirectly scattered light.

The actual energy per unit time incident on a surface element Q_a was expressed as the product of the measured energy of incidence Q_m and the empirical modifying equation

$$Q_a = Q_m \cdot \left(\frac{1}{C^* \{ (S_d)\exp(-D\tau/L) + C(\tau)[1-\exp(-D\tau/L)] \}} \right) \quad (11)$$

where

C^* = the fraction of incident energy measured by the surface element detector at normal incidence (i.e., normal incidence detector sensitivity)

S_d = angular sensitivity of detector based on the incident angle from the center of the light source to the center of the detector (relative to normal incidence)

$C(\tau)$ = a function of optical thickness

The complex scattering behavior, originating from multiple scattering and the nonisotropic scattering phase function, made it quite difficult to exactly determine $C(\tau)$. We assumed $C(\tau)$ equal to the hemispherically averaged sensitivity of the detector relative to the sensitivity at normal incidence, which was found to be 0.795. For the case of $\tau = 0$, equation (11) shows that the measured $\overline{FSS}$ factor was modified solely by the angular sensivity C^*S_d of the detector by assuming all the incident rays to the detector to be parallel to the line connecting the centers of the light source and detector. For the case of infinite optical thickness, the detector is assumed to receive incident energy from all directions with equal possibility. The modifier in equation (11) then approaches the reciprocal of the product of the normal incidence detector sensitivity and the hemispherically averaged sensitivity of the detector. For simplicity, the constant modifier for infinite optical thickness was also used as the modifier for cases when the light source and detector were located on the same enclosure wall.

The modified results for each surface element were further adjusted by using the smoothing technique which was mentioned previously. The extent to which the modified data has to be smoothed depends on the surface element position, light source position, and optical thickness. For representative positions of light source we can examine the absolute quantity being smoothed for all possible surface element positions and several different optical thicknesses on an average basis. For the light source positions 1, 2, and 6 indicated in Fig. 4, the modified results were smoothed by 2.6, 3.9, and 6.3 percent, respectively, to satisfy the conservation law.

Measurement of $\overline{FGS}$ Factors

To measure $\overline{FGS}$ directly, a uniformly diffuse cubic light source must be constructed. Such a device might be constructed using optical fibers with laser light introduced into a small cubic volume element filled with a scattering medium and surrounded with diffusing windows. The top of the cubic light source must then be connected to the mounting rod of the position-control device. Disregarding the difficult construction problem involved, it is doubtful that a truly diffuse cubic light source can be made by this technique. The most important drawback of such an $\overline{FGS}$ measurement is that the wall-

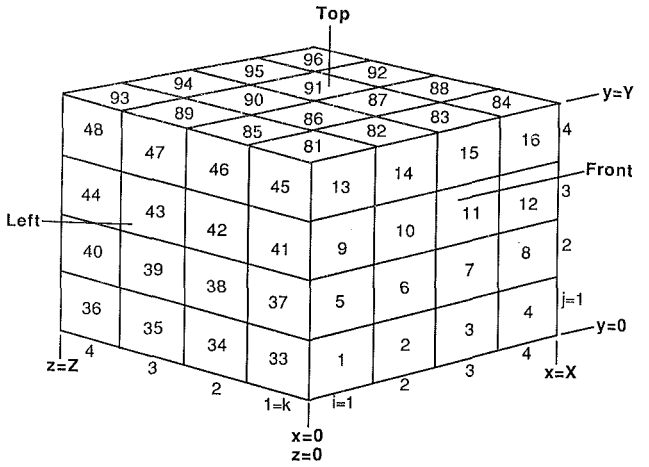

Fig. 4 Numbering of cube elements for exchange factors and pure radiation results presented in Tables 1-5.
Back, right, and bottom walls are parallel to front, left, and top walls, and consist of surface elements 17-32, 49-64, and 65-80, respectively. Surface elements 1-16 (33-48, 81-96) are directly oppposite 17-32 (49-64, 65-80).
The first 16 volume elements have the first 16 area elements as exterior surfaces, then the same "cube-stacking" continues in subsequent layers. Volumes 17, 33, and 49 have areas 34, 35, and 36 as exterior surfaces.
After exploiting symmetry, the surface elements 1, 2, and 6 are the unique positions for the light source.
There is no energy source inside the cube, and all walls are black. Surfaces for which $z = Z$, $x = X$, or $y = 0$ have unit emissive power, other surfaces are cold.

element photodetector cannot differentiate the contributions from each surface of the cubic light source; thus, the effect of the inherently nonisotropically sensitive photodetector cannot be corrected.

Because of this, we measured $\overline{FSG}$, and then transformed to $\overline{FGS}$ according to the reciprocity relationship expressed in equation (4). A 3.175-cm cubic detector was connected to a computer-controlled X-Y-Z position-control device which was composed of three stepping motors. For a given position of the detector, the signal detected by each surface of the cubic detector was recorded sequentially. Due to the nonisotropic sensitivity of the detector, the measured result was modified for each detector surface based on optical thickness, angular sensitivity, and the distance between the centers of the light source and detector surfaces. The modifying equation was the same as that for the $\overline{FSS}$ factors (equation (11)), except that the modifiers were assumed to be only the reciprocal of the product of the normal incidence detector sensitivity and the hemispherically averaged sensitivity of the detector for those detector surfaces which could not be "seen" by the light source.

The six modified results were summed to represent the total energy received by the cubic detector at a given position. It was not possible to determine the path lengths of those directly transmitted and indirectly scattered energies which penetrated the cubic volume element; hence, the absorptance of the cubic volume element based on its edge length, $1 - \exp(-\sigma L/4)$, was adapted for simplicity. Multiplying the received energy by the absorptance of the cubic volume element and dividing the result by the total incident energy, the $\overline{FSG}$ factor was obtained. The $\overline{FSG}$ factors were transformed to $\overline{FGS}$ factors, then scaled to satisfy energy conservation. For the light source positions 1, 2, 6, and 22 indicated in Fig. 4, the modified $\overline{FGS}$ factors were scaled by 18, 13.6, 9.4, and 10.7 percent, respectively, in the present work.

Estimation of $\overline{FGG}$ Factors

The measurement of $\overline{FGG}$ factors has the same experimental problems as the direct measurement of $\overline{FGS}$ factors. Fur-

Table 1 Comparison between experimental and analytical results of a set of surface-to-surface exchange factors for $\tau = 1$ and light source position 6 (Fig. 4) (values in parentheses are analytical results [4])

n	FS_6S_n	n	FS_6S_n	n	FS_6S_n	n	FS_6S_n
1	.00545 (.00830)	17	.01313 (.00832)	33	.02096 (.02075)	81	.00752 (.00808)
2	.01030 (.01450)	18	.01506 (.00977)	34	.02111 (.02096)	82	.00928 (.01068)
3	.00539 (.00878)	19	.01304 (.00868)	35	.01123 (.01092)	83	.00711 (.00845)
4	.00214 (.00368)	20	.00897 (.00601)	36	.00465 (.00517)	84	.00441 (.00462)
5	.01030 (.01450)	21	.01506 (.00977)	37	.03607 (.03603)	85	.01290 (.01097)
6	.02466 (.03389)	22	.01734 (.01158)	38	.03010 (.03082)	86	.01403 (.01406)
7	.00985 (.01518)	23	.01493 (.01024)	39	.01403 (.01406)	87	.01116 (.01146)
8	.00284 (.00507)	24	.01003 (.00699)	40	.00543 (.00625)	88	.00678 (.00659)
9	.00539 (.00878)	25	.01304 (.00868)	41	.02026 (.02123)	89	.00925 (.00802)
10	.00985 (.01518)	26	.01493 (.01024)	42	.02014 (.02162)	90	.01093 (.00981)
11	.00588 (.00936)	27	.01277 (.00911)	43	.01116 (.01146)	91	.00923 (.00846)
12	.00225 (.00403)	28	.00877 (.00630)	44	.00432 (.00550)	92	.00590 (.00544)
13	.00214 (.00368)	29	.00897 (.00601)	45	.00584 (.00741)	93	.00529 (.00465)
14	.00284 (.00507)	30	.01003 (.00699)	46	.00862 (.00949)	94	.00587 (.00549)
15	.00225 (.00403)	31	.00877 (.00630)	47	.00672 (.00656)	95	.00551 (.00494)
16	.00115 (.00229)	32	.00627 (.00452)	48	.00324 (.00368)	96	.00406 (.00349)

Note: For light source position 6, bottom and right walls are symmetrical to left and top walls respectively.

Table 2 Comparison between experimental and analytical results of surface-to-surface exchange factors (values in parentheses are analytical results [4])

	Light Source	Optical Thickness 0*	1.0	4.0
Back	1	.222 (.173)	.133 (.087)	.050 (.026)
	2	.246 (.198)	.154 (.106)	.059 (.037)
	6	.275 (.228)	.191 (.130)	.076 (.053)
Left	1	.310 (.336)	.341 (.358)	.350 (.358)
	2	.185 (.192)	.177 (.178)	.160 (.140)
	6	.223 (.241)	.224 (.232)	.211 (.197)
Right	1	.075 (.077)	.062 (.053)	.038 (.025)
	2	.117 (.120)	.103 (.098)	.075 (.060)
	6	.139 (.145)	.129 (.125)	.094 (.087)
Front	1	.008 (.000)	.060 (.090)	.172 (.209)
	2	-.003† (.000)	.083 (.118)	.225 (.280)
	6	.002 (.000)	.103 (.156)	.314 (.380)
Top	1	.075 (.077)	.062 (.053)	.038 (.025)
	2	.074 (.089)	.067 (.066)	.044 (.035)
	6	.139 (.145)	.129 (.125)	.094 (.087)
Bottom	1	.310 (.336)	.341 (.358)	.350 (.358)
	2	.381 (.401)	.416 (.434)	.436 (.447)
	6	.223 (.241)	.224 (.232)	.211 (.197)

* For the case of zero optical thickness, the analytical factors were calculated for optical thickness of 0.001 rather than zero due to program limitations.

† Negative values are a result of the smoothing technique, and are set to zero in radiative transfer calculation.

ther, it is also anticipated that the cubic light source and the cubic detector will mechanically interfere with each other for adjacent positions, presenting a difficult control problem for the X-Y-Z positioner. The measurement for the situation where one element is directly above the other is not possible due to the interference of the positioning rods. It appears most convenient to estimate the gas-to-gas direct-exchange areas, and then to transform them to $\overline{FGG}$ [3, 4, 13].

Larsen [4] showed that heat flux and temperature estimates are relatively insensitive to $\overline{FGG}$ factors for problems of small to moderate optical thicknesses. For the case of radiative equilibrium, $\overline{FGG}$ factors are not needed in the heat transfer analysis, but these factors must be used when the enclosure medium departs from radiative equilibrium, especially as optical thickness increases.

We did not attempt measurement of $\overline{FGG}$. For cases where significant departure from radiative equilibrium is expected, $\overline{FGG}$ values can be estimated by the methods suggested in [3, 4, 13].

Discussion of Results

For the measurement of $\overline{FSS}$ factors, there are 16 surface elements on each of the six enclosure walls. Referring to Fig. 4, the wall where the laser light is incident is defined as the front wall. By following the incident direction of light, the remaining walls are defined as back, left, bottom, right, and top walls. A set of $\overline{FSS}$ factors ($\tau = 1$ and light source position 6) is included in Table 1 to demonstrate the error associated with each individually measured $\overline{FSS}$ factor for the selected optical thickness and light source position. This set of data, in general, indicates the accuracies for those $\overline{FSS}$ factors which directly enter the zonal calculation.

Instead of presenting the detailed $\overline{FSS}$ factors here, we examine the sum of $\overline{FSS}$ factors on each wall. Both experimentally measured and analytically computed surface-to-surface exchange factors for optical thicknesses 0, 1, and 4 are included in Table 2. For the case of zero optical thickness, the most inaccurate results are for the back wall, with about 25 percent deviation between the experimental and analytical results. Due to wall reflections, 0.4 percent of the total energy transfer was detected at the front wall, which should receive no energy under the analytical assumption of perfectly black walls. The deviations on all other walls were generally less than 8 percent. The high percentage deviation on the back wall was also attributed to the wall reflections. For the cases of optical thicknesses 1 and 4, the high forward scattering of Rayleigh–Gans scattering gave the largest deviation to the back wall. However, the back wall generally only received a small amount of the total energy transfer, and its deviation was less than 6 percent even for the optically thin case (optical thickness = 1) if compared with the total energy transfer. Due to the reduced back-scattering present in the experiment in comparison with the assumed isotropic scattering, the front wall had the second largest deviation. Again, deviations were less than 6 percent for all cases if compared with the total energy transfer. For those walls having a large percentage of the total energy transfer, say over 40 percent, the deviations in energy balance were generally less than 4 percent, and would be less than 2 percent if compared with the total energy transfer.

The experimentally measured and analytically computed gas-to-surface exchange factors are included in Table 3. As observed for the $\overline{FSS}$ factors, the high forward scattering of the latex particles gave the largest deviation at the back wall for the experimentally measured $\overline{FGS}$ factors, and the measured factors at the front wall were smaller in comparison with those of the analytical prediction due to the reduced back-scattering. The small percentage of energy transfer to the back wall makes this deviation less important, but the appreciable deviation (e.g., light source at volume element 6) at the front wall, which has a large percentage energy transfer, has a significant effect on the total energy transfer.

With optical thicknesses 1 and 2 in a cubic enclosure with the boundary conditions specified in Fig. 4, the heat transfer results shown in Tables 4 and 5 for pure radiation are demonstrated by using the experimentally determined $\overline{FSS}$ and $\overline{FGS}$ factors, and compared with the analytical predictions. The percentage deviation between experiment and theory is small except for elements with relatively small heat flux.

Following the work discussed above, we also measured the $\overline{FSS}$ and $\overline{FGS}$ factors in a scale furnace enclosure which included slanted walls. The details can be found in [14]. Even though no analytical data are available for comparison, the

Table 3 Comparison between experimental and analytical results of gas-to-surface exchange factors (values in parentheses are analytical results [4])

Light Source		Optical Thickness 1.0		Optical Thickness 2.0	
Back	1	.051	(.040)	.039	(.030)
	2	.057	(.049)	.047	(.039)
	6	.071	(.060)	.063	(.051)
	22	.121	(.115)	.118	(.110)
Left	1	.282	(.293)	.294	(.303)
	2	.150	(.130)	.135	(.125)
	6	.176	(.168)	.170	(.166)
	22	.212	(.219)	.216	(.224)
Right	1	.051	(.040)	.039	(.030)
	2	.078	(.071)	.066	(.062)
	6	.100	(.090)	.090	(.082)
	22	.121	(.115)	.118	(.110)
Front	1	.282	(.293)	.294	(.303)
	2	.330	(.351)	.352	(.368)
	6	.376	(.424)	.417	(.453)
	22	.212	(.219)	.216	(.224)
Top	1	.051	(.040)	.039	(.030)
	2	.057	(.049)	.047	(.039)
	6	.100	(.090)	.090	(.082)
	22	.121	(.115)	.118	(.110)
Bottom	1	.282	(.293)	.294	(.303)
	2	.330	(.351)	.352	(.368)
	6	.176	(.168)	.170	(.166)
	22	.212	(.219)	.216	(.224)

Table 4 Comparison between experimental and analytical results of exchange factor method ($\tau = 1$) for a cubic enclosure with the boundary conditions specified in Fig. 4

		Emissive Power				Heat Flux	
k	j	i = 1	i = 2	i = 3	i = 4	#	q
1	4	.154(.120)	.191(.169)	.263(.228)	.385(.373)	1	.532(.498)
1	3	.191(.169)	.272(.240)	.348(.318)	.464(.471)	2	.686(.638)
1	2	.263(.228)	.348(.318)	.423(.396)	.536(.529)	3	.754(.718)
1	1	.385(.373)	.464(.471)	.536(.529)	.615(.627)	4	.822(.803)
						5	.399(.350)
2	4	.191(.169)	.272(.240)	.348(.318)	.464(.471)	6	.535(.487)
2	3	.272(.240)	.364(.344)	.455(.448)	.577(.604)	7	.623(.593)
2	2	.348(.318)	.455(.448)	.545(.552)	.652(.682)	9	.332(.270)
2	1	.464(.471)	.577(.604)	.652(.682)	.737(.772)	10	.447(.380)
						13	.241(.194)
3	4	.263(.228)	.348(.318)	.423(.396)	.536(.529)		
3	3	.348(.318)	.455(.448)	.545(.552)	.652(.682)		
3	2	.423(.396)	.545(.552)	.636(.656)	.728(.760)		
3	1	.536(.529)	.652(.682)	.728(.760)	.809(.831)		
4	4	.385(.373)	.464(.471)	.536(.529)	.615(.627)		
4	3	.464(.471)	.577(.604)	.652(.682)	.737(.772)		
4	2	.536(.529)	.652(.682)	.728(.760)	.809(.831)		
4	1	.615(.627)	.737(.772)	.809(.831)	.846(.880)		

Note: Values in parentheses are analytical results [4].

values obtained for those factors significant to the thermal analysis are believed to be accurate.

Conclusions

The technique of measurement of radiative exchange factors in a scale cube has been presented, along with results for that case. The accuracy of measured exchange factors is affected by wall reflections, absorption of radiative energy by the water used for particle suspension, the nonisotropic scattering phase function, and the accuracy of the detector sensitivity measurement. Except for the detector sensitivity measurement, all other error sources become less important for optically thick cases.

Table 5 Comparison between experimental and analytical results of exchange factor method ($\tau = 2$) for a cubic enclosure with the boundary conditions specified in Fig. 4

		Emissive Power				Heat Flux	
k	j	i = 1	i = 2	i = 3	i = 4	#	q
1	4	.117(.090)	.161(.139)	.229(.203)	.372(.363)	1	.528(.452)
1	3	.161(.139)	.243(.214)	.323(.299)	.466(.468)	2	.626(.593)
1	2	.299(.203)	.323(.299)	.403(.384)	.534(.532)	3	.707(.675)
1	1	.372(.363)	.466(.468)	.534(.532)	.628(.637)	4	.841(.776)
						5	.315(.280)
2	4	.161(.139)	.243(.214)	.323(.299)	.466(.468)	6	.450(.413)
2	3	.243(.214)	.353(.329)	.431(.443)	.597(.616)	7	.559(.523)
2	2	.323(.299)	.431(.443)	.508(.557)	.677(.701)	9	.234(.198)
2	1	.466(.468)	.597(.616)	.677(.701)	.771(.797)	10	.340(.303)
						13	.214(.128)
3	4	.229(.203)	.323(.299)	.403(.384)	.534(.532)		
3	3	.323(.299)	.431(.443)	.508(.557)	.677(.701)		
3	2	.403(.384)	.508(.557)	.586(.671)	.757(.786)		
3	1	.534(.532)	.677(.701)	.757(.786)	.839(.861)		
4	4	.372(.363)	.466(.468)	.534(.532)	.628(.637)		
4	3	.466(.468)	.597(.616)	.677(.701)	.771(.797)		
4	2	.534(.532)	.677(.701)	.757(.786)	.839(.861)		
4	1	.628(.637)	.771(.797)	.839(.861)	.883(.910)		

Note: Values in parentheses are analytical results [4].

The surface-to-surface and gas-to-surface exchange factors with small values deviate from the analytical values, but large factors generally can be obtained with good accuracy. As a result, good estimates of radiative heat transfer (which depend chiefly on the exchange factors with large values) can be obtained.

This work has developed and presented an experimental method to measure exchange factors. The method allows the zonal method to be extended to any geometry after a set of experimental measurements is obtained for that geometry.

The experimental method and results presented here point out how the assumptions inherent in both the Hottel zonal and exchange factor methods differ from real systems. It is not possible to design even a laboratory experiment that meets the constraints necessary to provide exact agreement between analytically predicted and measured exchange factors (i.e., diffuse source and detector, isotropically scattering medium, and black enclosure surfaces). The difference between the measured and analytical results might as well be viewed as shortcomings of the analysis, rather than of the experiment, because most of the differences are caused by factors that will be present in a real system. It may well be that the measured factors, when used in an analysis, will produce better agreement with heat transfer and temperature data from an operating furnace than will the very idealized analytically derived factors; this remains to be seen. In any case, the experimental method allows furnace calculations in geometries where it is impractical to compute factors analytically.

Acknowledgments

The authors wish to thank the National Science Foundation for the support of this research under Grant No. MEA-8210246.

References

1 Hottel, H. C., and Sarofim, A. F., *Radiative Transfer*, McGraw-Hill, New York, 1967.

2 Hottel, H. C., and Cohen, E. S., "Radiant Heat Exchange in a Gas-Filled Enclosure: Allowance for Nonuniformity of Gas Temperature," *AIChE Journal*, Vol. 4, No. 1, 1958, pp. 3–14.

3 Larsen, M. E., and Howell, J. R., "The Exchange Factor Method: An Alternative Basis for Zonal Analysis of Radiating Enclosures," ASME JOURNAL OF HEAT TRANSFER, Vol. 107, No. 4, 1985, pp. 936–942.

4 Larsen, M. E., "The Exchange Factor Method: An Alternative Zonal Formulation for Analysis of Radiating Enclosures Containing Participating Media," Ph.D. Dissertation, The University of Texas at Austin, Austin, TX, 1983.

5 Larsen, M. E., and Howell, J. R., "Least-Squares Smoothing of Direct-Exchange Areas in Zonal Analysis," ASME JOURNAL OF HEAT TRANSFER, Vol. 108, No. 1, 1986, pp. 239–242.

6 Wachtel, R. E., and La Mer, V. K., "The Preparation and Size Distribution of Some Monodisperse Emulsions," *Journal of Colloid Science*, Vol. 17, 1962, pp. 531–564.

7 Margolis, J. S., McCleese, D. J., and Hunt, G. E., "Laboratory Simulation of Diffuse Reflectivity From a Cloudy Planetary Atmosphere," *Applied Optics*, Vol. 11, No. 5, 1972, pp. 1212–1216.

8 Levi, L., *Applied Optics*, Vol. 2, Wiley, New York, 1980, p. 918.

9 Tilton, L. W., and Taylor, J. K., "Refractive Index and Dispersion of Distilled Water for Visible Radiation at Temperatures 0 to 60°C," *Journal of Research of the National Bureau of Standards*, Vol. 20, 1938, pp. 419–477.

10 Hale, G. M., and Querry, M. R., "Optical Constants of Water in the 200-nm to 200-μm Wavelength Region," *Applied Optics*, Vol. 12, No. 3, 1973, pp. 555–563.

11 van de Hulst, H. C., *Light Scattering by Small Particles*, Wiley, New York, 1957.

12 Woods, M. E., and Krieger, I. M., "Rheological Studies on Dispersions of Uniform Colloidal Spheres, I. Aqueous Dispersions in Steady Shear Flow," *Journal of Colloid and Interface Science*, Vol. 34, No. 1, 1970, pp. 91–99.

13 Edwards, D. K., and Balakrishnan, A., "Volume Interchange Factors for Nonhomogeneous Gases," ASME JOURNAL OF HEAT TRANSFER, Vol. 94, No. 2, 1972, pp. 181–187.

14 Liu, H. P., "Improved Method for Engineering Analysis of Radiative Heat Transfer in Furnaces," Ph.D. Dissertation, The University of Texas at Austin, Austin, TX, 1985.

Combined Radiation and Convection in Absorbing, Emitting, Nongray Gas-Particulate Tube Flow

S. Tabanfar

M. F. Modest

Department of Mechanical Engineering,
University of Southern California,
Los Angeles, CA 90089-1453

The interaction of thermal radiation with conduction and convection in thermally developing absorbing, emitting, nongray gas-particulate turbulent suspension flow through a circular tube is investigated. The contribution of thermal radiation is obtained through evaluation of the total hemispherical emittance of the particulate cloud and through evaluation of single band absorptances for molecular gases, modified to account for the interaction with the particles. The governing differential equation is derived as a (nonlinear) energy equation, coupled with integral equations to find the thermal radiation contributions. The energy equation is solved numerically by an implicit finite difference method with an iterative procedure. Qualitative results for Nusselt numbers are shown for a variety and range of parameters, such as optical thickness of particulates and single molecular gas bands, relative gas band position and band width, and temperature ratios (heated as well as cooled suspension flows).

Introduction

The study of heat transfer in flowing mixtures of gases and solids or liquid particles is of great importance in the design of furnaces, boilers, combustion chambers, cooling towers, rocket engines, etc. In a two-phase flow, an increase of heat transfer rates over that of a one-phase system is expected. The presence of the particles influences the heat transfer rates in several ways: (*i*) The particles penetrate into the laminar sublayer, causing a thinning of the viscous sublayer, thus increasing convective heat transfer; (*ii*) the presence of the particles may decrease the turbulent energy transport by damping the convective eddies; (*iii*) the radial motion of the particles enhances the energy exchange between the laminar sublayer and turbulent core; (*iv*) the particles have higher volumetric heat capacity than the gas, increasing the thermal entry length and, thus, the heat transfer rate. Furthermore, in high-temperature applications the interaction between particulate clouds, molecular gases, and walls by radiative heat transfer may become very important.

It has been demonstrated experimentally by Farbar and Morley [1], and also by Farbar and Depew [2, 3], that it is possible to increase heat transfer rates by adding solid particles to gas flow. This increase is moderate unless the particle mass loading ratio becomes very large. Tien [4] investigated analytically the heat transfer for a turbulently flowing fluid with suspended small solid particles in a circular pipe neglecting radiation effects. Echigo et al. [5, 6] and Tamehiro et al. [7] have studied the heat transfer in a flow of a gaseous suspension with radiatively absorbing and emitting particulates between parallel plates and in circular tubes. Chawla and Chan [8] investigated the combined convection-radiation in a gas-particulate laminar flow between parallel plates with isotropic scattering. Azad and Modest [9] studied the combined radiation and convection in absorbing, emitting, and anisotropically scattering gas-particulate tube flow. Realizing the shortcomings of a gray-gas analysis, Modest [10] studied the effects of nongray particle-molecular gas interaction on radiative heat fluxes in a one-dimensional medium, confined between parallel black walls, and later Tabanfar and Modest [11] extended the results to a one-dimensional cylindrical medium with black walls.

It is the purpose of this paper to investigate the combined convective and radiative effects in turbulent tube flow of an absorbing, emitting nongray gas-particulate suspension. A radiation model is developed to find the divergence of radiative flux for both particulate and gas phases. Employing these models in the energy equations for each phase, the resulting two coupled, nonlinear differential equations are solved numerically by an implicit finite difference method with an iterative procedure. The results are presented for a wide range of parameters.

Analysis

In the present study the following major assumptions are made:

1 The flow field of the two phases is hydrodynamically fully developed and has a turbulent velocity distribution.

2 Fluid and particle properties are constant.

3 The particles are uniformly distributed throughout the pipe cross section and are sufficiently small and numerous to be considered a continuum.

4 The time-mean velocities of the two phases are equal and the presence of the particles has no effect on the velocity profile, the eddy diffusivities for heat or momentum, or the friction factor for the gas.

5 The eddy diffusivity of the particles is negligible.

6 The energy transport by collisions between particles or with the wall are negligible.

7 The particles are small enough so that local temperatures of gas and particulates are essentially the same.

8 Viscous dissipation is not included.

9 The particulates absorb and emit with a constant and gray absorption coefficient, the gas may have a number of vibration-rotation bands in the infrared, and the medium is assumed to be nonscattering.

10 Radiative transfer in the axial direction is neglected as compared with the radial heat transfer; this has been shown to be a good approximation except for regions close to a temperature jump (inlet) [12].

11 The cylinder wall is black.

Contributed by the Heat Transfer Division and presented at the ASME Winter Annual Meeting, Miami Beach, FL, November 17-21, 1985. Manuscript received by the Heat Transfer Division September 3, 1985.

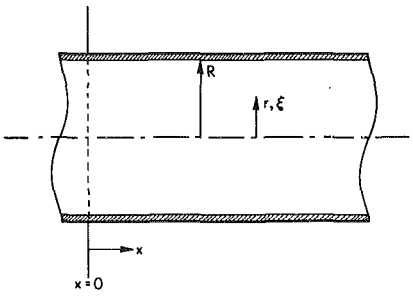

Fig. 1 Coordinate system for gas-particulate suspension flow

Some of the above assumptions are not necessarily very good. For example, assumptions 3, 4, and 5 are made primarily since at present no theory or experimental correlations exist to reliably predict the influence of these effects. However, if strong radiation is present these inaccuracies should become less and less important. The assumption of constant properties has been made simply to make the display of results more tractable.

Energy Equation. Based on the assumptions made, an energy balance based on the cylindrical coordinate system in Fig. 1 yields the basic equation governing the temperature field

$$(n_p V_p \rho_p c_p + \rho_g c_g) u \frac{\partial T}{\partial x} \tag{1}$$

$$= \frac{1}{r}\frac{\partial}{\partial r}\left[r(k_g + \rho_g c_g \epsilon_{H,g})\frac{\partial T}{\partial r}\right] - \nabla \cdot \mathbf{q}^R(r)$$

subject to the boundary conditions

$$r=0: \quad \frac{\partial T}{\partial r}=0; \qquad x=0: \quad T=T_{in}$$

$$r=R: \quad T=T_w \text{ (constant wall temperature)} \tag{2}$$

Here $\nabla \cdot \mathbf{q}^R$ is spectrally integrated divergence of radiative heat flux (its evaluation is discussed in detail later in this paper). No particle conductivity and diffusivity appear in equation (1) because of assumptions 5 and 6 above.

The above equations are similar to the ones employed by Tien [4] and by Azad and Modest [9]. The difference here is the use of a new radiation model, which extends [9] to include nongray gas radiation. Another difference is the use of a single energy equation for both phases (since gas and particulate temperatures are assumed to be the same). The assumption of negligible temperature difference between gas and particles, together with negligible scattering, makes the present model applicable to small particles, such as gas–soot mixtures. Equation (1) and the equation to find $\nabla \cdot \mathbf{q}^R$ are the governing equations with T and $\nabla \cdot \mathbf{q}^R$ to be determined. To establish the velocity distribution, the three-layer turbulent model for fully developed flow is used. In the laminar sublayer and the buffer layer, we use the models presented by Kays [13], and in the turbulent core the expression proposed by Reichardt [14] is employed. The eddy diffusivity for momentum $\epsilon_{M,g}$ is described by the Van Driest model modified by Spalding [15] for the wall region, and by the Reichardt model [14] for the turbulent core. The eddy diffusivity for heat $\epsilon_{H,g}$ is calculated using the standard assumption that $\epsilon_{M,g} \simeq \epsilon_{H,g}$. This has been presented in detail by Azad and Modest [9].

The governing equation and the boundary conditions may be nondimensionalized by introducing the following quantities

Nomenclature

$A_{pg}^{i(k)}$ = single band absorptance for evaluation of $\nabla \cdot \mathbf{q}_P^R$, equation (21)
$B_{pg}^{i(k)}$ = single band absorptance for evaluation of $\nabla \cdot \mathbf{q}_g^R$, equation (24)
c = specific heat at constant pressure
C_L = heat capacity loading ratio
C_2 = constant in Planck function = 1.4388 cm-K
d_p = particle diameter
$F_\eta, f_\eta^{(k)}$ = geometric functions
h = heat transfer coefficient for pipe flow
h_p = heat transfer coefficient for flow over solid particles
$I_{0\eta}, I_{b\eta}, I_\eta$ = (direction-integrated), (blackbody) spectral intensity
k_g = thermal conductivity of gas
M_R = dimensionless conduction–radiation parameter = $k_g/4\sigma T_{in}^3 R$
Nu_x = local Nusselt number
n_p = number of solid particles per unit volume
Pr = Prandtl number = $\mu_g C_g/k_g$
q^C, q^R, q^T = conductive, radiative and total flux; $q^T = q^C + q^R$
R = pipe radius
Re_D = gas Reynolds number = $2\bar{u}_g R/\nu_g$
r = radial distance
T = temperature
u = axial velocity
V_p = solid particle volume = $\pi d_p^3/6$
x = axial coordinate
α_i = band strength parameter
ϵ_H, ϵ_M = heat and momentum eddy diffusivities
η = wavenumber
θ = polar angle (Fig. 2), also dimensionless temperature, equation (3)
$\kappa_{g\eta}, \kappa_\eta$ = (gas) absorption coefficient
κ_p = gray particle absorption coefficient
μ = dynamic viscosity
ν = kinematic viscosity
ξ = dimensionless radial coordinate = r/R
ρ = density
σ = Stefan–Boltzmann constant
τ_{gi}, τ_p = gas and particle optical thickness
ψ = azimuthal angle (Fig. 2)
ω_i = band width parameter
$\Phi^{(k)}$ = total hemispherical emittance for particle cloud, equation (20)

Subscripts

av = average value
g = pertaining to gas
i = pertaining to ith gas band, or at its band center
in = inlet
mm = suspension mixed mean
p = pertaining to particles
pg = pertaining to particulate-gas interaction
w = pertaining to wall
η = spectral value

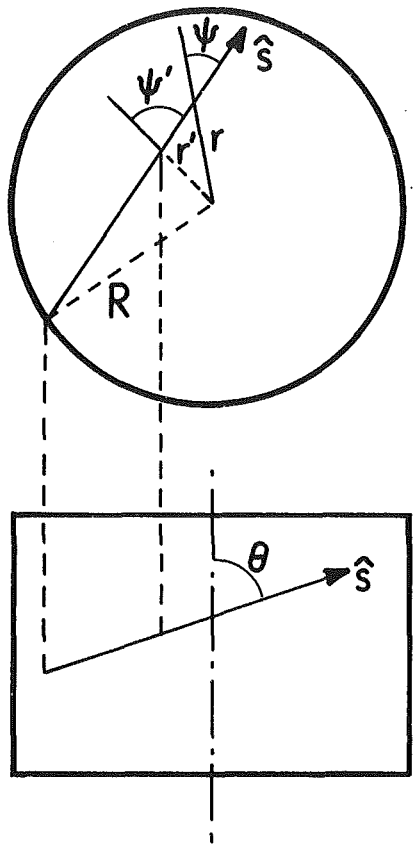

Fig. 2 Coordinate system for cylindrical geometry

$$\xi = r/R, \quad \bar{x} = x/R, \quad \theta = T/T_{in}, \quad \bar{q} = \frac{qR}{k_g T_{in}},$$

$$C_L = c_p n_p V_p \rho_p / c_g \rho_g, \quad f_1 = u/2\bar{u}, \quad f_2 = 1 + \frac{\epsilon_{M,g}}{\nu_g} \Pr \tag{3}$$

where $\bar{u}$ is the average fluid velocity. This leads to

$$f_1(1+C_L)\mathrm{Re}_D \Pr \frac{\partial\theta}{\partial\bar{x}} = \frac{1}{\xi}\frac{\partial}{\partial\xi}\left[\xi f_2 \frac{\partial\theta}{\partial\xi}\right] - \nabla\cdot\bar{q}^R(\xi) \tag{4}$$

with the boundary conditions

$$\bar{x}=0; \quad \theta=1; \quad \xi=0; \quad \frac{\partial\theta}{\partial\xi}=0; \quad \xi=1; \quad \theta=\theta_w \tag{5}$$

For numerical stability, equation (4) was further transformed by using a logarithmic transformation for the radial coordinates appropriate to turbulent and laminar flows, according to the method of Wassel and Edwards [16] and as used by Azad and Modest [9].

Radiation Model. A new model has been developed to evaluate the spectrally integrated divergence of the radiative heat flux accurately. The development is similar to the one by Tabanfar and Modest [11] where the spectrally integrated radiative flux was calculated, while for the present study the divergence of the total flux is needed. Direct calculation of $\nabla\cdot\mathbf{q}^R$ was preferred over finite differencing results from [11] for added accuracy.

In general, one may write for the directionally integrated radiative equation of transfer

$$\nabla\cdot\mathbf{q}_\eta^R = \kappa_\eta[4e_{b\eta} - I_{0\eta}] \tag{6}$$

where $\mathbf{q}_\eta^R$ is spectral radiative heat flux, $\kappa_\eta = \kappa_p + \kappa_{g\eta}$ is the spectral absorption coefficient, $e_{b\eta}$ is spectral emissive power, and $I_{0\eta}$ is spectral directionally integrated intensity. For ease of reading, $\nabla\cdot\mathbf{q}_\eta^R$ is broken into two parts, with $\nabla\cdot\mathbf{q}_{g\eta}^R$ being the radiation sources/sinks for the particulate and gas phases, respectively:

$$\nabla\cdot\mathbf{q}_{p\eta}^R = \kappa_p[4e_{b\eta} - I_{0\eta}] \tag{7}$$

$$\nabla\cdot\mathbf{q}_{g\eta}^R = \kappa_{g\eta}[4e_{b\eta} - I_{0\eta}] \tag{8}$$

Using the coordinate system shown in Fig. 2, the spectral direction-integrated intensity $I_{0\eta}$ in a one-dimensional cylindrical geometry is given by

$$I_{0\eta}(r) \equiv \int_0^\pi \int_0^{2\pi} I_\eta(\tau_s, \psi, \theta)\sin\theta\, d\psi d\theta \tag{9}$$

The spectral intensity I_η for a one-dimensional cylindrical medium has been evaluated previously [11] so that

$$I_{0\eta}(r) = 4\Bigg\{\int_r^R \frac{dI_{b\eta}(r')}{dr'}\int_0^{\pi/2}\int_0^{\pi/2}\Big[\exp$$
$$[-F_\eta(r, r', r\sin\psi)/\sin\theta] + \exp[-\{F_\eta(r\sin\psi, r', r\sin\psi)$$
$$+ F_\eta(r\sin\psi, r, r\sin\psi)\}/\sin\theta]\Big]\sin\theta\, d\theta d\psi dr'$$
$$+ \int_0^{\pi/2}\int_{r\sin\psi}^r \frac{dI_{b\eta}(r')}{dr'}\int_0^{\pi/2}\Big[\exp$$
$$-[\{F_\eta(r\sin\psi, r', r\sin\psi) + F_\eta(r\sin\psi, r, r\sin\psi)\}/\sin\theta]$$
$$-\exp[-F_\eta(r', r, r\sin\psi)/\sin\theta]\Big]\sin\theta\, d\theta dr'\, d\psi + \pi I_{b\eta}(r)\Bigg\} \tag{10}$$

where

$$F_\eta(a, b, c) \equiv \int_a^b \kappa_\eta(r'')r''\Big/\sqrt{r''^2 - c^2}\, dr'' \tag{11}$$

In equation (10) it was assumed that there is no temperature slip at the black wall. To simplify equation (10) a procedure similar to [10, 11] is followed. With the definition of

$$f_\eta^{(k)}(\kappa_\eta, r, r') \equiv \frac{4}{\pi}\int_0^{\pi/2}\int_0^{\pi/2}\Big\{\exp[-F_\eta(r, r', r\sin\psi)/\sin\theta]$$
$$+(-1)^k\exp[-\{F_\eta(r\sin\psi, r', r\sin\psi)$$
$$+F_\eta(r\sin\psi, r, r\sin\psi)\}/\sin\theta]\Big\}\left[\frac{r\cos\psi}{\sqrt{r'^2 - r^2\sin^2\psi}}\right]^k \sin\theta\, d\theta d\psi \tag{12}$$

This leads to

$$I_{0\eta}(r) = \int_r^R \frac{de_{b\eta}(r')}{dr'} f_\eta^{(0)}(\kappa_\eta, r, r')dr'$$
$$-\int_0^r \frac{de_{b\eta}(r')}{dr'} f_\eta^{(1)}(\kappa_\eta, r', r)dr' + 4e_{b\eta}(r) \tag{13}$$

Finally, substituting equation (13) into equation (7) and integrating over all wavenumbers results in

$$\nabla\cdot\mathbf{q}_p^R(r) = \kappa_p\Bigg\{\int_0^r \frac{dT}{dr'}\int_0^\infty \frac{de_{b\eta}(r')}{dT} f_\eta^{(1)}(\kappa_\eta, r', r)d\eta\, dr'$$
$$-\int_r^R \frac{dT}{dr'}\int_0^\infty \frac{de_{b\eta}(r')}{dT} f_\eta^{(0)}(\kappa_\eta, r, r')d\eta\, dr'\Bigg\} \tag{14}$$

Similarly, applying equation (13) in equation (8) and integrating over all wavenumbers results in

$$\nabla\cdot\mathbf{q}_g^R(r) = \int_0^r\int_0^\infty \kappa_{g\eta}\frac{de_{b\eta}(r')}{dr'} f_\eta^{(1)}(\kappa_\eta, r', r)d\eta dr'$$
$$-\int_r^R\int_0^\infty \kappa_{g\eta}\frac{de_{b\eta}(r')}{dr'} f_\eta^{(0)}(\kappa_\eta, r, r')d\eta dr' \tag{15}$$

The spectral absorption coefficient for many molecular gases may be approximated by the exponential-wide band model [17], i.e.

$$\kappa_{g\eta} = \sum_{i=1}^{N} \frac{\alpha_i(T)}{\omega_i(T)} \exp[-t|\eta_i - \eta|/\omega_i(T)] \tag{16}$$

with $t=1$ for bands with a head, and $t=2$ for symmetric bands. $\alpha_i(T)$ is the integrated intensity of the ith band, and $\omega_i(T)$ is the band wing decay width. Equation (16) gives accurate results for optically thick situations, i.e., if there is considerable line overlap, and if the gas is nearly opaque at the band center. This can be expected to be the case if gas radiation is strong enough to compete with particle radiation and convection. In general, both α_i and ω_i vary with temperature [17] and pressure. However, to reduce the complexity of the problem it will be assumed here that α_i and ω_i may be approximated by constant average values α_{iav} and ω_{iav}, i.e.,

$$\alpha_{iav} \equiv 2\int_0^1 \alpha_i(T)\xi d\xi, \quad \omega_{iav} \equiv 2\int_0^1 \omega_i(T)\xi d\xi \tag{17}$$

Using equation (17), equation (11) may now be evaluated as

$$F_\eta(a,b,c) = \kappa_p(\sqrt{b^2-c^2} - \sqrt{a^2-c^2}) + \sum_{i=1}^{N} \alpha_{iav}/\omega_{iav} \exp[-t|\eta_i - \eta|/\omega_{iav}](\sqrt{b^2-c^2} - \sqrt{a^2-c^2}) \tag{18}$$

Employing equation (18), making the common assumptions that the N bands overlap only negligibly and that the emissive power varies only slightly over each band and may be approximated by the value at the band center $e_{b\eta i}$, and after analytical integration over wavenumber, the divergence of the particle flux may be expressed as

$$\nabla \cdot \mathbf{q}_p^R(\xi) = \frac{\tau_p}{4M_R}\left\{\int_0^\xi \Phi^{(1)}(\tau_p\xi', \xi/\xi')\frac{d\theta^4(\xi')}{d\xi'}d\xi' - \int_\xi^1 \Phi^{(0)}(\tau_p\xi, \xi'/\xi)\frac{d\theta^4(\xi')}{d\xi'}d\xi' - \sum_{i=1}^{N}\frac{\omega_{iav}e_{b\eta i}(\theta_{in})}{\sigma T_{in}^4}\left[\int_0^\xi \frac{de_{b\eta i}(\xi')}{e_{b\eta i}(\theta_{in})d\xi'} A_{pg}^{i(1)}(\tau_p\xi', \tau_{gi}\xi', \xi/\xi')d\xi' - \int_\xi^1 \frac{de_{b\eta i}(\xi')}{e_{b\eta i}(\theta_{in})d\xi'} A_{pg}^{i(0)}(\tau_p\xi, \tau_{gi}\xi, \xi'/\xi)d\xi'\right]\right\} \tag{19}$$

where $M_R = k_g/4\sigma T_{in}^3 R$ is the conduction-radiation parameter, $\tau_{gi} = \alpha_{iav}R/\omega_{iav}$ is the optical thickness at the gas band center, $\tau_p = \kappa_p R$ is particle optical thickness, and the functions are defined as

$$\Phi^{(k)}(\tau_p, x) = \frac{4}{\pi}\int_0^{\pi/2}\int_0^{\pi/2}\left\{\exp[-\tau_p(\sqrt{x^2-\sin^2\psi} - \cos\psi)/\sin\theta] + (-1)^{(k)}\exp[-\tau_p(\sqrt{x^2-\sin^2\psi} + \cos\psi)/\sin\theta]\right\}\left[\frac{\cos\psi}{\sqrt{x^2-\sin^2\psi}}\right]^k \sin\theta\, d\theta d\psi \tag{20}$$

$$A_{pg}^{i(k)}(\tau_p, \tau_g, x) = \frac{4}{\pi}\int_0^{\pi/2}\int_0^{\pi/2}\left\{\exp[-\tau_p(\sqrt{x^2-\sin^2\psi} - \cos\psi)/\sin\theta]\mathrm{Ein}[\tau_g(\sqrt{x^2-\sin^2\psi} - \cos\psi)/\sin\theta] + (-1)^k\exp[-\tau_p(\sqrt{x^2-\sin^2\psi} + \cos\psi)/\sin\theta] \times \mathrm{Ein}[\tau_g(\sqrt{x^2-\sin^2\psi} + \cos\psi)/\sin\theta]\right\}\left[\frac{\cos\psi}{\sqrt{x^2-\sin^2\psi}}\right]^k \sin\, d\theta d\psi \tag{21}$$

Here

$$\mathrm{Ein}(x) = E_1(x) + \gamma + \ln(x) \tag{22}$$

E_1 is an exponential integral and $\gamma = 0.5772165\ldots$ is Euler's constant.

Returning to the evaluation of $\nabla \cdot \mathbf{q}_g^R$, using equations (16) and (18), and after analytical integration over wavenumber and nondimensionalizing, equation (15) can be expressed as

$$\nabla \cdot \mathbf{q}_g^R(\xi) = \frac{1}{4M_R}\sum_{i=1}^{N}\frac{\omega_i e_{b\eta i}(\theta_{in})}{\sigma T_{in}^4}\frac{1}{e_{b\eta i}(\theta_{in})}\tau_{gi} \times \left\{\int_0^\xi \frac{de_{b\eta i}(\xi')}{d\xi'}B_{pg}^{i(1)}(\tau_p\xi', \tau_{gi}\xi', \xi/\xi')d\xi' - \int_\xi^1 \frac{de_{b\eta i}(\xi')}{d\xi'}B_{pg}^{i(0)}(\tau_p\xi, \tau_{gi}\xi, \xi/\xi')d\xi'\right\} \tag{23}$$

where

$$B_{pg}^{i(k)}(\tau_p, \tau_g, x) = \frac{4}{\pi}\int_0^{\pi/2}\int_0^{\pi/2}\left\{\left[\exp[-\tau_p(\sqrt{x^2-\sin^2\psi} - \cos\psi)/\sin\theta] - \exp[-(\tau_p+\tau_g)(\sqrt{x^2-\sin^2\psi} - \cos\psi)/\sin\theta]\right]/\tau_g(\sqrt{x^2-\sin^2\psi} - \cos\psi) + (-1)^k\left[\exp[-\tau_p(\sqrt{x^2-\sin^2\psi} + \cos\psi)/\sin\theta] - \exp[-(\tau_p+\tau_g)(\sqrt{x^2-\sin^2\psi} + \cos\psi)/\sin\theta]\right]/\tau_g(\sqrt{x^2-\sin^2\psi} + \cos\psi)\right\}\left[\frac{\cos\psi}{\sqrt{x^2-\sin^2\psi}}\right]^k \sin\theta\, d\theta d\psi, \quad k=0,1 \tag{24}$$

In order to evaluate $\nabla \cdot \mathbf{q}^R$ the six functions $\Phi^{(k)}$, $A_{pg}^{i(k)}$, and $B_{pg}^{i(k)}$ $(k=0, 1)$ need to be known. In the case of constant properties (i.e., nonvarying τ_p and τ_{gi}) these functions are independent of the local temperature field and may be evaluated once and for all. A similar statement holds for $\mathbf{q}_w^R$ for which an additional two functions need to be evaluated [11].

Equation (4) is a parabolic nonlinear partial differential equation for θ. This equation is solved numerically by an implicit finite difference scheme combined with an iterative procedure. After the radial nodes are placed, the necessary auxiliary functions to find $\nabla \cdot \mathbf{q}^R$ and q_w^R are evaluated once and for all. Then for an assumed temperature profile, based on the previous axial step, the divergences of radiative heat flux and q_w^R are calculated. These values are then substituted into equation (4) to find new radial distributions for θ. This procedure is repeated until a prescribed convergence criterion is satisfied. For all calculations the radial lattice was divided into 80 equally spaced intervals (in transformed coordinates).

The volume-averaged two-phase mixed-mean temperature T_{mm} is defined as the temperature that would exist if the phases were in thermal equilibrium. In order to apply a check and balance on the code for numerical stability, T_{mm} was calculated both radially and axially [9]. The local Nusselt number for the flow is defined as

$$\mathrm{Nu}_x = \frac{2hR}{k_g} \tag{25}$$

and is based on the local heat transfer coefficient, defined by

$$h = q_w^T/(T_{mm} - T_w) \tag{26}$$

The Nusselt number, like the mixed-mean temperature, can be calculated by radial and axial integration [9]. The axial integration was used to check numerical stability and served as a

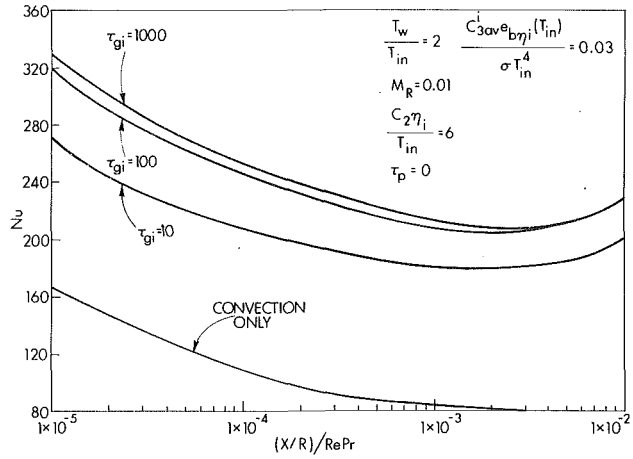

Fig. 3 Influence of gas optical thickness on Nusselt number development: heated wall

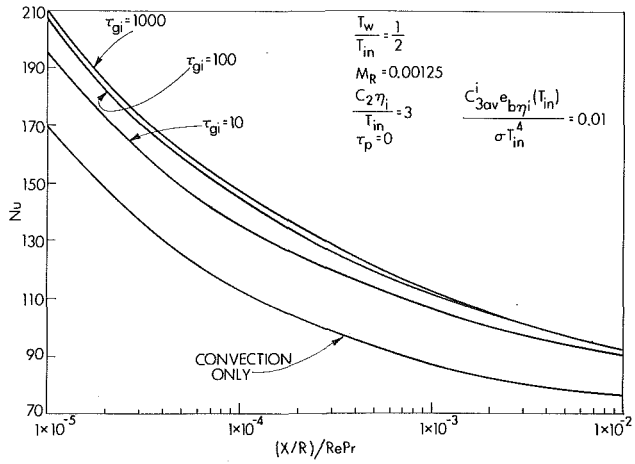

Fig. 4 Influence of gas optical thickness on Nusselt number development: cooled wall

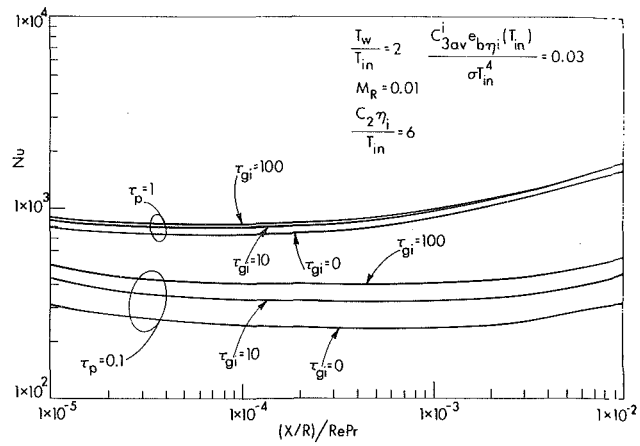

Fig. 5 Influence of gas-particulate radiation on Nusselt number development: heated wall

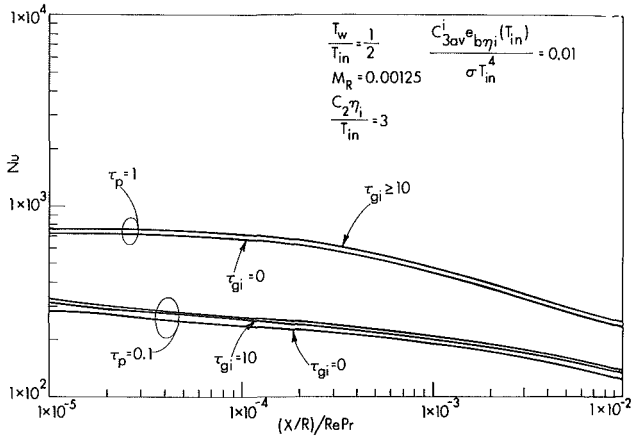

Fig. 6 Influence of gas-particulate radiation on Nusselt number development: cooled wall

criterion to establish the optimum number of radial nodes and axial steps.

Results and Discussion

To demonstrate the behavior of the particulate-gas interaction using the new radiation model, the total local Nusselt numbers and radiative heat flux ratios are found versus axial distance for different optical thicknesses of particulates and molecular gas bands, band position parameters, band width parameters, and wall temperature ratios. Since particulate-gas radiative interaction is of primary concern here, all results are for fixed values of Pr = 1, Re = 30,000, and a heat capacity loading ratio of $C_L = 2$. For different values of C_L, the curves for Nu are stretched by a factor of $(1 + C_L)$ [9]. An M_R of 0.01 was chosen for the cold gas/hot wall case, and 0.00125 for the hot gas/cold wall case, roughly corresponding to a 1-ft diameter burner with gas at 500 K and 1000 K. Since the gas radiation calculations are rather computer time intensive, only a single molecular-gas band is used in the following, in order to assess its qualitative importance. With a single band (and 81 radial nodes) CPU time on a VAX 750 is roughly 3 hr.

The effects of gas radiation (no particle radiation) on Nusselt number are shown in Figs. 3 and 4 for hot and cold walls, respectively. As expected, the Nusselt numbers increase with increasing optical thickness of the gas, but there is a limiting optical thickness for certain band position parameters and band width parameters, beyond which the Nusselt number is no longer affected. As the gas optical thickness at the band center increases, the photon mean free path decreases and, for very large τ_{gi}, much of the gas radiation is absorbed close to the point of emission (the center of the band becomes completely absorbing), but total gas band radiation does not decrease due to the always present optically thin band wings. If τ_{gi} is further increased (keeping the band width parameter constant), a wider part of the band center is completely absorbing, the band wings are shifted but otherwise remain the same, and the resulting gas radiation remains unaffected. Due to the nonlinear radiative contribution no fully developed temperature profile and, consequently, no asymptotic Nusselt number develops. For the heated wall case, the Nusselt number goes through a minimum at a certain downstream location, beyond which it tends to increase again. The location of the minimum moves toward the inlet with increasing importance of radiation. While Fig. 3 (and all following figures) is qualitatively correct for all values of x, it may be quantitatively inaccurate near the inlet because of the one-dimensional radiation model. deSoto [12] found axial radiation effects negligible beyond $x/R \simeq 6$.

For the hot medium/cold wall situation, the fluid temperature drops as it moves along the tube and, therefore, the importance of radiation is reduced with axial distance. While the Nusselt numbers are still higher than for the convection-only case, unlike the cold medium/hot wall situation the Nusselt number does not go through a minimum. Note that the value of the band width parameter $\omega_i e_{b\eta i}/\sigma T^4_{in}$ is

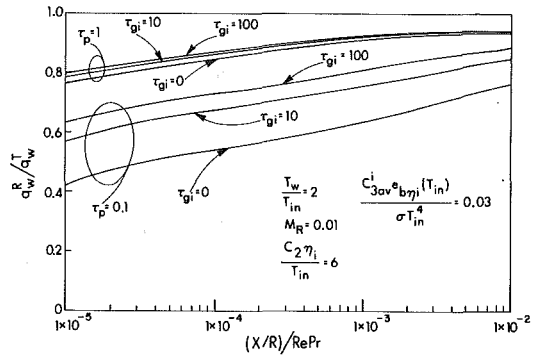

Fig. 7 Influence of gas-particulate radiation on radiative heat flux ratio: heated wall

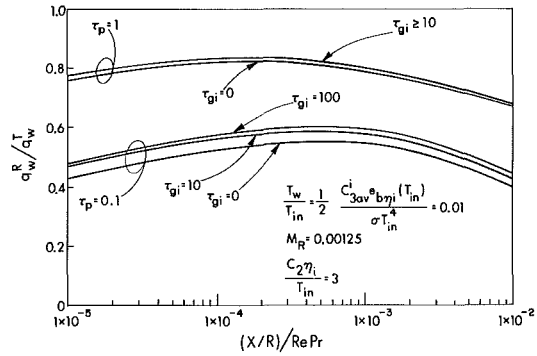

Fig. 8 Influence of gas-particulate radiation on radiative heat flux ratio: cooled wall

relatively high in Figs. 3 and 4. This higher value is chosen to make the effects of gas radiation more noticeable, since only a single band is considered here. The conduction–radiation ratio, band width, and band position parameters are all chosen so that they would have identical values if based on the hot temperature (the higher temperature between the inlet temperature and the wall temperature).

The effect of gas–particulate radiation is demonstrated in Fig. 5 for a hot wall and in Fig. 6 for a cold wall situation. As expected, the overall radiation and, consequently, the Nusselt numbers increase with optically thicker particulates [9]. For the hot wall case, this results in moving the minimum Nusselt number location closer to the inlet. In both figures for $\tau_p = 1$ the particle radiation is dominant and addition of gas beyond $\tau_{gi} = 10$ has little effect on the Nusselt numbers. Figures 7 and 8 show the radiative heat flux ratio at the wall q_w^R/q_w^T in a gas–particulate flow. For the hot wall situation, the radiative heat flux ratio increases with axial distance and becomes larger for optically thicker gas and particulates. For the cold wall situation the curves show that the radiative heat flux ratio increases to a maximum value at a certain axial position (due to high convective fluxes near the temperature jump at the inlet) and decreases beyond that point. The maxima occur farther downstream in cases with less radiation (smaller gas and particulate optical thickness). This is due to the fact that, when the radiation effects are small (optically thin cases), the fluid core remains hot for a longer distance resulting in increased convection.

To assess the importance of nongrayness most cases depicted in Figs. 3–6 were also run as gray gases, i.e., treating the gas as a gray medium with an equivalent optical thickness based on the Planck-mean absorption coefficient, evaluated at the inlet temperature

$$\tau_{g,Pl} = \frac{1}{\sigma T_{in}^4}\int_0^\infty \tau_{g\eta} e_{b\eta}(T_{in})\,d\eta = \tau_{gi}\,\frac{\omega^i_{av} e_{b\eta i}(T_{in})}{\sigma T_{in}^4} \tag{27}$$

While increasing the optical thickness of a nongray gas results in steadily increasing Nu, a gray gas behaves as was described earlier for the gas bandcenter: For small optical thickness little emission takes place resulting in small Nu increases. The Nusselt number continues to increase with $\tau_{g,Pl}$ until more and more of the gas radiation is absorbed close to the point of emission, reducing the heat transfer rate until, for an opaque gas, only convection remains. Obviously, a gray approximation can never replace a nongray analysis beyond the maximum point which lies around $\tau_{g,Pl} \simeq 1$ to 3; but even for relatively weak gas bands with $\tau_{gi} = 10$ (resulting in $\tau_{g,Pl} = 0.3$ and 0.1 for the hot and cold wall case, respectively) the error is very large: In the hot wall case without particles the minimum Nu for a gray approximation is 435 (i.e., outside the range shown in Fig. 3) as compared to 180 for the nongray analysis. For the cold wall case the error is smaller (since $\tau_{g,Pl} = 0.1$ is smaller) at roughly 50 percent as seen by examining the equivalent $\tau_p = 0.1$, $\tau_{gi} = 0$ case in Fig. 6. Obviously, larger values for τ_{gi} would make a gray approximation even more inaccurate.

Summary and Conclusions

The interaction of thermal radiation with conduction and convection in thermally developing, absorbing, emitting, nongray gas/particulate suspension flow through a circular tube with black walls has been investigated. A new model to evaluate gas and particulate radiation contributions has been introduced. The governing energy equations for both phases are solved numerically and the results for Nusselt numbers and wall radiative heat flux ratios are presented for wide ranges of radiation parameters.

The results obtained show that the effect of radiation from a single molecular gas band on overall heat transfer rates is, to a limited extent, qualitatively similar to that of gray particulates. The Nusselt numbers increase with increase of gas optical thickness (the increase of gas optical thickness beyond a certain value has almost no further effect on overall radiation), they go through a minimum at a certain downstream location for a hot wall situation, and decrease continuously with axial distance in cold wall cases. However, comparison with a gray gas approximation shows that such an analysis would nearly always result in unacceptable errors.

The increase of the band width parameter at constant gas optical thickness (broadening of the band) results in an increase of the effective band width and, therefore, higher gas radiation. The energy emitted from a molecular gas depends on its location in the spectrum. There is a wave number $\eta_{\max}$, at which the emissive power $e_{b\eta i}$ is a maximum for a given temperature ($T/\eta_{\max} = C_2/2.83$). If the combination of the gas band center location and gas temperature (T/η_i) is close to this value, the result is maximum gas radiation and a higher Nusselt number.

References

1 Farbar, L., and Morley, M. J., "Heat Transfer to Flowing Gas-Solids Mixtures in a Circular Tube," *Ind. Engng. Chem.*, Vol. 49, 1957, pp. 1143–1150.

2 Farbar, L., and Depew, C. A., "Heat Transfer Effects to Gas-Solids Mixtures Using Solid Spherical Particles of Uniform Size," *Ind. Engng. Chem. Fundam.*, Vol. 2, 1963, pp. 130–135.

3 Depew, C. A., and Farbar, L., "Heat Transfer to Pneumatically Conveyed Glass Particles of Fixed Size," ASME JOURNAL OF HEAT TRANSFER, Vol. 85, 1963, pp. 164–172.

4 Tien, C. L., "Heat Transfer by Turbulently Flowing Fluids-Solids Mixtures in a Pipe," ASME JOURNAL OF HEAT TRANSFER, Vol. 83, 1961, pp. 183–188.

5 Echigo, R., and Hasegawa, S., "Radiative Heat Transfer by Flowing

Multiphase Medum—Part I. An Analysis on Heat Transfer of Laminar Flow Between Flat Plates," *Int. J. Heat Mass Transfer*, Vol. 15, 1972, pp. 2519–2534.

6 Echigo, R., Hasegawa, S., and Tamehiro, H., "Radiative Heat Transfer by Flowing Multiphase Medium—Part II. An Analysis on Heat Transfer of Laminar Flow in an Entrance Region of Circular Tube," *Int. J. Heat Mass Transfer*, Vol. 15, 1972, pp. 2595–2610.

7 Tamehiro, H., Echigo, R., and Hasegawa, S., "Radiative Heat Transfer by Flowing Multiphase Medium—Part III. An Analysis on Heat Transfer of Turbulent Flow in a Circular Tube," *Int. J. Heat Mass Transfer*, Vol. 16, 1973, pp. 1199–1213.

8 Chawla, T. C., and Chan, S. H., "Combined Radiation and Convection in Thermally Developing Poiseuille Flow With Scattering," ASME JOURNAL OF HEAT TRANSFER, Vol. 102, 1980, pp. 297–302.

9 Azad, F. H., and Modest, M. F., "Combined Radiation and Convection in Absorbing Emitting and Anisotropically Scattering Gas-Particulate Tube Flow," *Int. J. Heat Mass Transfer*, Vol. 24, 1981, pp. 1681–1698.

10 Modest, M. F., "Radiative Heat Transfer in a Plane-Layer Mixture of Non-gray Particulates and Molecular Gases," *J. Quant. Spectrosc. Radiat. Transfer*, Vol. 26, 1981, pp. 523–533.

11 Tabanfar, S., and Modest, M. F., "Radiative Heat Transfer in a Cylindrical Mixture of Non-gray Particulates and Molecular Gases," *J. Quant. Spectrosc. Radiat. Transfer*, Vol. 30, 1983, pp. 555–570.

12 deSoto, S., "Coupled Radiation, Conduction and Convection in Entrance Region Flow," *Int. J. Heat Mass Transfer*, Vol. 11, 1968, pp. 39–53.

13 Kays, W. M., *Convective Heat and Mass Transfer*, McGraw-Hill, New York, 1966.

14 Reichardt, H., *Z. Angew., Math. Mech.*, Vol. 31, 1951, p. 208.

15 Spalding, D., *Conf. Intern. Development in Heat Transfer*, ASME, Boulder, CO, Part II, 1961, pp. 439–446.

16 Wassel, A. T., and Edwards, D. K., "Molecular Gas Radiation in a Laminar or Turbulent Pipe Flow," ASME JOURNAL OF HEAT TRANSFER, Vol. 98, 1976, pp. 101–107.

17 Edwards, D. K., and Menard, W. A., "Comparison of Models for Correlation of Total Band Absorption," *Appl. Opt.*, Vol. 3, 1964, p. 621.

K. Kheyrandish
Research Assistant.

C. Dalton
Professor.
Fellow ASME

J. H. Lienhard
Professor.
Fellow ASME

Heat Transfer/Phase Change Laboratory,
Mechanical Engineering Department,
University of Houston,
Houston, TX 77004

A Model for Fluid Flow During Saturated Boiling on a Horizontal Cylinder

A model has been developed to represent the vapor removal pattern in the vicinity of a cylinder during nucleate flow boiling across a horizontal cylinder. The model is based on a potential flow representation of the liquid and vapor regions and an estimate of the losses that should occur in the flow. Correlation of the losses shows a weak dependence on the Weber number and a slightly stronger dependence on the saturated liquid-to-vapor density ratio. The vapor jet thickness, which is crucial to the prediction of the burnout heat flux, and the shape of the vapor film are predicted. Both are verified by qualitative experimental observations.

Introduction

Flow boiling is one of the most efficient means for removing heat from a heater immersed in a liquid. In the nucleate boiling regime, it can yield extraordinarily high heat transfer coefficients – approaching 10^5 W/m^2-K – just below burnout. A rising demand for compact and efficient heat exchange has directed increasing attention to the use of nucleate flow boiling in contemporary processes.

Yet the prediction of nucleate boiling heat transfer coefficients has remained elusive. One problem has been the extreme sensitivity of the heat flux q to its various independent system variables: liquid velocity U_∞; heater surface condition; heater geometry; liquid subcooling; and liquid properties. The difficulties in predicting q are as grave for flow over the outside of submerged bodies as they are for flow within pipes and other conduits. Indeed, one can accurately say that during 50 years of focused work on nucleate boiling since Nukiyama's pioneering paper [1], we do not yet have one generally applicable prediction of q for any situation.

However, when q is specified independently and the wall temperature difference is dependent, we can simply let the temperature adjust itself, since it will be reasonably close to saturation in any event. The only problem is that we must not exceed the burnout heat flux q_{max}, for to do so would be to suffer an immediate and catastrophic temperature rise.

The prediction of q_{max} therefore becomes an issue of paramount practical importance, although it too has been plagued with difficulties. To date, there exist correlations for burnout within pipes, but no mechanistic predictions are available. Probably the first mechanistic burnout prediction of q_{max} in flow boiling was that of Lienhard and Eichhorn [2] for a saturated liquid in crossflow past a horizontal cylinder. But this prediction was also flawed in two ways: It involved an empirically determined constant and it did not include an explicit description of the hydrodynamic instability that led to burnout.

Lienhard and Eichhorn envisioned the vapor removal configuration shown in Fig. 1. (This configuration is consistent with the extensive photographic studies of Vliet and Leppert [3], Leppert and Pitts [4], and Min [5]. It is also similar to what we have observed in extensive visual studies to be described subsequently.) A simple "Mechanical Energy Stability Criterion" (MESC) was used in [2] to predict q_{max}. It required the occurrence of some form of hydrodynamic instability if the vapor carried kinetic energy into the wake system more rapidly than surface energy was lost from the wake system. Equating these two rates resulted in an expression for the dimensionless peak heat flux.

New data obtained by Hasan et al. in 1981 [6] gave a basis for clearly defining the regime of gravity influence. They found that gravity could strongly affect q_{max} if a "gravity influence parameter" G was not > 10, where

$$G = U_\infty/(g\sigma/\rho_f)^{1/4} \tag{1}$$

Many of their new data were shown to be gravity independent so they could be used to revise the sheet thickness expression; this was done using a semi-empirical prediction technique. The result was

$$\alpha = 0.000919r \tag{2}$$

Recently, Kheyrandish and Lienhard [7] argued that surface energy is not all lost in a control volume surrounding the wake, but much of it is transformed from the sheet into the periodically separating cylindrical bubbles. They extended the MESC as formulated in [2, 4] by introducing new information as to the periodicity of separation of these bubbles, and obtained a more accurate expression for the dimensionless peak heat flux ϕ

$$\phi \equiv \frac{\pi q_{max}}{\rho_g h_{fg} U_\infty} = \alpha\left[1 + \left(\frac{4}{\alpha We}\right)^{1/3}(1 - \sqrt{\pi(\phi - \alpha)}\mathrm{St})^{1/3}\right] \tag{3}$$

where the Weber number We and the Strouhal number St are defined in the nomenclature. Current work will almost certainly lead to additional modifications of the burnout theory. Equation (3) should therefore be viewed as an approximate result which is adequate for nondimensionalizations and comparisons we make here.

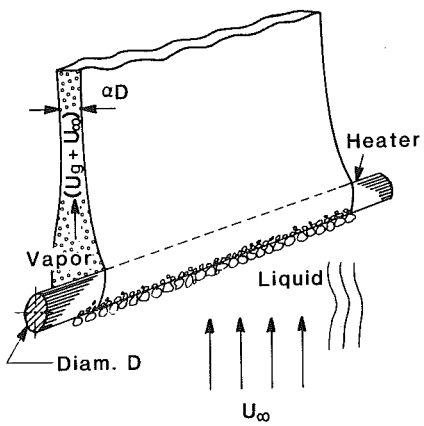

Fig. 1 Idealized vapor removal model for flow boiling over cylinder

Contributed by the Heat Transfer Division and presented at the 23rd National Heat Transfer Conference, Denver, Colorado, August 4–7, 1985. Manuscript received by the Heat Transfer Division November 5, 1985.

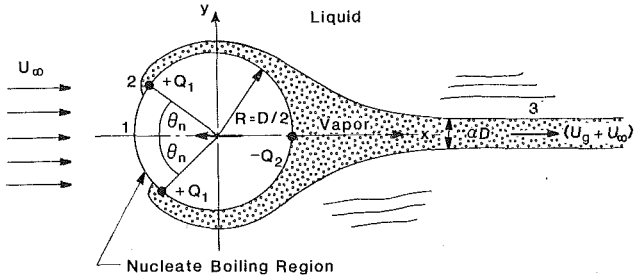

Fig. 2 Idealized potential flow model

While the MESC simplified the treatment of the problem, it nevertheless left one important element that could not be settled theoretically, namely the problem of establishing the vapor sheet thickness αD. Without that, the q_{max} prediction could not really be regarded as a true prediction.

The objective of this paper is therefore that of developing a prediction for α. We shall also illustrate the potential flow representation of the shape of the wake. Since no one has yet found a means to evaluate α experimentally, nor is there hope on the horizon that anyone soon will, we turn our attention instead to the methods of potential flow analysis to do so.

Visual Observations of the Flow

We have used the reconstructed apparatus of Hasan et al. [6] in the University of Houston Heat Transfer/Phase Change Laboratory to view flow nucleate boiling near burnout during crossflow over a horizontal cylinder. This visualization shows clearly that the nucleate boiling process is localized on a forward segment of the cylinder as indicated in Fig. 1. Escaping vapor bubbles merge and form a vapor film that covers most of the cylinder surface area. This film leaves in the form of a two-dimensional jet at the rear of the cylinder. One consequence of this vapor escape pattern is that the bulk of the cylinder is virtually insulated and almost all of the heat transfer takes place over the small forward segment. This segment subtends the angle $2\theta_n$ as shown in Fig. 2.

Since the nucleate boiling region is localized in a region close to the stagnation point and the remaining flow around the cylinder is to all intents and purposes "lubricated" by the flow of vapor, we are justified in assuming that the liquid motion around the cylinder can be treated as a potential flow.

Potential Flow Model

Single-Phase Kinematics. The kinematics of the flow field can be modeled using the concepts of potential flow. The flow field will be developed first for two identical phases with the correct dividing streamline pattern. In this context, the dividing streamline is the streamline that will subsequently become the vapor–liquid interface.

The complex velocity potential for a cylinder in a uniform flow field is given by

$$W(Z) = U(Z + R^2/Z) \tag{4}$$

where U is the uniform approach velocity, Z is the complex variable $(x+iy)$, and R is the radius of the cylinder. Fluid, which for the present is of the same phase as the approach fluid, is emitted into the flow from two sources, each of strength Q_1, located on the surface of the cylinder at angles $\pm\theta_n$ from the forward stagnation point on the cylinder. A sink of strength Q_2 is located at the rear stagnation point to cause a downstream convergence of the upper and lower dividing streamlines. A contraction occurs when $\alpha < 1$ in Fig. 1. In the event that the downstream streamlines diverge instead of converging ($\alpha > 1$), the sign of Q_2 changes and a source is located at the rear stagnation point. Since the sources and sinks are located on the surface of the cylinder, fluid is emitted in the interior of the cylinder as well as the exterior. Thus, a sink of strength $(Q_1 - Q_2/2)$ must be located at the center of the cylinder in order to preserve the shape of the cylinder.

Milne-Thomson's circle theorem [8] is used to put the complex velocity potential in its final form for a single-phase fluid

$$W(Z) = U(Z + R^2/Z) + (Q_1/2\pi)[\ln(Z + \mathrm{Re}^{i\theta_n}) + \ln(Z + \mathrm{Re}^{-i\theta_n})] - (Q_2/2\pi)\ln(Z + R) - [(Q_1 - Q_2/2)/2\pi]\ln Z \tag{5}$$

This model is shown in Fig. 2, where the angle θ_n is shown as 45 deg. This value should represent the physical situation quite accurately. Limited flow visualization studies seem to indicate that the vapor blanket is established at a value of θ_n near 45 deg. The region $|\theta_n| < 45$ deg is subject to bubble formation and will be dealt with later.

Nomenclature

D = diameter of cylindrical heater
G = gravity influence parameter, defined in equation (1)
g = gravitational acceleration
h_{fg} = latent heat of vaporization
MESC = mechanical energy stability criterion
L = energy loss per unit volume in the vapor; $L' = 2L/\rho_f U_\infty^2$
p = pressure; p_0 = upstream static pressure
Q = volumetric strength of source or sink; Q_v = volumetric vapor flow rate in the jet
q = nucleate boiling heat flux; q_{max} = peak or "burnout" q
R = $D/2$
r = ρ_f/ρ_g
St = Strouhal number $= D/U_\infty\tau$, equal to D/λ_H at burnout
U = approach velocity; U_∞ = liquid approach velocity (Fig. 3*a*); U'_∞ = vapor approach velocity (Fig. 3*b*)
u = x-direction velocity component; $u^* = u/U_\infty$
u_g = velocity of the vapor in the jet relative to the liquid bulk
W = complex velocity potential
We = Weber number $= \rho_g U_\infty^2 D/\sigma$
x, y = coordinate system (see Fig. 2)
x^*, y^* = x/R and y/r, respectively
Z = $x+iy$
α = ratio of vapor sheet thickness to D
θ_n = angle at which vapor film is established (see Fig. 2)
λ_H = Helmholtz unstable wavelength in the vapor sheet
ρ_f, ρ_g = saturated liquid and vapor densities, respectively
σ = surface tension
τ = period of bubble breakoff from sheet
ϕ = dimensionless peak heat flux $= \pi q_{max}/\rho_g h_{fg} U_\infty$
ψ = stream function; $\psi^* = \psi/UR$
ψ_D, ψ_D^* = values of ψ and ψ^* on the dividing streamline, respectively

Since we are interested in the interface (i.e., the dividing streamline) between the vapor and liquid regions, knowledge of the stream function is necessary. The stream function is the imaginary part of the complex potential

$$\psi = Uy - \frac{UR^2 y}{x^2+y^2} + \frac{Q_1}{2\pi}\left[\tan^{-1}\left(\frac{y+R/\sqrt{2}}{x+R/\sqrt{2}}\right) + \tan^{-1}\left(\frac{y-R/\sqrt{2}}{x+R/\sqrt{2}}\right)\right] - \frac{Q_2}{2\pi}\tan^{-1}\left(\frac{y}{x-R}\right) - \frac{(Q_1-Q_2/2)}{2\pi}\tan^{-1}\left(\frac{y}{x}\right) \quad (6)$$

We define the dimensionless variables

$$\psi^* \equiv \frac{\psi}{UR}, \quad x^* \equiv \frac{x}{R}, \quad y^* \equiv \frac{y}{R} \quad (7)$$

The dimensionless stream function becomes

$$\psi^* = y^* - \frac{y^*}{x^{*2}+y^{*2}} + \frac{Q_1}{2\pi RU}\left[\tan^{-1}\left(\frac{y^*+1/\sqrt{2}}{x^*+1/\sqrt{2}}\right) + \tan^{-1}\left(\frac{y^*-1/\sqrt{2}}{x^*+1/\sqrt{2}}\right)\right] - \frac{Q_2}{2\pi RU}\tan^{-1}\left(\frac{y^*}{x^*-1}\right) - \frac{Q_1-Q_2/2}{2\pi RU}\tan^{-1}\left(\frac{y^*}{x^*}\right) \quad (8)$$

Since the x-direction velocity is expressed as $u = \partial\psi/\partial y$, the dimensionless velocity may be defined as $u^* \equiv u/U = \partial\psi^*/\partial y^*$ and

$$u^* = 1 - \left[\frac{x^{*2}-y^{*2}}{(x^{*2}+y^{*2})^2}\right] + \frac{Q_1}{2\pi RU} \cdot \left[\frac{(x^*+1/\sqrt{2})}{x^{*2}+y^{*2}+\sqrt{2}(x^*+y^*)+1} + \frac{(x^*+1/\sqrt{2})}{x^{*2}+y^{*2}+\sqrt{2}(x^*-y^*)+1}\right] - \frac{Q_2}{2\pi RU}\left[\frac{x^*-1}{x^{*2}+y^{*2}-2x^*+1}\right] - \frac{(Q_1-Q_2/2)}{2\pi RU}\left(\frac{x^*}{x^{*2}+y^{*2}}\right) \quad (9)$$

From equations (8) and (9), we note that

$$\Psi^* \to y^*, \quad u^* \to 1 \quad (10)$$

as x^* becomes large, for all y^*. This indicates that for single-phase flow, the model gives equal velocities on either side of the dividing streamline for large x^*. This is consistent with Robertson [9] who says that the velocity ratio on either side of the dividing streamline u/U is equal to $(\rho_f/\rho_g)^{1/2}$, or for a single phase $u = U$. (Note that in equations (6)–(9), the angle θ_n has been taken to be 45 deg.) Varying the angle θ_n only had the effect of altering the shape of the dividing streamline near the location of the sources Q_1, and did not affect the size or shape of the wake.

Two-Phase Kinematics. The flow field described by equation (6) and shown in Fig. 3 is for a single-phase flow that can be either liquid or vapor. Since potential flow theory does not provide for discontinuous changes in fluid properties, we use the following strategy: We combine the liquid flow exterior to the dividing streamline with the vapor flow interior to it, as shown in the shaded portions of Fig. 3. This will be completely legitimate if both the geometry and the pressure are properly matched at the interfaces. The geometry of the flows will automatically be the same if the cylinder diameter and the jet thickness are taken to be the same in both the liquid and vapor potential models. To satisfy the second boundary condition, we notice that the pressure at the liquid and vapor stagnation points in Fig. 3 must be equal

$$p_0 + 1/2\rho_f U_\infty^2 = p_0 + 1/2\rho_g U_\infty'^2 \quad (11)$$

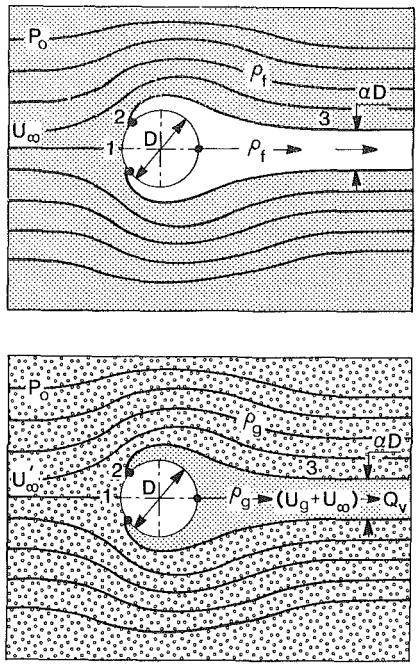

Fig. 3(*a*) Idealized liquid flow; (*b*) idealized vapor flow

In the liquid model between points 1 and 2, we have

$$p_0 + \frac{1}{2}\rho_f U_\infty^2 = p_2 + \frac{1}{2}\rho_f (2U_\infty \sin\theta_n)^2 \quad (12)$$

Here, we have assumed potential flow between points 1 and 2. Equation (12) may be rewritten in the following form

$$(p_0 - p_2)/\frac{1}{2}\rho_f U_\infty^2 = 4\sin^2\theta_n - 1 \quad (13)$$

Development of Losses

In the physical problem (flow boiling over a cylinder), nucleate boiling occurs in the region between 1 and 2 on the surface of the cylinder, and virtually all the vapor generation occurs in this area. Thus, the fluid flows in this region are highly disturbed by the generation of new bubbles. As these bubbles merge to form the continuous vapor film, their surface energy is dissipated. Thus, this region must be associated with some form of energy loss, which is related to surface tension. These losses, per unit volume of the vapor, are represented by L. Using equation (11) and the loss term L, we can write

$$p_0 + \frac{1}{2}\rho_f U_\infty^2 = p_0 + \frac{1}{2}\rho_g (u_g + U_\infty)^2 + L \quad (14)$$

between points 1 and 3 in the vapor model, where $(u_g + U_\infty)$ is the vapor velocity in the jet. Defining $L' = 2L/\rho_f U_\infty^2$, we may write equation (14) as

$$1 - L' = \frac{1}{r}(1 + u_g/U_\infty)^2 \quad (15)$$

Lienhard and Eichhorn [2] used an energy balance on the heater to show that u_g/U_∞ is related to the dimensionless peak heat flux by

$$(1 + u_g/U_\infty) = \phi/\alpha \quad (16)$$

From equations (15) and (16), we get

$$L' = 1 - \frac{(\phi/\alpha)^2}{r} \quad (17)$$

As was shown in [7], burnout is influenced by the type of heating (a-c or non-a-c); thus, the α prediction for a-c data

Table 1 Summary of available data and present prediction of α for flow boiling burnout on horizontal cylinders with a-c heating

D(mm)	U_∞(m/s)	ϕ	We	L'	(α)prediction
Isopropanol, r = 335, [6]					
0.5	1.46	1.836	0.142	0.946	0.454
	1.72	1.600	0.198	0.955	0.413
	2.01	1.476	0.270	0.958	0.398
	2.25	1.393	0.337	0.960	0.388
0.81	1.23	1.724	0.163	0.951	0.434
	1.47	1.547	0.233	0.956	0.408
	1.76	1.338	0.335	0.963	0.373
	1.94	1.246	0.408	0.966	0.358
	2.23	1.175	0.539	0.967	0.355
	2.43	1.117	0.641	0.969	0.348
1.50	1.23	1.389	0.304	0.961	0.381
	1.33	1.298	0.356	0.965	0.365
	1.47	1.255	0.436	0.965	0.365
	1.68	1.127	0.566	0.969	0.343
	1.94	1.007	0.755	0.973	0.325
	2.20	0.945	0.970	0.974	0.322
	2.40	0.881	1.159	0.977	0.314
Methanol, r = 615, [6]					
0.81	1.37	3.139	0.101	0.973	0.737
	1.58	2.971	0.135	0.974	0.744
	1.74	2.863	0.164	0.974	0.752
	1.85	2.767	0.185	0.975	0.750
1.51	1.33	2.593	0.176	0.979	0.694
	1.67	2.208	0.280	0.982	0.682
	1.82	2.042	0.332	0.984	0.674
Water, r = 1550, [7]					
0.5	2.0	8.68	0.02	0.990	1.93
	2.9	7.12	0.043	0.991	2.86

Table 2 Summary of available data and present prediction of α for flow boiling burnout on horizontal cylinders with non-a-c heating

D(mm)	U_∞(m/s)	ϕ	We	L'	(α)prediction
Freon-113, r = 196, [11]					
6.5	2.4	0.52	18.9	0.987	0.32
	4.0	0.414	52.5	0.989	0.27
	6.8	0.32	152	0.990	0.22
Freon-113, r = 196, [12]					
3.18	2.4	0.603	9.25	0.984	0.35
	4.0	0.496	25.7	0.987	0.31
	6.0	0.425	57.8	0.989	0.28
6.35	2.4	0.502	18.48	0.987	0.30
	4.0	0.390	51.3	0.989	0.25
	6.0	0.307	115.5	0.990	0.21
12.7	2.4	0.295	37.0	0.987	0.19
	4.0	0.262	102.7	0.989	0.18
	6.0	0.241	231.0	0.991	0.17
Water, r = 1450, [3]					
3.175	1.44	6.60	0.075	0.995	2.28
	2.07	5.23	0.154	0.996	2.04
	2.90	4.30	0.303	0.997	1.93

should be different from that of non-a-c data. Then L' may be correlated with r and We separately for each case. Based on the data presented in [3, 7] for water, in [6] for methanol and isopropanol, and in [11, 12] for Freon-113, we can calculate L' for a-c heated experiments [6, 7] and non-a-c heated experiments [3, 11, 12] as shown in Tables 1 and 2.

If the losses in the vapor result from a dissipation of kinetic energy as a consequence of surface tension forces, we may write

$$L = L(\rho_f, \rho_g, U_\infty, D, \sigma) \tag{18}$$

This reduces to the following dimensionless form

$$L' = L'(r, We) \tag{19}$$

Equations (18) and (19) are based only upon those observations for which $G > 10$. Thus, gravity will not influence the results.

Figures 4 and 5 show the dependence of L' on We for a-c and non-a-c data, respectively. Analysis of the data showed that the final form of correlation becomes

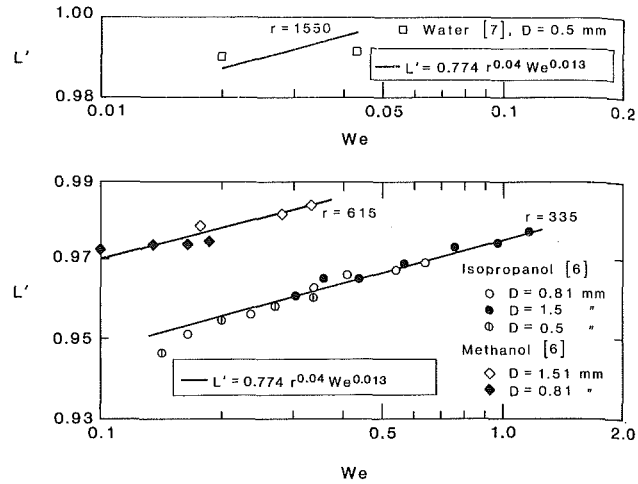

Fig. 4 Correlation of L' for a-c data

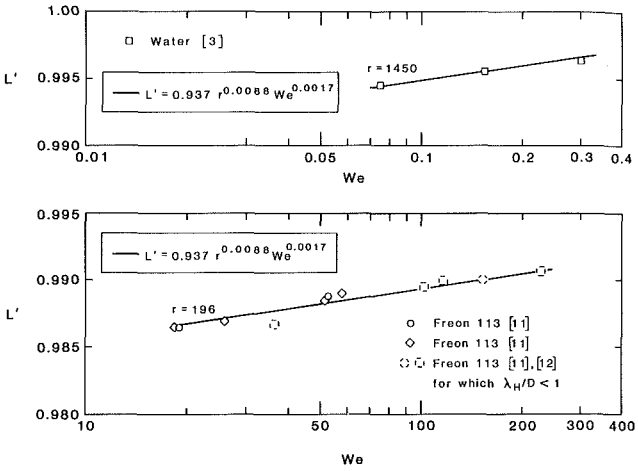

Fig. 5 Correlation of L' for non-a-c data

$$L' = 0.774 r^{0.04} We^{0.013} \tag{20}$$

for a-c data, and

$$L' = 0.937 r^{0.0088} We^{0.0017} \tag{21}$$

for non-a-c data, with an rms scatter of less than 4 percent in both cases. Even though the dependence on r and We is weak, the influence is sufficient to be considered important because small deviates of L' from unity are significant.

It was initially presumed (see Kheyrandish and Dalton [10]) that a second loss mechanism, related to the vapor viscosity (or vapor Reynolds number), existed between points 2 and 3 in the vapor film. This second loss could be the result of energy dissipation in the vapor shear layer, and the possible formation of nonshedding vortices behind the cylinder. However, analysis of the data as shown in Fig. 4 suggests that this dependence is very slight and cannot be verified over the range of variables for which data are presently available. Thus, it is reasonable to neglect this second loss mechanism.

Prediction of α

We are now in a position to predict the value of α. Rearranging equation (15) and substituting equation (20) into it, we get

$$u_g + U_\infty = U_\infty \sqrt{r(1 - 0.774 r^{0.04} We^{0.013})} \tag{22}$$

Finally, combining equations (16) and (22) yields the following equation for prediction of α for the a-c data

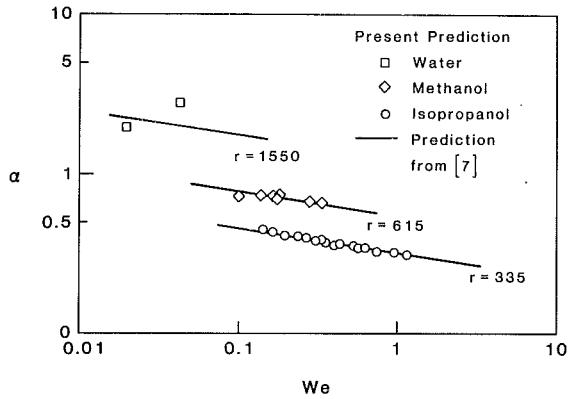

Fig. 6 Comparison of present prediction of α with prediction of [7] for a-c experiments

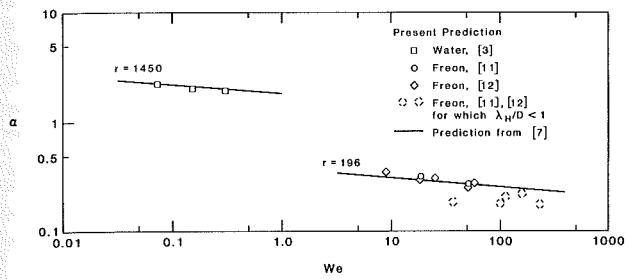

Fig. 7 Comparison of present prediction of α with prediction of [7] for non-a-c experiments

$$\alpha = \phi/\sqrt{r(1-0.774r^{0.04}We^{0.013})} \tag{23}$$

Following the same approach and using equation (21) gives the α prediction for the non-a-c data as

$$\alpha = \phi/\sqrt{r(1-0.937r^{0.0088}We^{0.0017})} \tag{24}$$

It must be noted that using equations (23) and (24) to predict α requires knowledge of peak heat flux. However, if an independent expression for α is found, then these equations may also be used to predict the dimensionless peak heat flux ϕ.

Figures 6 and 7 show a comparison between α values predicted by equations (23) and (24), and those predicted by the MESC in [7]. The two representations agree within an rms error of 3 percent. The MESC prediction is based on a mechanical energy balance on the vapor jet over a region beyond that in which our surface tension-related losses are present.

It was noted in [7] that prediction of α based on the MESC can only be properly used if a vapor wake actually exists. Therefore, when λ_H/D (where λ_H is the Helmholtz unstable wavelength in the walls of the vapor sheet) shrinks to the order of magnitude of unity, the present arguments become dubious. We have accordingly identified the data for which $\lambda_H/D \leq 1$ in Figs. 5 and 7.

Equation (2) is the prediction for α for a-c data given by Hasan et al. [6]. It shows dependence of α on r only, while the present predictions show a dependence on We as well as r. Equation (2) was obtained from data over a smaller range of variation of variables and its accuracy is limited to those data, Specifically, it underestimates α for larger values of r. The authors are unaware of any additional data on α for further comparison.

We note that the points for which $\lambda_H/D \leq 1$ compare poorly with the prediction from [7] in Fig. 7. This is to be expected since the vapor sheet is ill defined in this range.

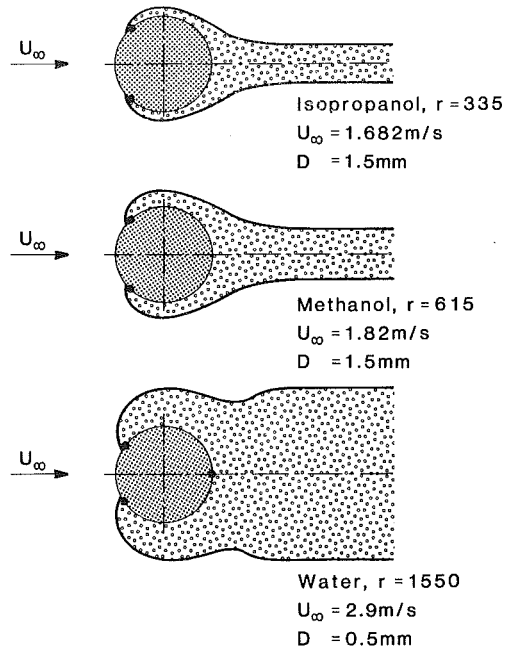

Fig. 8 Shape of the vapor film as predicted by potential flow analysis

Flow Representation

The vapor flow rate Q_v in the wake of the two-phase model (Fig. 2) can be obtained from an energy balance in the wake

$$\pi D q_{\max} = \rho_g Q_v h_{fg} \tag{25}$$

In terms of the variables in Fig. 2, we can write Q_v as $(Q_1 - Q_2/2)$. Rearranging equation (25) in terms of ϕ, we get

$$Q_v = DU_\infty \phi \tag{26}$$

and since the value of the stream function on the dividing streamline ψ_D is $Q_v/2$, it follows that

$$\psi_D = RU_\infty \phi \tag{27}$$

As we noted earlier, the velocity on either side of the single-phase flow dividing streamline must be the same and equal to the approach velocity. Thus, from Fig. 3(*b*) and equation (22), we can write for a-c data

$$U'_\infty = U_\infty \sqrt{r(1-0.774r^{0.04}We^{0.013})} \tag{28}$$

where U'_∞ is the approach velocity in the pure vapor model. Substitution of equations (27) for ψ and (28) for U into equation (6), and division by RU_∞ yields

$$\sqrt{r(1-0.774r^{0.04}We^{0.013})}\left(y^* - \frac{y^*}{x^{*2}+y^{*2}}\right) + \frac{Q_1}{2\pi RU_\infty}\left[\tan^{-1}\left(\frac{y^*+1/\sqrt{2}}{x^*+1/\sqrt{2}}\right) - \tan^{-1}\left(\frac{y^*-1/\sqrt{2}}{x^*+1/\sqrt{2}}\right)\right] - \frac{Q_2}{2\pi RU_\infty}\tan^{-1}\left(\frac{y^*}{x^*-1}\right) - \frac{(Q_1-Q_2/2)}{2\pi RU_\infty}\tan^{-1}\left(\frac{y^*}{x^*}\right) - \phi = 0 \tag{29}$$

as the equation of the interface between liquid and vapor in Fig. 2, where x^* and y^* are defined in equation (7). Equation (29) is plotted in Fig. 8 for three different cases and gives a clear picture of the idealized behavior of the vapor film for these three different examples. Note that for large x^* in equation (29), y^* approaches α as predicted by equation (23). A similar expression can be obtained for non-a-c data.

Conclusions

We have developed a model to represent the vapor film in crossflow nucleate boiling over a cylinder. We have incorporated a potential flow representation and an estimation of losses to develop predictions of the vapor jet thicknesses for a-c and non-a-c heating experiments. The loss mechanism was associated with the bubble formation region and was the result of surface-tension effects. The predicted behavior of the vapor film and jet has a qualitative similarity to what is observed in the physical problem. We do not presently have data available to make a quantitative comparison between our predictions and the actual vapor film and wake. However, our results are completely consistent with the approximate results given in [7].

Acknowledgments

We thank Professor Roger Eichhorn and Gene Ungar for their input during our group dialogue. We are grateful to both the NASA Lewis Research Center and the NSF for providing partial support for this work under Grants NAG 3-537 and MEA-8218708.

References

1 Nukiyama, S., "The Maximum and Minimum Values of the Heat Transmitted From Metal to Boiling Water Under Atmospheric Pressure," *J. Jap. Soc. Mech. Engr.*, Vol. 37, 1934, pp. 367–374 (transl. *Int. J. Heat Mass Transfer*, Vol. 9, 1966, pp. 1419–1433).

2 Lienhard, J. H., and Eichhorn, R., "Peak Boiling Heat Flux on Cylinders in a Crossflow," *Int. J. Heat Mass Transfer*, Vol. 19, 1976, pp. 1135–1142.

3 Vliet, G. C., and Leppert, G., "Critical Heat Flux for Nearly Saturated Water Flowing Normal to a Cylinder," ASME JOURNAL OF HEAT TRANSFER, Vol. 86, 1964, pp. 59–67.

4 Leppert, G., and Pitts, C. C., "Boiling," in: *Advances in Heat Transfer* T. F. Irvine, Jr. and J. P. Hartnett, eds., Vol. 1, Academic Press, New York, 1964.

5 Min, T. K., "Boiling on Cylinders in Cross-Flow Low-Velocity Peak Heat Flux Measurements for Water and Methanol," Master's Thesis, Mech. Engr. Dept., Univ. of Kentucky, Lexington, KY, 1975.

6 Hasan, M. Z., Hasan, M. M., Eichhorn, R., and Lienhard, J. H., "Boiling Burnout During Crossflow Over Cylinders, Beyond the Influence of Gravity," ASME JOURNAL OF HEAT TRANSFER, Vol. 103, 1981, pp. 478–484.

7 Kheyrandish, K., and Lienhard, J. H., "Mechanisms of Burnout in Saturated Flow Boiling Over a Horizontal Cylinder," *Multiphase Flow and Heat Transfer*, V. K. Dhir, J. C. Chen, and O. C. Jones, eds., HTD-Vol. 47, ASME, New York, 1985, pp. 25–31.

8 Milne-Thomson, L. M., "The Circle Theorem," *Proc. Camb. Phil. Soc.*, Vol. 36, 1940, pp. 246–250.

9 Robertson, J. M., *Hydrodynamics in Theory and Application*, Prentice-Hall, Englewood Cliffs, NJ, 1965.

10 Kheyrandish, K., and Dalton, C., "A Flow Model for Burnout in Saturated Boiling Over a Horizontal Cylinder," in: *Multiphase Flow and Heat Transfer*, V. K. Dhir, J. C. Chen, and O. C. Jones, eds., HTD-Vol. 47, ASME, New York, 1985, pp. 33–38.

11 Yilmaz, S., and Westwater, J. W., "Effect of Velocity on Heat Transfer to Boiling Freon-113," ASME JOURNAL OF HEAT TRANSFER, Vol. 102, 1980, pp. 26–31.

12 Broussard, R. A., and Westwater, J. W., "Diameter and Velocity Effects for Cross-Flow Boiling," *AIAA Journal*, Vol. 23, 1985, pp. 1615–1620.

T. P. Tsai

I. Catton
Fellow ASME

Mechanical, Aerospace and Nuclear Engineering,
University of California,
Los Angeles, CA 90024

The Effect of Flow From Below on Dryout Heat Flux

An experimental investigation of dryout heat flux in a saturated porous medium with forced flow from below has been conducted. Freon-113, methanol, and water were used as test fluids. Particle sizes were 0.59–0.79 mm, 1.6 mm, 3.2 mm, and 4.8 mm. The dryout heat flux increases as the inlet mass flux increases, and asymptotically approaches the total evaporation energy of the inlet flow. The pressure drop across the bed changes rapidly near the dryout point due to the formation of a dry zone.

Introduction

A number of hypothetical severe accidents have been postulated that would cause a light water reactor (LWR) core to become a rubble bed. The resulting rubble bed, made up of zirconium oxide, nuclear reactor fuel, and steel, is commonly called a debris bed. If the debris bed receives insufficient coolant, it can heat up and eventually melt, ultimately leading to melting or degradation of the surrounding steel structures. We will attempt to further delineate the conditions that determine whether such a postulated debris bed or damaged core is coolable, where "coolable" means all regions of the debris can be wetted.

The importance of dryout has led to numerous publications during the past decade. In the early 1970s, Sowa et al. [1] conducted the first experiment in this field. Later Gabor et al. [2] studied dryout using Joule heating at the Argonne National Laboratory for LMFBR safety analysis. Keowen [3] studied dryout heat fluxes of an inductively heated bed to try to answer some of the questions raised about the work of Gabor et al. [2]. His dryout heat flux data were found to be much higher than those of Gabor et al. In retrospect, the main cause of higher dryout heat flux seems to be the larger particle size used in Keowan's experiment. In the early studies, the particle size had not been varied systematically. Keowen's work was extended by Dhir and Catton [4] at UCLA. They developed a semi-empirical model for small particle beds, $D_p < 0.8$ mm, based on a number of experimental studies using various fluids. Besides Dhir and Catton's effort, Hardee and Nilson [5], Lipinski [6, 7], and others have developed models to predict dryout heat flux. As a result, dryout of a debris bed with coolant entering from above can be estimated, if the bed can be characterized.

Recently, Jakobsson [8] studied the effect of pressure on dryout. He found that the dryout heat flux can be scaled using the scaling factor proposed by Lienhard and Schrock [9] and Lienhard and Watanabe [10]. The scaled dimensionless dryout heat flux is only a function of reduced pressure and geometry. Thus, water behavior at high pressure can be simulated using different kinds of fluids through this scaling technique.

Since dryout under pool boiling conditions generally occurs at the bottom of a debris bed, a way to prevent dryout might be to pump liquid through the bed from below. Squarer and Peoples [11] conducted the first forced-flow dryout experiment showing that dryout may be controlled by a small amount of flow. Tsai et al. [12, 13] further studied the effect of forced flow by using Freon-113 and methanol as test fluids. The purpose of the present work is to investigate the dependence of dryout heat flux on flow from below. Both dryout heat flux and pressure drop are reported for a porous bed with forced flow from below and gravity driven entry of coolant from above.

Experimental Apparatus and Procedure

The experimental apparatus, shown in Fig. 1, consists of a 6.9 cm i.d. pyrex glass tube which constrains the particulate bed. Subcooled liquid (Freon-113, methanol, or water) flows up through the bed, which is supported by a sintered glass filter. The bed is inductively heated by a 40 cm multiturn copper coil powered by a 450 kHz, 10 kW power supply. Steel particles of 0.59–0.79 mm, 1.6 mm, 3.2 mm, and 4.8 mm diameter were used to form the porous bed. All of the particles were stainless steel, except for the 0.59–0.79 mm particles which were mild steel. The bed height was varied from 8 to 15 cm. The mass flux was controlled with a valve and measured with a calibrated flow meter.

The bed power distribution has been shown to be almost uniform as part of several previous studies [4, 12, 13]. Because the heating is nearly uniform, a single thermocouple gives an accurate measure of the early stages of bed heating. The startup time rate of change of the temperature is used to deter-

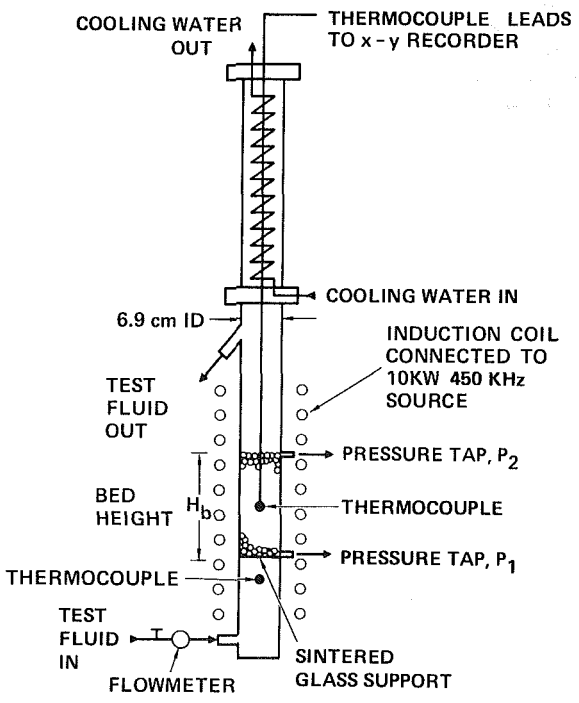

Fig. 1 Experimental apparatus

Contributed by the Heat Transfer Division for publication in the JOURNAL OF HEAT TRANSFER. Manuscript received by the Heat Transfer Division November 5, 1984.

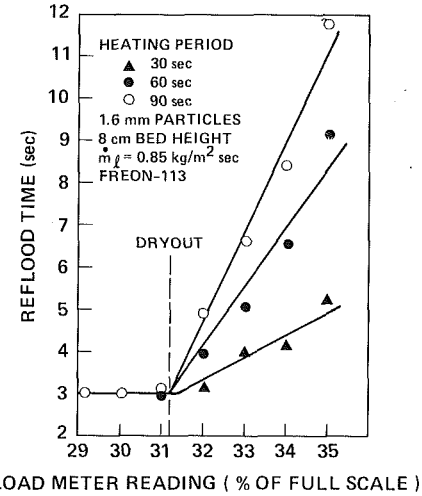

Fig. 2 Effect of different heating periods on reflood time

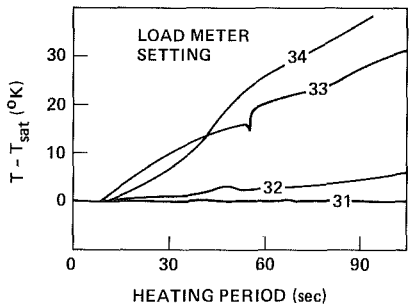

Fig. 3 Dryout zone temperature-time behavior of various load meter settings

mine the bed heat flux using the following equation, i.e., the total bed power per unit bed cross-sectional area

$$Q = (\epsilon\rho_l C_{pl} + (1-\epsilon)C_{ps}\rho_s)H_b\frac{dT_b}{dt} \quad (1)$$

Dryout of a submerged bed occurs when coolant can no longer reach some part of the bed. When there is no bottom flow, the dry zone forms at the bottom and the temperature in the dry zone begins to increase with time. With liquid flowing from below, the dry zone shifts upward. Locating a thermocouple where dryout is anticipated to occur is very difficult. To overcome this problem, Somerton et al. [14] suggested the reflood time be used to determine the occurrence of dryout. Reflood time is defined as the time it takes the coolant, displaced from the bed by the boiling process, to re-enter when the power is turned off. This time can be measured by watching how the liquid front moves up to a predetermined point at the surface of the bed. Once a dryout spot forms, the

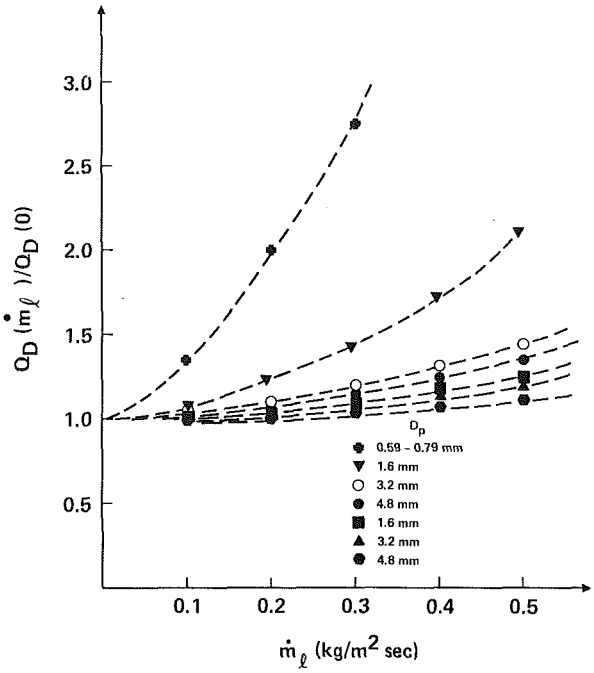

Fig. 4 Effect of flow on the dryout heat flux

reflood time will increase because the local superheat must first be removed by evaporation. If the input power is below the dryout heat flux, the whole bed is at the saturation temperature and the reflood time is almost constant. Once the dryout limit has been reached, the reflood time increases as a result of the formation and superheating of a dried-out region. In this situation the reflood time increases with increasing power and heating period. A typical graph of the reflood time is shown in Fig. 2 where the loading is directly proportional to the power. To verify that temperature measurement and the reflood time method were consistent, temperature was measured, with some difficulty, at the dryout location. It can be seen from Fig. 3 that the two methods are consistent. A detailed description of the reflood time method can be found in [14].

Results and Discussion

As pointed out by Squarer and Peoples [11], a small amount of bottom flow can greatly increase the dryout heat flux. From Fig. 4 one can see that the dryout heat flux increases monotonically with increase in bottom flow. The increase in dryout heat flux decreases with increasing particle size. For a 4.8 mm particle bed, the increase is only nominal. Data for methanol and Freon-113 are shown.

Nomenclature

C_{pl} = specific heat of liquid, J/kgK
D_p = particle diameter, m
g = earth's gravitational acceleration, m/s^2
H_b = bed height, m
h_{fg} = latent heat, J/kg
$\dot{m}_l$ = mass flux, kg/m^2-s
$\dot{m}_{lcr}$ = critical mass flux, kg/m^2-s
M = molecular weight
P = pressure, N/m^2
P_c = critical pressure, N/m^2
P_1 = pressure at bottom of bed, N/m^2
P_2 = pressure at top of bed, N/m^2
R = gas constant
Q = input heat flux, W/m^2
$Q_D(\dot{m}_l)$ = dryout heat flux at inlet mass flux = $\dot{m}_l$, W/m^2
Q_s = scaling factor, W/m^2
T_b = bed temperature, K
T_c = critical temperature, K
ρ_l = liquid density, kg/m^3
ρ_v = vapor density, kg/m^3
σ = surface tension, N/m
ΔP = $P_1 - P_2$, N/m^2
ΔP_D = ΔP at dryout point, N/m^2
ΔT_{sub} = subcooling, K

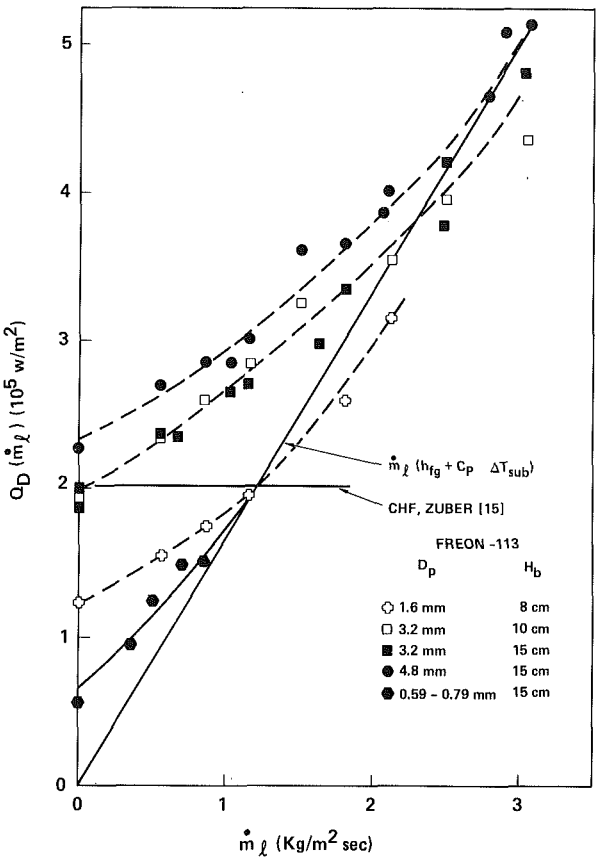

Fig. 5 Comparison of dryout heat flux with $\dot{m}(h_{fg} + C_{pl}\Delta T_{sub})$ for a Freon-113-saturated bed

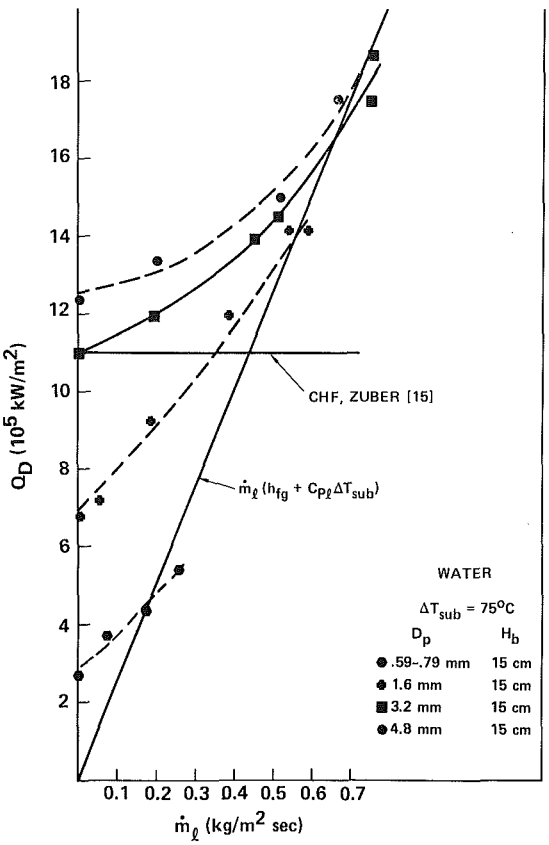

Fig. 7 Comparison of dryout heat flux with $\dot{m}(h_{fg} + C_{pl}\Delta T_{sub})$ for a water-saturated bed

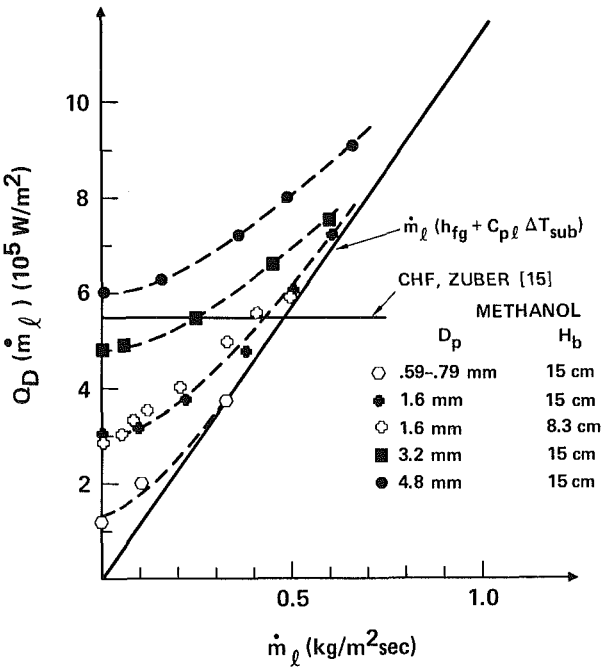

Fig. 6 Comparison of dryout heat flux with $\dot{m}(h_{fg} + C_{pl}\ \Delta T_{sub})$ for a methanol-saturated bed

As the amount of bottom flow increases, the dryout heat flux asymptotically approaches $\dot{m}_l(h_{fg} + C_{pl}\Delta T_{sub})$, the total evaporation energy of the inlet flow. This is shown in Figs. 5–7. For a sufficiently high flow rate, the dryout heat flux will become independent of particle size. At this point, it is really not a dryout process in the same sense as defined earlier. Also from the same figures, the discrepancy between the dryout heat flux and the total evaporation energy, $\dot{m}_l(h_{fg} + C_{pl}\Delta T_{sub})$, can be viewed as the effect of counterflow from the overlying liquid layer. The effect of countercurrent flow on Q_D becomes less and less important as the inlet flow increases, and eventually the bottom flow dominates the whole bed (see Figs. 8–10). It is noteworthy that the counterflow has a similar effect for different fluids and beds of different particle sizes. It indicates that one should be able to develop a correlation to express the counterflow effect in terms of appropriate dimensionless parameters. The dryout heat flux can then be expressed as the sum of counterflow part and the total evaporation energy of the inlet flow.

Before trying to derive an empirical expression for dryout heat flux, the critical mass flux $\dot{m}_{lcr}$ was defined as that at which the counterflow into the bed no longer contributes to raising the dryout heat flux. Obviously, if the inlet mass flux is higher than critical mass flux, the dryout heat flux is just equal to $\dot{m}_l(h_{fg} + C_{pl}\Delta T_{sub})$. The results of such a definition are shown in Fig. 11. It can be seen that smaller particle beds have a smaller critical mass flux. Experimental data from the three test fluids (Freon-113, methanol, and water) were used to obtain the following empirical expression for the critical mass flux

$$\frac{\dot{m}_{lcr}h_{fg}}{Q_s} = 5.78D_p^{0.51}\left[\frac{P}{P_c}\right]^{0.36} \tag{2}$$

where D_p has units of mm, P_c is the critical pressure of the test fluid, and Q_s is the scaling factor used by Jakobsson [8–10]

$$Q_s = \frac{P_c}{\rho_l - \rho_v}(g\sigma)^{1/4}\left[\frac{8}{3}\frac{M}{R}\frac{P_c}{T_c}\right]^{3/4} \tag{3}$$

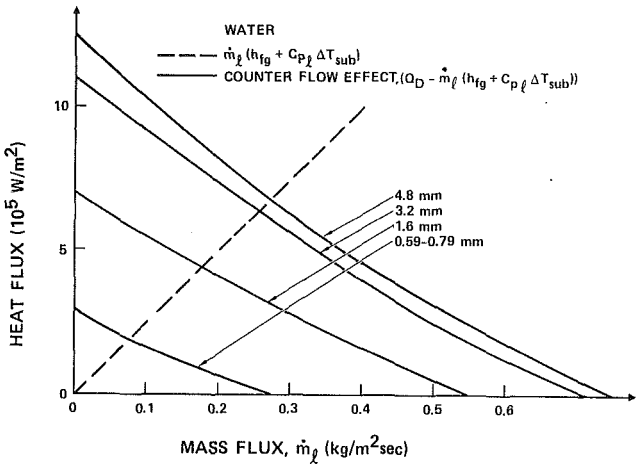

Fig. 8 Contribution to dryout heat flux by counterflow in a Freon-113-saturated bed

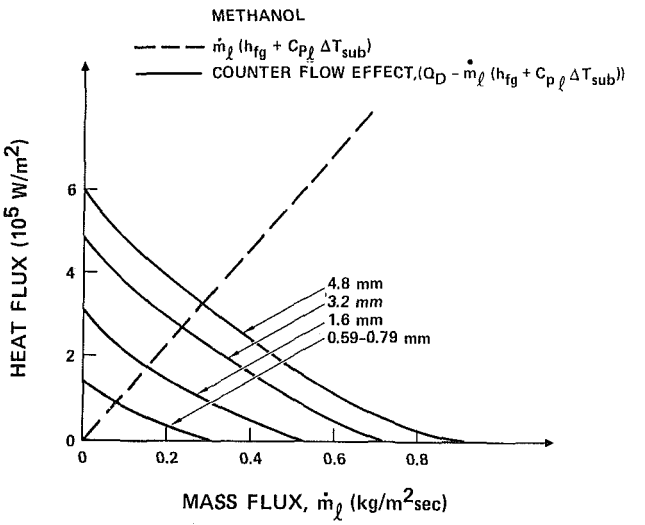

Fig. 9 Contribution to dryout heat flux by counterflow (methanol)

The dryout heat flux is then correlated using the critical mass flux expression, equation (2), and the scaling factor. The resulting expression is

$$\frac{Q_D - \dot{m}_l h_{fg}^*}{Q_s} = \begin{cases} 0 & \text{if} \quad \dot{m}_l \geq \dot{m}_{lcr} \\ 0.5\left[\dfrac{(\dot{m}_{lcr} - \dot{m}_l)h_{fg}^*}{Q_s}\right]^{0.78} D_P^{0.35}\left[\dfrac{P}{P_c}\right]^{0.023} & \text{if} \quad \dot{m}_l \leq \dot{m}_{lcr} \end{cases} \tag{4}$$

where $h_{fg}^* = h_{jg} + C_{pl}\Delta T_{sub}$.

Once again the particle diameter has units of mm. The calculated critical mass fluxes from equation (2) are within ±15 percent of measured data. In most cases, equation (4) predicts the results within ±20 percent. Combining equations (2) and (4), one can predict the dryout heat flux of a uniform bed with or without bottom flow. Further, the scaling incorporates the effect of pressure on dryout.

Forced flow from below requires that a sufficient liquid head exist. Therefore, pressure drop across the porous bed is an important parameter in dealing with debris bed coolability. Pressure drop measurements are shown in Figs. 12–17 for various flow rates as functions of input power.

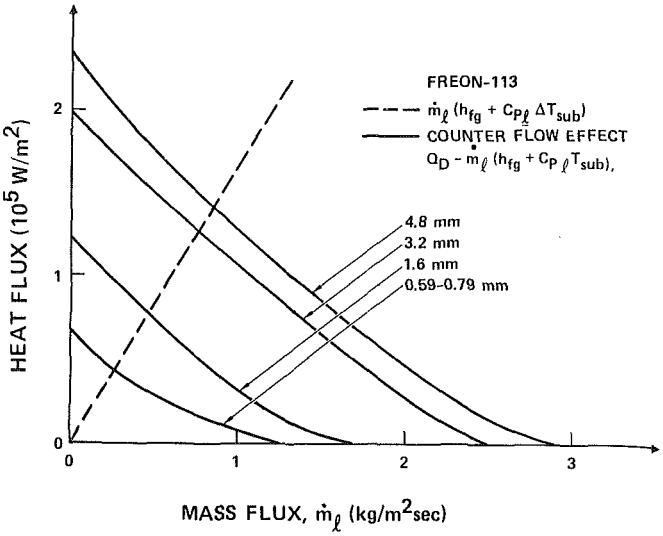

Fig. 10 Contribution to dryout heat flux by counterflow (water)

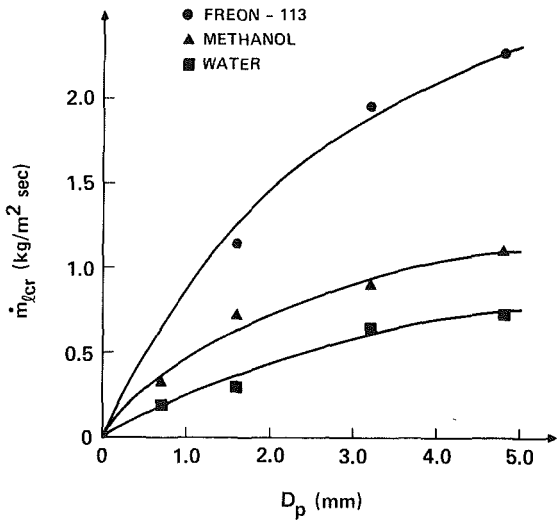

Fig. 11 Critical mass flux, $\dot{m}_{lcr}$, for Freon-113, methanol, and water-saturated beds; variation with particle diameter

Without input power, pressure drop is equal to the sum of hydrostatic pressure, friction loss, and inertial loss. At low input power, ΔP decreases slightly with increasing power because the hydrostatic head decreases with increasing void. Further increasing the input power will increase the amount of vapor flow. As a consequence, the friction loss will increase due to higher vapor velocity and the hydrostatic pressure drop will decrease due to the increase of void fraction. For some cases (methanol, $D_p = 1.6$ mm, 3.2 mm) the two effects cancel each other, so ΔP remains almost constant. However, when water was used, the increase in frictional ΔP seems to be much greater than the decrease in hydrostatic pressure resulting from the increase in void fraction. ΔP will increase until dryout occurs (see Figs. 12–17). The frictional loss is greater for small particle beds simply because the permeability is smaller. For all of the cases studied, ΔP was found to decrease rapidly once dryout occurs. The reason for the rapid change is the rapid increase in void once power exceeds the dryout heat flux. Thus the magnitude of the pressure change near the dryout point can be viewed as an indication of the size of the dry zone. A larger dry zone results in a more significant reduction in the magnitude of the pressure drop across the bed.

As shown in Figs. 18 and 19, the flow will push the dry zone

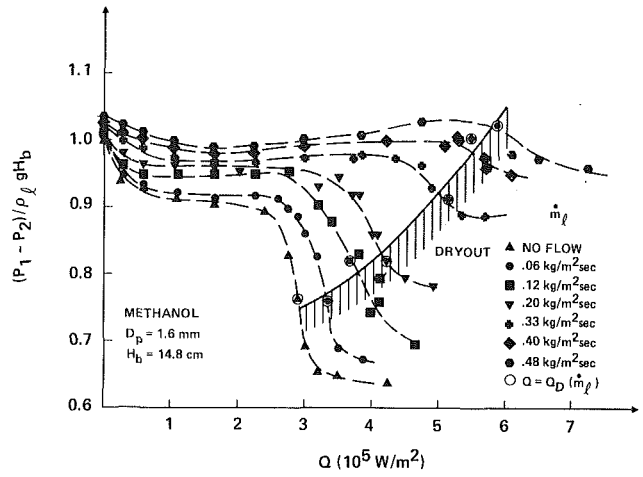

Fig. 12 Pressure drop across a methanol-saturated debris bed of 1.6 mm particles

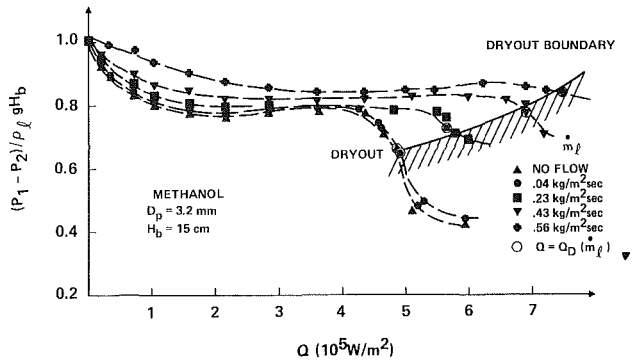

Fig. 13 Pressure drop across a methanol-saturated debris bed of 3.2 mm particles

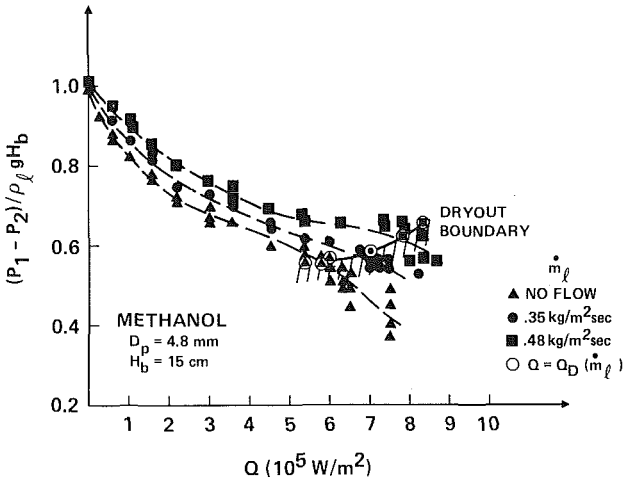

Fig. 14 Pressure drop across a methanol-saturated debris bed of 4.8 mm particles

upward and make it smaller. When the mass flux exceeds $\dot{m}_{lcr}$, the dryout heat flux approaches $\dot{m}_l(h_{fg} + C_{pl}\Delta T_{sub})$, and the dry zone is expected to be a very thin layer at top of the bed. The magnitude of change in ΔP at the dryout point is, therefore, relatively small.

In Fig. 20 pressure drop was plotted as a function of mass flow rate for various values of the input power. A dryout line is also shown. The area below the dryout line represents the region of dryout. In a reactor with a degraded core, the input power (decay heat) would be given and one could define how

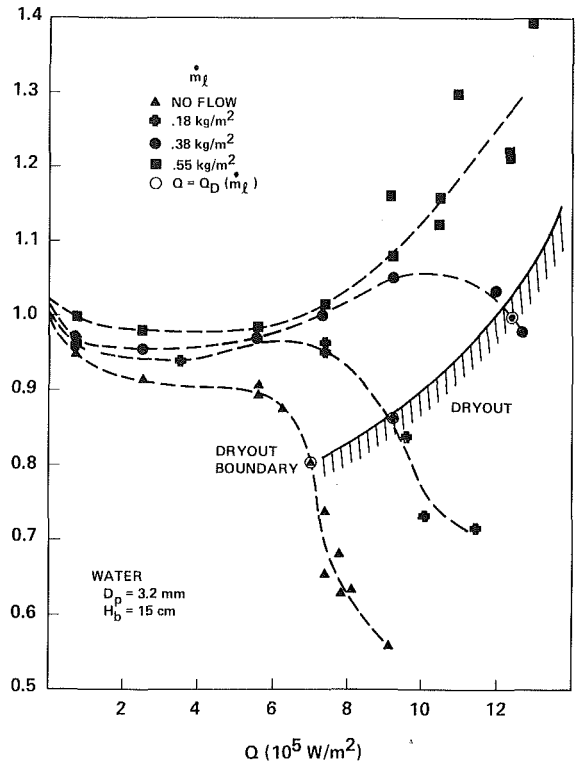

Fig. 15 Pressure drop across a water-saturated debris bed of 1.6 mm particles

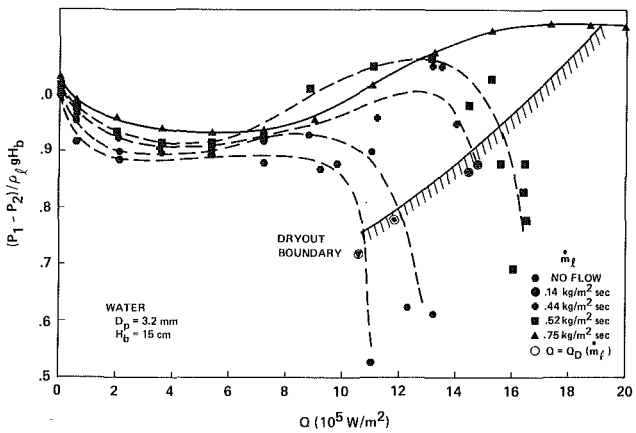

Fig. 16 Pressure drop across a water-saturated debris bed of 3.2 mm particles

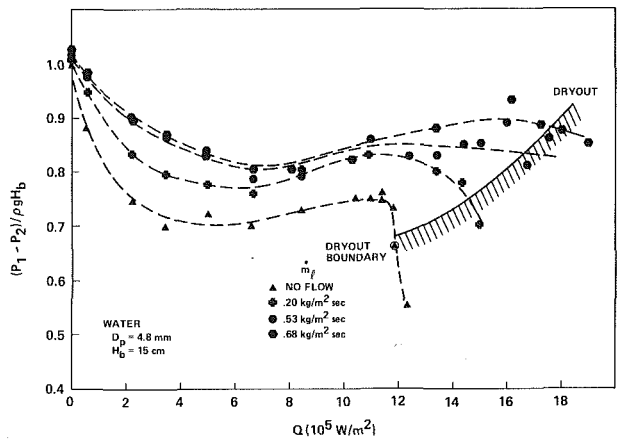

Fig. 17 Pressure drop across a water-saturated debris bed of 4.8 mm particles

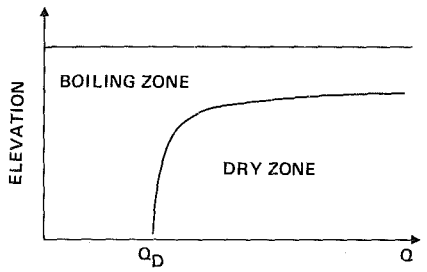

Fig. 18 Position of the dry zone as a function of input power when $\dot{m}_l = 0$

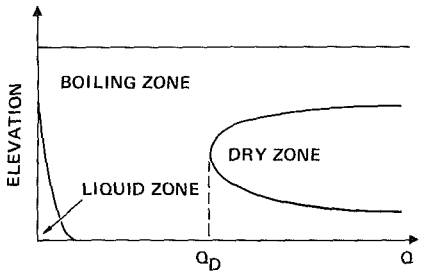

Fig. 19 Position of the dry zone as a function of input power with flow from below

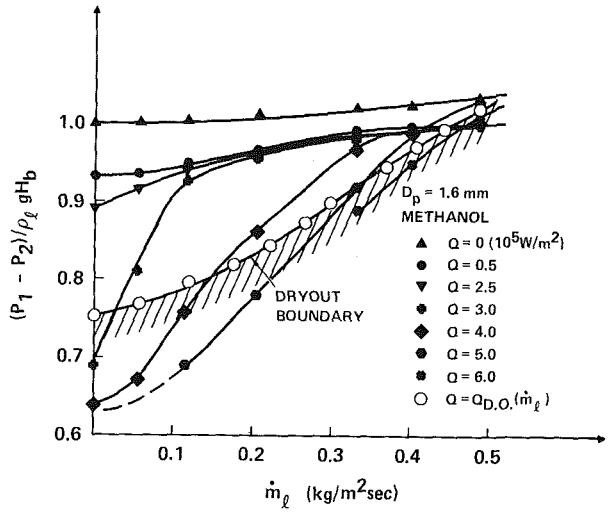

Fig. 20 Pressure drop as a function of mass flux for various values of power input

large the flow rate should be to avoid dryout. The pressure drop at the dryout point is plotted in Figs. 21 and 22 as a function of dryout heat flux for different particle sizes and flow rates. These figures would allow one to determine whether there is sufficient head to drive the flow and avoid dryout.

ΔP_D is found to be larger for smaller particles. A small particle bed has smaller permeability and therefore a bigger viscous loss. As mentioned earlier, different particle sizes could have the same dryout heat flux if the inlet mass flux were high enough, but the pressure drop would not be the same because of different permeabilities. Moreover, when the flow rate is high, $\Delta P_D/\rho_l g H_b$ may exceed 1. A liquid head higher than H_b would then be required to provide enough liquid to prevent dryout.

Concluding Remarks

A number of observations were made during this experimental study. Briefly, they are as follows:

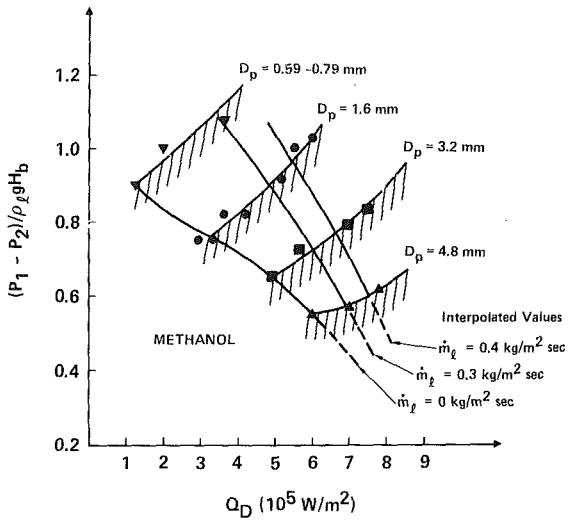

Fig. 21 Pressure drop at the dryout point (methanol)

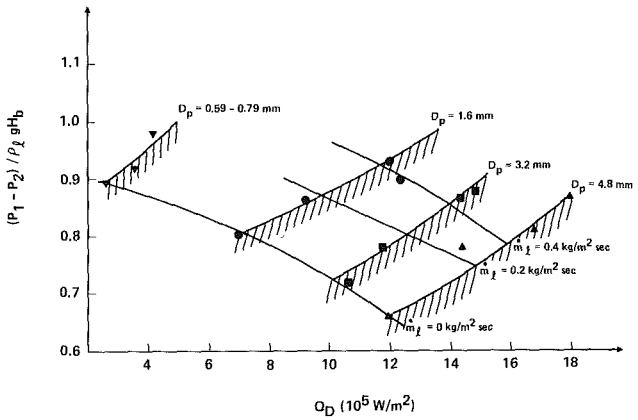

Fig. 22 Pressure drop at the dryout point (water)

1 The dryout heat flux increases monotonically as the inlet mass flux increases. The inlet flow has more influence on small particles than on large.

2 For all the particle sizes studied, the dryout heat flux asymptotically approaches the total evaporation energy of the inlet flow, $\dot{m}_l(h_{fg} + C_{pl}\Delta T_{sub})$, as the mass flow rate increases.

3 Counterflow from the overlying liquid becomes less important as the inlet flow increases, and the inlet flow dominates the whole bed once it exceeds a certain critical mass flux. For larger particle sizes, the critical mass flux is higher.

4 When there is no through flow, the dry zone is near the bottom of the bed. The inlet flow from below pushes the position of dry zone upward and has a tendency to make it smaller.

5 The magnitude of ΔP changes rapidly around the dryout point due to the formation of the dry zone in the bed when power exceeds dryout heat flux.

6 The pressure drop at the dryout point ΔP_D will be less for a lower mass flow rate than for a higher flow rate. Smaller particles have greater ΔP_D.

7 For sufficiently large flow rates, different size particles may have the same dryout heat flux, but the pressure drop will be different because the bed permeability is different.

Acknowledgments

The Electrical Power Research Institute is gratefully acknowledged for its support of this research project.

References

1 Sowa, E. S., Hesson, J. C., Gebner, R. H., and Goldfuss, G. T., "Heat Transfer Experiments Through Beds of UO_2 in Boiling Sodium," *Transactions ANS*, Vol. 14, 1971, p. 725.

2 Gabor, J. D., Sowa, E. S., Baker, L., Jr., and Cassulo, J. C., "Studies and Experiments on Heat Removal for Fuel Debris in Sodium," *Proceedings of the ENS/ANS Fast Reactor Safety Meeting*, Los Angeles, CA, Apr. 1974.

3 Keowen, R. S., "Dryout of a Fluidized Particulate Bed With Internal Heat Generation," M.S. Thesis, University of California, Los Angeles, CA, 1974.

4 Dhir, V. K., and Catton, I., "Study of Dryout Fluxes in Beds of Inductively Heated Particles," NUREC-0252 USNRC, 1977.

5 Hardee, H. C., and Nilson, R. H., "Natural Convection in Porous Media With Heat Generation," *Nuclear Science and Engineering*, Vol. 63, 1977, p. 119.

6 Lipinski, R. J., "A Particulate Bed Dryout Model With Upward and Downward Boiling," *Transactions ANS*, Vol. 35, 1980, p. 358.

7 Lipinski, R. J., "A One-Dimensional Particle Bed Dryout Model," *Transactions ANS*, Vol. 34, 1981, p. 386.

8 Jakobsson, J. O., "Pressure Dependence of Dryout Heat Flux in a Volume Heated Porous Bed," M.S. Thesis, University of California, Los Angeles, CA, 1983.

9 Lienhard, J. H., and Schrock, V. E., "The Effect of Pressure Geometry and the Equation of State Upon the Peak and Minimum Boiling Heat Flux," ASME JOURNAL OF HEAT TRANSFER, Vol. 85, 1963, p. 261.

10 Lienhard, J. H., and Watanabe, K., "On Correlating Peak and Minimum Boiling Heat Fluxes With Pressure and Heater Configuration." ASME JOURNAL OF HEAT TRANSFER, Vol. 87, 1965, p. 94.

11 Squarer, D., and Peoples, J. A., "Dryout in Inductively Heated Beds With and Without Forced Flow," *Transactions ANS*, Vol. 34, 1980, p. 537.

12 Tsai, F. P., Jakobsson, J., Catton, I., and Dhir, V. K., "Dryout of an Inductively Heated Bed of Steel Particles With Subcooled Flow From Below," *Thermal Hydraulics of Nuclear Reactors*, M. Merilo, ed., American Nuclear Society, 1983, p. 891.

13 Tsai, F. P., and Catton, I., "On Dryout Heat Flux and Pressure Drop of a Submerged Inductively Heated Bed With Flow From Below," *AIChE Symposium Series*, Vol. 79, 1983, p. 296.

14 Somerton, C. W., and Catton, I., "The Reflood Time as a Determination for Dryout," ASME JOURNAL OF HEAT TRANSFER, Vol. 106, 1984, p. 656.

15 Zuber, N., "Hydrodynamic Aspects of Boiling Heat Transfer," in: *Physics and Mathematics*, 1959, AECU-4439.

D. M. France
Mem. ASME

I. S. Chan

S. K. Shin

Department of Mechanical Engineering,
University of Illinois at Chicago,
Chicago, IL 60680

High-Pressure Transition Boiling in Internal Flows

Transition boiling heat transfer was studied for the case of internal flow of high-pressure water. Transition boiling results were determined from measurements from 138 steady-state tests conducted in a temperature-controlled facility. Water flowed vertically upward inside a tube with inside diameter = 10.1 mm and vertical length = 13.1 m, as it was heated by liquid sodium flowing countercurrent in a surrounding annulus. The water parameter range of the experiments was pressure 7-15.3 MPa and mass flux 0.7-3.2 Mg/m^2•s. A mathematical model was developed that predicted the transition boiling heat transfer coefficient well over the entire parameter range.

Introduction

The term transition boiling has been applied to boiling regimes in both pool and flow boiling situations. The hydrodynamics of the boiling fluid differ significantly among variations of these situations, but they are all characterized by some similar phenomena, and they are all regarded as transition boiling. In general, transition boiling is defined as the locally unstable region bounded by critical heat flux (CHF) and the stable post-CHF regime. The instability is characterized by periodic wetting and nonwetting of the heated surface by the liquid phase and results in time periods of high and low heat transfer as a consequence of liquid or vapor in contact with the heated surface, respectively. The present study is concerned with heat transfer in the transition boiling region of the internal two-phase flow of high pressure water. In the parameter range of interest, an annular flow regime exists prior to CHF with a liquid film on the heating surface (the tube wall) and a vapor core with entrained liquid droplets. The post-CHF region is a mist flow, and the transition boiling region connecting them is characterized by the breakdown of the liquid film on the wall in the presence of a vapor core. The distinguishing features of this study of transition boiling are the high pressure of the water, the internal flow condition, and the temperature-controlled experimental results from which transition boiling heat transfer information was calculated.

Transition boiling phenomena are relatively difficult to study experimentally. The most direct approach, widely utilized for general boiling studies, imposes a known and constant heat flux on the heated surface. This heat flux-controlled approach often precludes the establishment of a steady-state transition boiling region and/or leads to unmanageable temperatures of the heated surface. As a result, transition boiling data are sparse in the engineering literature in all situations, pool boiling and flow boiling. As discussed [1], other techniques have been used successfully in obtaining transition boiling measurements. They generally involve more complex experimental apparatus and data reduction techniques. The experimental results used in this investigation were obtained using one of these alternate techniques, liquid heating of the boiling surface. In this temperature-controlled situation, transition boiling is easily maintained in the test section under steady-sate conditions without problems with overly high temperatures. The purpose of this study was to calculate transition boiling heat transfer from results of extensive experiments on high-pressure water flowing inside tubes and to develop a mathematical presentation of these results. The temperature-controlled aspect of the experiments allowed the required information to be obtained, and the high water pressure employed (7-15.3 MPa) makes the results relatively unique.

There has been interest in transition boiling heat transfer in external flows in recent years. It is important to differentiate between transition boiling phenomena in internal and external flows where the hydrodynamics are significantly different. New results and conflicting interpretations with regard to external flows, such as the two transition boiling curve hypothesis [2], are currently being investigated, as summarized in a recent article [3]. These external flow experiments are characterized by a liquid stream outside of the wall boiling region, similar to a pool boiling situation. In contrast, transition boiling in internal flows occurring in the liquid-deficient region precludes the type of phenomena attributed to wetting of liquid from the stream on the heating surface in external flows. For example, it was noted [1] that different results are obtained at CHF and transition boiling by increasing or decreasing the heat flux to the surface in pool boiling, but no such phenomenon has been observed in steady-state internal flow boiling. Thus, internal flow transition boiling has not been found to be subject to the reported controversial aspects of the external flow case. However, transition boiling experiments are difficult to perform in all types of boiling, and as a consequence the available data are sparse.

High-Pressure Experiments

Transition Boiling Characteristics. Thermal fluctuations were measured and discussed at the heated surface of high pressure (13 MPa) water in transition boiling [4]. Water flowed internally upward inside a tube in a temperature-controlled experiment. The unstable nature of transition boiling, attributed to heated surface contact with liquid and vapor on an alternating basis, produced these temperature fluctuations. The amplitude of the heated surface temperature fluctuations was found to vary considerably as a function of test parameters of heat flux and water flow rate. The frequency was confined to a narrow band of 0.3 to 1.0 Hz. Similar results for frequency were reported in [5]. The heat flux to the boiling water, or the water heat transfer coefficient, calculated from measured fluctuating heated surface temperatures would also be oscillatory in nature. Time-averaged results would then be appropriate for overall heat transfer calculation applications. However, the average heat flux and average surface temperature could also be computed directly from measurements in the heating fluid. The thick tube wall (heated surface) of [4] and the heating fluid attenuated the amplitude of the thermal fluctuations initiated at the water/tube interface and were effectively an inherent low-pass filter. This approach of using the heating fluid measurements to obtain

Contributed by the Heat Transfer Division for publication in the JOURNAL OF HEAT TRANSFER. Manuscript received by the Heat Transfer Division December 14, 1984.

average water heat transfer parameters was adapted in this study.

Transition Boiling Heat Transfer Data. Experiments were performed at Argonne National Laboratory (ANL) and reported [6] for high-pressure water boiling as it flowed vertically inside a tube heated by liquid sodium flowing countercurrent in a surrounding annulus. The results of over 400 tests were discussed, with each test having CHF in the test section. The water pressure covered the range of 7 to 15.3 MPa, and the water mass flux range was 0.7 to 3.2 $Mg/m^2 \cdot s$. The results reported [6] were concerned with the critical heat flux point, but many of the tests included the transition boiling region as well. Selected tests from this group formed the data base for this investigation.

The experiments reported [6] were performed in the Steam Generator Test Facility (SGTF) which was described in some detail in [4, 7]. The facility will accommodate test tubes in excess of 21 m vertical length. The maximum nominal operating parameters are as follows: power = 1 MW, sodium volumetric flowrate = 0.0044 m^3/s at 650°C, water pressure = 16.5 MPa at 480°C, and water volumetric flowrate = 0.0082 m^3/s.

The SGTF test section is shown schematically in Fig. 1. It consists of a straight, vertical, round water tube with inside diameter = 10.1 mm, outside diameter = 15.9 mm, material 2 1/4 Cr-1 Mo steel, and heated length = 13.1 m. Water was force circulated upward in the tube, and sodium flowed countercurrent in the surrounding concentric annulus; the inside shell diameter was 31.5 mm. Spacers, which were designed to have minimal fin effect and low flow disturbance, were placed at 0.6 m and 0.9 m axial increments along the test section to maintain concentricity between the tube and shell. The mixed mean temperatures of the sodium and water at the test section inlet and outlet were measured with stainless steel sheated thermocouples (T.C.) placed in the flow as shown in Fig. 1. Two thermocouples were provided at each location, and mixers were placed upstream of the sodium stream thermocouples at the inlet and outlet to the test section. The principal instruments for determining the axial heat flux distribution were the 102 select wire, chromel-alumel thermocouples spot welded to the outside of the shell, as shown in Fig. 1. Also shown in Fig. 1 are internal thermocouples that were embedded in the water tube wall. The wall temperature measurements gave a clear indication of the transition boiling location in the test sections by virtue of the thermal fluctuations in this region. The shell thermocouple measurements (as well as flows, pressure, and test section inlet conditions) were used in an analysis of the sodium flow to produce water heat transfer results [6]. Mean values were obtained directly in the transition boiling region as a result of this heating fluid analysis.

Sodium flow was measured in the SGTF with an electromagnetic flowmeter and water flow with a turbine flowmeter. High accuracy pressure gages and pressure transducers were used to measure water pressure with an accuracy of ±0.02 MPa. All instrument calibrations were traceable to the National Bureau of Standards. Five parameters specified a test in the SGTF: water mass flux, water pressure, water inlet subcooling, sodium flow rate, and

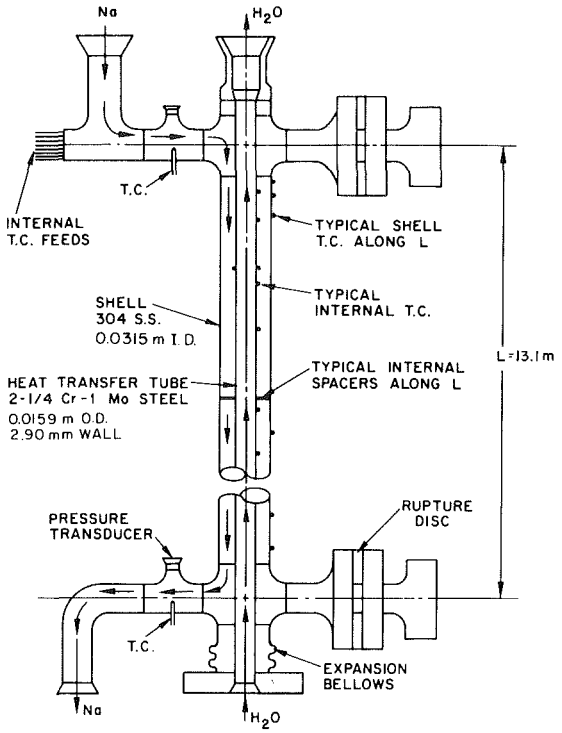

Fig. 1 Test section

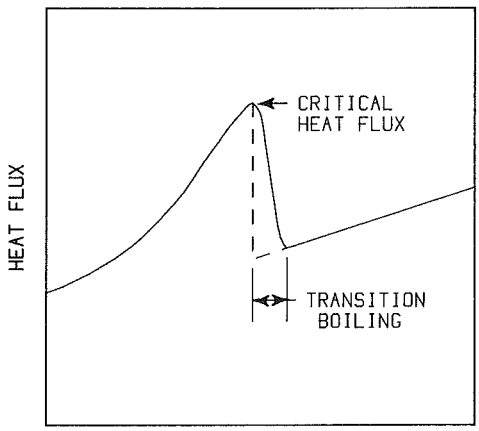

Fig. 2 Transition boiling in the test section

sodium temperature at the inlet to the test section. The axial heat flux distribution is shown schematically in Fig. 2 for a typical test where axial distance is measured in the direction of the water flow (upward). The solid line in Fig. 2 is indicative of the actual test section heat flux, and the transition boiling region is shown. Applications involving temperature-controlled flow boiling heat transfer require the prediction of this axial heat flux distribution. Calculations are generally per-

Nomenclature

G = water mass flux, $Mg/m^2 \cdot s$
h, H = heat transfer coefficient in transition boiling, $kW/m^2 \cdot °C$
H_{CHF} = heat transfer coefficient at CHF, $kW/m^2 \cdot °C$ (also designated H-CHF)
P = water pressure, MPa
Q = heat flux, kW/m^2
T_{sat} = water saturation temperature, °C
T_{wall} = temperature of heated surface, °C
ΔT = $T_{wall} - T_{sat}$, °C (also designated DTSAT)

Subscripts

CHF = conditions at the critical heat flux location

formed numerically including the various single-phase and two-phase flow regimes along the tube length. However, transition boiling heat transfer is usually neglected in high-pressure cases because of the lack of information concerning it. Consequently, the broken line of Fig. 2 is generally followed in applied situations, and the error involved in the predicted heat transfer may be appreciable.

All ANL tests [6] were conducted with subcooled water entering the test section, but the exit quality varied considerably among the tests. The tests were reviewed to specify a group that had transition boiling regimes present in the test section. Tests were selected as appropriate for this study only if the transition boiling region was followed by a clear post-CHF region such that test section end effects did not influence transition boiling heat transfer. It was found that 138 tests met this criterion, and these tests covered the entire experimental range of water pressure and flow rate.

Transition boiling heat transfer coefficients were calculated from the measurements made in 138 ANL tests [6]. The heat transfer coefficient was defined using the temperature difference between the heated surface (water tube wall at the inside diameter) and the equilibrium saturation temperature of the water. (Thermodynamic nonequilibrium effects are expected to be small in transition boiling due to the close proximity to the annular flow region and the relatively high values of water mass flux used in the tests.) In each test, the experimental heat transfer coefficient was determined at CHF and at several locations in the transition boiling region. The number of transition boiling coefficients determined depended on the length of the region and other parameters that affected the ANL data reduction method [6]. This method consisted of a numerical solution to the inverse heat transfer problem of thermally developing sodium flow in an annulus. The axial step size used was limited by the sodium flowrate and was larger for higher flow rates. However, a minimum of three values of heat transfer coefficient was obtained from the measurements of each test. A sample of the results is given in Fig. 3 where five coefficients were obtained from the measurements. The water pressure and mass flux for this test, No. R156, are given in Fig. 3, and the star symbols were obtained from the measurements. The heat transfer coefficient H was nondimensionalized with respect to the coefficient at CHF, H_{CHF}, to facilitate comparison with other test results, and $T_{wall} - T_{sat}$ is the temperature difference upon which the heat transfer coefficient was based as discussed previously.

Low-Pressure Experiments

Transition boiling of water in internal flows at pressures lower than the ANL experiments [6] were studied experimentally [8–10], and mathematical representations of the heat flux or heat transfer coefficient were formulated in each case. The tests of [8] were performed in a heat flux-controlled test section at atmospheric pressure. As a consequence of the heat flux controlled condition, transition boiling measurements were made under transient conditions. It was found that the transition boiling heat flux relative to the heat flux at CHF could be correlated by the term $\Delta T/\Delta T_{CHF}$. The resulting equation was

$$\frac{Q}{Q_{CHF}} = \left(\frac{\Delta T}{\Delta T_{CHF}}\right)^{-1.25} \tag{1}$$

The experiments of [9] were also performed at near-atmospheric water pressure. A temperature-controlled facility was used, and as a result, transition boiling was studied under steady-state conditions. Mercury flowing in an annulus provided heat to boil water flowing upward in a vertical tube. Experimental results for the transition boiling heat transfer coefficient were represented by a combination of convective and boiling terms. The boiling contribution was essentially related

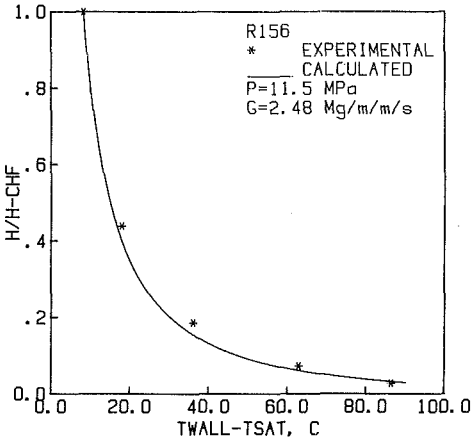

Fig. 3 Typical transition boiling heat transfer results

to the heat transfer coefficient at CHF by the use of an exponential function of the form

$$h \propto \exp[K_1(\Delta T - \Delta T_{CHF})] \tag{2}$$

where K_1 is a constant.

The third investigation [10] referenced in this section was a study of transition boiling data at a pressure of 7 MPa which is the lower limit of the pressure range of the ANL experiments [6]. It was found [10] that the transition boiling heat flux relative to the heat flux at CHF could be represented in an exponential form

$$\frac{Q}{Q_{CHF}} \propto \exp[\Delta T^{(K_2 + K_3 \Delta T)}] \tag{3}$$

where K_2 and K_3 are constants.

Although the mathematical relations developed in [8–10] for transition boiling heat transfer in relatively low-pressure water did not represent the high-pressure ANL data well, common elements from these results were successfully applied in developing a predictive relation for these data.

Results

Mathematical Formulation. Considering the successful representation of a significant amount of low-pressure transition boiling data by relations of the type given by equations (1)–(3), a similar approach was adopted for the high-pressure results determined from the experiments of [6]. All three low-pressure formulations rely on knowledge of conditions at CHF. In some applications, it is desirable to have a predictive equation for transition boiling heat transfer that is independent of CHF conditions, but in many cases the application involves the prediction of both CHF and transition boiling heat transfer. In the latter case, conditions at CHF are generally known, or predicted, prior to encountering transition boiling. In this situation there is no detriment to relating transition boiling phenomena to conditions at CHF. This technique proved to be successful previously [8–10], and it was retained in the current study acknowledging the application limits to situations in which CHF information is available or predictable.

It is evident from the formulation of equations (1)–(3) that transition boiling heat transfer in flow boiling is strongly influenced by the controlling parameter in pool boiling, the wall-to-fluid temperature difference ΔT. It is also seen that the reduction in heat flux and heat transfer coefficient, as a function of ΔT beyond CHF, has an exponential form. Thus, mathematical relations were conceived for representing the high-pressure transition boiling heat transfer coefficient as a function of ΔT and ΔT_{CHF} using exponential decay. The rationale for this approach was based on the suposition that the

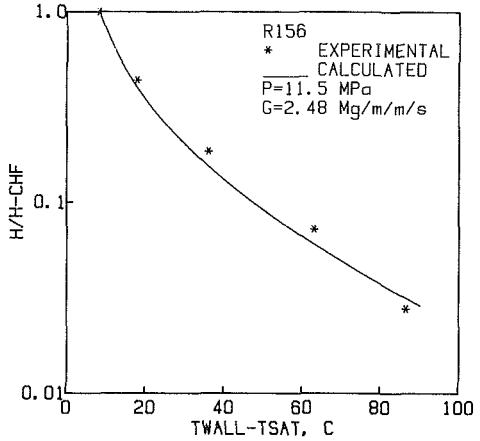

Fig. 4 Heat transfer at intermediate pressure and mass flux

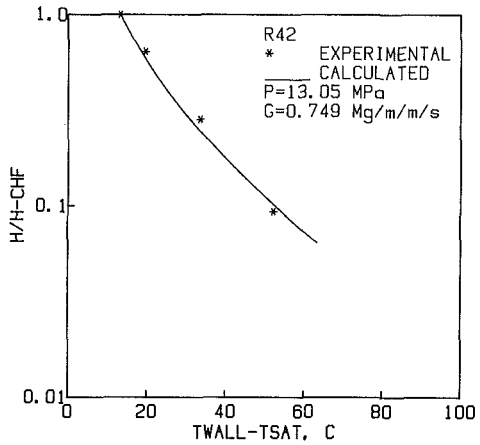

Fig. 5 Heat transfer at intermediate pressure and low mass flux

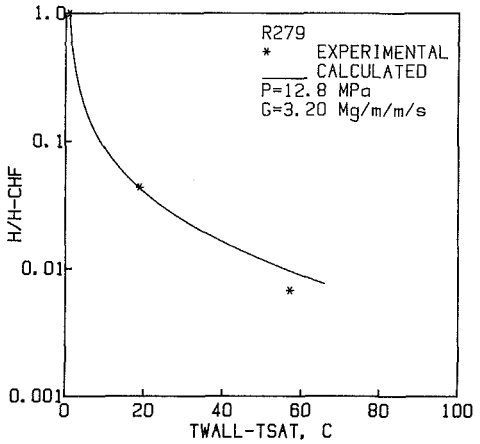

Fig. 6 Heat transfer at intermediate pressure and high mass flux

mathematical form that modeled the physical phenomena well at low pressure could be extended to higher pressures. The results were positive indicating the merit of this supposition.

Several mathematical functional forms were conceived with undetermined coefficients to be optimized with respect to data prediction. It was found that a relatively simple form represented the transition boiling heat transfer data well, and other more complex forms did not increase the accuracy of the data predictions in an amount sufficient to warrant the inclusion of the increased complexity. The resulting predictive equation is

$$\frac{h}{h_{CHF}} = \frac{\Delta T_{CHF}}{\Delta T} \exp[-C(\Delta T - \Delta T_{CHF})] \quad (4)$$

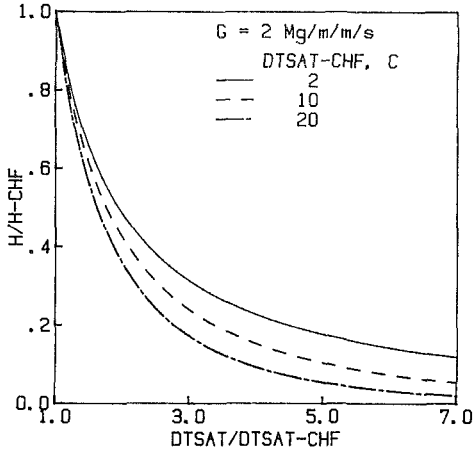

Fig. 7 Effect of CHF conditions

where the parameter C was optimized to the data using an error minimization computer code. It was found that this parameter was a weak function of the water mass flux and was essentially independent of water pressure over the high-pressure range of the data (7 to 15.3 MPa). The parameter C is given by

$$C = 0.0279 - 0.00556G \quad (5)$$

where the water mass flux G has the units of $Mg/m^2 \cdot s$ in equation (5), and C has the units of $°C^{-1}$.

Data Comparisons. Experimental results were previously presented in Fig. 3 for a typical test, No. R156, at intermediate values of water pressure and mass flux. The solid line in Fig. 3 is the calculation from equations (4) and (5), and the data prediction is considered to be very good. The exponential reduction in heat transfer coefficient beyond CHF is clear in Fig. 3, and the reduction spans an order of magnitude. As a consequence, the results of test R156 are shown on a logarithmic scale in Fig. 4, and all subsequent results use this scale. This scale represents the differences, between calculated and experimental results, better at low values of the heat transfer coefficient.

The results presented in Figs. 4–6 at an intermediate water pressure and three values of water mass flux, intermediate, low, and high, respectively, show good agreement between experiments and prediction in all cases. The rate of reduction of transition boiling heat transfer coefficient is significantly greater in the high mass flux case of Fig. 6 compared to the intermediate and low mass flux cases of Figs. 4 and 5. However, the mass flux produces this effect in an indirect manner through its relation to the critical heat flux. Higher mass fluxes are known to produce CHF at lower qualities perhaps due to a change in mechanism from departure from nucleate boiling (DNB) to liquid film dryout (LFD). The effects of CHF conditions are seen to be significant in Fig.7 where the results of equations (4) and (5) are presented for an intermediate value of mass flux and three values of ΔT_{CHF}. However, the direct effect of mass flux is shown to be small in Fig. 8 where the predictions of equations (4) and (5) are given for the entire experimental range of mass flux.

Not all of the results from the 138 tests employed in this study were predicted as well as the tests of Figs. 4–6. An example of a test, in which the differences between calculated and experimental heat transfer were among the largest considering all tests, is given in Fig. 9. Test No. R720 of Fig. 9 happens to be at the highest water pressure and lowest mass flux of the test series. However, this worst case comparison between calculation and experiment of Fig. 9 is not indicative of all of

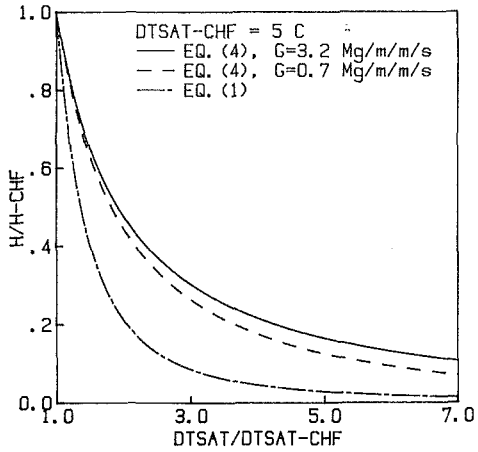

Fig. 8 Mass flux effect

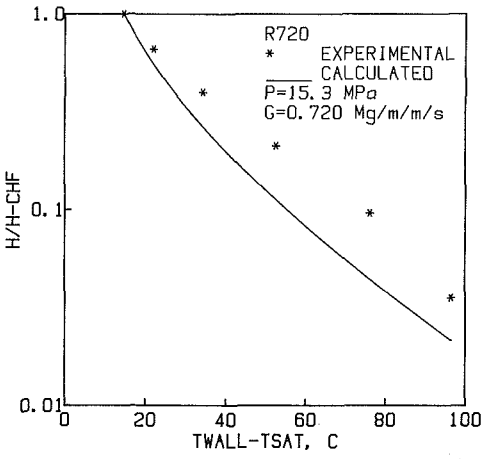

Fig. 9 Maximum Prediction Deviations from measurements

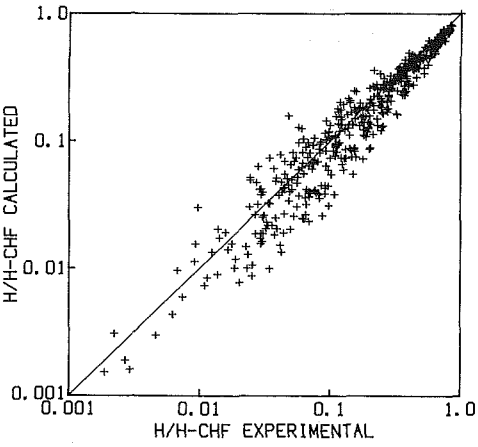

Fig. 10 Comparison of results from 138 tests

the tests at these parameters. No systematic errors in predictions were found as a function of water pressure or mass flux.

A composite of the calculated results of equations (4) and (5) compared with experimental transition boiling heat transfer coefficients, from all 138 tests used in this study, is given in Fig. 10. The comparison is considered to be good considering the difficulty of transition boiling experiments and the complexity of the data reduction methods. The results as represented by equations (4) and (5) are compared in Fig. 8 to the low-pressure model of equation (1). As discussed previously, the general trends are the same, but the low-pressure model does not extend well to high-pressure conditions.

Conclusions

Transition boiling heat transfer data were determined from the steady-state tests [6] of high-pressure water flowing inside a vertical tube. The temperature-controlled nature of the experiments allowed this information to be obtained. The combination of the high water pressure (7-15.3 MPa) and the temperature-controlled nature of the experiments makes these results relatively unique.

The average heat transfer coefficients determined from the experimental measurements in the transition boiling region were predicted well by equations (4) and (5). The form of these equations was developed from the extension of models that proved to be successful at lower water pressures. The predictions of equations (4) and (5) were considered good over the entire range of the experimental data, 7-15.3 MPa water pressure and 0.7-3.2 $Mg/m^2 \cdot s$ water mass flux.

The heat transfer coefficient results of equations (4) and (5) rely on knowledge of CHF conditions as do the low-pressure models [8–10]. In many applications, this requirement presents no restriction to use of the transition boiling results presented. For example, equations (4)–(5) could readily be incorporated into the analysis of a nuclear steam generator [11] which is a temperature-controlled boiling system. (This analysis neglected transition boiling heat transfer.) The analysis calculates CHF conditions, and this information is required whether or not transition boiling heat is included.

Acknowledgments

This study was performed under the auspices of the U.S. Department of Energy.

References

1 Collier, J. G., "Post-Dryout Heat Transfer – A Review of the Current Position," in: *Two-Phase Flows and Heat Transfer*, Vol. II, ed. S. Kakac and T. N. Veziroglu, Hemisphere, 1976, pp. 769–813.

2 Witte, L. C., and Lienhard, J. H., "On the Existence of Two Transition Boiling Curves," *Int. J. Heat Mass Transfer*, Vol. 25, 1982, pp. 771–778.

3 Bui, T. D., and Dhir, V. K., "Transition Boiling Heat Transfer on a Vertical Surface," *Basic Aspects of Two-Phase Flow and Heat Transfer*, ASME HTD Vol. 34, 1984, pp. 37–46.

4 France, D. M., Carlson, R. D., Chiang, T., and Priemer, R., "Characteristics of Transition Boiling in Sodium-Heated Steam Generator Tubes," ASME JOURNAL OF HEAT TRANSFER, Vol. 101, 1979, pp. 270–275.

5 Kebadze, B. V., Stroelov, V. S., Kul'pin, B. V., and Gavrilin, A. I., "Statistical Characteristics of the Temperature Fluctuations in a Direct-Flow Sodium Water Steam Generator," *Soviet Atomic Energy*, Vol. 39, 1976, pp. 870–873.

6 France, D. M., Carlson, R. D., Chiang, T., and Minkowycz, W. J., "Critical Heat Flux Experiments and Correlation in a Long, Sodium-Heated Tube," ASME JOURNAL OF HEAT TRANSFER, Vol. 103, 1981, pp. 74–80.

7 Stevens, H. C., and France, D. M., "Development of a Thermal/Hydraulic Test Facility for Full-Scale LMFBR Steam Generator Tubes," *Transactions of the American Nuclear Society*, Vol. 22, 1975, pp. 538–540.

8 Cheng, S. C., Ng, W. W. L., Heng, K. T., and Groeneveld, D. C., "Measurements of Transition Boiling Data for Water Under Forced Convective Conditions," ASME JOURNAL OF HEAT TRANSFER, Vol. 100, 1978, pp. 382–384.

9 Weisman, J., Kao, Y. K., and Rahrooh, G., "Transition Boiling Heat Transfer in a Vertical Round Tube," ASME Paper No. 79-HT-47, 1979.

10 Tong, L. S., and Young, J. D., "A Phenomenological Transition and Film Boiling Heat Transfer Correlation," *Proceedings of the Fifth International Heat Transfer Conference*, Vol. IV, Tokyo, 1974.

11 Oberjohn, W. J., Carter, H. R., and Schluderberg, D. C., "Thermal-Hydraulic Performance of a Consolidated Nuclear Steam Generator (CNSG) Module," ASME Paper No. 77-JPGC-NE-2, 1977.

Boiling Heat Transfer in Horizontal and Inclined Rectangular Channels

S. M. Morcos
A. Mobarak
M. Hilal
M. R. Mohareb

Mechanical Engineering Department,
Cario University,
Cario, Egypt

The present experimental investigation is concerned with boiling heat transfer of water inside both horizontal and inclined rectangular channels under a relatively low heat flux. These configurations simulate the absorber channel of line-focus solar concentrations under boiling conditions. The experimental facility includes electrically heated aluminum rectangular channels with aspect ratios of 2.67 and 0.37. The experimental results of the two-phase Nusselt number for the two aspect ratios and for the inclination angles 0, 15, 30, and 45 deg were correlated in terms of a ratio of the two-phase to the liquid-phase Reynolds number for the forced-convection vaporization region. The proposed correlations agree well with previous investigations. In the present work, classifications of the various flow patterns were made by direct observation through a glass window at the end of the test section.

Introduction

Line-focus parabolic trough solar concentrators have been used extensively to deliver thermal energy for industrial processes and other needs in the temperature range between 120 and 350°C. These parabolic concentrators have been under various developments to reduce their cost and improve the system performance. Consistent with these developments, rectangular channels may be considered more suitable as an absorber configuration since the reflected angular solar spectrum is facing the target surface in a strip instead of a line. Moreover, the concept of direct steam generation in the absorber of the line-focus concentrator is rather attractive as it lowers the collector operating temperature owing to the relatively high heat transfer coefficient associated with boiling flow. Lower operating temperatures would greatly increase the performance of a direct generation system compared to an unfired boiler system. May and Murphy [1] have analytically assessed the performance benefits of the direct generation of steam in the receiver tube of a line-focus collector, and have shown that such techniques could reduce the delivered cost of steam in excess of 25 percent.

Investigations of the boiling heat transfer inside circular horizontal and slightly inclined tubes for steam–water flows have been reported by Isbin et al. [2], Scruton and Chojnowski [3], and recently by Mobarak et al. [4]. Similar work has been regularly reported in the literature for refrigerants evaporating in horizontal tubes [5–13]. These investigations cover both the nucleate boiling and the two-phase forced-convection regions. Moreover, various correlations have been proposed for the boiling heat transfer coefficient inside horizontal tubes for water [4] and for refrigerant fluids [5–13]. Although the correlation proposed by Chen [14] was based on the experimental results for saturated forced-convection regions in vertical tubes, the experimental work of Scruton and Chojnowski [3], Gouse et al. [5, 6], and Reidle and Purcupile [12] has shown that Chen's correlation is satisfactory for horizontal tubes provided that all surfaces of the tube remain wetted and that stratification is not severe.

Experimental investigations of boiling two-phase flow in rectangular channels are rather limited. Davis and David [15] studied the heat transfer characteristics of high-quality steam–water flow in a horizontal rectangular channel 19.5 mm high, 6.6 mm wide, and 152.4 mm long. Sato et al. [16, 17] investigated the boiling two-phase flow of water in a vertical rectangular channel with a cross section of 15 × 10 mm and a heated length of 1100 mm. In the first part of their study [16], observation of the local flow patterns along the entire length of the test channel and the main factors affecting the transition of the flow pattern were reported. In the second part of the study, Sato et al. [17] correlated their nucleate boiling heat transfer data taking into consideration the contributions of nucleate boiling and of forced convection.

The present work is, therefore, concerned with the experimental investigation of the boiling two-phase flow in both horizontal and inclined rectangular channels under relatively low heat flux and mass flow rate in order to cover less investigated territory. Such configurations simulate the absorber channel of a line-focus solar collector under boiling conditions. The rectangular channel is electrically heated to approximate the conditions of the solar absorber with material of high thermal conductivity.

Experimental Apparatus

A schematic layout of the test loop is shown in Fig. 1. It was specially designed and constructed for this program to allow maximum flexibility in testing different test sections at various inclination angles, mass flow rates, wall heat fluxes, and channel aspect ratios.

The test loop shown in this figure is a low-pressure system with all the piping made of 12.5 mm nominal diameter galvanized steel tube. Water is circulated through the loop by a small centrifugal pump. After the pump, the flow splits into a test-section line and a bypass line for flow control.

In the test-section line, water flows into an upper constant head tank fitted with an overflow path. Then it passes through a control valve, a rotameter, the test section, and a heat exchanger before it returns to the accumulating tank, where it merges with the bypass line.

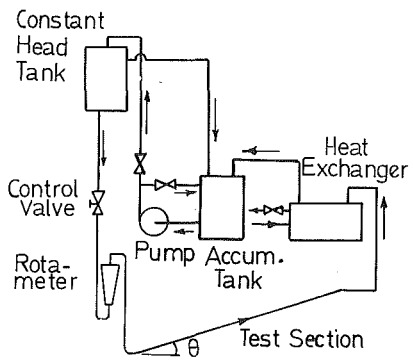

Fig. 1 Diagrammatic layout of test loop

Contributed by the Heat Transfer Division for publication in the JOURNAL OF HEAT TRANSFER. Manuscript received by the Heat Transfer Division August 5, 1985.

The main part of the test section is a rectangular aluminum channel of 20 × 10 mm outer dimensions with a wall thickness of 2 mm and a total length of 2.2 m. This yields two values of the aspect ratio of 2.67 and 0.37 for the rectangular channel. Uniform heating was applied to such relatively thick wall channels, which have high thermal conductivity, by a nickel-chrome wire closely wound around the rectangular channel in a uniform pitch. The wire has a strip cross section of 0.36 × 4.0 mm with 1.98 Ω/m. The maximum electric power of the wire heater is about 3 kW at 220 V. The wire is fixed at its two terminals by two copper rings connected to the measuring circuit, which includes an ammeter, a voltmeter, and an external variable resistance to adjust the input power to the circuit. This wire was electrically insulated from the channel by a thin layer of mica tape, and was also covered on the outside with another layer of mica tape.

An inlet cone made of brass, which has a circular cross section with 12.5 mm nominal diameter from one side and a rectangular cross section of 16 × 6 mm from the other side, was used to guide the flow from the circular cross section of the test loop to the rectangular cross section of the test section. A mixing chamber made of brass having a circular cross section of 20 mm nominal diameter was installed at the exit end of the rectangular channel in order to complete the mixing process.

At each end of the test section an aluminum flange of 40 × 30 mm was fixed to the channel. A rubber gasket was placed between the two flanges of the test-section channel, and the two flanges of the inlet cone and the mixing chamber, in order to minimize the axial conduction through the channel wall.

The test section and both the inlet part and the mixing chamber were covered by four layers of an asbestos cord thermal insulation in order to minimize the heat losses to the surroundings. The test section was supported on an adjustable table to the desired inclination angle.

In order to study the effect of the aspect ratio on the experimental results, the test section was allowed to rotate 90 deg around its longitudinal axis so that the aspect ratio could be changed from $AR = 2.67$ to 0.37. Moreover, a special end connection, having two glass windows 100 mm long each, is designed in such a way as to allow for direct observation of the flow regimes in the channel with $AR = 2.67$ and 0.37. This end piece was fixed at the end of the test section before the mixing chamber when it was required.

The fluid bulk and the wall temperatures were measured by chromel-alumel thermocouple wires 0.2 mm in diameter. The thermocouple potentials were measured with a precision manual potentiometer of 0.005 mV sensitvity. The inlet bulk fluid temperature was measured by a thermocouple probe installed directly in the fluid stream just prior to the inlet cone. The outlet bulk fluid temperature was measured by a thermocouple probe located after the mixing chamber to ensure good mixing of the water and the vapor through the mixing chamber. Four thermocouples were located at axial distances of 0.0, 0.45, 1.6, and 2.0 m downstream from the onset of the heating, for measuring the bulk fluid temperature along the channel.

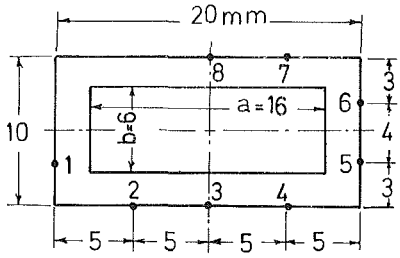

Fig. 2 Circumferential distribution of the wall thermocouple junctions

The outside wall temperatures were measured at six axial locations of 0.0, 0.3, 0.6, 0.9, 1.4, and 2.0 m from the onset of the heating. A guard heater of 50 mm was installed at the inlet end of the test-section channel to compensate for the axial conduction through the channel flange and the inlet cone.

In order to measure the circumferential wall temperature distribution at each axial location, eight thermocouple junctions were welded circumferentially around the rectangular channel as shown in Fig. 2. This distribution was selected in order to check the symmetry of the circumferential temperature profile around the meridional plane. Moreover, the above circumferential distribution of the wall thermocouples allows for the rotation of the test section by 90 deg about its axis so that a new value of the aspect ratio is obtained. The six bulk thermocouples as well as the 48 wall thermocouples were connected through two selector switches to the potentiometer and a common cold junction.

The dryness fraction of the wet steam at the exit of the test section was measured by periodically passing a wet sample through a specially designed surface condenser. Measurements of both the condensate and cooling water inlet and outlet temperatures enable the determination of the mass dryness fraction from the energy balance across the well-insulated surface condenser.

Experimental Procedure

The test loop shown in Fig. 1 was first filled completely with water from the upper constant head tank and air was bled from all high points of the system. Water was allowed to circulate in the test loop with the a-c power on for several hours, until it was sufficiently deaerated.

The testing generally proceeded by controlling the a-c power input to the test section through the variable external resistance, while the mass flow rate was maintained constant during each run by the control valve located upstream of the test section. The loop was allowed to operate at least 20 min before taking the data run, so that steady-state conditions were established and two successive readings, separated by 10 min, gave essentially the same value. Once steady state was

Nomenclature

a = channel inner width
AR = aspect ratio of the rectangular channel = a/b
b = channel inner height
C_1 = floating constant
D_e = equivalent hydraulic diameter = $2ab/(a+b)$
G = mass velocity
h = heat transfer coefficient
k = thermal conductivity
Nu = Nusselt number
p = pressure
q'' = uniform wall heat flux
Re = Reynolds number
T_b = bulk fluid temperature
T_{sat} = saturation temperature
T_w = wall temperature
x = vapor quality
θ = inclination angle
μ = dynamic viscosity
ρ = density

Subscripts

i = inside wall condition
l = liquid phase
v = vapor phase
TP = two-phase

Superscripts

$\bar{}$ = average condition

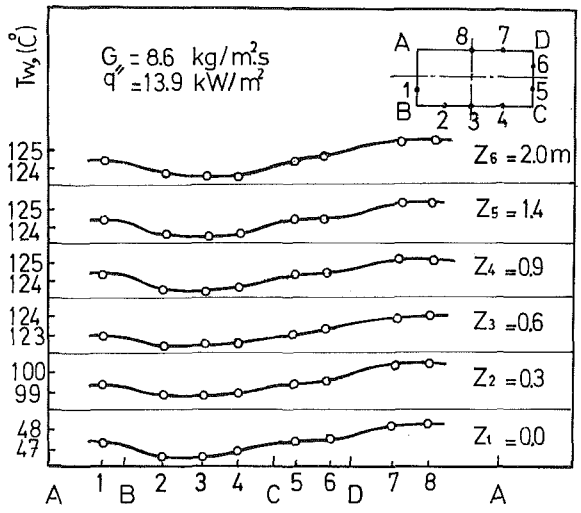

Fig. 3 Circumferential wall temperature distributions for AR = 2.67 and θ = 30 deg

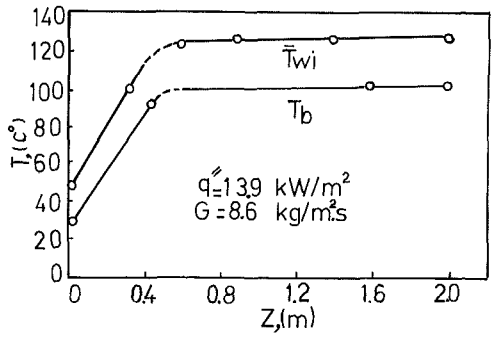

Fig. 4 Axial wall and bulk fluid temperature distributions for AR = 2.67 and θ = 30 deg

established, the readings for the mass flow rate, inlet, intermediate, and outlet bulk fluid temperatures, as well as the circumferential wall temperatures at the six axial locations and the electric power input, were recorded.

A wet vapor sample flowed at a constant rate into the surface condenser casing through a needle valve fixed in the outlet end of the test-section channel. This flow rate was measured as condensate leaving from the condenser. After the flow reached steady-state conditions, the inlet and outlet cooling water temperatures as well as condensate temperature were recorded.

The above experimental procedure was carried out for a test-section pressure of 118 kPa and mass flow rates of nearly 3, 6, 9, and 12 kg/h. For every mass flow rate, different runs were carried out for different input heat fluxes q'' of approximately 8, 10, 12, and 14 kW/m^2, over the entire length of the test section. All the previous runs were carried out for four values of the channel inclination angle of 0, 15, 30, and 45 deg to the horizontal.

After proceeding with the above experimental runs for the first aspect ratio of 2.67, the test section was turned 90 deg about its longitudinal axis, so that a new aspect ratio of 0.37 was obtained. The same experimennal procedures were repeated for the second aspect ratio.

Data Reduction

The heat input to the test section was based on the actual fluid enthalpy rise across the test section. The inside channel wall temperatures were obtained from the outside wall temperatures and the actual heat input using the one-dimensional conduction equation for the channel wall under steady-state conditions. This one-dimensional approach was used as it gives essentially the same results as the two-dimensional solution of the conduction equation [18]. The temperature difference was always less than 1.0°C for the two-phase flow. The circumferentially averaged wall temperature $\bar{T}_w$ was computed from the eight inner wall temperatures using numerical integration.

The values of the two-phase circumferentially averaged heat transfer coefficient h_{TP} at each measuring section were then calculated, using the heat flux based on the inside channel surface area q'' in the following manner

$$h_{TP} = \frac{q''}{\bar{T}_w - T_{\text{sat}}} \tag{1}$$

where T_{sat} is the saturation temperature.

Following the usual definitions, the two-phase circumferentially averaged Nusselt number Nu_{TP} and Reynolds number Re_{TP} can be written as

$$\text{Nu}_{TP} = \frac{h_{TP}\, D_e}{k_{TP}} \tag{2}$$

$$\text{Re}_{TP} = \frac{G\, D_e}{\mu_{TP}} \tag{3}$$

where $D_e = 2\,ab/(a + b)$ is the equivalent hydraulic diameter, k is the thermal conductivity, and μ is the dynamic viscosity. The properties of the two-phase mixture are based on the following formulae [19]

$$\frac{1}{\mu_{TP}} = \frac{x}{\mu_v} + \frac{1-x}{\mu_l} \tag{4}$$

$$\frac{1}{k_{TP}} = \frac{x}{k_v} + \frac{1-x}{k_l} \tag{5}$$

where l, v, and TP refer to liquid, vapor, and two-phase flow, respectively. Further details of the experimental apparatus, test procedure, and data reduction are given in [20].

Experimental Results and Discussion

The experimental results of the heat transfer coefficient for the single-phase flow were first obtained. These results were compared with the previous data for the heat transfer in rectangular channels [21]. The good agreement between the present results and the previous data verifies the proper operation of the test loop, together with the accuracy of the various measuring instruments.

The experimental results of the two-phase flow under low heat flux include the circumferential wall temperature distribution for various inclination angles of the test section. A typical set of these results is depicted in Fig. 3 for an inclined channel with θ = 30 deg under a constant heat flux q'' = 13.9 kW/m^2, mass velocity G = 8.6 kg/m^2•s and AR = 2.67. These curves reveal that the distributions are symmetric about the meridional plane of the channel. Moreover, at any axial location the temperature difference between the top and bottom walls, resulting from the buoyancy effects, is generally small and is less than 2°C.

The experimental results of the axial wall and bulk temperature distributions are plotted in Fig. 4 for an inclined channel with θ = 30 deg under a constant heat flux q'' = 13.9 kW/m^2, mass velocity G = 8.6 kg/m^2•s, and AR = 2.67. This figure shows the gradual increase in the mean wall temperature up to a value sufficient for the onset of the subcooled nucleate boiling. Then it remains constant at a few degrees above the saturation temperature. Similarly the bulk fluid temperature increases to the saturation temperature and then remains constant.

The experimental results of the two-phase circumferentially

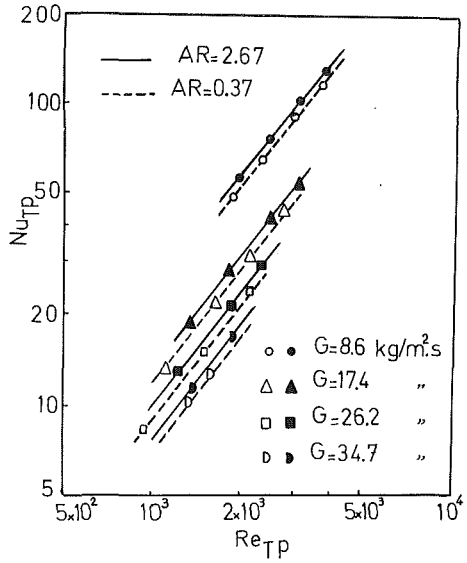

Fig. 5 Nusselt number Nu_{TP} variation with Reynolds number Re_{TP} for θ = 30 deg

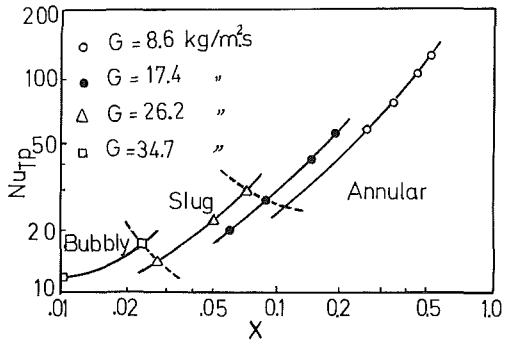

Fig. 6 Nusselt number Nu_{TP} versus vapor quality X for AR = 2.67 and θ = 30 deg

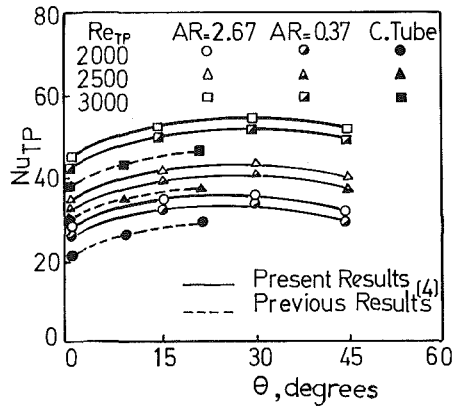

Fig. 7 Nusselt number Nu_{TP} variation with inclination angle θ

averaged Nusselt number Nu_{TP} at the exit of the test section are plotted in Fig. 5 as a function of the two-phase Reynolds number Re_{TP} for the two aspect ratios AR = 2.67 and 0.37 with an inclination angle θ = 30 deg. Examination of Fig. 5 indicates that Nu_{TP} depends not only on Re_{TP} but also on the mass velocity G. For the two aspect ratios, it is clear that these curves have the same trend and similarity. However, the effect of increasing the aspect ratio is to increase Nu_{TP} for given values of Re_{TP} and G.

The experimental data for Nusselt number Nu_{TP} are replotted as a function of the dryness fraction x, for different values of mass velocities G. Figure 6 represents these relations for AR = 2.67 and θ = 30 deg, in which it is noticed that Nu_{TP} increases with quality, and the rate of such increase is relatively small in the low-quality region and becomes high in the higher-quality region. The flow patterns are also shown in this figure where the two dotted curves show the boundaries between bubbly, slug, and annular flows.

A composite plot showing the values of Nu_{TP} at the exit of the channel as a function of the inclination angle θ is depicted in Fig. 7 for the two aspect ratios AR = 2.67 and 0.37. Figure 7 reveals that the optimum value of the inclination angle that yields the maximum value of Nu_{TP} is equal to 30 deg. This finding agrees with the experimental work of Morcos et al. [21], and the numerical results of Abou-Ellail and Morcos [22] for single-phase flow in rectangular channels. Figure 7 also shows the experimental data of Mobarak et al. [4] for boiling two-phase in inclined circular tubes, which have the same trend as the present results.

Flow Patterns

The mechanism of boiling heat transfer in horizontal and inclined channel is closely related to the distribution of the liquid and vapor phases, as well as the flow pattern. Therefore, in order to identify the boiling heat transfer phenomena in channel flow, it is necessary to know the flow conditions at the given location. As the flow patterns of boiling flow include many varieties, it is rather difficult to classify them in limited patterns. However, classification of flow patterns may be useful in understanding the following states.

In the present work, classifications of the various flow patterns were made by direct observation through the glass window at the end of the test section, using a 35 mm camera. Typical examples of the changes in the flow patterns are shown in Fig. 8 for the rectangular channel with AR = 0.37 and θ = 30 deg.

Starting with a relatively high mass velocity G = 26.2 kg/m²•s and a low heat flux q'' = 9.8 kW/m², Fig. 8(*a*) shows a typical example of bubbly flow with x = 0.005. Direct observation of this flow pattern indicates that the size distribution of the bubbles is basically nonuniform.

With a further increase in the heat flux to q'' = 11.6 kW/m², keeping the same mass velocity, the flow pattern changes to slug flow as shown in Fig. 8(*b*). In the slug flow the vapor piston is formed by coalescence of the flowing bubbles and the generated bubbles at the channel walls.

Figure 8(*c*) shows a typical example of the wavy-annular flow for G = 17.7 kg/m²•s, q'' = 9.8 kW/m², and x = 0.08. The wavy-annular flow pattern is usually accompanied by remarkable flow fluctuations.

In the range of still higher heat flux, and consequently higher vapor quality, no remarkable fluctuation was observed as the flow pattern changes to annular flow. Figure 8(*d*) shows an example of the annular flow for G = 17.7 kg/m²•s, q'' = 13.5 kW/m², and x = 0.16, where the vapor phase flows in the upper part of the channel and the liquid phase flows along the lower wall of the channel.

Based on these photographs, the classified flow patterns are plotted in Fig. 9 for AR = 2.67 and 0.37, taking the mass veloity G and the vapor quality x as coordinates. In the above figure the dotted lines show the boundaries between the various flow patterns. Near the boundaries, the types of the flow patterns are somewhat intermixed. Examination of Fig. 9 reveals that the transition from slug to annular flow occurs at a lower quality as the flow rate increases. However, the transition from bubbly to slug flow has the reverse tendency. These findings were also observed in the experimental work of Sato et al. [16].

Fig. 8(a) Bubbly flow: $G = 26.2$ kg/m^2•s, $q'' = 9.8$ kW/m^2, and $X = 0.005$

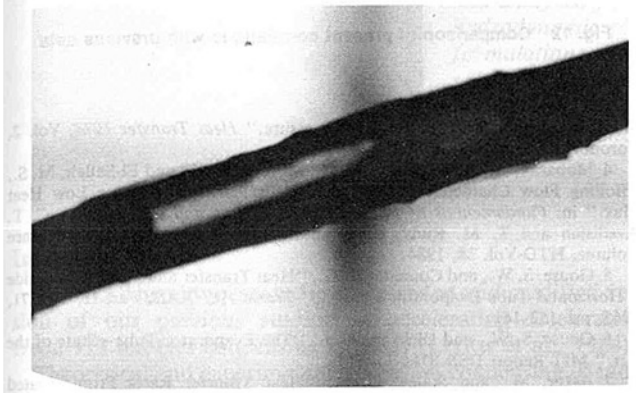

Fig. 8(b) Slug flow: $G = 26.2$ kg/m^2•s, $q'' = 11.6$ kW/m^2, and $X = 0.03$

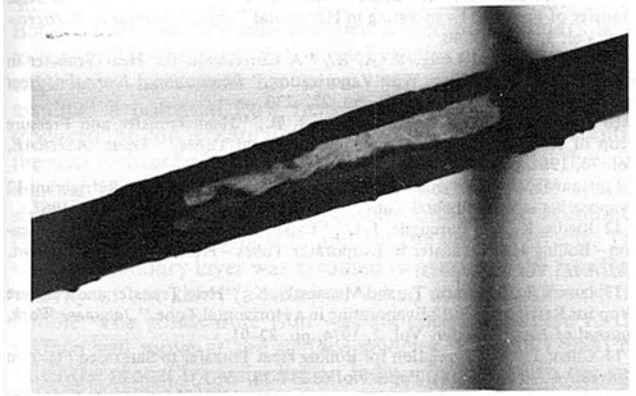

Fig. 8(c) Wavy-annular flow: $G = 17.7$ kg/m^2•s, $q'' = 9.8$ kW/m^2, and $X = 0.08$

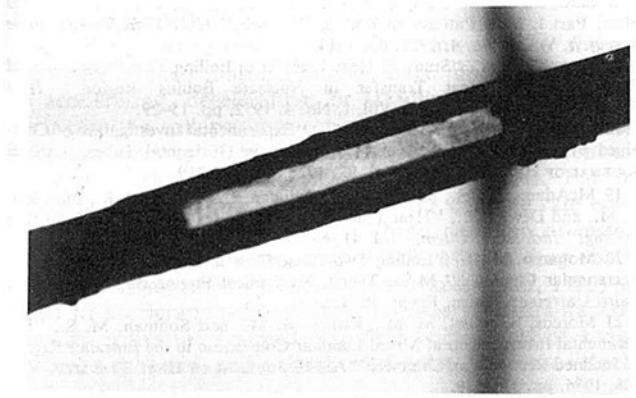

Fig. 8(d) Annular flow: $G = 17.7$ kg/m^2•s, $q'' = 13.5$ kW/m^2, and $X = 0.16$

Fig. 8 Flow patterns for $AR = 0.37$ and $\theta = 30$ deg

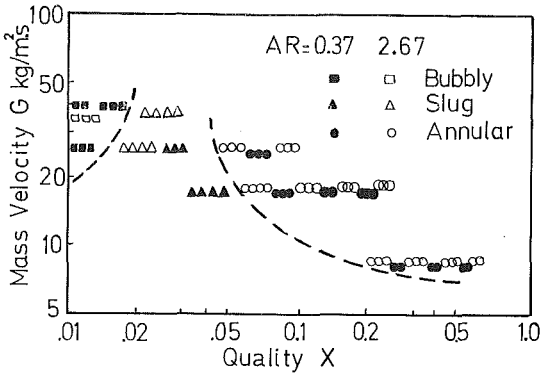

Fig. 9 Classified flow patterns for $AR = 2.67$ and 0.37

Correlation of Experimental Results

As indicated in Fig. 9, the flow regimes in most of the experimental runs for $AR = 2.67$ and 0.37 are those of slug-annular flows. Therefore, the correlation presented in this section will be primarily for the slug-annular flow patterns, which characterize the two-phase forced convection region, in the range of heat flux q'' from 8 to 14 kW/m^2 and mass velocity G from 8.6 to 34.4 kg/m^2•s.

Examination of Fig. 5 reveals that the representation of Nu_{TP} versus Re_{TP} for the various constant values of G is almost a parallel straight line of slope 1.25, which was also the case for other inclination angles. Moreover, the effect of the mass velocity was accounted for by the liquid Reynolds number defined as

$$\mathrm{Re}_l = \frac{G(1-x)D_e}{\mu_l}$$

When plotting Nu_{TP} versus Re_l for various constant values of Re_{TP}, the resulting parallel straight lines on the logarithmic scale have a constant slope of -0.78 for all inclination angles. This suggests that Nu_{TP} could be correlated in the following form

$$\mathrm{Nu}_{TP} = C_1 f(\theta)(\mathrm{Re}_{TP})^{1.25}(\mathrm{Re}_l)^{-0.78} \tag{6}$$

where C_1 is a floating constant and $f(\theta)$ is a function of the inclination angle θ. The best expression for $f(\theta)$ that has the same trend as the experimental results presented in Fig. 7 was found to be

$$f(\theta) = 1 + \sin\theta \cos(\theta + 30) \tag{7}$$

for the range of θ between 0 and 45 deg.

Using a least-square fitting of all the experimental data, the value of C_1 was then established at 0.31 for $AR = 2.67$. The final form of the correlation of Nu_{TP} for $AR = 2.67$ is given by

$$\mathrm{Nu}_{TP} = 0.31[1 + \sin\theta \cos(\theta + 30)](\mathrm{Re}_{TP}/\mathrm{Re}_l^{0.62})^{1.25} \tag{8}$$

In a similar manner, the correlation of the experimental results for Nu_{TP} for $AR = 0.37$ is given by

$$\mathrm{Nu}_{TP} = 0.27[1 + \sin\theta \cos(\theta + 30)](\mathrm{Re}_{TP}/\mathrm{Re}_l^{0.62})^{1.25} \tag{9}$$

Graphs of the two correlations expressed by equations (8) and (9) together with the various experimental data are depicted in Figs. 10 and 11 for $AR = 2.67$ and 0.37, respectively. These figures indicate that the present results for the boiling heat transfer coefficient for slug-annular flow could be predicted within ± 10 percent by the proposed correlations.

A comparison between the present correlations and the available correlations for the forced-convection vaporization region is depicted in Fig. 12. This figure shows the relatively good agreement between the present correlations and the ex-

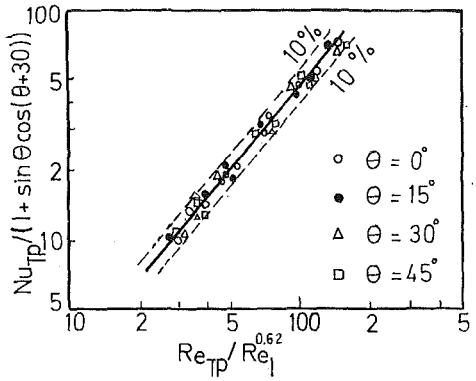

Fig. 10 Correlation of experimental results for AR = 2.67

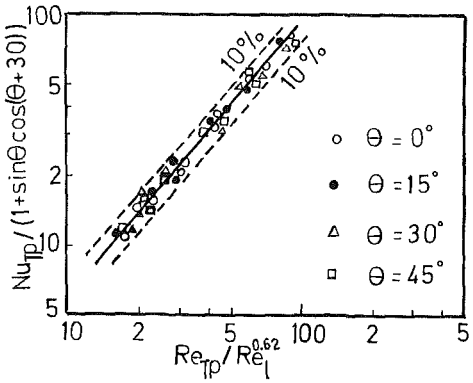

Fig. 11 Correlation of experimental results for AR = 0.37

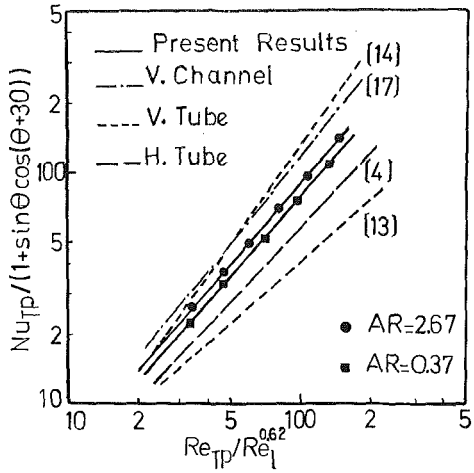

Fig. 12 Comparison of present correlations with previous data

perimental work of Sato et al. [17] for boiling flow of water in vertical rectangular channel. Figure 12 also shows a comparison with the well-established Chen correlation, which is higher than the present results due to the fact that Chen's correlation is based on data for vertical tubes. Also shown in Fig. 12 are the experimental results of Mobarak et al. [14], and Izumi et al. [13], which are lower than the present results as they are concerned with boiling flow characteristics in horizontal and slightly inclined circular tubes. However, the present correlations for both AR = 2.67 and 0.37 have the same trend as those of previous investigations.

Conclusions

The present experimental results reveal that Nu_{TP} for a given aspect ratio and inclination angle depends not only on Re_{TP} but also on the mass velocity G. The effect of increasing the aspect ratio is to increase Nu_{TP} for given values of Re_{TP} and G. Moreover, the optimum value of the inclination angle that yields the maximum value of Nu_{TP} is found equal to 30 deg.

In the forced-convection region, the present experimental results of Nu_{TP} for horizontal and inclined channels have been successfully correlated using a ratio of Re_{TP} to Re_l. The present correlations are in fair agreement with the experimental data of previous investigators.

References

1 May, K. E., and Murphy, L. M., "Performance Benefits of the Direct Generation of Steam in Line-Focus Solar Collectors," ASME *Journal of Solar Energy Engineering*, Vol. 105, 1983, pp. 126–133.

2 Isbin, H. S., et al., "Heat Transfer to Steam-Water Flows," *Proceedings of the 1961 Heat Transfer and Fluid Mechanics Institute*, Stanford University Press, 1961, pp. 70–78.

3 Scruton, B., and Chojnowski, B., "Two-Phase Heat Transfer in Serpentine Geometry Boiler Tubes at High Pressure," *Heat Transfer 1978*, Vol. 2, Toronot, 1978, pp. 55–60.

4 Mobarak, A., Abdel-Salam, M. S., Morcos, S. M., and El-Sallak, M. S., "Boiling Flow Characteristics in Inclined Circular Tubes Under Low Heat Flux," in: *Fundamentals of Phase Change: Boiling and Condenstion*, C. T. Avedisian and T. M. Rudy, eds., ASME 1984 WAM Bound Conference Volume, HTD-Vol. 38, 1984.

5 Gouse, S. W., and Coumou, K. G., "Heat Transfer and Fluid Flow Inside a Horizontal Tube Evaporator Phase I," *Trans. ASHRAE*, Part II, Vol. 71, 1965, pp. 152–161.

6 Gouse, S. W., and Dickson, A. J., "The Evaporator Tube – State of the Art," MIT Report DSR 8734-7, 1965.

7 Baker, M., and Staley, C. F., "Heat Transfer Rates From Heated Horizontal Tubes to Boiling Refrigerant 22," *ASHRAE Journal*, Vol. I, 1959, p. 83.

8 Worsoe-Schmidt, P., "Some Characteristics of Flow Pattern and Heat Transfer of Freon-12 Evaporating in Horizontal Tubes," *Journal of Refrigeration*, Vol. 3, 1960, p. 40.

9 Sachs, P., and Long, R. A. K., "A Correlation for Heat Transfer in Stratified Two-Phase Flow With Vaporization," *International Journal of Heat and Mass Transfer*, Vol. 2, 1961, pp. 222–230.

10 Johnston, R. C., and Chaddock, J. B., "Heat Transfer and Pressure Drop of Refrigerants Evaporating in Horizontal Tubes," *Trans. ASHRAE*, Vol. 70, 1964, pp. 163–172.

11 Chawla, J. M., "Heat Transfer and Pressure Drop for Refrigerant-12 Evaporating in a Horizontal Tube," *VDI Forschungschaft*, Vol. 523, 1967.

12 Riedle, K., and Purcupile, J. C., "Experimental and Analytical Investigation – Boiling Heat Transfer in Evaporator Tubes – Horizontal Flow," *Trans. ASHRAE*, Vol. 2271, 1973.

13 Izumi, R., Ishimaru, T., and Matsuzaki, K., "Heat Transfer and Pressure Drop for Refrigerant R-12 Evaporating in a Horizontal Tube," *Japanese Work, Journal of Heat Transfer*, Vol. 2, 1974, pp. 82–91.

14 Chen, J., "A Correlation for Boiling Heat Transfer to Saturated Fluids in Convective Flow," ASME Paper No. 63-HT-34, 1963.

15 Davis, E. J., and David, M. M., "Heat Transfer to High-Quality Steam-Water Mixtures Flowing in a Horizontal Rectangular Duct," *Canadian Journal of Chemical Engineers*, Vol. 39, June 1961, pp. 99–105.

16 Sato, T., et al., "Study of Heat Transfer in Boiling Two-Phase Channel Flow, Part I: Flow Patterns in Boiling Channels," *Heat Transfer – Japanese Research*, Vol. I, No. 4, 1972, pp. 1–14.

17 Sato, T., et al., "Study of Heat Transfer in Boiling Two-Phase Channel Flow, Part II: Heat Transfer in Nucleate Boiling Region," *Heat Transfer—Japanese Research*, Vol. I, No. 4, 1972, pp. 15–29.

18 Morcos, S. M., and Bergles, A. E., "Experimental Investigation of Combined Forced and Free Laminar Convection in Horizontal Tubes," ASME JOURNAL OF HEAT TRANSFER, Vol. 97, 1975, pp. 212–219.

19 McAdams, W. H., Kennel, W. E., Minden, C. S. L., Carl, R., Picornell, P. M., and Dew, J. E., "Heat Transfer at High Rates to Water With Surface Boiling," *Ind. Engr. Chem.*, Vol. 41, No. 9, 1949, pp. 1945–1953.

20 Mohareb, M. R., "Boiling Two-Phase Flow in Horizontal and Inclined Rectangular Channels," M.Sc. Thesis, Mechanical Engineering Department, Cairo University, Cairo, Egypt, 1984.

21 Morcos, S., Hilal, M. M., Kamel, M. M., and Soliman, M. S., "Experimental Investigation of Mixed Laminar Convection in the Entrance Region of Inclined Rectangular Channels," ASME JOURNAL OF HEAT TRANSFER, Vol. 108, 1986, pp. 574–579.

22 Abou-Ellail, M. M. M., and Morcos, S. M., *Combined Forced and Free Laminar Convection in the Entrance Region of Inclined Rectangular Channels, Numerical Methods for Non-linear Problems*, Pineridge Press, Swansea, United Kingdom, 1980, pp. 807–820.

Condensation of an Accelerating-Decelerating Bubble: Experimental and Phenomenological Analysis

Y. Lerner
H. Kalman
R. Letan

Department of Mechanical Engineering,
Ben-Gurion University of the Negev,
Beer-Sheva, Israel

An experimental and theoretical phenomenological study of accelerating-decelerating bubbles, condensing in an immiscible liquid, was conducted. The system consisted of a column of water, and bubbles of freon-113, 4–5 × 10^{-3} m in diameter. Shadowgraphing of the process has illustrated the wake formation behind the bubble, wake shedding, forward movement of vortices, and envelopment of the decelerating bubble in its wake. The bubble size, shape, and path were videotaped and analyzed for the collapse rate, and the instantaneous position. The visualized hydrodynamic phenomena provided a phenomenological basis for the theoretical formulations. The theoretical model postulated an eccentrically positioned vapor sphere in the collapsing bubble, a boundary layer and wake over the accelerating bubble, and a concentric vorticular envelope around the decelerating bubble. The theoretical-phenomenological predictions compared well with experiment.

Introduction

The work herein presented is an extended and modified version of our previous studies on accelerating-decelerating freon-113 bubbles condensing in water (Lerner et al., 1984).

Theoretical and experimental studies on condensing, steadily rising, hydrocarbon bubbles in water were conducted by Jacobs (Jacobs and Major, 1982; Jacobs et al., 1978) and Sideman (Isenberg and Sideman, 1970; Isenberg et al., 1970). Both Jacobs and Sideman assigned a thermal boundary layer to the bubble. In Sideman's model viscous effects were semi-empirically accounted for by a "velocity factor." Jacobs assumed a potential flow field around the bubble, and introduced the condensate film inside the bubble as a substantial thermal resistance in his model. In Sideman's model the condensate film was assumed negligible. Lerner (1983) synthesized and modified the two previous models. He accounted both for the condensate film and for the viscous effects. The viscous boundary layer was assumed to attenuate the free flow velocity to one third (a heuristic value) at the surface of the bubble. The condensate film was supposed to adhere to the surface and move at the surface velocity. Kalman (1984) refined the model by assigning an index of mobility to the surface of the bubble. The mobility of the surface was assumed to decrease with the size of the bubble (Lerner and Letan, 1985) varying between zero (rigid surface) and potential flow velocity (Jacobs model).

All the aforementioned models relate to the thermal resistance of the collapsing bubble. Each model is applicable to accelerating, decelerating, or steadily rising bubbles. In each case the collapse rate equation is coupled with the appropriate velocity. Sideman and Jacobs assigned a constant velocity to the collapsing hydrocarbon bubbles. For accelerating-decelerating freon bubbles the collapse rate equation was simultaneously solved with an equation of instantaneous velocity (Moalem et al., 1980), using a drag coefficient of a rigid sphere. Ullman (Lerner and Letan, 1985) applied to accelerating-decelerating bubbles the instantaneous velocity expression coupled with drag coefficients of a rigid sphere, a spheroid, and a distorted droplet. Then the velocity expression integrated with respect to time yielded the predicted path of the bubble. The curve which agreed best with experiment was selected and re-applied in the collapse rate equation.

Isenberg's model agreed very well with his experimental data (Isenberg and Sideman, 1970). Lerner's model (Lerner and Letan, 1985) almost overlapped those experiments. Conceptually, the two models differ, but practically the predicted curves are similar and close. Comparison of all the aforementioned models with experimental data of hydrocarbon bubbles (Kalman et al., 1986) illustrated a good agreement at the early stages of collapse. As collapse proceeded, additional effects, not accounted for in the available models, appeared to play a dominant role in the process. Those effects, or rather the physical phenomena which took place in the transient process of collapse, came to an expression in the "envelope model" (Kalman, 1984) applied to the freon bubbles (Lerner et al., 1984) as well as to the hydrocarbon bubbles (Kalman et al., 1986).

Theoretical Model

Qualitative visualization studies were conducted to gain an insight into the mechanism and the physical phenomena governing bubble collapse. The methods applied were: visualization of the temperature field by shadowgraphing, visualization of the flow pattern by color entrainment, screen-tracing of the videotaped bubble shape and path, and visualization of the condensate shape by dye injection. All those visualized phenomena have provided the physical basis for the postulated model of bubble collapse.

Shadowgraphs and screen-traced collapse are presented and discussed in this work. The color entrainment which complements the shadowgraphing studies and the visualization of condensate are illustrated and analyzed elsewhere (Kalman et al., 1987).

Shadowgraphing of the collapse process has outlined the thermal surroundings of the collapsing bubble. Representative examples of freon-113 bubbles collapsing in water are shown in two series of shadowgraphs in Fig. 1. Both series illustrate the same fundamental phenomena: A bubble of spherical shape breaks away from the nozzle, a thermal layer forms over the bubble, and a wake behind the bubble. The detached bubble reshapes into an ellipsoid. That stage corresponds to an ac-

Contributed by the Heat Transfer Division and presented at the 22nd National Heat Transfer Conference, Niagara Falls, New York, August 1984. Manuscript received by the Heat Transfer Division August 8, 1984.

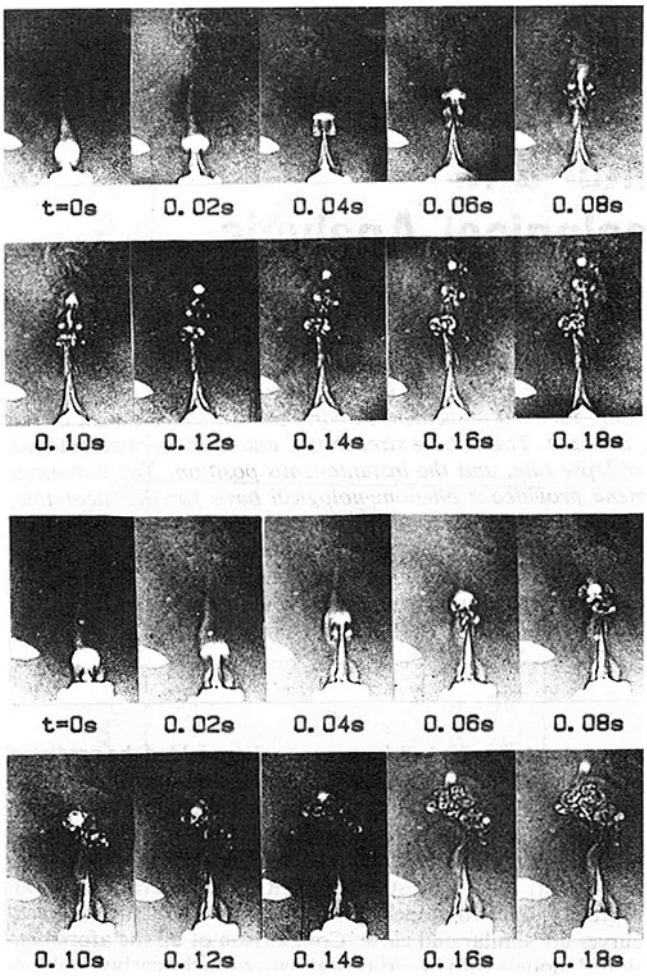

Fig. 1 Shadowgraphs of a freon-113 bubble condensing in water in two experiments

celeration period. Deceleration of the bubble follows. Vortices of the wake move forward and hinder the upper surface of the bubble, and a thermal cloud envelops the bubble. As the collapse process is completed the droplet moves through the cloud of vortices and away from it.

The thermal boundary layer and the thermal wake shadowgraphed in Fig. 1 relate also to a viscous boundary layer, and a viscous wake as later experimentally confirmed by entrainment of colored water (Kalman et al., 1987). These visualization studies led to an understanding of the nature of the thermal resistance outside the collapsing bubble.

The thermal resistance inside the bubble was explored also by visualization techniques. The vapor bubble appeared spherical, eccentrically positioned, and adhering to the top of the collapsing bubble. The condensate film was very thin away from the front stagnation point, and considerably thicker farther downstream (Kalman et al., 1987).

All these visualized phenomena served as a basis for the postulations of the model. The physical picture is more complex, therefore approximations had to be made by reasonable simplification of the assumptions. The model of the collapse process was postulated as follows:

- The bubble is spherical. An equivalent radius is used in zones where shape oscillations and distortion take place.
- The sphere of vapor is eccentrically positioned in the bubble at the top. The condensate film adheres to the surface of the bubble. It does not flow or drain. It grows in thickness as the collapse proceeds.
- The initial bubble consists of saturated vapor and noncondensible gases. The noncondensibles are uniformly distributed in the vapor.
- The bubble velocity is translational and time dependent. The drag coefficient may vary with size and shape.
- The liquid surrounding the bubble is immiscible, quiescent, infinite, and of constant temperature.
- A viscous liquid surrounds the bubble. A nonslip condition is assumed at the bubble surface. The flow field is potential outside the viscous boundary layer.
- A thermal boundary layer extends from the bubble surface into the viscous layer. The temperature field outside the thermal boundary layer is quasi-steady, i.e., it instantaneously adjusts to the shape and size of the collapsing bubble.
- In the acceleration zone a viscous boundary layer extends over the upper surface of the bubble, and a wake over the rear surface. In the deceleration zone the bubble settles into its wake. An "envelope" of vortices concentrically surrounds the bubble. The flow field outside the "envelope" is preserved.
- Collapse of the bubble is completed within the "envelope" of vortices.

Nomenclature

C_D = drag coefficient
CFW = condensation of freon in water
c_p = specific heat, J/kg•°C
D_H = horizontal diameter, m
D_V = vertical diameter, m
f = frequency of injection, bubble/s
g = gravitational acceleration, m/s^2
h = convection heat transfer coefficient, W/m^2•°C
H = position above the initial bubble, m
h_{fg} = heat of vaporization, J/kg
k = thermal conductivity, W/m•°C
m_v = mass of vapor
q = rate of heat transfer, W
R = radius of bubble, m
R_0 = initial radius, m
R_v = radius of vapor sphere
$\bar{R}$ = normalized radius = R/R_0
r = radius from the center of vapor sphere, m
T = temperature, °C
T_i = temperature at condensate–liquid interface, °C
T_s = saturation temperature, °C
T_s^* = saturation temperature at vapor partial pressure, °C
T_∞ = temperature of continuous liquid, °C
t = time, s
t_f = time at termination of collapse, s
t_m = time at maximum velocity of bubble, s
U_∞ = instantaneous velocity of rise, m/s
ΔT = temperature difference = $(T_s - T_\infty)$, °C
Nu = Nusselt number = $(2R \cdot h/k_l)$
Pr = Prandtl number = $(\mu \cdot c_p/k)_l$
Re = Reynolds number = $(2R \cdot U_\infty \cdot \rho_l/\mu_l)$
α = fraction of noncondensibles
γ = defined by equation (15)
δ_f = thickness of condensate, m
θ = angle from front stagnation point of vapor sphere
μ = viscosity, kg/m•s
ρ = density, kg/m^3
ϕ_s = normalized saturation temperature, equation (11)

Subscripts

f = condensate
l = continuous liquid
v = vapor

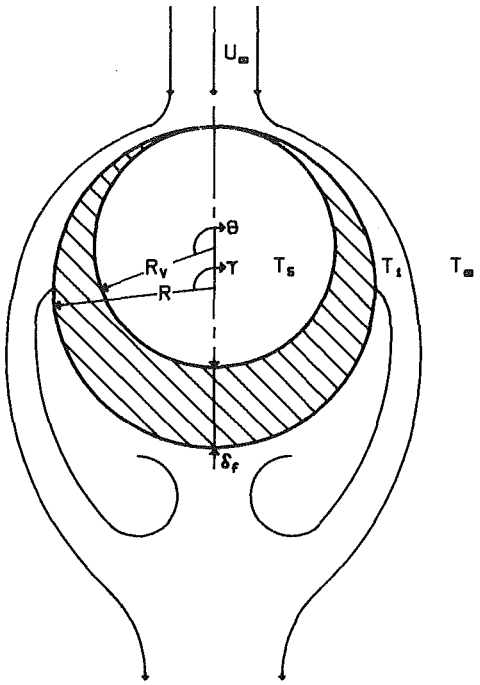

Fig. 2 Schematic representation of the model in acceleration

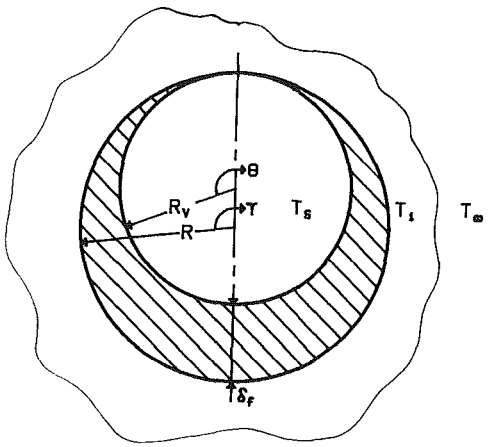

Fig. 3 Schematic representation of the model in deceleration

Based on these postulations the model is depicted in Figs. 2 and 3 for the accelerating and decelerating bubble, respectively. The collapse process, the instantaneous velocity curve, and the path of the bubble are schematically presented in Fig. 4. Further description of the process is made along with the formulations.

The quantitative formulations follow the postulations stated above. The rate of latent heat released by the condensing vapor is

$$q = -h_{fg} \frac{dm_v}{dt} \tag{1}$$

For $\rho_f >> \rho_v$, equation (1) may be expressed as

$$q = -4\pi R^2 \cdot \rho_v \cdot h_{fg} \cdot \frac{dR}{dt} \tag{2}$$

The condensed vapor forms the condensate in the bubble. The condensate film in both the accelerating and decelerating bubble is considered to envelop the sphere of vapor eccentrically. As the vapor sphere collapses, its isothermal boundary moves in. Solution of such a problem has to be handled by a tedious

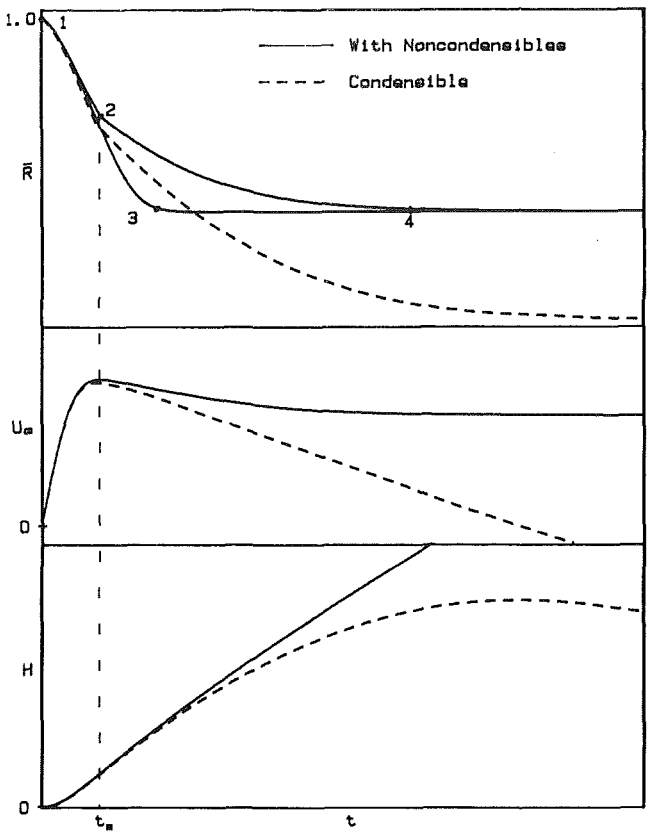

Fig. 4 Schematic representation of the collape process of an accelerating-decelerating bubble

numerical procedure. Therefore a shortcut has been taken, assuming a quasi-steady conduction across the condensate. It is also assumed that the centers of the eccentric spheres are close, and the radii of the inner sphere approximate also the direction of the temperature gradients in the outer sphere of condensate. The uncertainties of the physical process are in this case much greater than the error introduced by the simplified geometric procedure.

Thus, the heat released in condensation is transferred across the condensate film by conduction. At an angle θ the rate is

$$dq = -k_f \cdot (2\pi r^2 \cdot \sin\theta d\theta) \cdot \frac{dT}{dr} \tag{3}$$

Integration of this equation with the boundary conditions

$$r = R_v \qquad T = T_s$$
$$r = R_v + \delta_f \qquad T = T_i \tag{4}$$

yields

$$dq = \frac{2\pi k \cdot \sin\theta d\theta}{\left[\frac{1}{R_v} - \frac{1}{R_v + \delta_f}\right]} (T_s - T_i) \tag{5}$$

Then the heat is transferred from the condensate to the cooling liquid by convection

$$dq = h \cdot (T_i - T_\infty) \cdot 2\pi (R_v + \delta_f)^2 \sin\theta d\theta \tag{6}$$

Substituting Nu for h, combining equations (5) and (6), and integrating provides the instantaneous heat transfer rate from the bubble

$$q = \int_0^\pi \frac{\pi R_0 (T_s - T_\infty) \sin\theta d\theta}{\frac{1}{2k_f}\left[\frac{1}{\bar{R}_v} - \frac{1}{(\bar{R}_v + \bar{\delta}_f)}\right] + \frac{\bar{R}}{\mathrm{Nu} \cdot k_l \cdot (\bar{R}_v + \bar{\delta}_f)^2}} \tag{7}$$

where $\bar{\delta}_f = \delta_f/R_0$ and $\bar{R}_v = R_v/R_0$. By combining equations (2) and (7) the rate of bubble collapse is obtained

$$\frac{d\bar{R}}{dt} = -\frac{(T_s - T_\infty)}{4R_0^2 \cdot \rho_v \cdot h_{fg} \cdot \bar{R}^2}$$

$$\cdot \int_0^\pi \frac{\sin\theta d\theta}{\frac{1}{2k_f}\left[\frac{1}{\bar{R}_v} - \frac{1}{\bar{R}_v + \bar{\delta}_f}\right] + \frac{\bar{R}}{\mathrm{Nu} \cdot k_l (\bar{R}_v + \bar{\delta}_f)^2}} \tag{8}$$

For $\bar{R}_v$, we may substitute

$$\bar{R}_v = \left[\frac{\bar{R}^3 - \frac{\rho_v}{\rho_f}}{1 - \frac{\rho_v}{\rho_f}}\right]^{1/3} \tag{9}$$

and for $\bar{\delta}_f$, by geometric considerations

$$\bar{\delta}_f = [\bar{R}_v(2\bar{R} - \bar{R}_v) + (\bar{R} - \bar{R}_v)^2(\cos\theta)^2]^{1/2} - (\bar{R} - \bar{R}_v)\cos\theta - \bar{R}_v \tag{10}$$

In the presence of noncondensibles the apparent saturation temperature T_s^* has to be used instead of T_s. The apparent temperature driving force $(T_s^* - T_\infty)$ has been previously applied in the dimensionless form (Lerner and Letan, 1985; Jacobs and Major, 1982; Isenberg and Sideman, 1970)

$$\phi_s = \frac{T_s^* - T_\infty}{T_s - T_\infty} = \frac{\bar{R}^3 - \bar{R}_f^3}{\bar{R}^3 - \frac{\rho_v}{\rho_f}} \tag{11}$$

Substituting $(T_s^* - T_\infty)$ of equation (11) for $(T_s - T_\infty)$ in equation (6) yields

$$\frac{d\bar{R}}{dt} = -\frac{(T_s - T_\infty)}{4 \cdot \rho_v \cdot h_{fg}} \left[\frac{\bar{R}^3 - \bar{R}_f^3}{\bar{R}^3 - (\rho_v/\rho_f)}\right] \frac{1}{R_0^2 \cdot \bar{R}^2}$$

$$\cdot \int_0^\pi \frac{\sin\theta d\theta}{\frac{1}{2k_f} \cdot \left[\frac{1}{\bar{R}_v} - \frac{1}{(\bar{R}_v + \bar{\delta}_f)}\right] + \frac{\bar{R}}{\mathrm{Nu} \cdot k_l \cdot (\bar{R}_v + \bar{\delta}_f)^2}} \tag{12}$$

The fraction of noncondensibles affects the temperature driving force in the process by determining the apparent temperature of saturation. In this way the size of the bubble in the process, and the final size of the bubble, are also affected. The final bubble-droplet may move up, or fall down, the direction being determined by the residue of condensibles/noncondensibles. In Fig. 4 the collapse processes of bubbles with and without noncondensibles are compared: curve 1–2–4 against curve 1–2–CC (completely condensible). In the last case the velocity (CC) and path (CC) of the denser droplet are reversed. The fraction of noncondensibles is experimentally obtained from the measured initial and final radii (R_0 and R_f) of the bubble in the same way as calculated previously (Jacobs et al., 1978; Isenberg et al., 1970).

The thermal resistance outside the bubble, namely the convection over the bubble, was expressed as the convection heat transfer coefficient h in equation (6). Then Nu was substituted in equation (7) for h. In our previous work (Lerner et al, 1984) a mobile boundary layer was used over the accelerating bubble, and a conductive "envelope" over the decelerating bubble. The "mobility" was heuristically assigned to the bubble surface (Lerner and Letan, 1985). The "envelope" thickness was calculated using the wake volume correlated in the literature, and preserving the same volume for the "envelope" into which the bubble has settled concentrically. That approach, to be illustated and discussed later, has been presently abandoned for the more conventional approach.

The model of Lee and Barrow (1968) is used for convection over the accelerating bubble. Two regions are distinguished. Over the upper surface

$$0 < \gamma < \pi/2 \qquad \mathrm{Nu}_x = 0.898\,\mathrm{Re}^{1/2} \frac{\sin^4\gamma}{\left[\int_0^\gamma \sin^7\gamma d\gamma\right]^{1/2}} \tag{13}$$

and over the rear surface, in the wake

$$\frac{\pi}{2} < \gamma < \pi \qquad \mathrm{Nu} = 0.0447\,\mathrm{Re}^{0.78}\,\mathrm{Pr}^{1/3} \tag{14}$$

where

$$\gamma = \sin^{-1}\left[\frac{\bar{R}_v + \bar{\delta}_f}{\bar{R}} \cdot \sin\theta\right] \tag{15}$$

Equations (13) and (14) are applied to the accelerating bubble, namely in the time interval $0 \le t \le t_m$, where t_m corresponds to the instant at which the maximum velocity is reached (Fig. 4).

As deceleration commences, $t > t_m$, the bubble settles into its wake, and the vorticular envelope replaces the upper convective layer. Thus, the wake vortices envelop the whole surface, and equation (14) is applied in the range of

$$0 < \gamma < \pi$$

The Reynolds number in equations (13) and (14) involves the instantaneous velocity applied as previously (Lerner and Letan, 1985)

$$\frac{dU_\infty}{dt} = \frac{(\bar{R}^3 \cdot \rho_l - \rho_v) \cdot R_0 \cdot g - (3/8) \cdot \bar{R}^2 \cdot \rho_l \cdot U_\infty^2 \cdot C_D}{(\rho_v + \rho_l \cdot \bar{R}^3/2) \cdot R_0} \tag{16}$$

The drag coefficient C_D of a rigid sphere

$$C_D = \frac{24}{\mathrm{Re}} + \frac{6}{1 + \mathrm{Re}^{1/2}} + 0.4 \tag{17}$$

as well as the drag coefficients of a spheroid and a distorted droplet were previously examined (Lerner and Letan, 1985) for their effects on bubble velocity (equation (16)). Then, the velocity relation integrated with respect to time t yielded the path of the collapsing bubble

$$H = \int_0^t u_\infty dt \tag{18}$$

The path $H(t)$ as well as the collapse curve $\bar{R}(t)$ can be compared with measurements to examine the validity of the postulations.

Experimental Apparatus

Condensation experiments were conducted with bubbles of freon-113 in water. The process took place in a vertical square column, 10 × 10 cm in cross section, and 60 cm high. The walls of the column were made of glass plates. Beneath the glass column was installed a vapor generator made of a brass cylinder. It was filled with water, electrically heated, and thermostatically controlled. A copper tube passed through the vapor generator to the bottom of the glass column, and into the injection nozzle. Nozzles of 3 mm and 5 mm in diameter were used. The glass column was filled with water at a prescribed temperature, and open to the atmosphere. Five iron-constantan thermocouples were installed in the column, the copper tube, and the vapor generator. The bubble collapse process was photographically recorded in two ways: by shadowgraphing and by direct filming.

The shadowgraphing was used for visualization of the thermal boundary layer formation, the wake, and movement of

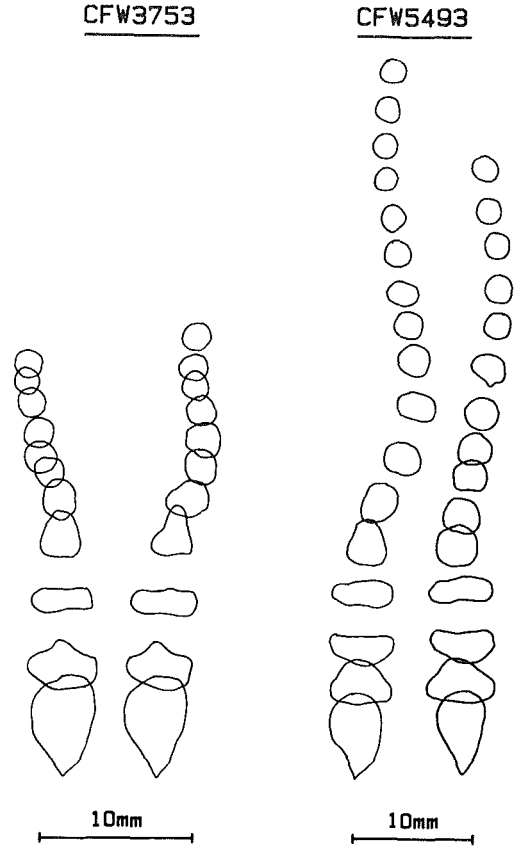

Fig. 5 Screen-tracing of a videotaped collapse of four freon-113 bubbles in water

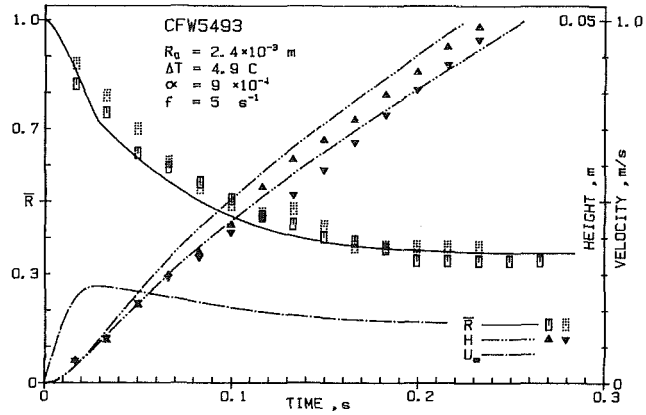

Fig. 6 Condensation of freon-113 bubbles in water: comparison of the model with experiment No. CFW5493

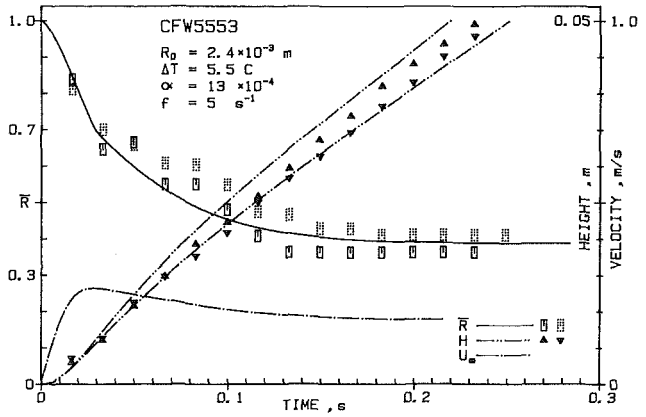

Fig. 7 Condensation of freon-113 bubbles in water: comparison of the model with experiment No. CFW5553

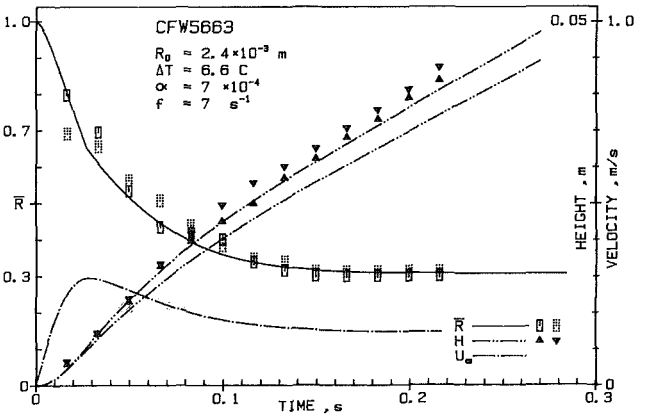

Fig. 8 Condensation of freon-113 bubbles in water: comparison of the model with experiment No. CFW5663

vortices. The results, although qualitative, provided an insight into the phenomena governing the process.

The direct filming of the bubble collapse process was applied to record the bubble size, bubble position, and the respective time lapse. These measurements gave quantitative information on the collapse rate, bubble velocity, and its path.

The shadowgraphing system consisted of a monochromatic light, lenses, a screen, and a cine-camera. The light source was a helium–neon laser, made by Spectra Physics, model 120, with a 0.65 mm beam diameter, 632.8 nm wavelength, and a power of 5 mW. Three lenses were used to illuminate uniformly the path of bubbles in the glass column. A screen was placed across the column to reflect the projected images into the camera. The cine-camera employed was Bolex H16 EBM Electric, Kern Vario-Switar 1:1, 9, f = 16 ÷ 100. Eastman Kodak 4-x Negative Film 7224 was used. The images projected on the screen were filmed at the speed of 50 frames per second, namely, photographs were taken at intervals of 0.02 s, as illustrated in Fig. 1.

The direct filming system consisted of a television camera, a video motion analyzer, a video timer, and a back illumination. The collapse of bubbles was filmed directly in the test column. A Sony Rotary Shutter camera RSC-1050 was employed. The rotary shutter enabled a movement analysis at the speed of 1/500 s. A Video Motion Analyzer SVM-1010 provided the combination of a television screen and a recording system. Pictures were recorded on a rotary magnetic disk, and then projected on the screen at the speed of 60 frames per second without blurring. Each projected picture on the screen could be halted to make the measurements of bubble diameter and position. A video timer VTG-33 connected to the camera exposed on a counter the time related to each picture. The time lapse between succeeding frames was used in calculations of the rate of collapse and bubble velocity. Illumination for the filming was provided at the back of the glass column.

The uncertainty in measurements corresponds to timing, bubble size, and position. For timing, the bubbles were videotaped at a frequency of 60 s^{-1}. The images projected on the screen were timed, and the time was digitally exposed with an accuracy of 0.01 s. The time lapse between images corresponded to 1/60 = 0.0166 s. To overcome that difficulty at least ten images were counted noting the time lapse of their appearance. That provided an accuracy of 0.001 s. The width of the graphic symbols in Figs. 6–16 corresponds to 0.004 s, i.e., the indicated error is four times larger than the error in timing.

To measure the radius of the bubble, the horizontal and ver-

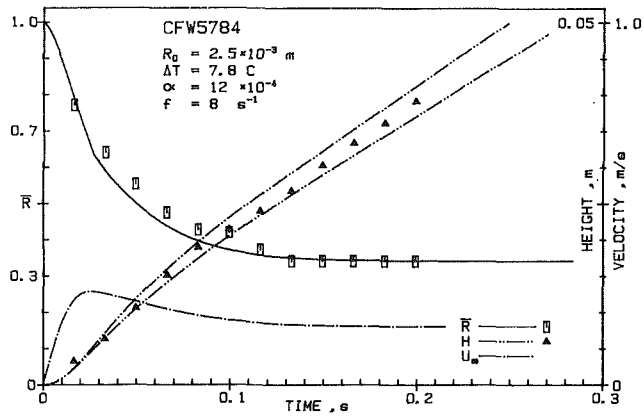

Fig. 9 Condensation of freon-113 bubbles in water: comparison of the model with experiment No. CFW5784

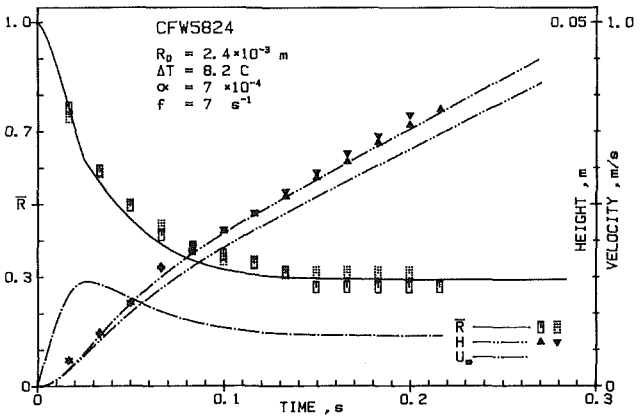

Fig. 10 Condensation of freon-113 bubbles in water: comparison of the model with experiment No. CFW5824

tical diameters of the bubble images projected on the screen were measured on a scale enlarged about four times actual size. The error in length measurements on the screen was about 0.5 mm, i.e., 0.12 mm of the actual diameter, or 0.06 mm of the actual radius. The error expressed in nondimensional form is $\Delta\bar{R}$ = 0.025–0.030 for R_0 = 2.0–2.4 mm. The height of the graphic symbols in Figs. 6–16 is also $\Delta\bar{R}$ = 0.030. Thus, the size of the graphic "point" respresents also the uncertainty in measurement.

For the position of the bubble, the height of any bubble along its path is measured from the position of the initial bubble. The error in length measurements is again 0.5 mm on the enlarged scale, and 0.12 mm on the actual scale. The graphic symbols correspond to a height of 1.15 mm, and are therefore ten times larger than the actual experimental error in bubble position.

Results and Discussion

The extensive visualization studies of freon-113 bubbles condensing in water included shadowgraphing (Fig. 1), color entrainment in wakes (Kalman et al., 1986), visualization of condensate (Kalman et al., 1987), and screen-tracing (Fig. 5). The color-entrainment experiments were conducted to outline and complement the flow patterns observed in shadowgraphs (Fig. 1). Visualization of the condensate shape was performed to ascertain the validity of the postulated envelope model (Kalman, 1984).

The screen-tracing presented in Fig. 5 pertains to two pairs of bubbles, each pair videotaped at the same experimental conditions. A train of images is traced for each bubble where between two successive images the time lapse corresponds to 0.0167 s (1/60 s). The "train" outlines the shape oscillations, the spacing between images, the position of a bubble at any instant both vertically and horizontally. As illustrated in Fig. 5, the initially formed bubble is of a prolate pear shape. It oscillates to an oblate shape, and is again expanded to a prolate shape. As the bubble decreases in size, it gradually shapes into a sphere. On detachment the bubble velocity is low, and two first images almost overlap. As the bubble accelerates, its velocity increases, and the next two images are considerably separated (CFW 3753). Then the bubble decelerates, and the images are again closely spaced, and overlapping.

The conventional equation (16) is used to predict the instantaneous velocity of the bubble, its maximum, and the terminal velocity obtained on termination of the collapse process. The predicted curve generally fits the observed path (Figs. 1, 6–16). However, the "train" of traced images (Fig. 5) shows also a minimum in the deceleration zone, and then again a higher terminal velocity. These deviations indicate that the conventional equation of instantaneous velocity may not represent or account for all the physical phenomena encountered in the process. The shadowgraphed wake phenomena (Fig. 1) illustrate qualitatively how and why these deviations may occur. The path obtained by integration of the instantaneous velocity relates to the vertical position only. It does not account for the oscillations due to wake shedding, or to phenomena associated with the bubble settling into its wake.

The shadowgraphs (Fig. 1) as well as the color entrainment studies (Kalman et al., 1987) have shown the two distinct zones of collapse. The measured instantaneous radii of the collapsing bubble have quantitatively validated the visualized phenomena. The two zones are schematically depicted by curve 1–2–4 in Fig. 4. Such curves are typical of the collapse process, and repeatedly shown in Figs. 6–16. The initial slope of the collapse rate is steep. In the vicinity of maximum velocity the slope abruptly changes to a slower decline. The break point in the curve was previously curve-fitted (Lerner et al., 1984) with the experimental points in the deceleration zone. In the present analysis the break point was chosen at the point of maximum velocity of the "rigid sphere." That, of course, yielded a larger deviation between the predicted curves and the experimental measurements, as illustrated in Figs. 6–16.

The collapse rate in the zones of acceleration (curve 1–2, Fig. 4) is presently described by the convective boundary layer and a wake over a rigid surface of the bubble (Fig. 2). Inside the bubble the condensate film of eccentric shape is supposed to adhere to the bubble surface. The last assumption is rather questionable, because the screen-traced images in Fig. 5 expose vigorous shape oscillations of the accelerating bubble, and consequently a mobile surface. However, the assumption of condensate adherence in that zone may be valid because of the interfacial forces across the very thin film. Thus, the collapse of the accelerating bubble is predicted by the model of an eccentrically shaped condensate film adhering inside the bubble, and by the conventional convective model of a boundary layer and wake outside the bubble.

In the zone of deceleration the bubble settles into its wake as visualized in Fig. 1. The collapse rate in that zone (curve 2–4 in Fig. 4) is described by the "envelope model" (Fig. 3), namely by a vorticular envelope outside the bubble, and the eccentric adhering condensate inside the bubble (Kalman, 1984). The full envelopment of the bubble is quantitatively formulated to take place instantaneously at the point of maximum velocity. Such postulation is a simplification of the physical process which commences at the point of maximum velocity, and extends over a time interval. The assumption concerning the shape of the condensate has been visually validated (Kalman et al., 1987). The adherence of the condensate to the surface of the decelerating bubble seems to be obvious. There are no shape oscillations; the surface of the bubble appears stabilized, gradually shaping into a sphere. On the outside, the

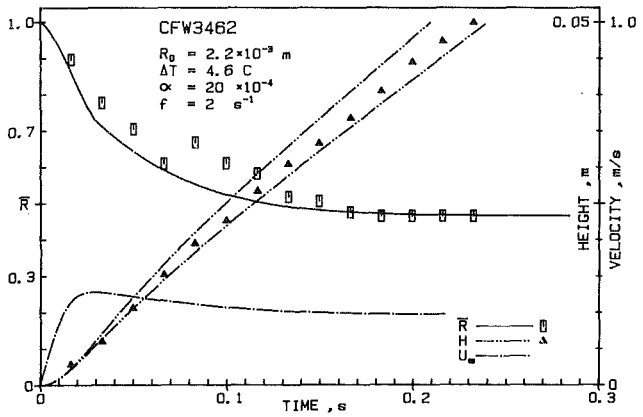

Fig. 11 Condensation of freon-113 bubbles in water: comparison of the model with experiment No. CFW3462

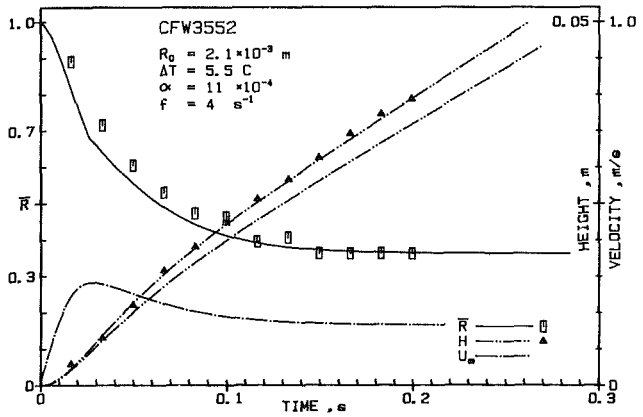

Fig. 12 Condensation of freon-113 bubbles in water: comparison of the model with experiment No. CFW3552

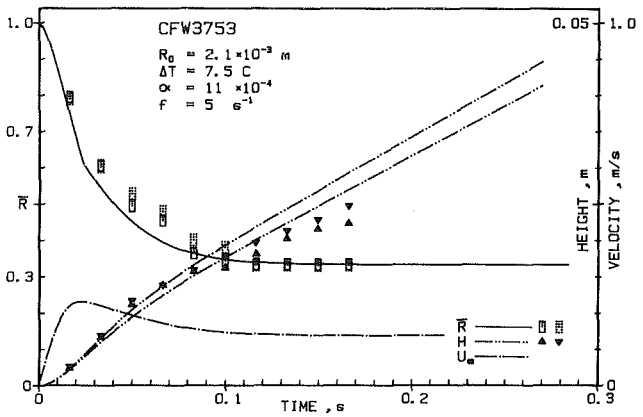

Fig. 13 Condensation of freon-113 bubbles in water: comparison of the model with experiment No. CFW3753

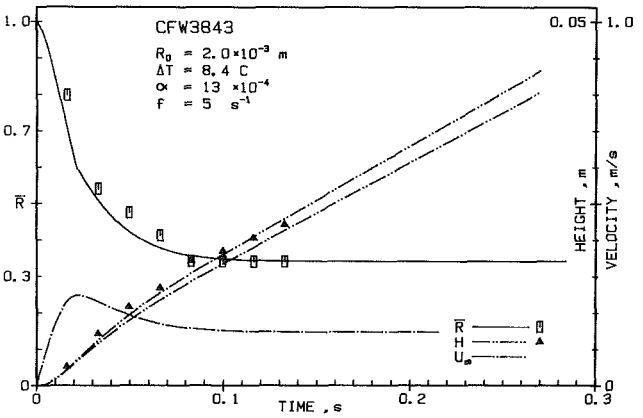

Fig. 14 Condensation of freon-113 bubbles in water: comparison of the model with experiment No. CFW3843

bubble is enveloped in a vorticular envelope. There is no unidirectional flow to motivate the surface. Therefore, it is physically feasible that the bubble surface is immobile in that zone, and the condensate adheres to the surface. Physically, there has to be some draining in the condensate layer due to the gravitational forces which preserve the eccentric upright position of the vapor sphere in the bubble. However, the condensate movement may be slow and of negligible effect on the thickness of the film within the present experimental range of temperature difference (Ja < 10). Thus, the collapse of the decelerating bubble is predicted by the model of an eccentrically shaped condensate adhering inside the bubble, and by the vorticular "envelope" model outside the bubble.

These two models, combined at the point of maximum velocity, are employed to predict the collapse rates in the experiments presented in Figs. 6–16.

The experimental program involved several parameters: temperature difference, fraction of noncondensibles, frequency of injection, and initial bubble size. Numerous experiments were conducted varying one of the parameters and fixing the others.

The experiments presented in this work (Figs. 5–16) were conducted at injection frequencies of 2–8 bubble/s. The initial radii were 2.4×10^{-3} m and $2.0 - 2.2 \times 10^{-3}$ m obtained in nozzles of 5×10^{-3} m and 3×10^{-3} m, respectively. The temperature difference experimented with ranged within 4.5–8.5°C, and the fractions of noncondensibles corresponded to $6 - 20 \times 10^{-4}$.

The injection frequency of $f \leq 8$ bubbles/s is below the frequency of interaction (Lerner and Letan, 1985). Thus, in that range the injection frequency does not serve as a parameter.

The measurements of time-dependent bubble size presented by Lerner et al. (1984) were repeated again by Kalman (1986), including measurements of path and screen-tracing of each bubble. Some of the techniques previously employed were further improved, and refined. Particular attention was paid to the initial size of the bubble, and to the instant of detachment. Only bubbles videotaped on detachment were analyzed. The repeated new experimental data are illustrated in Figs. 5–16. Some of these figures show experimental points pertaining to one or two bubbles measured at the same conditions.

The instantaneous radius of each bubble was calculated using the measured horizontal and vertical diameters

$$R = \frac{1}{2} (D_H^2 D_V)^{1/3} \tag{19}$$

The dimensionless form of the radius was plotted

$$\bar{R} = \left[\frac{D_H^2 \cdot D_V}{(D_H^2 \cdot D_V)_0} \right]^{1/3} \tag{20}$$

The uncertainty, in length measurements $\bar{R}$, was graphically represented by the height of the symbols. Another uncertainty, not indicated graphically, relates to the value of the equivalent radius, based on the assumption of horizontal symmetry and ellipsoidal shape. As illustrated in Fig. 5, the initial shape of the bubble is irregular; however as collapse proceeds the bubble reshapes, first into an ellipsoid, and then into a sphere.

Each of the experiments illustrated in Figs. 6–14 shows the measured radii, and the measured heights of the collapsing bubble. The theoretical curves of collapse, velocity of the sphere, and two path curves are drawn for each experiment. The point of maximum velocity of a sphere t_m is used for

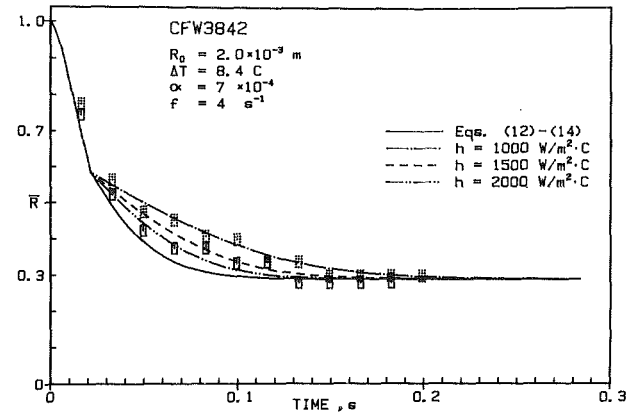

Fig. 15 Comparison of the model at four convection rates in the "envelope" with an experiment of two freon-113 bubbles condensing in water

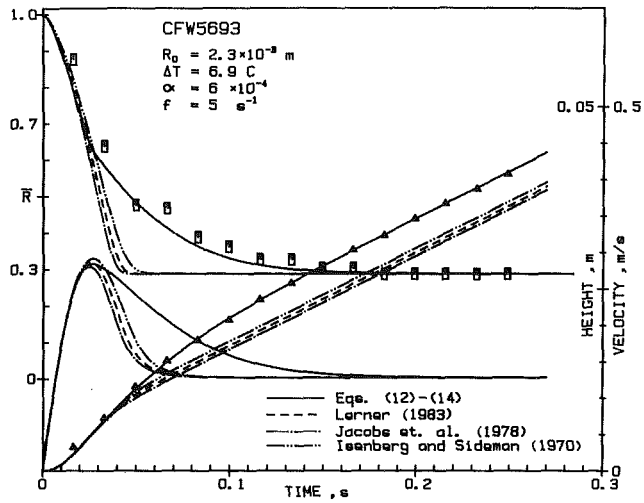

Fig. 16 Condensation of freon-113 bubbles in water: comparison of theoretical models with an experiment

distinction between the zones of acceleration and deceleration in the process of collapse.

Velocities of a sphere and of a spheroid were used for the two path curves (equation (18)), which are graphically illustrated. In the zone of acceleration the predicted curves of the sphere and the spheroid overlap and agree with the experimental results. In the zone of deceleration the experimental points are mostly found between the path curves or on the curves. In some experiments (Figs. 8 and 13) a considerable deviation is apparent. That may be associated with the irregular patterns of the bubble envelopment in its wake, a phenomenon not accounted for in the equation of velocity.

In the size range $R_0 = 2.0\text{–}2.4 \times 10^{-3}$ m there are no second-order effects except for those incorporated in the formulations. However it may be expected that bubbles 2–3 times larger exhibit surface mobility in the deceleration zone as well, inducing flow in the condensate film, and affecting the "envelope." On the other hand, bubbles much smaller than those experimented with may also exhibit their characteristic features related to their flow regime. In such cases the theoretical models have to be reformulated and adapted to the physical phenomena.

The temperature difference of 4.5–8.5°C appears to be satisfactorily expressed in the theoretical model. In our present experimental range the Jacob number is smaller than 10, and the heat transfer rates control the process of collapse. At much larger temperature differences, other effects not accounted for in the present formulations may become dominant.

The fraction of noncondensibles in the bubble controls the apparent saturation temperature T_s^* in the bubble. This way the presence of noncondensibles reduces the temperature driving force which affects the rate of collapse, the size of the bubble, and termination of the process. The fraction of noncondensibles presently experimented with was in the range of $6\text{–}20 \times 10^{-4}$, e.g., below 0.2 percent. These concentrations are very low and presumably do not affect the thermal resistance inside the bubble. At much higher concentrations the thermal resistance may become affected, and will have to be accounted for in the model.

The rate of convection over the bubble is also a variable to be analyzed. In our present model we have used the relations derived and correlated by Lee and Barrow (1968). In the zone of acceleration the application follows exactly the original application. In the zone of deceleration, however, the vorticular envelope all over the bubble is assmed to be as convective as the wake behind a sphere (equation (14)). That is, of course, an approximation. The other ultimate way to cope with such situations is to assume that the vorticular envelope performs as a conductive layer (Lerner et al., 1984).

The wake approximation yields a convection heat transfer coefficient which ranges within 4000–2000 W/m²•°C in the zone of deceleration. The conductive layer approximation leads to a value of about 1000 W/m²•°C. The actual rate is to be found between these extremes. An example of that problem is illustrated in Fig. 15, where two collapsing bubbles were measured at the same conditions. The convection over the bubbles is calculated using equations (13) and (14) for the accelerating bubble, and equation (14) for the decelerating bubble. The decelerating zone extends from $t_m = 0.02$ s to about $t_f = 0.15$ s. The convection heat transfer coefficient varies with the bubble size and velocity yielding $h = 3600$ W/m²•°C at $t_m = 0.02$ s, and $h = 2500$ W/m²•°C at $t_f = 0.15$ s. Additionally to the "wake convection" (equation (14)), the collapse model was calculated using three other convection heat transfer coefficients of constant value, $h = 1000$, 1500, 2000 W/m²•°C.

The four curves are drawn in the deceleration zone in Fig. 15. The figure shows that one bubble obeys the "wake convection" very closely, while the other bubble is closer to the curves obtained at a convection of 1000–1500 W/m²•°C.

The very different behavior of the two bubbles may be attributed to the irregular pattern of bubble envelopment in the wake. Examining again the experiments presented in Figs. 6–14 shows the "wake convection" usually provides a satisfactory description of the convection in the "envelope."

The other models of collapse are also compared with the present work in Fig. 16. The models of Jacobs (Jacobs et al., 1978), Sideman (Isenberg et al., 1970), and Lerner (at $n=3$, Lerner and Letan, 1985) overlap the present curve in the acceleration zone, as shown in Fig. 16. Beyond the point of maximum velocity ($t > t_m$) the three models continue the collapse rate at the same steep slope, and predict termination of the process much too soon. In experiment No. CFW5693, illustrated in Fig. 16, the termination is predicted by the three models at $t \simeq 0.04\text{–}0.06$ s as compared to the experimental value of 0.17 s. The "envelope" model, on the other hand, appears to describe the collapse process very closely in the zone of deceleration.

In calculations of velocity the conventional drag coefficient of a rigid sphere was applied to the four models. The velocity curves and the integrated path curves of the four models are shown in Fig. 16. The velocity affects the path, but has little effect on the collapse rate. However the radius of the bubble significantly affects the velocity curve.

The four models, conceptually so different, yield the same collapse rates for an accelerating bubble. These results may be attributed to the high rates of convection, and the very thin film of condensate. The significant difference between the

models appears in the deceleration zone, where the convection rate over the bubble is drastically reduced with the settling of the bubble into its vorticular "envelope." At a later stage of collapse the thicker condensate film also contributes a substantial part to the overall thermal resistance of the bubble.

The model presented herein may be further improved and refined to describe more closely the physical phenomena governing the collapse process. Additional experimental data on convection rates in the vorticular envelope, the time needed to complete the envelopment of the bubble in its wake, and the velocity of the "enveloped" bubble, could certainly contribute to closer predictions of the collapse rate.

Conclusions

Accelerating-decelerating bubbles show two distinct zones of collapse. In acceleration, the rate of collapse is steep. In deceleration, it is abruptly decreased.

The theoretical model depicts a vapor sphere eccentrically positioned inside the bubble, and the condensate film adhering to the surface of the bubble.

Two models are used to represent the thermal resistance outside the bubble. A boundary layer and a wake over a rigid surface serve to predict the rate of collapse of the accelerating bubble. A vorticular "envelope" is used to describe the collapse of the decelerating bubble. The combined model postulated, on phenomenological arguments, agrees well with experimental results.

References

Clift, R., Grace, J. R., and Weber, M. E., 1978, *Bubbles, Drops and Particles*, Academic Press, New York, pp. 106–107.

Isenberg, J., and Sideman, S., 1970, "Direct Contact Heat Transfer With Change of Phase: Bubble Condensation in Immiscible Liquids," *International Journal of Heat and Mass Transfer*, Vol. 13, pp. 997–1011.

Isenberg, J., Moalem, D., and Sideman, S., 1970, "Direct Contact Heat Transfer With Change of Phase: Bubble Collapse With Translatory Motion in Single and Two-Phse Systems," *Proceedings, 4th International Heat Transfer Conference*, Vol. 5, B.2.5.

Jacobs, H. R., Fannar, H., and Beggs, G. C., 1978, "Collapse of a Bubble of Vapor in an Immiscible Liquid," *Proceedings, 6th International Heat Transfer Conference*, Vol. 2, pp. 383–388.

Jacobs, H. R., and Major, B. H., 1982, "The Effect of Noncondensible Gases on Bubble Condensation in an Immiscible Liquid," ASME JOURNAL OF HEAT TRANSFER, Vol. 104, pp. 487–492.

Kalman, H., 1984, "Condensation of Bubbles," Preparatory Report for Ph.D. Candidacy, Ben-Gurion University, Beer-Sheva.

Kalman, H., 1986, "Condensation of Bubbles," Report for Ph.D. Thesis, Ben-Gurion University, Beer-Sheva.

Kalman, H., Ullman, A., and Letan, R., 1986, "Dynamics of a Condensing Bubble in Zones of Time-Dependent Velocity," *Proceedings, 8th International Heat Transfer Conference*, Hemisphere, New York.

Kalman, H., Ullmann, A., and Letan, R., 1987, "Visualization Studies of a Freon-113 Bubble Condensing in Water," ASME JOURNAL OF HEAT TRANSFER, this issue.

Lee, K., and Barrow, H., 1968, "Transport Processes in Flow Around a Sphere With Particular Reference to the Transfer of Mass," *International Journal of Heat and Mass Transfer*, Vol. 11, pp. 1013–1026.

Lerner, Y., 1983, "Condensation of Bubbles," M.Sc. Thesis, Ben-Gurion University, Beer-Sheva, Israel.

Lerner, Y., and Letan, R., 1985, "Dynamics of Condensing Bubbles: Effects of Injection Frequency," ASME Paper No. 85-HT-47.

Lerner, Y., Kalman, H., and Letan, R., 1984, "Condensation of an Accelerating-Decelerating Bubble: Experimental and Phenomenological Analysis," *Basic Aspects of Two-Phae Flow and Heat Transfer*, Symp. Vol. HTD-34, 22nd National Heat Transfer Conference, Niagara Falls, NY, pp. 1–10.

Moalem-Maron, D., Sokolov, M., and Sideman, S., 1980, "A Closed Periodic Condensation-Evaporation Cycle of an Immiscible, Gravity Driven Bubble," *International Journal of Heat and Mass Transfer*, Vol. 23, pp. 1417–1423.

Journal of Heat Transfer

Technical Notes

This section contains shorter technical papers. These shorter papers will be subjected to the same review process as that for full papers.

Two Functions Used in the Analysis of Crossflow Exchangers, Regenerators, and Related Equipment

F. E. Romie[1]

Introduction

Two families of functions, which will be designated as $G_n(x, y)$ and $F_n(x, y)$, find use in the analysis of crossflow heat exchangers [1–6], regenerators [7–11], packed beds [12–14], the transient response of heat exchangers [15–19], and related problems [20–22]. Larsen [14] gives four place tables for G_{-1}, G_0, G_1, F_0, and $F_1(x, y)$ (x and y; 0, (1), 20). However, in many applications the values of the functions are required for larger values of the index n, larger values of x and y, and for both arguments negative. The dual purpose of this note is to summarize some properties of the functions and to indicate a rapid method of finding their numerical values.

The functions find use in the analysis of systems, such as heat exchangers, in which fluid flows in contact with a solid that can be considered to have zero thermal conductivity in the direction of fluid flow but infinite thermal conductivity for flow of heat into solid. The functions F_n and G_n, under these circumstances, are applicable if the entrance fluid temperature has a prescribed dependence on time or a prescribed distribution across the entrance plane or if the initial temperature of the fluid or solid has a prescribed axial distribution. The functions can also be used to describe the fluid and solid temperatures in, for example, nuclear reactors in which the heat generation rate in the solid has a prescribed axial distribution and/or variation with time. Generally it is required that the prescribed quantities be expressed as polynomials of the time or location coordinates. The listed references, particularly [9, 11, 17, 23, 24], give some examples of the use of the functions. Many possible applications have yet to be addressed.

The functions G_0 and F_0 are usually attributed to Anzelius [12] and Schumann [13] and might therefore be termed the Anzelius–Schumann functions. The functions G_n and $F_n(x, y)$, $n>0$, are n-times successive integrals of G_0 and $F_0(x, y)$ with respect to the second argument y. Either set of functions can be translated into the other but the translation of the G_n set into the F_n set is so direct (contrast equations (13) and (34)) that the G_n set can be considered to be the generating set. The functions F_n (V_{n+1} in their notation) have been described by Serov and Korol'kov [23] and a closely related set by Lach and Pieczka [24]. The functions G_n do not appear to have been previously described, particularly in regard to their utility in finding numerical values for both sets.

Differential Equations

The functions $G_n(x, y)$ and $F_n(x, y)$ satisfy two first-order partial differential equations

$$\frac{\partial G_n(x, y)}{\partial y} = F_n - G_n = -\frac{\partial F_n(x, y)}{\partial x} \tag{1}$$

For $n \geq 0$, $G_n(x, 0) = 0$ and $F_n(0, y) = y^n/n!$. Particular values are

$$G_n(0, y) = (-1)^n \left(\sum_{r=0}^{n} \frac{(-y)^r}{r!} - e^{-y} \right), \qquad n \geq -1 \tag{2}$$

and $F_0(x, 0) = e^{-x}$ but, for $n>0$, $F_n(x, 0) = 0$. G_n and F_n go to zero as n becomes large.

The solution of equations (1), with $n = 0$, appears to have been first given by Nusselt [1] although Brinkley [20] refers to a function similar to $F_0(x, y)$ originated by Laplace.

Derivative Functions

$$G_{-1}(x, y) = \frac{\partial G_0}{\partial y} = e^{-(x+y)} I_0(2\sqrt{xy}) \tag{3}$$

$$= e^{-(x+y)} \sum_{r=0}^{\infty} \frac{x^r}{r!} \frac{y^r}{r!} \tag{4}$$

$$F_{-1}(x, y) = \frac{\partial F_0}{\partial y} = \pm e^{-(x+y)} \left(\frac{x}{y} \right)^{1/2} I_1(2\sqrt{xy}) \tag{5}$$

$$= e^{-(x+y)} \sum_{r=0}^{\infty} \frac{x^{r+1}}{(r+1)!} \frac{y^r}{r!} \tag{6}$$

In equation (5) the plus sign is for both arguments positive, the negative sign for both arguments negative.

$$G_{-2}(x, y) = \frac{\partial G_{-1}}{\partial y} = F_{-1} - G_{-1} \tag{7}$$

Particular values of the derivative functions are: $G_{-1}(0, y) = e^{-y}$, $F_{-1}(0, y) = 0$, $G_{-1}(x, 0) = e^{-x}$, and $F_{-1}(x, 0) = xe^{-x}$.

The following equations can be found from equations (3) and (5)

$$G_{-1}(x, y) = e^{\frac{ax}{1-a} - ay} G_{-1}\left(\frac{x}{1-a}, y(1-a) \right) \tag{8}$$

$$= e^{\frac{ay}{1-a} - ax} G_{-1}\left(x(1-a), \frac{y}{(1-a)} \right) \tag{8a}$$

[1] Palos Verdes Estates, CA 90274; Mem. ASME.

Contributed by the Heat Transfer Division for publication in the JOURNAL OF HEAT TRANSFER. Manuscript received by the Heat Transfer Division December 7, 1984.

$$F_{-1}(x, y) = (1-a)e^{\frac{ax}{1-a}-ay} F_{-1}\left(\frac{x}{1-a}, y(1-a)\right) \quad (9)$$

$$= \frac{e^{\frac{ay}{1-a}-ax}}{(1-a)} F_{-1}\left(x(1-a), \frac{y}{1-a}\right) \quad (9a)$$

Series Expansions, $n \geq 0$

For all x and y,

$$G_n(x, y) = e^{-(x+y)} \sum_{r=0}^{\infty} \frac{y^{r+n+1}}{(r+n+1)!} \sum_{p=0}^{r} \frac{(n+r-p)!}{(r-p)!n!} \frac{x^p}{p!} \quad (10)$$

or, for x and y nonnegative numbers

$$G_n(x, y) = e^{-(x+y)} \sum_{r=n}^{\infty} \frac{r!}{(r-n)!n!} \left(\frac{y}{x}\right)^{\frac{r+1}{2}} I_{r+1}(2\sqrt{xy}) \quad (11)$$

and

$$G_n(-x, -y) = e^{x+y} \sum_{r=n}^{\infty} (-1)^{r+1} \frac{r!}{(r-n)!n!} \left(\frac{y}{x}\right)^{\frac{r+1}{2}} I_{r+1}(2\sqrt{xy}) \quad (12)$$

Equation (10) is given in [9] in which $G_n = K_n y^n/n!$. Equation (11) can be found from [23] using, from equation (1), $G_n = e^{-x}\, \partial/\partial x(e^x F_n)$. Series expansions for $F_n(x, y)$ can be found, if desired, by noting from equation (1) that $F_n = e^{-y}\, \partial/\partial y\, (e^y G_n)$.

All following equations are for all n unless otherwise specified. However, for negative indices only F_{-1}, G_{-1}, and G_{-2} have been found to be useful and have therefore been defined.

Recurrence Relations

$$F_n(x, y) = G_n(x, y) + G_{n-1}(x, y) \quad (13)$$

$$G_{n+1}(x, y) = \frac{1}{n+1}\Big[(y-x-1-2n)\, G_n + (2y-n)G_{n-1} + yG_{n-2}\Big], \quad n \geq 0 \quad (14)$$

Equations (14) and (16) can be found from a recurrence equation in F_n given by Serov and Korol'kov [23].

Derivatives

$$\frac{\partial G_n(x, y)}{\partial y} = G_{n-1}(x, y) = -\frac{\partial F_n(x, y)}{\partial x} \quad (15)$$

$$\frac{\partial G_n(x, y)}{\partial x} = \frac{1}{x}\Big[nF_n(x, y) - yF_{n-1}(x, y)\Big], \quad n \geq 0 \quad (16)$$

$$\frac{\partial F_n(x, y)}{\partial y} = F_{n-1}(x, y) \quad (17)$$

Integrals ($a \neq 0, 1$)

$$\int_0^x G_n(t, y)dt = -F_{n+1}(x, y) + F_{n+1}(0, y) \quad (18)$$

$$\int_0^x e^t G_n(t, y)dt = e^x F_n(x, y) - F_n(0, y) \quad (19)$$

$$\int_0^x e^{at} G_n(t, y)dt = \frac{1}{a}\left(\frac{1-a}{a}\right)^n \Big[e^{\frac{ay}{1-a}}\left(1 - F_0\left(x(1-a), \frac{y}{1-a}\right)\right) + e^{ax} \sum_{r=0}^{n} \left(\frac{a}{1-a}\right)^r F_r(x, y) - \sum_{r=0}^{n} \left(\frac{a}{1-a}\right)^r F_r(0, y)\Big], \quad n \geq -1 \quad (20)$$

$$\int_0^y G_n(x, t)dt = G_{n+1}(x, y) - G_{n+1}(x, 0) \quad (21)$$

$$\int_0^y e^t G_n(x, t)dt = (-1)^n e^y \Big[\sum_{r=0}^{n} (-1)^r G_r(x, y) - \frac{y}{x} F_{-1}(x, y)\Big], \quad n \geq -1 \quad (22)$$

$$\int_0^y e^{at} G_n(x, t)dt = \frac{(-1)^{n+1}}{a^{n+1}}\Big[\frac{e^{\frac{ax}{1-a}}}{(1-a)} G_0\left(\frac{x}{1-a}, y(1-a)\right) - e^{ay} \sum_{r=0}^{n} (-a)^r G_r(x, y)\Big], \quad n \geq -1 \quad (23)$$

$$\int_0^x F_n(t, y)dt = -F_{n+1}(x, y) - F_n(x, y) + F_n(0, y) + F_{n+1}(0, y) \quad (24)$$

$$\int_0^x e^t F_n(t, y)dt = e^x\Big[F_n(x, y) + F_{n-1}(x, y)\Big] - F_n(0, y) - F_{n-1}(0, y) \quad (25)$$

$$\int_0^x e^{at} F_n(t, y)dt = \frac{1}{-a(1-a)}\Big[ae^{ax}F_n(x, y) - aF_n(0, y) + \left(\frac{1-a}{-a}\right)^n G_n\left(0, \frac{-ay}{1-a}\right) + \left(\frac{1-a}{a}\right)^n \Big\{e^{\frac{ay}{1-a}} F_0\left(x(1-a), \frac{y}{1-a}\right) - e^{ax} \sum_{r=0}^{n} \left(\frac{a}{1-a}\right)^r F_r(x, y)\Big\}\Big], \quad n \geq -1 \quad (26)$$

$$\int_0^y F_n(x, t)dt = F_{n+1}(x, y) - F_{n+1}(x, 0) \quad (27)$$

$$\int_0^y e^t F_n(x, t)dt = e^y G_n(x, y) - G_n(x, 0) \quad (28)$$

$$\int_0^y e^{at} F_n(x, t)dt = \frac{1}{(-a)^{n+1}}\Big[e^{\frac{ax}{1-a}} F_0\left(\frac{x}{1-a}, y(1-a)\right) - e^{ay} \sum_{r=0}^{n} (-a)^r F_r(x, y)\Big], \quad n \geq 0 \quad (29)$$

Laplace Transforms

Table 1 gives some basic Laplace transform pairs. Additional transform pairs are given in [17, 23]. In [17] $F_n = y^n H_n/n!$ and $G_n = y^n K_n/n!$. In [23] $F_n = V_{n+1}$.

Sums, ($a \neq 1$)

$$\sum_{0}^{\infty} (-a)^r G_r(x, y) = \frac{e^{\frac{ax}{1-a}-ay}}{1-a} G_0\left(\frac{x}{1-a}, y(1-a)\right) \quad (30)$$

Table 1 Some Laplace transform pairs

$F(s)$		$f(y)$
$\dfrac{e^{-\frac{xs}{s+1}}}{s^{n+1}}$,	$n \geq 0$	$F_n(x, y)$
$\dfrac{e^{-\frac{xs}{s+1}}}{(s+1)s^{n+1}}$,	$n \geq -1$	$G_n(x, y)$
$\dfrac{e^{-\frac{xs}{s+1}}}{(s+a)^{n+1}}$,	$n \geq 0$, $a \neq 1$	$\dfrac{e^{\frac{ax}{1-a}-ay}}{(1-a)^n} F_n\left(\frac{x}{1-a}, y(1-a)\right)$
$\dfrac{e^{-\frac{xs}{s+1}}}{(s+1)(s+a)^{n+1}}$,	$n \geq -1$, $a \neq 1$	$\dfrac{e^{\frac{ax}{1-a}-ay}}{(1-a)^{n+1}} G_n\left(\frac{x}{1-a}, y(1-a)\right)$
$\dfrac{e^{-\frac{xs}{s+1}}}{(s+1)^2}$		$\dfrac{y}{x} F_{-1}(x, y)$

$$\sum_0^\infty (-1)^r G_r(x, y) = \frac{y}{x} F_{-1}(x, y) \tag{31}$$

$$\sum_0^\infty (-a)^r F_r(x, y) = e^{\frac{ax}{1-a}-ay} F_0\left(\frac{x}{1-a}, y(1-a)\right) \tag{32}$$

$$\sum_0^\infty (-1)^r F_r(x, y) = G_{-1}(x, y) \tag{33}$$

$$\sum_0^n (-1)^r F_r(x, y) = G_{-1}(x, y) + (-1)^n G_n(x, y) \tag{34}$$

Exchange of Arguments

$$G_{-2}(y, x) = \frac{y}{x} F_{-1}(x, y) - G_{-1}(x, y) \tag{35}$$

$$G_{-1}(y, x) = G_{-1}(x, y) \tag{36}$$

$$G_0(y, x) = 1 - F_0(x, y) = 1 - G_0(x, y) - G_{-1}(x, y) \tag{37}$$

$$G_1(y, x) = F_1(x, y) + F_0(x, y) - 1 + x - y \tag{38}$$

$$F_{-1}(y, x) = \frac{y}{x} F_{-1}(x, y) \tag{39}$$

$$F_0(y, x) = 1 - G_0(x, y) \tag{40}$$

$$F_1(y, x) = F_1(x, y) - y + x \tag{41}$$

Numerical Evaluation

A rapid method of finding values of the functions involves finding values for $G_{-2}(x, y)$, $G_{-1}(x, y)$, and $G_0(x, y)$. The values of $F_n(x, y)$ and $G_n(x, y)$ can then be found using the two recurrence relations, equations (13) and (14). Equations (4), (6), and (10) are easily programmed for evaluation of G_{-2}, G_{-1}, and G_0. Baclic [11] suggests use of a rapid algorithm [25] for $I_r(Z)$ $(Z > 0)$, for the equations employing $I_r(2\sqrt{xy})$ and, for same equations, refers to a rapid method [26] that does not require evaluation of the modified Bessel functions.

The series for equations (10) and (11) converge more rapidly when $|y| < |x|$. Therefore, when $|y| > |x|$, evaluate $G_{-2}(y, x)$, $G_{-1}(y, x)$, and $G_0(y, x)$ and use equations (35), (36), and (37) to find $G_{-2}(x, y)$, $G_{-1}(x, y)$, and $G_0(x, y)$ before using the recurrence relations.

Use of the recurrence relations will give erroneous results for n sufficiently large. When the terms $(y-x-1-2n)$ and $(2y-n)$ of equation (14) are positive the recurrence relations involve only the sum of positive terms (x and y are here assumed positive). In this case, use of the recurrence equations will introduce no error. However, when one or both of the terms are negative, equation (14) involves differences with a consequent loss of significant digits as n increases. In this case, equations (10) or (11) can be programmed for $G_n(x, y)$ (n = 0, 1, 2, . . .) and $F_n(x, y)$ found using equation (13).

Generally, if $F_m(x, y)$ or $G_m(x, y)$ are required, then all values, n = 0, 1, 2, . . . ,m, are required.

Approximate Forms

For x and y positive and not too small, Klinkenberg [2] recommends any of three pair of equations for G_0 and F_0. The pair most amenable to the following usage is

$$G_0(x, y) = \frac{1}{2} \operatorname{erfc}\left[\left(x+\frac{1}{4}\right)^{1/2} - \left(y-\frac{1}{4}\right)^{1/2}\right] \tag{42}$$

$$F_0(x, y) = \frac{1}{2} \operatorname{erfc}\left[\left(x-\frac{1}{4}\right)^{1/2} - \left(y+\frac{1}{4}\right)^{1/2}\right] \tag{43}$$

in which erfc ( ) is the complementary error function. For x = 5 and y = 4 the error for both equations is less than ±0.3 percent. The accuracy improves as x and y increase. For x = 10 and y = 8 the error is about ±0.1 percent.

The function erfc $(-K)/2$ $(=(1+\operatorname{erf}(K))/2)$ approaches unity as K increases; for K = 2.7, erfc$(-K)/2$ = 0.99997. Equating the argument of the error function in equation (42) to $-K$ gives

$$y_c = x + \frac{1}{2} + 2K\left(x+\frac{1}{4}\right)^{1/2} + K^2 \tag{44}$$

With K equal to (say) 2.7 and $y \geq y_c$, the value of $G_0(x, y)$ will be sensibly unity and the values $G_{-1}(x, y)$ and $G_{-2}(x, y)$ will be sensibly zero. In particular, for the region $x \geq 0$ and $y \geq y_c$, use $G_0(x, y) = 1$, $G_{-1}(x, y) = 0$ and $G_{-2}(x, y) = 0$ with the recurrence equations (13) and (14) to find $G_n(x, y)$ and $F_n(x, y)$. The maximum error in evaluating $G_n(x, y)$ and $F_n(x, y)$ using this procedure occurs in $G_0(x, y)$ on the locus $y = y_c$. With K = 2.7, the error in $G_0(x, y)$ is less than ±0.007 percent.

Table 2 Reference values of G_0, G_{-1}, and G_{-2}

x	y	G_0	G_{-1}	G_{-2}
4	3	0.283050	0.143858	0.009750
−4	−3	−80025.1	173004.	−357734.

Reference Values

Table 2 gives, for reference purposes, values of G_{-2}, G_{-1}, and G_0 for arbitrarily selected arguments. In addition to the previously noted tabulation of Larsen [14], Serov and Korol'kov [23] tabulate G_{-1}, F_0, F_1, and $\exp(-2(x+y))F_0(-x, -y)$, (designated as N) for $x=0$ to 50 and $y=0$ to 100.

Acknowledgments

The author wishes to thank Dr. B. S. Baclic for the help provided in reviewing the original version of this note.

References

1 Nusselt, W., "Der Wärmeübergang im Kreuzstrom," *Zeitschrift des Vereines deutscher Ingenieure*, Vol. 55, 1911, pp. 2021-2024.

2 Klinkenberg, A., "Heat Transfer in a Cross-Flow Heat Exchanger and Packed Beds," *Industrial and Engineering Chemistry, Engineering, Design and Process Development*, Vol. 46, No. 11, Nov. 1954, pp. 2285-2289.

3 Baclic, B. S., and Gvozdenac, D. D., "ϵ-NTU-ω Relationships for Inverted Order Flow Arrangements of Two-Pass Crossflow Heat Exchangers," *Regenerative and Recuperative Heat Exchangers*, R. K. Shah and D. E. Metzger, eds., HTD Vol. 21, ASME, 1981, pp. 27-41.

4 Baclic, B. S., Sekulic, D. P., and Gvozdenac, D. D., "Exact Explicit Equations for Some Two and Three-Pass Crossflow Heat Exchangers Effectiveness—Part II," *Advanced Study Institute Proceedings on Low Reynolds Number Forced Convection in Channels and Bundles*, Ankara, Turkey, 1981, pp. 863-876.

5 Baclic, B. S., and Gvozdenac, D. D., "Exact Explicit Equations for Some Two- and Three-Pass Cross-Flow Heat Exchangers Effectiveness," *Heat Exchangers: Thermal Hydraulic Fundamentals and Design*, S. Kakac, A. E. Bergles, and F. Mayinger, eds., Hemisphere, Washington, 1981, pp. 481-494.

6 Baclic, B. S., Sekulic, D. P., and Gvozdenac, D. D., "Performances of Three-Fluid Single Pass Crossflow Heat Exchanger," *Proceedings of the Seventh International Heat Transfer Conference*, Hemisphere, Washington, 1982, Vol. 6, pp. 167-172.

7 Nusselt, W., "Der Beharrungszustand im Winderhitzer," *Zeitschrift des Vereines deutscher Ingenieure*, Vol. 72, 1928, pp. 1052-1054.

8 Nahavandi, A. N., and Weinstein, A. S., "A Solution to the Periodic-Flow Regenerative Heat Exchanger Problem," *Applied Sci. Res.*, Vol. 10, 1961, pp. 335-348.

9 Romie, F. E., "Periodic Thermal Storage: The Regenerator," ASME JOURNAL OF HEAT TRANSFER, Vol. 101, 1979, pp. 726-731.

10 Willmott, A. J., and Duggan, R. C., "Refined Closed Methods for the Contraflow Regenerator Problem," *International Journal of Heat and Mass Transfer*, Vol. 23, 1980, pp. 655-662.

11 Baclic, B. S., "The Application of the Galerkin Method to the Solution of the Symmetric and Balanced Counterflow Regenerator Problem," ASME *Journal of Heat Transfer*, Vol. 107, No. 1, 1985, pp. 214-221.

12 Anzelius, A., "Über Erwärmung vermittles durchströmender Medien," *Zeitschrift fur Angewandte Mathematik und Mechanik*, Vol. 6, 1926, pp. 291-294.

13 Schumann, T. E. W., "Heat Transfer: A Liquid Flowing Through a Porous Prism," *Franklin Institute Journal*, Vol. 208, 1929, pp. 405-416.

14 Larsen, F. W., "Rapid Calculation of Temperature in a Regenerative Heat Exchanger Having Arbitrary Initial Solid and Entering Fluid Temperatures," *International Journal of Heat and Mass Transfer*, Vol. 10, 1967, pp. 149-168.

15 Myers, G. E., Mitchell, J. W., and Lindeman, C. F., "The Transient Response of Heat Exchangers Having an Infinite Capacitance Rate Fluid," ASME JOURNAL OF HEAT TRANSFER, Vol. 92, 1970, pp. 269-275.

16 Tan, K. S., and Spinner, I. H., "Dynamics of a Shell-and-Tube Heat Exchanger With Finite Tube-Wall Heat Capacity and Finite Shell-Side Resistance," *Industrial and Engineering Chemistry Fundamentals*, Vol. 17, 1978, pp. 353-358.

17 Romie, F. E., "Transient Response of Gas-to-Gas Crossflow Heat Exchangers With Neither Gas Mixed," ASME JOURNAL OF HEAT TRANSFER, Vol. 105, 1983, pp. 563-570.

18 Romie, F. E., "Transient Response of the Counterflow Heat Exchanger," ASME JOURNAL OF HEAT TRANSFER, Vol. 106, 1984, pp. 620-626.

19 Romie, F. E., "Transient Response of the Parallel-Flow Heat Exchanger," ASME JOURNAL OF HEAT TRANSFER, Vol. 107, 1985, pp. 727-730.

20 Brinkley, S. R., "Heat Transfer Between a Fluid and a Porous Solid Generating Heat," *Journal of Applied Physics*, Vol. 18, June 1947, pp. 582-585.

21 Yang, W. J., Clark, J. A., and Arpaci, V. S., "Dynamic Response of Heat Exchangers Having Internal Heat Sources—Part IV," ASME JOURNAL OF HEAT TRANSFER, Vol. 83, 1961, pp. 321-338.

22 Goldstein, S., "On the Mathematics of Exchange Processes in Fixed Columns—I, Mathematical Solutions and Asymptotic Expansions," *Proceedings of the Royal Society*, Vol. A219, 1953, pp. 151-171.

23 Serov, E. P., and Korol'kov, B. P., *Dinamika parogeneratorov, (Dynamics of Steam Generators)*, Energiya, Moscow, 1972.

24 Lach, J., and Pieczka, W., "On the Properties of Some Special Functions Related to Bessel's Functions and Their Application in Heat Exchanger Theory," *International Journal of Heat and Mass Transfer*, Vol. 27, No. 12, 1984, pp. 2225-2238.

25 Amos, D. E., Daniel, S. L., and Weston, M. K., "CDC 6600 Subroutines IBESS and JBESS for Bessel Functions $I_\nu(x)$ and $J_\nu(x)$, $x \geq 0$, $\nu \geq 0$," *Transactions on Mathematical Software*, Association for Computing Machinery Inc., Vol. 3, pp. 76-95.

26 Baclic, B. S., Gvozdenac, D. D., and Dragutinovic, G. D., "Easy Way to Calculate the Breakthrough Curves in Absorption and Ion Exchange," Paper No. F2.6, presented at the 7th International Congress of Chemical Equipment Design and Automation, Praha, Czechoslovakia, Aug. 31-Sept. 4, 1981.

A New Simplified Formula for Crossflow Heat Exchanger Effectiveness

Chung-Hsiung Li[1]

I Introduction

The main objective of this study is to present a new and convenient formula for the effectiveness of a single-pass crossflow heat exchanger with both fluids unmixed. Recently, a survey of various solutions for the effectiveness of a crossflow heat exchanger with two unmixed fluids was given in a letter by Baclic and Heggs (1985). Based on this survey, the formula presented herein has not been obtained by any of the previous authors. The governing equations for the crossflow heat exchanger with two fluids unmixed can be found in the heat transfer text by Jakob (1957) and a heat exchanger text by Hausen (1983). The solution for this configuration was first obtained by Nusselt (1911, 1930). An explanation for the fact that different solutions were obtained by different authors from the same governing equations (as shown in the letter by Baclic and Heggs, 1985) is discussed by Li (in review).

This new formula is also much simpler, with regard to computer programming, than the simple formula given by Baclic (1978). Also, the formula given by Baclic was actually derived by Binnie and Poole (1937) fifty years ago. If the most fundamental recurrence formula of modified Bessel functions is substituted into the effectiveness formula obtained by Binnie and Poole, the new formula given by Baclic can be obtained immediately. From the Binnie and Poole formula, one has to compute the first kind of modified Bessel functions for the order from 0 to ∞, which will also be discussed in this paper.

II Formulation and Solution

The ϵ-N_{tu}-$C_{\min}/C_{\max}$ relationship stated by Kays and London (1964) is used to formulate the effectiveness of a single-pass crossflow heat exchanger with two fluids unmixed. ϵ is the thermal effectiveness and is a function of the number of heat transfer units ($N_{tu} = AU/C_{\min}$) and the heat capacity ratio ($C^* = C_{\min}/C_{\max}$). N_{tu} is a function of A, the heat transfer area, and U, the overall heat transfer coefficient. $C_{\min}$ and $C_{\max}$ are, respectively, the smaller and the larger of the two fluid heat capacity rates.

[1]Engineering Technologies Department, C-E Air Preheater, Combustion Engineering, Inc., Wellsville, NY 14895.

Contributed by the Heat Transfer Division for publication in the JOURNAL OF HEAT TRANSFER. Manuscript received by the Heat Transfer Division January 7, 1985.

Table 2 Reference values of G_0, G_{-1}, and G_{-2}

x	y	G_0	G_{-1}	G_{-2}
4	3	0.283050	0.143858	0.009750
−4	−3	−80025.1	173004.	−357734.

Reference Values

Table 2 gives, for reference purposes, values of G_{-2}, G_{-1}, and G_0 for arbitrarily selected arguments. In addition to the previously noted tabulation of Larsen [14], Serov and Korol'kov [23] tabulate G_{-1}, F_0, F_1, and $\exp(-2(x+y))F_0(-x, -y)$, (designated as N) for $x=0$ to 50 and $y=0$ to 100.

Acknowledgments

The author wishes to thank Dr. B. S. Baclic for the help provided in reviewing the original version of this note.

References

1 Nusselt, W., "Der Wärmeübergang im Kreuzstrom," *Zeitschrift des Vereines deutscher Ingenieure*, Vol. 55, 1911, pp. 2021-2024.

2 Klinkenberg, A., "Heat Transfer in a Cross-Flow Heat Exchanger and Packed Beds," *Industrial and Engineering Chemistry, Engineering, Design and Process Development*, Vol. 46, No. 11, Nov. 1954, pp. 2285-2289.

3 Baclic, B. S., and Gvozdenac, D. D., "ϵ-NTU-ω Relationships for Inverted Order Flow Arrangements of Two-Pass Crossflow Heat Exchangers," *Regenerative and Recuperative Heat Exchangers*, R. K. Shah and D. E. Metzger, eds., HTD Vol. 21, ASME, 1981, pp. 27-41.

4 Baclic, B. S., Sekulic, D. P., and Gvozdenac, D. D., "Exact Explicit Equations for Some Two and Three-Pass Crossflow Heat Exchangers Effectiveness—Part II," *Advanced Study Institute Proceedings on Low Reynolds Number Forced Convection in Channels and Bundles*, Ankara, Turkey, 1981, pp. 863-876.

5 Baclic, B. S., and Gvozdenac, D. D., "Exact Explicit Equations for Some Two- and Three-Pass Cross-Flow Heat Exchangers Effectiveness," *Heat Exchangers: Thermal Hydraulic Fundamentals and Design*, S. Kakac, A. E. Bergles, and F. Mayinger, eds., Hemisphere, Washington, 1981, pp. 481-494.

6 Baclic, B. S., Sekulic, D. P., and Gvozdenac, D. D., "Performances of Three-Fluid Single Pass Crossflow Heat Exchanger," *Proceedings of the Seventh International Heat Transfer Conference*, Hemisphere, Washington, 1982, Vol. 6, pp. 167-172.

7 Nusselt, W., "Der Beharrungszustand im Winderhitzer," *Zeitschrift des Vereines deutscher Ingenieure*, Vol. 72, 1928, pp. 1052-1054.

8 Nahavandi, A. N., and Weinstein, A. S., "A Solution to the Periodic-Flow Regenerative Heat Exchanger Problem," *Applied Sci. Res.*, Vol. 10, 1961, pp. 335-348.

9 Romie, F. E., "Periodic Thermal Storage: The Regenerator," ASME JOURNAL OF HEAT TRANSFER, Vol. 101, 1979, pp. 726-731.

10 Willmott, A. J., and Duggan, R. C., "Refined Closed Methods for the Contraflow Regenerator Problem," *International Journal of Heat and Mass Transfer*, Vol. 23, 1980, pp. 655-662.

11 Baclic, B. S., "The Application of the Galerkin Method to the Solution of the Symmetric and Balanced Counterflow Regenerator Problem," ASME *Journal of Heat Transfer*, Vol. 107, No. 1, 1985, pp. 214-221.

12 Anzelius, A., "Über Erwärmung vermittles durchströmender Medien," *Zeitschrift fur Angewandte Mathematik und Mechanik*, Vol. 6, 1926, pp. 291-294.

13 Schumann, T. E. W., "Heat Transfer: A Liquid Flowing Through a Porous Prism," *Franklin Institute Journal*, Vol. 208, 1929, pp. 405-416.

14 Larsen, F. W., "Rapid Calculation of Temperature in a Regenerative Heat Exchanger Having Arbitrary Initial Solid and Entering Fluid Temperatures," *International Journal of Heat and Mass Transfer*, Vol. 10, 1967, pp. 149-168.

15 Myers, G. E., Mitchell, J. W., and Lindeman, C. F., "The Transient Response of Heat Exchangers Having an Infinite Capacitance Rate Fluid," ASME JOURNAL OF HEAT TRANSFER, Vol. 92, 1970, pp. 269-275.

16 Tan, K. S., and Spinner, I. H., "Dynamics of a Shell-and-Tube Heat Exchanger With Finite Tube-Wall Heat Capacity and Finite Shell-Side Resistance," *Industrial and Engineering Chemistry Fundamentals*, Vol. 17, 1978, pp. 353-358.

17 Romie, F. E., "Transient Response of Gas-to-Gas Crossflow Heat Exchangers With Neither Gas Mixed," ASME JOURNAL OF HEAT TRANSFER, Vol. 105, 1983, pp. 563-570.

18 Romie, F. E., "Transient Response of the Counterflow Heat Exchanger," ASME JOURNAL OF HEAT TRANSFER, Vol. 106, 1984, pp. 620-626.

19 Romie, F. E., "Transient Response of the Parallel-Flow Heat Exchanger," ASME JOURNAL OF HEAT TRANSFER, Vol. 107, 1985, pp. 727-730.

20 Brinkley, S. R., "Heat Transfer Between a Fluid and a Porous Solid Generating Heat," *Journal of Applied Physics*, Vol. 18, June 1947, pp. 582-585.

21 Yang, W. J., Clark, J. A., and Arpaci, V. S., "Dynamic Response of Heat Exchangers Having Internal Heat Sources—Part IV," ASME JOURNAL OF HEAT TRANSFER, Vol. 83, 1961, pp. 321-338.

22 Goldstein, S., "On the Mathematics of Exchange Processes in Fixed Columns—I, Mathematical Solutions and Asymptotic Expansions," *Proceedings of the Royal Society*, Vol. A219, 1953, pp. 151-171.

23 Serov, E. P., and Korol'kov, B. P., *Dinamika parogeneratorov, (Dynamics of Steam Generators)*, Energiya, Moscow, 1972.

24 Lach, J., and Pieczka, W., "On the Properties of Some Special Functions Related to Bessel's Functions and Their Application in Heat Exchanger Theory," *International Journal of Heat and Mass Transfer*, Vol. 27, No. 12, 1984, pp. 2225-2238.

25 Amos, D. E., Daniel, S. L., and Weston, M. K., "CDC 6600 Subroutines IBESS and JBESS for Bessel Functions $I_\nu(x)$ and $J_\nu(x)$, $x \geq 0$, $\nu \geq 0$," *Transactions on Mathematical Software*, Association for Computing Machinery Inc., Vol. 3, pp. 76-95.

26 Baclic, B. S., Gvozdenac, D. D., and Dragutinovic, G. D., "Easy Way to Calculate the Breakthrough Curves in Absorption and Ion Exchange," Paper No. F2.6, presented at the 7th International Congress of Chemical Equipment Design and Automation, Praha, Czechoslovakia, Aug. 31-Sept. 4, 1981.

A New Simplified Formula for Crossflow Heat Exchanger Effectiveness

Chung-Hsiung Li[1]

I Introduction

The main objective of this study is to present a new and convenient formula for the effectiveness of a single-pass crossflow heat exchanger with both fluids unmixed. Recently, a survey of various solutions for the effectiveness of a crossflow heat exchanger with two unmixed fluids was given in a letter by Baclic and Heggs (1985). Based on this survey, the formula presented herein has not been obtained by any of the previous authors. The governing equations for the crossflow heat exchanger with two fluids unmixed can be found in the heat transfer text by Jakob (1957) and a heat exchanger text by Hausen (1983). The solution for this configuration was first obtained by Nusselt (1911, 1930). An explanation for the fact that different solutions were obtained by different authors from the same governing equations (as shown in the letter by Baclic and Heggs, 1985) is discussed by Li (in review).

This new formula is also much simpler, with regard to computer programming, than the simple formula given by Baclic (1978). Also, the formula given by Baclic was actually derived by Binnie and Poole (1937) fifty years ago. If the most fundamental recurrence formula of modified Bessel functions is substituted into the effectiveness formula obtained by Binnie and Poole, the new formula given by Baclic can be obtained immediately. From the Binnie and Poole formula, one has to compute the first kind of modified Bessel functions for the order from 0 to ∞, which will also be discussed in this paper.

II Formulation and Solution

The ϵ-N_{tu}-$C_{\min}/C_{\max}$ relationship stated by Kays and London (1964) is used to formulate the effectiveness of a single-pass crossflow heat exchanger with two fluids unmixed. ϵ is the thermal effectiveness and is a function of the number of heat transfer units ($N_{tu} = AU/C_{\min}$) and the heat capacity ratio ($C^* = C_{\min}/C_{\max}$). N_{tu} is a function of A, the heat transfer area, and U, the overall heat transfer coefficient. $C_{\min}$ and $C_{\max}$ are, respectively, the smaller and the larger of the two fluid heat capacity rates.

[1]Engineering Technologies Department, C-E Air Preheater, Combustion Engineering, Inc., Wellsville, NY 14895.

Contributed by the Heat Transfer Division for publication in the JOURNAL OF HEAT TRANSFER. Manuscript received by the Heat Transfer Division January 7, 1985.

Based on modified Bessel functions of the first kind, the formula derived by Binnie and Poole (1937) and stated as a new formula by Baclic (1978) can be written as

$$\epsilon = 1 - \exp[-(1+C^*)N_{tu}][I_0(2N_{tu}\sqrt{C^*}) + \sqrt{C^*}I_1(2N_{tu}\sqrt{C^*}) - \frac{1-C^*}{C^*}\sum_{n=2}^{\infty} C^{*n/2} I_n(2N_{tu}\sqrt{C^*})] \quad (1)$$

The purpose of this study is to present a new and simple formula for the effectiveness of a single-pass crossflow heat exchanger with both fluids unmixed as

$$\epsilon = 1 - \exp(-N_{tu}) - \exp[-(1+C^*)N_{tu}] \sum_{n=1}^{\infty} C^{*n} P_n(N_{tu}) \quad (2)$$

where

$$P_n(N_{tu}) = \frac{1}{(n+1)!}\sum_{j=1}^{n}(n-j+1)\frac{N_{tu}^{n+j}}{j!} \quad (3)$$

III Derivation

An analytical solution for the temperature distribution in a crossflow heat exchanger with two fluids unmixed was developed by Nusselt (1930) and stated by Hausen (1983). It can be written as

$$\frac{T_1' - T_2}{T_1' - T_2'} = \theta(x, y) = 1 - e^{-ax-by}\sum_{n=1}^{\infty}\frac{(ax)^n}{n!}\sum_{j=0}^{n-1}\frac{(by)^j}{j!} \quad (4)$$

where

$$a = C^* N_{tu} \text{ and } b = N_{tu} \quad (5)$$

The effectiveness of a crossflow heat exchanger can be expressed as

$$\epsilon = \frac{C_{\max}}{C_{\min}}\int_0^1 (1-\theta(1, y))dy$$

$$= \frac{b}{a}e^{-a}\sum_{n=1}^{\infty}\frac{a^n}{n!}\sum_{j=0}^{n-1}\frac{1}{b}\left(1 - e^{-b}\sum_{i=0}^{j}\frac{b^i}{i!}\right)$$

$$= 1 - e^{-a-b}\sum_{n=1}^{\infty}\frac{a^{n-1}}{n!}\sum_{j=0}^{n-1}\sum_{i=0}^{j}\frac{b^i}{i!} \quad (6)$$

From equation (6), one can cancel out one summation term and obtain

$$\epsilon = 1 - e^{-a-b}\sum_{n=1}^{\infty}\frac{a^{n-1}}{n!}\sum_{j=0}^{n-1}(n-j)\frac{b^j}{j!} \quad (7)$$

We can manipulate equation (7) to obtain equation (2) as follows

$$\epsilon = 1 - e^{-a-b}\sum_{n=1}^{\infty}\frac{a^{n-1}}{n!}\left[n + \sum_{j=1}^{n-1}(n-j)\frac{b^j}{j!}\right]$$

$$= 1 - e^{-b} - e^{-a-b}\sum_{n=2}^{\infty}\frac{a^{n-1}}{n!}\sum_{j=1}^{n-1}(n-j)\frac{b^j}{j!}$$

$$= 1 - e^{-b} - e^{-a-b}\sum_{n=1}^{\infty}\frac{a^n}{(n+1)!}\sum_{j=1}^{n}(n+1-j)\frac{b^j}{j!} \quad (8)$$

Substituting for a and b from equation (5) into equation (8), we can obtain equation (2).

IV Results and Discussion

The present analysis shows that the effectiveness of the single-pass crossflow heat exchanger with both fluids unmixed can be computed with equations (2) and (3). The main difference between the formula given by Binnie and Poole (1937) (i.e., equation (1)) and the one presented herein (i.e., equation (2)) is due to the fact that the former uses the modified Bessel function $I_n(2N_{tu}\sqrt{C^*})$ and the latter uses the polynomial function $P_n(N_{tu})$. Although one can obtain the numerical value of modified Bessel functions of the first kind from the recurrence formula for any order n, it requires values of $I_0(2N_{tu}\sqrt{C^*})$ and $I_1(2N_{tu}\sqrt{C^*})$ to start the calculation. $I_0(2N_{tu}\sqrt{C^*})$ and $I_1(2N_{tu}\sqrt{C^*})$ are power series with infinite terms; their values are usually computed from Chebyshev polynomial approximation functions (Abramowitz and Stegun, 1965). The accuracy of these values is restricted by the coefficients of the approximating polynomial functions. The $P_n(N_{tu})$ of equation (3) is a polynomial function with finite terms. One can compute N_{tu}^{n+1} from N_{tu}^n and N_{tu}^{n+2} from N_{tu}^{n+1} term by term, and obtain the value of $P_n(N_{tu})$ accurately. This shows that one can obtain the effectiveness of a crossflow heat exchanger with both fluids unmixed from equation (2) with a simpler and faster computer program.

References

Abramowitz, M., and Stegun, I. A., 1965, *Handbook of Mathematical Functions With Formulas, Graphs, and Mathematical Tables*, Dover, New York, p. 378.

Baclic, B. S., 1978, "A Simplified Formula for Cross-Flow Heat Exchanger Effectiveness," ASME JOURNAL OF HEAT TRANSFER, Vol. 100, pp. 746–747.

Baclic, B. S., and Heggs, P. J., 1985, "On the Search for New Solutions of the Single-Pass Crossflow Heat Exchanger," *Int. J. Heat Mass Transfer*, Vol. 28, pp. 1965–1976.

Binnie, A. M., and Poole, E. G. C., 1937, "The Theory of the Single-Pass Cross-Flow Heat Exchanger," *Proc. Cambridge Phil. Soc.*, Vol. 33, pp. 403–411.

Hausen, H., 1983, *Heat Transfer in Counterflow, Parallel Flow, and Cross Flow*, McGraw-Hill, New York, pp. 226–231 (translation edited by A. J. Willmott).

Jakob, M., 1957, *Heat Transfer*, Vol. II, Wiley, New York, pp. 217–227.

Kays, W. M., and London, A. L., 1964, *Compact Heat Exchangers*, McGraw-Hill, New York, pp. 18–19, 39.

Li, C. H., "A Note on the Exact Solution of the Single-Pass Crossflow Heat Exchanger Problem," submitted for review to *Int. J. Heat Mass Transfer*.

Nusselt, W., 1911, "Der Wärmeübergang im Kreuzstrom," *Zeitschrift des Vereines deutscher Ingenieure*, Vol. 55, pp. 2021–2024.

Nusselt, W., 1930, "Eine neue Formel für den Wärmedurchgang im Kreuzstrom," *Technische Mechanik und Thermodynamik*, Vol. 1, pp. 417–422.

Microwave Heating of Porous Media

Fabio Gori,[1] G. Biffi Gentili,[2] and L. Martini[1]

Nomenclature

A = soil surface
c = specific heat
E = electric field
f_0 = working frequency
g = gravitational constant
h = enthalpy
j = imaginary symbol
k = hydraulic permeability
N = number of soil layers
p = pressure
p_d = displacement pressure
q = energy per unit time and volume
S = water saturation of the soil
S_R = residual water saturation of the soil
T = temperature

[1]Dipartimento di Energetica dell'Università, 50139 Firenze, Italy.
[2]Dipartimento di Ingegneria Elettronica dell'Università, 50139 Firenze, Italy.

Contributed by the Heat Transfer Division for publication in the JOURNAL OF HEAT TRANSFER. Manuscript received by the Heat Transfer Division June 28, 1985.

Based on modified Bessel functions of the first kind, the formula derived by Binnie and Poole (1937) and stated as a new formula by Baclic (1978) can be written as

$$\epsilon = 1 - \exp[-(1+C^*)N_{tu}][I_0(2N_{tu}\sqrt{C^*}) + \sqrt{C^*}I_1(2N_{tu}\sqrt{C^*}) - \frac{1-C^*}{C^*}\sum_{n=2}^{\infty} C^{*n/2} I_n(2N_{tu}\sqrt{C^*})] \quad (1)$$

The purpose of this study is to present a new and simple formula for the effectiveness of a single-pass crossflow heat exchanger with both fluids unmixed as

$$\epsilon = 1 - \exp(-N_{tu}) - \exp[-(1+C^*)N_{tu}] \sum_{n=1}^{\infty} C^{*n} P_n(N_{tu}) \quad (2)$$

where

$$P_n(N_{tu}) = \frac{1}{(n+1)!}\sum_{j=1}^{n}(n-j+1)\frac{N_{tu}^{n+j}}{j!} \quad (3)$$

III Derivation

An analytical solution for the temperature distribution in a crossflow heat exchanger with two fluids unmixed was developed by Nusselt (1930) and stated by Hausen (1983). It can be written as

$$\frac{T_1' - T_2}{T_1' - T_2'} = \theta(x, y) = 1 - e^{-ax-by}\sum_{n=1}^{\infty}\frac{(ax)^n}{n!}\sum_{j=0}^{n-1}\frac{(by)^j}{j!} \quad (4)$$

where

$$a = C^* N_{tu} \text{ and } b = N_{tu} \quad (5)$$

The effectiveness of a crossflow heat exchanger can be expressed as

$$\epsilon = \frac{C_{\max}}{C_{\min}}\int_0^1 (1-\theta(1, y))dy$$

$$= \frac{b}{a}e^{-a}\sum_{n=1}^{\infty}\frac{a^n}{n!}\sum_{j=0}^{n-1}\frac{1}{b}\left(1 - e^{-b}\sum_{i=0}^{j}\frac{b^i}{i!}\right)$$

$$= 1 - e^{-a-b}\sum_{n=1}^{\infty}\frac{a^{n-1}}{n!}\sum_{j=0}^{n-1}\sum_{i=0}^{j}\frac{b^i}{i!} \quad (6)$$

From equation (6), one can cancel out one summation term and obtain

$$\epsilon = 1 - e^{-a-b}\sum_{n=1}^{\infty}\frac{a^{n-1}}{n!}\sum_{j=0}^{n-1}(n-j)\frac{b^j}{j!} \quad (7)$$

We can manipulate equation (7) to obtain equation (2) as follows

$$\epsilon = 1 - e^{-a-b}\sum_{n=1}^{\infty}\frac{a^{n-1}}{n!}\left[n + \sum_{j=1}^{n-1}(n-j)\frac{b^j}{j!}\right]$$

$$= 1 - e^{-b} - e^{-a-b}\sum_{n=2}^{\infty}\frac{a^{n-1}}{n!}\sum_{j=1}^{n-1}(n-j)\frac{b^j}{j!}$$

$$= 1 - e^{-b} - e^{-a-b}\sum_{n=1}^{\infty}\frac{a^n}{(n+1)!}\sum_{j=1}^{n}(n+1-j)\frac{b^j}{j!} \quad (8)$$

Substituting for a and b from equation (5) into equation (8), we can obtain equation (2).

IV Results and Discussion

The present analysis shows that the effectiveness of the single-pass crossflow heat exchanger with both fluids unmixed can be computed with equations (2) and (3). The main difference between the formula given by Binnie and Poole (1937) (i.e., equation (1)) and the one presented herein (i.e., equation (2)) is due to the fact that the former uses the modified Bessel function $I_n(2N_{tu}\sqrt{C^*})$ and the latter uses the polynomial function $P_n(N_{tu})$. Although one can obtain the numerical value of modified Bessel functions of the first kind from the recurrence formula for any order n, it requires values of $I_0(2N_{tu}\sqrt{C^*})$ and $I_1(2N_{tu}\sqrt{C^*})$ to start the calculation. $I_0(2N_{tu}\sqrt{C^*})$ and $I_1(2N_{tu}\sqrt{C^*})$ are power series with infinite terms; their values are usually computed from Chebyshev polynomial approximation functions (Abramowitz and Stegun, 1965). The accuracy of these values is restricted by the coefficients of the approximating polynomial functions. The $P_n(N_{tu})$ of equation (3) is a polynomial function with finite terms. One can compute N_{tu}^{n+1} from N_{tu}^n and N_{tu}^{n+2} from N_{tu}^{n+1} term by term, and obtain the value of $P_n(N_{tu})$ accurately. This shows that one can obtain the effectiveness of a crossflow heat exchanger with both fluids unmixed from equation (2) with a simpler and faster computer program.

References

Abramowitz, M., and Stegun, I. A., 1965, *Handbook of Mathematical Functions With Formulas, Graphs, and Mathematical Tables*, Dover, New York, p. 378.

Baclic, B. S., 1978, "A Simplified Formula for Cross-Flow Heat Exchanger Effectiveness," ASME JOURNAL OF HEAT TRANSFER, Vol. 100, pp. 746–747.

Baclic, B. S., and Heggs, P. J., 1985, "On the Search for New Solutions of the Single-Pass Crossflow Heat Exchanger," *Int. J. Heat Mass Transfer*, Vol. 28, pp. 1965–1976.

Binnie, A. M., and Poole, E. G. C., 1937, "The Theory of the Single-Pass Cross-Flow Heat Exchanger," *Proc. Cambridge Phil. Soc.*, Vol. 33, pp. 403–411.

Hausen, H., 1983, *Heat Transfer in Counterflow, Parallel Flow, and Cross Flow*, McGraw-Hill, New York, pp. 226–231 (translation edited by A. J. Willmott).

Jakob, M., 1957, *Heat Transfer*, Vol. II, Wiley, New York, pp. 217–227.

Kays, W. M., and London, A. L., 1964, *Compact Heat Exchangers*, McGraw-Hill, New York, pp. 18–19, 39.

Li, C. H., "A Note on the Exact Solution of the Single-Pass Crossflow Heat Exchanger Problem," submitted for review to *Int. J. Heat Mass Transfer*.

Nusselt, W., 1911, "Der Wärmeübergang im Kreuzstrom," *Zeitschrift des Vereines deutscher Ingenieure*, Vol. 55, pp. 2021–2024.

Nusselt, W., 1930, "Eine neue Formel für den Wärmedurchgang im Kreuzstrom," *Technische Mechanik und Thermodynamik*, Vol. 1, pp. 417–422.

Microwave Heating of Porous Media

Fabio Gori,[1] G. Biffi Gentili,[2] and L. Martini[1]

Nomenclature

A = soil surface
c = specific heat
E = electric field
f_0 = working frequency
g = gravitational constant
h = enthalpy
j = imaginary symbol
k = hydraulic permeability
N = number of soil layers
p = pressure
p_d = displacement pressure
q = energy per unit time and volume
S = water saturation of the soil
S_R = residual water saturation of the soil
T = temperature

[1]Dipartimento di Energetica dell'Università, 50139 Firenze, Italy.
[2]Dipartimento di Ingegneria Elettronica dell'Università, 50139 Firenze, Italy.

Contributed by the Heat Transfer Division for publication in the JOURNAL OF HEAT TRANSFER. Manuscript received by the Heat Transfer Division June 28, 1985.

t = time
u = internal energy
V = velocity
y = coordinate, gravity oriented
Z_c = compressibility factor
α = coefficient of convection
Δ = finite difference
$\epsilon = \epsilon' - j\epsilon''$ = complex permittivity
λ = effective thermal conductivity
μ = dynamic viscosity
ρ = density
ϕ = porosity

Subscripts

a = air
c = capillary
e = electromagnetic
ext = external
g = gas
i = variable
in = initial
r = solid pavement
s = steam
sat = saturated
v = at constant volume
w = water
$'$ = real part
$''$ = imaginary part
0 = void

Introduction

The technique actually used for recycling in place asphaltic concrete pavements is the following [1]:

- heating of the surface layer of the pavement with special infrared lamps (gas-fed);
- hot removal and remixing in place of the materials with the addition of new binder;
- in-line reconstruction of the pavement layer with rolling.

Such a technique is highly efficient and economic but it suffers an important disadvantage: The low thermal conductivity of the asphalt causes a strong temperature decrease with depth. Further on, the infrared radiation produces carbonization of the pavement skin with possible modification of the rheological properties of the bitumen.

The technology of microwave generators (Magnetron, Klystron, and Amplitron) has registered some recent advances. It is now possible, and in some cases convenient, to use microwave energy for industrial heating of low-thermal-conductivity materials.

Actually the microwaves are employed for drying wood, paper, and textiles, and for freeze-drying, cooking, and defrosting foods [2]. One of the most interesting features of the microwave process is the rate and uniformity of the heating inside the material. Some preliminary experiments have been carried out for recycling in place asphaltic concrete pavements [3].

The goal of the present paper is to propose a theoretical model capable of describing the phenomena occurring in a soil during a microwave heating process.

Theoretical Model

The electromagnetic and heat mass transfer analysis is carried out with reference to the physical model of Fig. 1.

Electromagnetic Analysis. The soil investigated is divided into $(N-1)$ homogeneous layers. The electrical field intensity and the other electromagnetic (EM) parameters are evaluated on the basis of the classical theory [4].

The power absorbed in each layer of the soil is given by the following relation

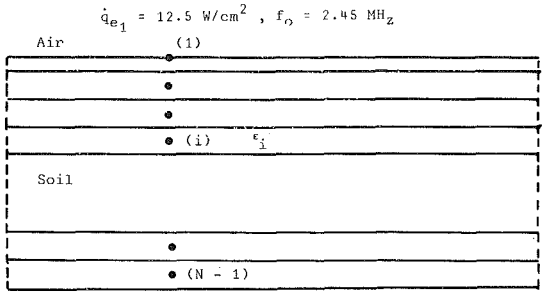

Fig. 1 Physical system

$$\dot{q}_e = 0.278 |E_i|^2 f_0 \epsilon_i'' \cdot 10^{-6} (\mathrm{W/cm^3}) \tag{1}$$

The permittivity of the layer ϵ_i takes into account the permittivities of the various components of the soil, i.e., air, solid, and water, with the following relation [5]

$$\sqrt{\epsilon} = (1-S)\phi\sqrt{\epsilon_a} + (1-\phi)\sqrt{\epsilon_r} + \left[S\phi + (1-S)\phi\,\frac{\rho_s}{\rho_w}\right]\sqrt{\epsilon_w} \tag{2}$$

The permittivities of the components depend on the temperature on the basis of the empirical relations of [6].

Heat and Mass Transfer Analysis. A layer of soil of constant porosity is subjected to a transient microwave process. The phenomenon is assumed one dimensional. The asphalt layer is generally represented in Fig. 1 where the numerical grid is reported on a homogeneous pavement.

Thermal boundary conditions are as follows. Natural convection is assumed on the upper surface because the microwave applicator is not contacting the pavement

$$\dot{q} = \alpha A (T - T_{\mathrm{ext}}) \tag{3}$$

and an adiabatic condition is assumed on the bottom surface. Boundary conditions for pressure on the bottom surface follow from the continuity of mass flow. The relative equations are not reported because of paper length.

Unsteady mass transfer in the soil takes into account the convective transport and neglects the molecular diffusion [7]. Mass conservation for air is

$$\frac{\partial}{\partial t}[\rho_a(1-S)] + \frac{\partial}{\partial y}[(1-S)\rho_a V_g] = 0 \tag{4}$$

and for water

$$\rho_w\left\{\frac{\partial S}{\partial t} + \frac{\partial}{\partial y}[(S-S_R)V_w]\right\} + \frac{\partial}{\partial t}[\rho_s(1-S)] + \frac{\partial}{\partial y}[\rho_s V_g (1-S)] = 0 \tag{5}$$

The residual saturation S_R is the minimum value of the connected liquid water for which V_w is not zero [8].

Energy conservation is written considering the effective thermal conductivity of the soil λ and the energy generated in the soil by the microwave process $\dot{q}_e$ [9].

Momentum conservations for gas and liquid phases are used in order to simplify the energy equation. For a soil with constant porosity and for constant water density it can be shown, with some algebraic passages, that the energy equation is given by

$$\frac{1}{\phi}\left\{\dot{q}_e + \lambda\,\frac{\partial^2 T}{\partial y^2}\right\} = \frac{\partial}{\partial t}\left\{(1-S)(\rho_s u_s + \rho_a u_a) + S\rho_w u_w + \frac{1-\phi}{\phi}\,\rho_r u_r\right\}$$

$$+\frac{\partial}{\partial y}\{V_g(1-S)(\rho_s h_s+\rho_a h_a)+V_w(S-S_R)\rho_w h_w\} \quad (6)$$

$$-(1-S)V_g\frac{\partial p_g}{\partial y}-(S-S_R)\frac{\partial p_w}{\partial y}V_w$$

Fluid velocities are calculated with Darcy's law [8], respectively, for the gas phase

$$(1-S)\phi V_g=-\frac{kg}{\mu_g}\left(\frac{\partial p_g}{\partial y}+\rho_g g\right) \quad (7)$$

and for the liquid phase

$$(S-S_R)\phi V_w=-\frac{k_w}{\mu_w}\left(\frac{\partial p_w}{\partial y}+\rho_w g\right) \quad (8)$$

where

$$kg=k\left(\frac{1-S}{1-S_R}\right)^2\left[1-\left(\frac{S-S_R}{1-S_R}\right)^2\right] \quad (9)$$

$$k_w=k\left(\frac{S-S_R}{1-S_R}\right)^4 \quad (10)$$

and the viscosities are dependent on the temperature as proposed in [10].

Capillary phenomena are taken into account and the liquid pressure is given by

$$p_w=p_g-p_c=p_s+p_a-p_c \quad (11)$$

Hysteresis is neglected and the capillary pressure p_c is approximated by the empirical expressions [11]

$$\left(\frac{p_d}{p_c}\right)^2(1-S_R)+S_R=S \quad \text{for } S\le S_{in} \quad (12)$$

$$p_d\left(\frac{1-S}{1-S_{in}}\right)\sqrt{\frac{1-S_R}{S_{in}-S_R}}=p_c \quad \text{for } S\ge S_{in} \quad (13)$$

Air is considered as a perfect gas.

Water vapor is considered superheated if the steam pressure is lower than the corresponding saturation pressure. The soil saturation S is deduced from the de/sorption isotherm [7].

The following state equations have been assumed

$$p_s=R_w Z_c T\,\rho_s \quad (14)$$

$$du_s=c_{v_s}dT \quad (15)$$

If the steam pressure is greater than p_{sat} the water vapor is assumed saturated and the Clapeyron equation is used

$$\frac{dp_s}{dT}=\rho_s\frac{h_s-h_w}{T} \quad (16)$$

Further on, the following empirical expressions have been derived in [12] from the steam tables [13]

$$d\,\rho_s=D_s dT \quad (17)$$

$$d(\rho_s u_s)=R_s dT \quad (18)$$

for the temperature range investigated.

The effective thermal conductivity of the asphalt has been taken from the data of [13].

Numerical Solution

Differential equations have been solved numerically with the finite difference scheme proposed in [14] called "tanks and tubes." The electromagnetic and thermodynamic variables are evaluated at the node i except for the fluid velocities for which the value on the surface between the nodes $i-1$ and i is employed.

Several numerical computations have been performed for soil with different layer depths and the numerical results have been found independent from the depth considered. Other details of the numerical solution can be found in [12].

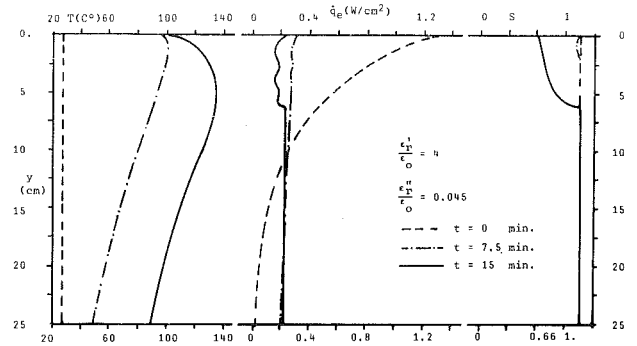

Fig. 2 Temperatures, absorbed power, and saturation in a saturated soil

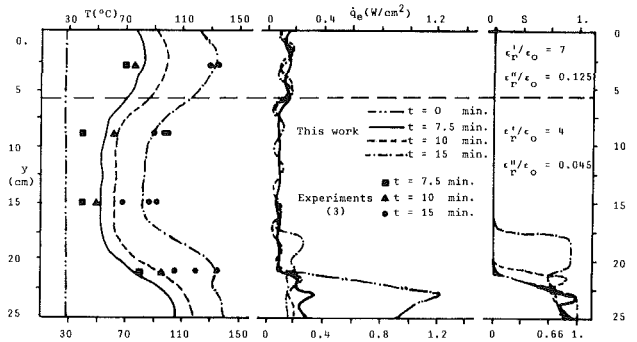

Fig. 3 Temperatures, absorbed power, and saturation versus soil depth

Presentation and Discussion of the Results

Presentation. Numerical solutions are presented in Figs. 2 and 3. The numerical values assumed for the soils examined are the following: $\phi = 0.3$, $S_R = 0.2$, $k = 10^{-6}$ m², $\lambda = 0.000605 + 4.633(T - 273.15)10^{-6}$ kW/mK.

In Fig. 2 are reported the temperature and the EM power absorbed in a soil fully saturated at the beginning of the treatment. The temperature, the absorbed EM power, and the saturation in the soil are shown after various times.

The same variables (T, $\dot{q}_e$, S) are reported in Fig. 3 along with the experimental data found in [3]. According to the constitution of the asphaltic concrete pavement a two-layer model is assumed with the values of dielectric complex constant reported in Fig. 3.

Discussion. In Fig. 2 numerical predictions have been obtained for a constant ϵ_r/ϵ_0. The profile of the EM power at $t = 0$ decreases strongly with the depth because the soil is fully saturated. The temperatures of the soil increase with time and after 15 min a partial vaporization of the liquid in the upper layer is predicted. A maximum in the temperature profile is detectable in correspondence of the saturated limit of the soil. At the same time the EM power absorbed in the upper layer is markedly reduced because the water content is decreased. Figure 2 shows some "wiggles" in the absorbed EM power profile, due to the EM standing waves induced by the stratified model assumed.

In Fig. 3 an asphalt layer of 25 cm, assumed in the theoretical analysis to reproduce the experimental condition, is placed on a semi-infinite calcar base. The asphalt layer is divided in two parts; the upper one (6 cm) is made of basalt and bitumen and the lower one by calcar and bitumen. The initial saturation profile in the soil has been assumed as sketched in Fig. 3 in accordance with the environmental conditions of the experiment [3] and the theory of capillary rise of water in a porous medium [7]. At $t = 0$ the EM power is mainly absorbed by the bottom layer. The consequent temperature in-

crease up to the partial vaporization produces a pressure gradient which causes the water to move upwards throughout the asphalt layer (17–21 cm). Regarding the temperature distribution it can be observed that the maximum in the temperature of the upper layer is due to the higher value assumed for ϵ_r''/ϵ_0 and to the decay of the electric field intensity with the depth.

As evidenced by Fig. 3, microwave energy absorbed in the upper layer (6 cm) is about two times that absorbed in the lower one (from 6 cm to 17.5 cm). This observation justifies the higher temperature in the upper layer.

Time evolution of temperature is finally compared with the experiments [3] because they are the only data available in the literature, to the knowledge of the authors. The experiments [3] have been performed with a Magnetron generator of 5 kW at 2.5 MHz. The radiator was a Horn Reflector type with an aperture of 0.04 m^2; the radiant surface was positioned parallel to the pavement at an height of about 20 cm. Several blocks of motorway pavements 25 cm high and 0.25 m^2 in area were placed on a calcar sublayer. Temperatures were monitored at different depths. The agreement between the numerical predictions of this work and the experimental results seems to be quite acceptable.

References

1 Chiostri, M., and Botto, M., "La rigenerazione in sito: una rivoluzione nelle tecniche manutentorie delle sovrastrutture stradali," Seminar on Recycling of Pavement Materials, Road Research Program of Economic Cooperation and Development (OECD), Rome, Mar. 1981.

2 Okress, E. C., *Microwave Power Engineering*, Academic Press, New York, 1968.

3 Botto, M., and Neri, F., "Ricerca sperimentale per l'impiego di microonde nella rigenerazione dei conglomerati bituminosi," Seminar on Recycling of Pavement Materials, Road Research Program of Economic Cooperation and Development (OECD), Rome, Mar. 1981.

4 Wait, J. R., *Propagation of Radio-Waves Over a Stratified Ground*, Pergamon Press, Oxford, 1953.

5 Wang, J. R., and Schmugge, T. J., "An Empirical Model for the Complex Dielectric Permittivity of Soils as a Function of Water Content," *IEEE Trans. on Geoscience and Remote Sensing*, GE-18, Oct. 1980, pp. 50–55.

6 von Hippel, A. R., *Dielectric Materials on Applications*, MIT Press, Cambridge, MA, 1954.

7 Luikov, A. V., *Heat and Mass Transfer in Capillary-Porous Bodies*, Oxford, Pergamon Press, 1966.

8 Corey, A. R., *Mechanics of Heterogeneous Fluids in Porous Media*, Water Resources Publications, Fort Collins, 1977.

9 van Wylen, G., and Sonntag, R. E., *Fundamentals of Classical Thermodynamics*, Wiley, New York, 1976.

10 Schubert, G., and Strauss, J. M., "Steam-Water Counter-flow in Porous Media," *Journal of Geophysical Research*, Vol. 84, B4, 1979, pp. 1621–1628.

11 McWhorter, D., and Suwada, D. K., *Ground-Water Hydrology and Hydraulics*, Water Resources Publications, Fort Collins, 1977.

12 Martini, L., "Modello termico di un processo di riscaldamento a microonde di mezzi porosi," Tesi di Laurea, Dipartimento di Ingegneria Elettronica, Facolta' di Ingegneria, Firenze, 1984.

13 Raznjevic, K., *Tabelle Termodinamiche*, Del Bianco, ed., Subotica, 1971.

14 Patankar, S. V., *Numerical Heat Transfer and Fluid Flow*, McGraw-Hill, New York, 1980.

Thermal Stratification Induced in a Circular Pipe by a Periodic Time-Dependent Temperature Imposed on the Boundary

L. Robillard,[1] P. Vasseur,[1,2] and H. T. Nguyen[1]

Nomenclature

R = radius of the pipe
Ra = Rayleigh number = $g\beta R^3 \Delta T_0'/\nu\alpha$
r = dimensionless radial cylindrical coordinate = r'/R
t = dimensionless time = $\alpha t'/R^2$
T = dimensionless temperature = $(T' - T_0')/\Delta T_0'$
u, v = dimensionless radial and angular velocities
β = thermal expansion coefficient
ρ = density
φ = angular coordinate
ψ = dimensionless stream function = ψ'/α
Ω = dimensionless vorticity = $\Omega' R^2/\alpha$
ω = dimensionless frequency or Strouhal number = $\omega' R^2/\alpha$
$'$ = refers to dimensional variable
$\bar{}$ = refers to a quantity averaged over one cycle
$*$ = refers to pure conduction regime
av = refers to spatially averaged quantity
i = refers to initial conditions
c = refers to the center of the pipe
w = refers to the value at the wall

[1]École Polytechnique, Université de Montréal, Department of Mechanical Engineering, Montreal, P.Q. – H3C 3A7, Canada.

[2]Assoc. Mem. ASME.

Contributed by the Heat Transfer Division for publication in the JOURNAL OF HEAT TRANSFER. Manuscript received by the Heat Transfer Division December 14, 1984.

1 Introduction

The laminar convective heat transfer in a horizontal circular tube has been treated intensively in the past for various time-dependent boundary conditions. Quack [1] has considered the case of a wall temperature increasing (or decreasing) linearly with time using a perturbation method. An experimental investigation of the same problem has been performed by Deaver and Eckert [2]. For this type of problem, the heating process is considered long enough for a quasi-steady state to be reached in which local temperature gradients, velocities, and other parameters become independent of time. Takeuchi and Cheng [3] have obtained a numerical solution (by finite difference method) for the same problem, extending the results obtained by Quack to more realistic Rayleigh numbers.

When a maximum density (such as the case of water at a temperature in the neighborhood of 4°C) is involved within the range of the cooling process, a steady state cannot develop and the flow field as well as the temperature field remains essentially time dependent. This particular situation has been studied experimentally and numerically by Gilpin [4], Cheng and Takeuchi [5], and Robillard and Vasseur [6]. Such a situation is characterized by an inversion process in the convective flow and in the thermal stratification of the core.

The problem investigated in the present paper concerns the case of a wall temperature varying sinusoidally with time. When the frequency is small, this problem can be related to the previously mentioned investigations in the sense that its time-dependent response should correspond piecewise to those of the constant cooling rate with the Rayleigh number adjusted to the wall temperature rate of change at a given time. Also the problem considered here is qualitatively similar to the cooling of a fluid with a maximum density when the wall temperature encompasses an extremum. However, no comparison can be made with previous results when the frequency is increased such that the corresponding period of oscillation becomes of the same order of magnitude as the characteristic transient time for the establishment of a quasi-steady state in the case of constant cooling rate.

2 Formulation of the Problem

Consider an infinitely long horizontal cylinder containing an incompressible fluid. It is assumed that initially the fluid is at rest and at a uniform temperature T_0'; at time $t' = 0$ the temperature of the boundary starts changing according to

$$T_w' = T_0' + \Delta T_0' \sin \omega' t' \tag{1}$$

The problem is to find the resulting fluid motion, temperature

crease up to the partial vaporization produces a pressure gradient which causes the water to move upwards throughout the asphalt layer (17–21 cm). Regarding the temperature distribution it can be observed that the maximum in the temperature of the upper layer is due to the higher value assumed for ϵ_r''/ϵ_0 and to the decay of the electric field intensity with the depth.

As evidenced by Fig. 3, microwave energy absorbed in the upper layer (6 cm) is about two times that absorbed in the lower one (from 6 cm to 17.5 cm). This observation justifies the higher temperature in the upper layer.

Time evolution of temperature is finally compared with the experiments [3] because they are the only data available in the literature, to the knowledge of the authors. The experiments [3] have been performed with a Magnetron generator of 5 kW at 2.5 MHz. The radiator was a Horn Reflector type with an aperture of 0.04 m^2; the radiant surface was positioned parallel to the pavement at an height of about 20 cm. Several blocks of motorway pavements 25 cm high and 0.25 m^2 in area were placed on a calcar sublayer. Temperatures were monitored at different depths. The agreement between the numerical predictions of this work and the experimental results seems to be quite acceptable.

References

1 Chiostri, M., and Botto, M., "La rigenerazione in sito: una rivoluzione nelle tecniche manutentorie delle sovrastrutture stradali," Seminar on Recycling of Pavement Materials, Road Research Program of Economic Cooperation and Development (OECD), Rome, Mar. 1981.

2 Okress, E. C., *Microwave Power Engineering*, Academic Press, New York, 1968.

3 Botto, M., and Neri, F., "Ricerca sperimentale per l'impiego di microonde nella rigenerazione dei conglomerati bituminosi," Seminar on Recycling of Pavement Materials, Road Research Program of Economic Cooperation and Development (OECD), Rome, Mar. 1981.

4 Wait, J. R., *Propagation of Radio-Waves Over a Stratified Ground*, Pergamon Press, Oxford, 1953.

5 Wang, J. R., and Schmugge, T. J., "An Empirical Model for the Complex Dielectric Permittivity of Soils as a Function of Water Content," *IEEE Trans. on Geoscience and Remote Sensing*, GE-18, Oct. 1980, pp. 50–55.

6 von Hippel, A. R., *Dielectric Materials on Applications*, MIT Press, Cambridge, MA, 1954.

7 Luikov, A. V., *Heat and Mass Transfer in Capillary-Porous Bodies*, Oxford, Pergamon Press, 1966.

8 Corey, A. R., *Mechanics of Heterogeneous Fluids in Porous Media*, Water Resources Publications, Fort Collins, 1977.

9 van Wylen, G., and Sonntag, R. E., *Fundamentals of Classical Thermodynamics*, Wiley, New York, 1976.

10 Schubert, G., and Strauss, J. M., "Steam-Water Counter-flow in Porous Media," *Journal of Geophysical Research*, Vol. 84, B4, 1979, pp. 1621–1628.

11 McWhorter, D., and Suwada, D. K., *Ground-Water Hydrology and Hydraulics*, Water Resources Publications, Fort Collins, 1977.

12 Martini, L., "Modello termico di un processo di riscaldamento a microonde di mezzi porosi," Tesi di Laurea, Dipartimento di Ingegneria Elettronica, Facolta' di Ingegneria, Firenze, 1984.

13 Raznjevic, K., *Tabelle Termodinamiche*, Del Bianco, ed., Subotica, 1971.

14 Patankar, S. V., *Numerical Heat Transfer and Fluid Flow*, McGraw-Hill, New York, 1980.

Thermal Stratification Induced in a Circular Pipe by a Periodic Time-Dependent Temperature Imposed on the Boundary

L. Robillard,[1] P. Vasseur,[1,2] and H. T. Nguyen[1]

Nomenclature

R = radius of the pipe
Ra = Rayleigh number = $g\beta R^3 \Delta T_0'/\nu\alpha$
r = dimensionless radial cylindrical coordinate = r'/R
t = dimensionless time = $\alpha t'/R^2$
T = dimensionless temperature = $(T' - T_0')/\Delta T_0'$
u, v = dimensionless radial and angular velocities
β = thermal expansion coefficient
ρ = density
φ = angular coordinate
ψ = dimensionless stream function = ψ'/α
Ω = dimensionless vorticity = $\Omega' R^2/\alpha$
ω = dimensionless frequency or Strouhal number = $\omega' R^2/\alpha$
$'$ = refers to dimensional variable
$\bar{}$ = refers to a quantity averaged over one cycle
$*$ = refers to pure conduction regime
av = refers to spatially averaged quantity
i = refers to initial conditions
c = refers to the center of the pipe
w = refers to the value at the wall

1 Introduction

The laminar convective heat transfer in a horizontal circular tube has been treated intensively in the past for various time-dependent boundary conditions. Quack [1] has considered the case of a wall temperature increasing (or decreasing) linearly with time using a perturbation method. An experimental investigation of the same problem has been performed by Deaver and Eckert [2]. For this type of problem, the heating process is considered long enough for a quasi-steady state to be reached in which local temperature gradients, velocities, and other parameters become independent of time. Takeuchi and Cheng [3] have obtained a numerical solution (by finite difference method) for the same problem, extending the results obtained by Quack to more realistic Rayleigh numbers.

When a maximum density (such as the case of water at a temperature in the neighborhood of 4°C) is involved within the range of the cooling process, a steady state cannot develop and the flow field as well as the temperature field remains essentially time dependent. This particular situation has been studied experimentally and numerically by Gilpin [4], Cheng and Takeuchi [5], and Robillard and Vasseur [6]. Such a situation is characterized by an inversion process in the convective flow and in the thermal stratification of the core.

The problem investigated in the present paper concerns the case of a wall temperature varying sinusoidally with time. When the frequency is small, this problem can be related to the previously mentioned investigations in the sense that its time-dependent response should correspond piecewise to those of the constant cooling rate with the Rayleigh number adjusted to the wall temperature rate of change at a given time. Also the problem considered here is qualitatively similar to the cooling of a fluid with a maximum density when the wall temperature encompasses an extremum. However, no comparison can be made with previous results when the frequency is increased such that the corresponding period of oscillation becomes of the same order of magnitude as the characteristic transient time for the establishment of a quasi-steady state in the case of constant cooling rate.

2 Formulation of the Problem

Consider an infinitely long horizontal cylinder containing an incompressible fluid. It is assumed that initially the fluid is at rest and at a uniform temperature T_0'; at time $t' = 0$ the temperature of the boundary starts changing according to

$$T_w' = T_0' + \Delta T_0' \sin \omega' t' \tag{1}$$

The problem is to find the resulting fluid motion, temperature

[1]École Polytechnique, Université de Montréal, Department of Mechanical Engineering, Montreal, P.Q. – H3C 3A7, Canada.

[2]Assoc. Mem. ASME.

Contributed by the Heat Transfer Division for publication in the JOURNAL OF HEAT TRANSFER. Manuscript received by the Heat Transfer Division December 14, 1984.

field, and heat transfer at the boundary when the steady periodic state is reached. Using the Boussinesq approximation, and assuming that the flow is two dimensional [5], the basic set of equations expressing the conservation of mass, momentum, and energy is reduced to the following dimensionless equations

$$\frac{\partial \Omega}{\partial t} = -J[\psi, \Omega] - \text{Pr Ra } J[T, r\cos\varphi] + \text{Pr } \nabla^2\Omega \tag{2}$$

$$\frac{\partial T}{\partial t} = -J[\psi, T] + \nabla^2 T \tag{3}$$

$$\Omega = -\nabla^2\psi \tag{4}$$

$$u = \frac{1}{r}\frac{\partial \psi}{\partial \varphi} \qquad v = -\frac{\partial \psi}{\partial r} \tag{5}$$

where

$$J[f_1, f_2] = \left[\frac{\partial f_1}{r\partial\varphi}\frac{\partial f_2}{\partial r} - \frac{\partial f_2}{r\partial\varphi}\frac{\partial f_1}{\partial r}\right]$$

other notations have the usual meaning defined in the nomenclature. Here the variables have been normalized by a characteristic time scale R^2/α, a length scale R, a temperature scale $\Delta T_0'$, and a reference temperature T_0. Pr $= \nu/\alpha$ appearing in equation (2) is the Prandtl number; ν and α are, respectively, the kinematic viscosity and thermal diffusivity, both referred to the temperature T_0'. In deriving equation (2), the equations of state $\rho = \rho_0[1 - \beta\,(T' - T_0')]$ was assumed. All properties were taken independent of pressure, viscous dissipation and the work done by pressure were neglected [7].

The dimensionless initial and boundary conditions are

$$\begin{aligned}
&\text{at } t=0\text{: } u=v=\psi=\Omega=T=0 && \text{everywhere;}\\
&\text{at } t>0\text{: } u=v=\psi=0;\ T=\sin\omega t && \text{on the wall}\\
&\frac{\partial u}{\partial\varphi}=v=\psi=\Omega=0;\ \frac{\partial T}{\partial\varphi}=0 && \text{on the symmetry line}
\end{aligned} \tag{6}$$

The governing parameters of the problem are the Rayleigh number Ra $= (gR^3/\alpha\nu)\,\beta\Delta T_0'$, the Strouhal number $\omega = \omega' R^2/\alpha$ and the Prandtl number Pr $= \nu/\alpha$. The Prandtl number for air and water is approximately 0.7 and 7 respectively. In the present study the arbitrary value of unity was chosen.

The rate of change of heat contained in the cavity is related to the heat transfer at the boundary by the following equation

$$\frac{\partial T_{av}}{\partial t} = 2Q_{av} \tag{7}$$

From the governing equations (2)–(3) and boundary conditions (6), it can be shown that

$$T(r, \varphi, t) = -T(r, \pi-\varphi; t+\pi/\omega) \tag{8a}$$

$$\psi(r, \varphi, t) = -(r, \pi-\varphi; t+\pi/\omega) \tag{8b}$$

which implies that the isotherms and flow patterns at any time will be repeated symmetrically across the horizontal diameter half a period later. It also follows from (8 *a*, *b*) that the time-averaged temperature and stream function satisfy the following symmetry across the horizontal diameter

$$\bar{T}(r, \varphi) = -\bar{T}(r, \pi-\varphi) \tag{9a}$$

$$\bar{\psi}(r, \varphi) = -\bar{\psi}(r, \pi-\varphi) \tag{9b}$$

3 Results and Discussion

3.1 Pure Conduction Regime. In the case of pure conduction the periodic steady-state solution of equation (3), with the boundary condition $T_w = \sin\omega t$, is independent of φ and may be obtained analytically [8] in the form:

$$T(r, t) = A\cos\omega t + B\sin\omega t \tag{10}$$

where

$$A = \frac{-bei(k)\ ber(kr) + ber(k)\ bei(kr)}{M_0^2(k)}$$

$$B = \frac{-ber(k)\ ber(kr) + bei(k)\ bei(kr)}{M_0^2(k)}$$

with $M_0(k) = \sqrt{ber^2(k) + bei^2(k)}$; $ber(x)$ and $bei(x)$ are the real and imaginary parts of the Bessel function $J_0(xe^{3\pi i/4})$.

When $\omega \to 0$, it can be deduced from equation (10) that differences between the temperature of an interior point and that of the boundary become vanishingly small compared to $\Delta T_0'$. Therefore the solution may be piecewise obtained from existing results for the same geometry with boundary submitted to a constant cooling (or heating) rate [3, 5]. This approach remains equally true when convection is involved. With increasing ω, the effect of the variation with time of the boundary temperature is limited to a narrow region near the wall in the case of pure conduction.

Also for the case of pure conduction, the temperature at any point, averaged over one cycle, must satisfy the following condition

$$\bar{T}(r) = \int_t^{t+2\pi/\omega} T(r, t)dt = 0 \tag{11}$$

However this is no longer true when convection is allowed.

3.2 Conduction Convection Regime. The set of equations (2)–(5) together with the initial and boundary conditions (6) has been solved by a finite difference method with an alternating direction implicit procedure and overrelaxation technique. A more detailed description can be found in [6]. Enough computer time was allowed to reach the periodic steady state which is characterized by the fact that the stream function and the temperature at every point repeat themselves periodically. The numerical approach was tested to reproduce pure conduction temperature distributions at Ra $\to$ 0.

First, it was found that, no matter how small the frequency is, the convective motion consists of a succession of flow reversals comparable to those already described in the case of water cooled at a constant rate through 4°C [4–6]. Figure 1 shows the sequence of flow (right) and temperature (left) fields taking place during one cycle. It should be noted from this figure that the streamline and isotherm patterns at any time are repeated symmetrically with respect to the horizontal diameter after half a period. This is in agreement with equations (8*a*, *b*).

When convection is present, T is no longer independent of φ, as it can already be observed on the sequence of Fig. 1. Numerical results for the temperature distributions along the horizontal diameter have been obtained for various Ra and ω_0. A comparison of those results with the pure conduction case indicates that the amplitude of the temperature is increased in the central region and that the temperature gradients near the boundary are steeper. More precisely the effect of convection is to increase both the amplitude and the number of harmonics of the temperature oscillations within the cavity. This clearly reflects the fact that convection is a nonlinear mechanism that essentially induces a distorted response of the system by generating higher harmonics from the applied boundary temperature.

3.3 Time-Averaged Temperature and Flow Fields. Let us now consider the time-averaged temperature and flow fields which are shown in Figs. 2(*a–d*). Those figures are obtained by numerically averaging the stream function and temperature values at each point during a complete period. One notes the symmetry of the isotherms and flow patterns with respect to the horizontal diameter, as predicted previously in equations (9 *a*, *b*). From these figures it appears that a sinusoidal time-dependent temperature at the boundary of a circular pipe can

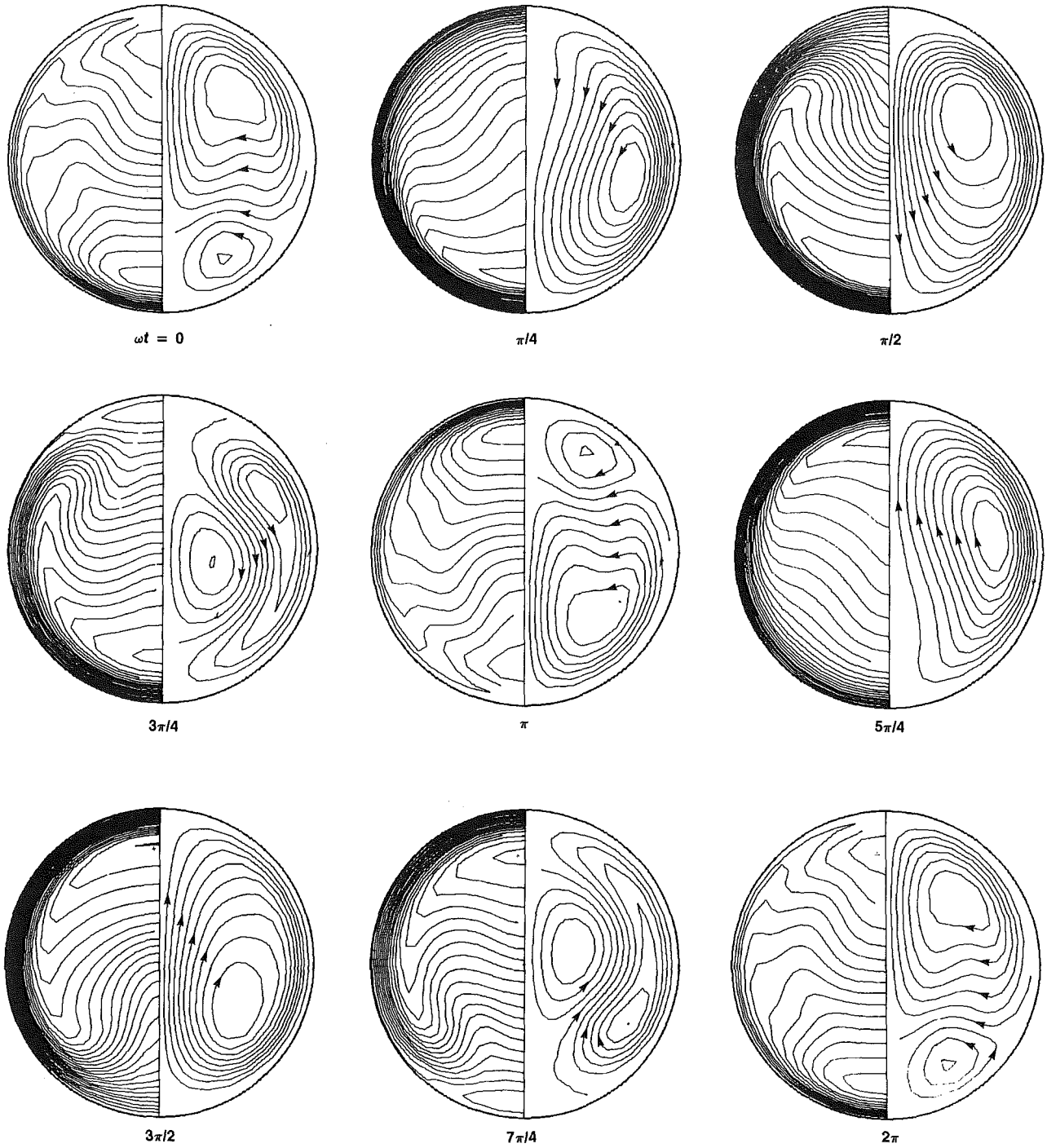

Fig. 1 Isotherms and streamlines at different times during one cycle for the case $\omega = 64$ and $Ra = 10^5$ ($\Delta T = 0.05$ between adjacent isotherms)

induce a nonzero time-averaged convective flow and a stable thermal stratification. The temperatures of the upper and lower halves of the pipe are above and below zero, respectively, with heat being conducted into the cold bottom and out of the hot top of the cavity, resulting in a time-averaged upward heat transfer. A first glance at Fig. 2 may lead to the wrong conclusion that there is no mechanism along the horizontal diameter to sustain that result. Firstly, there is an adverse vertical temperature gradient at such height and consequently no heat can be transported upward by conduction. Secondly, according to the streamline pattern of Figs. 2, it seems that no heat can be transported by convection across the horizontal diameter. However it should be remembered that the results of Fig. 2 represent time-averaged flow and temperature fields over one cycle. In fact, this is the transient flow field taking place during one cycle that produces an important mass exchange between the upper and the lower part of the cavity. Heat is conveyed across the horizontal diameter by this mass exchange.

Finally, Figs. 3(*a*, *b*) give Q and $(\bar{T})_{max}$, respectively, as functions of Ra, for ω equal to 10 and 64. Q is the net heat flux across the horizontal diameter during one cycle and $(\bar{T})_{max}$ is

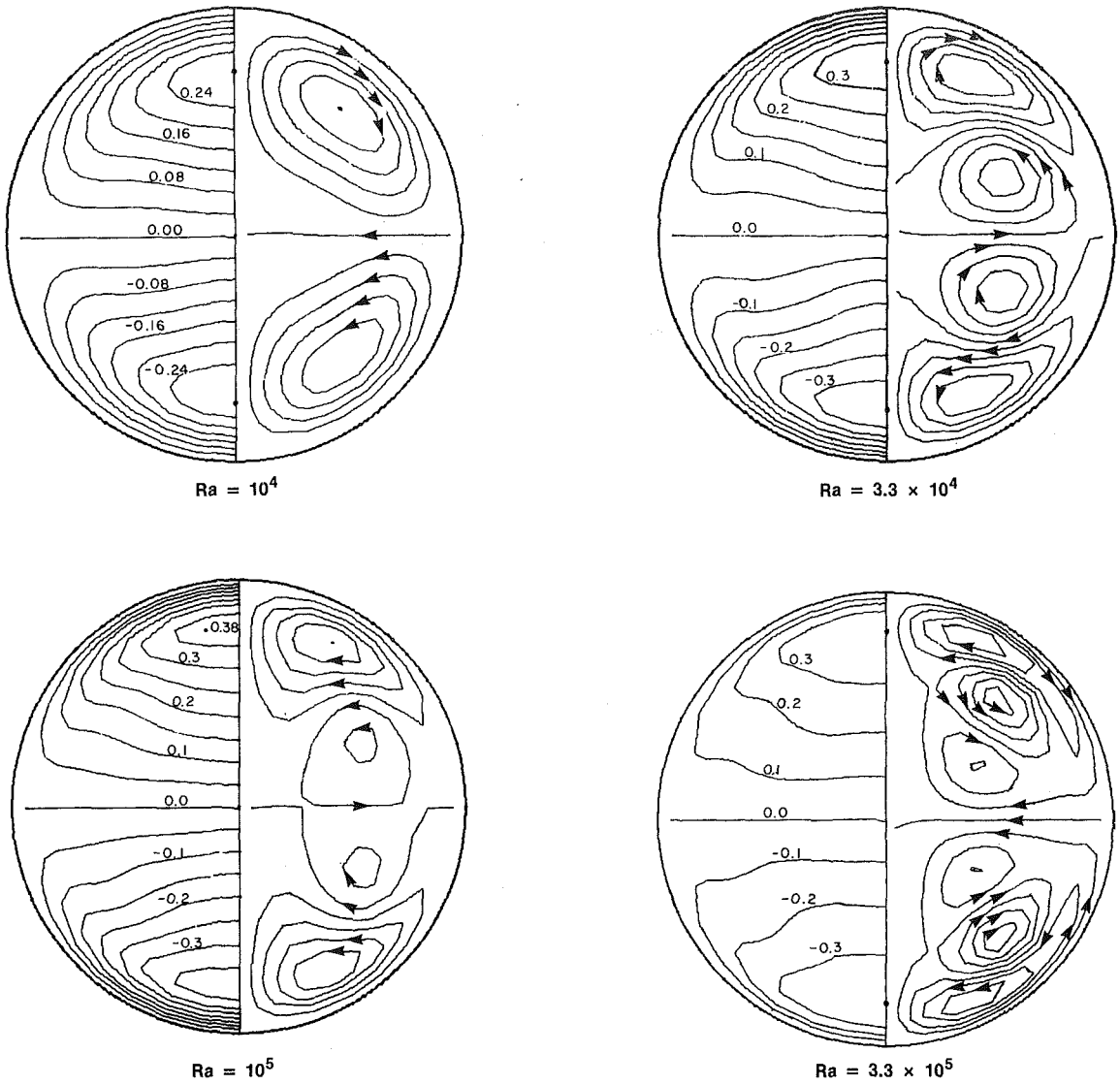

Fig. 2 Isotherm and streamline patterns obtained at each point by averaging the temperature and the stream function over one cycle (for *all cases*, $\omega = 64$)

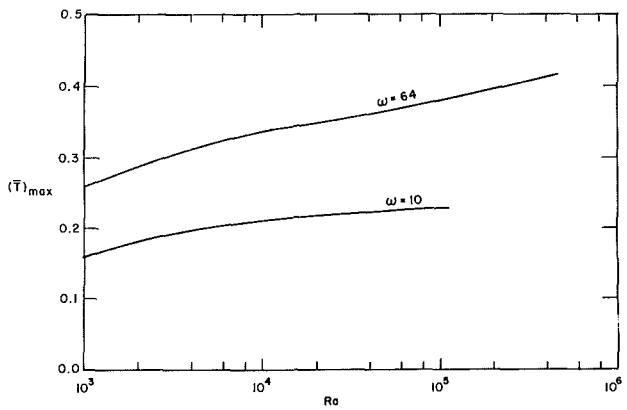

Fig. 3(*a*) Mean heat transfer across the cavity

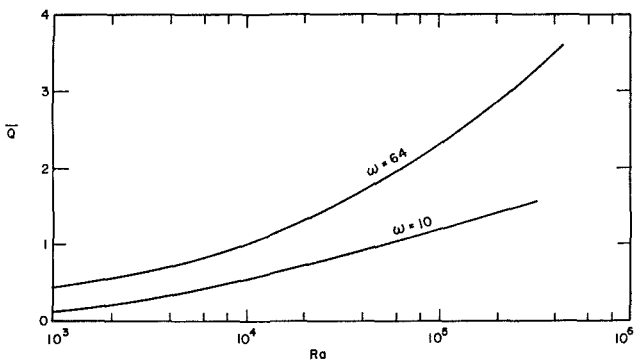

Fig. 3(*b*) Maximum mean temperature inside the cavity

the maximum value of the time-averaged temperature field. $(\bar{T})_{max}$ may be considered a measure of the stratification induced in the cavity. Solving for ω values beyond 64 within the same range of Rayleigh number would increase to some extent the stratification and the heat flux Q. However, the computer time then rapidly becomes prohibitive since the pure conduction itself involves a thermal boundary layer and consequently requires a much more refined mesh size.

Acknowledgments

This work was supported by the Natural Sciences and Engineering Research Council of Canada through Grants A-4197 and A-9201.

References

1 Quack, H., "Natürliche Konvektion innerhalb eines horizontalen Zylinders bei Kleinen Grashof Zahlen," *Warme- und Stoffübertragung*, Vol. 3, 1970, pp. 134–138.

2 Deaver, F. K., and Eckert, E. R. G., "An Interferometric Investigation of Convective Heat Transfer in a Horizontal Fluid Cylinder With Wall Temperature Increasing at a Uniform Rate," *Proceedings of the Fourth International Heat Transfer Conference*, Vol. 4, Paper NC11, ASME, New York, 1970.

3 Takeuchi, M., and Cheng, K., "Transient Natural Convection in Horizontal Cylinders With Constant Cooling Rate," *Warme- und Stoffübertragung*, Vol. 9, 1976, pp. 215–275.

4 Gilpin, R. P., "Cooling of a Horizontal Cylinder of Water Through Its Maximum Density Point at 4°C," *International Journal of Heat and Mass Transfer*, Vol. 18, 1975, pp. 1307–1314.

5 Cheng, K. C., and Takeuchi, M., "Transient Natural Convection of Water in a Horizontal Pipe With Constant Cooling Rate Through 4°C," ASME JOURNAL OF HEAT TRANSFER, Vol. 98, 1976, pp. 581–587.

6 Robillard, L., and Vasseur, P., "Convective Response of a Mass of Water Near 4°C to a Constant Cooling Rate Applied on Its Boundaries," *Journal of Fluid Mechanics*, Vol. 118, 1982, pp. 123–141.

7 Watson, A., "Numerical Studies on Two and Three Dimensional Laminar Convection Flows," Ph.D. Thesis, University of Hull, England, 1971.

8 Hildebrand, F. B., *Advanced Calculus for Applications*, Prentice-Hall, New York, 1963, p. 494.

Laminar Free Convection From a Sphere With Blowing and Suction

Ming-Jer Huang[1] and Cha'o-Kuang Chen[2]

Nomenclature

f = reduced stream function
$F(X)$ = prescribed surface function
g = gravitational acceleration
Gr = Grashof number for prescribed surface temperature
Gr* = Grashof number for prescribed surface heat flux
h = local heat transfer coefficient
k = thermal conductivity
Nu = local Nusselt number = hR/k
Pr = Prandtl number
R = radius of sphere
r = radial distance from symmetric axis to surface
T = fluid temperature
u,v = velocity components in x and y directions, respectively
x,y = dimensional coordinates
α = thermal diffusivity
β = coefficient of thermal expansion
$\tilde{\alpha},\tilde{\beta},\tilde{\gamma}$ = functions defined in equations (15)–(18), respectively
η = pseudosimilarity variable
θ = dimensionless temperature
ν = kinematic viscosity
ξ = transformed axial coordinate
ρ = fluid density
ψ = stream function

Subscripts

$w0$ = stagnation condition
w = surface condition

[1]Associate Professor, Department of Engineering Science, National Cheng Kung University, Tainan, Taiwan, Republic of China.

[2]Professor, Department of Mechanical Engineering, National Cheng Kung University, Tainan, Taiwan, Republic of China.

Contributed by the Heat Transfer Division for publication in the JOURNAL OF HEAT TRANSFER. Manuscript received by the Heat Transfer Division November 8, 1983.

Introduction

The effect of mass transfer on free convection from a vertical plate has been studied by Eichhorn (1960), Sparrow and Cess (1961), Merkin (1972), and Parikh (1974). Recently, Merkin (1975) gave an asymptotic series solution for two-dimensional bodies. Minkowycz and Sparrow (1979) studied a vertical cylinder in a natural convective flow. According to their conclusions, the heat transfer rate increases with suction and decreases with blowing.

The present note is concerned with the study of the influence of Prandtl number and surface mass transfer on a steady, laminar, free convective flow over a sphere with nonuniform surface temperature or heat flux.

Governing Equations

Consider a sphere of radius R which is situated in an otherwise quiescent environment having temperature T_∞. The coordinates x and y measure, respectively, the distance along the surface of sphere from the stagnation point and the distance normal to the surface. The surface subjected to mass transfer is maintained at an arbitrary temperature $T_w(x)$ or heat flux $q_w(x)$. By employing the Boussinesq approximation and assuming constant fluid properties, the laminar boundary layer equations described by Chiang et al. (1964) and Chen and Mucoglu (1977) are given as follows

$$\frac{\partial(ru)}{\partial x}+\frac{\partial(rv)}{\partial y}=0 \tag{1}$$

$$u\frac{\partial u}{\partial x}+v\frac{\partial u}{\partial y}=g\beta(T-T_\infty)\sin(x/R)+\nu\frac{\partial^2 u}{\partial y^2} \tag{2}$$

$$u\frac{\partial T}{\partial x}+v\frac{\partial T}{\partial y}=\alpha\frac{\partial^2 T}{\partial y^2} \tag{3}$$

where $r(x)=R\sin(x/R)$. The boundary conditions for equations (1)–(3) are

$$\left.\begin{aligned} &u=0,\ v=v_w(x),\ T=T_w(x)\ \text{ or }\ -k\frac{\partial T}{\partial y}=q_w(x) && \text{at } y=0\\ &u\to 0,\ T\to T_\infty && \text{as } y\to\infty \end{aligned}\right\} \tag{4}$$

To facilitate the solution of the above system of equations, it is necessary to transform these equations into a form exhibiting the effects of surface mass transfer and Prandtl number on the convective heat transfer. The transformation procedures are based on the prescribed surface temperature (PST) or prescribed surface heat flux (PHF). Let

$$X=x/R \text{ and } \xi=\int_0^X F(X)dX \tag{5}$$

with

$$\left.\begin{aligned} &\eta=y\mathrm{Gr}^{1/4}[F(X)]^{1/2}/R\\ &f(\xi,\eta)=\psi(x,y)[F(X)]^{1/2}/(\nu\xi\mathrm{Gr}^{1/4})\\ &\theta(\xi,\eta)=(T-T_\infty)/[(T_{w0}-T_\infty)F(X)] \end{aligned}\right\} \text{ for PST case} \tag{6}$$

and

Acknowledgments

This work was supported by the Natural Sciences and Engineering Research Council of Canada through Grants A-4197 and A-9201.

References

1 Quack, H., "Natürliche Konvektion innerhalb eines horizontalen Zylinders bei Kleinen Grashof Zahlen," *Warme- und Stoffübertragung*, Vol. 3, 1970, pp. 134–138.

2 Deaver, F. K., and Eckert, E. R. G., "An Interferometric Investigation of Convective Heat Transfer in a Horizontal Fluid Cylinder With Wall Temperature Increasing at a Uniform Rate," *Proceedings of the Fourth International Heat Transfer Conference*, Vol. 4, Paper NC11, ASME, New York, 1970.

3 Takeuchi, M., and Cheng, K., "Transient Natural Convection in Horizontal Cylinders With Constant Cooling Rate," *Warme- und Stoffübertragung*, Vol. 9, 1976, pp. 215–275.

4 Gilpin, R. P., "Cooling of a Horizontal Cylinder of Water Through Its Maximum Density Point at 4°C," *International Journal of Heat and Mass Transfer*, Vol. 18, 1975, pp. 1307–1314.

5 Cheng, K. C., and Takeuchi, M., "Transient Natural Convection of Water in a Horizontal Pipe With Constant Cooling Rate Through 4°C," ASME JOURNAL OF HEAT TRANSFER, Vol. 98, 1976, pp. 581–587.

6 Robillard, L., and Vasseur, P., "Convective Response of a Mass of Water Near 4°C to a Constant Cooling Rate Applied on Its Boundaries," *Journal of Fluid Mechanics*, Vol. 118, 1982, pp. 123–141.

7 Watson, A., "Numerical Studies on Two and Three Dimensional Laminar Convection Flows," Ph.D. Thesis, University of Hull, England, 1971.

8 Hildebrand, F. B., *Advanced Calculus for Applications*, Prentice-Hall, New York, 1963, p. 494.

Laminar Free Convection From a Sphere With Blowing and Suction

Ming-Jer Huang[1] and Cha'o-Kuang Chen[2]

Nomenclature

f = reduced stream function
$F(X)$ = prescribed surface function
g = gravitational acceleration
Gr = Grashof number for prescribed surface temperature
Gr* = Grashof number for prescribed surface heat flux
h = local heat transfer coefficient
k = thermal conductivity
Nu = local Nusselt number = hR/k
Pr = Prandtl number
R = radius of sphere
r = radial distance from symmetric axis to surface
T = fluid temperature
u,v = velocity components in x and y directions, respectively
x,y = dimensional coordinates
α = thermal diffusivity
β = coefficient of thermal expansion
$\tilde{\alpha},\tilde{\beta},\tilde{\gamma}$ = functions defined in equations (15)–(18), respectively
η = pseudosimilarity variable
θ = dimensionless temperature
ν = kinematic viscosity
ξ = transformed axial coordinate
ρ = fluid density
ψ = stream function

Subscripts

$w0$ = stagnation condition
w = surface condition

[1]Associate Professor, Department of Engineering Science, National Cheng Kung University, Tainan, Taiwan, Republic of China.

[2]Professor, Department of Mechanical Engineering, National Cheng Kung University, Tainan, Taiwan, Republic of China.

Contributed by the Heat Transfer Division for publication in the JOURNAL OF HEAT TRANSFER. Manuscript received by the Heat Transfer Division November 8, 1983.

Introduction

The effect of mass transfer on free convection from a vertical plate has been studied by Eichhorn (1960), Sparrow and Cess (1961), Merkin (1972), and Parikh (1974). Recently, Merkin (1975) gave an asymptotic series solution for two-dimensional bodies. Minkowycz and Sparrow (1979) studied a vertical cylinder in a natural convective flow. According to their conclusions, the heat transfer rate increases with suction and decreases with blowing.

The present note is concerned with the study of the influence of Prandtl number and surface mass transfer on a steady, laminar, free convective flow over a sphere with nonuniform surface temperature or heat flux.

Governing Equations

Consider a sphere of radius R which is situated in an otherwise quiescent environment having temperature T_∞. The coordinates x and y measure, respectively, the distance along the surface of sphere from the stagnation point and the distance normal to the surface. The surface subjected to mass transfer is maintained at an arbitrary temperature $T_w(x)$ or heat flux $q_w(x)$. By employing the Boussinesq approximation and assuming constant fluid properties, the laminar boundary layer equations described by Chiang et al. (1964) and Chen and Mucoglu (1977) are given as follows

$$\frac{\partial(ru)}{\partial x}+\frac{\partial(rv)}{\partial y}=0 \tag{1}$$

$$u\frac{\partial u}{\partial x}+v\frac{\partial u}{\partial y}=g\beta(T-T_\infty)\sin(x/R)+\nu\frac{\partial^2 u}{\partial y^2} \tag{2}$$

$$u\frac{\partial T}{\partial x}+v\frac{\partial T}{\partial y}=\alpha\frac{\partial^2 T}{\partial y^2} \tag{3}$$

where $r(x)=R\sin(x/R)$. The boundary conditions for equations (1)–(3) are

$$\left.\begin{aligned} &u=0,\ v=v_w(x),\ T=T_w(x)\ \text{ or }\ -k\frac{\partial T}{\partial y}=q_w(x) && \text{at } y=0\\ &u\to 0,\ T\to T_\infty && \text{as } y\to\infty \end{aligned}\right\} \tag{4}$$

To facilitate the solution of the above system of equations, it is necessary to transform these equations into a form exhibiting the effects of surface mass transfer and Prandtl number on the convective heat transfer. The transformation procedures are based on the prescribed surface temperature (PST) or prescribed surface heat flux (PHF). Let

$$X=x/R \text{ and } \xi=\int_0^X F(X)dX \tag{5}$$

with

$$\left.\begin{aligned} &\eta=y\mathrm{Gr}^{1/4}[F(X)]^{1/2}/R\\ &f(\xi,\eta)=\psi(x,y)[F(X)]^{1/2}/(\nu\xi\mathrm{Gr}^{1/4})\\ &\theta(\xi,\eta)=(T-T_\infty)/[(T_{w0}-T_\infty)F(X)] \end{aligned}\right\} \text{ for PST case} \tag{6}$$

and

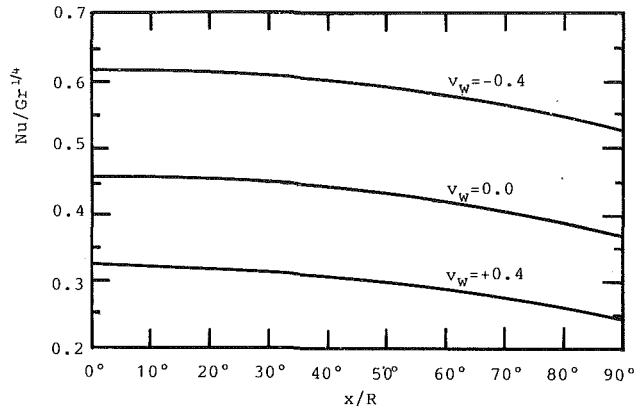

Fig. 1 Angular distributions of local Nusselt number for the PST case, Pr = 0.7

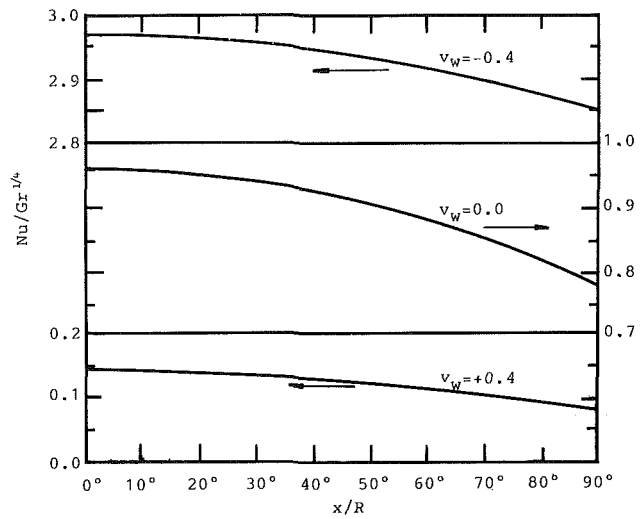

Fig. 2 Angular distributions of local Nusselt number for the PST case, Pr = 7.0

$$\left.\begin{aligned}
&\eta = y\mathrm{Gr}^{*1/5}[F(X)]^{1/2}/R \\
&f(\xi,\eta) = \psi(x,y)[F(X)]^{1/2}/(\nu\xi\mathrm{Gr}^{*1/5}) \\
&\theta(\xi,\eta) = [k\mathrm{Gr}^{*1/5}(T-T_\infty)]/[q_{w0}RF(X)]
\end{aligned}\right\} \quad \text{for PHF case} \tag{7}$$

where $\psi(x, y)$ is the stream function, defined as $ru = \partial(r\psi)/\partial y$ and $rv = -\partial(r\psi)/\partial x$. $F(X)$ is the function that describes the nonuniform surface condition, expressed as

$$F(X) = \begin{cases} (T_w(X) - T_\infty]/(T_{w0} - T_\infty) & \text{for PST case} \quad (8) \\ q_w(X)/q_{w0} & \text{for PHF case} \quad (9) \end{cases}$$

The Grashof number is defined as

$$\mathrm{Gr} = g\beta(T_{w0} - T_\infty)R^3/\nu^2 \tag{10}$$

and

$$\mathrm{Gr}^* = g\beta q_{w0}R^4/\nu^2 k \tag{11}$$

Substituting equations (5)–(11) into equations (1)–(4), the equations become

$$f''' - f'^2 + [1 + \tilde{\alpha}(X) + \tilde{\beta}(X)]ff'' + \frac{\sin X}{\xi}\theta = \xi\left(f'\frac{\partial f'}{\partial \xi} - f''\frac{\partial f}{\partial \xi}\right) \tag{12}$$

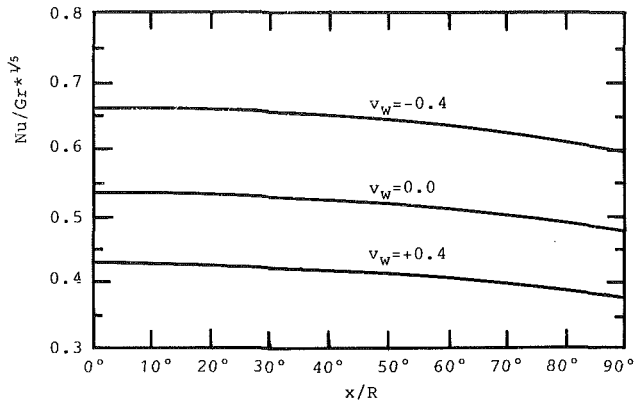

Fig. 3 Angular distributions of local Nusselt number for the PHF case, Pr = 0.7

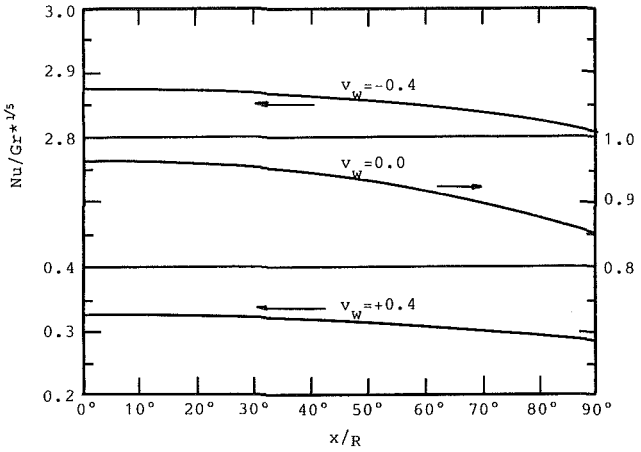

Fig. 4 Angular distributions of local Nusselt number for the PHF case, Pr = 7.0

$$\mathrm{Pr}^{-1}\theta'' + [1 + \tilde{\alpha}(X) + \tilde{\beta}(X)]f\theta' + 2\tilde{\beta}(X)f'\theta = \xi\left(f'\frac{\partial\theta}{\partial\xi} - \theta'\frac{\partial f}{\partial\xi}\right) \tag{13}$$

$$\left.\begin{aligned}
&\eta = 0;\ f' = 0,\ -\tilde{r}(X) = [1 + \tilde{\alpha}(X) + \tilde{\beta}(X)]f + \xi\frac{\partial f}{\partial\xi}, \\
&\qquad \theta = 1 \text{ or } \theta' = -[F(X)]^{-1/2} \\
&\eta \to \infty;\ f' \to 0,\ \theta \to 0
\end{aligned}\right\} \tag{14}$$

In the above equations primes denote partial differentiation with respect to η. $\tilde{\alpha}(X)$ and $\tilde{\beta}(X)$ are expressed in the following form

$$\tilde{\alpha}(X) = \xi\cos X/[F(X)\sin X], \tag{15}$$

$$\tilde{\beta}(X) = -\xi\frac{dF(X)}{dX}/\{2[F(X)]^2\} \tag{16}$$

$\tilde{\gamma}(X)$, which serves as the surface mass transfer parameter, is given by

$$\tilde{\gamma}(X) = \begin{cases} [R\,v_w(X)]/\{[F(X)]^{1/2}\nu\ \mathrm{Gr}^{1/4}\} \\ \qquad \text{for PST case} \quad (17) \\ [R\,v_w(X)]/\{[F(X)^{1/2}\nu\ \mathrm{Gr}^{*1/5}\} \\ \qquad \text{for PHF case} \quad (18) \end{cases}$$

The primary interest is the heat transfer rate and the wall shear stress. By using $h = q_w/(T_w - T_\infty)$, and $\tau_w = \mu\ \partial u/\partial y|_{y=0}$, and making use of equations (5)–(7), the following equations are obtained

Table 1 Values of $-\theta'(X, 0)$ and $f''(X, 0)$ for the PST case

Pr	v_w		x/R, degrees									
			0°	10°	20°	30°	40°	50°	60°	70°	80°	90°
	-1.2	$-\theta'(X,0)$	1.0055	1.0045	1.0016	.9968	.9900	.9812	.9702	.9570	.9414	.9231
		$f''(X,0)$	.7307	.7285	.7218	.7107	.6953	.6758	.6524	.6253	.5949	.5614
	-0.8		.7998	.7988	.7956	.7904	.7831	.7735	.7617	.7473	.7304	.7105
			.7690	.7668	.7601	.7490	.7336	.7142	.6907	.6636	.6331	.5993
	-0.4		.6165	.6155	.6123	.6069	.5994	.5896	.5774	.5628	.5455	.5252
			.7818	.7796	.7728	.7616	.7460	.7262	.7023	.6746	.6433	.6085
0.7	0.0		.4574	.4563	.4532	.4480	.4407	.4312	.4194	.4053	.3886	.3694
			.7678	.7655	.7586	.7471	.7311	.7108	.6863	.6577	.6253	.5892
	0.4		.3236	.3226	.3197	.3149	.3082	.2995	.2887	.2759	.2611	.2440
			.7298	.7274	.7204	.7086	.6923	.6715	.6464	.6171	.5838	.5466
	0.8		.2158	.2150	.2125	.2083	.2025	.1950	.1859	.1752	.1628	.1489
			.6735	.6711	.6640	.6521	.6357	.6147	.5894	.5599	.5263	.4889
	1.2		.1338	.1331	.1311	.1278	.1232	.1172	.1101	.1019	.0926	.0823
			.6061	.6037	.5967	.5850	.5688	.5481	.5232	.4942	.4614	.4250
	-1.2		8.4084	8.4082	8.4079	8.4073	8.4065	8.4055	8.4043	8.4029	8.4015	8.4001
			.1186	.1180	.1162	.1133	.1093	.1042	.0982	.0914	.0839	.0758
	-0.8		5.6304	5.6300	5.6287	5.6267	5.6239	5.6204	5.6162	5.6115	5.6064	5.6010
			.1749	.1741	.1716	.1674	.1617	.1546	.1460	.1362	.1254	.1136
	-0.4		2.9684	2.9670	2.9626	2.9553	2.9452	2.9320	2.9159	2.8966	2.8742	2.8485
			.2995	.2983	.2948	.2890	.2810	.2709	.2588	.2447	.2290	.2118
7.0	0.0		.9581	.9559	.9496	.9389	.9239	.9045	.8805	.8518	.8182	.7792
			.5034	.5019	.4975	.4901	.4800	.4670	.4514	.4332	.4127	.3898
	0.4		.1436	.1427	.1401	.1359	.1299	.1225	.1137	.1036	.0924	.0805
			.6526	.6507	.6449	.6353	.6220	.6049	.5843	.5600	.5323	.5012
	0.8		.0076	.0075	.0073	.0068	.0062	.0054	.0046	.0038	.0029	.0022
			.6810	.6788	.6719	.6604	.6444	.6241	.5994	.5704	.5373	.5002

Table 2 Values of $\theta(X, 0)$ and $f''(X, 0)$ for the PHF case

Pr	v_w		x/R, degrees									
			0°	10°	20°	30°	40°	50°	60°	70°	80°	90°
	-1.2	$\theta(X,0)$	.9950	.9958	.9981	1.0020	1.0075	1.0149	1.0241	1.0355	1.0492	1.0658
		$f''(X,0)$	.7277	.7259	.7203	.7110	.6981	.6817	.6620	.6389	.6129	.5839
	-0.8		1.2186	1.2198	1.2234	1.2295	1.2382	1.2496	1.2642	1.2820	1.3038	1.3301
			.8946	.8925	.8864	.8761	.8619	.8437	.8217	.7960	.7667	.7341
	-0.4		1.5050	1.5068	1.5121	1.5211	1.5339	1.5508	1.5722	1.5987	1.6308	1.6697
			1.0619	1.0596	1.0526	1.0409	1.0246	1.0037	.9783	.9485	.9143	.8758
0.7	0.0		1.8700	1.8726	1.8801	1.8927	1.9108	1.9346	1.9648	2.0020	2.0473	2.1018
			1.2276	1.2250	1.2168	1.2031	1.1840	1.1595	1.1296	1.0943	1.0535	1.0071
	0.4		2.3319	2.3355	2.3456	2.3628	2.3874	2.4198	2.4608	2.5112	2.5724	2.6460
			1.3936	1.3905	1.3808	1.3647	1.3422	1.3131	1.2776	1.2354	1.1867	1.1309
	0.8		2.9107	2.9155	2.9290	2.9516	2.9840	3.0267	3.0806	3.1468	3.2269	3.3231
			1.5635	1.5598	1.5484	1.5294	1.5027	1.4683	1.4262	1.3761	1.3180	1.2515
	1.2		3.6282	3.6345	3.6517	3.6809	3.7224	3.7771	3.8460	3.9306	4.0327	4.1548
			1.7410	1.7368	1.7233	1.7009	1.6695	1.6290	1.5793	1.5202	1.4516	1.3732
	-1.2		.1190	.1190	.1190	.1190	.1190	.1190	.1190	.1190	.1190	.1190
			.0142	.0141	.0139	.0135	.0130	.0124	.0117	.0109	.0100	.0090
	-0.8		.1784	.1784	.1784	.1784	.1784	.1785	.1785	.1785	.1785	.1786
			.0317	.0316	.0311	.0303	.0292	.0279	.0263	.0245	.0225	.0203
	-0.4		.3479	.3480	.3483	.3487	.3494	.3502	.3512	.3524	.3538	.3554
			.1135	.1130	.1117	.1094	.1062	.1022	.0974	.0919	.0856	.0787
7.0	0.0		1.0350	1.0365	1.0406	1.0477	1.0578	1.0711	1.0879	1.1087	1.1339	1.1642
			.5165	.5154	.5121	.5065	.4988	.4889	.4768	.4625	.4462	.4276
	0.4		3.0484	3.0535	3.0671	3.0899	3.1224	3.1648	3.2178	3.2822	3.3590	3.4493
			1.4475	1.4447	1.4357	1.4205	1.3992	1.3717	1.3378	1.2974	1.2502	1.1958
	0.8		7.3045	7.3145	7.3397	7.3817	7.4408	7.5174	7.6120	7.7253	7.8581	8.0116
			2.9668	2.9603	2.9389	2.9032	2.8530	2.7883	2.7086	2.6138	2.5034	2.3767

$$\left.\begin{aligned} \mathrm{Nu}/\mathrm{Gr}^{1/4} &= -\theta'(\xi, 0)[F(X)]^{1/2} \\ \tau_w/\left[\rho\left(\frac{\nu}{R}\right)^2 \mathrm{Gr}^{3/4}\right] &= \xi f''(\xi, 0)[F(X)]^{1/2} \end{aligned}\right\} \quad \text{for PST case} \tag{19}$$

and

$$\left.\begin{aligned} \mathrm{Nu}/\mathrm{Gr}^{*1/5} &= -1/\theta(\xi, 0) \\ \tau_w/\left[\rho\left(\frac{\nu}{R}\right)^2 \mathrm{Gr}^{*3/5}\right] &= \xi f''(\xi, 0)[F(X)]^{1/2} \end{aligned}\right\} \quad \text{for PHF case} \tag{20}$$

Numerical Results and Discussion

The system of equations (12) and (13), along with the boundary conditions (14), is solved by an implicit finite difference method (Cebeci and Bradshaw, 1977). Numerical calculations are carried out for fluids having Prandtl numbers of 0.7 and 7.0 over a sphere with suction ($\tilde{v}(X) < 0$) and blowing ($\tilde{v}(X) > 0$). Here only the results for the special cases of uniform surface temperature and uniform surface heat flux are presented. These cases correspond to the condition that $F(X)$ equals one.

The distributions of Nusselt number along the surface are illustrated in Figs. 1-2 for the PST case and in Figs. 3-4 for the PHF case. It can be seen from the figures that the Nusselt number decreases with blowing and increases with suction for both cases. In addition, it is also shown that the influence of surface mass transfer on the heat transfer rate is markedly different for different Prandtl numbers. The Nusselt number is more sensitive to surface mass transfer for high Pr than for

low Pr; whereas, the Nusselt number decreases, and is slightly affected by surface mass transfer, along the surface of sphere as measured from the stagnation point.

Table 1 shows $f''(X, 0)$ and $\theta'(X, 0)$ for the PST case and Table 2 expresses $f''(X, 0)$ and $\theta(X, 0)$ for the PHF case. For low Prandtl numbers ($Pr < 1$), the induced velocity of fluid due to density change is strongly affected by the temperature of fluid near the wall. When suction increases, the velocity and temperature profiles simultaneously move to the wall. The induced velocity of fluid becomes larger and the slope of velocity of fluid on the wall increases. Hence, the wall shear stress increases with increasing suction. However, as the suction becomes asymptotically large, most of the fluid is sucked up. The wall shear stress then begins to decrease.

Similarly, under the influence of blowing, the fluid is blown away. The location of maximum induced velocity of the fluid is shifted away from the wall. Therefore, the wall shear stress decreases as blowing increases. Thus, the results given in Table 1 for $f''(X, 0)$ with the low Prandtl number ($Pr = 0.7$) and with the prescribed surface temperature case are reasonable.

When the Prandtl number is greater than one, the influence of temperature on the velocity of fluid is restricted to a small region near the wall. As suction increases, the density of fluid in the momentum boundary layer is changed less due to the existence of temperature profiles. The induced velocity is not large enough to move most fluid. Therefore, with increasing suction, the wall shear stress decreases. On the other hand, as blowing increases, the induced velocity of fluid also increases. As a result, the wall shear stress increases.

As for the PHF case, it can be found from Table 2 that the wall surface temperature for blowing is higher than that for suction. This leads to the result that the effect of temperature on the induced velocity of fluid is larger for blowing than for suction. Thus, the wall shear stress increases with increasing blowing and decreases with increasing suction for both $Pr = 0.7$ and $Pr = 7.0$.

Conclusion

The present work is a contribution to the analysis of convective heat transfer of bodies subjected to surface mass transfer. The problem investigated in this note is a sphere. The results obtained provide further confirmation of the effects of surface mass transfer. The Nusselt number increases with suction and decreases with blowing. The wall shear stress increases or decreases with suction depending on the effect of temperature on the velocity of fluid at low/high Prandtl number with prescribed surface temperature. However, with prescribed surface heat flux the wall shear stress always increases with blowing and decreases with suction.

References

Cebeci, T., and Bradshaw, P., 1977, *Momentum Transfer in Boundary Layers*, Hemisphere, Washington, D.C.

Chen, T. S., and Mocoglu, A., 1977, "Analysis of Mixed Forced and Free Convection About a Sphere," *Int. J. Heat Mass Transfer*, Vol. 20, pp. 867–875.

Chiang, T., Ossin, A., and Tien, C. L., 1964, "Laminar Free Convection From a Sphere," ASME JOURNAL OF HEAT TRANSFER, Vol. 86, pp. 537–542.

Eichhorn, R., 1960, "The Effect of Mass Transfer on Free Convection," ASME JOURNAL OF HEAT TRANSFER, Vol. 82, pp. 260–263.

Merkin, J. H., 1972, "Free Convection With Blowing and Suction," *Int. J. Heat Mass Transfer*, Vol. 15, pp. 989–999.

Merkin, J. H., 1975, "The Effects of Blowing and Suction on Free Convection Boundary Layers," *Int. J. Heat Mass Transfer*, Vol. 18, pp. 237–244.

Parikh, P. G., Moffat, R., Kays, W. M., and Bershader, D., 1974, "Free Convection Over a Vertical Porous Plate With Transpiration," *Int. J. Heat Mass Transfer*, Vol. 17, pp. 1465–1474.

Sparrow, E. M., and Cess, R. D., 1961, "Free Convection With Blowing or Suction," ASME JOURNAL OF HEAT TRANSFER, Vol. 83, pp. 387–389.

Analysis of Laminar Flow and Heat Transfer in the Entrance Region of an Internally Finned Concentric Circular Annular Duct

P. Renzoni[1] and C. Prakash[2]

Introduction

The concentric circular annular duct is a common geometry in many fluid flow and heat transfer devices [1–4]. For the purpose of heat transfer augmentation, fins are often employed in the annular region, and such finned ducts find wide application in compact heat exchangers [5, 6]. The analysis of flow and heat transfer in this geometry is, therefore, quite important from an engineering standpoint. For fully developed conditions, the problem has already been analyzed [7–10]. However, no results are available for the developing flow in the entrance region. It is with this latter problem that the present paper is concerned.

Problem Statement

The situation being analyzed is shown schematically in Fig. 1. The problem concerns the prediction of steady, forced, laminar flow and heat transfer in the entrance region of an internally finned concentric circular annular duct. The fins are continuous, radial, assumed to be of zero thickness, and affixed on the inner tube. The symbols a, b, and h represent the inner tube radius, the outer tube radius, and the fin height, respectively. A uniform heat input Q' per unit axial length is applied at the inner tube, and the outer tube is insulated. It is assumed that the fins are made of a highly conducting material so that at any cross section the inner tube and the fins are assumed to be at a uniform temperature (which, of course, increases in the axial direction). The fluid is assumed to be incompressible and all properties are regarded as constant. Dissipation and compression work are neglected in the energy equation.

Solution Procedure

In an earlier investigation, Prakash and Liu [11] analyzed the entrance region flow in an internally finned circular duct. Except for the geometry, the present problem is identical to the one described in [11]. Hence, the same solution procedure as in [11] was applied, and the details will not be repeated. To summarize the salient features, the governing differential equations were integrated numerically using the control volume-based finite difference method of Patankar and Spalding [12]. The flow is assumed to be "parabolic" so that a marching procedure can be used along the axial direction. The computational domain consists of a sector of angular width π/N extending from one fin to midway to the next fin [see Fig. 1]. Here, N represents the number of fins. A 16 × 22 (angular × radial) grid was employed in the cross-stream plane. The grid was nonuniform, with grid lines packed near the solid walls and the fin tip. The fully developed results were obtained separately but using an identical grid layout. The fully developed results were obtained first. Then the results in the developing region were computed, and the solution was marched until the local friction factor and Nusselt number were within 1 percent of their fully developed values. This distance was covered in about 60 marching steps. A typical

[1]Graduate student, Department of Mechanical Engineering, Rensselaer Polytechnic Institute, Troy, NY 12181.

[2]Adjunct Assistant Professor, Mechanical Engineering Department, Rensselaer Polytechnic Institute, Troy, NY 12181; Assoc. Mem. ASME.

Contributed by the Heat Transfer Division for publication in the JOURNAL OF HEAT TRANSFER. Manuscript received by the Heat Transfer Division March 25, 1985.

low Pr; whereas, the Nusselt number decreases, and is slightly affected by surface mass transfer, along the surface of sphere as measured from the stagnation point.

Table 1 shows $f''(X, 0)$ and $\theta'(X, 0)$ for the PST case and Table 2 expresses $f''(X, 0)$ and $\theta(X, 0)$ for the PHF case. For low Prandtl numbers ($Pr < 1$), the induced velocity of fluid due to density change is strongly affected by the temperature of fluid near the wall. When suction increases, the velocity and temperature profiles simultaneously move to the wall. The induced velocity of fluid becomes larger and the slope of velocity of fluid on the wall increases. Hence, the wall shear stress increases with increasing suction. However, as the suction becomes asymptotically large, most of the fluid is sucked up. The wall shear stress then begins to decrease.

Similarly, under the influence of blowing, the fluid is blown away. The location of maximum induced velocity of the fluid is shifted away from the wall. Therefore, the wall shear stress decreases as blowing increases. Thus, the results given in Table 1 for $f''(X, 0)$ with the low Prandtl number ($Pr = 0.7$) and with the prescribed surface temperature case are reasonable.

When the Prandtl number is greater than one, the influence of temperature on the velocity of fluid is restricted to a small region near the wall. As suction increases, the density of fluid in the momentum boundary layer is changed less due to the existence of temperature profiles. The induced velocity is not large enough to move most fluid. Therefore, with increasing suction, the wall shear stress decreases. On the other hand, as blowing increases, the induced velocity of fluid also increases. As a result, the wall shear stress increases.

As for the PHF case, it can be found from Table 2 that the wall surface temperature for blowing is higher than that for suction. This leads to the result that the effect of temperature on the induced velocity of fluid is larger for blowing than for suction. Thus, the wall shear stress increases with increasing blowing and decreases with increasing suction for both $Pr = 0.7$ and $Pr = 7.0$.

Conclusion

The present work is a contribution to the analysis of convective heat transfer of bodies subjected to surface mass transfer. The problem investigated in this note is a sphere. The results obtained provide further confirmation of the effects of surface mass transfer. The Nusselt number increases with suction and decreases with blowing. The wall shear stress increases or decreases with suction depending on the effect of temperature on the velocity of fluid at low/high Prandtl number with prescribed surface temperature. However, with prescribed surface heat flux the wall shear stress always increases with blowing and decreases with suction.

References

Cebeci, T., and Bradshaw, P., 1977, *Momentum Transfer in Boundary Layers*, Hemisphere, Washington, D.C.

Chen, T. S., and Mocoglu, A., 1977, "Analysis of Mixed Forced and Free Convection About a Sphere," *Int. J. Heat Mass Transfer*, Vol. 20, pp. 867-875.

Chiang, T., Ossin, A., and Tien, C. L., 1964, "Laminar Free Convection From a Sphere," ASME JOURNAL OF HEAT TRANSFER, Vol. 86, pp. 537-542.

Eichhorn, R., 1960, "The Effect of Mass Transfer on Free Convection," ASME JOURNAL OF HEAT TRANSFER, Vol. 82, pp. 260-263.

Merkin, J. H., 1972, "Free Convection With Blowing and Suction," *Int. J. Heat Mass Transfer*, Vol. 15, pp. 989-999.

Merkin, J. H., 1975, "The Effects of Blowing and Suction on Free Convection Boundary Layers," *Int. J. Heat Mass Transfer*, Vol. 18, pp. 237-244.

Parikh, P. G., Moffat, R., Kays, W. M., and Bershader, D., 1974, "Free Convection Over a Vertical Porous Plate With Transpiration," *Int. J. Heat Mass Transfer*, Vol. 17, pp. 1465-1474.

Sparrow, E. M., and Cess, R. D., 1961, "Free Convection With Blowing or Suction," ASME JOURNAL OF HEAT TRANSFER, Vol. 83, pp. 387-389.

Analysis of Laminar Flow and Heat Transfer in the Entrance Region of an Internally Finned Concentric Circular Annular Duct

P. Renzoni[1] and C. Prakash[2]

Introduction

The concentric circular annular duct is a common geometry in many fluid flow and heat transfer devices [1-4]. For the purpose of heat transfer augmentation, fins are often employed in the annular region, and such finned ducts find wide application in compact heat exchangers [5, 6]. The analysis of flow and heat transfer in this geometry is, therefore, quite important from an engineering standpoint. For fully developed conditions, the problem has already been analyzed [7-10]. However, no results are available for the developing flow in the entrance region. It is with this latter problem that the present paper is concerned.

Problem Statement

The situation being analyzed is shown schematically in Fig. 1. The problem concerns the prediction of steady, forced, laminar flow and heat transfer in the entrance region of an internally finned concentric circular annular duct. The fins are continuous, radial, assumed to be of zero thickness, and affixed on the inner tube. The symbols a, b, and h represent the inner tube radius, the outer tube radius, and the fin height, respectively. A uniform heat input Q' per unit axial length is applied at the inner tube, and the outer tube is insulated. It is assumed that the fins are made of a highly conducting material so that at any cross section the inner tube and the fins are assumed to be at a uniform temperature (which, of course, increases in the axial direction). The fluid is assumed to be incompressible and all properties are regarded as constant. Dissipation and compression work are neglected in the energy equation.

Solution Procedure

In an earlier investigation, Prakash and Liu [11] analyzed the entrance region flow in an internally finned circular duct. Except for the geometry, the present problem is identical to the one described in [11]. Hence, the same solution procedure as in [11] was applied, and the details will not be repeated. To summarize the salient features, the governing differential equations were integrated numerically using the control volume-based finite difference method of Patankar and Spalding [12]. The flow is assumed to be "parabolic" so that a marching procedure can be used along the axial direction. The computational domain consists of a sector of angular width π/N extending from one fin to midway to the next fin [see Fig. 1]. Here, N represents the number of fins. A 16 × 22 (angular × radial) grid was employed in the cross-stream plane. The grid was nonuniform, with grid lines packed near the solid walls and the fin tip. The fully developed results were obtained separately but using an identical grid layout. The fully developed results were obtained first. Then the results in the developing region were computed, and the solution was marched until the local friction factor and Nusselt number were within 1 percent of their fully developed values. This distance was covered in about 60 marching steps. A typical

[1]Graduate student, Department of Mechanical Engineering, Rensselaer Polytechnic Institute, Troy, NY 12181.

[2]Adjunct Assistant Professor, Mechanical Engineering Department, Rensselaer Polytechnic Institute, Troy, NY 12181; Assoc. Mem. ASME.

Contributed by the Heat Transfer Division for publication in the JOURNAL OF HEAT TRANSFER. Manuscript received by the Heat Transfer Division March 25, 1985.

estimate of the dimensionless entrance length (to be defined later) is 0.01. The first dimensionless step size was taken to be 10^{-2} times this value; i.e., 10^{-4}. The subsequent step size Δz was gradually increased using the relation Δz = (1.1)(previous Δz). At each marching step, a sufficient number of iterations (usually five) was performed to ensure that the local value of the friction factor, Nusselt number, and velocity at some sample points had converged to four significant digits. Within these iterations, the unknown temperature of the inner tube and fins was iteratively updated as per the procedure described in [12]. The adequacy of the grid and the step size was justified by making comparisons with the results obtained by other investigators for fully developed flow in finned (and finless) annuli, and for entrance region flow in finless annuli. Agreement was generally within 1 percent.

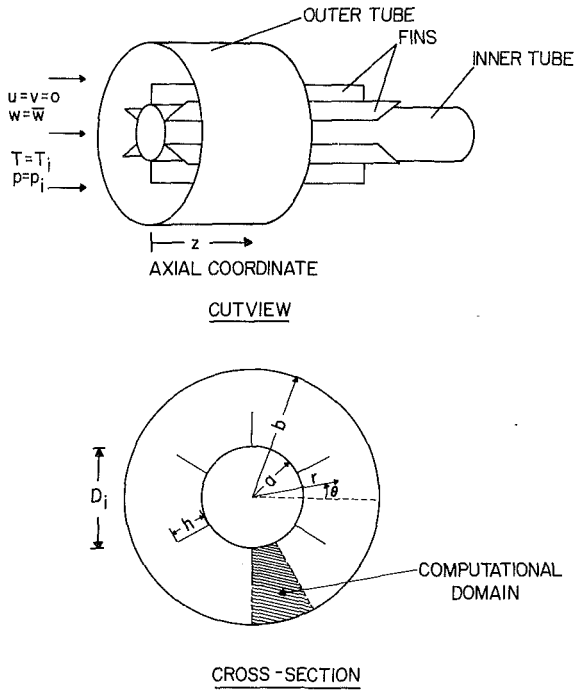

Fig. 1 An internally finned concentric circular annular duct

Dimensionless Parameters

In dimensionless form, the problem is characterized by the number of fins N, the dimensionless fin height $h/(b-a)$, the radius ratio b/a, and the fluid Prandtl number $\mathrm{Pr} = (\mu\, c_p/k)$. Here, μ, c_p, and k represent viscosity, specific heat, and the conductivity of the fluid, respectively. Computations were made for N = 8, 16, and 24; b/a = 1.25, 2, and 5; $h/(b-a)$ = 0, 0.5, and 1; and the Prandtl number was fixed at 0.707 corresponding to air. Due to the parabolic assumption, the Reynolds number is *not* a parameter of the problem and only serves to scale the axial coordinate. Based on the average axial velocity $\bar{w}$ and the inner tube diameter D_i, the Reynolds number may be defined as

$$\mathrm{Re} = \frac{\bar{w}\, D_i}{\nu} \tag{1}$$

where $\nu = \mu/\rho$ is the kinematic viscosity of the fluid, ρ being the fluid density. Alternately, the Reynolds number may be based on the equivalent hydraulic diameter D_h as

$$\mathrm{Re}_h = \frac{\bar{w}\, D_h}{\nu} \tag{2}$$

where D_h is defined as

$$D_h = \frac{4(\text{cross-sectional area})}{\text{wetted perimeter}} = \frac{4\pi(b^2 - a^2)}{(2\pi(a+b) + 2Nh)} \tag{3}$$

Table 1 Friction factor for fully developed flow

$\frac{b}{a} = 1.25$

$\frac{h}{b-a}$	$(f_h \mathrm{Re}_h)_{fd}$ N=8	N=16	N=24	$(f\,\mathrm{Re})_{fd}$ N=8	N=16	N=24
0	23.80			380.8		
0.5	20.83	19.40	18.72	434.2	510.8	607.6
1	17.58	15.03	14.21	463.1	589.8	777.4

$\frac{b}{a} = 2.0$

$\frac{h}{b-a}$	$(f_h \mathrm{Re}_h)_{fd}$ N=8	N=16	N=24	$(f\,\mathrm{Re})_{fd}$ N=8	N=16	N=24
0	23.63			23.63		
0.5	19.06	17.68	15.28	38.68	60.44	78.94
1	14.29	14.90	16.01	48.84	108.4	201.4

$\frac{b}{a} = 5.0$

$\frac{h}{b-a}$	$(f_h \mathrm{Re}_h)_{fd}$ N=8	N=16	N=24	$(f\,\mathrm{Re})_{fd}$ N=8	N=16	N=24
0	22.91			1.432		
0.5	17.89	11.96	7.940	3.822	5.440	6.242
1	14.73	15.35	15.65	6.699	18.54	36.31

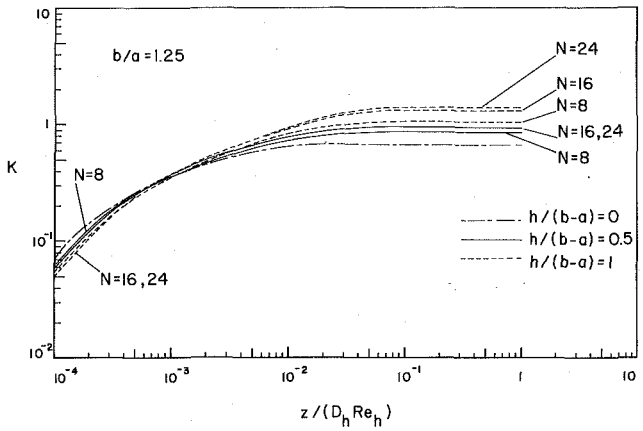

Fig. 2(*a*) Incremental pressure drop for a finned annular duct; *b/a* = 1.25

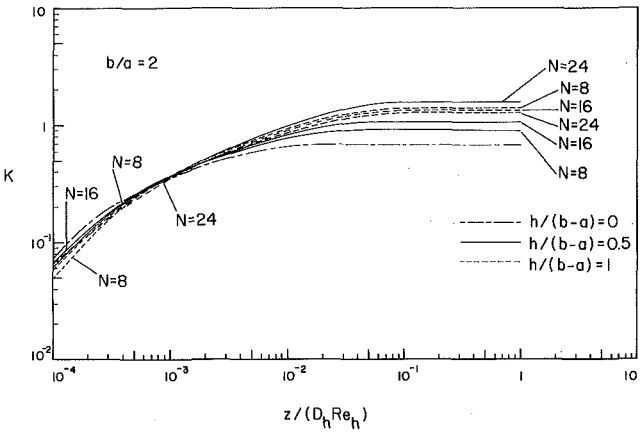

Fig. 2(*b*) Incremental pressure drop for a finned annular duct; *b/a* = 2

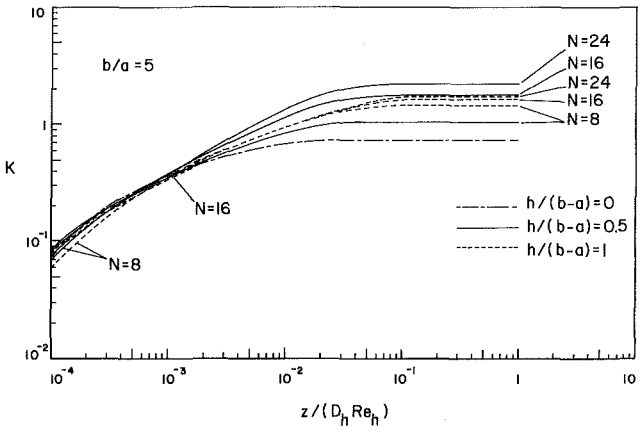

Fig. 2(*c*) Incremental pressure drop for a finned annular duct; *b/a* = 5

Either choice, i.e., (D_i, Re), or (D_h, Re_h), has its merits. In the present paper, both are used, and some results are presented both ways.

Pressure Drop Results

Let $\bar{p}(z)$ represent the cross-sectional average pressure at an axial location z. The local pressure gradient $(d\bar{p}/dz)$ can be expressed in dimensionless form as a *local* friction factor f defined as

$$f=\frac{(-d\bar{p}/dz)D_i/4}{(\rho\bar{w}^2)/2} \tag{4}$$

Table 2 Incremental pressure drop in the entrance region; values extrapolated from Fig. 2

	$K(\infty)$		
$\frac{h}{b-a}$ \ N	8	16	24
0	0.679		
0.5	0.864	0.951	0.956
1	1.07	1.33	1.42
	$\frac{b}{a}=1.25$		
$\frac{h}{b-a}$ \ N	8	16	24
0	0.692		
0.5	0.936	1.09	1.60
1	1.42	1.37	1.32
	$\frac{b}{a}=2.0$		
$\frac{h}{b-a}$ \ N	8	16	24
0	0.741		
0.5	1.06	1.78	2.23
1	1.46	1.64	1.77
	$\frac{b}{a}=5.0$		

or, using D_h as the characteristic length, as

$$f_h=\frac{(-d\bar{p}/dz)D_h/4}{(\rho\bar{w}^2)/2} \tag{5}$$

For the fully developed flow, the friction factor becomes inversely proportional to the Reynolds number, i.e., f Re (or f_h Re_h) becomes independent of z.

Let $\Delta p(z)$ represent the total pressure drop from inlet up to an axial location z. Often $\Delta p(z)$ is expressed as

$$\frac{\Delta p(z)}{(\rho\bar{w}^2/2)}=\frac{[\Delta p(z)]_{fd}}{(\rho\bar{w}^2/2)}+K(z) \tag{6}$$

where $[\Delta p(z)]_{fd}$ is the pressure that would have occurred if the flow were fully developed all the way from the inlet, and $K(z)$ represents the incremental pressure drop due to entrance effects. From the above definitions it follows that

$$\frac{\Delta p(z)}{(\rho\bar{w}^2/2)}=(f\mathrm{Re})_{fd}\left(\frac{4z}{D_i\mathrm{Re}}\right)+K(z)$$

$$=(f_h\mathrm{Re}_h)_{fd}\left(\frac{4z}{D_h\mathrm{Re}_h}\right)+K(z) \tag{7}$$

where $(f\ \mathrm{Re})_{fd}$ and $(f_h\ \mathrm{Re}_h)_{fd}$ represent the fully developed values of $(f\ \mathrm{Re})$ and $(f_h\ \mathrm{Re}_h)$, respectively. Thus, knowledge of $(f\ \mathrm{Re})_{fd}$ (or $(f_h\ \mathrm{Re}_h)_{fd}$) and $K(z)$ permits the calculation of the total pressure drop.

The fully developed friction factors as obtained in the present study are presented in Table 1. Both $(f\ \mathrm{Re})_{fd}$ and $(f_h\ \mathrm{Re}_h)_{fd}$ are provided for convenience.

Variation of the incremental pressure drop $K(z)$ is presented in Figs. 2(*a–c*). Plotted against the dimensionless axial distance $z/D_h\ \mathrm{Re}_h$, the results for different N, $h/(b-a)$, and b/a cases are found to fall close to each other in the near-entrance region. Near the inlet, the flow is characterized by thin boundary layers at the duct walls, and hence, higher fric-

tion losses. In addition, there is the pressure loss due to momentum flux associated with the changing velocity profile. As a result, the pressure loss is greater near the entrance as compared with the fully developed region. The incremental pressure loss K is, therefore, positive and increases with z. Further down, as the flow approaches the fully developed condition, the additional losses tend to zero, and hence, K approaches a constant value. These features are clearly illustrated by the results shown in Figs. 2(*a-c*).

The asymptotic value which K attains for large z is designated as $K(\infty)$ and it represents the total incremental pressure drop due to entrance effects. The value of $K(\infty)$, as obtained by graphically extrapolating the results of Figs. 2(*a-c*), are summarized in Table 2. Suppose that the radii a and b are fixed. Then, increasing the nubmer of fins N and/or increasing the fin height h increases the total solid-fluid contact area and the friction losses. In addition, increasing N and/or h implies a greater momentum flux change between the inlet and the fully developed velocity profiles. As a result, it is expected that $K(\infty)$ will increase with N and/or h, and this is clearly demonstrated by the results of Table 2. However, at the same time, increasing N and/or h is expected to reduce the length of the entrance region which has the competing effect of reducing $K(\infty)$. That this does happen is shown by the results corresponding to $b/a = 2$, $h/(b-a) = 1$ where $K(\infty)$ is found to decrease slightly with increasing N.

Estimate of the Hydrodynamic Entrance Length

As in [11], the hydrodynamic entrance length L_h is defined as the distance required for the *local* friction factor to be equal to 1.05 times the fully developed value. Variation of L_h so defined is presented in Table 3. In Table 3(*a*), the values of the dimensionless group $L_h/(D_h\mathrm{Re}_h)$ are listed. A more meaningful dimensionless representation would be $L_h/(D_i\ \mathrm{Re})$ from which the effect of N, h, b, and a for fixed mass flow rate can be easily discerned. This dimensionless group is listed in Table 3(*b*).

Consider the case of fixed a, b, and $\bar{w}$ (hence fixed D_i, Re, and mass flow through the passage). Under these conditions, an increase in number of fins and/or the fin height is expected to reduce the extent to which the boundary layers on the wall must grow for the flow to become fully developed; on the other hand, increasing N and/or h can increase the strength of the complex secondary cross-stream flow which may require a long axial length to decay. Thus, with fixed a, b, and mass flow rate, the entrance length L_h can have a mixed dependence on N and h. Such a behavior is displayed by the results of Table 3(*b*). Similar trends were observed in [11] for an internally finned circular duct. For fixed N, a, h, and $\bar{w}$ (hence D_i and Re_i), the effect of increasing b is always to increase L_h, which is expected; the farther the two tubes are from each other, the longer it takes for the boundary layers to merge and form a fully developed profile.

Heat Transfer Results

Let $T_w(z)$ be the peripherally uniform temperature of the inner tubes and the fins at an axial location z. By a heat balance, the local bulk temperature at z is given by

$$T_b(z) = T_i + \frac{Q'z}{\rho(c_p \bar{w}\ \pi(b^2-a^2))} \tag{8}$$

where T_i is the uniform temperature at the inlet. The *local* Nusselt number at z can be defined as

$$\mathrm{Nu}_h = \frac{Q'/(\pi D_i + 2Nh)}{(T_w - T_b)} \frac{D_h}{k} \tag{9}$$

or as

$$\mathrm{Nu} = \frac{Q'/(\pi D_i)}{(T_w - T_b)} \frac{D_i}{k} \tag{10}$$

Table 3 Estimate of the hydrodynamic entrance length L_h

(a): $L_h/(D_h\mathrm{Re}_h)$

$\frac{h}{b-a}$ \ N	8	16	24
0	0.0118		
1.5	0.0199	0.0249	0.0244
1	0.0303	0.0476	0.0529

$\frac{b}{a} = 1.25$

$\frac{h}{b-a}$ \ N	8	16	24
0	0.0122		
0.5	0.0237	0.0336	0.0560
1	0.0529	0.0516	0.0500

$\frac{b}{a} = 2.0$

$\frac{h}{b-a}$ \ N	8	16	24
0	0.0142		
0.5	0.0292	0.0531	0.0836
1	0.0574	0.0703	0.0775

$\frac{b}{a} = 5.0$

(b): $L_h/(D_i\mathrm{Re})$

$\frac{h}{b-a}$ \ N	8	16	24
0	0.000737		
0.5	0.000954	0.000946	0.000753
1.5	0.00115	0.00121	0.000968

$\frac{h}{b-a}$ \ N	8	16	24
0	0.0122		
0.5	0.0117	0.00983	0.0108
1	0.0155	0.00708	0.00398

$\frac{h}{b-a}$ \ N	8	16	24
0	0.227		
0.5	0.136	0.117	0.106
1	0.126	0.0582	0.0334

Table 4 Fully developed Nusselt number

$\frac{b}{a} = 1.25$

$\frac{h}{b-a}$	(a): $(Nu_h)_{fd}$ N=8	N=16	N=24	(b): $(Nu)_{fd}$ N=8	N=16	N=24
0	5.568			22.27		
0.5	4.215	3.765	3.501	25.37	31.62	38.99
1	3.327	3.113	3.340	27.94	44.33	71.88

$\frac{b}{a} = 2.0$

$\frac{h}{b-a}$	(a): $(Nu_h)_{fd}$ N=8	N=16	N=24	(b): $(Nu)_{fd}$ N=8	N=16	N=24
0	6.166			6.166		
0.5	3.673	2.537	1.590	11.89	16.63	17.42
1	3.235	3.933	4.372	21.21	64.65	133.9

$\frac{b}{a} = 5.0$

$\frac{h}{b-a}$	(a): $(Nu_h)_{fd}$ N=8	N=16	N=24	(b): $(Nu)_{fd}$ N=8	N=16	N=24
0	8.463			2.116		
0.5	2.619	1.062	.5597	7.376	8.010	8.078
1	3.461	3.493	3.433	26.11	82.04	165.0

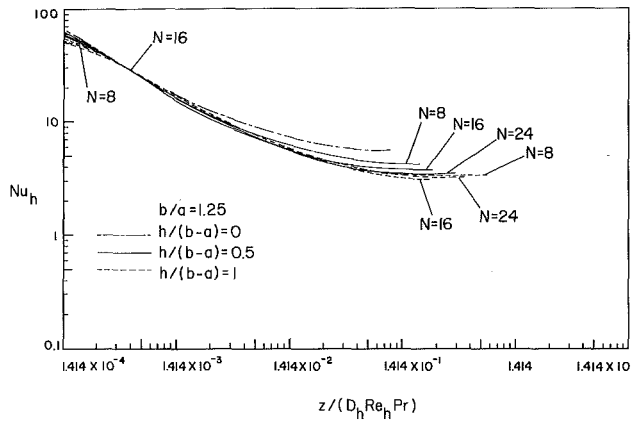

Fig. 3(a) Local Nusselt number for a finned annular duct; *b/a* = 1.25

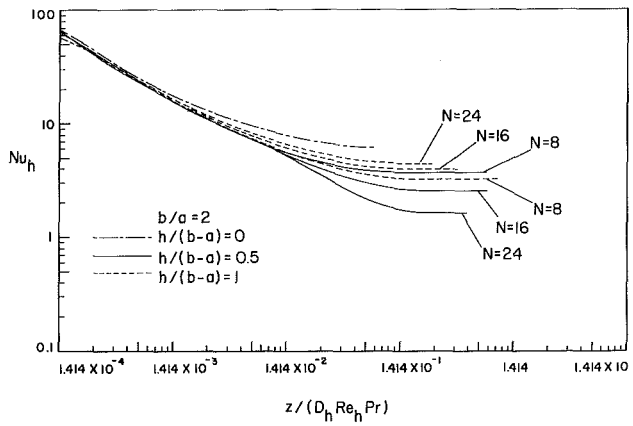

Fig. 3(b) Local Nusselt number for a finned annular duct; *b/a* = 2

Nu_h accounts for the total (inner tube + fin) surface area for computing the heat flux, and uses the hydraulic diameter D_h as the characteristic length. The subscript h on Nu_h is to designate the use of D_h. The Nusselt number Nu, as defined by equation (10), uses an average heat flux based on the inner tube area and uses the inner tube diameter D_i as the characteristic length. Whereas correlations can be developed more conveniently in terms of Nu_h, the effect of N, h, b, and a on the heat transfer performance can be discerned more easily and directly from Nu.

The fully developed Nusselt number values are listed in Table 4. Both $(Nu_h)_{fd}$ and $(Nu)_{fd}$ are provded for convenience. Consider $(Nu)_{fd}$, the variation of which is easier to interpret. Imagine that T_w and T_b are prescribed. Then, increasing the radius ratio b/a is expected to reduce the temperature gradients at the walls, leading to smaller heat flux and Nusselt number. However, for fixed $h/(b-a)$, which is the case in

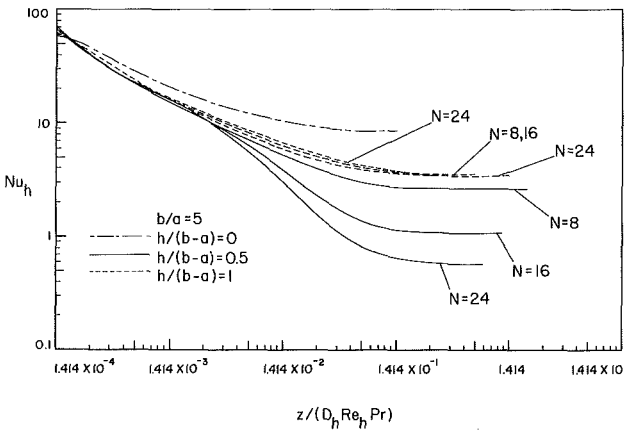

Fig. 3(c) Local Nusselt number for a finned annular duct; *b/a* = 5

Table 5 Estimate of thermal entrance length L_t

$\frac{b}{a} = 1.25$

$\frac{h}{b-a}$	(a): $L_t/(D_h \mathrm{Re}_h \mathrm{Pr})$ N = 8	16	24	(b): $L_t/(D_i \mathrm{Re}\ \mathrm{Pr})$ N = 8	16	24
0	0.0433			0.00270		
0.5	0.0728	0.0710	0.0763	0.00349	0.00270	0.00235
1	0.123	0.109	0.0898	0.00468	0.00277	0.00164

$\frac{b}{a} = 2.0$

$\frac{h}{b-a}$	N = 8	16	24	N = 8	16	24
0	0.0419			0.0419		
0.5	0.0738	0.135	0.190	0.0364	0.0396	0.0367
1	0.0972	0.0838	0.0924	0.0284	0.0115	0.00735

$\frac{b}{a} = 5.0$

$\frac{h}{b-a}$	N = 8	16	24	N = 8	16	24
0	0.0378			0.605		
0.5	0.109	0.180	0.262	0.510	0.396	0.333
1	0.107	0.132	0.153	0.235	0.109	0.0660

Table 4, increasing b/a also has the effect of increasing the total fin surface area which would tend to increase the total heat transfer from the fins. As a result, due to these two competing effects, $(\mathrm{Nu})_{fd}$ displays a mixed dependence on b/a in Table 4; for $h/(b-a) = 0$ and 0.5, $(\mathrm{Nu})_{fd}$ decreases with b/a, while for $h/(b-a) = 1$, it shows an increase with b/a.

The variation of the local Nusselt number is displayed in Figs. 3(*a-c*). As expected, the Nusselt number is very high in the entrance region. As the axial distance increases, the Nusselt number decreases, approaching asymptotically the fully developed values at large z.

Estimate of the Thermal Entrance Length

The thermal entrance length L_t is defined [6] as the distance required for the *local* Nusselt number to equal 1.05 times the fully developed value. Variation of L_t so defined is presented in Table 5. For fixed a, b, and $\bar{w}$ (hence fixed D_i, Re_i, and mass flow rate), the thermal entrance length L_t, like the hydrodynamic entrance length L_h, shows a mixed dependence on the number of fins N and the fin height h. As already explained, this behavior is due to two competing effects; increasing N and/or h reduces the extent to which boundary layers must grow for the flow to become fully developed, but increasing N and/or h increases the strength of the secondary cross-stream flow which may require a long axial length to decay. Keeping a and $\bar{w}$ fixed (hence fixed D_i and Re_i), the entrance length L_t increases with b for all N and h, which is expected.

Conclusions

Steady, laminar, forced convection flow and heat transfer in the entrance region of an internally finned concentric circular annular duct has been analyzed by numerically integrating the governing partial differential equations. The results presented include the variation of incremental pressure drop and the local Nusselt number in the entrance region. Estimates are provided for the hydrodynamic and thermal entrance lengths. Results display the expected large pressure gradients and heat transfer coefficients in the entrance region, approaching asymptotically the fully developed values at large axial distance. For prescribed inner and outer tube radii and mass flow rate, the entrance lengths show a mixed dependence on the number of fins and the fin height. For fixed inner tube radius, number of fins, fin height, and average axial velocity, the entrance lengths increase with increasing radius of the outer tube.

Acknowledgments

The authors are grateful to the Department of Mechanical Engineering, Aeronautical Engineering and Mechanics of the Rensselaer Polytechnic Institute for supporting this work under the auspices of this institute's BUILD program.

References

1 Heaton, H. S., Reynolds, W. C., and Kays, W. M., "Heat Transfer in Annular Passages: Simultaneous Development of Velocity and Temperature Fields in Laminar Flow," *Int. J. Heat Mass Transfer*, Vol. 7, 1964, pp. 763-781.

2 Sparrow, E. M., and Lin, S. H., "The Developing Laminar Flow and Pressure Drop in the Entrance Region of Annular Ducts," ASME *Journal of Basic Engineering*, Vol. 86, 1964, pp. 827-834.

3 Shah, V. L., and Farnia, K., "Flow in the Entrance of Annular Tubes," *Computers and Fluids*, Vol. 2, 1974, pp. 285-294.

4 Coney, J. E. R., and El-Shaarawi, M. A. I., "Developing Laminar Radial Velocity Profiles and Pressure Drop in the Entrance Region of Concentric Annuli," *Nuclear Science and Engineering*, Vol. 57, 1975, pp. 169-174.

5 Bergles, A. E., "Survey and Evaluation of Techniques to Augment Convective Heat and Mass Transfer," in: *Progress in Heat and Mass Transfer*, Vol. 1, Pergamon Press, Oxford, 1969, pp. 331-424.

6 Shah, R. K., and London, A. L., *Laminar Flow Forced Convection in Ducts*, Academic Press, New York, 1978.

7 Sparrow, E. M., Chen, T. S., and Jonsson, V. K., "Laminar Flow and Pressure Drop in Internally Finned Annular Ducts," *Int. J. Heat Mass Transfer*, Vol. 7, 1964, pp. 583-585.

8 Patankar, S. V., Ivanovic, M., and Sparrow, E. M., "Analysis of Turbulent Flow and Heat Transfer in Internally Finned Tubes and Annuli," ASME JOURNAL OF HEAT TRANSFER, Vol. 101, 1979, pp. 29-37.

9 de Lorenzo, B., and Anderson, E. D., "Heat Transfer and Pressure Drop

of Liquid in Double-Pipe Fin-Tube Exchangers," *Trans. ASME*, Vol. 67, 1945, pp. 697–702.

10 Clark, L., and Winston, R. E., "Calculation of Finside Coefficients in Longitudinal Finned-Tube Exchangers," *Chem. Eng. Prog.*, Vol. 51, 1955, pp. 147–150.

11 Prakash, C., and Liu, Ye-Di, "Analysis of Laminar Flow and Heat Transfer in the Entrance Region of an Internally Finned Circular Duct," ASME JOURNAL OF HEAT TRANSFER, Vol. 107, 1985, pp. 84–91.

12 Patankar, S. V., and Spalding, D. B., "A Calculation Procedure for Heat, Mass and Momentum Transfer in Three-Dimensional Parabolic Flows," *Int. J. Heat Mass Transfer*, Vol. 15, 1972, pp. 1787–1806.

Multilayer Rayleigh–Benard Instability via Shooting Method

C. A. Hieber[1]

Nomenclature

- a_i = dimensionless disturbance wave number for fluid layer i, $= (2\pi L_i/\lambda)$
- $C_{i,j}$ = dimensionless coefficients appearing in equation (1)
- D_i = dimensionless vertical derivative in fluid layer i, $= d/dZ_i$
- g = constant gravitational force per unit mass
- k = thermal conductivity of each fluid layer
- k_B = thermal conductivity of each barrier
- L_i = thickness of fluid layer i
- L_{B_i} = thickness of internal barrier i
- N = total number of internal barriers
- Ra_i = Rayleigh number for fluid layer i $= g\beta\Delta T_i L_i^3/\nu\alpha$
- T_C = uniform temperature of cold upper external wall
- T_H = uniform temperature of hot lower external wall
- W_i = dimensionless disturbance vertical velocity in fluid layer i
- $W_{i,j}$ = dimensionless functions appearing in equation (1) and defined by equations (2)–(4)
- Z_i = dimensionless vertical coordinate in fluid layer i, ranging between $-1/2$ (bottom) and $1/2$ (top)
- α = thermal diffusivity of each fluid layer
- β = volumetric coefficient of thermal expansion for each fluid layer
- δ_{jk} = Dirac delta function where $j, k = 1, 2, \ldots, 6$
- ΔT_i = temperature difference across fluid layer i
- θ_i = dimensionless temperature disturbance in fluid layer i
- $\theta_{i,j}$ = dimensionless functions appearing in equation (1) and defined by equations (2)–(4)
- λ = disturbance wavelength in horizontal plane
- ν = kinematic viscosity of each fluid layer

In recent papers by Catton and Lienhard (1984) and Lienhard (1987), consideration has been given to the Rayleigh–Benard stability problem for the multilayer situation interspersed with conductive solid walls, with possible application to solar collectors. The present note is concerned with pointing out and illustrating that this multilayer problem is readily amenable to a shooting technique. A general treatment of such an approach is given by Roberts and Shipman (1972), whereas examples of its application to hydrodynamic stability problems can be found in, e.g., Harris and Reid (1964) and Hieber and Gebhart (1971).

In particular, the stability problem in the present case constitutes a sixth-order linear system such that the general solution can be represented as the linear combination of six independent integrals. In terms of the disturbance velocity and temperature in each fluid layer i, this can be expressed as

$$W_i = \sum_{j=1}^{6} C_{i,j} W_{i,j}(Z_i), \qquad \theta_i = \sum_{j=1}^{6} C_{i,j}\theta_{i,j}(Z_i) \tag{1}$$

where $-1/2 \le Z_i \le 1/2$ and each $(W_{i,j}, \theta_{i,j})$ satisfies the sixth-order Rayleigh–Benard stability equations

$$(D_i^2 - a_i^2)^2 W_{i,j} = a_i^2\,\mathrm{Ra}_i\theta_{i,j} \tag{2}$$

$$(D_i^2 - a_i^2)\theta_{i,j} = -W_{i,j} \tag{3}$$

subject to the boundary conditions that, at the bottom of each layer,

$$W_{i,j}(-1/2) \equiv \delta_{j1}, \quad W'_{i,j}(-1/2) \equiv \delta_{j2}, \quad W''_{i,j}(-1/2) \equiv \delta_{j3}, \quad W'''_{i,j}(-1/2) \equiv \delta_{j4}, \quad \theta_{i,j}(-1/2) \equiv \delta_{j5}, \quad \theta'_{i,j}(-1/2) \equiv \delta_{j6} \tag{4}$$

where primes denote derivatives with respect to Z_i; δ_{jk} is unity if $j = k$ and is zero otherwise.

In particular, if we consider the typical case of no slip at each wall surface, then $W_i(-1/2)$ and $W'_i(-1/2)$ should vanish for every i, such that $C_{i,1}$ and $C_{i,2}$ should be zero for each i. Further, if the lowest wall temperature is fixed, then we require that $\theta_1(-1/2)$ should vanish, such that $C_{1,5} = 0$. In addition, the arbitrary scale of the disturbance field can then be conveniently fixed by taking $C_{1,6} \equiv 1$, such that $\theta'_1(-1/2) \equiv 1$. Accordingly, only two constants then remain to be determined in the lowest layer, namely $C_{1,3}$ and $C_{1,4}$. In particular, for specific values for a_1 and Ra_1, a Runge–Kutta procedure can be used to determine $(W_{1,j}, \theta_{1,j})$ for $j = 3$, 4, and 6 by integrating equations (2) and (3) across the lowest layer, starting with the behavior at $Z_1 = -1/2$ given in equation (4). Accordingly, $C_{1,3}$ and $C_{1,4}$ can then be determined by requiring that

$$C_{1,3}W_{1,3}(1/2) + C_{1,4}W_{1,4}(1/2) + W_{1,6}(1/2) = 0 \tag{5}$$

and

$$C_{1,3}W'_{1,3}(1/2) + C_{1,4}W'_{1,4}(1/2) + W'_{1,6}(1/2) = 0 \tag{6}$$

With the disturbance field in layer 1 so determined, one can then step across the partition between layers 1 and 2 by making use of closed-form results for the disturbance temperature field in terms of simple exponential functions. In particular, $\theta_2(-1/2)$ and $\theta'_2(-1/2)$ can then be directly related to $\theta_1(1/2)$ and $\theta'_1(1/2)$ for given values of k_B/k, L_{B_1}/L_1 and L_2/L_{B_1}. Accordingly, $C_{2,5} = \theta_2(-1/2)$ and $C_{2,6} = \theta'_2(-1/2)$ can be determined and, with $C_{2,1} \equiv 0 \equiv C_{2,2}$ (as noted above), the remaining two constants in layer 2 can then be determined by us-

[1]Senior Research Associate, Sibley School of Mechanical and Aerospace Engineering, Cornell University, Ithaca, NY 14853.

Contributed by the Heat Transfer Division for publication in the JOURNAL OF HEAT TRANSFER. Manuscript received by the Heat Transfer Division February 11, 1986.

of Liquid in Double-Pipe Fin-Tube Exchangers," *Trans. ASME*, Vol. 67, 1945, pp. 697–702.

10 Clark, L., and Winston, R. E., "Calculation of Finside Coefficients in Longitudinal Finned-Tube Exchangers," *Chem. Eng. Prog.*, Vol. 51, 1955, pp. 147–150.

11 Prakash, C., and Liu, Ye-Di, "Analysis of Laminar Flow and Heat Transfer in the Entrance Region of an Internally Finned Circular Duct," ASME JOURNAL OF HEAT TRANSFER, Vol. 107, 1985, pp. 84–91.

12 Patankar, S. V., and Spalding, D. B., "A Calculation Procedure for Heat, Mass and Momentum Transfer in Three-Dimensional Parabolic Flows," *Int. J. Heat Mass Transfer*, Vol. 15, 1972, pp. 1787–1806.

Multilayer Rayleigh–Benard Instability via Shooting Method

C. A. Hieber[1]

Nomenclature

- a_i = dimensionless disturbance wave number for fluid layer i, $= (2\pi L_i/\lambda)$
- $C_{i,j}$ = dimensionless coefficients appearing in equation (1)
- D_i = dimensionless vertical derivative in fluid layer i, $= d/dZ_i$
- g = constant gravitational force per unit mass
- k = thermal conductivity of each fluid layer
- k_B = thermal conductivity of each barrier
- L_i = thickness of fluid layer i
- L_{B_i} = thickness of internal barrier i
- N = total number of internal barriers
- Ra_i = Rayleigh number for fluid layer i $= g\beta\Delta T_i L_i^3/\nu\alpha$
- T_C = uniform temperature of cold upper external wall
- T_H = uniform temperature of hot lower external wall
- W_i = dimensionless disturbance vertical velocity in fluid layer i
- $W_{i,j}$ = dimensionless functions appearing in equation (1) and defined by equations (2)–(4)
- Z_i = dimensionless vertical coordinate in fluid layer i, ranging between $-1/2$ (bottom) and $1/2$ (top)
- α = thermal diffusivity of each fluid layer
- β = volumetric coefficient of thermal expansion for each fluid layer
- δ_{jk} = Dirac delta function where $j, k = 1, 2, \ldots, 6$
- ΔT_i = temperature difference across fluid layer i
- θ_i = dimensionless temperature disturbance in fluid layer i
- $\theta_{i,j}$ = dimensionless functions appearing in equation (1) and defined by equations (2)–(4)
- λ = disturbance wavelength in horizontal plane
- ν = kinematic viscosity of each fluid layer

In recent papers by Catton and Lienhard (1984) and Lienhard (1987), consideration has been given to the Rayleigh–Benard stability problem for the multilayer situation interspersed with conductive solid walls, with possible application to solar collectors. The present note is concerned with pointing out and illustrating that this multilayer problem is readily amenable to a shooting technique. A general treatment of such an approach is given by Roberts and Shipman (1972), whereas examples of its application to hydrodynamic stability problems can be found in, e.g., Harris and Reid (1964) and Hieber and Gebhart (1971).

In particular, the stability problem in the present case constitutes a sixth-order linear system such that the general solution can be represented as the linear combination of six independent integrals. In terms of the disturbance velocity and temperature in each fluid layer i, this can be expressed as

$$W_i = \sum_{j=1}^{6} C_{i,j} W_{i,j}(Z_i), \qquad \theta_i = \sum_{j=1}^{6} C_{i,j}\theta_{i,j}(Z_i) \tag{1}$$

where $-1/2 \le Z_i \le 1/2$ and each $(W_{i,j}, \theta_{i,j})$ satisfies the sixth-order Rayleigh–Benard stability equations

$$(D_i^2 - a_i^2)^2 W_{i,j} = a_i^2\,\mathrm{Ra}_i\theta_{i,j} \tag{2}$$

$$(D_i^2 - a_i^2)\theta_{i,j} = -W_{i,j} \tag{3}$$

subject to the boundary conditions that, at the bottom of each layer,

$$W_{i,j}(-1/2) \equiv \delta_{j1}, \quad W'_{i,j}(-1/2) \equiv \delta_{j2}, \quad W''_{i,j}(-1/2) \equiv \delta_{j3}, \quad W'''_{i,j}(-1/2) \equiv \delta_{j4}, \quad \theta_{i,j}(-1/2) \equiv \delta_{j5}, \quad \theta'_{i,j}(-1/2) \equiv \delta_{j6} \tag{4}$$

where primes denote derivatives with respect to Z_i; δ_{jk} is unity if $j = k$ and is zero otherwise.

In particular, if we consider the typical case of no slip at each wall surface, then $W_i(-1/2)$ and $W'_i(-1/2)$ should vanish for every i, such that $C_{i,1}$ and $C_{i,2}$ should be zero for each i. Further, if the lowest wall temperature is fixed, then we require that $\theta_1(-1/2)$ should vanish, such that $C_{1,5} = 0$. In addition, the arbitrary scale of the disturbance field can then be conveniently fixed by taking $C_{1,6} \equiv 1$, such that $\theta'_1(-1/2) \equiv 1$. Accordingly, only two constants then remain to be determined in the lowest layer, namely $C_{1,3}$ and $C_{1,4}$. In particular, for specific values for a_1 and Ra_1, a Runge–Kutta procedure can be used to determine $(W_{1,j}, \theta_{1,j})$ for $j = 3$, 4, and 6 by integrating equations (2) and (3) across the lowest layer, starting with the behavior at $Z_1 = -1/2$ given in equation (4). Accordingly, $C_{1,3}$ and $C_{1,4}$ can then be determined by requiring that

$$C_{1,3}W_{1,3}(1/2) + C_{1,4}W_{1,4}(1/2) + W_{1,6}(1/2) = 0 \tag{5}$$

and

$$C_{1,3}W'_{1,3}(1/2) + C_{1,4}W'_{1,4}(1/2) + W'_{1,6}(1/2) = 0 \tag{6}$$

With the disturbance field in layer 1 so determined, one can then step across the partition between layers 1 and 2 by making use of closed-form results for the disturbance temperature field in terms of simple exponential functions. In particular, $\theta_2(-1/2)$ and $\theta'_2(-1/2)$ can then be directly related to $\theta_1(1/2)$ and $\theta'_1(1/2)$ for given values of k_B/k, L_{B_1}/L_1 and L_2/L_{B_1}. Accordingly, $C_{2,5} = \theta_2(-1/2)$ and $C_{2,6} = \theta'_2(-1/2)$ can be determined and, with $C_{2,1} \equiv 0 \equiv C_{2,2}$ (as noted above), the remaining two constants in layer 2 can then be determined by us-

[1]Senior Research Associate, Sibley School of Mechanical and Aerospace Engineering, Cornell University, Ithaca, NY 14853.

Contributed by the Heat Transfer Division for publication in the JOURNAL OF HEAT TRANSFER. Manuscript received by the Heat Transfer Division February 11, 1986.

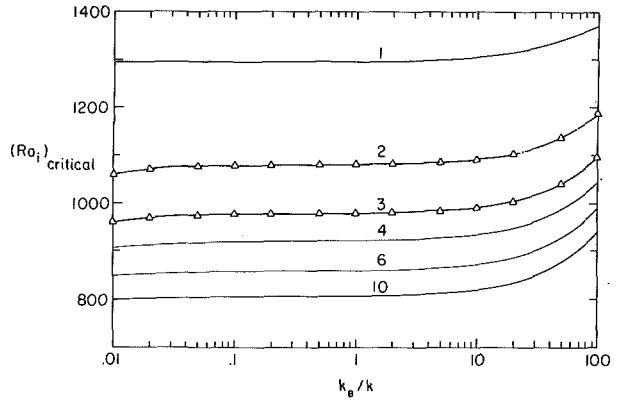

Fig. 1 Predictions for critical Rayleigh number for symmetric case in which $L_{B_i}/L_i = 0.002$ and $N = 1, 2, 3, 4, 6$, and 10. Curves indicate present results; results from Lienhard (1986) are denoted by Δ.

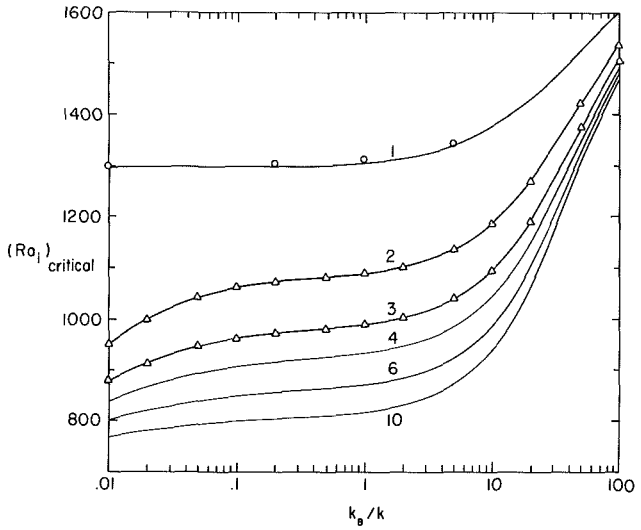

Fig. 2 Same as Fig. 1 but for $L_{B_i}/L_i = 0.02$. Results from Catton and Lienhard (1984) are denoted by ○ and results from Lienhard (1986) by Δ.

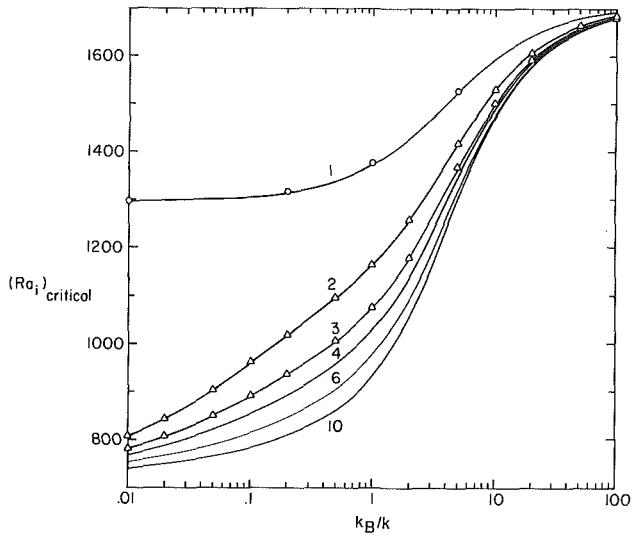

Fig. 3 Same as Fig. 2 but for $L_{B_i}/L_i = 0.2$

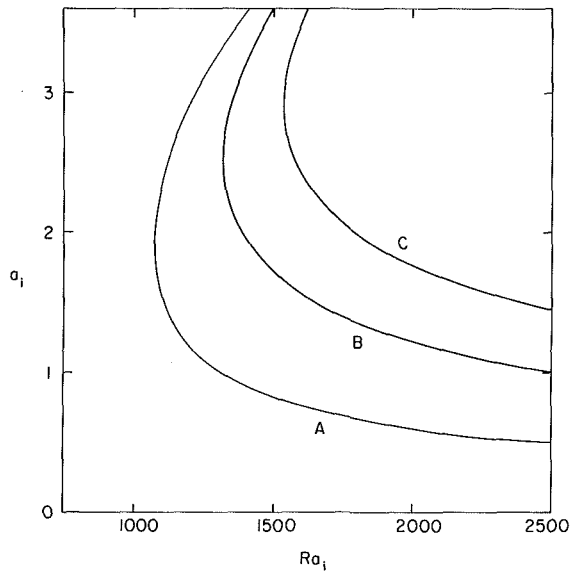

Fig. 4 Neutral stability curves corresponding to the three most unstable modes for the case $N = 3$, $k_B/k = 1$, and $L_{B_i}/L_i = 0.2$

ing the Runge-Kutta procedure to integrate across the layer and requiring that

$$C_{2,3}W_{2,3}(1/2) + C_{2,4}W_{2,4}(1/2) + C_{2,5}W_{2,5}(1/2) + C_{2,6}W_{2,6}(1/2) = 0 \quad (7)$$

and

$$C_{2,3}W'_{2,3}(1/2) + C_{2,4}W'_{2,4}(1/2) + C_{2,5}W'_{2,5}(1/2) + C_{2,6}W'_{2,6}(1/2) = 0 \quad (8)$$

resulting in values for $C_{2,3}$ and $C_{2,4}$. This procedure can be successively repeated until we reach the top layer, $i = N + 1$. Whether or not θ_{N+1} vanishes at $Z_{N+1} = 1/2$ will then determine whether or not we have an eigenvalue. If not, a Newton-Raphson iterative procedure has been found to work very well in the present problem for determining the Rayleigh number at a given wavenumber.

In effect, then, the shooting method in the present case reduces to a one-parameter problem, namely determining the Rayleigh number such that the thermal disturbance condition at the upper wall is satisfied. The resulting numerical program consists of approximately 300 lines of FORTRAN code which can handle an arbitrary number of layers with arbitrary thicknesses for each fluid layer and each wall. Although the code assumes that the outer walls are at fixed temperatures, the situation of poorly conducting outer walls could also be handled by a simple extension provided the thermal boundary conditions are linear, such as with a specified convective heat transfer coefficent.

For comparison, it might be noted that the approach followed by Catton and Lienhard (1984) is based upon the Galerkin method, as outlined by Chandrasekhar (1961), and requires determining the eigenvalues of a $2N \times 2N$ matrix when the disturbance velocity is represented in terms of N trial functions. In particular, Catton and Lienhard (1984) restrict their attention to the case of two fluid layers and note that "allowing the interlayer to be arbitrarily located between the heated and cooled surfaces dramatically increases the complexity of the problem." This is in contrast to the present shooting approach in which the location as well as the number and thicknesses of the interlayers can be handled by merely changing the data input accordingly. It should be noted that Lienhard (1987) has substantially improved the formulation of the earlier (1984) paper by essentially uncoupling the eigen-

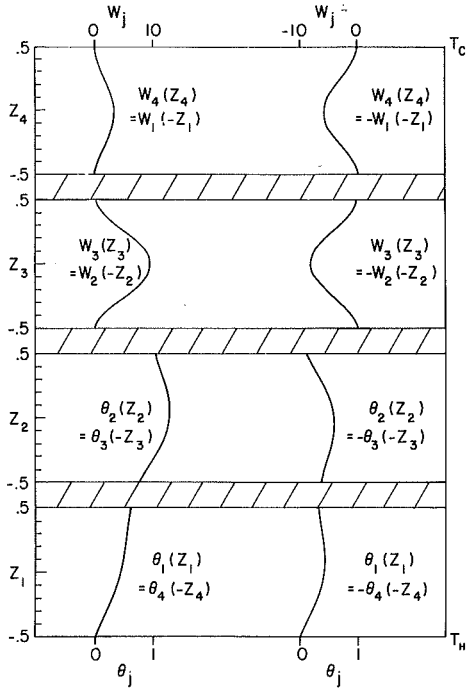

Fig. 5 Disturbance velocity and temperature profiles across the fluid layers corresponding to the minimum Ra_i along curves A (left) and B in Fig. 4. Note that $\theta_i(-1/2) \equiv 1$.

value problem between the various layers, thereby also being able to handle the multilayer situation with arbitrary relative thicknesses and locations.

As illustrations of the present shooting technique, results have been generated for the symmetric configuration in which all interior barriers are of the same thickness and all fluid layers are of the same thickness. In particular, results are shown for the critical Rayleigh number for $L_{B_i}/L_i = 0.002$ (Fig. 1), 0.02 (Fig. 2), and 0.2 (Fig. 3), together with corresponding predictions available from Catton and Lienhard (1984) and Lienhard (1986). It might be noted that the results in Figs. 1–3 correspond to the least-stable eigenfunction mode. For example, the value for $(Ra_i)_{critical}$ in Fig. 3 for $N = 3$ and $k_B/k = 1$ corresponds to the minimum value along curve A in Fig. 4. In particular, curve A is the locus of points in (a_i, Ra_i) along which the disturbance field is symmetric about the overall midpoint and the disturbance temperature has no zeroes other than at the upper and lower outer walls. On the other hand, the disturbance field along curve B in Fig. 4 is asymmetric with θ having only one interior zero, whereas that along curve C is symmetric with two interior zeroes. This is illustrated in Fig. 5 for the first two modes.

References

Catton, I., and Lienhard, J. H., V., 1984, "Thermal Stability of Two Fluid Layers Separated by a Solid Interlayer of Finite Thickness and Thermal Conductivity," ASME JOURNAL OF HEAT TRANSFER, Vol. 106, pp. 605–612.

Chandrasekhar, S., 1961, *Hydrodynamic and Hydromagnetic Stability*, Oxford University Press, London.

Harris, D. L., and Reid, W. H., 1964, "On the Stability of Viscous Flow Between Rotating Cylinders; Part 2: Numerical Analysis," *Journal of Fluid Mechanics*, Vol. 20, pp. 95–101.

Hieber, C. A., and Gebhart, B., 1971, "Stability of Vertical Natural Convection Boundary Layers: Some Numerical Solutions," *Journal of Fluid Mechanics*, Vol. 48, pp. 625–646.

Lienhard, J. H., V., 1987, "An Improved Approach to Conductive Boundary Conditions for the Rayleigh-Benard Instability," ASME JOURNAL OF HEAT TRANSFER, this issue.

Roberts, S. M., and Shipman, J. S., 1972, *Two-Point Boundary Value Problems: Shooting Methods*, American Elsevier, New York.

Air Resistance Coefficients for Perforated Plates in Free Convection

M. Ishizuka,[1] Y. Miyazaki,[1] and T. Sasaki[1]

1 Introduction

With the recent rapid increase in close packaging density, and higher power for electronic equipment, the cooling design involved in casings which enclose them has become more important. For the electronic equipment cooling design, data on flow path resistance in the casing are needed. The most significant factors in the flow resistance are considered to be vent perforations. However, all the resistance data for perforated plates were obtained for forced convective flows (higher Reynolds numbers), as reported by Collar (1939), Macphail (1939), and Taylor (1949). Smith and Van Winkle (1957) studied discharge coefficients through perforated plates at a wide Reynolds number range of 2000 to 20,000, and Kolodzie and Van Winkle (1958) also made a study at a 400 to 3000 Reynolds number range. Their work was limited to a lower porosity coefficient range of 0.023 to 0.158.

However, resistance data in air free convection paths have not been reported. Therefore, the measuring system for determining the resistance values for perforated plates in an air free convection path was designed. This note describes the measuring system and resistance values for perforated plates obtained by using the system.

2 Ventilation Model

Consider the ventilation model shown in Fig. 1, in which the temperature distribution is uniform. For steady state, expressions for energy balance and balance between fluid resistance and driving force due to buoyancy are as follows

$$Q = \rho C_p u A \Delta T \tag{1}$$

$$(\rho_\infty - \rho) g h = K_T \rho u^2/2 \tag{2}$$

Here, Q is dissipated power value, ρ is air density, C_p is air specific heat at constant pressure, u is air flow velocity, A is duct cross section, ΔT is temperature rise, g is gravity acceleration, h is distance between a resistance plate and input heater, and K_T is air flow resistance coefficient for the total system. The subscript ∞ expresses atmosphere. At constant pressure, from equations (1) and (2), we have

$$K_T = 2 \cdot g \cdot h \cdot \Delta T^3 / T_\infty (\rho C_p A/Q)^2 \tag{3}$$

Now, when K_0 is taken as the resistance coefficient value for the system without a perforated plate, net resistance coefficient K for the plate can be obtained by the following expression

$$K = K_T - K_0 \tag{4}$$

In addition, the following expression for the K value uncertainty will be obtained, as shown by Kline (1985), from equation (3)

$$|dK/K| = (9(d\Delta T/\Delta T)^2 + 4(dQ/Q)^2)^{1/2} \tag{5}$$

Here, other parameter uncertainties are neglected, in comparison to those for ΔT and Q.

[1] Researchers, Mechanical Engineering Laboratory, Research and Development Center, Toshiba Corporation, 4-1 Ukishima-cho, Kawasaki-ku, Kawasaki-city, 210, Japan.

Contributed by the Heat Transfer Division for publication in the JOURNAL OF HEAT TRANSFER. Manuscript received by the Heat Transfer Division April 15, 1985.

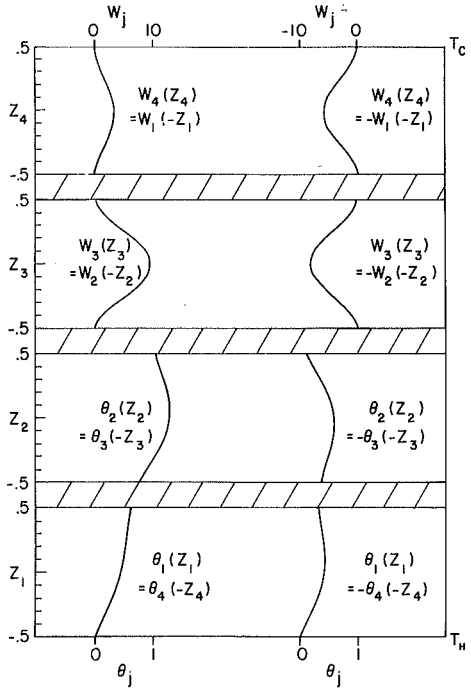

Fig. 5 Disturbance velocity and temperature profiles across the fluid layers corresponding to the minimum Ra_i along curves A (left) and B in Fig. 4. Note that $\theta_1(-1/2) \equiv 1$.

value problem between the various layers, thereby also being able to handle the multilayer situation with arbitrary relative thicknesses and locations.

As illustrations of the present shooting technique, results have been generated for the symmetric configuration in which all interior barriers are of the same thickness and all fluid layers are of the same thickness. In particular, results are shown for the critical Rayleigh number for $L_{B_i}/L_i = 0.002$ (Fig. 1), 0.02 (Fig. 2), and 0.2 (Fig. 3), together with corresponding predictions available from Catton and Lienhard (1984) and Lienhard (1986). It might be noted that the results in Figs. 1–3 correspond to the least-stable eigenfunction mode. For example, the value for $(Ra_i)_{critical}$ in Fig. 3 for $N = 3$ and $k_B/k = 1$ corresponds to the minimum value along curve A in Fig. 4. In particular, curve A is the locus of points in (a_i, Ra_i) along which the disturbance field is symmetric about the overall midpoint and the disturbance temperature has no zeroes other than at the upper and lower outer walls. On the other hand, the disturbance field along curve B in Fig. 4 is asymmetric with θ having only one interior zero, whereas that along curve C is symmetric with two interior zeroes. This is illustrated in Fig. 5 for the first two modes.

References

Catton, I., and Lienhard, J. H., V., 1984, "Thermal Stability of Two Fluid Layers Separated by a Solid Interlayer of Finite Thickness and Thermal Conductivity," ASME JOURNAL OF HEAT TRANSFER, Vol. 106, pp. 605–612.

Chandrasekhar, S., 1961, *Hydrodynamic and Hydromagnetic Stability*, Oxford University Press, London.

Harris, D. L., and Reid, W. H., 1964, "On the Stability of Viscous Flow Between Rotating Cylinders; Part 2: Numerical Analysis," *Journal of Fluid Mechanics*, Vol. 20, pp. 95–101.

Hieber, C. A., and Gebhart, B., 1971, "Stability of Vertical Natural Convection Boundary Layers: Some Numerical Solutions," *Journal of Fluid Mechanics*, Vol. 48, pp. 625–646.

Lienhard, J. H., V., 1987, "An Improved Approach to Conductive Boundary Conditions for the Rayleigh-Benard Instability," ASME JOURNAL OF HEAT TRANSFER, this issue.

Roberts, S. M., and Shipman, J. S., 1972, *Two-Point Boundary Value Problems: Shooting Methods*, American Elsevier, New York.

Air Resistance Coefficients for Perforated Plates in Free Convection

M. Ishizuka,[1] Y. Miyazaki,[1] and T. Sasaki[1]

1 Introduction

With the recent rapid increase in close packaging density, and higher power for electronic equipment, the cooling design involved in casings which enclose them has become more important. For the electronic equipment cooling design, data on flow path resistance in the casing are needed. The most significant factors in the flow resistance are considered to be vent perforations. However, all the resistance data for perforated plates were obtained for forced convective flows (higher Reynolds numbers), as reported by Collar (1939), Macphail (1939), and Taylor (1949). Smith and Van Winkle (1957) studied discharge coefficients through perforated plates at a wide Reynolds number range of 2000 to 20,000, and Kolodzie and Van Winkle (1958) also made a study at a 400 to 3000 Reynolds number range. Their work was limited to a lower porosity coefficient range of 0.023 to 0.158.

However, resistance data in air free convection paths have not been reported. Therefore, the measuring system for determining the resistance values for perforated plates in an air free convection path was designed. This note describes the measuring system and resistance values for perforated plates obtained by using the system.

2 Ventilation Model

Consider the ventilation model shown in Fig. 1, in which the temperature distribution is uniform. For steady state, expressions for energy balance and balance between fluid resistance and driving force due to buoyancy are as follows

$$Q = \rho C_p u A \Delta T \tag{1}$$

$$(\rho_\infty - \rho) g h = K_T \rho u^2/2 \tag{2}$$

Here, Q is dissipated power value, ρ is air density, C_p is air specific heat at constant pressure, u is air flow velocity, A is duct cross section, ΔT is temperature rise, g is gravity acceleration, h is distance between a resistance plate and input heater, and K_T is air flow resistance coefficient for the total system. The subscript ∞ expresses atmosphere. At constant pressure, from equations (1) and (2), we have

$$K_T = 2 \cdot g \cdot h \cdot \Delta T^3 / T_\infty (\rho C_p A/Q)^2 \tag{3}$$

Now, when K_0 is taken as the resistance coefficient value for the system without a perforated plate, net resistance coefficient K for the plate can be obtained by the following expression

$$K = K_T - K_0 \tag{4}$$

In addition, the following expression for the K value uncertainty will be obtained, as shown by Kline (1985), from equation (3)

$$|dK/K| = (9(d\Delta T/\Delta T)^2 + 4(dQ/Q)^2)^{1/2} \tag{5}$$

Here, other parameter uncertainties are neglected, in comparison to those for ΔT and Q.

[1] Researchers, Mechanical Engineering Laboratory, Research and Development Center, Toshiba Corporation, 4-1 Ukishima-cho, Kawasaki-ku, Kawasaki-city, 210, Japan.

Contributed by the Heat Transfer Division for publication in the JOURNAL OF HEAT TRANSFER. Manuscript received by the Heat Transfer Division April 15, 1985.

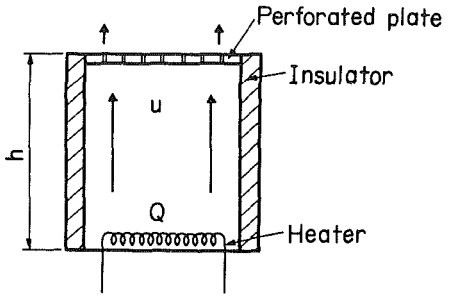

Fig. 1 Ventilation model

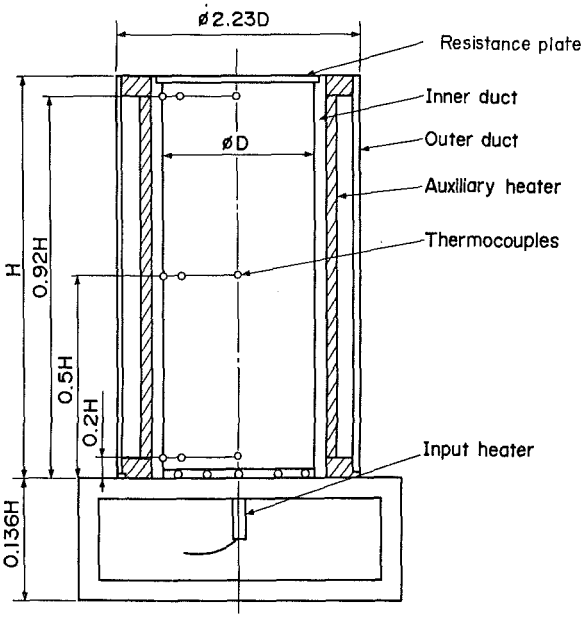

Fig. 2 Measuring system

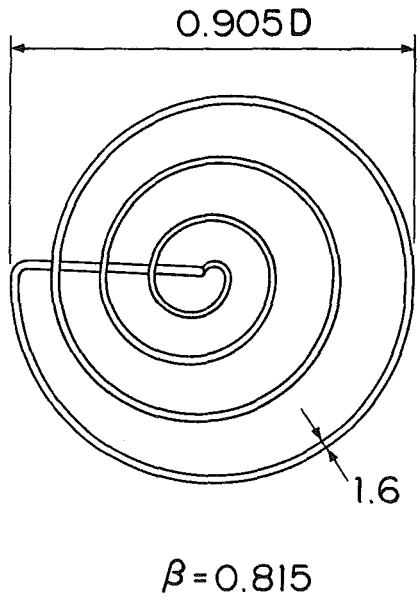

$\beta = 0.815$

Fig. 3 Input power heater shape

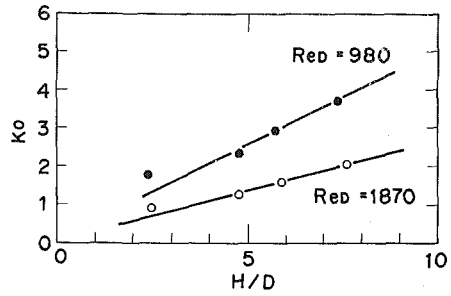

Fig. 4 Relationship between K_0 and H

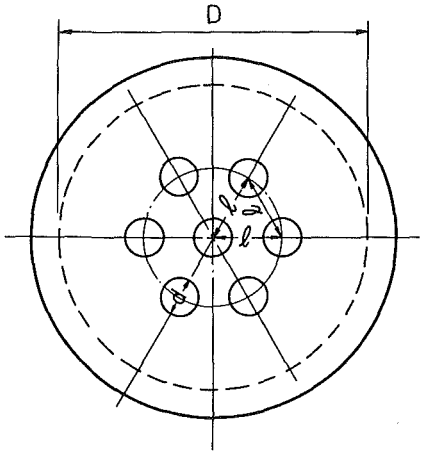

Fig. 5(a) Hexagonal

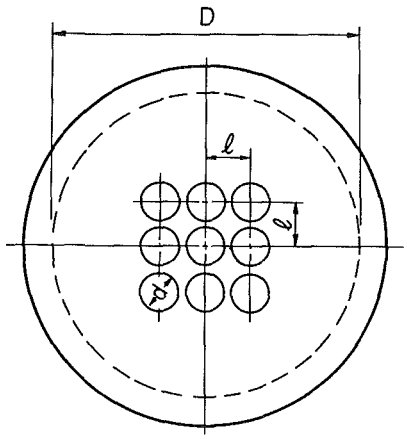

Fig. 5(b) Square

Fig. 5 Perforations for experimental perforated plates

3 Experiments

3.1 Measuring System. Figure 2 illustrates the measuring system designed in order to realize the ventilation model shown in Fig. 1.

The system consists of inner and outer ducts, the input power heater shown in Fig. 3 on the inner duct bottom, and a perforated plate on the top.

In order to make the inner duct as adiabatic as possible, a ribbon auxiliary heater was wound around the outer wall of the inner duct. The wall temperature and the center air temperature in the duct cross section are adjusted to within 2 percent of the wall temperature value by changing the ribbon heater voltage values. Duct diameter D is 77.2 mm. Height H is determined as $H = 5.7\ D$ by considering Fig. 4, which shows the relationship between the K_0 value and the height H. K_0 values were obtained as a function of Reynolds number Re_D, which is based on duct diameter, as follows

Table 1 Perforated plate dimensions

Plate No.	d (mm)	ℓ/d Ratio	t/d Ratio	β Ratio	Perforation pattern
P1	4.0	1.25	0.5	0.58	Hexagonal
P2		1.50		0.40	
P3		1.75		0.30	
P4		2.0		0.23	
P5	5.0	1.20	0.2	0.63	
P6		1.40		0.46	
P7		1.60		0.35	
P8		1.80		0.28	
P9	4.0	1.50	0.25	0.34	Square
P10			0.50		
P11	2.0	2.0	0.50	0.21	
P12	8.0	1.50	0.125	0.29	
P13			0.50		
P14	4.0	3.0	0.25	0.10	
P15			0.50		
P16			0.75		
P17			1.0		
P18			1.5		
P19			2.0		
P20	6.0	2.0	0.16	0.18	
P21			0.33		
P22			0.67		
P23			1.00		
P24			1.33		

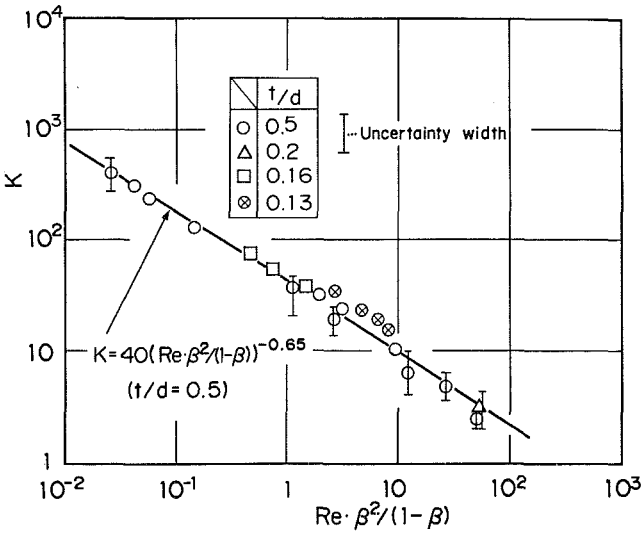

Fig. 6 Relationship among K, Re, and β

$$K_0 = 2300/\mathrm{Re}_D \tag{6}$$

3.2 Experimental Perforated Plates. Figure 5 shows the perforations for the experimental perforated plates. Figures 5(*a*) and 5(*b*) are hexagonal and square-shaped holes, respectively. Parameters for the 24 perforated plates are listed in Table 1. Perforated plates were made from drilled aluminum sheets.

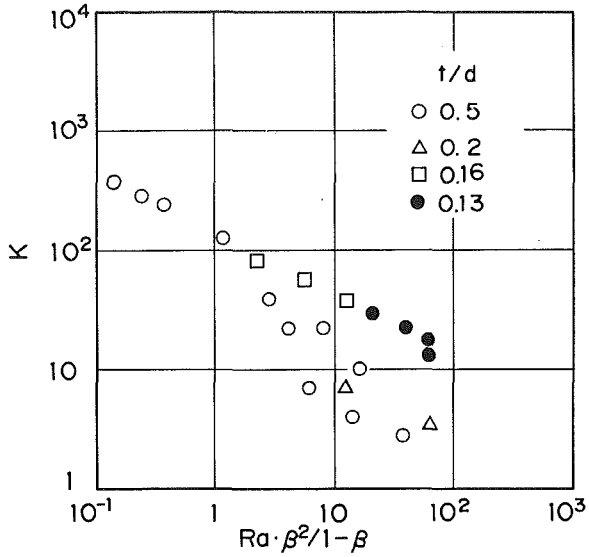

Fig. 7 Relationship between K and Ra

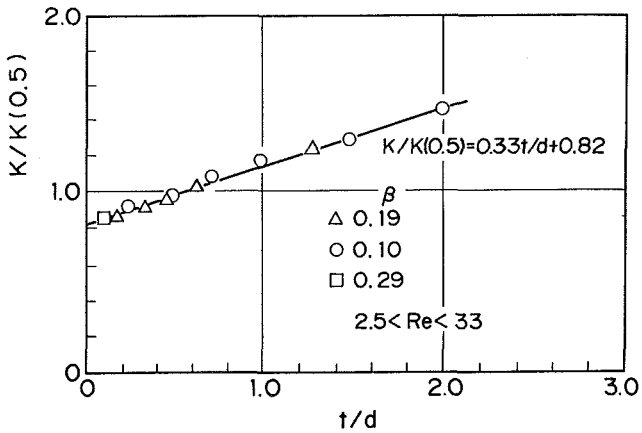

Fig. 8 Relationship between K/K(0.5) and t/d

3.3 Relationship Among Resistance Coefficient K, Reynolds Number Re, and Porosity Coefficient β. Figure 6 shows the relationship among resistance coefficient K, Reynolds number Re based on hole diameter d, and porosity coefficient β. Resistance coefficient K values are arranged as a function of $\mathrm{Re}\cdot\beta^2/(1-\beta)$, as shown in Fig. 6. All the data are correlated well with the following expression, from a practical point of view

$$K = 40(\mathrm{Re}\cdot\beta^2(1-\beta))^{-0.65}$$
$$2.5 < \mathrm{Re} < 82 \tag{7}$$
$$0.1 < \beta < 0.63$$

Especially when the plate thickness to hole diameter ratio t/d is 0.5, the K values were correlated very well with equation (7). In Fig. 6, finite-length lines, with open circular symbols showing measured values, define uncertainty width for the respective measure value. For a value without the line, it is shown that the values with uncertainty width are within the respective white symbols. Here, uncertainty width is obtained from equation (5), considering that temperature rise uncertainty $d\Delta T$ is estimated as ± 0.5 K and the heat leak at $dQ/Q = 2$ percent. The maximum uncertainty width was 25 percent, at $\beta = 0.63$, due to the small temperature rise.

3.4 Relationship Between Resistance Coefficient K and Rayleigh Number Ra. Figure 7 shows the relationship be-

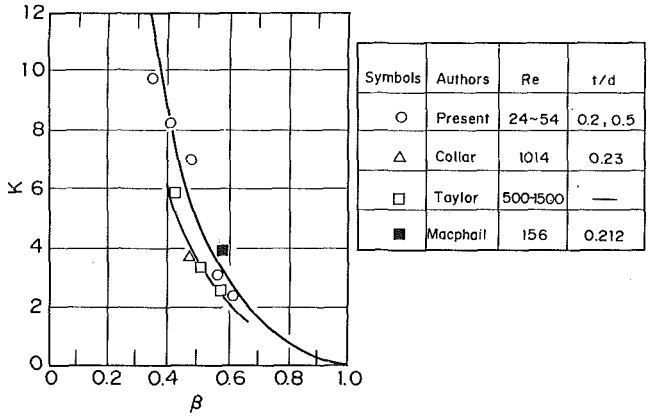

Fig. 9 Comparison between present data and data obtained by others

tween resistance value K and Rayleigh number Ra, based on hole diameter, as in Fig. 6. The correlation is poor, so it is clear that it is unsuitable to express the resistance coefficient as a function of Ra, since the item under consideration is not heat transfer, but purely an aerodynamic study.

3.5 Relationship Between Resistance Coefficient and K and Perforated Plate Thickness to Hole Diameter Ratio t/d. Figure 8 shows the relationship between resistance coefficient ratio $K/K(0.5)$ and plate thickness to hole diameter ratio t/d, where $K(0.5)$ denotes the resistance coefficient value at $t/d=0.5$. The reason is that the experimental results were correlated mainly at $t/d=0.5$ in Fig. 6. From Fig. 8, the linear correlation can be expressed with good approximation by the following equation

$$K/K(0.5)=0.25t/d+0.82 \tag{8}$$

4 Comparison Between Present Data and Data at Higher Reynolds Numbers

The comparison between present data ($Re<54$), and data obtained by Collar (1939), Macphail (1939), and Taylor (1949), is interesting.

Figure 9 shows the resistance coefficient K as a function of β for a wide Reynolds number range. From Fig. 9, it is suggested that, since the Reynolds number influence is much weaker than porosity coefficient influence for perforated plate resistance values, the Reynolds number influence should be neglected for β values which are larger than 0.4, from a practical point of view. However, for $Re<54$, it may be better to use equation (7).

5 Conclusions

A measuring system used to obtain resistance values for perforated plates in air free convection paths has been designed. Resistance coefficient value for perforated plates are presented. The results are very well correlated as functions of $Re\cdot\beta^2(1-\beta)$ and t/d. The results are very useful for designers who are concerned with electronic equipment thermal dissipation.

References

Collar, A. R., 1939, "The Effect of a Gauze on the Velocity Distribution in a Uniform Duct," Brit. Aero. Res. Coun. Rep. and Mem., No. 1867.

Kline, S. J., 1985, "The Purposes of Uncertainty Analysis," ASME *Journal of Fluids Engineering*, Vol. 107, pp. 153–160.

Kolodzie, P. A., and Van Winkle, M., 1957, "Discharge Coefficients Through Perforated Plates," *AIChE Journal*, Vol. 3, No. 3, pp. 305–312.

Macphail, D. C., 1939, "Experiments on Turning Vanes at an Expansion," Brit. Aero. Res. Coun. Rep. and Mem., No. 1876.

Smith, P. L., Jr., and Van Winkle, M., 1958, "Discharge Coefficients Through Perforated Plates at Reynolds Numbers of 400 to 3,000," *AIChE Journal*, Vol. 4, No. 3, pp. 266–268.

Taylor, G. I., and Batchelor, G. K., 1949, "The Effect of Wire Gauze on Small Disturbances in a Uniform Stream," *Quart. Journ. Mech. and Applied Math.*, Vol. 11, Pt. 1, pp. 3–29.

Visualization Studies of a Freon-113 Bubble Condensing in Water

H. Kalman,[1] A. Ullmann,[1] and R. Letan[1]

Several visualization methods have been applied in studies of organic bubbles condensing in water (Lerner et al., 1984; Kalman et al., 1986). The results, although qualitative in nature, have furnished an insight into the physical phenomena governing the process.

Shadowgraphing of the collapsing bubbles has outlined the thermal surroundings of the bubble (Lerner et al., 1984; Kalman et al., 1986). Shadowgraphs of a freon-113 bubble (Lerner et al., 1984) recorded in sequence have illustrated the formation of a thermal layer around the injected bubble. As the bubble detached from the nozzle, a wake appeared at the rear of the bubble. The bubble with its wake accelerated until a maximum velocity was reached. Then the bubble decelerated, the wake moved forward, and a thermal cloud enveloped the bubble. With the completion of the collapse process the bubble-droplet moved away from its thermal cloud.

The shadowgraphing has reflected the density gradients, i.e., the temperature field, but it has also led to an understanding of the flow phenomena around the bubble. It was almost obvious that the thermal boundary layer and the wake, as shadowgraphed in Fig. 1, related also to a viscous boundary layer and a viscous wake, respectively. The thermal shedding of the wake, as shown in the shadowgraph of Fig. 2, and further the envelopment of the bubble by the thermal cloud, were understood to correspond to the flow of the water surrounding the bubble. However, all that still remained to be experimentally proved by methods directly related to flow visualization. That goal was achieved by photographing the entrainment of colored water in the wake of a rising freon-113 bubble as illustrated in Figs. 3–5. These photographs complemented the shadowgraphs previously recorded (Lerner et al., 1984), and qualitatively proved that the thermal phenomena corresponded to the viscous flow. The details can be observed in Figs. 3–5, and compared with the respective shadowgraphs in the previous work.

Figure 3 illustrates the envelopment of the bubble in its wake in the zone of deceleration. Figure 4 shows the turning aside of the bubble, and the horizontal leveling of the wake with its bubble. Figure 5 shows the release of the bubble from its original colored wake. The same sequence was also observed in experiments with pentane bubbles condensing in water (Kalman et al., 1986).

The flow visualization experiments of the colored water were performed as follows: A vertical glass column, square in cross section, 10×10 cm, and 60 cm high was used in the experiments (Lerner et al., 1984). A nozzle, 3 mm in diameter, was installed at the bottom of the column, and connected to a vapor generator. Freon-113 was vaporized to form bubbles at the nozzle in the column filled with water. Purple water

[1]Mechanical Engineering Department, Ben-Gurion University of the Negev, Beer-Sheva, Israel.

Contributed by the Heat Transfer Division for publication in the JOURNAL OF HEAT TRANSFER. Manuscript received by the Heat Transfer Division August 8, 1984.

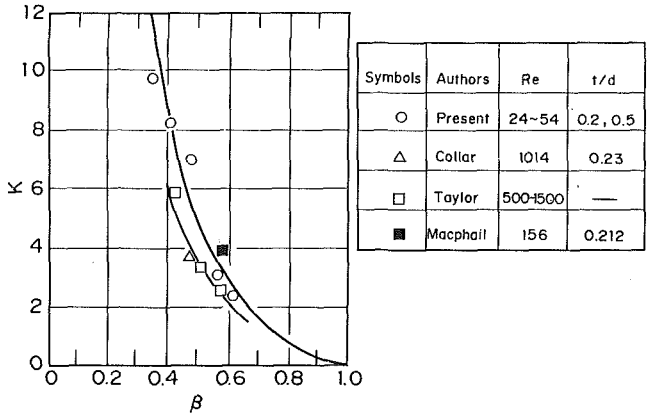

Fig. 9 Comparison between present data and data obtained by others

tween resistance value K and Rayleigh number Ra, based on hole diameter, as in Fig. 6. The correlation is poor, so it is clear that it is unsuitable to express the resistance coefficient as a function of Ra, since the item under consideration is not heat transfer, but purely an aerodynamic study.

3.5 Relationship Between Resistance Coefficient and K and Perforated Plate Thickness to Hole Diameter Ratio t/d. Figure 8 shows the relationship between resistance coefficient ratio $K/K(0.5)$ and plate thickness to hole diameter ratio t/d, where $K(0.5)$ denotes the resistance coefficient value at $t/d=0.5$. The reason is that the experimental results were correlated mainly at $t/d=0.5$ in Fig. 6. From Fig. 8, the linear correlation can be expressed with good approximation by the following equation

$$K/K(0.5)=0.25t/d+0.82 \tag{8}$$

4 Comparison Between Present Data and Data at Higher Reynolds Numbers

The comparison between present data ($Re<54$), and data obtained by Collar (1939), Macphail (1939), and Taylor (1949), is interesting.

Figure 9 shows the resistance coefficient K as a function of β for a wide Reynolds number range. From Fig. 9, it is suggested that, since the Reynolds number influence is much weaker than porosity coefficient influence for perforated plate resistance values, the Reynolds number influence should be neglected for β values which are larger than 0.4, from a practical point of view. However, for $Re<54$, it may be better to use equation (7).

5 Conclusions

A measuring system used to obtain resistance values for perforated plates in air free convection paths has been designed. Resistance coefficient value for perforated plates are presented. The results are very well correlated as functions of $Re\cdot\beta^2(1-\beta)$ and t/d. The results are very useful for designers who are concerned with electronic equipment thermal dissipation.

References

Collar, A. R., 1939, "The Effect of a Gauze on the Velocity Distribution in a Uniform Duct," Brit. Aero. Res. Coun. Rep. and Mem., No. 1867.

Kline, S. J., 1985, "The Purposes of Uncertainty Analysis," ASME *Journal of Fluids Engineering*, Vol. 107, pp. 153–160.

Kolodzie, P. A., and Van Winkle, M., 1957, "Discharge Coefficients Through Perforated Plates," *AIChE Journal*, Vol. 3, No. 3, pp. 305–312.

Macphail, D. C., 1939, "Experiments on Turning Vanes at an Expansion," Brit. Aero. Res. Coun. Rep. and Mem., No. 1876.

Smith, P. L., Jr., and Van Winkle, M., 1958, "Discharge Coefficients Through Perforated Plates at Reynolds Numbers of 400 to 3,000," *AIChE Journal*, Vol. 4, No. 3, pp. 266–268.

Taylor, G. I., and Batchelor, G. K., 1949, "The Effect of Wire Gauze on Small Disturbances in a Uniform Stream," *Quart. Journ. Mech. and Applied Math.*, Vol. 11, Pt. 1, pp. 3–29.

Visualization Studies of a Freon-113 Bubble Condensing in Water

H. Kalman,[1] A. Ullmann,[1] and R. Letan[1]

Several visualization methods have been applied in studies of organic bubbles condensing in water (Lerner et al., 1984; Kalman et al., 1986). The results, although qualitative in nature, have furnished an insight into the physical phenomena governing the process.

Shadowgraphing of the collapsing bubbles has outlined the thermal surroundings of the bubble (Lerner et al., 1984; Kalman et al., 1986). Shadowgraphs of a freon-113 bubble (Lerner et al., 1984) recorded in sequence have illustrated the formation of a thermal layer around the injected bubble. As the bubble detached from the nozzle, a wake appeared at the rear of the bubble. The bubble with its wake accelerated until a maximum velocity was reached. Then the bubble decelerated, the wake moved forward, and a thermal cloud enveloped the bubble. With the completion of the collapse process the bubble-droplet moved away from its thermal cloud.

The shadowgraphing has reflected the density gradients, i.e., the temperature field, but it has also led to an understanding of the flow phenomena around the bubble. It was almost obvious that the thermal boundary layer and the wake, as shadowgraphed in Fig. 1, related also to a viscous boundary layer and a viscous wake, respectively. The thermal shedding of the wake, as shown in the shadowgraph of Fig. 2, and further the envelopment of the bubble by the thermal cloud, were understood to correspond to the flow of the water surrounding the bubble. However, all that still remained to be experimentally proved by methods directly related to flow visualization. That goal was achieved by photographing the entrainment of colored water in the wake of a rising freon-113 bubble as illustrated in Figs. 3–5. These photographs complemented the shadowgraphs previously recorded (Lerner et al., 1984), and qualitatively proved that the thermal phenomena corresponded to the viscous flow. The details can be observed in Figs. 3–5, and compared with the respective shadowgraphs in the previous work.

Figure 3 illustrates the envelopment of the bubble in its wake in the zone of deceleration. Figure 4 shows the turning aside of the bubble, and the horizontal leveling of the wake with its bubble. Figure 5 shows the release of the bubble from its original colored wake. The same sequence was also observed in experiments with pentane bubbles condensing in water (Kalman et al., 1986).

The flow visualization experiments of the colored water were performed as follows: A vertical glass column, square in cross section, 10×10 cm, and 60 cm high was used in the experiments (Lerner et al., 1984). A nozzle, 3 mm in diameter, was installed at the bottom of the column, and connected to a vapor generator. Freon-113 was vaporized to form bubbles at the nozzle in the column filled with water. Purple water

[1]Mechanical Engineering Department, Ben-Gurion University of the Negev, Beer-Sheva, Israel.

Contributed by the Heat Transfer Division for publication in the JOURNAL OF HEAT TRANSFER. Manuscript received by the Heat Transfer Division August 8, 1984.

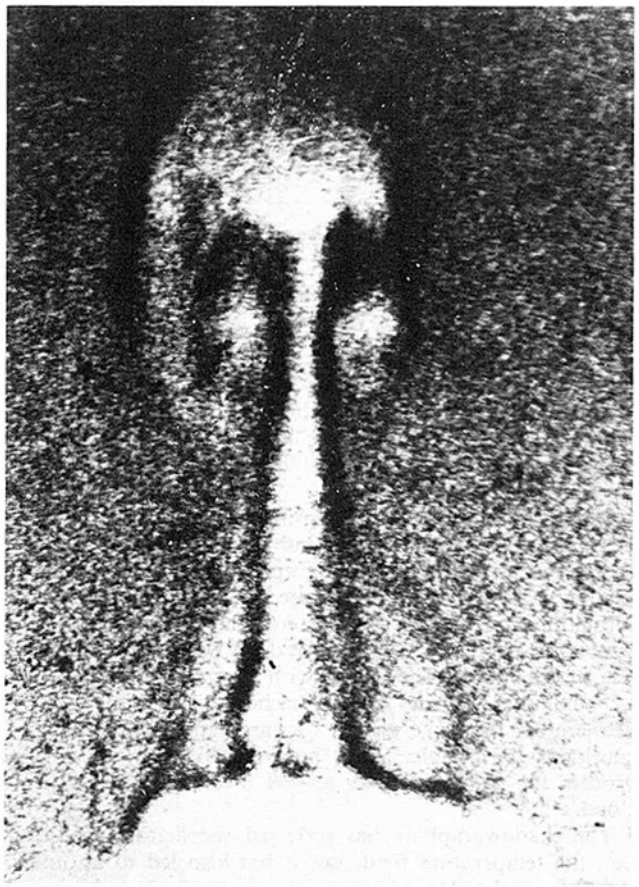

Fig. 1 Shadowgraph of a bubble, its wake and the thermal boundary layer (Lerner et al., 1984)

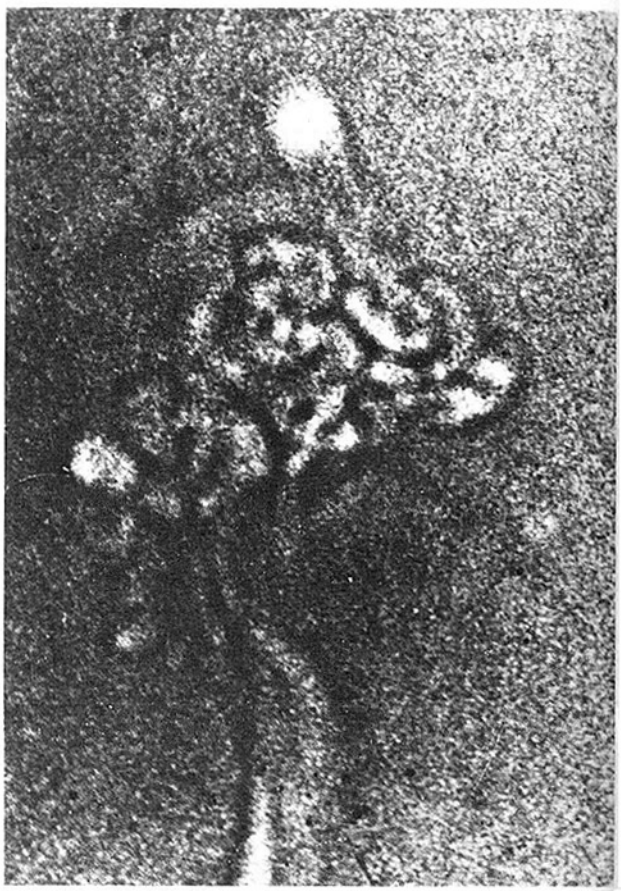

Fig. 2 Shadowgraph of a bubble, and its wake shedding (Lerner et al., 1984)

(colored with $KMnO_4$) was first poured into the column up to about 1 cm above the nozzle. Clear water was used above that layer to fill up the column to the top. Any bubble of freon-113 injected into the column entrained the purple water in its wake formed above the nozzle. Movements of the bubble and its purple wake were photographed using a cine-camera Arriflex, and Agfa film N-682, and a tungsten back light of 500 W.

A series of the colored wake photographs, of which Figs. 3–5 are samples, was recorded at a frequency of 40 frames/s. It showed the same sequence of events in the bubble collapse process as the shadowgraphs did in the previous work (Lerner et al., 1984). These two techniques of visualization have qualitatively provided the physical basis of the "boundary layer" and "envelope" models (Lerner et al., 1984; Kalman et al., 1986; Lerner and Letan, 1985) formulated for the external thermal resistance of the accelerating–decelerating bubble.

Visualization experiments were also conducted for an insight into the thermal resistance inside the bubble. To establish the character of the internal resistance, the flow and shape of the condensate film had to be investigated. The technique needed to detect flow of the very thin liquid film in a rising bubble was too complex to be employed in the present experiments. However, the shape visualization required a relatively simple experiment. The condensate shape has been photographed in two ways: by casting a shadow of the colorless bubble, and by coloring the liquid condensate.

In the first case a distant back illumination through the bubble was used to cast a "shadow" of the vapor bubble. Figure 6 shows two such freon-113 bubbles in water. In these photographs the vapor is shown black, and the external boundaries of the condensate are distinctly outlined. The vapor bubble appears to be spherical, eccentrically positioned,

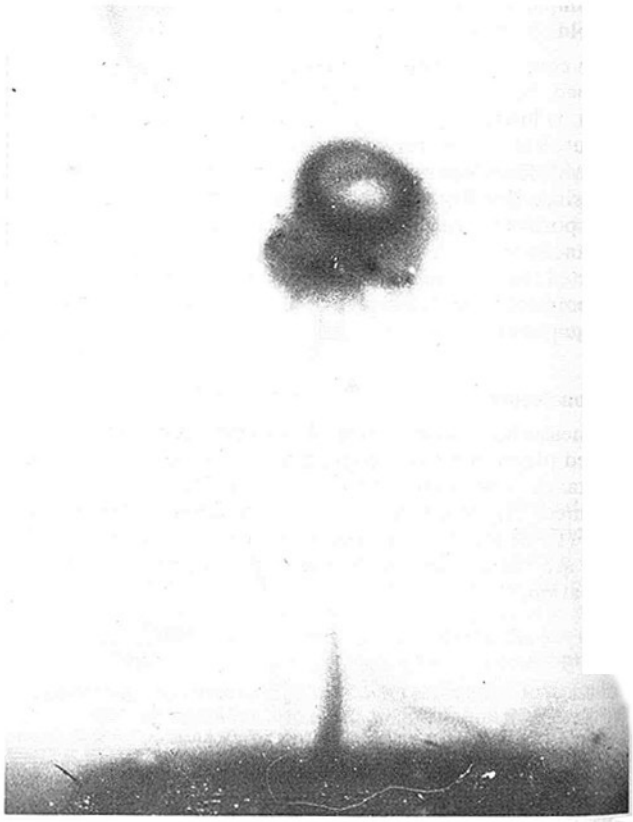

Fig. 3 Envelopment of a bubble in its entrained colored wake

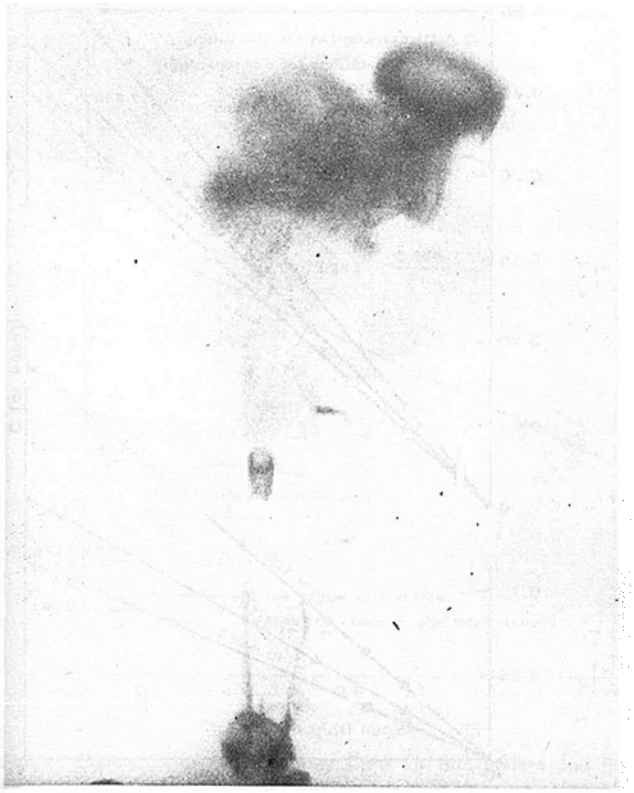

Fig. 4 Turning aside of the bubble from its colored wake

Fig. 5 Separation of the bubble from its colored wake

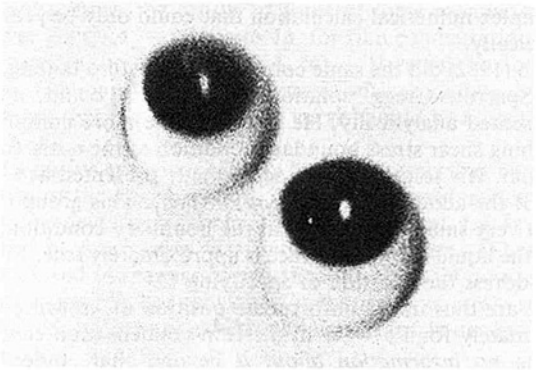

Fig. 6 "Shadow" of the vapor in a bubble

and adhering to the top at the interface of water. The condensate film does not show at all in the upper part of the bubble. It first appears at about 30 deg from the front stagnation point, and thickens considerably farther downstream. Thus, the black "shadow" of the vapor bubble has concealed the colorless thin film of liquid condensate enveloping the vapor bubble.

The experimentation was conducted in the same previously described square column. For the back illumination two flood

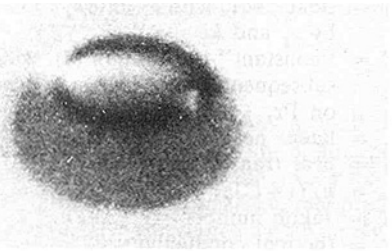

Fig. 7 Black-and-white photograph of a red-colored condensate in a bubble

bulbs, 150 W each, were used and fixed 1.1 m away from the column. A glass board covered with opaque tracing paper was used as a screen between the column and the light source. It was adjusted 0.2 m from the lights. In such optical arrangement the vapor bubble acted as a diverging lens, producing a black "shadow" in the photograph.

The distinction of the thin liquid film around the vapor bubble was achieved by using another technique of visualization of the condensate shape: Red organic dye was dissolved in the liquid freon-113. A droplet of the colored liquid was injected into hot water. It evaporated with the organic dye uniformly distributed in the vapor. It appeared colorless. Then the bubble moved into colder water, where it condensed. The red color showed up in the condensed liquid outlining the shape of the condensate, and the eccentric position of the vapor bubble. The very thin film of condensate in the upper part of the vapor bubble appeared as a weak coloration over the vapor, thus a colored "veil."

In reproduced black-and-white photographs the red condensate appears dark, and the "coloration" over the vapor is also observed. Figure 7 is such a black-and-white photograph reproduced from a color film. The physically spherical bubble is optically distorted in the photograph as those experiments were conducted in a circular tube, 5 cm in diameter.

In both Figs. 6 and 7, the eccentric position of the vapor bubble in the condensate is obvious. That shape was postulated in our condensation models, and quantitatively expressed in the mathematical formulations (Lerner et al., 1984; Kalman et al., 1986; Lerner and Letan, 1985).

References

Kalman, H., Ullmann, A., and Letan, R., 1986, "Dynamics of a Condensing Bubble in Zones of Time-Dependent Velocity," *Proceedings, 8th International Heat Transfer Conference*, Hemisphere, New York.

Lerner, Y., Kalman, H., and Letan, R., 1984, "Phenomenological and Experimental Analysis of an Accelerating-Decelerating Bubble Condensing in an Immiscible Liquid," *Basic Aspects of Two-Phase Flow and Heat Transfer*, Symposium Vol. HTD-34, 22nd National Heat Transfer Conference, pp. 1–10; ASME JOURNAL OF HEAT TRANSFER, this issue.

Lerner, Y., and Letan, R., 1985, "Dynamics of Condensing Bubbles: Effects of Injection Frequency," ASME Paper No. 85-HT-47.

Sensible Heat Correction in Laminar Film Boiling and Condensation

P. Sadasivan[1] and J. H. Lienhard[2]

Nomenclature

A_c = term inside the brackets in equation (1)

[1]Graduate Assistant, Mechanical Engineering Department, University of Houston, Houston, TX 77004.

[2]Professor, Mechanical Engineering Department, University of Houston, Houston, TX 77004; Fellow ASME.

Contributed by the Heat Transfer Division for publication in the JOURNAL OF HEAT TRANSFER. Manuscript received by the Heat Transfer Division May 12, 1986.

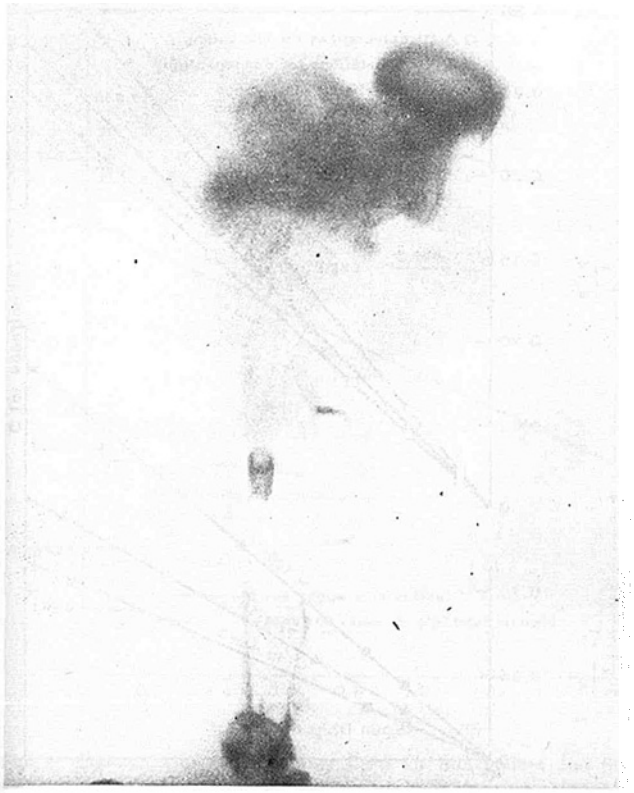

Fig. 4 Turning aside of the bubble from its colored wake

Fig. 5 Separation of the bubble from its colored wake

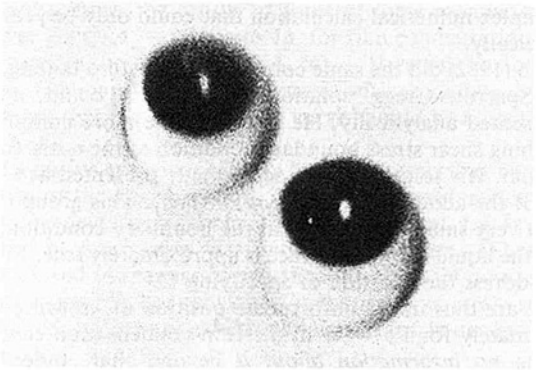

Fig. 6 "Shadow" of the vapor in a bubble

and adhering to the top at the interface of water. The condensate film does not show at all in the upper part of the bubble. It first appears at about 30 deg from the front stagnation point, and thickens considerably farther downstream. Thus, the black "shadow" of the vapor bubble has concealed the colorless thin film of liquid condensate enveloping the vapor bubble.

The experimentation was conducted in the same previously described square column. For the back illumination two flood

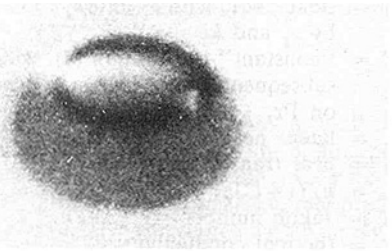

Fig. 7 Black-and-white photograph of a red-colored condensate in a bubble

bulbs, 150 W each, were used and fixed 1.1 m away from the column. A glass board covered with opaque tracing paper was used as a screen between the column and the light source. It was adjusted 0.2 m from the lights. In such optical arrangement the vapor bubble acted as a diverging lens, producing a black "shadow" in the photograph.

The distinction of the thin liquid film around the vapor bubble was achieved by using another technique of visualization of the condensate shape: Red organic dye was dissolved in the liquid freon-113. A droplet of the colored liquid was injected into hot water. It evaporated with the organic dye uniformly distributed in the vapor. It appeared colorless. Then the bubble moved into colder water, where it condensed. The red color showed up in the condensed liquid outlining the shape of the condensate, and the eccentric position of the vapor bubble. The very thin film of condensate in the upper part of the vapor bubble appeared as a weak coloration over the vapor, thus a colored "veil."

In reproduced black-and-white photographs the red condensate appears dark, and the "coloration" over the vapor is also observed. Figure 7 is such a black-and-white photograph reproduced from a color film. The physically spherical bubble is optically distorted in the photograph as those experiments were conducted in a circular tube, 5 cm in diameter.

In both Figs. 6 and 7, the eccentric position of the vapor bubble in the condensate is obvious. That shape was postulated in our condensation models, and quantitatively expressed in the mathematical formulations (Lerner et al., 1984; Kalman et al., 1986; Lerner and Letan, 1985).

References

Kalman, H., Ullmann, A., and Letan, R., 1986, "Dynamics of a Condensing Bubble in Zones of Time-Dependent Velocity," *Proceedings, 8th International Heat Transfer Conference*, Hemisphere, New York.

Lerner, Y., Kalman, H., and Letan, R., 1984, "Phenomenological and Experimental Analysis of an Accelerating-Decelerating Bubble Condensing in an Immiscible Liquid," *Basic Aspects of Two-Phase Flow and Heat Transfer*, Symposium Vol. HTD-34, 22nd National Heat Transfer Conference, pp. 1–10; ASME JOURNAL OF HEAT TRANSFER, this issue.

Lerner, Y., and Letan, R., 1985, "Dynamics of Condensing Bubbles: Effects of Injection Frequency," ASME Paper No. 85-HT-47.

Sensible Heat Correction in Laminar Film Boiling and Condensation

P. Sadasivan[1] and J. H. Lienhard[2]

Nomenclature

A_c = term inside the brackets in equation (1)

[1]Graduate Assistant, Mechanical Engineering Department, University of Houston, Houston, TX 77004.

[2]Professor, Mechanical Engineering Department, University of Houston, Houston, TX 77004; Fellow ASME.

Contributed by the Heat Transfer Division for publication in the JOURNAL OF HEAT TRANSFER. Manuscript received by the Heat Transfer Division May 12, 1986.

A_b = same as A_c with ν_f and k_f replaced by ν_g and k_g
C = "constant" in equation (2), which subsequently turns out to depend on Pr
h_{fg} = latent heat of vaporization
h = heat transfer coefficient
h'_{fg} = $h_{fg}(1 + C\text{Ja})$
Ja = Jakob number = $c_p\Delta T/h_{fg}$
k = thermal conductivity
Nu_x = hx/k_f for condensation and hx/k_g for boiling
Pr = Prandtl number
u = velocity component of fluid in the film, parallel with the wall
x = coordinate parallel with the heater or condenser wall
y = coordinate normal to the heater or condenser wall
ΔT = difference between saturation and wall temperatures
μ = dynamic viscosity
ν = kinematic viscosity
ρ = density

Subscripts

f = denoting a saturated liquid property
g = denoting a saturated vapor property

Problem

When Nusselt (1916) analyzed film condensation he obtained the following result for the local heat transfer:

$$\text{Nu}_x = \left[\frac{(\rho_f - \rho_g)gh_{fg}x^3}{4\nu_f k_f (T_{\text{sat}} - T_w)}\right]^{1/4} \left(\frac{h'_{fg}}{h_{fg}}\right)^{1/4} \tag{1}$$

where the conventional notation is defined in the Nomenclature section. In his results he recommended that the sensible heat required to cool the condensate below the local boiling point be accounted for by correcting the latent heat of vaporization h_{fg} as follows:

$$h'_{fg}/h_{fg} = (1 + C\text{Ja}) \tag{2}$$

where the Jakob number is $c_p\Delta T/h_{fg}$, and ΔT is the difference between the saturation and wall temperatures. He estimated $C = 3/8$. We can accordingly write equation (1) in the form

$$\text{Nu}_x = A_c^{1/4}(1 + C\text{Ja})^{1/4} \tag{3}$$

Bromley (1950) next adapted this development to the prediction of film boiling. He noted that Nusselt's boundary condition at the liquid-vapor interface $[(\partial u/\partial y) = 0]$ must be replaced by the condition $u \cong 0$ during film boiling. He also suggested that C might be 0.5 in this case. His result took the same form as Nusselt's

$$\text{Nu}_x = (A_b/4)^{1/4}(1 + C\text{Ja})^{1/4} \tag{4}$$

where A_b is the same as the bracketed term in equation (1), but with ν_f and k_f replaced by ν_g and k_g, and with Nu_x now based on k_g instead of k_f.

Bromley (1952) subsequently did a more precise prediction of C for film condensation and obtained $h'_{fg} = h_{fg}(1 + 0.4\text{Ja})^2$ which corresponds with $C \simeq 0.8$. He also suggested that this calculation might apply to film boiling as well. Rohsenow (1956) expanded this calculation to account for liquid crossflow at the liquid-vapor interface. He obtained $C = 0.675$ for film condensation, although he rounded it off to 0.68. Bromley admitted to having missed this extra term, in the printed discussion of Rohsenow's paper. He showed that with this error corrected he would have obtained $h'_{fg} = h_{fg}(1 + 0.34\text{Ja})^2$ which is virtually the same as Rohsenow's result. All of these calculations involved the implicit assumption that the Prandtl number was very large.

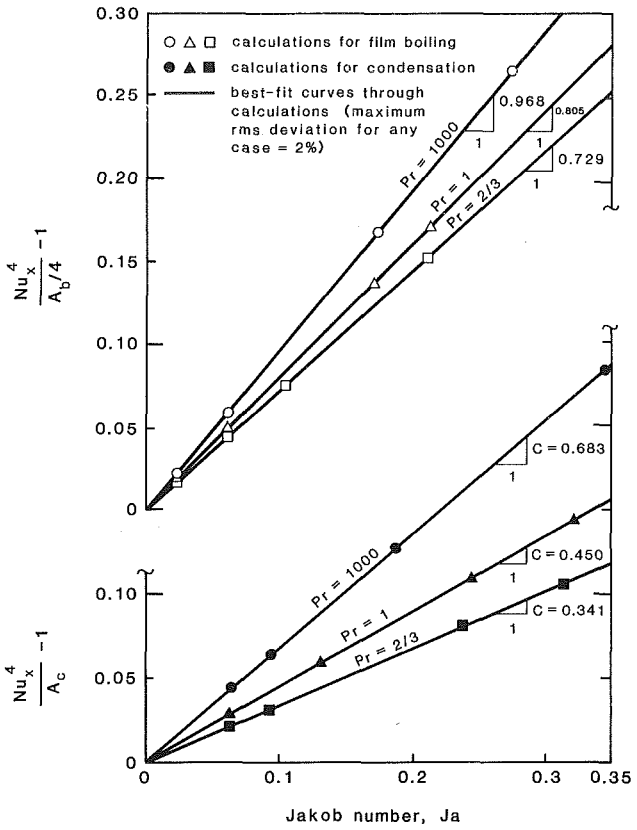

Fig. 1 Typical evaluations of C based on the exact solution of Sparrow and Gregg (1959) and the modified exact solution of Koh (1962)

Sparrow and Gregg (1959) provided a similarity solution of the boundary layer equations for the liquid film during film condensation. Their result showed exactly how the Nusselt number depended upon Pr and Ja. They remarked that their infinite Pr results appeared to bear out the value of $C = 0.675$. Their result had the disadvantage of being the result of a complex numerical calculation that could only be presented graphically.

Koh (1962) did the same computation for film boiling. Like the Sparrow-Gregg solution, his results could not be represented analytically. He also used the more complicated matching shear stress boundary condition at the outer edge of the film. His solutions were accordingly presented as a function of the additional group, $(\rho\mu)_g/(\rho\mu)_f$. This group is normally very small, implying that the boundary condition, $u = 0$, at the liquid-vapor interface is approximately true. Koh did not address the question of specifying C.

We are thus in the unfortunate position of knowing C approximately for $\text{Pr} = \infty$ in the film condensation case, and having *no information about it* beyond that. Indeed, the various similarity solutions have made it plain that C has to reflect inertial influences as sensible heat. If we want to write equations (3) and (4), we have to anticipate that C depends on Ja and Pr. Still, it would be extremely convenient to be able to solve film boiling and condensation problems accurately with no more than a latent heat correction because we must otherwise revert to complicated numerical solutions.

Furthermore, the influence of sensible heat becomes increasingly important in the case of film boiling since the numerical value of Ja is high enough to make the correction very important.

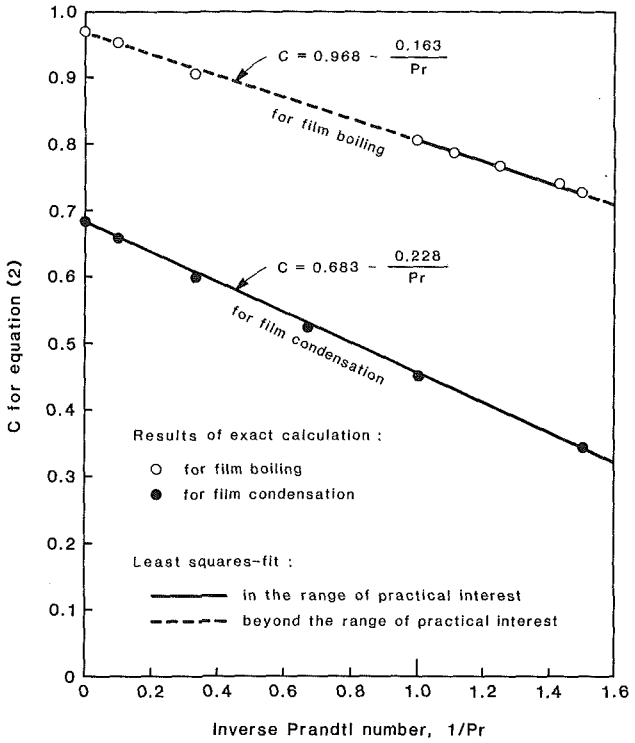

Fig. 2 Evaluation of the functions C(Pr) for film boiling and film condensation

A More Precise Evaluation of C

We have programmed the numerical solutions of both the Sparrow and Gregg equations, and the equations of Koh adapted to the limiting case in which $u = 0$ at the liquid-vapor interface. We have evaluated each set of equations over the range of Ja, for the range $0.6 < \text{Pr} < 1000$. A Pr equal to 1000 is close enough to infinity to make higher values unnecessary and Pr values below 0.6 become impractical. In the film boiling case, no single-component vapor yields a Pr below 2/3, and no liquid other than a liquid metal yields a Pr much below unity. And, of course, all of the present analyses fail at liquid metal conditions.

Figure 1 shows the results of three of these calculations in the form: $[\text{Nu}_x^4/A_c - 1]$ versus Ja, for film condensation, and three more in the form: $[\text{Nu}_x^4/(A_b/4) - 1]$ versus Ja, for film boiling. Comparing these coordinates with equations (3) and (4), we see that the slope of each curve should be numerically equal to C.

These curves are remarkable in how accurately they bear out the form of the h'_{fg} correction. The slope is constant for each Pr within a deviation that never exceeds 2 percent, for Ja up to 0.8; and in most cases was within one percent. (These Ja ranges exceed the ranges of practical interest.) Of course it is now clear that C is not constant. Furthermore, contrary to our expectation, it does not exhibit any significant Ja dependence, but rather $C = C(\text{Pr})$.

The resulting values of C are presented as functions of Pr^{-1} in Fig. 2 and once again the result is startling in its simplicity. The curves reveal that:

$$C_{\text{condensation}} = 0.683 - 0.228/\text{Pr} \tag{5}$$

$$C_{\text{film boiling}} = 0.968 - 0.163/\text{Pr} \tag{6}$$

It is interesting that for large Pr, equation (5) gives $C = 0.683$ which is higher than Rohsenow's limiting value by only 1.2 percent. We have also rerun Rohsenow's calculation using the film boiling boundary condition at the outer edge of the film and found that it gives 0.950. Thus the exact value of 0.968 is also higher than the Rohsenow type of calculation by only 1.9 percent.

Discussion

The sensible heat correction, which is itself a small correction for the Nusselt type of solution for film boiling or condensation, can thus be represented within two percent by equations (5) and (6). The accurate Nusselt number prediction in each case is thus completely represented within a very small fraction of a percent by

Condensation: $\text{Nu}_x/A_c^{1/4}$

$$= [1 + (0.683 - 0.228/\text{Pr})\text{Ja}]^{1/4} \tag{7}$$

Film boiling: $\text{Nu}_x/(A_b/4)^{1/4}$

$$= [1 + (0.968 - 0.163/\text{Pr})\text{Ja}]^{1/4} \tag{8}$$

We note that for the film boiling case (which is restricted to vapor Pr values that must lie in the range $2/3 \leq \text{Pr} \leq 1$) C is restricted to the narrow range $0.723 \leq C \leq 0.805$.

Equations (5) and (6) might show minor inaccuracy in either of two sets of circumstances. One is in a non-flat-plate geometry. However, since the plate geometry does not affect the film boundary conditions we expect it to have minimal effect on equations (5) and (6). The other circumstance is that for which significant drag is exerted on the liquid-vapor interface. We have noted that equation (6) is based on film boiling calculations whose accuracy deteriorates when $(\rho\mu)_g/(\rho\mu)_f$ is no longer small – at very high pressures, for example. In the case of condensation, both Chen (1961) and Koh et al. (1961) showed that the influence of vapor drag was negligible for Pr greater than the order of 10 and all Ja in ranges of practical interest. For Pr on the order of unity, both investigations showed that the influence of drag became noticeable for values of Ja much greater than 0.01.

A third circumstance – the superposition of forced flow outside the liquid-vapor interface – would doubtless have a serious influence on either result. In this case the boundary condition would be a specified value of u at the liquid-vapor interface – not $u = 0$ or $(\partial u/\partial y) = 0$. Equations (5) and (6) would certainly be altered in this case, and we recommend that they not be used for forced flows.

It is worth noting that all of these solutions deteriorate rapidly when the liquid-vapor interface becomes wavy or rippled.

Conclusion

1 For film condensation, equation (7) completely and accurately represents the Sparrow and Gregg exact solution in all ranges of practical interest.

2 For film boiling, equation (8) completely and accurately represents the Koh solution for negligible values of $(\rho\mu)_g/(\rho\mu)_f$, in all ranges of practical interest.

References

Bromley, L. A., 1950, "Heat Transfer in Stable Film Boiling," *Chem. Engr. Prog.*, Vol. 46, No. 5, pp. 221-227.

Bromley, L. A., 1952, "Effect of Heat Capacity of Condensate," *Ind. and Engr. Chem.*, Vol. 44, No. 12, pp. 2966-2969.

Chen, M. M., 1961, "An Analytical Study of Laminar Film Condensation: Part I – Flat Plates," ASME JOURNAL OF HEAT TRANSFER, Vol. 83, No. 1, pp. 48-54.

Koh, J. C. Y., 1962, "Analysis of Film Boiling on Vertical Surfaces," ASME JOURNAL OF HEAT TRANSFER, Vol. 84, No. 1, pp. 55-62.

Koh, J. C. Y., Sparrow, E. M., and Hartnett, J. P., 1961, "The Two-Phase Boundary Layer in Laminar Film Condensation," *International Journal of Heat and Mass Transfer*, Vol. 2, pp. 69-82.

Nusselt, W., 1916, "Die Oberflächenkondensation des Wasserdampfes," *Z. Deutsch. Ing.*, Vol. 60, pp. 541-546; 569-575.

Rohsenow, W. M., 1956, "Heat Transfer and Temperature Distribution in Laminar-Film Condensation," *Trans. ASME*, Vol. 78, pp. 1645-1648.

Sparrow, E. M., and Gregg, J. L., 1959, "A Boundary-Layer Treatment of Laminar-Film Condensation," ASME JOURNAL OF HEAT TRANSFER, Vol. 81, No. 1, pp. 13-18.